Lecture Notes in Electrical Engineering 305

Jiadong Sun
Wenhai Jiao
Haitao Wu
Mingquan Lu
Editors

China Satellite Navigation Conference (CSNC) 2014 Proceedings: Volume III

Springer

Lecture Notes in Electrical Engineering

Volume 305

For further volumes:
http://www.springer.com/series/7818

About this Series

"Lecture Notes in Electrical Engineering (LNEE)" is a book series which reports the latest research and developments in Electrical Engineering, namely:

- Communication, Networks, and Information Theory
- Computer Engineering
- Signal, Image, Speech and Information Processing
- Circuits and Systems
- Bioengineering

LNEE publishes authored monographs and contributed volumes which present cutting edge research information as well as new perspectives on classical fields, while maintaining Springer's high standards of academic excellence. Also considered for publication are lecture materials, proceedings, and other related materials of exceptionally high quality and interest. The subject matter should be original and timely, reporting the latest research and developments in all areas of electrical engineering.

The audience for the books in LNEE consists of advanced level students, researchers, and industry professionals working at the forefront of their fields. Much like Springer's other Lecture Notes series, LNEE will be distributed through Springer's print and electronic publishing channels.

Jiadong Sun · Wenhai Jiao
Haitao Wu · Mingquan Lu
Editors

China Satellite Navigation Conference (CSNC) 2014 Proceedings: Volume III

Springer

Editors
Jiadong Sun
China Aerospace Science
and Technology Corporation
Chinese Academy of Sciences
Beijing
China

Wenhai Jiao
China Satellite Navigation Office
Beijing
China

Haitao Wu
Navigation Headquarters
Chinese Academy of Sciences
Beijing
China

Mingquan Lu
Department of Electronic Engineering
Tsinghua University
Beijing
China

ISSN 1876-1100 ISSN 1876-1119 (electronic)
ISBN 978-3-642-54739-3 ISBN 978-3-642-54740-9 (eBook)
DOI 10.1007/978-3-642-54740-9
Springer Heidelberg New York Dordrecht London

Library of Congress Control Number: 2014937269

Printed on acid-free paper

Springer is part of Springer Science+Business Media (www.springer.com)

Preface

China's BDS Navigation Satellite System (BDS) has been independently developed, which is similar in principle to global positioning system (GPS) and compatible with other global satellite navigation systems (GNSS). The BDS will provide highly reliable and precise positioning, navigation and timing (PNT) services as well as short-message communication for all users under all-weather, all-time, and worldwide conditions.

China Satellite Navigation Conference (CSNC) is an open platform for academic exchanges in the field of satellite navigation. It aims to encourage technological innovation, accelerate GNSS engineering, and boost the development of the satellite navigation industry in China and in the world.

The 5th China Satellite Navigation Conference (CSNC 2014) is held on May 21–23, 2014, Nanjing, China. The theme of CSNC 2014 is BDS Application—Innovation, Integration and Sharing, which covers a wide range of activities, including technical seminars, academic exchange, forum, exhibition, lectures, as well as ION panel. The main topics are as:

1. BDS/GNSS Navigation Applications
2. Satellite Navigation Signal System, Compatibility and Interoperability
3. Precise Orbit Determination and Positioning
4. Atomic Clock Technique and Time-Frequency System
5. Satellite Navigation Augmentation and Integrity Monitoring
6. BDS/GNSS Test and Assessment Technology
7. BDS/GNSS User Terminal Technology
8. Satellite Navigation Models and Methods
9. Integrated Navigation and New Methods

The proceedings have 171 papers in nine topics of the conference, which were selected through a strict peer-review process from 479 papers presented at CSNC 2014.

We thank the contribution of each author and extend our gratitude to 165 referees and 36 session chairmen who are listed as members of an editorial board. The assistance of CNSC 2014's organizing committees and the Springer editorial office is highly appreciated.

Jiadong Sun

Editorial Board

The 5th China Satellite Navigation Conference (CSNC 2014)

Scientific Committee

Chairman
Jiadong Sun, China Aerospace Science and Technology Corporation

Vice-Chairman
Rongjun Shen, China
Jisheng Li, China
Qisheng Sui, China
Zuhong Li, China Academy of Space Technology
Shusen Tan, Beijing Satellite Navigation Center, China

Executive Chairman
Jingnan Liu, Wuhan University
Yuanxi Yang, China National Administration of GNSS and Applications
Shiwei Fan, China

Committee Members (By Surnames Stroke Order)
Xiancheng Ding, China Electronics Technology Group Corporation
Qingjun Bu, China
Liheng Wang, China Aerospace Science and Technology Corporation
Yuzhu Wang, Shanghai Institute of Optics and Fine Mechanics, Chinese Academy of Sciences
Guoxiang Ai, National Astronomical Observatories, Chinese Academy of Sciences
Shuhua Ye, Shanghai Astronomical Observatories, Chinese Academy of Sciences
Zhaowen Zhuang, National University of Defense Technology
Qifeng Xu, PLA Information Engineering University
Houze Xu, Institute of Geodesy and Geophysics, Chinese Academy of Sciences
Guirong Min, China Academy of Space Technology
Xixiang Zhang, China Electronics Technology Group Corporation
Lvqian Zhang, China Aerospace Science and Technology Corporation

Junyong Chen, National Administration of Surveying, Mapping and Geoinformation
Benyao Fan, China Academy of Space Technology
Dongjin Luo, China
Guohong Xia, China Aerospace Science and Industry Corporation
Chong Cao, China Research Institute of Radio Wave Propagation (CETC 22)
Faren Qi, China Academy of Space Technology
Sili Liang, China Aerospace Science and Technology Corporation
Shancheng Tu, China Academy of Space Technology
Rongsheng Su, China
Zhipeng Tong, China Electronics Technology Group Corporation
Ziqing Wei, Xi'an Institute of Surveying and Mapping

Organizing Committee

Secretary General
Haitao Wu, Navigation Headquarters, Chinese Academy of Sciences

Vice-Secretary General
Wenhai Jiao, China Satellite Navigation Office
Tao Peng, Academy of Satellite Application, China Aerospace Science and Technology Corporation
Wenjun Zhao, Beijing Satellite Navigation Center
Tao Peng, Satellite Application Research Institute of China Aerospace Science and Technology Corporation
Chuang Shi, Wuhan University
Weina Hao, Navigation Headquarters, Chinese Academy of Sciences

Committee Members (By Surnames Stroke Order)
Qun Ding, Xi'an Institute of Navigation Technology
Miao Yu, Beijing Institute of Space Science and Technology Information
Yinhu Ma, Navigation Satellite Systems Engineering Center, China Academy of Aerospace Electronics Technology
Ying Liu, China Satellite Navigation System Administration Office
Hao Zhang, International Cooperation of China Satellite Navigation System Administration Office
Wangming Yang, Nan Jing High Technology Industrial Development Zone Management Committee
Mingquan Lu, Tsinghua University
Xiuwan Chen, Peking University

Shuanggen Jin, Shanghai Astronomical Observatories, Chinese Academy of Sciences
Xiang'an Zhao, China Defense Science and Technology Information Center
Jing Zhao, Ministry of Science and Technology National Remote Sensing Center
Yuehu Hu, China Aerospace Science and Technology Corporation 20th Institute
Zhong Dou, National Time Service Center of Chinese Academy of Sciences

Contents

Part I
Precise Orbit Determination and Positioning

Chapter 1
Precise Orbit Determination for BeiDou Satellites During Eclipse Seasons

Jun Zhu, Jianrong Chen, Guang Zeng, Jie Li and Jiasong Wang

Abstract During the eclipse seasons, BeiDou IGSO/MEO satellites perform attitude maneuvers from yaw-steering to yaw-fixed, while the nominal yaw-angle is fixed to zero. Unfortunately, different levels of the orbit accuracy degradations in the Precise Orbit Determination (POD) process occur in this period. In this paper, a reduce-dynamic orbital model with additional pseudo-stochastic parameters is introduced to improve the orbit quality. The geometrical corrections in observations and the force variations related to attitude are modeled and investigated. The pseudo-stochastic orbit modeling techniques are applied for absorbing effects of the mis-modeled part of the attitude maneuvers. The POD results indicate a significantly improved performance of orbit with appropriate pseudo-stochastic parameters for BeiDou satellites during eclipse seasons.

Keywords Precise orbit determination (POD) · BeiDou navigation satellite system (BDS) · Solar radiation pressure (SRP) · Eclipse seasons

1.1 Introduction

During the period when the Sun is approximately located in the satellite's orbital plane, partial or total eclipses occur when the satellite will pass the night side of the Earth. As the Sun sensors of the attitude control system cannot keep track of

Foundation item: National Natural Science Foundation of China (41274018), GFZX0301040308-01.

J. Zhu (✉)
State Key Laboratory of Astronautic Dynamics, Xian 710043, China
e-mail: zhujun9306@126.com

J. Chen · G. Zeng · J. Li · J. Wang
Xi'an Satellite Control Center, Xian 710043, China

J. Sun et al. (eds.), *China Satellite Navigation Conference (CSNC) 2014 Proceedings: Volume III*, Lecture Notes in Electrical Engineering 305,
DOI: 10.1007/978-3-642-54740-9_1,

the Sun during this period, the Global Navigation Satellite System (GNSS) satellites cannot maintain the normal yaw attitude any more, but the different attitude maneuvers are performed for different GNSS satellites. During eclipse seasons the GPS-II/IIA satellites perform shadow-crossing maneuvers at the maximum rotation rate of the reaction wheels, and follow by a post-shadow recovery maneuver [1–4]. And the regime of the eclipsing GPS-IIR satellites contains only the noon and midnight turn maneuvers [5]. While the eclipsing GPS-IIF satellites follow a completely different yaw attitude scheme, midnight-turn yaw rate is kept constant to the value (about 0.06°/s) to get the satellites close to its nominal attitude when leaving the Earth's shadow [6]. GLONASS-M satellites take the similar shadow-crossing regime as the GPS-II/IIA satellites [7]. QZSS satellites perform an attitude maneuvers regime from yaw-steering to orbit-normal orientation in eclipse seasons, which is detailed in reference [8].

In the Precise Orbit Determination (POD) process, the attitude should be taken into account carefully, otherwise two problems appear: (1) the observations residuals increase due to the mis-modeled geometry position of the satellite's navigation antenna, and (2) the orbit integration errors increase due to the mis-modeled non-conservative forces, such as the Solar Radiation Pressure (SRP) and possibly albedo, suffering from the wrong orientation of the satellite's surfaces. According to the research in references [3–8], it is hardly to model the effect of the attitude maneuvers in POD process with sufficient accuracy, so there is usually a phenomenon of the orbit accuracy degrading in eclipse season.

During the eclipse seasons, BeiDou IGSO/MEO satellites perform attitude maneuvers from yaw-steering to yaw-fixed, which means the nominal yaw-angle is fixed to zero after the β angle is less than its allowed limitation [9, 10]. This attitude maneuver regime is similar as the QZSS satellites. Like other GNSS satellites, the POD accuracy of BeiDou satellites also degrades during these periods, but much worse due to the shortcoming of the regional tracking network or some other unknown reasons [10]. To improve the orbit quality of BeiDou IGSO satellites during eclipse seasons, the optimized POD strategies by estimating piece-wise orbit-normal and along-track (Y direction and B direction of DYB model [11]) parameters based on ECOM SRP model [12] and adjustable box-wing SRP model [13] are discussed in reference [10]. In this study we introduce extra pseudo-stochastic empirical parameters into a classical reduced-dynamic BDS POD scheme for the eclipsing BeiDou IGSO satellites, namely pseudo-stochastic orbit modelling techniques, as an efficient method to derive more precise satellite trajectories in the eclipse seasons.

1.2 Force Changes for Eclipsing BeiDou IGSO Satellites

For the eclipsing BeiDou IGSO satellites, non-conservative forces such as SRP force and the Thermal Re-Radiation (TRR) force change evidently due to shadow-crossing and attitude maneuvering. Three aspects are investigated: (1) in each

revolution the shadow-crossing event should occur, which leads to the once-per-revolution variations of the SRP forces from 0 to 1.2×10^{-7} m/s^2. (2) The transition of satellite attitude modes could cause the change of exposure surfaces. In yaw-steering regime, the body's +X surface is always exposed to Sun radiation, meanwhile the +Z and −Z surfaces take turn to expose to Sun. While in yaw-fixed regime, besides the ±Z surfaces, ±X surfaces and ±Y surfaces would be exposed to Sun alternatively. (3) In yaw-fixed regime, the solar panel is not perpendicular to the satellite-to-Sun direction any more, but there is a small angle (equals to the Sun's elevation with respect to the orbital plane) between the satellite-to-Sun direction and the normal direction of solar panel.

1.2.1 Solar Radiation Pressure

To investigate the variations of the solar radiation pressure forces for the BeiDou IGSO satellites in eclipse seasons, we adopt the empirical ECOM SRP model for BDS POD strategies. Total of 9 empirical parameters of the ECOM model can be corrected completely by fitting the observed data in the POD process. The integrated effects of the SRP forces, the TRR forces, and other non-conservative perturbation force of the satellite suffered in all directions can be calculated by using the empirical formula combined with the corrected SRP parameters.

Figure 1.1 shows the corrected SRP parameters of ECOM without a priori model for IGSO-4 satellite during the eclipse seasons, which represents the SRP forces of the satellite suffered in the DYX directions. In this period IGSO-4 switch its attitude mode from yaw-steering to yaw-fixed in 104th day of 2012. In this figure, both the direct solar pressure D0 (in the "Satellite—Sun" direction) and X0 (in the direction perpendicular to D0 within the "satellite—Sun—geocenter" plane, XC and XS are the period components in this direction) appeared abnormal fluctuations when attitude maneuvering. Obviously, the SRP represented by ECOM model (a set of parameters of constants and sine/cosine terms) in an estimated arc would have a continuous smooth trend. In the case of the attitude maneuvering, the ECOM model cannot accurately reflect the actual changes, which results in the POD accuracy degradation.

1.2.2 Thermal Re-Radiation

In the yaw-steering regime, the −X panels of IGSO satellites' body are always in shadow, while in the yaw-fixed regime ±X Panel take turns to be exposed, which will cause the temperature of the −X panel change significantly, shown in Fig. 1.2.

The TRR of solar panels can be calculated by [14]

$$F_i = \frac{2\sigma \cdot \varepsilon_i(T_i) \cdot A_i \cdot T_i^4}{3c} \tag{1.1}$$

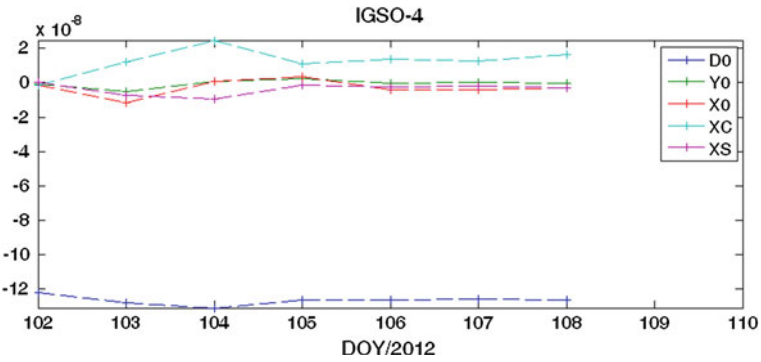

Fig. 1.1 SRP parameters of BeiDou satellites in eclipse seasons

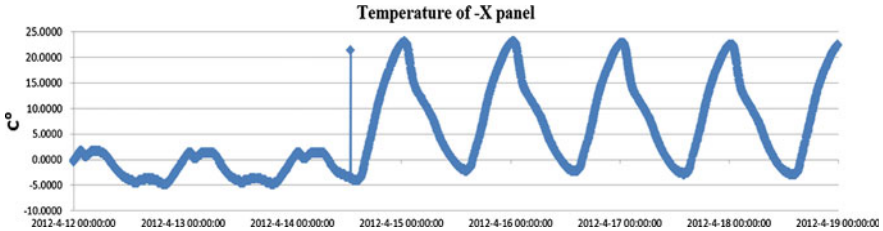

Fig. 1.2 X panel's temperature of BeiDou satellites in eclipse seasons

where c is the light speed, σ is the Boltzman constant, $\varepsilon_i(T_i)$ is the thermal re-radiation ratio, A_i is the area of the i-th panel, and T is temperature of the panel. For BeiDou IGSO/MEO satellites, it is virtually impossible to get the accurate emissivity ratio $\varepsilon_i(T_i)$ currently, and it is also unable to estimate the TRR effects of the multilayer and radiator exactly, so we can only get a rough estimation of the thermal radiation acceleration of $-$X panels at the level of 10^{-10} m/s^2.

1.3 Attitude-Related Geometric Correction

1.3.1 Antenna Phase Center

The average position of the Antenna Phase Center (APC) in body coordinates is defined as the antenna Phase Center Offset [15] (with respect to the antenna reference point, abbreviation for PCO). The instantaneous position of the APC also varies with the changes of the signal direction, which is defined as the Phase Center Variation (with respect to the mean antenna phase center, abbreviation for PCV). The ranging correction $\Delta\phi(\alpha, \eta)$ caused by PCO of satellite antenna is given by

$$\Delta\phi(\alpha, \eta) = \boldsymbol{r} \cdot \boldsymbol{e} = x_0 \sin\alpha \sin\eta + y_0 \cos\alpha \sin\eta + z_0 \cos\eta \tag{1.2}$$

where $\boldsymbol{e}$ is the unit vector of satellite-station in body-fixed coordinate system, α and η are azimuth and nadir. As the pre-launched PCOs of BeiDou satellites' navigation antennas have been published, we could calculate the ranging correction at given time by utilizing the actual attitudes. Usually the nominal attitudes are adopted in POD process, thus the deviations between the nominal values and the actual values will contribute to the ranging corrections. Given $\Delta\psi(t)$ as the error of yaw angle at time t, that is the rotation angle between the nominal body-fixed coordinate system and the actual body-fixed coordinate system around the Z-axis,then the relationship between the actual PCO (x_0, y_0, z_0) and the nominal value PCO $(\tilde{x}_0, \tilde{y}_0, \tilde{z}_0)$ existents as

$$(\tilde{x}_0, \tilde{y}_0, \tilde{z}_0)^{\mathrm{T}} = \boldsymbol{M}_{\mathrm{Z}}(\Delta\psi)(\, x_0 \quad y_0 \quad z_0\,)^{\mathrm{T}} \tag{1.3}$$

1.3.2 Phase Windup

Similar to GPS, another attitude-related geometric part of the ranging correction for BeiDou phase observation is the phase polarization effect, named as phase windup [16], which is caused by the rotation of the antennas of transmitter and the receiver around its polarization axis. As a major source of error for BeiDou carrier phase observation, the magnitude of phase windup could achieve several decimeters. A general formula for correcting phase windup is

$$\Delta\phi = \mathrm{sign}(\zeta)\arccos\left(\frac{\boldsymbol{D}_{\mathrm{T}} \times \boldsymbol{D}_{\mathrm{R}}}{|\boldsymbol{D}_{\mathrm{T}}| \cdot |\boldsymbol{D}_{\mathrm{R}}|}\right) \tag{1.4}$$

where

$$\begin{aligned}
\zeta &= \boldsymbol{T}_{\mathrm{R}} \cdot (\boldsymbol{D}_{\mathrm{T}} \times \boldsymbol{D}_{\mathrm{R}}),\\
\boldsymbol{D}_{\mathrm{T}} &= \boldsymbol{X}_{\mathrm{T}} - \boldsymbol{T}_{\mathrm{R}} \cdot (\boldsymbol{T}_{\mathrm{R}} \cdot \boldsymbol{X}_{\mathrm{T}}) - \boldsymbol{T}_{\mathrm{R}} \times \boldsymbol{Y}_{\mathrm{T}},\\
\boldsymbol{D}_{\mathrm{R}} &= \boldsymbol{X}_{\mathrm{R}} - \boldsymbol{T}_{\mathrm{R}} \cdot (\boldsymbol{T}_{\mathrm{R}} \cdot \boldsymbol{X}_{\mathrm{R}}) + \boldsymbol{T}_{\mathrm{R}} \times \boldsymbol{Y}_{\mathrm{R}},
\end{aligned}$$

$\boldsymbol{T}_{\mathrm{R}}$ is the phase propagation vector pointing from the satellite to the receiver, $\boldsymbol{D}_{\mathrm{T}}$ and $\boldsymbol{D}_{\mathrm{R}}$ are the effective dipole vectors of the receiver and the satellite antenna, $\boldsymbol{X}_{\mathrm{T}}$ and $\boldsymbol{Y}_{\mathrm{T}}$ are the unit vectors of the satellite antenna, $\boldsymbol{X}_{\mathrm{R}}$ and $\boldsymbol{Y}_{\mathrm{R}}$ are the unit vectors of the receiver antenna. For BeiDou satellites, $\boldsymbol{X}_{\mathrm{T}}$ and $\boldsymbol{Y}_{\mathrm{T}}$ are consistent with the unit vectors of the X-axis and Y-axis in the body-fixed coordinate system.

1.4 Pseudo-Stochastic Orbit Modeling

In the POD process for GNSS, the effects of the perturbations (SRP, TRR, and possibly albedo) acting on the satellite orbits should be modeled with sufficient accuracy to match the high-precision carrier phase observations (with accuracy of

1–3 mm). For BDS, there not yet an appropriate SRP model with sufficient accuracy. Although BeiDou IGSO/MEO satellites' manufacturer provides the geometric and physical properties of the satellite body and solar panel, but the analytical models based on these pre-launched parameters are not sufficiently accurate. Making use of these pre-launched parameters, we have also established a box-wing SRP model, and used it as a priori model in the POD process while estimating a set of ECOM parameters.

Figure 1.3 shows the variations of the five ECOM parameters with a priori Box-Wing model for the eclipsing IGSO-4 satellite. Contrast to Fig. 1.1, there is the consistent trend for SRP parameters in each corresponding direction after the attitude maneuvering. In addition, the direct SRP signed as D0 reaches 4×10^{-8} m/s^2, indicating large model errors of the used Box-wing model, and needs for further correction.

Either the empirical or the semi-empirical SRP model, are essentially realization of the reduced-dynamic POD. The general empirical formula (e.g. ECOM) is well suited for unknown forces with constant or once-per-revolution characteristics, but is not suited when trying to absorb effects due to momentum dumps or a slightly wrong attitude. On the other hand, the satellite orbiting the Earth is not a deterministic smooth motion, but often affected by many perturbations, such as shadow-crossing, attitude maneuverings, and solar storms, etc. Therefore, it is necessary to introduce many empirical parameters into POD process to absorb effects of unknown forces.

Pseudo-stochastic orbit modeling [17] may be considered as a realization of the well-known reduced-dynamic technique, which makes use of both the geometric strength of the GNSS observations and constraint of a deterministic equation of the orbital motion. Different from the stochastic orbit modeling based on a stochastic differential equation, this technique introduces additional parameters referred to as pseudo-stochastic into a classical least-squares (LS) orbit determination scheme, and they are characterized both by a priori known statistical properties like an expectation value and an a priori weight $\boldsymbol{W}$ given by an a priori variance σ_0. In this way, the traditional LS orbit determination problem is translated into a Bayesian estimation.

The use of pseudo-stochastic parameters proved to be a very powerful tool to improve the orbit quality. The widely-used instantaneous velocity pulses are suitable for absorb effects of an insufficiently known force field or events like thruster firings, or any other model deficiency. This technique were proposed by Beutler et al. in 1994, and were initially set up at CODE only for eclipsing satellites and for problem satellites in 1995. Making use of the pseudo-stochastic pulses, we can set up $n-1$ pulses $\Delta \boldsymbol{v}_i$ at the pre-determined epochs t_i in the complete time interval $I = [t_0, t_n]$. Then the corresponding variational equation is

$$\ddot{z}_{\Delta \boldsymbol{v}_i} = \boldsymbol{A}_0 \cdot \boldsymbol{z}_{\Delta \boldsymbol{v}_i} + \delta(t - t_i) \cdot \boldsymbol{e}(t) \tag{1.5}$$

where $\delta(t)$ denotes Dirac's delta distribution, $\boldsymbol{e}(t)$ denotes the predetermined direction (e.g. in radial, along-track and cross-track directions) of the pulses.

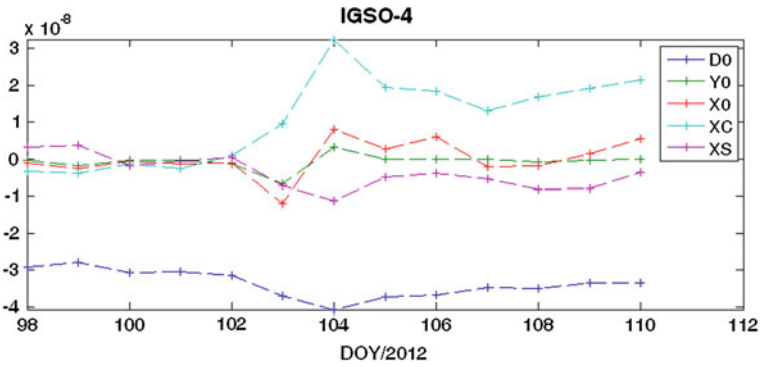

Fig. 1.3 SRP parameters with a priori box-wing model of BeiDou satellites in eclipse seasons

Obviously, the velocity $\dot{\boldsymbol{r}}$ of the improved orbit is discontinuous at the epochs t_i. Considering zero initial values, the partial derivatives w.r.t. the pseudo-stochastic pulses read as

$$\boldsymbol{z}_{ij} = \begin{cases} 0 & t < t_i \\ \sum_{k=1}^{6} \beta_{ij,k} \cdot \boldsymbol{z}_k(t) & t \geq t_i \end{cases} \quad j = 1, 2, 3 \tag{1.6}$$

From the condition equations

$$\boldsymbol{z}_{ij}(t_i) = \boldsymbol{0}; \quad \dot{\boldsymbol{z}}_{ij}(t_i) = \boldsymbol{e}_{ij} \tag{1.7}$$

the coefficients $\beta_{ij,k}$ can therefore be written as

$$\beta_{ij,k} = \frac{\partial E_k}{\partial \Delta v_{ij}} \tag{1.8}$$

The POD observed equation of the geocentric position vectors $\boldsymbol{r}_0$ at the observation times t_i corresponding to the pseudo-stochastic pulses may be brought into the form

$$\sum_{k=1}^{6} \frac{\partial o(\boldsymbol{r}_0(t_l))}{\partial E_k} \cdot \Delta E_k + \sum_{m=1}^{i} \sum_{j=1}^{3} \frac{\partial o(\boldsymbol{r}_0(t_l))}{\partial \Delta v_{mj}} \cdot \Delta v_{mj} - \Delta o_l = \varepsilon_l \tag{1.9}$$

where E_k is a set of six osculating elements, Δo_l is referred to as "observed minus computed".

Using Eq. (1.6), the partial derivatives associated with the pseudo-stochastic pulses may be written:

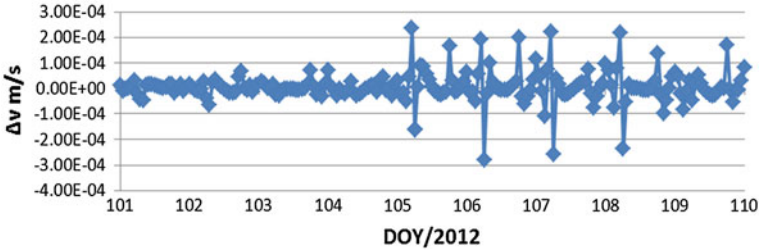

Fig. 1.4 Pseudo-stochastic velocity pulses of BeiDou IGSO satellites in eclipse seasons

$$\begin{aligned}\frac{\partial o(\boldsymbol{r}_0(t_l))}{\partial \Delta v_{mj}} &= \nabla(o(\boldsymbol{r}_0(t_l)))^{\mathrm{T}} \cdot \boldsymbol{z}_{mj}(t_l) \\ &= \nabla(o(\boldsymbol{r}_0(t_l)))^{\mathrm{T}} \cdot \sum_{k=1}^{6} \beta_{mj,k} \cdot \boldsymbol{z}_k(t_l)\end{aligned} \tag{1.10}$$

The additional parameters referred to as pseudo-stochastic introduced to the deterministic equation of motion are constrained by some priori information. In a LS orbit determination environment, additional knowledge is introduced in the form of artificial observations. The priori information is characterized hopefully on the knowledge of the deficiencies of the force field. While usually the initial value of zeros are expected for these parameters. The artificial observations referring to the epoch i read as

$$\Delta \boldsymbol{v}_i = 0 \tag{1.11}$$

The weight matrix $\boldsymbol{W}$ associated with these observations may be defined as the inverse of the variance-covariance matrix associated with these parameters [17]:

$$\boldsymbol{W} \doteq \sigma_0^2 \mathrm{cov}(\Delta \boldsymbol{v}_i)^{-1} \doteq \begin{pmatrix} \frac{\sigma_0^2}{\sigma_1^2} & 0 & 0 \\ 0 & \frac{\sigma_0^2}{\sigma_2^2} & 0 \\ 0 & 0 & \frac{\sigma_0^2}{\sigma_3^2} \end{pmatrix} \tag{1.12}$$

where σ_0 is the a priori RMS error of the (real) observation of unit weight and σ_k ($k = 1, 2, 3$) are the user-defined RMS errors associated with the three components of $\Delta \boldsymbol{v}_i$.

For comparison, Fig. 1.4 demonstrates changes of the estimated pseudo-stochastic velocity pulses in along-track direction for IGSO satellite in eclipse seasons, from which one can see the quite different trends and amplitude before and after the attitude mode switch, the first part of yaw-steering mode shows a steady trend at the level of 10–5 m/s, while after switching to yaw-fixed mode, the peak increases to 10–4 m/s. Further analysis showed that the peak appears at midday or midnight, which is probably due to the mutation of SRP in this short time period.

1.5 POD Results

This paper focuses on the eclipsing BDS I1 and I4 satellites in October 2013, the critical points are listed in Table 1.1. The orbit results discussed in this paper are based on data from parts of the BeiDou-capable stations of IGS M-GEX and a small network of four domestic stations. The classical double-difference processing strategy is adopted, and orbital arc length of 3 days is used, with two consecutive days orbit fit RMS as the orbit quality assessment.

The SRP model is crucial to POD results. The widely used classical ECOM model is built for GPS satellites. So within this paper, its adaptability for BDS IGSO/MEO satellites is investigated. The following subsets of the total 9 SRP parameters are considered for estimation in the POD process refer to [18]:

- 3 parameters: three constant terms in the three axes of DYX frame
- 5 parameters: three constant terms and one pair of sine/cosine terms in the X-direction of DYX frame
- 9 parameters: All of the constant term and period items.

Orbital internal consistencies of the 2-day orbit fit RMS for BeiDou IGSO and MEO satellites are listed in Tables 1.2 and 1.3 respectively. The orbit quality of the IGSO satellites with yaw-steering attitude mode is on the 20–30 cm level, and the 3D orbit fit RMS the MEO satellites is on the 10 cm level, except for the eclipsing I1 and I4 satellites with worse orbit quality of 44 and 21 cm 3D orbit fit RMS. Generally, five SRP parameters give the smallest RMS values for these 3-day solutions.

By using the pseudo-stochastic parameter to improve the orbit quality, its adaptability analysis needs to be carried out for BeiDou IGSO and MEO satellites. Different numbers of pseudo-stochastic velocity pulses are set up in along-track direction, and the results are lists in Tables 1.4 and 1.5.

The orbit fits listed in Tables 1.4 and 1.5 performing two different results for the IGSO and MEO satellites. For most IGSO satellite with yaw-steering attitudes, a 3-Day arc with a set of four pseudo-stochastic velocity pulses per day provides the best performance of 20–30 cm (except for I1), a further extension to twelve pseudo-stochastic velocity pulses result in no improvement, even a smaller degradation. However, the best results of all the MEO satellites are about 10 cm, which are derived from a strategy of only one pseudo-stochastic velocity pulses per day. When focused on the eclipsing satellites, the benefit of introducing pseudo-stochastic parameters is in particular pronounced for I1 and I4: the 2-Day orbit fits decrease to 44 and 21 cm accordingly, even close to the other normal IGSO satellites. We should take especial note of that, these POD tests for IGSO satellites are based on a regional tracking network, increasing too many pseudo-stochastic parameters may increase the instability of the solution.

The orbit qualities of 2-Day overlapping differences in three directions (radial, along-track, and cross-track) for eclipsing satellites I1 and I4 are shown in

Table 1.1 Day of Attitude mode transition for I1 and I4 in 2013

SVN	Day of yaw-steering to yaw-fixed mode	Day of yaw-fixed to yaw-steering mode
I1	284	292
I4	286	295

Table 1.2 2-Day orbit fit RMS values of BeiDou IGSO satellites in centimeters

SRP parameters	I1	I2	I3	I4	I5
3	69	35	35	48	33
5	44	26	31	21	19
9	60	84	69	68	66

Table 1.3 2-Day orbit fit RMS values of BeiDou MEO satellites in centimeters

SRP parameters	M1	M2	M3	M4
3	17	15	22	7
5	10	13	16	6
9	28	40	21	13

Table 1.4 2-Day orbit fit RMS values of BeiDou IGSO satellites in centimeters

Sto. per Day	I1	I2	I3	I4	I5
0	122	42	37	31	21
1	112	48	32	52	24
4	44	26	27	21	19
12	39	27	31	22	19

Table 1.5 2-Day orbit fit RMS values of BeiDou MEO satellites in centimeters

Sto. per Day	M1	M2	M3	M4
0	11	10	18	6
1	9	3	12	3
4	10	13	16	6
12	11	12	16	6

Figs. 1.5 and 1.6. In general, the addition of four pseudo-stochastic velocity pulses per day significantly improves the orbit quality of the eclipsing IGSO satellites: the radial accuracy is on the 20–40 cm level for yaw-fixed arcs, slightly below the accuracy for yaw-steering arcs. However, attitude mode transition seems to result in the worst RMS values for the arcs including the transition interval, and the deeper reason for this phenomenon remains to be further analyzed.

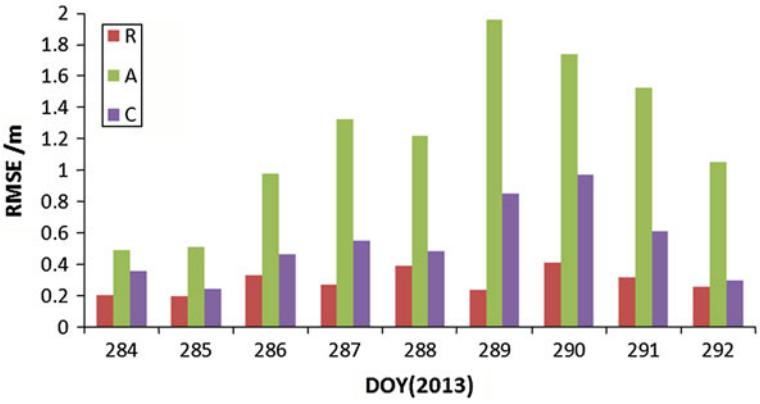

Fig. 1.5 Orbit overlapping difference of I1 in eclipse seasons

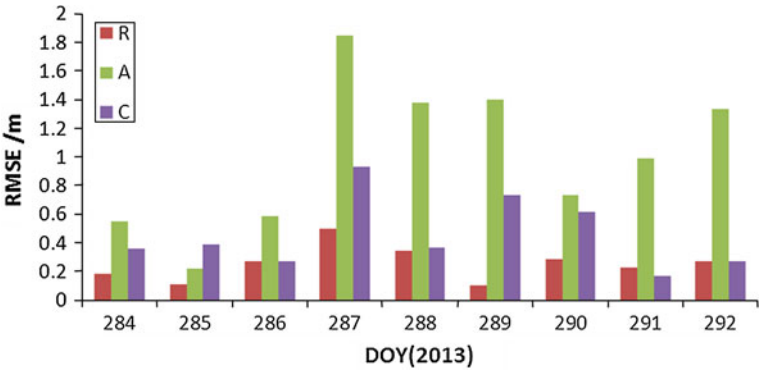

Fig. 1.6 Orbit overlapping difference of I4 in eclipse seasons

1.6 Summary and Conclusions

The POD problem for BeiDou IGSO and MEO satellite during the eclipse seasons were studied with the well-known pseudo-stochastic orbit modeling technique. The attitude-related geometric corrections and the force changes caused by attitude transition are focused on. The box-wing SRP model based on the pre-launch parameters seems to be not sufficiently accurate, and the estimated ECOM parameters perform irregularly after the attitude maneuver. Thus the pseudo-stochastic parameters are introduced to absorb the effects of insufficient SRP model and the attitude maneuvers. The POD tests were carried out with a tracking network of four domestic stations and some M-GEX stations. As a result, the ECOM model with five parameters represents the best adaptability for BeiDou IGSO and MEO satellites. More important, an appropriate set of the pseudo-stochastic orbit parameters can improve the orbit quality significantly: one pseudo-stochastic

velocity pulses per day gives the best radial accuracy of 10 cm for MEO satellites, four pseudo-stochastic velocity pulses per day gives the best performance for yaw-steering IGSO satellites with a radial accuracy of 20–30 cm. And for eclipsing IGSO satellites I1 and I4, the radial accuracy increases to 44 and 21 cm accordingly. Nevertheless, the attitude mode switch still results in somewhat lower accuracy for the Beidou satellites during eclipse seasons, so some deep reason still needs further analysis.

References

1. Bar-Sever YE (1996) A new model for GPS yaw attitude. J Geodesy 70:714–723
2. Kouba J (2009) A simplified yaw-attitude model for eclipsing GPS satellites. GPS Solutions 13:1–12
3. Rodriguez-Solano CJ, Hugentobler U, Steigenberger P et al (2013) Improving the orbits of GPS block IIA satellites during eclipse seasons. Adv Space Res 52:1511–1529
4. Weiss J, Bar-Sever Y, Bertiger W, Desai S, Haines B, Harvey N, Sibthorpe A (2012) Characterizing GPS block IIA shadow and post-shadow maneuvers. Geophysical Research Abstracts, 2012, 14, EGU2012-6850
5. Fliegel H, Gallini T (1996) Solar force modeling of block IIR global positioning system satellites. J Spacecraft Rockets 33(6):863–866
6. Dilssner F, Springer T, Enderle W (2011) GPS IIF yaw attitude control during eclipse season. AGU Fall Meeting, San Francisco, 9 Dec 2011
7. Dilssner F, Springer T, Gienger G, Dow J (2011) The GLONASS-M satellite yaw-attitude model. Adv Space Res 47:160–171. doi:10.1016/j.asr.2010.09.007
8. Hauschild A, Steigenberger P, Rodriguez-Solano C (2012) Signal, orbit and attitude analysis of Japan's first QZSS satellites Michibiki. GPS Solutions 16:127–133
9. Wang W, Chen G, Guo S et al (2013) A study on the BeiDou IGSO/MEO satellite orbit determination and prediction of the different yaw control mode. Proc Chin Navig Conf 3:31–40
10. Guo J, Zhao Q, Geng T et al (2013) Precise orbit determination for COMPASS IGSO satellites during yaw maneuvers. Proc Chin Navig Conf 3:41–53
11. Beutler G, Brockmann E, Gurtner W et al (1994) Extended orbit modeling technique at CODE processing center of the international GPS service for geodynamics (IGS): theory and initial results. Manuscr Geod 19:367–386
12. Springer TA, Beutler G, Rothacher M (1999) A new solar radiation pressure model for GPS satellites. GPS Solutions 2:50–62
13. Rodriguez-Solano CJ, Hugentobler U, Steigenberger P (2012) Adjustable box-wing model for solar radiation pressure impacting GPS satellites. Adv Space Res 49:1113–1128
14. Ziebart M, Adhya S, Sibthorpe A, Cross P (2003) GPS block IIR non-conservative force modelling: computation and implications. Proceedings of ION-GPS, pp 2671–2679
15. Schmid R, Steigenberger P, Gendt G et al (2007) Generation of a consistent absolute phase center correction model for GPS receiver and satellite antennas. J Geodesy 81:781–798
16. Wu JT, Wu C, Hajj GA, Bertiger WI et al (1993) Effects of antenna orientation on GPS carrier phase. Manuscr Geod 18:91–98
17. Jäggi A, Hugentobler U, Beutler G (2004) Efficient stochastic orbit modeling techniques using least squares estimators. In: Sansó F (ed) A window on the future of geodesy. Springer, Berlin, pp 175–180
18. Steigenberger P, Hugentobler U, Hauschild A et al (2013) Orbit and clock analysis of COMPASS GEO and IGSO satellites. J Geod 87:515–525. doi:10.1007/s00190-013-0625-4

Chapter 2
Research on the Combination of IGS Analysis-Center Solution for Station Coordinates and ERPs

Min Li and Tian-he Xu

Abstract This paper mainly focus on the issues of combining the station coordinates and ERPs based on the SINEX file, and discusses the constraints and normal equation's reconstruction in the SINEX file in details. The combination model and computational steps are given. A weighted-combination method based on the polynomial fitting residuals is proposed for the pole motion parameters. Computations and comparisons are performed using the proposed methods. The results show that the SINEX combination solution have the consistent accuracy with those provided by IGS. The accuracy of station coordinates in x and y direction is about 3, and 4 mm in direction z. The accuracy of pole motion parameters and their rate are 0.02 mas and 0.05 mas/d respectively. The accuracy of ERP solution based on the SINEX file is higher than that of the weighted-combination method.

Keywords Station coordinates · ERPs · SINEX · Transformation parameters · Polynomial fitting

M. Li (✉)
Chang'an University, Xi'an, Shanxi, China
e-mail: liminbmw760@163.com

T. Xu
State Key Laboratory of Geo-information Engineering, Xi'an, Shanxi, China

T. Xu
State Key Laboratory of Geodesy and Earth's Dynamics, Wuhan, Hubei, China

T. Xu
Xian Research Institute of Surveying and Mapping, Xi'an, Shanxi, China

T. Xu
State Key Laboratory of Astronautic and Dynamics, Xi'an, Shanxi, China

J. Sun et al. (eds.), *China Satellite Navigation Conference (CSNC) 2014 Proceedings: Volume III*, Lecture Notes in Electrical Engineering 305,
DOI: 10.1007/978-3-642-54740-9_2,

2.1 Introduction

Since 1999, IGS (International GNSS Services) have released many high-precision products including the global GNSS tracking station coordinates, velocity fields and the ERPs (Earth Rotation Parameters) etc. through a combination of at least seven AC (analysis-center) products [1]. IGS AC product combination is an important step for the IERS (International Earth Reference Services) to realize the ITRF (International Terrestrial Reference Frame) by fusing multi-source spatial geodetic data [1, 2]. For the IGS, the estimation of the station coordinates is the core task of realizing and maintaining the ITRF. Another important task is the determination of ERPs since they are necessary physical parameters in the conversion of Celestial coordinate system and Earth-Centered coordinate system, and they are also the basic data in satellite precise orbit determination, high accuracy positioning and navigation [3–5]. In order to facilitate and combine the AC products, IGS proposed the SINEX (Software INdependent EXchange) format file, from which the normal equation systems can be recovered. In this paper, we will focus on the issues of combination of the station coordinates and ERPs based on the SINEX file.

In this paper, we mainly focus on the theory and method of fusing the SINEX solutions. A weighted-combination method based on the polynomial fitting residuals is proposed for the pole motion parameters, computations and comparisons are performed using the proposed methods and some useful conclusions are obtained.

2.2 Strategy to Fuse the SINEX Solutions

During the combination, all the SINEX files from the ACs need to be preprocessed by rejecting the gross errors, eliminating the apriori constraints, apriori transformation of normal equations, unifying parameters apriori values, reconstructing normal equations and so on.

2.2.1 The Combination Model

The combination model is similar to that of ITRF, and here we don't consider the station velocity parameters. The model can be expressed as [6]:

$$X_s^i = X_c^i + X_k + D_k X_c^i + R_k X_c^i \tag{2.1}$$

where X_s^i is the solution for station i, X_c^i is the combined solution. T_k, D_k, R_k are the translation, scale and rotation parameters for the kth AC. For simplification, X_s^i is

replaced by X, seven transformation parameters is expressed as T_k, so the model written in the way of normal equations can be expressed as:

$$\begin{pmatrix} A1_s^T \\ A2_s^T \end{pmatrix} P_s \begin{pmatrix} A1_s & A2_s \end{pmatrix} \begin{pmatrix} X \\ T_k \end{pmatrix} = \begin{pmatrix} A1_s^T P_s B_s \\ A2_s^T P_s B_s \end{pmatrix} \tag{2.2}$$

where $A1_s$, $A2_s$ is the designed matrix defined by each station, which can be expressed as:

$$A1_s^i = \begin{pmatrix} I & 0 \\ 0 & I \end{pmatrix}, \quad A2_s^i = \begin{pmatrix} A_s^i & 0 \\ 0 & A_s^i \end{pmatrix} \tag{2.3}$$

where P_s is the weight matrix which is the inverse of each solution's variance-covariance matrix, B_s is the difference value of observation and calculation, A_s^i is the approximate coordinate values, i changes from 1 to n, n is the number of stations, the A_s^i is expressed as:

$$A_s^i = \begin{pmatrix} . & . & . & . & . & . & . \\ 1 & 0 & 0 & x_0^i & 0 & z_0^i & -y_0^i \\ 0 & 1 & 0 & y_0^i & -z_0^i & 0 & x_0^i \\ 0 & 0 & 1 & z_0^i & y_0^i & -x_0^i & 0 \\ . & . & . & . & . & . & . \end{pmatrix} \tag{2.4}$$

Equation (2.1) should be extended by adding the following equation if the ERP parameters are considered:

$$\begin{cases} x_s^p = x_c^p + R2_k \\ y_s^p = y_c^p + R1_K \\ \dot{x}_s^p = \dot{x}_c^p \\ \dot{y}_s^p = \dot{y}_c^p \\ LOD_s = LOD_c \\ UT_s = UT_c \end{cases} \tag{2.5}$$

Eq. (2.5) contains the pole motion vectors x_s^p and y_s^p and their transformation parameters $R1_k$ and $R2_k$, the pole motion velocity vectors $\dot{x}_s^p$ and $\dot{y}_s^p$, length of day LOD_s, universal time, UT_s. As the transformation parameters of LOD and UT vector is not obvious in the pure GPS intra-technique combination, so they are ignored.

2.2.2 The Combination Steps

2.2.2.1 Normal Equations Restoration

The process to restore the normal equations with the variance factor of unit weight $\hat{\sigma}_0^2$, estimation value $\hat{X}$, variance-covariance matrix $D_{\hat{X}}$, apriori value X^0, apriori variance-covariance D_{X^0} is described in detail in literature [5, 7]. Please notice that the normal equations restored here need to be revised during the next step, because when the parameters are pre-eliminated, the variance factor is no more accurate. It need to determinate the variance factor again through by iteration using Helmert variance component estimation [8]. The apriori standard deviation value in SOLUTION/ESTIMATE model is better to be used as apriori variance factor, otherwise the minus variance factor may occur during iteration.

2.2.2.2 Constraints Handling

One difficulty in the post-processing for GPS precise positioning and orbit determination with SINEX file is how to deal with the constraints well, the constraints added to each AC is not always appropriate and consistent, so it needs to be eliminated in advance.

We can identify the constraints though the first line in the SINEX file, it's shown with a mark: 0 stands for the fixed/tight constraint, 1 stands for the significant constraint, 2 stands for no constraint. Generally speaking, the constraints in the SINEX file can be classified into three parts [9]:

Case 0: the solutions are thought to be obtained by co-adjustment with the data unchanged during the process. Such kind of solutions is rare in the SINEX file now.

Case 1: the solutions are thought to be obtained by weighted parameters estimation, the apriori value and apriori variance-covariance matrix are given.

Case 2: the solutions need to be identified. Sometimes it's the loose constraints and a large variance such as 100 m is given. Sometimes it's the minimum constraints, seven or less than seven parameters and variance values are given in the apriori batch. Nowadays the latter is usually used in the IERS data combination and IGS weekly solution combination.

No fixed constraints are added to the station coordinates in all the SINEX files used in this paper, only the UT parameters are added with fixed constraints by several ACs. The process of eliminating the significant constraints is as follows:

$$N_f = D_{\hat{X}}^{-1} - D_{X^0}^{-1} \tag{2.6}$$

$$W_f = D_{\hat{X}}^{-1}\hat{X} - D_{X^0}^{-1}X^0 \tag{2.7}$$

Then we may get the unconstrained normal equations with N_f and W_f:

$$N_f X = W_f \tag{2.8}$$

As to the IGS SINEX files, the unconstrained matrix is almost singular after eliminating the significant constraints, because the matrix may be rank defect if it is related to the seven transformation parameters and their rates. Even if it's not rank defect, the normal equation maybe singular and the solution won't be stable. As to $N\hat{x} = b$, when it's singular, the module of N tends to be very small, the solution will change obviously if b changes a little. In this paper, we use the same procedures of ITRF to deal with the issues of rank defect and normal equation's singularity.

The combination work and realization of ITRF is mainly done by IGN in France. They add the minimum constraints before stacking the normal equations [5]. The principle of minimum constraints applied here is expressed as Similar Transformation constraints. It can be expressed by seven parameters transformation model as:

$$X_2 - X_1 = A\theta \tag{2.9}$$

where X_2, X_1 are station coordinates in two coordinate systems; θ is the transformation parameters expressed as in Eq. (2.1); A is the same as that of Eq. (2.4).

If we know several common points, θ can be solved by the principle of least-squares adjustment as:

$$\theta = \left(A^T P_x A\right)^{-1} A^T P_x (X_2 - X_1) \tag{2.10}$$

where P_x is the weight matrix of station coordinates, Let $B = (A^T P_x A)^{-1} A^T P_x$, we can get:

$$\theta = B(X_2 - X_1) \tag{2.11}$$

In order to eliminate the rank defection of Eq. (2.8), we introduce the condition equation expressed as:

$$B\left(\hat{X} - X_0\right) = 0, \left(\sum\nolimits_{\theta}\right) \tag{2.12}$$

The condition number equals to the number of rank defection, $\sum_\theta$ is the diagonal matrix, the value on the diagonal is the variance corresponding to the transformation parameters which is quite small. The corresponding normal equation of Eq. (2.12) is expressed as:

$$(B^T\Sigma_\theta^{-1}B)\hat{X} = (B^T\Sigma_\theta^{-1}B)X^0 \tag{2.13}$$

We may get the normal equation with minimum constraints if we combine Eq. (2.13) with Eq. (2.8):

$$\left(N_f + B^T\Sigma_\theta^{-1}B\right)\hat{X} = W_f + \left(B^T\Sigma_\theta^{-1}B\right)X_0 \tag{2.14}$$

From the equation above, we can find that the realization of Similar Transformation constraints is to transform the station coordinate of control net to the known coordinate system. As the added condition number equals to the number of rank defection and no extra constraints are introduced, so the benchmark information of the control net itself is not affected.

What need to be emphasized here is that the solutions to the normal equations with minimum constraints are still unstable, because the condition number is still very large and the normal equations are singular. So another organization in Germany called DGFI dealing with the realization of ITRF suggests to multiply a factor k^2 to the minimum constraints matrix, thus the condition number of the coefficient matrix in Eq. (2.14) is minimal. The minimum constraints is added after stacking the normal equations, thus the negative effect to the results caused by over parameterization is avoid.

The principle of Tykhonov-Phillips Regularization can also deal with the singular normal equations well, and the regularization parameters are solved by the Optimal Regularization method [5]. The results from this method are consistent but not the same as those of DGFI. As it's not studied in this paper, more details will not be shown here.

2.2.2.3 Normal Equation Systems Pre-processing

Apriori Helmert transformation to the normal equation systems without constraints is mainly to unify the reference benchmark and epoch, check the duplication of station names besides detecting and rejecting the gross error. The gross error can affect the following procedures a lot, for example the Helmert variance component estimation and the accuracy of the final combination and it should be detected by comparing the coordinates transformed by seven parameters with the ITRF solution at the same epoch.

2.2.2.4 Normal Equation Systems Reconstruction

Normal equation systems reconstruction means to classify, eliminate and merge the parameters, unify apriori value, stack the normal equations, introduce the transformation parameters and etc. The theory of parameter transformation is applied for all of them, which is the basic and core algorithm for estimating various parameters.

Suppose that two kinds of parameters as $\tilde{X}$ and $\hat{X}$, the transformation equation can be expressed as:

$$\hat{X} = C\tilde{X} + dx \tag{2.15}$$

where C is the coefficient matrix, dx is usually the constant matrix. Then the normal equation:

$$N\hat{X} = W \tag{2.16}$$

It can be rewritten as follows:

$$C^T NC\tilde{X} = C^T(W - Ndx) \tag{2.17}$$

Let, $\tilde{W} = C^T(W - Ndx)$ $\tilde{N} = C^T NC$ and $\tilde{W} = C^T(W - Ndx)$, we can get the following normal equation as:

$$\tilde{N}\tilde{X} = \tilde{W} \tag{2.18}$$

Equation (2.18) can be applied in a lot of aspects, such as apriori value unification and parameter pre-elimination. Apriori values of the unknown parameters in normal equations need to be unified before stacking, otherwise the normal equation should be transformed. For example, the parameter UT in ERPs supplied by GFZ is TAI-UT1 [10], while in most ACs it's the UT1 corrected with pole motion value, so they need to be unified. Parameter pre-elimination. Only the station coordinates and ERPs are considered in Eq. (2.1), so the parameters like apparent geocenter and satellite antenna phase bias are pre-eliminated.

It's not easy to solve the nine transformation parameters (seven for station coordinates and two for pole motion). The number of stations needs to be suitable for both the demand of benchmark and the robustness of normal equations. The rotation parameters for ERPs have better be solved every week.

2.2.2.5 Determination of Relative Weight Factor

The relative weight factor is determined for station coordinates and ERPs computation. Suppose the number of AC is N_i, P_k is the post-processing weight for

solution k, σ_0^2 is the post-processing variance factor and then the average post-processing variance for AC i can be expressed as:

$$\sigma_i^2 = \sum_{k=1}^{N_i} \sigma_0^2 p_k^{-1} / N_i \tag{2.19}$$

Then the relative weight factor for each AC is [11] :

$$w_i = \frac{1/\sigma_i^2}{\sum_{i=1}^{I} 1/\sigma_i^2 / I} \tag{2.20}$$

2.3 Strategy to a Weighted-Combination Method Based on the Polynomial Fitting Residuals

The weighted-combination method developed in this paper mainly aims at the combination of the pole motion parameters x^p, y^p. As the main period of pole motion is Chandler wobble and yearly wobble, the data for one year from all the ACs is used for fitting, the weight for each AC is determined by residuals, then we may carry out the combination. The fitting model is as follows [12]:

$$f(t) = a + bt + A_c \sin(2f_c t + \varphi_c)\pi + A_a \sin(2f_a t + \varphi_a)\pi \tag{2.21}$$

where a is constant terms for linear trend, b is the quotient term, A_c, A_a is the amplitude of Chandler wobble and yearly wobble, f_c, f_a is the corresponding frequency, φ_c, φ_a is the corresponding phase. For the convenient of computation, Suppose that $a_k = A_k \cos(\varphi_k)$, $b_k = A_k \sin(\varphi_k)$, then Eq. (2.21) can be written as:

$$f(t) = a + bt + \sum_{1}^{2} (a_k \sin(2\pi f_k t) + b_k \cos(2\pi f_k t)) \tag{2.22}$$

All the parameters in Eq. (2.22) can be solved by the principles of least-squares:

$$\hat{\beta} = \left(A^T A\right)^{-1} A^T l \tag{2.23}$$

where $\hat{\beta} = [\, a \quad b \quad a1 \quad b1 \quad a2 \quad b2 \,]^T$, A is the design matrix, l is the observation vector of pole motion data. The pole motion parameters can be fitted after solving Eq. (2.23) by least-squares without considering the observation accuracy of EOPs.

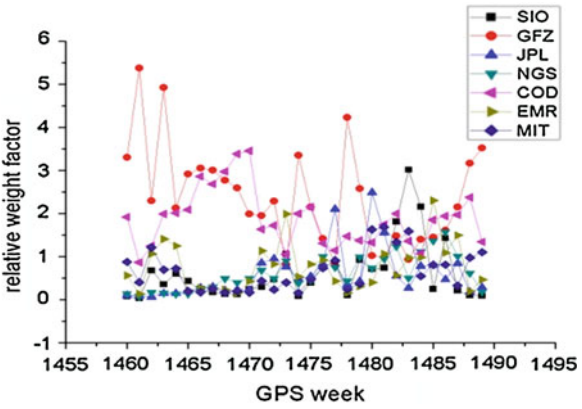

Fig. 2.1 Relative weight factors of 7 ACs

2.4 Calculation and Analysis

The SINEX files from 1460 to 1489 of GPS week in year 2008 are used with seven ACs, that is COD, EMR, GFZ, JPL, MIT, NGS and SIO. The relative weight factors determined by this paper are shown in Fig. 2.1. From it, we can find that GFZ and COD take a larger weight especially for the weeks before 1480. From weeks of 1480 to 1489, the parameters are added and new parameters are introduced in some ACs. For example, 120 and 170 parameters are added to the solutions of SIO and NGS separately. GFZ also introduces the satellite antenna phase bias, smaller differences of all the weight factors can be found in Fig. 2.1.

2.4.1 The Combination of Station Coordinates

The combination of station coordinates is based on ITRF05 reference frame with the file ITRF_IGS05.SNX. The reference epoch is the average epoch of all the weekly SINEX files. Three rotation parameters are not obvious while carrying out T-test to the transformation parameters, so they are rejected while computation. The standard deviation of the residuals between the combined solution and the each of the AC & ITRF in X, Y, Z direction are shown in Figs. 2.2, 2.3 and 2.4 respectively. The statistics information between the combined solution and that of ITRF is shown in Table 2.1.

From Figs. 2.2, 2.3 and 2.4, we can conclude that the standard deviation between the combined solution and those of ITRF in direction X and Y is from 2 to 4 mm, direction Z is from 2 to 4.5 mm. The standard deviation between the combined solution and that of each AC in direction X, Y and Z is almost below 7 mm and it is quite lower for that of COD and GFZ. Our solutions is almost equal to the IGS solutions shown in literature 1 whose standard deviation of each AC is under 3.5 mm in direction X, Y and 10 mm in direction Z.

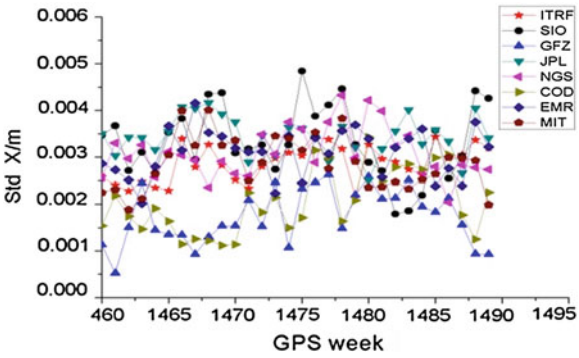

Fig. 2.2 Standard deviation in X direction between the combined solution and 7 ACs & ITRF

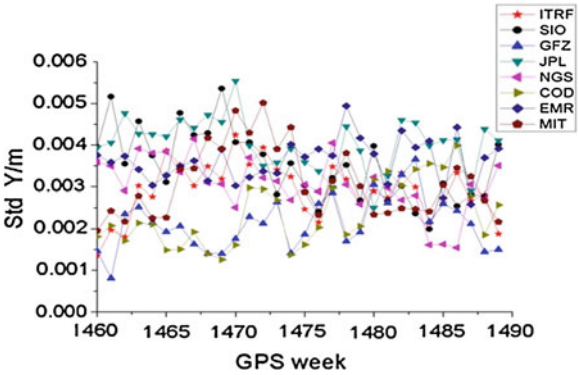

Fig. 2.3 Standard deviation in Y direction between the combined solution and 7 ACs & ITRF

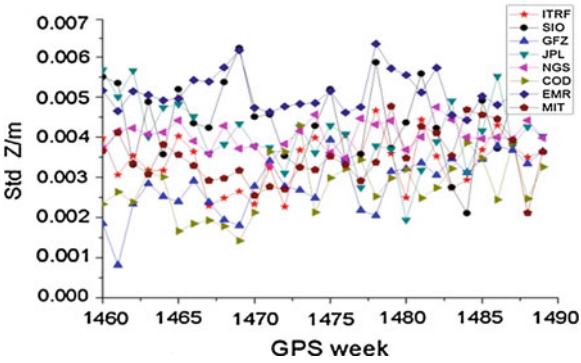

Fig. 2.4 Standard deviation in Z direction between the combined solution and 7 ACs & ITRF

According to Table 2.1, the maximum difference between the combined solutions and those of ITRF in all directions is less than 2 cm and the difference of standard deviation is between 3 and 4 mm. So, our results and IGS final results are at the same accuracy level.

Table 2.1 Statistics result of difference between the combined solution and ITRF in X, Y, Z direction

Difference	X	Y	Z
Maximum	0.0106	0.0093	0.0195
Minimum	−0.0087	−0.0091	−0.0201
Average	0.0007	0.0004	−0.0011
Standard deviation	0.0029	0.0028	0.0038

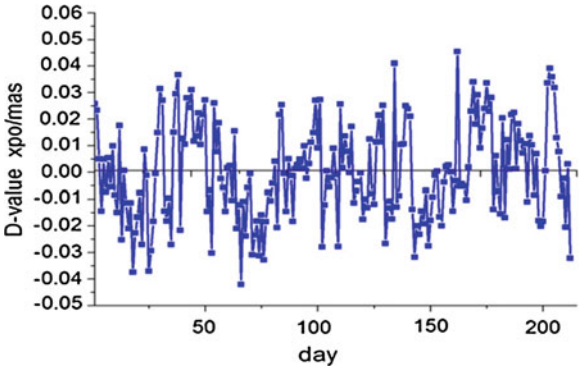

Fig. 2.5 Difference of xpo between the combined solutions and IGS

2.4.2 The Combination of ERPs

2.4.2.1 Combination of SINEX Solutions

The differences in ERPs between our solution and IGS solution are shown in Figs. 2.5, 2.6, 2.7, 2.8, 2.9 and 2.10, the statistical results are shown in Table 2.2.

From Figs. 2.5, 2.6, 2.7, 2.8, 2.9, 2.10 and Table 2.2, we can conclude that the maximum difference of pole motion vector between our combination results and IGS is less than 0.05 mas, the pole motion rate vector is less than 0.3 mas/d, the LOD is less than 0.015 ms and the UT is less than 0.07 ms. The maximum standard deviation of them is less than 0.02 mas, 0.06 mas/d, 0.002 and 0.013 ms separately. The accuracy of our results is comparative to those of literature [1].

2.4.2.2 The Weighted-Combination

The linear formula of Eqs. (2.22) and (2.23) are used to compute the standard deviation with the data of ERPs in 2008 of seven ACs, and then the weighted combination is performed. The results are shown in Figs. 2.11, 2.12 and Table 2.3.

From Figs. 2.11, 2.12 and Table 2.3, we can see that the standard deviation compared to the IGS solutions is about 0.05 mas while the corresponding RMS (Root-Mean-Square) of SINEX solutions is about 0.02 mas which obtained by only 30 weeks of data. So we can conclude that the accuracy of the combination

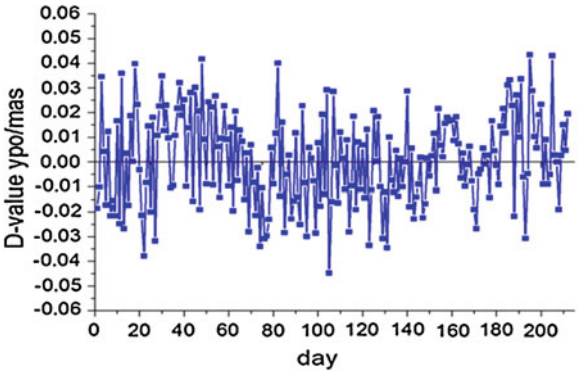

Fig. 2.6 Difference of ypo between the combined solutions and IGS

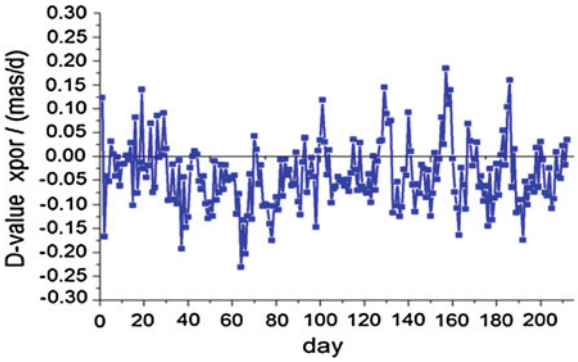

Fig. 2.7 Difference of xpor between the combined solutions and IGS

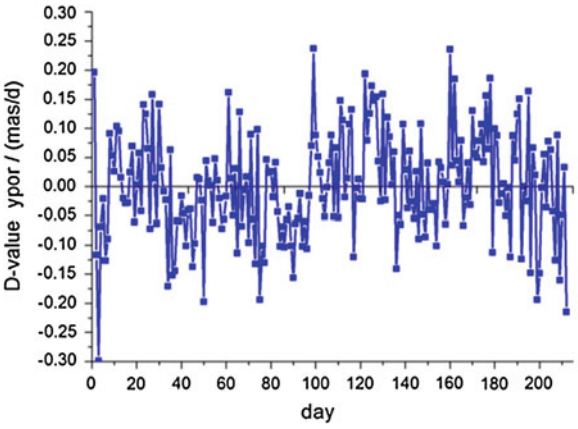

Fig. 2.8 Difference of ypor between the combined solutions and IGS

accuracy of SINEX is higher than that of the weighted-combination. However, the former needs to deal with a large amounts of computation relative to the normal equations, so the weighted-combination method is easier and more efficient which

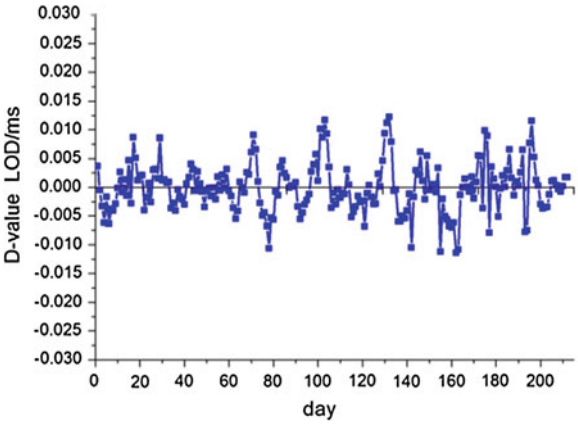

Fig. 2.9 Difference of LOD between the combined solutions and IGS

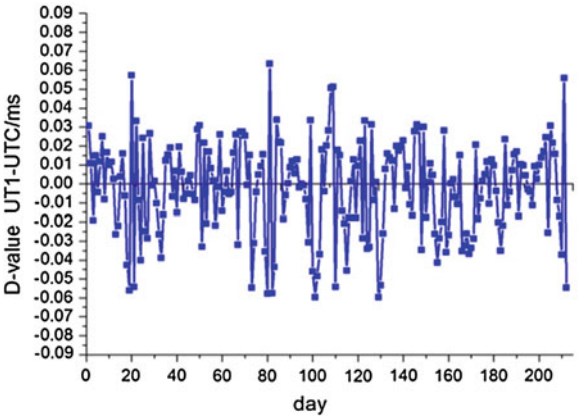

Fig. 2.10 Difference of UT between the combined solutions and IGS

Table 2.2 Statistics results of ERPs between the combined solutions and IGS

Difference	Xpo/mas	Ypo/mas	Xpor/mas/d	Ypor/mas/d	LOD/ms	UT/ms
Maximum	0.046	0.044	0.192	0.248	0.012	0.065
Minimum	−0.042	−0.047	−0.234	−0.300	−0.011	0.060
Average	−0.009	−0.004	−0.059	0.014	0.0013	0.005
Standard deviation	0.017	0.015	0.049	0.055	0.0021	0.013

can be used for fast combination of ERP. It should be noticed that the average difference of the weighted-combination is smaller than that of SINEX, which means that no obvious system error exists in the weighted-combination solutions.

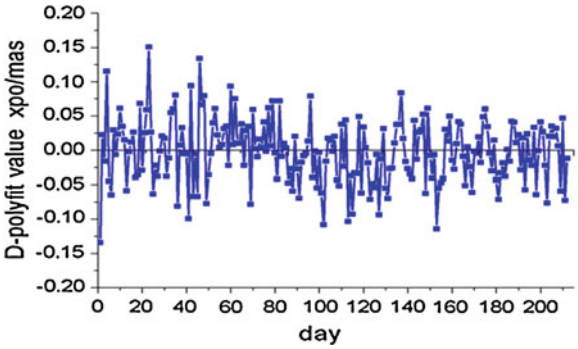

Fig. 2.11 Difference of xpo between the weighted-combination solutions and IGS

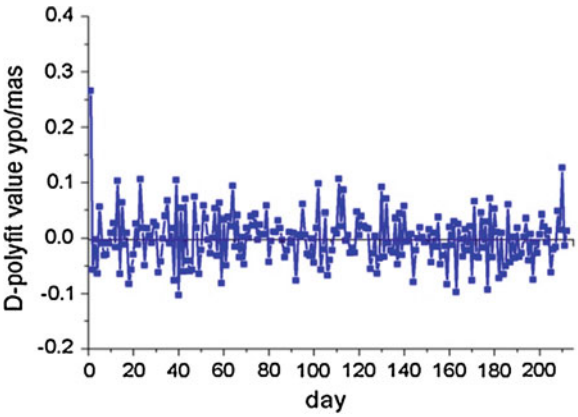

Fig. 2.12 Difference of ypo between the weighted-combination solutions and IGS

Table 2.3 Statistics results of pole parameters between the weighted-combination solutions and IGS

Difference	Xpo/mas	Ypo/mas
Maximum	0.151	0.266
Minimum	−0.134	−0.103
Average	−0.002	0.0007
Standard deviation	0.047	0.047

2.5 Conclusions

This paper mainly deals with the combination of station coordinates and ERPs based on weekly SINEX file provided by IGS. For the SINEX file of IGS, it's essential to deal with the constraints and properties of the normal equations well. The computation shows that the results from the combination of SINEX files have higher accuracy and are more reliable than those from the weighted-combination. The accuracy of former is consistent with IGS and higher efficiency for ERP combination solution can be obtained by by the latter. It can be concluded that a higher accuracy of ERP will be gotten if longer period of data is used.

Acknowledgments This work was supported by Natural Science Foundation of China (41174008) and the State Key Laboratory of Geodesy and Geodynamics Open Funded Projects (SKLGED2013-4-2-EZ) and the Open Foundation of State Key Laboratory of Astronautic and Dynamics (2014ADL-DW0101).

References

1. Ferland R, Piraszewski M (2009) The IGS-coordinates, Earth rotation parameters and apparent geocenter. Geodesy 83:385–392
2. Shi C, Zou R, Yao YB, Li M (2008) Systematic error analysis in data combination based on SINEX solution. J Wuhan Univ 33(6):608–611 (In Chinese)
3. Xu TH, Zhang LP (2013) Parameters determination based on daily GPS data of global IGS stations. J Geomatics Sci Eng 33(3):8–13 (In Chinese)
4. Li ZH, Huang JS (2005) GPS surveying and data processing. Wuhan University Press, Wuhan, pp 15–37
5. Yao YB (2004) Research on the algorithm and realization of post-processing for GPS precise positioning and orbit determination. Wuhan University, Wuhan (In Chinese)
6. Zou R (2009) The research of key technology on the realization and maintenance of TRF. Wuhan University, Wuhan (In Chinese)
7. Cui XZ, Yu ZZ, Tao BZ, Liu DJ (2001) General surveying adjustment. Wuhan University Press, Wuhan
8. Zhang XG (2009) Theory and algorithms of terrestrial reference frame. Information Engineering University, Zhengzhou (In Chinese)
9. Hugentobler URS, Schaer US, Fridez P (eds) (2009) Bernese GPS software, Version 5.0, Astronomical Institute, University of Berne, Switzerland
10. Heinkelmann R, Boehm J, Schuh H, Bolotin S, Engelhardt G (2007) Combination of long time-series of troposphere zenith delays observed by VLBI. Geodesy 81:483–501
11. Xu JY (2010) Research on the theory and method of predicting EOPs. Information Engineering University, Zhengzhou (In Chinese)
12. Thaller D (2008) Inter-technique combination based on homogeneous normal equation systems including station coordinates, Earth orientation and troposphere parameters, scientific technical report STR 08/15. GeoForschungsZentrum Potsdam

Chapter 3
Precise Orbit Determination for Haiyang 2A Satellite Using Un-differenced DORIS Code and Phase Measurements

Quan Zhou, Jing Guo and Qile Zhao

Abstract Currently, the third generation DORIS instrument named DGXX has been developed and equipped on Jason-2, Cryosat-2, Saral and Chinese Haiyang 2A satellite. Compared with the previous ones, the DGXX has seven measurement channels, and is able to provide synchronous dual frequency phase and code measurements. The orbits could be determinated based on the dual frequency phase and pseudo-range measurements directly, and the systematic errors could be analyzed. This contribution presents the algorithm for precise orbit determination with DORIS code and phase measurements. In addition, the orbit of HY2A are determinated from January to May 2012 using Position And Navigation Data Analyst software. The differences with respect to CNES POE orbits indicate that the accuracy in radial and 3D is 1.0 and 5.3 cm, respectively. Satellite laser ranging validation the accuracy of HY2A orbits is about 2.24 cm. Compared with the orbits computed with Doppler measurements, the accuracy of orbits computed with un-differenced phase observables in along-track and radial is a bit higher, the lower accuracy in cross-track maybe caused by inaccuracy receiver DORIS clock.

Keywords HY2A · DORIS · Pseudo-range and phase · Precise orbit determination

Q. Zhou (✉)
Test and Assessment Research Center, China Satellite Navigation office,
1 Fengyingdong Road, Beijing 10094, China
e-mail: zqatchina@163.com

J. Guo · Q. Zhao
GNSS Research Center, Wuhan University, 129 Luoyu Road, Wuhan 430079, China
e-mail: jingguo@whu.edu.cn

Q. Zhao
e-mail: zhaoql@whu.edu.cn

J. Sun et al. (eds.), *China Satellite Navigation Conference (CSNC) 2014 Proceedings: Volume III*, Lecture Notes in Electrical Engineering 305,
DOI: 10.1007/978-3-642-54740-9_3,

3.1 Introduction

Haiyang 2A (HY2A), launched on 16 August 2011 and developed by China Academy of Space Technology (CAST) and National Satellite Ocean Application Service (NSOAS), whose primary focus is scientific investigation of ocean topography, dynamics and environment [1, 2]. As we all know, satellite orbit is the foundation of altimeter data processing. Orbit error will directly affect the calculation of sea surface height, further effect the satellite altimetry products. For this reason, the precise orbit determination of HY2A is an important task of the satellite, and it is critical to determine their level of application. Three tracking systems for precise orbit determination (POD) are equipped to satisfy the required 10 cm threshold for POD, namely, Global Positioning System (GPS), Doppler Orbitography and Radiopositioning integrated by Satellite (DORIS) and Satellite Laser Ranging (SLR) [1, 2]. Particularly, the Doris instrument on HY2A is the first of a new generation, named DGXX. Compared with the previous two generations of DORIS-instrument, the new satellite receivers (DGXX) have now seven measurement channels, providing synchronous dual frequency phase and pseudo-range measurements other than Doppler measurements [3].

Though during the past few decades, a good amount of research have been made on the data processing theory and methods of DORIS system based on Doppler measurements [4–12]. However, with the envision and updating of the DORIS system [3, 13, 14], the research of numerical model and methods for new generation DORIS's pseudo-range and phase data processing is still limited: The oversea studies mainly carried by institute like on "Centre National d'Etudes Spatiales"(CNES) and "Institute Geo-graphique National"(IGN), etc., while this area in our country is still relative rarely studied, which reverse the DORIS phase date into Doppler data, without directly using pseudo-range and phase measurements, processed with existed data processing method. Using un-differenced dual frequency pseudo-range and phase measurements to determinate the satellite orbit can quickly provide satellite orbit owing to free from the error calibration of errors [15]. Furthermore, it also helps to followed-up study of systematic errors of DORIS: for example, the analysis of clock error of DORIS beacons and satellite receiver. Besides, since JASON-2, altimetry satellites will be equipped with DGXX receiver to determinate the precise orbits, the dual frequency pseudo-range and phase will become the main measurements. Though the GPS data processing methods can assistant the DORIS data processing, the characteristics of DORIS makes its processing methods differently. Thus, it is necessary to go deeper in the study of pseudo-range and phase measurements data processing theory and methods.

In this paper, using the PANDA software of GNSS Research Center of Wuhan University as a platform, we worked out the LEO satellites precise orbit determination (POD) Algorithm based on un-differenced dual frequency pseudo-range and phase measurements. At the same time, the precise orbit of HY2A from January to May 2012 has been determinated.

3.2 Measurements Models

As previously mentioned, the new generation of DORIS DGXX receiver can provide dual frequency pseudo-range and phase measurements. Unlike GPS pseudo-range measurements, the precision level of pseudo-range is around 1 km due to the influence of clock error of receiver and observation noise, which makes it failed to data preprocessing and POD, but can be applied in calculation of receiver clock using the reference time beacons' pseudo-range measurements. However, DORIS phase measurements precision level can reach to several millimeters [15], therefore, the orbits are determinated mainly based on the un-differenced phase measurements. In this sector, observation equations of pseudo-range and phase measurements are given respectively.

3.2.1 Pseudo-Range

Just like for GPS, [16] the equations of DORIS dual frequency pseudo-range can be expressed as follow:

$$C_1 = \rho + c(t_r - t^e) + I + T + \varepsilon_{C1} \tag{3.1}$$

$$C_2 = \rho + c(t_r - t^e) + \alpha^2 I + T + \varepsilon_{C2} \tag{3.2}$$

where C_1 and C_2 are the pseudo-range measurements on the first and second frequencies, t_r is receiver clock error, t^e is DORIS beacons clock error, I is the distance owing to the ionosphere propagation delay on the first frequency. T is the tropospheric propagation delay, α is the frequency ratio and can be expressed as $\alpha = f_1/f_2, \quad f_1 = 2036.25\,\text{MHz}, f_2 = 401.25\,\text{MHz}$, the ε_{c1} and ε_{c2} are observation noise for two frequencies.

The expression for the ionosphere-free pseudo-range combination is:

$$\begin{aligned} PC &= \frac{f_1^2}{f_1^2 - f_2^2} C_1 - \frac{f_2^2}{f_1^2 - f_2^2} C_2 \\ &= \rho + c(t_r - t^e) + T + \varepsilon_C \end{aligned} \tag{3.3}$$

In the DORIS system, only the clock error of the reference time beacons are known, the clock error of other beacons and the receiver clock error are unknown. Therefore, the receiver clock error need to be calculated firstly using the measurements of the time beacons:

$$t_r = \frac{PC - \rho - T + ct^e}{c} \tag{3.4}$$

3.2.2 Phase

The DORIS phase observation equations are:

$$\lambda_1 L_1 = \rho + c(t_r - t^e) - I + T + \lambda_1 N_1 + \varepsilon_{L_1} \tag{3.5}$$

$$\lambda_2 L_2 = \rho + c(t_r - t^e) - \alpha^2 I + T + \lambda_2 N_2 + \varepsilon_{L_2} \tag{3.6}$$

where N_1 and N_2 is the phase ambiguities for two frequencies, ε_{L_1} and ε_{L_2} are observation noise. Other parameters are the same as Eq. (3.3).

The ionosphere-free phase combination is:

$$\begin{aligned} LC &= \frac{\alpha^2 \lambda_1 L_1 - \lambda_2 L_2}{\alpha^2 - 1} \\ &= \rho + c(t_r - t^e) + T + N + \varepsilon_L \end{aligned} \tag{3.7}$$

N is the ambiguity of the ionosphere-free phase combination which is a constant during a pass. As for DORIS ground beacons, the stability of the clock is superior to 5.0E^{-13} and the tracking time during each signal pass is less than 30 min in most instances. Therefore, the DORIS beacons clock error can be represented by a polynomial of degree one over a pass:

$$t^e = a_0 + a_1(t - t_0) + \delta t^e \tag{3.8}$$

where a_0 is the constant term of the clock error, a_1 is the clock rate, t is the current signal transmit time, t_0 is the start time over a pass, δt^e is the higher order term error. If the receiver clock error is expressed as $(t_r + \delta t_r)$, we can get the following formula:

$$LC = (\rho + ct_r) + c(\delta t_r - \delta t^e) + T + N - ca_0 - ca_1(t - t_0) + \varepsilon_L \tag{3.9}$$

where $(\delta t_r - \delta t^e)$ is the remaining behavior of clock error. The N and $-ca_0$ are combined for B, $-ca_1(t - t_0)$ is reversed, the un-modeled behavior of the clock errors are ignored, we get the final ionosphere-free phase combination observation:

$$LC = (\rho + ct_r) + T + B + ca_1(t - t_0) + \varepsilon_L \tag{3.10}$$

3.3 Models and Parameters Used for Orbit Determination

In this work, using the un-differenced pseudo-range and phase measurements, the dynamic orbit of HY2A are determinated from January to May 2012 with Position And Navigation Data Analyst software of GNSS Research Center of Wuhan University. Table 3.1 summaries the force model, data, and parameters used for HY2A POD.

Table 3.1 The summary of POD strategy for HY2A satellite

Force model	Description
Static	EIGEN-6C (150 × 150)
Time-variable gravity field model	EIGEN-6C time-varying part
Secular rates for low degree coefficients	IERS conventions 2003
n-body	JPL DE405
Solid earth tides	IERS conventions 2003
Ocean tides	FES2004
Relativistic effects	IERS conventions 2003
Atmosphere drag	DTM94
Solar radiation pressure	Box-wing
Attitude	Nominal
Reference frame	
Inertial frame	J2000.0
Precession/nutation	IAU 2000A
EOP	IERS EOP 08 C04
SLR	ITRF2008-TRF-ILRS
DORIS	DPOD2008
Tracking data	
DORIS RINEX format	Un-differenced phase measurements,10 s intervals
Estimated parameters	
Ambiguities	One in each ambiguity arc for each station
Clock rate of ground beacons	One in each ambiguity arc for each station
Satellite initial state	Position and velocity at given initial epoch
Drag coefficient	Every 720 min
Constant empirical coefficients in along tracking	Every 720 min
Periodic empirical coefficients in along and cross tracking	Every 720 min
POD arc length	24 h

3.4 Orbit Validation

We determinated the HY2A dynamic orbit of the period from January to May 2012 using the above strategy. In this section, we will carry out detailed analysis on the orbital accuracy.

3.4.1 Orbit Comparison with Respect to CNES POE

Figure 3.1 shows the daily RMS value of orbit differences in along-track, cross-track, radial-track and 3D directions between the calculated orbit and CNES precise orbit ephemerides (POE). It can be seen that the RMS values of radial-track component is the smallest and the changing scales are small, whereas there are a relative bigger in the along-track and cross-track. The accuracy in radial-track, along-track, cross-track and 3D direction is 10.0, 33.9, 41.6 and 54.6 mm,

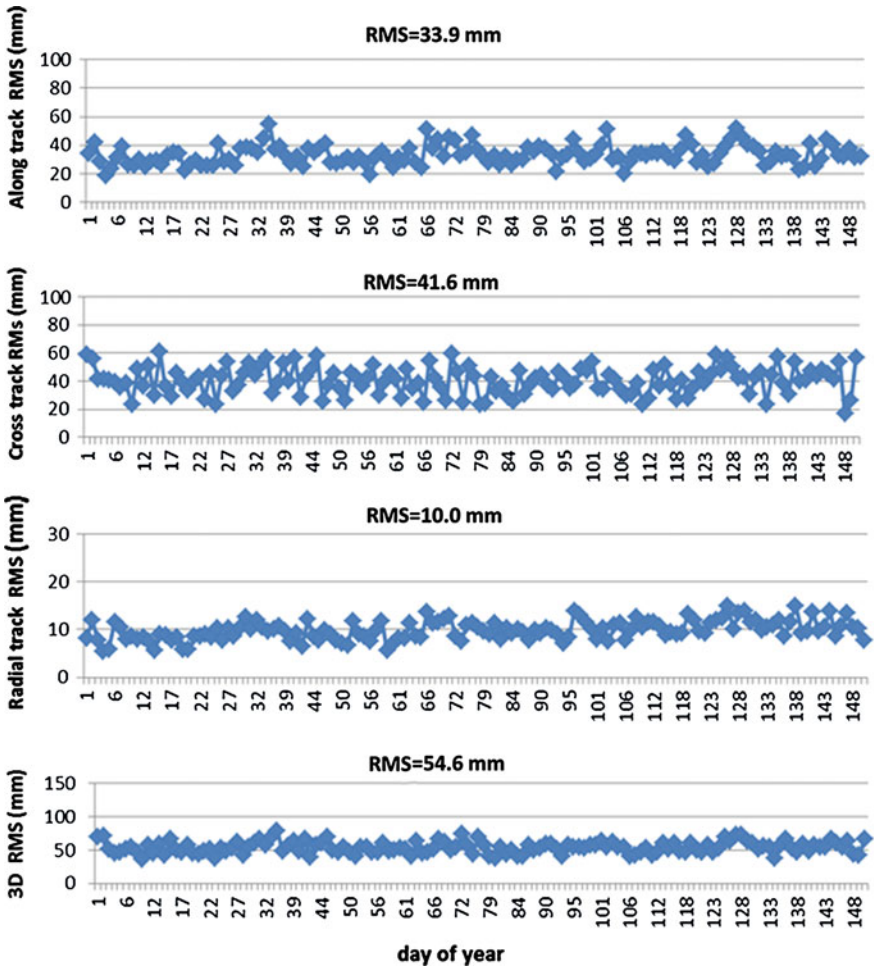

Fig. 3.1 RMS of orbit difference in the along-track, cross-track, radial-track and 3D direction of phase orbits with respect to CNES POE, the horizontal axis represents day of year

respectively. The reason for the poor accuracy in along-track may be the conservative force; for the cross-track direction, the reason is un-modeled behavior of the receiver clock error.

3.4.2 SLR Validation

SLR is a kind of independent tracking system. Using the SLR measurements to validate the orbital accuracy is the most effective orbit accuracy evaluation

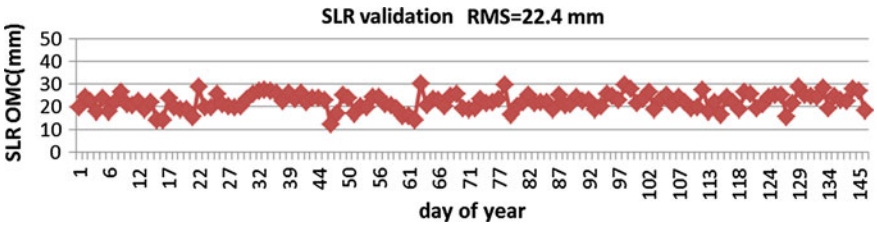

Fig. 3.2 SLR residuals on a network of fourteen reference stations

method. The laser retro-reflector arrays are equipped in HY2A and we do not use the SLR data to determinate the precise orbit, therefore, orbit accuracy can be validated by using the SLR measurements.

In this paper, the SLR observations data of HY2A from January to May 2012 is counted. Elevation mask angle is set to 15°. Figure 3.2 shows the RMS of the Observed minus Computed (O − C) residuals for HY2A satellite orbit. The overall RMS error of the residual is 22.4 mm and the average value is 0.74 mm. The results of the validation show that there is no significant systematic error between the computed orbit and the SLR system. The accuracy of the computed orbit can satisfy the demands for high precision orbit of HY2A scientific tasks.

3.4.3 Doppler Orbit and Un-differenced Phase Orbit Comparison with Respect to CNES POE

In order to analyze the impacts of observation on orbit determination results, The Doppler orbit of HY2A are determinated independently from 41th day to 150th day 2012 except un-differenced phase orbit. In Fig. 3.3 We compare Doppler and phase orbits with respect to CNES POE in along-track, cross-track, radial-track and 3D directions, blue for Doppler RMS and red for Phase RMS, respectively. The results indicated that the differences changes between Doppler orbit and phase orbit with respect to CENS POE are basically identical. Compared with the orbits computed with Doppler measurements, the accuracy of orbits computed with un-differenced phase observables in along-track and radial is a bit higher, the lower accuracy in cross-track maybe caused by inaccuracy receiver DORIS clock. As a whole, the accuracy of orbits computed with DORIS un-differenced phase observables is consistent with the accuracy of orbits computed with Doppler observables, especially the former being better than the latter in the radial direction.

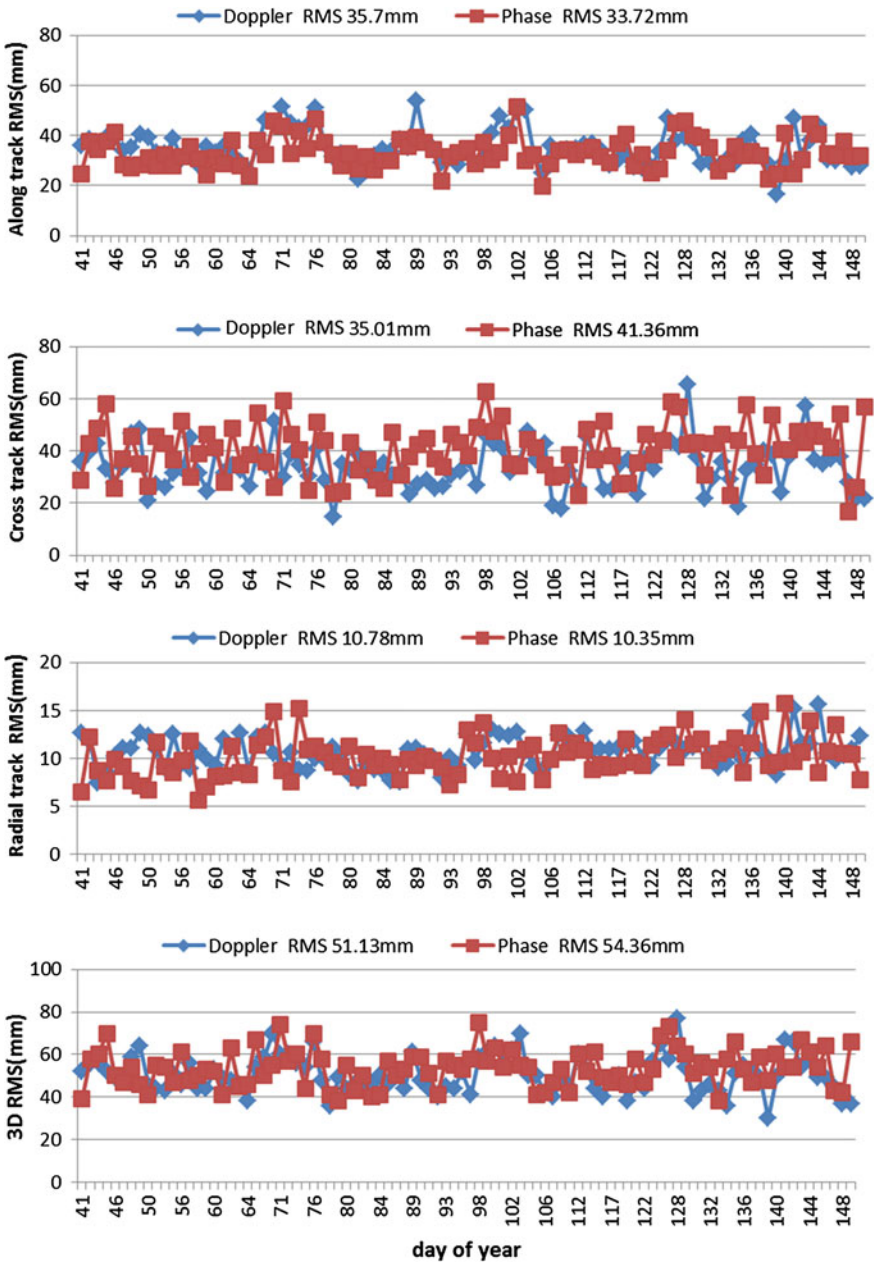

Fig. 3.3 RMS of orbit difference in the along-track, cross-track, radial-track and 3D direction of Doppler and phase orbits with respect to CNES POE, the horizontal axis represents day of year

3.5 Conclusions

In this paper, we determinated precise orbit for Haiyang 2A based on DORIS un-differenced dual frequency pseudo-range and phase measurements. These orbits are validated using orbit inter-comparison and SLR comparison. The difference with respect to CNES POE indicate the accuracy in radial and 3D is 1.0 and 5.3 cm, respectively. Satellite laser ranging validation the accuracy of HY2A orbits is about 2.24 cm. meanwhile we determinated the orbit using Doppler observables. Compared with the orbits computed with Doppler measurements, the accuracy of orbits computed with un-differenced phase observables in along-track and radial is a bit higher. All above demonstrates that we Chinese are fully capable to determinate precise orbit for LEO on the centimeter scale which can satisfy the demands for precise orbit determination of a number of satellite program in our country in the future.

References

1. Zhang Q, Zhang J, Zhang H, Wang R, Jia H (2013) The study of HY-2A satellite engineering development and in-orbit movement. Chin Eng Sci 15(7):12–18
2. Guo J, Zhao Q, Li M, Hu Z (2013) GPS-derived cm level orbits for HaiYang 2A satellite. J Wuhan Univ 2013(01):52–55, 131
3. Auriol A, Tourain C (2010) DORIS system: the new age. Adv Space Res 46(12):1484–1496. doi:10.1016/j.asr.2010.05.015
4. Jayles C (2009) Modelling of DORIS 2GM and Cryosat instruments. IDS technical documentation
5. Jayles C, Nhun-Fat B, Tourain C (2006) DORIS: system description and control of the signal integrity. J Geod 80:457–472
6. Mercier F, Cerri L (2009) Analysis of Jason-2 DORIS phase residuals and related POD results. IDS meetings
7. Mercier F (2010) DORIS phase and ionosphere effects. IDS meetings
8. Choi KR (2003) Jason-1 precision orbit determination using GPS combined with SLR and DORIS tracking data. The University of Texas, Austin
9. Cerri L, Ferrage P (2012) DORIS satellites models implemented in POE processing. SALP-NT-BORD-OP-16137-CN
10. Zelensky NP, Lemoine FG, Chinn1 DS, Pavlis1 DE, Rowlands DD, Le Bail K (2010) Improving DORIS troposphere modeling for Jason-1 and Jason-2. IDS meetings
11. Zelensky NP, Berthias JP, Lemoine FG (2006) DORIS time bias estimated using Jason-1, TOPEX/Poseidon and ENVISAT orbits. J Geod 80:497–506
12. Willis P, Desai SD, Bertiger WI, Haines BJ, Auriol A (2005) DORIS satellite antenna maps derived from long-term residuals time series. Adv Space Res 36:486–497
13. Lourme E (2009) Rinex DORIS 3.0. IDS technical documentation
14. Willis P, Fagard H, Ferrage P, Lemoine FG, Noll CE, Noomen R, Otten M, Ries JC, Rothacher M, Soudarin L, Tavernier G, Valette JJ (2010) The international DORIS service (IDS): toward maturity. Adv Space Res 45(12):1408–1420
15. Mercier F, Cerri L, Berthias JP (2010) Jason-2 DORIS phase measurement processing. Adv Space Res 45(12):1441–1454
16. Gurtner W, Estey L (2007) RINEX:the receiver independent exchange format version 3.0

Chapter 4
History, Present and Future of Solar Radiation Pressure Theory

Chen Junshou, Tan Wei, Li Chao, Zeng Guang and Yang Jie

Abstract It's a review article about the Solar Radiation Pressure Theory (SRPT). The applications of SRPT in asteroid dynamics, space debris long-term evolution and artificial satellite orbit determination were reviewed. The main SRPT development process and status was introduced from three aspects, which were empirical model, analytical model and semi-empirical model. Several factors, i.e. Second-incident effect, Self-Occlusion effect and Poynting-Robertson effect, were discussed in SRP model building. For SRPT application, the key role of SRP in long-term dynamic evolution of space debris was particularly expatiated on, and the state-of-art was presented. Then we focused on the SRPT application in Beidou Navigation and Positioning System. We demonstrated some existing problems for model building, physical material property perceiving and solution parameters. Finally, we gave the SRPT development prospect.

Keywords Solar Radiation Pressure · Model · Space Debris · Evolution · Beidou

4.1 Introduction

Solar radiation pressure is the most important non-conservative perturbation force in the motion of celestial body, such as asteroid, space debris, dust and high orbit artificial satellites. As early as the 1960s, a series of studies was carried out on the Solar Radiation Pressure Theory (SRPT) [1–4]. Applications of SRPT can be broadly divided into two fields, dynamical evolution of natural objects and satellite orbit calculation and long-term forecasts.

C. Junshou (✉) · T. Wei · L. Chao · Z. Guang · Y. Jie
State Key Labratory of Astronautic Dynamics, No. 462, Road Xianning East, Xi'an 710043, China
e-mail: aeric2003@gmail.com

J. Sun et al. (eds.), *China Satellite Navigation Conference (CSNC) 2014 Proceedings: Volume III*, Lecture Notes in Electrical Engineering 305,
DOI: 10.1007/978-3-642-54740-9_4,

In natural objects field, especially in the field of asteroid belt and near the earth asteroid dynamic evolution, solar radiation pressure plays a very important role. SRP, to a certain extent, affected process of the interplanetary dust falling to the sun through the Poynting-Robertson damping. For large objects, the effect is usually considered to be negligible. Solar radiation acceleration related to objects' area-mass ratio. Generally speaking, debris' area-mass ratio is higher, and for rocky sphere celestial is very low. Therefore, SRP on the asteroid's usually much smaller than the gravitational perturbation of the third body, and is ignored in most cases. Another important effect is SRP affect many natural celestial objects' thermal radiation. Since solar radiation is the main heat source of celestial radiation, thermal radiation and solar radiation pressure are closely related. This is particularly evident on the comet. Comet tail eruption of material was derived from solar radiation. Eruption of comet tail material was caused by solar radiation.

In early studies, Yarkovsky pointed out that due to the heat capacity of the asteroid was not 0, irradiated surface temperature of a rotating asteroid in the afternoon of was higher than that in the morning. Then it produced asymmetric secondary radiation, which made anterograde objects accelerate and retrograde objects slow down [5]. This effect is called "the Diurnal Yarkovsky Effect". Another Yarkovsky effect was found by Rubincam in the research of LAGEOS satellite [6], and is called "Seasonal Yarkovsky Effect". For objects whose rotation angle is not 0° or 180°, the hemisphere thermal radiation in the autumn is higher than that in the spring, and the cumulative effect is the semimajor axis of an asteroid decreases.

O'Keefe [7], Radvieskii [8] and Paddack [9] independently studied how the incident light changed the rotation of space objects. Rubincam revalidate their research and named "YORP Effect" [10]. This effect is caused by the net torque produced by SRP scattering on the asymmetric object surfaces. Rubincam studied the rotation rate variation of different shape targets at 0°/180° and 90° inclination angle. In 2005, Cuk and Burns [11] proposed "BYORP Effect" for dual planetary system (such as the Earth–Moon system), their result showed time-varying pressure torque also impacted on the relative orbit of dual planetary.

In 2004, C.C. Celestino studied micron grade debris' speed variation and long-term evolution compared with coplanar circular orbit near the geosynchronous orbit under SPR perturbation [12]. SPR changed the eccentricity of debris orbit, and produced the relative velocity variation. With the increase of the debris size, the maximum relative momentum and relative kinetic energy also increase. When the debris size increased from 1 to 100 microns, the relative momentum increased by 1,000 times, and the relative kinetic energy increases by 10^6 times.

At the same time, Kocifaj and Klawka [13] researched the dynamical behaviour of interstellar dust particles in the solar system. Interstellar dust particles were affected by the sun's gravitational field, solar radiation pressure, corpuscular radiation and the interstellar magnetic field, and SRP played an important role.

Unlike natural bodies, Satellite secondary radiation and solar radiation are the separation effects in SRPT of artificial satellites. This is because the satellite thermal control system changed the heat flow to some extent. In addition, solar

radiation pressure perturbation theory in artificial satellites mainly focuses on the satellite's orbit variation relative to earth, and Yarkovsky effect is not so important. Moreover, many low earth orbit satellites contain part of the shadow area, which has a considerable influence to satellite orbit.

With the continuous development of ocean observation satellites, satellite navigation and positioning systems, the requirement to orbit determination accuracy is increasing day by day. Up to 2009, the accuracy of GPS satellites' final orbit had reached 2.5 cm [14]. In China, the orbit determination accuracy of HY-2 satellite has reached centimeter grade, and Beidou navigation satellite positioning accuracy will also be at or near the GPS satellites in the future. These high precision applications put forward higher requirements to the perturbation theory and model.

SRP is one of the main non-conservative perturbation forces for artificial satellite in earth orbit. For satellite higher than 800 km, SRP perturbation effect on the orbit exceeds atmospheric perturbation, and becomes the most important non-conservative force [15].

SRPT is a key issue in any centimeter level's orbit determination. Precise radiation pressure model can further improve orbit determination accuracy, and are of high research value in manned space flight, space docking, satellite navigation and positioning, geodesy, etc.

For the orbiting satellites, its orbit is affected by multiple factors, such as the Earth's gravity field, the gravity of the sun, lunar and other planets, radiation perturbation, atmospheric drag, tides, Earth's radiation pressure, relativistic effects, etc. Even only for radiation perturbation, there are also solar radiation pressure, insulation radiation, heat sinks, solar panels thermal radiation, solar sail shunt thermal radiation, Earth albedo radiation, infrared radiation, etc. Precise radiation pressure model will help to separate radiation pressure perturbation from other perturbations, and to estimate the influence of atmospheric perturbation to satellite orbit. This will be also helpful to build a more accurate Atmospheric physics model, and evaluate the error of the atmospheric model.

Precise radiation pressure model can be utilized to the study of perturbation's physical mechanism. When the satellite orbit becomes abnormal, it can help to analyze satellites' fundamental physical forces, rather than boiled down to empirical forces. Moreover, it can be applied to satellite attitude control, and attitude adjustment without fuel. Back in 1976, K. C. Pande had preliminarily studied the possibility utilizing SRP to control spinning spacecraft's attitude [16]. In another way, radiation pressure force torque can be used to calculate the position of the sun relative to satellite. In 2010, Janssens [17] reported the technology of automatically tracking the sun using SRP in interplanetary navigation tasks. The result showed that, regardless of the satellite nutation, if satellite spin rate keeps constant, the angle of angular momentum precession with the sun is a constant near equilibrium points. In 2006, Li and Williams [18] researched methods of satellite formation reconfiguration utilizing solar radiation pressure. They established linear formation control equations through the analysis of differential radiation pressure. These equations showed that Sun–Earth equilibrium

points moved to new positions due to solar radiation perturbation. In 2010, Shahid and Kumar [19] published a study using radiation pressure to achieve formation control in the L2 Lagrange point double satellites formation. Over the same period, Varma and Kumar [20] studied the effects of radiation pressure on the stability of double satellites formation, and the method of utilizing radiation pressure to achieve stability control.

The existing studies have shown that SRP may also affected the long-term evolution of the satellite semimajor axis [21]. Research progress of SRPT can improve the accuracy of operating satellites' long-time orbit prediction. For satellites with large wings, radiation pressure may be used for orbit maintenance. For high orbit satellites to be retired, it is possible using SRP and J2 gravity perturbation to deorbit satellites. In 2006, Borja and Tun [22] discussed methods of applying SRP control to achieve deorbit, and SRP was auxiliary thrust force in the progress.

In deep space exploration, detectors with sails can take advantage of solar radiation in flight of the solar system. In 2012, Japan's Tomohiro Yamaguchi et al. [23] reported a method of mixed SRP estimation method for spinning solar sail spacecrafts. In 2013, Kezerashvili and Zquez-Poritz [24] studied Poynting Robertson effect to solar sail. They found that for solar sails cruising in the solar system, this effect could slow down the flight speed, and for spacecrafts round the solar system, it decreased the orbit semimajor axis and eccentricity.

4.2 Basic Principle

4.2.1 Interaction of Photons with Satellite Surfaces

Quantum mechanics theory claims that light travels in space there are both volatility and particles. A beam of light is a group of moving particles. Light perturbation is photons hit surfaces of satellite and produce pressure. For navigation satellites on medium earth orbit and synchronous orbit, perturbations belongs to radiation pressure theory includes: solar radiation, satellite thermal radiation, earth radiation. Solar radiation is momentum transformation of reflected or absorbed photons hit satellite body and wings. The thermal radiation's energy exchange between satellite and environment is the fundamental of setting up thermal radiation model. Radiation energy of heated satellite body can be radiated in the form of photons, and the flow rate of radiation energy is positively correlated with satellite's temperature. Earth radiation has two forms: earth albedo and earth thermal radiation. Earth albedo just exists in the earth hemisphere illuminated by the sun. Whereas, earth thermal radiation does not depend on sun light' incident angle, or whether satellite is in the in the earth's illuminated hemisphere or not. Earth thermal radiation always exists. Interaction of Solar radiation with solar sail is shown clearly in Fig. 4.1.

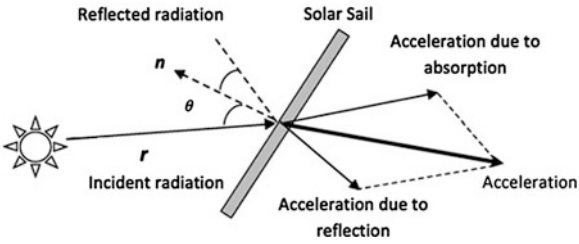

Fig. 4.1 Interaction of solar radiation with solar sail

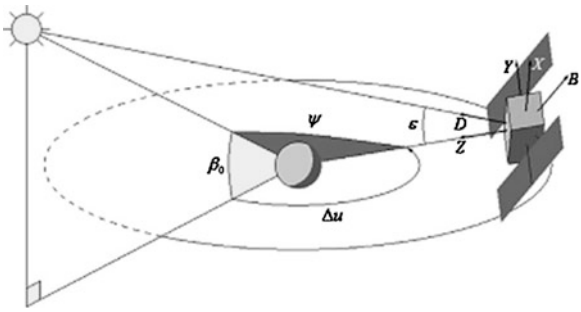

Fig. 4.2 Definition of coordinate system and parameters for satellite solar radiation pressure model

4.2.2 Coordinate Systems Definition

Most of solar radiation pressure models suppose SRP in some certain directions has the greatest impact on satellite orbits. Therefore, these directions can be defined as coordinate axes, and different models have different coordinate axis orientations and different solving parameters. The main coordinate axes are defined as Fig. 4.2. Origin of coordinate is satellite's nominal mass center. Z-axis is define as origin to the earth center. Y-axis stretches along wings. X-axis and Y, Z axis meet right-hand screw rule. D-axis is define as origin to the sun center. B-axis and D, Y axis meet right-hand screw rule and constitute DYB coordinate.

4.3 Solar Radiation Pressure Model

There are three types of solar radiation pressure model which are empirical model, analytical model and semi-empirical model. Empirical model use several fitting function with adjustable parameters to fit satellite orbit observations. The empirical model which can fit the observation well has a disadvantage of lacking of physical meaning. In practice, solar radiation pressure can't be separated from other experience perturbation. In the case of dramatic changes in the external environment (such as deep-space exploration), empirical model may lead to non-poor physical track. Analytical model using the material properties of the satellite

is established based on a series of physical principles derivation and calculation. The analytical model has the clear physical meaning, but the disadvantage is also obvious. Satellites in orbit face complex condition including not only eclipse, satellite temperature changing but also constantly changing of satellite attitude. So to establish a precise analysis model is quite difficult.

McMahon [25] indicated that a common model for solar pressure perturbation should be independent of the characteristics of satellite itself. This model perturbation theory can improve the understanding of the effect on the long-term, long-period, short-period orbit by solar pressure and can be applied to the satellite orbit determine the Earth.

4.3.1 Empirical Model

Colombo introduced the empirical model for GPS satellite firstly in 1989 [26]. After analyzing the orbital perturbation theory, Colombo point that GPS satellite ephemeris error can be corrected through a simple priori acceleration function with several adjustable parameters. Ignore the complex reason to causing errors (e.g. non-spherical gravitational and earth radiation pressure). The resonant frequency of every cycle of satellite orbit is 0 or 1. Applying Hill equation to analysis orbit perturbations in radial, tangential and normal directions, the Colombo model could be established based on priori orbit observation data. The basic assumption of the model is non-theoretical perturbation forces can be described by several periodic functions including adjustable parameters, although perturbation forces may be quit complicate. The proposed model includes perturbation acceleration in radial, tangential and normal directions, which were denoted as R, S, and W, respectively. These three accelerations are given by

$$\begin{cases} R(u) = R_0 + R_C \cos u + R_S \sin u \\ S(u) = S_0 + S_C \cos u + S_S \sin u \\ W(u) = W_0 + W_C \cos u + S_S \sin u \end{cases} \tag{4.1}$$

where u is satellite's latitude. This model was initially used to compensate for the Earth's gravity field, and was not separately considered solar radiation pressure perturbation.

In 1994, Beutler et al. [27] proposed another model containing nine parameters. It used the same functions as Eq. (4.1), but changed the three directions of perturbation accelerations as: the first direction from satellite to the sun, the second direction along satellite' solar panels, and the third direction defined by right-hand rule. The coordinate system definition is shown in Fig. 4.2. The three are denoted as D, Y and B, respectively. The model is expressed as

$$\begin{cases} D(u) = D_0 + D_C \cos u + D_S \sin u \\ Y(u) = Y_0 + Y_C \cos u + Y_S \sin u \\ B(u) = B_0 + B_C \cos u + B_S \sin u \end{cases} \tag{4.2}$$

One of empirical models' disadvantages is they lack of priori information. To compensate this shortcoming, the model proposed by Fliegel et al. [28, 29] can be used as a priori information.

In order to get a radiation pressure model containing appropriate priori information, Springer et al. [30] proposed a model based on CODE's data for several years in 1999. It can be expressed as

$$\begin{cases} D = D_0 \\ Y = Y_0 \\ B = B_0 \\ Z(\Delta u) = Z_1 \sin \Delta u \\ X(\Delta u) = X_1 \sin \Delta u + X_3 \sin 3\Delta u \end{cases} \tag{4.3}$$

This model contained 6 parameters, and have significant simplification compared with previous two empirical models. There are two new directions in this model, Direction Z and Direction X. Z axis is from satellite to the earth. X-axis and Z-axis, Y-axis together constitute right-handed Cartesian coordinate system. Δu in Eq. (4.3) represents the difference between satellite and the sun's latitude in orbital plane.

Currently CODE uses an improved version of model (4.3) as a priori information to generate the final orbit, and applies model (4.2) to fit Orbit tracking data. The difference is their model just solves 5 parameters, which are D_0, Y_0, B_0, B_C and B_S. Their results showed that this model compliance with measured data of GPS satellites quit well.

4.3.2 Analytical Model

The analytical model is established based on the optical characteristics of satellite materials, where the satellite physical dimension, satellite optical reflection imbibition properties, satellite orbit position, satellite attitudes and satellite umbra is synthesized. Besides, the fundamental information for the analytical model can be supported by the satellite manufacturer.

In the Cannonball model [31], which is one sort of simple solar pressure radiation model, it is assumed that the optical properties hold the same all around the spheroidal satellite surface. The solar pressure radiation force is along with the straight line joining the sun and satellite. This model was first created for LAGEOS mission, and this satellite had a similar shape to cannonball. The advantage of this model is easy to expressed perturbations in the form of potential function [32].

Therefore, it was widely used in the analysis of long-term dynamics evolution for space debris.

Spacecraft tasks often require a higher fidelity model of radiation pressure model than Cannonball model. The next step in establishment of radiation pressure model is to use polyhedron to simulate the satellite's geometry. Many spacecrafts could be modeled as "Box-Wing" shape, such as TOPEX/Poseidon [33] and GRACE [34]. Polyhedral SRP models can still apply analytical method to solve radiation perturbation problems. However, because this model needs to calculate radiation pressure on each plane at every position, that requires numerical calculations. With the introduction of more and more spacecraft details, solution of perturbation forces are more dependent on numerical method, such as micro-model [35]. Micro-model can introduce a lot of spacecraft details, and simulates its shape through CAD method. It can even assign different optical properties to each part. This kind of models with high fidelity adopts light-tracing method and can include self-shielding effect and secondary reflection effect [36].

In the early days of satellite on-orbit operation, it lacks of much observation data. The analytical model can be treated as priori information, and plays an important role. However, these models are often difficult to conforms well with realistic situation. Satellite surfaces will gradually aging, so there are uncertain parts in the optical properties of satellite. Sometimes, satellite may operate in non-nominal attitude. All these factors can introduce errors.

4.3.3 Semi-empirical Models

In addition to empirical model and analytical model, there are some semi-empirical models. These models utilized analytical model as priori parameters, and accepted empirical model to calculate the correction coefficients. These models can obtain higher accuracy. Main semi-empirical models are JPL model and Adjustable Box-wing model.

In order to process Jet Propulsion Laboratory (JPL)'s GPS satellite orbit measurement data, Barsever and Kuang proposed a model similar to Eq. (4.3) [37]. Then, JPL's Bar-Sever and Yoaz E considered SRP and satellite thermal radiation, and utilizing the GPS precise ephemeris provided regularly to the International GNSS Service (IGS), they established JPL pressure model for Block II/IIA.

JPL model has two different modes. The first mode is used for satellites in full sunlight, and nominal attitude is known. Models in this mode is purely numeric. It uses the earth–satellite–sun three points determined angle ε as the only variable representing the position of satellite, and uses flourier series to fit precise ephemeris. This model's solving optimal parameters are expressed in the BYD coordinate system. The second mode is used for satellites in earth shadow. Models in the second mode is purely analytical model obtained by modified T20 model. T20 model assumed that antenna center always points to the earth center. This

nominal attitude is not always appropriate. The points that not satisfied the nominal attitude's requirement are: points that satellite closest to the sun (noon), points that satellite farthest to the sun (midnight), and as long as 45 min' eclipse season. In order to adapt to the situation of non-nominal attitude, perturbation forces calculated by T20 model are decomposed into two parts, one part acting on main body and one part acting on solar panels. JPL model's accuracy is better than the T20 model which was the standard model. JPL model improved the accuracy of the analytical model through the comprehensive utilization of priori observational data and analytical model. It also solved the problem that SRP model was not always available in practice applications. This modeling method is a good reference for solar radiation pressure theory studies.

In 2011, Sibthorpe proposed a model using the GPS Solar Pressure Model presented by Barsever as priori acceleration terms and added random parameters. Sibthorpe et al. [38] compared the model with Eq. (4.2). Random parameters used in the JPL model were: constant deviations in Y and D directions, time-varying parameters in X and Z directions, and small random variables in Y directions. This method can be named as "Reduced Dynamics method".

In 2012, Rodriguez-Solano et al. [39] analyzed advantages and disadvantages of existing models, and established an adjustable box-wing model for GPS satellite based on the interaction of solar radiation with satellite surfaces. This model considered the physical interaction mechanism of photons with solar panels, and contained adjustable optical property parameters for satellite surfaces. Therefore, it could be as close to satellites observation data as possible. The adjustable box-wing model was also a compromise between analytical model and empirical model.

Adopting the GPS satellite precise ephemeris by the Center for Orbit Determination in Europe (CODE), this model was compared with ECOM model in precise orbit determination and orbit prediction verification. Results showed that, it was not only very close to GPS satellite observation data, but its accuracy was similar to ECOM radiation pressure model in precision orbit determination. What's more, to achieve this orbit prediction accuracy, ECOM model needs years' data, but Adjustable Box-Wing Model just needs one day's orbit observation data. This advantage provides quite a good solution to the SRP model establishment in situation of lacking large observation data.

4.4 Problem and Prospect

4.4.1 Applicability of Models

Most of existing models are built for GPS satellites, and there are still lacking of radiation pressure models for Beidou Navigation System. Most radiation pressure models for Beidou Navigation System are modified on GPS SRP models. Whereas,

on the one hand, structures of Beidou navigation satellite, surfaces' optical properties and thermal control systems are quite different from GPS satellites, on the other hand, the yawing model for Beidou navigation satellites drift is totally different from GPS satellites, blindly using GPS radiation pressure model will produce quite serious problems.

In October 2011, attitude control mode of one Beidou IGSO satellites changed from "Dynamic Bias" to "Zero Bias", and it was found that these satellites' orbit determination error significantly increased. Meanwhile, there were similar phenomenon in other IGSO satellites. Every IGSO had "Dynamic Bias" to "Zero Bias" convention 2 time periods per year. During these periods, service of Beidou IGSO satellites affected.

The yawing mode convention of Beidou IGSO satellites is different from GPS satellites. We should build corresponding SRP model for the special case. The present problem is that orbit determination software have not been modified for Beidou IGSO stallites' yawing control mode. It results in the short-time termination of service for orbit determination and prediction during "Zero Bias" yawing periods.

Therefore, we need to target specific satellite type and specific attitude control mode, and establish appropriate radiation pressure model. We suggest to analyze the relationship between radiation perturbation forces and attitude angles, theoretically established the transformation matrix from Euler angles matrix to radiation perturbation forces, and experimentally determine the matrix parameters. This may be helpful to improve the accuracy of orbit dynamics model, and to perform better in high orbit satellites' orbit determination and orbit control.

4.4.2 Perception and Modeling to the Optical Properties of Satellite and Nature Body

From Sect. 4.1 and above it gives rise to another question. Why we cannot build appropriate radiation pressure perturbation model for Beidou satellite IGSO? The reason may be we still haven't deeply understood the physical interaction mechanism of photons with satellites. Hence the SRP model based on satellite's optical properties can't be built.

On the other hand, GPS satellites have a more mature radiation pressure model. It is because there were comprehensive and deep research on analysis model in the early times. So we can establish radiation pressure functions in experience models similar to that in analysis model. Analysis models are the fundamental of experience models. If we study Beidou satellite radiation pressure perturbation problem blindly from the perspective of empirical model, and ignore the physical meaning behind it, it will be difficult to find high-precision empirical optical pressure model.

4.4.3 Problem of Model Solving Parameters

Solar radiation pressure is the main error source in orbit determination of high orbit satellite. Spring in Bern University pointed out that most of the models' improvement were achieved by adding numbers of solving parameters [40]. However, these added parameters will weak other estimated parameters. It results in decreases in orbit prediction accuracy. Sometimes the more parameters solved, the higher accuracy within observation phase, the poorer in orbit prediction. Therefore, an important research question is how to improve the accuracy of SRP model in the condition: not adding solving parameters but just remaining the parameters with physical meaning and dynamics value.

4.4.4 Summary and Outlook

Solar radiation pressure theory is developing toward two directions, empirical models and analytical models. Empirical models tend to study how models achieve higher accuracy in orbit determination. Meanwhile, analytical models tend to study more complicate structures, such as the international space station, macro surface force, finite element analysis, etc. In theory's fundamental research, some more complicate effects are of concern, such as secondary reflection effect, self-shielding effect, Poynting-Robertson damping effect. Moreover, widespread applications of high-precision onboard accelerometer also opened a door for radiation pressure perturbation theory.

In application aspects, SRPT's research scope is greatly expanded. It has a wide range of applications or prospects in interplanetary exploration, formation control, satellite deorbit, celestial bodies and debris dynamics evolution, and other fields. Especially in the field of space debris dynamics evolution, a considerable number of literature has emerged since 2013. It is currently the most active area of research in space debris and radiation pressure perturbation directions.

References

1. Tea PL Jr (1965) Some thoughts on radiation pressure. Am J Phys 33(1965):190–195
2. Edwards DK, Bevans JT (1965) Radiation stresses on real surfaces. AIAA J 3(3):522–523
3. Falken SN, Hsu CT (1965) Specular and lambert reflection problems in radiation dynamics. AIAA J 3(7):1356–1359
4. Shahrokhi F, Clark HT (1968) Determination of solar radiation forces on satellite materials. AIAA J 6(8):1569–1570
5. Hartmann WK (1999) Reviewing the Yarkovsky effect: new light on the delivery of stone and iron meteorites from the asteroid belt. Meteorit Planet Sci 34:A161–A167
6. Rubincam DP (1995) Asteroid orbit evolution due to thermal drag. J Geophys Res 100(E1):1585–1594

7. O'Keefe JA (1976) Tektites and their origin. Elsevier, Amsterdam
8. Radzievskii VV (1954) A mechanism for the disintigration of asteroids and meteorites. Dokl Akad Nauk SSSR 97:49–52
9. Paddack SJ (1969) Rotational bursting of small celestial bodies: effects of radiation pressure. J Geophys Res 74(17):4379–4381
10. Rubincam DP (2000) Radiative spin-up and spin-down of small asteroids. Icarus 148:2–11
11. Cuk M, Burns J (2005) Effects of thermal radiation on the dynamics of binary neas. Icarus 176:418–431
12. Celestino CC, Winter OC, Prado AFBA (2004) Debris perturbed by radiation pressure: relative velocities across circular orbits. Adv Space Res 2004(34):1177–1180
13. Kocifaj M, Klawka J (2004) Dynamical behaviour of interstellar dust particles in the solar system. J Quant Spectrosc Radiat Transfer 2004(89):165–177
14. Dow J, Neilan R, Rizos C (2009) The international GNSS service in a changing landscape of Global Navigation Satellite Systems. J Geodesy 3–4:191–198
15. Vokrouhlichy D, Farinella P, Mignard F (1993) Solar radiation pressure perturbations for earth satellites I: a complete theory including penumbra transitions. Astron Astrophys 280:295–312
16. Pande KC (1976) Attitude control of spinning spacecraft by radiation pressure. J Spacecraft 13(12):765–768
17. Janssens F (2010) Automatic sun tracking with solar radiation pressure in interplanetary missions. Toronto, Ontario, Canada
18. Li H, Williams T (2006) Reconfiguration of Sun–Earth libration point formations using solar radiation pressure. J Spacecraft Rockets 43(6):1328–1339
19. Shahid K, Kumar KD (2010) Formation control at the Sun–Earth L2 libration point using solar radiation pressure. J Spacecraft Rockets 47(4):614–615
20. Varma S, Kumar KD (2010) Multiple satellite formation flying using differential solar radiation pressure. Toronto, Ontario, Canada
21. Likhachev VN, Sazonov VV, Ul'Yashin AI (2004) Evolution of the orbit of an Earth satellite with a solar sail. Cosm Res 42(1):79–83
22. Borja JA, Tun D (2006) Deorbit process using solar radiation force. J Spacecraft Rockets 43(3):685–687
23. Yamaguchi T, Mimasu Y, Tsuda Y et al (2012) Hybrid estimation of solar radiation pressure for a sail spacecraft. J Spacecraft Rockets, AIAA Early Edition, 1–4
24. Kezerashvili RY, Zquez-Poritz JFV (2013) Effect of a drag force due to absorption of solar radiation on solar sail orbital dynamics. Acta Astronaut 2013(84):206–214
25. Mcmahon JW (2011) An analytical theory for the perturbative effect of solar radiation pressure on natural and artificial satellites. University of Colorado
26. Colombo OL (1989) The dynamics of global positioning orbits and the determination of precise ephemerides. J Geophys Res Atmos 94(B7):9167–9182
27. Beutler G, Jäggi A, Hugentobler U (2006) Efficient satellite orbit modelling using pseudo-stochastic parameters. J Geodesy 80(7):353–372
28. Fliegel H, Gallini T, Swift E (1992) Global positioning system radiation force model for geodetic applications. J Geophys Res Atmos 97(B1):559–568
29. Fliegel H, Gallini T (1996) Solar force modeling of block IIR Global Positioning System Satellites. J Spacecraft Rockets 33(6):863–866
30. Spring TA (1999) Modeling and validating orbits and clocks using the global positioning system. University of Berne, Berne
31. Lucchesi D (2001) Reassessment of the error modelling of non-gravitational perturbations on lageos ii and their impact in the lense-thirring determination. part I. Planet Space Sci 49:447–463
32. Scheeres DJ (1999) Satellite dynamics about small bodies: averaged solar radiation pressure effects. J Astronaut Sci 47(1):25–46
33. Marshall JA, Luthcke SB (1994) Modeling radiation forces acting on Topex/Poseiden for precision orbit determination. J Spacecraft Rockets 31(1):99–105

34. Cheng M, Ries J, Tapley B (2008) Assessment of the solar radiation model for grace orbit determination. Adv Astronaut Sci 129:501–510
35. Rim H (2006) Radiation pressure modeling for icesat precision orbit determination. Keystone, Co
36. Ziebart M (2004) Generalized analytical solar radiation pressure modeling algorithm for spacecraft of complex shape. J Spacecraft Rockets 41(5):840–848
37. Bar-Sever Y, Kuang D (2004) New empirically derived solar radiation pressure model for GPS satellites. Interplanetary Network Progress Report, pp 42–159
38. Sibthorpe A, Bertiger W, Desai SD (2011) An evaluation of solar radiation pressure strategies for the GPS constellation. J Geodesy 85(8):505–517
39. Rodriguez-Solano CJ, Hugentobler U, Steigenberger P (2012) Adjustable box-wing model for solar radiation pressure impacting GPS satellites. Adv Space Res 2012(49):1113–1128
40. Springer T, Beutler G, Rothacher M (1999) A new solar radiation pressure model for GPS. Adv Space Res 23(4):673–676

Chapter 5
BeiDou/GPS Indirect Fusion Precision Orbit Determination

Guang Zeng, Bing Gong, Jia Song Wang, Jie Li and Jun Zhu

Abstract A BeiDou/GPS indirect fusion process method based on double-difference data was proposed in this article. Based on the multi-mode navigation data from the 6 internal stations and 10 foreign stations of M-GEX (The IGS Multi-GNSS Global Experiment) combined with the GPS data from 120 IGS (International GPS Service) stations, an accuracy verification test of orbit determination was developed. The results show that the accuracy of satellite orbit overlap is about 10 cm in radial direction for BeiDou IGSO. For MEO the accuracy is 15 cm in radial direction and for GEO is about 20 cm. The orbit RMS for GPS satellite is about 2 cm by comparing with IGS final products.

Keywords BeiDou/GPS · POD · Double-difference · Fusion process

5.1 Introduction

Navigation system can provide navigation and timing capability. The precise orbit of the navigation satellite is the basis for precise positioning on the ground. Improving the accuracy of the orbit is an effective way to enhance the performance of the whole navigation system. Internationally the POD (precise orbit determination) of GPS is much more mature. GPS' final orbit from IGS (International GPS Service) can reach an accuracy less than 2.5 cm. Many internal research institutions can also achieve a similar accuracy. The strategy used widely is introducing receiver data of global tracking network to orbit determination processing.

Foundation item: National Natural Science Foundation of China (41274018), GFZX0301040308-01.

G. Zeng (✉) · B. Gong · J. S. Wang · J. Li · J. Zhu
State Key Lab of Astrodynamics, Xi'an 710043, China
e-mail: zengguang_04@163.com

J. Sun et al. (eds.), *China Satellite Navigation Conference (CSNC) 2014 Proceedings: Volume III*, Lecture Notes in Electrical Engineering 305,
DOI: 10.1007/978-3-642-54740-9_5,

The challenges of Beidou POD include: fewer stations and unreasonable distribution, complex constellation composition, different attitude control mode and so on. For a new navigation system, multi-system data fusion is an effective way to improve the accuracy of the orbit and the clock error.

Based on the BETS (BeiDou Experimental Tracking Stations) data, Ref. [1] achieve a fusion POD of BeiDou and GPS by processing dual-mode receiver data. However, the POD using non-difference data need to estimate an additional bias between navigation systems which increases the complexity of data processing. Reference [2] achieves a POD of BeiDou based on double-difference data. However, fusion POD of dual system is not tested and MEO orbit accuracy is not validated. In 2020, BeiDou will become a global navigation system which is mainly composed of MEO. So an orbit determination accuracy verification test of is necessary for BeiDou MEO satellites.

A BeiDou/GPS indirect fusion process method based on double-difference data was proposed in this article based on the multi-mode navigation data from the 6 internal stations and 10 foreign stations of M-GEX, combined with the single-mode GPS data from 120 IGS stations. First of all GPS satellites orbit was estimated together with station ZTD (tropospheric zenith delay) parameters, station coordinates and EOP (earth rotation parameters). Then, fix the station coordinates and other public parameters, estimate the Beidou satellite orbit using the Beidou data received by dual-mode receiver. Orbit determination accuracy of MEO, IGSO and GEO were verified at last.

5.2 Model

5.2.1 Observation Model

The receivers used in the experiment can collect multi-frequency code and phase pseudo-range data. For BeiDou $f = (B_1, B_2, B_3)$ and for GPS $f = (L_1, L_2, L_5)$. The receiver i receives f frequency signal of satellite j can form the code pseudo-range $P_{i,f}^j$ and phase pseudo-range $\Phi_{i,f}^j$. The observation equation is:

$$\begin{cases} P_{i,f}^j = \rho_i^j + c(\Delta t_i - \Delta t^j + b_i + b^j) + \varepsilon_P \\ \Phi_{i,f}^j = \rho_i^j + c(\Delta t_i - \Delta t^j + b_i + b^j) + n_i^j + \delta n_i^j + \varepsilon_\Phi \end{cases} \tag{5.1}$$

In the equation above, ρ_i^j is original distance of satellite and stations:

$\rho_i^j = |x_i(t_r) - x^j(t_t)| + \Delta\rho_{trp} + \Delta\rho_{ion} + \Delta\rho_{mp} + \Delta\rho_{rel} + \Delta\rho_{pc}$. $x_i(t_r)$ is the position of the receiver i at reception time t_r, $x^j(t_t)$ is the position of the satellite j at signal transmission time t_t, $\Delta\rho_{trp}$ is tropospheric delay, $\Delta\rho_{ion}$ is ionospheric delay, $\Delta\rho_{rel}$ is relativistic affection, $\Delta\rho_{pc}$ is offset and variation of phase center, ε_P is measurement error, ε_Φ is phase measurement error, n_i^j is initial phase ambiguity,

δn_i^j is polarization effects of phase, c is light speed, Δt_i, Δt^j are receiver and satellite clock error, b_i, b^j are receiver and satellite hardware delay.

If two receivers (i_1, i_2) track two satellites (j_1, j_2) at the same time, we can form the double-difference observation data like this:

$$\begin{cases} DDP(f, i_1, i_2, j_1, j_2) = \left(P_{i_1,f}^{j_1} - P_{i_1,f}^{j_2}\right) - \left(P_{i_2,f}^{j_1} - P_{i_2,f}^{j_2}\right) \\ DD\Phi(f, i_1, i_2, j_1, j_2) = \left(\Phi_{i_1,f}^{j_1} - \Phi_{i_1,f}^{j_2}\right) - \left(\Phi_{i_2,f}^{j_1} - \Phi_{i_2,f}^{j_2}\right) \end{cases} \tag{5.2}$$

By forming the double-difference, the influence of the satellite clock error and receiver clock error can been eliminated to avoid the huge number of clock error parameters in data processing. On the other hand, by eliminating the influence of the hardware delay, the double-difference ambiguity can keep integer character. Ambiguity fixed technique can be introduced in double-difference processing.

Based on the observations of dual frequencies (L1, L2 or B1, B2), ionosphere-free linear combination can be formed to eliminate the influence of the first order ionosphere. Ionosphere-free linear combination can be expressed:

$$Q_{f_3} = \frac{1}{f_1^2 - f_2^2}\left(f_1^2 Q_{f_1} - f_2^2 Q_{f_2}\right), \quad Q = (P, \Phi) \tag{5.3}$$

5.2.2 Orbit Determination Model

Multi-GNSS processing should be implemented in a unified space-time framework. Time system selected in this article is GPST and the reference frame is IGS08. Double-difference code and phase which are formed by ionosphere-free linear combination are used in the processing. The weight ratio of Code and phase data is 1:100. sampling rate of 300 s. Select the 5° cutoff angle and introduce the elevation-dependent weighting to reduce the correlation between the troposphere parameters and the station altitude.

The initial Solar radiation pressure model of GPS is T10 and T20. For Beidou any initial Solar radiation pressure model isn't used. In the POD processing, 5 parameters of Solar radiation pressure model parameters are estimated for GPS and Beidou satellites including the constant parameters of three directions (D, Y, X) and periodical parameter of the X direction.

5.3 Processing Strategy

The POD experiment in this article is based on the multi-mode navigation data from the 6 internal stations and 10 foreign stations of M-GEX. The strategy of BeiDou/GPS indirect fusion precision orbit determination is described below:

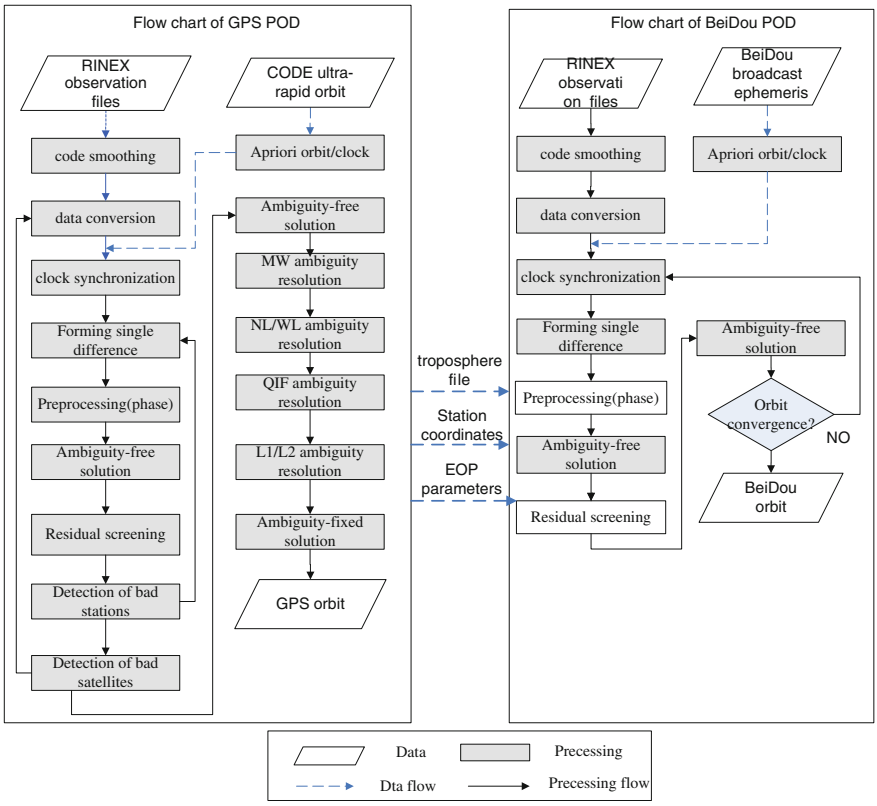

Fig. 5.1 Flow chart of BeiDou/GPS indirect fusion POD

First, GPS satellites orbit was estimated together with station ZTD parameters, station coordinates and EOP based on the data from the 6 internal stations of Beidou tracking network and 10 foreign stations of M-GEX combined with the single-mode GPS data from 120 IGS stations. Then, fix the ZTD parameters, coordinates of Beidou and M-GEX stations as well as EOP parameters. Finally, estimate 6 orbit elements and 5 parameters of Solar radiation pressure of Beidou satellites based on the data from the 6 internal stations of Beidou tracking network and 10 foreign stations of M-GEX.

In the global network data processing of GPS, one session contains daily data. The flow chart is shown in Fig. 5.1. The input data are the raw RINEX observation data, the ultra-rapid orbit forecasted by CODE (the Center for Orbit Determination in Europe) as well as EOP from IERS (International Earth Rotation and Reference Systems Service). First of all, smooth the code pseudo-range data by using phase data. After clock synchronization, an OBS-MAX (observation data maximum) strategy is used to form a single-difference baseline. Then, cycle slips are detected and repaired if possible. Secondly, the residual error is edited based on the

ambiguity float solution in a double-difference level. Then, the bad stations and satellites are excluded. If a bad satellite is detected, this process flow returns to the data format conversion step. If a bad station is detected, the observation files related will be deleted and the baseline will be reformed. Thirdly, ambiguity fixed strategy is selected according to the length of baseline. Finally, the final solution is generated by combining three-days normal equation including GPS orbits, station coordinates, EOP as well as station ZTD parameters. On account of the fact that the ultra-rapid orbit of CODE can reach an accuracy of less than 10 cm, the orbit improvement iteration of GPS is only done once.

Different from GPS, the initial orbit and clock error information used in the POD of BeiDou are from the broadcast ephemeris. To estimate the BeiDou orbit, three days arc is selected. Ionosphere-free linear combination is formed by combining the code and carrier pseudo-range of B1 and B2 frequency (weight ratio of 1:100). The parameters estimated include six orbital elements, 5 Solar radiation pressure parameters (D0, Y0, X0, XC, XS), a set of stochastic pulses and carrier phase ambiguities. As the initial orbit accuracy can only reach meter level, so an iterative loop of orbit improvement is done until convergence. Note that any ambiguity resolution strategy is not done for the POD of Beidou.

5.4 Observation Network

5.4.1 M-GEX

Around the needs of multi-GNSS (GPS/BeiDou/GLONASS/GALILEO) era, the International GNSS Service (IGS) organized a global multi-GNSS test named IGS M-GEX. Now, IGS M-GEX has become an important platform to promote the application of multi-GNSS.

The major task of IGS M-GEX is to complete the global multi-GNSS signal tracking experiment in addition to the conventional IGS business. The experiment focuses on the new available GNSS signals, including modern signals of GPS&GLONASS as well as all of other available signals e.g. BeiDou, Galileo, QZSS and SBAS (Space-based Augmentation System).

5.4.2 Orbit Determination Experiment Data Sources

The data used in the BeiDou POD experiment is from internal 6 stations (Beijing, Wuhan, Xi'an, Shanghai, Kunming, Urumchi) and 10 stations of IGS M-GEX. The particular information of M-GEX station used is listed in Table 5.1. The whole BeiDou satellites tracking network is shown in Fig. 5.2.

Table 5.1 M-GEX stations used in POD

Station	Country	Latitude (°)	Longitude (°)	Altitude (m)	Receiver	Antenna
ABMF	France	16.26	−61.53	−25.0	TRIMBLE NETR9	TRM57971.00
BRST	France	48.38	−4.50	65.8	TRIMBLE NETR9	TRM57971.00
CUT0	Australia	−32.00	115.89	24.0	TRIMBLE NETR9	TRM59800.00
DLF1	Netherlands	51.99	4.39	74.2	TRIMBLE NETR9	LEIAR25.R3
GRAC	France	43.75	6.92	1,319.8	TRIMBLE NETR9	TRM55971.00
KIR8	Sweden	67.88	21.06	498.0	TRIMBLE NETR9	LEIAR25.R3
MAR7	Sweden	60.59	17.26	74.2	TRIMBLE NETR9	LEIAR25.R3
ONS1	Sweden	57.40	11.92	44.4	TRIMBLE NETR9	LEIAR25.R3
REUN	France	−21.21	55.57	1,558.4	TRIMBLE NETR9	TRM55971.00
UNB3	Canada	45.95	−66.64	22.85	TRIMBLE NETR9	TRM57971.00

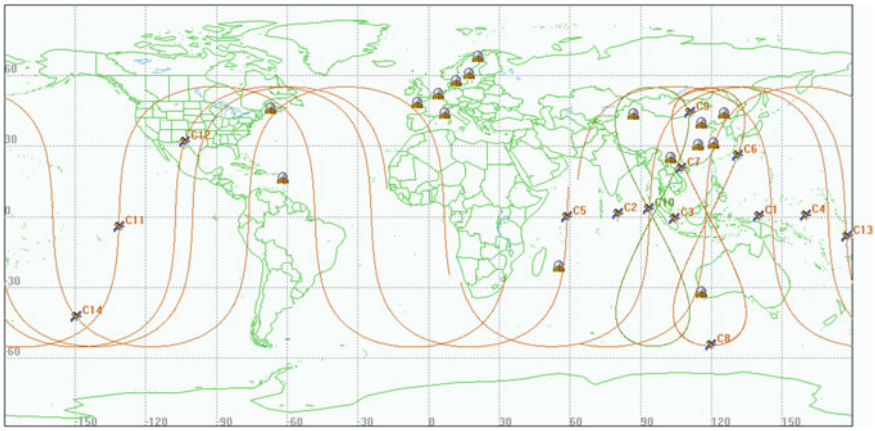

Fig. 5.2 Tracking network for BeiDou satellites

The data used in the GPS POD experiment is from about 120 IGS stations besides the multi-mode data used in BeiDou POD.

5.4.3 BeiDou MEO Satellite Observations Conditions

The visible condition has been significantly improved by introducing the stations of IGS M-GEX. If only the 6 internal BeiDou tracking stations are used, the length of tracking arc for MEO is about 8 h. This quantity can be increased to over 20 h by introducing the stations of IGS M-GEX as shown in Fig. 5.3.

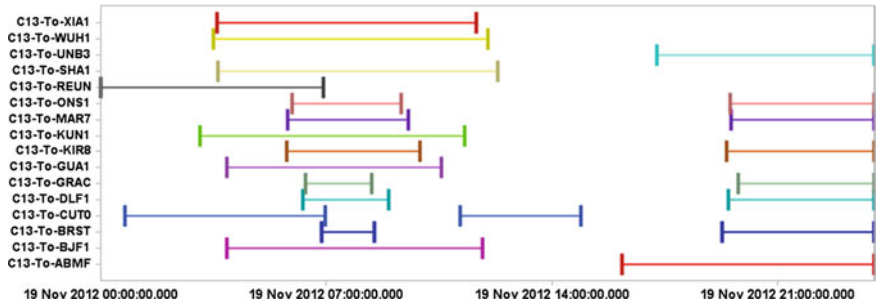

Fig. 5.3 Tracking arc for BeiDou MEO satellite (introducing M-GEX)

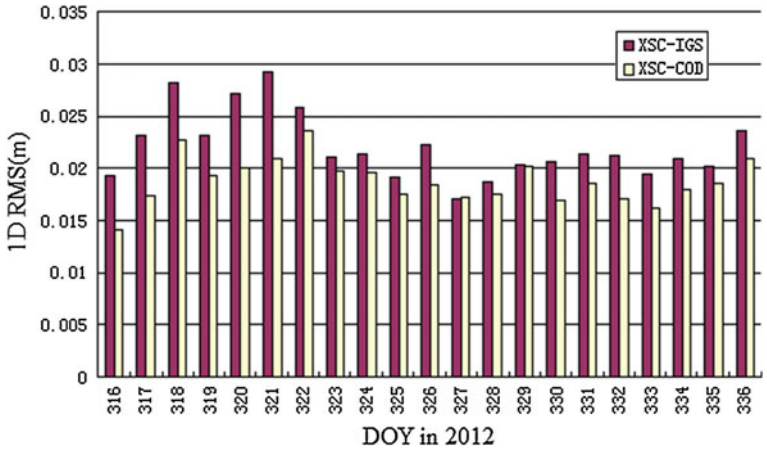

Fig. 5.4 GPS orbit error (compare with CODE and IGS)

In the early days of a new navigation system, to increase the tracking coverage is an effective way to improve the accuracy of orbit determination under the condition of limited dynamics model accuracy.

5.5 Results

5.5.1 POD of GPS

The data used in GPS POD experiment are from the 6 internal stations, 10 foreign stations of M-GEX and 120 IGS stations over a span of 3 weeks from 2012-11-11 to 2012-12-02. The estimated parameters include GPS orbit, ZTD parameters, station coordinates and EOP. Figure 5.4 illustrates the POD result of GPS. Compared with IGS final orbit, the orbit error (1D RMS) is 2.2 cm.

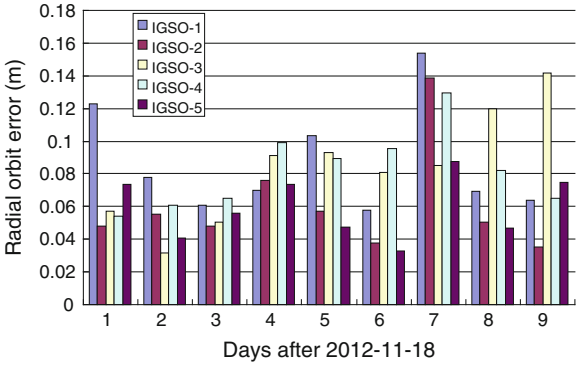

Fig. 5.5 Arc overlap result of BeiDou IGSO satellites

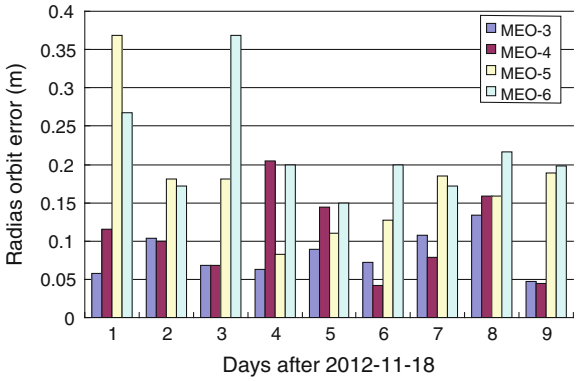

Fig. 5.6 Arc overlap result of BeiDou MEO satellites

5.5.2 POD of BeiDou

The data used in BeiDou POD experiment are from the 6 internal stations and 10 foreign stations of M-GEX, over a span of 12 days from 2012-11-15 to 2012-11-26.

The orbit determination accuracy is verified by orbital overlap method which is to compute the difference of overlapping 2 days ephemeris by comparing the neighboring determination results using 3 days observations.

The result shows: for IGSO satellites the radial error is 7.5 cm (Fig. 5.5) and the 1D RMS is 26 cm, for MEO satellites the radial error is 14 cm (Fig. 5.6) and the 1D RMS is 38 cm for GEO satellites the radial error is 24 cm (Fig. 5.7).

From the result we can see the orbit determining accuracy for GEO-4 is significantly worse than others. To analyze the causes, it is just because the position of GEO-4 is in the east of constellation (Fig. 5.2). The poor observation geometry can't form effective constraint for satellite position parameters.

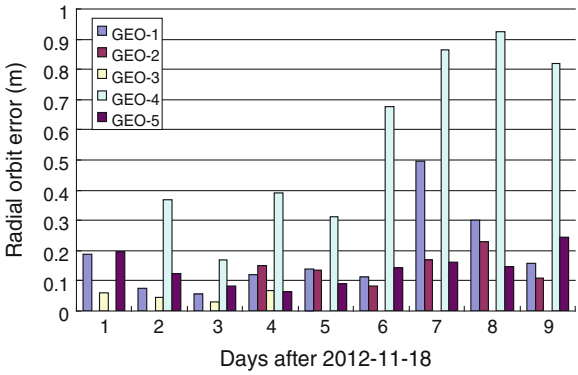

Fig. 5.7 Arc overlap result of BeiDou GEO satellites

5.6 Conclusion

A BeiDou/GPS indirect fusion process method based on double-difference data was proposed in this article. Based on the multi-mode navigation data from the 6 internal stations and 10 foreign stations of M-GEX combined with the GPS data from 120 IGS stations, an orbit determination accuracy verification experiment was developed. The orbit overlapping verified that the POD of BeiDou can reach such accuracy: for IGSO satellites, the radial error is 7.5 cm and the 1D RMS is 26 cm, for MEO satellites the radial error is 14 cm and the 1D RMS is 38 cm, for GEO satellites the radial error is 24 cm. The orbit 1D RMS for GPS satellite is about 2 cm by comparing with IGS final products.

References

1. Shi C, Zhao QL, Li M et al (2012) Precise orbit determination of Beidou satellites with precise positioning. Sci China Earth Sci 55:P1079–P1086
2. Zhu J, Wang J, Zeng G, Li J, Chen J (2013) Precise orbit determination of BeiDou regional navigation satellite system via double-difference observations. In: Proceedings of lecture notes in electrical engineering, China satellite navigation conference (CSNC) 2013, vol 245. pp 241–252

Chapter 6
The Influence Analysis of the Satellite Clock Performance with the Satellite Troubles

Xin Shi, Li Liu, Xianghua Hu, Gang Yao, Jing Li, Shuanglin Huang and Tao Cui

Abstract All kinds of environment factors have great influence on the in-orbit running of the satellite clock. Because of the scarce onboard experience in the national self-developing satellite clock, the influence analysis on the in-orbit running environment of the satellite clock is very necessary. In this paper, the variety of the satellite clock performance with the satellite troubles has been analyzed by using the Least Mean Square algorithm. Through computing the frequency accuracy, frequency drift rate and frequency stability of the satellite clock before and after the satellite troubles, the influence on the satellite clock performance of the satellite troubles has been deep studied. According to the experiment results, there is no obvious change of the satellite clock performance with the satellite troubles, so the satellite troubles have no obvious influence on the satellite clock.

Keywords Satellite troubles · Frequency accuracy · Frequency drift rate · Satellite clock performance

6.1 Introduction

The satellite clock is the time base onboard the satellite of the navigation signal forming and the system range measuring, which performance directly determines the navigation satellite time accuracy and the user navigation positioning precision. The in-orbit running of the satellite clock is influenced by all kinds of environment

X. Shi (✉) · L. Liu · X. Hu · G. Yao · J. Li · S. Huang
Beijing Satellite Navigation Center, Beijing 100094, China
e-mail: 876359113@qq.com

T. Cui
North China Institute of Computing Technology, Beijing 100083, China

J. Sun et al. (eds.), *China Satellite Navigation Conference (CSNC) 2014 Proceedings: Volume III*, Lecture Notes in Electrical Engineering 305,
DOI: 10.1007/978-3-642-54740-9_6,

factors and there's no onboard experience in the national self-developing satellite clock, so the satellite clock performance influence should be analyzed from the satellite clock running state change and the space environment.

In this paper, the variety of the satellite clock performance with the satellite troubles has been analyzed to evaluate the satellite troubles influence on the satellite clock performance. The analysis results would provide the reference to the development of the national satellite navigation and positioning system.

6.2 Clock Performance Analysis Methods

6.2.1 Least Mean Square Algorithm

For the satellite clock difference sequence, the Least Mean Square algorithm was used to get the poly-fit parameters according to which the poly-fit error was calculated.

In normal instance, for the relation between any satellite clock reading T and the system time t can be expressed by a two-degree polynomial, that is,

$$T - t = a_0 + a_1(t - t_0) + a_2(t - t_0)^2 \tag{6.1}$$

In this equation, a_0, a_1 and a_2 is respectively the clock difference, clock velocity and half acceleration of the difference between the satellite clock time and the system time at t_0. If the second length of clock reading is even, a_2 is equal to 0.

Defining z is the clock difference observation value between the satellite clock and the system time at t, there is,

$$z(t) = T - t \tag{6.2}$$

Obviously, if the observation time is t_j, the observation error is v_j, then the error equation is,

$$z(t_j) + v_j = a_0 + a_1(t_j - t_0) + a_2(t_j - t_0)^2 \tag{6.3}$$

If $\hat{a}_0,\ \hat{a}_1,\ \hat{a}_2$ is respectively the evaluation of the clock parameters of a_0, a_1 and a_2, there is,

$$\hat{z}(t_j) = \hat{a}_0 + \hat{a}_1(t_j - t_0) + \hat{a}_2(t_j - t_0)^2 \tag{6.4}$$

According to the Least Mean Square algorithm, $\hat{a}_0,\ \hat{a}_1,\ \hat{a}_2$ can be obtained by clock observation data time and time, that is,

$$\begin{bmatrix} \hat{a}_0 \\ \hat{a}_1 \\ \hat{a}_2 \end{bmatrix} = \begin{bmatrix} n & \sum_{j=1}^{n} \Delta t_j & \sum_{j=1}^{n} \Delta t_j^2 \\ \sum_{j=1}^{n} \Delta t_j & \sum_{j=1}^{n} \Delta t_j^2 & \sum_{j=1}^{n} \Delta t_j^3 \\ \sum_{j=1}^{n} \Delta t_j^2 & \sum_{j=1}^{n} \Delta t_j^3 & \sum_{j=1}^{n} \Delta t_J^4 \end{bmatrix}^{-1} \begin{bmatrix} \sum_{j=1}^{n} z_j \\ \sum_{j=1}^{n} z_j \Delta t_j \\ \sum_{j=1}^{n} z_j \Delta t_j^2 \end{bmatrix} \tag{6.5}$$

Among the above equation, n is the observation times, $\Delta t_j \equiv t_j - t_0$.

On the other hand, the relation between the system time poly-fit value error m_t and the single time error m_x, which express the relation between the time poly-fit precision and the observation precision, is analyzed in the theory. At the condition of the equal precision observation, if the observation times is $n = 2\ m + 1$, and

$$t_j = t_0 + j\tau \quad j = -m, \ldots, -1, 0, 1, \ldots m \tag{6.6}$$

there is,

$$\begin{bmatrix} \hat{a}_0 \\ \hat{a}_1 \\ \hat{a}_2 \end{bmatrix} = \begin{bmatrix} 2m+1 & 0 & b \\ 0 & b & 0 \\ b & 0 & c \end{bmatrix}^{-1} \begin{bmatrix} \sum_{j=-m}^{m} z_j \\ \tau \sum_{j=1}^{m} j\left(z_j - z_{-j}\right) \\ \tau^2 \sum_{j=1}^{m} j^2\left(z_j + z_{-j}\right) \end{bmatrix} \tag{6.7}$$

In the above equation,

$$b = 2\sum_{j=1}^{m} \Delta t_j^2 = \frac{\tau^2}{3} m(m+1)(2m+1) \tag{6.8}$$

$$c = 2\sum_{j=1}^{m} \Delta t_j^4 = \frac{\tau^4}{15} m(m+1)(2m+1)(3m^2 + 3m - 1) \tag{6.9}$$

Therefore,

$$\begin{bmatrix} \hat{a}_0 \\ \hat{a}_1 \\ \hat{a}_2 \end{bmatrix} = \frac{1}{nbc - b^3} \begin{bmatrix} bc & 0 & -b^2 \\ 0 & nc - b^2 & 0 \\ -b^2 & 0 & nb \end{bmatrix} \begin{bmatrix} \sum_{j=-m}^{m} z_j \\ \tau \sum_{j=1}^{m} j\left(z_j - z_{-j}\right) \\ \tau^2 \sum_{j=1}^{m} j^2\left(z_j + z_{-j}\right) \end{bmatrix} \tag{6.10}$$

then the system time t at any time is expressed by

$$t = T - \left[\hat{a}_0 + \hat{a}_1(t - t_0) + \hat{a}_2(t - t_0)^2\right] \tag{6.11}$$

Without doubt, the accuracy of the system time provided by the satellite clock is mainly determined by the estimating precision. According to the error diffusion equation, the relation between the system time poly-fit error m_t and the single time error m_x is expressed,

If $\Delta t = t - t_0 = km\tau$, then

$$m_t^2 = \frac{45m^2k^2(mk^2 - 1) + 9(3m^2 + 3m - 1)(mk^2 + m + 1)}{(2m + 3)(m + 1)(4m^2 - 1)} m_x^2 \tag{6.12}$$

Because under the normal condition $m \gg k > 1$, the above equation is approximately

$$m_t^2 = \frac{45k^4}{8m} m_x^2 \tag{6.13}$$

or

$$m_t = \frac{3k^2}{4}\sqrt{\frac{10}{m}} m_x \tag{6.14}$$

When the observation time or poly-fit time is long, the instability of the satellite clock would be operating [1], at this time, there is the observation equation,

$$z(t_j) = a_0 + a_1(t_j - t_0) + a_2(t_j - t_0)^2 + \Delta(t_j) \tag{6.15}$$

Among this equation, $\Delta(t_j) = \sigma_y \cdot (t_j - t_0)$ is the error caused by the satellite clock instability, which is defined as σ_y.

According to the above analysis, the poly-fit error is,

$$m_t^2 = \frac{45k^4}{8m} m_x^2 + \sigma_y^2 \cdot (t - t_0)^2 \tag{6.16}$$

6.2.2 Clock Performance Estimation Algorithm

6.2.2.1 Frequency Accuracy

Considering the frequency drift rate influence on the frequency accuracy, short-term high-frequency clock difference data is used to calculate the frequency accuracy. Through one-degree poly-fit by using the high-frequency clock

difference data, the one-degree polynomial coefficient A is obtained, which is the frequency accuracy, the model is,

$$X_i = X_0 + (t - t_0)A + \varepsilon_i \tag{6.17}$$

Among the above equation, X_i is the clock difference at t_i, X_0 is the clock difference at t_0, A is the one-degree polynomial coefficient of the time model, which is the clock frequency accuracy A.

But in the real computing process, the frequency accuracy calculated in different time is diverse because of the space disturbing factors such as different data measure accuracy and different satellite clock noise level. Thus, the frequency accuracy should be analyzed with the frequency drift rate.

6.2.2.2 Frequency Drift Rate

The frequency drift rate of the satellite clock can be estimated by using long-term clock velocity. The one-degree polynomial coefficient can be obtained once a day by using 15 days longer satellite-ground clock data, which is the clock velocity. Then the clock acceleration can be got from calculating the variance rate of the clock velocity, which is the clock frequency rate.

Because the frequency rate and its acceleration can be obtained by the two-degree difference of the clock difference data, with only different units, the frequency rate based on the clock difference data can be obtained through assuring the acceleration of the two-degree time model. In order to get the more accurate frequency drift rate, the regression analysis method can be adopted to assure the coefficient of the time model and get the satellite clock accuracy and drift rate, according to the Least Mean Square principle.

Because of the influence of the internal parts aging and the environment changing, the frequency will decrease with the time increase, which linear rate is called frequency drift rate. The frequency drift is the basic characteristic of the frequency source's long-term running work, which is defined as the continuous frequency source output frequency. The average variance of the output frequency in unit time is called aging rate for the crystal vibrator.

A group sampling value y_i of the relative frequency bias measured at an interval according to time sequence,

$$y_i = \frac{1}{\tau} \int_{t_i}^{t_i+\tau} y(t)dt \tag{6.18}$$

The sampling period is T. The day drift rate D can be obtained by using the Least Mean Square algorithm, which calculating process is as the frequency bias working out. The poly-fit result is,

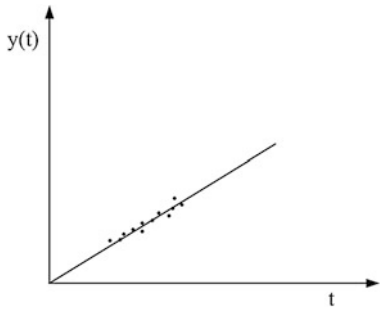

Fig. 6.1 Frequency drift ploy-fit

$$D = \frac{\sum_{i=1}^{N}(y_i - \bar{y})(t_i - \bar{t})}{\sum_{i=1}^{N}(t_i - \bar{t})^2} \tag{6.19}$$

The poly-fit sketch map is as Fig. 6.1.

6.2.2.3 Frequency Stability

The frequency stability is the random frequency value of the frequency standard. The frequency stability in the time area is the random wave level of the average frequency in some time interval, which is called sampling time. The time area frequency stability is showed by the square root of double-sampling variance (Allan Variance).

The sampling time and group number of the time area frequency stability estimation is ruled as Table 6.1.

The day drift rate stability can be calculated by the data measured by the day drift according to the Allan Variance formula as (6.20) or (6.21).

$$\sigma_y^2(\tau) = \frac{1}{2(M-1)}\sum_{i=1}^{M-1}[y_{i+1} - y_i]^2 \tag{6.20}$$

$$\sigma_y^2(\tau) = \frac{1}{2(N-2)\tau^2}\sum_{i=1}^{N-2}[x_{i+2} - 2x_{i+1} + x_i]^2 \tag{6.21}$$

There are many kinds of data sources, including onboard phase difference data, satellite-ground two-way time transfer data [2], laser two-way time transfer data, receiver pseudo-range phase data [3] and so on. The calculated clock difference accuracy has diverse with different data source. In order to estimate the satellite clock stability, the data accuracy in the sampling time should be better than the error caused by the clock stability. So, considering the clock difference accuracy

Table 6.1 Sampling time and group number

Sampling time τ	Sampling groups m
1 s	100
10 s	50
100 s	30
1 d	14

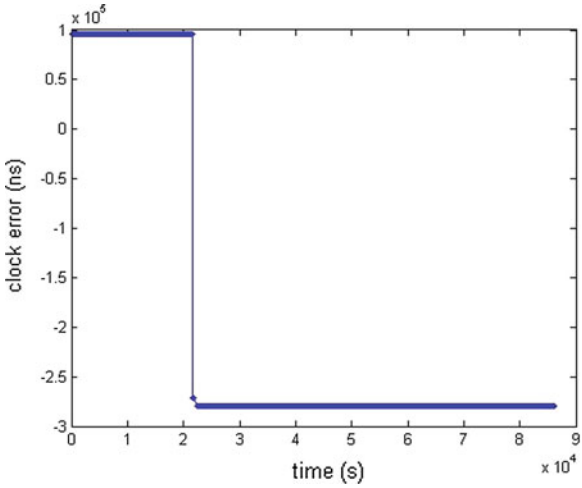

Fig. 6.2 Clock difference result

calculated by all kinds of data, the mid-short term stability under 1,000 s should adopt onboard phase difference data and laser two-way time transfer data. The stability longer than 10,000 s should use satellite-ground two-way time transfer data and receiver pseudo-range phase data besides the above two kinds of data.

6.3 Satellite Trouble Influence Analysis

6.3.1 Trouble Description

Some satellite occurred a trouble and the clock difference had a large hopping, which is as Fig. 6.2.

The satellite clock performance variance was analyzed by the Least Mean Square algorithm and the clock performance estimation algorithm.

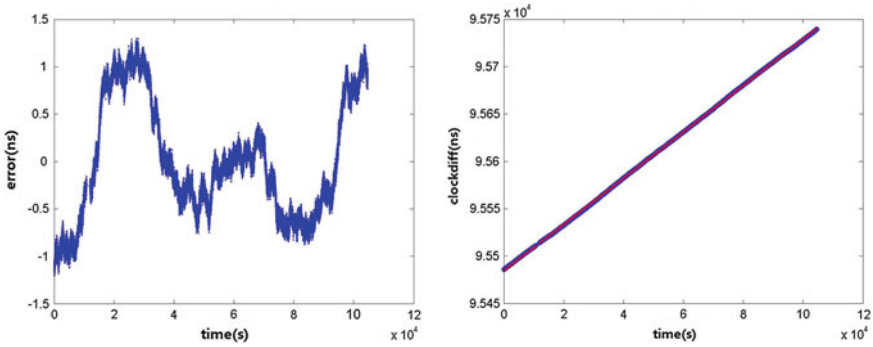

Fig. 6.3 Two degree poly-fit error of satellite clock difference before the trouble

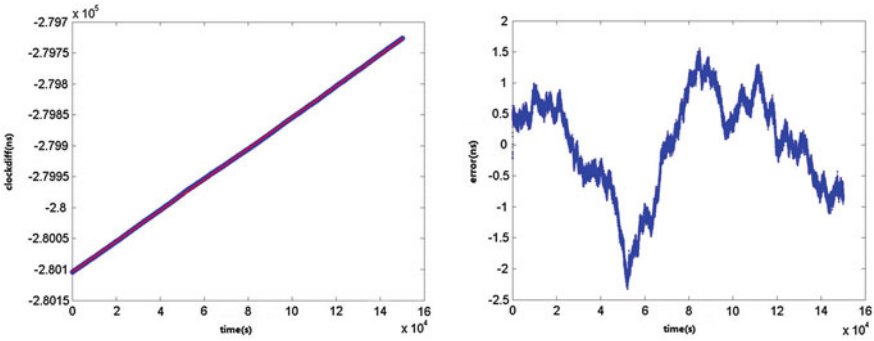

Fig. 6.4 Two degree poly-fit error of satellite clock difference after the trouble

6.3.2 Real Measured Data Experimental Result

6.3.2.1 Satellite Clock Difference Poly-Fit Error Analysis

Through analyzing the satellite clock difference result of fore-and-aft satellite trouble by using the Least Mean Square algorithm, the two-degree poly-fit result of the satellite clock difference before and after the satellite trouble is respectively as Figs. 6.3 and 6.4.

With the a_0 compensation, the clock difference data after the satellite trouble recovery was added to the clock difference data before the trouble, which is analyzed by two-degree poly-fit and the result is as Fig. 6.5.

From the above result, the compensated satellite clock two-degree poly-fit error inter-accordant precision is better than 2.5 ns. The error change of fore-and aft satellite trouble is less than 1 ns, which is shown as Fig. 6.5. The satellite clock

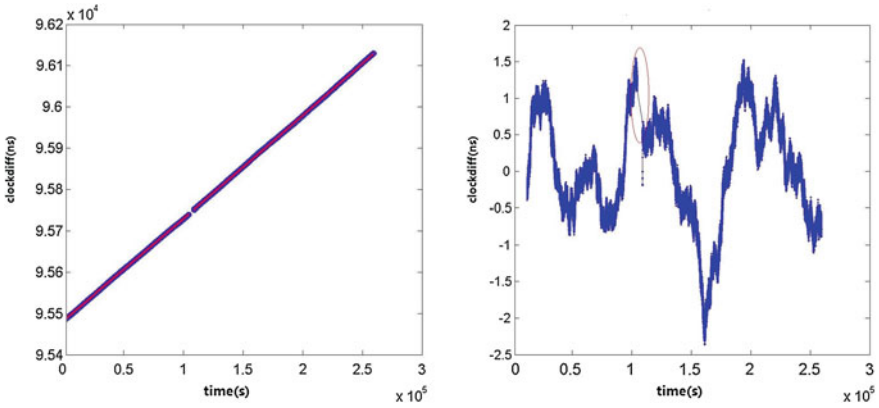

Fig. 6.5 Two degree poly-fit error of satellite clock difference after the compensation

Table 6.2 Satellite clock performance difference between fore-and-aft satellite trouble

Period	Frequency accuracy	Frequency drift rate	Allan 10,000 s stability	Allan day stability
Before trouble	1.8273E−12	4.9991E−14	6.7446E−14	4.0020E−14
After trouble	2.7243E−12	3.0774E−14	6.4101E−14	3.8844E−14

two-degree poly-fit error before and after the satellite trouble is in the error scope of the measuring noise. So the satellite trouble has no obvious influence on the satellite clock comparative result.

6.3.2.2 Satellite Clock Performance Analysis

The satellite clock performance was analyzed by the clock performance estimation algorithm with the data before and after the satellite trouble. The statistic result is as Table 6.2.

The clock different data Allan variance [4] curve before the satellite trouble is as Fig. 6.6.

The clock different data Allan variance curve after the satellite trouble is as Fig. 6.7.

From the above analysis, the 10,000 s stability difference is 3.345E−15 and day stability difference is 1.176E−15 before and after the satellite trouble. The 10,000 s and day stability instability caused by measuring error is respectively 3E−14 and 3E−15. So the 10,000 s and day stability difference before and after the satellite trouble is in the scope of the instability caused by the measuring error [5]. The satellite trouble has no obvious influence on the satellite clock performance.

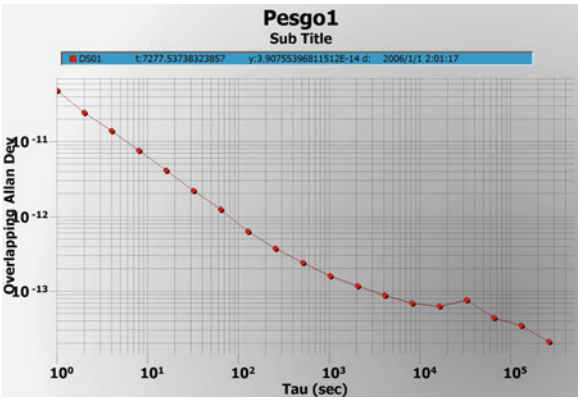

Fig. 6.6 Clock difference Allan variance curve before trouble

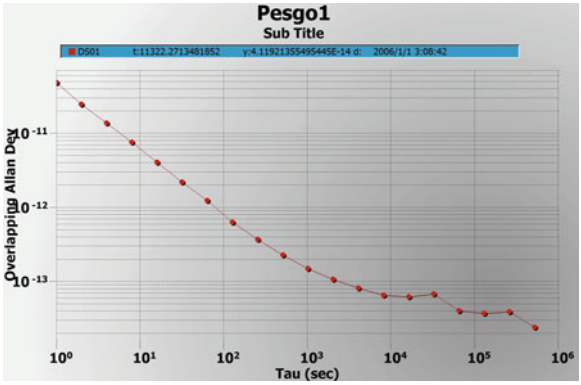

Fig. 6.7 Clock difference Allan variance curve after trouble

6.4 Conclusion

The difference of the satellite clock two-degree poly-fit error before and after the satellite trouble is caused by the measuring noise. The satellite trouble has no obvious influence on the satellite clock comparative result.

The 10,000 s and day stability difference before and after the satellite trouble is in the scope of the instability caused by the measuring error. The satellite trouble has no obvious influence on the satellite clock performance.

References

1. Weiss MA (1985) Weighting and smoothing of data in GPS common view time transfer. In: Proceedings of precise time and time interval systems and applications meeting, pp 261–275
2. Plumb J (2003) Carrier phase time transfer using global positioning system. University of Colorado, Colorado

3. Kirchner D (1991) Two2way time transfer via communication satellites. Proc IEEE 79(7):983–990
4. Riley WJ (2002) The Hadamard variance. Hamilton Technical Services
5. User manual—Stable32 frequency stability analysis. Hamilton Technical Services, 2005

Chapter 7
Analysis of Effect About Solar Radiation Pressure for Satellite Yaw Attitude

Meihong Li, Hui Yang, Lifang Yuan and Zhaozhao Gao

Abstract In order to meet the demands of energy and thermal control, inclined orbit satellite usually has the yaw attitude control. Now, the general yaw attitude methods have the theoretic dynamic offset, approximate dynamic offset and dynamic-zero offset. For the navigation position system, different yaw attitude controls of inclined orbit satellite will affect the solar radiation pressure dynamic model of precise orbit determination. The paper will research the different yaw attitude methods and compare with the foreign navigation satellite. The paper researches the yaw attitude in different control modes for the native and foreign navigation inclined orbit satellite. According to satellite characteristic, it analysis the effects about solar radiation pressure for different yaw attitude controls by differential area method, and gives the compensation model. It has the significances reference to improve the precise orbit determination.

Keywords Yaw attitude · Solar radiation pressure · Orbit determination

7.1 Introduction

In order to meet the demands of energy and thermal control, inclined orbit satellite usually has the yaw attitude control. Now, the general yaw attitude methods have the theoretic dynamic offset, approximate dynamic offset and dynamic-zero offset. For the navigation position system, different yaw attitude controls of inclined orbit satellite will affect the solar radiation pressure dynamic model of precise orbit determination. The paper will research the different yaw attitude methods and compare with the foreign navigation satellite. So, it need to analysis the effects about solar radiation pressure for different yaw attitude controls.

M. Li (✉) · H. Yang · L. Yuan · Z. Gao
China Academy of Space Technology, Beijing, PR China
e-mail: meihong_li@163.com

J. Sun et al. (eds.), *China Satellite Navigation Conference (CSNC) 2014 Proceedings: Volume III*, Lecture Notes in Electrical Engineering 305,
DOI: 10.1007/978-3-642-54740-9_7,

The paper researches the yaw attitude in different control modes for the native and foreign navigation inclined orbit satellite. According to satellite characteristic, it analysis the effects about solar radiation pressure for different yaw attitude controls by differential area method, and decreases the difference one order of magnitude by the compensation model. It has the significances reference to improve the precise orbit determination.

7.2 Yaw Attitude Methods

7.2.1 The Theoretic Dynamic Offset

For inclined orbit satellite inclination is 55°, the angle range of sun to the orbit plane is very large. If solar panels track the sun projection in orbit plane by single degree of freedom, which will can't need the satellite energy demand. So, it can make the sun in body XOZ plane by the yaw attitude control, and solar panels can track the sun with real-time by rolling Y-axes of body, which can need the satellite energy demand. Besides, the yaw attitude control usually make the sun in body +XOZ plane (or +XOZ plane) when considering the thermal control requirements.

Yaw formula as follows [1–3]:

When it makes the sun in body +XOZ plane, then

$$\varphi = \text{atan}(\tan\beta, \sin\mu) \tag{7.1}$$

When it makes the sun in body −XOZ plane, then

$$\varphi = \text{atan}(-\tan\beta, -\sin\mu) \tag{7.2}$$

where, β is the sun's elevation of satellite orbit plane, and μ is geometry angle between the satellite and the midnight of the orbit.

The yaw rate can be obtained from the formula (7.1) and (7.2):

$$\dot{\varphi} = \dot{\mu} \cdot \text{atan}\,\beta \cdot \cos\mu/(\sin^2\mu + \tan^2\beta) \tag{7.3}$$

where, $\dot{\mu}$ is the orbit rate and fixed.

When $\mu = 0°$ or $\mu = 180°$,

$$\dot{\varphi} = \pm\dot{\mu}/\tan\beta \tag{7.4}$$

Figure 7.1 shows the curves of the theoretic yaw attitude, the yaw rate and the sun's elevation. As can be seen by formula (7.4) and Fig. 7.1, when the β is small and $\mu = 0°$ or $\mu = 180°$, the yaw rate gets very big, which cause the actuator control moment and angular momentum gets very large, and margins gets small.

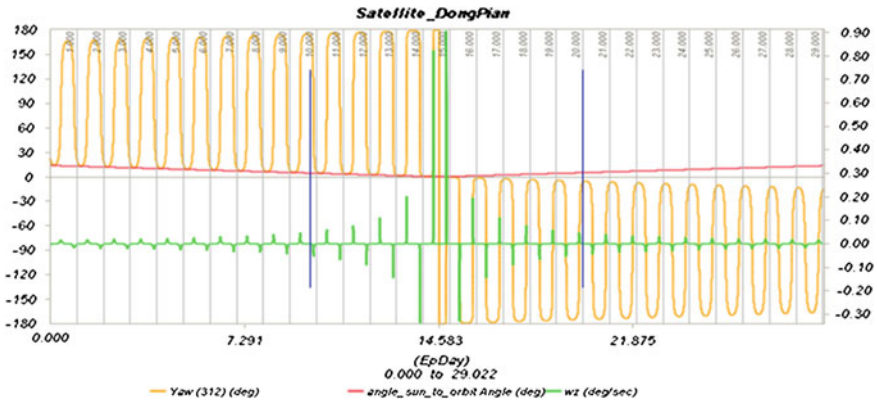

Fig. 7.1 *Curve* the theoretic yaw attitude, the yaw rate and the sun's elevation

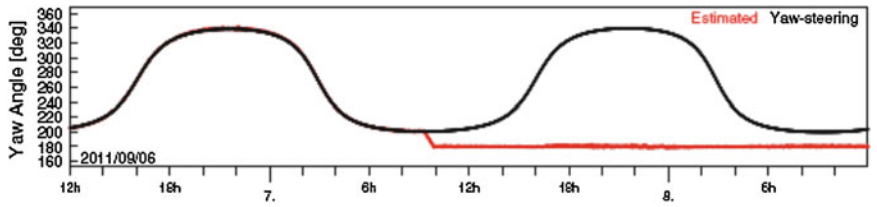

Fig. 7.2 *Curve* QZSS IGSO yaw attitude ($|ß| < 20°$)

So, it takes the approximate dynamic offset method or zero offset method, when the β is small and $\mu = 0°$ or $\mu = 180°$.

7.2.2 The Dynamic-Zero Offset

The dynamic-zero offset method is the same as the theoretic dynamic offset except for small β. When the β is small, the yaw keeps at zero. QZSS IGSO satellite just takes such method. Figure 7.2 shows the curves of QZSS IGSO yaw attitude ($|ß| < 20°$) [4].

7.2.3 The Approximate Dynamic Offset

The approximate dynamic offset method is the same as the theoretic dynamic offset except for small β and $\mu = 0°$ or $\mu = 180°$. Table 7.1 gives the GPS yaw method of approximate dynamic offset [5].

Table 7.1 GPS yaw method of approximate dynamic offset

	GPS II/IIA	GPSIIR	GPSIIF-1
Max yaw rate (°/s)	0.10/0.13	0.2	0.11
Noon maneuver	$\|ß\| < 3.6/4.9°$, using max yaw rate	$\|ß\| < 2.4°$, using max yaw rate, max duration 15 min	$\|ß\| < 4°$, yaw rate 0.11°/s, max duration 27 min
Shadow crossing	Using max yaw rate all time in the shadow	$\|ß\| < 2.4°$ and in the shadow, using max yaw rate, max duration 15 min	$ß\| < 2.4°$ and in the shadow,,yaw rate 0.06°/s, max duration 54 min

7.3 Analysis of Solar Radiation Pressure for Different Satellite Yaw Attitude

According to satellite characteristic, this section calculates the satellite area in sunlight by differential area method and analysis the solar radiation pressure for different yaw attitude controls. At the same time, it compares the difference of solar radiation pressure for dynamic-zero offset and approximate dynamic offset with the theoretic dynamic offset.

All the follow data is from the same duration of IGSO dynamic-zero. And solar radiation pressure is discussed in the orbit reference frame.

7.3.1 Solar Radiation Pressure for the Theoretic Dynamic Offset

Figure 7.3 shows IGSO Solar radiation pressure for the theoretic dynamic offset. By Fig. 7.3 we can see that:

For the theoretic dynamic offset, solar radiation pressure has the same variation every day. Starting with 12:00 a.m., solar radiation pressure changes like a sine function in the X-axis direction and like a cosine function in the Z-axis direction except for shadow.

When the satellite in the shadow, the solar radiation pressure is zero and not influenced by the attitude. So, in order to simply analysis, it will ignore the shadow.

7.3.2 Solar Radiation Pressure for the Dynamic-Zero Offset

The solar radiation pressure in zero offset is consistent with the theoretic dynamic offset. Figure 7.4 shows IGSO Solar radiation pressure for the zero offset.

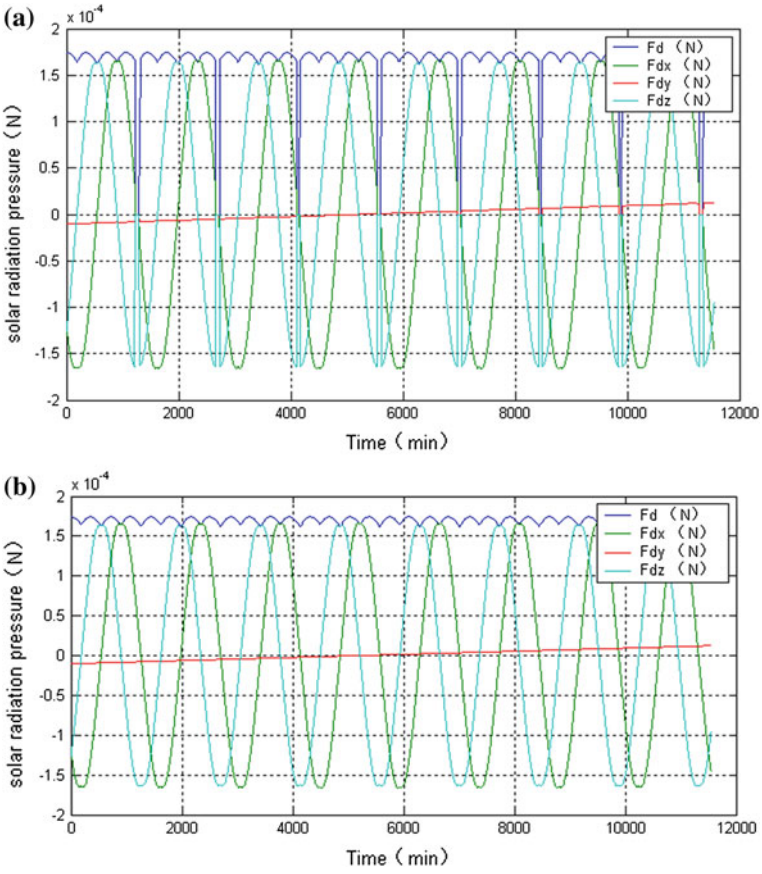

Fig. 7.3 **a** IGSO Solar radiation pressure for the theoretic dynamic offset (considering shadow). **b** IGSO Solar radiation pressure for the theoretic dynamic offset (ignoring shadow)

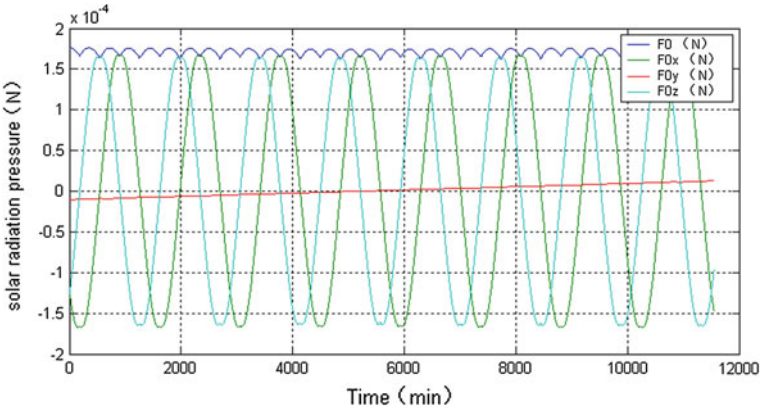

Fig. 7.4 IGSO Solar radiation pressure for the zero offset

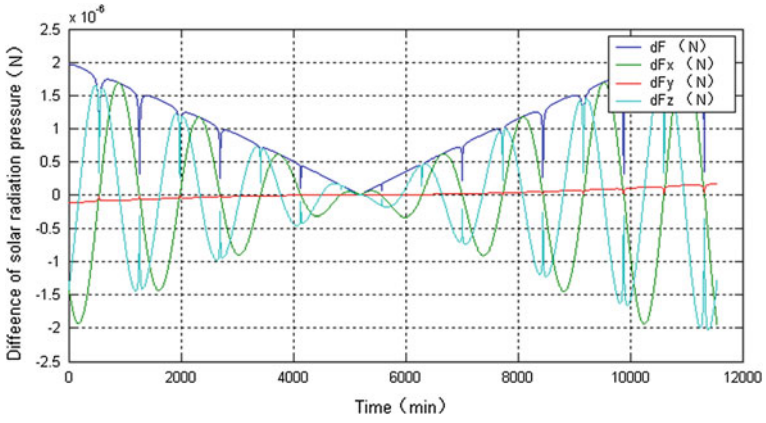

Fig. 7.5 The pressure difference: zero offset minus dynamic offset

Figure 7.5 shows the difference of the solar radiation pressure between the dynamic offset and zero offset. As can be seen:

1. Compared with the theoretic dynamic offset, the solar radiation pressure in zero offset increases.
2. The pressure difference between zero offset and dynamic offset reaches the maximum at conversion time, the minimum in the middle. The pressure difference dF, dFx, dFz are about 3×10^{-6} N and dFy is about 2×10^{-7} N.
3. The pressure difference between zero offset and dynamic offset has regularity in every direction. The magnitude of pressure difference decreases linearly and then increases linearly except for shadow. Starting with 12:00 a.m., the pressure difference changes like a sine function in the X-axis direction and like a cosine function in the Z-axis direction except for shadow.
4. At midnight, the satellite is in the shadow and the pressure difference is zero. At midday, the pressure difference focuses in the Z-axis direction, and no component in the X-axis direction.

7.3.3 Solar Radiation Pressure for the Approximate Dynamic Offset

The solar radiation pressure in approximate dynamic offset is consistent with the theoretic dynamic offset. Figure 7.6 shows the difference of the solar radiation pressure between the approximate dynamic offset and theoretic dynamic offset. As can be seen:

1. Compared with the theoretic dynamic offset, the solar radiation pressure in approximate dynamic offset increases at midday and midnight. The pressure

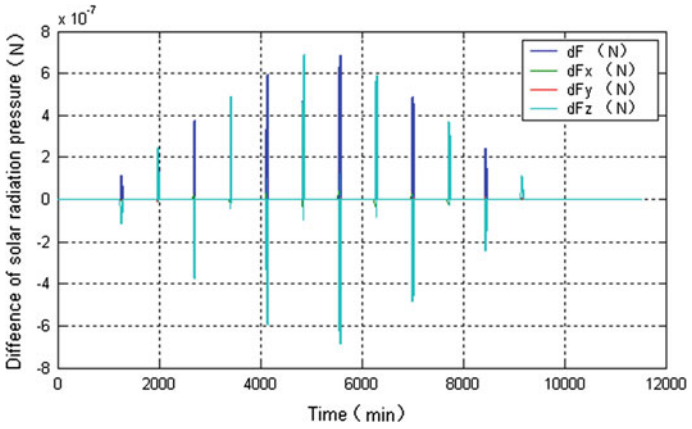

Fig. 7.6 The pressure difference: approximate dynamic offset minus dynamic offset

increases in the +Z-axis direction at midday and increases in the −Z-axis direction at midnight.

2. The pressure difference between approximate dynamic offset and dynamic offset reaches the maximum when the sun's elevation is zero (Figs. 7.7, 7.8). The pressure difference dF, dFz are about 3×10^{-6} N and dFx, dFy are about 2×10^{-7} N.
3. At midnight, the satellite is in the shadow and the pressure difference is zero.
4. Fz is the radial pressure of solar radiation. When analyzing the impact of Fz to the satellite semi-major axis, eccentricity needs to be considered. Generally, the IGSO/MEO eccentricity not more than 0.001. Seen by the follow formula, the effect of Fz to the semi-major axis will be reduced two orders of magnitude.

$$\frac{da}{dt} = \frac{2}{n\sqrt{1-e^2}}[Fa_z \cdot e \cdot \sin f + Fa_x(1 + e \cdot \cos f)] \tag{7.5}$$

where, Fa_z is the radial acceleration, Fa_x is the tangentially acceleration.

7.4 Compensation Analyses for Differences

GPS satellite just adds the experience compensation force to the solar radiation pressure model and gradually improves the accuracy of orbit determination. Learning from the development of GPS satellite pressure model, we can establish the compensation model for pressure difference caused by yaw models. Considering the pressure difference by dynamic-zero offset higher than approximate

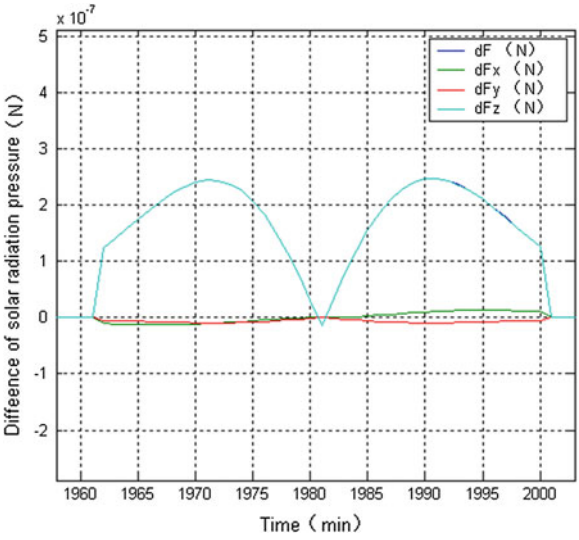

Fig. 7.7 The pressure difference at midday: approximate dynamic offset minus dynamic offset

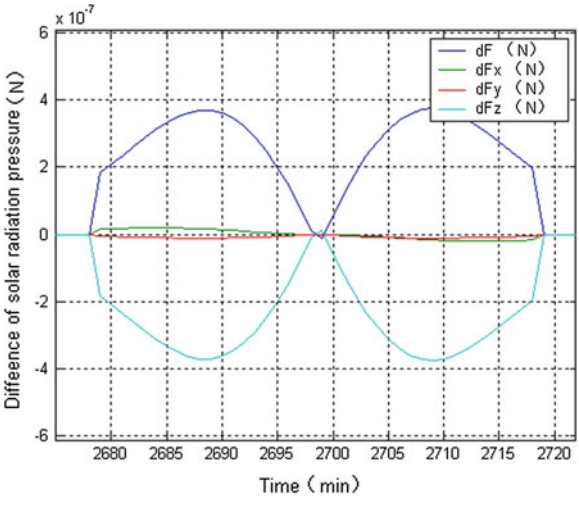

Fig. 7.8 The pressure difference at midnight: approximate dynamic offset minus dynamic offset

dynamic offset an order of magnitude, this section only analysis the compensation model for pressure difference caused by dynamic-zero offset.

For the pressure difference is zero at midnight, firstly it can ignore the midnight to establish the compensation model easily. Then for the midnight, it just needs to set the model value at zero.

Define the zero offset starting time as time 0, the time t in zero offset as variable. The following formula (7.6) gives the relationship between the compensation force YdF and t.

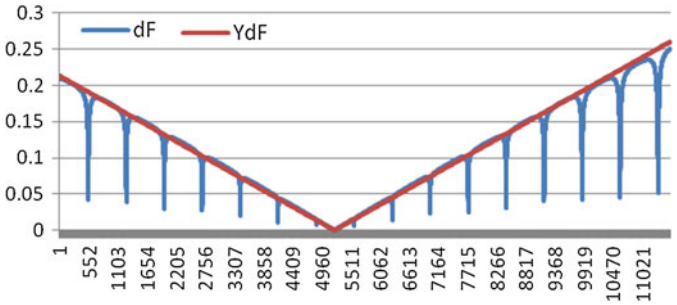

Fig. 7.9 The compensation curves YdF for the difference magnitude dF (10^{-5} N)

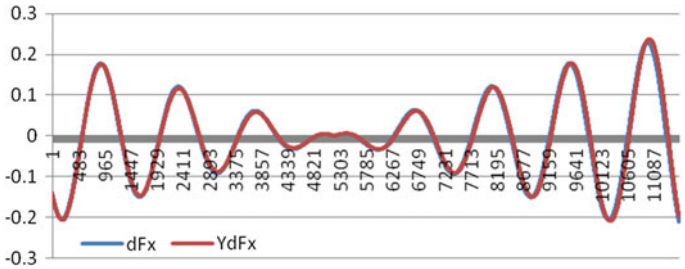

Fig. 7.10 The compensation curves YdFx for the difference in X-axis direction dFx (10^{-5} N)

$$
\begin{aligned}
\mathrm{YdF} &= \begin{cases} -\mathrm{kt} + \mathrm{b} & \mathrm{t} \le \mathrm{t}^* \\ \mathrm{kt} - \mathrm{b} & \mathrm{t} > \mathrm{t}^* \end{cases} \\
\mathrm{YdF}x &= \mathrm{YdF} \times \sin(\mathrm{w}(\mathrm{t} - \mathrm{t}_0)); \\
\mathrm{YdFz} &= \mathrm{YdF} \times \cos(\mathrm{w}(\mathrm{t} - \mathrm{t}_0)); \\
\mathrm{w} &= 2\pi/\mathrm{T}; \\
\mathrm{b} &= -\mathrm{kt}^*
\end{aligned}
\tag{7.6}
$$

where, t_0 is the first midday time from the zero offset starting time. t* is the first midday time from the zero offset starting time. k is the linear slope of pressure difference. T is the satellite cycle time. Now, dFy magnitude is very small and about 2×10^{-7} N, so it needs not to establish the compensation model for that.

Figures 7.9, 7.10, 7.11 and 7.12 shows the compensation curves and compensation errors for the pressure in zero offset. As can be seen:

(1) By establishing the compensation model, it can reduce the pressure difference an order of magnitude. The magnitudes of pressure difference dF, dFx, dFz are about 3×10^{-6} N. When establishing the compensation model, the magnitudes are about 5×10^{-7} N except for midday time.

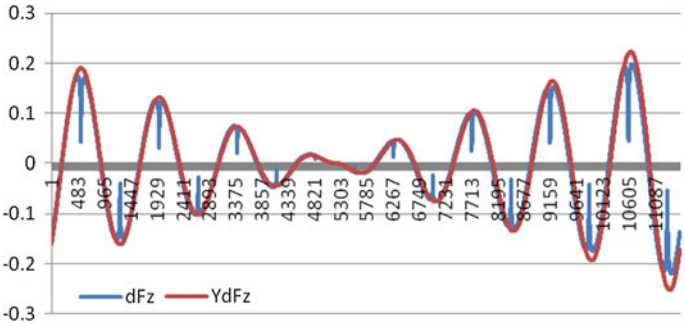

Fig. 7.11 The compensation curves YdFz for the difference in Z-axis direction dFz (10^{-5} N)

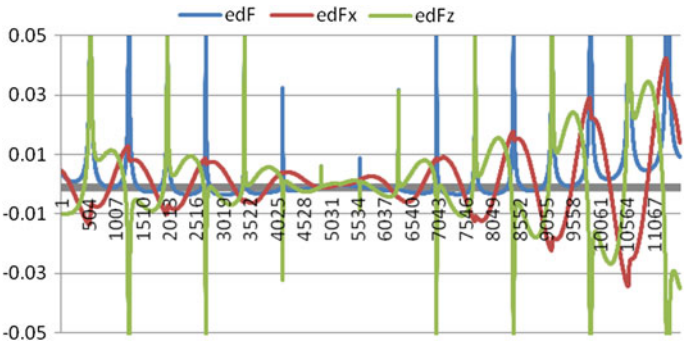

Fig. 7.12 The compensation errors (10^{-5} N)

(2) At midday, the compensation error focuses in the Z-axis direction, and no component in the X-axis direction. The variation of satellite semi-major axis is mainly caused by the force in X-axis direction. It needs to consider the eccentricity if the force in Z-axis direction. So, the effect of compensation error to the satellite semi-major axis will be reduced two orders of magnitude at midday (Fig. 7.12).

7.5 Conclusion

By the analysis above, for the typical satellite analyzed, it has follow conclusions:

(1) The solar radiation pressures for different yaw attitude controls have the same variations, only the order of magnitude different.

(2) Compared with the theoretic dynamic offset, The pressure difference dF, dFx, dFz in zero offset are about 3×10^{-6} N. By establishing the compensation model, it can reduce an order of magnitude.
(3) Compared with the theoretic dynamic offset, The pressure difference dF, dFz in approximate dynamic offset are about 8×10^{-7} N and dFx, dFy are about 2×10^{-7} N.

References

1. Bar-Sever YE (1996) A new model for GPS yaw-attitude. J Geodesy 70:714–723
2. Kouba J (2009) A simplified yaw-attitude model for GPS yaw-attitude. GPS Solut 13:1–2
3. Zhang B, Ou J et al (2010) Yaw attitude of eclipsing GPS satellites and its impact on solutions from precise point positioning. Chin Sci Bull 55(32):3687–3693
4. Hauschild A, Steigenberger P, Rodriguez-Solano C (2012) Signal, orbit and attitude analysis of Japan's first QZSS satellite Michibiki. GPS Solut 16:127–133
5. Wang W (2013) A study on the BeiDou IGSO/MEO satellite orbit determination and prediction of the different yaw control mode. China Satellite Navigation Conference 2013 Proceeding, vol 3, pp 31–40

Chapter 8
A Novel Algorithm on Sub-meter Level Real-Time Orbit Determination Using Space-Borne GPS Pseudo-Range Measurements

Xuewen Gong, Fuhong Wang and Wanke Liu

Abstract The real-time onboard orbit determination using GPS measurements has been rapidly developed in recent years due to its global coverage, abundant observations and low-cost. It can provide accurate orbital parameters for many space tasks such as LEO satellite orbit control and earth observation. The position and velocity accuracy of traditional real-time orbit determination algorithm using space-borne GPS pseudo-range measurements are always up to 1.0 m and 1.0 mm/s (3DRMS) because of an inevitable limitation of error of GPS broadcast ephemeris, thus it is difficult to meet the real-time high-precision requirements of High-resolution Earth Observations System and other space missions. Through thoughtful analysis of the variation of broadcast orbit and clock offset errors, a novel real-time orbit determination method using GPS pseudo-range observations was present in this paper. The new method estimates corresponding parameters in the Kalman filtering algorithm to absorb the slowly varying errors of broadcast orbits and clock offsets, so as to achieve orbit results with accuracies of sub-meter level in position and sub mm/s in velocity. Then a simulative test is carried out to process the space-borne GPS dual frequency pseudo-range data of consecutive 31 days from GRACE-A satellite using the auto-developed software SATODS. The test demonstrates that the position and velocity errors (3DRMS) of orbit results of the new method are reduced to 0.4–0.6 m and 0.4–0.6 mm/s respectively, which means orbital accuracies are improved by more than 40 % compared to the traditional one. Additionally, the new method has the same strategies in dynamic model and data pre-processing as the traditional one, so it would not increase computational burden visibly and has a very strong practical value.

Keywords Pseudo-range · Space-borne GPS · Real-time orbit determination · Sub-meter

X. Gong (✉) · F. Wang · W. Liu
School of Geodesy and Geomatics, Wuhan University, Wuhan, Hubei, China
e-mail: gongxuewen@whu.edu.cn

J. Sun et al. (eds.), *China Satellite Navigation Conference (CSNC) 2014 Proceedings: Volume III*, Lecture Notes in Electrical Engineering 305,
DOI: 10.1007/978-3-642-54740-9_8,

8.1 Introduction

In recent years, real-time precise orbit determination using global, abundant and low-cost GPS measurements onboard low Earth orbit (LEO) satellites has been widely applied to many space missions such as LEO satellite orbit control and earth observation [1].

Because of the real-time restrictions and autonomy demands, the traditional real-time orbit determination method usually only uses pseudo-range as main observations and broadcast ephemeris as position reference [1] and its position and velocity error (3DRMS) of determined orbits are always up to 1.0 m and 1.0 mm/s [2]. On the other hand, with the gradual improvement of the spatial resolution of earth observation and real-time requirements [3], a much higher accuracy is required in many remote sensing and science missions such as altimetry, gravimetry, SAR interferometry, or atmospheric sounding call for a sub-meter or decimeter position accuracy and a sub mm/s velocity knowledge [3]. Obviously, the traditional orbit determination method is difficult to meet these requirements, and a new and more accurate one becomes a key issue needed to be resolved.

Although Legacy Accuracy Improvement Initiative (LA-II) about GPS broadcast ephemeris has been implemented successfully at present, the overall error of broadcast orbits and clock offsets is still up to 2.0 m [4, 5], which means the error of broadcast ephemeris remains to be the main bottleneck to improve the accuracy of space-borne GPS real-time orbit determination. In an effort to overcome this bottleneck, a new real-time orbit determination method using GPS phase observations and broadcast ephemeris is studied by Montenbruck et al. [6–9] and it has raised the position and velocity accuracy of determined orbits to 0.5 m and 0.5 mm/s respectively, owing to the new dynamic ambiguities of phase data that can absorb the errors of broadcast orbits and clock offsets partly. Although the real-time orbit determination method using phase data can obtain a higher accuracy, it also increases the complexity of data processing because of the carrier phase observations included. In addition, it is difficult to detect and repair all cycle slips of the space-borne phase observations, which, to some extent, reduces the reliability of space-borne GPS real-time orbit determination. Moreover, the real-time orbit solvers using phase data take a lot of computational resources, and autonomous orbit operations are always carried out on space-borne processors with very limited computing capability, so a higher demand must be set on the space-borne processor and it makes more difficult to achieve engineering applications. Hence domestic aerospace sector mainly adopts the traditional real-time orbit determination method using pseudo-range measurements at present.

Through in-depth analysis on the impact and characteristic of broadcast ephemeris error that restricts to improve the accuracy of real-time orbit determination further, a novel real-time orbit determination method using pseudo-range measurements is put forward in this paper. This new method remains the pseudo-range as the main observations and sets corresponding parameters in the Kalman filter model to absorb the slowly varying errors of GPS broadcast orbits and clock offsets under

the constraints of highly precise dynamic models, so as to achieve higher precise real-time orbits of LEO. The new method avoids using phase observations and complex processing on cycle slips and ambiguity of phase data, which is a potential advantage and contributes to obtain sub-meter level real-time orbit results without increasing the computational burden significantly. Based on a simulative test carried out to process the space-borne GPS data from GRACE-A satellite, the accuracy and computational efficiency of this new method will be validated.

8.2 Broadcast Ephemeris Error and Its Variation Characteristic

8.2.1 Impact of Broadcast Ephemeris Error

The traditional orbit determination method always uses pseudo-range as main observations and processes real-time broadcast ephemeris to achieve GPS satellites' orbits and clock offsets. Supposed δ^j as the transmitter clock offset of GPS satellite, δ_R as the receiver clock bias, c as the speed of light in vacuum, $\left(X^j, Y^j, Z^j, c\delta^j\right)$ as the position and clock offset of GPS satellite determined by broadcast ephemeris, and $(X, Y, Z, c\delta_R)$ as the position and clock bias of GPS receiver on LEO satellite; the dual frequency GPS pseudo-range measurements P_1^j and P_2^j can be combined to remove the first order ionosphere effects and get the ionosphere-free combination: $P^j = \left(\alpha P_1^j - P_2^j\right)/(\alpha - 1)$, where, $\alpha = (f_1/f_2)^2$, is the square ratio of two carrier phase frequencies; supposed ε_P^j as the combination measurement noise, including multipath; so the simplified pseudo-range observation equation can be obtain by formula (8.1):

$$P^j = \sqrt{(X - X^j)^2 + (Y - Y^j)^2 + (Z - Z^j)^2} - c\delta^j + c\delta_R + \varepsilon_P^j \tag{8.1}$$

As is known to all, the position and clock offset of GPS satellite determined by broadcast ephemeris have a notable difference with their true values. The projection of this discrepancy in the direction of signal propagation path is denoted as "Signal-In-Propagation Path Error" (SIPPE). Apparently, SIPPE is a comprehensive error of GPS satellite orbit and clock offset and directly affects the positioning result. Supposed $(X^*, Y^*, Z^*, c\delta^*)$ as the true position and clock offset of GPS satellite (determined by precise ephemeris released by IGS), the formula of computing SIPPE is expressed as:

$$\begin{aligned} SIPPE = &\left[\sqrt{(X - X^*)^2 + (Y - Y^*)^2 + (Z - Z^*)^2} - c\delta^*\right] \\ &- \left[\sqrt{(X - X^j)^2 + (Y - Y^j)^2 + (Z - Z^j)^2} - c\delta^j\right] \end{aligned} \tag{8.2}$$

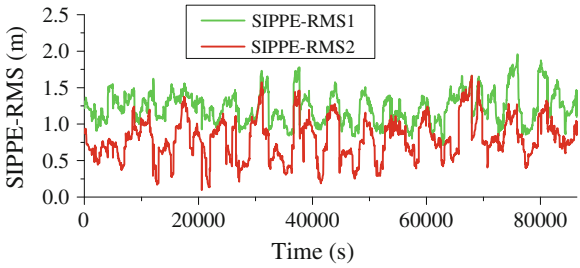

Fig. 8.1 The SIPPE before and after absorption of receiver clock bias parameter

According to Eqs. (8.1) and (8.2), It is evident that SIPPE of GPS broadcast ephemeris and the receiver clock bias parameter ($c\delta_R$) can't be separated, so for each epoch of orbit determination, the same part of SIPPEs of all visible GPS satellites is absorbed into the receiver clock bias parameter, and the residual parts will inevitably enter the location parameters of receiver (X, Y, Z), which is the key limitation to improve the accuracy of traditional real-time orbit determination.

In order to analyze SIPPE's impact on orbit accuracy roughly, an example about GRACE-A satellite (DOY = 209, 2008) is shown as follows. Considering that for each epoch the arithmetic mean value of SIPPEs of all visible GPS satellites is absorbed by the receiver clock bias parameter and for every GPS satellite the residual part is equal to SIPPE minus the arithmetic mean, Fig. 8.1 shows the root mean square (RMS) of the original SIPPEs of all visible GPS satellites and the RMS value of the residual parts of all ones in each epoch, and the former is abbreviated as SIPPE-RMS1 and latter SIPPE-RMS2. Comparing SIPPE-RMS1 and SIPPE-RMS2, it can be seen that the receiver clock bias parameter has absorbed most of SIPPE, but SIPPE-RMS2 is still up to 0.2–1.5 m and the residual part of SIPPE is still in sub-meter or meter level. Therefore, it turns out that the residual error of SIPPE is a major limitation to make the accuracy of the traditional real-time orbit determination using GPS pseudo-range measurements beyond meter-level.

8.2.2 Characteristic of Broadcast Ephemeris Error

As is described above, SIPPE of broadcast ephemeris is one of the most major influence factors to improve the accuracy of real-time orbit determination, so an in-depth analysis of its characteristic and the corresponding processing method must be enforced so as to achieve more accurate real-time orbit results. According Eq. (8.2), it can be seen that SIPPE is different with the traditional Signal-In-Space Range Error (SISRE) and associated with not only ephemeris error but also receiver's position.

Supposed that the receiver is in the center of earth, so it is capable of tracking every GPS satellite continuously. The true orbit and clock offset of GPS PRN02 satellite are determined by precise ephemeris released by IGS, then Fig. 8.2 shows the radial, along-track, and cross-track error (R, A, C) of GPS broadcast ephemeris,

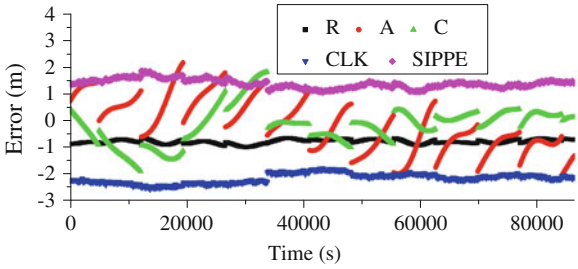

Fig. 8.2 GPS broadcast ephemeris error (PRN02-geocenter)

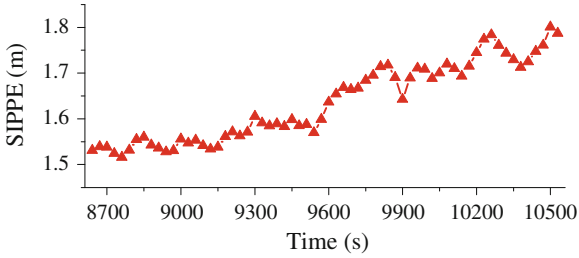

Fig. 8.3 GPS broadcast ephemeris error (PRN02-GRACE-A)

the satellite clock offset error *CLK*, and SIPPE in DOY = 209, 2008. Several features can be displayed: (1) The error of GPS satellite orbit and clock offset are about in 2.0–3.0 m; (2) The orbit and clock offset error and SIPPE exhibit a big jump when the broadcast ephemeris updates every 2 h; (3) The curve of satellite orbit error is smooth and varying slowly, but the curve of clock offset error exists small random changes; and their rate of change are all less than 1.0 mm/s.

If the receiver is onboard LEO satellites such as GRACE-A, it can't be long continuously tracking every GPS satellite, so only SIPPE of PRN02 satellite's broadcast ephemeris in a short arc is given in Fig. 8.3. The same characteristic can be seen: SIPPE of GPS satellite's broadcast ephemeris varies slowly, but exists a small random change because of the clock offset error's random changes.

Based on the analysis above, it can be concluded that whether the receiver is in the geocenter or onboard LEO satellites, SIPPE of GPS satellites' broadcast ephemeris exists obvious slowly varying characteristics.

8.3 Sub-meter Level Real-Time Orbit Determination Method

8.3.1 Setting Error Absorption Parameter

As is mentioned above, SIPPE of GPS satellites' broadcast ephemeris exists obvious slowly varying characteristics, so a novel processing strategy on SIPPE is put forward in the new sub-meter level real-time orbit determination method in

order to achieve much higher orbit accuracy. The SIPPE's processing strategy is described as follows: for each visible GPS satellite, a corresponding error absorption parameter with a featured stochastic model is set in the observation Eq. (8.1) to assimilate the residual SIPPE that can't be absorbed by the receiver clock bias parameter under the constraints of highly precise dynamic models.

Supposed *sippe* as the error absorption parameter of GPS satellite, then the Eq. (8.1) can be updated as:

$$P^j = \sqrt{(X - X^j)^2 + (Y - Y^j)^2 + (Z - Z^j)^2} - c\delta^j + sippe^j + c\delta_R + \varepsilon^j \tag{8.3}$$

A random walk process is used to represent the slowly varying characteristic of *sippe* as is described above; the stochastic model of random walk process can be presented with a difference equation:

$$sippe_{k+1} = sippe_k + w_k \tag{8.4}$$

where, $sippe_k$ is the value of *sippe* at t_k, w_k is a random variable with Gaussian white noise. If broadcast ephemeris updates or tracking new satellites occurs, the parameter *sippe* and its process noise should be reinitialized. Within a continuous tracking arc, the assignment of process noise of *sippe* is set based on SIPPE's rate of change.

8.3.2 Kalman Filter Model

Compared with the traditional real-time orbit determination method, the new one is similar in many aspects such as data reprocessing methods, dynamic models, satellite equation of state, compensation algorithm of empirical acceleration, et al. and details can be found in Refs. [1] and [2], but the new method has some difference in real-time filtering estimation because of an additional error absorption parameter *sippe*. Integrating with the dynamical compensation algorithm, taking into account both the impact of imperfect dynamics model of LEO satellite and the estimated parameters related in observation model, the estimated state vector of new method is expanded as follows:

$$X = \left[\vec{r}, \vec{v}, b, \dot{b}, a_R, a_T, a_N, C_d, C_r, sippe^1, sippe^2, \ldots, sippe^n\right] \tag{8.5}$$

where, $\vec{r}$ and $\vec{v}$ are the position and velocity vector of LEO satellite in Geocentric inertial coordinate frame, b and $\dot{b}$ are the clock bias and rate of GPS receiver, (a_R, a_T, a_N) are the radial, tangential and normal compensated accelerations, (C_d, C_r) are the radiation pressure and drag coefficients. Each GPS satellite corresponds to an error absorption parameter, so the state vector is 13 + n-dimensional if observing n GPS satellites.

The Kalman filter model of sub-meter level real-time orbit determination can be expressed as:

$$\begin{cases} X_k = \Phi_{k,k-1} X_{k-1} + W_k \\ Y_k = H_k X_k + V_k \end{cases} \tag{8.6}$$

where, $\Phi_{k,k-1}$ is the state transition matrix and its associated derivation formula refers to Refs. [1] and [2]; W_k is the process error vector, the first-order Gauss-Markov random process is used to express the process noise of compensation acceleration, the random walk process is used to represent the characteristic of the radiation pressure and drag coefficients and the error absorption parameters; Y_k is the observation vector at t_k; H_k is the design matrix (also known as observation matrix); V_k is observation error vector.

8.4 Data Processing and Analysis

According to the mathematical model of sub-meter level real-time orbit determination method as is stated above, we upgrade the SATODS software in Ref. [2], so the new software can realize not only the traditional orbit determination method, but also the new one. We use the two methods to simulate processing the space-borne GPS measurement data from GRACE-A satellite in real-time and assess the accuracy of real-time orbit results by comparing to GRACE-A's precise ephemeris released by Jet Propulsion Laboratory (JPL). The dynamic models and other orbit determination strategies of two methods are the same and listed in Table 8.1.

8.4.1 Real-Time Orbit Accuracy

The traditional real-time orbit determination method using pseudo-range measurements is abbreviated as "T-RTOD-PSEUDO", and the sub-meter level real-time orbit determination using pseudo-range measurements presented in this paper is abbreviated as "SL-RTOD-PSEUDO". Figures 8.4 and 8.5 are comparison of the position and velocity error (3DRMS) of these two real-time orbit determination methods used for processing space-borne GPS data of GRACE-A satellite(-DOY = 209–219, 2008) respectively. As can be seen, the position and velocity accuracy of "T-RTOD-PSEUDO" are 0.8–1.0 m and 0.8–1.0 mm/s, while the accuracies of "SL-RTOD-PSEUDO" are 0.4–0.6 m and 0.4–0.6 mm/s respectively, which means the accuracy of the new method is improved by more than 40 % when compared to the traditional one.

Figure 8.6 shows the positional error curves of two real-time orbit determination method in radial, along-track and cross-track direction when processing the GPS data of GRACE-A in DOY = 209, 2008. It can be seen that the position error

Table 8.1 The same strategies used in two orbit determination methods

Model/Parameter	Selection in real-time
Earth gravity field	EGM2008 70 × 70
N-body gravitation	Low precision model, Moon and Sun's position are computed by analytic method
Earth tides	Low precision model, k_{20} solid only
Drag model	Modified Harris-Priester model (density), fixed effective area, estimated C_d parameter
Radiation pressure model	Cannonball model, fixed effective area, estimated C_r parameter
Empirical acceleration	Kinetic model compensation (DMC), a first-order Gauss-Markov stochastic model

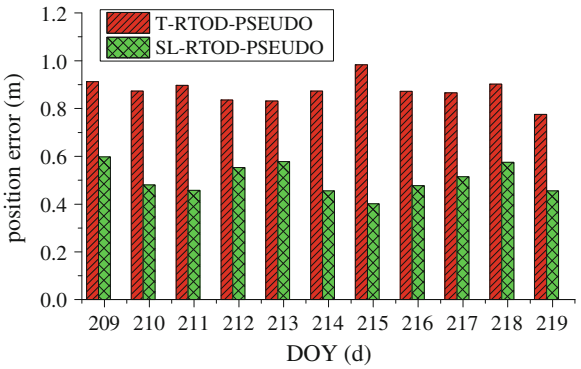

Fig. 8.4 The position error of two orbit determination methods

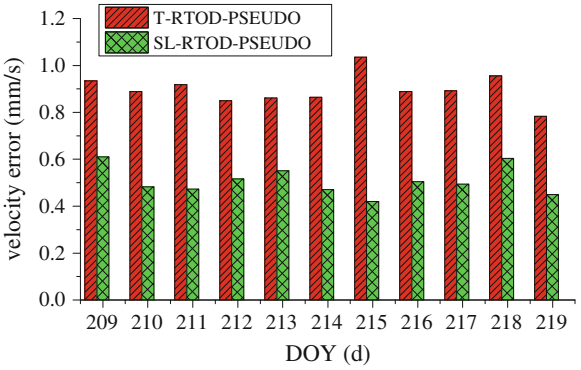

Fig. 8.5 The velocity error of two orbit determination methods

of the new method presented in this paper is always less than the one of the traditional method whether the filter is converged or not, and especially the radial error of the new method does not exist obvious fluctuation with large amplitude. Of course, it means that the new method has a good absorption of broadcast ephemeris error in signal propagation path (SIPPE).

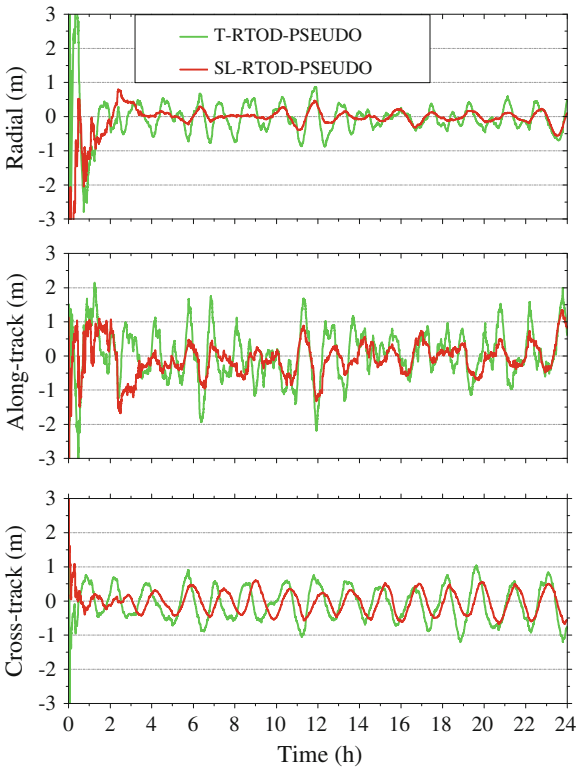

Fig. 8.6 The R/A/C position error of two orbit determination methods

8.4.2 Error Absorption

The reason why the proposed new method is superior to the traditional one is that the same part of all visible GPS satellites' SIPPEs is only absorbed by receiver clock bias parameter and the residual errors are inevitably included in the determined orbit results when using the traditional one, while, in the new method, not only the receiver clock bias parameter can absorb the same part of all visible GPS satellites' SIPPEs, but also the setting error absorption parameters are able to absorb the residual part of SIPPE. Figure 8.7 shows PRN02 satellite's original SIPPE and the corresponding absorbed part of two real-time orbit determination methods within a continuous tracking arc. It can be seen that the absorbed error of new method is closer to original SIPPE than the traditional one, which means the new method can do better to absorb SIPPE.

Figure 8.8 shows the RMS value of PRN02 satellite's original SIPPE and its residual parts of two real-time orbit determination methods. It can be seen that the new method presented in this paper can absorb more SIPPE than the traditional one and its residual error is smaller. If we define the absorbed error as RMS of original SIPPE minus RMS of residual SIPPE, Error Absorption Rate (EAR) is equal to the absorbed error divided by RMS of original SIPPE. Then it can be

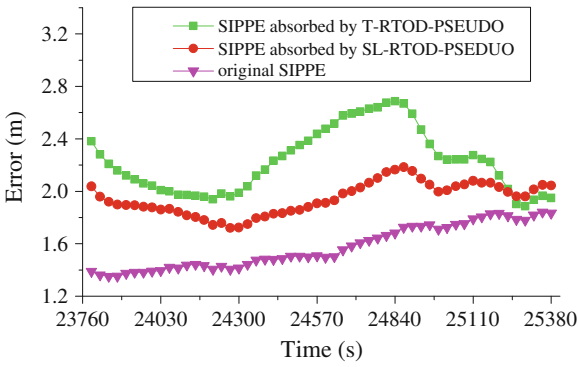

Fig. 8.7 SIPPE and the absorbed part by orbit determination

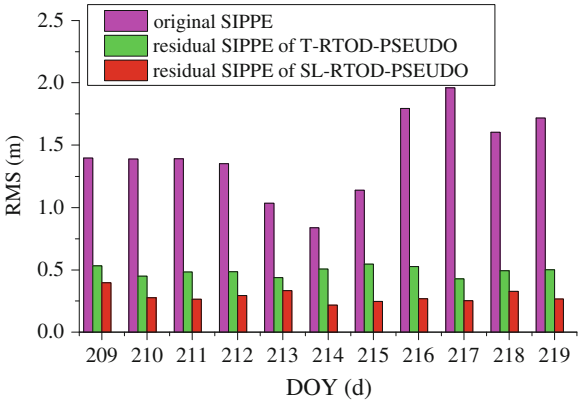

Fig. 8.8 The residual error of SIPPE

found that EAR of the new method presented in this paper is more than 75 % and it is much higher than the traditional one.

8.4.3 Computational Efficiency

As is stated above, the new method presented in this paper can greatly improve the accuracy of orbit determination. Compared to the traditional method, the new one adopts the same strategies in dynamic model, data pre-processing, and et al., but has a higher dimensional state vector, so the computational complexity may be increased to some extent. Compared to the real-time orbit determination method using carrier phase data proposed by Montenbruck et al., calculations will be more efficient because of avoiding processing phase observations. The real-time orbit determination that uses carrier phase as main observations is abbreviated as "RTOD-PHASE". Table 8.2 shows the comparison of main computational items of three orbit determination methods.

Table 8.2 Main computational items

Computational items	T-RTOD-PSEUDO	SL-RTOD-PSEUDO	RTOD-PHASE
Dimension	13	13+n	13+n
Gross error detection of pseudo-range	yes	yes	yes
Cycle slip detection of phase	no	no	yes
Processing ambiguity	no	no	yes
Pseudo-range measurement updating	yes	yes	yes
Phase measurement updating	no	no	yes

Table 8.3 The computational time in a single epoch

Method	Time (ms)
T-RTOD-PSEUDO	4.971
SL-RTOD-PSEUDO	5.743
RTOD-PHASE	9.180

Three methods are applied to process space-borne GPS data of GRACE-A on a 1.6 GHz AMD E-350 processor. A complete solver in a single epoch is accomplished every 30 s, including time updating, data preprocessing and measurement updating. The average computational time of a complete solver in a single epoch is showed in Table 8.3. Apparently, the new method does not increase the computational burden visibly when compared to the traditional one and it is much less time-consuming than the real-time orbit determination method using phase data.

8.5 Conclusions

The sub-meter level space-borne GPS real-time orbit determination method presented in this paper remains the pseudo-range as the main observations and sets error absorption parameters to absorb the broadcast ephemeris error in the signal propagation path (SIPPE), thereby improving the accuracy of orbit determination by more than 40 % compared to the traditional one. The new method avoids complex processing on cycle slips and ambiguities of phase data, without increasing the computational burden significantly, achieving sub-meter level (0.5 m, 0.5 mm/s) orbit results that are comparable to the real-time orbits arising from phase measurements, which contributes a lot to the satellite platforms that demand high-precision real-time orbital parameters.

Acknowledgements This paper is supported by National Natural Science Foundation (41374035).

References

1. Fuhong W (2006) Theory and software development on autonomous orbit determination with spaceborne GPS measurements. Wuhan University, Wuhan
2. Fuhong W (2010) A Kalman filtering algorithm for precision real-time orbit determination with space-borne GPS measurements. Geomatics Inf Sci Wuhan Univ 35(6):653–656
3. Deren L, Qinxi T, Rongxing L et al (2012) Current issues in high-resolution Earth observation technology. Sci China Earth Sci 42(6):1043–1051
4. Zhenghang L, Wenwu D, Zhao L (2008) Error analysis of orbit determined by GPS broadcast ephemeris. J Geodesy Geodyn 28(1):49–54
5. Wenkun Y, Wujiao D, Changsheng C et al (2012) Accuracy analysis of GPS/GLONASS broadcast ephemeris. Geotech Inv Surv 8:79–83
6. Montenbruck O, Ramos-Bosch P (2008) Precision real-time navigation of LEO satellites using global positioning system measurements. GPS Solutions 12(3):187–198
7. Wermuth M, Hauschild A, Montenbruck O et al (2012) TerraSAR-X precise orbit determination with real-time GPS ephemerides. Adv Space Res 50(5):549–559
8. Montenbruck O, Hauschild A, Andreset Y et al (2013) (Near-) real-time orbit determination for GNSS radio occultation processing. GPS Solutions 17(2):199–209
9. Mander A, Bisnath S (2013) GPS-based precise orbit determination of low earth orbiters with limited resources. GPS Solutions 17(4):587–594

Chapter 9
Real-Time Monitoring of Strong Ground Motion Using 50 Hz GNSS Data of Continuous Operation Reference Station (CORS)

Zhang Xi, Huang Dingfa, Liao Hua, Feng Wei and Li Meng

Abstract High-rate GNSS plays an important role in monitoring the process of strong ground motion, such as seismic activity. To achieve real-time monitoring, a reasonable solution and filtering method are needed, especially for the 50 Hz data. Based on the analysis of differential and combination method, effects of ionosphere and troposphere have obvious trend within a short time, but cannot be treated as linear trend completely. To monitor real time surface deformation accurately, a newly developed strategy is proposed in this paper, it can effectively reduce atmospheric error of double-difference in real-time. 50 Hz data are obtained during Lushan earthquake (Ms7.0), Sichuan, China; the coseismic deformations are captured successfully on the sites of continuous operation reference station (CORS) stations. With 3D grid searching method, the obtained earthquake focus is basically consistent with USGS published results. It shows that the proposed method is effective and reasonable for strong ground motion monitoring by using high-rate GNSS observations, especially for seismic activity.

Keywords CORS · High-rate GNSS · Morphological filtering · Sliding monitoring model · Strong ground motion · Coseismic deformation

Z. Xi · H. Dingfa (✉) · F. Wei · L. Meng
School of Geosciences and Environmental Engineering, Southwest Jiaotong University, Chengdu 610031, China
e-mail: dfhuang@swjtu.edu.cn

Z. Xi
e-mail: zhangxi@my.swjtu.edu.cn

F. Wei
e-mail: fengwei99@gmail.com

L. Meng
e-mail: nemon818@163.com

L. Hua
Sichuan Seismological Bureau, Chengdu 610041, China
e-mail: sc.liaohua@126.com

J. Sun et al. (eds.), *China Satellite Navigation Conference (CSNC) 2014 Proceedings: Volume III*, Lecture Notes in Electrical Engineering 305,
DOI: 10.1007/978-3-642-54740-9_9,

9.1 Introduction

Especially for seismic activity, strong ground motion, with great motion amplitude and short duration, still has no other better monitoring tool except seismographs so far [1]; But affected by the cost and near-field saturation phenomenon, the early warning capability of seismograph is limited. With worldwide continuous operation reference station (CORS) station construction is further into the application stage, many achievements embodied the superiority of GNSS technology in high-precision deformation monitoring [2, 3]. And it becomes possible to capture high-frequency events with high-rate GNSS technology [4–8]. However, affected by solver efficiency, the traditional method of coordinate solver is difficult to achieve high-precision monitoring in real-time, especially for 50 Hz data. New solver strategy is particularly critical.

Morphological filtering technology is a nonlinear filtering technology, which is built on mathematical morphology, has a complete theoretical system. With its superior computing performance and filtering effect, this technology has been successful in the field of image processing, artificial intelligence, digital signal analysis [9–11]. But there has not been applied to the GNSS data processing.

Based on the situation that duration of strong ground motion is short, experiments analyzed the characteristics of GNSS observation's errors in the period. The results show that errors about receiver and satellite are unpredictable, but variation of atmospheric delay has good trend. In order to achieve rapid solver for the displacement of CORS station and capture strong motion events promptly, a sliding window forecast method for correcting residuals has been proposed based on Morphological filtering.

In this paper, six stations' data (50 Hz) of Sichuan CORS are traced to the period of Lushan earthquake (Ms7.0). Seismic dynamic deformation at each station's location is captured successfully; through extracting arrival times of seismic waves, origin time and hypocentre are preliminarily found with grid search method. The results are consistent with Wu [12] and USGS, which demonstrate that this method is effective.

9.2 The Sliding Monitoring Model

Due to the short duration of strong ground motion, most of the GPS observation errors are apparently correlative between two epochs. The equation of differential observation between the current time and the time before the motion can be expressed as formula (9.1):

$$\lambda\delta\varphi_r^s = \delta\rho_r^s + \delta O^s + \delta T_r^s + c * \delta(\tau_r - \tau^s) - \delta I_r^s + \delta M + \varepsilon \tag{9.1}$$

where r and s identify receiver and satellite respectively, λ is carrier wavelength, φ is GPS carrier phase observation, ρ is the distance between receiver and satellite, O is orbit error, T is troposphere delay, I is ionosphere delay, τ_r and τ^s are clock error of receiver and satellite, M is multipath effect, ε is observational noises, δ is epoch differential operator.

Phase shift of multipath effect can be expressed as $M = \frac{2D}{\lambda} * \sin(\theta)$, where D is the distance between reflector and receiver, θ is the incident angle. Generally, It's similar in a short time, and its impact is limited for epoch differential observation [13].

Static coordinate (x_0, y_0, z_0) of CORS station can be accurately calculated with historical data; then, the formula (9.1) can be transformed into the following form:

$$\lambda\delta\varphi_r^s - \left(\rho_{ir}^s - \rho_{0r}^s\right) = \frac{(x_{0r} - x^s) * d_x + (y_{0r} - y^s) * d_y + (z_{0r} - z^s) * d_z}{\rho_{ir}^s} + Corrections_r^s \tag{9.2}$$

where (x^s, y^s, z^s) is the satellite coordinate, ρ_0 is the distance between receiver and satellite at time t_0, ρ_i is the distance between receiver's static coordinate and satellite at time t_i, *Corrections* is the comprehensive correction term include troposphere delay, receiver clock bias, satellite clock bias and orbit error (d_x, d_y, d_z) is the deformation of our concern.

The basic idea of sliding monitoring is:

- Setting the sliding window's length T_1 and event trigger threshold σ;
- Obtaining the CORS station coordinate (x_0, y_0, z_0) accurately with historical data;
- Forecasting future T_2 time's correction *Corrections*[] of each satellite;
- Updating *Corrections*[], if the real-time deformation is less than σ within T_2 time;
- Forecasting future T_1 time's correction *Corrections*[], if the real-time deformation is greater than σ within T_2 time.

9.3 Characteristics of Epoch Differential Corrections

In order to calculate the displacement of CORS station, it's necessary to accurately grasp the variation of corrections. Generally, the time of main shock is not more than 100 s, 3 min 50 Hz data of ZHJI station and JIGE station (They belong to Sichuan CORS, and its distance is about 164 km) are processed and analysed. And IGS ultra-fast precision ephemeris is adopted. Due to space limitations, the expansion analysis is only for three representative satellites, the changes of their elevations are described in Fig. 9.1.

Receiver clock bias, part of atmospheric delay and satellite related error are suppressed by the difference between satellites, and the Fig. 9.2 shows that

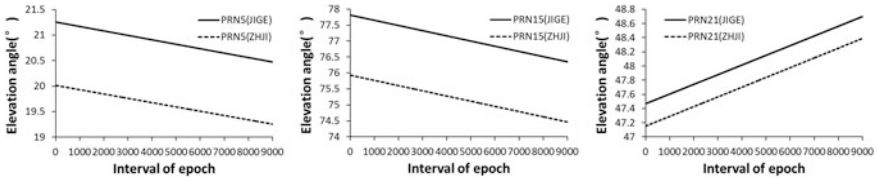

Fig. 9.1 Elevation of PRN5, PRN15, PRN21 on station ZHJI and JIGE during the test

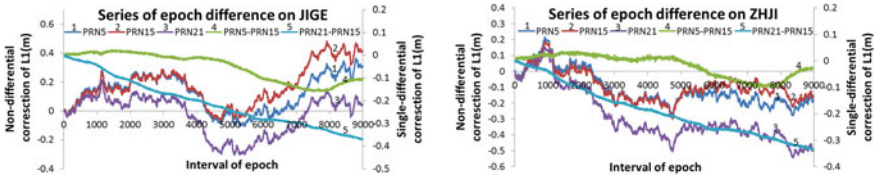

Fig. 9.2 Series of epoch differential correction on L1 non-difference and single-difference

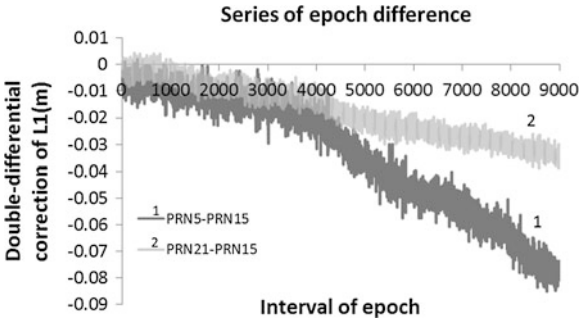

Fig. 9.3 Series of epoch differential correction on L1 double-difference

fluctuation of differential observation between satellites is decreased significantly. We can see receiver clock bias is the main factor that cause abnormal fluctuations of observations, its value cannot be forecasted with a simple model. So, satellite difference is necessary.

The quality of satellite differential observation is affected by atmospheric delay and satellite related error, in which satellite related errors and part of atmospheric delay are suppressed by double difference. By using double difference between ZHJI and JIGE, series of epoch differential correction are shown in Fig. 9.3.

By using IGS ultra-fast precision ephemeris, the accuracy of satellite orbit will be better than 5 cm, and the impact will be less than 1 mm for double differential observations on 200 km baseline [14]. Therefore, atmospheric delay is the main factor affected the series in Fig. 9.3. Combining Figs. 9.1 and 9.3, we can see atmospheric variation of the low elevation satellite is more remarkable, and suggest elevation of usable satellite should not less than 20° in high-precision solver (Fig. 9.2).

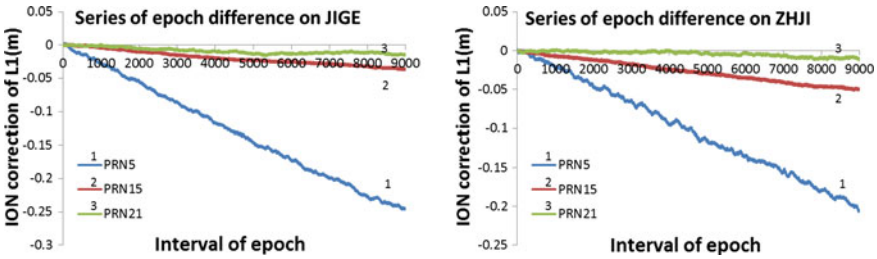

Fig. 9.4 Ionospheric correction series of epoch difference on L1

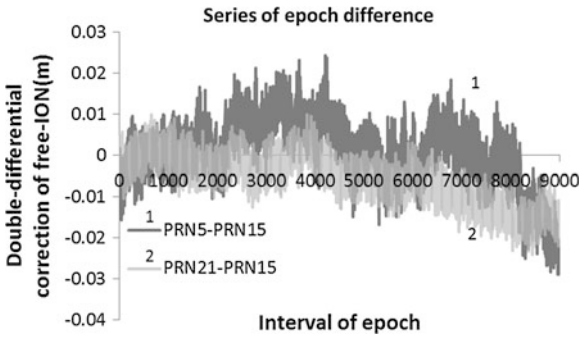

Fig. 9.5 Correction series of epoch difference on ionospheric-free observation

We all know atmospheric delay include ionosphere delay and troposphere delay. In order to further clarify their variation characteristics, L1 * $\lambda 1$ − L2 * $\lambda 2$ observation (Hereinafter referred to as I observation) is considered. Because the relative deviation between L1 and L2 is stable and variation of higher-order ionospheric effects is limited in a short time, series of epoch difference on I observation is only related with the first-order ionospheric effect, and the following relationship exists:

$$\Delta I_1 = \left(-\frac{f_2^2}{f_2^2 - f_1^2} \right) * \Delta I \tag{9.3}$$

where Δ is epoch differential factor, I_1 is ionospheric effect on L1, f_1 and f_2 is the frequency of L1 and L2 respectively. Situation of ionospheric effect on each station's L1 observation during the test is shown in Fig. 9.4:

As shown in Fig. 9.4, ionospheric correction is almost linear trend, and more remarkable for the low elevation satellite. If ionospheric-free observation is adopted, series of epoch difference will be like the Fig 9.5.

Compared with Fig. 9.3, the slope of correction series has decreased, which is more conducive to construct forecast model. Above analysis shows that the receiver clock bias is the main factor cause abnormal fluctuation of correction series, and it can be eliminated by single differential observation, but the single

differential correction series of epoch difference still is irregular after correcting the satellite-related error with ultra-fast precision ephemeris, so double differential observation is the only viable method for real-time deformation monitoring.

9.4 Morphological Filter

According to the basic idea of sliding monitoring, the forecast should include short-term forecast and long-term forecast. Where the purpose of short-term forecast is to detect the moment of strong motion timely, long-term forecast is to solve the ground motion process. We can see the overall trend of the series in Figs. 9.3 and 9.5 is almost linear, but fluctuations still exist. So it cannot represent actual variation of the series by using a simple linear model. Because the value of future correction is related to the current data, we propose to forecast the future correction with the reverse sequence of morphological filtering result.

9.4.1 Expression of Morphological Filtering

Morphological filtering is an important method for digital signal processing, it can reduce the noise of digital signal through the operation, such as erosion, dilation, opening, closing and their combinations. Its algorithm is high efficiency, and performance is good; which is very suitable for real-time data processing. The basic principle is described in related articles [9–11], not be repeated here. The filter combining opening-and-closing with closing-and-opening (Abbreviated as "OC-CO") is adopted in this paper, and its expression is the following formula.

$$y_{g(j)}(i) = [OC(f(i)) + CO(f(i))]/2 \tag{9.4}$$

where $\{f(i)(i = 1, \ldots, n)\}$ is the input signal, $y(i)$ is the output signal, $\{g(j)(j = 1, \ldots, m)\}$ is a structuring element, $OC(f(i)) = f \circ g \bullet g$ is morphological opening-and-closing operation, $CO(f(i)) = f \bullet g \circ g$ is morphological closing-and-opening operation, $f \circ g = f \ominus g \oplus g$ and $f \bullet g = f \oplus g \ominus g$ exist. The expression of erosion and dilation is shown as follows:

$$(f \ominus g)(i) = \min_{j=0,1,\ldots,m-1} \{f(i+j) - g(j)\}, \quad (i = 1, \ldots, n-m) \tag{9.5}$$

$$(f \oplus g)(i) = \max_{j=0,1,\ldots,m-1} \{f(i-j) + g(j)\}, \quad (i = 1, \ldots, n) \tag{9.6}$$

where $\ominus$ and $\oplus$ represent erosion and dilation operation respectively, m is length of structural element. Corresponding expression of OC-CO filter can be derived from the formula (9.5) and formula (9.6),

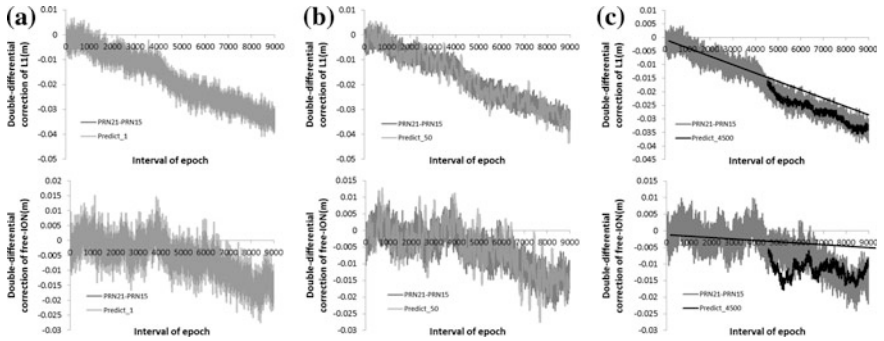

Fig. 9.6 Comparison chart of the observed and forecast values

9.4.2 Quality Analysis of Correction

According to the variation characteristics of epoch differential correction series on double differential observation, we tried to forecast corrections of 1 epoch, 50 epochs and 4,500 epochs respectively for "PRN21-PRN15" of Figs. 9.3 and 9.5 by using a structure with 20 zero elements, results of forecast are shown in Fig. 9.6:

In the Fig. 9.6, chart (a) and (b) have displayed the real time forecast correction and future 50 epochs' corrections. Comparing with observed sequence, the forecast sequences record the morphology of observed sequence, but 1.5 mm error and 4 mm error are imported respectively. Sequence of future 4,500 epochs' correction is shown as chart (c), we can see sample linear predictive model deviate from the trend of observed sequence, because linear model has ignored current trend, but the method mentioned above considered the current trend.

9.5 Dynamic Monitoring of Lushan Earthquake

Lushan earthquake (Ms7.0) occurred at 8:02 Beijing time on April 20, 2013, in Ya'an-Lushan, Sichuan Province, the hypocenter from USGS is (30.308° B, 102.888° L, 14 km H), the seismic esthesia is strong on Sichuan region, the seismic process was recorded by some stations of Sichuan CORS. In order to verify practicality of this method, six stations are selected include five stations nearby the epicenter and one station far away from it.

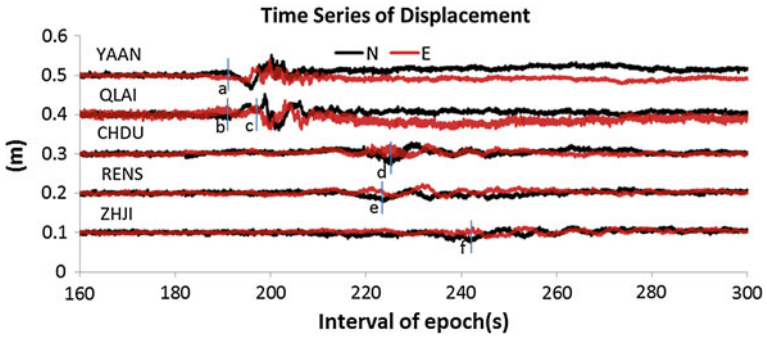

Fig. 9.7 Time series of horizontal displacement on each station

9.5.1 Dynamic Displacement of CORS Stations

JIGE station, the farthest one (about 360 km away from the epicenter), is selected as reference station; 5 min data (50 Hz) during the earthquake are used, and double difference of ionospheric-free observation is adopted; Coordinates of stations are post processing results of GAMIT, orbit file is IGS ultra-fast precision ephemeris; Setting the time length $T_1 = 120$ s and $T_2 = 1$ s; The process of long-term forecast will be triggered, when horizontal displacement is greater than 2 cm. Figure 9.7 has shown the dynamic displacement of each station.

In Fig. 9.7, these stations have felt the earthquake in varying degrees; Specifically, vibration is more violent on YAAN station and QLAI station, and their displacements respectively are (1.7, −0.9 cm) and (0.7, −1.5 cm) on coordinate (N, E) after the main shock; but few displacement on CHDU, RENS, ZHJI.

9.5.2 Hypocenter Search

Arrival times of seismic waves are indispensable to the determination of the hypocenter, but affected by noise, it is difficult to determine the arrival times with GPS observation, especially for small magnitude earthquake.

In Fig. 9.8, we can see that all of QLAI, CHDU, RENS, and ZHJI located in the same direction of USGS epicenter point, so their waveforms should be consistent in some extent. In Fig. 9.7, point a and point b are the seismic start of sequence; Points of c, d, e, f, are roughly determined to the same point of seismic wave; And arrival times of CHDU, RENS, ZHJI can be calculated approximately with the time difference between point b and point c. Learn from Liu's research [15], S-wave speed is about 4.0 km/s in this seismic area.

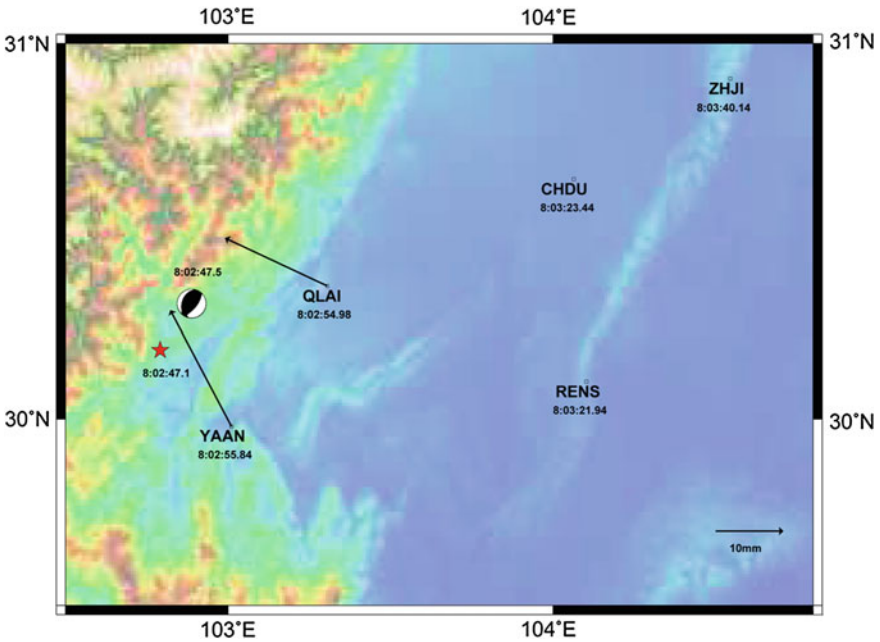

Fig. 9.8 Displacements and arrival times based on GPS observation

With grid search method, hypocenter (30.19° B, 102.74° L, 1.6 km H) and origin time (8:02:47.1) are found; the coordinate (B, L) of hypocenter and the origin time are consistent with the results of USGS, but quality of the depth is poor.

9.6 Conclusions

Experiments show that receiver related error and satellite related error are disorderly, there is no sample model fit for them, but atmospheric variation has obvious trend in a short time. So, double differential observation is the only viable method for real-time accurately monitoring with long-term forecast of correction.

Results of dynamic monitoring are consistent with USGS and associated researchers, and the average time for the whole calculation of one epoch is less than 20 ms. Which demonstrated the capability about dynamic monitoring of strong ground motion with high-rate GPS observation, and the morphological filter is effective. It is worth noting that:

- So far, for small magnitude earthquake, the capability of inversion is limited with GPS observation;

- The quality of inversion is closely related to distribution of stations and matching degree between the predictive factor and the actual variation of correction;
- There is some bias for the displacement between dynamic monitoring and post-processing

Analysis shows that forecast value deviate with the actual value at some epochs. It is not accurately to replace the value of future correction with the reverse sequence of morphological filtering result, more effective method is needed.

Acknowledgements The authors herby acknowledge with thanks to the financial supporting from National Natural Science Foundation of China (No. 41374032), National Hi-Tech Research and Development Program (863) (No. 2012AA12A209), and a grant from Spark Program of China Seismological Bureau (No. XH12039). The thanks are also extended to Sichuan Seismological Bureau for the supporting of GNSS CORS observations.

References

1. Chen Y, Song JL (2013) Review of the development history and present situation on seismographs. Prog Geophys 28(3):1311–1319 (in Chinese)
2. Gu GH (2007) Recent progress in researches on crustal movements through GNSS (GPS) observations. Recent Dev World Seismolog 7:9–15
3. Li YH, Shen YZ (2011) Impact of temporal correlation of GPS observations on baseline solution. Geomatics Inf Sci Wuhan Univ 36(4):427–430
4. Fang RX (2010) High-rate GPS data non-difference precise processing and its application on seismology. Ph.D. thesis, Wuhan University, Wuhan
5. Feng W, Huang DF, Li M et al (2013) Ground motion monitoring during strong shake with high-rate GPS double-differenced residual model. Chin J Geophys 56(9):3022–3028
6. Yin HT, Gan WJ, Xiao GR et al (2009) Progress on monitoring strong earthquake ground motions using high-rate GPS. Prog Geophys 24(6):2012–2019 (in Chinese)
7. Zhang XH, Guo F, Guo BF et al (2012) Coseismic displacement monitoring and wave picking with high-frequency GPS. Chin J Geophys 55(6):1912–1918
8. Avallone A, Marzario M, Cirella A et al (2011) Very high rate (10 Hz) GPS seismology for moderate-magnitude earthquakes: the case of the Mw 6.3 L'Aquila (central Italy) event. J Geophys Res: Solid Earth (1978–2012) 116(B2)
9. Zuo Q, Shi ZK (2003) An real-time algorithm for license plate extraction based on mathematical morphology. J Image Graph 3:281–285
10. Zhang JC, Wu XJ (2007) Research on applications of morphological filtering in real-time signal processing. Chin J Sens Actuators 20(4):828–831
11. Chen H, Guo K, Hu Y (2009) A study on application of mathematical morphology to seismic signal processing. Prog Geophys 24(6):1995–2002 (in Chinese)
12. Wu YQ, Jiang ZS, Wang M et al (2013) Preliminary results pertaining to coseismic displacement and preseismic strain accumulation of the Lushan M S7. 0 earthquake, as reflected by GPS surveying. Chin Sci Bull 58(20):1910–1916
13. Yuan LG, Huang DF, Ding XL et al (2004) On the influence signal multipath effects in gps carrier phase surveying. Acta Geod Cartogr Sin 33(3):210–215
14. Li CG, Huang DF, Zhou DW et al (2007) On real-time precise orbit biases correction technique for GPS/VRS network. J Geodesy Geodyn 27(1):96–99
15. Liu QY, Li Y, Chen JH et al (2009) Wenchuan Ms8. 0 earthquake: preliminary study of the S-wave velocity structure of the crust and upper mantle. Chin J Geophys 52(2):309–319

Chapter 10
Forecast of Equivalent Clock Correction and Its Application

Nan Xing, Xiaogong Hu, Yueling Cao, Ranran Su and Xiaoli Wu

Abstract Beidou Navigation Satellite System provides two kinds of services: basic navigation service and wide area differential service. To enhance the positioning accuracy, both services are challenged by orbit error reduction problem, especially during yaw-steering mode. Besides basic information, additional parameters, such as satellite pseudorange differential correction, could efficiently correct satellite orbit error and clock error. However, since it needs to be calculated in real-time, differential correction is only broadcast to authorized users. Through investigation of the historical record, we find that shortly (an hour) forecasting for differential correction is doable. We proposed two forecasting methods in this work, and tested them with real observation data. We find that positioning precision of basic navigation service could be efficiently improved with the forecasted differential correction, in some cases could even reach the level of wide area differential service.

Keywords Beidou Navigation Satellite System · Satellite pseudorange differential correction · Positioning accuracy

N. Xing (✉)
Beijing Research Institute of Telemetry, Beijing 100076, China
e-mail: nanx@shao.ac.cn

X. Hu · Y. Cao
Shanghai Astronomical Observatory, Chinese Academy of Sciences, Shanghai 200030, China

R. Su · X. Wu
Beijing Global Information Center of Application and Exploitation, Beijing 100094, China

J. Sun et al. (eds.), *China Satellite Navigation Conference (CSNC) 2014 Proceedings: Volume III*, Lecture Notes in Electrical Engineering 305,
DOI: 10.1007/978-3-642-54740-9_10,

10.1 Introduction

Satellite-based augmentation system (SBAS) is usually an external complement to satellite navigation service system. Based on ground stations that locate at accurately-surveyed points, SBAS can create additional correction messages and broadcast such complementary differential information with GEO satellites to improve user positioning precision [1–3]. Taking advantage of special GEO/IGSO/MEO constellation combination, Beidou Navigation Satellite System (BDS) itself can simultaneously provide basic navigation service and wide area differential service [4]. Basic navigation information is modulated in code D1 of IGSO/MEO and code D2 of GEO, and it includes satellite clock error, satellite orbit, ionospheric delay correction information, etc., which are adequate for basic service such as positioning, navigation, timing and so on. Besides that, the wide area differential service messages contain additional parameters from satellite-based augmentation system, such as satellite pseudorange differential correction (refer as pcor hereafter), ionospheric grid and regional integrity, leading much more accurate services [5]. Current positioning accuracy of basic navigation service is better than 10 m, wide area differential service could enhance this accuracy by about 2 m, or even 4–5 m for some particular region [6].

For wide area differential service, the enhancement of service accuracy is essentially due to the specific analysis of the satellite orbital error, clock error, medium model error and other main error sources. In view that the main impact of the satellite orbital error on pseudorange is in radial direction, BDS combine radial orbital error and the clock error into pcor to eliminate both errors. Such method could significantly reduce the computational complexity. Currently, pcor is updated every 18 s, effectively improving the user range error (URE) about 1 m.

On the other hand, BDS has two attitude control modes: orbit-normal mode and yaw-steering mode [7]. Theoretically, under different attitude control modes, orbit determination strategy needs to be adjusted, such as solar radiation pressure modeling, antenna phase center correcting, etc. Therefore the change of attitude control mode could affect the calculation accuracy of relevant navigation message, such as satellite orbital error, which is sensitively related to solar radiation pressure models.

Currently used solar radiation pressure model is consistent with yaw-steering mode. In this mode, user equivalent range error (UERE) for basic navigation service is about 2.5 m [8], for wide area differential service, UERE is about 1 m. In the orbit-normal mode, UERE for basic navigation service is much larger. In the worst situation, it could be even 30 m. This is due to the inconsistency between solar radiation pressure model and the attitude control modes. The pcor information can effectively overcome such issue, so the differential range error for authorized user at orbit-normal mode remains to be around 1 m.

As the requirement for services accuracy is increasing, how to improve the accuracy of basic navigation service under existing conditions, especially how to make basic navigation service efficiently use pcor and other information to ensure positioning accuracy stable, become a new challenge for the BDS.

The basic navigation message is only updated once per hour, pcor cannot be broadcasted to users in real time as wide area differential information. However, since the pcor describes the error of orbit and clock error, it should have remarkable varying characteristics. We therefore suggest to summarize these characteristics based on its historical information, make accurate short-term forecasting of the pcor, and then broadcast results along with the basic message to users. It is not only help offset the impact of changes in the attitude control modes, but also an effective method of improving the overall positioning accuracy of basic navigation service.

We firstly analyzed the time-varying characteristics of pcor with its historical measured data in Sect. 10.1. Based on this, two short-term forecasting methods for pcor were proposed in Sect. 10.2, and the pros and cons of each method is briefly reviewed. In Sect. 10.3, we tested these two methods with real data, and analyzed the application results. Our conclusion and discussions are given in Sect. 10.4.

10.2 Analysis on Time-Varying Characteristics of Pcor

The constellation of BDS is composed of three types of satellites: GEO, IGSO and. In order to achieve accurate forecast of pcor, we first analyze the time-varying characteristics of different satellites pcor. With the historical data of different satellites pcor on 2012-09-20, we find:

1. The value of pcor will jump on the hour, but keep continuous in the next hour.
2. Pcor sometimes occurs abnormal changes during certain hours.
3. The structure of pcor within one clock hour is relatively simple. Basically it is linear trend, and the linear slops for two adjacent hours are similar (Fig. 10.1).

Our understanding of above features are as follows: Firstly, the calculation of pcor is based on the navigation messages, and the messages were broadcasted on the hour, so there could be a slight jump for the pcor on the starting point of each clock hour; secondly, the changes of the pcor is mainly derived from satellite orbit errors and clock error, and the performance of satellite orbit errors and clock error is usually simple and linear, consequently, changes of pcor could be described by a continuous linear change; Finally, the pcor is sensitive with the abnormal changes of satellite status, such as when IGSO and MEO becomes available or un available, pcor will also behaves as abnormal changing, until enough data was accumulated and latest messages were updated.

10.3 Short-Term Pcor Forecast Methods

Based on the above analysis, we propose that without considering the satellite unusual circumstances, as long as we get two key information, we can effectively forecast pcor: the value of pcor on the starting point of each hour and the slop within every hour when we use linear function to fit the data. Without considering

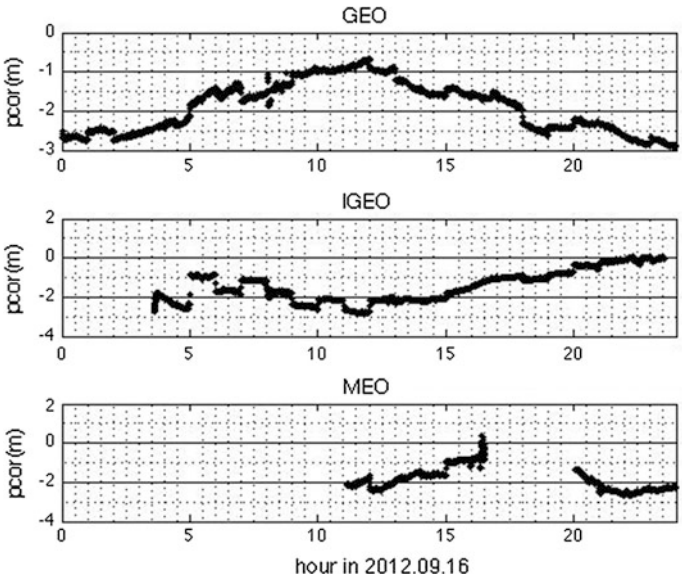

Fig. 10.1 Pcor time-varying characteristic of GEO (*top*), IGSO (*middle*) and MEO (*bottom*)

the unusual circumstances of satellite, the value of pcor on the starting point of each hour should be related with orbit and clock error, while the hourly slope does not have obvious variation, but the slop values for two adjacent hours usually have small changes.

We thus propose a simple forecasting method: fit the data of pcor in the first hour with linear function, and assume the behavior of pcor in next hour will follow the variation of this hour, thus make forecasting (hereinafter referred to as linear method). The advantage of this method is simple, thus it is relatively adaptable for difference situations. If the forecasting accuracy can significantly improve the results, it was easy to be converted into practical technology and to be used for online service.

Figure 10.2 presents the forecasting results of three satellites under yaw-steering mode, namely GEO4, IGSO2 and MEO3 on 2012-09-19 (three stars is randomly selected, so the result is robust). In the top panel, the blue line represents the original data and the green line is the result of linear forecast method. In the bottom panel, the green line shows the difference between the original pcor and forecasting results, the RMS value shows between two panels. We find that the linear method could well forecast pcor, and it has a good performance for GEO satellites, but somewhat worse for dramatic IGSO and MEO satellites. This is because such method does not take into account the value jumping on the starting point of each hour, and the jumping appearance for GEO satellites is relatively small, comparing with IGSO and MEO satellites.

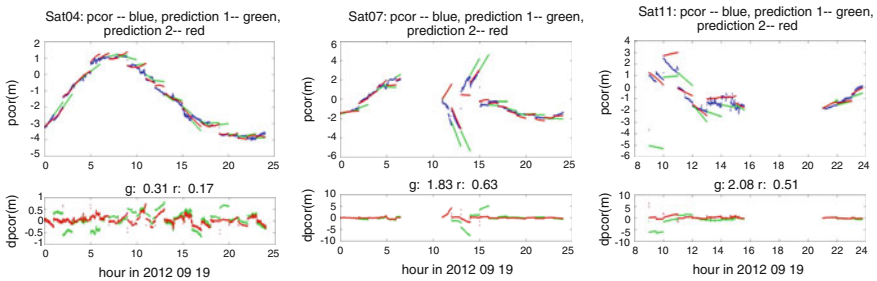

Fig. 10.2 Forecast result of pcor in 2012.9.19 (*left* GEO, *middle* IGSO, *right* MEO)

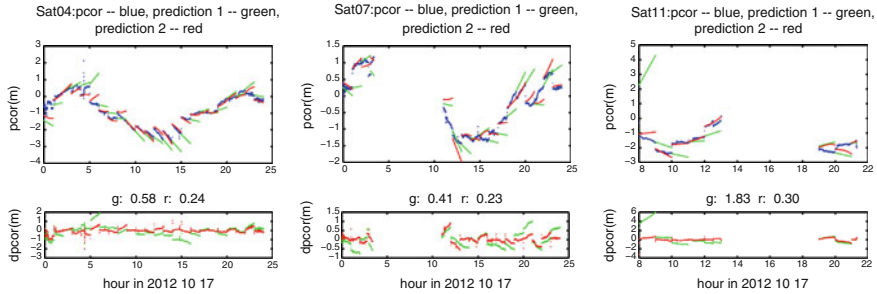

Fig. 10.3 Forecast result of pcor in 2012.10.17 (*left* GEO, *middle* IGSO, *right* MEO)

For the same three satellites, we tested the linear method with data when IGSO/MEO satellite are at orbit-normal mode on 2012-10-17. Forecasting results are shown in Fig. 10.3. We found that during orbit-normal mode, although the forecast could follow the main trend, but the forecasting accuracy is not high.

For wide area differential service, pcor is calculated based on the current hour (to avoid confusion, hereafter remark as the first hour) satellite clock error and ephemeris parameters in the broadcasted message. Since the forecasted pcor for second hour in the linear method is all based on the first hour information, it could be deviated by the old message of the first hour. The difference between real pcor data and the forecasting one could come from this. We thus propose to deduce the difference of clock error and ephemeris parameters between the two adjacent hour messages on top of the linear method (hereinafter referred to as linear correction method). Red lines in Figs. 10.2 and 10.3 show the results of this method. Compares the forecasting results for the two methods we can see that the modified method is better than simple linear method, especially in the orbit-normal mode or satellite orbit period, the RMS values obtained by the modified linear method can be reduced more than 50 % compared to the linear method. Since the orbital error and clock errors are easy to achieve short-term forecasting, this method could also be converted into practical technology. However, it should be noted that compared to linear method, such modified method would increase the processing load on the computer, thereby is much expensive for applying to engineering.

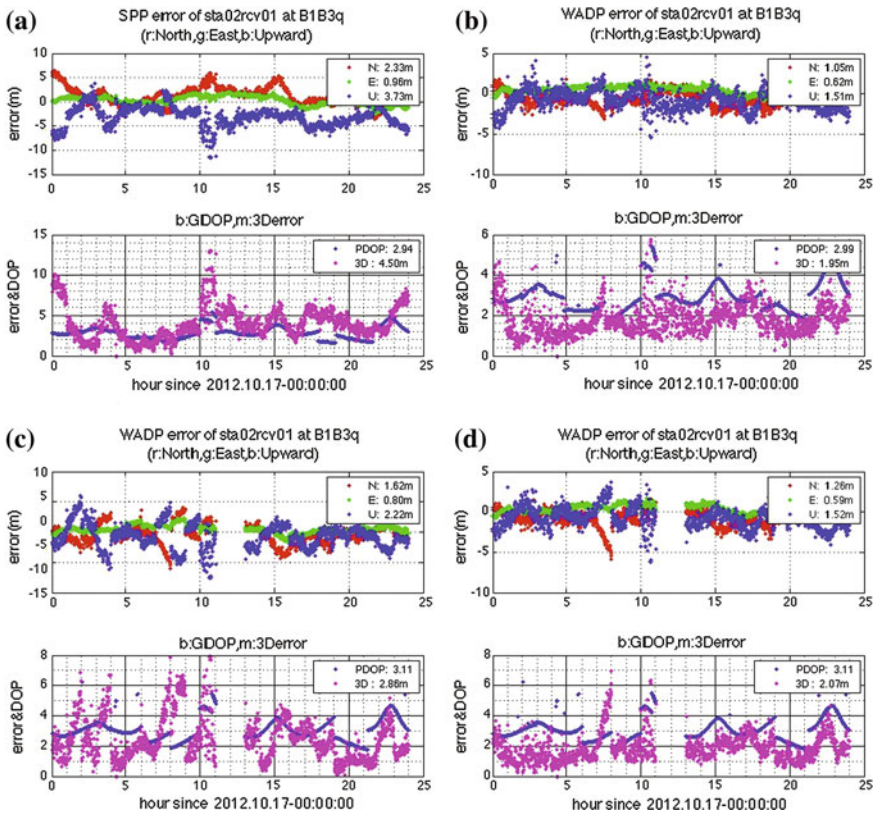

Fig. 10.4 Position accuracy of different methods in 2012.10.17

10.4 Application of Forecasted Pcor in Positioning

To further test the role of forecasting short-term pcor, we firstly carried out both linear method and modified linear method and then applied forecasting values to correct user's measurement data, testing how it affects positioning accuracy. Figure 10.4 is for 2012-10-17 data in Beijing. Figure 10.4a present the dual-frequency average user positioning accuracy without forecasting accuracy pcor for basic navigation service, and Fig. 10.4b is for wide area differential service. On the other hand, Fig. 10.4c, d present results that are used forecasting pcor (4c is with linear method and 4d is with modified linear method). The top sub-graphs in each figures show position error in north, east and up directions, which are denoted with red, green and blue line respectively. Position error in 3D is presented in bottom sub-graphs with pink line while position dilution of precision (PDOP) with blue. It is obvious that both forecasting method can effectively improve basic navigation service user's positioning accuracy, and modified forecasting method is better than

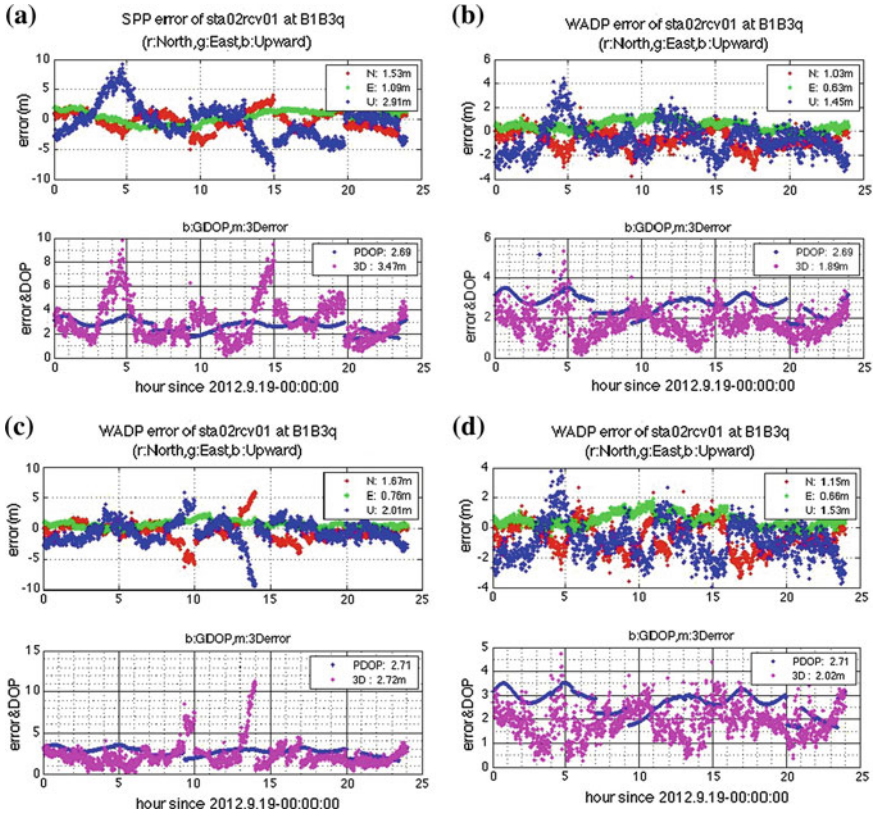

Fig. 10.5 Position accuracy of different methods in 2012.9.19

the linear method. Nevertheless, the results with modified linear method could be even close to wide area differential service user positioning accuracy.

For comparison, we also applied two methods to real data on 2012-09-19 in Beijing. As shown in Fig. 10.5, IGSO/MEO satellites are in yaw-steering mode, and two forecasting methods can improve the basic navigation service user positioning accuracy. Modified linear method seems to be better than linear method.

In order to verify the effectiveness and universality in the whole service area for the two forecasting methods, we randomly adopt 10 stations dispersedly within the service area, and perform again above tests for both method, the results are shown in Table 10.1. One can see that both forecasting methods could improve the positioning accuracy of basic navigation service in the whole service area, and modified linear method is superior to linear method, service accuracy with it could be even close to authorized users service accuracy.

Table 10.1 Positioning accuracy of 10 stations within service area

	2012-9-19				2012-10-17			
	A*	B	C	D	A	B	C	D
Beijing	3.47	1.89	2.72	2.02	4.50	1.94	2.86	2.07
Sanya	2.59	1.51	2.51	1.67	6.96	2.84	3.68	3.01
Kashgar	4.38	3.70	4.77	4.07	6.40	5.73	6.70	5.57
Chendu	3.82	2.26	3.33	2.56	6.26	2.98	3.91	3.23
Urumqi	4.72	3.90	5.47	4.23	6.81	5.96	7.12	5.70
Changchun	3.36	2.76	4.21	3.15	6.18	4.44	5.60	4.55
Shantou	2.58	1.51	2.43	1.68	6.04	1.70	2.71	1.84
Hailar	5.86	4.20	5.89	4.43	7.48	4.71	5.42	5.00
Ningbo	3.99	2.80	3.20	2.89	5.02	2.58	2.98	2.60
Lhasa	6.34	5.70	6.20	5.87	8.81	6.44	7.24	6.31

**A* basic navigation service, *B* wide area differential service, *C* linear method, *D* modified linear method

10.5 Summary

Pcor can effectively correct orbital error and reduce the effects on positioning accuracy caused by yaw mode changing or other factor. We thus propose to forecast pcor in short-term for basic navigation service, aiming at improving the service accuracy for basic navigation service.

In this work, we firstly analyzed the historical data of pcor, and found that within each hour, pcor has continuous and slowly varying features, one can use a simple linear function to fit the data. And slight jump characteristics exist on the hour, since the calculation of pcor is based on the navigation messages, and the messages were broadcasted on the hour.

Based on the above analysis, we propose two methods for short-term pcor forecast: linear method and modified linear method. We compared the forecasting results and the real data for both methods, and proved the validation of these two methods. The liner method is easier for converting into practical technology, but the modified method has higher forecasting accuracy.

We also applied the forecasting results to improve positioning accuracy of basic navigation service, it turns out that both methods could effectively reduce the effects from attitude-control mode changing for the whole service area, and also improve the overall positioning accuracy for basic navigation service. Sometimes even close to the wide area differential service accuracy.

References

1. Song WL, Tan SS (2007) The current status and development of WAAS technique. Radio Eng China 37(6):50–52 (in Chinese)
2. Hein GW (2000) From GPS and Glonass via EGNOS to Galileo-positioning and navigation in the third millennium. GPS Solut 3(4):39–47

3. Ashley WL, Umberto G, Fernandez JL (2006) EGNOS: a step closer to operational qualification. In: Proceedings of the 19th international technical meeting of the Satellite Division of the Institute of Navigation (ION GNSS), Fort Worth Convention Center, Fort Worth, pp 906–912
4. www.beidou.gov.cn/xtjs.html. (EB/OL)
5. China Satellite Navigation Office (2013) BeiDou navigation satellite system signal in space interface control document basic navigation service signal (version 2.0)
6. Cao YL, Hu XG, Wu B et al (2012) The wide-area difference system for the regional satellite navigation system of COMPASS. Sci China Phys Mech Astron 55(7):1307–1315
7. Zhou SS, Hu XG, Zhou JH et al (2013) Accuracy analyses of precise orbit determination and timing for COMPASS/Beidou-2 4GEO/5IGSO/4MEO constellation. In: Proceedings of China satellite navigation conference (CSNC), 2013
8. China Satellite Navigation Office (2013) BeiDou navigation satellite system open service performance standard (version 1.0)

Chapter 11
Multi-GNSS Processing Combining GPS, GLONASS, BDS and GALILEO Observations

Hongzheng Cui, Geshi Tang, Songjie Hu, Baiyan Song, Huicui Liu, Jing Sun, Peng Zhang, Cuilan Li, Maorong Ge and Chao Han

Abstract Coexistence and development of four kinds of Global Satellite Navigation System, GPS, GLONASS, BDS, and GALILEO have initially established. In order to benefit from multi-GNSS applications, including increase in usable SVs, signals and frequencies, increase in availability and coverage, more robust and reliable services, and so on, firstly we need to obtain the precise multi-GNSS orbit and clock in a unified space and time frame. Based on the knowledge of the EPOS and EPOS-RT (Earth Parameter and Orbit determination System in Real-Time) software package, Beijing Aerospace Control Center (BACC) has been working on his own software package for multi-GNSS data processing. This paper firstly introduces the multi-GNSS processing strategies in detail, and adopts additional inter system biases parameter (ISB) except the normal IGS and GFZ observation model and dynamic model. On the basis of above strategies and the observation data from a network of multi-GNSS capable receivers from the IGS Multi-GNSS EXperiment (MGEX) and a regional BDS station network operated by China, the experiments and simulation are carried out. The results are validated against products from other institutes and by overlap comparison. The impact on orbit and clock precision by combined processing against single system processing is investigated and the improvement on precise point positioning (PPP) is also evaluated.

Keywords Multi-GNSS · Combined data processing · Inter system biases (ISB) · Orbit overlap · Precise point positioning (PPP)

H. Cui (✉) · G. Tang · S. Hu · B. Song · H. Liu · J. Sun · P. Zhang · C. Li
Flight Dynamics Laboratory, Beijing Aerospace Control Center, Beijing 100094, China
e-mail: H.Z.Cui@hotmail.com

H. Cui · C. Han
School of Astronautics, Beijing University of Aeronautics and Astronautics, Beijing 100191, China

M. Ge
German Research Center for Geosciences, Potsdam, Germany

J. Sun et al. (eds.), *China Satellite Navigation Conference (CSNC) 2014 Proceedings: Volume III*, Lecture Notes in Electrical Engineering 305,
DOI: 10.1007/978-3-642-54740-9_11,

11.1 Introduction

Three Global Navigation Satellite Systems (GNSS) are currently operational, namely GPS and GLONASS for providing global positioning service and BDS (BeiDou-2) for providing regional positioning service. Other systems are under development in particular the European Galileo. There will be at least four operational GNSS in the near future. The success of all available systems applications and the acceptance of the new systems is a "must", but the transition from single-system to multi-GNSS applications is a challenge, because of the upgraded hardware and tracking networks, implemented Multi-GNSS capable analysis software packages, algorithms, and models. In order to summary the necessary knowledge to analyze observation data in a combined multi-GNSS data processing and explore the application of multi-GNSS in different fields we need to analyse the precision of combined processing which can reach, specially for combined orbit determination and positioning. CODE has started with a rigorously combined analysis of GPS and GLONASS measurements in May 2003 [1], and other ACs of the IGS, ESOC, and GFZ followed this approach [2], and Prange [3] from CODE introduced the first experiences about MGEX data analysis combining GPS, GLONASS, and GALILEO observations with the accuracy reaching 3.5 cm for G01, 3.5 cm for R24, and 8.5–17 cm for GALILEO. Meindl [4], Li [5], and He [6] in their Ph.D dissertation introduced the multi-GNSS processing algorithms, and models. Uhlemann [7] from GFZ and Hackel [8] from TUM conducted combination GPS/GALILEO estimation with the 3D overlapping accuracy of GALILEO reaching 5–8 cm and 2–3 cm respectively. Liu [9] analysed the combined GPS/BDS orbit determination, and 3D RMS of GEO, IGSO and MEO is 155, 33, and 18 cm, the radial precision is basically better than 10 cm. Qu [10] realized the GPS/BDS static and kinematic PPP and the result indicated that the precision of BDS static and kinematic PPP reaches centimeter level, and combined PPP improves the precision and convergence time than single system. Tegedor [11] first analysed the multi-GNSS orbit determination and PPP including GPS, GLONASS, BDS and GALILEO, and the accuracy for GALILEO and BDS MEO/IGSO reaches sub-decimeter and for BDS GEO reaches decimeter, and the accuracy and convergence time improved. Especially, MGEX and JAXA Multi-GNSS Demonstration Campaign push the change from GPS-only to multi-GNSS [12].

The papers above have rarely discussed the full Multi-GNSS processing combining GPS, GLONASS, BDS and GALILEO observations; and the characteristic on inter system biases parameters involved the four systems which is vital to obtain precise Multi-GNSS orbit and clock in a unified time and space frame. This paper firstly introduces the Multi-GNSS processing activities at iGMAS (international GNSS Monitoring and Assessment Service) Analysis Center (BAC) at BACC. Then, describes the research strategies briefly including data, processing strategies, and impact analysis, and based on the strategies conducts experiments and simulation study for combined processing. The results are validated against

products from other institutes and by overlap comparison. The impact on orbit and clock precision by combined processing against single system processing is investigated and the improvement on precise point positioning (PPP) is also evaluated. Finally, the results of experiments are analyzed in detailed before the conclusions are drawn.

11.2 Multi-GNSS Processing at BAC

The BDS constellation composed of 14 GEO satellites has deployed by 2012 and begins to provide positioning services for Asia-Pacific region. In order to provide services of GNSS performance monitoring, promote service assurance, improve service performance, ensure the interoperability of OS signals for four systems, GPS/GLONASS/GALILEO/BDS, a subgroup on iGMAS is established in 6th meeting of ICG in Sep 2011 [13]. The iGMAS components involve Tracking Stations network (TS), Operational Center (OC), Data Center (DC), Analysis Center (AC), Combination Center (CC), and Monitoring and Assessment Center (MAC), and core products include precise satellite orbit and clock, tracking station coordinate and receiver clock, Zenith Total Delay (ZTD), Earth Orientation Parameter (EOP) parameters, global statistical integrity and Ionospheric map. BACC is doing the work about operation and maintenance the iGMAS Analysis Center (BAC) [14], and producing the precision products to the users with equivalent accuracy to well-known institutes, such as IGS and CODE.

With regard to Multi-GNSS processing, BAC implements combined processing capability for four systems based on the knowledge of the EPOS and EPOS-RT software package. The Multi-GNSS precise products including orbit and clock, ZTD, EOP parameters, global statistical integrity and Ionospheric map, and this paper just focuses on the combined orbit and clock.

11.3 Research Strategy

The observation data from a network of multi-GNSS capable receivers from the MGEX tracking network and a regional BDS station network operated by China from day 321 to 334 in 2013. There are 17 tracking stations shown in Fig. 11.1, and the station name, inclusive systems, and receiver type are listed in Table 11.1 with exceptional staion named gua1 traking three systems.

Taking advantage of GPS observation and mature models to do joint orbit determination in a unified time and space frame to improve the orbit of other systems, and using the GPS orbit and clock from joint solution as the external check, we adopt joint orbit determination of GPS and GLONASS/BDS/GALILEO, firstly fixing the coordinate of station, receiver clock and tropospheric parameters using GPS precise ephemeris and clock, and then seting inter-system bias (ISB)

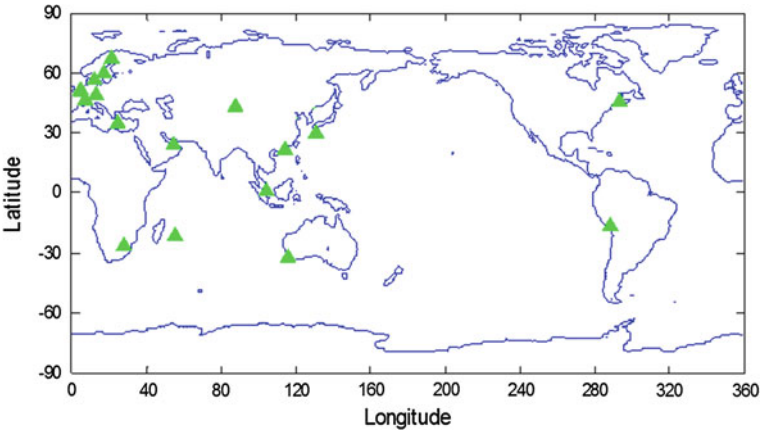

Fig. 11.1 The multi-GNSS capable ground tracking stations

Table 11.1 The multi-GNSS capable ground tracking stations summary

No.	Station name	Systems	Receiver type
1	unb3	G/R/C/E	Trimble NetR9
2	cut0	G/R/C/E	Trimble NetR9
3	dlf1	G/R/C/E	Trimble NetR9
4	zim3	G/R/C/E	Trimble NetR9
5	kri8	G/R/C/E	Trimble NetR9
6	mar7	G/R/C/E	Trimble NetR9
7	ons1	G/R/C/E	Trimble NetR9
8	reun	G/R/C/E	Trimble NetR9
9	gmsd	G/R/C/E	Trimble NetR9
10	areg	G/R/C/E	Trimble NetR9
11	brux	G/R/C/E	POLARX4TR
12	wtzz	G/R/E	JAVAD TRE_G3TH
13	jfng	G/R/C/E	Trimble NetR9
14	wark	G/R/C/E	Trimble NetR9
15	gua1	G/R/C	UNICORE UB4B0I
16	kun1	G/R/C/E	UNICORE UB4B0I
17	cny1	G/R/C/E	UNICORE UB4B0I

between GPS and GLONASS/BDS/GALILEO as a parameter to be estimated. Table 11.2 summaries the satellite force models and GFZ standard observation modeling except Yaw-control model used in three day solution, which are kept the same for all the network configurations.

For impact analysis, we compare the GPS/GLONASS orbit and clock to IGS final orbit and clock products to evaluate the accuracy, and the accuracy of BDS/GALILEO orbit and clock and can be validated by checking the orbit differences of overlapping time span between two adjacent three-day, as shown in Fig. 11.2.

Table 11.2 The satellite force models and observation parameters

Satellite force models	Description
	GPS/GLONASS/BDS/GALILEO
Mean earth gravity	EGM96 8 × 8
N-body	DE 405 (SUN MOON MERC VENU MARS JUPI SATU)
Solid earth tide	IERS 2003
Ocean tide	CSR 4.0
Solar radiation	BERN model with 5 parameters
Relativity	IERS 2003
Atmospheric drag	None
Empirical force	None
Integrator	Step: 60 s, Adams order: 11
Observation parameters	Description and prior information
Tracking data	GPS/GLONASS/BDS/GALILEO: zero-difference, combination of LC and PC, 30 s sampling
GNSS satellite orbit	GNSS initial position: 10.0 m, GNSS initial velocity: 0.1 m/s
Ground station coordinates	GPS-based PPP
Satellite clock	White noise: 30,000 m
Receiver clock	White noise: 9,000 m
Troposphere zenith delay	Random walk: 0.2 + 0.02 m/sqrt(h)
Xpole-Ypole, Xpole-Ypole rate	Fixed IERS EOPC
UT1, UT1 rate	Fixed IERS EOPC
Integer ambiguity	10,000.0 cycle
Solar radiation pressure	Parameter estimation
ISB	White noise: 900 m
PCO/PCV	GPS/GLONASS: IGS absolute correction BDS/GALILEO: only PCO Stations: not corrected for BDS/GALILEO; IGS absolute correction for GPS/GLONASS

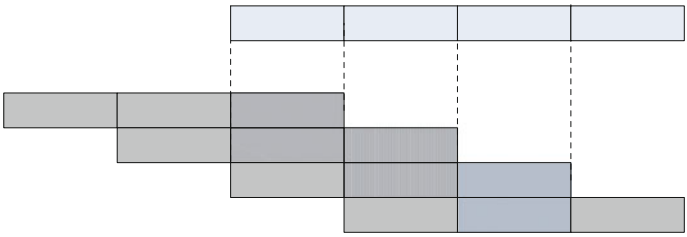

Fig. 11.2 Three-day sliding window with one-day step-size

In addition, the characteristic on inter system biases parameters involved the four systems and the the improvement on precise point positioning against single system are investigated.

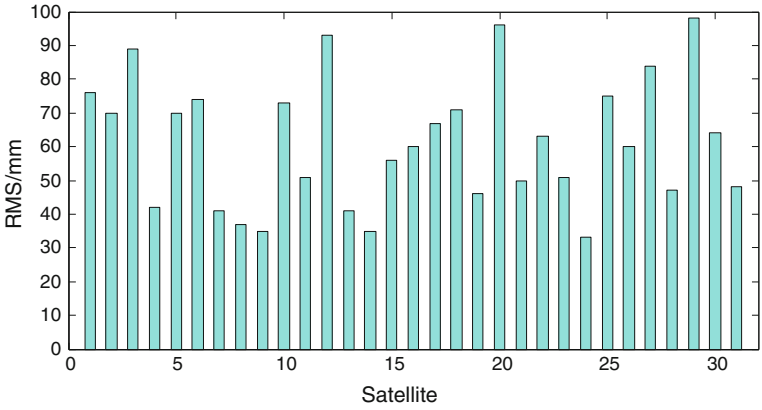

Fig. 11.3 The mean RMS of GPS orbit compared with IGS final orbit from day 321 to 334 in 2013 (unit: mm)

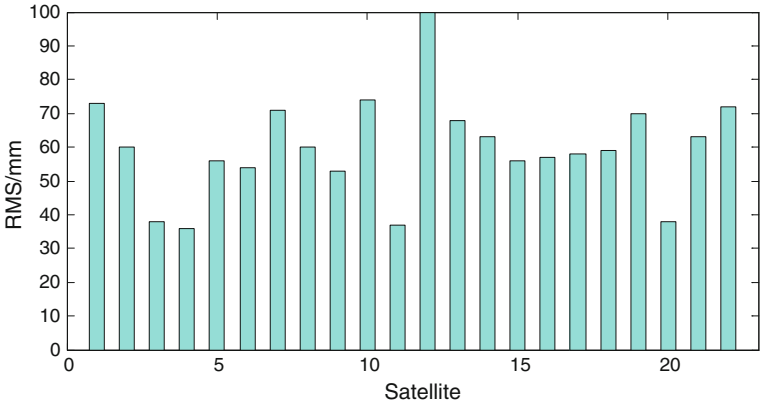

Fig. 11.4 The mean RMS of GLONASS orbit compared with IGS final orbit from day 321 to 334 in 2013 (unit: mm)

11.4 Experiments and Simulation Study

To investigate what is achievable with the current Multi-GNSS processing at BAC, the experiments are carried out with above strategis, and the satellite orbit and clock, ISB characteristics, and PPP results are compared and assessed. The results are shown in Figs. 11.3, 11.4, 11.5, 11.6, 11.7, 11.8, 11.9, 11.10, 11.11, 11.12 and 11.13.

As shown in Figs. 11.3 and 11.4, the mean 3D RMS of GPS and GLONASS orbit compared with IGS final product can reaches 3–9 cm.

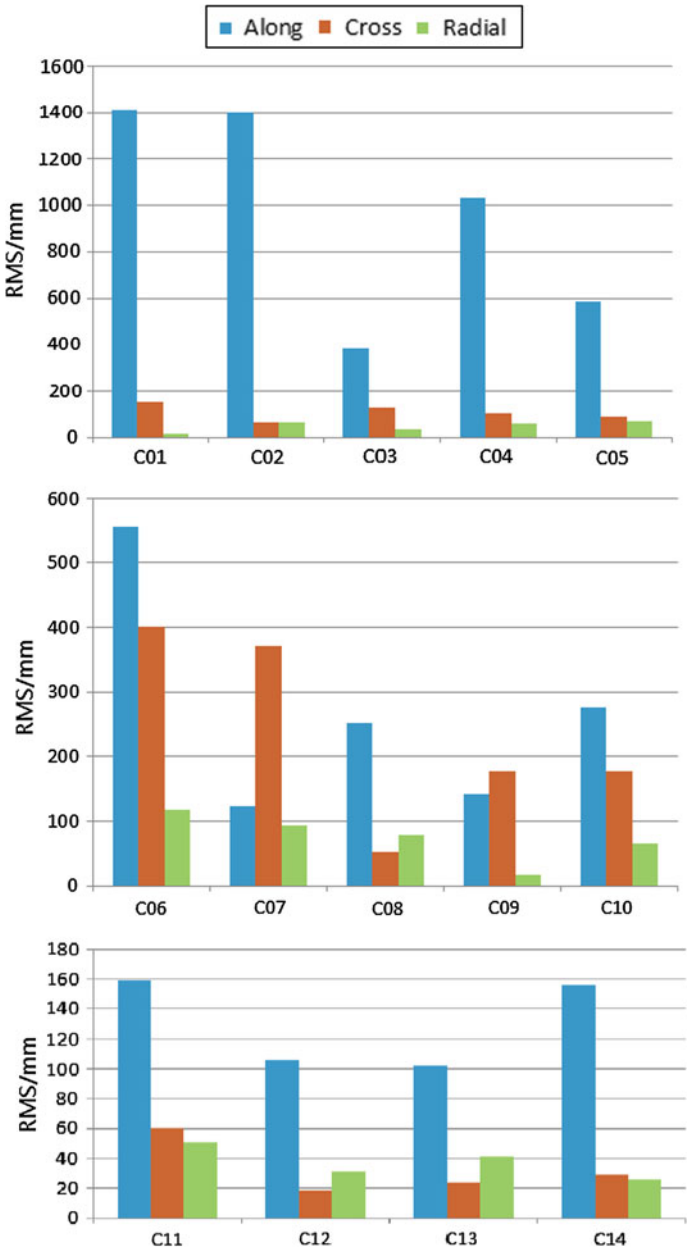

Fig. 11.5 The mean RMS of BDS orbit overlapping orbit difference from day 321 to 334 in 2013 (unit: mm)

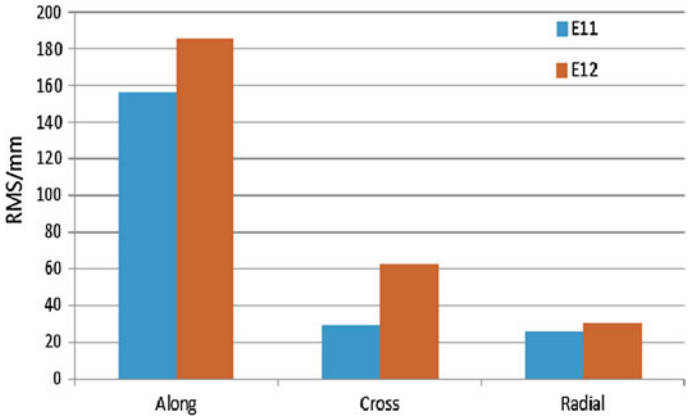

Fig. 11.6 The mean RMS of GALILEO orbit overlapping orbit difference from day 321 to 334 in 2013 (unit: mm)

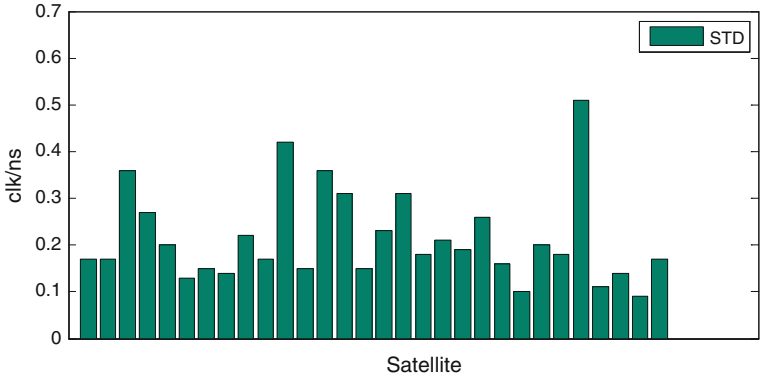

Fig. 11.7 The mean STD of GPS clock compared with IGS final clock from day 321 to 334 in 2013 (unit: ns)

As shown in Fig. 11.5, the accuracy for BDS in along direction is worse than in cross and radial direction, especially for GEO satellites. The mean 3D RMS of overlapping orbit reaches 300, 20 and 10 cm for GEO, IGSO and MEO respectively. And the radial RMS of BDS overlapping orbit can reach approximate and below 10 cm for GEO, IGSO, and MEO.

As shown in Fig. 11.6, the orbit assessment is done from overlaps from 3-day solution, and the orbit accuracy in radial direction of E11 and E12 can reach 2 cm.

As shown in Figs. 11.7 and 11.8, the mean STD of GPS and GLONASS clock compared with IGS final product can reach 0.25 ns approximately.

Figures 11.9 and 11.10 show that the mean STD is 0.37 ns for BDS satellite Clock, and GALILEO clock is 0.25 ns.

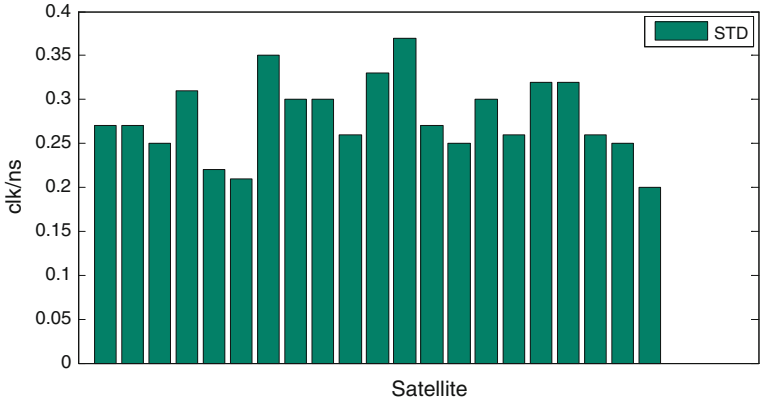

Fig. 11.8 The mean STD of GLONASS clock compared with IGS final clock from day 321 to 334 in 2013 (unit: ns)

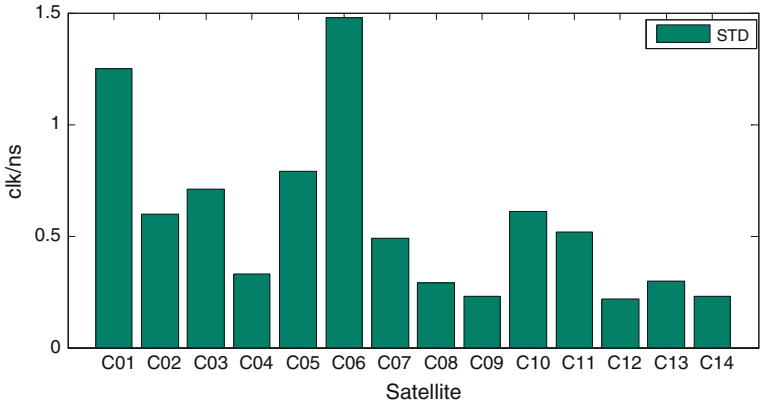

Fig. 11.9 The mean STD of BDS clock overlapping clock difference from day 321 to 334 in 2013 (unit: ns)

Figures 11.11 and 11.12 present the ISB between of GPS and BDS for all stations, and the ISBs on different days have the same change trend. The BRUX station equipped with POLARX4TR has more variety than other stations, and the dlf1, zim3, kir8, mar7, ons1, gmsd, and areg have commendable stability.

Using GPS one-day static PPP coordinates as reference, the average accuracy of PPP with different systems as shown in Fig. 11.13, and better PPP performance following Multi-GNSS can be achieved.

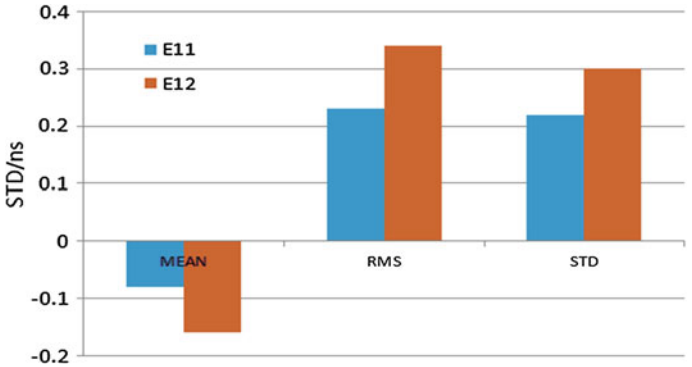

Fig. 11.10 The mean STD of GALILEO clock overlapping clock difference from day 321 to 334 in 2013 (unit: ns)

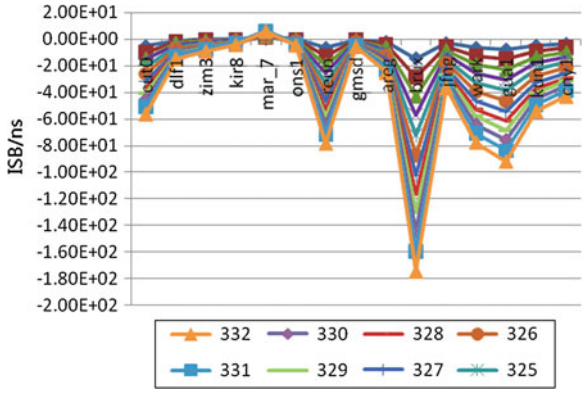

Fig. 11.11 ISB between of GPS and BDS for all stations (unit: ns)

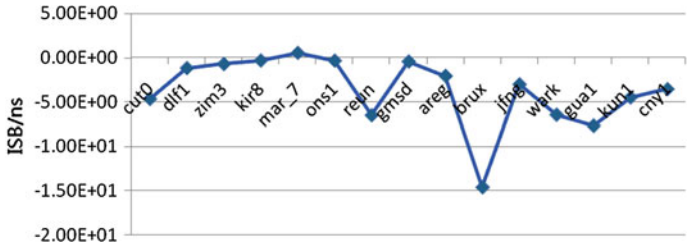

Fig. 11.12 The mean ISB between of GPS and BDS for all stations (unit: ns)

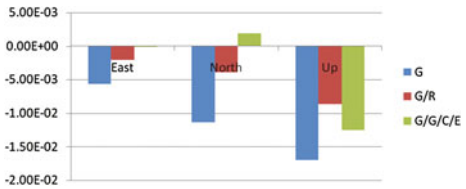

Fig. 11.13 BJSH station one-day static PPP (unit: m)

11.5 Conclusion

The preliminary research shows that the processing strategies at BACC is feasible and builds up a good basis for Multi-GNSS data analysis and other scientific research based on GNSS in the future. In the future research, the refinement of satellite attitude control model, the PCO/PCV correction, and the IFB should be taken into account, and the Multi-GNSS ambiguity fixing in data processing and positioning should be researched. This paper focuses on the rapid, and in the future work the Ultra-rapid resolution, real-time resolution, Multi-day combination resolution and routine performance assessment will be carried out, and hope to apply the high precision products to China space missions.

References

1. Dach R, Brockmann E, Schaer S, Beutler G, Meindl M, Prange L, Bock H, Jäggi A, Ostini L (2009) GNSS processing at CODE: status report. J Geodesy 83(3–4):353–365. doi:10.1007/s00190-008-0281-2
2. Springer T, Dach R (2010) GPS, GLONASS, and more. GPS World 21(6):48–58
3. Prange L, Dach R, Lutz S, Schaer S, Meindl M, Jäggi A (2012) MGEX data analysis at CODE—first experiences. IGS Workshop, Olsztyn, Poland, 23–27 Jul 2012
4. Meindl M (2011) Combined analysis of observations from different global navigation satellite systems. PhD thesis, University of Bern
5. Li M (2011) Research on multi-GNSS precise orbit determination theory and application. PhD thesis, University of Wuhan
6. He L (20113) The research on multi-GNSS satellites precise orbit determination. PhD thesis, University of Tongji
7. Uhlemann M, Gendt G et al (2012) GFZ's global multi-GNSS network and first data processing results. IGS Workshop, Olsztyn, Poland, 23-27 Jul 2012
8. Hackel S, Steigenberger P, Montenbruck O et al (2012) GALILEO IOV ORBIT DETERMINATION AND VALIDATION. IGS Workshop, Olsztyn, Poland, 23-27 Jul 2012
9. Liu Y, Lou Y D et al (2013) Beidou regional navigation system network solution and precision analysis. In: China Satellite navigation conference. Springer, Berlin
10. Qu L Zhao Q Li M et al (2013) Precise point positioning using combined Beidou and GPS observation. In: China Satellite navigation conference. Springer, Berlin
11. Tegedor J et al (2013) Multi-constellation precise point positioning including GPS, GLONASS, Galileo and BeiDou. GNSS PPP workshop

12. Weber R (2012) IGS M-GEX—the IGS multi-GNSS global experiment. Workshop on GNSS Biases, Bern, 18–19 Jan 2012
13. Yang (2012) Working progress of iGMAS. IGS workshop
14. Cui H et al (2013) Initial data processing assessment of the COMPASS satellite navigation system. In: 64th international astronautical congress

Chapter 12
GPS Receiver Clock Modelling for Kinematic-Based Precise Orbit Determination of Low Earth Orbiters

Yang Yang, Xiaokui Yue, Yong Li, Chris Rizos and Andrew G. Dempster

Abstract This paper describes a GPS receiver clock model that can improve the accuracy of kinematic orbit determination for spacecraft in low earth orbit. The receiver clock error is commonly estimated on an epoch-by-epoch basis, along with the satellite's position. However, due to the high correlation between the spacecraft orbit altitude and the receiver clock parameters, estimates of the radial component are degraded in the kinematic-based approach. Using clocks with high stability, e.g., ultra-stable oscillators, the highly predictable frequency behaviour of the receiver oscillator can be fully exploited to improve the positioning accuracy, especially for the radial component. A simple two-state model is used to describe the deterministic and stochastic property of the receiver clock. In particular, the clock parameters are estimated as time offset and frequency offset. Additionally, residual non-deterministic random errors such as frequency white noise, flicker noise and random-walk noise are modelled. The test results of GRACE flight data indicate that the positioning accuracy could be improved significantly. In particular, the radial component error was reduced by over 60 %.

Keywords Kinematic orbit determination · Clock modelling · Allan variance

12.1 Introduction

With the ever-increasing number of scientific applications of satellites in low Earth orbit (LEO) the precise determination of the position and velocity of the satellite is a necessity. Traditionally external observations from ground stations have been

Y. Yang (✉) · X. Yue
National Key Laboratory of Aerospace Flight Dynamics (AFDL),
Northwestern Polytechnical University, Xi'an, China
e-mail: yiyinfeixiong@gmail.com

Y. Yang · Y. Li · C. Rizos · A. G. Dempster
University of New South Wales, Sydney, Australia

J. Sun et al. (eds.), *China Satellite Navigation Conference (CSNC) 2014 Proceedings: Volume III*, Lecture Notes in Electrical Engineering 305,
DOI: 10.1007/978-3-642-54740-9_12,

used for satellite orbit determination. However, more and more space missions benefit from the use of an autonomous navigation system, which can estimate a satellite's state using the measurements available on-board. Since the beginning of the 1990s, the U.S. Global Positioning System (GPS) has been used for spacecraft navigation, providing high precision orbit information with minimum ground intervention. Based on the improvement of GPS data quality, the purely kinematic precise orbit determination (KPOD) [1, 2] approach has become an attractive alternative method for LEO satellites to dynamic and reduced-dynamic orbit determination methods (DPOD) [3, 4]. The KPOD makes use of a precise point positioning (PPP) approach for epoch-wise solution of the satellite's state from GPS observations. Important advantages of this approach are that it requires no a priori knowledge of spacecraft motion, and the positioning solutions are obtained very quickly.

To use the range-based positioning principle, the time of signal flight must be known, which in the case of one-way ranging is equal to the time of signal reception minus the time of signal transmission. As both clocks, on the GPS satellite and the LEO satellite, are synchronised to GPS time, the clock errors due to the oscillator instability/error must be accounted for. The GPS satellite clock error can be corrected using the clock model in the broadcast message, or using the IGS (International GNSS Service) precise clock products depending on the application [5]. However, the receiver clock error remains unknown. In general, the LEO orbit state and clock estimates are correlated. The receiver clock time error or "offset" is commonly treated as an unknown parameter and estimated along with LEO satellite positions at every observation epoch within the orbit determination algorithm. There are some drawbacks associated with epoch-by-epoch clock offset estimation. One is that suitable GPS geometry, including observations to at least four satellites must be available all the time. Additionally there is high correlation between the satellite orbit altitude and the receiver clock parameters [6, 7].

A clock is essentially an oscillator generating a periodic signal and a counter that keeps count of the number of cycles or oscillations [8]. The fundamental characteristic of a clock is its frequency stability. If clocks with high stability are used on board, e.g. ultra-stable oscillators (USO), the frequency behaviour of the receiver oscillator can be exploited to improve the positioning accuracy, especially for the radial coordinate [9, 10]. In this paper a two-state clock functional model and stochastic model, implemented within a Kalman filter, are investigated.

The paper is organised as follows: the functional model of GPS observations for KPOD is presented in Sect. 12.2. Section 12.3 introduces a two-state clock model. With the aid of the Allan deviation or the spectral density coefficients of the oscillator, the covariance matrix is obtained. In Sect. 12.4 a set of flight data from the Gravity Recovery and Climate Experiment (GRACE) mission is used for testing of the proposed receiver clock error model. The positioning results are compared with the standard KPOD method, and the estimated clock parameters (clock time offset and frequency offset) are analysed.

12.2 Functional Model of GPS Observations

12.2.1 Ionosphere-free Combination of GPS Observations

The GPS observation equations can be written as:

$$\begin{aligned} PR_r^{s,f} &= \rho_{r,PR}^{s,f} + c(cl_r - cl^s) + I_r^{s,f} + PCO^{s,f} + PCO_r^f + M_{r,PR}^{s,f} + v_{r,PR}^{s,f} \\ CP_r^{s,f} &= \rho_{r,CP}^{s,f} + c(cl_r - cl^s) - I_r^{s,f} + \lambda^f N_r^{s,f} + \lambda^f \left(\phi_{r,0}^f + \phi_0^{s,f}\right) + PCO^{s,f} \\ &\quad + PCO_r^f + \lambda^f \phi_r^{s,f} + M_{r,CP}^{s,f} + v_{r,CP}^{s,f} \end{aligned} \tag{12.1}$$

where the superscript s and f indicate the GPS satellite and the signal frequency respectively, and subscript r indicates the receiver. The terms in the equations are:

PR, CP	Code phase and carrier phase observation [m]
ρ_{PR}, ρ_{CP}	Geometric distance between receiver and GPS satellite [m]
I	Ionospheric delay [m]
c	Speed of light: 299,792,458 [m/s]
cl	Clock error, including relativistic corrections [s]
λ	Signal wavelength at frequency f [m]
N	Carrier phase integer ambiguity [cycle]
ϕ_0	Initial phase of carrier phase [cycle]
PCO	Phase centre offset [m]
ϕ	Relative rotation between GPS and receiver antennas [cycle]
M	Multipath effects [m]
v	Unmodelled code phase and carrier phase errors [m]

When two frequencies are used, the first order ionosphere effects can be mitigated, via the ionosphere-free combination of the measurements:

$$\begin{aligned} PR_{r,IF}^s &= \frac{f_1^2}{f_1^2 - f_2^2} PR_r^{s,1} - \frac{f_2^2}{f_1^2 - f_2^2} PR_r^{s,2} \\ CP_{r,IF}^s &= \frac{f_1^2}{f_1^2 - f_2^2} CP_r^{s,1} - \frac{f_2^2}{f_1^2 - f_2^2} CP_r^{s,2} \end{aligned} \tag{12.2}$$

Combining Eqs. (12.1) and (12.2), the ionosphere-free observations can be written as:

$$\begin{aligned} PR_{r,IF}^s &= \rho_{r,PR}^{s,f} + c(cl_r - cl^s) + PCO_{PR_{IF}}^s + PCO_{r,PR_{IF}} + M_{r,PR_{IF}}^s + v_{PR_{IF}}^s \\ CP_{r,IF}^s &= \rho_{r,CP}^{s,f} + c(cl_r - cl^s) + A_{IF}^s + PCO_{CP_{IF}}^s + PCO_{r,CP_{IF}} + \phi_{r,IF}^s + M_{r,CP_{IF}}^s + v_{CP_{IF}}^s \end{aligned} \tag{12.3}$$

It should be noted that the carrier phase ambiguity, A_{IF}^{S}, is no longer an integer quantity, hence it will be estimated as a floating value and no integer ambiguity fixing procedure is applied.

12.2.2 Relativistic Clock Effects

Clocks in orbit are subjected to relativistic frequency shifts. For precise orbit determination these effects must be corrected for. The relativistic frequency shifts have both constant and time-varying components [11]:

$$\frac{d\tau}{dt} = -\frac{1}{c^2}\left(\frac{v^2}{2} + U(r)\right) \tag{12.4}$$

where c is the vacuum speed of light, r and v are position and velocity of satellite in the earth-centred earth-fixed frame, and U is the earth's gravitational potential.

For GPS satellite clocks, only the first term of the gravitational potential is retained based on a Keplerian orbit assumption, and the constant component is easily computed. Consequently only the periodic component of the relativistic effect needs to be corrected for:

$$\tau_{per} = -\frac{2}{c^2}\mathbf{r}\cdot\mathbf{v} \tag{12.5}$$

However, LEO satellites will be more affected by the J_2 term in the model of the Earth gravity. It is therefore necessary to use a numerical integration procedure to take J_2 into account. A more general expression for the relativistic effects of LEO satellite clocks is given in [12].

12.2.3 Phase Windup Effects

The phase windup effect occurs in carrier phase measurements due to changes in the orientation between the transmitting and the receiving antenna. The rapid motion of the spaceborne receiver may result in more significant effects of phase windup because of the difference in attitudes between the transmit and receive antennas. The changing orientation may either be calculated from LEO satellite attitude determination information or by assuming a nominal attitude. More details of the phase windup correction can be found in [13].

12.2.4 Phase Centre Offset Correction

When IGS GPS precise orbit and clock products are used in the orbit determination, the GPS satellite phase centre offset (PCO) should be applied. This is

because these products are generated with respect to the GPS satellite's centre of mass, however the measurements are made to the antenna phase centre [5]. Similarly, the PCO of the spaceborne GPS receiver should also be accounted for. The spaceborne receiver has a specific installation on the satellite body according to the mass centre which results in a fixed antenna reference point (ARP), consequently the receiver PCO between the ARP and the phase centre must be applied [14].

12.2.5 Multipath Effects

Multipath is an effect linked to signal reflections in the environment of the receiver. By use of an ionosphere-free observable for KPOD, the multipath effect remains as one of the most significant error sources due to code phase measurements. The amplitude variations of multipath effects are typically larger at lower elevation angles, hence an appropriate elevation angle threshold (e.g. 5°) could significantly mitigate the multipath errors.

12.3 GPS Receiver Clock Modelling

High-fidelity frequency standards are used in many GPS signal tracking applications. These frequency standards are typically divided into different categories, such as quartz crystal oscillators, and rubidium and cesium atomic clocks [15]. Several space missions (including GRACE) have been using ultra-stable quartz oscillators (USO). Based on the high-stability property of USO, the receiver clock time offsets can be predicted using a simple two-state model. The high-quality oscillators installed on the two GRACE satellites have frequency stabilities of the order of $\sigma_y(\tau) = 1\text{–}3 \times 10^{-13}$ with $\tau = 1\text{–}1{,}000$ s [16]. Weinbach and Schön [10] analysed the feasibility of GRACE receiver clock modelling using USO. In theory, a linear model of the GRACE USO can be used for time intervals of up to 60 s.

12.3.1 A Two-state Receiver Clock Model

In general, the receiver clock error can be described as a simple deterministic model (e.g. a linear polynomial) with a stochastic model:

$$clk_n = a_0 + a_1 n\tau_0 + \cdots + a_m (n\tau_0)^m + \varepsilon_n \tag{12.6}$$

where clk_n denotes the receiver clock error at epoch n, a_0 and a_1 denote the initial clock time offset and fractional frequency offset respectively, a_m is the high order

polynomial coefficient, τ_0 is the sampling interval and ε_n is the unmodelled random noise. The clock term can be classified into two effects: deterministic errors including terms of a_0, a_1, $\cdots a_m$, and non-deterministic random errors such as white noise, flicker noise and random walk noise. Since a_0 and a_1 are the dominant terms in the clock error, the clock parameters to be estimated along with LEO positions are these two coefficients:

$$\begin{bmatrix} \dot{a}_0 \\ \dot{a}_1 \end{bmatrix} = \begin{bmatrix} 0 & 1 \\ 0 & 0 \end{bmatrix} \begin{bmatrix} a_0 \\ a_1 \end{bmatrix} + \begin{bmatrix} w_{a_0} \\ w_{a_1} \end{bmatrix} \tag{12.7}$$

with process noise:

$$E\left(\begin{bmatrix} w_{a_0} & w_{a_1} \end{bmatrix}^T \begin{bmatrix} w_{a_0} & w_{a_1} \end{bmatrix}\right) = Q_w \tag{12.8}$$

For high quality clocks, the time offset noise originating from the instability itself is small and will not accumulate over time. Consequently the dominant time offset is the accumulated error originating from frequency instability [17]. The covariance matrix components are derived by means of the power spectral density (PSD) coefficients (h_0, h_{-1} and h_{-2}) of the oscillator [15]:

$$Q_w = \begin{bmatrix} \frac{h_0}{2}\Delta t + 2h_{-1}\Delta t^2 + \frac{2}{3}\pi^2 h_{-2}\Delta t^3 & \frac{h_0}{2} + 4h_{-1}\Delta t + \frac{8}{3}\pi^2 h_{-2}\Delta t^2 \\ \frac{h_0}{2} + 4h_{-1}\Delta t + \frac{8}{3}\pi^2 h_{-2}\Delta t^2 & \frac{h_0}{2\Delta t} + 2h_{-1} + \frac{2}{3}\pi^2 h_{-2}\Delta t \end{bmatrix} \tag{12.9}$$

where h_0, h_{-1} and h_{-2} describe the impact of white frequency, flicker frequency and random walk frequency noise, respectively. These coefficients can be calculated from the relationship between the Allan Variance and PSD [17].

12.3.2 Clock Frequency Stability Analysis Tools

In the time domain the frequency stability is typically represented by statistical measures such as variances. The standard variance is not suitable for a variety of reasons, but other variances such as the Allan Variance, or its variants, are particularly useful [17]. To define frequency stability the modified Allan Variance is useful:

$$Mod\sigma_y^2(n\tau_0) = \frac{1}{4n^4\tau_0^2(N-3n+1)} \sum_{j=1}^{N-3n+1} \left(\sum_{i=j}^{j+n-1} x_{i+2n} - 2x_{i+n} + x_i \right)^2 \tag{12.10}$$

In addition, the median is a useful statistical parameter to define the estimated frequency centre value assuming no outliers [18]. The median absolute deviation

(MAD) is a robust way to set the criterion for an outlier. It is the median of the (scaled) absolute deviations of the data points from their median value, and is defined as:

$$MAD = Median\{|y(i) - Median\{y(i)\}|/0.6745\} \tag{12.11}$$

The factor 0.6745 makes the MAD equal to the standard deviation for normally distributed data. An outlier criterion of 5 times of the MAD is usually a good choice.

12.4 Case Study Using GRACE Data

The GRACE mission is used for testing the receiver-aided KPOD performance, as the two identical satellites are both equipped with USOs. The USO can provide the required short term frequency stability and a relative receiver synchronisation of better than 150 ps [16].

The GRACE data, known as Level 1B data, is archived by JPL's Physical Oceanography Distributed Active Archive Center (PODAAC) and is available to the science community [19]. PODAAC provides GPS flight data products in the format of GPS1B. The Level 1B data also includes a GPS Navigation (GNV) product that contains reduced-dynamic precise orbit determination solutions. The relativistic effects are corrected in the observations generated in the Level 1B RINEX files of the GRACE mission. Therefore the relativistic clock correction mentioned in Sect. 12.2.2 need not be considered when processing the GRACE data [10].

The 24 h dataset of the GRACE B spacecraft, with data interval of 10 s, from the 11th September 2005, has been selected to test the proposed clock-aided KPOD (KPOD-CLK) algorithm. The standard KPOD solutions were adopted as the benchmark solutions. Both results are compared with the GNV products.

The estimated receiver clock frequency is shown in Fig. 12.1 (left). Most of the data points stay inside the 5MAD threshold with an approximate zero slope, while there are still some outliers present. Figure 12.1 (right) is a plot of the modified Allan deviation of the estimated clock time offset with interval of 10 s. The estimated clock stabilities range from 10^{-12} to 10^{-13} with averaging time τ = 10–1,000 s for GRACE-B. This is slightly worse than the results presented in [20], and is due to the correlation between the clock time offsets and the position estimates. With the decimetre-level accuracy of the orbit solution obtained from the KPOD-CLK algorithm compared with the DPOD solutions (accurate at the centimetre-level), the clock time offset estimation will obviously deteriorate. Additionally, the clock correction in [20] is derived from carrier phase measurements only, which have far less noise than the code phase measurements.

The orbit residuals in the Radial, In-track and Cross-track (RIC) coordinate components and receiver clock time offsets estimated using KPOD-CLK algorithm

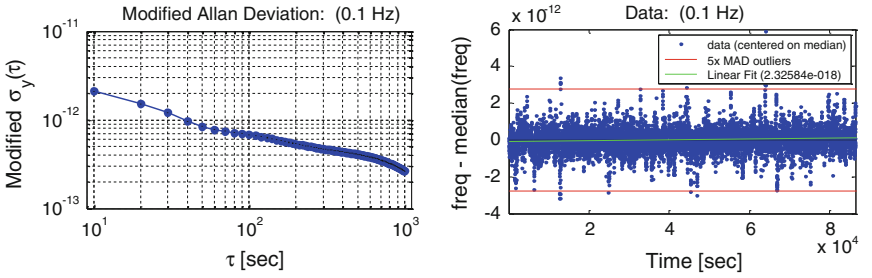

Fig. 12.1 Receiver clock stability and estimated receiver clock frequency offset of GRACE B using KPOD-CLK algorithm

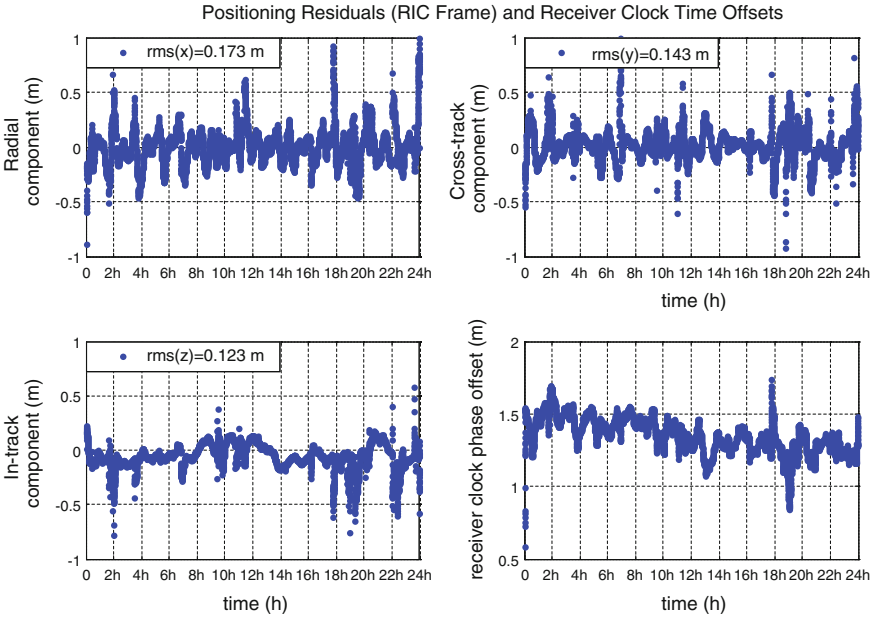

Fig. 12.2 Positioning residuals in RIC frame and estimated receiver clock time offsets using KPOD-CLK algorithm

are plotted in Fig. 12.2. The RMS errors are 0.173, 0.143 and 0.123 m for three components. The clock time offsets are smooth, except for some discontinuous points at the initial epochs. This is due to the uncertainty of the initial setting for receiver clock frequency offset, as it requires some time for the Kalman filter to converge.

The KPOD-CLK positioning performance is compared with the normal KPOD algorithm without receiver clock modelling in Table 12.1. Orbit determination

Table 12.1 Positioning residuals comparison between two KPOD methods with and without receiver clock modelling in terms of RMS errors

	Radial component	In-track component	Cross-track component
KPOD (m)	0.43	0.18	0.16
KPOD-CLK (m)	0.17	0.14	0.12
Improved ratio (%)	60.1	23.1	25.9

performance benefit from a precise receiver clock model that brings down the RMS errors. In particular, the radial component of the orbit positioning residuals reduces by more than 60 %.

12.5 Concluding Remarks

The use of a precise two-state receiver clock model was successfully demonstrated for the GRACE B satellite. The orbit determination performance was improved, especially for the radial direction. In the view of current progress of clock technology it is expected that miniaturised and inexpensive high-precision oscillators with very low power consumption will be increasingly used in future satellite missions. The proposed KPOD-CLK algorithm is therefore a useful alternative to standard KPOD algorithms.

Acknowledgments China Scholarship Council (CSC) is gratefully acknowledged for supporting the first author's visiting periods at the University of New South Wales.

References

1. Montenbruck O (2003) Kinematic GPS positioning of LEO satellites using ionosphere-free single frequency measurements. Aerosp Sci Technol 7(5):396–405
2. Švehla D, Rothacher M (2003) Kinematic and reduced-dynamic precise orbit determination of low earth orbiters. Adv Geosci 1:47–56
3. Yunck TP et al (1990) Precise tracking of remote sensing satellites with the global positioning system. Geosci Remote Sens, IEEE Trans 28(1):108–116
4. Montenbruck O et al (2005) Reduced dynamic orbit determination using GPS code and carrier measurements. Aerosp Sci Technol 9(3):261–271
5. Kouba J (2009) A guide to using international GNSS Service (IGS) products (available electronically at http://igscb.jpl.nasa.gov/igscb/resource/pubs/UsingIGSProductsVer21.pdf) (Unpublished)
6. Yeh T-K et al (2009) Determination of global positioning system (GPS) receiver clock errors: impact on positioning accuracy. Measure Sci Technol 20(7)
7. Weinbach U, Schon S (2012) Improved GPS receiver clock modeling for kinematic orbit determination of the GRACE satellites. In: European frequency and time forum (EFTF)
8. Galleani L, Tavella P (2010) Time and the kalman Filter. Control Syst, IEEE 30(2):44–65

9. Chan F-C, Pervan B (2009) Stochastic modeling of GPS receiver clocks for improved positioning and fault detection performance. In: Proceedings of the 22nd international technical meeting of the satellite division of the institute of navigation (ION GNSS-2009), Savannah, GA
10. Weinbach U, Schön S (2013) Improved GRACE kinematic orbit determination using GPS receiver clock modeling. GPS Solutions 17(4):511–520
11. Petit G, Luzum B (2010) IERS conventions. IERS Tech Note 36:179
12. Larson KM et al (2007) An assessment of relativistic effects for low Earth orbiters: the GRACE satellites. Metrologia 44(6):484
13. Psiaki ML, Mohiuddin S (2007) Modeling, analysis, and simulation of GPS carrier phase for spacecraft relative navigation. J Guid Control Dyn 30(6):1628–1639
14. Montenbruck O et al (2009) Antenna phase center calibration for precise positioning of LEO satellites. GPS Solutions 13(1):23–34
15. Brown RG, Hwang PY (2012) Introduction to random signals and applied kalman filtering with MATLAB exercises. 2012: Wiley Global Education
16. Dunn C et al (2002) The instrument on NASA's GRACE mission: augmentation of GPS to achieve unprecedented gravity field measurements. In: Proceedings of the 15th international technical meeting of the satellite division of the institute of navigation (ION GPS 2002). Portland, OR, Sep 2002
17. Allan DW (1987) Time and frequency(time-domain) characterization, estimation, and prediction of precision clocks and oscillators. IEEE Trans Ultrason Ferroelectr Freq Control 34(6):647–654
18. Riley W (2003) Techniques for frequency stability analysis. In: IEEE international frequency control symposium, Tampa, FL
19. Case K, Kruizinga G, Wu S (2002) GRACE level 1B data product user handbook. JPL Publication D-22027
20. Tseng T-P et al (2013) Assessing antenna field of view and receiver clocks of COSMIC and GRACE satellites: lessons for COSMIC-2. GPS Solutions, pp 1–12

Chapter 13
Application of Improved LLL Lattice Reduction in BDS Ambiguity Decorrelation

Kai Xie, Hongzhou Chai, Zongpeng Pan, Huarun Wang, Bingquan Dong and Liu Ming

Abstract In the process of BDS navigation and positioning, fast and precise ambiguity resolution plays a key role in improving the efficiency and precision of positioning. In cases of highly correlated ambiguities, since the searching space is too large, it takes a long time to fix the ambiguities. Therefore, it is very necessary to deccorelate the covariance matrix. In essence, the decorrelation process is the closest vector problem in Lattice Theory. On the basis of proving the equality of lattice reduction and decorrelation, the LLL decorrelation algorithm is analyzed and it is improved on the basis of QR decomposition. BDS triple-frequency data is adopted to carry the experiment. The decorrelation effect of the LLL and the improved LLL algorithm are analyzed from aspects of spectral condition number, average correlation coefficient and reduction time. It is proved that the improved LLL algorithm has better decorrelation effect although it requires longer reduction time.

Keywords Ambiguity resolution · Decorrelation · LLL lattice reduction · Gram-Schmidt orthogonal transformation · QR decomposition

13.1 Introduction

The BeiDou Navigation Satellite System run by China began to provide navigation and positioning service to the Asian-Pacific region. As the key problem of realizing precise kinematic positioning, the correct resolution of integer ambiguities has aroused concern of experts all over the world. Least-squares Ambiguity Searching Method [1] and Fast Ambiguity Resolution Approach (FARA) [2] etc. adopt direct searching method to obtain the optimal integer ambiguity resolution.

K. Xie (✉) · H. Chai · Z. Pan · H. Wang · B. Dong · L. Ming
Geospatial Information Institute, Information Engineering University, Zhengzhou 450000, China
e-mail: nicholas4413@163.com

J. Sun et al. (eds.), *China Satellite Navigation Conference (CSNC) 2014 Proceedings: Volume III*, Lecture Notes in Electrical Engineering 305,
DOI: 10.1007/978-3-642-54740-9_13,

But since the ambiguities are highly correlated, the searching efficiency is low. Teunissen [3] proposed the LAMBDA method which decorrelates the covariance matrix at first and then search the integer resolution. It promotes the efficiency and success rate greatly. In terms of ambiguity decorrelation, other representative methods mainly include Multi-dimensional Gaussian Integer Decorrelation [3], United Decorrelation [4] and Inverse Integer Cholesky Decomposition [5]. These methods are all based on LDL^T decomposition which realizes the orthogonalization of the covariance matrix. Integer ambiguity resolution is actually the closest vector problem in Lattice Theory. The definition of lattice is originated from geometry. Lagrange [6] studied secondary homogeneous type and proposed a two-dimensional integer scheme method which used the Lagrange reduction to find the shortest vector of a two-dimensional lattice in polynomial time. This method is called Lattice Reduction. Gauss [7], Hermite [8] and Minkowski [9] improved the reduction base. But in cases of high-dimensional lattice base, these methods cannot realize finding the lattice base in polynomial time. In order to solve this problem, Lenstra et al. [10] proposed LLL lattice reduction. During recent years, Hassibi and Boyed [11] and Grafarend [12] apply the LLL lattice reduction into ambiguity decorrelation and performs well. Liu [13] expatiates the application of LLL reduction in ambiguity resolution and analyzes the performance.

On the basis of analyzing the LLL reduction principles, the equality of lattice reduction and ambiguity decorrelation is proved. The LLL decorrelation algorithm is improved based on QR decomposition. BDS triple-frequency data is used to evaluate the performance. It is shown that the improved LLL decorrelation algorithm has promoted the performance obviously. But this method has a disadvantage of relatively long reduction time which needs further improvement.

13.2 Double-Differenced Ambiguity Resolution Model

The observation equation of BDS relative positioning is as follows:

$$\boldsymbol{y} = \boldsymbol{A}\boldsymbol{a} + \boldsymbol{B}\boldsymbol{b} + \boldsymbol{e} \quad \boldsymbol{Q}_y \tag{13.1}$$

where $\boldsymbol{y}$ denotes the carrier phase observable, $\boldsymbol{a}$ denotes the double-differenced ambiguity parameter, $\boldsymbol{b}$ denotes the baseline vector, $\boldsymbol{e}$ denotes the observation noise, $\boldsymbol{A}, \boldsymbol{B}$ denote the designed matrix, $\boldsymbol{Q}_y$ denotes the variance-covariance matrix.

According to the least-squares evaluation principle, the following problem is to be solved

$$\min \|\boldsymbol{y} - \boldsymbol{A}\boldsymbol{a} - \boldsymbol{B}\boldsymbol{b}\|^2_{\boldsymbol{Q}_y}, \quad \boldsymbol{a} \in \boldsymbol{Z}^m, \boldsymbol{b} \in \boldsymbol{R}^m \tag{13.2}$$

where $\|\cdot\|^2_{\boldsymbol{Q}_y} = (\cdot)^T \boldsymbol{Q}_y^{-1} (\cdot)$.

Equation (13.2) can be decomposed as follows

$$\|\boldsymbol{y}-\boldsymbol{A}\boldsymbol{a}-\boldsymbol{B}\boldsymbol{b}\|_{\boldsymbol{Q}_y}^2=\|\hat{\boldsymbol{e}}\|_{\boldsymbol{Q}_y}^2+\|\hat{\boldsymbol{a}}-\boldsymbol{a}\|_{\boldsymbol{Q}_{\hat{a}}}^2+\left\|\hat{\boldsymbol{b}}(\boldsymbol{a})-\boldsymbol{b}\right\|_{\boldsymbol{Q}_{\hat{b}|\hat{a}}}^2 \tag{13.3}$$

where

$$\begin{aligned}\hat{\boldsymbol{e}}&=\boldsymbol{y}-\boldsymbol{A}\hat{\boldsymbol{a}}-\boldsymbol{B}\hat{\boldsymbol{b}}\\ \hat{\boldsymbol{b}}(\boldsymbol{a})&=\hat{\boldsymbol{b}}-\boldsymbol{Q}_{\hat{b}\hat{a}}\boldsymbol{Q}_{\hat{a}}^{-1}(\hat{\boldsymbol{a}}-\boldsymbol{a})\\ \boldsymbol{Q}_{\hat{b}|\hat{a}}&=\boldsymbol{Q}_{\hat{b}}-\boldsymbol{Q}_{\hat{b}\hat{a}}\boldsymbol{Q}_{\hat{a}}^{-1}\boldsymbol{Q}_{\hat{a}\hat{b}}\end{aligned} \tag{13.4}$$

In Eq. (13.4), $\hat{\boldsymbol{a}}$ denotes float ambiguity resolution, $\hat{\boldsymbol{b}},\hat{\boldsymbol{b}}(\boldsymbol{a})$ denote float and fixed baseline vector respectively.

Therefore, Eq. (13.2) equals

$$\min\|\hat{\boldsymbol{a}}-\boldsymbol{a}\|_{\boldsymbol{Q}_{\hat{a}}}^2 \tag{13.5}$$

Since ambiguities are correlated, searching for the fixed ambiguities directly will cost a lot of time. The covariance matrix needs to be decorrelated at first.

Firstly, conduct $\boldsymbol{L}\boldsymbol{D}\boldsymbol{L}^{\mathrm{T}}$ decomposition to $\boldsymbol{Q}_{\hat{a}}$. Then conduct $\boldsymbol{Z}$ transformation to it to obtain a matrix with smaller covariance

$$\boldsymbol{Q}_{\hat{a}}=\boldsymbol{L}\boldsymbol{D}\boldsymbol{L}^{\mathrm{T}} \tag{13.6}$$

$$\boldsymbol{Q}_{\hat{z}}=\boldsymbol{Z}\boldsymbol{Q}_{\hat{a}}\boldsymbol{Z}^{\mathrm{T}}=\boldsymbol{L}\boldsymbol{D}\boldsymbol{L}^{\mathrm{T}} \tag{13.7}$$

where $\boldsymbol{D}=diag(\boldsymbol{d}_1,\ldots,\boldsymbol{d}_n)$, $\boldsymbol{Z}$ denotes integer unimodular matrix. $\boldsymbol{Q}_{\hat{z}}$ is nearly orthogonal after transformation and the diagonal elements of $\boldsymbol{D}$ are sorted in an increasing order [14]

$$\left|\bar{\boldsymbol{l}}_{\boldsymbol{ij}}\right|\le 1/2,\quad i>j \tag{13.8}$$

$$\boldsymbol{d}_{\boldsymbol{k}}+\bar{l}_{k,k-1}^2\bar{\boldsymbol{d}}_{k-1}\ge\bar{\boldsymbol{d}}_{k-1},\quad k=1,2,\ldots,n \tag{13.9}$$

13.3 The LLL Algorithm

The conditions of LLL lattice reduction are introduced. The equality of lattice reduction and ambiguity decorrelation is proved. Gram-Schmidt orthogonal transformation in LLL reduction is used to conduct the decorrelation.

13.3.1 Equality of Lattice Reduction and Decorrelation

Suppose vectors $\boldsymbol{b}_1, \boldsymbol{b}_2, \ldots, \boldsymbol{b}_n \in \boldsymbol{R}^n$ are n linearly independent n dimensional vectors, all combinations of $\boldsymbol{b}_1, \boldsymbol{b}_2, \ldots, \boldsymbol{b}_n$ consist n dimensional lattice $\boldsymbol{L}(\boldsymbol{b}_1, \boldsymbol{b}_2, \cdots, \boldsymbol{b}_n)$ written as

$$\boldsymbol{L}(\boldsymbol{b}_1, \boldsymbol{b}_2, \ldots, \boldsymbol{b}_m) = \sum_{i=1}^{n} t_i \boldsymbol{b}_i \quad t_i \in Z \tag{13.10}$$

$[\boldsymbol{b}_1, \boldsymbol{b}_2, \ldots, \boldsymbol{b}_n]$ is called a group of bases of this lattice. If they satisfy

$$\left|l_{k,j}\right| = \frac{\left\langle \boldsymbol{b}_k, \boldsymbol{b}_j^* \right\rangle}{\left|\boldsymbol{b}_j^*\right|^2} \le \frac{1}{2}, \quad 1 \le j < k \le n \tag{13.11}$$

$$\delta \left\|\boldsymbol{b}_{k-1}^*\right\|^2 \le \left\|\boldsymbol{b}_k^*\right\|^2 + l_{k,k-1}^2 \left\|\boldsymbol{b}_{k-1}^*\right\|^2, \quad k = 2, 3, \ldots, n; \quad \frac{1}{4} < \delta \le 1 \tag{13.12}$$

This sorted group of bases $[\boldsymbol{b}_1, \boldsymbol{b}_2, \ldots, \boldsymbol{b}_n]$ is called LLL reduction base reducted with parameter δ. $\boldsymbol{b}_j^*$ denotes the Gram-Schmidt orthogonal base. Equation (13.11) denotes that base vectors $\boldsymbol{b}_j, \boldsymbol{b}_k$ should be as orthogonal as possible. Equation (13.12) denotes the length restriction of near two base vectors. It has the strongest restriction when $\delta = 1$.

On the basis of analyzing the conditions of lattice reduction, the decorrelation method can be unified in the lattice theory frame. As is known, $\boldsymbol{Q}_{\hat{a}}$ can be decomposed as the product of a lower-triangle matrix and its transposed matrix

$$\boldsymbol{Q}_{\hat{a}\hat{a}} = \boldsymbol{G}^{\mathrm{T}} \boldsymbol{G} \tag{13.13}$$

Conduct Gram-Schmidt orthogonal transformation to matrix G in Eq. (13.13)

$$\boldsymbol{G} = \begin{bmatrix} \left\|g_1^*\right\| & 0 & \cdots & 0 \\ 0 & \left\|g_2^*\right\| & \cdots & 0 \\ \vdots & \vdots & \ddots & \vdots \\ 0 & 0 & \cdots & \left\|g_n^*\right\| \end{bmatrix} \cdot \begin{bmatrix} 1 & l_{1,2} & \cdots & l_{1,n} \\ 0 & 1 & \ddots & \vdots \\ 0 & 0 & \ddots & l_{n-1,n} \\ 0 & 0 & 0 & 1 \end{bmatrix} \tag{13.14}$$

Substitute Eq. (13.14) into (13.13), we have

$$\boldsymbol{Q}_{\hat{a}\hat{a}} = \begin{bmatrix} 1 & 0 & 0 & 0 \\ l_{1,2} & 1 & 0 & 0 \\ \vdots & \ddots & \ddots & 0 \\ l_{1,n} & \cdots & l_{n-1,n} & 1 \end{bmatrix} \cdot \begin{bmatrix} \left\|g_1^*\right\|^2 & 0 & \cdots & 0 \\ 0 & \left\|g_2^*\right\|^2 & \cdots & 0 \\ \vdots & \vdots & \ddots & \vdots \\ 0 & 0 & \cdots & \left\|g_n^*\right\|^2 \end{bmatrix} \cdot \begin{bmatrix} 1 & l_{1,2} & \cdots & l_{1,n} \\ 0 & 1 & \ddots & \vdots \\ 0 & 0 & \ddots & l_{n-1,n} \\ 0 & 0 & 0 & 1 \end{bmatrix} \tag{13.15}$$

In Eq. (13.15), element $\left\|g_i^*\right\|^2$ is the diagonal element of $\boldsymbol{D}$ in corresponding $\boldsymbol{LDL}^{\mathrm{T}}$ decomposition. Equation (13.9) equals (13.12) when $\delta = 1$.

13.3.2 The LLL Decorrelation Algorithm

As is known, a complete orthogonal base can be obtained from matrix $\boldsymbol{G}$ by Gram-Schmidt orthogonal transformation. The process is as follows.

Firstly, the row vectors of matrix $\boldsymbol{G}$ can be transformed one by one

$$\boldsymbol{g}_i^* = \boldsymbol{g}_i - \sum_{j=1}^{i-1} l_{ij}\boldsymbol{g}_j^* \quad i \le n \tag{13.16}$$

where $\boldsymbol{g}_i$ denotes the row vector of matrix $\boldsymbol{G}$. $\boldsymbol{g}_i^*$ denotes the vector after orthogonalization. n denotes the matrix dimension. l_{ij} denotes the transformation coefficient.

$$l_{ij} = \left\langle \boldsymbol{g}_i, \boldsymbol{g}_j^* \right\rangle \Big/ \left\langle \boldsymbol{g}_j^*, \boldsymbol{g}_j^* \right\rangle \quad j < i \tag{13.17}$$

where $\langle , \rangle$ denotes the inner product of two vectors.

In order to satisfy the conditions of integer transformation, the transformation coefficient needs to be rounded, so Eq. (13.16) becomes

$$\boldsymbol{g}_i^* = \boldsymbol{g}_i - \sum_{j=1}^{i-1} [l_{ij}]_{\mathrm{int}}\boldsymbol{g}_j^* \quad i \le n \tag{13.18}$$

where $[\,]_{\mathrm{int}}$ denotes rounding.

Since rounding brings about errors, g_i^* and g_j^* cannot be orthogonal. This problem can be solved by iteration.

$$(\boldsymbol{g}_i^*)^k = (\boldsymbol{g}_i)^{k-1} - \sum_{j=1}^{i-1} [l_{ij}^k]_{\text{int}} (\boldsymbol{g}_j^*)^k \quad i \le n \tag{13.19}$$

where

$$l_{ij}^k = \left\langle (\mathbf{g}_i)^{k-1}, (\mathbf{g}_j^*)^k \right\rangle / \left\langle (\mathbf{g}_j^*)^k, (\mathbf{g}_j^*)^k \right\rangle \quad j < i \tag{13.20}$$

when $\left| [l_{ij}^k]_{\text{int}} \right| \le \frac{1}{2}$, the iteration stops.

Suppose the transformation matrix of the ith time is $\boldsymbol{L}^i$. The iteration stops after k times. So

$$\boldsymbol{Q}_{\hat{a}} = (\boldsymbol{L}^k)^T \cdots (\boldsymbol{L}^1)^T \boldsymbol{Q}_{\hat{z}} (\boldsymbol{L}^1) \cdots (\boldsymbol{L}^k) \tag{13.21}$$

Suppose $\boldsymbol{Z} = \left[(\boldsymbol{L}^k)^{\mathrm{T}} \cdots (\boldsymbol{L}^1)^{\mathrm{T}} \right]^{-1}$, then $\boldsymbol{Q}_{\hat{z}}$ can be denoted as follows

$$\boldsymbol{Q}_{\hat{z}} = \boldsymbol{Z} \boldsymbol{Q}_{\hat{a}} \boldsymbol{Z}^{\mathrm{T}} \tag{13.22}$$

Above is the transformation process of the LLL decorrelation algorithm.

13.3.3 The Improved LLL Algorithm

The LLL algorithm uses the Gram-Schmidt orthogonal transformation to decompose matrix $\boldsymbol{G}$ into the product of an orthogonal matrix and an upper triangular matrix. According to the Matrix Theory, matrix $\boldsymbol{G}$ can also be decomposed into a unitary matrix and an upper triangular matrix by the QR decomposition. Therefore the QR decomposition is considered to improve the LLL algorithm.

Suppose $\boldsymbol{z} \in \boldsymbol{C}^n$ is a unit vector. Let $\boldsymbol{u} = \frac{\boldsymbol{x} - \alpha \boldsymbol{z}}{\|\boldsymbol{x} - \alpha \boldsymbol{z}\|_2}$, then for any $\boldsymbol{x} \in \boldsymbol{C}^n$, there is a matrix $\boldsymbol{H}$,which makes $\boldsymbol{H}\boldsymbol{x} = \alpha \boldsymbol{z}$, where $\mathbf{H} = \mathbf{I} - 2\mathbf{u}\mathbf{u}^H$, $|\alpha| = \|\mathbf{x}\|_2$ and $\alpha \boldsymbol{x}^{\mathrm{H}} \boldsymbol{z}$ is a real number.

According to the thought above, suppose $\boldsymbol{u}_i = \frac{\boldsymbol{x}_i - \alpha_i \boldsymbol{z}_i}{\|\boldsymbol{x}_i - \alpha_i \boldsymbol{z}_i\|_2}$, where $\boldsymbol{z}_i = \left[0 \cdots \underset{i}{1} \cdots 0 \right]^T$. An orthogonal matrix can be formed

$$\boldsymbol{H}_i = \boldsymbol{I} - 2\boldsymbol{u}_i \boldsymbol{u}_i^{\mathrm{T}} \tag{13.23}$$

Multiple$\boldsymbol{H}_i$ to $\boldsymbol{G}_{i-1}$ on the left side, we have

$$\boldsymbol{G}_i = \boldsymbol{H}_i \boldsymbol{G}_{i-1} \tag{13.24}$$

where $\boldsymbol{G}_0 = \boldsymbol{G}$. The last $n - i$ elements of the ith vector of matrix $\boldsymbol{G}_i$ are zeros and the diagonal element is α_i.

Multiple $\boldsymbol{H}_i$ to $\boldsymbol{G}$ successively, we have

$$\boldsymbol{H}_{n-1}\boldsymbol{H}_{n-2}\ldots\boldsymbol{H}_1\boldsymbol{G} = \boldsymbol{R} \tag{13.25}$$

Since $\boldsymbol{H}_1, \boldsymbol{H}_2, \ldots, \boldsymbol{H}_{n-1}$ are all orthogonal matrixes, suppose $\boldsymbol{Q} = (\boldsymbol{H}_{n-1}\boldsymbol{H}_{n-2}\ldots\boldsymbol{H}_1)^{-1}$, then we have

$$\boldsymbol{G} = \boldsymbol{Q}\boldsymbol{R} \tag{13.26}$$

Thereby matrix $\boldsymbol{G}$ can be decomposed into the product of orthogonal matrix $\boldsymbol{Q}$ and upper triangular $\boldsymbol{R}$. The left steps are the same as the LLL algorithm based on Gram-Schmidt orthogonal transformation.

13.4 Experiments Analysis

In order to analyze the decorrelation effect of the LLL algorithm and the improved LLL algorithm, spectral condition number, average correlation coefficient and reduction time are used to evaluate them. The processor of the computer is Intel Core(TM)2 with the main frequency of 2.93 Ghz. The memory is 2 GB.

Two Trimble R9 receivers are used to collect triple frequency BDS data from UTC 10:20:21 to UTC14:32:02 on Dec. 29th 2012 to carry out the experiments. The baseline length is 30.4 m. The sampling rate is 1 s and the cut-off elevation is 10°. Valid epochs are 15102. Approximate positions of the two receivers are provided by single-epoch pseudorange point positioning. The number of common visible satellites is shown in Fig. 13.1.

13.4.1 Spectral Condition Number

The spectral condition number of covariance matrix before and after decorrelation is shown in Fig. 13.2. The corresponding decorrelation algorithms from top to bottom are: original, the LLL algorithm, the improved LLL algorithm.

As is shown in Fig. 13.2, the spectral condition number of covariance matrix before decorrelation fluctuates from 10 to 12. It then fluctuates from 4 to 8 after decorrelation and the range of the improved LLL algorithm is smaller than the LLL algorithm.

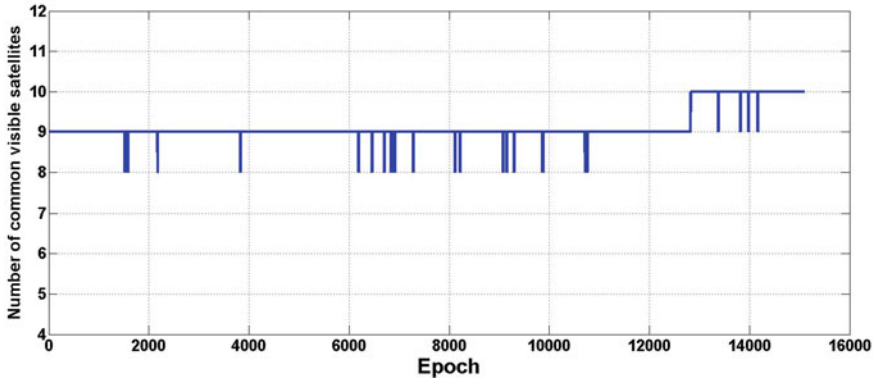

Fig. 13.1 Number of common visible satellites

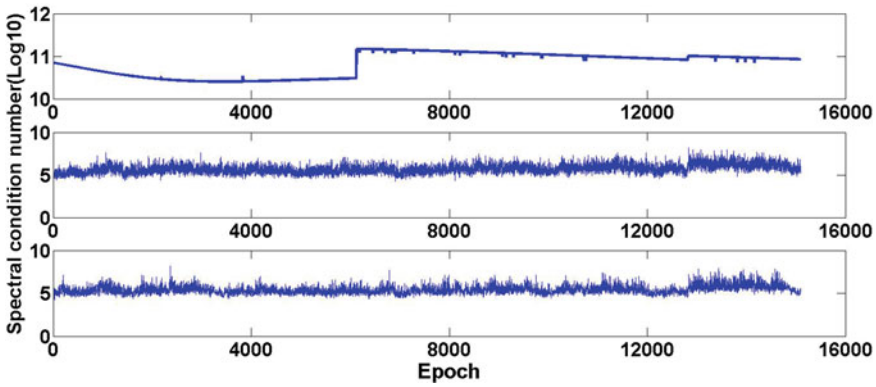

Fig. 13.2 Spectral condition number

13.4.2 Average Correlation Coefficient

The average correlation coefficient of covariance matrix before and after decorrelation is shown in Fig. 13.3. The corresponding decorrelation algorithms from top to bottom are: original, the LLL algorithm, the improved LLL algorithm.

As is shown in Fig. 13.3, the average correlation coefficient of covariance matrix before decorrelation fluctuates from 0.5 to 0.7. After the LLL decorrelation, the average correlation coefficient fluctuates from 0.17 to 0.32 which is obviously smaller than before. After the improved LLL, the average correlation coefficient fluctuates from 0.14 to 0.21 which is better than LLL algorithm.

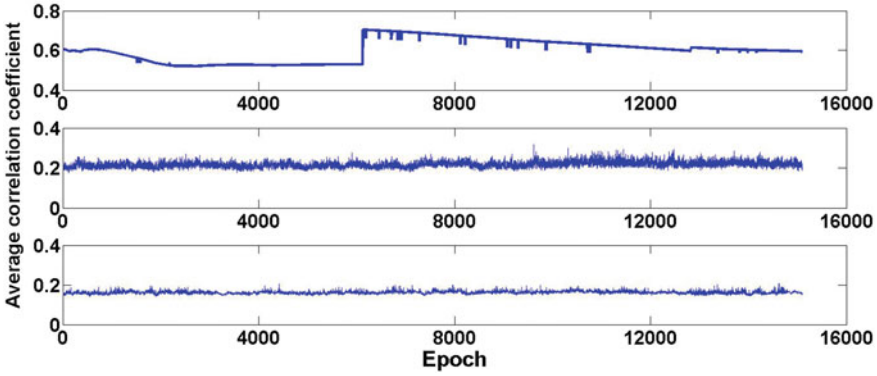

Fig. 13.3 Average correlation coefficient

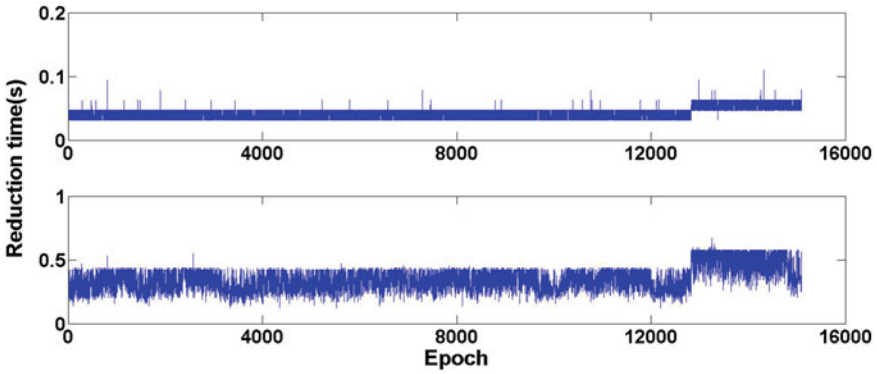

Fig. 13.4 Reduction time

13.4.3 Reduction Time

The reduction time of the LLL algorithm and the improved LLL algorithm is shown in Fig. 13.4. The corresponding decorrelation algorithms from top to bottom are: the LLL algorithm and the improved LLL algorithm.

As is shown in Fig. 13.4, the reduction time of the LLL algorithm fluctuates from 0.03 s to 0.11 s while it takes longer for the improved LLL algorithm which fluctuates from 0.13 s to 0.67 s. Therefore the reduction time indicator of LLL algorithm is better than the improved LLL algorithm.

Table 13.1 Comparison of indicators between LLL and improved LLL algorithm

Decorrelation algorithms	Spectral condition number (Log10)	Average correlation coefficient	Reduction time (s)
Original	10.82	0.60	
LLL algorithm	5.71	0.22	0.04
Improved LLL algorithm	5.40	0.16	0.35

13.4.4 Comprehensive Assessment

In order to comprehensively evaluate the decorrelation performance of the two algorithms, taking all the three indicators into consideration, a comparison between the LLL algorithm and the improved LLL algorithm is made by averaging each indicator.

As is shown in Table 13.1, the spectral condition number of the original matrix is as big as 10.82. After the LLL algorithm decorrelation, it decreases to 5.71 and the spectral condition number of the improved LLL algorithm is as small as 5.40. As same as the trend of the spectral condition number, the average correlation coefficient of the matrix before and after the LLL decorrelation and the improved LLL decorrelation decreases from 0.60 to 0.22 and 0.16 respectively. It indicates that the effect of the improved LLL algorithm is better than the LLL algorithm which realizes better orthogonalization of the reduction bases.

However, the reduction time of the improved LLL algorithm is obviously worse than the LLL algorithm which indicates a longer period of time required for the improved LLL algorithm to finish the decorrelation. The reason is analyzed as follows [15], for a certain matrix $\boldsymbol{A} \in \boldsymbol{R}^{m\times n}$, $rank(\boldsymbol{A}) = n$, it requires more flops to commit the QR decomposition than the Gram-Schmidt orthogonal transformation which leads to low efficiency of the improved LLL algorithm.

Taking all the factors into consideration, we can come to the conclusion that the improved LLL algorithm can better orthogonalize the covariance matrix which means better decorrelation effect. But due to the big computation load of QR decomposition, the improved LLL algorithm needs longer reduction time which means worse real-time capacity.

13.5 Conclusions

On the basis of proving the equality of the lattice reduction and ambiguity decorrelation, the LLL decorrelation algorithm is introduced. And it is improved based on the QR decomposition. The BDS triple-frequency data is used to carry out the experiments. The performances of the LLL algorithm and the improved LLL algorithm are compared from aspects of spectral condition number, average

correlation coefficient and reduction time. The results have shown that the improved LLL algorithm can realize better orthogonalization of the reduction bases which means better decorrelation effect. But due to a longer period of reduction time and worse real-time capacity, the improved LLL algorithm is more suitable for static baseline resolution.

In terms of the low reduction efficiency of the LLL algorithm based on QR decomposition, various orthogonal transformation algorithms will be tested for improvement.

References

1. Hatch RS (1990) Instantaneous ambiguity resolution. Kinematic systems in geodesy, surveying, and remote sensing. Springer, Tokyo, p 299–380
2. Frei E (1990) Rapid static positioning based on the fast ambiguity resolution approach FARA: theoty and first results. Manuscripta Geodaet 15(6):326–356
3. Teunissen PJG. (1993) Least-squares estimation of the integer GPS ambiguities. In: Proceedings of international association of geodesy general meeting, Beijing, China, Aug 1993
4. Liu LT, Hsu HT, Zhu YZ et al (1999) A new approach to GPS ambiguity decorrelation. J Geodesy 73(10):478–490
5. Xu P (2001) Random simulation and GPS decorrelation. J Geodesy 75(7):408–423
6. Lagrange JL (1773) Recherches D'arithmetique. Nouveaux memories de l'Academie de Berlin. p 265–312
7. Fan L (2013) Research on method of integer ambiguity estimation with lattice theory. Information Engineering University, Zhengzhou
8. Hermite C (1850) Extraits de lettres de M. Hermite à M. Jacobisur differents objets de la théorie des nombres, deuxième letter. Reine Angew Math 40:279–290
9. Minkowski H (1896) Geometrie der zahlen. Springer, Stuttgart
10. Lenstra AK, Lenstra HW, Lovasz L (1982) Factoring polynomials with rational coefficients. Mathematische Annalen 261(4):515–534
11. Hassibi A, Boyed S (1998) Integer parameter estimation in linear models with applications to GPS. IEEE Trans Sign Proces 46(11):2938–2952
12. Grafarend EW (2000) Mixed integer-real valued adjustment (IRA) problems: GPS initial cycle ambiguity resolution by means of the LLL algorithm. GPS Solutions 4(2):31–44
13. Liu J, Yu X, Zhang X (2012) GNSS ambiguity resolution using the lattice theory. Acta Geodaet Cartogr Sin 41(5):636–645
14. Chang XW, Zhou T (2007) Miles: matlab package for solving mixed integer least squares problems. GPS Solutions 11(4):289–294
15. Gloub GH, van Loan CF (1993) Matrix computation. The Johns Hopkins University Press, Baltimore

Chapter 14
Research on High Accuracy Prediction Model of Satellite Clock Bias

Xueqing Xu, Xiaogong Hu, Yonghong Zhou and Yezhi Song

Abstract Time basis of satellite navigation system is achieved by the satellite clock bias (SCB) prediction, while the SCB prediction accuracy will also affect the positioning accuracy of real-time navigation users. With the development of our Beidou satellite navigation system, the accuracy requirements of the SCB prediction is higher and higher, general quadratic polynomial extrapolation method have failed to meet the SCB forecast accuracy for each satellite. There is an urgent need to develop the SCB prediction program for each satellite, here we use a combined method of least squares and auto-regressive model (LS + AR) from the EOP forecasting, to predict and assess SCB with data from IGS. Results show that the combined LS + AR method can improve the SCB forecast accuracy effectively.

Keywords SCB prediction · Least squares · Auto-regressive model

14.1 Introduction

The long-term reliable forecasting of satellite clock error is an important pre-requisite for autonomous navigation satellite orbit determination. Satellite clock cannot be compared to the ground time reference continuously while the satellites is in space orbit, when the satellite run into the arcs which cannot be observed by ground stations, the synchronization between satellite clock and the system time

X. Xu (✉) · X. Hu · Y. Zhou · Y. Song
Shanghai Astronomical Observatory, Chinese Academy of sciences,
Nandan Road No.80, Xuhui, Shanghai 200030, China
e-mail: xqxu@shao.ac.cn

X. Xu
Key Laboratory of Planetary Sciences, Chinese Academy of Sciences,
Shanghai 200030, China

J. Sun et al. (eds.), *China Satellite Navigation Conference (CSNC) 2014 Proceedings: Volume III*, Lecture Notes in Electrical Engineering 305,
DOI: 10.1007/978-3-642-54740-9_14,

can be only maintained by satellite clock himself, in order to get continuous satellite clock results, satellite clock error should be predicted necessarily [8, 5].

Prediction accuracy of the navigation satellites atomic clocks determines the ephemeris updated frequency, and the complexity and workload of satellite navigation ground operation control system, and the prediction accuracy is not only related with its physical characteristics, but also restricted by the complexity of the prediction algorithm [13, 15, 16]. Now the forecasting models about the satellite clock error at home and abroad are: (1) the linear model (LM) [9, 14] (2) quadratic polynomial model (QPM) [10, 19] (3) gray model (GM) [3, 4, 11, 17, Liu et al. 2006; Li et al. 2009] (4) Kalman filters model (Kalman Filter) [9, 14], and other methods etc. [6].

The above prediction methods are suitable for the deterministic part of the satellite clock error prediction (the part can be expressed by quadratic polynomial or periodic function), and ignoring the prediction of uncertainty part in satellite clock error (the part cannot be directly expressed by the model, also known as the residuals), resulting in prediction accuracy restriction in part of the satellite clock error series. For example, Cui (2005) pointed out that using the second-order polynomial model (QPM) for long-term forecasting of satellite clock error, the cumulative error will be extended with increasing forecast time, and cannot meet the large span clock error prediction. Lu et al. [12] pointed out that the application of gray system model GM (1, 1) to the prediction of satellite clock error, can reduce the satellite clock error epoch for modeling and improve forecast accuracy, which shows some advantages, but deficiencies in gray model will cause large errors in the actual forecasting sometimes. Xu (2009) gave the 90-day forecast results by quadratic polynomial method and gray model, the prediction accuracy is in the order of microseconds to 10 μs, while 1 μs clock error will lead to 300 m users range error (URE), which is difficult to meet the guidance accuracy needs during wartime.

This paper will learn the mature experience from forecasting on the Earth Orientation Parameters (EOP), use a jointed method by least-squares and auto regression model, abbreviated as LS + AR model, and predict the different satellite clock error sequences with IGS GPS satellite clock error data, to estimate the clock error accuracy of different prediction span. Specifically which is firstly analyze the data features of each satellite clock error sequence, and then create a specific model mainly contains the constant term, linear term, polynomial term and periodic terms, to isolate the main parts and residuals by fitting the clock error sequences, and the main parts and residuals parts are predicted by different methods, while the clock error value is derived by adding main term prediction and residuals prediction finally.

14.2 Methods

This paper selects AR (p) model but not the complex ARMA (p, q) as the forecasting model for clock error residuals series, mainly because the estimation accuracy of ARMA (p, q) model coefficient is poorer than the AR (p) model, and

the total order (p + q) is higher the estimation accuracy is worse, while a higher-order AR (p) model is actually equivalent to a low-level ARMA (p, q) model, and the coefficient estimation of AR (p) model is more convenient and accurate compared with ARMA (p, q) model. We adopt the final prediction error criterion (FPE) to identify the order p of AR (p) model for each forecasting step, and use the Burg algorithm to solver the coefficients of AR (p) model, which means that the AR (p) model is updated for each forecasting step, and the new AR (p) model is more reasonable and accurate. The principles of fitting models and AR (p) model are briefly described as follows.

14.2.1 Fitting Model

Due to the different nature of main and residuals terms in the clock error sequence, the two parts usually need to be processed separately. We firstly identify the main periods of clock error sequence by the spectral analysis method, and then establish a model mainly contains the constant term, linear term, polynomial term and periodic terms, to isolate the main parts and residuals by fitting the clock error sequences, where the main periods are a week, 24 h and 12 h.

The fitting model is expressed as follows, which includes linear terms, polynomial and periodic terms:

$$Y_t = a + bt + ct^2 + \sum_{k=1}^{n} d_k \sin(2\pi t/P_k + \phi_k) + \varepsilon_t \tag{14.1}$$

where, a is the constant term, b is the linear coefficient, c is the quadratic coefficient, t is time, P_k, d_k and ϕ_k are period signals, amplitude and phase of periodic signals in satellite clock errors sequence, and ε_t is the noise.

According to the principle of least squares, the predictions of the clock error main terms can be extrapolated by the fitted model coefficients above, while the residual part in the clock error series is difficult to obtain by a simple linear model, and should be derived by other methods; here we select the classical autoregressive model (AR model).

14.2.2 AR Model

For a stationary random sequence $z_t(t = 1, 2, \ldots, N)$, the AR (p) model is expressed as follows,

$$z_t = \sum_{i=1}^{p} \varphi_i z_{t-i} + a_t. \tag{14.2}$$

where, a is zero-mean white noise, p is order of the model, $\varphi_1, \varphi_2, \ldots, \varphi_p$ are autoregressive coefficients, and obtained through solving the Yule-Walker equations by means of the Burg recursion [2] method.

The optimum order p is determined by Akaike's Final Prediction Error (FPE) criterion that corresponds to the smallest FPE [1],

$$\mathrm{FPE}(p) = \mathrm{P}_p(N + p + 1)/(N - p - 1), \tag{14.3}$$

$$\mathrm{P}_p = 1/(N - p) \sum_{t=p+1}^{N} \left(z_t - \sum_{j=1}^{p} \varphi_j z_{t-j} \right)^2. \tag{14.4}$$

14.3 An Example

Currently, GPS system totally contains 31 network working satellites, including 11 Block IIA satellites, 12 Block IIR satellites, seven Block IIR-M satellites and a Block IIF satellite. This example selects the PRN01, PRN05, PRN09, PRN16, PRN24 and PRN26 six satellites for analysis, which represent six types of GPS clock error: 1. Block IIA Cs; 2. Block IIA Rb; 3. Block IIR Rb; 4. Block IIR-M Rb; 5. Block IIF Cs; 6. Block IIF Rb.

This investigation employs the two weeks data set of clock error, during March 24, 2013 to April 6, 2013 from the International GNSS Service (IGS) official website for modeling and forecasting. The original data sampling interval is 30 s, in order to improve the computational efficiency; we adjust the data sampling interval into 6 min, and make the forecasting in the future 3 days containing short term to long-term changes in clock error. And the accuracy verification is obtained by comparing the model predicted values with clock error data, where the prediction spans are mainly selected as 2, 12, 24 and 72 h.

14.3.1 Prediction Error Estimates

We select the max absolute error (Max), mean absolute error (Mean), and root mean squared error (RMS) as the indicator to assess the prediction accuracy.

$$Max_i = \max\left|{p_j}^i - {o_j}^i\right|, \quad j = 1, \cdots, n. \tag{14.5}$$

$$Mean_i = \frac{1}{n} \sum_{j=1}^{n} \left|{p_j}^i - {o_j}^i\right| \tag{14.6}$$

Table 14.1 Statistics about the max, mean and RMS of GPS satellite clock bias prediction

PRN	T/h	Max/ns	Mean/ns	RMS/ns
01	2	0.190	0.062	0.076
	12	0.766	0.586	0.596
	24	2.538	2.333	2.336
	72	17.311	16.993	16.996
05	2	0.116	0.036	0.045
	12	0.744	0.276	0.331
	24	0.875	0.378	0.445
	72	6.092	6.539	6.097
09	2	0.844	0.317	0.452
	12	3.336	1.193	1.550
	24	4.109	1.451	1.805
	72	14.870	11.054	11.277
16	2	0.574	0.246	0.294
	12	0.860	0.436	0.515
	24	1.605	1.031	1.104
	72	8.006	7.154	7.165
24	2	2.983	1.172	1.452
	12	5.511	2.648	3.008
	24	10.635	6.293	7.001
	72	26.273	23.448	23.588
26	2	0.593	0.167	0.215
	12	1.546	0.880	0.906
	24	3.430	2.487	2.519
	72	16.902	14.765	14.790

$$RMS_i = \sqrt{\frac{1}{n}\sum_{j=1}^{n}(p_j{}^i - o_j{}^i)^2} \tag{14.7}$$

where, o is the EOP observations, p is the EOP predictions, i is the prediction interval, n is the number of total predictions.

14.3.2 Result Analysis

For each clock error prediction interval (2, 12, 24 and 72 h), 100 predictions are made by means of LS + AR method, and the maximum absolute error (Max), mean absolute error (Mean) and the mean square error (RMS) are calculated and listed in Table 14.1, the unit is nanoseconds (ns).

As an example, Figs. 14.1 and 14.2 displays the clock error original sequence, decomposed fitting sequence and residuals of typically rubidium clock error

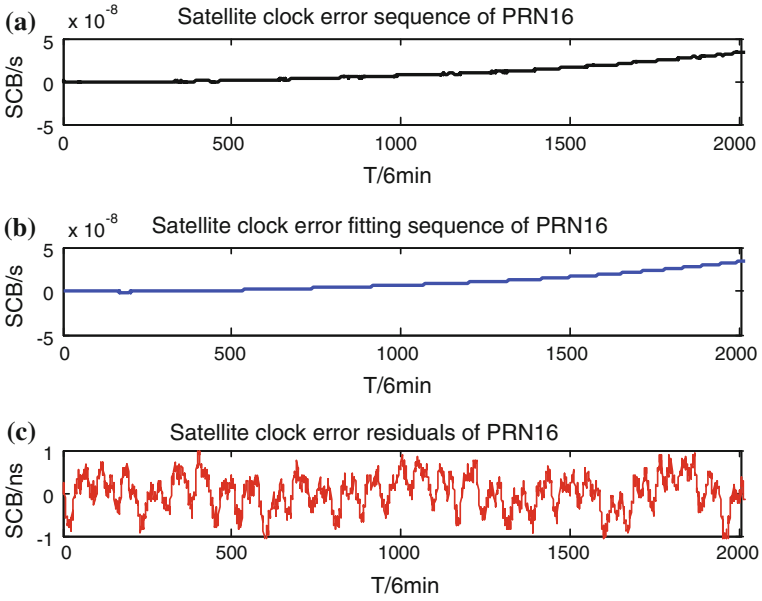

Fig. 14.1 SCB series, model fitting series and residual series of PRN16

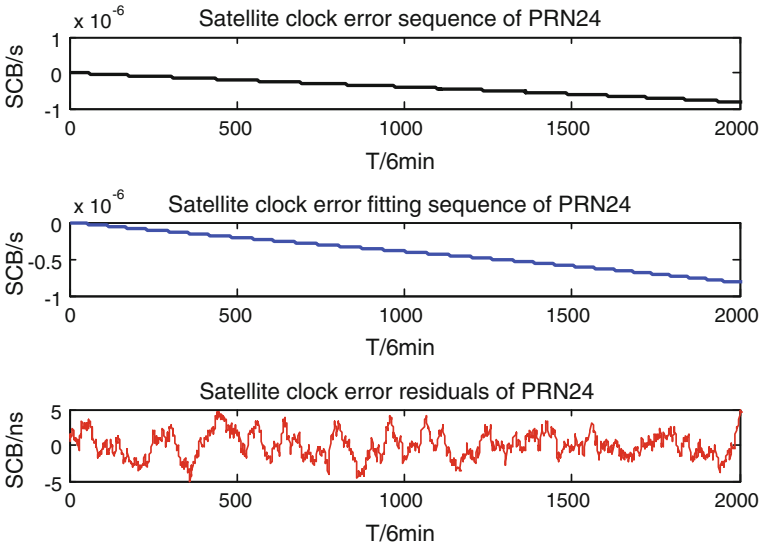

Fig. 14.2 SCB series, model fitting series and residual series of PRN24

sequence from PRN16 satellite and cesium clock error sequence from PRN24 satellite.while Figs. 14.3 and 14.4 shows the 24 h prediction result of the two satellite clock error series.

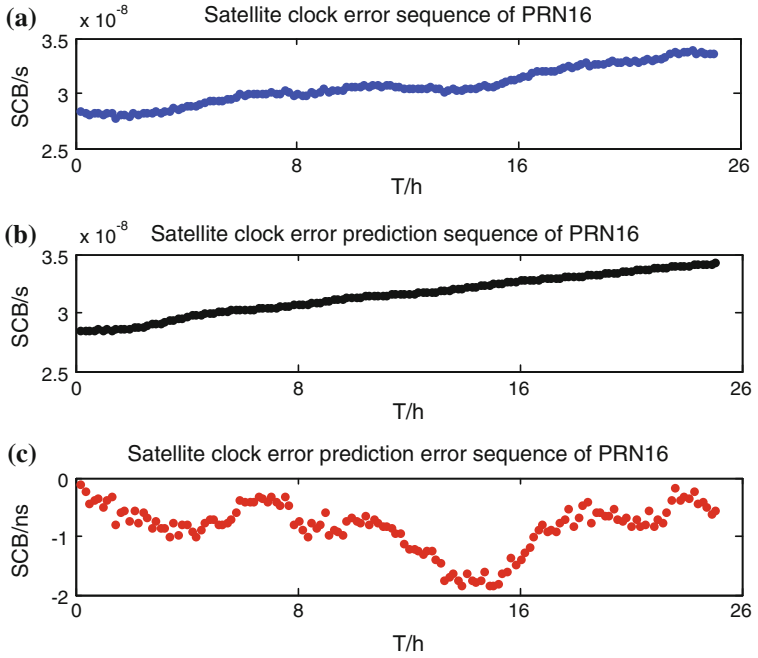

Fig. 14.3 24 h SCB series, prediction series and prediction error of PRN16

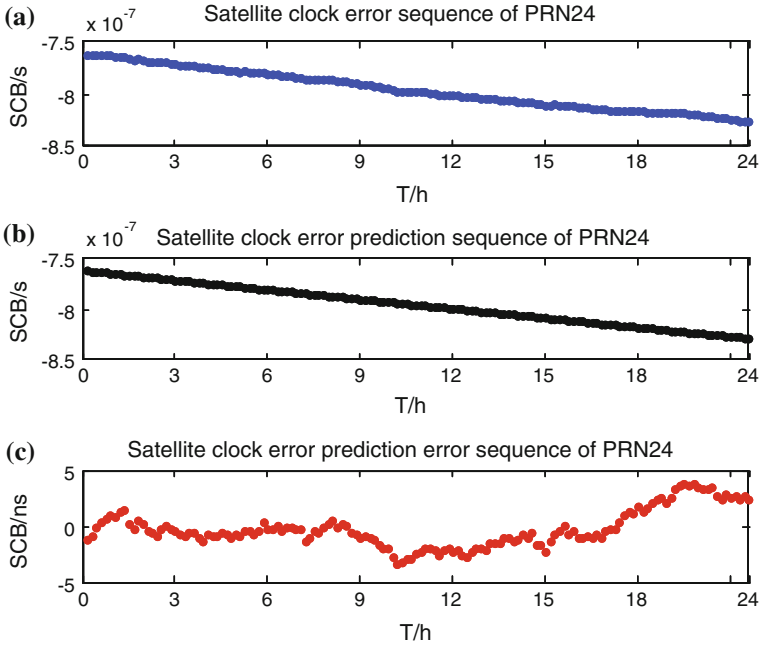

Fig. 14.4 24 h SCB series, prediction series and prediction error of PRN24

We can get some information from Figs. 14.1 and 14.2, that the PRN16 rubidium clock error sequence shows more stable residuals after model fitting, which is in the order of 2 ns; while PRN24 cesium clock error sequence remain a bigger residuals after model fitting about 10 ns, which shows that the stability of cesium clocks is worse than the rubidium clock. Meanwhile, it is shown from Table 14.1 and Figs. 14.3, 14.4, that PRN09, PRN24 are cesium clock, whose 12 h short-term forecast accuracy is poor, in the order of nanoseconds; while PRN01, PRN05, PRN16, PRN26 are rubidium clocks, the 12 h forecast accuracy of them are Higher, and are both in the sub-nanosecond magnitude. And for 24 and 72 h long-term forecasting, the cesium clock PRN24 perform most unstable, the RMS are 7 and 23.5 ns respectively, while the rubidium clock PRN05 and PRN16 perform best, which remains a nanosecond magnitude for the medium and long-term forecast accuracy.

14.4 Conclusion

In this study, we perform the short and medium-term predictions of the GPS clock error by means of LS + AR method, based on the IGS clock error sequence during March 24, 2013 to April 6, 2013. The prediction intervals range from 1 to 72 h. We get two information from the GPS satellite clock error sequence, on the one hand, the different types of satellite clock showing a law that is, the stability of rubidium clock is higher than cesium clock overall, and rubidium clock shows higher prediction accuracy than cesium clock for short-term and long-term forecasting. On the other hand, the LS + AR model reduce error accumulation by modeling each data series differently, which can effectively improve the prediction accuracy of the satellite clock error.

Acknowledgments The research is supported by the NSFC grant (11303073,11373057, 11073045), STCSM (06DZ22101). We thank the International GNSS Service (IGS) for providing the GPS satellite clock error data.

References

1. Akaike H (1971) Autoregressive model fitting for control. Ann Inst Stat Math 23:163–180
2. Brockwell PJ, Davis RA (1996) Introduction to time series and forecasting. Springer, New York
3. Cui X, Jiao W (2005) Grey system model for the satellite clock error predicting. Geomatics Inform Sci Wuhan Univ 30(5):447–450
4. Dai W, Jiao W, Li W (2009) Research on prediction of GPS block IIR atomic clock error. J Geodesy Geodyn 29(4):111–115
5. Guo H (2004) Frequency analysis theory and methods of navigation satellite atomic clocks. Information Engineering University, Zhengzhou

6. Guo H, Yang S, Yang Y (2007) Numerical prediction methods for clock difference based on two-way satellite time and frequency transfer data. Geomatics Inform Sci Wuhan Univ 32(1):43–46
7. Wei L, Chen P, Jinzhong M (2009) Application of gray system model in short-term predicting for the satellite clock error. J Surveying Mapp 6:32–35
8. Liu L (2004) Relativity theory of time comparison and high accuracy time synchronization technology. Information Engineering University, Zhengzhou
9. Liu X, Wu X, Zhao R et al (2011) Analysis of long-term clock bias forecast effects of several time prediction models. J Surveying Mapp 1:15–18
10. Liu X, Wu X, Tian Y (2010) Study on atomic prediction of time based on interpolation model with tchebytchev polynomials. J Geodesy Geodyn 30(1):77–82
11. Liu Y, Dang Y, Zheng Z (2011) Study and improvement for the model in satellite clock error long-term forecast. Hydrographical Surveying Charting 31(2):21–23
12. Lu X, Jia X, Cui X (2006) The optimization method of gray system theory for the satellite clock error short-term predicting. Eng Surveying Mapp 15(6):12–14
13. Wang Q, Li L, Gong Y (2010) Study of GPS satellite clock's behaviours and prediction. Sci Survey Mapp 35(2):36–39
14. Xu J, Zeng A (2009) Application of ARIMA (0, 2, q) model to prediction of satellite clock error. J Geodesy Geodyn 29(5):116–120
15. Zheng Z, Lu X (2008) Comparison and precision analysis of several GPS satellite clock bias prediction methods. J Shandong Univ Sci Technol 27(4):6–15
16. Zhu L (2006) Research on time comparison and performance analysis of atomic clocks. Information Engineering University, Zhengzhou
17. Zhu L, Wu X, Li C (2007) The two models for prediction of satellite clock error analysis. J Spacecraft TT&C Technol 26(3):39–43
18. Zhu X, Xiao H, Yong S et al (2008) The Kalman algorithm used for satellite clock offset prediction and its performance analysis. J Astronaut 29(3):966–970
19. Zhu L, Li C, Liu L (2009) Research on methods for prediction clock error based on domestic hydrogen atomic clock. J Geodesy Geodyn 29(1):148–151

Chapter 15
A New Relative Positioning Method Based on Un-differenced BDS Observation

Zongpeng Pan, Hongzhou Chai, Min Wang, Kai Xie, Huarun Wang, Bingquan Dong and Ming Liu

Abstract Aiming at the characteristics of the Beidou satellite navigation system (BDS), we introduce a new relative positioning method based on un-differenced observation. Unlike the relative positioning which always uses conventional double-difference approach to eliminate the satellite and receiver side errors and the common errors on the propagation path, this method preprocesses data similar to Precise Point Positioning (PPP) and uses ionosphere-free combination to relative positioning. During this process, one hand satellite clock errors are estimated as unknown parameters and use to establish the relationship between base station and rover, on the other hand ambiguity don't need to be fixed. The experiment result which based on resolving one week BDS observation data shows, the coordinate accuracy can reach millimeter and centimeter-level precision in horizontal and vertical direction when using this method for relative positioning over thousands of kilometers.

Keywords Beidou satellite navigation system · Un-differenced observation · Relative positioning · Satellite clock errors · Precise point positioning

15.1 Introduction

In recent years, application research and industrialization of the Beidou satellite navigation system [1–3] have been rapid development. It mainly concentrates in low-precision navigation applications [4, 5]. For high-precision positioning application research is relatively less and focuses on the short baseline relative positioning [6, 7] or precise point positioning (PPP) [8–12]. However, the relative

Z. Pan (✉) · H. Chai · M. Wang · K. Xie · H. Wang · B. Dong · M. Liu
Institute of Surveying and Mapping, Information Engineering University, Zhengzhou 450000, China
e-mail: panzongpeng@yeah.net

J. Sun et al. (eds.), *China Satellite Navigation Conference (CSNC) 2014 Proceedings: Volume III*, Lecture Notes in Electrical Engineering 305,
DOI: 10.1007/978-3-642-54740-9_15,

positioning for long distances is less concerned. The reason for this phenomenon is that (1) the Beidou satellite antenna phase center offsets (PCO) only give as factory value and the accuracy is not enough. For a short baseline, the satellite attitude is nearly in the same direction and PCO can be eliminated by double-differences between two stations. When it comes to the long baseline, the influence of the PCO can't be completely eliminated, if mandatory fixed ambiguities, it will lead to poor positioning accuracy [13]. So for Beidou long-distance relative positioning, using double differences positioning method to obtain high precision of ambiguity fixed solution is still not reached. (2) Only a few institutions capable of BDS precision orbit determination and clock errors calculation [14–16], and limited to the distribution and number of the ground-based observation stations, meanwhile, satellite model parameters (such as solar pressure model, the antenna PCO) also cannot be obtained precisely, the accuracy of orbit and clock offsets need to be improved [14, 15]. When long baseline relative positioning uses the broadcast ephemeris, the positioning accuracy is influenced by the ephemeris errors. Meanwhile, using the estimated Beidou precision orbit and clock errors to PPP, the positioning result is only a few centimeters [8–12].

Combined advantages with the relative positioning [17] and PPP [18, 19], this paper presents a new relative positioning method based on un-differenced observation. Unlike the relative positioning which always uses conventional double-difference approach to eliminate the satellite or receiver side errors and the public errors on the propagation path, there are not difference between rover station and base, but preprocesses data similar to PPP to eliminate and reduce the impact of errors, therefore more observations are available and the measurements are independent from each other. For the observation equations, in order to establish the relationship between the base station and rover, the satellite clock errors are treated as unknown parameters to be estimated which reducing the dependence on the precision of satellite clock errors. At the same time, the ambiguity is not fixed, directly use float solution, so the data processing is simple.

15.2 Un-differenced Relative Positioning

Assumed that the unit of carrier phase and pseudo range measurements is in meters, the i epoch, un-differenced ionosphere free carrier phase and pseudo range observation equations can be expressed as follows

$$\begin{aligned} v^j_{Lc,k}(i) &= \rho^j_k(i) + cdt_k(i) - cdt^j(i) + M(i)dT_k(i) + \lambda N^j_{Lc,k} - \lambda\Phi^j_{Lc,k}(i) \\ v^j_{Pc,k}(i) &= \rho^j_k(i) + cdt_k(i) - cdt^j(i) + M(i)dT_k(i) - P^j_{Pc,k}(i) \end{aligned} \tag{15.1}$$

where the subscript k for the station number, superscript j for satellites number, c for the speed of light in vacuum, dt_k as the receiver clock errors, dt^j as the satellite clock errors, ρ^j_k as geometric distance between satellite and receiver, dT_k

for tropospheric zenith delay (ZTD), M for the mapping function, $N^j_{Lc,k}$ as the ionosphere free ambiguity, $\Phi^j_{Lc,k}$ and $P^j_{Pc,k}(i)$ as the ionosphere free combination of carrier and pseudo range measurements, respectively, $v^j_{Lc,k}$ and $v^j_{Pc,k}$ for the carrier phase and pseudo range measurement noise and other errors, λ is the wavelength of ionosphere free combination.

In the un-differenced relative positioning, the base station coordinates and satellite orbital positions are fixed as known values. Linearized the rover station observation equations, then the base and the rover station observation equations can be expressed as follows

Base station

$$\begin{aligned} v^j_{Lc,B}(i) &= cdt_B(i) - cdt^j(i) + M(i)dT_B(i) + \lambda N^j_{Lc,B} + l^j_{Lc,B}(i) \\ v^j_{Pc,B}(i) &= cdt_B(i) - cdt^j(i) + M(i)dT_B(i) + l^j_{Pc,B}(i) \end{aligned} \tag{15.2}$$

Rover station

$$\begin{aligned} v^j_{Lc,R}(i) &= (\frac{x_0 - x^j}{\rho^j_0})dx + (\frac{y_0 - y^j}{\rho^j_0})dy + (\frac{z_0 - z^j}{\rho^j_0})dz \\ &\quad + cdt_R(i) - cdt^j(i) + M(i)dT_R(i) + \lambda N^j_{Lc,R} + l^j_{Lc,R}(i) \\ v^j_{Pc,R}(i) &= (\frac{x_0 - x^j}{\rho^j_0})dx + (\frac{y_0 - y^j}{\rho^j_0})dy + (\frac{z_0 - z^j}{\rho^j_0})dz \\ &\quad + cdt_R(i) - cdt^j(i) + M(i)dT_R(i) + l^j_{Pc,R}(i) \end{aligned} \tag{15.3}$$

where $l^j_{Lc,B}, l^j_{Pc,B}, l^j_{Lc,R}, l^j_{Pc,R}$ as pre-fits of the base station and rover station ionosphere free carrier and pseudo range measurements. x_0, y_0, z_0 as approximate coordinates of the rover station, x^j, y^j, z^j for satellite position and can be obtained from precise ephemeris. Now the parameters to be estimated in the observation equations are receiver clock errors, satellite clock errors, tropospheric zenith delay, and ambiguity and rover station coordinate corrections.

When using the above equations to estimate unknown parameters, the equations are singular, because the satellite and receiver clock errors and ambiguity parameters are linear correlation. Therefore, the same as satellite clock errors estimation, it must choose base station receiver clock as reference clock and fix it, then solve the rover receiver clock errors and satellite clock errors relative to the reference clock. Then Eq. (15.2) can rewrite as

$$\begin{aligned} v^j_{Lc,B}(i) &= -cdt^j(i) + M(i)dT_B(i) + \lambda N^j_{Lc,B} + l^j_{Lc,B}(i) \\ v^j_{Pc,B}(i) &= -cdt^j(i) + M(i)dT_B(i) + l^j_{Pc,B}(i) \end{aligned} \tag{15.4}$$

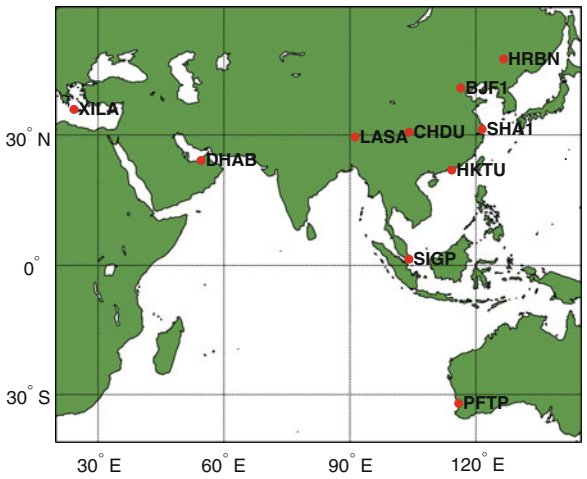

Fig. 15.1 Station distribution

combined Eqs. (15.3) and (15.4) can resolve the rover station coordinate corrections.

The above equations are not difference, therefore more observations are available and the measurements are independent from each other. The relationship between rover and base station is established and maintained via satellite clock errors, and it can not only absorb un-modeled errors, and then improve the positioning accuracy but also can reduce the dependence on the precision and sampling rate of satellite clock offsets which are important in PPP.

15.3 Experiments and Results Analysis

15.3.1 Data Collection

The experiments uses one week BDS observational data from April 2, 2013 to April 8, day of year for 092–098 days, which provided by Beidou Experimental Tracking Stations (BETS) and the corresponding precise orbit and clock products which provided by the GNSS Research Center of Wuhan University. Figure 15.1 shows the station distribution. The receivers which use in the experimental network were core-Star's UR240-type dual-frequency receiver, antenna type is UA240. Observation data are the B1 and B2 pseudo range and carrier phase measurements. During positioning, station coordinates are fixed to the true value which used in orbit determination, in order to self-consistent with the precise orbit coordinates.

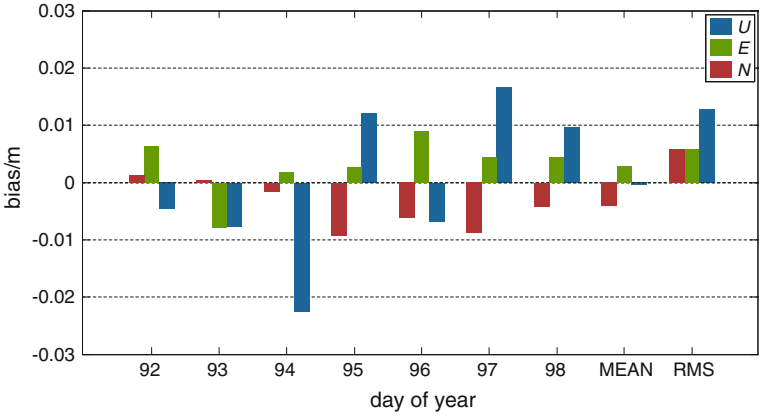

Fig. 15.2 One week positioning results of HRBN station (Bias)

Table. 15.1 One week positioning results of HRBN station (Bias)

DOY	N (m)	E (m)	U (m)
092	0.0013	0.0063	−0.0046
093	0.0003	−0.0078	−0.0076
094	−0.0016	0.0018	−0.0225
095	−0.0093	0.0026	0.0121
096	−0.0062	0.0089	−0.0068
097	−0.0088	0.0044	0.0167
098	−0.0042	0.0044	0.0097
Mean	−0.0041	0.0029	−0.0004
RMS	0.0057	0.0057	0.0128

15.3.2 Un-differenced Baseline Solution Analysis

When using un-differenced relative positioning to resolve baseline, the base station clock errors and station coordinates are fixed. The base station and rover station data preprocessing method is identical with the precise point positioning. Combined base and rover station observation equations to estimate rover position parameters. There is one week of baseline solution from BJF1 station to HRBN station, as shown in Fig. 15.2. BJF1 is the base station, HRBN as the rover station. The baseline length is 1,049.3 km.

As can be seen from Fig. 15.2, compared with the known coordinates of HRBN stations, un-differenced relative positioning results are in the order of millimeters in the horizontal direction, the positioning accuracy in the direction of the zenith is 1–2 cm. Detail statistical results of HRBN station is shown in Table 15.1.

As can be seen from Table 15.1, the coordinate consistency of HRBN station is better in one week of positioning results. The average of the coordinate accuracy

Table. 15.2 One week positioning results of rover stations (RMS)

Base station	Rover station	Baseline length (km)	N (m)	E (m)	U (m)
BJF1	HRBN	1,049.3	0.0057	0.0057	0.0128
CHDU	HKTU	1,368.9	0.0087	0.0091	0.0265
CHDU	BJF1	1,514.4	0.0073	0.0095	0.0312
CHDU	SHA1	1,663.8	0.0127	0.0228	0.0302
CHDU	HRBN	2,551.1	0.0074	0.0178	0.0325
HKTU	SIGP	2,547.2	0.0345	0.0295	0.0465
XILA	DHAB	3,139.2	0.0152	0.0518	0.1019
SIGP	PFTP	3834.8	0.0590	0.0746	0.1291
BJF1	SIGP	4367.7	0.0412	0.0338	0.0721

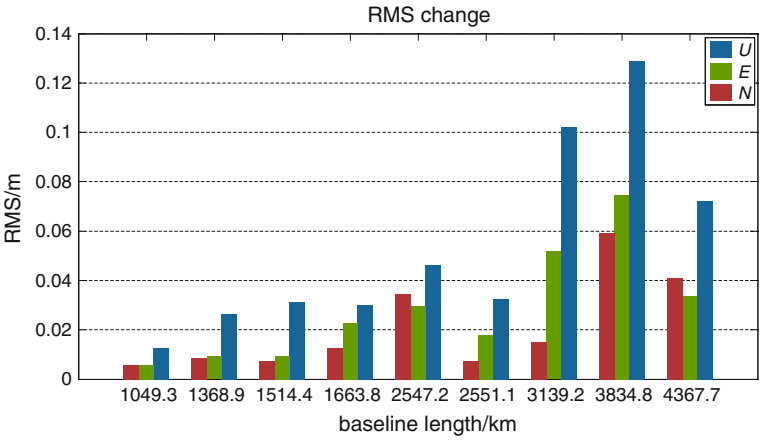

Fig. 15.3 Station positioning results compare among different baseline length

of the week, N direction is −0.0041 m, E direction is 0.0029 m, U direction is −0.0004 m. The RMS of the positioning results, N direction is 0.0057 m, E direction is 0.0057 m, U direction is 0.0128 m. Meanwhile, in order to better illustrate the validity of un-differenced relative positioning method, the positioning results of other baselines are listed in Table 15.2. In the baseline length column, left for the base station, right for the rover station.

It can be seen from Table 15.2, using un-differenced relative positioning method for precise positioning of Beidou system, when the baseline range from 1,000 to 2,500 km, the RMS of the coordinate accuracy can be ensured at millimeter to centimeter in the horizontal direction, and the RMS of the north direction is slightly better than the east direction's. The RMS of the positioning accuracy in the zenith direction is within a few centimeters, the maximum is not more than 5 cm. When the baseline length exceeds 3,000 km, significantly decreased positioning accuracy of the results, a few centimeters in the horizontal direction, the maximum is 0.1291 m in the zenith direction. From Fig. 15.3, it can show this trend.

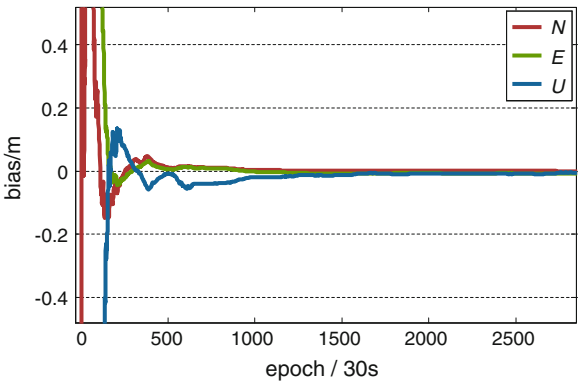

Fig. 15.4 HRBN station static positioning bias along with the observational time (DOY 093)

With the growth of distance between the stations, the positioning accuracy is gradually decreased. There are reasons, using un-differenced relative positioning method to positioning, the relationship between the two stations is established and maintained by satellite clock errors. When the distance between two stations are faraway, the common number of visible satellites will decrease. Then the relationship between the base station and rover will be weakened, resulting in a decline accuracy of satellite clock errors and positioning accuracy of results. Meanwhile, the BJF1 to SIGP (4,367.7 km) baseline solution is better than the XILA to DHAB (3,139.2 km) baseline solution and SIGP to PFTP (3,834.8 km) baseline solution, which may be caused by the distribution of stations and data quality, because the XILA station and DHAB station can only observe a few numbers of satellites.

In summary, using un-differenced relative positioning method to Beidou long baseline solution can obtain millimeter positioning results in horizontal direction and centimeter in zenith direction. It also shows that the Beidou satellite navigation system can meet the requirements of the long-distance precise relative positioning.

15.3.3 Convergence Analysis

Un-differenced relative positioning method without difference between stations, so common errors between the two stations can't be eliminated. It must use the accurate model to correct the errors or treat as unknown parameters to be estimated. Because the influence of the pseudo-range noise and other errors are not modeled, un-differential relative positioning need some time to converge to centimeter-level positioning accuracy. There are convergence time of HRBN station as shown in Figs. 15.4 and 15.5, the day of year for the 093 and 095. Where BJF1 is the base station, HRBN is the rover station.

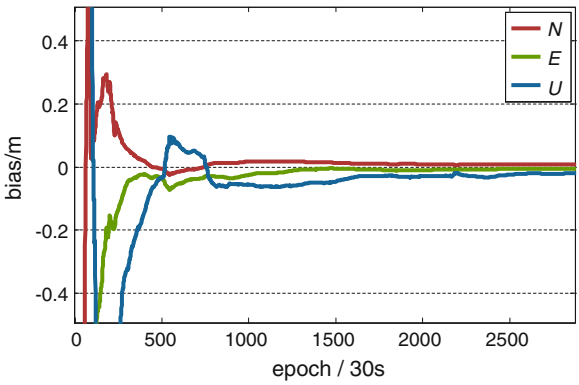

Fig. 15.5 HRBN station static positioning bias along with the observational time (DOY 095)

Comparing Figs. 15.4 and 15.5, the positioning results of the different DOY can converge to the millimeter and centimeter. But the convergence time is different. The faster case only need half an hour [20, 21] which is consistent with the convergence time of PPP. In bad case, the convergence time may require 2–3 h. The reasons for this phenomenon may be different data quality in different days, meanwhile the accuracy of satellite orbit and clock products may also cause the results of convergence time inconsistency, which need further study.

15.4 Conclusions

This paper presents a new relative positioning method based on un-differenced observation. Compared with the traditional relative positioning method, which has the following advantages, (1) the observation equations for the two stations without difference, therefore more observations are available and the measurements are independent from each other. (2) The satellite clock errors are treated as unknown parameters to be estimated which build relationship between base station and rover station, and reducing dependence on the accuracy of the satellite clock errors. (3) Data processing is flexible and the ambiguity is not fixed, directly use float solution and precise positioning results can be obtained. If the float ambiguity is fixed, it can also improve the positioning accuracy of the results.

Using un-differenced relative positioning method to precise positioning of Beidou satellite navigation system, the experiment results with BDS data show that: when the baseline range from 1,000 to 2,500 km, the RMS of the coordinate accuracy can be ensured at millimeter to centimeter in the horizontal direction, and the RMS of the north direction is slightly better than the east direction's. The RMS of the positioning accuracy in the zenith direction is within a few centimeters. Above all, un-differenced relative positioning method can be applied to long-distance precise relative positioning of Beidou satellite navigation system.

Acknowledgments Thanks to the GNSS Research Center of Wuhan University for providing the Compass orbit and clock products. This work was supported by National Natural Science Foundation of China (41274045).

References

1. Yang Y, Li J, Xu J, Tang J, Guo H, He H (2011) Contribution of the compass satellite navigation system to global PNT users. China Sci Bull 56(26):2813–2819
2. CSNO (China Satellite Navigation Office) (2012) BeiDou navigation satellite system signal in space interface control document (Open Service Signal B1I), Version 1.0, Dec 2012
3. Yang Y, Li J, Wang A, Xu J, He H, Guo H et al (2014) Preliminary assessment of the navigation and positioning performance of BeiDou regional navigation satellite system. Sci China Earth Sci 57(1):144–152
4. Wu X, Hu X, Wang G, Zhong H, Tang C (2013) Evaluation of COMPASS ionospheric model in GNSS positioning. Adv Space Res 51(6):959–968
5. Cai C, Gao Y, Pan L, Dai W (2013) An analysis on combined GPS/COMPASS data quality and its effect on single point positioning accuracy under different observing conditions. Advances in space research. http://dx.doi.org/10.1016/j.asr.2013.02.019
6. Shi C, Zhao Q, Hu Z, Liu J (2013) Precise relative positioning using real tracking data from COMPASS GEO and IGSO satellites. GPS Solution 17(1):103–119
7. Montenbruck O, Hauschild A, Steigenberger P, Hugentobler U, Teunissen P, Nakamura S et al (2013) Initial assessment of the COMPASS/BeiDou-2 regional navigation satellite system. GPS Solutions 17(2):211–222
8. Zhao Q, Guo J, Li M, Qu L, Hu Z, Shi C et al (2013) Initial results of precise orbit and clock determination for COMPASS navigation satellite system. J Geodesy 87(5):475–486
9. Li X, Ge M, Zhang H, Nischan T, Wickert J et al (2013) The GFZ real-time GNSS precise positioning service system and its adaption for COMPASS. Adv Space Res 51(6):1008–1018
10. Zhou S, Cao Y, Zhou J, Hu X, Tang C, Liu L et al (2012) Positioning accuracy assessment for the 4GEO/5IGSO/2MEO constellation of COMPASS. Sci China Phys Mech Astron 55(12):2290–2299
11. Li W, Teunissen P, Zhang B, Verhagen S (2013) Precise point positioning using GPS and compass observations. In: Proceedings of China satellite navigation conference (CSNC) 2013, vol 244. Springer, Berlin, pp 367–378
12. Zhou S, Hu X, Wu B, Liu L, Qu W, Guo R et al (2011) Orbit determination and time synchronization for A GEO/IGSO satellite navigation constellation with regional tracking network. Sci China Phys Mech Astron 54(6):1089–1097
13. Zhou W (2013) Research and realization on theories and methods of precision positioning base on BeiDou navigation satellite system. Institute of Surveying and Mapping, Information Engineering University, Zhengzhou, China, pp 79–96
14. Shi C, Zhao Q, Li M, Tang W, Hu Z, Lou Y et al (2012) Precise orbit determination of Beidou satellites with precise positioning. Sci China Earth Sci 55(7):1079–1086
15. Steigenberger P, Hugentobler U, Hauschild A, Montenbruck O et al (2013) Orbit and clock analysis of compass GEO and IGSO satellites. J Geodesy 87(6):515–525
16. Zhou S, Hu X, Zhou J, Chen J, Gong X, Tang C et al (2013) Accuracy analyses of precise orbit determination and timing for COMPASS/Beidou-2 4GEO/5IGSO/4MEO constellation. In: Proceedings of China satellite navigation conference (CSNC) 2013, vol 245. Springer, Berlin, pp 89–102
17. Blewitt G (1989) Carrier phase ambiguity resolution for the global positioning system applied to geodetic baselines up to 2000 km. J Geophys Res 94(B8):10187–20203
18. Zumberge JF et al (1997) Precise point positioning for the efficient and robust analysis of GPS data from large networks. J Geophys Res 102(B3):5005–5017

19. Kouba J, Héroux P (2001) Precise point positioning using IGS orbit and clock products. GPS Solution 5(2):12–28
20. Geng J, Teferle FN, Meng X, Towards PPP-RTK, Dodson AH (2011) Ambiguity resolution in real-time precise point positioning. Adv Space Res 47(10):1664–1673
21. Geng J, Meng X, Dodson A, Ge M, Teferle F (2010) Rapid re-convergences to ambiguity-fixed solutions in precise point positioning. J Geodesy 84(12):705–714

Chapter 16
Zero-Differenced Multi-GNSS Joint Precise Orbit Determination of BeiDou Satellites Based on Ambiguity Fixing

Weiping Liu, Jinming Hao, Jianwen Li and Mingjian Chen

Abstract A method of zero-differenced multi-GNSS joint precise orbit determination of BeiDou satellites based on ambiguity fixing was present. The realization of ambiguity fixing was focused on. The real data was analyzed, and the results show that the three dimensional precision of GEO, IGSO and MEO can respectively reach 1.263, 0.241 and 0.134 m. The radial precision of the three types of satellites is averagely better than 10 cm, and that of IGSO and MEO is mostly better than 5 cm. After ambiguity fixing, the three dimensional precision of BDS is improved 21.8 % averagely, and the tangential precision is improved most obviously, especially for GEO.

Keywords BeiDou navigation satellite system · Ambiguity fixing · Zero-differenced precise orbit determination · Multi-GNSS processing · SLR

16.1 Introduction

By the end of 2012, BDS (BeiDou Navigation Satellite System) had achieved the goal of the second step of "three-step" development strategy. The system, which contains five Geostationary Earth Orbit satellites (GEO), five Inclined Geosynchronous Orbit satellites (IGSO), and four Medium Earth Orbit satellites (MEO) in operation, has begun providing regional service for the Asia-Pacific [1, 2].

With the development of BDS, the method of precise orbit determination for BDS has been improved gradually. Zhou et al. [3] and Du [4] has researched precise orbit determination of GEO. Su, Guo, et al. has analysed the method of rapid orbit recovery for GEO [5, 6]. Mao, Zhou, et al. has studied the method

W. Liu (✉) · J. Hao · J. Li · M. Chen
College of Navigation and Aerospace Engineering, Information Engineering University, Zhengzhou, China
e-mail: lwpchxy@sina.com; lwpchxy@163.com

J. Sun et al. (eds.), *China Satellite Navigation Conference (CSNC) 2014 Proceedings: Volume III*, Lecture Notes in Electrical Engineering 305,
DOI: 10.1007/978-3-642-54740-9_16,

of GEO and IGSO joint precise orbit determination [7, 8]. Montenbruck et al. [9] has analyzed the initial assessment of BDS, and the three-dimensional orbit precision is about 1–10 m. Ge et al. [10] has studied the method of orbit determination of single BDS, and the 3D RMS of GEO and IGSO can respectively reach 3.3 and 0.5 m. Shi et al. [11] and Zhao et al. [12] has achieved the radial precision of 10 cm for BDS orbit based on BeiDou Experimental Tracking Stations [11, 12]. Steigenberger et al. [13, 14] has analyzed the strategy of BDS orbit determination based on Bernese software, which is like the method used in Galileo. Liu et al. [15] has studied BDS and GPS joint orbit determination.

In general, there are two different kinds of methods to determinate BDS orbit: (1) precise orbit is estimated by BDS data only; (2) Multi-GNSS data is processed to determinate BDS orbit. In the second kind, the method, which may be named as zero-differenced BDS/GPS joint precise orbit determination for BeiDou satellites, is used at most [11, 14]. The processing flow is followed as: At first, station coordinates, receiver clock and troposphere zenith delays are estimated by GPS observation data and precise orbit and clock. Secondly, BDS orbit is solved when these parameters are fixed. The method has been validated by real data processing [16, 17]. Because of the bad structure of observation network, ambiguity parameters are kept float in the method, which affects the accuracy of BDS orbit. With the development of BDS, Multi-GNSS Experiment of IGS, BeiDou Experimental Tracking Stations of Wuhan University [11], and international GNSS Monitoring and Assessment System [18, 19] have established many BDS observation stations, which can improve the structure of observation network, and provide favorable conditions for ambiguity fixed in the network solutions. In the context, the method of ambiguity fixed in the network solutions is studied, and is used in the zero-differenced BDS/GPS joint precise orbit determination of BeiDou satellites to improve the accuracy of BDS orbit.

The paper has studied a method of zero-differenced BDS/GPS joint precise orbit determination of BeiDou satellites based on ambiguity fixed. The realization of ambiguity fixing is focused on. The real data is analyzed, and the method is validated.

16.2 Method of Precise Orbit Determination

The method, which is used in the paper, is given in the Fig. 16.1. Different from the method of the reference [11] and [14], ambiguity is fixed in the paper. Zero-differenced ambiguity doesn't have the integer property in the influence of the initial phase deviation at satellites and receivers. Ambiguity fixing is only fit for double-differenced observation. For fixing ambiguity in zero-differenced orbit determination, we should process with the following three steps: double-differenced ambiguity selection, double-differenced ambiguity fixing, and ambiguity integer constraints.

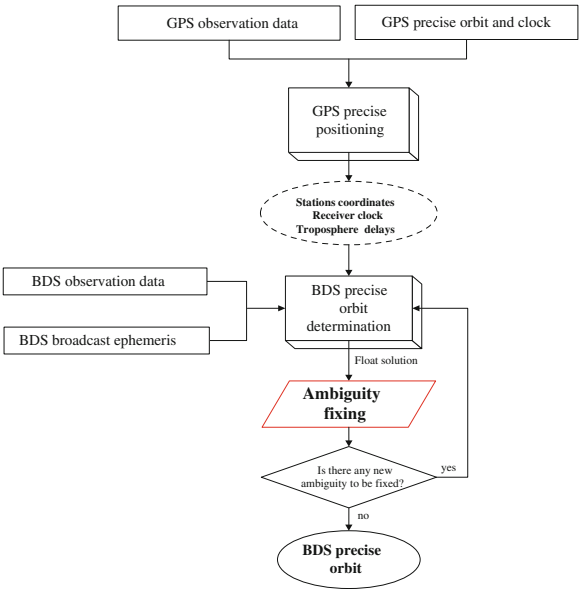

Fig. 16.1 Flow chart of precise orbit determination

16.2.1 Double-Differenced Ambiguity Selection

In BDS precise orbit determination, we use zero-differenced ionosphere-free combination pseudo-range and carrier-phase data. The observation equation of zero-differenced ionosphere-free combination carrier-phase can express as

$$\begin{aligned} L_{ck}^{i} &= (f_1^2 L_{1k}^{i} - f_2^2 L_{2k}^{i})/(f_1^2 - f_2^2) \\ &= \rho_k^i - f_2^2 \Delta\rho_k^i/(f_1^2 - f_2^2) + \gamma_{ck}^i \end{aligned} \tag{16.1}$$

where ρ_k^i is the geometry range between satellite i and station k, which contains orbit parameters. f_1 and f_2 are the frequency of the B_1 and B_2 carrier-phases, respectively. $\Delta\rho_k^i$ is the differential delay between B_1 and B_2 phase centers. γ_{ck}^i is the ambiguity bias of zero-differenced ionosphere-free combination carrier-phase, which can express as

$$\gamma_{ck}^{i} = (f_1^2 \lambda_1 b_{1k}^{i} - f_2^2 \lambda_2 b_{2k}^{i})/(f_1^2 - f_2^2) \tag{16.2}$$

where λ_1 and λ_2 are respectively the wavelengths of B_1 and B_2, and b_1 and b_2 are the ambiguity parameters.

At first, the float solution and variance of zero-differenced ionosphere-free ambiguity can be obtained through the processing in the Fig. 16.1. Based on the

theory of double-differenced carrier-phase, every four zero-differenced ambiguities can establish one double-differenced ambiguity [20]. We have

$$\begin{aligned}\gamma_{ckl}^{ij} &= (\gamma_{ck}^{i} - \gamma_{ck}^{j}) - (\gamma_{cl}^{i} - \gamma_{cl}^{j}) \\ &= (f_1^2\lambda_1 n_{1kl}^{ij} - f_2^2\lambda_2 n_{2kl}^{ij})/(f_1^2 - f_2^2)\end{aligned} \tag{16.3}$$

$$\sigma_{ckl}^{ij} = \left(\sigma_{ck}^{i2} + \sigma_{cl}^{i2} + \sigma_{ck}^{j2} + \sigma_{cl}^{i2}\right)^{1/2} \tag{16.4}$$

where n_{1kl}^{ij} and n_{2kl}^{ij} are respectively the double-differenced ambiguities of B_1 and B_2, which have the integer property.

In real data processing, only independent double-differenced ambiguities are selected. The usual selection methods are: (1) by the increasing order of the variances of the float ionosphere-free ambiguities; (2) by the increasing order of the length of baselines. Ge et al. [21] has analyzed the deficiencies of the two methods, and proposed the selection method which is at baseline and network level according to the possibility of ambiguity fixing. We use the method in the paper.

16.2.2 Double-Differenced Ambiguity Fixing

For fixing the independent double-differenced ambiguities, we can transform Eq. (16.3) as follows,

$$\begin{aligned}\gamma_{ckl}^{ij} &= [f_2^2\lambda_2 n_{\delta kl}^{ij} + (f_1^2\lambda_1 - f_2^2\lambda_2)n_{1kl}^{ij}]/(f_1^2 - f_2^2) \\ &= f_2^2\lambda_2 n_{\delta kl}^{ij}/(f_1^2 - f_2^2) + \lambda_I n_{1kl}^{ij}\end{aligned} \tag{16.5}$$

where $n_{\delta kl}^{ij} = n_{1kl}^{ij} - n_{2kl}^{ij}$ is the wide-lane ambiguity, $\lambda_I = c/(f_1 + f_2)$ is the narrow-lane wavelength, and n_{1kl}^{ij} is the narrow-lane ambiguity.

The wide-lane combinations of pseudo-range and carrier-phase can read as

$$\begin{aligned}L_{\delta k}^{i} &= (f_1 L_{1k}^{i} - f_2 L_{2k}^{i})/(f_1 - f_2) \\ &= \rho_k^i + I_k^i f_1 f_2/(f_1^2 - f_2^2) + \lambda_\delta b_{\delta k}^i + \Delta\rho_k^i f_2/(f_1 - f_2)\end{aligned} \tag{16.6}$$

$$\begin{aligned}P_{\delta k}^{i} &= (f_1 P_{1k}^{i} - f_2 P_{2k}^{i})/(f_1 + f_2) \\ &= \rho_k^i + I_k^i f_1 f_2/(f_1^2 - f_2^2) - \Delta\rho_k^i f_2/(f_1 + f_2)\end{aligned} \tag{16.7}$$

where $\lambda_\delta = c/(f_1 + f_2)$ is the wide-lane wavelength, $b_{\delta k}^i$ is the zero-differenced wide-lane ambiguity, I_k^i is the ionosphere delay, and other symbols are the same with Eq. (16.1).

From Eqs. (16.6) and (16.7), we have

$$b_{\delta k}^{i} = \frac{1}{\lambda_{\delta}}\left[L_{\delta k}^{i} - P_{\delta k}^{i} - 2\Delta\rho_{k}^{i} f_2/(f_1 - f_2)\right] \tag{16.8}$$

For eliminating observation noise and multipath effect, we can get the zero-differenced wide-lane ambiguity through the average value from a lot of epochs. The double-differenced wide-lane ambiguity reads as

$$n_{\delta kl}^{ij} = \langle b_{\delta k}^{i}\rangle - \langle b_{\delta l}^{i}\rangle - \langle b_{\delta k}^{j}\rangle + \langle b_{\delta l}^{i}\rangle \tag{16.9}$$

$$\sigma_{\delta kl}^{ij} = \left(\sigma_{\delta k}^{i2} + \sigma_{\delta l}^{i2} + \sigma_{\delta k}^{j2} + \sigma_{\delta l}^{i2}\right)^{1/2} \tag{16.10}$$

where $\sigma_{\delta j}^{i2} = \frac{1}{N_j^i}\left(\langle b_{\delta j}^{i2}\rangle - \langle b_{\delta l}^{i}\rangle^2\right)$, $\langle\rangle$ indicates the average value form some epochs, and N_j^i is the number of epochs.

The double-differenced wide-lane ambiguity is decided whether to be fixed according to the probability function [22]

$$P_0 = 1 - \sum_{n=1}^{\infty}\left[erfc\left(\frac{n-(b-I)}{\sqrt{2}\sigma}\right) - erfc\left(\frac{n+(b-I)}{\sqrt{2}\sigma}\right)\right] \tag{16.11}$$

where $erfc(x) = \frac{2}{\sqrt{\pi}}\int_x^{\infty} e^{-t^2}\mathrm{d}t$, b and σ^2 are the estimation and variance of the ambiguity, I is the nearest integer to b. We usually take the confidence level α as 0.1 %, and when $P_0 > 1 - \alpha$, b is fixed to I.

With Eqs. (16.3) and (16.4), we introduce the fixed wide-lane ambiguity into Eq. (16.5) and get the estimation and variance of the narrow-lane ambiguity. And then, we can decide whether the narrow-lane ambiguity is fixed by Eq. (16.11).

At last, we can get the fixed double-differenced ionosphere-free ambiguities by introducing the fixed wide-lane and narrow-lane ambiguities into Eq. (16.5).

16.2.3 Ambiguity Integer Constraints

The observation equation of zero-differenced orbit determination for BDS in the Fig. 16.1 can express as

$$\boldsymbol{v} = \boldsymbol{A}\boldsymbol{x} + \boldsymbol{l} \quad \boldsymbol{P} \tag{16.12}$$

$$\boldsymbol{x} = -\left(\boldsymbol{A}^T\boldsymbol{P}\boldsymbol{A}\right)^{-1}\boldsymbol{A}^T\boldsymbol{P}\boldsymbol{l} = -\boldsymbol{N}^{-1}\boldsymbol{w} \tag{16.13}$$

$$\boldsymbol{C}_{\boldsymbol{x}} = \sigma_0^2\boldsymbol{N}^{-1} \tag{16.14}$$

$$\sigma_0^2 = \frac{(\boldsymbol{l}^T \boldsymbol{P} \boldsymbol{l} - \boldsymbol{x}^T \boldsymbol{w})}{(n-t)} \tag{16.15}$$

where $\boldsymbol{v}$ is the residual vector with dimension n, $\boldsymbol{A}$ is the design matrix with dimension $n \times t$, $\boldsymbol{l}$ is $O - C$, $\boldsymbol{P}$ is the weight matrix, $\boldsymbol{N}$ is the normal equation matrix, $\boldsymbol{w}$ is the free term of normal equation, $\mathbf{C_x}$ is the covariance matrix, and σ_0^2 is the unit weight variance.

We may introduce the fixed double-differenced ionosphere-free ambiguities into the normal equation as additional constraint condition. The virtual observation equation can read as

$$\boldsymbol{v_b} = \boldsymbol{D'x} - \boldsymbol{b}_c^{-d} \quad \boldsymbol{P_b} \tag{16.16}$$

where $\boldsymbol{b}_c^{-d}$ is the fixed double-differenced ionosphere-free ambiguities, $\boldsymbol{D'}$ is the ambiguity mapping matrix, $\boldsymbol{P_b}$ is the weight matrix of the virtual observation, the elements of which should be evidently larger than the observation weight, e.g. 10^{10}.

According to the theory of condition adjustment, the solution of the original problem with the ambiguity integer constraints can express as

$$\boldsymbol{x}_{new} = -\left(\boldsymbol{A}^T \boldsymbol{P} \boldsymbol{A} + \boldsymbol{D'}^T \boldsymbol{P_b} \boldsymbol{D'}\right)^{-1} \left(\boldsymbol{A}^T \boldsymbol{P} \boldsymbol{l} - \boldsymbol{D'}^T \boldsymbol{P_b} \boldsymbol{b}_c^{-d}\right) = -\boldsymbol{N}_{new}{}^{-1} \boldsymbol{w}_{new} \tag{16.17}$$

$$\boldsymbol{C_x} = \sigma_0^2 \boldsymbol{N}_{new}{}^{-1} \tag{16.18}$$

$$\sigma_0^2 = \frac{(\boldsymbol{l}^T \boldsymbol{P} \boldsymbol{l} + \boldsymbol{b}_c^{-dT} \boldsymbol{P_b} \boldsymbol{b}_c^{-d} - \boldsymbol{x}_{new}{}^T \boldsymbol{w}_{new})}{(n + n_b - t)} \tag{16.19}$$

where n_b is the number of fixed ambiguities.

In practice, the following sequential formulas are used:

$$\boldsymbol{N}_{new}{}^{-1} = \boldsymbol{N}^{-1} - \left(\boldsymbol{N}^{-1} \boldsymbol{D'}^T\right) \beta \left(\boldsymbol{D'} \boldsymbol{N}^{-1}\right) \tag{16.20}$$

$$\boldsymbol{x}_{new} = \boldsymbol{x} + \left(\boldsymbol{N}^{-1} \boldsymbol{D'}^T\right) \beta \left(\boldsymbol{b}_c^{-d} - \boldsymbol{D'x}\right) \tag{16.21}$$

$$\beta = \left(\boldsymbol{P_b}^{-1} + \boldsymbol{D'} \boldsymbol{N}^{-1} \boldsymbol{D'}^T\right)^{-1} \tag{16.22}$$

where β is a scalar of one fixed ambiguity.

16.3 Numerical Examples and Analysis

To validate the method in the paper, an experiment is processed here. The experiment span is 2013.09.05–2013.09.09, and BDS/GPS data with 30 s interval from global 34 stations is analyzed. By the way, 16 stations are from M-GEX

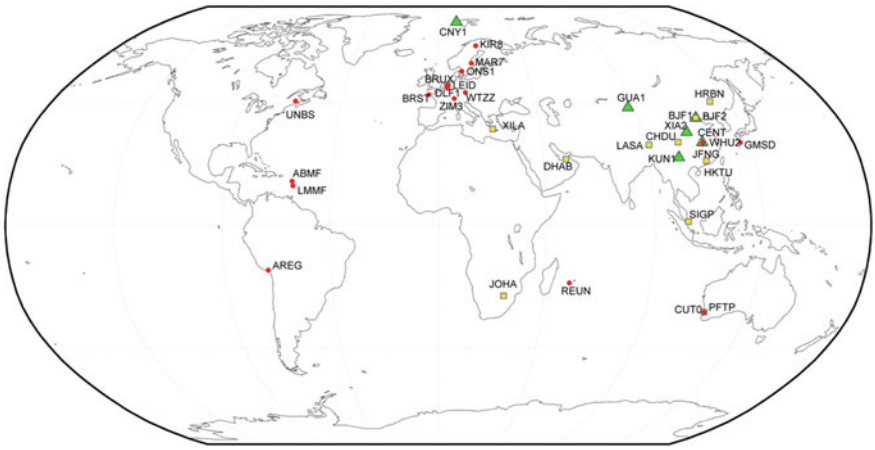

Fig. 16.2 Station layout

Table 16.1 Strategy of data processing

Name	Models and parameters
Orbit-arc length	3 days
Observation	Zero-differenced ionosphere-free combination pseudo-range and carrier-phase
Elevation cutoff angle	100
Sampling rate	30 s
EOP	Fixed IERS EOPC
Station coordinates	IGS08,Fixed GPS solution
Relativistic effects	Corrected
Tidal displacements	Solid earth, pole tide, ocean loading (IERS 2010)
Troposhere modeling	Saastamoinen + GMF, Fixed GPS solution
Ionosphere modeling	Ionosphere-free combination
Satellite clock	White noise
Receiver clock	Fixed GPS solution and the signal delay between GPS and BDS estimation
Orbit parameters	6 orbit state parameters and 5 Bern solar parameters estimation

(red circle), 12 stations are from BETS (yellow square), and 6 stations are from iGMAS (green triangle). The distribution of stations is given in Fig. 16.2.

Two cases are used, and the strategy of them is mostly same as Table 16.1. The difference between them is only in the ambiguity processing.

Case 1: Ambiguity is kept float.
Case 2: Ambiguity is fixed by the method in the paper, and the processing steps are given in Fig. 16.1.

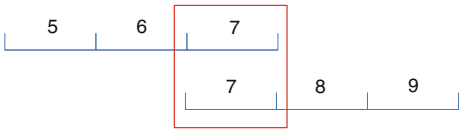

Fig. 16.3 Method of overlapped-arcs comparison

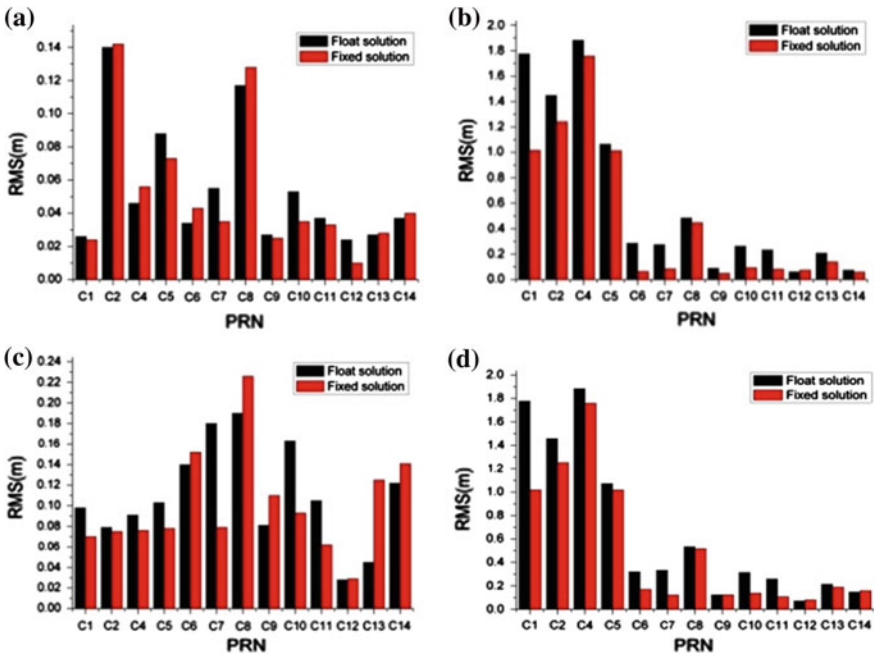

Fig. 16.4 Results of overlapped-arcs precision. **a** R, **b** T, **c** N, **d** 3D

The precision of BDS orbit is validated by checking the difference of the overlapped arcs, as Fig. 16.3. Figure 16.4 and Table 16.2 have given RMS of BDS orbit in the radial, tangential, normal and three-dimensional direction. Because of the maneuver, the result of C03 is not given here.

From Fig. 16.4 and Table 16.2, we can see:

1. On average, the three-dimensional precision of GEO, IGSO and MEO can reach 1.548, 0.325 and 0.173 m in Case 1 and 1.263, 0.214, and 0.134 m in Case 2, respectively. After ambiguity fixing, the three-dimensional precision of all satellites is improved by 21.8 % on average.
2. The tangential precision of BDS orbit can be improved most obviously by ambiguity fixing. The improvement of GEO, IGSO and MEO can respectively reach 0.285, 0.132 and 0.055 m. Although that of GEO is the most, the precision of GEO is also the worst in the tangential direction compared with IGSO and MEO.

Table 16.2 Statistics of overlapped-arcs errors (Units: m)

Type	PRN	R		T		N		3D	
		Case 1	Case 2	Case 1	Case 2	Case 1	Case 2	Case 1	Case 2
GEO	C1	0.026	0.024	1.775	1.017	0.098	0.070	1.778	1.020
	C2	0.140	0.142	1.448	1.242	0.079	0.075	1.457	1.252
	C4	0.046	0.056	1.882	1.757	0.091	0.076	1.884	1.759
	C5	0.088	0.073	1.065	1.014	0.103	0.078	1.073	1.019
	Average	**0.075**	**0.074**	**1.543**	**1.258**	**0.093**	**0.075**	**1.548**	**1.263**
IGSO	C6	0.034	0.043	0.286	0.064	0.140	0.152	0.320	0.170
	C7	0.055	0.035	0.275	0.085	0.180	0.079	0.333	0.121
	C8	0.117	0.128	0.485	0.448	0.190	0.226	0.534	0.517
	C9	0.027	0.025	0.089	0.049	0.081	0.110	0.123	0.123
	C10	0.053	0.035	0.263	0.094	0.163	0.093	0.314	0.137
	Average	**0.057**	**0.053**	**0.280**	**0.148**	**0.151**	**0.132**	**0.325**	**0.214**
MEO	C11	0.037	0.033	0.234	0.082	0.105	0.062	0.259	0.107
	C12	0.024	0.010	0.061	0.074	0.028	0.029	0.071	0.080
	C13	0.027	0.028	0.208	0.139	0.045	0.125	0.214	0.189
	C14	0.037	0.040	0.074	0.059	0.122	0.141	0.147	0.158
	Average	**0.031**	**0.028**	**0.144**	**0.089**	**0.075**	**0.089**	**0.173**	**0.134**

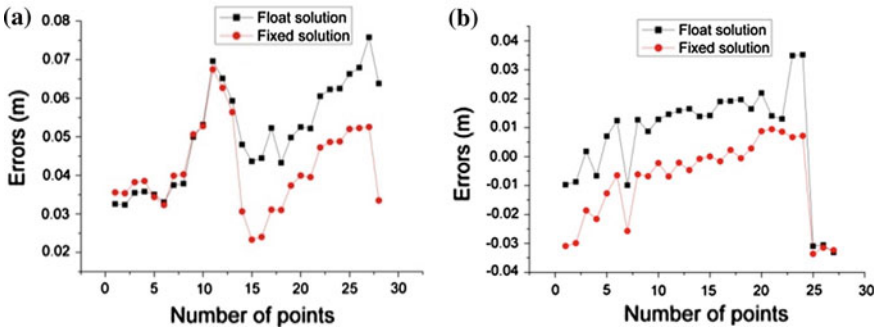

Fig. 16.5 SLR check results of orbit determination. **a** C10, **b** C11

3. After ambiguity fixing, the radial precision of three types of satellites can be better than 10 cm on average, and that of IGSO and MEO can be better than 5 cm, except C08. The three-dimensional precision of C04 and C08 is worse than that of the same type of satellites, which may be related to network structure and observation quality.

Because the difference of the overlapped arcs can only illustrate internal precision, we validate the orbit accuracy of C10 and C11 by the SLR data. The results are given in Fig. 16.5.

From Fig. 16.5, the SLR validation results of C10 and C11, which chiefly reacts the radial precision, are improved from 0.051 and 0.019 m in Case 1 to 0.043 and 0.016 m in Case 2. The results are coincident with the above analysis.

16.4 Conclusions

The increasing number of BDS stations has improved the structure of BDS observation network, which is good for ambiguity fixing. In the context, a method of zero-differenced multi-GNSS joint precise orbit determination of BeiDou satellites based on ambiguity fixed is present in the paper. The analysis shows that the three-dimensional precision of GEO, IGSO and MEO can reach 1.263, 0.214, and 0.134 m by the method in the paper. The radial precision of three types of satellites can be better than 10 cm on average, and that of IGSO and MEO can generally be better than 5 cm. After ambiguity fixing, the three-dimensional precision of BDS is averagely improved by 21.8 %. The improvement is the most in the tangential direction, especially for GEO. The results have also been validated by SLR.

We also find that the orbit precision of GEO is obviously worse than that of IGSO and MEO, and the orbit precision of BDS is also worse than that of GPS. With the improvement of network structure, BDS dynamic model, and Multi-GNSS data processing methods, these problem may be solved in the future, and the precision of BDS can be improved too.

Acknowledgments We would like to thank the data provider Information Engineering University which is one of the analysis centers of iGMAS! We also want to thank Pro. Maorong Ge in GFZ, Pro. Qile Zhao, PhD. Min Li, and PhD. Xi Su in Wuhan University for their support and help!

References

1. Yang Y (2010) Progress, contribution and challenges of compass/Beidou satellite navigation system. Acta Geodaetica Cartogr Sin 39(1):1–6
2. China Satellite Navigation Office (2012) BeiDou navigation satellite system signal in space interface control document 1.0. Beijing, pp 1–3
3. Zhou J, Chen L, Hu X et al (2010) The precise orbit determination of GEO navigation satellite with multi-types observation. Sci Sin Phys Mech Astron 40(5):520–527
4. Du L (2006) A study on the precise orbit determination of geostationary satellites. Information Engineering University, Zhengzhou
5. Mao Y, Du Y, Song X et al (2011) GEO and IGSO joint precise orbit determination. Sci Sin Phys Mech Astron 54(6):1009–1013
6. Zhou S, Hu X, Wu B et al (2011) Orbit determination and time synchronization for a GEO/IGSO satellite navigation constellation with regional tracking network. Sci Sin Phys Mech Astron 54(6):1089–1097
7. Su H (2000) Precise orbit determination of global navigation satellite system of second generation. University of Munchen, Berlin, pp 95–109

8. Guo R, Zhou J, Hu X et al (2011) A strategy of rapid orbit recovery for the geostationary satellite. Acta Geodaetica Cartogr Sin 40:19–25
9. Montenbruck O, Hauschild A, Steigenberger P et al (2013) Initial assessment of the COMPASS/ BeiDou-2 regional navigation satellite system. GPS Solutions 17(2):211–222
10. Ge M, Zhang HP, Jia XL et al (2012) What is achievable with the current compass constellation. GPS World 1:29–34
11. Shi C, Zhao QL, Li M et al (2012) Precise orbit determination of Beidou Satellites with precise positioning. Sci China Earth Sci 55:1079–1086
12. Zhao Q, Guo J, Li M et al (2013) Initial results of precise orbit and clock determination for COMPASS navigation satellite system. J Geod 87(5):475–486
13. Steigenberger P, Hugentobler U, Montenbruck O et al (2011) Precise orbit determination of GIOVE-B based on the CONGO network. J Geod 85(6):357–365
14. Steigenberger P, Hugentobler U, Hauschild A et al (2013) Orbit and clock analysis of compass GEO and IGSO satellites. J Geod 87(6):515–525
15. Liu Y, Lou Y, Shi C et al (2013) BeiDou Regional navigation system network solution and precision analysis. In: Proceedings of China satellite navigation conference (CSNC) 2013, Guangzhou, 15–17 May 2013
16. Li M, Zhao Q, Shi C et al (2012) Precise orbit determination of Beidou satellites by Beidou/ GPS Data. CSNC2012, Guangzhou
17. Liu W, Hao J, Li J et al (2013) A method of precise orbit determination of BeiDou navigation satellite. J Geomatics Sci Technol 30(3):247–250
18. Jiao W, Ding Q, Li J et al (2011) Monitoring and assessment of GNSS open services. Sci Sin Phys Mech Astron 41(5):521–527
19. Jiao W (2012) Architecture and current development of iGMAS. CSNC2012, Guangzhou
20. Blewitt G (1994) Carrier phase ambiguity resolution for the global positioning system applied to geodetic baselines up to 2000 km. J Geophys Res 94(B8):10187–10203
21. Ge M, Gendt G, Dick G et al (2005) Improving carrier-phase ambiguity resolution in global GPS network solutions. J Geod 79(1–3):103–110
22. Dong D, Bock Y (1989) Global positioning system network analysis with phase ambiguity resolution applied to crustal deformation studies in California. J Geophys Res 94(B4): 3949–3966

Chapter 17
BDS Satellites and Receivers DCB Resolution

Qiang Zhang, Qile Zhao, Hongping Zhang and Guo Chen

Abstract Using GNSS observation data to establish high-precision ionospheric model has an important role in precise point positioning, real-time navigation and ionosphere research. One of the main error sources to accurately estimate total electron content (TEC) is Differential Code Bias (DCB). At present, the international GNSS Service (IGS) daily publish GPS and GLONASS satellites DCB and IGS tracking station receivers DCB, BeiDou Navigation Satellite System (BDS) has not provided the BDS satellites DCB services. Based on BeiDou Experimental Tracking Stations (BETS), and use a combination of ionospheric residual method to resolve BDS satellites DCB and BETS tracking station receivers DCB at B1 and B2 frequencies. The results show that, BDS satellites DCB are between −8 and 16 ns at B1 and B2 frequencies and their stabilities are basically better than 0.5 ns. Because of the satellite elevation, IGSO satellites DCB have highest stabilities, followed by MEO satellites, and GEO satellites have worst stabilities, especially C04 and C05; BETS tracking station receivers DCB are basically between −5 and −25 ns, and their stabilities are better than 1.5 ns.

Keywords BDS · Ionosphere · DCB · TEC

17.1 Introduction

GNSS signal is transmitted from the satellite internal part to the transmitting antenna and from receiver antenna to digital IF output and the time delay is known as the hardware delay. Difference between different frequency signal (carrier phase or pseudorange code) time delay is called the hardware delay bias. Delay bias between the pseudorange code is called Differential Code Bias (DCB), and

Q. Zhang (✉) · Q. Zhao · H. Zhang · G. Chen
GNSS Research Center, Wuhan University, Wuhan, Hubei Province, China
e-mail: zhangqiang@whu.edu.cn

J. Sun et al. (eds.), *China Satellite Navigation Conference (CSNC) 2014 Proceedings: Volume III*, Lecture Notes in Electrical Engineering 305,
DOI: 10.1007/978-3-642-54740-9_17,

between the carrier phase is called Uncalibrated Phase Delays (UPD) [1]. DCB product released by IGS Ionosphere Working-group show that, the magnitudes for the GPS satellites DCB at P1 and P2 frequencies are −10 to 10 ns. It will result in 30 TECU errors, without considering the satellites DCB (for GPS L4 combination frequency, 1 ns is about 2.86 TECU) [2].

Ionosphere Association Analysis Centers JPL, CODE, ESOC use different methods to estimate global ionospheric model, while satellites and receivers DCB as the by-product are estimated at the same time [3–6], but UPC uses a combination of ionospheric residual method to separate satellites DCB [7]. IGS daily release combined satellites DCB computed by the four IAACs using a weighted-mean method [8], its stabilities are better than 0.1 ns. Some domestic academics have done some research on the GPS DCB, and their study results are basically in line with each other [9, 10]. BeiDou Navigation Satellite System has completed the satellites constellation network in Asia-Pacific region, including 5 GEO + 5 IGSO + 4 MEO, and has provided positioning, navigation, timing services since 27 December 2012. Wuhan University has been building BDS continuous observation network named BeiDou Experimental Tracking Stations (BETS) since 2011, now, it includes about 20 tracking stations at home and abroad 20 [11]. Li Zishen proposed a "two-step method" to estimate BeiDou satellites DCB according to BeiDou tracking stations distribution, which overcame the impact of some satellites DCB instability effectively [12]. Wu Xiaoli, as the first academic to verify the BeiDou satellites DCB solving strategies using tri-frequency data, analyzes that the stabilities of BeiDou satellites DCB is slightly worse than the IGS satellites DCB, and the accuracy is better than 0.5 ns with the satellites constellation has only 4 satellites [13, 14].

Based on BETS dual-frequency observations in 2013, using a combination of ionospheric residual method, BeiDou satellites and BETS tracking station receivers DCB are estimated in this paper.

17.2 DCB Estimation Method

17.2.1 BDS Ionospheric Code Post-fit Residuals

BDS observations include carrier phase observations and pseudorange observations, and the three frequencies are B1 = 1,561.098 MHz, B2 = 1,207.14 MHz, B3 = 1,268.52 MHz. This paper only analyzes BeiDou satellites and receivers DCB at B1 and B2 frequencies.

BeiDou dual frequency pseudorange and carrier phase observation equations are expressed as:

$$P_{f,j}^{i} = R_{j}^{i} + c\delta_{j} - c\delta^{i} + I_{f,j}^{i} + d_{jtrop}^{i} + b_{f,j} + b_{f}^{i} + \varepsilon_{P,f,j}^{i} \tag{17.1}$$

$$L_{f,j}^{i} = R_{j}^{i} + c\delta_{j} - c\delta^{i} - I_{f,j}^{i} + d_{jtrop}^{i} - \lambda_{f}(d_{f,j}^{i} + N_{f,j}^{i}) + \varepsilon_{L,f,j}^{i} \tag{17.2}$$

where i is sequence number of satellites, j is number of stations, $f(=1,2)$ stands for frequency, R_j^i is the geometric distance between the station j and the satellite i, δ_j is clock bias for station j, δ^i is clock bias for satellite i, I_j^i is ionospheric delay, d_{jtrop}^i is tropospheric delay, $b_{f,j}$ is receiver pseudorange code hardware delays, $b^{f,i}$ is satellite pseudorange code hardware delays, $d_{f,j}^i$ is receiver and satellite carrier phase advance, $N_{f,j}^i$ is carrier phase integer ambiguity, $\varepsilon_{f,j}^i$ are measurement noise.

Difference the station and satellite observation equations at B1 and B2 frequencies, it will get a combination of ionospheric residual $P4, L4$, the combination equations are expressed as:

$$P_{4,j}^{i} = P_{1,j}^{i} - P_{2,j}^{i} = I_{1,j}^{i} - I_{2,j}^{i} + (DCB_j + DCB^{i}) \tag{17.3}$$

$$L_{4,j}^{i} = L_{1,j}^{i} - L_{2,j}^{i} = -(I_{1,j}^{i} - I_{2,j}^{i}) - (B1 - B2) \tag{17.4}$$

where DCB^i is satellite differential code bias, DCB_j is receiver differential code bias, $B_f = d_{f,j}^i + N_{f,j}^i$ is non-integer ambiguity at B1 and B2 frequencies.

As the pseudorange measurements have lager noise, and carrier phase measurements need to resolve ambiguity, usually carrier phase smoothed pseudorange measurements are used as data preprocessing strategies. Smoothed pseudorange measurements are expressed as:

$$P_{4,sm} = w_t P_4(t) + (1 - w_t) P_{4,ex}(t) \quad t > 1 \tag{17.5}$$

$$P_{4,ex}(t) = P_{4,sm}(t-1) + [L_4(t-1) - L_4(t)] \quad t > 1 \tag{17.6}$$

where t is epoch number, w_t is a weight factor related with t. Before pseudorange measurements are smoothed, cycle slip detection and gross errors elimination should be done. In this paper, M-W combination observations and ionospheric residual observations are used to detect cycle slip and remove gross errors.

Because of the impact of higher-order terms in ionosphere delay is very small, we only consider the first-order term, and the ionospheric delay is expressed as:

$$I_j^i = \frac{40.28}{f^2} STEC \tag{17.7}$$

Combine Eqs. (17.7) and (17.3), and take the smoothed pseudorange measurements $P_{4,sm}$ in place of P_4, the ionospheric residuals equations can be obtained as follows:

$$P_{4,sm} = F \cdot STEC + (DCB_j + DCB^i) \tag{17.8}$$

where $F = 40.28 \cdot (\frac{1}{f_1^2} - \frac{1}{f_2^2})$ stands for that the total electron content is converted to ionospheric delay in unit of m.

17.2.2 Regional Ionospheric TEC Modeling

In order to estimate more stable DCB, we need to get more accurate ionospheric delay. Global ionospheric model usually uses 15-order spherical harmonic function model, and regional ionospheric model usually uses polynomial model, generalized trigonometric series and the low-order spherical harmonic function model [15].

Ionosphere is mainly in the 60–1,000 km space from the earth's surface. To simplify the TEC estimation method, usually a Single Layer Model (SLM) is assumed, and the STEC is projected to VTEC. CODE currently uses an improved single model (MSLM), its projection function is:

$$VTEC = M(z) \cdot STEC \tag{17.9}$$

$$M(z) = \cos(\arcsin(\frac{R}{R+H}\sin(\alpha z))) \tag{17.10}$$

where z is satellite elevation angle, $R = 6{,}371$ km is radius of the earth, $H = 506.7$ km is the height of projection function, $\alpha = 0.9782$ is the coefficient factor.

This paper describes the ionospheric delay with spherical harmonic function model, the function is expressed as:

$$VTEC = E(\beta, s) = \sum_{n=0}^{n_{\max}} \sum_{m=0}^{n} \tilde{P}_{nm}(\sin\beta) \cdot (\tilde{C}_{nm}\cos(ms) + \tilde{S}_{nm}\sin(ms)) \tag{17.11}$$

CODE estimates spherical harmonic function model based on about 240–260 global stations, the model accuracy is generally 1–8 TECU, it is about 1.4 TECU in Europe, 2.3 TECU in China (Fig. 17.1). In this paper, spherical harmonic function model published by CODE is used to compute ionospheric TEC in China region.

17.2.3 DCB Estimation Strategy

Satellites and receivers DCB are influenced by temperature and pressure, for satellites, DCB are quite stable because of the temperature control, pressure control are very precise for the atomic frequency and standard signal generator,

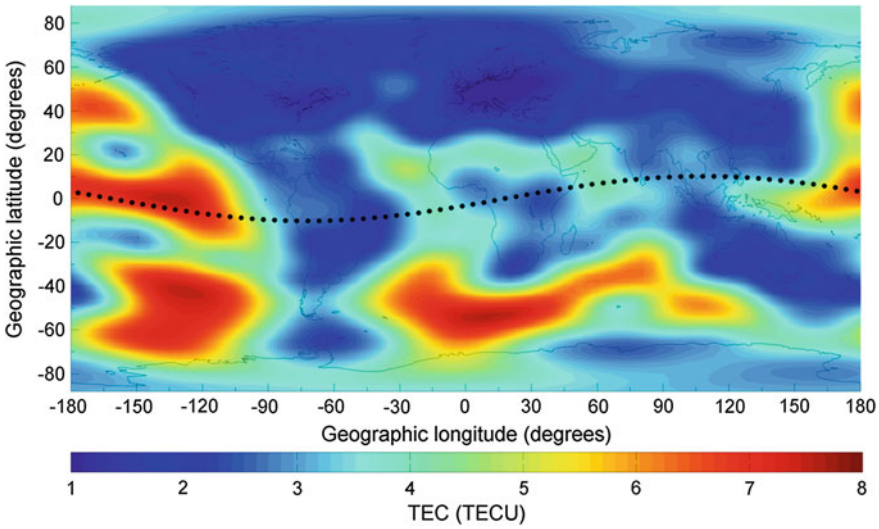

Fig. 17.1 Accuracy of CODE global ionospheric model

and for receivers, DCB are slightly worse, but the change in a day is very small. This paper assumes that satellites and receivers DCB are constants in a single day.

According to Eq. (17.8), make the difference between ionospheric residuals and ionospheric delays as pseudo observations in least square equations, there have the following equations:

$$\begin{cases} V = B \cdot X_{DCB} - L \\ X_{DCB} = [X^i_{DCB} \quad X_{j,DCB}] \\ L = P_{4,sm} - F \cdot STEC \end{cases} \tag{17.12}$$

where V are residuals, B is design matrix, X_{DCB} is the estimated parameters including satellites and receivers DCB.

In the absence of a priori satellite DCB or receiver DCB, the rank deficiency of design matrix is 1. Taking into account that the BDS have been providing officially services, this paper adopts the method that the sum of all the 14 BeiDou satellites DCB is 0, as follows:

$$\begin{cases} S \cdot X^i_{DCB} = 0 \\ \underset{1\times 14}{S} = [1, \ldots, 1] \end{cases} \tag{17.13}$$

According to the basic principle of least square with constrained conditions, we can get the following equations:

$$\begin{cases} X_{DCB} = [X^i_{DCB} \quad X_{j,DCB}] = (N_{BB} + S^T S)^{-1} W \\ D_{XX} = \sigma_0^2 \cdot (N_{BB} + S^T S)^{-1} \\ N_{BB} = B^T P B \\ W = B^T P L \\ \sigma_0^2 = \frac{V^T P V}{n - n^i - n_j} \\ P = \frac{\sigma^2}{(1/\sin e)^2} \end{cases} \tag{17.14}$$

where D_{XX} is the covariance matrix of satellites and receivers DCB, σ_0 is posteriori error, n is the observation numbers, n^i is BeiDou satellites number, n_j is stations number, P is weight related with satellite elevation angle.

17.3 Experiment and Result Analysis

This paper selects 14 stations (including 8 domestic stations, 6 foreign stations) in BETS in a whole year of 2013, BDS satellites and BETS tracking station receivers DCB are evaluated at B1 and B2 frequencies, BETS network stations and satellites constellation are shown in Fig. 17.2, BDS satellites types are shown in Table 17.1.

17.3.1 BDS Satellites DCB Analysis

BDS satellites DCB in year 2013 are shown in Fig. 17.3. There are 12 sub-figures standing for BDS satellites DCB time series from January, 2013 to December, 2013. As can be seen from the Fig. 17.3, generally, the stabilities of BDS satellites DCB are very stable, the magnitudes for 14 BDS satellites are −8–16 ns. From January to December, the variations are very small in a month, and the satellites DCB stabilities of last several months are slightly better than the first months. Because the constraints using that the sum of all BDS satellites DCB is 0, when the control system adjust a satellite attitude or internal status of a satellite is not stable, all the satellites will have jumps as a whole, such as 82nd, 101st, 123rd, 268th days, but the magnitudes are small.

BDS satellites DCB standard deviations are shown in Fig. 17.4. It can be seen from Fig. 17.4, in a whole year, 5 IGSO satellites DCB stabilities are the highest, 5 GEO satellites and 4 MEO satellites DCB stabilities are roughly equal, but C04 and C05 are slightly worse. IGSO satellites DCB are generally within 0.3 ns; MEO satellites DCB are generally within 0.5 ns; GEO satellite C01, C02, C03 are generally within 0.4 ns, C04 and C05 are about 0.5 ns, the largest value reaches 0.7 ns. Considering BDS satellites constellation in Fig. 17.2, it can be seen that, for C04, C05, C11, tracking stations in China region have very low satellites

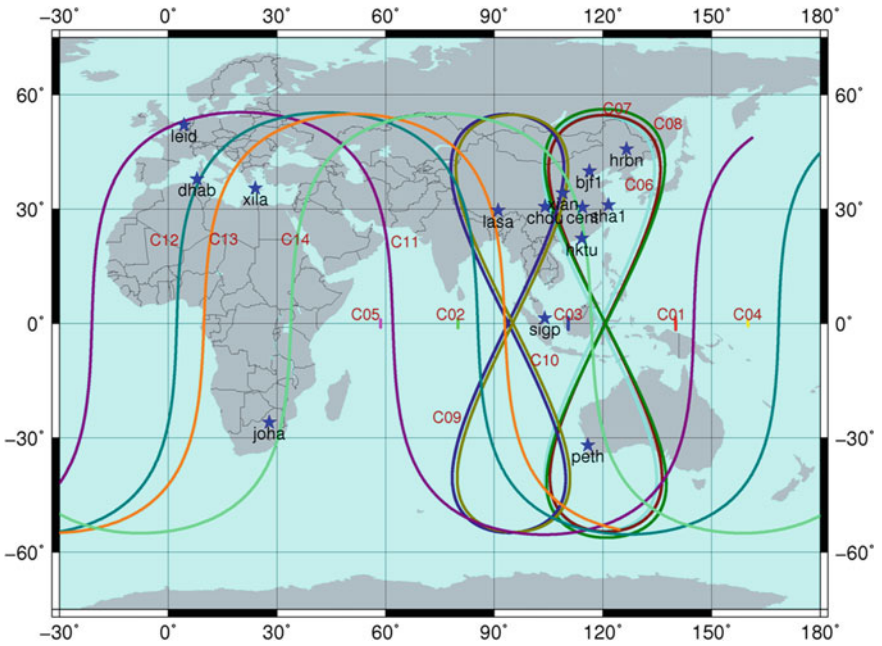

Fig. 17.2 BDS BETS network stations and satellites constellation

Table 17.1 BDS satellites types

PRN	Type	PRN	Type	PRN	Type
C01	GEO	C06	IGSO	C11	MEO
C02	GEO	C07	IGSO	C12	MEO
C03	GEO	C08	IGSO	C13	MEO
C04	GEO	C09	IGSO	C14	MEO
C05	GEO	C10	IGSO		

elevation angles, the observations have more errors like multipath errors, in a word, the satellites DCB have a strong influence with elevation angles.

17.3.2 BETS Tracking Station Receivers DCB Analysis

Figure 17.5 shows 14 tracking station receivers DCB in the BETS, all the receivers in the network are BDS/GPS dual-mode dual-frequency receivers made by Unicore Communications, Inc. It can be seen in Fig. 17.5 that, all receivers DCB are basically −5 to −25 ns, and their stabilities are good. The bjf1 station DCB has 3 big changes at 65th, 238th, 287th days; cent station DCB has big change at 84th

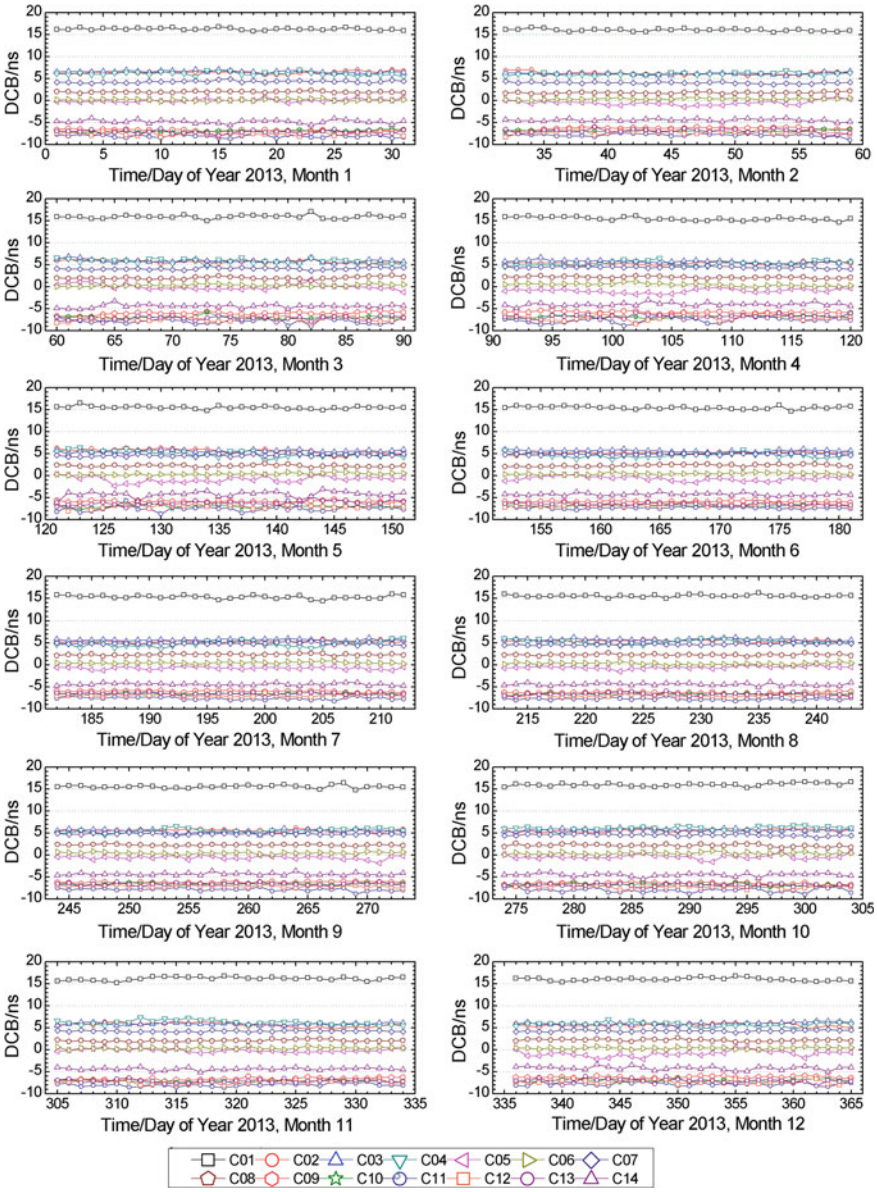

Fig. 17.3 BDS satellites DCB time series

day; xila station DCB becomes stable since 163rd day, but has big changes since December; hktu station DCB has big changes in 260th day, the probable reason is the replacement of receivers.

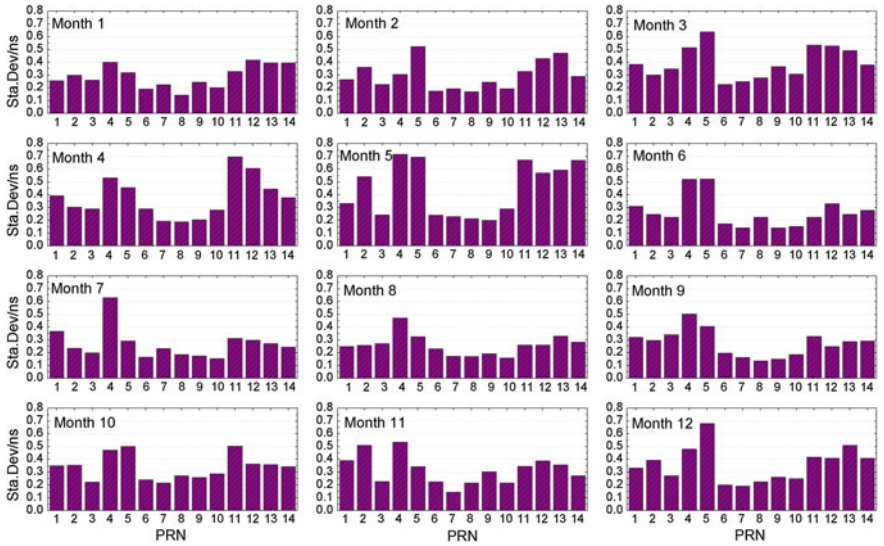

Fig. 17.4 BDS satellites DCB standard deviations

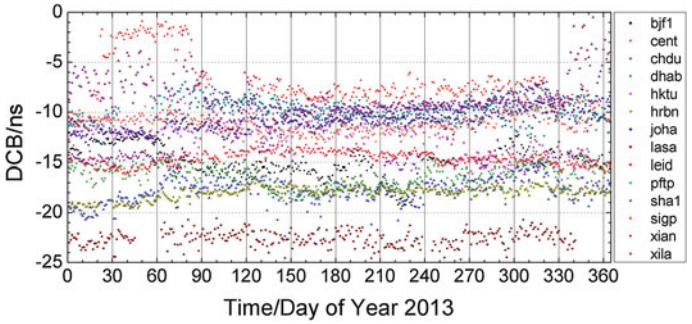

Fig. 17.5 BETS tracking station receivers DCB time series

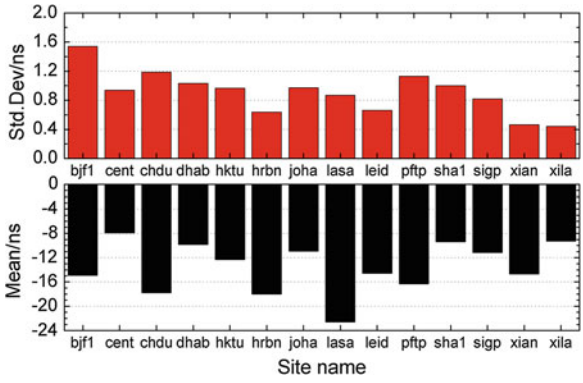

Fig. 17.6 Receivers DCB mean value and standard deviation

Figure 17.6 shows receivers DCB mean value and standard deviations, it can be seen from Fig. 17.6, BETS receivers DCB stabilities are better than 1.6 ns, the maximum value for receivers DCB is bjf1 station, about 1.54 ns.

17.4 Conclusion

Since BDS has not provided satellites DCB services, this paper based on BETS, using ionospheric residuals combination method, has evaluated BDS satellites and receivers DCB preliminarily. Researches show that, the magnitude for BDS satellites DCB are −8 to 16 ns at B1 and B2 frequencies, their stabilities are generally better than 0.5 ns, while, IGSO satellites DCB stabilities are the highest, followed by MEO satellites, GEO satellites have the worst stabilities, especially C04 and C05; the magnitude for BETS tracking station receivers are −5 to −25 ns, their stabilities are better than 1.6 ns. The experimental results have a good reference value for the analysis of single point positioning and creating more accurate ionospheric delay model.

Acknowledgments This work was partially sponsored by National Natural Science Foundation of China (Grant No. 41231174 and Grant No. 41204009), partially sponsored by National "863 Program" of China (Grant No. 2013AA122501), and partially sponsored by the "111 Project" of China (Grant No. B07037). The first author would like to thank Mr. Xiaotao Li for providing BDS data and Mr. G. Wang at Wuhan University for giving some advice. Thanks also go to the editor in chief and three anonymous reviewers for their valuable comments and improvements to this manuscript.

References

1. Ge M, Gendt G, Rothacher M et al (2008) Resolution of GPS carrier-phase ambiguities in precise point positioning (PPP) with daily observations. J Geodesy 82(7):389–399
2. Ciraolo L, Azpilicueta F, Brunini C et al (2007) Calibration errors on experimental slant total electron content (TEC) determined with GPS. J Geodesy 81(2):111–120
3. Komjathy A, Sparks L, Wilson BD et al (2005) Automated daily processing of more than 1000 ground-based GPS receivers for studying intense ionospheric storms. Radio Sci 40(6):RS6006
4. Mannucci AJ, Wilson BD, Yuan DN et al (1998) A global mapping technique for GPS-derived ionospheric total electron content measurements. Radio Sci 33(3):565–582
5. Schaer S (1999) Mapping and predicting the earth's ionosphere using the global positioning system. University of Berne, Berne
6. Feltens J, Dow JM (2006) Realized and planned improvements in ESA/ESOC ionosphere modelling. IGS Workshop, Darmstadt
7. Hernández-Pajares M, Juan JM, Sanz J et al (1998) Global observation of the ionospheric electronic response to solar events using ground and LEO GPS data. J Geophys Res Space Phys 103(A9):20789–20796
8. Hernández-Pajares M, Juan JM, Sanz J et al (2009) The IGS VTEC maps: a reliable source of ionospheric information since 1998. J Geodesy 83(3–4):263–275

9. Zhang HP (2006) Research on China area ionosphere monitoring and delay correction based on ground-based GPS. Shanghai astronomical observatory. Chinese Academy of Science, China
10. Jin R, Jin S, Feng G (2012) M_DCB: Matlab code for estimating GNSS satellite and receiver differential code biases. GPS Solutions 16(4):541–548
11. Shi C, Zhao QL, Li M et al (2012) Precise orbit determination of Beidou Satellites with precise positioning. Sci China Earth Sci 55(7):1079–1086
12. Li ZS, Yuan Y, Li H et al (2012) Two-step method for the determination of the differential code biases of COMPASS satellites. J Geodesy 86(11):1059–1076
13. Wu XL, Ping JS, Liu L et al (2011) Hardware delay resolution for regional satellites navigation system. Geomatics Inf Sci Wuhan Univ 36(10):1218–1221
14. Fan JC, Wu XL, Li YX et al (2013) COMPASS satellites DCB parameter accuracy assessment based on tri-frequency data. Chin Space Sci Technol 33(4):62–70
15. Yuan YB, Ou JK (2005) A generalized trigonometric series function model for determining ionospheric delay. Prog Nat Sci 15(8):1015–1019

Chapter 18
Initial Research on Comparison of PPP-Inferred GPS- and BDS-PWV in China Region

Wenwen Li, Min Li, Lizhong Qu, Xing Su and Qile Zhao

Abstract Due to the special constellation design with GEO, IGSO and MEO, the BeiDou System (BDS) now is available to provide a good coverage over the China region. This makes it possible to study the precipitable water vapor (PWV) inversion with only BeiDou observations using the precise point positioning (PPP) method. This paper selected 5 stations among the BETS (BeiDou Experiment Tracking Stations) network with GPS/BDS dual-mode dual-frequency data for the research. By the PPP approach, the zenith tropospheric delay (ZTD) was estimated at each station using only BDS or GPS observations respectively. And then the PWV was obtained by a conversion factor and the zenith wet delay retrieved from the estimated ZTD. The results show that due to the bias of 1–10 mm existing between the BDS- and GPS-derived ZTD, the inferred BDS-PWV and GPS-PWV is biased about 0.1–2 mm. And the final mean bias and STD of BDS- and GPS-PWV difference of all 5 stations is 0.78 and 1.73 mm. It is concluded that the PWV inferred from BDS can reach similar precision comparing to the GPS-PWV in the China region.

Keywords BeiDou system · Precipitable water vapor · GPS · Tropospheric delay · PANDA

18.1 Introduction

The precipitable water vapor (PWV) is the key parameter of the weather analysis and numerical weather prediction. Bevis [1] first proposed the method that retrieves the PWV from zenith tropospheric delay (ZTD) estimations using the precise

W. Li (✉)
School of Geodesy and Geomatics, Wuhan University, Wuhan 430079, China
e-mail: cheeselee@whu.edu.cn

W. Li · M. Li · L. Qu · X. Su · Q. Zhao
Research Center of GNSS, Wuhan University, 129 Luoyu Road, Wuhan 430079, China

J. Sun et al. (eds.), *China Satellite Navigation Conference (CSNC) 2014 Proceedings: Volume III*, Lecture Notes in Electrical Engineering 305,
DOI: 10.1007/978-3-642-54740-9_18,

positioning approach with ground-based GPS observations. And after that, a series of GPS meteorology experiments like GPS/STORM, WWAVE successfully proved that the feasibility of using GPS as a precise approach to obtain the PWV (GPS-PWV), as well as the ground-based GPS-PWV can reach as high precision as the radiosonde and water vapor radiometer [2, 3]. Now the precision of GPS-PWV can reach 1–2 mm, and it has already been widely used in the meteorology studies.

As one of the GNSS systems, the BeiDou system (BDS) now has 14 satellites (5GEO + 5IGSO + 4MEO) in service, and it was officially announced to provide operational positioning service over the Asia–Pacific region on Dec 27th 2012. Due to the special constellation design, BDS is available to provide a good coverage over the China region. This makes it possible to study the precipitable water vapor (PWV) inversion with only BeiDou observations using the precise point positioning (PPP) method.

The key point of the PWV inversion using ground-based GNSS observations is to estimate the ZTD precisely. Being able to get the absolute ZTD at each station, the PPP technique is widely adopted in the GPS meteorology research [4–6]. But the precision of the PPP-estimated ZTD is limited by the precision of the navigation satellite ephemeris and clock products, and also has a strong correlation with the positioning accuracy of the vertical component. The BeiDou Experiment Tracking Stations (BETS) network, which is constructed by Wuhan University, is able to provide tracking measurements of BDS satellites globally. On this basis, Wuhan University can provide the daily precise BDS satellites ephemeris and clock products. The studies of Shi et al. [8], Zhao et al. [7] and Qu et al. [9] showed that the precision of PPP using only BDS observations with these products can reach a similar precision as the GPS. Xu et al. [10] also computed the BDS satellites precision orbit and clock with the BETS observations. And he then estimated the ZTD by using 4-days' BDS or GPS observations respectively for comparison. Their results showed that ZTD derived from GPS and BDS agrees with each other with a bias and STD of about 2–3 and 5–6 mm, respectively.

In this paper, we selected 5 stations among the BETS network in the China region with BDS/GPS dual-mode dual-frequency observations. By using the IGS final GPS precise ephemeris and clock products and the Wuhan University precise BDS ephemeris and clock products, the ZTDs are estimated with only BDS or GPS observations respectively, and then used for the PWV inversion. On this basis, we analyzed the difference of the GPS-PWV and BDS-PWV. And the BDS-PWV precision is evaluated using the GPS-PWV as a reference.

18.2 Data and Method

18.2.1 Data

For the studies of BDS precision orbit determination and precise positioning, Wuhan University has been constructed the BETS network since 2011 on a global scale.

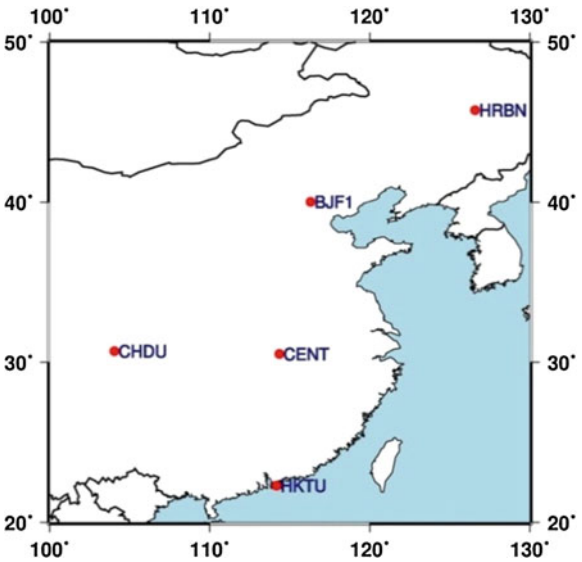

Fig. 18.1 Distribution of selected stations

Currently the total number of stations is 14. We selected 5 stations among the BETS network in the China region, as shown in Fig. 18.1. These stations are all equipped with the UNICORE receivers and can provide BDS/GPS dual-mode dual-frequency observations. The data from Aug. 11th to Sep. 12th in 2013 of these stations are processed using the PANDA (Positioning And Navigation Data Analyst) software.

The PPP technique needs the precise navigation satellite ephemeris and clock products to provide a steady and high accuracy spatial and time benchmark. IGS has been providing the GPS precision ephemeris and clock products since 2001. And now the precision of these products can be better than 5 cm. Wuhan University now provides the daily BDS precision ephemeris and clock products by using the BETS data. Zhao et al. [7] studied these precise products and claimed the precision of IGSO and MEO can now reach 10 cm in radial direction. In this paper we adopted the IGS final GPS ephemeris and clock products for GPS PPP processing, as well as the Wuhan University BDS ephemeris and clock products for BDS PPP processing.

18.2.2 PWV Inversion Using PPP Method

18.2.2.1 ZTD Estimation with PPP Approach

GNSS PPP technique uses the PC, LC observations to conduct the basis observation model, which allows elimination of the ionospheric delay, and still suffers error from receiver clock, the tropospheric delay, and multipath effects. The detail observation equation is:

$$\begin{aligned} P^j(i) &= \rho^j(i) + c\left(\delta t(i) - \delta T^j(i)\right) + ZTD(i) \cdot M\left(\theta^j(i), e^j(i)\right) + \varepsilon_p \\ \varphi^j(i) \cdot \lambda &= \rho^j(i) + c\left(\delta t(i) - \delta T^j(i)\right) + ZTD(i) \cdot M(e^j(i), \alpha^j(i)) + N^j(i) \cdot \lambda + \varepsilon_\varphi \\ ZTD &= ZHD + ZWD \end{aligned} \tag{18.1}$$

In (18.1), i is the epoch number, j is the satellite number. $P^j(i)$, $\varphi^j(i)$ are the PC, LC observations, λ is the ionospheric-free wave length. $\rho^j(i)$ is the geometry distance between the satellite and the station. $\delta t(i)$, $\delta T^j(i)$ are the clock errors of the receiver and the satellite respectively. $ZTD(i)$ is the ZTD including the zenith hydrostatic delay (ZHD) part and the zenith wet delay (ZWD) part. $M(e^j(i), \alpha^j(i))$ is the mapping function related to the satellite elevation angle $e^j(i)$ and azimuth angle $\alpha^j(i)$. $N^j(i)$ is the ionosphere-free ambiguity. $\varepsilon_p, \varepsilon_\varphi$ are the observation noise and the multipath effect of the PC, LC observations.

In the PPP processing, the station coordinates, the receiver clock error at every epoch and the ZTD are the parameters to be estimated. Since the ZHD usually can take over 90 % of the total ZTD and it changes slowly, it can be computed by the empirical model such as the Saastamoinen, Hopfield model with the ground meteorological data. However, the ZWD is affected seriously by the weather conditions, and can vary from cm to several-decimeter level. So it is always estimated using piecewise-constant or rand walk models. The above ZTD model is based on the isotropic atmosphere assumption, but when taking the effect of the anisotropic atmosphere into consideration, the gradients in the horizontal north-south and east-west directions also need to be estimated [4].

18.2.2.2 PWV Computation with ZWD

The ZWD can be retrieved from the PPP-inferred ZTD by subtracting the ZHD. The ZWD and PWV are in a simple linear relationship:

$$PWV = \Pi \cdot ZWD \tag{18.2}$$

In (18.2), Π is the conversion factor, which is a function of the weighted average atmospheric temperature. The detail equation of Π is:

$$\Pi = 10^6 \cdot \left[\rho_w R_v \left(\frac{k_3}{T_m} + k_3 - \frac{m_w}{m_d} k_1\right)\right]^{-1} \tag{18.3}$$

In (18.3), the $\rho_w$is the water density, $R_v$is the vapor gas constant, k_1, k_2, k_3 are three constants. m_w, m_d are the molar mass of dry air and water vapor respectively. Since high accuracy T_m computation needs the radiosonde profiles which are usually not available, most published studies to date adopt the suggestion that T_m is linearly related to surface temperature or use numerical weather models. In this paper, we used the global T_m grid model provided by the GGOS, which is in $2^\circ \times 2.5^\circ$ grid and update every 6 h. Yao et al. [11] showed that the precision of the

Table 18.1 GPS and BDS PPP processing strategy

	GPS PPP	BDS PPP
Observations	PC, LC	PC, LC
Elevation cutoff	7°	7°
Weighting strategy	Elevation dependent weight	Elevation dependent weight
Satellite orbit and clock	Fixed, IGS final ephemeris and clock products (300 s)	Fixed, Wuhan University precise ephemeris and clock products
Satellite antenna PCO and PCV	igs08.atx	Not considered
Receiver antenna PCO and PCV	Not considered	Not considered
Phase wind-up	Corrections applied	Corrections applied
Station displacement	Solid earth tide, ocean tide loading, pole tide	Solid earth tide, ocean tide loading, pole tide
	IERS 2003	IERS 2003
Station coordinates	Estimated	Estimated
Receiver clock error	Estimated as white noise	Estimated as white noise
ZTD	Saastamoinen + PWC	Saastamoinen + PWC
	Estimate ZTD every 2 h and gradients in horizontal north-south and east-west directions every day	Estimate ZTD every 2 h and gradients in horizontal north-south and east-west directions every day
Mapping function	GMF	GMF

T_m grid model can reach 2.2 K when compared to the T_m derived from radiosonde profiles. This can make the mean conversion error of the PWV less than 1 %.

18.3 Processing Strategy

We adopted the PANDA software for PPP processing. The detail processing strategy is described in Table 18.1.

The Saastamoinen model needs the surface meteorological data for ZHD computation, which is not provided by the BETS network stations. So in this paper we use the GPT model for the surface pressure and temperature at each station [12]. This will not affect the final BDS-PWV precision assessment due to the same model adopted for both BDS PPP and GPS PPP.

18.4 Experiment and Analysis

18.4.1 PPP Positioning and ZTD Estimations Comparison

Since the precision of ZTD estimations is strongly correlated with the vertical positioning precision, the positioning difference can indicate the ZTD estimation

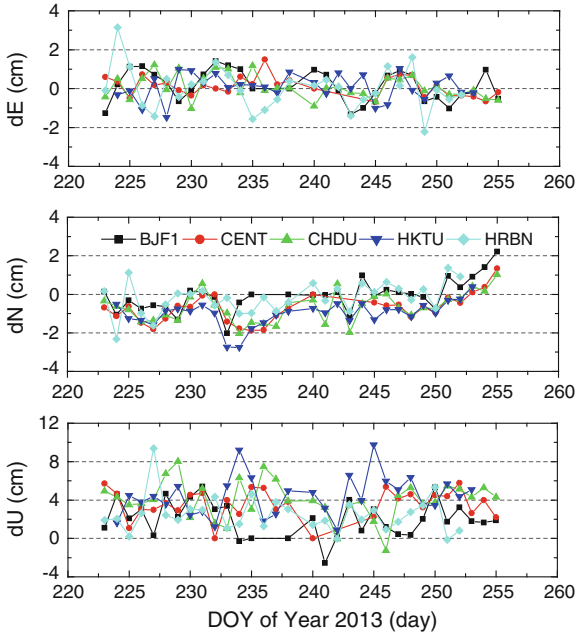

Fig. 18.2 BDS and GPS PPP positioning results comparison

difference. In Fig. 18.2, the GPS and BDS daily estimated coordinate difference of the 5 stations is compared. It is shown that the position difference of the horizontal component is very small, and mostly are under 1–2 cm. But the vertical difference can be as large as 10 cm, and suffers from an obvious bias of about 2–4 cm. This may be due to the fact that the precise ephemeris and clock products of BDS are less accurate than that of GPS.

The retrieved ZWD from the BDS or GPS estimated ZTD is also compared. In Fig. 18.3, the ZWD difference at site CHDU and HRBN is shown. It can be seen that the changing trends of the BDS- and GPS-derived ZWD agree with each other well, but there still exists some systematic errors. Table 18.2 shows the bias, STD (standard deviation) and RMS (root-mean-square) of the ZWD difference. The statistics results indicate that all the ZWD difference has some bias ranging from 1–10 mm, and absolute value of the bias increases while the latitude decreases. For the HKTU station, the bias reaches 11 mm at maxim, but for other selected stations the bias are all below 6 mm. The STD values are all about 10–20 mm. For overall mean statistics, the mean bias is about 4.8 mm and the mean STD 10.9 mm. Xu et al. [10] studied the ZWD difference of GPS and BDS using a local CORS network in Hebei Province, which is close the station BJF1 and HRBN. Their results indicate the mean bias of the GPS and BDS PPP-derived ZWD is about 2.8 mm with mean STD 4.8 mm. The bias at BJF1 and HRBN of this study is close that of Xu et al. [10], while the STD is rather higher. This may be because Xu explored the experiment on a shorter time scale of only 4-days.

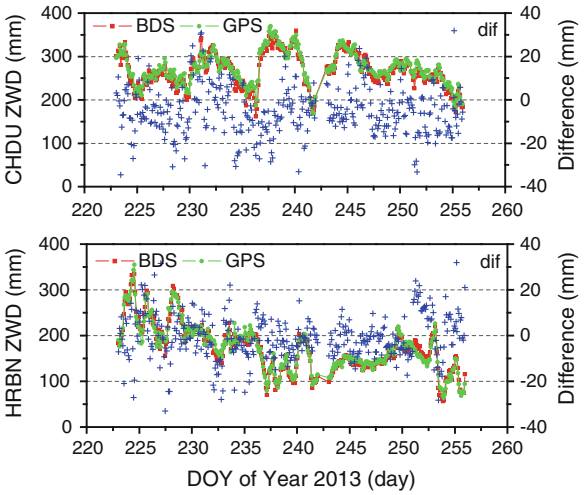

Fig. 18.3 ZWD comparison from BDS- and GPS-estimated ZTD at CHDU and HRBN station

Table 18.2 Statistics of the difference between BDS- and GPS-estimated ZWD

	Bias (mm)	STD (mm)	RMS (mm)
BJF1	−1.133	10.280	10.343
CENT	−5.524	9.778	11.231
CHDU	−5.463	11.294	12.546
HRBN	−0.776	9.578	9.610
HKTU	−11.412	13.659	17.800
Mean	−4.862	10.918	12.306

18.4.2 BDS- and GPS-PWV Comparisons

Using the retrieved ZWD and the conversion factor computed with the Tm model, the PWV can then be obtained. Figure 18.4 shows the BDS- and GPS-PWV and their difference at site CHDU and HRBN. It can be seen clearly that the BDS-PWV coincides well with the GPS-PWV with little difference. This is due to the fact that 6.4–6.5 mm ZWD difference causes only 1 mm PWV difference, and in Fig. 18.3 the maximum ZWD difference is about 40 mm. Table 18.3 is the correlation coefficient of the BDS- and GPS-PWV. And it can be seen all of the coefficients of the 5 stations are over 0.94, indicating the BDS- and GPS-PWV coincide with each other very well.

In Fig. 18.5, the bias, STD and RMS of the BDS- and GPS-PWV difference at all 5 selected stations are shown. The mean bias of the PWV difference is about 0.1–2 mm (expect HKTU, all other 4 stations has a bias less than 1 mm), this is caused by the bias in the BDS- and GPS-derived ZWD. The statistics shows the mean bias and STD of BDS- and GPS-PWV difference is about 0.78–1.73 mm. Since currently precision of GPS-PWV can reach 1–2 mm when compared to the radiosonde and other meteorological measurements, the BDS-PWV now can reach a similar precision in the China region.

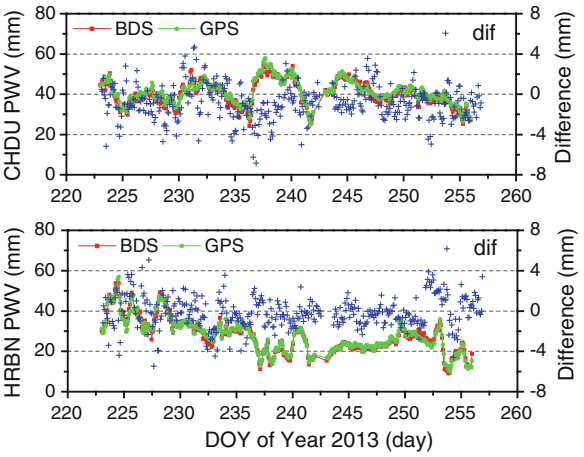

Fig. 18.4 BDS- and GPS-PWV comparison at CHDU and HRBN

Table 18.3 Correlation coefficient of BDS- and GPS-PWV of each station

	Correlation coefficient
BJF1	0.9911
CENT	0.9829
CHDU	0.9609
HKTU	0.9439
HRBN	0.9839

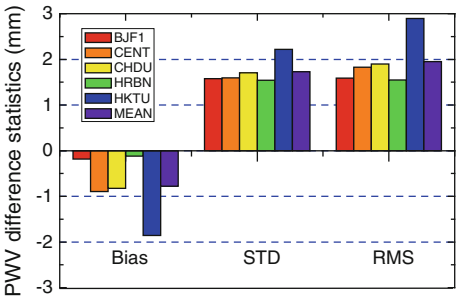

Fig. 18.5 BDS- and GPS-PWV difference statistics

18.5 Conclusions

This paper selected 5 stations from the BETS network in China region for research. About 33-day dual-frequency data are processed using the PPP approach for accurate ZTD estimations with only BDS or GPS data respectively. And by subtracting the ZHD from the BDS and GPS estimated ZTD, the BDS- and GPS-derived ZWD are obtained and used for PWV inversion. The research results indicate that the BDS and GPS derived ZWD suffers from a systematic bias of about 1–10 mm, which is varied with station latitude, while the STD of the ZWD

difference is about 10 mm. This causes a bias about 0.1–2 mm of the BDS- and GPS-PWV difference, with STD about 2 mm. The final mean bias and STD of BDS- and GPS-PWV difference is 0.78 and 1.73 mm. Since currently precision of GPS-PWV is about 1–2 mm, it is concluded that the BDS-PWV now can reach a similar precision with the GPS-PWV in the China region.

Acknowledgments This work was sponsored by the National Natural Science Foundation (Grant No.41204029, 41274049, 41325015) and the BeiDou Outstanding Youth Foundation (Grant No. CSNC2012-QY-1).

References

1. Bevis M, Businger S, Herring TA et al (1992) GPS meteorology: remote sensing of atmospheric water vapor using the global positioning system. J Geophys Res: Atmos (1984–2012) 97(D14):15787–15801
2. Businger S, Chiswell SR, Bevis M et al (1996) The promise of GPS in atmospheric monitoring. Bull Am Meteorol Soc 77(1):5–18
3. Tregoning P, Boers R, O'Brien D et al (1998) Accuracy of absolute precipitable water vapor estimates from GPS observations. J Geophys Res Atmos 103(D22):28701–28710. doi:10.1029/98jd02516
4. Ye S, Zhang S, Liu J (2008) Precision analysis of precise point positioning based tropospheric delay estimation. Geomatics Inf Sci Wuhan Univ 33(8):788–791
5. Chen Y, Liu Y, Wang X, Li P (2007) GPS real-time estimation of precipitable water vapor-Hong Kong experiences. Acta Geodaetica Cartogr Sin 36(1):9–12
6. Zhang X, He X, Guo B et al (2010) Near real time pw inversion based on zero-differenced GPS observation. Geomatics Inf Sci Wuhan Univ 35(7):806–810
7. Zhao Q, Guo J, Li M et al (2013) Initial results of precise orbit and clock determination for COMPASS navigation satellite system. J Geod, 1–12
8. Shi C, Zhao Q, Li M et al (2012) Precise orbit determination of BeiDou satellites with precise positioning. Sci Chin Earth Sci 55(7):1079–1086
9. Qu L, Zhao Q, Li M et al (2013) Precise point positioning using combined BeiDou and GPS observations. In: Proceedings of China satellite navigation conference (CSNC), pp 241–252
10. Xu A, Xu Z, Ge M et al (2013) Estimating zenith tropospheric delays from BeiDou navigation satellite system observations. Sensors 13(4):4514–4526
11. Yao YB, Zhang B, Yue SQ et al (2013) Global empirical model for mapping zenith wet delays onto precipitable water. J Geod, 1–10
12. Boehm J, Heinkelmann R, Schuh H (2007) Short note: a global model of pressure and temperature for geodetic applications. J Geod 81(10):679–683. doi:10.1007/s00190-007-0135-3

Chapter 19
Optimal Estimation for Inter-Satellite Observation Equipment Systematic Error

Guifen Tang, Weifen Yang, Bin Wu, Li Liu and Zhiqiao Chang

Abstract Inter-satellite link enables continuous observation when mobile satellite is not visible. However, whether we can get continuous clock error base on inter-satellite links is the key that inter-satellite links coming into practical. Thus, precision for inter-satellite observation equipment system error become the bottleneck for inter-satellite links showing their strengths. Paper gives integrated solver for inter-satellite observation equipment system error with redundant observation. To further enhance the inter-satellite equipment system solver poor accuracy, the paper analyzes relative motion between the satellite signal space for inter-satellite delay effects, and inter-satellite pseudo-range measurement error correction model were refined. Finally, we make experiment with simulation data to verify the validity and effectiveness for the proposed theories and methods.

Keywords Inter-satellite ranging · Systematic error · Time synchronization

19.1 Introduction

With the development of satellite navigation systems modernization, research-based inter-satellite link become a new hotspot in the realm of navigation [1–4]. Inter-satellite links realize continuous observation for mobile satellite, when they

G. Tang (✉) · L. Liu · Z. Chang
Beijing Satellite Navigation Center, Beijing 100094, China
e-mail: guifentang@nudt.edu.cn

W. Yang
Haidian Information Center, Beijing 100063, China

G. Tang · B. Wu
Shanghai Astronomical Observatory, The Chinese Academy of Sciences,
Shanghai 200030, China

J. Sun et al. (eds.), *China Satellite Navigation Conference (CSNC) 2014 Proceedings: Volume III*, Lecture Notes in Electrical Engineering 305,
DOI: 10.1007/978-3-642-54740-9_19,

are not visible. This provides more choices for high-precision time synchronization and precise orbit determination. However, due to inter-satellite observation technology is still in the experimental stage [2], is not mature, the current research on inter-satellite links are mostly still the method of data simulation [5], implementation technology, etc.

Inter-satellite observation technology brings unlimited reverie for more precise time synchronization. Based on the existing time than on experience, the pseudo-range two-way method can eliminate the most common errors, which has higher accuracy for time compare. Considering that there are redundancy observations for inter-satellite, it is tend use inter-satellite two-way method to implement inter-satellite time compare, which can be obtained higher accuracy for inter-satellite time compare.

In addition, similar to the satellite-ground time synchronization technology [6], in order to achieve inter-satellite two-way time compare, we need deduct inter-satellite equipment devices delay from the pseudo-observation In advance. If the value of equipment delay is wrong or changing, then the calculated clock errors inevitably affected by these systematic errors, which ultimately affect the inter-satellite time transfer accuracy. Systematic errors between inter-satellite equipment become an important factor restricting the precision time synchronization among the satellite. Its precision not only restricts the accuracy of misclosure between inter-satellite and satellite-ground, but also affected the clock difference consistency by the different inter-satellite topologies.

Due to the limited load-bearing capacity of the satellite, Navigation satellite does not been equipped with online calibration system for equipment devices delay. It is necessary to locate, separate and calculate systematic errors between inter-satellite observation equipment from the perspective of integrated data processing.

So, this paper studies the solver for systematic errors inter-satellite observation equipment the difference between star systems integrated distance measuring equipment problem.

In fact, inter-satellite observation equipment systematic error is more complex than traditional systematic errors between satellite-ground equipment, not only including inter-satellite systematic errors between devices, but also with systematic errors between satellite-ground equipment.

Firstly, this paper gives calculation model for systematic errors between inter-satellite observation equipment. We also analyzed each signal delay model. Because navigation satellites have high-speed relative motion, we found that the traditional satellite-ground signal spatial delay model does not apply to inter-satellite ranging signal. To achieve high-precision inter-satellite equipment systematic errors, we refine the delay model for inter-satellite ranging signal, and give the method for optimal estimation inter-satellite equipment systematic errors. Finally, we make Experiment with simulation data to verify the validity and effectiveness for the proposed theories and methods.

19.2 The Method for Calculating Inter-Satellite Equipment Systematic Errors

19.2.1 Calculation Model

For inter-satellite ranging, there is delay during the signal propagation, and each satellite in turn transmit the measurement signal, therefore, inter-satellite pseudo-range observations equation can be expressed as:

$$\begin{aligned}\rho_{BA}(T_0) =& \left|\vec{r}_A(T_0) - \vec{r}_B\left(T_0 - \frac{\rho'_{BA}}{c}\right)\right| \\ &+ \Delta t_A(T_0) - \Delta t_B\left(T_0 - \frac{\rho_{BA}}{c}\right) + \tau_{BA}^{others} + \tau_B^S + \tau_A^R\end{aligned} \tag{19.1}$$

$$\begin{aligned}\rho_{AB}(T_1) =& \left|\vec{r}_B(T_1) - \vec{r}_A\left(T_1 - \frac{\rho'_{AB}}{c}\right)\right| \\ &+ \Delta t_B(T_1) - \Delta t_A\left(T_1 - \frac{\rho_{AB}}{c}\right) + \tau_{AB}^{others} + \tau_A^S + \tau_B^R\end{aligned} \tag{19.2}$$

where $\rho_{BA}(T_0)$ is satellite A received pseudo-range from satellite B at time T0, $\rho_{AB}(T_1)$ is satellite B received pseudo-range from satellite A at time T1, $\Delta t_A(T_0)$ is clock error between satellite A with ground frequency at moments T0, $\Delta t_B(T_1)$ is clock error between satellite B with ground frequency at moments T1, τ_{BA}^{others} is the total signal propagation spatial delay on the path from satellite A to B, τ_{AB}^{others} is the total signal propagation spatial delay on the path from satellite B to A, which would be described in detail in the next section, $\tau_B^S,\ \tau_A^R,\ \tau_A^S,\ \tau_B^R$ is Satellite B send equipment delay, Satellite A receive equipment delay, Satellite A send equipment delay, Satellite B receive equipment delay respectively.

Using prediction ephemeris and clock errors, bi-directional pseudo-range can be imputed to time T0:

$$\begin{aligned}\rho'_{BA}(T_0) =& |\vec{r}_A(T_0) - \vec{r}_B(T_0)| + \Delta t_A(T_0) \\ &- \Delta t_B(T_0) + \tau_{BA}^{others} + \tau_B^S + \tau_A^R\end{aligned} \tag{19.3}$$

$$\begin{aligned}\rho_{BA}(T_0) =& |\vec{r}_B(T_0) - \vec{r}_A(T_0)| + \Delta t_B(T_0) \\ &- \Delta t_A(T_0) + \tau_{BA}^{others} + \tau_B^S + \tau_A^R\end{aligned} \tag{19.4}$$

Adding the above two equations, remove the satellite clock error, we can get:

$$\begin{aligned}\frac{\rho_{AB}(T_0) + \rho_{BA}(T_0)}{2} =& |\vec{r}_B(T_0) - \vec{r}_A(T_0)| + \frac{\left(\tau_{BA}^{others} + \tau_{AB}^{others}\right)}{2} \\ &+ \frac{\tau_B^S + \tau_A^R + \tau_A^S + \tau_B^R}{2}\end{aligned} \tag{19.5}$$

$$\tau_B^S + \tau_A^R + \tau_A^S + \tau_B^R = \rho_{AB}(T_0) + \rho_{BA}(T_0) - 2 \times |\vec{r}_B(T_0) - \vec{r}_A(T_0)| + \tau_{BA}^{others} + \tau_{AB}^{others} \tag{19.6}$$

19.2.2 Inter-Satellite Ranging Signal Spatial Delay Model Refinement

In general, the signal spatial delay correction items include: ionospheric corrections, tropospheric corrections, Sagnac effect correction, relativistic corrections, etc., the following discussion were spatial delay correction model for inter-satellite ranging signals.

First, the height of navigation satellites were more than 20,000 km, the tropospheric will not be affected for inter-satellite ranging, and secondly, due to the inter-satellite links usually high or ultra-high frequency signal, for two-way satellite time comparison the effect by ionosphere also can be ignored.

Therefore, the focus of inter-satellite ranging is the correction terms which are relative to satellite motion. Specifically in the relativistic effect and Sagnac effect correction, the following were described.

1. Relativistic effects corrections for inter-satellite pseudo-range ranging.

Relativistic effects, navigation system pseudo-range and carrier measurements are affected by the general and special relativity effects, according to the definition of the theory of relativity, relativistic effects will be extended to the inter-satellite links and can be correct for inter-satellite links for pseudo-range measurements. For Satellite *j,* frequency Deviation for satellite *i* is:

$$\Delta f = \frac{\mu}{c^2}\left(\frac{1}{r_j} - \frac{1}{r_i}\right) \cdot t_i + \frac{1}{2c^2}\left(v_j^2 - v_i^2\right) \cdot t_i \tag{19.7}$$

where, the first term effects is general relativity correct, the second term is special relativity effect correction. Further time deviation can be obtained:

$$\Delta t = \frac{\mu f_i}{c^2}\left(\frac{1}{r_j} - \frac{1}{r_i}\right) + \frac{f_i}{2c^2}\left(v_j^2 - v_i^2\right) \tag{19.8}$$

where $\mu = 3.98600436 \times 10^{14}\,\mathrm{m}^3/\mathrm{s}^2$ is earth's gravitational constant; r_i, r_j is pseudo-range observations from satellite i, j respectively, v_i, v_j is the speed for satellite i, j respectively, f_i is standstill frequency in Inertial coordinate system.

2. Sagnac effect for Inter-satellite pseudo-range corrections ranging

Sagnac effect is a rotating coordinate system of a particular phenomenon, refers to the direction opposite to the circumferential loop transfer beam there is a time difference, the rotation in the same direction of the light beam time longer than the

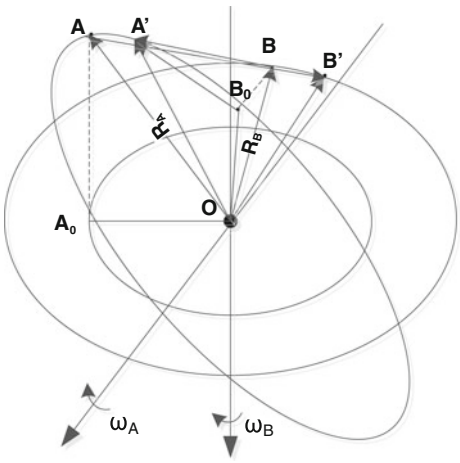

Fig. 19.1 Sagnace effect to inter-satellite link

opposite direction of the light beam passing time, the size of the loop area and rotational speed related.

When the time T has two satellites were located at positions A, B, and sends timing signals to each other under the control of the local clock, the rotation of the satellite around the earth, the signal arrival time at each satellite, the position of has changed, At this location A' (B'). So, the actual path of the signal propagation time scale is not $A \rightarrow B$ (or $B \rightarrow A'$), but $A \rightarrow B'$ or $B \rightarrow A'$. Then the transmission delay caused by the difference of these two pathways is Sagnac effect,which can be shown in Fig. 19.1.

According to the light propagation delay formulas for any two points, we can get Sagnac effect correction for any two points as follows:

$$\begin{aligned}
\Delta t_{A\rightarrow B} &= \frac{\overline{R}_{AB'} \cdot \overline{v}_{B'}}{c^2} \\
&= \frac{\left(\overline{R}_{B'} - \overline{R}_A\right) \cdot \left(\overline{\omega}_{B'} \times \overline{R}_{B'}\right)}{c^2} \\
&= \frac{\left(\overline{R}_{B'} \times \overline{R}_A\right) \cdot \overline{\omega}_{B'}}{c^2} \\
&= -\frac{2S_{\Delta AOB'}\left(\overline{n}_{RB'} \times \overline{R}_{RA}\right) \cdot \overline{\omega}_{B'}}{c^2} \\
&= -\frac{2S_{\Delta A_0OB'} \cdot \overline{\omega}_{B'}}{c^2}
\end{aligned} \tag{19.9}$$

where $S_{\Delta AOB'}$ is area of the triangle formed satellite A, geocentric and satellite B $\cdot$ $S_{\Delta A_0OB'}$ is $S_{\Delta AOB'}$'s projection surface in satellite B's orbit. $\overline{\omega}_{B'}$ is the satellite B's angular velocity around the earth, $\overline{v}_{B'}$ is the speed of satellite B stars in the Earth is rotating coordinate system, $\overline{R}_{B'}$ is the geometric distance from Satellite B to Geocentric, $\overline{R}_A$ is the geometric distance from Satellite A to Geocentric.

Similarly, we can get Sagnac effect of the signal path $B \rightarrow A'$:

$$\begin{aligned} \Delta t_{B\rightarrow A'} &= \frac{\overline{R}_{A'B} \cdot \overline{v}_{A'}}{c^2} \\ &= \frac{2S_{\Delta A'OB_0} \cdot \overline{\omega}_{A'}}{c^2} \end{aligned} \tag{19.10}$$

where $S_{\Delta A'OB_0}$ is $S_{\Delta A'OB}$'s projection surface in satellite A's orbit.

$$\Delta t_{Sagnac} = \frac{2S_{\Delta A_0OB'} \cdot \overline{\omega}_{B'}}{c^2} + \frac{2S_{\Delta A'OB_0} \cdot \overline{\omega}_{A'}}{c^2} \tag{19.11}$$

From the above equation if the two satellites in the same orbital plane, then the same angular velocity, is approximately equal to the projected area, when affected by the Sagnac effect is large relatively.

19.2.3 Optimal Estimation for Inter-Satellite Observation Equipment Systematic Errors

Using Eq. (19.5) as the observation equation, we can get the optimal estimation for inter-satellite observation equipment systematic errors. Let $X, L, A,$ can be respectively expressed by the following:

$$\begin{aligned} \underset{2m,1}{X} &= \begin{bmatrix} a_1 \\ a_2 \\ \vdots \\ a_m \\ b_1 \\ b_2 \\ \vdots \\ b_m \end{bmatrix}, \quad \underset{\frac{m(m-1)}{2},1}{L} = \begin{bmatrix} c_{12} \\ \vdots \\ c_{1m} \\ c_{23} \\ \vdots \\ c_{2m} \\ \vdots \\ c_{m-1,m} \end{bmatrix} \\ \underset{\frac{m(m-1)}{2},2m}{A} &= \begin{bmatrix} 1\,1\,0\,0\cdots\,0\,0_m\;1\,1\,0\,0\,\cdots 0\,0_m \\ 0\,1\,1\,0\,\cdots\,0\,0_m\;0\,1\,1\,0\,\cdots 0\,0_m \\ 0\,0\,1\,1\,\cdots\,0\,0_m\;0\,0\,1\,1\,\cdots\,0\,0_m \\ \cdots \\ 00\,0\,0\,\cdots\,1\,1_m\,0\,0\,0\,0\,\cdots\,1\,0_m \end{bmatrix} \end{aligned} \tag{19.12}$$

Table 19.1 Simulation of observations device delay

Satellite ID	Send delay (ns)	Receive delay (ns)
PRN13	2,453	5,683
PRN14	1,070	2,535
PRN25	5,320	706
PRN22	3,145	2,697

where

$$\begin{aligned} C_{ij} &= \tau_i^S + \tau_j^R + \tau_j^S + \tau_i^R \\ &= \rho_{ij} + \rho_{ji} - 2 \times \left|\vec{r}_j - \vec{r}_i\right| + \tau_{ij}^{others} + \tau_{ji}^{others} \end{aligned} \tag{19.13}$$

Let $V = AX - L$, So based on least squares estimation, we can get:

$$X = (A^T A)^{-1} A^T L \tag{19.14}$$

A solution must satisfy the following formula in the formula:

$$\frac{m(m-1)}{2} \geq 2m, \quad \text{that is } m \geq 5 \tag{19.15}$$

There are more than five satellites with inter-satellite links, that we can calculate inter-satellite observation equipment system error. If fixing a satellite receiver, transmitter delay, we need only 4 satellite observations with each other to get adjustment calculation. For the entire constellation and associated ground time synchronization system occurs, we choose the anchor observation equipment as a benchmark to calculate the constellation systematic error.

19.3 Experiments and Results Analysis

In order to verify the correctness and the effectiveness of method the proposed in this paper, we chose four GPS satellites simulation experiments. They are satellite PRN13, PRN14, PRN25 and PRN25 in the orbital plane I, and satellite PRN22 in the orbital plane II. Use IGS published ephemeris and clock errors precise simulation of approximately four hours between the satellites observed data, while among a group of simulated satellite observation equipment delay.

Table 19.1 shows the result of the observation equipment delay for the experiment, which is obtained by the method proposed by this paper. In the experiment we fix PRN13 as a benchmark, while its delay as known value. According the result, we know that the precision solver for inter-satellite equipment systematic error is better than 0.7 ns (Table 19.2).

In order to investigate the accuracy of the inter-satellite equipment systematic error, we calculate the inter-satellite clock errors with the calculated equipment

Table 19.2 The result of observation equipment delay

Satellite ID	Send delay (ns)	The error of send delay (ns)	Receive delay (ns)	The error of receive delay (ns)
PRN13	2,453	–	5,683	–
PRN14	1,070.64	0.64	2,534.92	0.08
PRN25	5,320.40	0.4	7,05.97	0.03
PRN22	3,144.94	0.06	2,697.26	0.26

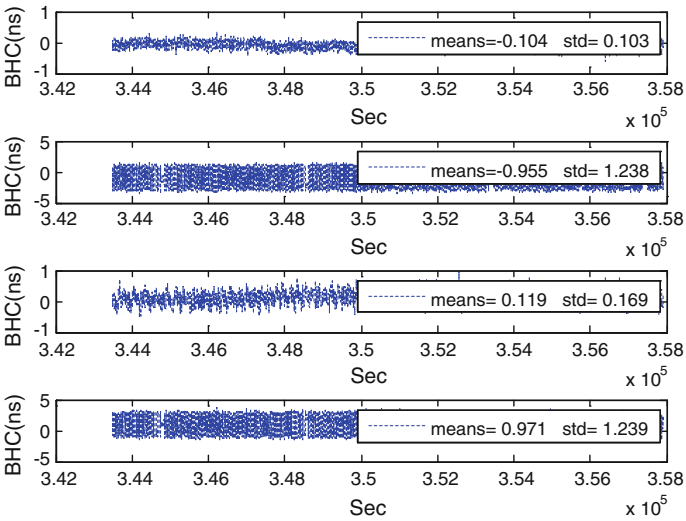

Fig. 19.2 Misclosure for any three satellite clocks

delay. We also calculate misclosure for any three satellite clocks shown in Fig. 19.2. Experiment results show that the solution method for inter-satellite equipment delay proposed in this paper has the accuracy of better than 1 ns.

19.4 Conclusion

This paper gives an integrated method using redundancy inter-satellite ranging observation for calculating inter-satellite equipment systematic error. In order to further enhance the inter-satellite equipment systematic error accuracy, this paper analyzes the effect to the spatial signal delay causing by satellite high-speed relative motion, and refine correction model for inter-satellite ranging. Finally, To test the method proposed by this paper, this paper use IGS precise ephemeris and clock error parameters simulating inter-satellite ranging data, and calculate systematic error for inter-satellite observation devise. The result shows that systematic error accuracy calculating by the proposed method can be better than 1 ns.

References

1. Shuai P, Qu G (2005) Time synchronization techniques of the autonomous navigation of navigation constellation. Trans Space Navig 26(6):768–772
2. Song XY, Jiax X, Mao Y (2009) Two steps time synchronizing method for auto-navigation with crosslink ranging measurement. Geomatics Inf Sci Wuhan Univ, 1297–1300
3. Huang F, Lu X, Wu H, Bian Y (2010) An algorithm of dynamic two way time transfer based on inter-satellite range variation. Geomatics Inf Sci Wuhan Univ, 13–16
4. Zhu J (2011) Research on orbit determination and time synchronizing of navigation satellite based on crosslinks. HuNan Changsha National University of Defense Technology
5. Zhu J, Wen Y, Chen Z et al (2008) Research on modeling and simulation of semi-autonomous orbit determination for satellite navigation constellation. 2008 Asia simulation conference-7th international conference on System Simulation and Scientific Computing, Beijing
6. Liu X (2008) Study on high precision time synchronization method in satellite navigation and positioning system. PLA Information Engineering University, HeNan Zhengzhou

Chapter 20
Compass RDSS Positioning Accuracy Analysis

Rui Guo, Ranran Su, Li Liu, Guangming Hu and Zhiqiao Chang

Abstract The RDSS service is an important component in the Compass system, which is accomplished by the GEO satellites with the restriction of known elevation. The RDSS observation model was deduced, and the positioning model was given with the elevation restriction. RDSS positioning tests were implemented with real observation data, the results were as follows: (1) the PDOP value was improved greatly to 1.5, with elevation restriction; (2) the RDSS observation noise is about 0.6 ns, which was greater than the pseudoranging and phase ranging in the RNSS; (3) the horizontal accuracy could reach 4.6 m in the Beijing region; (4) the main factors influenced the positioning accuracy include the elevation error, the time delay of both satellites and ground equipment, therefore in order to realize 10 m horizontal position accuracy, the elevation error should be less than 10 m, and the equipment time delay should be less than 10 ns.

Keywords GEO · RDSS · Positioning · Elevation · Equipment time delay

20.1 Introduction

With the vigorous development of the satellite navigation system, GPS and GLONASS the two global system have been built, China and the European Union launched the global satellite navigation plan. GPS, GLONASS, Galileo and Beidou (Compass) have become the world's four largest satellite navigation system, which have attracted the attention of the world [1–3]. They are both in their own independent system to strengthen its national security and economic security, and providing services to its compatibility and publicity to all over the world civil

R. Guo (✉) · R. Su · L. Liu · G. Hu · Z. Chang
Beijing Satellite Navigation Center, Beijing 100094, China
e-mail: guorui@shao.ac.cn

J. Sun et al. (eds.), *China Satellite Navigation Conference (CSNC) 2014 Proceedings: Volume III*, Lecture Notes in Electrical Engineering 305,
DOI: 10.1007/978-3-642-54740-9_20,

market, meeting the people's increasing positioning, navigation, timing and other requirements.

Radio determination satellite service (RDSS) is an important component of the Compass satellite navigation system and the characteristic. The positioning principle is completed by the ground control system, with users' location determination and calculation in the ground control system [4].

The scholars at home and abroad has carried out many related research work on RDSS, mainly including RDSS positioning algorithm, signal design, generalized RDSS design and expansion, RDSS and SINS integrated navigation and so on. A series of achievements have been made, which has enriched the connotation of satellite navigation system. But the results were mainly based on simulation and theory analysis, there was no systematic analysis and demonstration of the quantitative analysis of RDSS service performance based on real observation data [5–11].

This tests and analysis were carried out based on the traditional RDSS service in this paper. The Compass RDSS positioning model was deduced with the restriction of elevation. Tests were implemented using the user real observation data in the Beijing region. The RDSS observation noise was evaluated. The HDOP characteristics was analysed according to the COMPASS satellite constellation. The RDSS user positioning accuracy was tested and analysed, which was considered as being correlated with the equipment time delay error and the elevation error. Several beneficial conclusions were gained.

20.2 Mathematic Model

The RDSS service is an active positioning mode, with a 4-way ranging observation. Firstly the center station transmits C-band out-station uplink signals, which are transferred to S-band downlink signals by the GEO satellite, each GEO satellite with two beam signals. Secondly the RDSS user responses one beam signal according to its position and signal intensity, and transmits the L-band uplink signal to several GEO satellites, which is transferred to C-band downlink signal. Finally the center station responses all the C-band downlink signals to accomplish the 4-way ranging and to process the user position [12, 13] (Fig. 20.1).

The RDSS observation model is as follows:

$$\begin{aligned}\rho &= \rho_{Out\_C} + \rho_{Out\_S} + \rho_{In\_L} + \rho_{In\_C} \\ &= R_{OutC} + \Delta D_{OutCTrop} + \Delta D_{OutCIono} + \Delta D_{OutCSagnac} + \Delta D_{OutCRel} + \Delta D_{OutCAnt} \\ &\quad + R_{OutS} + \Delta D_{OutSTrop} + \Delta D_{OutSIono} + \Delta D_{OutSSagnac} + \Delta D_{OutSRel} + \Delta D_{OutSAnt} + c \cdot \tau_{Out} \\ &\quad + R_{InL} + \Delta D_{InLTrop} + \Delta D_{InLIono} + \Delta D_{InLSagnac} + \Delta D_{InLRel} + \Delta D_{InLAnt} \\ &\quad + R_{InC} + \Delta D_{InCTrop} + \Delta D_{InCIono} + \Delta D_{InCSagnac} + \Delta D_{InCRel} + \Delta D_{InCAnt} + c \cdot \tau_{In} + \varepsilon\end{aligned} \tag{20.1}$$

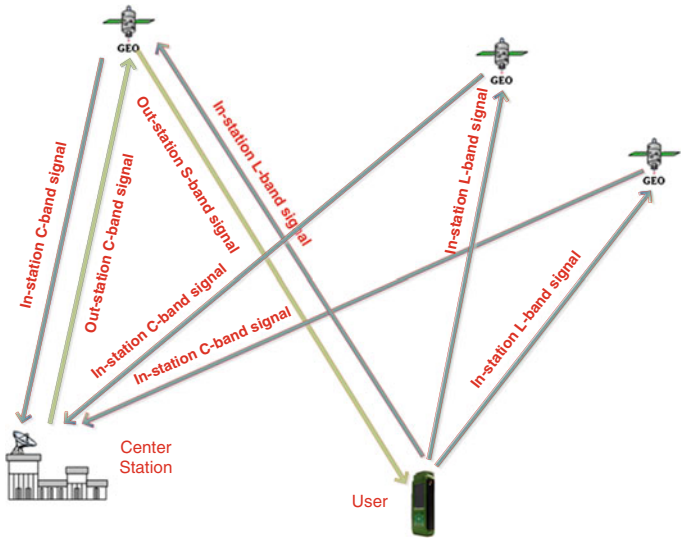

Fig. 20.1 RDSS positioning sketch map

R_* is the geometric range between the satellite and the ground (the center station or the user). ΔD_{*Trop} and ΔD_{*Iono} are the troposphere and ionosphere delay. $\Delta D_{*Sagnac}$ is the sagnac effect. ΔD_{*CRel} is the general relativistic correction. ΔD_{*Ant} is the antenna phase center correction (the satellite or the station). ε is the observation noise.

τ_{Out} is the equipment time delay of out-station link, including the center-station transmit time delay and satellite out-station transfer time delay.

τ_{In} is the equipment time delay of in-station link, including the user transmit time delay, the satellite in-station transfer time delay and the center station receive time delay.

For the troposphere delay, we could introduce the experiential GPT model, because the center station could not the user atmospheric parameters. For the ionosphere delay, we could correct it with the Klobuchar 8 parameters or 14 parameters models.

In the observation course, the center station could calculate the pseudorange signal out-station time according the user response frame ID. Therefore the ρ_{Out_C} and ρ_{In_C} observations could be calculated by satellite aberration iteration. The observation could be deduced as follows:

$$\begin{cases} \rho' = \rho - \rho_{Out\_C} - \rho_{In\_C} \\ \rho' = \rho_{Out\_S} + \rho_{In\_L} = R_{OutS} + R_{InL} + \Delta D \\ \Delta D = \Delta D_{OutSTrop} + \Delta D_{OutSIono} + \Delta D_{OutSSagnac} + \Delta D_{OutSRel} + \Delta D_{OutSAnt} \\ \qquad + \Delta D_{InLTrop} + \Delta D_{InLIono} + \Delta D_{InLSagnac} + \Delta D_{InLRel} + \Delta D_{InLAnt} \end{cases} \tag{20.2}$$

In the Eq. (20.2), the user position parameters are included in both the R_{OutS} and R_{InL} parameters. If the visual satellites m are greater than 2, the position parameters could be estimated with the elevation restriction. We implement the linearization in Eq. (20.2), the error equation is as follows:

$$\begin{cases} V_1 = (\dfrac{X_{OutSat} - X_0}{\rho_{OutSat0}} + \dfrac{X_{InSat1} - X_0}{\rho_{InSat10}})dX + (\dfrac{Y_{OutSat} - Y_0}{\rho_{OutSat0}} + \dfrac{Y_{InSat1} - Y_0}{\rho_{InSat10}})dY \\ \quad + (\dfrac{Z_{OutSat} - Z_0}{\rho_{OutSat0}} + \dfrac{Z_{InSat1} - Z_0}{\rho_{InSat10}})dZ + (\rho_1{}' - \rho_{OutSat0} - \rho_{InSat10} - \Delta D_{10}) \\ V_2 = (\dfrac{X_{OutSat} - X_0}{\rho_{OutSat0}} + \dfrac{X_{InSat2} - X_0}{\rho_{InSat20}})dX + (\dfrac{Y_{OutSat} - Y_0}{\rho_{OutSat0}} + \dfrac{Y_{InSat2} - Y_0}{\rho_{InSat20}})dY \\ \quad + (\dfrac{Z_{OutSat} - Z_0}{\rho_{OutSat0}} + \dfrac{Z_{InSat2} - Z_0}{\rho_{InSat20}})dZ + (\rho_2{}' - \rho_{OutSat0} - \rho_{InSat20} - \Delta D_{20}) \\ \quad \cdots\cdots\cdots\cdots\cdots\cdots\cdots\cdots\cdots\cdots\cdots\cdots\cdots\cdots \\ V_m = (\dfrac{X_{OutSat} - X_0}{\rho_{OutSat0}} + \dfrac{X_{InSatm} - X_0}{\rho_{InSatm0}})dX + (\dfrac{Y_{OutSat} - Y_0}{\rho_{OutSat0}} + \dfrac{Y_{InSatm} - Y_0}{\rho_{InSatm0}})dY \\ \quad + (\dfrac{Z_{OutSat} - Z_0}{\rho_{OutSat0}} + \dfrac{Z_{InSatm} - Z_0}{\rho_{InSatm0}})dZ + (\rho_2{}' - \rho_{OutSat0} - \rho_{InSatm0} - \Delta D_{m0}) \end{cases} \tag{20.3}$$

$[X_{OutSat}, Y_{OutSat}, Z_{OutSat}]$ is the out-station satellite position, and $[X_{InSatm}, Y_{InSatm}, Z_{InSatm}]$ is the in-station satellite position. $[X_0, Y_0, Z_0]$ is the user approximate position. $\rho_{OutSat\,0}$ is the approximate range between out-station satellite and the user. $\rho_{InSatm\,0}$ is the approximate range between in-station satellite and the user. $[dX, dY, dZ]$ is the user position parameter correction.

As the GEO satellites are located in the equator, the satellite geometry is very poor for the ground users. Especially for the 2 GEO satellites, the ground elevation data base is needed to process user position parameters. The error equation should be added a new observation, which is showed in Eq. (20.4) with φ and λ are user latitude and longitude respectively.

The user position parameters could be calculated with the least square method, and the navigation and positioning could be accomplished.

$$V_{m+1} = \cos(\varphi) * cos(\lambda) * dX + \cos(\varphi) * sin(\lambda)dY + \sin(\varphi) * dZ \tag{20.4}$$

20.3 Tests and Analysis

The RDSS positioning tests were implemented using the RDSS user observation in the region from August 17 to August 18 in 2013. The ranging error and HDOP were analysed. The positioning error characteristic was analysed based on different error sources.

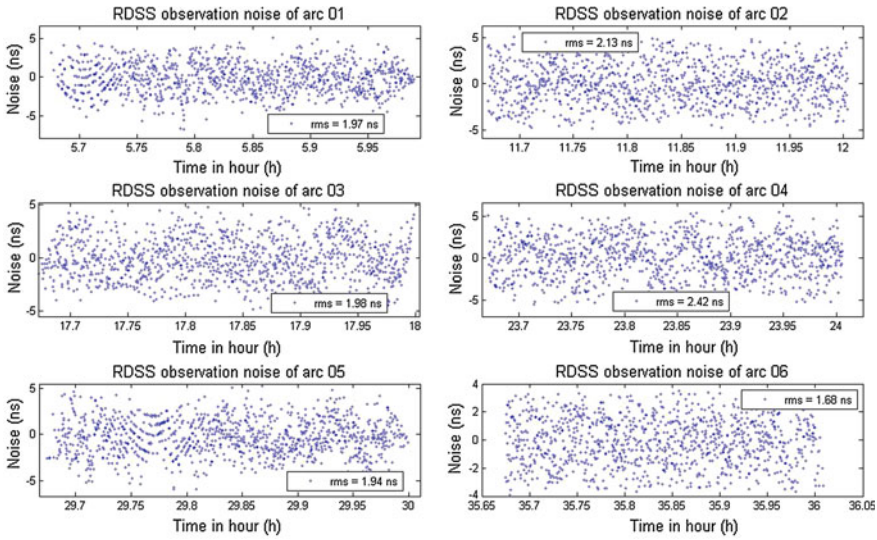

Fig. 20.2 RDSS ranging noise

Table 20.1 RDSS ranging noise (ns)

Arc-1	Arc-2	Arc-3	Arc-4	Arc-5	Arc-6	Mean
1.97	2.13	1.98	2.42	1.94	1.68	2.02

20.3.1 Ranging Error

The ranging accuracy is an important guarantee for navigation and positioning. RDSS is the four-way ranging mode. The measured data were acquired from August 17 to August 18 in 2013, we used 6 20-min observing data to analyse the ranging error, with a high order polynomial to fit the ranging data. We removed the trend in the data with the polynomial, and counted the fitting residual of each period (Fig. 20.2, Table 20.1).

Results showed that, the average fitting RMS 6 time period was about 2 ns, about 0.6 m, the measurement accuracy was obviously poorer than RNSS positioning in the pseudorange and phase measurement accuracy.

20.3.2 HDOP

The Compass navigation system contains 5 GEO satellites, at least 2 GEO satellites were needed to achieve positioning navigation and positioning, with the elevation restriction. The HDOP value was showed and analysed in the Beijing region with different satellites number (Table 20.2).

Table 20.2 RDSS users' HDOP in the Beijing region

SatNum = 2		SatNum = 3		SatNum = 4	
Satellite combination	HDOP	Satellite combination	HDOP	Satellite combination	HDOP
(01,02)	1.825	(01,02,03)	1.780	(01,02,03,04)	1.593
(01,03)	2.374	(01,02,04)	1.672	(01,02,03,05)	1.541
(01,04)	3.428	(01,02,05)	1.641	(01,02,04,05)	1.627
(01,05)	1.782	(01,03,04)	1.850	(01,03,04,05)	1.604
–	–	(01,03,05)	1.729	Mean	1.591
–	–	(01,04,05)	1.671	SatNum = 5	HDOP
Mean	2.352	Mean	1.724	Mean	1.522

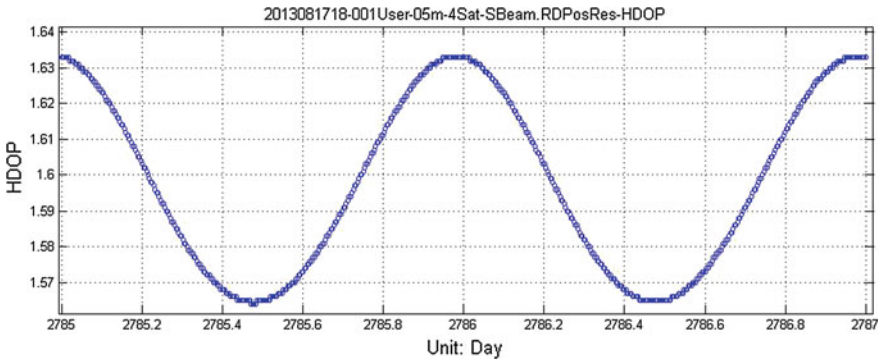

Fig. 20.3 RDSS users' HDOP in the Beijing region (4 GEO)

The above results showed that, with 2 satellites, 3 satellites, 4 satellites and 5 satellites, the average HDOP were respectively 2.352, 1.724, 1.591 and 1.522. If the satellite number increased to 3, the HDOP value was greatly improved. If the satellite number increased to 4 and 5, the HDOP value was improved limitedly, which could improve the system availability, and reduce the risk of positioning accuracy deterioration with satellites faults.

20.3.3 Effect of Elevation Errors

In the RDSS positioning mode, the elevation error would affect the positioning accuracy, because the accuracy of the elevation database was limited. In this positioning test, the user coordinates was known, we tested the positioning errors with different elevation errors, in order to analyse the error characteristic (Figs. 20.3, 20.4, Table 20.3).

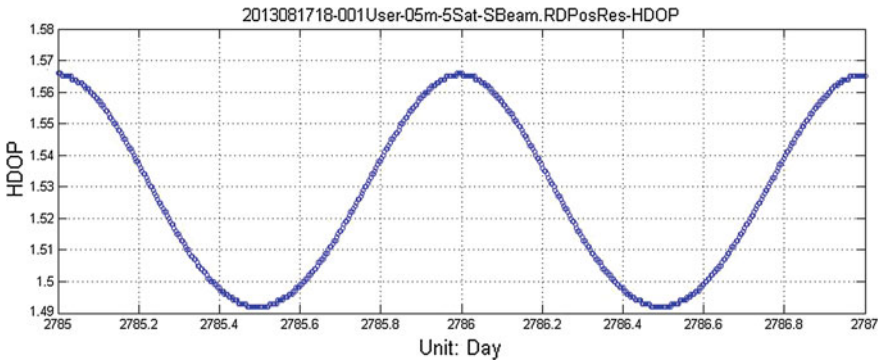

Fig. 20.4 RDSS users' HDOP in the Beijing region (5 GEO)

Table 20.3 Effect of elevation errors on RDSS user positioning accuracy (Unit: m)

Elevation error (m)	East–West error (m)	North–South error (m)	Horizontal error (m)
5	4.118	2.196	4.667
6	3.840	2.876	4.797
7	3.573	3.633	5.096
8	3.322	4.428	5.535
9	3.088	5.243	6.085
10	2.877	6.071	6.718
11	2.693	6.907	7.413
12	2.543	7.748	8.155
13	2.434	8.593	8.931
14	2.370	9.440	9.733
15	2.355	10.29	10.556

Results showed that if the elevation error was 5 m, the RDSS horizontal accuracy was about 4.7 m. If the elevation error reached 10 and 15 m, the horizontal errors were about 7 and 10 m respectively.

The 1-day periodic position errors were visible in Fig. 20.5, which were induced by the GEO satellites orbit errors with the coherent variety period.

20.3.4 Effect of Time Delay Errors

In the RDSS positioning mode, the time delay errors were an key factor to affect the users' positioning accuracy. The time delays included the center-station transmit time delay, the satellite out-station transfer time delay, the user transmit time delay, the satellite in-station transfer time delay and the center-station receive time delay.

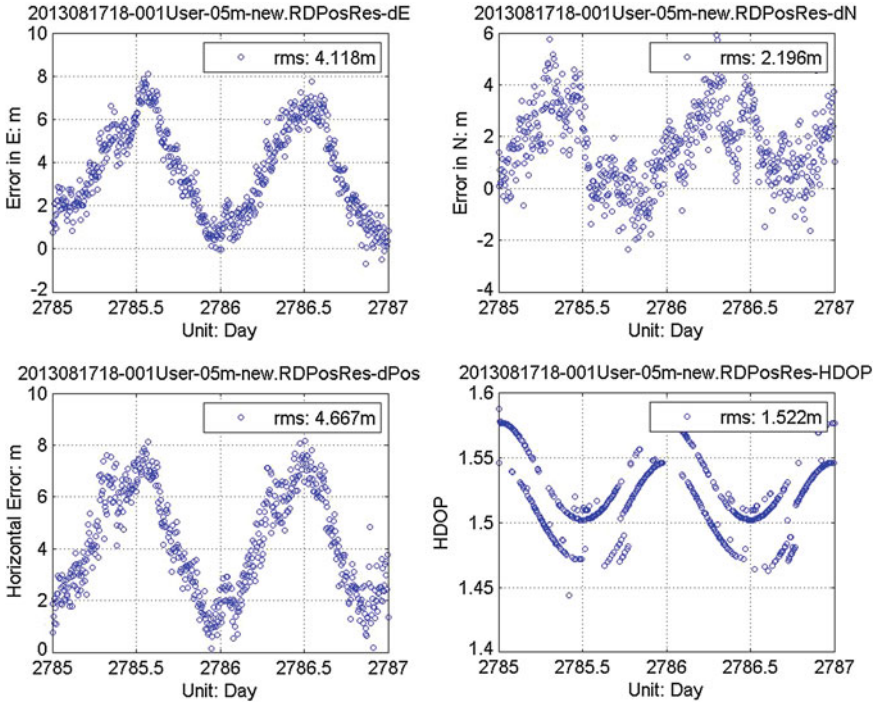

Fig. 20.5 Effect of 5 m elevation error on RDSS user positioning accuracy

Table 20.4 Effect of time delay errors on RDSS user positioning accuracy

Time delay errors (ns)	East–West error (m)	North–South error (m)	Horizontal error (m)
0	4.118	2.196	4.667
3	4.528	1.827	4.882
6	4.966	1.592	5.215
9	5.414	1.537	5.628
12	5.869	1.680	6.105

The time delays were variant. In order to analyse the effect on positioning accuracy, we only consider the comprehensive time delay. Tests were also carried out with the RDSS observation data in the Beijing region, and 5 m elevation was introduced in the positioning process in order to be realistic with real environment (Table 20.4).

Results above showed that the positioning accuracy could reach 4.667 m with the time delay given by the factory. If the time delays reached 3, 6, 9 and 12 ns, the users' positioning horizontal error could reach 6–7 m. Therefore in order to accomplish 10 m horizontal accuracy, the time delay error should be restricted with 10 ns.

20.4 Conclusions

The RDSS observation model was deduced in this paper. And the positioning algorithm was also given with the restriction of known elevation. The tests and analysis were carried out with real RDSS observation data in the Beijing region. Results were as follows:

1. The average RDSS ranging noise was about 2 ns (0.6 m), which was poorer than the pseudoranging and phase observation accuracy.
2. With the restriction of known elevation, the HDOP could reach 2.3 with 2 GEO satellites, which could be improved greatly and reached 1.7 with 3 GEO satellites. If the GEO satellites was 4 or 5, the HDOP could reach 1.5, the navigation availability could be improved obviously, which could reduce the position accuracy deterioration with the single satellite abnormity.
3. The RDSS horizontal positioning accuracy was about 4.7 m in the Beijing region, with the support of 5 GEO satellites.
4. The RDSS positioning accuracy was restricted by the elevation errors and time delay errors. In order to realize 10 m horizontal position accuracy, the elevation error should be less than 10 m, and the equipment time delay should be less than 10 ns.

Acknowledgments Supported by the National Natural Science Foundation Project (2013, 41204022) and the 863 program of Science and Technology Department (2013AA122402), and the 5th Chinese postdoctoral science fund special projects.

References

1. Robert MA (1989) Radio determination satellite services and standards. The National Defense Industry Press, Beijing
2. Tan S (2007) Engineering for satellite navigation position. The National Defense Industry Press, Beijing, pp 26–32
3. Tan S (2009) Theory and application of comprehensive RDSS Position and report. Acta Geodaeticaet Cartographica Sinica 38(1):1–5
4. Wen R, Liu Z, Ge X et al (2010) Analysis of S Band RDSS service global extension. Telecommun Eng 50(6):121–124
5. Xing N, Su R, Zhou J et al (2013) Analysis of RDSS positioning accuracy based on RNSS wide area differential technique. Sci China Phys Mech Astron 56(10):1995–2001
6. Zhan J, Pang J, Zhang G et al (2011) Modeling and simulation testing of RDSS timing. Scientia Sinica Phys Mech Astron 41(5):620–628
7. Zheng C, Li D, Wang X et al (2010) A motion based method and emulation of RDSS integer ambiguity. J Geomatics Sci Technol 27(3):169–175
8. Tang B, Liu Q, Zhang Y et al (2012) Design of monitor and calibration method for BD RDSS user equipment test system. GNSS World China 37(1):13–16
9. Liu Y, Liu G, Chen X et al (2012) Discussion on adding RDSS to IGSO satellite in 2nd generation Beidou navigation satellite system. J Geodesy Geodyn 32(3):72–75

10. Lin X, Liu J (2003) The study on improvement of “Beidou” double-star navigation system and it’s algorithm. Chin J Space Sci 23(2):149–154
11. Lin X, Liu J, Yuan X et al (2004) One integrated navigation system of RDSS/SINS based on pseudo-range. J Shanghai JiaoTong Univ 38(10):1737–1740
12. Li QL, Liu Z, Xue YQ et al (2006) Modeling and simulation in RDSS system. J Syst Simul 18(5):1199–1203
13. Xu L, Yuan H, Fan J et al (2007) Study on a method of calculating the ionosphere TEC using RDSS system observation data. Chin J Space Sci 27(4):286–291

Chapter 21
BDS Precise Orbit Determination with iGMAS and MGEX Observations by Double-Difference Method

Junhong Liu, Bing Ju, Defeng Gu, Jing Yao, Zhen Shen and Xiaojun Duan

Abstract The double-difference method is used to determine the BeiDou Navigation Satellite System (BDS) orbit with 5 stations of the first phase of international GNSS Monitoring and Assessment Service (iGMAS) and 8 stations of Multi-GNSS Experiment (MGEX). The code multipath errors RMS of B1, B2 and B3 are 0.45, 0.43 and 0.26 m for iGMAS observations, respectively, which are comparable to that of MGEX stations. The average carrier phase errors RMS is 1.79 cm for iGMAS observations and 0.82 cm for MGEX data. Moreover, the precise orbit determination (POD) results of BDS with only 5 iGMAS stations are presented. The post-fit residuals RMS of the double-difference ionosphere-free code and carrier phase are 1.9 m and 7.4 mm. The accuracies of GEO, IGSO and MEO are 0.34, 0.20, 0.71 m in the radial component, while the 3D-RMS are 1.48, 0.66 and 3.05 m. Furthermore, 8 MGEX stations are added to solve the BeiDou satellites orbit. The radial RMS of orbit overlapping is approximately 0.2 m. The 3D-RMS is 0.88 m for GEO and 0.61 m for MEO. The tracking geometry is enhanced by adding the MGEX stations, which improves the accuracies of GEO and MEO satellites. However, the overlapping RMS of IGSOs is not improved. Additionally, the RMS of phase post-fit residuals is beyond 2 cm for some baselines and is obviously larger than that of the baselines between iGMAS stations. The enlarged residuals indicate some potential discordance for the observations between iGMAS and MGEX stations.

Keywords BeiDou Navigation Satellite System (BDS) · International GNSS monitoring and assessment service (iGMAS) · Multi-GNSS experiment (MGEX) · Precise orbit determination (POD)

J. Liu · B. Ju · D. Gu (✉) · J. Yao · Z. Shen · X. Duan
College of Science, National University of Defense Technology, Changsha 410073, China
e-mail: gudefeng05@163.com

J. Sun et al. (eds.), *China Satellite Navigation Conference (CSNC) 2014 Proceedings: Volume III*, Lecture Notes in Electrical Engineering 305,
DOI: 10.1007/978-3-642-54740-9_21,

21.1 Introduction

The BeiDou Navigation Satellite System (BDS) is independently developed and operated by China. The BDS adopts its own time (BeiDou Time, BDT) and coordinate system (China Geodetic Coordinate System 2000, CGCS2000) [1]. The first phase of the BDS was completed at the end of 2012 and can provide navigation services for the Asia-Pacific area [2]. The second phase of the BDS will provide better services for world-wide users by 2020 [3, 4].

The accuracy of BeiDou satellites orbit is a main factor influencing the BDS service capability. Some initial precise orbit determination results of BeiDou satellites are obtained in the recent years. Zhao et al. used COMPASS Experimental Tracking Network (CETN) observations to determine the BDS navigation satellites orbit. The 48 h orbit overlap comparison shows that the root mean square (RMS) values are less than 10 cm in the radial component [5]. He et al. [6] analyzed the impact of the tracking geometry to improve BDS satellites orbits accuracy. Montenbruck et al. [7] presented an initial characterization and performance assessment of the COMPASS system. Zhu et al. [8] used a regional tracking network to determine the BDS satellites orbit. The obtained orbit accuracy is about 20 cm in radial component. Zhou et al. [9] showed that the accuracies of BeiDou satellite orbit overlap are about 0.2, 1.2 and 0.6 m in R/T/N direction for a regional monitor network. In addition, Wang et al. [10] proposed two models to improve the IGSO and MEO satellites orbit accuracy during the conversion between yaw steering and orbit normal mode. Guo et al. investigated the reason of orbit accuracy degradation during yaw maneuvers of IGSO and presented two approaches to improve the POD accuracy [11]. Zhang et al. [12, 13] studied a method of the maneuvering orbit determination and prediction.

At present, with the limited ground tracking network the BDS precise orbit could not reach the similar quality of GPS. The tracking geometry will be more optimizing for BDS by adding the MGEX station, which might improve the accuracy of BDS satellites orbit. The GEO, IGSO and MEO satellites orbits accuracies with just 5 stations of the first phase of iGMAS are presented in this paper. Furthermore, the orbits of BeiDou satellites are solved again by adding 8 MGEX stations and the accuracies are compared with the results of only iGMAS stations.

21.2 Tracking Network and Observations Quality

The tracking network including 5 iGMAS stations and 8 MGEX stations is used in POD of BDS. 8 days (from days 340 to 347 in 2012) of tracking data are collected to finish this study. During this period, only a few observations for 5 satellites C02, C04, C05, C13 and C14 are available. Therefore, this paper focuses on the other 9 satellites including 2 GEOs (C01, C03), 5 IGSOs (C06, C07, C08, C09, C10), and

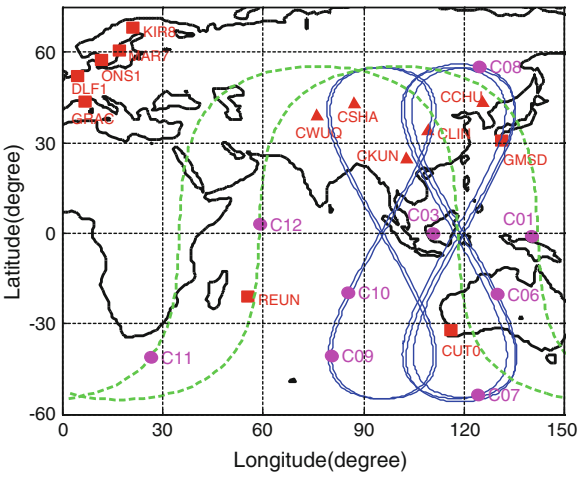

Fig. 21.1 Tracking network and BeiDou Satellites

2 MEOs (C11, C12). The 13 tracking stations and 9 satellites are illustrated in Fig. 21.1 to show the observing geometry.

In Fig. 21.1, the triangles are the iGMAS stations, the rectangles are the MGEX stations and the circles are the BeiDou satellites. Figure 21.1 shows that only 2 stations (CUT0, REUN) are located in the southern hemisphere. Besides, 5 MGEX stations (KIR8, MAR7, DLF1, ONS1, GRAC) are located in the Europe, where the stations can not receive the signals from the GEOs and can only receive a few observations with a low elevation from IGSOs.

The pseudorange multipath errors of B1 (MP1) and MP2 are computed according to the two frequencies pseudorange and carrier phase. The MP3 is estimated by the observations of B1 and B3. The carrier phase errors (PE) are assessed by the geometry-free and ionosphere-free linear combination (Eq. 21.1) with a triple-carrier phase observations [7].

$$\begin{aligned} GIF &= \frac{1}{f_1^2 - f_2^2}\left(f_1^2 L_1 - f_2^2 L_2\right) - \frac{1}{f_1^2 - f_3^2}\left(f_1^2 L_1 - f_3^2 L_3\right) \\ &\approx -0.088N_1 - 0.369N_2 + 0.459N_3 + \varepsilon_{GIF} \end{aligned} \tag{21.1}$$

Where L_i is the carrier phase of B_i in meters, f_i is the frequency of B_i, and N_i is the carrier phase ambiguities (i = 1,2,3). ε_{GIF} includes the phase wind-up effects, phase center variations, receiver noise and multipath of carrier phase. The RMS of ε_{GIF} is approximate 2.49 times of the single frequency carrier phase errors if the carrier phase errors are the same level in each frequency observations. Therefore, the standard deviation of the combination observations represents a weighted of carrier phase errors. The average pseudorange multipath errors and carrier phase errors of each station from days 341 to 343 are summed up in Table 21.1.

In Table 21.1, the pseudorange multipath errors RMS for iGMAS stations observations of B1, B2 and B3 are 0.45, 0.43 and 0.26 m respectively, while the

Table 21.1 Pseudorange multipath errors and carrier phase errors from days 341 to 343 in 2012

Station		MP1 (m)	MP2 (m)	MP3 (m)	PE (cm)
iGMAS	CCHU	0.41	0.40	0.27	1.29
	CKUN	0.45	0.45	0.27	1.35
	CLIN	0.45	0.49	0.24	1.05
	CSHA	0.44	0.41	0.23	3.84
	CWUQ	0.50	0.42	0.29	1.43
	Mean	0.45	0.43	0.26	1.79
MGEX	CUT0	0.57	0.43	0.30	0.93
	GMSD	0.31	0.35	0.26	0.97
	REUN	0.42	0.53	–	–
	KIR8	0.42	0.46	0.34	0.70
	MAR7	0.51	0.64	0.42	0.70
	ONS1	0.52	0.57	0.41	0.82
	DLF1	0.45	0.57	–	–
	GRAC	0.39	0.39	–	–
	Mean	0.45	0.49	0.35	0.82

Broken lines for no observations at B3

RMS are 0.45, 0.49 and 0.35 m for MGEX stations observations. Additionally, the RMS of the carrier phase errors is 1.79 cm for iGMAS stations measurements and is 0.82 cm for that of MGEX. The numerical values show that the carrier phase errors RMS for iGMAS data is approximately twice as large as that of MGEX data.

The National University of Defense Technology Orbit Determination Toolkit (NUDTTK) software has been employed to evaluate the observations quality and finish the POD of BeiDou satellites. This software is independently developed by NUDT and could be used to process many kinds of satellite measurements including spaceborne observations of GPS, SLR data, DORIS data and observations of BDS and GPS on ground.

21.3 Precise Orbit Determination

21.3.1 POD Strategy

In this paper the observations for 3 days are used to obtain a 3-day solution. The orbit quality is assessed by the post-fit residuals and orbit overlap of two adjacent 3-day solutions. The RMS of the orbit differences between the last day in the first 3-day solution and the middle day of the later 3-day solution are computed as an index of orbit accuracy. The observation models, dynamical models and the parameters applied in POD are listed in Table 21.2.

Table 21.2 Summary of models and parameters applied in POD

Observation models	
Observations	Double-Difference ionosphere-free code and phase combination of B1 and B2 with 60 s sampling
Elevation cutoff	10°
Weight for observations	2 mm and 0.5 m for raw phase and code data. An elevation-dependent weighting is sin(2e) for the elevation(e) lower than 30°
Troposphere model	Saastamoinen model as an initial (Climate model from GPT and mapping function from GMF models) and estimated in POD
Reference frame	
Time system	GPS Time
Inertial frame	J2000.0
Terrestrial frame	ITRF 2005
Precession-nutation	IERS Conventions 2003
EOP	IERS Standard Rapid EOP
Orbit models	
Geopotential	GGM02(12×12)
Solid Earth tides, pole tide and ocean tide	IERS Conventions 2003
Third-body	JPL DE405
Relativistic effects	Schwarzschild item
Solar radiation pressure model	CODE 9 parameters model
Parameters estimated	
Orbit parameters	Position, velocity and 9 solar radiation parameters
Station coordinates	With a constraint of 5 cm for each component
Troposphere parameters	Piece-wise linear zenith delay of each station per 2 h
Ambiguity	Non-integral solution

21.3.2 POD Results with iGMAS Network

To assess the orbit estimated by the 5 stations, a detailed orbit quality is shown by the RMS of the differences in the radial, along-track, cross-track and 3D. The statistical results for the orbit are presented in Fig. 21.2.

MG, MI and MM are the mean RMS of GEOs, IGSOs and MEOs in Fig. 21.2. Figure 21.2 shows that the RMS of IGSOs is smaller than the other two types of satellites. The mean RMS of the three types of satellites is listed in Table 21.3.

From the orbit RMS in Table 21.3, with 5 iGMAS tracking stations, IGSOs have the smallest RMS in radial component of 0.20 m compared to 0.34 and 0.71 m for GEOs and MEOs, respectively. In addition, the RMS in the position reaches 1.48, 0.66 and 3.05 m for GEOs, IGSOs and MEOs, respectively.

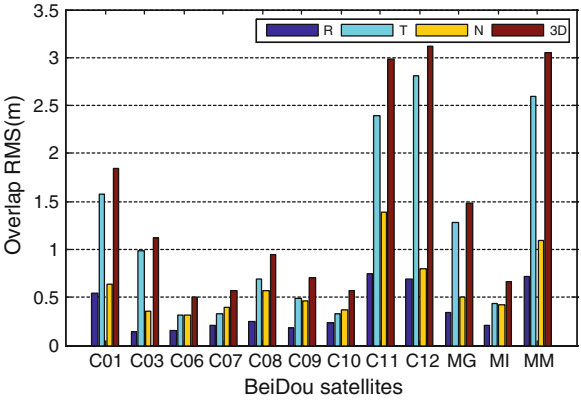

Fig. 21.2 The average orbit overlapping RMS of the orbits estimated by iGMAS network for each satellite and the mean of each satellite type

Table 21.3 Mean orbit overlapping RMS of three types of satellites for iGMAS network (m)

Types of satellites	radial	Along-track	Cross-track	3D
GEO	0.34	1.28	0.50	1.48
IGSO	0.20	0.43	0.42	0.66
MEO	0.71	2.60	1.09	3.05

The regional tracking network with 5 iGMAS stations can receive only a few observations from MEOs. The number of MEOs observations is approximate a half of IGSOs and is about a quarter of GEOs. Therefore, the orbits of MEOs are predicted in most of the time, which is the main factor increasing the RMS of the orbit overlap.

The RMS of the post-fit residuals is another important index to access the orbit quality. The errors of double-difference ionosphere-free combination data are about 6 times of the raw observations errors.

Figure 21.3 shows that the RMS of post-fit residuals is about 1.9 m for code double double-difference ionosphere-free observations, and it is approximate 7.4 mm for carrier phase measurements. Furthermore, the distribution of the code and carrier phase post-fit residuals is similar to the white noise, which indicates the observations are well fitted by the POD models.

The zenith delay parameter for every 2 h of each station is also estimated by a piece-wise linear function in POD. Furthermore, the tabular points of the function are constrained using a first-order Gauss-Markov process. The zenith delay including the estimated parameters and the values from the initial model can be used to generate the product of the troposphere. The zenith delay parameters from days 341 to 343 are illustrated in Fig. 21.4.

Figure 21.4 shows that the estimated zenith delay parameters present a high stability for every station. The results vary from −5 to 10 cm.

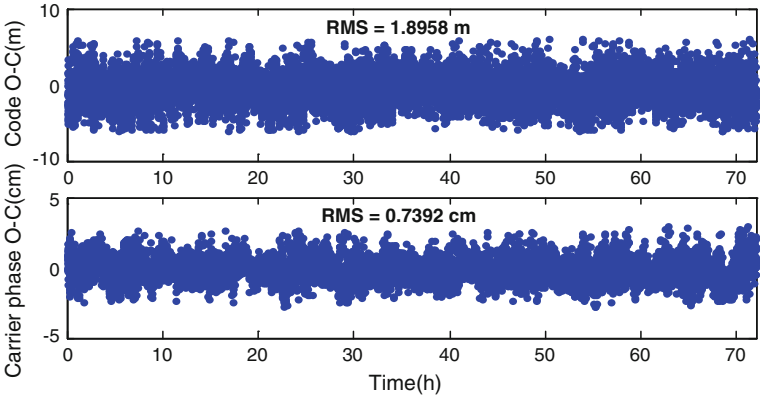

Fig. 21.3 The double-difference ionosphere-free observations post-fit residuals of the baseline between CSHA and CLIN only used iGMAS network

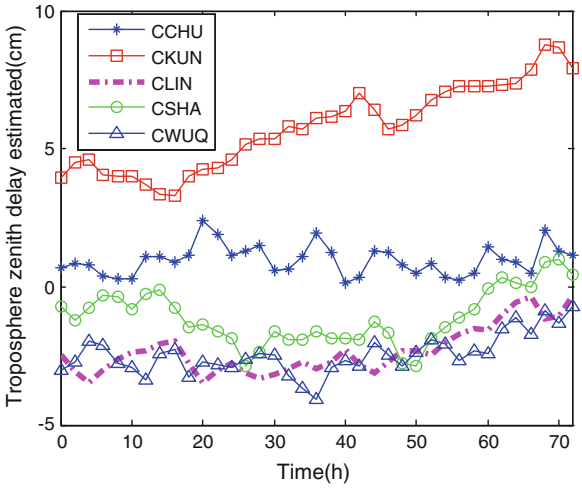

Fig. 21.4 Troposphere zenith delay estimation results of iGMAS network solution

21.3.3 POD Results with iGMAS and MGEX Network

The observations of 8 MGEX stations are processed together with that of 5 iGMAS stations. The quality of the estimated orbits is shown in Fig. 21.5.

Figure 21.5 shows that the orbit overlapping RMS for MEOs is the smallest, and the radial component accuracy is better than 20 cm on average. A detailed assessment of the orbit quality adding the MGEX stations are listed in Table 21.4.

Compared to the results of 5 iGMAS stations, the average orbit overlapping RMS of GEO and MEO satellites are obviously reduced by adding the MGEX stations.

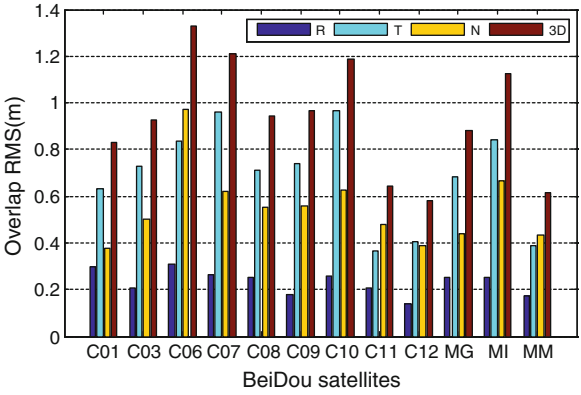

Fig. 21.5 POD results used iGMAS and MGEX network

Table 21.4 The average orbit overlapping RMS of three types of satellites for iGMAS and MGEX network (m)

Types of satellites	Radial	Along-track	Cross-track	3D
GEO	0.25	0.68	0.44	0.88
IGSO	0.25	0.84	0.67	1.13
MEO	0.17	0.39	0.43	0.61

The radial RMS and 3D-RMS of GEOs are 0.25 and 0.88 m (Table 21.4). Respectively the RMS of MEOs in the radial, along-track, cross-track and 3D are 0.17, 0.39, 0.43 and 0.61 m. From Fig. 21.1, it is obvious that the two MGEX stations (GMSD and CUT0) enhance the tracking geometry to GEOs. Therefore, the orbit overlapping RMS of GEOs is reduced significantly. For the MEO satellites, all of the 8 MGEX stations can receive the signals from MEOs. As a consequence, the RMS of orbit overlapping is also degraded for MEOs. Nevertheless, the RMS of IGSOs becomes larger than the iGMAS network solution.

The post-fit residuals of the RMS are analyzed. The RMS of code residuals are almost no variation. Even so the carrier phase residuals are enlarged (Fig. 21.6).

Figure 21.6 shows the post-fit residuals RMS is approximate 2.92 cm for the baseline between CWUQ and KIR8 and is 2.81 cm for the baseline between CKUN and CUT0. The RMS is about 4 times as that of iGMAS stations solution (Fig. 21.3). The baselines are divided into 3 types. The first one is the baselines consisted by iGMAS stations. The second one is the baselines consisted by iGMAS station and MGEX station. The third one is the baselines consisted by MGEX stations. The RMS of post-fit residuals of each baseline is listed in Table 21.5.

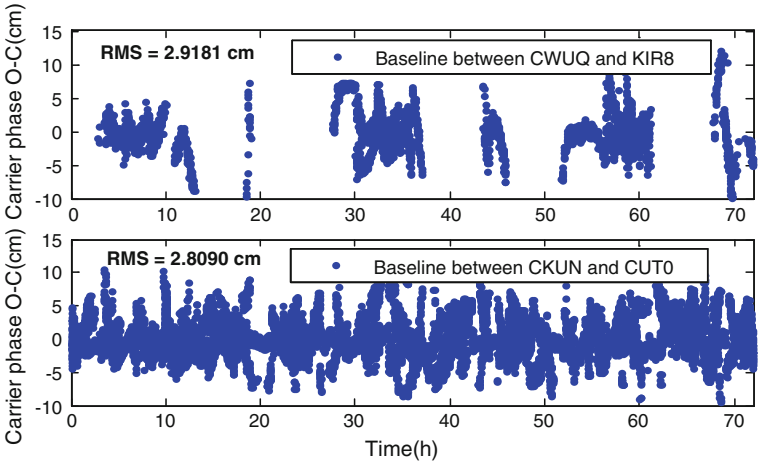

Fig. 21.6 The post-fit residuals of double-difference ionosphere-free carrier phase observations for the iGMAS and MGEX network solution during the days 341 to 343

Table 21.5 The post-fit residuals RMS of the Baselines used in POD

Types of baselines	Station A	Station B	Length (km)	RMS (cm)	Mean (cm)
iGMAS and iGMAS	CSHA	CWUQ	1030.6	0.94	0.96
	CKUN	CLIN	1205.3	0.95	
	CCHU	CLIN	1739.9	0.93	
	CLIN	CSHA	2143.1	1.02	
MGEX and MGEX	MAR7	ONS1	469.8	1.76	2.11
	DLF1	ONS1	772.4	1.86	
	KIR8	MAR7	831.6	1.91	
	DLF1	GRAC	933.8	2.04	
	CUT0	REUN	5827.1	2.99	
iGMAS and MGEX	CCHU	GMSD	1545.1	1.21	2.31
	CWUQ	KIR8	4463.8	2.92	
	CKUN	CUT0	6188.1	2.81	

The baselines consisted by iGMAS stations have the smallest RMS of post-fit residuals (Table 21.5). The average RMS of the 4 baselines consisted by iGMAS stations is 0.96 cm. By contrast the RMS of the other two types' baselines is larger, and the value is beyond 2 cm for some baselines. Table 21.5 presents some discordance between the iGMAS and MGEX observations.

The posit-fit residuals RMS will increase if some differences exist between the coordinate of iGMAS stations and MGEX stations. Moreover, there may be some neglected corrections in the observations. Additionally, a lot of observations of IGSOs with low elevation are employed in POD, which is another possible reason of enlarging the post-fit residuals.

21.4 Conclusions

The tracking geometry of 5 iGMAS stations and 8 MGEX stations to BeiDou satellites is demonstrated in this paper. Subsequently, the observations quality of each station is evaluated. Moreover, two tracking networks (iGMAS station only and adding MGEX stations) are used in POD of BeiDou satellites. The quality of the estimated orbits is assessed. 4 conclusions are obtained from this study.

1. The RMS of code multipath errors of B1, B2 and B3 are 0.45, 0.43 and 0.26 m for iGMAS observations, respectively, which are comparable to that of MGEX stations. The RMS of carrier phase errors is 1.79 cm for iGMAS and 0.82 cm for MGEX data.
2. With 5 iGMAS tracking stations, the orbit overlapping RMS of GEOs, IGSOs and MEOs are 0.34, 0.20 and 0.71 m in the radial component, while the 3D-RMS reach 1.48, 0.66 and 3.05 m respectively. The RMS of post-fit residuals is 1.9 m for the code observations and is 7.4 mm for carrier phase.
3. Adding 8 MGEX stations, the orbits overlapping RMS is obviously reduced for GEOs and MEOs. The RMS of the radial component is 0.25 m for GEOs and 0.17 m for MEOs, while the 3D-RMS is 0.88 and 0.61 m. However, the orbit quality is not improved for IGSOs, the overlapping RMS of which is 0.25 m in radial component and 1.13 m in position on average.
4. The post-fit phase residuals RMS of some baselines exceed 2 cm, which is much larger than that of baselines consisted by iGMAS stations. Some potential discordance may exist between iGMAS and MGEX observations.

Acknowledgements The authors are grateful to iGMAS and Crustal Dynamics Data Information System (CDDIS) for providing the observations.

This work is co-supported by international GNSS Monitoring and Assessment Service (iGMAS), National Natural Science Foundation of China (61002033, 61370013), the Program for New Century Excellent Talents in university and the Project-sponsored by SRF for ROCS, SEM in China

References

1. China Satellite Navigation Office (2012) BeiDou navigation satellite system signal in space interface control document. Available from: http://gge.unb.ca/test/beidou_icd_english.pdf
2. China Satellite Navigation Office (2012) Progress report of Compass/Beidou satellite navigation system. Space Int 4:6–11
3. Sun FP, Liu S, Zhu XH et al (2012) Research and progress of Beidou satellite navigation system. Sci China Inf Sci 55(12):2899–2907
4. China Satellite Navigation Office (2012) Development of BeiDou navigation satellite system. The 7th meeting of International Committee on GNSS, Beijing
5. Zhao Q, Guo J, Li M et al (2013) Initial results of precise orbit and clock determination for COMPASS navigation satellite system. J Geodesy 87(5):475–486

6. He L, Ge M, Wang J et al (2013) Experimental study on the precise orbit determination of the BeiDou navigation satellite system. Sensors 13(3):2911–2928
7. Montenbruck O, Hauschild A, Steigenberger P, Nakamura S et al (2012) Initial assessment of the COMPASS/BeiDou-2 regional navigation satellite system. GPS Solutions 17(2):211–228
8. Zhu J, Wang J, Zeng G et al (2013) Precise orbit determination of BeiDou regional navigation satellite system via double-difference observations. In: 2013 Proceedings on China satellite navigation conference (CSNC), Wuhan
9. Zhou S, Hu X, Zhou J et al (2013) Accuracy analyses of precise orbit determination and timing for COMPASS/Beidou-2 4GEO/5IGSO/4MEO constellation. In: 2013 Proceedings on China satellite navigation conference (CSNC), Wuhan
10. Wang W, Chen G, Guo S et al (2013) A study on the Beidou IGSO/MEO Satellite orbit determination and prediction of different yaw control mode. In: 2013 Proceedings on China satellite navigation conference (CSNC), Wuhan
11. Guo J, Zhao Q, Geng T et al (2013) Precise orbit determination for COMPASS IGSO Satellites in Yaw Maneuvers. In: 2013 Proceedings on China satellite navigation conference (CSNC), Wuhan
12. Zhang JL, Qiu HX, Yong Y et al (2013) Application of thrust force model in GEO's orbit determination in case of Maneuvers. In: 2013 Proceedings on China satellite navigation conference (CSNC), Wuhan
13. Zhang JL, Qiu HX, Yong Y et al (2013) Study of determination orbit of COMPASS-GEO after Maneuvers with short segmental arc. In: 2013 Proceedings on China satellite navigation conference (CSNC), Wuhan

Chapter 22
Combined Autonomous Orbit Determination of GEO/IGSO Satellites on the Space-Based Probe

Peng Liu and Xi-Yun Hou

Abstract Nowadays, the orbit determination (OD) of GEO/IGSO satellites mainly depends on the observation data from the ground stations. While the ground stations are not available, the orbits of the GEO/IGSO satellites can not be precisely determined by themselves. One effective approach to increase the OD accuracy and to realize the autonomous orbit determination of the GEO/IGSO satellites is to add the highly accurate inter-satellite range data. But a serious problem of merely using this type of data is the uncertainty of the orbital plane of the GEO/IGSO satellites. So external references such as the ground stations or the special celestial bodies in space are needed. The research in this work is to replace the ground stations with some probes located on some special orbits. These special orbits are carefully chosen so that the uncertainty of the orbital plane of the GEO/IGSO satellites can be significantly eliminated in autonomous OD and thus make the combined autonomous OD of the GEO/IGSO satellites and the probes possible.

Keywords GEO/IGSO satellite · Inter-satellite range data · Orbit determination · Collinear libration point · Distant retrograde orbit

22.1 Introduction

Currently, navigation and guidance of GEO/IGSO satellites mainly rely on the support from ground stations. With more and more GEO/IGSO satellites and communication missions, the idea of building a GEO/IGSO satellite constellation

P. Liu (✉) · X.-Y. Hou
School of Astronomy and Space Science, Nanjing University, Nanjing, China
e-mail: pengliu123@gmail.com

P. Liu · X.-Y. Hou
Institute of Space Environment and Astrodynamics, Nanjing University, Nanjing, China

J. Sun et al. (eds.), *China Satellite Navigation Conference (CSNC) 2014 Proceedings: Volume III*, Lecture Notes in Electrical Engineering 305,
DOI: 10.1007/978-3-642-54740-9_22,

which can be determined autonomously is proposed. The applications of the constellation require precise orbits of GEO/IGSO satellites. The highly accurate inter-satellite range data is a good choice to enhance the OD accuracy [1]. But a serious problem of merely using this type of data is the uncertainty of the orbital plane of the satellites [2]. So external references such as the ground stations or the special celestial bodies in space are needed. The usual solution to this problem is to add the ground station's support. While the ground stations are not available, the orbits of the GEO/IGSO satellites can not be precisely determined by themselves. The purpose of this paper is to take the place of the ground stations with the probes located on the collinear libration point (CLP) orbit in the Earth–Moon system or the distant retrograde orbit (DRO) around the Moon. Different from the simple substitution, the spatial state of the probe is unknown beforehand, it is needed to be determined combined with GEO/IGSO satellites. Therefore, it is the combined autonomous orbit determination (CAOD) in fact.

CLPs are special equilibrium points of the circular restricted three-body problem (CRTBP). Different from GEO/IGSO satellites, CLP probes are in the region where the gravitational force from the Earth and the Moon are comparable to each other. The introduction of CLP provides an absolute reference orientation for GEO/IGSO satellites. Due to this fact, the CAOD of the GEO/IGSO satellites and the CLP probes is possible. However, the CLP probe is not the only choice for the CAOD of the GEO/IGSO satellites. Theoretically speaking, any kind of orbits that can provide an absolute reference orientation for GEO/IGSO satellites can play the same role as the CLP probe. In our study, another kind of special orbit—distant retrograde orbit (DRO) around the Moon is also studied. The research shows that the DROs are competitive to the CLP orbits, not only because the OD results are comparable to each other, but also because the DROs usually have much better stability properties than the CLP orbits. Although this research is studied in the CRTBP, it can be simply generalized to the real force model of the Earth–Moon system.

22.2 Circular Restricted Three-Body Problem

Usually, the probe's motion is described in a frame rotating with the two primaries. This frame is called the synodic frame. In the synodic frame, use the following dimensionless parameters

$$[M] = m_1 + m_2,\ [L] = \overline{P_1P_2} = a,\ [T] = \sqrt{a^3/G[M]}$$

the equation of motion (EOM) of the probe is as follows

$$\ddot{r} + 2(-\dot{y}, \dot{x}, 0)^T = (\partial\Omega/\partial r)^T \tag{22.1}$$

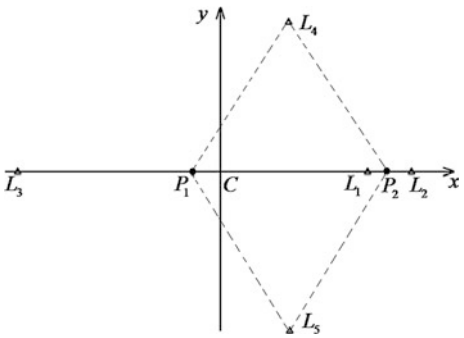

Fig. 22.1 The barycenter synodic frame and the five libration points

where

$$\Omega = \left[x^2+y^2+\mu(1-\mu)\right]/2+(1-\mu)/r_1+\mu/r_2$$
$$\mu = m_2/(m_1+m_2)$$

$m_1, m_2 (m_1 > m_2)$ are the masses of the two primaries, r_1, r_2 are the distances of the probe from the two primaries.

It is well known that there are five libration points in the CRTBP. Theoretically speaking, small bodies can remain static on these points in the synodic frame. Figure 22.1 shows the locations of these five libration points in the barycenter synodic frame. Three of them (L_1, L_2, L_3) are called collinear libration points (CLPs), and the other two (L_4, L_5) are called triangular libration points (TLPs). In this study, only L_1 is our focus because it is closer to the Earth.

22.3 Collinear Libration Point

22.3.1 Stability of the CLP

Generally speaking, motions around the CLPs are unstable. Nevertheless, conditionally stable orbits still exist, such as the periodic halo orbits and the quasi-periodic Lissajous orbits. Both kinds of orbits can be used as nominal orbits of the CLP probes. Halo orbits are usually preferable due to their periodicity and better visibility from the Earth. In the following studies, we'll focus on halo orbits. Nevertheless, all the methods also go for Lissajous orbits. Figure 22.2 depicts one halo orbit around L_1 point in the Earth–Moon system.

Using the third-order analytical solution [3] or even higher order analytical solutions [4] as the initial seed for the numerical correction algorithms for periodic orbits [5], we can compute the halo orbits. In our work, a 15th order analytical solution is used as the initial seed and usually 2–3 iterations are enough to get the

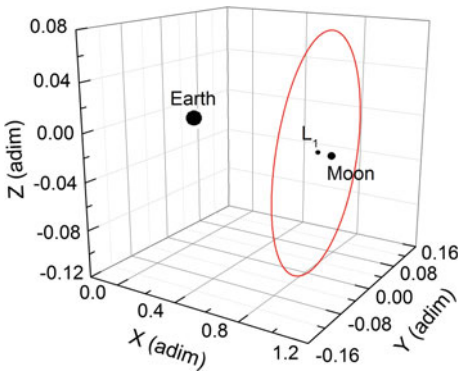

Fig. 22.2 A halo orbit around L_1 point in the Earth–Moon system

initial state of small halo orbits to the machinery accuracy. Using the well-known predictor-corrector algorithm, we can go from smaller halo orbit to larger halo orbits [6]. Due to the nonlinear effects, some properties of the halo orbits such as period and stability also change with the orbit amplitudes.

Denote the state vector of the probe as $X = (x, y, z, \dot{x}, \dot{y}, \dot{z})$ and briefly denote the EOM of Eq. (22.1) as

$$\dot{X} = F(X) \tag{22.2}$$

Starting from the initial point $X_0 = X(t_0 = 0)$, the trajectory under the law of Eq. (22.2) can be denoted as

$$X(t) = X(X_0, t) \tag{22.3}$$

The periodic orbit (such as the halo orbit) satisfies

$$X(t = T) - X_0 = 0 \tag{22.4}$$

The *Monodromy* matrix of a periodic orbit is defined as

$$M = \left.\frac{\partial X(t)}{\partial X_0}\right|_{t=T} \tag{22.5}$$

where the right hand side of Eq. (22.5) is the station transition matrix (STM) of the periodic orbit. For Hamiltonian systems such as the CRTBP, eigenvalues of the matrix M should appear in conjugate and in pairs [7]. I.e., if λ is the eigenvalue of M, then $\bar{\lambda}, \lambda^{-1}, \bar{\lambda}^{-1}$ should also be the eigenvalues of M. For halo orbits of small to moderate amplitudes, the eigenvalues of M are usually of the form [8]

$$\left(1, 1, a, a^{-1}, e^{ib}, e^{-ib}\right) \tag{22.6}$$

where a, b are real numbers and usually $a \neq 1$ for halo orbits. Denote the eigenvalue pair of the matrix M as $\left(\lambda_i, \lambda_i^{-1}\right)$, the stability parameter is defined as [9]

$$s_i = \lambda_i + \lambda_i^{-1} \tag{22.7}$$

Usually for the eigenvalue pair of $\left(\lambda_i, \lambda_i^{-1}\right) = \left(e^{ib}, e^{-ib}\right), b \neq 0, \ |s_i| < 2$, the motion is in the space spanned by the eigenvalues of this eigenvalue pair and is linearly stable. For the eigenvalue pair of $\left(\lambda_i, \lambda_i^{-1}\right) = (a, a^{-1}), a \neq 1, \ |s_i| > 2$, the motion is linearly unstable. Generally, the parameter s_i can be used as an indicator of the stability of the motion. The motion around the period orbit is stable if $|s_i| < 2$ and unstable if $|s_i| > 2$ and critical if $|s_i| = 2$.

For a three dimensional periodic orbit in the CRTBP model, the eigenvalues of the *Monodromy* matrix should satisfy [8]

$$(\lambda - 1)^2\left(\lambda^2 + p_1\lambda + 1\right)\left(\lambda^2 + p_2\lambda + 1\right) = 0 \tag{22.8}$$

where

$$\begin{aligned} p_1 &= \frac{1}{2}\left(\alpha + \sqrt{D}\right), \ p_2 = \frac{1}{2}\left(\alpha - \sqrt{D}\right) \\ D &= \alpha^2 - 4(\beta - 2) \\ \alpha &= 2 - Tr(M), \ \beta = \frac{1}{2}\left[\alpha^2 + 2 - Tr\left(M^2\right)\right] \end{aligned}$$

Obviously $s_i = -p_i$.

Due to the following symmetry of Eq. (22.1)

$$(x, y, z, \dot{x}, \dot{y}, \dot{z}, t) \leftrightarrow (x, y, -z, \dot{x}, \dot{y}, -\dot{z}, t) \tag{22.9}$$

Actually we have two families of halo orbits around each CLP. These two families have members symmetric to each other with respect to the $x - y$ plane [3]. In our studies, the halo orbit we used is the one that most of the orbit is above the $x - y$ plane (the north halo). The halo orbit has two intersection points with the $x - z$ plane, we choose the z coordinate of the upper intersection point as the amplitude parameter of the halo orbit. Figure 22.3 shows the curve of the stability parameter with respect to the amplitude parameter for the L_1 point. The continuation process is terminated at the point where $D < 0$ in Eq. (22.8) (In this case, if $\alpha \neq 0$, the eigenvalues are complexes with nonzero real parts).

Judging from Fig. 22.3, we know that with increasing out of plane amplitude, the stability parameter s_1 of the halo orbit reduces. Since the motion around the halo orbit deviates from it at a speed proportional to $e^{at} \sim e^{s_1 t}$ [where a is the eigenvalue in Eq. (22.6)], the probe deviates at a slower speed for large halo orbits given the same initial deviation from the nominal orbit. Thus the control frequency could be smaller. From the view point of orbit control, it's better to use a larger

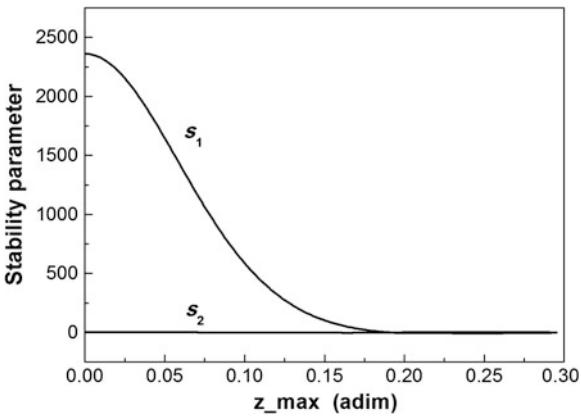

Fig. 22.3 The curves of the stability parameter versus the amplitude parameter for the halo families around L_1 in the Earth–Moon system

halo orbit. Note that the length unit in Figs. 22.2 and 22.3 is the mean distance between the Earth and the Moon, i.e., 384747.981 km.

22.3.2 OD Accuracy of CLP Probe and GEO/IGSO Satellites

The CAOD problem of a CLP probe and GEO/IGSO satellites is the most important and the most basic one in our studies. In numerical simulations, the out-of-plane amplitude of the halo orbit around L_1 point is taken to be 30,780 km. The CLP probes and GEO/IGSO satellites are integrated simultaneously in the Earth-centered inertial frame. At each "observation" epoch, the inter-satellite range data is generated by the differences in their positions. In order to simplify our studies, only random errors (with a threshold of one meter) are added to the "observation" data. In the following simulations, without specifications, the sample interval is taken to be 10 min. One remark should be made. Different sample data with different intervals may lead to different OD results, but will not change the results qualitatively.

First, the OD problem of the CLP probe and GEO satellite is investigated. Table 22.1 shows the OD results of L_1 probe and GEO satellite according to different lengths of data. In Table 22.1 and all the following tables, the OD accuracy of the GEO/IGSO is expressed by the radial (R), transverse (T) and normal (N) errors, and the OD accuracy of the CLP probe is expressed by position error (r) and velocity error($\dot{r}$).

From Table 22.1, we can see that, for 1-day length of data, the orbits of L_1 probe and GEO satellite cannot be determined. The reason is maybe that 1-day arc is very short for L_1 probe and GEO satellite, and the geometry between them is poor. Due to the fact, the B matrix is ill or even rank deficient. However, the OD accuracy of L_1 probe and GEO satellite can be up to 10 m level for 3-day length of data and 1 m level (the observation accuracy) for 5-day length of data.

Table 22.1 The OD results of L_1 probe and GEO satellite according to different lengths of data

Days	GEO satellite			L_1 probe	
	R(m)	T(m)	N(m)	r(m)	$\dot{r}$(m/s)
1	–	–	–	–	–
2	2.61	32.16	104.19	642.64	5.88×10^{-3}
3	0.07	2.03	9.52	29.09	1.43×10^{-4}
5	0.04	0.25	1.01	2.80	1.68×10^{-5}
10	0.02	0.08	0.73	0.45	2.35×10^{-6}
15	0.01	0.05	0.53	0.31	1.88×10^{-6}
20	0.01	0.04	0.37	0.12	6.67×10^{-7}

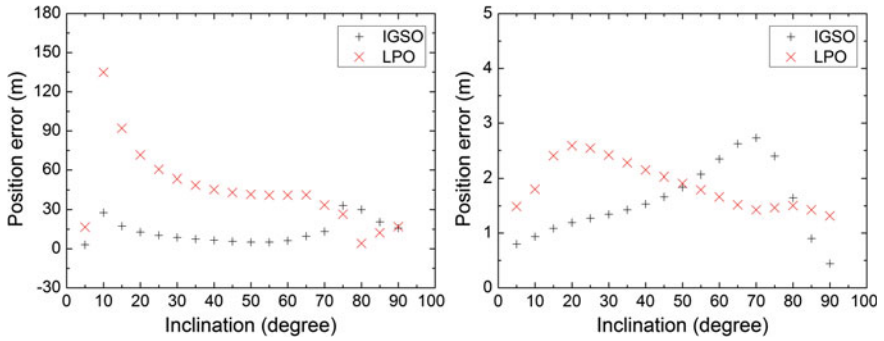

Fig. 22.4 *Left* The OD results of L_1 probe and IGSO satellites for 3-day lengths of data. *Right* The OD results of L_1 probe and IGSO satellites for 5-day lengths of data

Second, the OD problem of the CLP probe and IGSO satellites is investigated. Different from GEO satellite, the inclination of IGSO satellite is not zero. So different geometries between L_1 probe and IGSO satellites may be have a influence on the OD accuracy. The left frame of Fig. 22.4 shows the OD accuracy for 3-day and the right frame of Fig. 22.4 shows 5-day length of data. We can simply see that the OD accuracy is better when the inclination of IGSO satellite is near 50° and 90°.

22.4 Distant Retrograde Orbit Around the Moon

22.4.1 Stability of the DRO

The DROs belong to a special symmetric retrograde family of the CRTBP model which terminates onto a colliding orbit with the second primary. For DROs very close to the Moon, the influence from the Earth is negligible and the DROs are approximately retrograde circular orbits around the Moon in a two-body frame. This fact can be used to provide initial seeds for the numerical correction algorithm

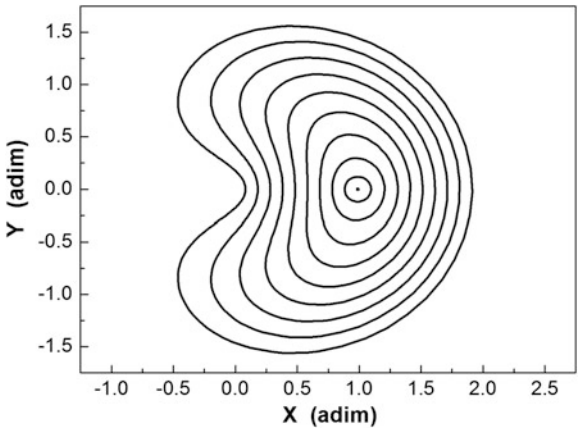

Fig. 22.5 Some examples of the DRO family with different amplitudes

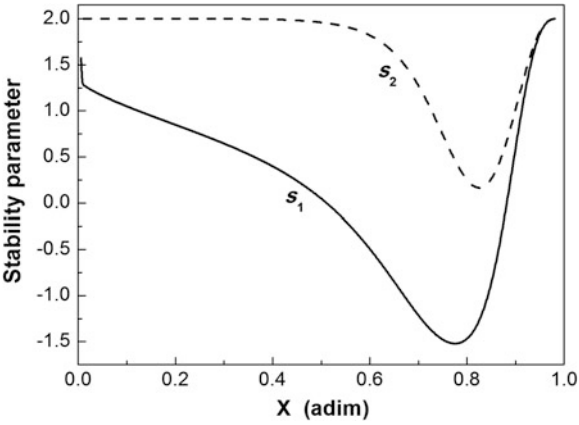

Fig. 22.6 The curves of the stability parameter versus the amplitude parameter for the DRO

of the periodic orbit. Figure 22.5 shows several example DROs with different amplitudes. With increasing amplitudes, the Earth's influence becomes stronger and stronger and the shape of the DROs deviates further and further from a circular orbit. Figure 22.6 shows the two stability parameters of this family before it collides with the Earth. The abscissa of this frame is the x coordinate of the left intersection point of the orbit with the x axis. With increasing amplitude, the planar stability parameter s_1 first comes down and then increases again. Same thing happens to the vertical stability parameter s_2.

From Figs. 22.5 and 22.6, we know that these DROs are generally stable. Similar to the halo orbits in the CLP case, we can also have periodic spatial orbits bifurcating from the planar DRO family. However, when the amplitude of the planar DRO is too large and even exceed the sphere of the Moon's gravitational action, the influence of the Earth's gravity will be significant. In fact, to test the effects of the vertical component of the DRO in the CAOD process, it's unnecessary to use a periodic orbit. We can choose a DRO with moderate planar

Table 22.2 The OD results of the DRO probe and GEO satellite according to different lengths of data

Days	GEO satellite			DRO probe	
	R(m)	T(m)	N(m)	r(m)	$\dot{r}$(m/s)
1	–	–	–	–	–
2	1.28	52.55	465.33	1,680.67	1.89×10^{-2}
3	0.05	0.31	5.34	32.79	2.61×10^{-4}
5	0.04	0.10	0.85	2.26	1.26×10^{-5}
10	0.005	0.06	1.16	0.45	2.25×10^{-6}
15	0.01	0.03	1.08	0.17	9.78×10^{-7}
20	0.02	0.05	0.67	0.10	4.50×10^{-7}

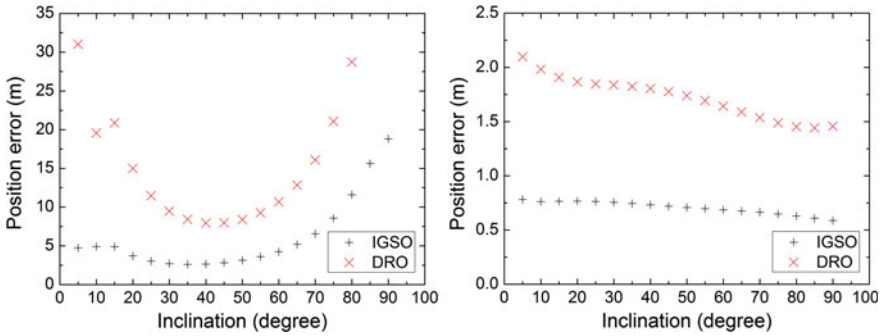

Fig. 22.7 *Left* The OD results of the DRO probe and IGSO satellites for 3-day lengths of data. *Right* The OD results of the DRO probe and IGSO satellites for 5-day lengths of data

amplitude and add a vertical displacement to it. The obtained orbit is usually quasi-periodic. Due to the planar and vertical stability of the DRO orbit, the quasi-periodic orbit is stable if the vertical displacement is not too large.

22.4.2 OD Accuracy of DRO Probe and GEO/IGSO Satellites

Similar to the halo orbits in the CLP case, the CAOD problem of a DRO probe and GEO/IGSO satellites is investigated. The planar amplitude of the DRO is 4×10^4 km, and the vertical displacement is 2×10^4 km. The numerical simulation condition is the same to that of the CLP. Table 22.2 shows the OD results of DRO probe and GEO satellite according to different lengths of data. The left frame of Fig. 22.7 shows the OD accuracy of DRO probe and IGSO satellites for 3-day length of data. The right frame of Fig. 22.7 shows the OD accuracy for 5-day length of data.

From Table 22.2, we can see the OD results of DRO probe and GEO satellite are similar to those of CLP. From Fig. 22.7, we can also simply see that for 3-day length of data the OD accuracy of DRO probe and IGSO satellites is better when the inclination of IGSO satellite is near 40°.

22.5 Conclusion

This paper investigates the CAOD problem of GEO/IGSO satellites on the basis of CLP orbits in the Earth–Moon system and DROs around the Moon. The research shows that the OD accuracy of GEO/IGSO satellites may be up to the observation accuracy only using the inter-satellite range data between the probe and the GEO/IGSO satellites.

Acknowledgments This work was supported by national Natural Science Foundation of China (Grant Nos. 11033009, 11078001, 11203015), National Basic Research Program of China (Grant No. 2013CB834100) and National High Technology Research and Development Program 863 of China (Grant No. 2012AA121602).

References

1. Kato M, Sasaki S, Tanaka K et al (2008) The Japanese lunar mission SELENE: science goals and present status. Adv Space Res 42:294–300
2. Liu L, Liu YC (2000) The rank deficiency on inter-satellite measurement in the autonomous orbit determination. J Spacecr TT&C Technol 19(3):13–16 (in Chinese)
3. Richardson DL (1980) Analytic construction of periodic orbits about the collinear points. Celest Mech Dyn Astron 22:241–253
4. Jorba À, Masdemont J (1999) Dynamics in the centre manifold of the collinear points of the restricted three body problem. Physica D 132:189–213
5. Doedel EJ et al (2007) Elemental periodic orbits associated with the libration points in the circular restricted 3-body problem. Int J Bifurcat Chaos 17:2615–2677
6. Munoz-Almaraz FJ et al (2003) Continuation of periodic orbits in conservative and Hamiltonian systems. Physica D 181:1–38
7. Arnold VI (1999) Mathematical methods of classical mechanics, 2nd edn. World Publishing Corporation, Beijing
8. Gómez G, Masdemont J, Simó C (1998) Quasihalo orbits associated with libration points. J Astronaut Sci 46:135–176
9. Bray TA, Goudas CL (1967) Three dimensional oscillations about L1, L2, L3. Adv Astron Astrophys 5:71–130

Chapter 23
Modeling and Performance Analysis of GPS/GLONASS/BDS Precise Point Positioning

Pan Li and Xiaohong Zhang

Abstract The main challenge of dual-frequency precise point positioning (PPP) is that it requires about 30 min to obtain a centimeter level accuracy. Currently, PPP is generally conducted with GPS only using the ionosphere-free combination. Along with the competition of the first phase of the Beidou Navigation Satellite System (BDS) which comprising 5 satellites in Geostationary Orbit (GEO), 5 in Inclined Geosynchronous Orbit (IGSO) and 4 in Medium Earth Orbit (MEO) by the end of 2012, the regional navigation capabilities has been formed and the visibility and availability have been significantly improved for users in the Asia-Pacific regional area. Attention has been paid to improve the performance of PPP by combining BDS and other navigation satellite system (GPS/GLONASS). This study introduces a single-differenced (SD) between-satellite PPP model which can process any single-system or multi-system GNSS (GPS/GLONASS/BDS) raw dual-frequency carrier phase measurements. In this model, the GPS satellite with the highest elevation is selected as the reference satellite to form the SD between-satellite measurements. Thus the GPS receiver clock offset is canceled and only a system time offset between GPS and other GNSS system is estimated for the observations of GLONASS or BDS. In the proposed model, noisy pseudorange measurements are ignored thus modeling the pseudorange stochastic model is not required. The stochastic model for SD measurements and states can be easily realized by mapping that for undifferenced measurements and states. Also the correlation of the SD measurements is considered. Using a 7-day data set from 10 multiple system GNSS stations, we have investigated the performance of single-system PPP, GPS/GLONASS PPP and GPS/GLONASS/BDS PPP, including convergence speed and positioning accuracy. The contribution of BDS observation to the performance of multi-GNSS PPP is analyzed and assessed with special

P. Li (✉) · X. Zhang
School of Geodesy and Geomatics, Wuhan, China
e-mail: lipan.whu@gmail.com

X. Zhang
e-mail: xhzhang@sgg.whu.edu.cn

J. Sun et al. (eds.), *China Satellite Navigation Conference (CSNC) 2014 Proceedings: Volume III*, Lecture Notes in Electrical Engineering 305,
DOI: 10.1007/978-3-642-54740-9_23,

concern. Numerous experimental results indicate that after adding BDS observations, the convergence time can be reduced by 10–12 % for GPS PPP, and reduced by about 5–7 % for GPS/GLONASS PPP further. Besides, BDS observations can contribute to improving the accuracy of kinematic PPP with 3 h observations. After adding BDS observations, the RMS in kinematic mode is improved by 14.3, 7.1 and 7.5 % for GPS PPP while 11.1, 16.7 and 6.5 % for GPS/GLONASS PPP, in the east, north and up directions, respectively. For GPS/GLONASS/BDS PPP, an accuracy of 1–2 cm in horizontal and 2–3 cm in vertical directions can be achieved in kinematic mode while an accuracy of less than 1 cm in horizontal and 1–2 cm in vertical directions can be achieved in static mode.

Keywords GPS/GLONASS/BDS · Multi-GNSS · Precise point positioning · Convergence speed · Positioning accuracy

23.1 Introduction

Precise Point Positioning (PPP) is one of the representative techniques for high accuracy GNSS-based positioning [1, 2] (the other is Network-based Real-Time Kinematic). Based on pseudorange and carrier phase observations from a standalone GNSS receiver and the IGS precise orbit and clock products, PPP positioning accuracy can reach cm- to dm-levels for static or kinematic applications on a global scale. PPP has been demonstrated to be a powerful and efficient technology for scientific and civilian applications, such as near real-time GPS meteorology [3, 4] and crustal deformation monitoring [5, 6]. Although PPP has advantages such as high computational efficiency, not requiring dedicated reference stations, it requires a long convergence time to achieve a desired accuracy. Besides, compared with network double difference solution, PPP suffers from a relative poor accuracy for observations covering a short time interval, such as 3 h [7]. These problems have impeded its further application in many areas and are more significant in the conventional GPS-PPP solution.

Along with the competition of the first phase of the Beidou Navigation Satellite System (BDS) which comprising 5 satellites in Geostationary Orbit (GEO), 5 in Inclined Geosynchronous Orbit (IGSO) and 4 in Medium Earth Orbit (MEO) by the end of 2012, the regional navigation capabilities has been formed and the visibility and availability have been significantly improved for users in the Asia-Pacific regional area. Attention has been paid to improve the performance of PPP with BDS or combining BDS and GPS. Based on simulated data, Yang et al. [8] pointed out the contribution of BDS to user's PNT by analysis of visible satellites and dilution of precision (DOP) values. Shi et al. [9] determined the precise orbit of BDS satellites, with the radial accuracy better than 10 cm; using observations come from a regional reference network named 'Beidou Experimental Tracking Stations' (BETS). Based on achieved orbit and clock products, Shi et al. [9]

showed that static PPP and kinematic RTK can also achieve centimeter level and 5–10 cm respectively. Also with continuous measurement data from BETS, Liu et al. [10] analyzed the impact of different ambiguity resolution strategy on precision orbit determination of BDS and then compared the positioning results of BDS network solution and BDS PPP. The results show that BDS static PPP solution can achieve horizontal accuracy better than 1.4 cm and vertical accuracy better than 3 cm, which is a little worse than BDS network solution, but basically at the same level. Moreover, Li et al. [11] presented an initial performance assessment of dual-frequency un-differenced PPP for GPS, BDS and combined GPS/BDS, using three days datasets of two stations. Their results show that the combined GPS/BDS PPP can shorten the convergence time, but not necessarily improve positioning results by much if the satellites of the single GNSS system already have a good receiver-satellite geometry.

These studies preliminary demonstrated that cm-level positioning accuracy can be achieved using BDS observation covering 24 h. Nowadays, with the recovery of the GLONASS system, many researchers have also studied combined PPP with GPS and GLONASS observations. Their results indicated that the convergence speed can be accelerated by combined PPP [12, 13]. As mentioned above, all these studies are based on dual-system GNSS observations (GPS/GLONASS or GPS/BDS). However, three-system combined PPP with GPS/GLONASS/BDS has not been discussed in the literature until now. Whether three-system combined PPP can shorten the convergence time and improve the positioning accuracy of PPP is an important problem worthy of study and discussion.

This study introduces a single-differenced (SD) between-satellite PPP model which can process any single-system or multi-system GNSS (GPS/GLONASS/BDS) raw dual-frequency carrier phase measurements. In this model, the GPS satellite with the highest elevation is selected as the reference satellite to form the SD between-satellite measurements. Thus the GPS receiver clock offset is canceled and only a system time offset between GPS and other GNSS system is estimated for the observations of GLONASS or BDS. In the proposed model, noisy pseudorange measurements are ignored thus modeling the pseudorange stochastic model is not required. The stochastic model for SD measurements and states can be easily realized by mapping that for undifferenced measurements and states. Based on the post-processing BDS orbit and clock products from Wuhan University GNSS Center (WHU) and GPS/GLONASS products from ESA, and the multi-GNSS observations from MGEX project of IGS and CUTIN university, this contribution aims at investigating the effect of add BDS observations on the positioning performance of GNSS PPP. Also in which, the positioning results of single-system PPP, GPS/GLONASS, GPS/GLONASS/BDS multi-GNSS PPP are compared. In the following sections, the single-differenced-between-satellite PPP algorithm for dual-frequency single and multi-GNSS systems is presented. Then experimental design and data processing strategy are described in Sect. 23.3. In Sect. 23.4, numerical results are presented and analyzed.

23.2 Method

For a satellite s observed by receiver r, the pseudorange and carrier phase observations can be expressed as:

$$P_{r,j}^{s,G} = \rho_r^s + c\left(dt_r^G - dt^{s,G}\right) + T^{s,G} + I_{r,j}^{s,G} + B_{r,j}^G - B_j^{s,G} + e_{r,j}^{s,G} \tag{23.1}$$

$$L_{r,j}^{s,G} = \rho_r^s + c\left(dt_r^G - dt^{s,G}\right) + T^{s,G} - I_{r,j}^{s,G} + \lambda_j^G\left(N_{r,j}^{s,G} + b_{r,j}^G - b_j^{s,G}\right) + \varepsilon_{r,j}^{s,G} \tag{23.2}$$

where G refers to a satellite system (GPS/GLONASS/BDS, etc.); the subscript $j(=1, 2)$ refers to a given frequency; ρ is the geometric distance; c is the speed of light; dt_r and dt^s are the clock errors of receiver and satellite, respectively; T is the slant troposphere delay; $I_{r,j}^s$ is the slant ionospheric delay at the j frequency; N is the integer ambiguity; $b_{r,j}$ and b_j^s are the receiver-dependent and satellite-dependent uncalibrated phase delays (UPD) at the j frequency, respectively; λ_j is the wavelength of the frequency j; $B_{r,j}$ is the signal delay from receiver antenna to the signal correlator in the receiver; B_j^s is signal delay from satellite signal generation to signal transmission from satellite antenna; e is the pseudorange measurement noise; ε is measurement noise of carrier phase.

23.2.1 A Simple Review on Undifferenced PPP Model

Ionosphere-free combination observables are normally used in PPP to eliminate the first-order ionospheric delays in the pseudorange and carrier phase measurements. The undifferenced ionosphere-free GPS PPP model has been well presented and discussed in detail by many authors such as Kouba and Héroux [1], Zumberge et al. [2]. Furthermore, one can refer to Cai and Gao [12], Li et al. [11] for a clear study on the undifferenced ionosphere-free combined GPS/GLONASS, GPS/BDS PPP model, including both functional and stochastic components.

In undifferenced PPP, the pseudorange should be assigned with an appropriate weight to separate the receiver clocks and the ambiguities, especially for GLONASS. As reported by Cai and Gao [12], the GLONASS code observation residuals are about twice as large as those of GPS, caused by GLONASS satellite-dependent code hardware delay and errors in the GLONASS precise products. Hence, they empirically assign about half the weights of GPS code observations to GLONASS code observations to weaken the effect of larger GLONASS code observation residuals on the positioning results. How to suitably model the code observation to mitigate the impact of multipath, code hardware delay is still a research question to high-precision PPP.

Moreover for combined PPP model with multi-GNSS observations, instead of estimating a receiver clock parameter for each satellite system observation, it is preferable to introduce a system time difference parameter as it can reflect the

difference between different system times. Therefore a receiver clock error for GLONASS and BDS can be described as follows, when they are integrated with GPS:

$$dt_r^{GLO} = dt_r^{GPS} + dt_{r\_sys}(GPS - GLO) \tag{23.3}$$

$$dt_r^{BDS} = dt_r^{GPS} + dt_{r\_sys}(GPS - BDS) \tag{23.4}$$

where $dt_{r\_sys}(GPS - GLO)$ is the GPS-GLONASS system time difference while $dt_{r\_sys}(GPS - BDS)$ denotes the GPS-BDS system time difference.

23.2.2 Functional Model of Single-Difference Between-Satellite PPP

In fact, for most applications except for time transfer [14], the receiver clock offsets are often not of concern and can be ignored. Therefore, we apply the single-difference between-satellite on the undifferenced ionosphere-free carrier phases to eliminate the GPS receiver clocks errors and the receiver-dependent uncalibrated phase delays (UPD) [15]. In this SD model, no epoch-wise receiver clock parameter need to be estimated in single-system PPP because the receiver clock offset is eliminated. While in multi-system PPP the system time offset between GPS and GLONASS is estimated for the GLONASS observations and that between GPS and BDS is estimated for the BDS observations. In this case we do not need pseudorange measurements to separate the receiver clocks and the ambiguities so that we do not need to rigorously model the pseudorange measurements.

Specifically, our PPP algorithm implementation is based on a Kalman-filter. The filter processes SD ionosphere-free linear combinations of carrier phase measurements. The satellite with healthy observations and the highest elevation is selected as the reference for single-system PPP. However, for multi-GNSS PPP involving GPS, the GPS satellite with healthy observations and the highest elevation is selected as the reference. Assuming m satellites were simultaneously tracked by receiver r, then the linearized equations for the undifferenced carrier phase observation of all satellites can be formed as follows:

$$\underset{m\times 1}{y} = \underset{m\times(m+6)}{A} \cdot \underset{(m+6)\times 1}{x} + \underset{m\times 1}{\varepsilon_y}, \quad \varepsilon_y \sim N\left(0, Q_{yy}\right) \tag{23.5}$$

$$x = \left[X, Y, Z, ZWD, dt_{r\_sys}(GPS - GLO), dt_{r\_sys}(GPS - BDS), N_{if}^s\right]^T \tag{23.6}$$

SD measurements can be easily formed by mapping that of undifferenced measurements using the transformation matrix. With this method, the correlation of the SD measurements is also considered. The unknown vector in the PPP includes three position coordinate, a wet zenith tropospheric delay (ZWD), two system time

offset $dt_{r\_sys}(GPS - GLO)$ and $dt_{r\_sys}(GPS - BDS)$ (fixed to zero if no observation from corresponding satellite system) and the undifferenced float ambiguities N_{if}^{s}, where $s = 1 \ldots m$. The quantity Q_{yy} takes the form of a diagonal matrix with its diagonal elements $Q_{ii} = \sigma_0^2 / \sin^2(E_r^s)$, E_r^s is the elevation angle of each satellite and σ_0 is the standard deviation of the GNSS observation at zenith.

23.2.3 Stochastic Model of Single-Difference Between-Satellite PPP

The Extended Kalman Filter (EKF) is utilized in the parameter estimation, and the corresponding dynamic model can be denoted as:

$$x(i+1) = \Phi_{i+1,i} \cdot x(i) + \omega(i), \quad \omega \sim N(0, Q_{\omega\omega}) \tag{23.7}$$

$\Phi_{i+1,i}$ is the corresponding transition matrix, ω is the normally-distributed process noise with zero-mean and variance-covariance (VC) matrix $Q_{\omega\omega}$. The matrix $Q_{\omega\omega}$ can be denoted as:

$$Q_{\omega\omega} = diag\left\{ q_p \cdot \Delta t, q_{zwd} \cdot \Delta t, q_{t(GPS/GLO)} \cdot \Delta t, q_{t(GPS/BDS)} \cdot \Delta t, \underset{m \times m}{0} \right\} \tag{8}$$

where Δt is the time interval between adjacent epochs. For the Kalman filter, the spectral density values for the ZWD and the system time difference parameter are empirically set to $q_{zwd} = 10^{-8}$ m^2/s and $q_{t(GPS/GLO)} = q_{t(GPS/BDS)} = 10^{-6}$ m^2/s, respectively. The ambiguity parameters and static position coordinates are considered as constants. But in kinematic mode, the kinematic position coordinates are modeled as white noise and the diagonal element of q_p is 10^4 m^2/s. The initial standard deviation values for phase observations of three GNSS systems are all set to 0.003 m. During the filtering, the state vector is predicted from the previous epoch to the current epoch using a system model. The state vector and the associated covariance matrix are then resolved with the observations in the measurement update process.

23.3 Data Processing and Experimental Strategy

GNSS measurements recorded in 30-s intervals from about 10 stations observed during DOY 264 to 270 in 2013 are used in this study (Table 23.1). Precise final GPS/GLONASS satellite orbit and clock corrections are provided by the European Space Agency (ESA) while the final BDS orbits and clock products are provided

Table 23.1 The information of stations

Site	Lat (°)	Lon (°)	Receive type	Antenna type	Agency
CUAA	−32.0	115.9	JAVAD TRE_G3T DELTA	TRM59800.00 SCIS	Curtin Univ
CUBB	−32.0	115.9	JAVAD TRE_G3T DELTA	JAV_GRANT-G3T NONE	Curtin Univ
CUT1	−32.0	115.9	SEPT POLARX4	TRM59800.00 SCIS	Curtin Univ
CUT2	−32.0	115.9	TRIMBLE NETR9	TRM59800.00 SCIS	Curtin Univ
CUT3	−32.0	115.9	JAVAD TRE_G3T DELTA	TRM59800.00 SCIS	Curtin Univ
GMSD	30.6	131.0	TRIMBLE NETR9	TRM59800.00 SCIS	IGS
JFNG	30.5	114.5	TRIMBLE NETR9	TRM59800.00 NONE	IGS
KZN2	55.8	49.1	TRIMBLE NETR9	TRM59800.00 SCIS	IGS
NNOR	−31.0	116.2	SEPT POLARX4	SEPCHOKE_MC NONE	IGS
REUN	−21.2	55.6	TRIMBLE NETR9	TRM55971.00 NONE	IGS

by Wuhan University GNSS Research Center. We also apply the absolute antenna phase centers model [16]. The 'antex' file generated and released by the International GNSS Service (IGS) which includes Phase Center Offset (PCO) and Phase Center Variation (PCV) corrections information for both satellites and receivers are used for precise data processing. It should be mentioned that only a preliminary PCO of BDS satellites is available for BDS from IGS, therefore, PCO and PCV corrections cannot be corrected for BDS observations accurately. The elevation cut-off angle is set to 7°.

For each station, the 24 h dataset is divided into 8 sessions, so each session is 3 h. This length of data should be long enough to ensure the convergence of the position solutions in most cases. The processing results of the first 90 min of observations are mainly used for analyzing the convergence time, while the results of the second 90 min of observations are mainly used for analyzing the positioning accuracy. In this study, "convergence" means "obtaining a 3D positioning error less than 1 dm". The positioning error is just the difference of the position solution and the true coordinate benchmarks from IGS weekly solution. We also check the errors of 20 epochs after. Only when the errors of all 20 epochs are within the limit, we consider the position has converged in this epoch [13].

23.4 Experimental Results and Analysis

In total there are about 560 positioning tests used in the experiment. The positioning performance of single- and multi-system PPP is analyzed based on different processing models, namely GPS-only, GLONASS-only, BDS-only, combined GPS/GLONASS, combined GPS/BDS and combined GPS/GLONASS/BDS PPP.

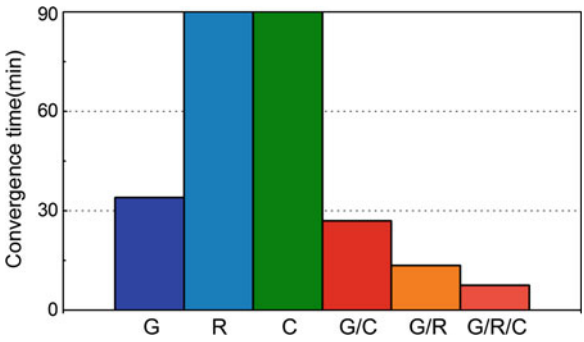

Fig. 23.1 Convergence time of kinematic PPP for the observations of the 3rd session from station REUN on DOY 264, 2013

23.4.1 The Convergence Speed Results

The forward-Kalman-filter PPP is applied to all 3-h-long observations in both the static and kinematic mode. The convergence time of each solution is recorded.

First we take the kinematic PPP results of the 3rd session from REUN station on DOY 264, 2013 as a typical example to compare the convergence time of six processing models. Details are given in Fig. 23.1. We can find that over 90 min are required to achieve the convergence for GLONASS-PPP and BDS-PPP, while only 34.0 min are needed for GPS-PPP. Compared with GPS-PPP, the convergence time is reduced by 7 min in GPS/BDS PPP while compared with GPS/GLONASS-PPP; the convergence time is reduced by 6 min in GPS/GLONASS/BDS PPP. Hence a faster convergence speed is achieved by adding BDS observation.

Figure 23.2 shows the average convergence time of kinematic PPP on each day over all test stations. For each PPP model, the average convergence time shows a good agreement over days. There are no significant daily variations in the average convergence time. The average convergence time of static PPP also had the same rule. Similar phenomenon can be also found in static PPP.

Statistical results of the convergence time for all observations are plotted in Fig. 23.3 for static and kinematic PPP. As can be seen, in static mode, the average convergence time is 25.7 min for GPS-PPP, which is obviously shorter than that of GLONASS-PPP and BDS-PPP. For GPS-PPP, the convergence time can be further reduced by 10.5 % by adding BDS observation and by 38.9 % by adding GLONASS observation. A shortest convergence time of 15.0 min is achieved by three-system PPP. Compared with that of GPS/GLONASS PPP, the convergence time is further improved by 4.5 % after adding BDS observations. Owing to a relatively weaker model, the average convergence time of kinematic PPP is significantly longer than that of static PPP, for single- and multi- system solutions. The statistical results of kinematic PPP are as follows: The average convergence time is 45.1 min for GPS PPP while 39.6 min for GPS/BDS PPP. It is reduced significantly by 12.2 % after adding BDS observations. The average convergence time is 20.7 min for GPS/GLONASS PPP while 19.3 min for GPS/GLONASS/

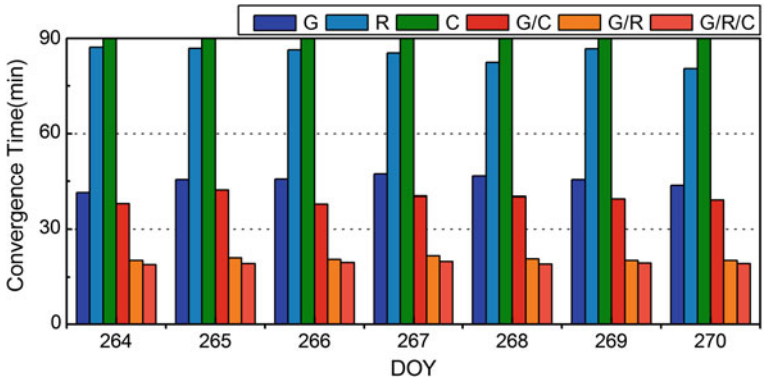

Fig. 23.2 Average convergence time of kinematic PPP per day

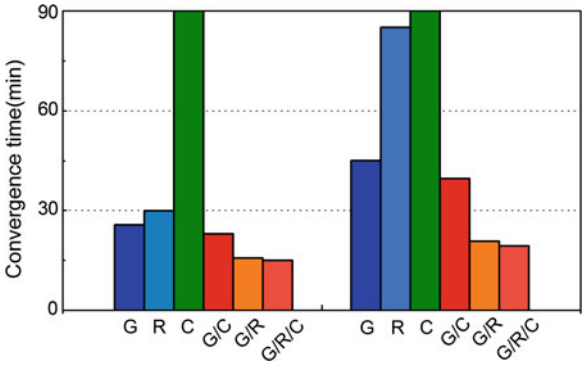

Fig. 23.3 Average convergence time of static (*left*) and kinematic (*right*) PPP

BDS PPP. It is reduced further by 6.8 % with BDS observations combined. As shown, the overall convergence time is reduced more significantly compared to static PPP. This is because adding BDS observations leads to enhancement of strength of geometry and redundancy in kinematic PPP.

As we know, PPP solutions are sensitive to satellite orbit and clock products and the error correction model. Currently, the Beidou orbit and clock products from WHU have a lower accuracy than GPS/GLONASS products from ESA. Moreover, PCO and PCV, one of the major error sources, cannot be corrected accurately for BDS observations. Therefore, the convergence time of BDS-PPP is longer than GPS-PPP and GLONASS-PPP and compared with GLONASS, BDS has a smaller contribution to rapid convergence to combined PPP in current situation.

Table 23.2 Average RMS of all tests in east, north and up directions for static PPP (cm)

	G	R	C	G/C	G/R	G/R/C
E	1.5	3.0	9.8	1.5	0.9	0.9
N	0.6	1.1	5.5	0.6	0.5	0.5
U	1.6	2.5	17.0	1.6	1.5	1.4

23.4.2 The Positioning Accuracy Results

In this part, the positioning accuracy of single- and multi-system PPP solutions is compared. We have calculated the root mean square (RMS) values of the positioning biases over all sessions. For static PPP, as shown in Table 23.2, the average RMS of conventional GPS-PPP solution is only 1.5, 0.6 and 1.6 centimeters in the east, north and up directions, respectively. The highest positioning accuracy is achieved by three-system PPP. We find that it has nearly no impact on the positioning accuracy whether adding BDS observation or not. This is because that the model strength of static PPP is strong enough so that the effect of the low-precision BDS observation can be negligible. A higher positioning accuracy is expected if exact PCO and PCV information is provided for BDS and precise clock offset and orbit of BDS satellites are routinely provided with a precision of several centimeters.

For kinematic PPP, we first take the 3-h-long observation of the 1st session from CUT2 station on DOY 264, 2013 as a representative example to analyze the positioning performance of different PPP models. The epoch-wise coordinate biases in three directions are plotted in Fig. 23.4. The bias in up direction gets larger from 300th to 360th epoch for GLONASS PPP. Only a dm-level positioning accuracy can be obtained by BDS-PPP. The positioning bias of GPS-PPP is relatively smaller and stable compared with GLONASS-PPP and BDS-PPP. Combining multi-GNSS observations, a more stable and accuracy positioning results can be obtained. Furthermore, the epoch-wise 3D coordinate biases are given in Fig. 23.5. It clearly shows that, BDS observation can contribute to improving positioning accuracy, no matter combined with GPS or GPS/GLONASS. The best positioning results with a precision of 2–3 cm is achieved by GPS/GLONASS/BDS PPP.

We have calculated the average RMS of all sessions; see Table 23.3. Comparing GPS-PPP and GPS/BDS-PPP, we find that the RMS can be improved by 14.3, 7.1 and 7.5 % in east, north and vertical directions after BDS observation is involved in the processing. Besides, Comparing GPS/GLONASS-PPP and GPS/GLONASS/BDS-PPP, we can find that the RMS can be further improved by 11.1, 16.7 and 6.5 % in three directions after BDS observation is involved in the processing. For each PPP model, the accuracy of the east component is considerably worse than that of the north component because that the integer ambiguity have not be correctly resolved. Generally speaking, the accuracy of the east component is lower than that of north component for a PPP float solution [17, 18].

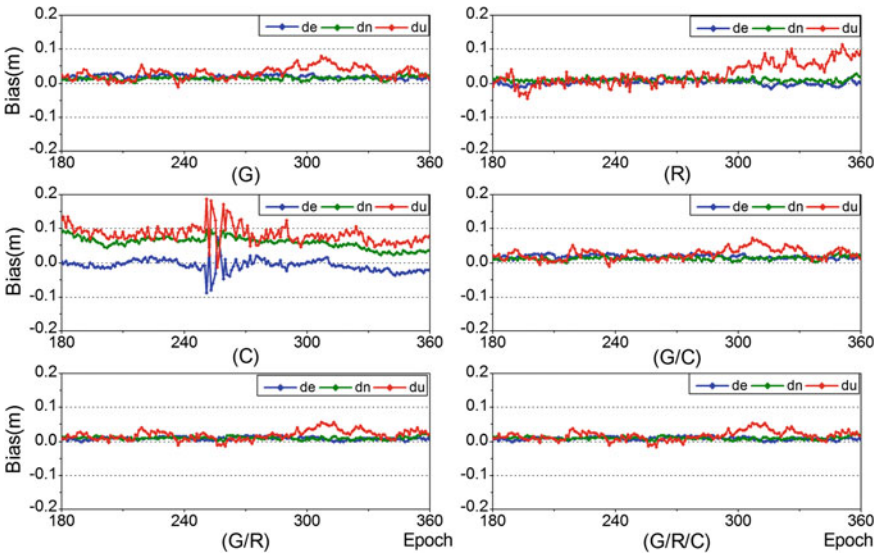

Fig. 23.4 Coordinate biases of kinematic PPP for the observations of the 1st session from station CUT2 on DOY 264, 2013, with different PPP models, in east, north and up directions, respectively

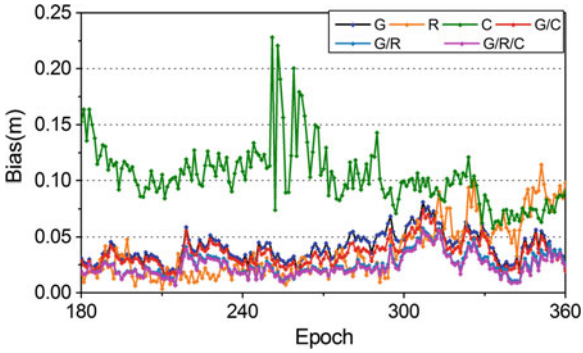

Fig. 23.5 3D coordinate biases of kinematic PPP for the observations of the 1st session from station CUT2 on DOY 264, with different PPP models

Table 23.3 Average RMS of all tests in east, north and up directions for kinematic PPP (cm)

	G	R	C	G/C	G/R	G/R/C
E	2.8	16.5	26.1	2.4	1.8	1.6
N	1.4	6.7	14.3	1.3	1.2	1.0
U	4.0	21.6	37.1	3.7	3.1	2.9

23.5 Conclusions and Remarks

This study introduces a single-differenced between-satellite precise point positioning model which can process single or multiple system GNSS (GPS/GLONASS/BDS) raw dual-frequency carrier phase measurements. Based on the BDS products from WHU and GPS/GLONASS products from ESA, about 560 3 h-long datasets have been used in the numerical analysis and the positioning results of single- and multi-GNSS PPP are reported. The main conclusions are as followed:

1. Adding BDS observations can contribute to accelerating the convergence speed of PPP. The convergence time can be reduced by 10–12 % for GPS PPP, and reduced by about 5–7 % for GPS/GLONASS PPP further, after adding BDS observation. A shortest convergence time is achieved by three-system PPP.
2. BDS observations can contribute to improving the accuracy of kinematic PPP with 3 h observations. After adding BDS observations, the RMS in kinematic mode is improved by 14.3, 7.1 and 7.5 % for GPS PPP while 11.1, 16.7 and 6.5 % for GPS/GLONASS PPP, in the east, north and up directions, respectively. For GPS/GLONASS/BDS PPP, an accuracy of 1–2 cm in horizontal and 2–3 cm in vertical can be achieved in kinematic mode while an accuracy of less than 1 cm in horizontal and 1–2 cm in vertical can be achieved in static mode.

The performance of multi-GNSS PPP is expected to be further improved with more accuracy of precise products and exact PCO and PCV information provided for BDS in future.

Acknowledgments This study was supported by National 973 Project China (Grant No. 2013CB733301) and National Natural Science Foundation of China (Grant No. 41074024, No. 41204030) and the Fundamental Research Funds for the Central Universities (No.: 2012214020207). Thanks to GNSS Research Center of Wuhan University for providing the BDS orbit and clock products, ESA for providing the GPS/GLONASS orbit and clock products. The authors also thank IGS-MGEX and Curtin University for providing the Multi-constellation GNSS data.

References

1. Kouba J, Héroux H (2001) Precise point positioning using IGS orbit and clock products. GPS Solutions 5(2):12–28
2. Zumberge J, Heflin M, Jefferson D, Watkins M, Webb F (1997) Precise point positioning for the efficient and robust analysis of GPS data from large networks. J Geophys Res 102(B3):5005–5017
3. Gendt G, Dick G, Reigber C, Tomassini M, Liu Y, Ramatschi M (2004) Near real time GPS water vapor monitoring for numerical weather prediction in Germany. J Meteorol Soc Japan. Ser. II 82(1B):361–370
4. Rocken C, Johnson J, Van Hove T, Iwabuchi T (2005) Atmospheric water vapor and geoid measurements in the open ocean with GPS. Geophys Res Lett 32(12):L12813

5. Calais E, Han JY, DeMets C, Nocquet JM et al (2006) Deformation of the North American plate interior from a decade of continuous GPS measurements. J Geophys Res 111:B6402
6. Hammond WC, Thatcher W (2005) Northwest basin and range tectonic deformation observed with the global positioning system, 1999–2003. J Geophys Res Solid Earth 110(B10405B10)
7. Zhang XH, Li P, Guo F (2013) Ambiguity resolution in precise point positioning with hourly data for global single receiver. Adv Space Res 51(1):153–161
8. Yang YX, Li JL, Xu JY, Tang J, Guo HR, He HB (2011) Contribution of the Compass satellite navigation system to global PNT users. Chin Sci Bull 56(26):2813–2819. doi:10.1007/s11434-011-4627-4
9. Shi C, Zhao QL, Li M, Tang WM, Hu ZG, Lou YD, Zhang HP, Niu XJ, Liu JN (2012) Precise orbit determination of Beidou satellites with precise positioning. Sci China Earth Sci 55(7):1079–1086
10. Liu Y, Lou Y, Shi C et al (2013) BeiDou regional navigation system network solution and precision analysis. In: Proceedings of the 4th China satellite navigation conference (CSNC), Wuhan, China, 15–17 May 2013
11. Li W, Teunissen PJG, Zhang B, Verhagen S (2013) Precise point positioning using GPS and Compass observations. In: Proceedings of the 4th China satellite navigation conference (CSNC), Wuhan, China, 15–17 May 2013
12. Cai C, Gao Y (2013) Modeling and assessment of combined GPS/GLONASS precise point positioning. GPS Solutions 17(2):223–236
13. Li P, Zhang XH (2013) Integrating GPS and GLONASS to accelerate convergence and initialization times of precise point positioning. GPS Solutions. doi:10.1007/s10291-013-0345-5
14. Defraigne P, Baire Q (2011) Combining GPS and GLONASS for time and frequency transfer. Adv Sp Res 47(2):265–275
15. Blewitt G (1989) Carrier phase ambiguity resolution for the global positioning system applied to geodetic baselines up to 2000 km. J Geophys Res 94(B8):10187–10203
16. Rebischung P, Griffiths J, Ray J, Schmid R, Collilieux X, Garayt B (2012) IGS08: the IGS realization of ITRF2008. GPS Solutions 16(4):483–494
17. Ge M, Gendt G, Rothacher M, Shi C, Liu J (2008) Resolution of GPS carrier-phase ambiguities in precise point positioning (PPP) with daily observations. J Geodesy 82(7):389–399
18. Zhang XH, Li P (2013) Assessment of correct fixing rate for precise point positioning ambiguity resolution on global scale. J Geodesy 87(6):579–589

Chapter 24
Fitting Method and Accuracy Analysis of Broadcast Ephemeris in Hybrid Constellation

Feng He, Xiaogong Hu, Li Liu, Huang Hua, Shanshi Zhou, Shan Wu, Li Gu, He Zhao and Xiao Liu

Abstract Broadcast ephemeris parameter is an important reflection of navigation system service performance. In hybrid constellation, GEO, IGSO and MEO satellites have different dynamic characteristics which lead to different fitting performances. In this article, the basic physical meaning of ephemeris parameters are analyzed, and the evaluation for the variation characteristics of fitting parameters is carried on. Several improved algorithms are proposed from the aspect of mathematical processing, which effectively eliminates the unsuitability in the parameter fitting of GEO. The fitting accuracy of 3 types of satellites are analyzed based on the 16-parameter model, and then the evaluation of fitting performance is completed. It is proved in the experiments: the high accuracy can be realized for the 3 types of satellites, and even the accuracy is prior to 1 cm for most time. For GEO, the accuracy can be sub-centimeter, while the accuracy can be millimeter for IGSO and MEO satellites. In summary, the 16-parameter model is enough to meet the centimeter level application requirement.

Keywords Hybrid constellation · Ephemeris fitting · Biased estimate · Satellite navigation

F. He (✉) · L. Liu · H. Hua · S. Wu · L. Gu · H. Zhao · X. Liu
Beijing Satellite Navigation center, Beijing 100094, China
e-mail: hefeng@shao.ac.cn

X. Hu · S. Zhou
Shanghai Astronomical Observatory, Chinese Academy of Sciences, Shanghai 200030, China

J. Sun et al. (eds.), *China Satellite Navigation Conference (CSNC) 2014 Proceedings: Volume III*, Lecture Notes in Electrical Engineering 305,
DOI: 10.1007/978-3-642-54740-9_24,

24.1 Introduction

Ephemeris parameters are approximation to precision orbit, which can be obtained by analytical solution and numerical fitting. The accuracy of ephemeris is determined by precision orbit, and it is also related to the fitting algorithm, communication transmission capacity and user algorithm. As regard to satellite navigation system, taking different types of satellites into consideration, the designed suitable satellite ephemeris model and fitting algorithm are necessary for the improvement of navigation service performance.

Among all the satellite navigation systems [1], the kepler roots model is applied in GPS which includes the reference epoch t_{oe}, 6 kepler root parameters, 6 short-period amplitude harmonic correction items, and 3 long-period correction items. For GLONASS, a satellite position-velocity-acceleration parameter based model is applied for ephemeris parameter model.

The kepler roots based ephemeris parameter model has a characteristic of clear physical meaning, so it is applied in most navigation systems. There have been some results for the model application in domestic researches. The strategy of rotation coordinate plane is proposed [2–5], with which the singularity caused by low inclination angle is solved. The non-singularity roots based fitting method is studied [6], with which the singularity brought by low eccentricity is eliminated. The Inversion method with QR decomposition is given for the improvement of ill-conditioned equation [7]. Besides, the 18-parameter model is studied which is designed in the new signal of GPS [8, 9], and the differences between the 2 models (16&18) is analyzed which gives an important reference information for the ephemeris parameters application. Since the ephemeris parameter model is designed for MEO satellite in GPS, the unsuitability may exist when the model is applied to GEO and IGSO satellites. Thus, the improvement for the fitting algorithm should be studied while the ephemeris parameters fitting accuracy also need to be evaluated.

In this article, the comprehensive analysis for ephemeris parameter application performance is carried on including the ephemeris parameter meaning, fitting algorithm and fitting accuracy. The basic dynamic meaning of ephemeris parameters is described and the concentrated explanation for short-term perturbation parameters and long-term perturbation parameters is made. 2 types of improved ephemeris fitting algorithms are proposed, with which the parameter fitting unsuitability of GEO satellites is eliminated. The fitting performance for 3 types of satellites is analyzed, and the optimal fitting strategies is deduced, while the comprehensive evaluation for ephemeris model is realized.

24.2 Basic Meaning of Broadcast Ephemeris Parameters

The ephemeris parameter model consists of kepler roots and perturbation variation parameters, in which every parameter has certain physical background. Though can not make a full description for the perturbed motion of satellite, the 16-

parameter model has a certain consistency to the laws of physics, and the physical meaning for parameter design is as following.

$(\sqrt{A}, e, i_0, \Omega_0, \omega, M)$ are kepler root parameters, and they approximately be the same as the mean root of reference epoch (Ω_0 need to be imputed to the start epoch of the week). Based on the parameters, the orbit roots or position-velocity parameters in any time can be calculated with the perturbation variation parameters mentioned in the following part of the article. (C_{rs}, C_{rc}, C_{us}, C_{uc}, C_{is}, C_{ic}) are amplitude of short-period correction items, and the corresponding correction argument is $2\Phi_k$, the short-period correction in ephemeris user algorithm equation is given below.

$$\begin{aligned} \delta u_k &= C_{us} \sin 2\Phi_k + C_{uc} \cos 2\Phi_k \\ \delta r_k &= C_{rs} \sin 2\Phi_k + C_{rc} \cos 2\Phi_k \\ \delta i_k &= C_{is} \sin 2\Phi_k + C_{ic} \cos 2\Phi_k \end{aligned} \tag{24.2.1}$$

The short-period corrections are not designed every orbital root in ephemeris parameters, instead, the correction is designed for the trace argument u, radial distance r and orbital inclination angle i. The short-period amplitude parameters number will reach 12 if the corrections are designed for every orbital root, and the overmuch parameters will bring bad influence to fitting computation.

All the short-period items can be imputed to three-axis, and that are the direction of R, T and N. The correction of distance r is equal to that of radial direction R, the correction of trace argument u is equal to that of tangential direction T, the correction of inclination angle i is equal to that of normal direction N, so 6 parameters can complete the expression of orbital short-period items which can meet the requirement of accuracy and limited communication resources. Only the main short-period item is absorbed by the short-period correction items in ephemeris, and the rest periodic items are left in the other parameters.

Δn is the correction of average angular velocity, M and ω can not be solved separately in fitting since they have a high correlation which caused by the low eccentricity of navigation satellite, so the long-term correction can be expressed by one parameter. From the aspect of ephemeris parameters design, the long-term correction and long-period correction of M and ω are absorbed by Δn, while the long-term correction and long-period correction of Ω are absorbed by $\dot{\Omega}$, and the long-period correction of *idot* is absorbed by i.

As the same situation of short-period correction parameters, the corrections of long-term and long-period are equal to the corrections on the three-axis, among which Δn is the correction of trace direction, *idot* and $\dot{\Omega}$ are the correction of orbital plane swing direction. The radial long-period variability can be ignored when the fitting arc is short, so there is not radial long-period correction in 16-parameter model. At last, the meaning of all parameter is obvious, and that can make a good description for satellite orbit.

Table 24.1 Statistics table for ephemeris fitting parameters results

Parameter	Min value/Max value			Over-exceeding (%)
	GEO	IGSO	MEO	
URE	2.440E−2	1.665E−3	8.519E−3	–
	6.135E−2	9.953E−2	6.624E−2	
Δn	−2.477E−9	1.923E-11	9.636E-10	G:2.4 I:0 M:0
±3.7e−9	4.841E−9	9.285E-10	1.372E-9	
	−2.488E−9			**G:2.6 I:0 M:0**
	4.956E−9			
idot	−3.064E−10	−4.479E−10	−1.083E−10	0
±9e−10	3.029E−10	5.344E−10	2.615E−10	
C_{rc}	−1.347E3	−1.016E3	8.755E1	0
±2048	1.283E3	5.402E2	3.667E2	
C_{rs}	−1.287E3	−1.752E2	−2.301E2	0
±2048	1.379E3	9.597E2	6.980E1	

24.3 Improved Methods of Broadcast Ephemeris Parameters Fitting

There is potentially inadaptability when the 16-parameter model is applied to GEO and IGSO satellites because it is originally designed for MEO. The algorithm improvement can be taken into consideration from the aspects of fitting strategy and fitting standard, and that will contribute to high precision fitting results.

24.3.1 Analysis of Parameter Variation Range

The continuous 6-month ephemeris parameter variation result for GEO, IGSO, and MEO is depicted in Table 24.1 with real satellite orbit data, among which the bold represents the fitting result of 3-hour-arc, and the rest is for the result of 4-hour-arc. The fitting URE (User Range Error) is computed, while the minimum value and maximum value of some parameters are given as well as the interface range in GPS ICD document and percentage of parameter's exceeding interface range.

According to the fitting result of the 3 types of satellites above, for GEO satellite, the parameters with wide variation range include *idot*, C_{rc}, C_{rs} and Δn, and the interface ranges are enough for most computed parameter(the redundancy is more than 50 %) except the parameter of Δn. For IGSO and MEO satellites, though there are still some parameters which also have wide variation range, the interface is enough for every parameter and the redundancy is evident (more than 50 %). In short, the parameter interface range is completely available for IGSO and MEO, but there is possibility of exceeding interface range for GEO parameters.

24.3.2 Adjustable Arc and Bias Estimate Based Algorithm

The ridge evaluation is a kind of important biased estimate method, and it can reduce the ill-condition of equation while compressing the value of parameter. Thus, the parameter can be controlled in the interface range as well as meeting the fitting accuracy standard.

In ephemeris fitting, the observation equation for least squares adjustment is:

$$V = AX + L \tag{24.3.1}$$

Where the vector of observation is:

$$L = (x_1, y_1, z_1, x_2, y_2, z_2 \ldots, x_n, y_n, z_n)$$

The vector of solved parameter is:

$$X = (A^T PA)^{-1} A^T PL \tag{24.3.2}$$

The vector of X is:

$X = (\sqrt{a}, e, i_0, \Omega_0, \omega, M, \Delta n, \dot{\Omega}, idot, C_{rs}, C_{rc}, C_{us}, C_{uc}, C_{is}, C_{ic})$, which includes 15 parameters, V is the vector of observation residuals, A is the coefficient matrix, and P is the observation weight matrix.

The normal matrix is $N = (A^T PA) + PX$. Among which, A and P are the same meaning as in formula (24.3.2), PX is the added weight matrix for parameter compressing. Suppose the parameters which are highly related to the range-exceeded parameter have the number of i, j, k in the vector, and $PX_i, PX_j, PX_{\mathrm{k}}$ are respectively the i, j, k element in the diagonal of the matrix, while the other elements are all zero in PX. Thus, the parameters of i, j, k in vector of X can be compressed. In the computation of ephemeris fitting, the range-exceeded parameter should be fixed below the range, and the biased estimate strategy is carried on with the fitting arc of 3 and 4 h. The standard for the ridge weight selecting depends on the requirement of fitting accuracy, for which the weight is given from 2^2 to 2^{10} until the accuracy is meet. The experiment is done for GEO satellite, and the result is showed in Figs. 24.1, 24.2.

According to the fitting result, the value of Δn is controlled below the interface range through fixing parameter and compressing with ridge evaluation when Δn exceeds the interface range. It proves that the method combining adjusting arc length and biased estimate is effective for eliminating the phenomena of parameter's exceeding the interface range.

24.3.3 URE Criterion Based Ephemeris Fitting Algorithm

The least square adjustment is carried out under the criterion of minimum 3D (direction) position error according to the current algorithms, but as regard to

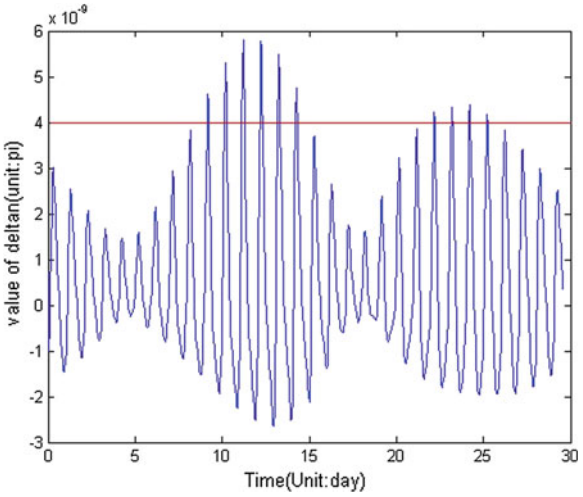

Fig. 24.1 Value of Δn for the previous algorithm

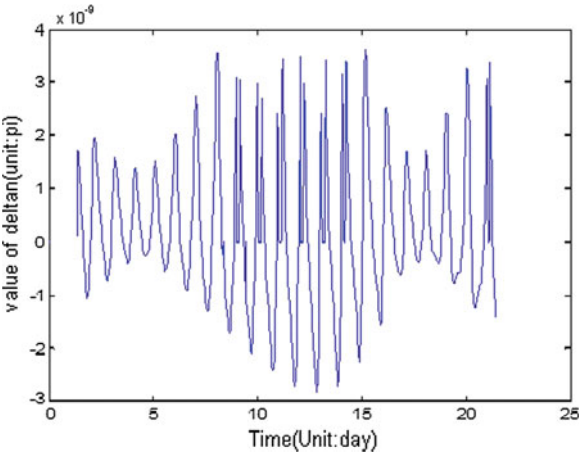

Fig. 24.2 Value of Δn for the new algorithm

satellite navigation system, the most influenced factor for user is the radical error of the orbit, or URE. For ephemeris fitting, it means that minimum 3D position fitting error can not be equal to the minimum URE fitting error, and the criterion of minimum URE is more consistent with the application requirement of user. Therefore, it is necessary to adjust the criterion for ephemeris fitting.

There is a projection relation from satellite position error to different directions in orbital coordinate system, according to which the formula of getting URE from different projection errors is given below.

$$URE_{\text{err}} = \sqrt{1.0 \times \Delta \mathrm{R}^2 + 0.09 \times (\Delta T^2 + \Delta N^2)} \tag{24.3.3}$$

In the formula, it is obvious that the radial projection error has the largest weight in URE while the other two errors have relatively little weights, because of which the observations of R, T, N should be granted different weights in the process of adjustment, and then the little error brought to direction of R can lead to the result which have a lower URE fitting error.

The adjusted criterion algorithms is showed below.

The least square adjustment observation formula for ephemeris fitting is given by

$$V = AX + L \tag{24.3.4}$$

hence:

$$L = -AX + V \tag{24.3.5}$$

where L is CTS (Conventional Terrestrial System) coordinate vector, X is parameter vector which need to be solved.

After coordinate transformation for both sides of the formula, then

$$G \times L = G \times (-AX + V) \tag{24.3.6}$$

New observation formula after rotation is given by

$$V' = A'X + L' \tag{24.3.7}$$

where A' is the new coefficient matrix, L' is the new orbital coordinate observation vector (R_1, T_1, N_1, R_2, T_2, N_2…, R_n, T_n, N_n), on this condition, the obtained parameter solution is

$$X = (A'^T P' A')^{-1} A'^T P' L' \tag{24.3.8}$$

where P' is the new weight matrix of observation vector, the error controlling of 3D position can be realized through the adjustment of weight in the matrix. It is more consistent to achieve the goal of minimum URE and realize the optimal controlling for the solution with the strategy of setting larger weight for the element of R.

The experiments of ephemeris fitting with new algorithms are carried out based on the real POD data of GEO during the fitting failure period, and the direction of R, T and N are granted different weight values, in which the weight value of R is set as n × 100 (n from 1 to 10), while the weight value of T and N are both set as 1. The circulation computing is proceed until the solution meet the requirement of accuracy, and the result of new algorithm and old algorithm are depicted in Table 24.2.

According to the experiment result, there is obvious increasing iteration number in the process of the old algorithm. Though, all groups of ephemeris fitting

Table 24.2 Fitting result for different algorithms

Time	Iterations of original	Iterations of new
Time1	Divergence	18
Time2	36	11
Time3	38	12
Time4	86	15
Time5	45	11

efficiency is improved and the divergence is eliminated with the new URE criterion algorithm of parameter weighted assignment, and the result is qualified for the accuracy and computation efficiency.

24.4 Fitting Accuracy Analysis for Broadcast Ephemeris Parameter

In this section, the comprehensive evaluation for fitting accuracy of 3 types of satellites is carried out with the 16-parameter model.

24.4.1 Fitting Accuracy Analysis for Different Strategies

The fitting parameter is closely related to the satellite perturbation period since the ephemeris parameter is a approximate description for satellite orbit, so a long-time fitting result can lead to a comprehensive and objective evaluation. In the experiment, about 6 months' orbit data is adopted including GEO, IGSO and MEO satellites, while the fitting accuracy standard is set to be 0.05 m.

The statistic result of GEO, IGSO and MEO satellites is given in Table 24.3, and the fitting computation is carried out with the arc length of 2–5 h.

According to the fitting accuracy result for 3 types of satellites, all types of satellites have the possibility of exceeding the standard of 0.05 m, and the percentage for different satellites ranges from 0.25 to 82 %. When the fitting arc is adapted to 3 h, the fitting error can be controlled below 0.05 m.

For GEO satellite, the computation rapidly turns to be convergence with the fitting arc of 3 and 4 h though there is still some errors beyond the standard of 0.05 m. The iteration numbers for the arc of 2 and 5 h increase sharply, and the result can not meet the standard of 0.05 m. As regard to the reason for different fitting performances, the ephemeris parameters are an approximate description for satellite orbit, so the parameters are not enough for longer orbit arc while that will be redundant for shorter orbit arc. It is also proposed from the analysis that 3-hour-arc is the best program for GEO fitting, and the followed analysis is carried on based on 3-hour-arc for GEO.

Table 24.3 Statistics ephemeris fitting accuracy result for different types of satellites

Sat type	Arc	Average iterations	Min/Max (m)	Exceed percent (%)
GEO	2 h	27	4.394E−3 6.881E−1	2.5
	3 h	**12**	**1.313E−2 4.999E−2**	**0**
	4 h	12	2.440E−2 6.135E−2	0.25
	5 h	More than 80	1.044E−2 1.003E−1	55
IGSO	**2 h**	**3**	**1.164E−4 4.996E−2**	**0**
	3 h	**3**	**2.066E−4 4.993E−2**	**0**
	4 h	3	1.665E−3 9.953E−2	0.58
	5 h	More than 80	1.091E−3 2.734E−1	21
MEO	**2 h**	**3**	**1.601E−4 4.999E−2**	**0**
	3 h	**3**	**1.054E−3 4.998E−2**	**0**
	4 h	More than 80	8.519E−3 6.624E−1	12.8
	5 h	More than 80	1.532E−2 2.239E−1	82

For IGSO and MEO satellites, 2-hour-arc and 3-hour-arc are better for fitting accuracy. There are errors beyond 0.05 m when the arc turn out to be 4 h, while the result becomes bad on the condition of 5-hour-arc. In conclusion, 2 hour-arc and 3-hour-arc are the best strategy for MEO and IGSO satellites.

24.4.2 Ultimate Fitting Accuracy Analysis

In order to make some further analysis, the suppose is given that the statistic result after 80 iterations is the ultimate fitting accuracy. The fitting computation is carried out based on the same data of Sect. 24.4.1, and the result of different types of satellites is given in Table 24.4.

According to the fitting result, for GEO, the ultimate accuracy is prior to 0.03 m, and the average fitting error is lower than 0.01 m in a long period. For IGSO and MEO satellites, general speaking, the fitting error is better under the condition of 2 hour-arc and 3-hour-arc, and the maximum error is lower than 3 cm while average value can be 1–2 mm. For 3 types of satellites, the ephemeris fitting accuracy can be prior to 0.05 m for 16-parameter model, and even the accuracy is prior to 1 cm for most time. For GEO, the accuracy can be sub-centimeter, while the accuracy can be millimeter for IGSO and MEO satellite. In Summary, the ephemeris fitting accuracy can be ignored in the navigation services of users.

Table 24.4 Statistics ephemeris fitting accuracy result for different types of satellites

Sat type	Arc	Fitting error (m)	
		Max	Average
GEO	3 h	2.523E−2	7.929E−3
IGSO	2 h	2.546E−2	1.745E−3
	3 h	4.611E−2	5.344E−3
MEO	2 h	6.616E−3	1.971E−3
	3 h	4.529E−2	1.246E−2

24.5 Conclusion

In the article, the analysis and experiments are carried out based on the 16-parameter model of GPS, which includes the ephemeris parameter meaning, fitting algorithm and fitting accuracy, and the conclusion is given as following:

1. Under the condition of 16-parameter model, for GEO, there are some problems including the fact that the parameters' variation is too wide and the fitting efficiency is reduced sometimes. The parameter variation range is confined through the method of adjusted length and ridge estimate, and the efficiency is improved with the method that the URE criterion is taken as the constraints and the fitting solving standard is adapted.
2. With 16-parameter model, different fitting arcs can lead to different accuracies. The optimal fitting arc for GEO is 3 h while that of MEO and IGSO is 2 h. The high accuracy can be reached for 3 types of satellites, and even the accuracy is prior to 1 cm for most time. For GEO, the accuracy can be sub-centimeter, while the accuracy can be millimeter for IGSO and MEO satellites.

References

1. Songjie HU (2005) Research on the broadcast ephemeris parameters of GPS and GLONASS. J Spacecraft TT & C Technol 26(3):5–8
2. Chen L, Han C, Chen J (2007) The research of satellites broadcast ephemeris parameters fitting arithmetic. Sci Surveying Mapp 32(3):12–14
3. Huang Y, Hu XG, Wang XY (2006) Precision analysis of broadcast ephemeris for medium and high orbit satellite. Proc Astron 24(1):81–87
4. Gao Y, Xi X, Wang W (2007) An improved fitting algorithm design of broadcast ephemeris for GEO satellite. J Natl Univ Defense Technol 29(5):18–22
5. Ruan R, Jia X, Wu X, Feng L (2011) Broadcast ephemeris parameters fitting for GEO satellites based on coordinate transformation. J Mapp Surveying 40:145–150
6. Huang H (2012) Study on broadcast ephemeris model and fitting algorithm of navigation satellite. Nanjing University, Nanjing

7. Cui X (2006) Solving similar GPS broadcast ephemeris parameters using Givens transformation 28(4):P22–25
8. Cui X, Jiao W, Jia X (2006) Comparisons of two kinds of GPS broadcast ephemeris parameter algorithms. Chin J Space Sci 26(5):382–387
9. Cui X, Jiao W, Jia X (2004) The fitting algorithm of GPS broadcast ephemeris parameters. J Inst Mapp Surveying 21(4):244–246

Chapter 25
Kinematic Wide Area Differential Corrections for BeiDou Regional System Basing on Two-Way Time Synchronization

Yueling Cao, Xiaogong Hu, Jianhua Zhou, Bin Wu, Li Liu, Shanshi Zhou, Ranran Su, Zhiqiao Chang and Xiaoli Wu

Abstract Real-time wide area differential corrections are provided to BeiDou authorized users to satisfy the need of high-accuracy navigation service. The algorithm of wide area differential corrections are studied based on independent two-way time synchronization system and the performance of two kinds of differential modes with one-dimensional (also the equivalent satellite clock correction introduced in BeiDou ICD file) or four-dimensional correction are comparatively analyzed. The results show that for the current one-dimensional mode, the correction accuracy will decrease when the orbital errors are large, especially for the situations such as quickly orbit determination recovery after satellite failure or maneuver. While for the four-dimensional mode, the stability and precision of the separation of ephemeris and satellite clock parameters are seriously limited by the regional monitoring network. Applying the two-way time synchronization observations, the high-precision separation of orbital and satellite clock errors is realized with kinematic method, and with actual observations, the processing results show that user differential range error may be minimized to decimeter level and the positioning accuracy is also improved by 40 % in the area lacked monitor stations. The four-dimensional mode may process in real-time and once be applied in BeiDou Wide Area Differential Augmentation System, the accuracy, continuity and availability of the system will all be improved.

Y. Cao (✉) · X. Hu (✉) · B. Wu · S. Zhou
Shanghai Astronomical Observatory, Chinese Academy of Sciences,
Shanghai 200030, China
e-mail: caoyueling@shao.ac.cn

X. Hu
e-mail: hxg@shao.ac.cn

Y. Cao
Graduate University of Chinese Academy of Sciences, Beijing 100049, China

J. Zhou (✉) · L. Liu · R. Su · Z. Chang · X. Wu
Beijing Global Information Application and Development Center, Beijing 100094, China
e-mail: marui_168@sohu.com

J. Sun et al. (eds.), *China Satellite Navigation Conference (CSNC) 2014 Proceedings: Volume III*, Lecture Notes in Electrical Engineering 305,
DOI: 10.1007/978-3-642-54740-9_25,

Keywords Time synchronization system · Separation of orbital and clock error · DOP

25.1 Introduction

As the application of satellite navigation technology in the national economy and military defense, Global Navigation Satellite System (GNSS) is becoming more and more important. Therefore China has for more than a decade pursued the build-up of the autonomous GNSS, BeiDou.

To serve its own purposes, BeiDou adopts a unique system design, in extensive use of Geostationary Earth Orbit (GEO) and Inclined Geosynchronous Satellite Orbit (IGSO) satellites which are more suitable for regional services. Several challenges are facing Beidou precise orbit determination: (1) Strong statistic correlations between GEO's orbit and clock estimates; (2) Domestic monitoring network is unable to provide enough tracking coverage, especially for MEO satellites. Consequently, the accuracy of broadcast ephemeris would be decreased. By providing the real-time differential corrections for orbits and clocks, the accuracy of the navigation system will be greatly improved.

After fully consideration of compatibility with currently exiting GNSS system and prevention of their deficiencies, BeiDou is designed to simultaneously provide open service and authorized service using the same control and operation segment. The differences between the two modes of services and the differential correction models adopted in authorized service are detailed in Ref. [1].

Given the regional monitoring network of BeiDou, orbital and clock differential corrections are combined as one, as Equivalent Satellite Clock Error, which is limited ability of orbital error correction for the situations of satellite maneuver, or orbit determination fast recovery. In the paper the high-precision four-dimensional corrections of orbital and satellite clock errors is realized with kinematic method and the law of error propagation is analyzed with Dilution of Precision (DOP). Basing on the exclusive time synchronization (TS) observations of two-way radio-wave time transfer system, the satellite clock errors were estimated. Meanwhile station clocks were obtained from common view time transfer of reference stations, improving the accuracy of station clock estimation. The assessment of the four-dimensional differential correction model is conducted with real observation data, and the results show that the algorithm in the paper provides an effective supplement of Equivalent Satellite Clock Error model and has significance for BeiDou wide-area differential correction system construction.

Table 25.1 The difference of orbital error projection coefficients among stations

Projection direction	GEO 4		GEO 5	
	Max difference	Direction	Max difference	Direction
Radial	0.002	East–West	0.005	East–West
Tangential	0.050	North–South	0.060	North–South
Normal	0.070	North–South	0.080	North–South

25.2 Analysis of Ephemeris Error Projection Difference

By using broadcast ephemeris and high-precision known reference station coordinates, geometric range, satellite clock bias could be calculated. Ionospheric delay, tropospheric delay could also be corrected by Model.

Pseudo-range residual is computed by removing geometric range, satellite clock bias, ionospheric delay, and tropospheric delay from the CNMC smoothed pseudo-range [1] and can be simplified as:

$$\Delta\rho_i^j = C\Delta t_i - \varepsilon_{orb} - \varepsilon_{satclk} + \varepsilon_i^j \tag{25.1}$$

where $\Delta\rho_i^j$ is pseudo-range residual, $C\Delta t_i$ is station clock; ε_{orb} and ε_{satclk} are orbital and satellite clock errors in broadcast ephemeris; ε_i^j is observation noise.

The satellite clock errors translate into pseudo-range measurements, but projections of satellite orbital errors vary with observation directions. According to Ref. [1], the equivalent satellite clock parameter is used to correct satellite clock errors and orbit radial errors as well as average projection of orbit tangential and normal errors in combination.

The characters of orbital error projected in different directions were analyzed by the projection coefficients. If dR, dT, dN are three-dimensional orbital errors in ephemeris, the projection of orbital errors in the line of sight could be expressed as $\varepsilon_{orb} = a_i \cdot dR + b_i \cdot dT + c_i \cdot dN$, where a_i, b_i, c_i are corresponding projection coefficients.

Take the eastern GEO-5 (60 °E) and the Western GEO-4 (160 °E) satellites in BeiDou navigation system as an example. The projection coefficients of orbital errors upon different regional monitor stations are computed and compared, and the statistic results are listed in Table 25.1. The distribution of the stations and satellites in test is given in Fig. 25.1.

The results show that the projection difference of orbital errors to different reference stations could reach to several meters once the orbit tangential and normal errors reach to several ten thousand meters in the situation of satellite maneuver, orbit determination fast recovery or IGSO satellite attitude control. The equivalent satellite clock correction does not take into account the effect of orbital error projection difference, which may degrade the service accuracy of wide area differential system in these special situations.

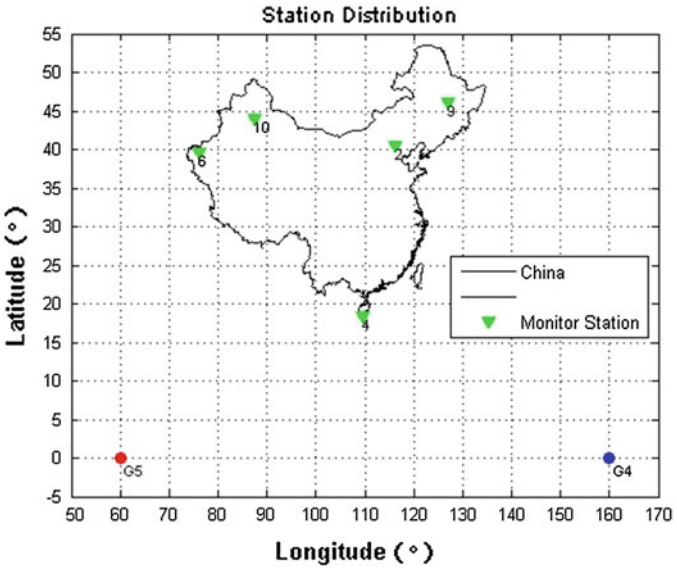

Fig. 25.1 Regional reference stations and GEO satellites distribution map

25.3 Four-Dimensional Differential Correction Model

25.3.1 Algorithm of Separation of Orbital and Clock Errors

In order to improve the availability and accuracy of wide area differential system for special situations such as satellite maneuver or satellite attitude control, four-dimensional differential correction model is studied, which separates the orbital and clock errors in broadcast ephemeris.

Station clock, satellite clock errors and orbital radial errors in Eq. (25.1) are highly correlated. If they were solved simultaneously, the normal equation would be seriously ill-conditional, which caused solution has large deflection compared with accurate solution.

In the paper, common view time synchronization method is applied to compute station clocks first. The satellite clock errors are estimated basing on independent two-way time synchronization observations. Then three-dimensional orbital errors could be solved. The computation processing is given in Fig. 25.2.

For the high stability of master station clock, it is taken as the common reference for the other reference stations. Master station clock could be calculated as follows:

$$\Delta t_{sta,M} = \frac{1}{P_{staM}} \sum_{j=1}^{N} \frac{\Delta \rho_M^j}{\sigma^2_{\Delta \rho_M^j} + (URA^j)^2} \tag{25.2}$$

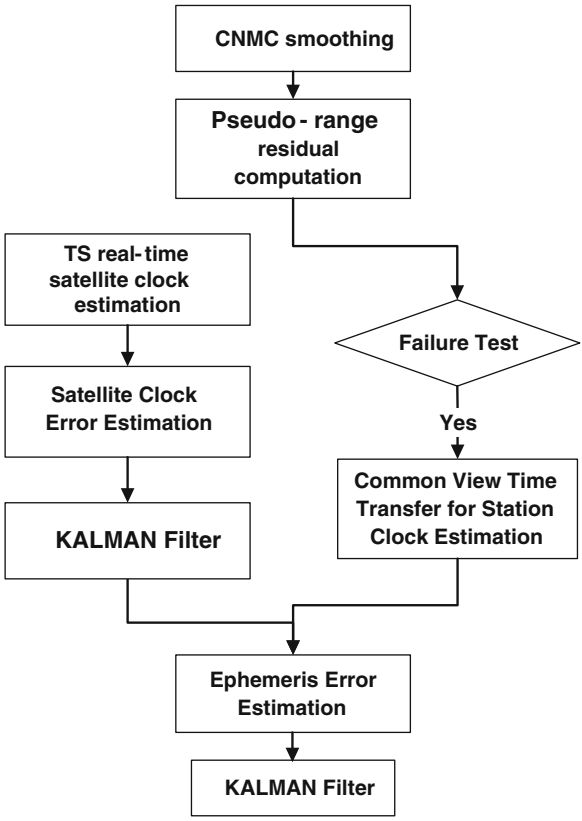

Fig. 25.2 The processing of separation for orbital and clock errors

where, $\Delta t_{sta,M}$ is master station clock; $\Delta\rho_M^j$ is Pseudo-range residual; $\sigma^2_{\Delta\rho_M^j}$ is observation errors; P_{staM} is weight.

The difference of pseudo-range residuals between master station and reference station is computed as $\Delta_{i,M}^j = \Delta\rho_i^j - \Delta\rho_M^j$. The results include the difference of orbital projection errors and the difference of station clocks. The first term could be ignored for regional monitoring network and the quality of BeiDou broadcast ephemeris. A good estimate of the clock difference can be achieved using multiple common satellites as follow:

$$dclk_{sta,i} = \Delta t_{sta,i} - \Delta t_{sta,M} = \frac{1}{N_{i,M}} \sum_{j=1}^{N_{i,M}} \Delta_{i,M}^j \tag{25.3}$$

Common view time transfer is used to remove the station clock from pseudo-range residual in Eq. (25.1) when combined with the master clock estimate, and we have all of the measurements in terms of synchronization.

Meanwhile, the satellite clock could be estimated basing on independent two-way Time Synchronization observations which are exclusive for BeiDou.

$$\begin{aligned}\Delta T_{AS} &= \frac{1}{2}(R_A - R_S) + \frac{1}{2}\left[\left(\tau_A^T + \tau_S^R\right) - \left(\tau_S^T + \tau_A^R\right)\right] + \frac{1}{2}\left(\tau_{AS}^{ion} - \tau_{SA}^{ion}\right) \\ &+ \frac{1}{2}\left(\tau_{AS}^{tro} - \tau_{SA}^{tro}\right) + \frac{1}{2}\left(\tau_{AS}^{G} - \tau_{SA}^{G}\right) + \frac{1}{2}(\Delta\tau_{AS} - \Delta\tau_{SA})\end{aligned} \tag{25.4}$$

where ΔT_{AS} is real-time satellite clock from TS; A indicates ground stations; S indicates satellites; R_A and R_S are two-way time synchronization observations between satellite and ground station; τ_A^T and τ_S^T are respectively station and satellite transmitting equipment time delay; τ_A^R and τ_S^R are respectively station and satellite receiving equipment time delay; τ_{AS}^{ion} and τ_{SA}^{ion} are two-way ionospheric delay; τ_{AS}^{tro} and τ_{SA}^{tro} are two-way tropospheric delay; τ_{AS}^{G} and τ_{SA}^{G} are two-way gravitational delay; $\Delta\tau_{AS}$ and $\Delta\tau_{SA}$ are two-way time delay caused by the movement of the targets.

The precision of satellite clock estimation from two-way radio-wave time transfer measurements is better than 1 ns [2]. A Kalman filter [3] is used to reduce the noise of TS satellite clock. The satellite clock error, ε_{satclk}, is then estimated with the comparisons of real-time TS satellite clock and broadcast satellite clock.

The estimates of satellite and station clock bias are separated and removed from pseudo-range residual:

$$\tilde{\Delta\rho_i^j} = \Delta\rho_i^j - C \cdot dclk_{sta,i} - C \cdot \Delta t_{sta,M} - \varepsilon_{satclk} \tag{25.5}$$

Then we set up kinematic observation equation for orbital errors estimation:

$$\tilde{\Delta\rho_i^j} = a_{x,ij} \cdot dx_i^j + b_{y,ij} \cdot dy_i^j + c_{z,ij} \cdot dz_i^j + \varepsilon_i^j \tag{25.6}$$

where $\begin{pmatrix} dx_i^j & dy_i^j & dz_i^j \end{pmatrix}$ are orbital errors.

Using observations from multiple stations and satellites, real-time three-dimensional orbital errors could be achieved. A Kalman filter is implemented with a measurement update [3].

25.3.2 Analysis of Dilution of Precision

For satellites, Dilution of Precision (DOP) could be used to specify monitoring network geometry effect on satellite kinematic differential accuracy for observations of navigation systems. DOP are calculated as:

$$XDOP_j = \sqrt{Q_{j,xx}},\ YDOP_j = \sqrt{Q_{j,yy}},\ ZDOP_j = \sqrt{Q_{j,zz}}$$

Table 25.2 The statistical results of DOP

SatID	RDOP	TDOP	NDOP	PDOP	SatID	RDOP	TDOP	NDOP	PDOP
GEO1	2.2	17.3	15.2	23.1	IGSO6	4.2	31.2	17.9	36.2
GEO3	2.1	18.2	11.8	21.8	IGSO7	4.1	30.5	18.0	35.6
GEO4	6.9	38.4	36.7	53.6	IGSO8	4.0	29.4	16.8	34.1
GEO5	4.2	28.0	19.6	34.5	IGSO9	4.2	30.8	17.0	35.4
MEO11	7.5	22.3	29.3	37.6	IGSO10	3.8	28.4	16.4	33.0
MEO12	4.6	18.3	16.1	24.8	**Mean**	**4.3**	**26.6**	**19.5**	**33.6**

where, $Q_{j(xx,yy,zz)}$ is diagonal elements in covariance matrix of Eq. (25.6).

For purposes of analysis, these DOP were transformed into (R, T, N) orbital coordinates and expressed as RDOP, TDOP and NDOP. DOP value could reflect the law of error propagation for kinematic four-dimensional differential correction model.

Observation data on 2012/06/21 of 10 stations were processed to calculate the correction of orbital and clock errors, and the corresponding DOP values were analyzed. Mean value of DOP in three-dimensional directions are evaluated. For non-GEO satellites, DOP values would diverge caused by the sets and rises of satellites and values whose Position DOP less than 150 were used in statistic (Table 25.2).

Table 25.2 shows that the magnification of error propagation for satellite three-dimensional positioning is about 34, in which about 4.3 in Radial direction, 26.6 in the Tangential direction and 19.5 in the Normal direction.

25.4 Results and Discussion

Basing on real-time CNMC phase smoothing pseudo-range, the paper verified the effectiveness of the two differential models under situations of satellite maneuver fast recovery and normal service, and the performance of the two models were compared with real data.

25.4.1 The Analysis for Satellite Maneuver Recovery

BeiDou observation data on day of 173 in 2012 were processed, for IGSO-8 satellite was planned maneuver from 0 to 2 o'clock. The recovery of orbit determination lasted next 6 h. The satellite returned to normal until 8 o'clock. Satellites in the constellation except IGSO-8 were under normal service all day.

The orbital errors increased rapidly after satellite maneuver especially in Radial direction reaching to 10^4 orders of magnitude, as well as in Tangential and Normal directions to tens of thousands of meters.

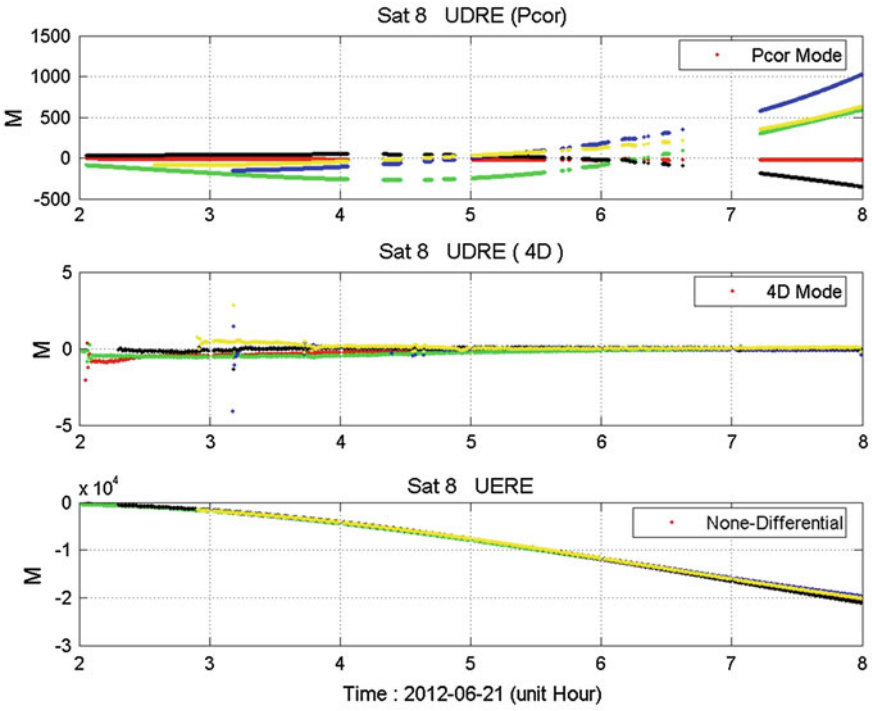

Fig. 25.3 Comparison of UDRE and UERE during IGSO-8 satellite maneuver recovery (*Top* UDRE results from one-dimensional differential model; *Middle* UDRE results from four-dimensional differential model; *Bottom* UERE results from none-differential model; *Colors* indicate different monitor stations)

Compared to User Equivalent Range Errors (UERE) in open service, UDRE in authorized service corrected with differential corrections was used to evaluate the accuracy of differential models. Figure 25.3 gives UDRE and UERE of IGSO-8 during the period of satellite quickly orbit determination recovery. The colors indicated different monitor stations. UDRE in top and middle of Fig. 25.3 were related to one- and four-dimensional differential model respectively. And in bottom of Fig. 25.3 were corresponding UERE.

The discontinuous curves in top of Fig. 25.3 indicated that the one-dimensional differential correction could not be calculated resulting from data excluded for errors. Compared to the one-dimensional differential model, the four-dimensional differential model provided corrections with much better continuity.

The RMS statistic of UDRE and UERE of IGSO-8 for different monitor stations is listed in Table 25.3. The computation of RMS statistic is given in Eq. (25.6)

$$RMS_i^j = \sqrt{(mean_i^j)^2 + (\mathrm{std}_i^j)^2} \tag{25.6}$$

Table 25.3 RMS of UDRE and UERE of IGSO-8 (meter)

Mode	Sta9	Sta2	Sta4	Sta6	Sta10
UDRE with one-dimensional differential mode	123.27	17.44	265.13	425.72	240.39
UDRE with four-dimensional differential mode	0.09	0.30	0.33	0.20	0.21
UERE with none-differential mode	11088.9	10782.4	10670.6	11607.8	11441.9

Table 25.3 shows that in the period of IGSO-8 satellite quickly orbit determination recovery, IGSO-8 orbit errors are too large to be corrected by equivalent satellite clock, UDRE is about 100 m. But UDRE with the four-dimensional differential correction is just a few decimeters. It indicates that the accuracy, availability and continuity of the wide-area differential service can be significantly improved with four-dimensional differential model.

For the two kinds of differential correction mode, real-time pseudo-range single point positioning errors are analyzed for different monitor stations, including the RMS of positioning errors, PDOP (Positioning Dilution Of Precision) and the number of available satellites (Fig. 25.4).

In Fig. 25.4, red bars represent the one-dimensional mode and blue bars represent the four-dimensional mode. The locations of the monitor stations in Fig. 25.4 are listed from northeast, middle, south to the west of the regional tracking area and the distributions are distinguished by three yellow bars.

The results show that in eastern China, the positioning accuracy is equivalent for the two kinds of differential models where monitor stations are densely distributed. But in the area lacked monitor stations such as northeastern, southern and western China, the positioning accuracy is improved by 40 % with the four-dimensional differential corrections. The four-dimensional differential model provides a useful source to realize the sub-meter wide-area differential positioning for regional navigation system.

Otherwise, in the period of IGSO-8 satellite quickly orbit determination recovery, the satellite is not available for service with equivalent satellite clock differential correction. While with the four-dimensional differential corrections, the satellite is available. This is significant for the improvement of the satellite navigation system availability, as the majority of the BeiDou constellation are GEO and IGSO satellites, whose orbit maneuver frequently.

25.4.2 The Analysis for Normal Service

The performance of the two kinds of differential models is also compared under normal navigation service situation, with normal satellite observations of July 21th, 2012.

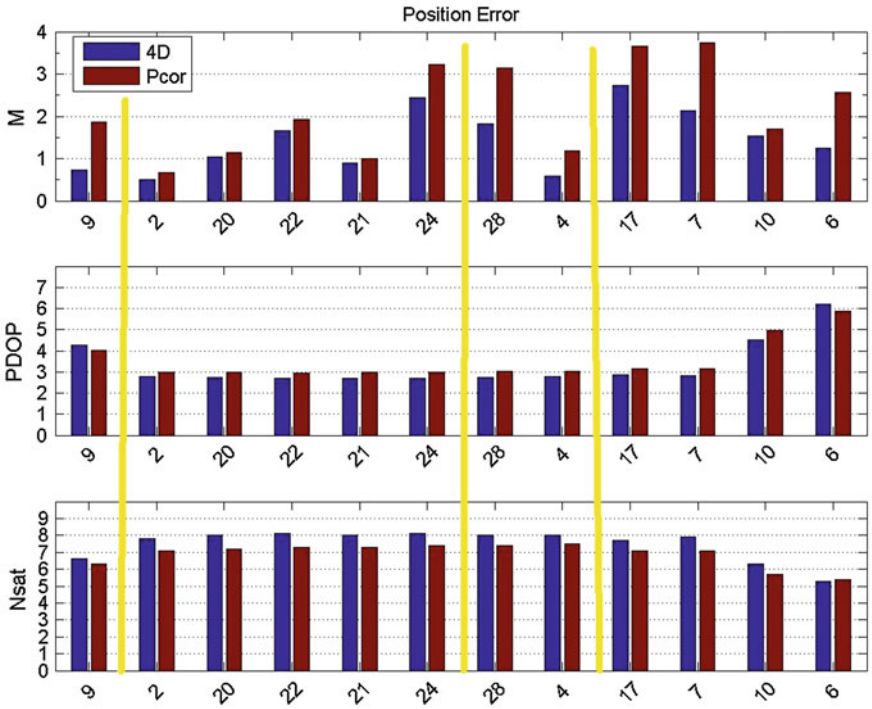

Fig. 25.4 Position error (*top*), DOP (*middle*) and satellite number (*bottom*) (*blue bars* indicate four-dimensional model; *Red bars* indicate one-dimensional model; X label is station number)

In Fig. 25.5, real-time pseudo-range single point positioning errors are analyzed through three monitor stations, distributed in the eastern, southern and western China separately. Where blue color represents the positioning results with one-dimensional differential correction, green color represents the positioning results with four-dimensional differential correction and red color represents the positioning results with none-differential under open service.

The statistical results of positioning errors are listed in Table 25.4. It shows that under normal service, the accuracy of two differential models is equivalent when monitor stations are densely distributed. While in the station sparse distribution region, the four-dimensional separation model is better than equivalent satellite clock model. Since equivalent satellite clock model correct the satellite clock error as well as the average projection of orbital errors of all the monitor stations, the model accuracy partly related to monitor station distribution. Applying real-time multipath error correction, the pseudo-range accuracy is much improved which is favorable to the high precision separation of ephemeris and clock errors. The four-dimensional model leads to about 1 m accuracy of real-time pseudo-range differential positioning.

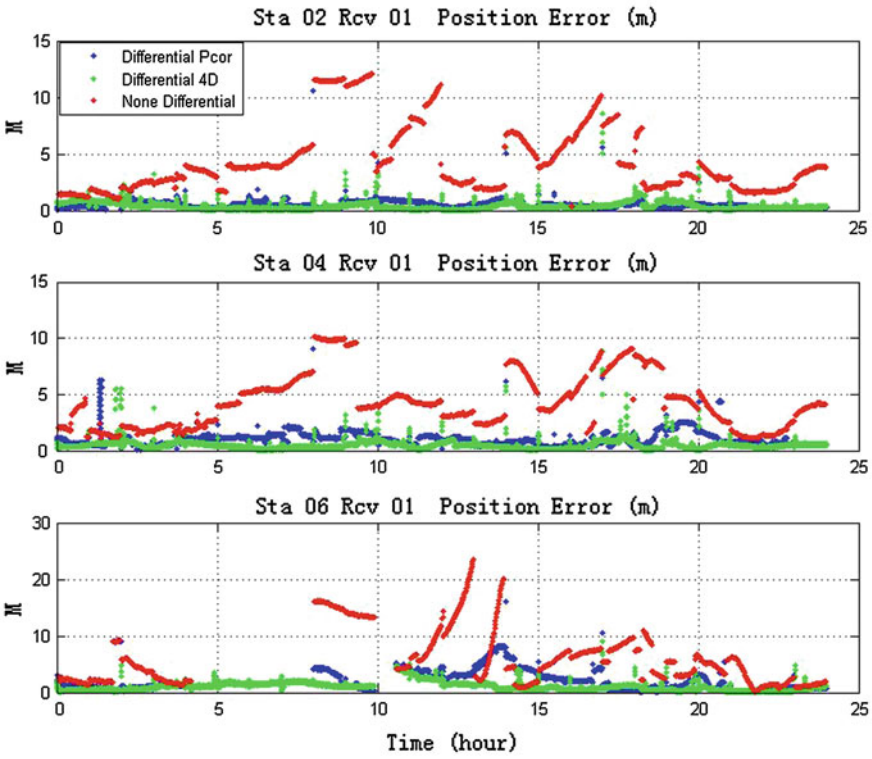

Fig. 25.5 The Real-time positioning error (*top* eastern station; *middle* southern station; *bottom* western station; *blue line* indicates one-dimensional differential model; *green line* indicates four-dimensional differential model; *red line* indicates none-differential model)

Table 25.4 RMS of real-time positioning errors (meter)

Mode	Sta2	Sta4	Sta6
One-dimensional differential model	0.598	1.184	2.875
four-dimensional differential model	0.524	0.607	1.299
None-differential	5.295	4.957	7.658

25.5 Conclusions

The performance of two kinds of wide area differential models with one-dimensional (the equivalent satellite clock) or four-dimensional (the separation of orbital and clock errors) are comparatively analyzed. And the validation of four-dimensional differential correction for BeiDou regional system is confirmed with actual observation.

The results show that for equivalent satellite clock model, the correction accuracy will decrease in the area lack of monitor stations and is not suitable for the situations such as quickly orbit determination recovery after satellite failure or maneuver.

Applying the independent two-way time synchronization observation, the precision separation of orbital and clock errors is realized. As the orbital errors are provided in three-dimensional, it reduces the dependence of the model on the distribution of monitor stations. Compared with one-dimensional model, the positioning accuracy is improved by 40 % in the area lack of monitor stations. And the UDRE is reduced to decimeter level for the situations of quickly orbit determination recovery after satellite failure or maneuver, equivalent with the normal service satellites. The accuracy, continuity and availability are all improved for the wide area differential correction system with the four-dimensional correction model provided in the paper.

Acknowledgements This work was supported by the National Natural Science Foundation of China (Grant No. 11203059, 41204023, 11203058, 11103068) and the Shanghai Key Laboratory of Space Navigation and Position Techniques. Grant No. 12DZ2273300.

References

1. Cao YL, Hu XG et al (2012) The wide-area difference system for the regional satellite navigation system of COMPASS. Sci China Phys Mech Astron 55(7):1307–1315
2. Zhou SS, Cao YL et al (2012) Positioning accuracy assessment for the 4GEO/5IGSO/2MEO constellation of COMPASS. Sci China Phys Mech Astron 55(12):2290–2299
3. Tsai YJ (1999) Wide area differential operation of the global positioning system: ephemeris and clock algorithms. Stanford University
4. www.beidou.gov.cn/System Introduction
5. Zhou SS, Hu XG, Wu B et al (2011) Orbit determination and time synchronization for a GEO/IGSO satellite navigation constellation with regional ephemeris and clock algorithms tracking network. Sci China Phys Mech Astron 54:1089–1097
6. Cai CL, Li XH, Wu HT (2009) An analysis of the wide area differential method of geostationary orbit satellites. Sci China Ser G 52:310–314
7. Karl S, Zeta AI, Peter S et al (2001) WAAS measurement processing, reducing the effects of multipath. ION GPS 2001

Chapter 26
Earth Rotation Parameters Determination Using BDS and GPS Data Based on MGEX Network

Tianhe Xu, Sumei Yu and Jiajin Li

Abstract Earth rotation parameters (ERPs) are necessary parameters to achieve mutual transformation of the celestial reference frame and earth-fix reference frame. They are very important for satellite precise orbit determination (POD), high-precision space navigation and positioning. In this paper, the determination of ERPs including polar motion (PM), polar motion rate (PMR) and length of day (LOD) are presented using BDS and GPS data of June 2013 from MEGX (Multi-GNSS Experiment) network based on least square (LS) estimation with constraint condition. BDS and GPS data of 16 stations from MGEX network are the first time used to estimate the ERPs. The results show that the RMSs of x and y component errors of PM and PM rate are about 0.92 mas, 1.0 mas, 0.20 mas/d and 0.32 mas/d respectively using BDS data. The RMS of LOD is about 0.028 ms/d using BDS data. The RMSs of x and y component errors of PM and PM rate are about 0.19 mas, 0.21 mas, 0.18 mas/d respectively using GPS data. The RMS of LOD is about 0.021 ms/d using BDS data. The optimal relative weight is between 1:2 and 1:3. The accuracy improvements of BDS is about 14 % in X component of PM, 8 % in Y component of PM, 21 % in X component of PM rate and 17 % in Y component of PM rate. There is no obvious improvement in LOD when BDS data is involved. System biases between BDS and GPS are resolved and they are different with different station and very stable day to day with about 20 cm accuracy.

T. Xu (✉)
State Key Laboratory of Geo-information Engineering, Xi'an, Shanxi, China
e-mail: thxugfz@163.com

T. Xu
State Key Laboratory of Geodesy and Earth's Dynamics, Wuhan, Hubei, China

T. Xu
Xian Research Institute of Surveying and Mapping, Xi'an, Shanxi, China

S. Yu · J. Li
Chang'an University, Xi'an, Shanxi, China

T. Xu
State Key Laboratory of Astronautic and Dynamics, Xi'an, Shanxi, China

J. Sun et al. (eds.), *China Satellite Navigation Conference (CSNC) 2014 Proceedings: Volume III*, Lecture Notes in Electrical Engineering 305,
DOI: 10.1007/978-3-642-54740-9_26,

Keywords Earth rotation parameter · IGS · Polar motion · Length of day · Least square

26.1 Introduction

Earth rotation parameters (ERPs) are necessary parameters to achieve mutual transformation of the celestial reference frame and earth-fix reference frame [1]. They include four time-varying rotational angels consisting of the polar motion coordinates (PMx, PMy), the universal time (UT1), together with the length of day (LOD, equivalent to the time rate of change of UT1). The PM is an important parameter to characterize the movement of Earth, which is used to describe the instantaneous movement of the earth's rotation axis in the body and the polar position on the earth surface is changing slowly [2]. EOP is the necessary parameters to achieve mutual conversion of the celestial reference frame and earth reference frame, and it is very important for high-precision space navigation and positioning. Modern measurement techniques such as VLBI, SLR, GPS and DORIS can provide people with high precision and high spatial and temporal resolution of Earth Orientation Parameters [3–9]. Nowadays, the International GPS Service (IGS) has been distributing, as part of its product combinations, three distinct ERP series: the IGS Utra-rapid series, the IGS Rapid series and the IGS Final series [10–13]. They are the combination of all IGS Analysis Centers (AC). In ERP determination, China drops behind to aboard such as America and Europe countries and is still under the way. The most fruit in this field is represented by ERP prediction with high accuracy [14–18]. With the development of BDS and open for public service, it is urgent and important task for us to study the ERP determination using BDS data. In this paper, we report on ERP determination using BDS and GPS data based on MGEX network in order to give some reference or advice on the ERP determination using BDS.

26.2 ERP Determination Using LS with Constraint Condition

For ERP determination using GNSS data, ionosphere free linear combination to eliminates the first order ionospheric path delay is usually used. For the code and carrier phase observations the ionosphere free combination can be expressed as

$$PC_i^j = \rho + c \cdot (dt_i - dT^j) + d_{i,trop}^j + \varepsilon_{PC} \tag{26.1}$$

$$LC_i^j = \rho + c \cdot (dt_i - dT^j) + d_{i,trop}^j + \lambda B_i^j + \varepsilon_{LC} \tag{26.2}$$

where PC_i^j and LC_i^j are ionosphere free combination of code and carrier phase respectively. ρ is the geometric distance from GPS satellite to GOCE satellite. c is the light speed; dt_i and dT^j are receiver clock offset and satellite clock offset respectively. $d_{i,trop}^j$ is the tropospheric refraction; λB^j is the ambiguity parameter of ionosphere free combination. ε_{PC} and ε_{LC} are code and carrier phase noise respectively. After linearization from Eqs. (26.2) and (26.3), the error equations can be expressed asEquation ID="Equ3"> V_{pc} = PC_{i}^{\,j} - \phi_{m} = AX + c \cdot dt_{i} - c \cdot dT^{\,j} + d_{i,trop}^{\,j} + \phi_{nm} + \varepsilon_{pc} \eqno\rm(26.2)

$$V_{lc} = LC_i^j - \phi_m = AX + c \cdot dt_i - c \cdot dT^j + d_{i,trop}^j + \lambda B_i^j + \phi_{nm} + \varepsilon_{lc} \tag{26.4}$$

where ϕ_m is the error corrections which can be calculated by models such as solid Earth tide, ocean tide and antenna phase centre corrections. X *is* the position correction vector expressed as (dx, dy, dz); A *is* the design matrix for position parameters expressed as $\left(\frac{x_i - x^j}{\rho}, \frac{y_i - y^j}{\rho}, \frac{y_i - y^j}{\rho}\right)$; ϕ_{nm} includes other non-modelling corrections such as multipath error, GPS orbit errors and atmospheric errors. ε_{pc} and ε_{lc} are the residual vector of ionosphere free combination.

In order to compute the difference vector between the observing station and GPS satellite, both positions must be given in the same reference frame. Therefore, we need to know Earth orientation parameter between the two frames when analyzing GPS data. The transformation between the celestial and the Earth-fixed coordinate system may be performed by means of equation

$$\vec{r}_{CIS} = P^T(t) R_1(\Delta\varepsilon) R_2(-\Delta\phi \sin\varepsilon_0) R_3(-\Theta_{GM}) R_1(y_p) R_2(x_p) \vec{r}_{CTS} \tag{26.5}$$

where $P(t)$ is the rotation matrix referring to precession and $R_i(\alpha)$characterizes a rotation around axis i, about angle α. $\vec{r}_{CIS}$ and $\vec{r}_{CTS}$ are the position vectors of a station in the terrestrial and inertial systems, respectively. $\Delta\varepsilon$ and $\Delta\phi$ denote the nutation in longitude and obliquity, ε_0 denotes the mean obliquity of the ecliptic, and Θ_{GM} stands for the Greenwich mean sidereal time.

Unfortunately, due to correlations with the orbital elements, a subset of the Earth orientation parameter is not directly accessible to the GPS such as UT1-UTC and the nutation parameters. Therefore the possible solved parameters by GPS data are PM, and LOD, which is called ERPs without UT1-UTC in this paper.

Based on the error Eqs. (26.4) and (26.5) and the dynamic Eq. (26.1), orbit determination can be performed using least square batch strategy. When a prior or constraint condition are known, it is better for us to solve the observation equation by least square with constraint condition, which can be expressed as:

$$\begin{cases} V = AX - L & P \\ V_x = X - X_0 & P_{X_0} \end{cases} \tag{26.6}$$

where P and P_{X_0} are weight matrices of observation and constraint condition. The estimator of least square with constraint condition can be written as:

$$\begin{aligned} X &= X_0 + \delta X \\ \delta X &= (A^T P A + P_{X_0})^{-1} A^T P \delta L \\ \delta L &= L - A X_0 \end{aligned} \tag{26.7}$$

It is very flexible to set up the solved parameter in GNSS data processing according to our need or concern. For example, if we want to do POD, we can added a strong constraint on the station coordinate. For ERP determination, we can use the predicted ERPs as X_0 and added a loose constraint condition to get the solution of ERPs.

26.3 ERP Determination Using BDS and GPS Data

The functional model and stochastic model should be adjusted when combing the BDS and GPS data for ERP determination based on the above error equations. The adjusted error equations can be written as:

$$V_{BDS} = A_{BDS} X_{COM} + B_{BDS} X_{BDS} + X_{ISB} - L_{BDS} \tag{26.8}$$

$$V_{GPS} = A_{GPS} X_{COM} + B_{GPS} X_{GPS} - L_{GPS} \tag{26.9}$$

where the formula (26.8) and (26.9) are the error equation of BDS and GPS. The difference lies in the parameter estimation of system biases between BDS and GPS for the determination ERP combining BDS and GPS data. The parameters are set to constant in the same station and same observation session and solved with other unknown parameters.

In the aspect of stochastic model, the relative weight should be considered between BDS and GPS data since they are different in the quality and accuracy. The commonly used methods for relative weight determination follow in two types: experiential method and variance component estimation. The former is simple and easy but no strict background adjustment. The latter is strict and perfect but very complex and need to iteration with huge computation. In this paper, an approach combing experiential method and numerical testing method are presented for determining the relative weight reasonably.

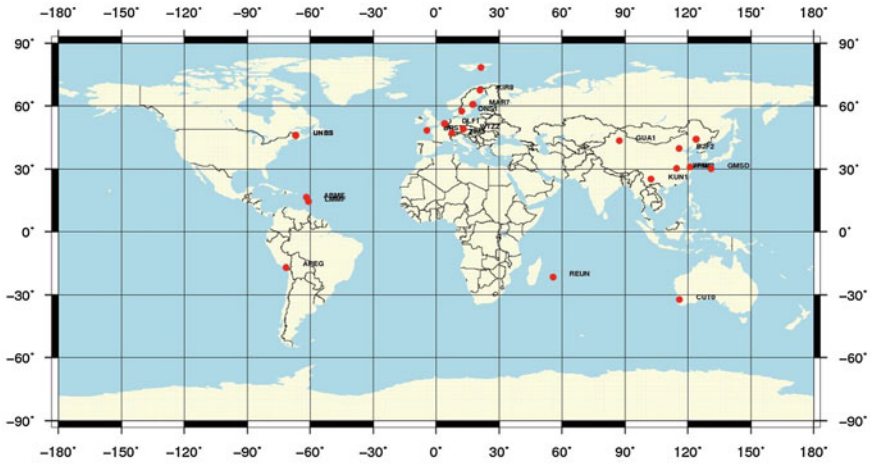

Fig. 26.1 The station distribution with BDS and GPS receiver of MEGX network

26.4 Computations and Comparisons

The BDS and GPS data of 15 IGS stations belong to MGEX network span from 1/6/2013 to 30/6/2013 are used for the test ERPs determination. The selected stations including areg, brst, brux, cut0, dlf1, gmsd, jfng, kir8, mar7, ons1, reun, unb3, unbs, wtzz, zim3 and their distribution are shown in Fig. 26.1. The zero-difference code and carrier phase observations are used. It should be pointed out that the UT1 cannot be determined only by GPS data since GPS provides distance observation. According to this reason, a strong constraint of 0.1 ms on UT1 are added and loose constraint of 300 mas, 300 mas, 30 mas/d, 30 mas/d, 20 ms/d on PM, PMR and LOD are added respectively in LS estimation. The estimated parameters include the initial orbit vector per day, five parameters of solar radiation pressure per day, satellite and receiver clock offset per epoch, ambiguity and ZTD per hour per station, ERPs per day. The following three schemes are performed.

Scheme 1: ERP determination using GPS data
Scheme 2: ERP determination using BDS data
Scheme 3: ERP determination using BDS and GPS data.

The time series EOP 08C04 file provided by the IERS is used as reference for evaluation the accuracy of ERP determination. The absolute value of x and y component of PM errors per day are shown in Figs. 26.2 and 26.3 respectively. The absolute value of x and y component of PM rate errors per day are shown in Figs. 26.4 and 26.5 respectively. The absolute value of LOD errors per day are given in Fig. 26.6. The RMSs of ERP are shown in Fig. 26.7. The RMSs of ERP with different relative weight between BDS and GPS are listed in Table 26.1. All the

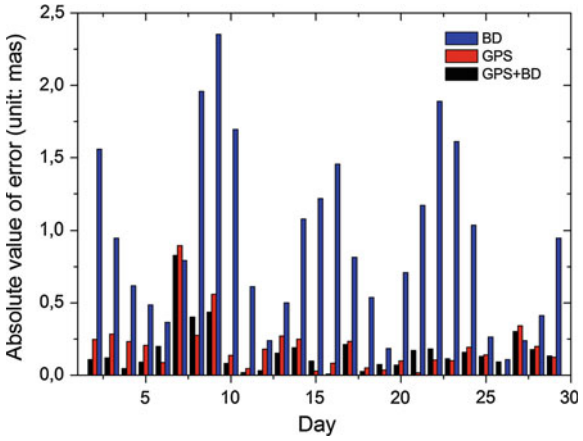

Fig. 26.2 The absolute value of x-component error of pole motion

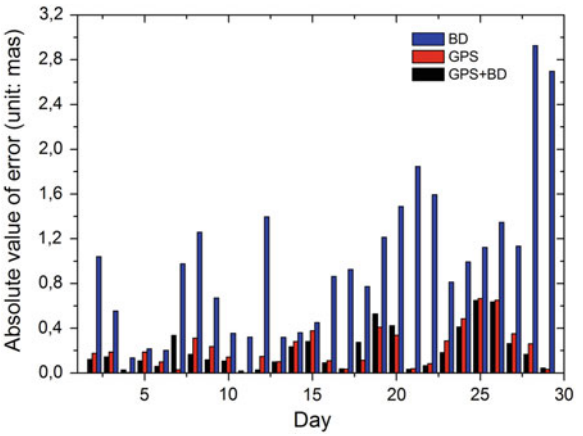

Fig. 26.3 The absolute value of y-component error of pole motion

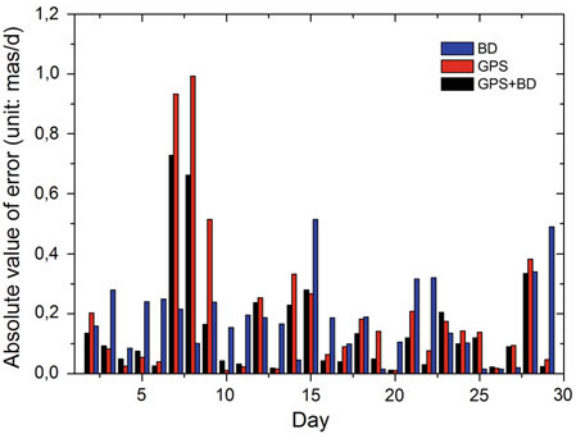

Fig. 26.4 The absolute value of x-component error of pole motion rate

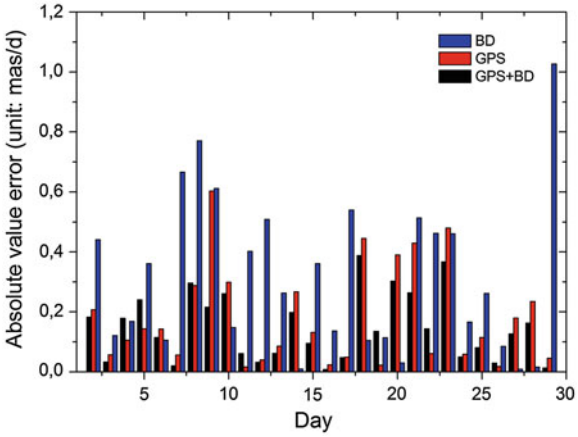

Fig. 26.5 The absolute value of y-component error of pole motion rate

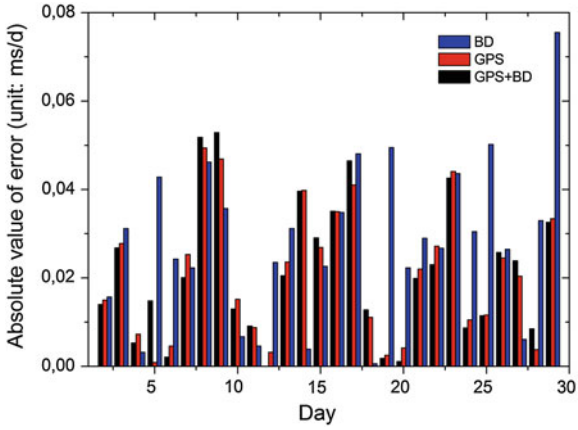

Fig. 26.6 The absolute value of LOD error

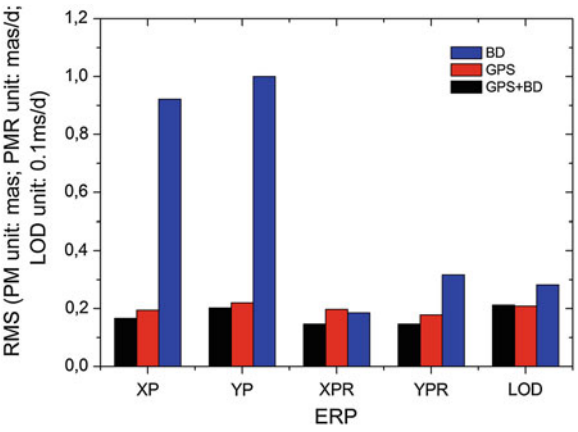

Fig. 26.7 The RMS of ERP errors

Table 26.1 The RMS of ERP errors using BDS and GPS with different relative weight (PM unit: mas, PM rate unit: mas/d; LOD unit: ms/d)

ERP	1:1	2:1	3:1	4:1	5:1
XP	0.1560	0.1624	0.1664	0.1733	0.1753
YP	0.2463	0.2246	0.2023	0.2143	0.2175
XPR	0.1416	0.1442	0.1464	0.1510	0.1528
YPR	0.1480	0.1431	0.1469	0.1509	0.1525
LOD	0.0213	0.0212	0.0212	0.0212	0.0212

Table 26.2 The RMS of ERP using BDS, GPS and GPS+BD (relative weight is 1:3) (PM unit: mas, PM rate unit: mas/d; LOD unit: ms/d)

ERP	GPS	BD	GPS+BD	BD contribution (%)
XP	0.1944	0.9217	0.1664	14.4
YP	0.2197	1.0001	0.2023	8.1
XPR	0.1854	0.1973	0.1464	21.0
YPR	0.1785	0.3167	0.1469	17.7
LOD	0.0209	0.0282	0.0212	−1.4

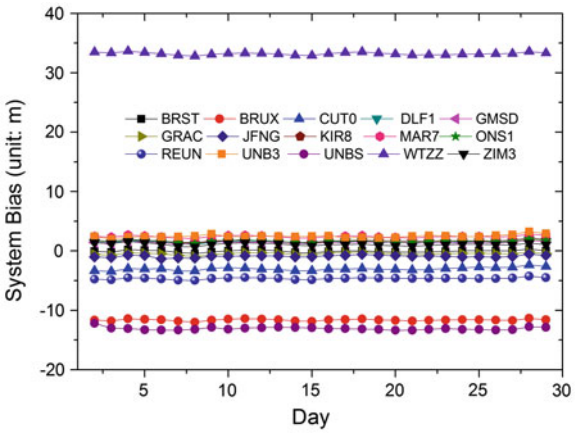

Fig. 26.8 System bias between BDS and GPS of stations

RMSs of ERP errors are listed in Table 26.2. The system biases between BDS and GPS are shown in Fig. 26.8 and Table 26.3.

From the above results, the following conclusions can be drawn.

1. The relative weight between BDS and GPS is better to chose as one to two or one to three for the determination of ERP when combing them. In this case, the accuracy of ERP can be improved to some extent.
2. The RMSs of x and y component error of PM is about 0.19 mas and 0.21 mas by using GPS data. The RMS of x and y component error of PM is about 0.92

Table 26.3 The statistical results of system bias between BDS and GPS of stations (unit: m)

Station	Mean	STD
BRST	−0.062	0.177
BRUX	−11.637	0.152
CUT0	−3.048	0.258
DLF1	1.471	0.172
GMSD	1.395	0.165
GRAC	−0.485	0.178
JFNG	−0.914	0.174
KIR8	1.701	0.165
MAR7	2.394	0.172
ONS1	1.607	0.167
REUN	−4.646	0.157
UNB3	2.480	0.238
UNBS	−13.073	0.246
WTZZ	33.205	0.210
ZIM3	1.087	0.224

mas and 1.0 mas by using BDS data, which are obviously larger than those by GPS data.

3. The RMSs of x and y component error of PM is about 0.15 mas by combining BDS and GPS data. The accuracy of ERP determination is improved to some extent, and the improvements of x and y component of PM are about 14 and 8 % respectively.
4. The RMSs of x and y component error of PM rate is about 0.18 mas/d by using GPS data of MEGX network. The RMSs of x and y component error of PM rate is about 0.20 mas/d and 0.32 mas/d by using BDS data of MEGX network, which are the same accuracy level to those by GPS data.
5. The RMSs of x and y component error of PM is about 0.16 mas/d and 0.2 mas/d by combining BDS and GPS data. The accuracy of ERP determination is improved to some extent, and the improvements of x and y component of PM rate are about 21 % and 17 % respectively.
6. The RMS of LOD errors is about 0.021 ms/d determined from GPS data and about 0.028 ms/d from BDS data. The RMS of LOD errors is about 0.021 ms/d by combining BDS and GPS data, which is equivalent to those by using just GPS data.
7. The system biases between BDS and GPS when combing them to determine the EPRs. They are different in different stations. The maximum of the them can reach several tens of meters which needs to be estimated in ERP determination. The estimated system biases are very stable and their accuracy is about 20 cm.

26.5 Conclusion

GNSS technique is one of the important approach to determine the ERPs of pole motion, pole motion rate and length of day. However, the whole Earth orientation parameters cannot be obtained just by GNSS, and need other space techniques such as VLBI, SLR and DORIS et al. The computational results in this paper show that the ERPs can be independently obtained by BDS data, although the accuracy of pole motion is obvious lower than those of GPS. The difference must be shortened when the global BDS will be established. The accuracies of pole motion rate and length of day is almost on the same level between GPS and BDS using MEGX network. The ERP accuracy can be further improved to some extent when the BDS data is combined in GPS data.

Acknowledgments This work was supported by Natural Science Foundation of China (41174008) and the Open Foundation of State Key Laboratory of Geodesy and Earth's Dynamics (SKLGED2013-4-2-EZ) and the Open Foundation of State Key Laboratory of Astronautic and Dynamics (2014ADL-DW0101) and the Foundation for the Author of National Excellent Doctoral Dissertation of China (2007B51).

References

1. Zheng DW, Yu NH (1996) Earth rotation and it's relations to geophysical phenomena: the changes of length of the day. J Adv Geophys 11(2):81–101 (In Chinese)
2. Beutler G (1998) The role of GPS in space geodesy. In: Teunissen PJG, Kleusberg A (eds) GPS for geodesy, 2nd edn. Springer, Berlin
3. Bizouard C, Gambis D (2005) The combined solution C04 for earth orientation parameters consistent with international reference frame 2005. http://hpiers.obspm.fr/eoppc/products/combined/C04_05.guide.pdf
4. Gambis D (2004) Monitoring earth orientation using space-geodetic techniques: state-of-the - art and prospective. J Geodesy 78(4–5):295–303
5. Ferland R, Piraszewski M (2009) The IGS-combined stations coordinates, earth rotation parameters and apparent geocenter. J Geodesy 83:385–392
6. Ray J, Kauba J, Altamimi Z et al (2005) Is there utility in rigorous combinations of VLBI and GPS earth orientation parameters? J Geodesy 79(9):505–511
7. Rummel R, Rothacher M, Beutler G (2005) Integrated global geodetic observing system (IGGOS)—science rationale. J Geodyn 40:357–362
8. Thaller D (2007) Inter-technique combination based on homogeneous normal equation systems including station coordinates, Earth orientation and troposphere parameters. Scientific technical report STR08/15, GFZ 2007
9. Englich S, Jorge P et al (2007) Determination of earth rotation variations by means of VLBI and GPS and comparison to conventional models. Vermessung Geoinfo 2:104–112
10. Li P (1994) Determination of earth rotation parameters and adjustment of a global geodetic network using the global positioning system. Technical report. Department of Geodesy and Geomatics Engineering, University of New Brunswick, Canda
11. Mireault Y, Kouba J, Ray J (1999) IGS earth rotation parameters. GPS Solution 3(1):50–72
12. Hefty J, Rothacher M et al (2000) Analysis of the first year of Earth rotation parameters with a sub-daily resolution gained at CODE processing centre of the IGS. J Geodesy 74:479–487

13. IGS Central Bureau (eds) (2002) 2002–2007 IGS strategic plan. Jet Propulsion Laboratory, Pasadena, California
14. Xu T, Zhang L, Li M et al (2013) Earth rotation parameters determination based on daily GPS Data of global IGS stations. Geomatics Sci Eng 33(3):8–13
15. Zhang Y, Wang Q, Zhu J et al (2011) Combination of weighted least square and AR model with application in pole motion prediction. Astron Prog 29(3):343–352
16. Xu X, Zhou YH (2010) High precision prediction method of earth orientation parameters. J Spacecraft TT&C Technol 29(2):70–76 (In Chinese)
17. Weixing Z, Wanke L, Xiaoying G (2011) Influence analysis of prediction errors on automats orbit determination. J Geodesy Geodyn 31(5):106–110 (In Chinese)
18. Li B (2010) Prediction of Earth rotation variation based on ARMA model. Global Positioning Syst 35(1):1–5

Chapter 27
SPODS Software and Its Result of Precise Orbit Determination for GNSS Satellites

Rengui Ruan, Xiaolin Jia, Xianbing Wu, Laiping Feng and Yongxing Zhu

Abstract The Satellite Positioning and Orbit Determination System (SPODS) is a tool for data analysis of global navigation satellite systems such as GPS, BeiDou, GLONASS, and Galileo. It has being designed and developed at Xi'an Research Institute of Surveying and Mapping since 2011. A brief introduction of the main models and methods employed in SPODS was presented in this paper. Experiments of precise orbit determination for GPS and GLONASS as well as integrated orbit determination for multi-GNSS were carried out with observation data collected from IGS tracking network. Compared with IGS final orbit, the accuracy in RTN components are 0.008, 0.011 and 0.012 m for GPS orbits, and are 0.019, 0.047 and 0.054 m for GLONASS orbits. The rms of orbit arc boundary discontinuities in RTN components are 0.054, 0.135 and 0.204 m for Galileo satellites, and 0.203, 3.486 and 0.155 m for BeiDou GEO satellites, 0.093, 0.171 and 0.249 m for BeiDou IGSO satellites, 0.040,0.120 and 0.177 m for BeiDou MEO satellites. It's worth to notice that the accuracy of GPS orbit with SPODS is comparable with that of IGS Analysis Centers.

Keywords GPS · GLONASS · BeiDou · Galileo · Precise orbit determination · SPODS software

R. Ruan (✉) · X. Jia · X. Wu · L. Feng · Y. Zhu
Xi'an Research Institute of Surveying and Mapping, Xi'an 710054, China
e-mail: rrg2002me@163.com

R. Ruan · X. Jia · X. Wu · L. Feng · Y. Zhu
State Key Laboratory of Geo-information Engineering, Xi'an 710054, China

J. Sun et al. (eds.), *China Satellite Navigation Conference (CSNC) 2014 Proceedings: Volume III*, Lecture Notes in Electrical Engineering 305,
DOI: 10.1007/978-3-642-54740-9_27,

27.1 Introduction

In the past two decades, GPS/GNSS has become one of the most important technologies for space geodesy. Nowadays, several programs of GNSS (such as BeiDou, Galileo, QZSS and so on) are in progress, along with the continuously increasing stability and performance of GPS and GLONASS, which promises a new era of multi-GNSS for research and application. Some well-known institutions (such as Jet Propulsion Laboratory (JPL), Astronomical Institute, University of Bern (AIUB, CODE), German Research Centre for Geosciences (GFZ), Massachusetts Institute of Technology (MIT)) have always been in a leading position in the field of GNSS research and applications, with long-term technology accumulation and high precision GPS data processing tools such as GIPSY, Bernese, EPOS and GAMIT developed in early 1990s. During the last 3 years, a new tool for GNSS data processing named SPODS (Satellite Positioning and Orbit Determination System) has being designed and developed at Xi'an Research Institute of Surveying and Mapping. Wei et al. [16] exhibits the performance of SPODS for precise orbit determination, positioning and earth rotation parameters solution with GPS data for the first time. Since the SPODS software is little known to the GNSS community, a brief introduction of the main models and methods employed in SPODS is presented in this paper. In order to comprehensively demonstrate the performance of SPODS for GNSS precise orbit determination, experiments with observation data collected from IGS tracking stations were carried out and the orbit accuracy of GPS, GLONASS, BeiDou and Galileo were evaluated.

27.2 SPODS: Models and Methods

In the SPODS software, un-differenced ionosphere-free carrier-phase and code pseudorange observations are used. Data processing starts with a procedure of preprocessing to detect carrier phase cycle slip and bad observations according to the method of TurboEdit [4]. The observation equation is carefully modeled with various correction and unknown parameters are solved with the method of weighted least squares iteratively and the bad observation and cycle slip are detected by checking post-fit residuals. The iteration ends until no cycle slip and outlier is detected. Afterwards, ambiguity fixing is performed with the method according to Ge Maorong [9]. The independent DD-ambiguities [3, 8, 9, 12] are selected firstly on the constellation level and then on the network level. The decision to fixing or not the wide-lane [3] and narrow-lane DD-ambiguity depends on whether their fixing probabilities are larger than 99 %.

The PECE method of Adams-Bashforth-Moulton with RKF 8/7 start procedure is used for satellite orbit extrapolation. The force acting on the satellite from various sources including: earth's geopotential, gravity of the moon, the sun, and the planetary, solar radial pressure and general relativistic effects are considered.

Variation of geopotential caused by solid earth tide and pole tide according to IERS conventions (2003) [11] is also taken into account, and the acceleration generated by geopotential is expressed in the function of satellite coordinates x, y, z [5, 13]. The position of the moon, the sun, and the planetary are interpolated with JPL DE405. Perturbation from solar radial pressure is computed with constant and periodic acceleration in D, Y and B direction named as ECOM model [14].

The inertial frame is realized to GCRS according to geocentric, mean equator and equinox of 2000 Jan 1.5 (J2000.0) and the terrestrial frame of ITRF2005 realized of ITRS is used. The interconnection between ITRS and GCRS is realized by IAU2000A Precession-Nutation Model [11] with earth oriental parameters from IERS Bulletin A (earth rotation parameters are adjusted). The variation of pole motion and UT1 caused by diurnal and sub-diurnal ocean tide as were as diurnal and semidiurnal nutation effect are considered [11].

Corrections employed to the observations include: offset and variation of the antenna phase center for both satellites and receivers computed with data from IGS ANTEX file, periodic clock variation of the theory of relativity, the wind-up effect of carrier-phase, ionosphere and troposphere delay and site-displacement caused by solid earth tide, pole tide and ocean tide-loading. The attitude of satellite including in eclipse period is carefully modeled [6, 7, 10] e.g. GYM-95 is use for GPS satellites [1]. The zenith delay of troposphere is computed using the Saastamoinen model with temperature and pressure from the GPT model and mapped to path delay using the dry GMF mapping function [2]. The tidal displacement of stations is computed according to IERS Conventions (2003) [11].

27.3 Experiments and Result

Experiments with observation data from IGS tracking stations were carried out to validate the performance of SPODS for orbit determination for GPS, GLONSS, BeiDou and Galileo satellites.

In the routine data processing with SPODS, observation data spanning 1 day with sample interval of 5 min are used. The sigma of un-differenced PC and LC are 2.0 m and 2 cm for zenith, and increase with decreasing elevation angle E using the function $1/\sin^2 E$ and the observation with elevation angle smaller than 10° are excluded.

All station coordinates are adjusted with a priori constrain of 1 km in each component except some 10 stations are selected as reference station with precise coordinates from the file IGS05.snx and a prior constrain of 2 cm for each component. The position and velocity of satellites at the initial epoch and parameters of ECOM (D0, Y0, B0, Bc and Bs) are adjusted with approximate values obtained by fitting the broadcast ephemeris. EOP product of IERS Bulletin A are used and Daily x and y pole offsets, pole-rates, and LOD are adjusted. For each station, the wet zenith delay is adjusted every 2 h as constant parameters and the north and

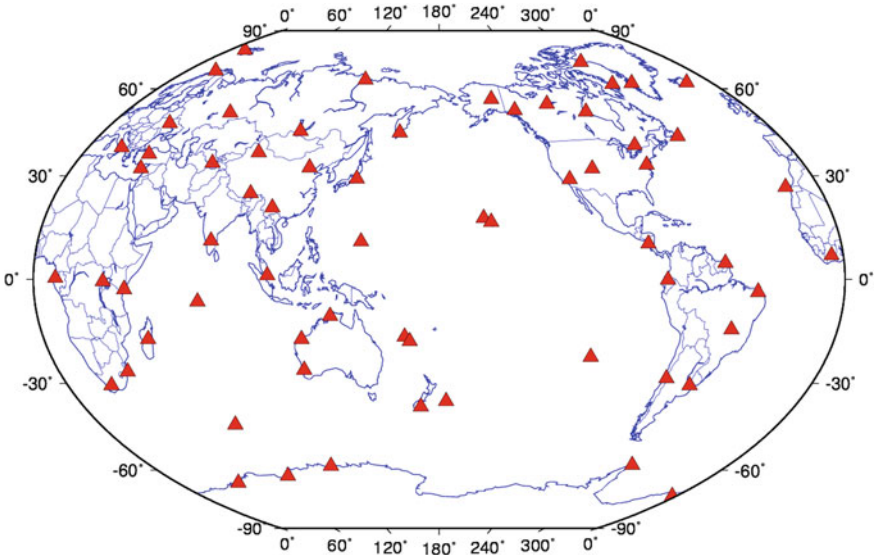

Fig. 27.1 Distribution of stations for GPS orbit determination

east gradient are estimated every 24 h. Ambiguity fixing is performed for the ambiguities of GPS, Galileo and BeiDou observations, while ambiguities of GLONASS observations remain float.

In case of data processing for multi-GNSS, the inter-system bias is estimated for each receiver, especially for GLONASS, 1 bias parameter for each receiver-satellite pair is estimated.

In this paper, the experiments for GPS and GLONASS data processing are strictly according to the routine strategy, while for the experiment of multi-GNSS, the strategy are slight different that data spanning 2 days and EOP parameters were fixed to IERS product of Bulletin A.

27.3.1 GPS

To validate the performance of the SPODS software for GPS orbit determination, GPS data from about 64 IGS tracking stations during March 16–31, in 2011, were collected. Figure 27.1 shows the station distribution.

The obtained GPS orbits are compared with the IGS final GPS orbits, and the differences (errors) were expressed in R, T, N components. Figure 27.2 shows that daily rms in R component are smaller than 0.01 m, while in T and N components are smaller than 0.015 m and the mean rms are 0.008, 0.011 and 0.012 m for RTN respectively.

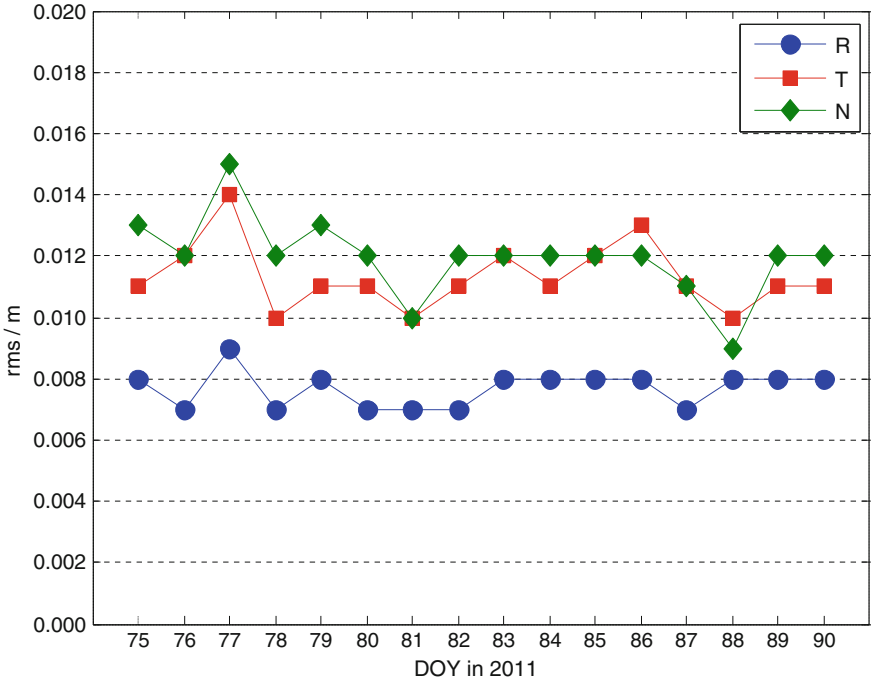

Fig. 27.2 The rms errors in RTN of GPS orbits compared with IGS final GPS orbits

We also compare the final GPS orbit from IGS Analysis Centers (ACs) with the IGS final GPS orbit and the daily ID rms of the differences were shown in Fig. 27.3 together with that of SPODS noted by XRI. It can be concluded that the orbit obtained with SPODS is comparable with those of IGS ACs, which also indicates that models and methods employed in SPODS have a good consistency with IGS ACs.

27.3.2 GLONASS

To validate the performance of the SPODS software for GLONASS orbit determination, observation data from about 73 IGS tracking stations during March 16–31, in 2011, were collected. Figure 27.4 shows the station distribution.

The obtained GLONASS orbits are compared with the IGS final GLONASS orbits, and the differences (errors) were expressed in R, T, N components. Figure 27.5 shows that daily rms in R component is about 0.02 m, while in T and N component are between 0.04 and 0.06 m and the mean rms are 0.019, 0.047 and 0.054 m respectively.

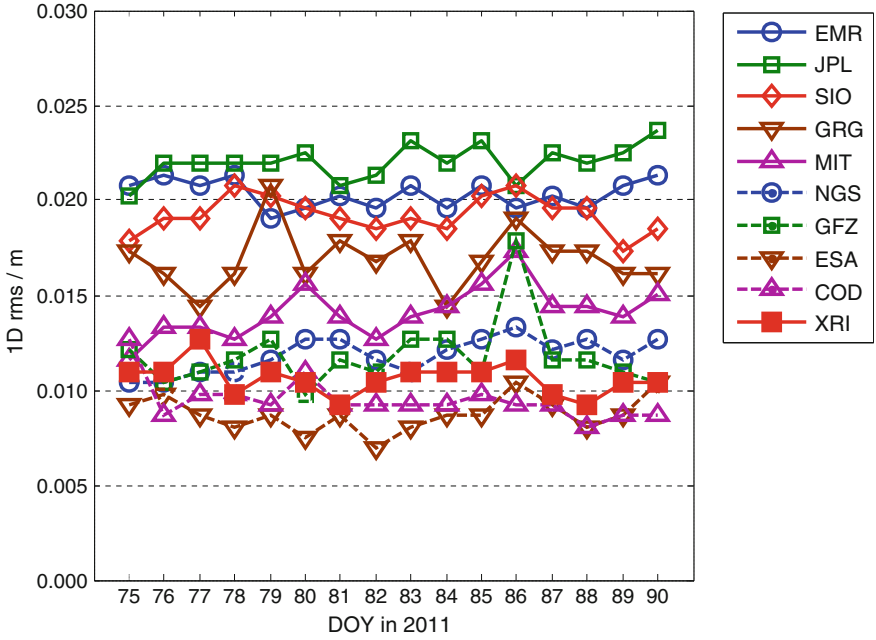

Fig. 27.3 The ID rms of GPS orbit from XRI and IGS ACs compared with IGS final GPS orbit

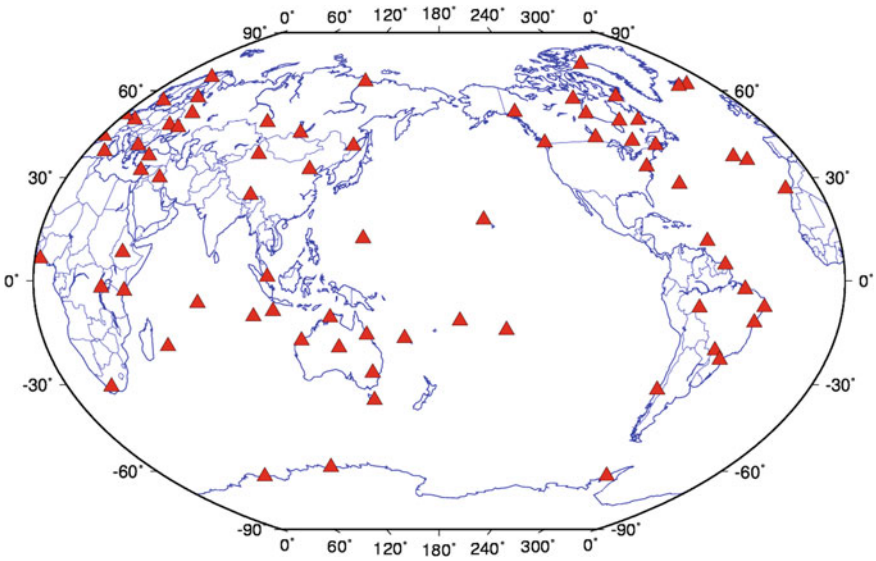

Fig. 27.4 Distribution of stations for GLONASS orbit determination

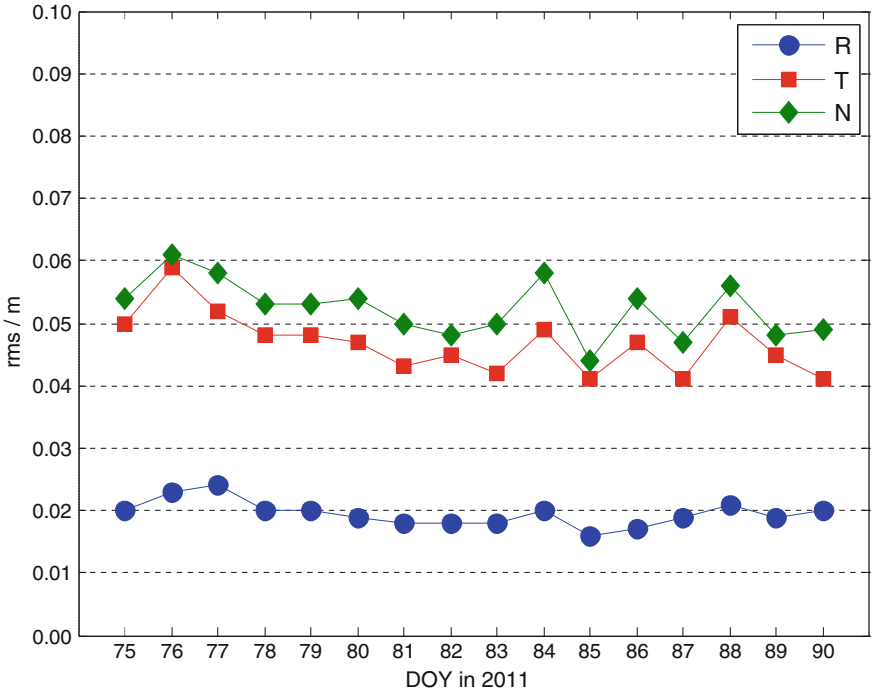

Fig. 27.5 The rms errors in RTN of GLONASS orbits compared with IGS final GLONASS orbits

Again, we compute the daily 1D rms of the final GLONASS orbit from 4 IGS ACs (GRG, ESA, GFZ and CODE) compared with the IGS final GLONASS orbits and presented them in Fig. 27.6 together with that of SPODS. It's obvious that the GLONASS orbit of SPODS is on the same level with GRG but evidently worse than that of GFZ, CODE and ESA.

27.3.3 Multi-GNSS

At present, in the sky, there are 4 In-Orbit-Validate (IOV) satellites of Galileo and 14 operational satellites of BeiDou including 4 in middle earth orbit (MEO), 5 in inclined geostationary earth orbit (IGSO) and 5 in geostationary earth orbit. To validate the performance of the SPODS software for Galileo/BeiDou orbit determination and the ability for multi-GNSS date processing, observation data of some 25 stations of IGS MGEX from 01 to 30, in Nov. 2013, were collected. These stations are equipped with multi-GNSS receivers of type SEPT POLARX4 or TRIMBLE NETR9. Figure 27.7 shows the station distribution. Carrier-phase and

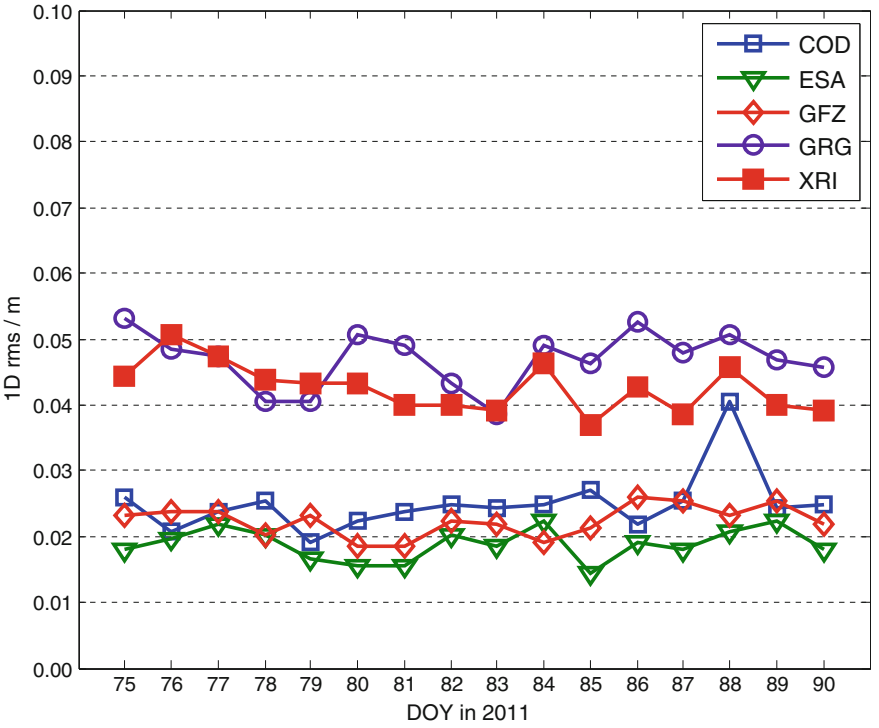

Fig. 27.6 The ID rms of GLONASS orbit from XRI and IGS ACs compared with IGS final GLONASS orbit

pseudorange observations on GPS L1 and L2, BeiDou B1 and B2, Galileo E1 and E5 and GLONASS L1 and L2 are used.

As a quality indicator for the internal consistency of the orbits, arc boundary discontinuities of two consecutive and un-overlapped arcs are used, i.e., the differences in RTN components of the orbit positions at midnight. The principle to compute arc boundary discontinuities is illustrated by Fig. 27.8,

Tables 27.1 and 27.2 show the rms of arc boundary discontinuity in RTN for the Galileo and BeiDou Satellites respectively. For Galileo satellites, the rms in R component are between 0.04 and 0.06 m, while in T and N components are between 0.10 and 0.25 m, the mean rms over all Galileo satellites are 0.054, 0.135 and 0.204 m. For BeiDou MEO satellites (C11–C14), the rms in R component are between 0.02 and 0.07 m, in T component are around 0.12 m, in N component are between 0.12 and 0.20 m, the mean rms in RTN are 0.040, 0.120 and 0.177 m. For IGSO satellites (C06–C10), the rms in R component are between 0.04 and 0.15 m; in T component are between 0.12 and 0.24 m, in N component are between 0.20 and 0.33 m, mean rms are 0.093, 0.171 and 0.249 m. For GEO satellites (C01–C05), the rms in R component are 0.14 and 0.28 m, in T component are between 1.6 and 6.3 m, in N component are smaller than 0.3 m, mean rms in RTN

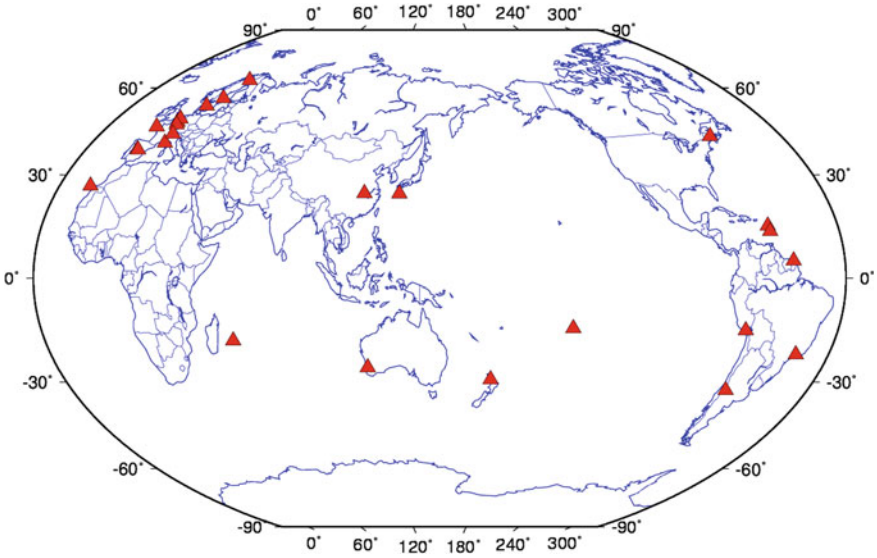

Fig. 27.7 Distribution of Stations for multi-GNSS orbit determination

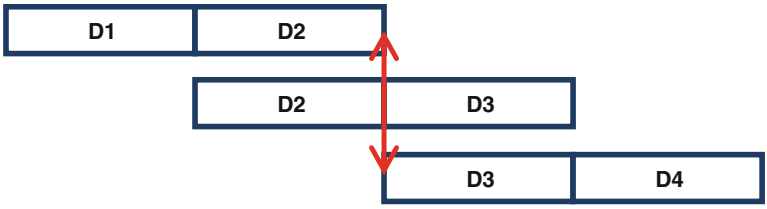

Fig. 27.8 Illustration for computation of arc boundary discontinuities

Table 27.1 The rms of arc boundary discontinuity of Galileo satellites in RTN components (m)

ID	R	T	N
E11	0.060	0.105	0.161
E12	0.062	0.125	0.199
E19	0.044	0.158	0.219
E20	0.049	0.154	0.237

component are 0.203, 3.486 and 0.155 m. The precision of BeiDou orbits are equivalent with the results reported by other institutions [15, 17].

For the sake of completeness, Figs. 27.9 and 27.10 show the rms of arc boundary continuities in RTN components of GPS and GLONASS satellites. For GPS satellites, the rms in R component are smaller than 0.05 m, in T and N components are mostly below 0.01 m, mean rms in RTN are 0.029, 0.072 and

Table 27.2 The rms of arc boundary discontinuity of BeiDou satellites in RTN components (m)

ID	R	T	N
C01	0.142	6.239	0.180
C02	0.274	1.739	0.175
C03	0.201	1.632	0.079
C04	0.253	2.033	0.060
C05	0.144	5.787	0.279
C06	0.046	0.122	0.239
C07	0.071	0.166	0.207
C08	0.149	0.205	0.233
C09	0.073	0.129	0.327
C10	0.127	0.235	0.237
C11	0.065	0.127	0.191
C12	0.032	0.132	0.206
C13	0.037	0.100	0.157
C14	0.028	0.120	0.156

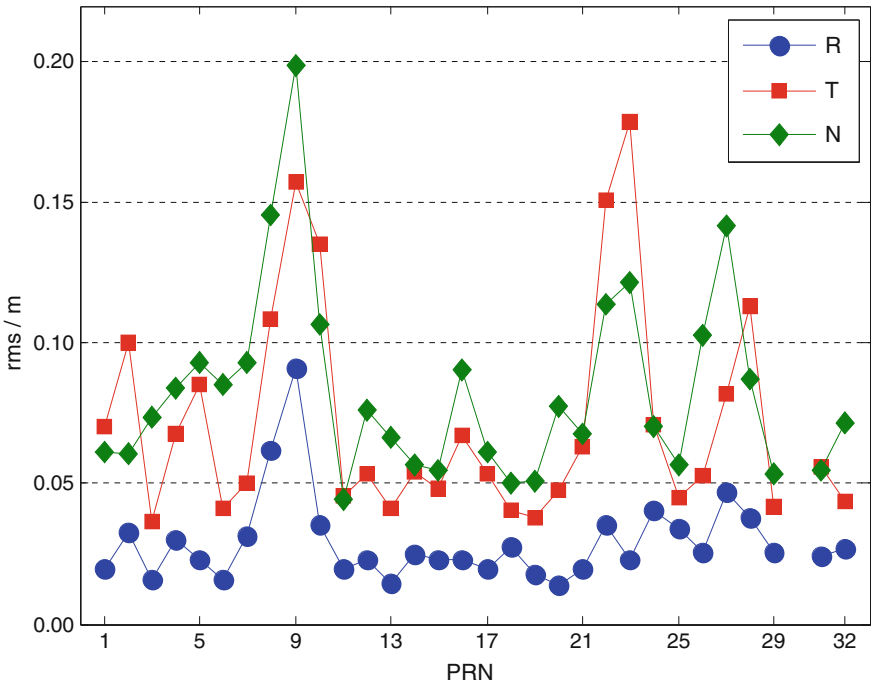

Fig. 27.9 The rms of arc boundary discontinuity of GPS satellites in RTN

0.083 m. For most GLONASS satellites, the rms in R component are smaller than 0.05 m, in T and N component below 0.15 m, mean rms in RTN are 0.045, 0.135 and 0.142 m.

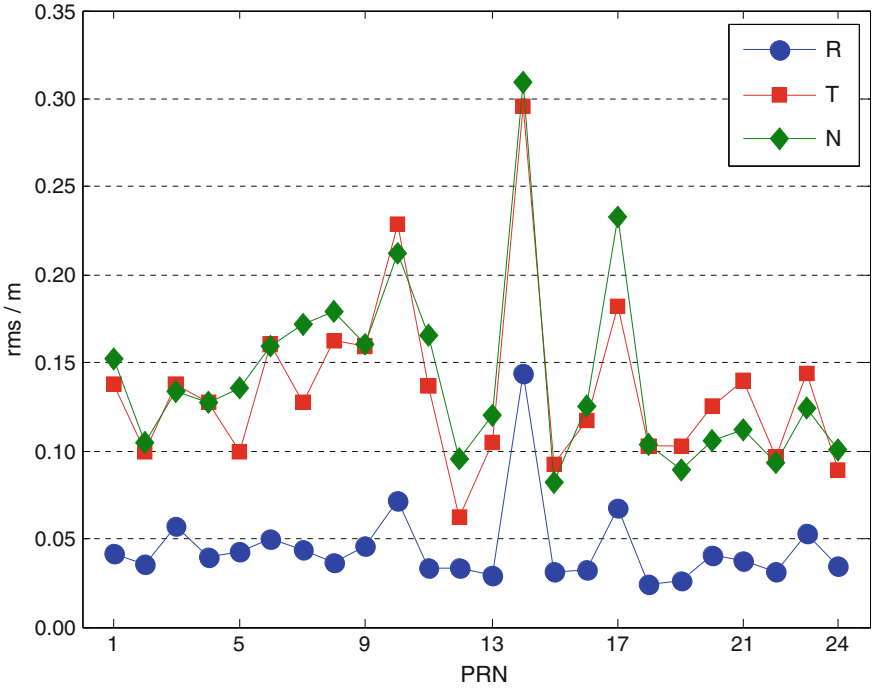

Fig. 27.10 The rms of arc boundary discontinuity of GLONASS satellites in RTN

27.4 Summary

The SPODS software designed and developed at Xi'an Institute of Surveying and Mapping now possess the ability for high precise data processing of GPS, GLONASS, BeiDou and Galileo. Experiment of GPS orbit determination show that, compared with IGS final orbit, the rms of consistency in RTN components are 0.008, 0.011 and 0.012 m. By comparing with the GPS orbit of IGS ACs on 1 d rms, it's indicated that the accuracy of GPS orbit with SPODS is on the same level with the IGS ACs. The rms of the resulting GLONASS satellite orbit compared with IGS final GLONASS orbit are 0.019, 0.047 and 0.054 m respectively in RTN components, which are equal with that of GRG and larger than that of ESA, GFZ and COD. Experiments for multi-GNSS orbit determination with observation data collected from about 25 MGEX stations in November 2013 were carried out. The results show the rms of arc boundary discontinuity for Galileo satellites are 0.054, 0.135 and 0.204 m in RTN respectively. The rms of discontinuity in RTN are 0.203, 3.486 and 0.155 m for BeiDou GEO satellites; 0.093, 0.171 and 0.249 m for BeiDou IGSO satellites; and 0.040, 0.120 and 0.177 m for BeiDou MEO satellites.

References

1. Bar-Sever YE (1997) A new model for yaw attitude of global positioning system satellites. J Geodesy 70:714–723
2. Beohm J, Neill A, Tregoning P, Schuh H (2006) Global mapping function (GMF): a new empirical mapping function based on numerical weather model data. Geophy Res Lett 33
3. Blewitt G (1989) Carrier phase ambiguity resolution for the global positioning system applied to geodetic baselines up to 2000 km. J Geophys Res 94:10187–10203
4. Blewitt G (1990) An automatic editing algorithm for GPS data. Geophys Res Lett 17:199–202
5. Cunningham LE (1970) On the computation of the spherical harmonic terms needed during the numerical integration of the orbital motion of an artificial satellite. Celest Mech 3:207–216
6. Dilssner F (2010) GPS IIF-1 satellite antenna phase center and altitude modeling. Inside GNSS
7. Dilssner F, Springer T, Gienger G, Dow J (2011) The GLONASS-M satellite yaw-attitude model. Adv Space Res 47:160–171
8. Dong D-N, Bock Y (1989) Global positioning system network analysis with phase ambiguity resolution applied to crustal deformation studies in California. J Geophys Res 94:3949–3966
9. Ge M, Gendt G, Dick G, Zhang FP (2005) Improving carrier-phase ambiguity resolution in global GPS network solutions. J Geodesy 2005:103–110
10. Kouba J (2008) A simplified yaw-attitude model for eclipsing GPS satellites. GPS Solutions
11. IERS conventions (2003) IERS Technical Note 32, IERS, Frankfurt am Main
12. Mervart L (1995) Ambiguity resolution techniques in geodetic and geodynamic applications of the global positioning system. University of Berne, Switzerland
13. Montenbruck O, Gill E (2001) Satellite orbits models, methods, and applications. Springer, Berlin
14. Springer TA (1999) Modeling and validating orbits and clocks using the global positioning system. Astronomical Institute, University of Berne, Switzerland
15. Steigenberger P, Hugentobler U, Hauschild A, Montenbruck O (2013) Orbit and clock analysis of Compass GEO and IGSO satellites. J Geodesy 87:515–525
16. Wei Z, Ruan R, Jia X, Wu X, Song X, Mao Y, Feng L, Zhu Y (2014) Satellite positioning and orbit determination system SPODS: theory and test. Acta Geodaetica Cartogr Sin 43:1–4 (in Chinese)
17. Zhao Q, Guo J, Li M, Qu L, Hu Z, Shi C, Liu J (2013) Initial results of precise orbit and clock determination for COMPASS navigation satellite system. J Geodesy 2013:475–486

Chapter 28
Research on Feature Extraction Method of No-Modeling System Error in BeiDou Orbit Determination Residual

Lue Chen, Geshi Tang, Hongzheng Cui, Ming Chen, Huicui Liu and Mei Wang

Abstract BeiDou navigation satellite precise orbit determination is one of the key technologies in BeiDou satellite navigation system application. To analyze the no-modeling system error in BeiDou navigation satellite system, this paper proposes Ensemble Empirical Mode Decomposition (EEMD) and Hilbert spectrum method for orbit determination residual feature extraction. Firstly, the feature extraction principle of EEMD and Hilbert spectrum is analyzed, and the method model of feature extraction is established, then Pseudo-range and carrier phase orbit determination residuals in BeiDou satellite navigation system are analyzed, finally, the proposed method is applied to multi-stations GEO receiving multiple BeiDou navigation satellite signals for the orbit residuals analyzing. The results show that the proposed method can accurately extract the 86,400 s period feature which is closely related to the time period items with one day in the BeiDou orbit residuals. It is very important for separating the no-modeling system error in BeiDou navigation satellite orbit determination residuals for improving the orbit determination precision.

Keywords BeiDou navigation satellite · Orbit determination residual · Feature extraction · Ensemble Empirical Mode Decomposition · Hilbert spectrum

L. Chen (✉) · G. Tang · H. Cui · M. Chen · H. Liu · M. Wang
Science and Technology on Aerospace Flight Dynamics Laboratory, Beijing 100094, China
e-mail: luechen0912@163.com

L. Chen · G. Tang · H. Cui · M. Chen · H. Liu · M. Wang
Beijing Aerospace Control Center, Beijing 100094, China

J. Sun et al. (eds.), *China Satellite Navigation Conference (CSNC) 2014 Proceedings: Volume III*, Lecture Notes in Electrical Engineering 305,
DOI: 10.1007/978-3-642-54740-9_28,

28.1 Introduction

At present, China is running and constructing BeiDou navigation satellite system which is an important component in global navigation satellite system (GNSS), it is the national critical infrastructure [1], and it plays an important role in the areas of industrial production and people's life. Precise orbit determination is one of the key technologies in satellite navigation system. The observation of BeiDou satellite contains pseudo-range and carrier phase observation. Orbit determination residual directly expresses the orbit determination inner average precision. There are lots of reasons for generating no-modeling system error in BeiDou orbit determination calculating, for example, multipath, satellite orbit, ionosphere delay, troposphere delay, satellite clock error [2]. Ionosphere, troposphere, satellite clock errors can be corrected by modeling, but for some difficult modeling errors are usually simply ignore these impacts, and these no-modeling system errors in orbit determination residuals are one of the most error resources in BeiDou satellite precise orbit determination. This paper proposes the orbit determination residual feature extraction method of Ensemble Empirical Mode Decomposition (EEMD) and Hilbert spectrum, and it is used to precisely extract feature information in BeiDou orbit determination residuals. It is expected to isolate the no-modeling system errors in BeiDou orbit determination residuals for improving the orbit determination precision.

28.2 Theory of Orbit Determination Residual Feature Extraction

BeiDou orbit determination residual is defined as observation subtract from theoretical calculation value, BeiDou orbit determination residual directly expresses the BeiDou orbit determination precision. Orbit determination residual is a time sequence, thus it can be analyzed by the method of time sequence analyzing.

In addition, BeiDou orbit residuals typically exhibit nonlinear and non-stationary characteristics, this paper researches the residual analysis using the advanced frequency analysis method developed rapidly in recent years. EEMD method combined with Hilbert spectrum analysis was firstly introduced into orbit residual analysis, to achieve high-precision BeiDou orbit residual feature extraction. EEMD method originated from Empirical Mode Decomposition (EMD) method [3] which is an important method creation, it rapidly used in Geophysics, image processing, wireless communications, nonlinear analysis, fault diagnosis, etc. [4–6]. And EMD method also used in GPS/Pseudolite Positioning research [7]. The following introduces the basic theory of feature extraction in BeiDou orbit residual analyzing.

28.2.1 The Empirical Mode Decomposition

The EMD method is able to decompose a signal into some IMFs. An IMF is the function that satisfies the two following conditions: (1) in the whole data set, the number of extrema and the number of zero-crossings must either equal or differ at most by one, and (2) at any point, the mean value of the envelope defined by local maxima and the envelope defined by the local minima is zero. An IMF represents simple oscillatory mode embedded in the signal. With the simple assumption that any signal consists of different simple IMFs, the EMD method was developed to decompose a signal into IMF components. The EMD process of a signal $x(t)$ can be described as follows:

Step 1: Identify all the local extrema (the combination of both maxima and minima) of the signal $x(t)$, connect all these local maxima (minima) with a cubic spline as the upper (lower) envelope;

Step 2: Calculate the mean $m(t)$ of the upper and lower envelope, the difference between the signal $x(t)$ and $m(t)$ as the first component $h_1(t)$:

$$h_1(t) = x(t) - m(t) \tag{28.1}$$

Judge whether $h_1(t)$ satisfy two conditions of IMF existence, if not, $h_1(t)$ will be treated as signal to repeat step (1) and (2) until $h_1(t)$ satisfy the conditions, this is the sifting process. Then the first IMF ($c_1(t)$) is designated as

$$c_1(t) = h_1(t). \tag{28.2}$$

Huang et al. also suggested a criterion for stopping the sifting process. This is accomplished by limiting the size of the standard deviation, denoted as S_d, which is calculated from two consecutive sifting results as

$$S_d = \sum_{t=0}^{T} \frac{|(h_{k-1}(t) - h_k(t))|^2}{h_k^2(t)} \tag{28.3}$$

where T is the time span of signal, $h_{(k-1)}(t)$ and $h_{(k)}(t)$ are two continuous processing results. The value of S_d is usually determined between 0.2 and 0.3.

Step 3: Remove $c_1(t)$ from the rest of the signal by

$$r_1(t) = x(t) - c_1(t) \tag{28.4}$$

Treat $r_1(t)$ as a new signal and repeating the same sifting process as described above, we can then obtain the second IMF 28 ($c_2(t)$). Finally, we can obtain a series of IMFs $c_i(t)$ $(i = 1, 2, \ldots, n)$ and the final residue $r_n(t)$. The sifting process can be stopped by any of the following predetermined criteria: either when the component $c_n(t)$ or the residue $r_n(t)$ becomes less than the predetermined value of substantial consequence, or when the residue $r_n(t)$ becomes a monotonic

function from which no more IMF can be extracted. Summing up all the IMFs and the final residue, we should be able to reconstruct the original signal $x(t)$ by

$$x(t) = \sum_{i}^{n} c_i(t) + r_n(t). \tag{28.5}$$

28.2.2 Ensemble Empirical Mode Decomposition

The principle of EEMD method is that [8]: Utilizing the statistical characteristics of frequency uniform distribution of Gaussian white noise, Gaussian white noise is added to the original signal to make it continuous in different scales to avoid mode mixing.

The discontinuity of IMFs causes the phenomenon of mode mixing in EMD, and the capability of EMD getting reasonable IMFs is determined by local extrema and the extrema distribution intervals. When there are not enough extrema, the decomposition will stop; when the extrema distribution intervals of the signal are not uniform, fitting error of upper and lower envelope of the extrema will appear, to induce mode mixing.

The method of EEMD avoiding mode mixing is implemented as follows: Firstly, on the base of the established criterion of adding white noise in EEMD, the amplitude standard deviation coefficient of white noise is determined. After white noise with uniform scales and const amplitude standard deviation is added to the original signal, the signal will have enough extrema to provide a condition for avoiding mode mixing; Then, the signal with added Gaussian white noise is decomposed by EMD to get corresponding IMFs, and all the corresponding IMFs are ensemble calculated using the principle that the average statistical of uncorrelated random sequences is equal to zero, to eliminate effects of added Gaussian white noise to real IMFs; Finally, IMFs of ensemble calculation are as the final results of EEMD.

The specific steps of EEMD are as follows:

Step 1: Gaussian white noise $n_i(t)$ with zero mean value and constant amplitude standard deviation is added to original signal, as

$$y_i(t) = y(t) + n_i(t) \tag{28.6}$$

where $y_i(t)$ is the signal with the ith time added Gaussian white noise.

A criterion of adding white noise is a key problem in EEMD method, because the amplitude of added white noise can directly affect the decomposition effect of avoiding mode mixing. According to the requirement of avoiding mode mixing and the characteristics of EEMD, the added white noise should not affect effective

high frequency components, which refers to contain the components of fault information of high frequency in signal, and should change the distribution characteristics of extrema intervals of low frequency in signal. In this paper, based on mechanism analysis and many experiments, a criterion of adding white noise in EEMD method is proposed, as

$$0 < \alpha < \frac{\sigma}{2} \tag{28.7}$$

where α is the ratio coefficient of amplitude standard deviation of the added white noise, ε_n, to amplitude standard deviation of the original signal, ε_o, as $\alpha = \frac{\varepsilon_n}{\varepsilon_o}$; σ is ratio coefficient of amplitude standard deviation of the effective high frequency components in original signal, ε_h, to amplitude standard deviation of the original signal, ε_o, as $\sigma = \frac{\varepsilon_h}{\varepsilon_o}$. In most cases, we suggest the value of α, which can meet the requirement of avoiding mode mixing in signal, is $\frac{\sigma}{4}$ in (28.7), as $\alpha = \frac{\sigma}{4}$.

Step 2: $y_i(t)$ is decomposed by EMD to get the respective IMFs denoted by $c_{ij}(t)$ and a residue of data denoted by $r_i(t)$. Where $c_{ij}(t)$ expresses the jth IMF of decomposition of the ith added Gaussian white noise to signal.

Step 3: The above corresponding IMFs are calculated by an ensemble average way to get the final IMFs as the results of EEMD, as

$$c_j(t) = \frac{1}{N}\sum_{i=1}^{N} c_{ij}(t) \tag{28.8}$$

where $c_j(t)$ expresses the jth IMF of EEMD.

28.2.3 Hilbert Spectrum

The definition of Hilbert transform is as follows,

$$H[x(t)] = \frac{1}{\pi}\int_{-\infty}^{\infty} \frac{x(\tau)}{t-\tau} d\tau \tag{28.9}$$

where $H[\,]$ is Hilbert operator.

Using Hilbert spectrum to demodulate BeiDou orbit residual progress is as follows, the original signal $x(t)$ is transformed to $\hat{x}(t)$ by Hilbert transform, and $\hat{x}(t)$ is as the imaginary of the original signal. And the envelope of the original signal $P(t) = \sqrt{x^2(t) + \hat{x}^2(t)}$, then the envelope is calculated by FFT spectrum to obtain the Hilbert spectrum.

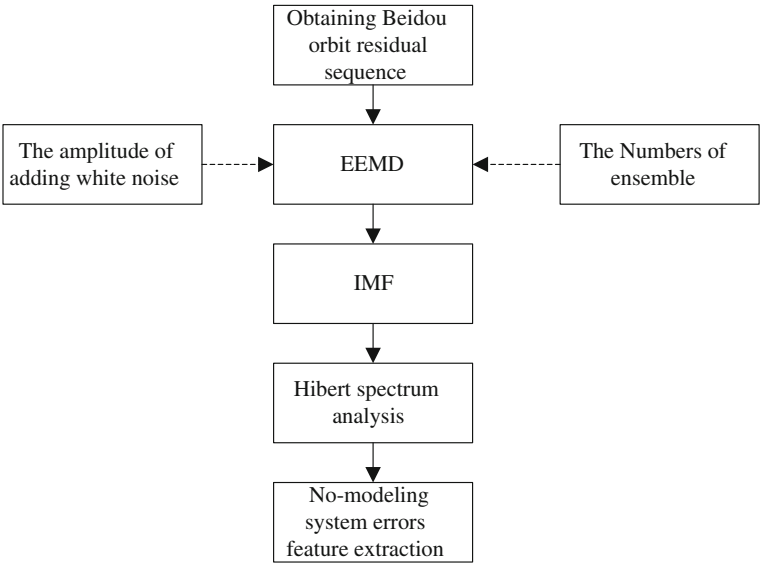

Fig. 28.1 BeiDou orbit residual non-modeling system error feature extraction flow chart

Based on the above principle, this paper proposes EEMD and Hilbert spectrum method for BeiDou orbit determination residual feature extraction. The processing progress is as shown in Fig. 28.1.

28.3 Orbit Determination Residual Characteristic Analysis

This section introduce BeiDou orbit determination residual characteristic analysis based on pseudo-range and carrier phase, the orbit data comes from iGMAS analysis center of Beijing aerospace control center, and the sample frequency is 1/30, this means 30 s obtains 1 data, and there are 3 days' orbit data. Figure 28.2 shows the pseudo-range orbit determination residual waveform of Station CUT0 and Satellite CO1, and Fig. 28.3 shows the carrier phase orbit determination residual waveform of Station CUT0 and Satellite CO1. Figure 28.4 shows the pseudo-range orbit determination residual waveform of Station GSMD and Satellite CO3, and Fig. 28.5 shows the carrier phase orbit determination residual waveform of Station GSMD and Satellite CO3.

From these above figures, it can be found that the pseudo-range orbit determination residual waveform of CUT0-CO1 is disorder, and it contains lots of random noise. But period modulation information is present by carefully analyzing. The carrier phase orbit determination residual waveform of CUT0-CO1 is disorder, but there is no obvious regular feature in this waveform. The pseudo-range orbit

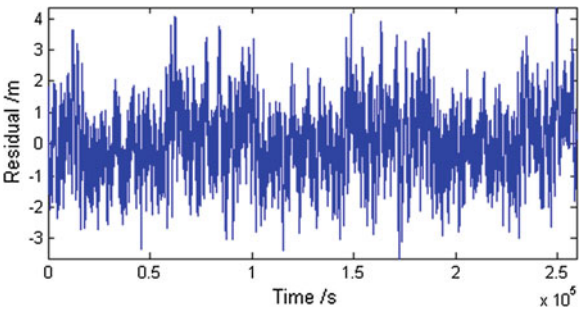

Fig. 28.2 Pseudo-range orbit determination residual of CUT0-CO1

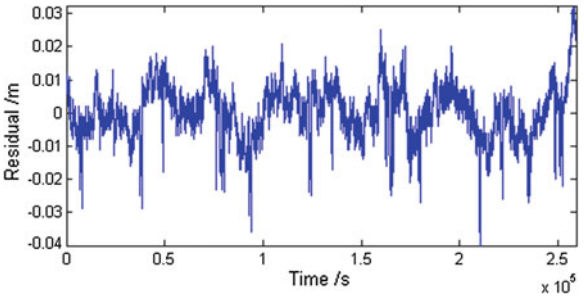

Fig. 28.3 Carrier phase orbit determination residual of CUT0-CO1

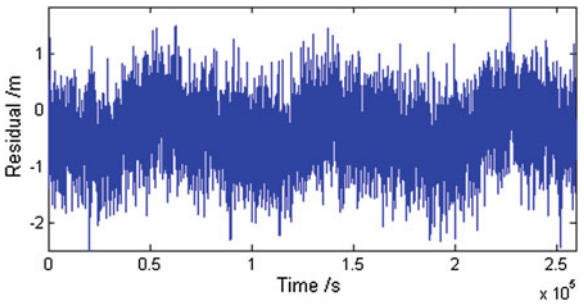

Fig. 28.4 Pseudo-range orbit determination residual of GSMD-CO3

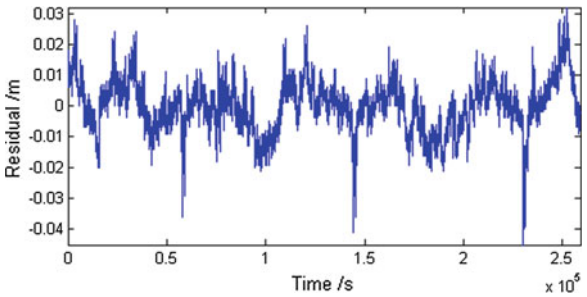

Fig. 28.5 Carrier phase orbit determination residual of GSMD-CO3

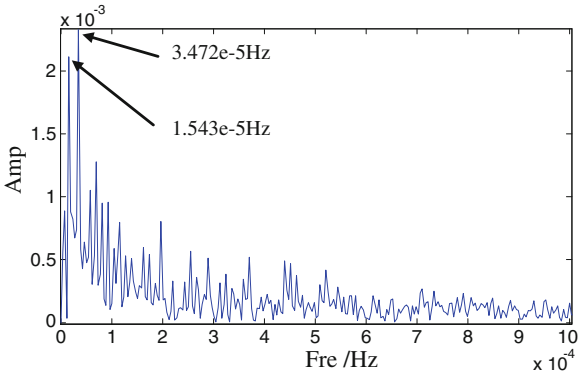

Fig. 28.6 FFT spectrum of carrier phase orbit determination residual of CUT0-CO1

determination residual waveform of GSMD-CO3 contains lots of random noise, the waveform presents a uniform distribution. The carrier phase orbit determination residual waveform of CUT0-CO3 is disorder, but there are three obvious descend peaks. Thus, it shows that BeiDou orbit determination residuals contain enrich information, the waveforms do not present ideal random distribution. It can be inferred that BeiDou orbit determination residuals contain feature information which can be extracted. If this information can be extraction effectively, the no-modeling system errors in orbit residual could be effectively separated.

28.4 Experimental Analysis

As shown in the above section, Fig. 28.3 shows the carrier phase orbit determination residual waveform of Station CUT0 and Satellite CO1. The FFT spectrum of this orbit residual is shown in Fig. 28.6. In Fig. 28.6, there are two obvious peak frequencies, they are respectively 1.543E−5 and 3.472E−5 Hz, and the according time periods are respectively 64,809 and 28,802 s. According to the physical meaning of orbit determination residual and the motion feature of GEO, we could not get more information of these two frequencies, thus, the residual data is analyzed by the proposed method in the above sections.

Figures 28.7 and 28.8 show the IMF results of EEMD of CUT0-CO1 orbit determination residuals. There are 8 IMFs and 1 residual component. And the adding white noise coefficient is set with 0.2, and the ensemble numbers is set with 100.

Then, the IMFs obtained from EEMD results are calculated by Hilbert spectrum, and the calculated results are shown in Figs. 28.9 and 28.10. In Fig. 28.9, the obvious peak frequencies 2.315E−5 and 6.944E−5 Hz could be easily found. In Fig. 28.10, the obvious peak frequencies 1.157E−5, 2.315E−5 and 3.472E−5 Hz could be easily found.

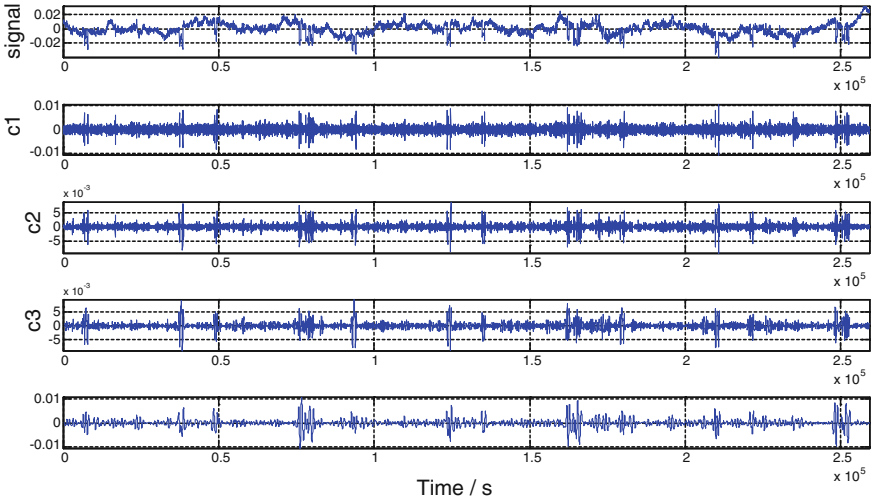

Fig. 28.7 First EEMD result of carrier phase orbit determination residual of CUT0-CO1

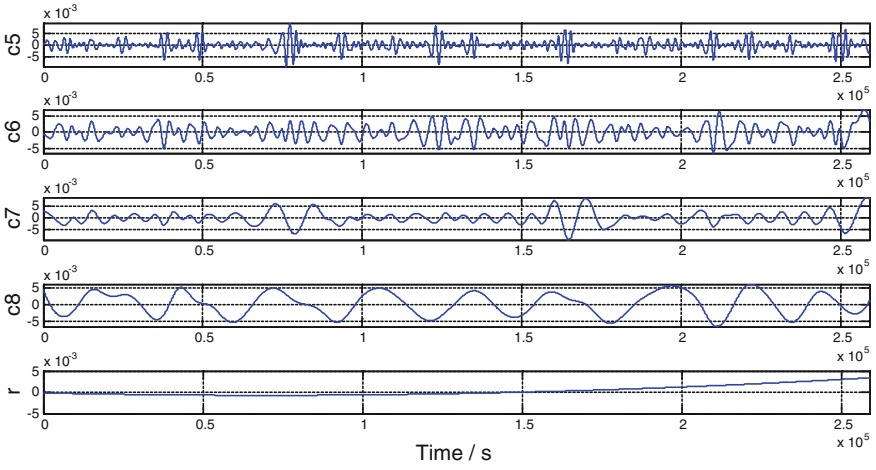

Fig. 28.8 Second EEMD result of carrier phase orbit determination residual of CUT0-CO1

In Fig. 28.10, the real frequency of 1.517E−5 is 1.5174074075E−5 Hz before rounding. The feature frequencies in Figs. 28.9 and 28.10 are transformed to time period shown in Table. 28.1. It can be found that, 1.517E−5 Hz in Hilbert spectrum is strictly corresponding 86,400 s, which is the time of 1 day. And the other frequencies are the 2nd, 3rd, 6th harmonic frequencies. Thus, it is preliminarily considered that there is a period information related to 1 day in BeiDou

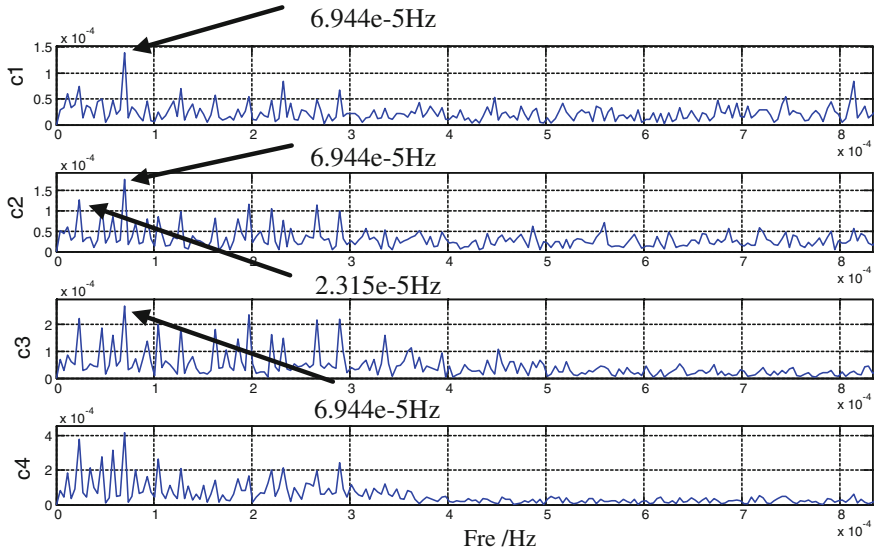

Fig. 28.9 First Hilbert spectrum of orbit determination of EEMD result in CUT0-CO1

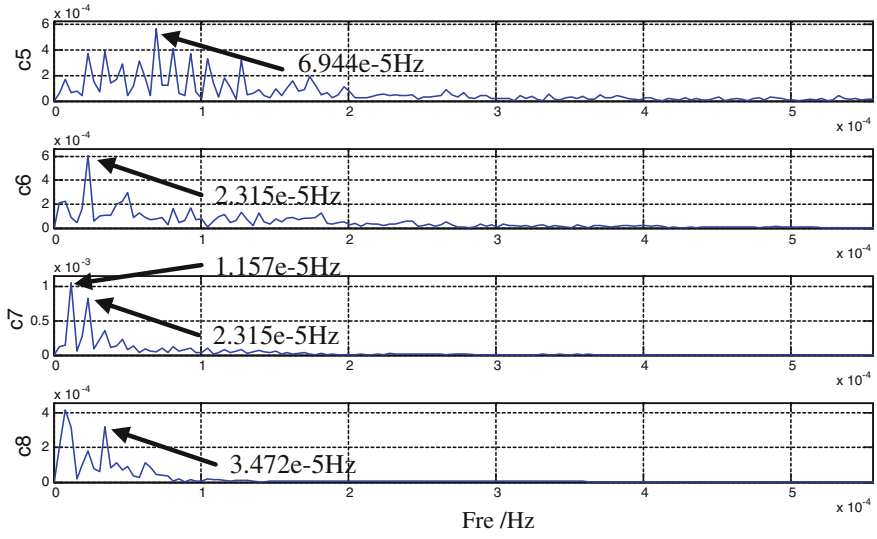

Fig. 28.10 Second Hilbert spectrum of orbit determination of EEMD result in CUT0-CO1

orbit determination residual. According to the motion of BeiDou orbit, It is inferred that there is feature information which is strictly corresponding to BeiDou satellite orbit moving period in BeiDou orbit determination residual.

Table 28.1 Feature frequency and period

Feature frequency (Hz)	Time period (s)
1.157E−5	86,400
2.315E−5	43,200
3.472E−5	28,800
6.944E−5	14,400

Table 28.2 The most obvious frequency feature in orbit determination

Nums	Receiving station	BeiDou satellite	Pseudo-range residual frequency (Hz)	Carrier phase residual frequency (Hz)
1	CUT0	CO1	1.157E−5	1.157E−5
			2.315E−5	2.315E−5
2	CUT0	CO3	/	1.157E−5
			2.315E−5	2.315E−5
3	CUT0	CO4	1.157E−5	/
			2.315E−5	2.315E−5
4	CUT0	CO5	2.315E−5	1.157E−5
			5.788E−5	/
5	GSMD	CO1	1.157E−5	1.157E−5
			2.315E−5	3.472E−5
6	GSMD	CO3	/	2.315E−5
			2.315E−5	3.472E−5
7	GSMD	CO4	1.157E−5	2.315E−5
			2.315E−5	3.472E−5
8	JFNG	CO1	/	1.157E−5
			2.315E−5	3.472E−5
9	JFNG	CO3	1.157E−5	1.157E−5
			/	3.472E−5
10	JFNG	CO4	1.157E−5	1.157E−5
			2.315E−5	3.472E−5

To further verification of the above inference, the orbit residuals of Station CUT0/GSMD/JFNG receiving different BeiDou navigation satellite signal are analyzed, and the most obvious two feature frequencies are recorded in Table. 28.2. Where, '/' expresses that there is only one feature frequency in Hilbert spectrum, and the other feature frequencies are weak. From Table 28.2, it is further verified that there is one period information related to 1 day in BeiDou orbit determination residual. Maybe, the reason why the harmonic frequencies based on 1.157E−5 Hz exist in orbit residual is that, BeiDou navigation satellite signals from the transmitter to the receiver through propagation paths in complex conditions, lots of effects exist, such as multipath [9], propagation medium, etc. The signals received by the receivers generate mutual modulation, and the nonlinear coupling phenomena appears. The nonlinear coupling phenomena mainly present

the frequency sidebands existing. In addition, it can be found that the proposed method can more effectively and accurately extract the feature information which is submerge in noise than traditional FFT spectrum.

28.5 Conclusion

1. This paper proposes an EEMD and Hilbert spectrum feature extraction method of BeiDou orbit determination residual, and it accurately extract the feature information of the no-modeling system errors in BeiDou GEO navigation satellite.
2. The proposed feature extraction method is better than traditional FFT spectrum in extracting effective feature in BeiDou orbit determination residual, and this method has higher reliability, and higher sensitivity.
3. There are obvious feature frequencies 1.157E−5 Hz and its harmonic frequencies in pseudo-range and carrier phase orbit determination residual, which are related to the time of one day (86,400 s).
4. The following research work will focus on the extracted feature frequency's modeling in orbit determination, and removing this system error, and verifying the modeling's accuracy and reliability by orbit determination experiment.

Acknowledgements The authors offer our sincere appreciation for Station CUT0/GSMD/JFNG providing BeiDou navigation satellite pseudo-range and carrier phase observation. This work was supported by the key project of National Nature Science Foundation of China (No. 41304026).

References

1. Yang Y (2010) Progress, contribution and challenges of Compss/BeiDou satellite navigation system. Acta Geodacticaet Cartographica Sinica 39(1):1–6
2. Cui H, Tang G et al (2013) Initial data processing assessment of the BeiDou satellite navigation system. In: 64th International Astronautical Congress, B.2.1.1, Beijing, China
3. Huang NE, Shen Z, Long SR (1998) The Empirical mode decomposition and the Hilbert spectrum for nonlinear and non-stationary time series analysis. Proc R Soc Lond 454:903–995
4. Flandrin P, Gonçalves P, Rilling G (2005) EMD equivalent filter banks: from interpretation to applications. Hilbert-Huang transform and its applications
5. Zi Y, Chen L, He Z (2010) Fault diagnosis of rotating machinery using adaptive ensemble empirical mode decomposition method. In: 23rd international proceedings of advances in maintenance and condition diagnosis technologies towards sustainable society, COMADEM, Naro, Japan, pp 409–416
6. Lue C, Yanyang Z, Zhengjia H, Wei C (2009) Research and application of ensemble empirical mode decomposition principle and 1.5 dimension spectrum method. J Xi'an Jiaotong Univ 43(5):94–98

7. Liu C, Wang J, Xu C, Gao J (2010) Integration of GPS/Pseudolites baseline solution based on empirical mode decomposition. Geomatics Inf Sci Wuhan Univ 35(8):996–1000
8. Wu Z, Huang NE (2009) Ensemble empirical mode decomposition: a noise-assisted data analysis method. Adv Adapt Data Anal 1:1–41
9. Liu H, Li X, Ge L, Rizos C, Wang F (2011) Variable length LMS adaptive filter for pseudorange multipath mitigation. GPS Solution 15(1):29–38

Chapter 29
Fast PPP Ambiguity Resolution Using a Sparse Regional Reference Network

Yihe Li and Yang Gao

Abstract Precise point positioning real-time kinematic (PPP-RTK) can achieve fast ambiguity resolution and precise positioning with the satellite fractional cycle biases (FCBs) and atmospheric correction derived from a dense regional reference network. However, the interpolated atmospheric corrections based on a sparse reference network with inter-station distances of more than 100 km are not precise enough to facilitate reliable PPP ambiguity resolution. In this contribution, a new method is proposed for fast PPP ambiguity resolution within a sparse regional reference network. First, code biases, FCBs, biased ionospheric and tropospheric delays at the reference stations are estimated with known positioning using the regional sparse reference network data. Then, the biased ionospheric and tropospheric corrections at a user station are generated using a distance-based linear interpolation of the ionospheric and tropospheric delays available at the reference stations. To strengthen the observation model, the interpolated ionospheric and tropospheric delays derived from the sparse network are all considered as pseudo-observations with a given variance-covariance matrix which will be adaptively estimated according to the reference network density to describe the level of the constraint strength. To get a realistic constraint variance, atmospheric constraint variance is estimated with a certain window length. By a proper tuning of the variance-covariance matrix applied for the atmospheric pseudo-observations, the method can adapt any scale of the regional reference network. The ambiguity fixing performance and the resulted position accuracy are assessed with medium and large reference networks. The validation confirms that the new strategy can fix ambiguity within 1 min for a medium network and within 7 min for a larger network while provide centimeter-level positioning solution ambiguity with 20.8 s for a medium network and within 71.9 s for a larger network.

Y. Li (✉) · Y. Gao
Department of Geomatics Engineering, The University of Calgary, Calgary, Canada
e-mail: yihli@ucalgary.ca

J. Sun et al. (eds.), *China Satellite Navigation Conference (CSNC) 2014 Proceedings: Volume III*, Lecture Notes in Electrical Engineering 305,
DOI: 10.1007/978-3-642-54740-9_29,

Keywords PPP-RTK · Regional sparse reference network · Ionosphere-constraint model · Adaptive constraint variance estimation

29.1 Introduction

Precise point positioning (PPP) is the technique to derive centimeter-level positioning accuracy using a single receiver and the precise clock and orbit products from International GNSS Service (IGS) [1]. It has drawn the increasing research attentions over the past years and has been applied to various applications, for instance, estimating the tropospheric delays for meteorology, monitoring the earthquakes and tsunamis, precision agriculture etc. [2–4]. Typically, dual-frequency code and phase measurements are used to form linear ionosphere-free observations (L3) for removing the first-order ionosphere effects. Apart from the position coordinates, ambiguities, receiver clock bias and troposphere zenith wet delay (ZWD) parameters are also estimated in PPP solution. Integer ambiguity fixing has the potential to significantly shorten the time-to-fixed- solution (TTFS) and improve the PPP positioning accuracy when fractional cycle biases (FCBs) are available to recover the integer feature of integer ambiguities [5–7]. But this approach would still require approximate 20–30 min to reliably fix the integer ambiguities.

The ionosphere and troposphere are considered as two key dominating error sources limiting the capability of carrier phase fast ambiguity resolution (AR) and the positioning precision [8]. Due to lack of precise ionospheric model, the positioning model is based on the L3 observations in which both wide-lane (WL) and narrow-lane (NL) ambiguities are to be fixed. The large noise of the range observations (which are definitely needed for WL ambiguity fixing) and the short NL wavelength result in a long initialization time for ambiguity-fixing. Besides, once the tropospheric ZWD parameter is estimated along with coordinate parameters, the model is seriously ill-conditioned due to its strong correlation with the height parameter as recognized by Dodson et al. [9]. Thus, it cannot be precisely solved without long period observation accumulation. In general, the residual tropospheric delays are typically modeled as a first-order Gauss-Markov random walk process, and a filtering technique, such as Kalman filtering, is often used. In a static scenario, the results from Tralli and Lichten [10] suggested that a few minutes of GPS observations provide sufficient strength to resolve centimeter-level zenith delay fluctuations.

To reliably resolve the ambiguities, both of the ionospheric and tropospheric errors have to be kept as small as possible. Shi [11] proposed a troposphere constraint method to improve the PPP ambiguity resolution as well as height solution by using the station-based IGS troposphere ZWD product. This method essentially specifies the correlation between the RZTD and three position components. However, the external troposphere corrections are chosen as the station-based IGS troposphere ZWD product which is probably not the optimal choice in practice. Ge et al. [12] proposed a network real-time kinematic positioning (NRTK) strategy

using pre-fit undifferenced observation residuals of the reference network with linear combination to remove biases and recover the integer feature of the ambiguities at user stations. Li et al. [13] retrieved atmospheric delays as corrections from data derived by a regional dense network to accelerate convergence. However, both of the above two methods ignore the retrieved atmospheric delay errors and can be only suitable for networks with short inter-station distances. In order to achieve fast or instantaneous AR with medium or long inter-station distances, both ionospheric and tropospheric errors have to be considered after a priori corrections. Therefore, the ionosphere-weighted model in which the ionospheric delays are treated stochastically instead of deterministically [14–19] is introduced into PPP AR. Its popularity stems from improving the model strength through adding prior stochastic information of ionospheric delays in term of zero-valued ionospheric pseudo-observations and stochastic model. Moreover, the relative variation of the ionosphere delay between consecutive epochs is also taken into account in term of pseudo-observations. Li [20] improved PPP ambiguity resolution performance considering the ionospheric characteristics by adding spatial and temporal constraints after correcting the slant delay using the IGS Global-Ionospheric-Maps (GIMs). As a result, the convergence time can be reduced by 30 %.

The accuracy of the interpolated atmospheric corrections at the user station depends on the density of the regional reference network. For a sparse reference network with the inter-station distance more than 100 km, the interpolated atmospheric corrections could be not precise enough to facilitate reliable PPP ambiguity resolution. The choice of the ionospheric constraint variance should correspond to the expected statistical behaviour of the noise of the ionospheric delays. In this contribution, we will propose a new method for fast PPP ambiguity resolution using the corrections of a sparse regional reference network. To get a realistic constraint variance, atmospheric constraint variance is adaptively estimated according to the reference network density with a certain window length. The performance of our proposed method is demonstrated by using both networks with medium and long inter-station distances. The rest of the paper is organized as follows. Our new method is presented in Sect. 29.2, two experiments are demonstrated in Sect. 29.3, and conclusions are given out in Sect. 29.4.

29.2 Regional Augmentation PPP with Atmospheric Constraint

29.2.1 Augmentation Information from Regional Reference Network

Undifferenced GPS code and phase observations on frequencies L1 and L2 are denoted as

$$\begin{cases} P_1 = \rho + d_{orb} + c(dt^r - dt^s) + T + I + b^r_{P_1} - b^s_{P_1} + \varepsilon_{P_1} \\ P_2 = \rho + d_{orb} + c(dt^r - dt^s) + T + \frac{f_1^2}{f_2^2} I + b^r_{P_2} - b^s_{P_2} + \varepsilon_{P_2} \\ L_1 = \rho + d_{orb} + c(dt^r - dt^s) + T - I - \lambda_1 N_1 + b^r_{L_1} - b^s_{L_1} + \varepsilon_{L_1} \\ L_2 = \rho + d_{orb} + c(dt^r - dt^s) + T - \frac{f_1^2}{f_2^2} I - \lambda_2 N_2 + b^r_{L_2} - b^s_{L_2} + \varepsilon_{L_2} \end{cases} \tag{29.1}$$

where, $i = 1, 2$ denotes the L1 and L2 frequencies, P_i and L_i are the raw code and phase measurements (m), ρ is the geometric distance between receiver and satellite (m), d_{orb} is the satellite orbit error (m), c is the speed of light in vacuum (m/s); dt^r and dt^s are the common receiver and satellite clock biases (s), T is the tropospheric delay (m), I is the first-order ionospheric delay, f_i is the frequency (H_z), λ_i is the carrier phase wavelength (m), N_i is the integer ambiguity (cycle); $b^r_{P_i}$ and $b^s_{P_i}$ are the observable-dependent receiver and satellite code biases (m); $b^r_{L_i}$ and $b^s_{L_i}$ are the observable-dependent receiver and satellite FCB (m); ε_{P_i} and ε_{L_i} are the code and phase observation errors including multipath noises (m).

Since the coordinates of all stations of a regional reference network and precise satellite orbits are known, the dry component of tropospheric delays can be corrected with a priori model, and the remaining ZWD delay is modeled as piece-wise constants, the WL and NL ambiguities (N_{NL} and N_{WL})can be resolved in a few minutes. Once the WL and NL ambiguities are fixed on the reference stations, the L1 and L2 integer ambiguities can be easily derived, and the ZWD delay, the satellite and receiver clock biases (dt^s and dt^r) as well as the FCBs ($b^s_{L_3}$ and $b^r_{L_3}$) and code biases ($b^s_{P_3}$ and $b^r_{P_3}$) can be computed accurately using L3 and P3 observation equations as follows

$$\begin{aligned} P_3 &= \rho + d_{orb} + \left(cdt^r + b^r_{P_3}\right) - \left(dt^s + b^s_{P_3}\right) + T + \varepsilon_{P_3} \\ L_3 &= \rho + d_{orb} + \left(cdt^r + b^r_{L_3}\right) - \left(dt^s + b^s_{L_3}\right) + T - \lambda_3(17N_{NL} + 60N_{WL}) + \varepsilon_{L_3} \end{aligned} \tag{29.2}$$

The FCBs and code biases w.r.t L3 observation are as follows,

$$\begin{aligned} b^s_{L_3} &= \frac{f_1^2}{f_1^2 - f_2^2} b^s_{L_1} - \frac{f_2^2}{f_1^2 - f_2^2} b^s_{L_2}, \qquad b^r_{L_3} = \frac{f_1^2}{f_1^2 - f_2^2} b^r_{L_1} - \frac{f_2^2}{f_1^2 - f_2^2} b^r_{L_2} \\ b^s_{P_3} &= \frac{f_1^2}{f_1^2 - f_2^2} b^s_{P_1} - \frac{f_2^2}{f_1^2 - f_2^2} b^s_{P_2}, \qquad b^r_{P_3} = \frac{f_1^2}{f_1^2 - f_2^2} b^r_{P_1} - \frac{f_2^2}{f_1^2 - f_2^2} b^r_{P_2} \end{aligned} \tag{29.3}$$

Therefore, the undifferenced observation equation shown in Eq. (29.1) corrected by code biases and FCBs shown in Eq. (29.3) is expressed as

$$\begin{cases} P_1 - b^r_{P_3} + b^s_{P_3} = \rho + d_{orb} + c(dt^r - dt^s) + T + I + b^r_{P_1} - b^s_{P_1} - b^r_{P_3} + b^s_{P_3} + \varepsilon_{P_1} \\ P_2 - b^r_{P_3} + b^s_{P_3} = \rho + d_{orb} + c(dt^r - dt^s) + T + \frac{f_1^2}{f_2^2} I + b^r_{P_2} - b^s_{P_2} - b^r_{P_3} + b^s_{P_3} + \varepsilon_{P_2} \\ L_1 - b^r_{L_3} + b^s_{L_3} = \rho + d_{orb} + c(dt^r - dt^s) + T - I - \lambda_1 N_1 + b^r_{L_1} - b^s_{L_1} - b^r_{L_3} + b^s_{L_3} + \varepsilon_{L_1} \\ L_2 - b^r_{L_3} + b^s_{L_3} = \rho + d_{orb} + c(dt^r - dt^s) + T - \frac{f_1^2}{f_2^2} I - \lambda_2 N_2 + b^r_{L_2} - b^s_{L_2} - b^r_{L_3} + b^s_{L_3} + \varepsilon_{L_2} \end{cases} \tag{29.4}$$

Moving all known quantities in Eq. (29.4) to the right of equation, the term including the ionospheric delay and combination of FCBs and code biases are then derived straightforwardly as follows

$$\begin{cases} I + \frac{f_2^2}{f_1^2 - f_2^2}\left(b^s_{P_1} - b^s_{P_2} - b^r_{P_1} + b^r_{P_2}\right) = P_1 - \rho - c(dt^r - dt^s) - T - b^r_{P_3} + b^s_{P_3} + \varepsilon_{P_1} \\ \frac{f_1^2}{f_2^2}\left(I + \frac{f_2^2}{f_1^2 - f_2^2}\left(b^s_{P_1} - b^s_{P_2} - b^r_{P_1} + b^r_{P_2}\right)\right) = P_2 - \rho - c(dt^r - dt^s) - T - b^r_{P_3} + b^s_{P_3} + \varepsilon_{P_2} \\ I - \frac{f_2^2}{f_1^2 - f_2^2}\left(b^s_{L_1} - b^s_{L_2} - b^r_{L_1} + b^r_{L_2}\right) = \rho + c(dt^r - dt^s) + T - \lambda_1 N_1 - L_1 + b^r_{L_3} - b^s_{L_3} + \varepsilon_{L_1} \\ \frac{f_1^2}{f_2^2}\left(I - \frac{f_2^2}{f_1^2 - f_2^2}\left(b^s_{L_1} - b^s_{L_2} - b^r_{L_1} + b^r_{L_2}\right)\right) = \rho + c(dt^r - dt^s) + T - \lambda_2 N_2 - L_2 + b^r_{L_3} - b^s_{L_3} + \varepsilon_{L_2} \end{cases} \tag{29.5}$$

For simplification, we call the term including the ionospheric delay and combination of phase and code biases code and phase biased ionospheric delays I^b_P and I^b_L which are derived from the either P1 or P2 code and L1 or L2 phase observations and can be written as

$$\begin{cases} I^b_P = I + \frac{f_2^2}{f_1^2 - f_2^2}\left(b^s_{P_1} - b^s_{P_2} - b^r_{P_1} + b^r_{P_2}\right) \\ I^b_L = I - \frac{f_2^2}{f_1^2 - f_2^2}\left(b^s_{L_1} - b^s_{L_2} - b^r_{L_1} + b^r_{L_2}\right) \end{cases} \tag{29.6}$$

In practice, the I^b_P derived from P1 or P2 observations are respectively used for correcting the P1 or P2 observations at user station. The I^b_L derived from L1 or L2 observations are respectively used for correcting the L1 or L2 observations at user station.

As a summary, the augmentation information provided by reference stations are biased ionospheric delays, tropospheric ZWD, the satellite clock, as well as and code biases and FCB corrections, which will be used by user station for carrying out PPP solution.

29.2.2 Interpolation of Ionospheric and Tropospheric Corrections

The reference-station-specific slant ionospheric and tropospheric corrections are used to generate the correction at user station, which are usually interpolated by using distance-based linear interpolation [21],

$$T_{u,k} = \frac{\sum_{i=1}^{i=n} \frac{1}{D_i} T_{i,k}}{\sum_{i=1}^{i=n} \frac{1}{D_i}} \tag{29.7}$$

where, $T_{i,k}$ and $T_{u,k}$ are the tropospheric correction for epoch k, reference station i and user station u, D_i is the distance from reference station i to user station. The biased ionospheric correction derived from code and phase observations for epoch k at user station u ($I^b_{P,u,k}$ and $I^b_{L,u,k}$) at user station can be interpolated as,

$$I^b_{P,u,k} = \frac{\sum_{i=1}^{i=n} \frac{1}{D_i} I^b_{P,i,k}}{\sum_{i=1}^{i=n} \frac{1}{D_i}} = I_{u,k} + \frac{f_2^2}{f_1^2 - f_2^2}\left(b^s_{P_1} - b^s_{P_2}\right) + \frac{f_2^2}{f_1^2 - f_2^2} \frac{\sum_{i=1}^{i=n} \frac{1}{D_i}\left(b^r_{P_2,i} - b^r_{P_1,i}\right)}{\sum_{i=1}^{i=n} \frac{1}{D_i}} \tag{29.8}$$

$$I^b_{L,u,k} = \frac{\sum_{i=1}^{i=n} \frac{1}{D_i} I^b_{L,i,k}}{\sum_{i=1}^{i=n} \frac{1}{D_i}} = I_{u,k} - \frac{f_2^2}{f_1^2 - f_2^2}\left(b^s_{L_1} - b^s_{L_2}\right) - \frac{f_2^2}{f_1^2 - f_2^2} \frac{\sum_{i=1}^{i=n} \frac{1}{D_i}\left(b^r_{L_2,i} - b^r_{L_1,i}\right)}{\sum_{i=1}^{i=n} \frac{1}{D_i}} \tag{29.9}$$

where $I_{i,k}$ and $I_{u,k}$ are the ionospheric correction for epoch k, reference station i and user station u.

29.2.3 Fast Ambiguity Resolution at User Station Using Ionospheric and Tropospheric Constraint Equations

For a sparse reference network, the interpolated ionospheric and tropospheric corrections are not accurate enough for fast ambiguity resolution. Therefore, we still introduce the residual ionospheric delay δI and tropospheric delay δT for the observation equation at user station after applying satellite clock dt^s, interpolated tropospheric T_u, biased ionospheric corrections ($I^b_{P,u}$ and $I^b_{L,u}$), satellite code biases and FCBs. Then the observation equation at user station after correction is rewritten as

$$\begin{cases} P_1 - I^b_{P,u} - T_u + cdt^s + b^s_{P_3} = \rho + d_{orb} + cdt^r + B^r_{P_{1,u}} - B^s_{P_{1,u}} + \delta T + \delta I + \varepsilon_{P_1} \\ P_2 - \frac{f_1^2}{f_2^2} I^b_{P,u} - T_u + cdt^s + b^s_{P_3} = \rho + d_{orb} + cdt^r + B^r_{P_{2,u}} - B^s_{P_{2,u}} + \delta T + \frac{f_1^2}{f_2^2}\delta I + \varepsilon_{P_2} \\ L_1 + I^b_{L,u} - T_u + cdt^s + b^s_{L_3} = \rho + d_{orb} + cdt^r + B^r_{L_{1,u}} - B^s_{L_{1,u}} + \delta T - \delta I - \lambda_1 N_1 + \varepsilon_{L_1} \\ L_2 + \frac{f_1^2}{f_2^2} I^b_{L,u} - T_u + cdt^s + b^s_{L_3} = \rho + d_{orb} + cdt^r + B^r_{L_{2,u}} - B^s_{L_{2,u}} + \delta T - \frac{f_1^2}{f_2^2}\delta I - \lambda_2 N_2 + \varepsilon_{L_2} \end{cases} \tag{29.10}$$

where $B^r_{P_{*,u}}$, $B^r_{L_{*,u}}$ and $B^s_{P_{*,u}}$ and $B^s_{L_{*,u}}$ are mixed code biases and FCBs for receiver and satellite which are combination of biases at user and reference stations as follows

$$\begin{cases} B^r_{P_{1,u}} = b^r_{P_1,u} - \frac{f_2^2}{f_1^2 - f_2^2} \frac{\sum_{i=1}^{i=n} \frac{1}{D_i}\left(b^r_{P_{2,i}} - b^r_{P_{1,i}}\right)}{\sum_{i=1}^{i=n} \frac{1}{D_i}}, & B^s_{P_{1,u}} = \frac{f_2^2}{f_1^2 - f_2^2}\left[\left(b^s_{P_{1,u}} - b^s_{P_{2,u}}\right) - \frac{\sum_{i=1}^{i=n} \frac{1}{D_i}\left(b^s_{P_{1,i}} - b^s_{P_{2,i}}\right)}{\sum_{i=1}^{i=n} \frac{1}{D_i}}\right] \\ B^r_{P_{2u}} = b^r_{P_2,u} - \frac{f_1^2}{f_1^2 - f_2^2} \frac{\sum_{i=1}^{i=n} \frac{1}{D_i}\left(b^r_{P_{2,i}} - b^r_{P_{1,i}}\right)}{\sum_{i=1}^{i=n} \frac{1}{D_i}}, & B^s_{P_{2,u}} = \frac{f_1^2}{f_1^2 - f_2^2}\left[\left(b^s_{P_{1,u}} - b^s_{P_{2,u}}\right) - \frac{\sum_{i=1}^{i=n} \frac{1}{D_i}\left(b^s_{P_{1,i}} - b^s_{P_{2,i}}\right)}{\sum_{i=1}^{i=n} \frac{1}{D_i}}\right] \\ B^r_{L_{1,u}} = b^r_{L_1,u} + \frac{f_2^2}{f_1^2 - f_2^2} \frac{\sum_{i=1}^{i=n} \frac{1}{D_i}\left(b^r_{L_{2,i}} - b^r_{L_{1,i}}\right)}{\sum_{i=1}^{i=n} \frac{1}{D_i}}, & B^s_{L_{1,u}} = \frac{f_2^2}{f_1^2 - f_2^2}\left[\left(b^s_{L_{1,u}} - b^s_{L_2}\right) - \frac{\sum_{i=1}^{i=n} \frac{1}{D_i}\left(b^s_{L_{1,i}} - b^s_{L_{2,i}}\right)}{\sum_{i=1}^{i=n} \frac{1}{D_i}}\right] \\ B^r_{L_{2,u}} = b^r_{L_2,u} + \frac{f_1^2}{f_1^2 - f_2^2} \frac{\sum_{i=1}^{i=n} \frac{1}{D_i}\left(b^r_{L_{2,i}} - b^r_{L_1,i}\right)}{\sum_{i=1}^{i=n} \frac{1}{D_i}}, & B^s_{L_{2,u}} = \frac{f_1^2}{f_1^2 - f_2^2}\left[\left(b^s_{L_{1,u}} - b^s_{L_{2,u}}\right) - \frac{\sum_{i=1}^{i=n} \frac{1}{D_i}\left(b^s_{L_{1,i}} - b^s_{L_{2,i}}\right)}{\sum_{i=1}^{i=n} \frac{1}{D_i}}\right] \end{cases} \tag{29.11}$$

As the code biases and FCBs for one satellite at user stations is the same value as those at the reference stations, namely $b^s_{P_{1,u}} = b^s_{P_{1,i}}$, $b^s_{P_{2,u}} = b^s_{P_{2,i}}$, $b^s_{L_{1,u}} = b^s_{L_{1,i}}$, $b^s_{L_{2,u}} = b^s_{L_{2,i}}$. Thus, these satellite biases at user station will be compensated with the biased interpolated ionospheric correction $I^b_u \cdot B^s_{P_{1,u}} = B^s_{P_{2,u}} = B^s_{L_{1,u}} = B^s_{L_{2,u}} = 0$. On the other hand, despite that the receiver bias at user station is different with those at the reference stations, the receiver biases on the estimated biased ionospheric correction is the same to all visible satellites at the user station. Thus, it can be absorbed by user receiver code bias and FCBs ($B^r_{P_{1,u}}$, $B^r_{P_{2,u}}$, $B^r_{L_{1,u}}$ and $B^r_{L_{2,u}}$). Therefore, such systematic biases have no effect on ionospheric corrections and the ambiguity-fixing at the user stations.

Since the interpolated ionospheric and tropospheric corrections are available at the user station, but exists some errors caused by either spatial extent of reference network or different elevations for the same satellites, we can form the following constraint equation to fast ambiguity resolution

$$\begin{cases} \delta I_k = \delta I_{k,0} + \varepsilon_{\delta I_k}, \quad \varepsilon_{\delta I_k} \sim N\left(0, \sigma^2_{\delta I_k}\right) \\ \delta T_k = \delta T_{k,0} + \varepsilon_{\delta T_k}, \quad \varepsilon_{\delta T_k} \sim N\left(0, \sigma^2_{\delta T_k}\right) \end{cases} \tag{29.12}$$

where $\delta I_{k,0}$ and $\delta T_{k,0}$ are the deterministic errors of interpolated ionospheric and tropospheric correction vector, which are generally given as zero. $\varepsilon_{\delta I_k}$ and $\varepsilon_{\delta T_k}$ are assumed to be random errors, the corresponding variances are $\sigma^2_{\delta I_k}$ and $\sigma^2_{\delta T_k}$. The ionospheric and tropospheric differences of the adjacent epochs can also use to form the constraint equation as follows

$$\begin{cases} \delta I_{r,k} - \delta I_{r,k-1} = w_{\delta I_k}, \quad w_{\delta I_k} \sim N\left(0, \sigma^2_{w_{\delta I_k}}\right) \\ \delta T_k - \delta T_{k-1} = w_{\delta T_k}, \quad w_{\delta T_k} \sim N\left(0, \sigma^2_{w_{\delta T_k}}\right) \end{cases} \tag{29.13}$$

where k is the current epoch; $k-1$ is the previous epoch; w_{I_k} and w_{T_k} are the differences of ionospheric and zenith tropospheric correction errors from previous epoch to current epoch; $\sigma^2_{w_{\delta I_k}}$ and $\sigma^2_{w_{\delta T_k}}$ are the variance of $w_{\delta I_k}$ and $w_{\delta T_k}$. The variances of Eqs. (29.12) and (29.13) must reflect the actual accuracies of the interpolated ionospheric and tropospheric corrections. If the variance is much smaller than its actual accuracy, it will result in the estimated ambiguities with considerable biases. Conversely, if the variance is much larger than its actual accuracy, it will cause constraint equation ineffective for improving the AR efficiency.

The variances of the interpolated ionospheric and tropospheric corrections can be properly estimated with the observations of a reference network using the following method. Firstly, we choose one station as simulated user station from n stations of a reference network, and interpolate the biased ionospheric correction for the user station using the remaining n-1 stations, then compute the difference between the estimated and interpolated ionospheric corrections as

$$\delta I_{r,k} = I^b_{r,k} - \frac{\sum_{i \in S} \frac{1}{D_{ri}} I^b_{i,k}}{\sum_{i \in S} \frac{1}{D_{ri}}}, \quad S = 1, 2, \ldots r-1, r+1, \ldots n \tag{29.14}$$

where r stands for the simulated user station, $I_{r,k}$ and $I_{i,k}$ are estimated ionospheric correction vector at simulated user station and the other $n-1$ stations. $\delta I_{r,k}$ is the difference between the estimated and interpolated ionospheric corrections at simulated user stations. Secondly, the variances $\sigma^2_{\delta I_k}$ and $\sigma^2_{w_{\delta I_k}}$ are computed by considering the distance between the simulated user and other reference stations. To avoid an over-optimistic constraint variance, the maximum value of interpolated error for all observed satellite is used. The $\sigma^2_{\delta I_k}$ and $\sigma^2_{w_{\delta I_k}}$ are written as

$$\sigma^2_{I_k} = \frac{\sum_{i=1}^{i=n} \frac{1}{D_i} \max\left(\delta I_{i,k}\right)^2}{\sum_{i=1}^{i=n} \frac{1}{D_i}} \tag{29.15}$$

$$\sigma^2_{w_{I,k,k-1}} = \left(\frac{\sum_{i=1}^{i=n} \frac{1}{D_i} \max\left(\delta I_{i,k} - \delta I_{i,k-1}\right)^2}{\sum_{i=1}^{i=n} \frac{1}{D_i}} \right) \tag{29.16}$$

In order to obtain confident variance estimates, we take the mean of latest m epochs estimates as,

$$\sigma_{I_k}^2 = \frac{\sum_{j=k-m+1}^{k} \sigma_{\delta I_j}^2}{m} \tag{29.17}$$

$$\sigma_{w_{I,k}}^2 = \frac{\sum_{j=k-m+1}^{k} \sigma_{w_{\delta I,j}}^2}{m} \tag{29.18}$$

The window length m should be reasonable chosen, because if it is too long, the computed constraint variance will be smooth to describe the detail of observation environment; while if it is too short, the estimate will be unstable. In our study, we take $m = 8$ for 15 $_{\mathrm{S}}$ data interval. For the variance of tropospheric corrections, we can be estimated with the same way as ionospheric corrections.

The constraint level is reflected through the variance of the pseudo-observations, which is estimated with the reference network. The estimated variance is usually large in the sparse network, and small in a dense network, hence our proposed method can adapt any scale of reference network. Moreover, L1 and L2 observation equations are directly used to solve the L1 and L2 ambiguities and the LAMBDA method [22] is used to fix integer ambiguity.

29.3 Experiments and Results

In order to demonstrate the performance of the proposed methodology, two test networks of different spatial extent have been analyzed, called the network with medium inter-station distances and the network with long inter-station distances. The test networks were constructed by using several GPS stations of USA Continuously Operating Reference Stations (CORS) (Figs. 29.2, 29.8). Stations P505, P480, P510 and P510 constitute the medium reference network with inter-station distances of 41.4–65.3 km. 10 Stations located inside this network were chosen as a simulated user receiver with average distances to the reference stations of 36.4, 56.2, 28.6 and 60.3 km, respectively. The observation sampling interval is 15 s. The large network consists of stations SG04, SG10, SG46 and SG48 with inter-station distances of 65.2–114.7 km. And the stations SG01, SG42 and SG47 were simulated as user receivers with average distances to the reference stations of 84.5, 56.6, 62.9 and 80.8 km, respectively. The observation interval is also 15 s. The medium network was designed in such a way that it closely reflects the geometry and size of current CORS with an average station separation of 50 km. The elevation cut-off angle is 10°. The LAMBDA method is applied to conduct ambiguity resolution. Both ratio test and success rate are applied to validate the ambiguities [23]. The ratio threshold value is 2 and the success probability applied is 0.99 [24] (Fig. 29.1).

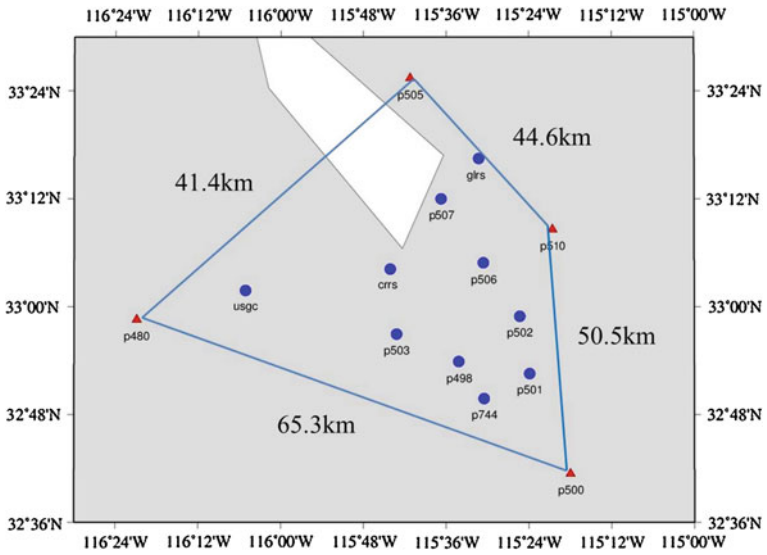

Fig. 29.1 Medium reference network, the *red triangle*—reference network, *blue circle*—user stations

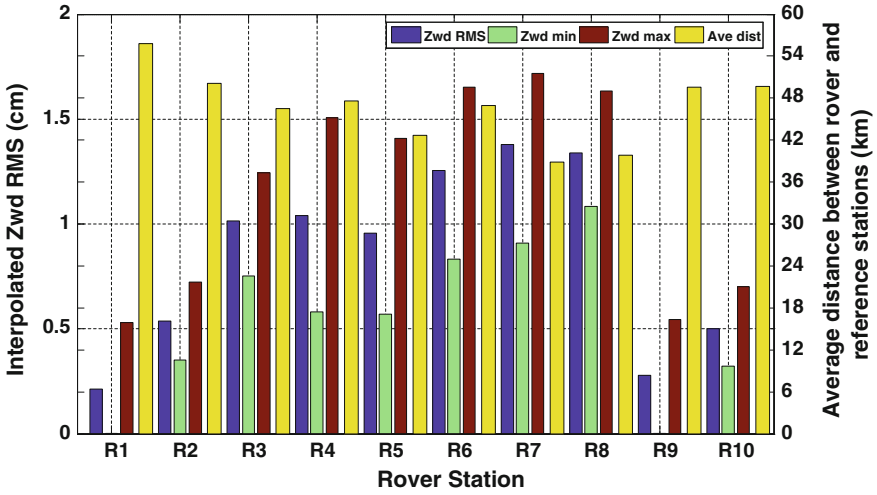

Fig. 29.2 Interpolated ZWD statistics compared to estimated ZWD at 10 user stations

The orbit and clock corrections are generated using the predicted orbits with initial condition fitted by using IGR orbits with 42 h arc length [25] and real-time estimated clocks [26]. The satellite FCBs are computed from a set of regional stations within USA in order to have a better fit to the region [13]. We process the

GPS data at the user stations in PPP mode and fix the integer ambiguities. Two PPP AR schemes are implemented for the purpose of comparison. Scheme 1 uses the traditional PPP AR mode which forms L3 observables of carrier-phases and pseudo-ranges while the tropospheric delay is estimated together with the position and ambiguity parameters. Scheme 2 uses the PPP AR mode augmented with regional network using our proposed method. The simulated user station is also processed as a reference station in advance in order to obtain the ionospheric and tropospheric delays for assessing the interpolated corrections from the other reference stations. The PPP ambiguity fixing at user station use interpolated ionospheric and tropospheric corrections.

29.3.1 Medium Network

Taking the zero-differenced (ZD) ionospheric and tropospheric delays retrieved at the four reference stations, we interpolate the ionospheric and tropospheric corrections for the user stations epoch by epoch, and present statistic results in Figs. 29.2 and 29.3 for tropospheric and ionospheric corrections, respectively. Figure 29.2 shows several interpolated ZWD statistics of 10 user stations. The ZWD RMSs for user stations are from 0.2 to 1.4 cm, which is essentially reflects the average spatial extent between user station and reference stations. Figure 29.3 shows the RMSs statistics of interpolated ionospheric corrections, which are derived from the differences between the estimated and interpolated corrections, and the differences for the user station crrs are shown in left panel of Fig. 29.4. The variances of interpolated slant ionospheric corrections achieve 2.1–5.2 cm in Fig. 29.3, which are significantly larger than those of ZWD and its variation is not very consistent with average spatial extent between user station and reference stations as ZWD. From right panel of Fig. 29.4 we can see that $\sigma_{\delta I_k}$ show in red envelops most of interpolated ionospheric errors, which is big enough to avoid bias in the AR while constraint with $2\sigma_{\delta I_k}$ shown in green is obviously loose compared to the actual interpolated correction error. Besides, $\sigma_{\delta I_k}$ is much larger than interpolated ionospheric errors, especially during the UTC 16:00 to 24:00 when is the day time at that region and the ionosphere activities are relatively strong. This result shows that the proper constraint variance can be determined when the ionosphere is quiet. When the ionosphere is active, bigger constraint variance would be determined, which would affect AR efficiency but not cause bias in AR model.

The TTFS of all 10 user stations in medium network is computed and counted. A typical cumulative distribution of PPP TTFS with 10 rover stations is shown in Fig. 29.5. The probabilities of TTFS are 7.0, 88.6, 95.1, and 95.5 % for the observation time with 15, 30, 45 min and 1 h, respectively. The average TTFS is 21.9 min. The results show that the longer the observation time is used the higher the TTFS can be achieved. As the longer the observation time used in float PPP

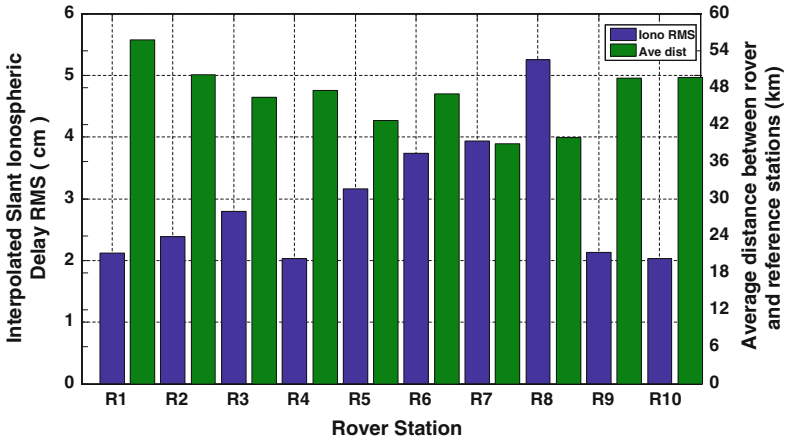

Fig. 29.3 Interpolated ionospheric statistics compared to estimated ionospheric delay at 10 user stations

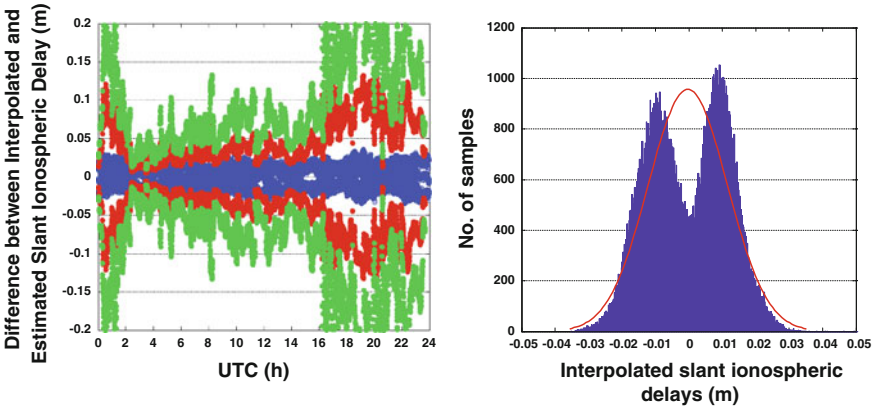

Fig. 29.4 Difference between interpolated and estimated ZD ionospheric delays over 24 h at user station crrs (*blue circle in left panel*). The *red circle* presents σ_{I_k} while the *green circle* presents $2\sigma_{I_k}$. The *right panel* shows the distribution of difference between interpolated and estimated ZD ionospheric delays over 24 h

solution the more accurate the float ambiguity, and so the more reliably integer ambiguity can be fixed. The TTFS probability is improved significantly when the length of the observation time increases from 15 to 30 min. In comparison, only a small improvement is found when the observation time lengthens are increased to 45 min and 1 h. With regional augmented tropospheric and ionospheric

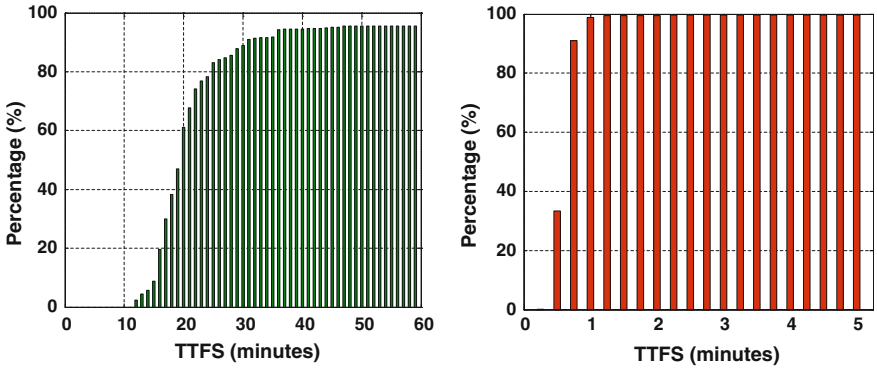

Fig. 29.5 Cumulative distribution of TTFS (scheme 1 vs. scheme 2)

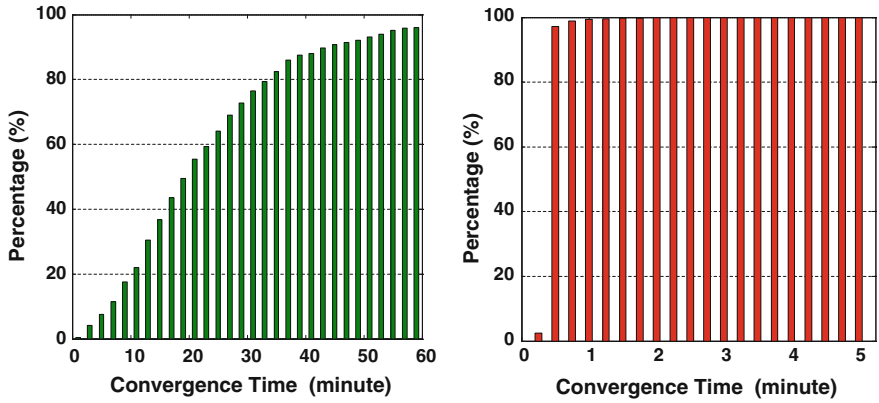

Fig. 29.6 Cumulative distribution of convergence time (scheme 1 vs. scheme 2)

corrections, the probability of TTFS can achieve 93.5 % only using 1 min observations. It can be seen that the scheme 1 requires 19.5 min to fix the L1 and L2 ambiguities while the scheme 2 successfully fixed ambiguity within 1 min. For ambiguity-float kinematic PPP results, as shown in Fig. 29.6, the average convergence time is 22.5 min for the scheme 1 while only 30.8 s for the scheme 2. Here, the 'convergence' means a 3D positioning error achieves less than 10 cm (Fig. 29.6).

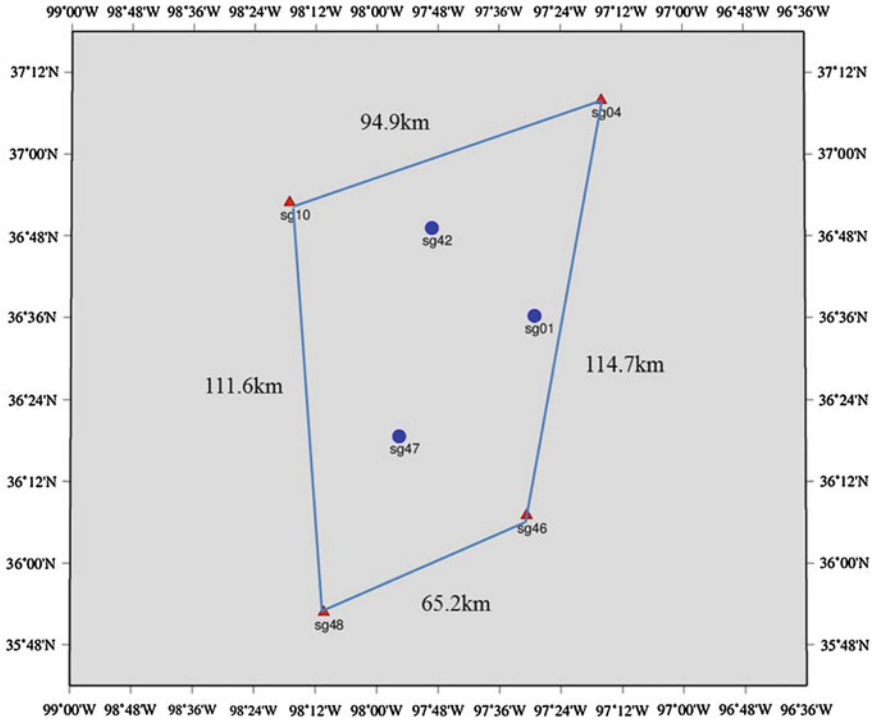

Fig. 29.7 Large regional network distribution, the *red triangle*—reference network, *blue circle*—user stations

Table 29.1 Interpolated atmospheric correction accuracy with large network

User station	Ave dist (km)	Interpo. ZWD RMS (cm)	Interpo. Iono RMS (cm)
Sg01	69.6	1.8	5.7
Sg42	73.5	2.0	6.8
Sg47	71.9	2.1	7.3

29.3.2 Large Network

Table 29.1 shows the accuracies of interpolated ionospheric and tropospheric corrections for the large network with average distance of about 70 km as shown in Fig. 29.7. It can be seen that both of the interpolated ZWD and ionospheric correction error become bigger compared to the RMS of interpolated ZWD errors using a medium network. However, the RMS of interpolated ionospheric error achieves 5.7–7.3 cm centimeters, which are significant and cannot be neglected. Figure 29.8 shows the difference between the interpolated and estimated ZD ionospheric delays over an 8-h period when the ionosphere is quiet and the

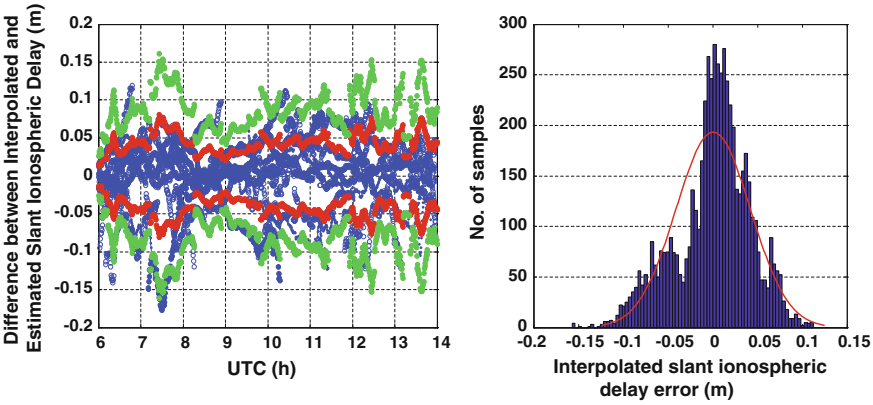

Fig. 29.8 Difference between interpolated and estimated ZD ionospheric delays over 8 h at rover station sg01 (*blue circle in left panel*). The *red circle* presents σ_{I_k} while the *green circle* presents $2\sigma_{I_k}$. The *right panel* shows the distribution of difference between interpolated and estimated ZD ionospheric delays

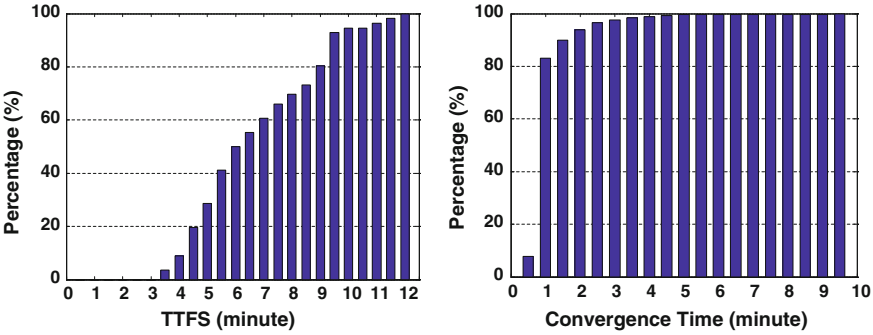

Fig. 29.9 Cumulative distribution of TTFS and convergence time of large network (scheme 2)

ionospheric constraint variance. For the large network, it can be seen that σ_{I_k} shown in red only envelops about 60 % of the interpolated ionospheric errors. That means this constraint variance is still optimistic for 40 % of ionospheric errors. If we use $2\sigma_{I_k}$ as the constraint variance, more than 90 % of ionospheric errors can be enveloped. In practice, a conservative constraint variance should be given to avoid bias in ambiguities. Thus, it's better to use $2\sigma_{I_k}$ as the constraint variance for large networks.

For large networks, a typical cumulative distribution of PPP TTFS and convergence time with 3 user stations is shown in Fig. 29.9. Both of TTFS and convergence time increase compared to the results of medium network, but still have significant improvement. The TTFS probability achieves 28.6 and 94.6 % when the observation time is 5 and 10 min. The average TTFS is 6.9 min. For

ambiguity-float kinematic PPP, the percentage of convergence time achieves 83.3, 93.8 and 99.6 % for the observation time with 1, 2 and 5 min, respectively, and on average the convergence time is 71.9 s.

29.4 Conclusions

We have developed a new strategy to augment PPP by mitigating the spatial errors by using ionospheric and tropospheric corrections derived from a sparse regional reference network, so that fast ambiguity fixing can be achieved for users within the network coverage. Since the ionospheric and tropospheric correction errors vary with the spatial geometry of the reference network, the atmospheric constraint variance is adaptively determined for different networks in real time. The method has been validated with two regional networks. From the experimental results, the ZWD correction errors are less than 1 cm on average while the ionospheric correction error is about 3 cm for medium size networks. Thus, the performance of PPP capable of fast ambiguity resolution can be comparable to NRTK. Despite both interpolated ZWD and ionospheric correction errors increase for large networks, the average convergence time and TTFS can achieve 71.9 s and 6.9 min, respectively. With this proposed method, it can extend the inter-station distances to more than 100 km for current reference RTK networks but still can achieve centimeter level position solutions within 10 min.

References

1. Kouba J (2009) A guide to using international GNSS service (IGS) products. http://igscb.jpl.nasa.gov/components/usage.html
2. Dixon K (2006) StarFire TM: a global SBAS for sub decimetre precise point positioning. In: Proceedings of ION GNSS 2006, Institute of Navigation, Fort Worth, Texas, pp 2286–2296
3. Dousa J (2010) The impact of errors in predicted GPS orbits on zenith troposphere delay estimation. GPS Solutions 14:229–239
4. Shi C, Lou Y, Zhang H, Zhao Q, Geng J, Wang R, Fang R, Liu J (2010) Estimating seismic displacement of the Mw8.0 wenchuan earthquake from high-rate GPS observations. Adv Space Res 46(2):228–235
5. Ge M, Gendt G, Rothacher M, Shi C, Liu J (2008) Resolution of GPS carrier-phase ambiguities in precise point positioning (PPP) with daily observations. J Geodesy 82(7):389–399
6. Laurichesse D, Mercier F, Berthias JP, Broca P, Cerri L (2009) Integer ambiguity resolution on un differenced GPS phase measurements and its application to PPP and satellite precise orbit determination. Navigation 56(2):135–149
7. Collins P (2008) Isolating and estimating un-differenced GPS integer ambiguities. In: Proceedings of ION national technical meeting, San Diego, US, pp 720–732
8. Li B, Feng Y, Shen Y, Wang C (2010) Geometry-specified troposphere decorrelation for subcentimeter real-time kinematic solutions over long baselines. J Geophys Res 115:B11404
9. Dodson A, Shardlow P, Hubbard L, Elgered G, Jarlemark P (1996) Wet tropospheric effects on precise relative GPS height determination. J Geod 70:188–202. doi:10.1007/BF00873700

10. Tralli D, Lichten S (1990) Stochastic estimation of tropospheric path delays in global positioning system geodetic measurements. Bull Geodesy 64:127–159. doi:10.1007/BF02520642
11. Shi J (2012) Precise point positioning integer ambiguity resolution with decoupled clocks. PhD thesis, Department of Geomatics Engineering University of Calgary, UCGE Report 20367
12. Ge M, Zou X, Dick G, Jiang W, Wickert J, Liu J (2010) An alternative Network RTK approach based on un differenced observation corrections ION GNSS, Portland, Oregon
13. Li X, Zhang X, Ge X (2011) Regional reference network augmented precise point positioning for instantaneous ambiguity resolution. J Geodesy 85:151–158
14. Teunissen P (1997) The geometry-free GPS ambiguity search space with a weighted ionosphere. J Geodesy 71(6):370–383
15. Odijk D (2000) Weighting ionospheric corrections to improve fast GPS positioning over medium distances. In: Proceedings of ION GPS-2000, Institute of Navigation, Alexandria, pp 1113–1123
16. Horemuz M, Sjoberg LE (2002) Rapid GPS ambiguity resolution for short and long baselines. J Geodesy 76:381–391
17. Wielgosz P, Kashani I, Grejner-Brzezinska D (2005) Analysis of long-range network RTK during severe ionospheric storm. J Geodesy 79(9):524531
18. Wielgosz P (2011) Quality assessment of GPS rapid static positioning with weighted ionospheric parameters in generalized least squares. GPS Solutions 15:89–99
19. Li Y, Shen Y (2011) INS aided ambiguity resolution for GPS/INS integrated kinematic positioning, ION GNSS
20. Li X (2012) Improving real-time PPP ambiguity resolution with ionospheric characteristic consideration. In: Proceedings of ION GPS 2012 Nashville TN Sept 17–21
21. Gao Y, Li Z, McLellan JF (1997) Carrier phase based regional area differential GPS for decimeter-level positioning and navigation. In: Proceedings of 10th international technical meeting of the Satellite Division of US Institute of Navigation, Kansas, City, pp 1305–1313, Sept 16–19
22. Li B, Verhagen S, Teunissen PJG (2013) GNSS integer ambiguity estimation and evaluation: LAMBDA and Ps-LAMBDA. In: Proceedings of China satellite navigation conference (CSNC) 2013, lecture notes in electrical engineering, vol 24. Wuhan, pp 291–301
23. Verhagen S (2005) On the reliability of integer ambiguity resolution. Navigation 52(2):99–110
24. Li P, Zhang X (2013) Integrating GPS and GLONASS to accelerate convergence and initialization times of precise point positioning. GPS Solutions 15:315–324
25. Choi K, Ray J, Griffiths J, Bae T (2012) Evaluation of GPS orbit prediction strategies for the IGS Ultra-rapid products. GPS Solutions. doi:10.1007/s10291-012-0288-2
26. Hauschild A, Montenbruck O (2009) Kalman-filter-based GPS clock estimation for near real-time positioning. GPS Solutions 13:173–182

Chapter 30
Optimization of GEO Navigation Satellite Station Shifts Impulsives

Ying Liu, Guoqiang Zhao and Jing Li

Abstract In order to increase system availability, optimization of control of the drift orbit of GEO navigation satellites for station shifts is studied. Given the orbit drift time, comparing to the traditional method that adjusts phase by changing the semimajor axis, we employ the primer vector theory and assess the whole improvement process. The detailed algorithm is presented to determine the number, time, and position of the impulsives. At the end of program, the numerical optimization method BFGS is used to improve the model. As shown by the problem analyzed, we can get better result by applying the presented method.

Keywords GEO station shifts · Primer vector theory · Trajectory optimization

30.1 Introduction

After a Geostationary Earth Orbit (GEO) navigation satellite is positioned at the initial geostationary orbit, station shifts will take place due to various reasons and the satellite and change the subsatellite longitude. Considering the key role of GEO satellites in Beidou navigation satellite constellation, it is of high significance to study issues related to drift control for the GEO satellites station shifts because this shall help save satellite propellants, increase the availability of GEO satellites and thus increase the overall system availability of the system. The Refs. [1–3] introduce the traditional method of orbit control in detail. The traditional method

Y. Liu
Beijing Institute of Tracking and Telecommunications Technology, Beijing 100094, China
e-mail: liu2ying@163.com

G. Zhao · J. Li (✉)
State Key Laboratory of Astronautic Dynamics, Xi'an 710043, China
e-mail: sciwalker@126.com

J. Sun et al. (eds.), *China Satellite Navigation Conference (CSNC) 2014 Proceedings: Volume III*, Lecture Notes in Electrical Engineering 305,
DOI: 10.1007/978-3-642-54740-9_30,

adjusts the orbit semimajor axis and changes the relative angular velocity. Thus the satellite moves to the target position. Another orbit control is performed to reduce the satellite's relative drift speed and it is reinserts into another GEO. Given the mission requirements, different strategies are designed corresponding to different time durations.

Given the orbit drift time duration, the initial and the target position vector are specified. The essence of the traditional control strategy is to solve the Lambert problem. The Ref. [4] tells that the Lambert solution is not the optimal result of two position vector as the transfer time is fixed. The optimal trajectory should satisfy the necessary condition of the primer vector. The paper also gives the improvement process. The Ref. [5] analyze the optimization of evasion maneuvers. The Ref. [6] apply the feature to search the optimal multi-impulse launch opportunities.

We apply the primer vector theory to improve the GEO navigation satellite station shifts and present the detailed calculation procedure. The BFGS numerical method is employed to optimize the fuel consumption.

30.2 Primer Vector Theory

30.2.1 Problem Formulation

The primer vector is introduced by Lawden [4] in 1963. The primer vector is defined to be the costate variable associated with the velocity vector's. Consider the problem that the spacecraft is subject only to the central force of the Earth gravity and the thrust of its own propulsion system.

$$\dot{\boldsymbol{r}} = \boldsymbol{v} \tag{30.1}$$

$$\dot{\boldsymbol{v}} = \boldsymbol{g} + \Gamma \boldsymbol{u} \quad \boldsymbol{g} = -\frac{\mu}{r^3}\boldsymbol{r} \tag{30.2}$$

$$\dot{J} = \Gamma \tag{30.3}$$

where $\boldsymbol{r}$ and $\boldsymbol{v}$ denote the position and velocity vectors in the Earth centered inertial system. The Earth's gravitational constant is denoted by μ and its value is 398,600.14 km^3/s^2. Γ is thrust acceleration $0 \le \Gamma \le \Gamma_{max}$ and $\boldsymbol{u}$ is the unit vector of control variables. For the assumption that the velocity change is finished at the negligible duration, the thrust capability of the satellite is not bounded and can be replaced by an impulsive without in any way affecting its position. That is $\Gamma = 0$ or $\Gamma \to \infty$. Generally, J is the characteristic velocity to be minimized expressed by

$$J(t_f) = \int_{t_0}^{t_f} \Gamma \, dt \tag{30.4}$$

where t_0 and t_f denote the initial and final time, respectively. Equation 30.1–30.3 is the formulation of the satellite under the control of gravity and thrust.

To obtain the optimal fuel consumption solution, we should solve the optimal control problem in the interval of $t_0 \leq t \leq t_f$.

30.2.2 Necessary Conditions for Optimal Orbit Transfer

According to the dynamic equation 30.1–30.3, the Hamilton function is constructed as

$$H = \boldsymbol{\lambda}_r^T \boldsymbol{v} + \boldsymbol{\lambda}_v^T \boldsymbol{g} + (\boldsymbol{\lambda}_v^T \boldsymbol{u} + \lambda_J)\Gamma \tag{30.5}$$

The symbol $\boldsymbol{\lambda}_r$, $\boldsymbol{\lambda}_v$, λ_J denote the corresponding costates of $\boldsymbol{r}$, $\boldsymbol{v}$ and J, respectively. The costate equation is as follows

$$\dot{\boldsymbol{\lambda}}_r = -\frac{\partial H}{\partial \boldsymbol{r}} = -G(\boldsymbol{r})\boldsymbol{\lambda}_v \tag{30.6}$$

$$\dot{\boldsymbol{\lambda}}_v = -\frac{\partial H}{\partial \boldsymbol{v}} = -\boldsymbol{\lambda}_r \tag{30.7}$$

$$\dot{\boldsymbol{\lambda}}_J = -\frac{\partial H}{\partial J} = 0 \tag{30.8}$$

where $\mathbf{G}(\boldsymbol{r})$ is called the Gravity Gradient Matrix

$$G(\boldsymbol{r}) = \mu(3\boldsymbol{r}\boldsymbol{r}^T - r^2\boldsymbol{I})/r^5 \tag{30.9}$$

and $\boldsymbol{I}$ is the identity matrix.

Due to the Pontryagin Maximization (or Minimization) Principle, $\boldsymbol{\lambda}_r$ and $\boldsymbol{\lambda}_v$ are determined by the boundary conditions. And

$$\boldsymbol{\lambda}_J = -1 \tag{30.10}$$

To maximizing the function (30.5), the dot product $\boldsymbol{\lambda}_v \boldsymbol{u}$ should be maximized. So the direction of $\boldsymbol{\lambda}_\mathbf{v}$ and u should be aligned. We denote $\boldsymbol{\lambda}_\mathbf{v}$ by $\boldsymbol{p}$ and call it the Primer Vector. According to the Eq. (30.7), we have

$$\dot{\boldsymbol{p}}(t) = -\boldsymbol{\lambda}_r(t) \tag{30.11}$$

The Hamilton function is formulated as

$$H = \boldsymbol{p}^T \boldsymbol{g} - \dot{\boldsymbol{p}}^T \boldsymbol{v} + (p-1)\Gamma \tag{30.12}$$

In the situation of impulsive $\Gamma \to \infty$, $(p-1)\Gamma$ should always be zero to make the expression meaningful. So the Eq. (30.12) can be written as

$$H = \boldsymbol{p}^T \boldsymbol{g} - \dot{\boldsymbol{p}}^T \boldsymbol{v} \tag{30.13}$$

The primer can be obtained by solving the equation as follows

$$\ddot{\boldsymbol{p}}(t) = G(\boldsymbol{r})\boldsymbol{p} \tag{30.14}$$

The following conditions must be satisfied over an optimal trajectory:

1. The primer can be obtained by Eq. (30.14). The primer and its first time derivative must be continuous everywhere.
2. The magnitude p of the primer must not exceed 1 on the trajectory and $p = 1$ at the impulsive time.
3. The impulsive direction must be aligned with the primer at the time.
4. Due to the condition 2, the primer reaches a maximum at all interior impulsives $\dot{p} = \dot{\boldsymbol{p}}^T \boldsymbol{p} = 0$.

30.3 Optimization Procedure of Orbit Transfer Design

Necessary conditions are already given in the previous section for optimal impulsive transfer orbit. The current section shall explain how to transform a non-optimal orbit into an optimal orbit. Lion and Handelsman demonstrated how to get an approaching solution to provide first-order propellant consumption with a method encompassing increase of intermediate impulsives and terminal glide, thus improving non-optimal impulsive orbits, when the main vectors computed for the non-optimal orbits do not meet necessary conditions. An iterative process is established to get solutions to converge to the necessary conditions.

30.3.1 Calculation of the Primer Vector

A reference trajectory should be ready before the primer vector calculation. The reference trajectory is usually not optimal. We calculate the primer vector along the nonoptimal orbit. Usually the lambert solution is used between the two point.

$$\boldsymbol{p}_0 = \frac{\Delta \boldsymbol{V}_0}{|\Delta \boldsymbol{V}_0|} \quad \boldsymbol{p}_f = \frac{\Delta \boldsymbol{V}_f}{|\Delta \boldsymbol{V}_f|} \tag{30.15}$$

where $\boldsymbol{p}_0$ and $\boldsymbol{p}_f$ denote the primer vector at the initial and final time. $\Delta \mathbf{V}_0$ and $\Delta \mathbf{V}_f$ denote the characteristic velocity at the initial and final time.

From the Eq. (30.14), the primer vector can be calculated by the transition matrix.

$$\begin{pmatrix} \boldsymbol{p}(t) \\ \dot{\boldsymbol{p}}(t) \end{pmatrix} = \begin{pmatrix} \phi_{11} & \phi_{12} \\ \phi_{21} & \phi_{22} \end{pmatrix} \begin{pmatrix} \boldsymbol{p}_0 \\ \dot{\boldsymbol{p}}_0 \end{pmatrix} \tag{30.16}$$

and we have

$$\dot{\boldsymbol{p}}_0 = \phi_{12}^{-1}\left(\boldsymbol{p}_f - \phi_{11}\boldsymbol{p}_0\right) \tag{30.17}$$

So we have known the initial primer vector state $\boldsymbol{p}_0, \dot{\boldsymbol{p}}_0$. Using the Eq. (30.16), we can obtain the primer vector state at any time on the trajectory.

30.3.2 Procedure of Optimization

1. Given the initial position, the final position and the orbit drift time, we can acquire the initial solution of the primer vector and the transition matrix.
2. Then we check the primer magnitude of the whole trajectory. If the primer magnitude p(t) exceeds 1 at the interior point, the two impulsive transfers are not optimal. We should add the third impulsive at the time t_{m} when the magnitude p(t) is maximized.

$$\delta \boldsymbol{r}_m = cA^{-1}\frac{\boldsymbol{p}_m}{|\boldsymbol{p}_m|} \tag{30.18}$$

where

$$A = \phi_{22}(t_m, t_f)\phi_{12}^{-1}(t_m, t_f) - \phi_{22}(t_m, t_0)\phi_{12}^{-1}(t_m, t_0) \tag{30.19}$$

$$c = \frac{\beta\frac{\Delta \boldsymbol{V}_f}{|\Delta \boldsymbol{V}_f|} - \alpha\frac{\Delta \boldsymbol{V}_0}{|\Delta \boldsymbol{V}_0|} - 1}{\frac{\left[\alpha\cdot\alpha - \frac{(\alpha\cdot\Delta \boldsymbol{V}_0)^2}{|\Delta \boldsymbol{V}_0|^2}\right]}{|\Delta \boldsymbol{V}_0|} + \frac{\left[\beta\cdot\beta - \frac{(\beta\cdot\Delta \boldsymbol{V}_f)^2}{|\Delta \boldsymbol{V}_f|^2}\right]}{|\Delta \boldsymbol{V}_f|}} \tag{30.20}$$

$$\alpha = \phi_{12}^{-1}(t_m, t_0)A^{-1}\frac{\boldsymbol{p}_m}{|\boldsymbol{p}_m|} \tag{30.21}$$

$$\beta = \phi_{12}^{-1}(t_m, t_f)A^{-1}\frac{\boldsymbol{p}_m}{|\boldsymbol{p}_m|} \tag{30.22}$$

We can get t_{m} and p_{m} by check the trajectory process. And the transition matrix A can be calculated by the corresponding pieces of trajectory.

3. Then we should solve two Lambert problems. One is the trajectory that is from the initial position to the position $\boldsymbol{r}_m + \delta\boldsymbol{r}_m$. And the corresponding time duration is $t_m - t_0$. The other trajectory is from the position $\boldsymbol{r}_m + \delta\boldsymbol{r}_m$ to the end position. Now we get a three impulsive trajectory and we can make the characteristic velocity smaller by adjusting the interior impulsive's time and position. And the descent value can be expressed by

$$dJ = (\boldsymbol{p}_m^+ - \boldsymbol{p}_m^-)d\boldsymbol{r}_m - (\boldsymbol{p}_m^+\boldsymbol{V}_m^+ - \boldsymbol{p}_m^-\boldsymbol{V}_m^-)dt_m \tag{30.23}$$

The labels "+" and "−" denote the state before and after the impulsive.

4. We check the primer magnitude of the whole trajectory again. If the primer vector satisfy the necessary condition. Then the iteration process ends. Or the same improvement iteration should continue.

30.3.3 Numerical Optimization Algorithm

We propose the *Broyden-Fletcher-Goldfarb-Shanno* (BFGS) optimization algorithm with numerical stability [7].

1. Given the initial point $\boldsymbol{x}^{(1)}$ and the tolerance *tol*.
2. The matrix H_1 is the identity matrix. Calculate the gradient at $\boldsymbol{x}^{(1)}$.
3. Make $\boldsymbol{d}^{(k)} = -\boldsymbol{H}_k\boldsymbol{g}_k$.
4. From make one-dimension search at $\boldsymbol{x}^{(k)}$,

$$f(\boldsymbol{x}^{(k)} + \lambda_k\boldsymbol{d}^{(k)}) = \min_{\lambda \geq 0} f(\boldsymbol{x}^{(k)} + \lambda\boldsymbol{d}^{(k)})$$

and $\boldsymbol{x}^{(k+1)} = \boldsymbol{x}^{(k)} + \lambda_k\boldsymbol{d}^{(k)}$.

5. Check convergence criterion. If $\frac{|f(\boldsymbol{x}^{(k+1)}) - f(\boldsymbol{x}^{(k)})|}{|f(\boldsymbol{x}^{(k+1)})| + |f(\boldsymbol{x}^{(k)})|} < \frac{tol}{2}$ is satisfied, then stop the iteration. The end point is $\boldsymbol{x}^{(k+1)}$. Or continue the procedure 6.
6. Make $\boldsymbol{g}_{k+1} = \nabla f(\boldsymbol{x}^{(k+1)})$, $\boldsymbol{p}^{(k)} = \boldsymbol{x}^{(k+1)} - \boldsymbol{x}^{(k)}$, $\boldsymbol{q}^{(k)} = \boldsymbol{g}_{(k+1)} - \boldsymbol{g}_k$. Calculate $\boldsymbol{H}_{(k+1)}$ using BFGS formula.

$$\boldsymbol{H}_{(k+1)} = \boldsymbol{H}_k + \frac{\boldsymbol{p}^{(k)}\boldsymbol{p}^{(k)T}}{\boldsymbol{p}^{(k)T}\boldsymbol{q}^{(k)}} - \frac{\boldsymbol{H}_k\boldsymbol{q}^{(k)}\boldsymbol{q}^{(k)T}\boldsymbol{H}_k^T}{\boldsymbol{q}^{(k)T}\boldsymbol{H}_k\boldsymbol{q}^{(k)}} + \left[\boldsymbol{q}^{(k)T}\boldsymbol{H}_k\boldsymbol{q}^{(k)}\right]\boldsymbol{u}\boldsymbol{u}^T$$

$$\boldsymbol{u} = \frac{\boldsymbol{p}^{(k)}}{\boldsymbol{p}^{(k)T}\boldsymbol{q}^{(k)}} - \frac{\boldsymbol{H}_k\boldsymbol{q}^{(k)}}{\boldsymbol{q}^{(k)T}\boldsymbol{H}_k\boldsymbol{q}^{(k)}}$$

The iteration continues until the specified number is achieved. Or return the procedure 3.

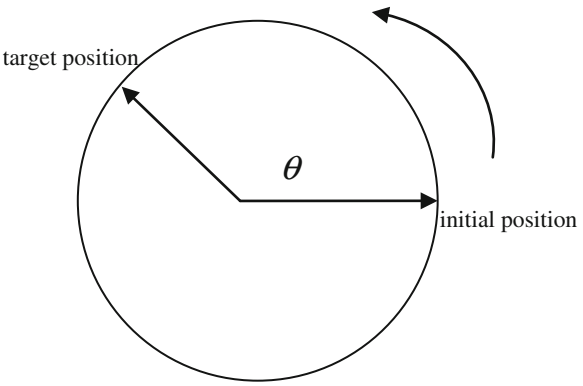

Fig. 30.1 GEO satellite station shifts

30.4 Numerical Example

Assume the satellite is at the initial position (Fig. 30.1) at the beginning. The phase difference between the target position and the initial position is θ. For computing convenience, the quantities about length, time, are nondimensionalized by GEO radius (42,164 km), period (86,164 s) and thus μ is $4\pi^2$. The initial position vector is (1, 0, 0), θ is 288°. The orbit drift time duration for station shifts is 2.3.

Computing the Lambert problem and we get the following parameters.

The first impulsive time: 0
The first impulsive vector: (0.5443, 0.3857, 0)
The second impulsive time: 2.3
The second impulsive vector: (−0.1987, −0.6369, 0)
The whole impulsive magnitude: 1.3343.

The primer magnitude varies as the Fig. 30.2.

According to the primer vector theory, an impulsive should be added at the time where the primer magnitude is maximal. Finishing the process and the primer magnitude is as Fig. 30.3.

In the later part of Fig. 30.3, the primer magnitude still exceeds 1 obviously. So another impulsive is added and the BFGS algorithm is performed to optimize the whole trajectory. The final primer magnitude trajectory is as Fig. 30.4.

From the Fig. 30.4, we can see that the primer magnitude is always not exceeds 1. The necessary conditions of optimal trajectory are satisfied. The final result is that the optimal station shifts should perform 4 impulsives. The characteristic velocity is 1.1884 and it is 0.1459 less than the two-impulsive station shifts. It is about 704 m/s after transformed into international standard. The four impulsives are summarized as follows:

The first impulsive time: 0
The first impulsive vector: (0.1815, 0.3987, 0)

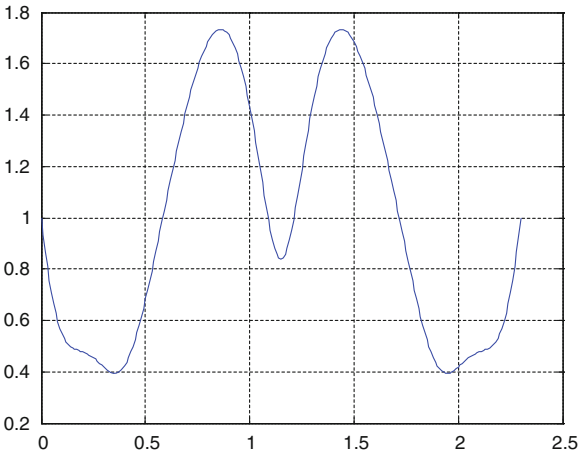

Fig. 30.2 The primer magnitude of the two-impulsive station shifts

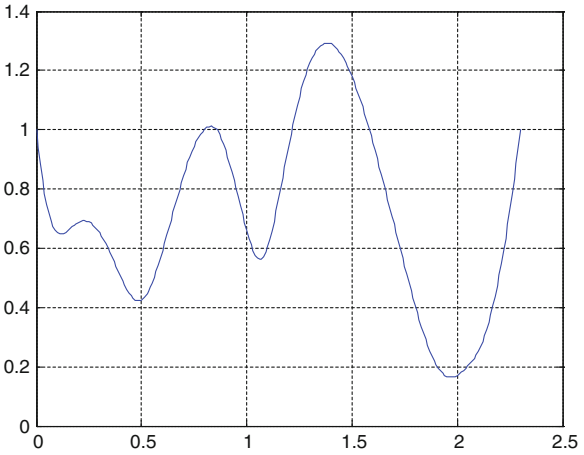

Fig. 30.3 The primer magnitude after adding an impulsive in interior part of the two-impulsive station shifts

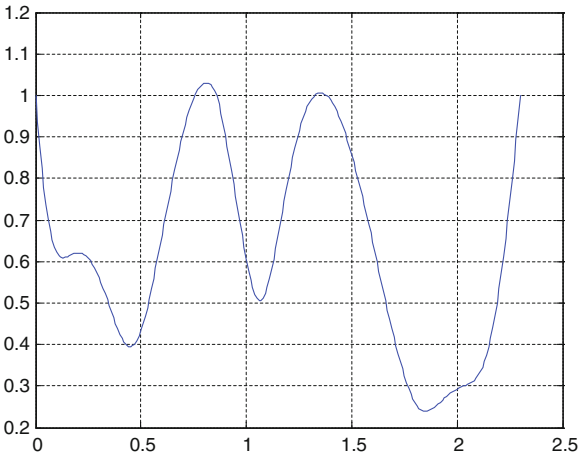

Fig. 30.4 The primer magnitude after adding two impulsives in interior part of the two-impulsive station shifts

The second impulsive time: 0.7941
The second impulsive vector: (0.0905, −0.1273, 0)
The third impulsive time: 1.5059
The third impulsive vector: (0.1498, −0.0483, 0)
The fourth impulsive time: 2.3
The fourth impulsive vector: (−0.3221, −0.2950, 0)
The whole impulsive magnitude: 1.1884.

30.5 Conclusion

The paper focuses on optimization of GEO Navigation Satellite station shifts impulsives. According to the nonoptimal orbit drift trajectory, we employ the primer vector theory and present the detailed algorithm to determine the number, time, and position of the impulsives. Combining the numerical optimization method BFGS, we can get better orbit drift strategies for station shifts and reduce fuel consumption.

References

1. Li H (2011) Geostationary satellite orbital analysis and collocation design strategies. National Defence Industrial Press, Beijing
2. Soop EM (1999) Handbook of geostationary orbits. National Defence Industrial Press, Beijing
3. Li Y (2003) The principle of station-keeping and maneuver strategies of geostationary communication satellites. J Spacecraft TT&C Technol 22(4):53–61
4. Jezewski DJ (1975) Primer vector theory and applications. NASA-TR-R-454, Washington, DC
5. Zhao R (2008) Space weapon orbit design. Chinese Astronautic Press, Beijing, pp 203–303
6. Qiao D (2007) Study of transfer trajectory design method for deep space exploration and application to small body exploration. Harbin Institute of Technology, Harbin, pp 30–34
7. Press WH, Teukolsky SA, Vetterling WT, Flannery BP (2005) Numerical recipes in C++: the art of scientific computing. Publishing House of Electronics Industry Press, Butterworths

Chapter 31
Orbit Determination and Error Analysis Based on GNSS Crosslink Ranging Observations

Yinan Meng, Shiwei Fan, Xiaoyong Song, Jun Lu and Chengeng Su

Abstract When traditional L-band navigation signals applied for high-orbit spacecraft orbit determination, there come problems such as few visual navigation satellites and low accuracy due to the limited antenna beam angle. Global Navigation Satellite System (GNSS) equipped with inter-satellite distance measuring equipment provides a more effective means for high-orbit spacecraft orbit determination. In this paper the ranging errors of GNSS crosslink were analyzed, and high-orbit satellite orbit determination experiments were performed based on the current crosslink ranging accuracy level, using the geometric method and kinetic method respectively. Results show that, kinetic method performs better with fewer available observations, but the improvement is not obvious with sufficient observations. Whether or not the user clock error is solved has significant effects on results of geometric method. The orbit determination accuracy reaches about a hundred meters level if the solution includes clock error; however, the accuracy can achieve within several meters if excludes clock error.

Keywords GNSS crosslink · Error analysis · Orbit determination · Geometric method · Kinetic method

Y. Meng (✉) · S. Fan · J. Lu · C. Su
Beijing Institute of Tracking and Telecommunication Technology, Beijing 100094, People's Republic of China
e-mail: mengyinan0915@163.com

X. Song
Xi'an Research Institute of Surveying and Mapping, Xi'an 710054, People's Republic of China
e-mail: sxyong_chd@sohu.com

J. Sun et al. (eds.), *China Satellite Navigation Conference (CSNC) 2014 Proceedings: Volume III*, Lecture Notes in Electrical Engineering 305,
DOI: 10.1007/978-3-642-54740-9_31,

31.1 Introduction

Global Navigation Satellite System (GNSS) such as GPS and GLONASS has built a crosslink network serving with both high-precision measurement and inter-satellite communication [1] to fulfill autonomous navigation [2], which also prospects an international trend of extensive application for GNSS. The ranging type GNSS crosslink will provide a new and effective means for autonomous orbit determination of spacecrafts [3]. On account of the wide scanning range of crosslink beam, GNSS crosslink signals can be tracked on higher orbits than the conventional navigation signals, especially for high-orbit spacecraft, for which the number of available ranging observations increases greatly.

There have been many discussions about GNSS crosslink, mainly about the frequency [4], the geometry characteristics [5], or the link scheme [6] of crosslink network itself, but no researches of extensive application have been reported yet.

However, GNSS crosslink network has to help realise overseas management and control, as well as autonomous orbit determination and time synchronization [7]. While GNSS satellites carrying out the above normal tasks, the available ranging observations for the external user spacecraft will be reduced. With less than 4 available GNSS crosslinks, it will lead to the failure of geometric positioning. In this article, dynamic orbit determination method combining GNSS crosslink measurements with dynamic models is applied in condition of insufficient observations. On basis of the analyzed ranging errors, orbit determination experiments using geometric method and dynamic method are conducted, and the accuracies are compared.

31.2 Basic Principles and Mathematical Models

Dynamic orbit determination method is adopted in circumstance of insufficient GNSS crosslink observations. The essence is the procedure of orbit improvement, namely using the observations to improve the estimated initial kinetic parameters. The user spacecraft kinetic equation (equation of state) as well as the GNSS crosslink observation equation need to be established first.

With more than 4 crosslink measurements, geometric orbit determination method can be applied. High-orbital spacecraft orbit parameters can be obtained by least square fitting, similar to the single point positioning of ground navigation users.

31.2.1 Observation Model and Error Correction

Considering the various error sources in the observation path, the pseudorange observation equation of GNSS crosslink can be expressed in detail as follows:

Table 31.1 Ranging errors of GNSS crosslink

Error sources	Modify method	Time constant	Mean square error
GNSS ephemeris error ($\delta \boldsymbol{r}^{\mathrm{S}}$)	broadcast message	Update every 1 h	$\sigma_{ephe} \approx 0.2$ m
GNSS clock error (δt^{S})	broadcast message	Update every 1 h	$\sigma_{clk} \approx 0.3$ m(1 ns)
Crosslink device delay (Δt)	calibration	Static error	$\sigma_{chan} \approx 0.06$ m(0.2 ns)
Antenna phase center error ($\delta \rho_{pco}$)	calibration	Static error	$\sigma_{pco} \approx 0.002$ m
Rrelativistic effect ($\delta \rho_{rel}$)	formula	$\approx$16 h	$\sigma_{rel} \approx 0.02$ m
Multipath ($\delta \rho_{multi}$)	–	$\approx$100 s	$\sigma_{multi} \approx 0.5$ m
Receiver noise ($\delta \rho_{noise}$)	–	White noise	$\sigma_{noise} \approx 0.1$ m

$$\rho = R + c\delta t_u - c\delta t^S + c\left(\Delta t_u + \Delta t^S\right) + \delta\rho_{pco} + \delta\rho_{rel} + \delta\rho_{multi} + \delta\rho_{noise} + \varepsilon_\rho \tag{31.1}$$

where ρ is the pseudorange measurement of GNSS crosslink; $\boldsymbol{r}$ and $\boldsymbol{r}^{\mathrm{S}}$ are the positions of user and navigation satellite respectively, and $R = \left\|\boldsymbol{r} - \boldsymbol{r}^S\right\|$ is the geometric distance between them; δt_u and δt^{S} are the on-board clock error of user and navigation satellite respectively; Δt_u and Δt^{S} are the device delay of transmitting and receiving crosslink equipment respectively; $\delta\rho_{pco}$ is the error of antenna phase center offset; $\delta\rho_{rel}$ is the error of relativistic effect; $\delta\rho_{multi}$ is the error of multipath effect; $\delta\rho_{noise}$ is the receiver measurement noise; ε_ρ is the integrated effect of the residual distance errors.

In Eq. (31.1), the position and clock error of the navigation satellite can be obtained by the GNSS broadcast message [8], the antenna phase center offset error and device delay can be calibrated previously, the relativistic effect can be modified through periodic drift correction formula [9], the receiver measurement noise can be estimated through the corresponding model [10], and the impact of multipath delay effects on ranging can be assumed using the experience value. User ranging errors caused by various error sources are shown in Table 31.1.

User equivalent ranging error is:

$$\sigma_\rho = [\sigma_{ephe}^2 + \sigma_{clk}^2 + 2\sigma_{chan}^2 + 2\sigma_{pco}^2 + \sigma_{rel}^2 + \sigma_{multi}^2 + \sigma_{noise}^2]^{1/2} \approx 0.630 \text{ m} \tag{31.2}$$

Thus the corrected observation equation can be written as:

$$\rho_C = R + b + \varepsilon \tag{31.3}$$

where ρ_C is the error corrected pseudorange measurement; $b = c\delta t_u$ is the receiver clock error (in distance); ε is the observing error.

Linearizing Eq. (31.3) near $\boldsymbol{r}^*$ and b^*, the approximate position and clock error value of the user spacecraft, one can obtain:

$$\rho_C = \rho_C{}^* + \frac{(\boldsymbol{r}^* - \boldsymbol{r}^S)^T}{R^*}\Delta\boldsymbol{r} + \Delta b + \varepsilon \tag{31.4}$$

where $R^* = \left\|\boldsymbol{r}^* - \boldsymbol{r}^S\right\|$; $\rho_C{}^* = R^* + b^*$; $\Delta\boldsymbol{r}$ and Δb are the improved value relative to the approximate value $\boldsymbol{r}^*$ and b^*.

Given $L = \rho_C - \rho_C{}^*$, Eq. (31.4) can be written as:

$$L = \begin{bmatrix} \frac{(\boldsymbol{r}^* - \boldsymbol{r}^S)^T}{R^*} & 1 \end{bmatrix} \begin{pmatrix} \Delta\boldsymbol{r} \\ \Delta b \end{pmatrix} + \varepsilon \tag{31.5}$$

31.2.2 Dynamic Model

In inertial coordinate system, the user's dynamics equation can be simplified as:

$$\ddot{\boldsymbol{r}} = f(\boldsymbol{r}, \dot{\boldsymbol{r}}, \boldsymbol{p}, t) = -\frac{GM_E}{r^3}\boldsymbol{r} + \boldsymbol{a}_p(\boldsymbol{r}, \dot{\boldsymbol{r}}, \boldsymbol{p}, t) \tag{31.6}$$

where $\boldsymbol{r}$, $\dot{\boldsymbol{r}}$ and $\ddot{\boldsymbol{r}}$ are the postion, velocity and acceleration of the user respectively, $r = \|\boldsymbol{r}\|$; GM_E is the Earth's gravitational constant; $\boldsymbol{p}$ is the dynamic parameters; t is time. The first term on right side of the equation is the two-body motion acceleration, the second term represents the perturbation acceleration, that is, all except the acceleration forces caused by the central gravitation, including perturbation that can be modeled, such as non-spherical gravitation, sun and moon gravitation, solar radiation pressure main items, and the residual perturbation that requires empirical model fitting.

In this article, compensating empirical acceleration parameters a_R, a_T, a_N in three directions of radial, tangential, normal, and solar radiation pressure coefficient C_r are selected as kinetic parameters, that is $\boldsymbol{p} = [a_R, a_T, a_N, C_r]^T$. Different constraints are imposed to the three empirical acceleration parameters to ensure the stability of solution.

Set the dynamic state vector as $\boldsymbol{X}_p = (\boldsymbol{r}, \dot{\boldsymbol{r}}, \boldsymbol{p})^T$, and the corresponding system state equation is:

$$\dot{\boldsymbol{X}}_p = F(\boldsymbol{X}_p, t) + \boldsymbol{w}_p = [\dot{\boldsymbol{r}} \quad \boldsymbol{a} \quad \boldsymbol{0}]^T + \boldsymbol{w}_p \tag{31.7}$$

where $\boldsymbol{a} = \ddot{\boldsymbol{r}} = f(\boldsymbol{X}_p, t)$ is the perturbation forces calculated according to models and $\boldsymbol{w}_p$ is the dynamic model noise.

31.2.3 Clock Error Model

Random process is usually used to simulate the receiver clock error, including white noise, integrated white noise, flicker noise and so on. In this article, the user

clock error b and the frequency difference f will be modeled with random walk process as follows:

$$\begin{cases} \dot{b} = f + w_f \\ \dot{f} = w_g \end{cases} \tag{31.8}$$

where w_f and w_g are assumed as Gauss white noise process with zero mean.

Set the clock error vector as $\boldsymbol{X}_b = \left(b, \dot{b}\right)^T$, thus the state equation is:

$$\dot{\boldsymbol{X}}_b = F(\boldsymbol{X}_b, t) + \boldsymbol{w}_b = \begin{bmatrix} \dot{b} \\ 0 \end{bmatrix} + \begin{bmatrix} w_f \\ w_g \end{bmatrix} \tag{31.9}$$

31.2.4 Dynamic Model

Set the state vector as $\boldsymbol{X} = \left[\boldsymbol{X}_p, \boldsymbol{X}_b\right]^T = \left[\boldsymbol{r}, \dot{\boldsymbol{r}}, a_R, a_T, a_N, C_r, b, \dot{b}\right]^T$, then the simultaneous equation of Eqs. (31.7) and (31.9) can be written as:

$$\dot{\boldsymbol{X}} = F(\boldsymbol{X}) + \boldsymbol{w} \tag{31.10}$$

where $\boldsymbol{w} = \left[\boldsymbol{w}_p \quad \boldsymbol{w}_b\right]^T$ is the state noise vector with covariance matrix of $\boldsymbol{\Sigma}_{w_k}$.

Given correction vector as $\boldsymbol{x} = \boldsymbol{X} - \boldsymbol{X}^*$, one can obtain state transition equation as follows:

$$\boldsymbol{x} = \Phi(t, t_0)\boldsymbol{x}_0. \tag{31.11}$$

Equation (31.5) can be rewritten as:

$$L = \boldsymbol{H}\boldsymbol{x} + \varepsilon \tag{31.12}$$

where $\boldsymbol{H} = \left[\frac{(\boldsymbol{r}^* - \boldsymbol{r}^S)^T}{R^*} \quad \boldsymbol{0}_{3\times1} \quad \boldsymbol{0}_{4\times1} \quad 1 \quad 0\right]$.

Assuming there are a sequence of GNSS crosslink observations L_1–L_l at time of t_1–t_l, thus

$$L_k = \boldsymbol{H}_k\boldsymbol{x}_k + \varepsilon_k = \boldsymbol{H}_k\Phi(t_k, t_0)\boldsymbol{x}_0 + \varepsilon_k, \quad k = 1, \cdots l \tag{31.13}$$

where the covariance matrix of ε_k is $\boldsymbol{\Sigma}_k$.

31.2.4.1 Kalman Filtering Algorithm

As state noise and observation noise both satisfy the statistical characteristics of zero mean white Gauss noise, Kalman filtering algorithm is as follows:

1. state prediction

$$\begin{aligned} \bar{\boldsymbol{x}}_k &= \boldsymbol{\Phi}_{k,k-1}\hat{\boldsymbol{x}}_{k-1} \\ \boldsymbol{\Sigma}_{\bar{x}_k} &= \boldsymbol{\Phi}_{k,k-1}\boldsymbol{\Sigma}_{\hat{x}_{k-1}}\boldsymbol{\Phi}_{k,k-1}^T + \boldsymbol{\Sigma}_{w_k} \end{aligned} \tag{31.14}$$

2. the measurement update

$$\begin{aligned} \hat{\boldsymbol{x}}_k &= \bar{\boldsymbol{x}}_k + \boldsymbol{K}_k(L_k - \boldsymbol{H}_k\bar{\boldsymbol{x}}_k) \\ \boldsymbol{K}_k &= \boldsymbol{\Sigma}_{\bar{x}_k}\boldsymbol{H}_k^{\mathrm{T}}[\boldsymbol{H}_k\boldsymbol{\Sigma}_{\bar{x}_k}\boldsymbol{H}_k^{\mathrm{T}} + \boldsymbol{\Sigma}_k]^{-1} \\ \boldsymbol{\Sigma}_{\hat{x}_k} &= [\boldsymbol{I} - \boldsymbol{K}_k\boldsymbol{H}_k]\boldsymbol{\Sigma}_{\bar{x}_k} \end{aligned} \tag{31.15}$$

Given a set of initial state reference value $\boldsymbol{X}^*(t_0)$, the priori parameters to be estimated $\bar{\boldsymbol{x}}_0$ and the priori covariance matrix $\boldsymbol{\Sigma}_{\bar{x}_0}$, the optimal estimation $\hat{\boldsymbol{x}}$ of moment t can be obtained using Eqs. (31.14) and (31.15), resulting in the improved orbit:

$$\hat{\boldsymbol{X}} = X^* + \hat{\boldsymbol{x}} \tag{31.16}$$

31.2.4.2 Least Squares Algorithm

Least Squares Algorithm is applied to the geometric orbit determination method. The crosslink observation equation can be written as follows:

$$\boldsymbol{L} = \boldsymbol{H}\boldsymbol{x} + \varepsilon \tag{31.17}$$

where $\boldsymbol{L} = [L_1\, L_2 \ldots L_M]^T$ is the observation vector, and $\boldsymbol{H} = \left[\boldsymbol{H}^{(1)}\, \boldsymbol{H}^{(2)} \ldots \boldsymbol{H}^{(M)}\right]^T$ is the matrix of coefficient.

If the user clock error is included while resolving, the forms of $\boldsymbol{H}^{(k)}$ and $\boldsymbol{x}$ are as follows:

$$\boldsymbol{H}^{(k)} = \begin{bmatrix} \frac{(\boldsymbol{r}^* - \boldsymbol{r}^{S(k)})^T}{R^{(k)*}} & 1 \end{bmatrix}, \quad \boldsymbol{x} = \begin{bmatrix} \boldsymbol{r} - \boldsymbol{r}^* \\ b - b^* \end{bmatrix} \tag{31.18}$$

and are as follows if the user clock error is excluded:

$$\boldsymbol{H}^{(k)} = \left[\frac{(\boldsymbol{r}^* - \boldsymbol{r}^{S(k)})^T}{R^{(k)*}}\right], \quad \boldsymbol{x} = \boldsymbol{r} - \boldsymbol{r}^* \tag{31.19}$$

According to the least squares theory, the solution to Eq. (31.17) is:

$$\begin{aligned} \boldsymbol{x} &= (\boldsymbol{H}^T\boldsymbol{P}\boldsymbol{H})^{-1}\boldsymbol{H}^T\boldsymbol{P}\boldsymbol{L} \\ \boldsymbol{\Sigma}_{\boldsymbol{x}} &= \sigma^2(\boldsymbol{H}^T\boldsymbol{P}\boldsymbol{H})^{-1} \end{aligned} \tag{31.20}$$

31.3 Simulation Calculations

31.3.1 Conditions of Simulation Experiments

The simulated GNSS constellation is composed of 3 Geostationary Earth Orbital (GEO) satellites, 3 Inclined Geo Synchronous Orbital (IGSO) satellites and 24 Medium Earth Orbital (MEO) satellites with configuration of Walker-δ 24/3/1, height of 21,500 km, inclination angle of 55°. The simulated GNSS crosslink is dynamic pointing type with beam angle of 4° and scanning range of ±70°.

The orbital parameters of the user spacecraft equipped with GNSS crosslink receiver are as a GEO satellite with height of 42,164.17 km, inclination angle of 0° and eccentricity ratio of 0.

The simulation period is from February 1, 2012 to April 2, 2012. The dynamic models include: earth gravitational field with 8th-order JGM3 model, sun and moon gravitation with ephemeris of JPL DE 405, solid tide with IERS 2003 model, solar radiation pressure with sphere model together with scaling factor and Y direction parameter, earth oriental parameter given by IERS Bulletin B.

As ranging errors analysed in Table 31.1, set the random error as 0.65 m and the residual system error as 0.2 m. Clock errors of navigation satellite and user spacecraft adopt the GPS actual measurement. Inter-satellite ranging measurement can be one-way or dual-way. For one-way measurement, user clock error needs to be estimated, and for dual-way, only obit parameters need to be estimated.

In the following experiments, numbers of GNSS crosslink signals available to the user spacecraft are set as no more than 4 or more than 4 in different circumstances.

31.3.2 Results of Simulation Experiments

31.3.2.1 Orbit Error Without Measurements

Directly applying the prior dynamic parameters to orbit prediction without crosslink measurement correction, the error relative to simulated standard orbit is shown as in Fig. 31.1.

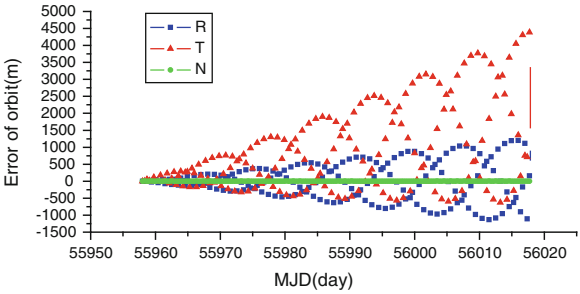

Fig. 31.1 Error of orbit prediction without crosslinks

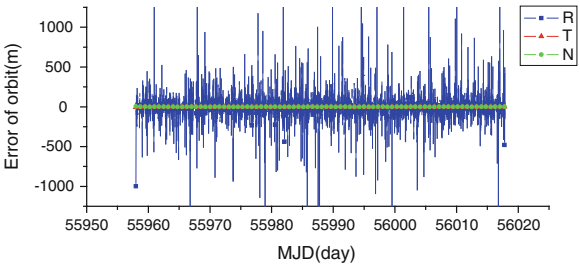

Fig. 31.2 Result of including clock error with 4 links

It shows that the main errors exist in the along-track and radial directions and increase significantly over time, reaching up to several kilometers after 60 days.

31.3.2.2 Orbit Error of Geometric Method

While using geometric method, user's position and clock error are both estimated. Take notice that fewer than 4 observations leads to failure of positioning. With four or more crosslinks, the geometric method orbit error relative to simulated standard orbit is shown as in Figs. 31.2 and 31.3.

Figures 31.2 and 31.3 show that, when user's position and clock error both be estimated, the average position error with only four crosslinks is about two hundred meters, and deteriorates significantly in worse geometry situation. As the crosslink number reached 4–8, the accuracy improves but is still around 60 m. It also shows that the error in radial direction is obviously lager than the other two directions. Since the accuracy of geometric method mainly depends on the geometry of measurements, however, most of the crosslinks of GEO user and GNSS satellites are away from the equatorial plane.

To avoid the impact of user clock error, dual-way crosslink measurements can be employed to eliminate the clock error directly. When the clock error is not estimated, the geometric method significantly improves, as shown in Figs. 31.4 and 31.5.

Figures 31.4 and 31.5 show that orbit determination accuracy improves significantly when user clock error excluded. This is mainly due to the improvement

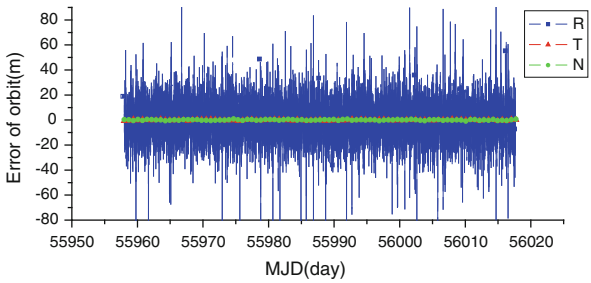

Fig. 31.3 Result of including clock error with more than 4 links

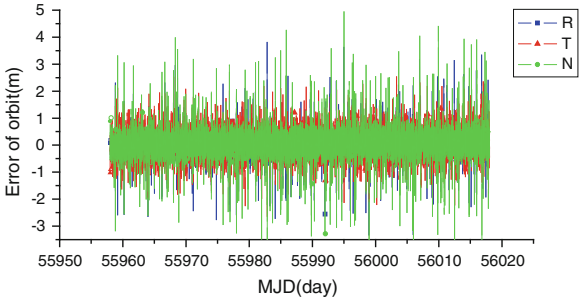

Fig. 31.4 Result of excluding clock error with 4 links

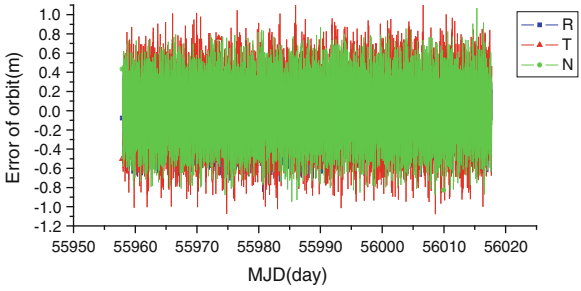

Fig. 31.5 Result of excluding clock error with more than 4 links

of positioning geometry, with DOP value decreasing from more than 30 to close to 1. Generally speaking, the accuracy of geometric orbit determination varies with the observation geometry, and improves as the number of crosslinks improves.

31.3.2.3 Orbit Error of Dynamic Method

In the dynamic method, number of crosslink observations is less important than in the geometric method. With four or more crosslinks, the geometric method orbit error relative to simulated standard orbit is shown as in Figs. 31.6 and 31.7.

Compared with Figs. 31.4 and 31.5, Figs. 31.6 and 31.7 shows that dynamic method reaches higher accuracy and stability than geometric method under the

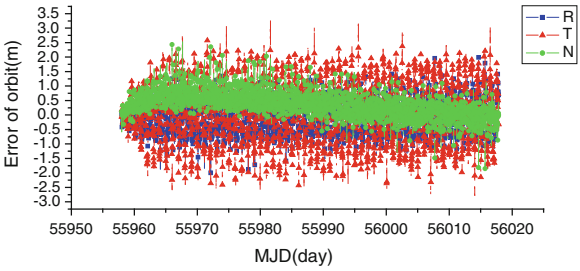

Fig. 31.6 Result of excluding clock error with 4 links

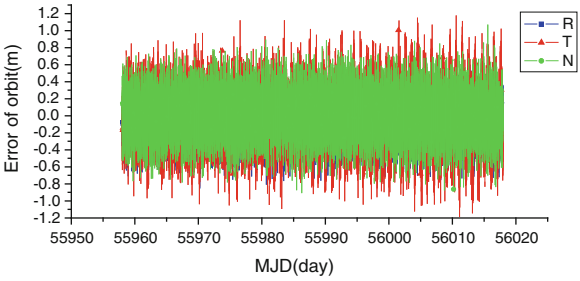

Fig. 31.7 Result of excluding clock error with more than 4 links

same observation geometry conditions, but the improvement is less obvious with more crosslink measurements. The main advantage of dynamic method is that orbit determination accuracy is less effected by measuring geometry, resulting in good orbit stability.

It should be noticed that user clock error needs to be estimated as well while using single way crosslink measurement, which may leads to worse DOP value. Equations in Sect. 31.2.4 can still be applied for a filter of orbit determination, but this calls for higher dynamic model accuracy and preliminary orbit precision. The specific effects of user clock errors on orbit determination needs further analysis.

31.4 Conclusions

On account of the limited antenna beam angle, the traditional L-band navigation signals cannot be applied for high-orbit spacecraft precise orbit determination. Global Navigation Satellite System equipped with the crosslink network provides a more effective means for the high-orbit spacecraft orbit determination since there would be more signals available for the wide range. As the ranging errors of GNSS crosslink analyzed in this paper, it can reach a relatively high ranging accuracy. Results of the high-orbital satellite orbit determination experiments show that kinetic method performs better than geometric method with fewer available observations, while the improvement is not obvious with sufficient observations. Besides, whether to solve the user clock error or not has significant effects for

geometric method: the orbit determination accuracy reaches about a hundred meters level if the solution includes clock error, but can achieve within several meters if excludes clock error.

Using GNSS crosslink ranging observations for orbit determination is a new direction, which will expand the application field of GNSS, and makes excellent prospects especially for the high-orbital precise orbit determination.

References

1. Ollie L, Boyd L, Gower A et al (2005) GPS III system operations concepts. IEEE Aerosp Electron Syst Mag 20(1):P10–P18
2. Fernández FA (2010) Inter-satellite ranging and inter-satellite communication links for enhancing GNSS satellite broadcast navigation data. Available via http://www.Sciencedirect.com/
3. Fan S, Meng Y, Gao W et al (2013) Summarizing on the development of spacecraft orbit determination technology. J Geomatics Sci Technol 30(6):P549–P554
4. Marine KP, Anderson P, Langer J (2003) Crosslink for the next-generation GPS. In: IEEE Aerospace conference, Big Sky, MT, 8–15 Mar 2003
5. Yang N, Li C (2007) ISL analysis of navigation satellite system. GNSS World China 2:P17–P20
6. Zhou J, Yang L, Xu B et al (2011) An improved satellite link scheme with beam restriction for the navigation constellation. In: 2011 China satellite navigation conference, Shanghai, 18–20 May 2011
7. Holmes JK, Raghavan SC (2004) A summary of the new GPS IIR-M and IIF modernization signals. In: IEEE 60th Vehicular technology conference, Los Angeles, CA, 26–29 Sept 2004
8. ARINC Research Corporation (2003) Navstar GPS space segment/navigation user interfaces, ICD-GPS-200C. Available via http://www.navcen.uscg.gov/pubs/gps/icd200/default.htm(amend the comma ',' after 'navcen' to dot '.')
9. Li J (1995) Satellite precision orbit determination. Chinese PLA Publishing House, Beijing
10. Kaplan ED, Hegarty CJ (2006) Understanding GPS: principles and applications, 2nd edn. Artech House Inc., Boston

Part II
Atomic Clock Technique and Time-Frequency System

Chapter 32
A Novel Method for Navigation Satellite Clock Bias Prediction Considering Stochastic Variation Behavior

Yu Lei, Zhaopeng Hu and Danning Zhao

Abstract Considering that the satellite clock bias (SCB) is composed of a trend part, periodic item and stochastic component, a novel method incorporating the polynomial model adding a few cyclic terms and least squares support vector machines (LS-SVM) for clock bias prediction is proposed in this paper. The trend part and periodic item are firstly modeled by the polynomial model adding a few cyclic terms according to the physical characteristics of satellite clocks. Then, the polynomial fitting residuals, namely the stochastic component, is modeled based on the LS-SVM. Finally, the forecasted results for the trend part, periodic item and stochastic component are aggregated to produce the final prediction value for the clock bias. For verification and testing, the GPS clocks are taken as an example and the short-term prediction experiments are carried out. The simulation results have demonstrated that the proposed prediction method outperforms the IGU-P solutions at least on a daily basis.

Keywords Satellite clock bias (SCB) · Stochastic variation · Least squares support vector machines (LS-SVM) · Prediction model

32.1 Introduction

The satellite clock bias (SCB) is one of main error sources to be eliminated in precise positioning. Taking GPS for example, the accuracy of the final GPS clock products provided by IGS has been shown to be roughly 75 ps RMS, which can achieve centimetre precision in real-time precise point positioning (RTPPP), but

Y. Lei (✉) · Z. Hu · D. Zhao
National Time Service Center, Chinese Academy of Sciences, Xi'an 710600, China
e-mail: leiyu@ntsc.ac.cn

Y. Lei · Z. Hu · D. Zhao
University of Chinese Academy of Sciences, Beijing 100039, China

J. Sun et al. (eds.), *China Satellite Navigation Conference (CSNC) 2014 Proceedings: Volume III*, Lecture Notes in Electrical Engineering 305,
DOI: 10.1007/978-3-642-54740-9_32,

with a 13-days delay. The performance of clock prediction based on the broadcast ephemeris and the IGS ultra-rapid predicted (IGU-P) products is about 5 and 3 ns RMS, respectively. These two clock solutions have not shown acceptably high-quality prediction performance, though they are available in real-time. Consequently, it is greatly significant to improve the accuracy of clock prediction [1–6].

It is difficult to predict the satellite clock behaviour accurately. One reason for the fact is that satellite clocks in space can be easily impacted on by various factors like environment and temperature and this leads to complicated aspects such as periodic and stochastic variations, which are not sufficiently described by traditional models such as a linear model, quadratic polynomial model, grey model and so on. These models are appropriate to describe the variations of a stationary clock rather than a non-stationary clock. This is because that all these models consider the trend term or both the trend and cyclic items, but ignore the random part [5, 6].

Combing the polynomial model with a few cyclic items which highlights the trend item and periodic item modelling and the least squares support vector machines (LS-SVM) that can capture the nonlinear patterns in the random term, this study proposes a novel hybrid methodology for clock bias prediction. The simulation results have verified the feasibility and effectiveness of the proposed method.

32.2 The Physical Characteristics of Atomic Clocks on Board

The output of an atomic clock can be expressed as $V(t) = [V_0 + \varepsilon(t)] \sin(2\pi\upsilon_0 t + \phi(t))$, where υ_0 and V_0 are the nominal frequency and amplitude of the output signal, and $\varepsilon(t)$ and $\phi(t)$ are the random fluctuations of the amplitude and phase, respectively. The normalized phase bias $x(t) = \phi(t)/(2\pi\upsilon_0)$ evolves over time in terms of deterministic and random laws. For example, the phase bias, namely clock bias, is often modeled as the following quadratic polynomial.

$$x(t) = x_0 + y_0 t + \frac{1}{2} z t^2 + \psi(t) \tag{32.1}$$

where $x_0 = x(0)$ and $y_0 = y(0)$ represent the phase and frequency bias at the initial instant t_0; $\psi(t)$ is a stochastic noise process; and z is the linear variations of the frequency bias, referred to as frequency drift or aging usually. In fact, the value of z can be set to 0 for the clocks of the GPS Block IIR, IIR-M and IIF satellites [4].

Originally, the quadratic polynomial model is very appropriate for the case of a stationary clock, though on-board clocks show non-stationary behaviour like periodic variations which can not been described by this model. Senior et al. [7] offered enough evidence to support the periodic behaviour in all types of GPS satellite clocks. To predict the satellite clock behaviour, a more general representation of satellite clocks is desirable and the clock bias can be modelled as below.

$$x(t) = x_0 + y_0 t + \frac{1}{2} z t^2 + \sum_{i=1}^{n} \left(a_i \cos(\omega_i t) + b_i \sin(\omega_i t)\right) + \psi(t) \tag{32.2}$$

where the frequency of the sinusoidal variations, ω_i, is confirmed corresponding to the main clock period that can be detected by using the spectrum analysis method; x_0, y_0, z, a_i and b_i can be estimated with the least square methodology; and the random term, $\psi(t)$, considered as the white gauss noise, is always ignored. Heo et al. [3] and Xu et al. [5] improved the prediction precision of GPS onboard clocks with the period term and random term modelled.

32.3 Least Squares Support Vector Machines for Regression

LS-SVM developed by Suykens and Vandewalle [8] in 1999 is an improvement of the support vector machines (SVM). LS-SVM performs by mapping the input data into a high-dimension feature space nonlinearly, and then runs the linear regression in this feature space. This allows us to formulate the nonlinear relationship between input data and output data. Basically, LS-SVM defines the regression function as

$$f(\boldsymbol{x}) = \boldsymbol{w}^T \varphi(\boldsymbol{x}) + b \tag{32.3}$$

where $\boldsymbol{w}$ represents the weight vector; b is the bias term and $\varphi(\cdot)$ denotes the nonlinear mapping function which maps the input vectors into a high-dimension feature space.

Consider a given training data set $\boldsymbol{x}_i$, y_i, $i = 1, 2, \ldots, l$ with input data, $\boldsymbol{x}_i$, and output data, y_i. In LS-SVM, the regression problem can be regard as the following optimization problem based on the structure risk minimization principle.

$$\begin{cases} \min\limits_{\boldsymbol{w},\boldsymbol{e}} J(\boldsymbol{w},\boldsymbol{e}) = \frac{1}{2}\boldsymbol{w}^T\boldsymbol{w} + \frac{\gamma}{2}\sum\limits_{i=1}^{l} e_i^2 \\ s.t. \quad y_i = \boldsymbol{w}^T\varphi(\boldsymbol{x}_i) + b + e_i \quad i = 1, 2, \ldots, l \end{cases} \tag{32.4}$$

where e_i represents the approximation error from the training data set and γ is penalty parameter employed for limiting the minimization of estimation error and function smoothness.

In order to handle the optimization problem of Eq. (32.4), the Lagrange function is formulated and the Karush-KuhnTucker (KKT) conditions are used for Eq. (32.4) to obtain the solutions. As a consequence, Eq. (32.4) can be changed into

$$\begin{bmatrix} 0 & \boldsymbol{I}_v^T \\ \boldsymbol{I}_v & \boldsymbol{\Omega} + \gamma^{-1}\boldsymbol{I} \end{bmatrix} \begin{bmatrix} b \\ \boldsymbol{\alpha} \end{bmatrix} = \begin{bmatrix} 0 \\ \boldsymbol{y} \end{bmatrix} \tag{32.5}$$

where $\boldsymbol{I}_v = [\,1 \quad 1 \quad \ldots \quad 1\,]^T$, $\boldsymbol{\alpha} = [\alpha_1, \alpha_2, \ldots, \alpha_l]^T$, $\boldsymbol{y} = [y_1, y_2, \ldots, y_l]^T$, and the Mercer condition has been applied to matrix $\boldsymbol{\Omega}$ with $\Omega_{ij} = \varphi(\boldsymbol{x}_i)^T \varphi(\boldsymbol{x}_j)$. By solving the above linear system, the LS-SVM for regression can be obtained from

$$y = f(\boldsymbol{x}) = \sum_{i=1}^{l} \alpha_i K(\boldsymbol{x}, \boldsymbol{x}_i) + b \tag{32.6}$$

where $K(\boldsymbol{x}, \boldsymbol{x}_i)$ is the kernel function.

32.4 Methodology

32.4.1 Integrated Prediction Model

In reality, the SCB series can be treated as superposition of the trend part, periodic term and random component. So motivated by the nature, this paper proposes an integrated model combing the polynomial model adding cyclic terms and LS-SVM model. The combined model uses the polynomial model with cyclic terms to extract trend and periodic terms of clock series, and then utilizes LS-SVM to model the residuals. As LS-SVM owns the wonderful capacity of nonlinear mapping and parallel processing, it can be employed to forecast the non-stationary and nonlinear time series. On the other hand, the time series of polynomial fitting residuals has definite internal regularity. This kind of information processing method is just what LS-SVM is good at, while it is difficult for traditional analytical methods. Thus, LS-SVM is applied to model and forecast the residuals.

The forecasting process of the proposed integrated model is shown in Fig. 32.1.

1. Clock bias data preprocessing: this subsection addresses the issues that the integrated model predicts the clock bias in the presence of outliers, missing data and data transition. For outliers and missing data, the 3σ principle is used to detect and remove outliers, and then the interpolation method is utilized to interpolate these data points and the missing data. As to data transition, the anomalies are disposed of by employing a moving method, and then corrected based on the interpolation approach. After the data preprocessing, the integrated model can be constructed.
2. The clock bias of n epochs is modeled by the polynomial model adding cyclic terms, and then the trend item, periodic item and random term are extracted. Furthermore, the random term is modeled by the LS-SVM model.

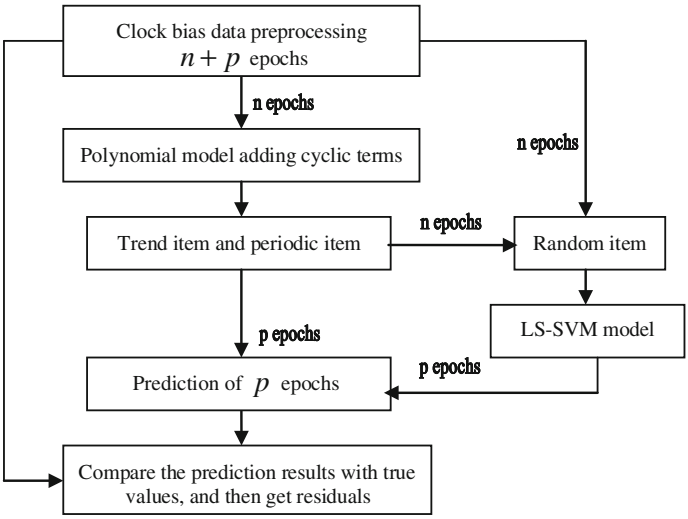

Fig. 32.1 Flow chart of clock bias prediction with the integrated model

3. The polynomial model adding cyclic terms is used to predict the trend part and periodic part of the following clock bias series of p epochs, while the LS-SVM model is employed for forecasting the random part, and then the predicted results for the trend part, periodic term and random item are aggregated to produce the final forecasted value for the clock bias.

32.4.2 Modelling the Clock Bias Residuals Based on the LS-SVM

The fitting residuals of the polynomial model adding cyclic terms, namely the stochastic term, can exhibit complexly dynamical behaviour that the traditional modelling techniques are not able to capture effectively. Hence, the LS-SVM is applied to the prediction of the residuals, because it provides the possibility of assessing linear or nonlinear components of the coupling between variables, and more importantly, it is one of the fundamental tools in nonlinear unknown system modelling. On the assumption that the time series of fitting residuals$\{\psi(i), i = 1, 2,\ldots,n\}$, is a nonlinear dynamical system, the time evolution of the system can be caught by mapping past output items to future outputs $y_k = f(\vec{x}_k)$, where $\vec{x}_k = [\psi(k-1), \psi(k-2), \ldots, \psi(k-m)]^T$ and $y_k = \psi(k)$ is an observable output. f can be attained from the predictive mapping f: $R^m \rightarrow R$ as described in Sect. 32.1.3, which is the centerpiece of modeling.

Table 32.1 The structure of input vectors and output vectors

No.	Input vectors	Output vectors
1	$\psi(m), \psi(m-1), \ldots, \psi(1)$	$\psi(m+1)$
$\vdots$	$\vdots$	$\vdots$
$k-m$	$\psi(k-1), \psi(k-2), \ldots, x(k-m)$	$\psi(k)$
$\vdots$	$\vdots$	$\vdots$
$n-m$	$\psi(n-1), \psi(n-2), \ldots \psi(n-m)$	$\psi(n)$

The training samples are arranged, as depicted in Table 32.1. In process of modeling, LS-SVM analyzes the training data set, which results in a LS-SVM model built. During the prediction stage, the LS-SVM model is utilized to predict the future random term $\hat{\psi}(n+1)$ in one-step-ahead, based on the historical data $\{\psi(n), \psi(n-1), \ldots, \psi(n-m+1)\}$. Let $\psi(n+1) = \hat{\psi}(n+1)$, thus a new time series $\{\psi(n+1), \psi(n), \ldots, \psi(n-m+2)\}$ can be gained, which is as the input vectors for next instant. In this way, the desired output that corresponds to the model input can be obtained and the multi-step prediction for the random item can be achieved.

Selecting inappropriate parameters can lead to under-fitting or over-fitting of the LS-SVM model. To establish a LS-SVM model efficiently, model parameters must be accurately determined. These parameters include:

1. The kernel function: The kernel function is employed to construct a nonlinear decision hyper-surface on the LS-SVM input space. In general, utilizing the RBF kernel function is capable of yielding accurate forecasting. Hereby, the RBF kernel function is adopted as the kernel function of the LS-SVM model.
2. The regularization parameter, γ, balances the approximation accuracy and complexity of the LS-SVM model.
3. The bandwidth of the kernel function, σ, called as the kernel parameter, describes the variance of the RBF kernel function.

The grid search (GS) method together with k-fold cross-validation [9], is the commonly used parameter choice approach for LS-SVM regression. In this study, this approach is introduced for the purpose of choosing the parameters γ and σ.

32.5 Simulation Results

32.5.1 Data and Experiment Description

In general, the IGS offers three kinds of GPS clock products; the accuracy of the IGS final products is highest in all IGS products, but they are released with a delay of approximately 13 days; the IGS ultra-rapid observed (IGU-O) products are distributed for real-time or near real-time applications four times one day with an

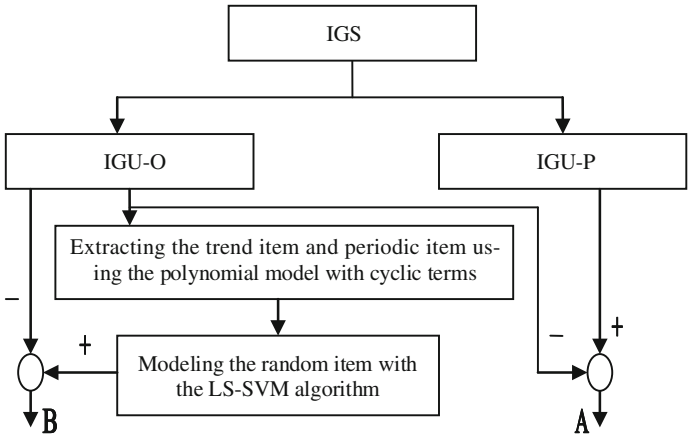

Fig. 32.2 Schematic diagram of the performance test and evaluation

initial latency of about 3 h and the precision of the IGU-O and IGU-P products is about 0.15 and 3 ns RMS, respectively. The IGU-O products are very suitable as the initial values of the proposed model for the one-day-ahead forecasting, because they are highly accurate and can be available on a daily basis. Therefore, in this research, the IGU-O products are used to build, test and evaluate the proposed model. The prediction of the proposed model which is built upon the IGU-O products is compared with respect to the IGU-P solutions as well.

The IGU-O clock bias of 29 October 2011 is used to predict the satellite clock bias over the next 24 h, and the IGU-O and IGU-P clock bias of 30 October 2011 are used to check the forecasting ability of the proposed model based the evaluation criteria. The sample interval of these products is 15 min. Eight GPS satellites in orbit are randomly selected, whose types include Block IIA, IIR, IIR-M and IIF. The number of the selected satellites is PRN03, PRN06, PRN08, PRN10, PRN14, PRN25, PRN26 and PRN31, respectively. Several tests to evaluate the proposed model for clock prediction have been carried out, as illustrated in Fig. 32.2, where A and B represent the prediction residuals of IGU-P and the proposed model, respectively.

32.5.2 Experiment Procedures

The proposed algorithm is implemented in a robust software code (in MATLAB language) and several separate tests have been conducted to evaluate the proposed model for clock prediction, which are 3-, 6-, 12-, 24-h-ahead prediction test. Integrity check is firstly performed so as to exclude the anomalies existing in the clock data.

After the data preprocessing, the trend item is extracted from the clock bias sequence in terms of its physical property. Herein, the clocks of Block IIA satellites are fitted by quadratic polynomial, whereas the other satellites by one order polynomial. Then, the spectrum analysis approach is applied to the fitting residuals for detecting notable periodic items (the first three items are taken in this study). Once main periods are determined, the cyclic term can be extracted.

After the trend item and periodic term are extracted, the random item is modeled by the LS-SVM based on the RBF kernel. The method of GS with cross-validation is adopted to the choice of γ and σ so as to improve the generality ability of the LS-SVM model. The basic concept is to cross-validate the prediction results with data samples. The implementation process is detailed as below.

1. Parameter setting: the searching bound and step of the parameters γ and σ are set. As to γ, the bound and step are set to $1–10^5$ and 10, while $1–10^4$ and 10 forσ, respectively.
2. Data preparation: the training samples are randomly separated into k parts. $k-1$ parts are used to train the LS-SVM model, while the leaving part is as the validation series. The prediction values can be calculated from the LS-SVM model using given set of parameters γ, σ. Then, the prediction variance of the validation series relative to the forecasting values can be obtained. For each set of parameters validation series is sampled for k times. Thus, the k variance can be estimated. The mean of the k variance for each set of parameters, $\bar{C}(\gamma, \sigma)$ can be finally derived.
3. Stop the search process until all given values of γ and σ have been scanned.
4. The values of γ and σ that make the smallest $\bar{C}(\gamma, \sigma)$are considered as the optimal model parameters.

It should be pointed out that the k value depends on the size of data samples. In this study, the candidate values are 3, 4 or 5. At last, the prediction value of the clock bias can be calculated based on the forecasted results of the trend term, periodic term and random term.

32.5.3 Results and Discussion

The prediction residuals of the proposed model and IGU-P solutions are shown in Fig. 32.3. The classified statistics results of the prediction precision are given in Table 32.2.

From Fig. 32.3 and Table 32.2, it can be concluded that:

1. The prediction error curves of eight GPS satellites converge within 5 ns, and the prediction precision is within 3 ns RMS based on the proposed model.
2. Figure 32.3 shows that the 3- and 6-h-ahead prediction consequences are very similar between the proposed model and IGU-P products, but the IGU-P starts to diverge afterwards.

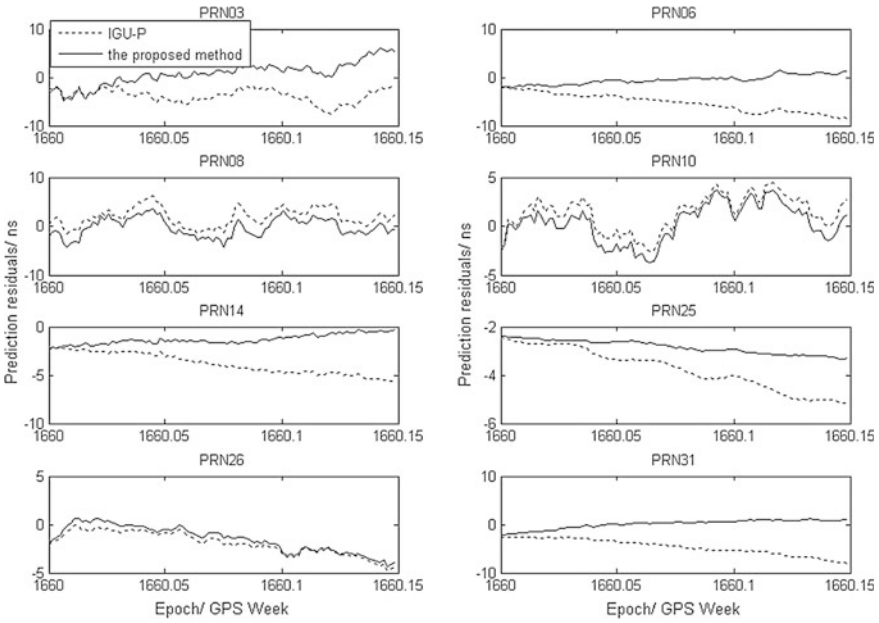

Fig. 32.3 24-h prediction residuals of the IGU-P products and proposed model

Table 32.2 Statistics of the prediction precision for the eight GPS clocks based on the proposed model and IGU-P

RMS	Clock type	3 h		6 h		12 h		24 h	
(ns)		A	B	A	B	A	B	A	B
PRN03	IIA Cs	3.32	2.89	3.11	2.72	3.81	2.00	4.05	2.56
PRN06	IIA Rb	2.47	1.79	3.08	1.71	3.77	1.33	5.65	1.06
PRN08	IIA Cs	1.13	1.10	2.04	2.03	2.58	2.23	2.67	1.88
PRN10	IIA Cs	1.73	1.19	1.86	0.99	1.64	1.62	2.32	2.00
PRN14	IIR Rb	2.33	2.03	2.46	1.85	2.95	1.70	4.02	1.41
PRN25	IIF Rb	2.62	2.46	2.69	2.51	3.05	2.60	3.89	2.87
PRN26	IIA Rb	1.10	0.97	0.88	0.73	1.08	0.75	2.34	2.07
PRN31	IIR-M Rb	2.64	1.78	2.69	1.40	3.31	1.01	4.97	0.93

A IGU-P, *B* the proposed strategy

3. In Table 32.2, the results demonstrate that the 3- and 6-h prediction accuracy of the proposed model is comparable with that of the IGU-P products. However, the proposed model can give better performance than the IGU-P solutions for the 12- and 24-h-ahead prediction, and the most significant improvement is 81.3 % as far as the RMS is concerned. In addition, it can be seen that the improvement percentage of PRN10 and PRN26 is smaller than that of the other

satellites. Explanation why the proposed strategy improves noticeably or slightly for different satellite clocks needs to be investigated.

It takes the proposed method less than eight minutes to train the LS-SVM model and predict the clock bias, which can make the algorithm available for real-time prediction of clock bias.

32.6 Conclusion

Considering that the satellite clock bias is made up of the trend part, periodic item and random component, this study develops an integrated model combing the polynomial model adding several cyclic terms and LS-SVM for clock bias prediction. Besides the trend term, the proposed prediction strategy comprises a few cyclic terms to overcome the periodic effects, as well as a random corrected term in order to capture stochastic variation behavior, which is not sufficiently described by conventional models. The trend item and periodic item are modeled by employing the polynomial model adding several cyclic terms, while the random item is modeled by the LS-SVM algorithm that can capture linear or nonlinear patterns existing in the stochastic series. Additionally, the grid search methodology together cross-validation is used to find the optimal parameters of LS-SVM so as to improve the prediction accuracy.

The proposed prediction scheme fully takes into account the physical characteristics of atomic clocks in space, which results in higher precision than conventional prediction solutions available for 24-h-ahead prediction. The simulation results show that the proposed method outperforms the IGU-P solutions in terms of prediction precision on a daily basis indicating that, specifically, the stochastic activities from satellite clocks can be captured. Also, it is worth mentioning that the proposed prediction model is remarkably more stable more than the IGU-P clock model.

It should be noted that the performance of the proposed method is affected by the LS-SVM parameters at a certain extent. Thus, how to select the optimal parameters of LS-SVM needs to be studied on furthermore.

References

1. Broederbauer V, Opize M, Weber R (2007) Automated quasi-realtime prediction of GNSS clock corrections. Geoinformation 95:53–58
2. Zheng ZY, Chen YQ, Lu XS (2009) An improved grey model and its application research on the prediction of real-time GPS satellite clock errors. Chin Astron Astrophy 33:72–89
3. Heo YJ, Cho J, Heo MB (2010) Improving prediction accuracy of GPS satellite clock with periodic variation behaviour. Meas Sci Technol 21:531–539

4. Huang GW, Zhang Q, Xu GC (2014) Real-time clock offset prediction with an improved model. GPS Solutions 18:95–104
5. Xu B, Wang Y, Yang XH (2013) A hybrid model for navigation satellite clock error prediction. Comput Intell 465:307–316
6. Li XY, Dong XR, Zheng K et al (2013) Research of satellite clock error prediction based on RBF neural network and ARMA model. Lec Notes Electr Eng 245:325–334
7. Senior KL, Ray JR, Beard RL (2008) Characterization of periodic variations in the GPS satellite clocks. GPS Solutions 12:211–225
8. Suykens J, Vandewalle J (1999) Least squares support vector machine classifiers. Neural Process Lett 19:293–300
9. Duan K, Keerthi SS, Poo AN (2003) Evaluation of simple performance measures for tuning SVM hyperparameters. Neurocomputing 51:41–49

Chapter 33
Preliminary Performance Evaluation of Beidou Spaceborne Atomic Clocks

Peiyuan Zhou, Lan Du, Zhongkai Zhang, Yu Lu and Yueyong Lian

Abstract The performance of spaceborne atomic clock is one of the key factors that impact the accuracy of satellite navigation system positioning, navigation and timing (PNT). With the officially operation of Chinese Beidou satellite navigation system at the end of 2012, it is extremely necessary to conduct a comprehensive evaluation of the performance of the spaceborne atomic clocks. Firstly, this paper introduces two performance evaluation indices of spaceborne atomic clock and their calculation methods, namely the frequency stability and short-term prediction precision. Then, based on the measured data of Beidou satellite clock error, we make an analysis of the performance indices of the atomic clock, and the results was compared with the GPS spaceborne rubidium clocks, and thus obtained some useful conclusions, which has important significance to improve Beidou satellite navigation system.

Keywords Spaceborne atomic clock · Frequency stability · Short-term prediction

33.1 Introduction

In satellite navigation and positioning applications, the measurement of exact location is actually accurate time measurement. Without high-precision frequency standards, it is impossible to achieve high-precision positioning, navigation and timing (PNT) service [1]. As a core part of the navigation satellite payload, atomic clocks provide space time benchmark for the forming of satellite navigation signals and ranging measurements. Obviously, its performance directly determines the accuracy of positioning, navigation and timing of the satellite navigation system.

P. Zhou · L. Du (✉) · Z. Zhang · Y. Lu · Y. Lian
College of Navigation and Aerospace Engineering, Information Engineering University, Zhengzhou, Henan Province, China
e-mail: lan.du09@gmail.com; 953304030@qq.com

J. Sun et al. (eds.), *China Satellite Navigation Conference (CSNC) 2014 Proceedings: Volume III*, Lecture Notes in Electrical Engineering 305,
DOI: 10.1007/978-3-642-54740-9_33,

Rubidium atomic clock can meet the accuracy requirements of satellite navigation systems, plus additional advantages such as low price, small size, low mass (less than cesium clock), high short-term stability and many others, have been widely used in satellite navigation systems, such as China's Beidou satellite navigation system, European Galileo system and the latest satellite blocks of GPS.

The performance of spaceborne atomic clock is affected by multiple factors, such as space environment, data sampling interval and noise levels. Therefore it is necessary for satellite navigation systems to evaluate the performance of its onboard atomic clocks during orbit and to check whether the clock's actual operating conditions are consistent with the design specifications and its impact on PNT services. In recent years, scholars had done a lot of work about performance evaluation of atomic clock [2–8]. However, these efforts are mainly directed against the GPS spaceborne atomic clock, and there is little research on other satellite navigation systems, especially on the Beidou spaceborne atomic clocks. By the end of 2012, China's Beidou regional navigation system went into operation making China the world's third country to own an independent satellite navigation system; it is of great importance to assess the performance of the Beidou spaceborne atomic clock.

Main indicators used for the performance evaluation of atomic clocks are frequency stability and short-term prediction accuracy. Based on mature GPS atomic clock evaluation methods and taking the characteristics of Beidou onboard rubidium clock into account, this paper calculates the performance of Beidou atomic clocks using measured clock bias. What's more, similar indicators of running GPS spaceborne rubidium clocks (Block IIA, Block II R, Block II RM and Block II F) and Beidou rubidium clocks were compared to arrive at some meaningful conclusions.

33.2 Atomic Clock Performance Evaluation Methods

In order to have a comprehensive understanding of the Beidou spaceborne atomic clock, taking into account the characteristics of rubidium clocks, this paper selects frequency stability (overlapping Hadamard variance) and short-term forecast accuracy of quadratic polynomial to assess rubidium clocks. Following are brief introductions, definitions and calculation methods of these indicators.

33.2.1 Frequency Stability

Frequency stability of navigation satellite atomic clocks refers to random fluctuations of the sampling frequency value due to internal noise; it can be used to describe the average random frequency variation [8]. Time-domain variance is often used to characterize frequency stability.

There are many commonly used time domain variance, among which overlapping Hadamard variance can make full use of known data through the formation of all possible three sampling, which can largely improve the confidence of frequency stability estimation. Furthermore, it is not subjected to frequency drift, so it can be used in the stability evaluation of rubidium clocks [8–10].

For clock bias series (namely phase data) $\{x_i,\ i = 1,\ 2,\ \ldots,\ N\}$, having sampling interval τ_0 and length N, its overlapping Hadamard variance can be calculated by the following equation [9]:

$$H\sigma_y^2(\tau) = \frac{1}{6\tau^2(N-3m)} \sum_{i=1}^{N-3m} \left[x_{i+3m} - 3x_{i+2m} + 3x_{i+m} - x_i\right]^2 \tag{33.1}$$

where, $\tau = m\tau_0$ and $1 \le m \le \mathrm{int}\left(\frac{N-1}{3}\right)$, and m is the averaging factor.

For corresponding frequency series $\{y_i,\ i = 1,\ 2,\ \ldots,\ M\}$, having sampling interval τ_0 and length M, $M = N - 1$. So overlapping Hadamard variance based on frequency data can be calculated by the following equation:

$$H\sigma_y^2(\tau) = \frac{1}{6\tau^2(M-3m+1)} \sum_{j=1}^{M-3m+1} \sum_{i=j}^{j+m-1} \left[y_{i+2m} - 2y_{i+m} + y_i\right]^2 \tag{33.2}$$

where, the averaging factor m ranges are $1 \le m \le \mathrm{int}\left(\frac{M}{3}\right)$.

33.2.2 Short-Term Prediction Accuracy

Prediction accuracy satellite clock bias depends mainly on the following aspects: satellite clock frequency stability, the length of time forecasting, prediction models and the quality of observational data [1, 8]. Among them, the satellite clock frequency stability reflects its forecasting capability; clock error prediction model should also consider the complexity of the prediction model parameters. Polynomial model is the most commonly used model in clock error prediction, and its forecasting accuracy is sufficient in short-term ranges [11], its equation:

$$x_i = a_0 + a_1 t_i + a_2 t_i^2 + \cdots + a_m t_m^m + e_i \tag{33.3}$$

where, $a_0,\ a_1,\ \ldots, a_m$ are fitting parameters, m is polynomial orders determined by atomic clock types, and e_i is modeling error.

Rearranging Eq. (33.3) in matrix form, we get:

$$\boldsymbol{X} = \boldsymbol{Ha} + \boldsymbol{e} \tag{33.4}$$

where, $\boldsymbol{X}$ are n-dimensional observation vector, $\boldsymbol{a}$ are $m+1$-dimensional unknown parameters vector, $\boldsymbol{e}$ are n-dimensional error vector, and $\boldsymbol{H}$ are $n \times (m+1)$-dimensional design matrix:

$$\boldsymbol{H} = \begin{bmatrix} 1 & t_1 & \cdots & t_1^m \\ 1 & t_2 & \cdots & t_2^m \\ \vdots & \vdots & \vdots & \vdots \\ 1 & t_n & \cdots & t_n^m \end{bmatrix} \tag{33.5}$$

In order to resist the effect of gross error in the clock bias observation sequence, we introduced the method of resistance estimation [12]. Then, solution to the unknown parameters vector is:

$$\hat{\boldsymbol{a}} = \left(\boldsymbol{H}^T \bar{\boldsymbol{P}} \boldsymbol{H}\right)^{-1} \boldsymbol{H}^T \bar{\boldsymbol{P}} \boldsymbol{X} \tag{33.6}$$

The corresponding variance factors are:

$$\sigma_0^2 = \frac{\boldsymbol{V}^T \bar{\boldsymbol{P}} \boldsymbol{V}}{n - m - s} \tag{33.7}$$

where s refers to the number of $\bar{p}_i = 0$, $\bar{\boldsymbol{P}}$ is equivalent weight matrix, its elements can be calculated as following equation:

$$\bar{p}_i = \begin{cases} p_i & |v_i/\sigma_{v_i}| \le k_0 \\ p_i \frac{k_0}{|v_i/\sigma_{v_i}|} \left(\frac{k_1 - |v_i/\sigma_{v_i}|}{k_1 - k_0} \right)^2 & k_0 < |v_i/\sigma_{vi}| \le k_1 \\ 0 & |v_i/\sigma_{v_i}| > k_1 \end{cases} \tag{33.8}$$

where $k_0 \in (1.0, 2.0)$and $k_1 \in (2.5, 4.5)$.

After calculating of the unknown parameters $\hat{\mathbf{a}}$, prediction value $\hat{x}_{t+L}$ in epoch (t+L) using polynomial prediction model can be expressed as:

$$\hat{x}_{t+L} = \boldsymbol{H}_{t+L}^T \hat{\boldsymbol{a}} \tag{33.9}$$

where, t are the start epoch of predicting, and L are the number of prediction epochs, and

$$\hat{\boldsymbol{a}} = \begin{bmatrix} \hat{a}_0 & \hat{a}_1 & \cdots & \hat{a}_m \end{bmatrix}^T,$$
$$\boldsymbol{H}_{t+L}^T = \begin{bmatrix} 1 & t_{t+L} & t_{t+L}^2 & \cdots & t_{t+L}^m \end{bmatrix}.$$

Root mean square error of prediction can be calculated as:

$$RMS = \sqrt{\frac{\sum_{i=1}^{L} (\hat{x}_{t+i} - x_{t+i})^2}{L}} \tag{33.10}$$

where, observation data x_{t+i} is used for the assessing of RMS.

33.3 Analysis of Results

Currently, satellite clock bias (phase) observational data is provided directly by satellite navigation system, therefore, the work of this paper is based on the satellite clock bias data. Our work was conducted according to the following steps.

1. Data acquisition and preprocessing. Mainly includes the detection and elimination of gross error, data interpolation and interval equalization, etc.
2. Calculating overlapping Hadamard variance based on the satellite clock bias sequence to get the frequency stability indicators.
3. Using polynomial fitting by the data of a day, with robust estimation method to solve the clock bias model parameters, then short-term clock bias prediction was conducted using the model, and the root mean square error was calculated.
4. After obtaining frequency drift, frequency stability and short-term forecast accuracy indicators from the above step, comprehensive analysis and evaluation was conducted, as well as comparison of relevant indicators with GPS spaceborne rubidium clocks.
5. Conclusions were drawn about the performance of spaceborne atomic clocks.

Due to regional restrictions of ground tracking network, the clock bias data of Beidou MEO and IGSO satellites had long intermittent dead time. In order to get more accurate and objective performance evaluation of Beidou spaceborne atomic clocks, atomic clocks in the Beidou GEO satellites was selected only, namely G01, G02, G03, G05 of data length 121 days (MJD 56382 to MJD 56503), and G04 of data length 60 days (MJD 56442 to MJD 53503), having sampling interval of 5 min.

In addition, in order to have further analysis of the present domestic spaceborne performance indicators of the rubidium clocks, this article also calculate same performance indicators of GPS using IGS clock bias data of data length 120 days (MJD 56338 to 56458), having sampling interval of 5 min. Rubidium standard of four block was chose (Block type IIA, Block II R, R-M Block II and Block II F), GPS rubidium standard information was shown as in Table 33.1 [13].

Table 33.1 Information of GPS spaceborne rubidium clocks

Satellite number	Satellite blocks	Launch time(year)
PRN 06	Block IIA	1994
PRN 02	Block IIR	2004
PRN 05	Block IIR-M	2009
PRN 01	Block IIF	2011

33.3.1 Analysis of Frequency Stability

This paper uses the overlapping Hadamard variance for spaceborne rubidium standard frequency stability analysis, using the same algorithm to calculate the frequency stability of Beidou and GPS atomic clocks at the same time. With limited space, only the results of Beidou GEO 01 and GPS PRN 02 (Block IIR) were shown in this paper (Figs. 33.1 and 33.2).

Frequency stability indicators of the rest of 7 satellites was obtained using the same processing method, results was listed, as shown in Table 33.2 and Fig. 33.3

As can be seen from the results above, three of five Beidou spaceborne rubidium clocks had stability indicators order of 10E−14 at day average intervals, while the rest of two Beidou satellites had stability indicators order of 10E−13 at day average intervals. Meanwhile two of four GPS spaceborne rubidium clocks had stability indicators order of 10E−15 at day average intervals, while the rest of two GPS satellites had stability indicators order of 10E−14at day average intervals in which Block IIF had the highest frequency stability. In addition, it can be seen from Fig. 33.3 that all GPS onboard rubidium clock stability indicators are better than Beidou rubidium clock.

33.3.2 Analysis of Short-Term Prediction Accuracy

In order to evaluate the performance of atomic clocks, this paper calculates the accuracy of the short-term prediction based on polynomial model, using the robust estimation method to get the fitting parameters. Firstly, the paper solves polynomial model with one-day long clock bias data, then conduct satellite clock bias prediction of 24 h, finally calculates the RMS of prediction values and true values. Taking into account the performance characteristics of rubidium atomic clocks, a quadratic polynomial model was chosen to fit the known clock bias and get the quadratic polynomial coefficients a1, a2 and a3 (i.e., the phase, frequency offset and drift) as shown in Table 33.3.

As can be seen from the above table, GPS rubidium clock performance is better than the Beidou rubidium clock in terms of clock frequency drift. With the above clock bias model, one day long clock bias prediction was conducted as well as the calculation of 24 h RMS. Results was listed as shown in Table 33.4, and its plot shown in Fig. 33.4.

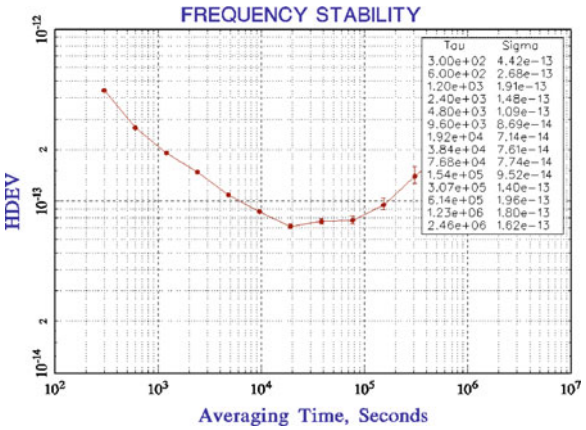

Fig. 33.1 Frequency stability of Beidou satellite GEO 01

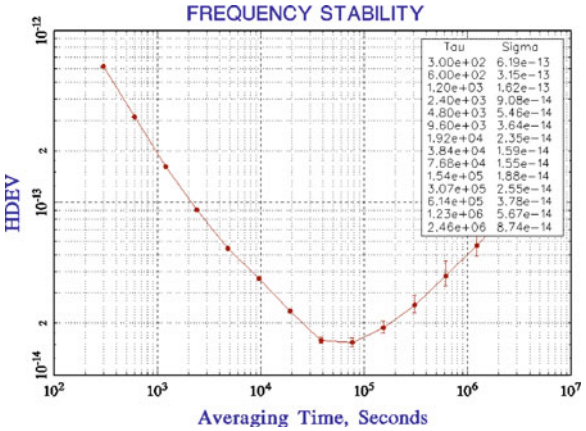

Fig. 33.2 Frequency stability of GPS satellite PRN 02

Table 33.2 Results of spaceborne atomic clocks frequency stability analysis

Satellite number	Frequency stability of one day (10E−14)
BDS G01	7.9271
BDS G02	21.1010
BDS G03	8.4013
BDS G04	6.5497
BDS G05	35.9670
PRN 01	0.4705
PRN 02	1.5661
PRN 05	0.8950
PRN 06	5.0524

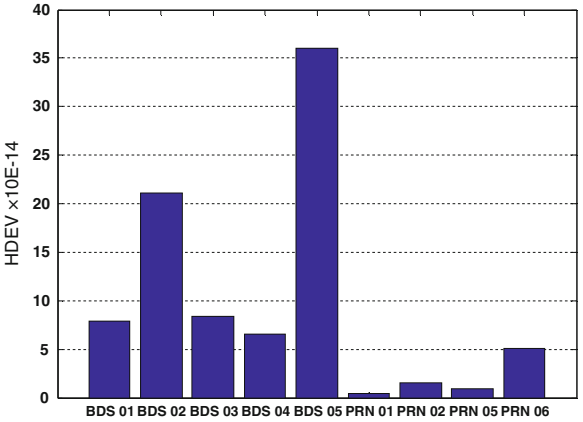

Fig. 33.3 The results of spaceborne atomic clocks frequency stability analysis

Table 33.3 Coefficients of quadratic polynomial fitting of spaceborne atomic clocks

Satellite number	Phase (10E−5)	Frequency offset (10E−5)	Frequency drift(10E−7)
BDS G01	−0.00008	0.1799	−0.0698
BDS G02	−0.00024	−0.3641	0.3749
BDS G03	−0.00001	0.0386	0.0543
BDS G04	2.99194	−0.1286	−0.1386
BDS G05	15.08760	−0.4867	0.0339
GPS PRN 01	0.05475	0.0234	0.0121
GPS PRN 02	41.85676	0.0134	0.0066
GPS PRN 05	−38.37740	−0.0154	0.0006
GPS PRN 06	34.66907	−0.1256	−0.0166

Table 33.4 Short-term prediction accuracy of spaceborne atomic clocks

Satellite number	RMS(10E−9s)
BDS G01	4.2131
BDS G02	52.033
BDS G03	4.2655
BDS G04	2.9605
BDS G05	15.146
GPS PRN 01	0.86915
GPS PRN 02	0.48951
GPS PRN 05	0.4258
GPS PRN 06	1.3109

Conclusions can be drawn from the above results that the short-term prediction accuracy of GPS is better than Beidou short-term prediction accuracy; and worst short-term prediction accuracy of Beidou is 5.2033 ns, while the worst prediction

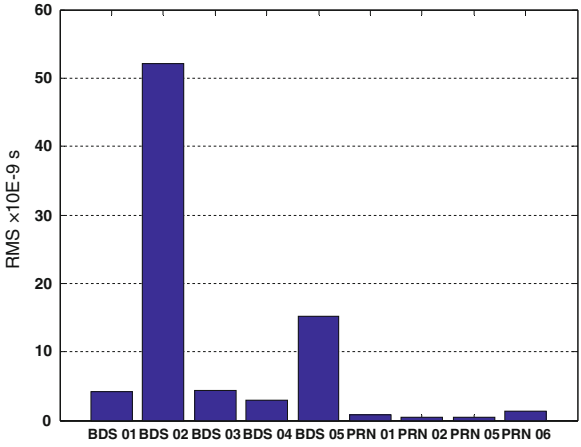

Fig. 33.4 Results of short-term prediction accuracy of spaceborne atomic clocks

accuracy of GPS is 0.04258 ns. The basic law of prediction accuracy is consistent with atomic clock's frequency stability. Therefore, when using the same data length, the same calculation method and the same sample interval, the short-term prediction accuracy of the atomic clock can be used to characterize the stability indicators.

33.4 Conclusions

In GEO satellites of Beidou navigation systems, three of five (G01, G03, G05) have frequency stability in magnitude of 10E−14, the other two have frequency stability in magnitude of 10E−13; while the frequency stability of GPS is basically in magnitude of 10E−14, and some newest spaceborne clocks reached a magnitude of 10E−15. On the other hand, variation of the short-term prediction accuracy has a similar law, but the prediction accuracy of Beidou has been able to meet most PNT application requirements. Therefore, we can draw a preliminary conclusion that the performance of the Beidou Rubidium atomic clocks is equal to the initial blocks of GPS Rubidium atomic clocks, but there is an obvious gap compared with the newest block Rubidium clocks of GPS.

It should be noted that, the analysis of GPS clocks are based on clock bias data provided by IGS having high precision, while analysis of Beidou clocks are based on untreated measured clock bias data, although we have introduced robust estimation method to improve the precision of evaluation, results may be affected by various unknown errors; in addition, GPS satellites are MEO satellites and Beidou is GEO satellites, having orbit at different heights, its space environment is also inconsistent. Therefore, the next step will be to study the performance of spaceborne atomic clock with high precision post-processing data as well as the performance evaluation method of Beidou MEO and IGSO satellites.

Acknowledgments This work is supported by project of National Natural Science Foundation of China (41174025, 41174026, and 41174027).

References

1. Zheng Z, Lu X, Chen Y (2008) Improved grey model and application in real-time GPS satellite clock bias prediction. In: Fourth international conference on natural computation, 2008. ICNC'08, vol 2. IEEE, pp 419–423 (Oct)
2. Riley Jr WK (1992) Rubidium atomic frequency standards for GPS block 2R. In: ESA special publication vol 340, pp 231–238 (Jun)
3. Senior KL, Ray JR, Beard RL (2008) Characterization of periodic variations in the GPS satellite clocks. GPS Solutions 12(3):211–225
4. Epstein M, Freed G, Rajan J (2004) GPS IIR rubidium clocks: in-orbit performance aspects. In: ITT Aerospace/Communications Div Clifton NJ
5. Waller P, Gonzalez F, Hahn J, Binda S, Piriz R, Hidalgo I, Cerretto G (2008) In-orbit performance assessment of GIOVE clocks. In: European Space Agency, Noordwijk (Netherlands)
6. Oaks J, Senior K, Largay M, Beard R, Buisson J (2005) NRL analysis of GPS on-orbit clocks. In: Frequency control symposium and exposition, 2005. Proceedings of the 2005 IEEE international. IEEE, pp 12–18 (Aug)
7. Jia XL, Feng LP, Mao Y, Yang HY (2010) Performance evaluation of GPS on-board clock. J Time Freq 2:007
8. Guo H (2006) Study on the analysis theories and algorithms of the time and frequency characterization for atomic clocks of navigation satellites. Information Engineering University
9. Riley WJ (2007) User manual: stable32 frequency stability analysis version 1.5. 0. Hamilton technical services, Beaufort, SC
10. Hutsell ST, Reid WG, Crum JD, Mobbs HS, Buisson JA (1996) Operational use of the Hadamard variance in GPS. Naval Observatory Alternate Master Clock Schriever Afb Co
11. Senior K (2004 April) Report from the IGS clock products working group. In: 16th meeting of the CCTF, vol 1
12. El Ghaoui L, Lebret H (1997) Robust solutions to least-squares problems with uncertain data. SIAM J Matrix Anal Appl 18(4):1035–1064
13. http://glonass-iac.ru/en/GPS/

Chapter 34
Real-Time Atomic Clock Anomaly Detection and Processing Based on Generalized Likelihood Ratio Test

Peiyuan Zhou, Lan Du, Zhongkai Zhang and Yu Lu

Abstract As a core part of the navigation satellite payload, the performance of spaceborne atomic clocks directly decides the accuracy of GNSS Positioning Navigation Timing (PNT) service. Through continuously monitoring of clock bias, fast anomaly detection and processing can be realized, and thus, ensuring that satellite navigation system can meet the requirements of various end users. The paper combines principles of Generalized Likelihood Ratio Test (GLRT) with polynomial clock model based on clock types, and then a new method of real-time atomic clock anomaly detection and processing was put forward: firstly, anomaly detection was carried out based on the real-time GLRT detector, then short-term clock bias forecast and extrapolation was conducted by using the polynomial clock model, and based on steps above, eliminate the anomaly points and replace it with extrapolation values. Simulation examples was given based on GPS satellite clock bias provided by IGS, the results show that the method can detect and handle atomic anomalies fast and effectively (especially abnormal frequency jumps), and it can guarantee the integrity of clock bias.

Keywords Atomic clock anomaly detection · GLRT detector · Clock bias model

34.1 Introduction

Atomic clock is one of the key components of many complex systems, such as telecommunications network systems, power systems, and global navigation satellite systems [1]. Atomic clock, having excellent metrological characteristics, is the basis for these applications. But due to power outages, equipment failures,

P. Zhou · L. Du (✉) · Z. Zhang · Y. Lu
College of Navigation and Aerospace Engineering, Information Engineering University, Zhengzhou, Henan Province, China
e-mail: lan.du09@gmail.com; 953304030@qq.com

J. Sun et al. (eds.), *China Satellite Navigation Conference (CSNC) 2014 Proceedings: Volume III*, Lecture Notes in Electrical Engineering 305,
DOI: 10.1007/978-3-642-54740-9_34,

and external disturbances, in the long-term operation lifespan of atomic frequency standard, there are various data anomalies such as frequency drift, phase transitions and frequency hopping, etc. [2]. Therefore, real-time monitoring of atomic clocks should be conducted as well as real-time anomaly detection and treatment strategies, ensuring that a warning signal was sent to the end user in a short time when anomaly happens.

In recent years, scholars had done a lot of meaningful work about atomic clock anomaly analysis and processing, and various effective atomic clock anomaly detection algorithms had been put forward, such as least-squares method, Allan variance method, robust estimation based on the median (MAD), Kalman filter method and maximum likelihood ratio test method [3–8], etc. While these algorithms have their own advantages, these methods have some deficiencies in real-time situations. The least squares method, Allan variance method and robust estimation based on the median (MAD) method is mainly used for data post-processing, Kalman filter, maximum likelihood method is complex in parameter selection. In order to ensure real-time navigation and positioning needs of end users, the strategies of real-time atomic clock anomaly identification, interpretation and processing requires further study.

Studies have shown that atomic clock frequency data obey Gaussian distribution, the mean and variance of which is time-dependent [5]. Therefore, based on atomic clock frequency characteristics, combined with the generalized maximum likelihood estimation and the polynomial clock bias model, we propose a convenient and reliable real-time atomic clocks anomaly detection and processing algorithm. Simulation results show that the algorithm can efficiently detect and process clock anomalies, achieving satisfying results.

34.2 Real-Time Atomic Clock Anomaly Detecting and Processing Algorithm Based on Generalized Likelihood Ratio Test

In order to achieve real-time detection and processing of abnormal atomic clocks, this paper put forward some improvements to the original generalized likelihood ratio test, namely, we propose a new threshold selection method. Then we use this method to detect anomalies, while use real-time clock error prediction model to calculate the estimated value of the anomalies for repairing.

34.2.1 Generalized Likelihood Ratio Test (GLRT)

Generalized likelihood ratio test is a quick and effective way to detect changes in the mean and variance. The studies of reference [5] have shown that atomic clock

frequency data obey Gaussian distribution under normal operating mode. Thus, the GLRT method can be used in real-time anomaly detection of atomic clocks.

34.2.1.1 Basic Principles of GLRT

Based on the premise that atomic clock frequency data obey Gaussian distribution, we can design two assumptions H_0 and H_1 to describe changes in their model parameters. H_0 (Null hypothesis) assumes that sample data obey Gaussian probability density function; H_1 (alternative hypothesis) assumes that the mean and variance of the sample data has been changed. These assumptions can be described by the following equation:

$$\begin{cases} H_0 : y[n] : N(\mu_0, \sigma_0), & n = 0, \ldots, N-1 \\ H_1 : \begin{cases} y[n] : N(\mu_0, \sigma_0), & n = 0, \ldots, n_0 - 1 \\ y[n] : N(\mu_1, \sigma_1), & n = n_0, \ldots, N-1 \end{cases} \end{cases} \tag{34.1}$$

Where, n_0 refers to the unknown transition point to be estimated, N is the length of sample data, μ_0, μ_1, σ_0, σ_1 is model parameters in assumption H_0 and H_1 respectively.

In order to judge above assumptions, we introduce: $\hat{\mu}_{0\_H_0}$ and $\hat{\sigma}_{0\_H_0}$ as maximum likelihood estimation value of model parameters in null hypothesis; while $\hat{\mu}_{0\_H_1}$, $\hat{\sigma}_{0\_H_1}$, $\hat{\mu}_{1\_H_1}$ and $\hat{\sigma}_{1\_H_1}$ as maximum likelihood estimation value of model parameters under the alternative hypothesis. Thus, the GLRT method's criterion used for judging the alternative hypothesis can be described by the following equation (detailed derivation see ref. (34.4)):

$$T(Y) = \log(L_G(y)) = N \log\left(\frac{\hat{\sigma}_{0\_H_0}}{\hat{\sigma}_{1\_H_1}}\right) - \hat{n}_0 \log\left(\frac{\hat{\sigma}_{0\_H_1}}{\hat{\sigma}_{1\_H_1}}\right) > \gamma \tag{34.2}$$

Where N is the length of sample, $\hat{n}_0$ is the estimated point of anomaly, and γ is the threshold value.

Thus, when taken γ as a given value, the anomaly detection can be carried out.

34.2.1.2 Improvement in the Selection of Threshold Value

In the computing process of GLRT method, the selection of threshold value is the crux of the algorithm. Common method to get a threshold value is calculating the ROC curve [5, 9], in which the probability of correct detection (PD) and probability of false alarm (PFA, assuming choose assumptions established) have to be calculated. Although such a method can be used to determine a reliable and accurate threshold, it requires Monte Carlo experiments to select the threshold which means a large amount of calculation. So this method is not suitable for real-time anomaly detection. Therefore, this paper proposes a new method to quickly determine the value of threshold, the steps are:

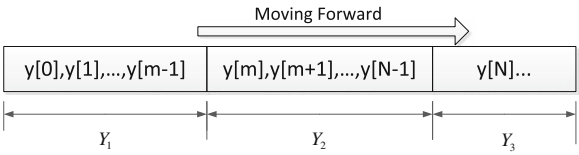

Fig. 34.1 Diagram of data structure

Step 1: Segment of sample data. Normal known data is divided into three parts, Y_1, Y_1 and Y_3, and Y_3 is assumed to be "unknown" data, the data structure is shown in Fig. 34.1.

As can be seen from the above diagram, we know that: Y_1 and Y_2 obeys the same Gaussian distribution $N(\mu_0, \sigma_0)$, an after adding unknown data $y[N]$ in the known series Y_2, if $y[N]$ is a normal point, Y_2 still obey $N(\mu_0, \sigma_0)$, or Y_2 will obey $N(\mu_1, \sigma_1)$.

Step 2: Carried out GLRT detection process to get the reasonable ranges of threshold in no abnormal situations. Assuming that anomaly point $\hat{n}_0 = m$, one can calculate the T(Y) value, the value obtained at this time should be within the threshold range. Continue sliding window and after conducting detection process in the whole Y_3 series, we get a T(Y) sequence. These values are all within the threshold range, so threshold value can be set as:

$$\gamma = \max(T(Y)) \tag{34.3}$$

Select Y_3 series for getting the threshold (to train the GLRT detector), when it is long enough, it can better take into account normal fluctuations in the sequence, avoiding misjudge normal fluctuations as "anomaly."

34.2.2 Real-Time Clock Bias Model

In order to timely detect and process abnormal atomic clocks so that it does not affect the overall satellite navigation system service, fast treatment must be carried out after removing the anomalies. Since normal and known sequences are available, it can be used to create sophisticated clock error model, and then high precision prediction value of outliers can be calculated for real-time users.

There are many common atomic clock bias models, such as polynomial model, gray system model, Kalman filter model, etc. [10]. Taking the complexity and computational time of these algorithms into account, we use the most simple and highly accurate short-term forecasting polynomial model to fit the known data. Frequency drift characteristics of different onboard atomic clocks vary, so for spaceborne cesium and rubidium clocks polynomial model can be expressed respectively as:

$$X = \begin{cases} a + bt + \varepsilon(t); & Cs\ Clock \\ a + bt + ct^2 + \varepsilon(t); & Rb\ Clock \end{cases} \tag{34.4}$$

Where, a, b and c are unknown polynomial parameters of the model, $\varepsilon(t)$ is model errors.

Solved polynomial model parameters by least squares method, and then use the model to predict. It should be noted that atomic clocks anomaly detecting process are often based on frequency data, while the atomic clock bias (i.e. phase) data is used for the prediction, so there must be a conversion between frequency data and phase data.

34.2.3 Algorithm Description

Based on the above-mentioned method, we designed real-time atomic clock anomaly detection and processing algorithm based on GLRT detector and polynomial clock bias model. The main steps are as follows:

Step 1: Data interception. Getting normal clock bias data X from historical sequence and its corresponding frequency sequence Y;
Step 2: Determine the threshold. Use GLRT detector to calculate T(Y) sequence using the known frequency sequence, set the maximum T(Y) as threshold;
Step 3: Anomaly detection. After determining the threshold, we can start using GLRT detector to process unknown data points. For an unknown point, we get a T(Y) by GLRT detector. If T(Y) is smaller than threshold, continue moving the window; If not, use the clock bias sequence to establish polynomial model, get the estimated clock bias value and the corresponding clock frequency estimates of abnormal point, replace the original point, while sending anomaly warning to end-users;
Step 4: Sliding window. According to "one in one out" principle, delete the first point of the window, add an unknown point;
Step 5: Abnormal warning. Go back to step 1, repeat these steps, and record continuous warning; When the number of continuous warning exceeds N/5, it indicates the occurrence of persistent atomic clock frequency hopping, and then we need to re-select clock error sequence and frequency sequence;

In the process, attention should be paid to several points: (1) clock error just plays the role as the known sequence data to establish clock bias model; (2) conversion have to be made when a new point was added; (3) the threshold value have to be re-calculated when a new point was added;

34.3 Verification and Analysis of Cases

In common spaceborne atomic clocks anomalies, missing signal is due to the atomic clock completely malfunctioning, and frequency drift in most cases can be manually modeled to predict and correct. And simple onboard atomic clock phase

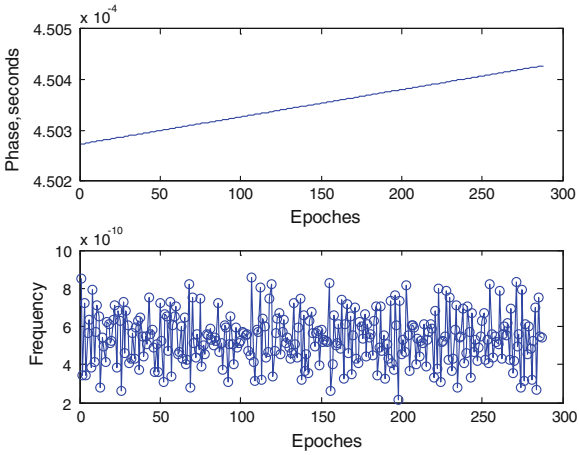

Fig. 34.2 Phase and frequency data of GPS PRN 02 space-borne atomic clock

transition occurs rarely, and it is indirectly reflection of frequency hopping [2]. This section will use the GPS post-processing clock bias data to simulate some cases, so that effectiveness of this algorithm can be verified.

34.3.1 Data Source

Frequency hopping is usually divided into transient and persistent hopping. In the case of real-time detection of anomalies, persistent accumulation of transient hopping can be seen as a persistent hopping. Therefore, two cases are designed based on GPS post-processing clock bias data: (1) single-point frequency hopping (2) consecutive multi-point frequency hopping. Then use anomaly detection and processing algorithm in this paper to verify the effectiveness of the algorithm.

Data used here are provided by IGS in 8 September 2013, having sampling period of 5 min, and GPS PRN 02 satellite was selected as a research object, the clock bias and frequency data are shown as in Fig. 34.2.

As can be seen from Fig. 34.2, the frequency of the data is basically obeying Gaussian distribution, which confirmed the precondition. Since the atomic clock abnormal events is of small probability, making it difficult to get clock bias data with anomalies, we use the method in [11] to simulate some human-made "anomalies", that is to superimpose abnormal values on the normal clock bias data to characterize the anomaly. This paper added artificial "temporary transition" in the frequency sequence at $n = 170$ and $n = 233, 234, 235$, the magnitude are about 2 and 3 times the magnitude of mean frequency of the sequence. The sequence after adding anomalies was shown in Fig. 34.3.

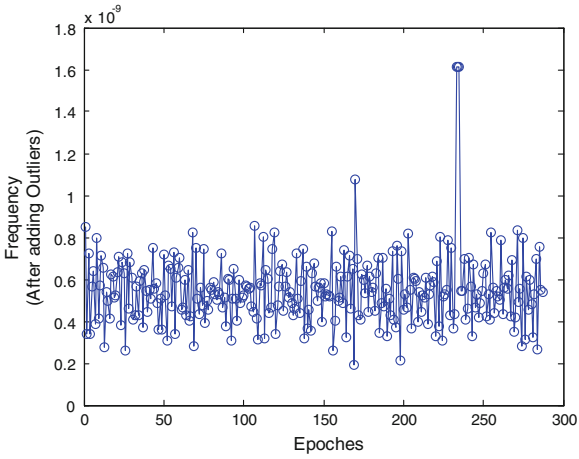

Fig. 34.3 Frequency data of GPS PRN 02 after adding anomalies

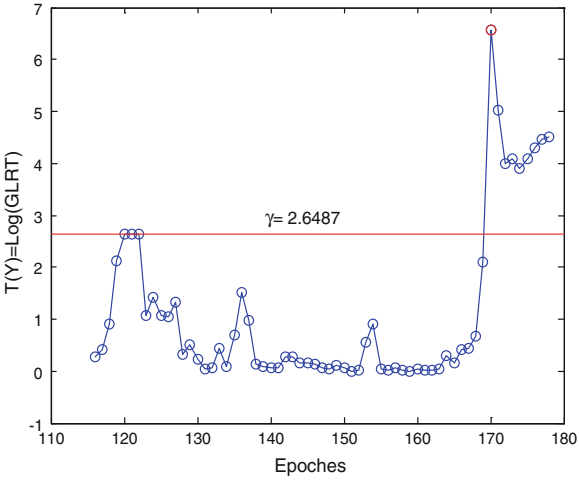

Fig. 34.4 First warning of anomaly

34.3.2 Analysis of Results

From history clock bias data without abnormal point, this paper capture a sequence of length 150, so that the length of the sliding window is 116 while sub windows Y_1 and Y_2 have length of 100 and 15 respectively (n_0=100), "unknown" sequence to be detected Y_3 have length of 30. Carry the GLRT detector in Y_3 to calculate T(Y) values. When the window slides 30 times, we take the maximum T(Y) value as the threshold, then $\gamma = 2.6487$.

After determining the threshold, continue sliding window, starting GLRT detector to assess unknown data, the process get $T(Y) = 6.572 > \gamma$ in the first abnormal point, therefore the point can be regard as frequency hopping point, then a warning was issued immediately, as shown in Fig. 34.4

Table 34.1 T(y) values of abnormal point and nearby points ($\gamma = 2.6487$)

Point	168	169	170	171	172
T(Y)	0.6677	2.111	**6.572**	5.033	3.996

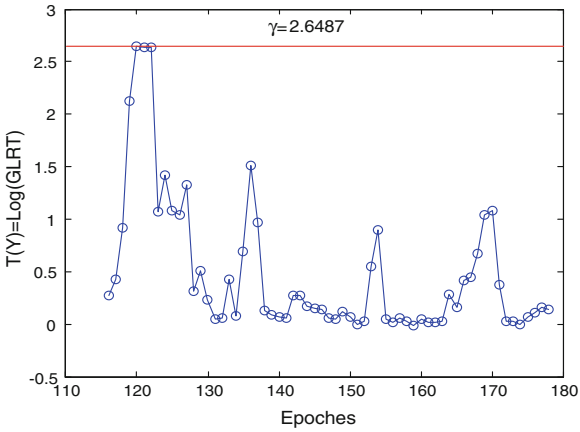

Fig. 34.5 T(Y) sequence after repairing the first abnormal point

For making comparisons, T(Y) value of several points near the abnormal point was calculated, as shown in Table 34.1.

As can be seen from Table 34.1, T(Y) value is far greater than near points in point Number 170 and points after anomaly occurred are greater than the threshold, too. Thus, conclusion can be reached that an abnormal point will affect distribution of the whole sequence. Therefore, the method of GLRT detector to have n_0 fixed while sliding data window is quite reasonable.

When processing the abnormal point, use the known clock bias sequence to establish polynomial model, and then extrapolate to get an estimate value of the abnormal point, and replace it with its estimated value for repairing. In order to verify whether the algorithm is effective or not, the GLRT detector was calculated in the sequence after repairing again. As can be seen in Fig. 34.5, and then there is no anomaly warning in point 170, it means that the anomaly has been processed successfully.

It can be seen from the above example that this algorithm is effective on positioning anomaly as well as dealing with atomic clock single frequency hopping. Furthermore, the polynomial model used for repairing abnormal point is also of high accuracy, the bias between estimated value and true value is 1.454e−11 s, the algorithm have effective control of repairing error.

After repairing of the first abnormal point, continue sliding window and conduct GLRT detection. T(y) values in this process was shown as in Fig. 34.6. As can be seen from Fig. 34.6, when detector find the second anomaly, the threshold is 2.6487, while $T(Y) = 16.69$ in the abnormal point. Therefore, the point is regarded as frequency hopping point and a warning signal is released.

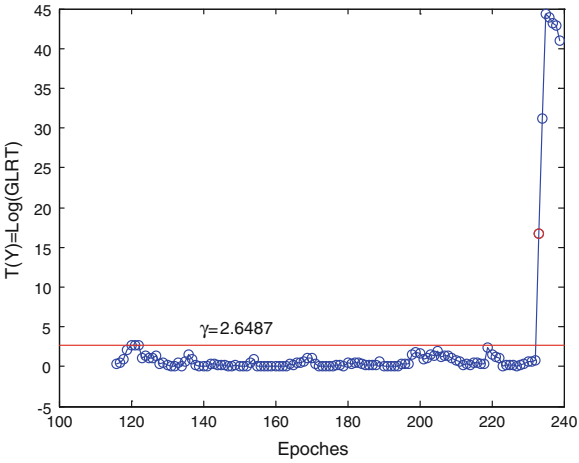

Fig. 34.6 Second warning of anomaly

Table 34.2 T(y) of abnormal points and nearby points ($\gamma = 2.6487$, the data in brackets are T(Y) values after repairing abnormal point)

Point	231	232	233	234	235
T(Y)	0.6466	0.735	**16.69** (0.7474)	**15.45** (1.093)	**4.00** (2.089)

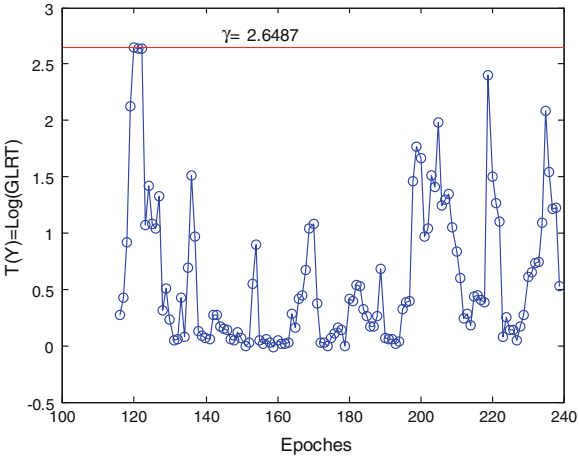

Fig. 34.7 T(y) sequence after repairing all abnormal points

Continue sliding window and detect unknown data, three continuous frequency hopping point can be detected. The average repairing bias of these abnormal points is 1.04e−10 s. Table 34.2 lists the T(Y) values before and after anomaly repairing. It can be seen from the table that our algorithm had detected three frequency hopping points and repair them effectively by polynomial model at sub-nanoseconds level (Fig. 34.7).

34.4 Conclusions

This paper presents real-time atomic clock anomaly detection and processing algorithm based on GLRT detector and high-precision clock bias model. Through simulation of two kinds of frequency hopping (single hop and multi continuous hop), it can be seen that the proposed algorithm can not only effectively detect common frequency hopping (temporary and permanent frequency hop), but also give timely warning and repair the abnormal point. The algorithm is simple and effective as well as high degree of automation, which is of significance for practical engineering application. The next step, we will try to improve this algorithm further, and apply it in real-time Beidou atomic clock anomaly detection and processing.

Acknowledgments This work is supported by project of National Natural Science Foundation of China (41174025, 41174026, and 41174027).

References

1. Morikawa T (2001) Spaceborne atomic clock. IEIC technical report. Institute of Electronics, Information and Communication Engineers, vol 101, no. 157, pp 75–81
2. Viðarsson L, Pullen S, Green G, Enge P (2001) Satellite autonomous integrity monitoring and its role in enhancing GPS user performance. In: Proceedings of the institute of navigation GPS, pp 690–702
3. Guo H (2006) Study on the analysis theories and algorithms of the time and frequency characterization for atomic clocks of navigation satellites. Information Engineering University
4. Huang Xin-ming G, Gang XWO (2011) A Real-time anomaly monitoring algorithm for satellite clock based on Kalman filter. J Astronaut Metrol Meas 5:003
5. Nunzi E, Galleani L, Tavella P, Carbone P (2007) Detection of anomalies in the behavior of atomic clocks. IEEE Trans Instrum Meas 56(2):523–528
6. Nunzi E, Carbone P (2008) Monitoring signal integrity of atomic clocks by means of the GLRT. Metrologia 45(6):S103
7. Galleani L, Tavella P (2005) Tracking nonstationarities in clock noises using the dynamic Allan variance. In: Proceedings of the 2005 IEEE international Frequency control symposium and exposition, IEEE, Aug 2005, pp 392–396
8. Weiss M, Shome P, Beard R (2010, November). On-board GPS clock monitoring for signal integrity. In Proceedings of the 42th annual precise time and time interval (PTTI) applications and planning meeting, Nov 2010
9. Nunzi E, D'Ippolito D (2009). A novel theoretical analysis of fault detection for atomic clock. In: advanced methods for uncertainty estimation in measurement. AMUEM 2009. IEEE international workshop on, IEEE, July, pp 85–88
10. Cui XQ, Jiao WH (2005) Grey system model for the satellite clock error predicting. Geomatics Inf Sci Wuhan Univ 30(5):447–450
11. Fei N (2008) Theory and technique on GNSS integrity augment. Zheng Zhou: dissertation submitted to Information Engineering University

Chapter 35
Frequency Stability Estimation of BDS GEO On-Board Clock Based on Satellite Transponded Carrier Doppler

Hang Gong, Yuanling Li, Rui Ge, Xiangwei Zhu, Jing Yuan and Feixue Wang

Abstract In GNSS systems, frequency stability of satellite on-board clock will affect satellite clock offset modeling and prediction, and then impact the accuracy of positioning and timing, so frequency stability estimation of satellite on-board clock is of great significance for GNSS systems. This paper proposes a frequency stability estimation method for BDS GEO on-board clock based on satellite transponded carrier doppler. Frequency offset of on-board clock is estimated by self-transmitting and self-receiving transponded carrier doppler of ground station, and then the frequency stability can be estimated. Theoretical realization principle of the method is analyzed, and is validated using BDS observation. Experimental show that frequency stability estimation results of this method are basically consistent with that of network method and the relative deviation is less than 10 % within average interval of 1000 s.

Keywords BeiDou navigation satellite system · Transponded carrier doppler · Satellite on-board clock · Frequency stability

35.1 Introduction

The frequency stability parameter of satellite on-board clock is very important for applications such as clock prediction and simulation modeling in GNSS system. For GPS systems, the basic method for satellite clock stability estimation is to use the

H. Gong (✉) · Y. Li · R. Ge · X. Zhu · F. Wang
College of Electronic Science and Engineering, National University of Defense Technology, Changsha 410073 Hunan, People's Republic of China
e-mail: gonghang@nudt.edu.cn

F. Wang
e-mail: wangfeixue_nnc@163.com

J. Yuan
PLA Unit 94789, Nanjing 210016 Jiangsu, People's Republic of China

J. Sun et al. (eds.), *China Satellite Navigation Conference (CSNC) 2014 Proceedings: Volume III*, Lecture Notes in Electrical Engineering 305,
DOI: 10.1007/978-3-642-54740-9_35,

IGS precise clock products, but it is limited to GPS and GLONASS system currently, does not apply to BeiDou Navigation Satellite System (BDS/Compass) and Galileo systems. On the other hand, the commonly used precise orbit determination and time synchronization method (denoted as ODTS method) requires continuous observation of large ground monitoring networks and complex clock determination algorithm, it can not be achieved based on a single station observation.

Several single station estimation methods are analyzed and compared in literature [1–4], in which the method based on precise ephemeris is not applicable at this stage of BDS system [1, 2]; the carrier phase fitting method is too optimistic [2]; the method based on smoothed broadcast ephemeris has a relatively high precision, and can preferably be applied at this stage of the BDS system, but there are some errors due to that the geometric distance is calculated by the predicting satellite broadcast ephemeris [3]; and the method combining satellite two-way with one-way carrier ranging is sensitive to carrier phase cycle slips [4].

This paper proposes a single station frequency stability estimation method based on satellite transponded carrier doppler applying to BDS GEO satellite.

35.2 Principle of Method

The principle of this method is shown in Fig. 35.1. C-band transponders are installed on GEO satellites of BDS system for time synchronization between stations, two-way satellite time synchronization devices are configured in some monitoring stations of the BDS system (transmitting and receiving devices are denoted as TW transmitter and TW receiver respectively) [5]. TW receiver of this station can simultaneously receive ranging signal of itself transponded by GEO while receiving ranging signal of the other stations. The carrier doppler observation of TW receiver includes frequency offset of satellite on-board clock, so the frequency offset can be calculated by the transponded carrier doppler observation, and then the frequency stability can be estimated [4]. For ease of description, the frequency stability estimation method of satellite on-board clock based on such satellite transponded carrier doppler herein is denoted as STCD method for short.

The following section will analyze the calculating method of the frequency offset between satellite and ground TW receiver using transponded carrier doppler observations.

Using spread spectrum ranging system, transmitted signal of TW transmitter is:

$$s_T(t) = a_1 x(t) \sin[2\pi(f_T + \Delta f_t)t + \theta_t] \tag{35.1}$$

where, a_1 is the amplitude of transmitted signal; $x(t)$ is modulated pseudo-random code; f_T is the nominal carrier frequency of uplink transmission; Δf_t is carrier frequency bias of uplink transmission; θ_t is the initial phase. Since the modulation data will not affect ranging, the modulated data in signal is not considered in Eq. (35.1).

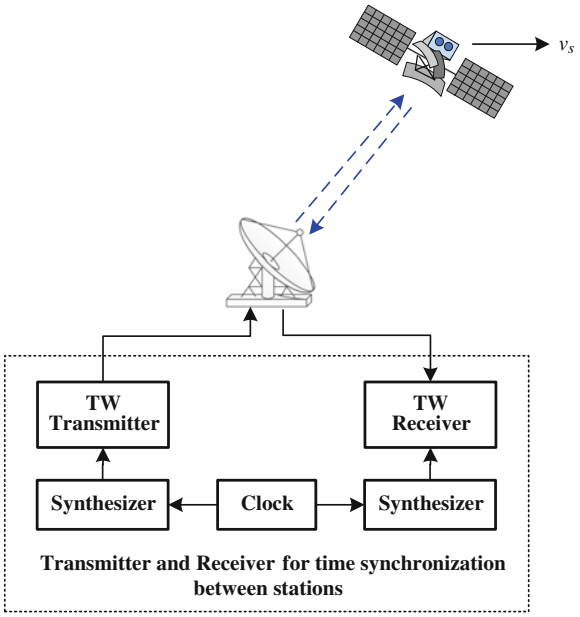

Fig. 35.1 Principle of STCD method

The uplink transmission signal received by satellite is [6]:

$$s_{SR}(t) = a_2 x\left[t - \tau_{g1}(t)\right] \sin\left\{2\pi(f_T + \Delta f_t)\left[t - \tau_{p1}(t)\right] + \theta_t\right\} \tag{35.2}$$

where, a_2 is the amplitude of received signal; $\tau_{g1}(t)$ is code propagation delay (group delay) of uplink transmission; $\tau_{p1}(t)$ is carrier propagation delay (phase delay) of uplink transmission. $\tau_{p1}(t)$ is a time-variant propagation delay. With a first-order expansion of the time-variant delay, $\tau_{p1}(t)$ can be modeled as [6]:

$$\tau_{p1}(t) = \tau_{p10} + \left[\frac{d\tau_{p1}(t)}{dt}\right] t \tag{35.3}$$

where, τ_{p10} is the initial propagation delay of uplink transmission. Then the received signal is:

$$s_{SR}(t) = a_2 x\left[t - \tau_{g1}(t)\right] \sin\{2\pi[f_T + \Delta f_t + f_{d1}(t)]t - 2\pi(f_T + \Delta f_t)\tau_{p10} + \theta_t\} \tag{35.4}$$

where, $f_{d1}(t)$ is the carrier doppler of uplink transmission:

$$f_{d1}(t) = (f_T + \Delta f_t)\left[-\frac{d\tau_{p1}(t)}{dt}\right] \tag{35.5}$$

When the satellite receives $s_{SR}(t)$, it will convert its carrier frequency to f_R and transmit the signal back to ground. Then the transmitted signal of satellite transmitter is:

$$\begin{aligned} s_{ST}(t) = a_3 x\left[t - \tau_{g1}(t)\right] \sin\{2\pi[f_T + \Delta f_t + f_{d1}(t) - f_{SL}]t \\ - 2\pi(f_T + \Delta f_t)\tau_{p10} + \theta_t - \theta_s + \pi/2\} \end{aligned} \tag{35.6}$$

where, f_{SL} is local oscillator frequency when the satellite converts f_T to f_R; θ_s is the initial phase of that oscillator. Thus the radio frequency signal received by TW receiver is:

$$\begin{aligned} s_R(t) = a_4 x\left[t - \tau_{g1}(t) - \tau_{g2}(t)\right] \sin\{2\pi[f_T + \Delta f_t + f_{d1}(t) \\ - f_{SL}]\left[t - \tau_{p2}(t)\right] - 2\pi(f_T + \Delta f_t)\tau_{p10} + \theta_t - \theta_s + \pi/2\} \end{aligned} \tag{35.7}$$

where, a_4 is the amplitude of received signal; $\tau_{g2}(t)$ is code propagation delay (group delay) of downlink transmission; $\tau_{p2}(t)$ is carrier propagation delay (phase delay) of downlink transmission. Similar to $\tau_{p1}(t)$, $\tau_{p2}(t)$ is also a time-variant delay, with a first-order expansion model as:

$$\tau_{p2}(t) = \tau_{p20} + \left[\frac{d\tau_{p2}(t)}{dt}\right] t \tag{35.8}$$

where, τ_{p20} is the initial propagation delay of downlink transmission. Thus the received signal is:

$$\begin{aligned} s_R(t) = a_4 x\left[t - \tau_{g1}(t) - \tau_{g2}(t)\right] \sin\{2\pi[f_T + \Delta f_t + f_{d1}(t) - f_{SL} + f_{d2}(t)]t \\ - 2\pi[f_T + \Delta f_t + f_{d1}(t) - f_{SL}]\tau_{p20} - 2\pi(f_T + \Delta f_t)\tau_{p10} + \theta_t - \theta_s + \pi/2\} \end{aligned} \tag{35.9}$$

where, $f_{d2}(t)$ is the carrier doppler of downlink transmission:

$$f_{d2}(t) = [f_T + \Delta f_t + f_{d1}(t) - f_{SL}]\left[-\frac{d\tau_{p2}(t)}{dt}\right] \tag{35.10}$$

When the TW receiver receives $s_R(t)$, it will down-convert the signal to an intermediate frequency signal $s_{IF}(t)$, and then carry out carrier tracking and pseudo-code correlation and other process. The intermediate frequency signal $s_{IF}(t)$ after radio frequency front-end process is:

$$\begin{aligned} s_{IF}(t) = a_5 x\left[t - \tau_{g1}(t) - \tau_{g2}(t)\right] \sin\{2\pi[f_T + \Delta f_t + f_{d1}(t) - f_{SL} + f_{d2}(t) - f_{RL}]t \\ - 2\pi[f_T + \Delta f_t + f_{d1}(t) - f_{SL}]\tau_{p20} - 2\pi(f_T + \Delta f_t)\tau_{p10} + \theta_t - \theta_s - \theta_r + \pi\} \end{aligned} \tag{35.11}$$

where, f_{RL} is the local oscillator when the TW receiver down-converts f_R to f_{IF}; θ_r is the initial phase of the local oscillator; then we have:

$$\begin{cases} f_{SL} = f_T - f_R + \Delta f_{SL} \\ f_{RL} = f_R - f_{IF} + \Delta f_{RL} \end{cases} \tag{35.12}$$

where, Δf_{SL} and Δf_{RL} are the local oscillator frequency bias of the satellite transponder and the receiver down convertor respectively, and Δf_{SL} includes the frequency offset of satellite on-board clock:

$$\Delta f_{SL} = \frac{f_{SL}}{f_0}\Delta f_s = \frac{f_T - f_R}{f_0}\Delta f_s = (f_T - f_R)\delta f_s \tag{35.13}$$

where, Δf_s is the frequency of on-board base clock (such as 10.23 MHz), and $\delta f_s = \Delta f_s / f_0$ is relative frequency offset of on-board base clock.

So the intermediate frequency signal of TW receiver is:

$$\begin{aligned} s_{IF}(t) = a_5 x\left[t - \tau_{g1}(t) - \tau_{g2}(t)\right] \sin\{2\pi[f_{IF} + \Delta f_t + f_{d1}(t) + f_{d2}(t) - \Delta f_s - \Delta f_r]t \\ - 2\pi[f_R + \Delta f_t + f_{d1}(t) - \Delta f_s]\tau_{p20} - 2\pi(f_T + \Delta f_t)\tau_{p10} + \theta_t - \theta_s - \theta_r + \pi\} \end{aligned} \tag{35.14}$$

After carrier and code tracking the TW receiver will recover a local carrier signal with the same frequency and phase as $s_{IF}(t)$. The carrier frequency of nominal IF signal minus that of the local recovery carrier signal derives the carrier doppler measurements. Thus the carrier doppler observation of TW receiver is:

$$F_d(t) = -f_{d1}(t) - f_{d2}(t) - \Delta f_T + \Delta f_{SL}(t) + \Delta f_{RL} + \varepsilon(t) \tag{35.15}$$

where, $\varepsilon(t)$ is observation noise of carrier doppler, and

$$f_{d1}(t) = -(f_T + \Delta f_T)\left[\frac{v_s(t)}{c} + s'(t) - \tau'_{i1}(t) + \tau'_{tr}(t)\right] \tag{35.16}$$

$$f_{d2}(t) = -[f_R + \Delta f_T + f_{d1}(t) - \Delta f_{SL}(t)]\left[\frac{v_s(t)}{c} - s'(t) - \tau'_{i2}(t) + \tau'_{tr}(t)\right] \tag{35.17}$$

Let

$$\begin{cases} k_1 = \frac{v_s(t)}{c} + s'(t) - \tau'_{i1}(t) + \tau'_{tr}(t) \\ k_2 = \frac{v_s(t)}{c} - s'(t) - \tau'_{i2}(t) + \tau'_{tr}(t) \end{cases} \tag{35.18}$$

Then

$$\begin{aligned} F_d(t) = (1 - k_2)\Delta f_{SL}(t) + (k_1 - k_1 k_2) f_T + k_2 f_R \\ + (k_1 + k_2 - k_1 k_2 - 1)\Delta f_T + \Delta f_{RL} + \varepsilon(t) \end{aligned} \tag{35.19}$$

Thus

$$\delta f_s(t) = \frac{[F_d(t) - (k_1 - k_1k_2)f_T - k_2f_R - (k_1 + k_2 - k_1k_2 - 1)\Delta f_T - \Delta f_{RL}]}{(1 - k_2)(f_T - f_R)} \tag{35.20}$$

The relative frequency offset of on-board base clock between satellite and ground TW receiver can be calculated by Eq. (35.20), and then the frequency stability of on-board can be estimated [7]:

$$\sigma_y^2(y) = \frac{1}{2(N - 2m)} \sum_{k=1}^{N-2m} [\delta f_s(k + m) - \delta f_s(k)]^2 \tag{35.21}$$

35.3 Implementation Process

Based on the above discussion, the implementation process of the STCD method is shown in Fig. 35.2, and it is carried out as follows:

1. The transmission time of satellite for each observation is calculated;
2. Satellite position and the relative velocity between satellite and ground TW receiver is calculate by broadcast ephemeris;
3. The gradient of atmospheric propagation delay, Sagnac effect, and relativity errors in carrier doppler observation are corrected;
4. The satellite on-board clock frequency offset with respect to ground receiver clock is calculated using Eq. (35.20), and its short-term stability is computed consequently by Eq. (35.21).

35.4 Experiments and Analysis

Precise clock offset of BDS system can not be obtained as a means of validation for the moment, and there is no published frequency stability result of BDS on-board clock currently, except for part of satellite stability results of February 2012 with average interval above 100 s using ODTS method by literature [8]. In this paper, experiment is carried out based on the same time observations of two BDS monitoring stations 01 and 03 with a distance of about 3,000 km, and the results of the two stations using STCD method are compared to validate themselves to another, with the results of literature [8] as a comparison. Both the two stations

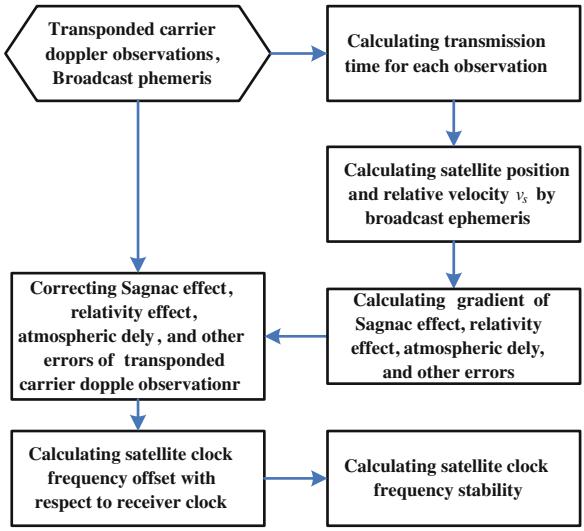

Fig. 35.2 Flow chart of STCD method

installed two-way satellite time synchronization devices, and the receivers use the same clock reference from a hydrogen maser which is disciplined by BDT (BDS system time), so the stability of receiver clock is better than satellite on-board clock, and the clock offset calculated by Eq. (35.21) can be used for frequency stability estimation of satellite on-board clocks.

The time period of experiment is from BDT 2012-12-02 00:00:00 to 2012-12-03 00:00:00. The ionospheric-free carrier phase combination of B1 and B3 frequency is used to estimate the frequency stability of SV01 (GEO) on-board clock. Comparison of the results of stations 01 and 03 are shown in Fig. 35.3.

As can be seen from Fig. 35.3, the results of station 01 and 03 using this method agree well with each other, and the relative error of average interval within 1,000 s is less than 10 %. The results of average interval above 100 s are basically consistent with the literature [8]. Because it is not the comparison of the same observation period, a certain bias is involved in the results, but the effectiveness of this STCD method can be explain to a certain extent.

This STCD method is currently available for frequency stability estimation of the BDS satellite SV01 and SV03 on-board clock. Estimation results of the two satellites on-board clock for the same period are shown in Fig. 35.4.

As can be seen from Fig. 35.4, the stability of current two BDS SV01 and SV03 satellite on-board clocks are basically consistent. The statistical average characteristics are shown in Table 35.1, in which the results of average interval of 100–10,000 s agree well with that in literature [8].

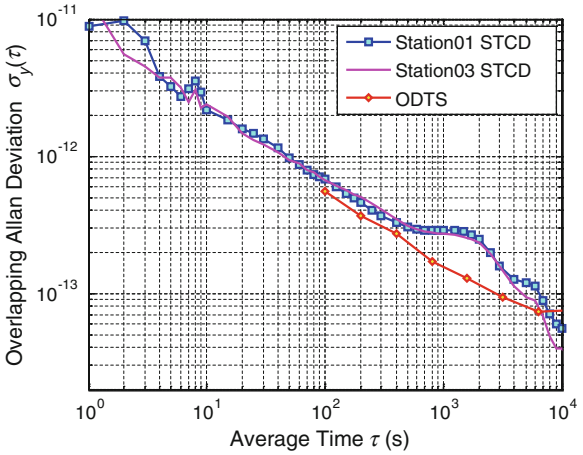

Fig. 35.3 Estimation result comparison between station 01 and station 03 by STCD method

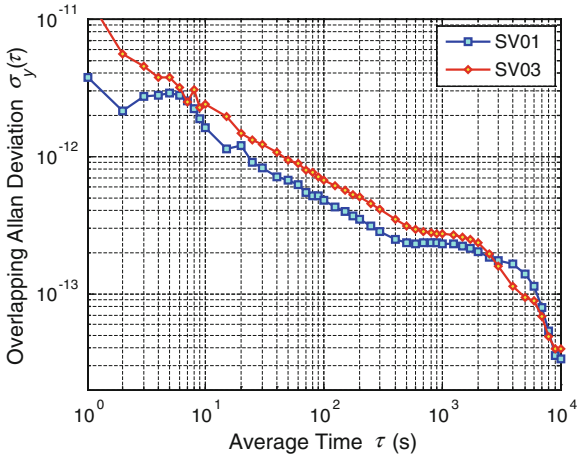

Fig. 35.4 Frequency stability estimation of BDS SV01 and SV03 on-board clocks

Table 35.1 Average frequency stability of BDS SV01 and SV03 on-board clocks

Average interval	STCD method	ODTS method
1	9.1×10^{-12}	/
10	2.0×10^{-12}	/
100	5.8×10^{-13}	5×10^{-13}
1,000	2.5×10^{-13}	2×10^{-13}
10,000	3.7×10^{-14}	7×10^{-14}

35.5 Conclusion

This paper proposed a frequency stability estimation method for BDS GEO satellite on-board clock based on satellite transponded carrier doppler. This method was validated using BDS observation. The experiment results of this

method were consistent with the complexity ODTS algorithm. Finally, the frequency stability of current BDS SV01 and SV03 on-board clocks are estimated by the proposed method, the results show that the stability of these satellite clocks are basically consistent. The frequency stability of current BDS on-board clocks is approximately 9×10^{-12} at average time of 1 s and 3×10^{-13} at 1,000 s.

Satellite on-board clock frequency stability can be monitored in real-time using this method. So the proposed method can be used for integrity monitoring of BDS GEO satellite on-board clock, and it is also applicable to frequency stability estimation for frequency standard of other satellite with transponders. When the satellite on-board clock stability is better than receiver clock, the method also provides a receiver clock stability estimation approach.

References

1. Gong H, Yang WK, Wang Y et al (2012) Comparison of short-term stability estimation methods of GNSS on-board clock. Lecture notes in Electrical Engineering, v 160 LNEE. In: Proceedings of the 3rd China satellite navigation conference. Berlin: Springer, pp 503–513
2. Delporte J, Boulanger C, Mercier F (2011) Straight forward estimations of GNSS on-board clocks. In: Proceedings of 2011 joint conference of the IEEE international frequency control symposium and European frequency and time forum. San Francisco, California, USA
3. Gong H, Liu ZJ, Peng J, Wang FX (2013) Estimation method of GNSS on-board clock short-term stability based on smoothed broadcast ephemeris. Geomatics Inf Sci Wuhan Univ 38(7):837–841
4. Gong H, Yang WK, Liu ZJ, Zhu XW, Wang FX (2013) Estimation method of BDS on-board clock short-term stability combining satellite two-way with one-way carrier ranging. J Nat Univ Defense Technol 35(3):158–163
5. Yang XH, Ma LM, Sun BQ et al (2011) The method of time synchronization based on the combination of COMPASS GEO pseudo- range and two-way data. In: Proceedings of 2011 joint conference of the IEEE international frequency control symposium and European frequency and time forum. San Francisco, California, USA
6. Jin SG (2012) Global navigation satellite systems: signal, theory and applications. InTech, Croatia, pp 14–16
7. Ferre-Pikal et al (2008) IEEE standard definitions of physical quantities for fundamental frequency and time metrology—random instabilities. The institute of Electrical and Electronics Engineers Inc., New York, pp 26–29
8. Han CH (2012) Time synchronization and in-orbit performance assessment of compass on-board clocks. In: Invited presentation of 3rd China satellite navigation conference. Guangzhou, China

Chapter 36
Simple Precise Time Signal Delivery Over Fiber Link Scheme

Yitang Dai, Zhongle Wu, Tianpeng Ren, Feifei Yin, Kun Xu, Jintong Lin and Geshi Tang

Abstract The capability of transferring time signal to remote locations with high stability and accuracy for synchronization is crucial for many important occasions, involving very long-baseline interferometry, coherent radio telescope arrays, modern particle accelerator, and the Deep Space Network. The widely used satellite methods of time and frequency transfer are unable to preserve the stability delivered by modern timekeeping sources. To meet these high stability requirements, optical fiber link has been used to transfer frequency and time reference, which however still suffers from mechanical perturbation and temperature variation along the link and degrades the phase stability at the remote end. Over the past decade, researchers mainly focused on the frequency dissemination, and the transfer stability is now sufficient for most frequency standards. However, the time signal transfer stability is far below frequency reference, which is typically at the nanosecond accuracy level. We propose and demonstrate a stable time signal delivery scheme over fiber link utilizing frequency stabilization technology. In the scheme, we utilizing the frequency reference to compensate the link-length variation, and the total transfer delay is kept constant. Precise time signal is regenerated at the remote end. The fiber link we used in this paper is 10-km, and the long-term fiber delay variation is more than 800 ps. We obtain a time deviation of 40 ps at 1-s and falling to 2.3 ps at 1,000-s averaging time for time transfer. The time delay resolution of scheme is 1 ps, and the compensation range is in direct proportion with the fiber length. The proposed scheme shows a potential ability to

Y. Dai · Z. Wu · F. Yin · K. Xu (✉) · J. Lin
State Key Laboratory of Information Photonics and Optical Communications, Beijing University of Posts and Telecommunications, Beijing 100876, China
e-mail: xukun@bupt.edu.cn

T. Ren · G. Tang
Science and Technology on Aerospace Flight Dynamics Laboratory, Beijing 100094, China

T. Ren · G. Tang
Beijing Aerospace Control Center, Beijing 100094, China

J. Sun et al. (eds.), *China Satellite Navigation Conference (CSNC) 2014 Proceedings: Volume III*, Lecture Notes in Electrical Engineering 305,
DOI: 10.1007/978-3-642-54740-9_36,

precisely transfer time signal and frequency reference simultaneously, which is very suitable for long range time and frequency transfer.

Keywords Time and frequency delivery · Fiber link · Time deviation

36.1 Introduction

Current research on microwave frequency references and optical atomic clocks offers the potential to produce frequency references with short-term instabilities of a few parts in 10^{16} for a 1 s averaging time [1]. These highest precision atomic clocks are usually very complex and not portable, maintained by certain laboratories, with very limited access. The ability to remotely transfer time signal and frequency reference to remote locations without introducing any additional instability is of greatly needed for many important occasions, such as the test of fundamental physical principles, development of next-generation accelerator-based x-ray sources, long-baseline coherent radio telescope arrays, and the accurate mapping of the Earth's geoid [2]. For example, in the Atacama Large Millimeter Array (ALMA) radio astronomy project, the local oscillator reference signal arriving at remote antennas with a maximum path length up to 18 km must be stabilized under one picosecond, in order to achieve the unprecedented sensitivity and angular resolution [3, 4].

The widely used satellite methods of time and frequency transfer are unable to preserve the stability delivered by modern timekeeping sources. To meet these high stability requirements, optical fiber link has been used to transfer frequency and time reference, which however still suffers from mechanical perturbation and temperature variation along the link and degrades the phase stability at the remote end. Over the past decade, researchers mainly focused on the frequency dissemination, and the transfer stability is now sufficient for most frequency standards. Different frequency transfer schemes based on fiber links have been proposed and demonstrated, basically two types [5]. The first one is in-loop tunable delay lines, such as the piezoelectric fiber stretcher or motor-driven tunable optical delay line. The second type is that the frequency standard at the center station is phase-tuned so that the phase at the remote end is stable, such as a voltage-controlled oscillator (VCO) or a cavity-length-changeable passively mode-locked laser. However, these schemes are not suitable for long range time signal transfer. For the first type, due to the large temperature-dependent delay variation of standard fiber, RF delivery over tens of kilometers requires a significant tunable range which will beyond the dynamic range of tunable delay lines. For the second type, because time signal is a wide-band signal, the VCO can only compensate single-frequency signal. Therefore, the time signal transfer stability is far below frequency reference, which is typically at the nanosecond accuracy level.

Recently, a time synchronization at 50 ps precision level was demonstrated in a frequency transfer fiber link [6], however, the time compensation and frequency compensation are achieved separately. Reference [7] fulfilled the joint stable time and frequency transfer in the same transmission path, but the time delay resolution is limited by the delay-locked loop integrated circuit.

In this paper, we propose and demonstrate the extension of our frequency transfer scheme [6] to the time transfer capability. We use the frequency reference to stabilize the time signal. Precise time signal and frequency reference are simultaneously regenerated at the remote end of fiber link. By utilizing the fiber's inherent chromatic dispersion, link-length variation caused by the environment variation are compensated. As the delay fluctuation of the fiber link is corrected, the time signal and the frequency signal are stabilized at the same time. In a 50-km fiber link, we obtain a time deviation of 2.1 ps (for time transfer) and an Allan Deviation of 1.42×10^{-15} (for frequency transfer) at 1,000-s averaging. The time delay resolution of scheme is 1 ps, and the compensation range is in direct proportion with the fiber length, which is very suitable for long range time and frequency transfer.

36.2 Principle

The proposed time signal transfer scheme is illustrated in Fig. 36.1. The stable transfer scheme consists of a large tunable-range optical delay and a regular phase detector. Rather than acting directly on the optical length of the fiber link like a broadly proposed optical compensation system, the scheme takes advantage of the chromatic dispersion in optical fiber. Utilizing the fiber's inherent chromatic dispersion, link-length variation caused by the environment change are compensated. As the delay fluctuation of the fiber link is corrected, the frequency signal can be stably transferred to the remote end. Because the time signal follows the same transmission path as the frequency signal, its delay is also stabilized by the system. Therefore, stable time can be regenerated at the remote end.

The radio frequency signal to be transferred is also regarded as a calibration signal. At the center station, the calibration frequency reference signal RF_1 and time signal are modulated on the optical carrier which comes from a computer-controlled tunable laser diode (TLD) via a Mach-Zehnder modulator (MZM), where the time signal is BPSK modulated by RF_2. Assume that the initial wavelength of the optical carrier is λ_0. After the modulator and an optical circulator, the optical signal is injected into the standard single mode fiber (SMF) spool which is located at the laboratory. The fiber delay fluctuation that results from the environment variation is τ. At the remote end, part of the optical signal is transferred back to the center station through the same fiber link via a Faraday rotator mirror (FRM). The round-trip transmitted optical signal is detected by a fast photo detector which recovers the calibration signal. The recovered calibration signal is filtered out and compared to the original frequency reference signal through an

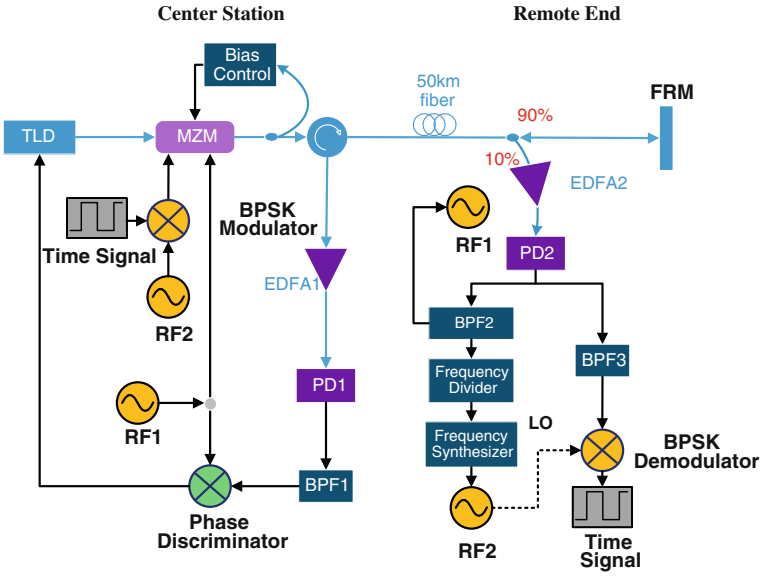

Fig. 36.1 Simple precise time signal delivery over fiber link scheme

electronic phase detector. Phase error signal is extracted which contains twice the phase perturbation of the fiber link under the assumption that the forward and backward propagations through the same fiber link experiences the same time delay. The output of the phase detector is then used to alter the wavelength of the tunable laser by a computer. The wavelength of the tunable laser is shifted using a classic proportional—integral-derivation (PID) algorithm according to the round—trip phase fluctuation. By tuning the wavelength of the TLD to λ we can get the following equation:

$$D \cdot L \cdot (\lambda - \lambda_0) + \tau = 0 \tag{36.1}$$

where D is the dispersion factor of the fiber and L is the length of the fiber.

The whole scheme acts as a long phase locking loop. After the loop is locked, at the remote end, the other part of the optical signal is filtered and recovered by a photo detector. The RF_1 is filtered out. This is the stably transferred frequency reference. We frequency divide this signal to synthesize RF_2 to demodulate the time signal. The stabilized time signal as well as frequency signal can be regenerated at the remote end.

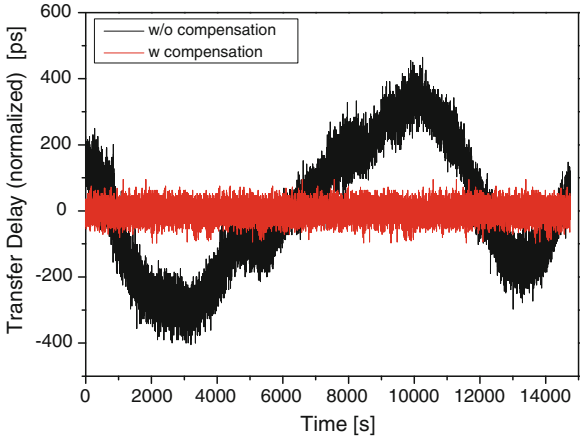

Fig. 36.2 Measured transfer delay of the time signal without (*black*) and with compensation (*red*)

36.3 Experiment and Results

36.3.1 Time Stability

A proof-of-concept experiment is carried out and the setup is shown in Fig. 36.1. In the experiment, because we do not have an atomic clock, the frequency reference is synthesized by an analog signal generator and is set at 1,210 MHz. The time signal is generated by a arbitrary waveform generator. It generates an output square wave signal with an 8.4 ns rise and fall time and a 0.1 % duty ratio at a rate of 1.2 kHz. The tunable wavelength range of our TLD is from 1,525 to 1,568 nm and the minimum $\Delta\lambda$ is about 1 pm. A modulator bias-controller is used to lock the MZM at quadrature point.

Experimentally, we compare the time signal delivery stability without and with the proposed fluctuation compensation. In the uncompensated delivery, the wavelength of the optical carrier is fixed at 1,550 nm while the other conditions remain the same as those in the compensated situation.

In the experiment, we measure the time delay fluctuations of our system. In 15,000 s measuring time, the temperature changes more than 5° in the laboratory. Time transfer delay of the time signal is measured 1-s a time with a time interval counter and shown in Fig. 36.2. During the whole 15,000 s recording time, the uncompensated time transfer delay (normalized) is as large as 800 ps (shown in Fig. 36.2, black line). When the wavelength tuning driven by the PID phase tracking is on, the time transfer delay is about ± 50 ps (shown in Fig. 36.2, red line). We can see with compensation, the time delay is independent with temperature change. The time transfer delay suppression ratio will be greater for larger fiber length fluctuation.

The time deviation calculated from the transfer delay measurement is shown in Fig. 36.3. In the compensated link, the time deviation is monotonically decreasing

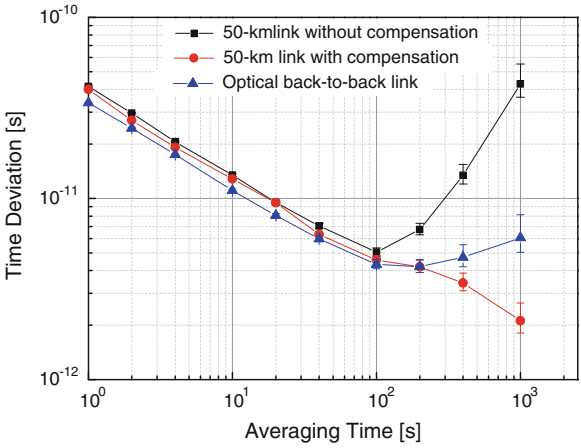

Fig. 36.3 Time deviation of time signal transfer with and without compensation. *Black square* 50 km without compensation; *red circle* 50 km with compensation; *blue triangle* optical back-to-back link transfer

with averaging time, while the uncompensated link is not. The short-term jitter of the time signal, measured in a 1-s period, was 40 ps, which is similar with the uncompensated one. For averaging time of 1,000-s, the time deviation fall to 2.3 ps, whereas for uncompensated situation, it reached back to 50 ps. The time deviation of time signal reference was also measured. The time deviation of compensated link is approaching to that of the reference signal. This shows that the compensation scheme ensures the time signal preserving the stability in the long-term transfer. In our formal work [3], we measured the frequency transfer stability in a 54-km fiber link. A 0.854 ps root mean square time jitter is achieved after compensation. The time signal transfer is expected to achieve this accuracy level if we use better time interval measurement equipment. The proposed scheme shows a potential ability to precisely transfer time signal and frequency reference simultaneously.

36.3.2 Frequency Stability

Next, we examined the frequency transfer capability of our system. We measured the frequency stability with and without compensation. The Allan Deviation calculated from a 15,000-s measurement is shown in Fig. 36.4. The Allan Deviation of the compensated link was monotonically decreasing with averaging time, from 1.12×10^{-12} at 1-s falling to 1.42×10^{-15} for an averaging time of 1,000-s. The uncompensated link was even worse, and was degraded by the fluctuation. We also measured the optical back-to-back stability of our system. In this test, the 50-km fiber was replaced by a 1-m fiber, and the other situation remained the same. We can see the degradation introduced by the time signal, and the Allan Deviation of the compensated link is almost the same with the optical back-to-back stability.

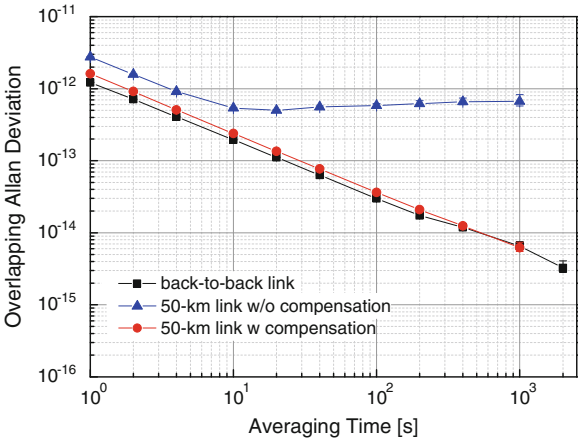

Fig. 36.4 Allan deviation of frequency signal transfer with and without compensation

36.4 Conclusion

In conclusion, we have presented a scheme allowing time and frequency simultaneously transfer in a fiber link with active compensation of the propagation delay. The scheme takes advantage of the chromatic dispersion in optical fiber, and the time signal and frequency reference are stabilized at the remote end at the same time. We have demonstrated a stability of the time signal transfer over 50-km fiber with a time deviation around 40 ps at 1-s and 2.3 ps for 1,000-s averaging. We have also tested the performance of our frequency transfer. We obtained an Allan Deviation of about 1.42×10^{-15} for an averaging time of 1,000-s. The compensation range is in direct proportion with the fiber length, which is very suitable for long range time and frequency transfer. It may have important applications in radio astronomy.

Acknowledgments This work was supported in part by National 973 Program (2012CB315705), NSFC Program (61302016), and the Fundamental Research Funds for the Central Universities.

References

1. Foreman SM, Holman KW, Hudson DD, Jones DJ, Ye J (2007) Remote transfer of ultrastable frequency references via fiber networks. Rev Sci Instrum 78:021101
2. Calhoun M, Huang S, Tjoelker RL (2007) Stable photonic links for frequency and time transfer in the deep-space network and antenna arrays. Proc IEEE 95(10):1931–1946
3. Cliche JF, Shillue B (2006) Precision time control for radioastronomy-maintaining femtosecond synchronization in the Atacama large millimeter array. IEEE Control Syst Mag 26(1):19–26
4. Tarenghi M (2008) The Atacama large millimeter/submillimeter array: overview & status. Astrophys Space Sci 313:1–7

5. Zhang A, Dai Y, Yin F, Ren T, Xu K, Li J, Ji Y, Lin J, Tang G (2013) Stable radio-frequency delivery by λ dispersion-induced optical tunable delay. Opt Lett 38(14):2419–2421
6. Wang B, Gao C, Chen WL, Miao J, Zhu X, Bai Y, Zhang JW, Feng YY, Li TC, Wang LJ (2012) Precise and continuous time and frequency synchronization at the 5×10^{-19} accuracy level. Sci Rep 2:556
7. Krehlik P, Sliwczynski L, Buczek L, Lipinski M (2012) Fiber-optic joint time and frequency transfer with active stabilization of the propagation delay. IEEE Trans Instrum Meas 61(10):2844–2851

Chapter 37
Satellite Clock Offset Determination and Prediction with Integrating Regional Satellite-Ground and Inter-Satellite Data

Li Liu, Xin Shi, Guifen Tang, Lan Du, Lingfeng Zhu and Rui Guo

Abstract Time synchronization between Satellites is the foundation for satellite navigation system, which is realized by satellite-ground clock offset determination and prediction. Therefore, satellite clock offset determination and prediction is a key technique for satellite navigation systems. At present, precise time synchronization between satellites by inter-satellite link and auto-time synchronization is considered to be important development direction for navigation domain. A satellite clock offset determination and prediction method by integrating regional satellite-ground observation data and inter-satellite observation data is discussed. We first introduce some common used methods for satellite clock determination, and then discuss the principle and data process model for satellite clock determination based on inter-satellite link dada. We provide the method of Helmert variance components estimation to determine and predict satellite clock based on integrating satellite-ground and inter-satellite observation data. At last, we analyse the performance for our method by using real observation data and simulation data, the result shows the method overcomes the defects of regional monitoring network and improves the precise of prediction form 8 to 1.5 ns for MEO satellite when the satellites can't been observed. The method also increases the satellite clock data when the satellites can be observed, which can improved the precise and reliability for determination and prediction satellite clock offset.

Keywords Navigation satellite · Time synchronization · Inter-satellite link · Clock offset determination · Clock offset prediction

L. Liu (✉) · X. Shi · G. Tang · L. Zhu · R. Guo
Beijing Satellite Navigation Center, Beijing 100094, China
e-mail: lliu@shao.ac.cn

L. Du
Information Engineering University, Zhengzhou 450052, China

J. Sun et al. (eds.), *China Satellite Navigation Conference (CSNC) 2014 Proceedings: Volume III*, Lecture Notes in Electrical Engineering 305,
DOI: 10.1007/978-3-642-54740-9_37,

37.1 Introduction

The distance between satellite and user is the base observation value for the satellite navigation user, which is obtained by measuring the transmission delay. So satellite navigation system should have a high precise time scale in order to realize the high precise navigation and positioning [1]. The high precise time scale that the satellite navigation system provides to the user is realized by the accuracy time of the navigation satellite. In order to make the time which is broadcast by the satellite deputize for the ground time scale, the satellite clock should be synchronized by the ground time scale termly or periodically. Thus, the difference between the satellite time and ground time can be maintained in a stated bias scope. Synchronization satellite clock means to compute the clock offset between the satellite clock and the system time. For the navigation satellite, synchronization satellite clock is realized by the determination and prediction of the satellite clock offset. In fact, the clock offset parameters a0, a1, a2 of the navigation message is obtained by predicting the satellite clock offset determination result. Therefore, high precise time synchronization is the core of the satellite navigation system and the accurate satellite clock offset determination and prediction is one of the key techniques.

The satellite clock offset determination gradually adopts the direct observations of ground station measuring the navigation satellites, using orbit and clock offset integrated determination method, two-way satellite-ground time transfer method, pseudo code and laser ranging method to realize concretely [2–5]. The national and foreign scholars have deep studied in the satellite clock offset parameters prediction methods, such as polynomial model, gray model, AR time serial analysis, nerve network model, etc. [6–9]. Considering the physical characteristics of the satellite clock and the restriction of broadcast link, one-degree or two-degree polynomial model is the normal expression in satellite navigation system.

With the emergence of the inter-satellite link auto-navigation concept and the realization on some GPS satellites, the auto-determination technique of navigation satellite clock offset and orbit based on the inter-satellite link has become one of the study hotspots in satellite navigation domain [10–12]. Especially for that area where can only realize the regional stations setting, how to use the inter-satellite link data to remedy the shortage of the regional satellite-ground link data in order to realize high precise satellite clock offset determination and prediction has become a problem.

Aimed at overcoming the shortage of MEO satellite clock offset prediction just using the regional satellite-ground monitoring network, a method of integrating the regional satellite-ground and inter-satellite data for satellite clock offset determination and prediction is discussed in this paper. The Helmert variance components estimation method is performed to determine and predict satellite clock offset based on integrating the satellite-ground and inter-satellite observation data. At last, some available conclusions had been gained by the experimentation analysis with the real and simulated data.

37.2 Satellite Clock Offset Determination Method and Characteristic Analysis

37.2.1 Satellite Clock Offset Determination Method Base on the Satellite-Ground Link

The satellite clock offset determination methods base on the satellite-ground link include orbit and clock offset integrated determination method, two-way satellite-ground time transfer method, pseudo code and laser ranging method [2–5], etc. The methods and their characteristics analysis are shown as the following.

1. **Orbit and clock offset integrated determination method**

In order to maintain the precise synchronization between on-board clock and system time, GPS and GALILEO system adopt an auto-adjusted closed loop method with the synchronous determination of the satellite clock offset and the satellite orbit. Its principle is that: the orbit determination and time synchronization monitor stations which are distributed in the global world take its atomic clock as the standard, receive the signals transmitted by the satellites and measure the double-frequency pseudorange and carrier phase observation; then the observation data of these monitor stations are transferred to the master station; the master station takes the main clock as the standard, analyzes and processes the smoothed pseudorange data by the Kalman filter, computes the new satellite orbit and clock offset results; at last, the satellite orbit and clock offset computed by the master station are fitted as the navigation message parameters and then injected to the satellites.

The advantage of this method is the synchronous calculation of the orbit and clock offset with the simple equipment. The disadvantage is that the orbit error and the clock offset error can not be separated and the measured clock offset can not represent the real clock characteristics.

2. **Two-way satellite-ground time transfer method**

In order to realize the higher-precise satellite clock offset determination and separate the orbit error and the clock offset error at the same time, the two-way satellite-ground time transfer method can be adopted for the independent accurate determination. Its principle is that: The satellite S and the ground station produce and broadcast the pseudo code ranging signals with the control of the native clock. The ground station observes the down-link pseudorange at its native clock time (this pseudorange includes the minus satellite clock offset). The satellite S observes the up-link pseudorange at its clock time (this pseudorange includes the plus satellite clock offset). At the same time, the satellite transmits its up-link pseudorange observation to the ground station through the communication link. The ground station calculates the difference of its measured down-link pseudorange and the received up-link pseudorange. Thus, the clock offset between the

satellite and the ground station can be obtained. Assuming that the ground station clock is synchronous with the system time (clock offset is zero or known), the clock offset determination of the satellite to the system time is accomplished.

The advantage of this method is that the common errors (such as the troposphere delay, satellite ephemeris error, ground station coordinate and so on) are eliminated, and the ionosphere delay error related to the signal frequency is greatly weakened. So that time transfer precision is highly improved. The determined satellite clock offset represents the satellite clock characteristic and the satellite clock offset is separated from the orbit error, which provides the basis of the precise orbit determination at some special cases such as during periods of satellite orbit maneuvering and orbit recovery. The disadvantage is that the equipment and system realization is complex and there is system bias in different equipment.

3. **Pseudo code and laser ranging method**

The principle of the pseudo code and laser ranging method is that: the ground station transmits the laser signal to the satellite with the control of its native clock. The signal echoes immediately when it arrives at the satellite and the reflected signal is received by the ground station. Thus the laser two-way range observation is obtained. The pseudorange observation received by the ground receiver contains the clock offset of the satellite to the ground station and the station-satellite distance. But the ground laser range just contains the station-satellite distance. So that, the clock offset between the satellite clock and the ground clock can be obtained through deducting the station-satellite distance obtained by the laser range in the observed pseudorange.

The realization of this method not only need to install laser reflection prism in the satellite, but also need to install the corresponding laser ranging equipment and navigation receiver with apposition common clock. It is difficult to realize totally automation because the equipment is complex and restricted with the weather. So this method can only be a verification method.

37.2.2 Satellite Clock Offset Determination Method Base on the Inter-Satellite Link

As the two-way satellite-ground time transfer method, assuming that two satellites A and B send the time signal T_A and T_B to each other at their native clock time, the time signal sent by the satellite A is received by the satellite B at the clock time T'_A passing through the delay τ'_{AB} and measures the delay R_{AB}. At the same time, the time signal sent by the satellite B is received by the satellite A at the clock time T'_B passing through the delay τ'_{BA} and measures the delay R_{BA}. Then the two satellites exchange their own observation and calculate their relative clock offset.

Based on the principle of the two-way time synchronization, the formula is given:

$$\begin{cases} R_{AB} = \tau'_{AB} - \Delta T_{AB} = \tau_{AB} + \tau^e_A + \tau^r_B + \Delta\tau_{AB} - \Delta T_{AB} \\ R_{BA} = \tau'_{BA} + \Delta T_{AB} = \tau_{BA} + \tau^e_B + \tau^r_A + \Delta\tau_{BA} + \Delta T_{AB} \end{cases} \tag{37.1}$$

In the above formula, τ_{AB} and τ_{BA} is the geometrical delay between the two satellites at the unitary calculating time, τ^e_i and τ^r_i (i = A or B) is respectively the sending and receiving delay, $\Delta\tau_{AB}$ and $\Delta\tau_{BA}$ is respectively the transmission delay of the two links (mainly including plasma delay, gravitation delay and motion delay), $\Delta T_{AB} = \Delta T_A - \Delta T_B$ is the relative clock offset between the satellite A and B, ΔT_A and ΔT_B is respectively the relative clock offset between the satellites A, B and the system time.

The above two formulae minus and ignore the error of influence less than 0.1 ns, the formula of calculating the inter-satellite relative clock offset is:

$$\begin{aligned} \Delta T_{AB} = {} & \frac{1}{2}(R_{AB} - R_{BA}) + \frac{1}{2}[\tau_{AB} - \tau_{BA}] + \frac{1}{2}\left[\left(\tau^e_A + \tau^r_B\right) - \left(\tau^e_B + \tau^r_A\right)\right] \\ & - \frac{1}{2c}\left[\frac{\left(X^i_A - X^i_B\right)\cdot V^i_A \cdot (\tau_{BA} - \Delta T_{BA})}{\rho_{AB}} + \frac{\left(X^i_A - X^i_B\right)\cdot V^i_B \cdot (\tau_{AB} - \Delta T_{AB})}{\rho_{AB}}\right] \end{aligned} \tag{37.2}$$

The above formula is the principle formula of calculating the inter-satellite relative clock offset with the two-way time synchronization, in which the first item is the time difference measured by the two satellites, the second item is the geometrical delay difference between the two satellites, the third item is the sending and receiving delay difference between the two satellites equipment, and the last item is the transmission correction difference between the two links.

The above obtained clock offset is the relative clock offset between the two satellites A and B. But we need the clock offset of the non-direct satellite-ground link satellite (generally assuming it is the satellite A) to the system time. So the clock offset of the known satellite B to the system time must be obtained and the clock offset of the satellite A can be calculated by the following formula.

$$\Delta T_A = \Delta T_{AB} + \Delta T_B \tag{37.3}$$

The clock offset of the satellite B to the system time ΔT_B can be obtained by the above satellite-ground link observation. When the satellite B can not directly observe with the ground station, the clock offset can be obtained by the conversion through the other satellite which has satellite-ground link observation and inter-satellite link observation. The more errors accumulate because of the twice inter-satellite observation conversion.

37.3 Integrated Satellite Clock Offset Determination and Prediction with the Satellite-Ground and Inter-Satellite Data

After the satellite clock offset determination, the clock offset parameters should be predicted in order to provide satellite clock offset service to the users.

Because GEO satellite can maintain continuous observation with the ground, it can adopt the short-term prediction result to realize higher clock offset predicting precision. But MEO satellite can not maintain continuous observation with the ground after its observed arc, mid-term (more than 10 h) predicting precision will fall greatly by only use the regional satellite-ground observation data. The inter-satellite data can remedy the shortage of the satellite-ground data.

On the other hand, considering the different observation precision, the observation quantity and the different data distribution of the two technical methods, the different data should be weighted with different values, when satellite clock offset parameters are predicted with the satellite-ground and inter-satellite data. The national and foreign scholars have deeply studied in weight determination problem of the different data and put forward many new methods. At present, there are major three methods [13–15]: using the standard variance provided by the observation data, adopting experiential weight, adopting variance component estimation. In order to unify the two kinds of data, the Helmert variance component estimation method is adopted in this paper and the basic model is shown as following:

$$V = AX - L \tag{37.4}$$

In this formula,

$$V = \begin{bmatrix} V_1 \\ V_2 \end{bmatrix}, \quad A = \begin{bmatrix} A_1 \\ A_2 \end{bmatrix}, \quad X = \bar{X} - \bar{X}_0, \quad L = \begin{bmatrix} L_1 \\ L_2 \end{bmatrix} \tag{37.5}$$

L1 and L2 is respectively m_1 and m_2 dimension vector, $\bar{X}$ and $\bar{X}_0$ is respectively the true value and the initial value of the estimated parameter, A is the differential coefficient matrix of the observation value to the state vector.

Then the estimated value of the parameter correction value is:

$$\hat{X} = N^{-1}U \tag{37.6}$$

In this formula,

$$N = A^T PA = A_1^T P_1 A_1 + A_2^T P_2 A_2 = N_1 + N_2 \tag{37.7}$$

$$U = A^T PL = A_1^T P_1 L_1 + A_2^T P_2 L_2 = U_1 + U_2 \tag{37.8}$$

P1 and P2 is respectively the weight matrix of the satellite-ground and inter-satellite observation value. Because the covariance of the observation value is

generally unknown, the weight matrix P1 and P2 is not suitable in the first calculation. If the unit weight variance of the two groups of observation data is respectively σ_1^2 and σ_1^2, then:

$$P_1 = \sigma_1^2 \sum_1^{-1} \tag{37.9}$$

$$P_2 = \sigma_2^2 \sum_2^{-1} \tag{37.10}$$

σ_1^2 and σ_2^2 can be estimated by using the above calculated residual error. According to the Helmert variance component estimation method, the linearity function can be obtained:

$$G\hat{Y} = W \tag{37.11}$$

In this formula,

$$G = \begin{bmatrix} m_1 - 2tr(N^{-1}N_1) + tr(N^{-1}N_1)^2 & tr(N^{-1}N_1N^{-1}N_2) \\ tr(N^{-1}N_1N^{-1}N_2) & m_2 - 2tr(N^{-1}N_2) + tr(N^{-1}N_2)^2 \end{bmatrix} \tag{37.12}$$

$$\hat{Y} = \begin{bmatrix} \hat{\sigma}_1^2 & \hat{\sigma}_2^2 \end{bmatrix}^T \quad W = \begin{bmatrix} V_1^T P_1 V_1 & V_2^T P_2 V_2 \end{bmatrix}^T \tag{37.13}$$

The estimated value of the unit weight variance through parameter adjustment method is:

$$\hat{Y} = G^{-1}W \tag{37.14}$$

At the actual data processing, the iterative computation is need. The main iteration steps are:

1. set the initial weight of two types observations using the priori variance of unit weight, and calculate the $V_1^T P_1 V_1$ and $V_2^T P_2 V_2$ of two kinds observation in accordance with the parameter adjustment;
2. using (37.14) formula, calculate the first estimated value $\hat{\sigma}_1^{2(1)}$ and $\hat{\sigma}_2^{2(1)}$ of variance factor of the two types observation;
3. reset the weight of two types observation with posterior variance;
4. again execute the parameter adjustment with the new weight of two types observation;
5. repeat (2)–(4), until $\sigma_1^{2(n)} \approx \sigma_2^{2(n)}$.

37.4 Experimentation Analysis with the Real Measurement Data

In order to testify the accuracy and feasibility of the method proposed in this paper, we simulated long-time continuous satellite-ground link satellite clock offset of two GEO satellites A and B as the real value, from which we got one-by-one the relative clock offset between the two GEO satellites according to the time. We took the relative clock offset as the satellite clock offset real value obtained from the inter-satellite link. Then we simulated data according to the MEO satellite observed time, that is: in the MEO satellite observed arc and we took the clock offset of the satellite A as the clock offset observation value of the MEO satellite. In the MEO satellite non-observed time, in order to simulate the random error of the inter-satellite measurement and the system bias of the transition through the different satellite equipment, we took the relative clock offset of the two satellites plus the random error (variance is 0.25 ns) and the random system bias (variance is 0.25 ns) as the inter-satellite link simulated data, converted the satellite B real clock offset to the satellite A simulated clock offset (this result is that the satellite A real clock offset plus the above random errors), took the simulated satellite clock offset as the MEO satellite clock offset obtained from the inter-satellite link, at the same time, still took the satellite A clock offset of the corresponding time as the MEO satellite clock offset real value. Thus we can estimate the clock offset prediction precision obtained from the different methods. The following is the satellite clock offset prediction precision analysis with only the regional satellite-ground data and the integrated satellite-ground and inter-satellite data (Fig. 37.1).

37.4.1 Satellite Clock Offset Prediction Precision Analysis with only the Regional Satellite-Ground Data

The statistics show that the regional setting stations has less than 30 % orbit coverage to some MEO satellites. That is to say, the MEO is not observed about two-part of the period and the longest time of non-directly observing can achieve 20 h. Therefore, with only the regional satellite-ground observation data, MEO satellite clock offset is mostly maintained by the mid-term or long-term prediction results, which will makes the clock offset precision rapidly decrease when the MEO satellite is out and just into the regional. The following is the satellite clock offset prediction result with only the regional satellite-ground link.

In order to compare, the following figure the 24 h prediction error of GPS satellite clock. The data is obtained from IGS precise clock offset. G03 is the BLOCK IIA satellite launched in the early period, G21 is the BLOCK IIR satellite, G29 is the BLOCK IIR-M satellite, G25 is the BLOCK IIF satellite.

From the Fig. 37.2, the clock offset prediction precision of the GPS BLOCK IIA satellite (G03) is worse, the 2-h prediction precision is about 4 ns and 24-h is

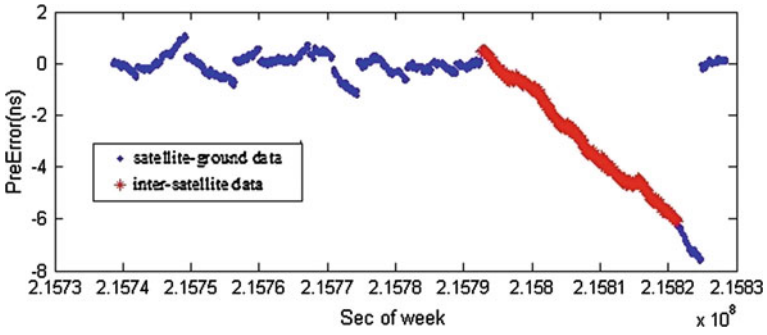

Fig. 37.1 Satellite clock offset prediction result with only the regional satellite-ground data

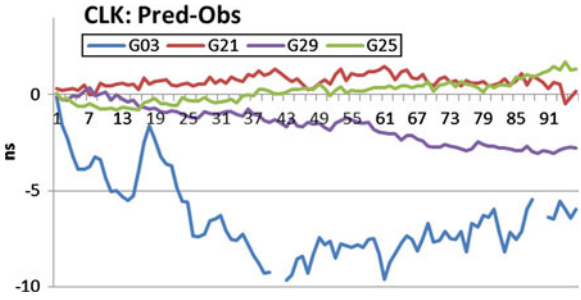

Fig. 37.2 24 h prediction error of GPS satellite clock

about 10 ns; BLOCK IIR and BLOCK IIR-M satellites is much better than BLOCK IIA, the 24-h prediction error is less than 3 ns; BLOCK IIF satellite is more stable and its 24-h predicted error is below 2 ns.

37.4.2 Satellite Clock Offset Prediction Precision Analysis with the Integrated Satellite-Ground and Inter-Satellite Data

In order to make an experimentation analysis of the satellite clock offset prediction method with the integrated satellite-ground and inter-satellite data in this paper, we calculated the above simulated satellite-ground and inter-satellite data and got the satellite clock offset prediction results as following (Fig. 37.3).

The experimentation results show that the integration of the regional satellite-ground data and the inter-satellite data not only remedy the shortage of the regional ground monitoring network but also improve the clock offset prediction precision from 8 to 1.5 ns when the MEO is not observed.

In order to validate the accuracy and the stability of the Hermlert variance component estimation method, the simulation experiment used six arcs of the

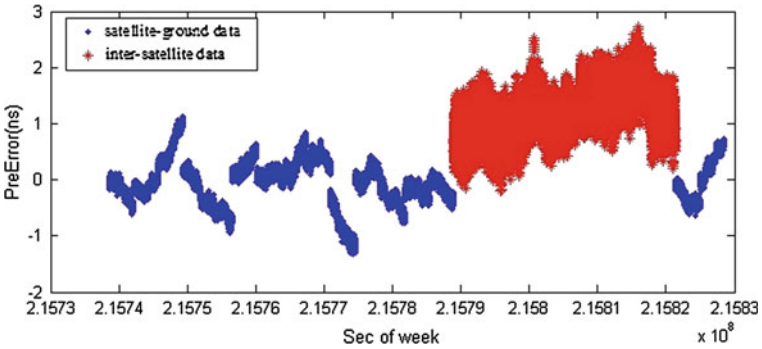

Fig. 37.3 Satellite clock offset prediction results with integrating satellite-ground and inter-satellite data

Table 37.1 The weight and mean variance of satellite-ground and inter-satellite data calculated by the Helmert variance component estimation method

Arc	Satellite-ground weight	Inter-satellite weight	Satellite-ground mean variance (ns)	Inter-satellite mean variance (ns)
Arc1	89.93	1.86	0.105	0.734
Arc2	213.64	1.96	0.068	0.715
Arc3	225.66	1.87	0.067	0.731
Arc4	102.95	1.81	0.098	0.743
Arc5	223.10	1.98	0.067	0.711
Arc6	255.34	1.85	0.063	0.736

MEO satellite observed and non-observed time. The experiment results are in the following (Table 37.1).

From the experiment results, when the satellite-ground and inter-satellite data are integrated and processed, the mean variance are uniform by using the Hermert variance component estimation and the real simulated data. The data weight varies with the observation data precision. When the observation data precision is higher, the weight is bigger. It shows that the Hermert variance component estimation calculation results totally reflect the observation data precision, which can avoid the unsuitable weight problem caused by the satellite-ground and inter-satellite initial difference.

37.5 Conclusions

From the studied results of this paper, the conclusions can be drawn as following:

1. The high precise relative clock offset between two satellites can be calculated using the observation values of two-way inter-satellite link, with the assistant of

satellite-ground link data, the MEO satellite clock offset in its non-observed arc can be obtained, thus the shortage of the regional stations setting to the MEO satellite observed arc. For the regional observed arc, the integrating of the satellite-ground and the inter-satellite link data improve the reliability of the satellite clock offset determination and prediction results, because of the added inter-satellite clock offset at the same time.

2. It is an effectual method to improve the satellite clock offset prediction precision by using the inter-satellite data. The testing results show that the satellite clock offset prediction precision in the MEO non-observed arc decreases from 8 to 1.5 ns, through integrating the regional satellite-ground and inter-satellite data, which can greatly improve the satellite clock offset service capability.
3. When the satellite-ground and inter-satellite data are integrated and processed, Helmert variance component estimation method can avoid the unsuitable weight problem caused by the initial adjustment.
4. At the time of the satellite-ground and inter-satellite data is integrated and processed, the system bias between the inter-satellite and the satellite-ground data should be considered especially. If it is not eliminated or controlled greatly, the system bias will be magnified in clock offset prediction, and the performance of satellite clock offset parameters will be influenced.

Acknowledgements Funding information: Project supported by the National Natural Science Foundation of China (Grant No. 41174027), National 863 plans projects (Grant No. 2012AA8113009).

References

1. Xu Q-F (2001) Measure of interspace and geotectonic–satellite navigation and precision positioning. People liberator arming publishing company, Beijing
2. Liu L (2004) Relativity time synchronization and technique of time synchronization. People liberator arming information and engineering university, vol 4
3. Liu L, Zhu L-F, Han C-H (2009) Model of satellite-ground wireless double direction time synchronization and experimentation analysis. Astron Trans 50(2):189–196
4. Liu L, Zhu L-F, Han C-H (2009) Experimentation analysis of satellite-ground and ground-ground double direction time synchronization. Dissertation proseminar of navigation satellite orbit ascertaining and time synchronization, Xi An, vol 6
5. Yang F-M, Li X (2003) Evolution of laser time synchronization technique. Thesis of countrywide conference about time and frequency in 2003
6. Zheng Z-Y, Lu X-S (2008) Comparison and precision analysis of several GPS satellite clock bias prediction methods. J Shandong Univ Sci Technol (Nat Sci) 27(4):6–11
7. Zhu L-F, Wu X-P, Li C, Dong Z (2007) Vice analysis of gray system model for the satellite clock error predicting. J Astron Metrol Meas, vol 4
8. Guo C-J, Teng Y-L (2011) Application of neural network in satellite clock bias short-term prediction. Sci Surveying Mapp 36:198–200
9. Liu Y-Y, Dang Y-M, Zhang C-F (2012) Application of a combined model in satellite clock bias prediction. Sci Surveying Mapp 37:17–19

10. Ping S (2004) Autonomous navigation technology for navigation constellation: autonomous synchronization among satellites. Aerocraft Meas Control Trans, vol 4
11. Chen J-P, You Z, Jiao W-H (2005) Research on autonav of navigation satellite constellation based on crosslink range and inter-satellites orientation observation. J Astronaut, vol 1
12. Zhang Y (2005) Study on autonomous navigation of constellation using inter-satellite measurement. National defence technology university
13. Yang Y-X, Song L-J, Xu T-H (2002) Robust parameter estimation for geodetic correlated observations. Acta Geodaet Et Cartographic Sin, vol 2
14. Liu C-J, Ma G-F, Qiao S-B (2005) Variance component estimation with gross errors or systematic errors. Bull Surveying Mapp, vol 10
15. Liu C, Ma G (2002) Blunder test and robust solution of variance component estimation for Helmert type. Wtusm Bull Sci Technol, vol 6

Chapter 38
The Influence of Satellite Elevation on Monitoring GNSS System Time Offset

Lin Zhu, Huijun Zhang, Xiaohui Li and Xue Zhang

Abstract Multi-system satellite navigation is an important development direction of Global Navigation Satellite Systems (GNSS) in the future. Because the system time of each satellite navigation system is independent, monitoring GNSS system time offset has become one of key issues solved in multi-system navigation. However, the monitoring accuracy of system time offset is affected by different elevations of satellites. First of all, the influence of satellite elevation on the signal propagation delay errors and monitoring results of system time offset is analyzed. On this basis, six kinds of weighting method based upon satellite elevation are proposed. Finally, with test data provided by a platform that monitors GNSS system time offset at National Time Service Center (NTSC), how various elevation weighting methods and cut-off elevation have an effect on monitoring results are verified. The results show that, for GPS and GLONASS, the monitoring accuracy is different adopting different elevation weighting methods, and the suitable cut-off elevation is 10°.

Keywords Satellite elevation · Weighting method · System time offset · Measuring method

L. Zhu (✉) · H. Zhang · X. Li · X. Zhang
National Time Service Center, The Chinese Academy of Sciences, Lintong, Shaanxi, China
e-mail: zhulin@ntsc.ac.cn

L. Zhu · H. Zhang · X. Li · X. Zhang
Key Laboratory of Precision Navigation Positioning and Timing, Chinese Academy of Sciences, Lintong, Shaanxi, China

X. Zhang
Graduate School of Chinese Academy of Sciences, Beijing, China

J. Sun et al. (eds.), *China Satellite Navigation Conference (CSNC) 2014 Proceedings: Volume III*, Lecture Notes in Electrical Engineering 305,
DOI: 10.1007/978-3-642-54740-9_38,

38.1 Introduction

With the increasing GNSS and the rapidly development of BeiDou Navigation Satellite System, compatibility and interoperability of GNSS is one of inevitable developement direction of Global Navigation Satellite Systems (GNSS). However, as a key component of GNSS, interoperability of GNSS system time is one of key issues that must be solved. Each satellite navigation system has an independent and stable operating system time scale. Although every navigation system time is transferred with UTC, time offset still exists. The time offset between any two satellite navigation systems is called as system time offset [1–3]. It is one of key factors to implement interoperability of GNSS system time that the system time offset be precisely measured.

At the first of this paper, measuring GNSS system time offset is researched. And then, the influence of satellite elevation on Measuring GNSS system time offset is analyzed. Next, various weighting methods based on satellite elevation are proposed. Finally, using test data provided by a monitoring platform of GNSS system time offset at National Time Service Center (NTSC), the influence of various elevation weighting methods on monitoring results are verified.

38.2 Measurement and Error Analysis of GNSS System Time Offset

38.2.1 Resume of Measuring GNSS System Time Offset

In the current development of GNSS system time offset transfer method, the system time offset can be determined by two methods: user-level and system-level [1, 4, 5].

For the user-level method, system time offsets are determined as an uncertain parameter in user receivers. While measuring time offset between two navigation systems, two navigation systems are used, signals from five satellites are received, and then five unknowns (3D position, user clock offset and time offset of two navigation systems) are resolved. The number of unknown increases with the number of applied navigation systems. In the second method, the system time offsets are monitored and then broadcast in the navigation messages to users. (Four satellites in view can determine user position).

In the “open sky” conditions, the monitoring accuracy from these two resolving methods is closed to each other. However, in environments with limited signal availability, especially in so-called “urban canyons”, many advantages, such as fewer unknowns, lower DOP, and lower errors of system time broadcasted offset are existed in system-level method. By comparison, the system-level method is fitter to measuring GNSS time offset [1, 6]. Therefore, the system-level method to measure GNSS system time offset is studied in this paper.

Table 38.1 Errors analysis

Error	Value (ns)
Reference error of monitoring station	2.0
Satellite clock errors	4.5
Satellite orbit errors	4.5
Ionospheric delays	3.0
Tropospheric delays	1.5
Receiver noise and multipath effects	3.0
Measurement noise errors	0.5

Nowadays, there are two techniques in system-level to measure GNSS system time offset. The first is to measure system time offset directly between time-frequency centers of different satellite navigation systems by time transfer links. The second is to measure the system time offset by receiving signal-in-space (SIS) with geodetic time receivers.

The second technique is used by measuring platform of GNSS system time offset at NTSC. The large number of researches and analyses are relied on test data collected by this platform.

38.2.2 Errors Analysis

To measure system time offset with the second technique, the main errors affecting the measuring accuracy are summarized in Table 38.1 [4, 7].

According to Table 38.1, the errors of measuring system time offset with single satellite is estimated as: $\sqrt{2^2 + 4.5^2 + 4.5^2 + 3^2 + 1.5^2 + 3^2 + 0.5^2} \approx 8.06$ ns.

From the satellite constellation distribution, in the case of good observation conditions, the number of visible satellites for each GNSS system is more than 8. Indeed, the number of visible satellites which satellite elevation exceeds 30° is more than 4. Because of the errors of each satellite is standalone, the errors of measuring system time offset with 4 visible satellites are estimated as: $8.06/\sqrt{4} = 4.03$ ns, about 4 ns. Thus, compared with measuring system time offset with single satellite, the monitoring accuracy of system time offset is effectively improved with more satellites.

38.3 The Influence of Satellite Elevation on Monitoring Accuracy

The errors related to elevation are ionospheric delays and tropospheric delays in measuring system time offset by receiving signal-in-space (SIS). In order to study the influences of satellite elevation on system time offset, it is the chief issue to

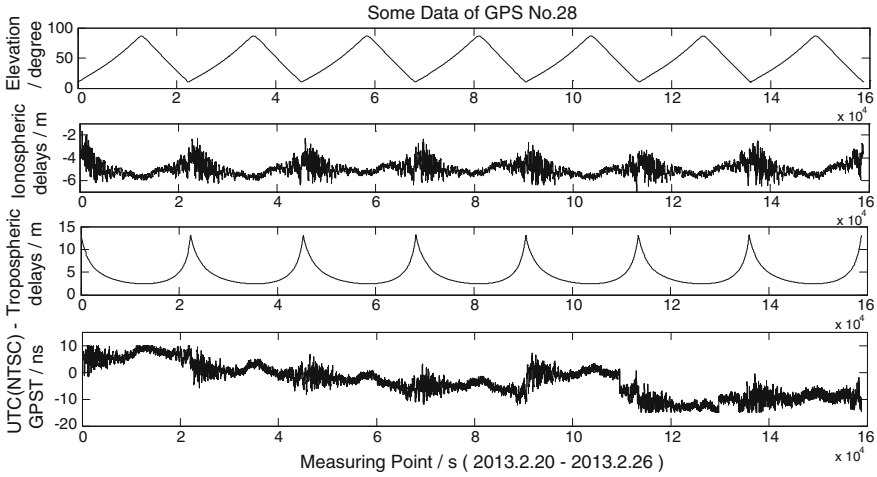

Fig. 38.1 Elevations ionospheric delays, tropospheric delays and monitoring results for GPS 28

analysis the relationships of satellite elevation, ionospheric delays, tropospheric delays and measuring results.

Because that there isn't suitable reference standard that the time offset between GPST and GLONASST. The results of UTC(NTSC)-GPST and UTC(NTSC)-GLONASST as measuring results. And those results are evaluated compared with data in BIPM circular T.

On the antenna side, the propagate path that signal through the atmosphere is longer, and the propagate errors are more. And on the receiver side, if the elevation is lower, the large number of multipath errors is introduced to measure system time offset. Thus, the satellite cut-off elevation is set to 10°

The data for GPS No. 28 and GLONASS No. 4 at visible periods from 20 February 2013 to 26 February 2013 is collected for analysis. It contains elevation, ionospheric delays, tropospheric delays and the system time offset (UTC (NTSC)-GPST or UTC (NTSC)-GLONASST). And then, the cut-off elevation is set to 10°. Comparative results are shown in Figs. 38.1 and 38.2.

As can be seen in above two figures, for GPS and GLONASS, there are some relationships of satellite elevation, ionospheric delays, tropospheric delays and measuring results: the satellite elevation is smaller, the fluctuation of ionospheric delays, tropospheric delays and measuring results is sharper; and the satellite elevation is greater, the fluctuation of ionospheric delays, tropospheric delays and measuring results is slighter [7].

In order to identify the specific relationship between satellite elevation with the ionospheric delays, tropospheric delays and measuring results (UTC (NTSC)-GPST or UTC (NTSC)-GLONASST), some data for GPS No. 28 and GLONASS No. 4 at visible periods on 20 February 2013 is analyzed. And the cut-off elevation is set to 10°. Finally, the distributions of the ionospheric delays, tropospheric

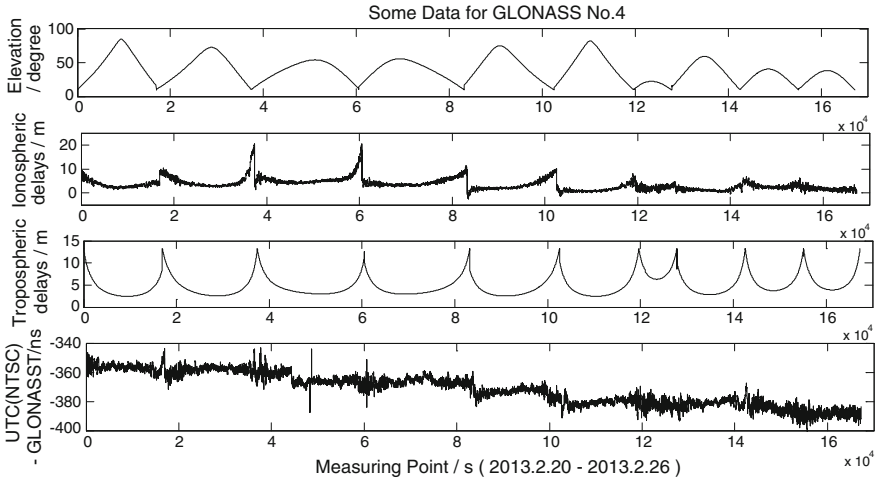

Fig. 38.2 Elevation, ionospheric delays, tropospheric delays and monitoring results for GLONASS 04

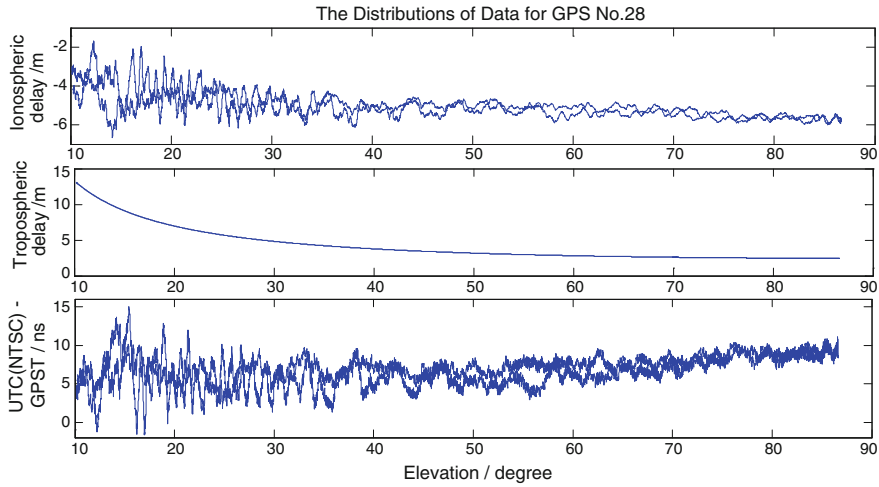

Fig. 38.3 Ionospheric delays, tropospheric delays and monitoring results for GPS 28 at elevation

delays and measuring results with satellite elevation are determined. The results are shown in Figs. 38.3 and 38.4.

As can be seen from the above two figures, if elevation is greater than 30°, the fluctuation of ionospheric delays, tropospheric delays and measuring results is slighter; otherwise, if elevation is smaller than 30°, the fluctuation of comparing data is sharper.

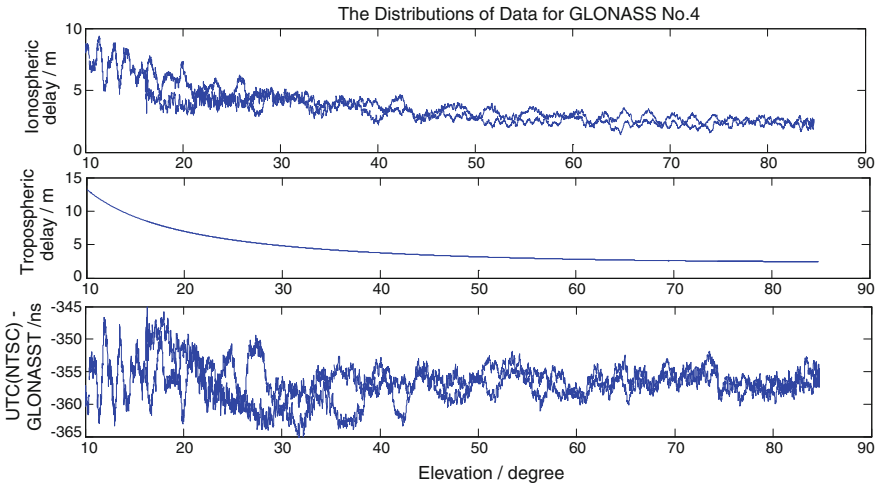

Fig. 38.4 Ionospheric delays, tropospheric delays and monitoring results for GLONASS 04 at elevation

Upon above analysis, it will improve measuring accuracy that taking data which elevation greater 30° measure system time offset while using single satellite. Nevertheless, numerous satellites owned different elevations can be monitored at one monitoring station. In order to improve usage rate of satellites and to balance some influences of each error on measuring results, it is necessary that take the most appropriate method of integrated much satellite's data of different elevation.

38.4 The Influence of Different Weighting Methods on Monitor of System Time Offset

For fully exploiting all satellites data with different elevations at the same time, some different weighting methods based on elevation are constructed to measure system time offset. The influences of taking different weighting functions on measuring results are different. And these influences are compared in this paper.

38.4.1 Various Weighting Methods

According to above conclusions, 6 kinds of simple or common weighting methods based on elevation to measure system time offset are discussed. These weighting methods are expressed as follows [8]:

1. Equal weight function, the weights assigned to

$$p = \frac{1}{N} \tag{38.1}$$

2. Linear function, the weights assigned to

$$\mathrm{p} = \frac{el_i}{\sum_{i=1}^{N} el_i} \tag{38.2}$$

3. Quadratic function, the weights assigned to

$$\mathrm{p} = \frac{el_i^2}{\sum_{i=1}^{N} el_i^2} \tag{38.3}$$

4. Cubic function, the weights assigned to

$$\mathrm{p} = \frac{el_i^3}{\sum_{ii=1}^{N} el_i^3} \tag{38.4}$$

5. Inverse function, the weights assigned to

$$\mathrm{p} = \frac{1/el_i}{\sum_{i=1}^{N} 1/el_i} \tag{38.5}$$

Table 38.2 RMS errors of UTC (NTSC)-GPST at elevations (ns)

	10°	15°	20°	25°	30°	35°	40°
Equal weight function	*3.27*	*3.21*	3.20	*3.35*	*3.25*	*3.54*	*3.59*
Linear function	3.38	3.78	3.38	3.49	3.43	3.81	3.90
Quadratic function	3.75	3.76	3.76	3.83	3.81	4.15	4.25
Cubic function	4.22	4.23	4.23	4.26	4.26	4.51	4.59
Inverse function	3.42	3.26	3.25	3.42	3.30	3.38	3.36
The sin function	3.39	3.41	3.50	3.88	3.64	3.79	3.93

Table 38.3 RMS errors of UTC (NTSC)-GLONASST at elevations (ns)

	10°	15°	20°	25°	30°	35°	40°
Equal weight function	4.04	4.09	3.99	4.18	4.16	4.11	4.42
Linear function	*3.81*	*3.86*	*3.89*	4.02	4.02	4.00	4.37
Quadratic function	3.86	3.87	3.91	*3.98*	*3.99*	*3.98*	*4.36*
Cubic function	3.95	3.95	3.96	3.99	4.00	4.00	4.38
Inverse function	4.92	4.78	4.27	4.50	4.48	4.28	4.53
The sin function	4.56	4.49	4.72	4.87	4.81	4.62	4.47

6. The Sin function, the weights assigned to

$$p = \frac{\sin^2(el_i)}{\sum_{i=1}^{N} \sin^2(el_i)} \tag{38.6}$$

In these functions, p is weights, N is the number of satellites, el is elevation (degrees).

38.4.2 Experiment Results

Based on the experiment data provided by a platform that monitors GNSS system time offset at National Time Service Center (NTSC), the influences of different weighting methods on measuring system time offset are analyzed. Thus, the suitable weighting method and cut-off elevation are determined.

The satellite elevation and measuring results (UTC(NTSC)-GPST and UTC(NTSC)-GLONASST) are collected from March, 2013 to August, 2013. In order to avoid introduce much more atmospheric delays and multipath errors, the cut-off elevation is set from 10° to 40°(Interval of the cut-off elevation is 5°). Meanwhile, the RMS is calculated by measuring results and data in BIPM circular T. The analytical results are shown in Tables 38.2 and 38.3.

Some conclusions are shown in Tables 38.2 and 38.3: for GPS, the RMS is smaller if equal weight function is adopted to measure system time offset; for GLONASS, the linear function is appropriate weighting if elevation is less than 20°, whereas the quadratic function is more suitable than others for other cut-off elevations. Meanwhile, observing many satellites can reduce the error introduced by small elevations at the same time. Mass data demonstrate that the RMS will be small if the cut-off elevation is set to 10°.

38.5 Conclusions

Based on the analysis of measuring errors of GNSS system time offset, the influence of satellite elevation on measuring system time offset is researched. And then, the effects of various weighting methods based on elevation and various cut-off elevations on measuring system time offset are discussed.

Thus, several conclusions are demonstrated:

- Firstly, it is inverse ratio relationship between satellite elevation with ionospheric delays, tropospheric delays and measuring results using single satellite;
- Secondly, for GPS, when taking equal weight function to measure system time offset, the measuring accuracy is better; and for GLONASS, linear function and quadratic function are suitable weighting function;
- Finally, the suitable cut-off elevation is 10° for almost weighting functions when satellites are observed at the same time.

Acknowledgments This paper is supported by Supported by "Western Light Talents training program of CAS"Project (Y109YR2701), 2010, Research on GNSS system time offset monitoring and prediction.

References

1. Moudrak A, Konovaltsev A, Furthner J, Hornbostel A, Hammesfahr J (2004) GPS Galileo time offset: how it affects positioning accuracy and how to cope with it. In: ION GNSS 17th international technical meeting of the satellite division, Long Beach, CA, pp 660–669
2. Merino MMR et al (2001) An integrated GNSS concept, Galileo & GPS, benefits in terms of accuracy, integrity, availability and continuity. ION GPS, pp 11–14
3. Zhang H, Li X, Xu L (2010) Monitoring and prediction of GNSS system time difference. In: China satellite navigation conference, Beijing, May, pp 471–476
4. Zhu L, Zhang H, Li X et al (2013) Measurement and correction method of the system time offset of multimode satellite navigation. In: Proceedings of SPIE 8759. Eighth international symposium on accuracy engineering measurement and instrumentation, p 87591. doi:10.1117/12.2014845
5. Hahn J, Powers E (2005) Implementation of the GPS to Galileo time offset (GGTO). In: Proceedings of the 2005 joint IEEE international frequency control symposium and precise

time and time interval (PTTI) systems and applications meeting (IEEE 05CH37664C), 29–31 Aug 2005, Vancouver, Canada , pp 33–212
6. Li X, Xu L, Zhang H et al (2011) Study on the interoperability of system time. In: China satellite navigation conference, Shanghai, May, pp 319–325
7. Zhu L (2013) Research on one-station and multi-station combined monitoring method of GNSS system time offset. University of Chinese Academy of Sciences
8. Zhou X Error theory and experiment data processing. Beihang University Press, Beijing, 1986

Chapter 39
A Method to Estimate Frequency Stability of an Atomic Clock with Discontinuous Frequency Data

Pengfei Wang, Shenghong Xiao, Feng Zhao, Fang Wang, Shengguo He, Qiang Hao, Xianglei Wang, Zhiwu Cai and Ganghua Mei

Abstract The BeiDou Navigation System has currently no sufficient ground stations to support continuous monitoring frequency data of the atomic clocks contained in the MEO satellites. As a result, the obtained frequency data of MEO satellite clocks are discontinuous, which makes it difficult to estimate the frequency stability of the clocks. To overcome the difficulty, a method of calculation using discontinuous frequency data to estimate frequency stability of an atomic clock is presented in this paper. The calculation can be divided to three steps. Firstly, the discontinuous frequency data are fitted with a polynomial function, and the residuals are obtained after removal of the systematic deviation. Secondly, the discontinuous residuals are linked up to form a new group of continuous residuals, and based on which frequency stability is calculated. Finally, the obtained long-term frequency stability is modified by using bias function developed by Barnes. The method has been tested on a set of frequency data, with length of 4 months, of a rubidium atomic clock. The Allan variance stabilities obtained by the method are in good agreement with those of the calculation based on the original data, which implies that the method is basically feasible.

P. Wang · F. Zhao · F. Wang · S. He · Q. Hao · G. Mei (✉)
Wuhan Institute of Physics and Mathematics, Chinese Academy of Sciences, Wuhan 430071, China
e-mail: mei@wipm.ac.cn

P. Wang
e-mail: wpengfee@foxmail.com

P. Wang · F. Zhao · F. Wang · S. He · Q. Hao · G. Mei
Key Laboratory of Atomic Frequency Standards, Chinese Academy of Sciences, Wuhan 430071, China

P. Wang · S. He · Q. Hao
University of Chinese Academy of Sciences, Beijing 100080, China

S. Xiao · X. Wang · Z. Cai
Beijing Satellite Navigation Center, Beijing 100094, China

J. Sun et al. (eds.), *China Satellite Navigation Conference (CSNC) 2014 Proceedings: Volume III*, Lecture Notes in Electrical Engineering 305,
DOI: 10.1007/978-3-642-54740-9_39,

Keywords Satellite navigation system · MEO satellites · Space rubidium atomic clock · Frequency stability

39.1 Introduction

The BeiDou Navigation System contains GEO, IGSO and MEO satellites [1]. The system is now still a regional one with all ground monitor stations built in China. Based on the stations, continuous time or frequency data of atomic clocks in the GEO and IGSO satellites can be obtained, but obtained data of clocks contained in the MEO satellites are always discontinuous. As the result, there is a serious difficulty to estimate the frequency stability, especially the long-term stability, for the MEO satellite clocks. To overcome the difficulty, a method using time-discontinuous frequency data to estimate frequency stability of an atomic clock is presented. In this paper, we outline main procedures of the method, give a calculation example. Based on analysis of the calculation results, we believe the method is basically feasible.

39.2 Estimation Method

The clock offset of a space atomic clock can be generally written as [2]:

$$x(t) = f(t) + \varepsilon(t) \tag{39.1}$$

where $f(t)$ is the clock offset modeling function, describing systematic clock deviation in time or frequency from the reference, and $\varepsilon(t)$, the clock residual, describing random fluctuation in time or frequency of the clock. All the information about frequency stability of an atomic clock is contained in $\varepsilon(t)$.

The clock offset function is normally obtained from the polynomial fitting of clock data [3], and has the form:

$$f(t) = \sum_{k=0}^{K} a_k t^k = a_0 + a_1 t + \cdots + a_K t^K \tag{39.2}$$

and the residual $\varepsilon(t)$ is then obtained by the removal of $f(t)$ from $x(t)$:

$$\varepsilon(t) = x(t) - f(t) \tag{39.3}$$

In calculation of the frequency stability of an atomic clock, Allan variance [4], $\sigma(2, \tau, \tau)$, is mostly used. At least 16 frequency data are needed to get a credible value of frequency stability at a sampling time, which means that, to obtain the stability at one day, the clock should be tested continually at least 16 days.

The orbital period of an MEO satellite is about 13 h, during which a ground station could acquire a set of clock data with length of 2–5 h. Therefore, the monitored clock data is always composed of many sets, i.e. discontinuous. One set of data has length of 20,000 s at most, enabling to estimate frequency stability with sampling time of 1,000 s, but not sufficient to estimate the middle-term or long-term stability, and the later is more important than the former for a space clock.

It seems to us, to estimate long-term frequency stability of the MEO satellite clock based only one ground monitoring station, that what we could only do is making use of discontinuous frequency data. Main idea of our method is to make a continuous link of the discontinuous data, and then consider the error introduced by linking procedure.

The calculation model of the method data is showed in Fig. 39.1. The dots represent frequency data composed of M sets, Δ_n is time interval between the nth set the $(n + 1)$th one. According to Fig. 39.1, each of the frequency data and its corresponding measurement time could be easily marked. For example, the frequency data of the ith group are written as:

$$F\left[\sum_{n=1}^{i-1}(N_n+\Delta_n)+1\right],\quad F\left[\sum_{n=1}^{i-1}(N_n+\Delta_n)+2\right]\ldots F\left[\sum_{n=1}^{i-1}(N_n+\Delta_n)+N_i\right].$$

and their corresponding measurement times are written as:

$$T\left[\sum_{n=1}^{i-1}(N_n+\Delta_n)+1\right],\quad T\left[\sum_{n=1}^{i-1}(N_n+\Delta_n)+2\right]\ldots T\left[\sum_{n=1}^{i-1}(N_n+\Delta_n)+N_i\right].$$

Polynomial fitting of the frequency data is a needed to determine $f(t)$ expressed in Eq. (39.2). The residual is then obtained after the removal of $f(t)$ from each frequency data. The obtained residual of the mth data in the ith set is:

$$\begin{aligned}\varepsilon\left[\sum_{n=1}^{i-1}(N_n+\Delta_n)-m\right]&=F\left[\sum_{n=1}^{i-1}(N_n+\Delta_n)-m\right]\\&\quad-\sum_{k=0}^{K}b(k)\left\{T\left[\sum_{n=1}^{i-1}(N_n+\Delta_n)-m\right]\right\}^k\end{aligned}\tag{39.4}$$

Through Eq. (39.4), a new set of continuous residual data could be easily constructed, which contains $N_1 + N_2 + \ldots + N_M$ individual data, and based on which, frequency stability could be calculated.

It should be pointed out, in the link process, the time dependence of noises may be destroyed, which would be main source of calculation error. The frequency stability of an atomic clock is determined mainly by five types of noise [4, 5], which are white phase modulation noise (WPM), flicker phase modulation noise (FPM), white frequency modulation noise (WFM), flicker frequency modulation

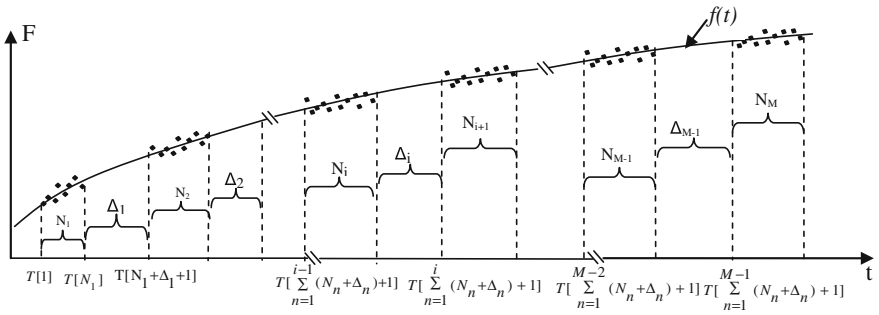

Fig. 39.1 Frequency data measured time-discontinuously (*scatter points*)

noise (FFM) and random walk frequency modulation noise (RWFM). Except for WFM, all the other four noises are time-dependent, and the dependence could be characterized by self-correlation function R(τ). The Fourier transform of R(τ) is power spectral density S(f) [6], whose description in time-domain is $\sigma(2, \tau, \tau)$. In the link process, R(τ) should be destroyed, then $\sigma(2, \tau, \tau)$ should be affected too.

The differences between continuous measurement and discontinuous measurement could be discussed through the model showed in Fig. 39.2, in which T is measurement cycle and τ is sampling time or averaging time. $\tau < T$ means the measurement is discontinuous and the obtained Allan variance is $\langle\sigma(2, T, \tau)\rangle$; while $\tau = T$ means the measurement is continuous and the obtained Allan variance is $\langle\sigma(2, \tau, \tau)\rangle$. Only $\langle\sigma(2, \tau, \tau)\rangle$ is what we want since it reflects real property of an atomic clock. Barnes [7] introduced a bias function to describe the relationship between $\langle\sigma^2(2, T, \tau)\rangle$ and $\langle\sigma^2(2, \tau, \tau)\rangle$:

$$B_2(T, \tau) = \frac{\langle\sigma^2(2, T, \tau)\rangle}{\langle\sigma^2(2, \tau, \tau)\rangle} \tag{39.5}$$

Equation (39.5) implies that, $\langle\sigma^2(2, \tau, \tau)\rangle$, result of continuous measurement, can be obtained from $\langle\sigma^2(2, T, \tau)\rangle$, result of discontinuous measurement, provided $B_2(T, \tau)$ is known.

Not $\langle\sigma(2, \tau, \tau)\rangle$ but $\langle\sigma(2, T, \tau)\rangle$ is what we really get when we make use of the linked residuals to estimate frequency stability. Comparing Figs. 39.1 and 39.2, we find the two measurement methods are quite similar, and the main difference is that r defined by T/τ is constant in Fig. 39.2 but being not in Fig. 39.1. To make use of Eq. (39.5) to modify our calculation result, we introduce concepts of average T and τ with forms respectively as follows:

$$\begin{aligned} T &\approx \frac{\tau_0}{M-1}\sum_{n=1}^{M-1}(N_n + \Delta_n) \\ \tau &\approx \frac{\tau_0}{M}\sum_{n=1}^{M} N_n \end{aligned} \tag{39.6}$$

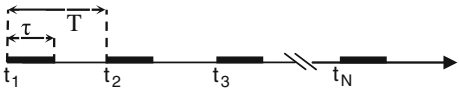

Fig. 39.2 A frequency measurement method

In Eq. (39.6), τ is actually the average length of each data set in Fig. 39.1, and T is the sum of τ and average time gap between two adjacent sets. τ_0 is the sampling time.

The bias function $B_2(T, \tau)$ is dependent on noise type and the ratio *r*. Determination of $B_2(T, \tau)$ will be discussed next in the calculation example.

39.3 An Calculation Example of the Method

We use a set of rubidium clock output frequency data to test the method introduced above. The original data, obtained through continuous measurement of 4 months, with sampling time of 100 s, is shown in Fig. 39.3. Part of the data is selected to simulate the measurement results of an MEO satellite clock, which is shown in Fig. 39.4. In the selection, length of a data set is randomly chosen to be in 2–5 h, and the time gap between adjacent sets, in 13–20 h.

Firstly the three order polynomial fitting curve of discontinuous frequency data was performed, obtaining $f(t)$ as red line shown in Fig. 39.4. Then, according to Eq. (39.4), we calculate and link clock residuals to form a new set of continuous residuals, as shown in Fig. 39.5. The new set of data has a length of 21 days, enabling to calculate 10,000 s stability and day stability. Allan variance stabilities were obtained based on the new set of data, and so were those based on the original residuals data. Comparing the results shown in Fig. 39.6, it can be found that the two results are in good agreement when τ is smaller than 10,000 s, and there is a considerable difference when τ exceeds 10,000 s.

The modification of long-term frequency stability ($\tau > 10{,}000$ s) is discussed below. The discussion should be based on analysis of the influence of different types of noise on frequency stability. As is well known, when the five types of noise are uncorrelated, the Allan variance $\langle\sigma^2_{\text{total}}\rangle$ is the sum of five variances contributed by the five types of noise:

$$\langle\sigma^2_{total}\rangle = \langle\sigma^2_{WPM}\rangle + \langle\sigma^2_{FPM}\rangle + \langle\sigma^2_{WFM}\rangle + \langle\sigma^2_{FFM}\rangle + \langle\sigma^2_{RWFM}\rangle \tag{39.7}$$

Relationship of Allan variances of the five types of noise with τ is given in Table 39.1 [4].

Since WPM and WFM are high frequency noises, they could be neglected in our case when averaging time is bigger than 100 s. On the other hand, RWFM is a noise with very long periods, and actually in Fig. 39.6 we does not found increase in instability, or more accurately, the instability as τ does not increase when τ is smaller than 4,000 s, therefore it can be assumed that in 200–1,000 s of τ region,

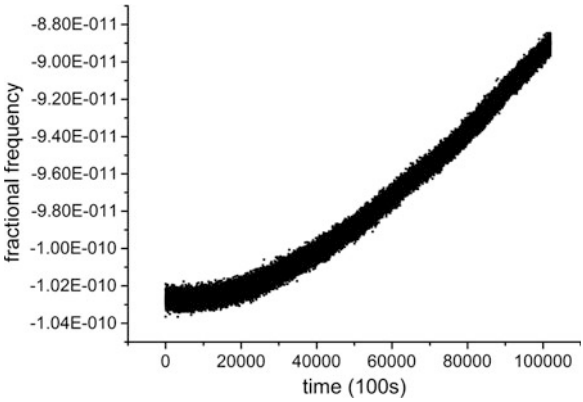

Fig. 39.3 The fractional frequency data of a rubidium clock

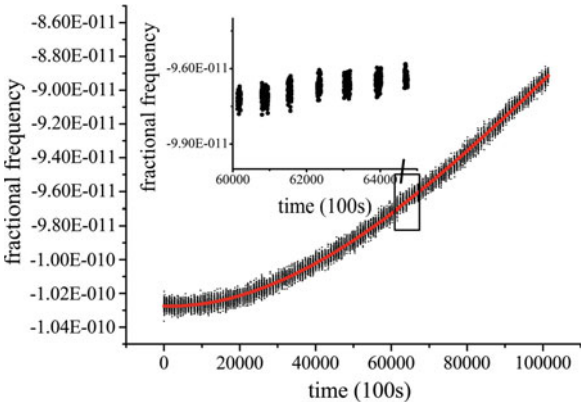

Fig. 39.4 Time-discontinuous frequency data and three order clock offset function curve (*red line*)

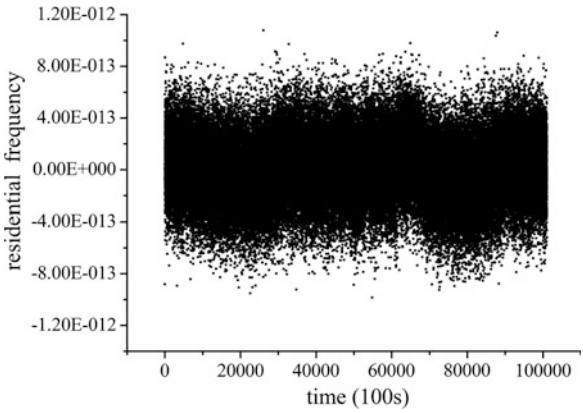

Fig. 39.5 Three order residuals of the linked data

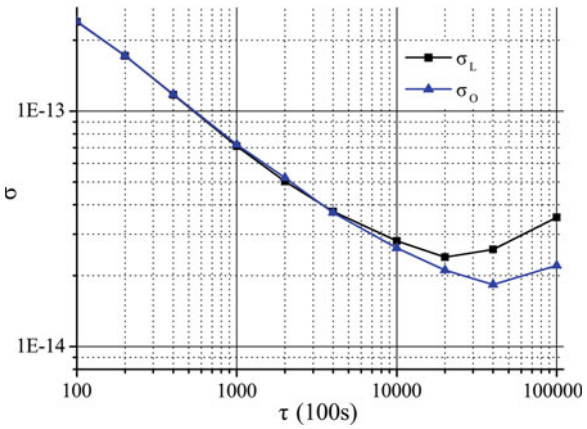

Fig. 39.6 Allan variance calculated from the linked data (σ_L), and that from the original data (σ_O)

Table 39.1 Relationship between Allan variance and sampling time τ for different types of noises

	WPM	WFM	WFM	FFM	RWFM
$\langle\sigma(2, \tau, \tau)\rangle$	$\propto\tau^{-1}$	$\propto\tau^{-1}$	$\propto\tau^{-1/2}$	$\propto\tau^{0}$	$\propto\tau^{1/2}$

the stability is contributed by only by the WFM and the FFM noises, and Eq. (39.7) could be rewritten as:

$$\langle\sigma^2_{total}\rangle \approx \langle\sigma^2_{WFM}\rangle + \langle\sigma^2_{FFM}\rangle \tag{39.8}$$

According Table 39.1, $\langle\sigma^2_{\mathrm{WFM}}\rangle$ is proportional to τ^{-1}, and $\langle\sigma^2_{\mathrm{FFM}}\rangle$ is a constant, we have the relations:

$$\begin{aligned}\langle\sigma^2_{total}\rangle\big|_{\tau=\tau_1} &\approx \langle\sigma^2_{WFM}\rangle\big|_{\tau=\tau_1} + \langle\sigma^2_{FFM}\rangle \\ \langle\sigma^2_{total}\rangle\big|_{\tau=\tau_2} &\approx \frac{\tau_1}{\tau_2}\langle\sigma^2_{WFM}\rangle\big|_{\tau=\tau_2} + \langle\sigma^2_{FFM}\rangle\end{aligned} \tag{39.9}$$

In our previous calculation we knew that $\langle\sigma^2_{\mathrm{total}}\rangle|_{\tau=400}$ is 1.288×10^{-26} and $\langle\sigma^2_{\mathrm{total}}\rangle|_{\tau=1,000}$ is 5.256×10^{-27} (see Fig. 39.6), thus from Eq. (39.9) we get that $\langle\sigma^2_{\mathrm{FFM}}\rangle$ is 1.733×10^{-28} and $\langle\sigma^2_{\mathrm{WFM}}\rangle|_{\tau=1,000}$ is 5.083×10^{-27}.

When τ exceeds 10,000 s, contribution of RWFM should be considered, and Eq. (39.7) could be written as:

$$\langle\sigma^2_{total}\rangle \approx 5.083 \times 10^{-27} \times 1,000/\tau + 1.733 \times 10^{-28} + \langle\sigma^2_{RWFM}\rangle \tag{39.10}$$

where the unit of τ is second. Considering the effect of link of data, $\langle\sigma^2_{\mathrm{RWFM}}\rangle$ should be written as $\langle\sigma^2_{\mathrm{RWFM}}(2, \mathrm{T}, \tau)\rangle$ more accurately, while what we really want is $\langle\sigma^2_{\mathrm{RWFM}}(2, \tau, \tau)\rangle$. Thus, the long-term frequency stability should be modified.

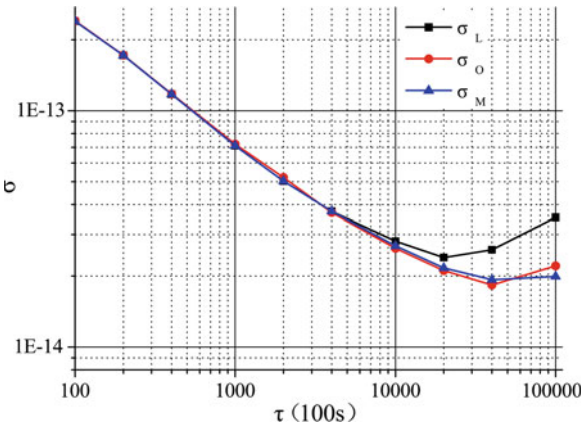

Fig. 39.7 Three calculated results of Allan variance. σ_O is obtained with original data, σ_M and σ_L are obtained with linked data and with and without modification respectively

According to Eq. (39.6), T is calculated to be 59,400 s and τ to be 12,600 s, from which we know that r is 6.5, and the bias function B_2 is 6.5 according to reference [7]. Finally, the long-term frequency stability is modified to be:

$$\langle \sigma^2_{total} \rangle \approx 5.083 \times 10^{-27} \times 1,000/\tau + 1.733 \times 10^{-28} + \langle \sigma^2_{RWFM} \rangle / 6.5 \quad (39.11)$$

Modification calculation was performed only for the results with τ exceeding 10,000 s according to Eq. (39.11). In fact, modification of the results is not necessary with τ no larger than 10,000 s, if we see the results shown in Fig. 39.6. The results with and without modification, together with the results calculated with original data, are shown in Fig. 39.7. From Fig. 39.7 we see that the modification leads a much better agreement of long-term stability with those obtained from original data.

In order to verify further the applicability of the method, two more groups of discontinuous frequency data are generated from the original data. In one group, the length of data set is randomly chosen in 3–6 h with a mean time being 4.5 h (16,200 s), and the time gap between adjacent sets is the same as the example above, while in the other group, the length of data set is the same as the example above, and the time gap between adjacent sets is randomly chosen in 13–16 h with a mean time being 14.5 h (52,200 s). The calculated results are shown in Table 39.2, in which the original results are given also for comparison.

The results obtained from the discontinuous data are very close to those obtained from the original data when sampling time is no larger than 10,000 s, in this case no modification is needed. The deviation of the result without modification from the original result occurs when sampling time is above 10,000 s, and it increases with the sampling time. The modified results, however, are much more close to the original results, and the maximum deviation is less than 3×10^{-15}.

Comparison of results shown in Fig 39.7 and Table 39.2 suggests effectiveness of the proposed method. In the method, however, average values are used for T and τ, which is not exactly the same case in Barnes's model. The error introduced by this treatment is worth further studying.

Table 39.2 Allan variances calculated by the residuals of three groups of discontinuous frequency data

Sampling time (s)		1×10^4	2×10^4	4×10^4	1×10^5
$\tau = T$	σ_O (10^{-14})	2.62	2.11	1.83	2.21
$\tau = 12{,}600$ s	σ_L (10^{-14})	2.81	2.39	2.58	3.53
T = 59,400 s	σ_M (10^{-14})	2.69	2.16	1.93	1.99
$B_2 = 6.5$					
$\tau = 16{,}200$ s	σ_L (10^{-14})	2.66	2.55	2.80	3.09
T = 59,400 s					
$B_2 = 4.0$	σ_M (10^{-14})	2.50	2.21	2.14	2.39
$\tau = 12{,}600$ s	σ_L (10^{-14})	2.72	2.42	2.45	3.54
T = 52,200 s	σ_M (10^{-14})	2.61	2.19	1.99	1.96
$B_2 = 5.7$					

σ_O is obtained with original data, σ_L and σ_M are obtained with linked data and with and without modification respectively

39.4 Summary

A method using discontinuous frequency data to estimate frequency stability of an atomic clock is presented in this paper. The process of method can be divided to three steps. Firstly, the discontinuous data are fitted with a polynomial function, and the clock residuals are obtained after removal of systematic deviation. Secondly, the discontinuous residuals are linked up to form a new set of continuous residuals with sufficient length, and frequency stability is calculated based on the new set of data. Finally, long-term frequency stability is modified by using the bias function developed by Barnes. The method was tested with experimentally obtained frequency data. Part of the data was selected to construct a discontinuous frequency data. The Allan variance stability was calculated by using both of the discontinuous data and original data, and the two results are in good agreement. This suggests effectiveness of the method. The method may be useful in frequency stability estimation of an atomic clock in the MEO satellite by using only one ground monitor station.

References

1. Web: http://www.beidou.gov.cn/xtjs.html
2. Barnes JA et al (1971) Characterization of frequency stability. IEEE Trans Instrum Meas 20(2)
3. Guo H (2006) Study on the analysis theories and algorithms of the time and frequency characterization for atomic clocks of navigation satellites, p 144
4. Allan DW (1996) Statistics of atomic frequency standards. Proc IEEE 54(2):221–230
5. Rutman J, Walls FL (1991) Characterization of frequency stability in precision frequency sources. Proc IEEE 79(6):952–960
6. Riehle F (2004) Frequency standards: basics and applications. WILEY-VCH Verlag GmbH & Co. KGaA, Germany, pp P54–P57
7. Barnes JA (1969) Tables of bias functions, B_1, and B_2, for variances based on finite samples of processes with power law spectral densities. NBS Tech. Note 375, Jan 1969

Chapter 40
Study to Spaceborne Rubidium Atomic Clocks Characteristics and Ground Test Requirements

Jun Xie

Abstract This paper summarizes the experience and results throughout the development process of the Spaceborne Rubidium Atomic Frequency Standard (SRAFS) in Beidou navigation satellite system, analyzes the characteristics of SRAFS, as well as the effect of different states between the in orbit operation status and the ground test status. It presents the ground test program and the main requirements in the development process of SRAFS and puts forward issues need to pay attention, so that the technology level and product quality of the China SRAFS are improved and standardized.

Keywords Spaceborne rubidium atomic frequency standard (SRAFS) · SRAFS characteristics · Ground test

40.1 Introduction

By the establishment of the time reference and the space position reference, the satellite navigation system becomes the basic infrastructure to provide users with high-precision, highly reliable positioning, velocity and timing services.

The spaceborne atomic clock is the core device to build the time reference and the space position reference. Its performance and product quality directly affect the measurement accuracy and service performance of satellite navigation system.

The design principle and the realization principles of Spaceborne Rubidium Atomic Frequency Standard (SRAFS) are basically the same as the ground used rubidium atomic clock. However, due to differences of the application environment and the special requirements of the satellite, it causes the differences between

J. Xie (✉)
China Academy of Space Technology, 5142 Box 56 Subbox Beijing 100094, China
e-mail: xiebook@sina.com

J. Sun et al. (eds.), *China Satellite Navigation Conference (CSNC) 2014 Proceedings: Volume III*, Lecture Notes in Electrical Engineering 305,
DOI: 10.1007/978-3-642-54740-9_40,

the SRAFS and the ground used rubidium atomic clock, such as the product scheme design selection, various module design, component and material selection, test evaluation and experiment verification.

Currently, the Beidou navigation satellite system (BDS) relies on SRAFS to generate the high-precision, highly reliable time and frequency reference signal for satellite. With the construction and development requirements of BDS, the research work of SRAFS as well as engineered products made a series of achievements and progress. The data analysis to ground experiment and in-orbit status is continuously improved and standardized [1].

This paper summarizes the experience and results throughout the development process of the Spaceborne Rubidium Atomic Frequency Standard (SRAFS) in Beidou navigation satellite system, analyzes the characteristics of SRAFS, as well as the effect of different states between the in orbit operation status and the ground test status. It presents the ground test program and the main requirements in the development process of SRAFS and puts forward issues need to pay attention, so that the technology level and product quality of the China SRAFS are improved and standardized.

40.2 SRAFS Milestones in China

The study of atomic clock originated from 1950s in China. In 1965 the first prototype of the ground cesium frequency standard was born. In 1973 the first prototype of the ground rubidium frequency standard was developed [2]. But until 1999 the spaceborne atomic clock product engineering research was officially included in the pre-research program, and the study to engineered product of the SRAFS was carried out.

In 2004 with the official approval of BDS project, rubidium atomic clock is determined to be the spaceborne device by the satellite system. Meanwhile, the technical specification, the interface requirements and the engineering requirements were proposed, which accelerates the SRAFS development process in China. Under the unified organization of satellite systems, according to the spaceborne product requirements, a number of domestic units conscientiously sum up experiences, strengthen research and exchanges, and achieved fruitful results.

At 15:00 on September 9, 2006, China's first SRAFS with Shijian 8 satellite was successfully launched from the Jiuquan Satellite Launch Center. After the SRAFS was powered on in-orbit, the acquisitioned telemetry data was sent back to the ground station, compared and analyzed with the ground test data. The results showed that this rubidium atomic clock product works properly in orbit after experiencing the rocket launch, the low pressure and the vacuum environment, the interface between SRAFS and the satellite platform is matching, and its performance in-orbit meets the specification.

On April 14, 2007, a Beidou navigation satellite configured with 4 domestic SRAFS was successfully launched at the Xi'chang Satellite Launch Center. After

the satellite into orbit, 2 of the 4 SRAFSs were switched on. According to the transmitted telemetry data, the SRAFSs working status meet the design requirement. Its telemetry parameters such as lock time, light intensity signal and rubidium signal coincide with the ground results of vacuum environment experiment. The Beidou satellite designs the phase measuring device for the two working SRAFS, the in-orbit data verifies the stable status of the two SRAFSs.

Since 2009, China's Beidou navigation satellites launched are configured with domestic SRAFS, which constitutes the foundation to achieve the BDS's function and performance.

During the development process of the Beidou's SRAFS, a series of problems have been solved such as anti-mechanic environment impact, thermal interface matching, and electromagnetic compatibility, under the condition of normal temperature and pressure measurement and under vacuum testing. Lots of in-orbit data of SRAFSs are collected and compared with the ground testing results, the SRAFS difference characteristics between ground and in-orbit are clear. Based on the above analysis, the necessary experiment and test program are standardized.

At present, we proposed higher performance requirements to the SRAFS of Beidou navigation satellite, that the specification of long-term frequency stability and frequency drift rate is near to 10^{-14}. Therefore, the SRAFS characteristics need to be further analyzed, and set up targeted and effective experiment and test verification during the ground development process. The test program and requirement of SRAFS need to be standardized.

40.3 SRAFS Compositions

A SRAFS is generally composed of physical part, circuit part, power supply part and structural component.

The physical part comprises rubidium lamp, filter bubble, absorption bubble (some products integrate filter bubble and absorption bubble), C field coil, microwave resonate cavity, magnetic shield, heater, photo detector and so on.

The circuit part comprises voltage controlled crystal oscillator, servo circuit, frequency multiplier, frequency synchronizer, amplifier, thermal control circuit, and so on.

The power part provides various voltage and current signal for the physical part, circuit part, and provides power on and off function of SRAFS. The acquisition circuit of telemetry data and the remote command circuit are generally integrated into the power part.

The structural part includes the necessary shielding design, heat transfer design, support and connection design, and buffer protection structure.

By comparing the SRAFS compositions with the ground rubidium atomic clock, the physical part of SRAFS has the characteristics of anti-mechanic environment impact, thermal interface design and miniaturization; the circuit part and the power part have the characteristics of component selection, electromagnetic

design, heater circuit design, power requirement; the structural part requires small size, light weight and highly integrated design [3].

The design and development process of the SRAFS parts must be in accordance to the spaceborne product standards, and are required to be verified by the ground experiment and test.

40.4 SRAFS Development Requirements and Characteristics

According to the product design and production processes, after the process of design, production, experiment and test verification, it needs to take the tests and experiments of the subsystem and the satellite system level. In this process, most of the time SRAFS works under the normal temperature and pressure, which is completely different from the in-orbit environment (such as pressure and temperature).

During the ground debugging and testing process, SRAFS needs to often power on and off for several times. The working time period after power on is not very long. It does not reflect the long-term performance of SRAFS. This working status is different from the in-orbit working mode with long-term and continuous power supply.

In the satellite launch process SRAFS experiences the shock, noise and vibration impact caused by the rocket launch and the satellite separation process. The environment varies from the normal pressure to the low pressure, the final vacuum status.

After the satellite into orbit, SRAFS needs to be long-term working under the space radiation environment to reliably provide high precision and highly stability signal.

Since the differences of the working environment (pressure, temperature and space radiation), working status (power on or off, the duration of continuous power on, working environment), the mechanic response of the satellite experienced, requirement for long life and high reliability and quality, SRAFS has the following development requirements and characteristics:

40.4.1 High Precision and High Stability

As SRAFS provides the time and frequency reference for the satellite, its output signal performance needs to meet the design requirement of the satellite system such as frequency accuracy, frequency stability, frequency drift rate and signal power.

High precision and high stability performance are the primary requirement to SRAFS. It is also the necessary condition for the navigation satellite to use SRAFS.

40.4.2 Adaption to Various Environments

SRAFS needs to adapt the impact and changes of mechanical environment, thermal environment, pressure changes, electromagnetic environment and space radiation. It needs to meet the ground testing requirements of subsystem and satellite system level. It needs to reach the life requirements of 3 year storage and 12 year in-orbit work after the ground acceptance test.

40.4.2.1 Mechanical Environment

During the SRAFS design and development process, the special effective technology is need to ensure stable and reliable support and connection among rubidium lamp, filter bubble, absorption bubble, C field coil, crystal oscillator and various circuit boards. SRAFS components do not have the phenomenon of displacement, deformation and damage after shock, noise and vibration process.

Before and after the mechanical environment experiment, SRAFS performance needs to be checked whether any change appears.

40.4.2.2 Thermal Environment

Due to the ground conditions, the ground debugging, experiment and use are often carried out under the laboratory (about 18–28 °C) environment. While after the satellite into orbit, the satellite system designs and configures specific thermal cabin for SRAFSs, whose bottom board temperature is controlled in about 0 °C, and the temperature shift range is less than 1 °C within an orbital period. In the other words: the temperature condition to develop and use the SRAFS is quite different after the satellite into orbit such as the configured temperature value, the range of temperature change and the rate of temperature change.

As the difference existence of the above thermal environment, when SRAFS is under the normal temperature and pressure debugged and tested, the performance specification in the vacuum environment and temperature range between −10 and +10°C (generally configured as about 0 °C) in orbit needs to be fully considered. The SRAFS performance must meet the specification requirements under the various conditions and environment. Mean while, the SRAFS design needs to ensure the basic rubidium function to adapt the laboratory temperature condition during the test and experiment of subsystem and satellite system level. At least its accuracy of output frequency and short-term frequency stability meet the

specification requirement, and it ensures the SRAFS will not be damaged and keep the good quality and life due to the wide range of temperature changes and higher temperature.

The working temperature difference of SRAFS on the ground and in-orbit is one of the difficulties for the SRAFS design and development process, which needs to take special design methods and carry out repeated test verification under different status.

40.4.2.3 Pressure Change

Pressure changes may cause the different working status of SRAFS's physical part, and the change of internal heat transfer path.

During the ground debugging and test process, SRAFS's internal heat transfer changes by convection, radiation and conduction. Since no air and pressure in orbit, there is not the heat transfer path by convention, the internal heat transfer paths change inevitably. SRAFS design and development process must take targeted measures to pressure change, that ensure SRAFS keep the same performance and quality under the air pressure change.

40.4.2.4 Electromagnetic Environment

SRAFS is signal source with high precision and high stability. It has a high electromagnetic interference requirement. As a satellite comprises plenty of internal cable, high power amplifier, multiple frequency source and magnetic moment, different operation status of satellite may cause internal changes of electromagnetic environment. In addition, spaceborne product needs to highly integrated and miniaturization. SRAFS design must fully consider the balance the product layout of each module, and take the effective technology for electrical isolation and magnetic shielding.

40.4.2.5 Radiation Environment

After satellite into orbit the spaceborne product will be long-term operating in the environment of space radiation and earth's magnetic field. The solar electromagnetic radiation, the solar flares, the geomagnetic storms and others may generate lots of charged particles and plasma, and may result the changes of product's component and raw material, which may eventually cause the function and performance changes of spaceborne products [4].

Therefore, the SRAFS design needs to fully consider the impact of space radiation environment to the selected component and raw material, good protection design and effective test verification to total dose of ionizing radiation effects, displacement damage effects, single event effects, and effects of surface charge and

discharge. In addition, it needs to control the quality loss coefficient and the deflated loss coefficient of raw material, meets the requirements of derating design and safety margin factor, and ensures the stability and reliability of the SRAFS performance and function.

40.4.2.6 Ground Testing Requirement of Subsystem and Satellite System

After the power on of SRAFS, the temperature control circuit of each SRAFS parts needs a period of time to get into their balance status. Then the output signal is locked and its frequency accuracy and short-term frequency stability may meet the technical specification requirements.

During the ground testing process of subsystem and satellite system, since the requirement of satellite development and testing program, SRAFS are often switched on and off for many times. Incorrect operation of switch on and off may cause negative effect to SRAFS.

For the presence of multiple operations of switch on and off with short working time after power on, SRAFS's parameters need to have good consistent characteristic and avoid the presence of significant parameter difference after multiple operations of power supply. Furthermore, the SRAFS designer needs to propose according to the product's features using requirements during the test and operation process of subsystem and satellite system level such as status of power supply, time interval and temperature range. These methods may ensure the safety and quality of SRAFS.

40.4.3 High Integration, Light Weight and Low Power Requirements

Because of the capacity constraints of rocket, spaceborne product requires high integration, small size and light weight as well as low power. Therefore, in the premise of ensuring the function and performance of SRAFS, right design program (including components and raw materials) and advanced technologies must be selected.

During the high integration and miniaturization process of SRAFS, some negative factors need to be considered due to the weight limitation for the thermal design, electromagnetic compatibility design and security design. High integration may cause internal signal coupling and radiation effect that increase the difficulties of safety shielding and isolation methods. Small size enlarges the thermal effects among internal components and modules that thermal control method is not easy to take. Light weight may constraint the use of magnetic shielding and filter. These

factors and effects must be paid full attention and a reasonable balance during the design and development process of SRAFS.

40.4.4 Long Life and High Reliability Requirements

As the spaceborne product has the non-maintenance characteristic, SRAFS has the long life and high reliability requirements.

SRAFS design needs to obey component derating requirement, complete reliability model and prediction, analyze failure model and propose preventive methods, carry out the special reliability experiments for both physical part and circuit part, and take the necessary life experiment. Meanwhile, the frequency, power and other parameters of SRAFS need to quantified control for the key parts, such as physical part, crystal oscillator circuit, servo circuit, thermal control circuit and microwave cavity. This quantified control ensures the quality and reliability to reach the product target of long life, high reliability, continuity and stability in orbit.

40.4.5 Remote Command and Telemetry Function

User may control the power supply as well as some adjustments of the ground-used rubidium clock by the designed buttons and switches on the device, and its working status displays on the device screen. While the control to a SRAFS has to send the command signals by the remote control circuit, and drive the SRAFS circuit (including switches, relays or state memory) to operate. A SRAFS has at least 2 commands: product switched on command and switched off command.

SRAFS telemetries are the key parameters to directly reflect the working status and performance of the in-orbit product. The telemetry generally includes switch working state, lock indicator, signal quantity of light intensity, rubidium signal status and temperatures.

40.5 Ground Experiment and Testing Requirements

For the development requirement and product characteristics, SRAFS needs to take the following program of the ground experiments and test during the ground development process: initial performance test under normal temperature and pressure, power pull side experiment, mechanical experiment, magnetic experiment, high temperature burn-in experiment, temperature circling experiment, thermal vacuum experiment, final performance test under the thermal vacuum environment [5].

Comparing with other spaceborne products, in the above experiments SRAFS has certain requirements need special attention. The follows proposes the testing requirements focusing on the verification program related to the performance specification of SRAFS.

40.5.1 Tests Under Normal Temperature and Pressure

The working environment of SRAFS in—orbit is different from that in the normal laboratory temperature and pressure. The experiment and test in the normal temperature and pressure target to verify the basic working status, parameter range of telemetries, executing state of remote command. Some performance may be also tested like the frequency accuracy, phase noise, output power, signal spectrum, and the short-term frequency stability from 10 to 1,000 s sampling period.

It needs to carry out multiple tests for the basic working status, parameter range of telemetries, executing state of remote command, and establish the envelop of normal range. Only the SRAFS is stably locked, the frequency accuracy is tested after the SRAFS locked. 10–100 s frequency stability is tested at least 3 h after the SRAFS powered on. 1000 s frequency stability needs to be taken 3 days after powered on. The multiple testing data present the basic performance characteristics of a SRAFS, and will be compared with the related data measured during the test of subsystem and satellite system level for further analysis.

40.5.2 Temperature Circling Test

As the satellite platform provides temperature range guarantee to SRAFS from -10 to $+10$ °C, the temperature circling experiment for each SRAFS is required.

Under the working status of low temperature, the heating capability and power consumption need to be focused, the temperature control capability is verified and the main performance specifications of SRAFS are tested, such as frequency accuracy, output signal power, signal spectrum and short-term stability.

Under the working status of high temperature, besides the above mentioned parameters, the temperature changes in key parts need to in particular concerned by checking the telemetries of SRAFS. The temperature coefficients must meet the SRAFS design to ensure that the working temperature of rubidium lamp does not overheat.

40.5.3 Thermal Vacuum Test

The ground thermal vacuum experiment of SRAFS is the most important experiment before the product's delivery to the satellite. Based on the long term experiment and test in a vacuum environment, it may give the sufficient assessment to the SRAFS output signal data during preheating process, balancing process and burn-in process. These tests may provide the general characteristics and the prediction value of SRAFS after the satellite into orbit.

SRAFS has requirement to the device of thermal vacuum test. Besides providing the required vacuum level, the device needs to have ability of accurate temperature control, can acquisition data from multiple paths, and may continuously process mass data and output their tabulations and graphics.

According to the plenty of experiment data in the vacuum environment, the analysis result shows: that when SRAFS is powered on in vacuum environment, the output signal frequency and the short-term frequency stability under 100 s may reach balance after about 3 days; the 1,000 s frequency stability may reach balance after about 7 days; and the long-term frequency stability and the days drift rate may begin to be tested at least 20 days after continuous power up.

Based on the series data obtained from the previous domestic SRAFSs, it is required that SRAFS has to carry out at least 2 months continuous experiment and test in thermal vacuum environment. The long-term stability given from this test may basically reflect the characteristics of this SRAFS. The analysis to the days drift rate in 2 months may draw its changing trends. In general, the drift rate may be further reduced gradually after the 2 month.

SRAFS test has the following requirements for thermal vacuum experiment:

1. According to the experiment standard of spaceborne product, multiple cycle of normal vacuum tests are required. Even if some SRAFS telemetry is designed with different value under the conditions of thermal vacuum and normal temperature and pressure, but the telemetry under the same condition must keep stability.
2. After completion of the general program for spaceborne product, the bottom board temperature of the vacuum cabin needs to be reconfigured to a certain value (usually set at 0 °C, according to the temperature in-orbit reference), and then take a long-term thermal vacuum test. In the first 7 days, the frequency accuracy, output power, 10 ms to 1,000 s frequency stability are measured. The transients change process of the output signal just after SRAFS powered on and the change trends of its telemetry parameters need to be paid attention.
3. After 7 day thermal vacuum experiment, under the premise that the tested SRAFS meets the required function and performance, the experiment keeps the same status and is continuously carried out for 2 months. During this process, it focuses on the change trend analysis to the days drift rate of the output signal frequency, and the changes of telemetry parameter. The parameters should be continuous and smooth without any change dramatically.

40.6 Conclusions

Comparing with the ground-used rubidium clock, SRAFS has the special differences such as the operation environment, use requirement and product design. SRAFS provides high-precision and high stability output signal, may adapt various environment, and has the characteristics of high integration, light weight, low power, long life and high reliability.

This paper summarizes and analyzes the SRAFS characteristics, combining the Beidou's development experience, proposes and standardizes the ground experiment requirements of SRAFS. It is helpful to ensure and promote the technology level and product quality of domestic SRAFS, and is significative to develop higher performance SRAFS in the future.

References

1. Xie J, Wang J, Mi H (2012) Analysis of Beidou navigation satellites in-orbit state. In: China Satellite Navigation Conference (CSNC) 2012 proceedings, lecture notes in electrical engineering 161. Springer, Berlin, pp 111–122. doi:10.1007/978-3-642-29193-7_25
2. Wang Y (2012) Proceedings of the atomic clock and time frequency system (in Chinese). National Defense Industry Press, pp 144–149
3. White J, Beard R (2001) Why the space clock is different. In: Proceedings of the 33rd annual PTTI meeting, pp 7–16
4. Cai Z (2005) Spacecraft anti-radiation design. From CAST, spacecraft electric product stability design series (in Chinese)
5. Xu F (2002) Satellite engineering (in Chinese). China Aerospace Press, China, pp 257–273

Part III
Integrated Navigation and New Methods

Chapter 41
Target Localization for MIMO Radar with Unknown Mutual Coupling Based on Sparse Representation

Jianfeng Li and Xiaofei Zhang

Abstract Multiple-input multiple-output (MIMO) radars have attracted lots of attention for their special advantages. As a key issue, target localization method for MIMO radar has also been studied by lots of researchers. However, most of these methods are based on the ideal array model, and the practical unknown mutual coupling will make them have great performance degradation or even fail to work. Sparse representation (SR) has obtained a rapid development in the field of array signal processing over the past few years for its loose requirement for data amount and high-resolution feature. But only one-dimensional angle is considered, and the unknown mutual coupling will make the dictionary hard to construct when apply it for MIMO radar target localization. Even if the mutual coupling is compensated, the two-dimensional angle in MIMO radar will make the dictionary very huge, as well as enhance the inter-correlation of the dictionary. As a result, it brings higher complexity without performance improvement. However, according to our study, both the influences of mutual coupling and two-dimensional angle are occurred in space domain, but the output data of MIMO radar contains both the information in space and time domains. Thus, the influenced space domain is avoided and Doppler frequency in the time domain is utilized in this paper and not only the mutual coupling is avoided, but also a one-dimensional dictionary for the Doppler frequency can be obtained. The Doppler frequency can be firstly obtained via the sparse recovery technique, and meanwhile, the influenced direction matrix can be acquired from the non-zero rows of the recovered matrix. According to the special characteristic of the mutual coupling in uniform linear array (ULA), select the special rows of the direction matrix to eliminate the effect of mutual coupling and estimate the angles. The estimated target parameters (two-dimensional angles and Doppler frequency) are automatically paired, and the proposed algorithm has better estimation performance and can detect more targets than the subspace-based method and SR-based method. Simulation results verify the effectiveness of the algorithm.

J. Li (✉) · X. Zhang
College of Electronic and Information Engineering, Nanjing University of Aeronautics and Astronautics (NUAA), Nanjing, China
e-mail: lijianfengtin@126.com

J. Sun et al. (eds.), *China Satellite Navigation Conference (CSNC) 2014 Proceedings: Volume III*, Lecture Notes in Electrical Engineering 305,
DOI: 10.1007/978-3-642-54740-9_41,

Keywords MIMO radar · Unknown mutual coupling · Target localization · Sparse representation

41.1 Introduction

As a new system radar, multiple-input multiple-output (MIMO) radar utilizes antenna array to transmit signals that are orthogonal to each other, and utilizes array to receive the reflect wave. Compared to conventional phased-array radar, it has greater spatial freedom and bigger array aperture, so it can improve the target detecting ability and the parameter estimation resolution [1–5]. As a key issue for MIMO radar, target parameter estimation methods in MIMO radar have been studied and researched by lots of scholars. Subspace methods like Reduced-dimension multiple signal classification (RD-MUSIC) method [5], Root-MUSIC method [6] and Estimation of signal parameters via rotational invariance technique (ESPRIT) method [7–9], and the iteration methods like Parallel factor analysis (PARAFAC) methods [10, 11] all can obtain pretty well parameter estimation performance. Parameter estimation based on sparse representation (SR) [12] has also been applied for target localization in MIMO radar [13] for its loose requirement for data amount and high-resolution feature. But the two-dimensional angle in MIMO radar will not only increase the complexity, but also degrade the estimation performance.

The methods mentioned above are all based on the perfect array manifold, which is always influenced by practical mutual coupling between the antennas. The unknown mutual coupling will make the above methods have performance degradation, or even fail [14, 15]. An angle estimation method for MIMO radar based on the subspace (referred to as "ESPRIT-like") was proposed in 14, and the mutual coupling can be eliminated via the removing of the data of some antennas, which can lead to the array aperture loss. Reference [15] proposed a one-dimensional direction of arrival (DOA) estimation method for antenna array based on SR. The removing of some outputs is also needed, but it can obtain high resolution estimation for application of SR.

In summary, the unknown mutual coupling and two-dimensional angle bring up problems for target localization in MIMO radar. But it should be noted that the output of MIMO radar contains information in both space and time domain. Thus, in this paper, the influenced information in the space domain is avoided, and Doppler frequency is utilized to construct the dictionary based on the information in the time domain. The problems caused by the unknown mutual coupling and two-dimensional angle are avoided. The Doppler frequency can be estimated firstly based on SR, then the two-dimensional angle can be obtained through the recovered data. The simulation demonstrate that the proposed algorithm has better estimation performance and can detect more targets than the ESPRIT-like method [14] and SR method [15].

41.2 Data Model

As Fig. 41.1 shows, assume that the transmit and receive arrays of bistatic MIMO radar system are M-element and N-element uniform linear arrays (ULAs), respectively. The arrays are both located in the y-axis with half-wavelength spacing between adjacent antennas. Assume that there are K targets located in the y–z plane with (θ_k, ϕ_k) being the direction of departure (DOD) and direction of arrival (DOA) of k-th target. According to [4–6], the output of the matched filters at the receiver can be expressed as,

$$\mathbf{x}(t) = [\tilde{\mathbf{a}}_r(\phi_1) \otimes \tilde{\mathbf{a}}_t(\theta_1), \ldots, \tilde{\mathbf{a}}_r(\phi_K) \otimes \tilde{\mathbf{a}}_t(\theta_K)]\mathbf{s}(t) + \mathbf{n}(t) \tag{41.1}$$

where $\mathbf{s}(t) = [s_1(t), \ldots, s_K(t)]^T$, and $s_k(t) = \beta_k e^{j2\pi f_k t/f_s}$ with β_k, f_k and f_s being the reflecting coefficient, Doppler frequency, and the pulse repeat frequency, respectively. $\mathbf{n}(t)$ is an MN $\times$ 1 Gaussian noise vector. $\tilde{\mathbf{a}}_r(\phi_k) \otimes \tilde{\mathbf{a}}_t(\theta_k)$ is the Kronecker product of the receive and the transmit steering vectors for the k-th target, and they are influenced by the mutual coupling in practice

$$\tilde{\mathbf{a}}_r(\phi_k) = \mathbf{C}_r \mathbf{a}_r(\phi_k) \tag{41.2.a}$$

$$\tilde{\mathbf{a}}_t(\theta_k) = \mathbf{C}_t \mathbf{a}_t(\theta_k) \tag{41.2.b}$$

where $\mathbf{C}_r$ and $\mathbf{C}_t$ represent the mutual coupling matrices (MCM), and they can be expressed as banded symmetric Toeplitz matrices [14, 15]

$$\mathbf{C}_r = toeplitz\left(c_0^r, \ldots, c_n^r, 0, \ldots, 0\right) \tag{41.3.a}$$

$$\mathbf{C}_t = toeplitz\left(c_0^t, \ldots, c_m^t, 0, \ldots, 0\right) \tag{41.3.b}$$

where $c_p^r (p = 0, \ldots, n)$ and $c_q^t (q = 0, \ldots, m)$ stand for the mutual coupling coefficients. $\mathbf{a}_r(\phi_k)$ and $\mathbf{a}_t(\theta_k)$ are the steering vectors without considering the mutual coupling, and they are expressed as Vandermonde structures

$$\mathbf{a}_r(\phi_k) = \left[1, u_k, \ldots, u_k^{N-1}\right]^T \tag{41.4.a}$$

$$\mathbf{a}_t(\theta_k) = \left[1, v_k, \ldots, v_k^{M-1}\right]^T \tag{41.4.b}$$

where $u_k = e^{-j\pi \sin \phi_k}$ and $v_k = e^{-j\pi \sin \theta_k}$.

Collect J snapshots in the time domain, then the output will be

$$\mathbf{X} = [\mathbf{x}(1), \ldots, \mathbf{x}(J)] = \tilde{\mathbf{A}}\mathbf{S} + \mathbf{N} \tag{41.5}$$

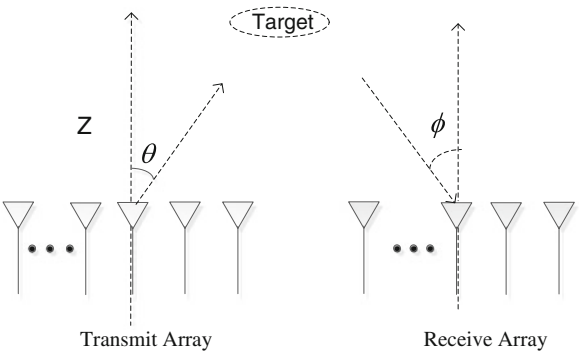

Fig. 41.1 Framework of MIMO radar

where $\tilde{\mathbf{A}} = [\tilde{\mathbf{a}}_r(\phi_1) \otimes \tilde{\mathbf{a}}_t(\theta_1), \ldots, \tilde{\mathbf{a}}_r(\phi_K) \otimes \tilde{\mathbf{a}}_t(\theta_K)]$, $\mathbf{N} = [\mathbf{n}(1), \ldots, \mathbf{n}(J)]$, is the noise matrix with zero mean and covariance matrix $\sigma^2\mathbf{I}_{MN}$. $\mathbf{S} = [\mathbf{s}(1), \ldots, \mathbf{s}(J)]$. Which can be expressed as

$$\mathbf{S} = \mathbf{\Phi}\mathbf{B}^H \tag{41.6}$$

where $\mathbf{\Phi} = diag(\beta_1, \beta_2, \ldots, \beta_K)$, $\mathbf{B} = [\mathbf{b}(f_1), \mathbf{b}(f_2), \ldots, \mathbf{b}(f_K)]$, and

$$\mathbf{b}(f_k) = \left[e^{-j2\pi f_k/f_s} \quad e^{-j4\pi f_k/f_s} \quad \ldots \quad e^{-j2J\pi f_k/f_s} \right]^T \tag{41.7}$$

41.3 Target Localization for MIMO Radar with Unknown Mutual Coupling

It can be shown that the direction matrix $\tilde{\mathbf{A}}$ contains the different delays caused by the locations of the antennas, i.e. the difference in the space domain. But it can also be shown that $\tilde{\mathbf{A}}$ contains two-dimensional angle (DOD and DOA) information and is influenced by unknown mutual coupling. The other side, the matrix $\mathbf{B}$ represents the difference in the time domain, and it contains only the information of the Doppler frequency. Furthermore, it is independent from the mutual coupling. In the follow section, we will start from matrix $\mathbf{B}$ and complete the target localization.

41.3.1 Doppler Frequency Estimation Based on SR

Obtain the conjugate transpose of the output data as

$$\begin{aligned}\mathbf{Y} &= \mathbf{X}^H \\ &= \mathbf{S}^H \tilde{\mathbf{A}}^H + \mathbf{N}^H \\ &= \mathbf{B}\boldsymbol{\Phi}^H \tilde{\mathbf{A}}^H + \mathbf{N}^H \\ &= \mathbf{B}\boldsymbol{\Omega} + \mathbf{N}^H\end{aligned} \tag{41.8}$$

where $\boldsymbol{\Omega}=\boldsymbol{\Phi}^H\tilde{\mathbf{A}}^H$. Use $\bar{f}_1,\bar{f}_2,\ldots,\bar{f}_L$ to denote all the possible Doppler frequencies, and construct one-dimensional dictionary $\boldsymbol{\Theta} = [\mathbf{b}(\bar{f}_1),\ldots,\mathbf{b}(\bar{f}_L)]$ according to (41.7). Obviously, $\boldsymbol{\Theta}$ contains all the K columns of B. Correspondingly, expand $\boldsymbol{\Omega}$ to a taller sparse matrix Q, which satisfies

$$\mathbf{Q}(l,:) = \begin{cases} \boldsymbol{\Omega}(k,:) & \text{if } \bar{f}_l = f_k, \quad k = 1,\ldots,K \\ \mathbf{0}_{1\times MN} & \text{other} \end{cases} \quad l = 1,\ldots,L \tag{41.9}$$

where $\mathbf{Q}(l,:)$ is the l-th row of Q. According to the construction above, it can be shown that $\mathbf{B}\boldsymbol{\Omega} = \boldsymbol{\Theta}\mathbf{Q}$. Thus the data in (41.8) can be expressed as

$$\mathbf{Y} = \boldsymbol{\Theta}\mathbf{Q} + \mathbf{N}^H \tag{41.10}$$

It can be indicated that if the sparse matrix $\mathbf{Q}$ can be recovered from $\mathbf{Y}$, then the Doppler frequency can be estimated via the positions of the non-zero rows in $\mathbf{Q}$. The problem can be formulated as

$$\begin{aligned} &\text{minimize } \|\mathbf{Q}\|_{1,2} \\ &\text{sugject to } \|\mathbf{Y} - \boldsymbol{\Theta}\mathbf{Q}\|_F \le \xi \end{aligned} \tag{41.11}$$

where $\|\mathbf{Q}\|_{1,2} \triangleq \sum_{l=1}^{L} \|\mathbf{Q}(l,:)\|_2$, $\|\cdot\|_2$, denotes the 2-norm of a vector. ξ is the up bound of the fitting error, and it is determined by the noise variance. The calculation method of ξ has been presented in Refs. [12, 15]. Here a simple calculation method is given, according to (41.10)–(41.11),

$$\begin{aligned}\xi \approx \left\|\mathbf{N}^H\right\|_F &= \sqrt{tr\left(\mathbf{N}^H\mathbf{N}\right)} = \sqrt{tr\left(\mathbf{N}\mathbf{N}^H\right)} = \sqrt{tr\left(\sigma^2\mathbf{I}_{MN}\right)} \\ &= \sqrt{MN\sigma^2}\end{aligned} \tag{41.12}$$

where $tr(\cdot)$ is the trace of a matrix. According to the subspace methods in [5–9], the noise variance σ^2 in (41.12) can be estimated via the mean of the (MN-K) smaller eigen-values of the receive data $\mathbf{X}$.

Substitute the obtained ξ and (41.11) into sparse recovery tool SPGL1 [16], then the sparse matrix Q can be obtained. The positions of non-zero rows or the

rows that have relative larger absolute values in Q will give the estimations of Doppler frequencies.

41.3.2 Two-Dimensional Angle Estimation for the Targets

The positions of non-zero rows in the sparse matrix Q give the estimations of the Doppler frequencies, and according to (41.9), the non-zero rows themselves are the estimation of the matrix $\mathbf{\Omega}$. As $\mathbf{\Omega} = \mathbf{\Phi}^H \tilde{\mathbf{A}}^H$, then

$$\tilde{\mathbf{A}} = \mathbf{\Omega}^H \mathbf{\Phi}^{-1} \tag{41.13}$$

As $\mathbf{\Phi}$ is a diagonal matrix, the direction matrix $\tilde{\mathbf{A}}$ can be estimated via the normalization of each columns of $\mathbf{\Omega}^H$. The k-th column of $\tilde{\mathbf{A}}$ can be written as $\tilde{\mathbf{a}}_k = \tilde{\mathbf{a}}_r(\phi_k) \otimes \tilde{\mathbf{a}}_t(\theta_k)$, and take each M elements of $\tilde{\mathbf{a}}_k$ to form a column, then a matrix $\tilde{\mathbf{F}}_k$ with the dimension $M \times N$ can be obtained

$$\tilde{\mathbf{F}}_k = \tilde{\mathbf{a}}_t(\theta_k)\tilde{\mathbf{a}}_r^T(\phi_k) \tag{41.14}$$

After the singular value decomposition (SVD) of $\tilde{\mathbf{F}}_k$, $\mathbf{F}_k = \mathbf{U}\mathbf{\Lambda}\mathbf{V}^H$, the largest left singular vector and the right singular vector are u and v, respectively. Then

$$\tilde{\mathbf{a}}_t(\theta_k) = \mathbf{u}/\mathbf{u}(1), \ldots, \tilde{\mathbf{a}}_r(\phi_k) = (\mathbf{v}/\mathbf{v}(1))^* \tag{41.15}$$

Now the steering vectors $\tilde{\mathbf{a}}_t(\theta_k)$ and $\tilde{\mathbf{a}}_r(\phi_k)$ are obtained, but the angles can not be estimated directly for the internal unknown mutual coupling. Define the select matrices as

$$\mathbf{J}_1 = [\mathbf{0}_{(N-2n)\times n}, \mathbf{I}_{(N-2n)\times(N-2n)}, \mathbf{0}_{(N-2n)\times n-1}] \tag{41.16.a}$$

$$\mathbf{J}_2 = [\mathbf{0}_{(M-2m)\times m}, \mathbf{I}_{(M-2m)\times(M-2m)}, \mathbf{0}_{(M-2m)\times m}] \tag{41.16.b}$$

Then

$$\mathbf{J}_1\tilde{\mathbf{a}}_r(\phi_k) = \mathbf{J}_1\mathbf{C}_r\mathbf{a}_r(\phi_k) = \alpha_{rk}\mathbf{a}_{r1}(\phi_k) \tag{41.17.a}$$

$$\mathbf{J}_2\tilde{\mathbf{a}}_t(\theta_k) = \mathbf{J}_2\mathbf{C}_t\mathbf{a}_t(\theta_k) = \alpha_{tk}\mathbf{a}_{t1}(\theta_k) \tag{41.17.b}$$

where $\alpha_{rk} = \sum_{p=-n}^{n} c_{|p|}^r u_k^{p+n}$, $\alpha_{tk} = \sum_{q=-m}^{m} c_{|q|}^t v_k^{q+m}$, $\mathbf{a}_{r1}(\phi_k)$ and $\mathbf{a}_{t1}(\theta_k)$ are the first ($N-2n$) and ($M-2m$) rows of $\mathbf{a}_r(\phi_k)$ and $\mathbf{a}_t(\theta_k)$, respectively. They still have Vandermonde structures.

Let $\bar{M} = M - 2m$ and $\bar{N} = N - 2n$, as α_{rk} and α_{tk} are both scalars, which can be eliminated via normalization. Thus after the processing of (41.17a), $\mathbf{a}_{r1}(\phi_k)$ and $\mathbf{a}_{t1}(\theta_k)$ can be obtained. Their phases are $\mathbf{p}_{rk} = -\text{angle}(\mathbf{a}_{r1}(\phi_k)) =$

$[0, \pi \sin \phi_k, \ldots, (\bar{N}-1)\pi \sin \phi_k]^T$ and $\mathbf{p}_{tk} = -\text{angle}(\mathbf{a}_t(\theta_k)) = [0, \pi \sin \theta_k, \ldots, (\bar{M}-1)\pi \sin \theta_k]^T$ Let $\mathbf{g}_r = [0, \pi, \ldots, (\bar{N}-1)\pi]$ and $\mathbf{g}_t = [0, \pi, \ldots, (\bar{M}-1)\pi]$, and then the least squares (LS) solutions of $\sin \phi_k$ and $\sin \theta_k$ are $\sin \phi_k = \mathbf{g}_r^+ \mathbf{p}_{rk}$ and $\sin \theta_k = \mathbf{g}_t^+ \mathbf{p}_{tk}$, respectively, where $(\cdot)^+$ is the generalized inverse of a matrix. Finally, the two-dimensional angles can be estimated as

$$\hat{\theta}_k = \sin^{-1}(\mathbf{g}_t^+ \mathbf{p}_{tk}),\ \hat{\phi}_k = \sin^{-1}(\mathbf{g}_r^+ \mathbf{p}_{rk}) \tag{41.18}$$

41.3.3 Summary of the Algorithm

The steps of the algorithm for target localization in MIMO radar with unknown mutual coupling based on SR are summarized below,

1. Obtain the conjugate transpose of the receive data Y, and construct the one-dimensional dictionary $\boldsymbol{\Theta}$ of the Doppler frequency via (41.7).
2. According to ξ obtained in (41.12) and (41.11), use sparse recovery tool SPGL1 to recover the sparse matrix Q.
3. Utilizes the positions of non-zero rows in the sparse matrix Q to estimate Doppler frequencies, and utilizes the non-zero rows themselves to estimate the direction matrix $\tilde{\mathbf{A}}$.
4. Reshape each column of $\tilde{\mathbf{A}}$, and according to (41.15)–(41.18), obtain the estimation of the two-dimensional angle after the SVD and selecting matrices.

Remark 1 Both the estimations of the Doppler frequencies and angles are corresponding to the non-zero rows of Q, so the estimated parameters are automatically paired.

Remark 2 According to (41.16)–(41.17), selecting matrices are also utilized in this paper, and it may also lead to the array aperture loss. But it should be noted that selecting matrices are utilized after the estimations of the direction matrices, so it will not influence the maximum detectable number of targets. In the simulation below, it can be shown that the proposed algorithm can detect more targets than the other two methods with the same number of antennas.

41.4 Simulation Results

Define the root mean square error (RMSE) of the angle estimation as $\frac{1}{K}\sum_{k=1}^{K}\sqrt{\left(\frac{1}{1{,}000}\sum_{w=1}^{1{,}000}\left[\left(\hat{\theta}_{k,w}-\theta_k\right)^2+\left(\hat{\phi}_{k,w}-\phi_k\right)^2\right]\right)}$, where $\hat{\theta}_{k,l}$ and $\hat{\phi}_{k,l}$ are the estimations of DOD and DOA in the w-th Monte Carlo trail, respectively.

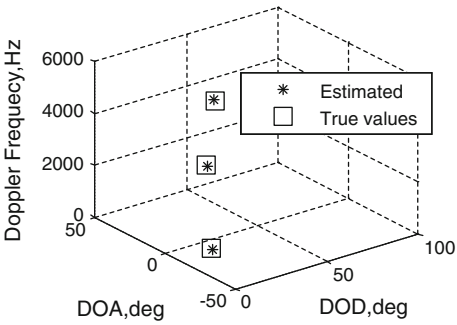

Fig. 41.2 Estimation result of the proposed algorithm

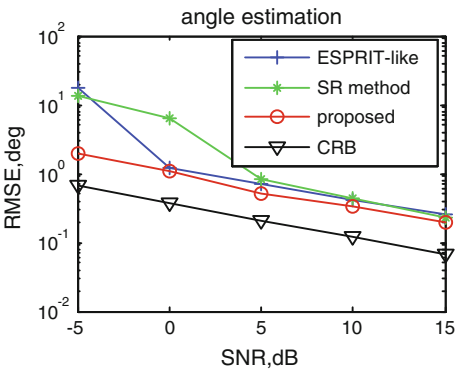

Fig. 41.3 Angle estimation performance comparison

Assume that there are $K = 3$ targets with the angles being $(\theta_1, \phi_1) = (10°,-20°)$, $(\theta_2, \phi_2) = (30°, 10°)$ and $(\theta_3, \phi_3) = (50°, 30°)$. The mutual coupling coefficients in the transmit and receive arrays are $[1, 0.2 + 0.1j]$ and $[1, -0.3 - 0.2j]$, respectively.

Figure 41.2 shows the Doppler frequency and angle estimation result of the proposed algorithm when $M = 8$, $N = 6$, $J = 50$ and Signal to noise ratio (SNR) is 0 dB. For comparison, the true values are also shown in the figure. It can be indicated that the DOD, DOA and Doppler frequency can be estimated clearly.

The angle estimation performance comparison between our algorithm, ESPRIT-like method [14], SR method [15] and Cramer–Rao Bound (CRB) [17] is presented in Fig. 41.3. $M = 8$, $N = 6$, $J = 50$ are used, and it can be found that the proposed algorithm has smaller RMSE than the other two, especially in low SNR. In addition, the proposed is very close to the CRB.

Figure 41.4 is the estimation result of the three algorithms when the number of antennas is small ($M = 5$, $N = 4$, $J = 50$). As there are only a few antennas, ESPRIT-like method and SR method are both failed, but the proposed algorithm can still accurately estimate the two-dimensional angles. So the proposed algorithm can detect more targets than the other two methods with the same number of antennas.

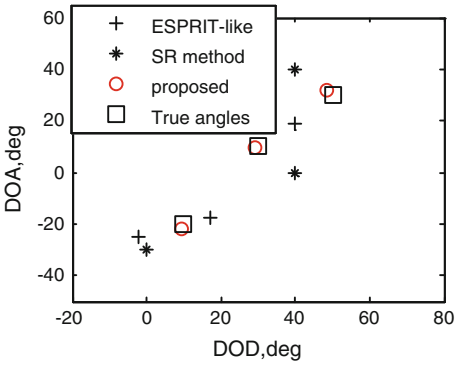

Fig. 41.4 Angle estimation result with few antennas

41.5 Conclusion

In this paper, the target localization problem for bistatic MIMO radar with unknown mutual coupling is studied, and a method based on SR is proposed. The SR of the Doppler frequency is utilized, and the method can obtain high resolution angle estimation benefit from the application of SR. Meanwhile, the adverse influences caused by the mutual coupling and two-dimensional angle in the space domain can be avoided. The simulation and comparison in the paper verify the effectiveness of the proposed algorithm.

Acknowledgments This work is supported by China NSF Grants (61371169,61071164), Funding of Jiangsu Innovation Program for Graduate Education (CXZZ13_0165), Funding for Outstanding Doctoral Dissertation in NUAA (BCXJ13-09), Priority academic program development of Jiangsu high education institutions and the Fundamental Research Funds for the Central Universities (NS2013024,kfjj130114)

References

1. Fishler E, Haimovich A, Blum RS, Cimini LJ, Chizhik D, Valenzuela RA (2004) MIMO radar: an idea whose time has come. In: Proceedings of IEEE radar conference, pp 71–78
2. Sharma R (2010) Analysis of MIMO radar ambiguity functions and implications on clear region. In: Proceedings of IEEE radar conference, pp 544–548
3. Li J, Liao G, Griffiths H (2011) Bistatic MIMO radar space-time adaptive processing. In: Proceedings of IEEE international radar conference, pp 498–502
4. Bekkerman I, Tabrikian J (2006) Target detection and localization using MIMO radars and sonars. IEEE Trans Signal Process 5(10):3873–3883
5. Zhang X, Xu L, Xu L, Xu D (2010) Direction of departure (DOD) and direction of arrival (DOA) estimation in MIMO radar with reduced-dimension MUSIC. IEEE Commun Lett 14(12):1161–1163
6. Bencheikh ML, Wang YD, He HY (2010) Polynomial root finding technique for joint DOA DOD estimation in bistatic MIMO radar. Signal Process 90(9):2723–2730
7. Duofang C, Baixiao C, Guodong Q (2008) Angle estimation using ESPRIT in MIMO radar. Electron Lett 44(12):770–771

8. Jinli C, Hong G, Weimin S (2008) Angle estimation using ESPRIT without pairing in MIMO radar. Electron Lett 44(24):1422–1423
9. Yunhe C (2010) Joint estimation of angle and Doppler frequency for bistatic MIMO radar. Electron Lett 46(2):170–172
10. Zhang X, Xu Z, Xu L, Xu D (2011) Trilinear decomposition-based transmit angle and receive angle estimation for multiple-input multiple-output radar. IET Radar Sonar Navig 5(6):626–631
11. Nion D, Sidiropoulos ND (2009) Adaptive algorithms to track the PARAFAC decomposition of a third-order tensor. IEEE Trans Signal Process 57(6):2299–2310
12. Malioutov D, Cetin M, Willsky AS (2005) A sparse signal reconstruction perspective for source localization with sensor arrays. IEEE Trans Signal Process 53(8):3010–3022
13. Liu Y, Wu M, Wu S (2010) Fast OMP algorithm for 2D angle estimation in MIMO radar. Electron Lett 46(6):444–445
14. Zheng ZD, Zhang J, Zhang JY (2012) Joint DOD and DOA estimation of bistatic MIMO radar in the presence of unknown mutual coupling. Signal Process 92(12):3039–3048
15. Dai J, Zhao D, Ji X (2012) A sparse representation method for DOA estimation with unknown mutual coupling. IEEE Antennas Wirel Propag Lett 11:1210–1213
16. Berg EV, Friedlander MP (2007) SPGL1: a solver for large-scale sparse reconstruction. http://www.cs.ubc.ca/labs/scl/spgl1
17. Stoica P, Nehorai A (1990) Performance study of conditional and unconditional direction-of-arrival estimation. IEEE Trans Signal Process 38(10):1783–1795

Chapter 42
Navigation Using Invariants of Gravity Vectors and Gravity Gradients

Xiaoyun Wan and Jinhai Yu

Abstract The paper develops and analyzes the application of invariants of gravity vectors and gravity gradients in gravity matching navigation. Compared with the traditional method based on gravity gradient tensors, there is no need for the attitude signal in the method of invariants. The invariants are introduced firstly and the formulas to calculate them are given; and then the thought of matching navigation is discussed and some algorithms are introduced. By using the accurate gravity field model which was well developed previously, some numerical simulations are conducted to test the feasibility of the algorithm. It indicates that the accuracy of the matching navigation based on invariants of gravity vectors and gravity gradients are same as that of the navigation based on components of gravity vectors and gravity gradients when there is no attitude observation error. However, if attitude errors exist, the matching navigation using the method of invariants has an obvious advantage with a much higher accuracy. Since in many cases, attitude observation with high accuracy is difficult, such as conditions under water, the method of navigation given in the paper can be used more conveniently. Similarly, the idea can also be used in matching navigation using information of geomagnetic field.

Keywords Gravity vectors · Gravity gradients · Invariants · Navigation and positioning

X. Wan (✉)
Qian Xuesen Laboratory of Space Technology, Youyi Road 104, Beijing 100094, China
e-mail: wxy191954@126.com

X. Wan · J. Yu
College of Earth Science, University of Chinese Academy of Sciences, Yuquan Road 19, Beijing 100049, China
e-mail: yujinhai@ucas.ac.cn

J. Sun et al. (eds.), *China Satellite Navigation Conference (CSNC) 2014 Proceedings: Volume III*, Lecture Notes in Electrical Engineering 305,
DOI: 10.1007/978-3-642-54740-9_42,

42.1 Introduction

Gravity matching navigation is passive, so it can meet the requirements of submarine for high accuracy navigation in long time. Many countries conducted many investigations on this kind of navigation. Metzger and Jircitanno [1] introduced the technology of navigation using gravity gradients to improve the accuracy of inertial navigation; Jekeli [2] discussed the effect of gravity field on inertial navigation; Behazd and Behrooz [3] introduced the principle of the Iterative Closest Contour Point (ICCP) algorithm. Wang and Bian [4] discussed ICCP algorithm for gravity aided inertial navigation and [5] investigated the Terrain Contour Matching (TERCOM) algorithm; [6] introduced the application of maximum correlation in gravity aided navigation; Liu [7] and [8] both systemically investigated the gravity aided inertial navigation and performed many simulation experiments; Tong et al. [9] proposed a new matching algorithm based on local gravity map using two-dimension Gaussian function.

Most of the above mentioned investigations focus on the algorithm of matching navigation, such as different kinds of search algorithm, the construction of back ground model and so on, but few work was involved in the physical quantity for matching. The current popular quantities for matching are gravity anomalies or gravity gradients. For the former, the latitude is needed which would cause some errors since the position is not known; for the latter, there are 6 components for a gravity gradient tensor where attitude data should be known. The paper investigates the application of invariants of gravity vector and gravity gradient tensor in matching navigation. This paper firstly discusses the fundamental principles and algorithm in the Sect. 42.2, where a theory of invariants and the matching function are both introduced; the Sect. 42.3 gives some numerical experiments to test the feasibility of the algorithm; finally some conclusions are given.

42.2 Algorithm of Navigation

42.2.1 Invariants of Gravity Vectors and Gravity Gradient Tensor

Letting x, y, z be three axes of the coordinate system, as for gravity vector we have,

$$g = |\mathbf{g}| = \sqrt{g_x^2 + g_y^2 + g_z^2} \tag{42.1}$$

where g_x, g_y, g_z mean three components of gravity vector $\mathbf{g}$. For gravity gradients, we have the following values,

$$\begin{cases} B = v_{xx}v_{yy} + v_{yy}v_{zz} + v_{xx}v_{zz} - \left(v_{xy}^2 + v_{yz}^2 + v_{xz}^2\right) \\ C = v_{xy}^2 v_{zz} + v_{yz}^2 v_{xx} + v_{xz}^2 v_{yy} - v_{xx}v_{yy}v_{zz} - 2v_{xy}v_{yz}v_{xz} \end{cases} \tag{42.2}$$

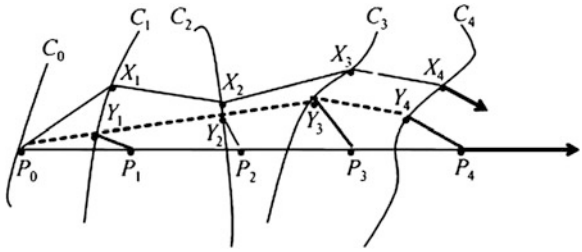

Fig. 42.1 Principle of ICCP[3]

where $v_{xx}, v_{yy}, v_{zz}, v_{xy}, v_{xz}, v_{yz}$ mean all the components of a gravity gradient tensor. As we all know, g is module of gravity vector **g**, which does not change with changes of coordinate system; according to [10, 11] and etc., values of B, C are both constant in different coordinate systems at the same position. The above mentioned values are the so called invariants. The paper is aimed at discussing their application in navigation and positioning.

42.2.2 Matching Function

In theory if function of gravity potential is known, based on the three functions given by (42.1), (42.2), the three unknown parameters about position such as x, y, z or r, θ, λ can be derived. [11] preliminarily discusses this point. The paper is aimed at discussing the application of invariants in another angle. It's that the initial positions are determined with inertial navigation technology and then the trajectory is modified by gravity and gravity gradient observation data. The core is matching algorithm. In the paper, ICCP is adopted, the principle of which is shown in Fig. 42.1, where $P_i\,(i = 0, 1, 2, \ldots, N)$ are trajectories provided by inertial navigation; $X_i\,(i = 0, 1, 2, \ldots, N)$ denotes the true trajectories; $C_i(i = 1, 2, \ldots, N)$ denotes the contour values of gravity or gravity gradients. The core of ICCP is to search the points where the gravity values are closest to the gravity observation values near the measured points by inertial technology, named as $Y_i\,(i = 1, 2, \ldots, N)$. The constraints also include the distance between the two neighbor points. By iteration searching, we can let Y_i move to X_i step by step[4].

Matching values adopted in the paper are the so called invariants, which are g, B and C. The paper mainly discusses the two-dimensional navigation and the optimal function is defined as follows,

$$d = w_\theta \left(\frac{\Delta\theta}{P_\theta}\right)^2 + w_\lambda \left(\frac{\Delta\lambda}{P_\lambda}\right)^2 + w_g \left(\frac{\Delta g}{P_g}\right)^2 + w_B \left(\frac{\Delta B}{P_B}\right)^2 + w_C \left(\frac{\Delta C}{P_C}\right)^2 \tag{42.3}$$

where $\Delta\theta$, $\Delta\lambda$ mean co-latitude and longitude differences between the search points and the measured points by inertial technology; Δg, ΔB, ΔC mean differences of invariants between gravity information of search points and the observation values;

$P_\theta, P_\lambda, P_g, P_B, P_C$ are normalization factors to unify the dimension; where $w_\theta, w_\lambda, w_g, w_B, w_C$ are weight functions which are all equal to 1 in the paper. In Eq. (42.3), the terms related with θ, λ are used to restrain the distance, which guarantees that the matching points are not far from the measured points which are given by inertial technology in the first step; the terms related with g, B, C are aimed at constraining the matching degree between gravity information, the values of which are smaller, the superiority is higher.

For comparison, the paper does similar computing using each component of gravity vectors and gravity gradients. The optimal function is:

$$d = w_\theta\left(\frac{\Delta\theta}{P_\theta}\right)^2 + w_\lambda\left(\frac{\Delta\lambda}{P_\lambda}\right)^2 + w_{g_x}\left(\frac{\Delta g_x}{P_{g_x}}\right)^2 + w_{g_y}\left(\frac{\Delta g_y}{P_{g_y}}\right)^2 + w_{g_z}\left(\frac{\Delta g_z}{P_{g_z}}\right) + w_{v_{xx}}\left(\frac{\Delta v_{xx}}{P_{v_{xx}}}\right)^2 + w_{v_{yy}}\left(\frac{\Delta v_{yy}}{P_{v_{yy}}}\right)^2 + w_{v_{zz}}\left(\frac{\Delta v_{zz}}{P_{v_{zz}}}\right)^2 + w_{v_{xy}}\left(\frac{\Delta v_{xy}}{P_{v_{xy}}}\right)^2 + w_{v_{xz}}\left(\frac{\Delta v_{xz}}{P_{v_{xz}}}\right)^2 + w_{v_{yz}}\left(\frac{\Delta v_{yz}}{P_{v_{yz}}}\right)^2 \tag{42.4}$$

Where $P_{g_i}(i = x, y, z)$, $P_{v_i}(i = xx, yy, zz, xy, xz, yz)$ denote normalization functions for each components respectively. The values of them are given as standard deviation of each components from the back ground data; $w_{g_i}(i = x, y, z)$, $w_{v_i}(i = xx, yy, zz, xy, xz, yz)$ are weight functions and values are all equal to 1; $\Delta g_i\,(i = x, y, z)$, $\Delta v_i\,(i = xx, yy, zz, xy, xz, yz)$ denotes the differences between gravity information of searched points and the observation values.

In the paper the whole search processing is conducted by iterations. The first step is to find out the points which let d smallest by using the gravity information and the initial position Pos 0 provided by inertial navigation. The points are named as Pos. In the second step, data fitting of Pos are conducted by quadratic polynomial, and then let fitted data replace the start points for a new search like the first step. The iteration continues until an enough small value of d is reached. Different from ICCP algorithm, when the "closest" points are found preliminarily, translation matrix and rotation matrix to correct the initial points don't need to be computed and instead data fitting with quadratic polynomial are conducted in the paper.

42.3 Numerical Tests

Assuming that EGM08 is the real gravity field model, gravity vector and gravity gradient data are simulated with former 360 degrees and orders of EGM08 in the districts where θ and λ are located in 71.35284°–72.495849°, 130.098054°–131.983554° respectively. The intervals in the directions of θ and λ are both 500 m and r is a constant with the value of 6,378,136.30 m. Invariants of g and B computed by these data are shown in Fig. 42.2. From the figure, we can find that the invariants g and B indicate obviously different characteristics. g shows a strong dependence on the value of θ, but B does not. Due to these differences, the points

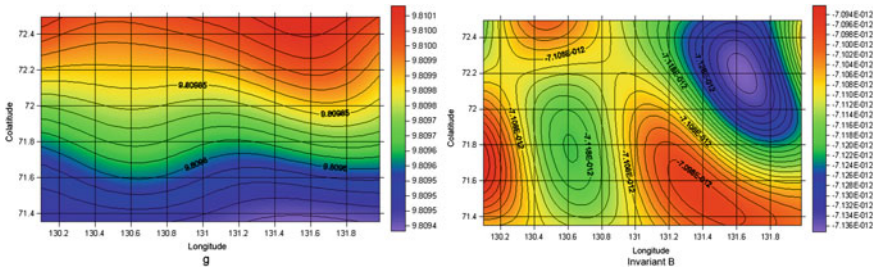

Fig. 42.2 Values of g (m/s^2) and B (s^{-4})

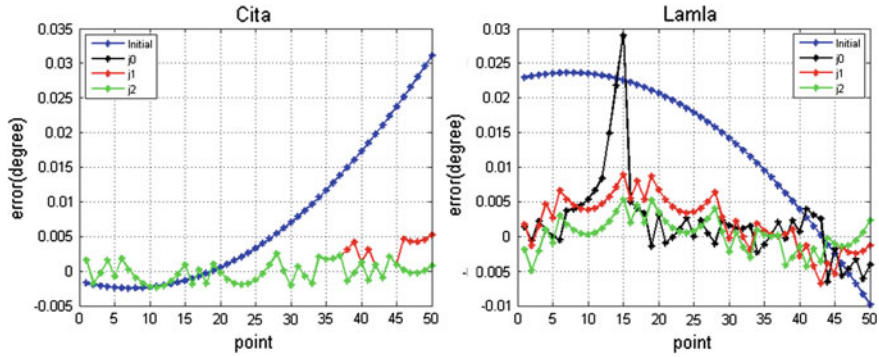

Fig. 42.3 Results of co-latitude and longitude

can be determined by gravity information. In fact, invariants C and B have quite similar properties. Due to the limitation of length of the paper, the figure of C is not given here.

In order to verify the algorithm proposed in the paper, firstly let $\theta = 71.80172°$, $\lambda = 130.531082°$, $\dot{\theta} = 0.000115°/\text{s}$, $\dot{\lambda} = 0.000286°/\text{s}$ be the start point and let $\ddot{\theta} = 5.729578 \times 10^{-6°}/\text{s}^2$, $\ddot{\lambda} = 5.729578 \times 10^{-6°}/\text{s}^2$ be the acceleration. Then simulate 50 points in time interval with 8 s as the measured points and then let $\theta_0 \imath = 71.8°$, $\lambda_0 = 130.554°$, $\dot{\theta}_0 = 0.000143°/\text{s}^2$, $\dot{\lambda}_0 = 0.000258°/\text{s}^2$ be the start point, and let $\ddot{\theta} = 5.15662 \times 10^{-6°}/\text{s}^2$, $\ddot{\lambda} = 6.302536 \times 10^{-6°}/\text{s}^2$ be acceleration. And do the same computation, the results are seen as true trajectories. Finally by using gravity information (given in the true trajectories) and the measured points, do a navigation with the method introduced in the former section. Figure 42.3 shows the convergence maps of co-latitude and longitude where *Initial* denotes the differences of the start points and true points; *j*0 denotes the differences between the initial matching points and the true points; *j*1 denotes the differences between the searched points obtained from one iteration and the true pints; *j*2 denotes the differences between the final results and true points. The iteration number is 20. Figure 42.4 gives the matching results by using invariants of gravity vectors and

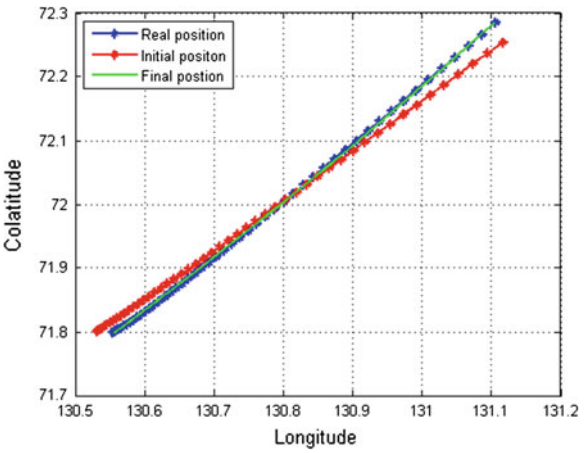

Fig. 42.4 Matching result of invariants

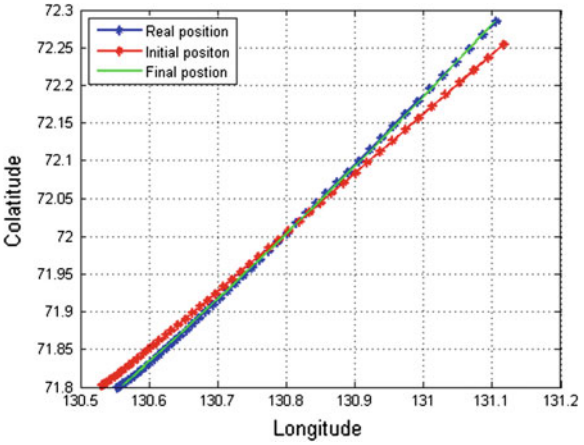

Fig. 42.5 Matching results of components

Table 42.1 Results without lattitude errors (units: °)

	Co-latitude	Longitude
Invariants	0.001240773	0.0017772
Components	0.001239175	0.0019401

gravity gradients; Fig. 42.5 shows the results by using each component of gravity vectors and gravity gradients.

Table 42.1 gives the absolute mean values of the differences between the final results and the true values. Obviously, the accuracy of the results from invariants and components are almost the same with each other. If the spherical distance of 1° is equal to 100 km, the final position errors are about 216 m which is consistent with the resolution of the background gravity data. It means that gravity aided inertial navigation is effective, whatever based on invariants or based on each component of gravity vectors and gravity gradients.

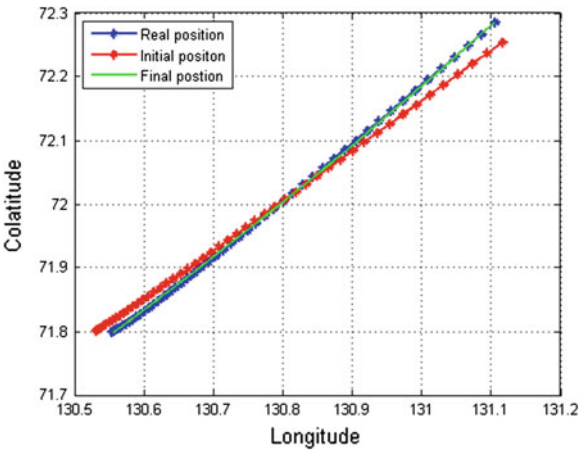

Fig. 42.6 Matching results of invariants

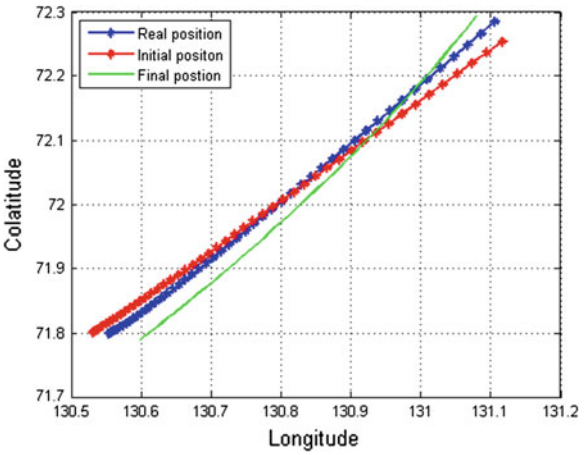

Fig. 42.7 Matching results of components

Table 42.2 Results without lattitude errors (units: °)

	Colatitude	Longitude
Invariants	0.001240773	0.0017772
Components	0.016441781	0.0231259

Actually coordinates system should be maintained during gravity vectors and gravity gradients observing. However in some circumstances, the coordinates are difficult to be maintained with a high accuracy, such as underwater conditions. Now assume that the gravity information including the gravity vectors and gravity gradients is rotated around z with an angle of 0.1° in the anticlockwise direction. Then do the same calculation as the above-mentioned experiment and the final results are shown in Figs. 42.6, 42.7, and Table 42.2.

Obviously, due to the error of orientation, there are large errors in the positioning results based on each component of gravity vectors and gravity gradients. The mean position error exceeds 2 km. This can be explained by the fact that the observed values of gravity vectors and gravity gradient tensors are not consistent with their values from the reference map. However, the positioning results obtained from the method of invariants are still accurate. It means that the method of invariants is superior to the method based on each component of gravity vectors and gravity gradients if attitude observation errors exist.

42.4 Conclusions and Discussions

By using the invariants of gravity vectors and gravity gradients, the paper proposes a new idea of matching navigation. Some numerical tests are conducted to test the superiority of the algorithm which is affected little by attitude observation errors, so it would be very helpful in matching navigation in some special circumstances, such as underwater conditions. Although the experiment mainly discusses two-dimensional navigation, the algorithm can also be applied into three-dimensional navigation. Due to the paper length limitation, the related discussion would not be given here.

Acknowledgments Thanks for the support from the National Natural Science Fund of China (Nos. 41074015, 41104047, 41104014, 41304022, 61203226).

References

1. Metzger H, Jircitanno A (1976) Inertial Navigation performance improvement using gravity gradient matching techniques. J SPACECRAFT 13(6):323–324
2. Jekeli C (1997) Gravity on precise, short-term, 3-D free-inertial navigation. J Inst Navig 44(3):347–357
3. Behzad K, Behrooz K (1999) Vehicle localization on gravity maps. In: Proceeding of SPIE-the international society for optical engineering, pp 182–191
4. Wang Z, Bian S (2008) ICCP algorithm for gravity aided inertial navigation. Acta geodaetica et cartogarphica sinica 37(2):147–151
5. Yan L, Cui C, Wu H (2009) A gravity matching algorithm based TERCOM. Geom Inf Sci Wuhan Univ 34(3):261–264
6. Xia B, Wang H (2009) Gravity matching aided navigation of maximum correlation. Opt Precision Eng 17(4):832–838
7. Liu F (2010) Research for gravity gradient aided inertial navigation system. Harbin Engineering University, Harbin
8. Wang W (2009) Underwater navigation methods based on gravity and environmental features. Harbin Engineering University, Harbin

9. Tong Y, Bian S, Jiang D et al (2012) A new integrated gravity matching algorithm based on approximated local gravity map. Chin J Geophys 55(9):2917–2924
10. Yu J, Zhao D (2010) The gravitational gradient tensor's invariants and the related boundary conditions. Sci China Earth Sci 40(2):178–187
11. Wan X (2013) Gravity field recovery using GOCE gradient data and its application. Univ Chin Acad Sci, Beijing

Chapter 43
Walking Status Detection for Pedestrian Navigation

Ling Yang, Yong Li and Chris Rizos

Abstract Pedestrian Navigation System (PNS) is useful for emergency responders, security personnel, and wide range augmented reality applications. Since the majority of these pedestrian navigation applications require walking from outdoor to an indoor destination point, the Inertial navigation System (INS) which is self-contained and immune to jamming/interference are preferred to be used. Due to the sensor properties, a navigation solution of a stand-alone inertial system will drift rapidly, so it relies on external corrections to maintain the system stability and reliability, such as Global Positioning System (GPS). In addition to seeking for external compensation, taking use of constraints deduced from the particular properties of pedestrian application is also well presented. Compared with using external augmentation, these constraints are advantaged of keeping the system independence. In this paper, the walking status detection based on inertial sensor's properties is investigated. Two constraints are considered to reduce the divergence of the navigation solution caused by the signal errors of accelerometer and gyroscope. One is position update by step detection and the other is the heading angle constraint based on walking status detection. Experiments results show that different walking status: static, walking forward, or turning, can be well distinguished by the signal properties during walking.

Keywords Pedestrian navigation · Step detection · Walking status detection

L. Yang (✉) · Y. Li · C. Rizos
School of Civil and Environmental Engineering, UNSW, Sydney, Australia
e-mail: ling.yang1@student.unsw.edu.au

Y. Li
e-mail: yong.li@unsw.edu.au

C. Rizos
e-mail: c.rizos@unsw.edu.au

J. Sun et al. (eds.), *China Satellite Navigation Conference (CSNC) 2014 Proceedings: Volume III*, Lecture Notes in Electrical Engineering 305,
DOI: 10.1007/978-3-642-54740-9_43,

43.1 Introduction

A navigation system that tracks the location of a person is useful for firefighters or other emergency first responders, for location-aware computing, personal navigation assistance, mobile 3D audio, augmented reality, and other applications. Such a system may be referred to as a Pedestrian Navigation System (PNS). Many approaches have been successfully developed for PNS, which do not need external devices except IMU sensors. The main advantage of inertial sensor-based systems is that they are self-contained, environment-independent and can provide instantaneous position, velocity and attitude measurements. In an inertial pedestrian navigation procedure, the positions are computed by detecting the user's step and propagating the estimated step length in the direction of motion [2, 8]. With a foot-mounted inertial system, frequent zero velocity updates (ZUPTs) during stance phases are used to eliminate the distance error accumulation over time and thus to maintain the system stability for longer period [3, 7]. On the other hand, an INS stand-alone system accumulates large errors in orientation due to the bias in the gyroscopes, which cannot be eliminated by ZUPTs. To reduce the attitude drift without using external information, Borestein et al. [1] proposed Heuristic Drift Reduction (HDR) method, which makes use of the fact that many indoor corridors or paths are straight. Jiménez et al. [4] detected a straight walk by analyzing the orientation change.

Theoretically, the moving speed and distance can be obtained by integrating the acceleration signal. But for indoor pedestrian application, the acceleration is small, so it can hardly be separated from sensor noise, offset drift, and tilt variation. In this paper, the signal properties during walking are investigated and two types of constraint are considered to reduce the divergence of the navigation solution caused by the signal errors of accelerometer and gyroscope. One is the position update by step detection and the other is the heading angle constraint based on walking status detection. The second constraint is based on the assumption that the heading angle will change gradually during turning period and keep constant when going straight forward without considering any external disturbance or measurement noises.

The paper is organized as follows. The step detection algorithm and step length estimation are given in Sect. 43.2; the walking status detection are presented in Sects. 43.3, 43.4, experiments conducted in both outdoors and indoors are then given to assess the performance of the proposed method. Finally the concluding remarks of the study are drawn in Sect. 43.5.

43.2 Step Detection

While people walk, the vertical acceleration fluctuates periodically due to the motion mechanism. This periodical signal stands for the steps people walked, as shown in Fig. 43.1. By step detection algorithm, the position is computed by

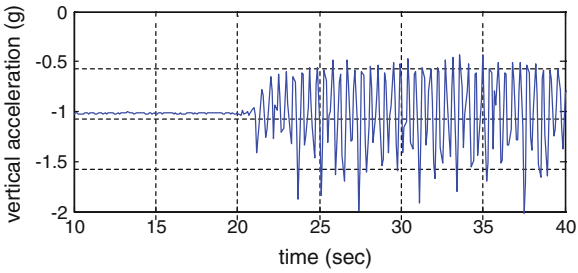

Fig. 43.1 Accelerometer outputs at down axis (output rate = 10 Hz)

staring from initial coordinates, x_0, y_0, and initial heading angle ψ_0. The horizontal coordinates are propagated by

$$\begin{cases} x_k = x_{k-1} + s_k * \cos\psi_k \\ y_k = x_{k-1} + s_k * \sin\psi_k \end{cases} \tag{43.1}$$

where s_k is the step length with index k, and the heading angle update depends on the pedestrian walking status, either keep constant or derived from the angular rate measurement from the gyro. The detailed walking status detection method will be discussed in the following section.

In this paper, a simple peak identification algorithm is used to detect the number of steps. It can be seen that the vertical acceleration signal fluctuates to peak twice every step. Hence a step is finished between two local maximum or minimal peaks.

For indoor pedestrian walking, the acceleration is small, the sensor noise, offset drift, and tilt variation thus play an obvious impact on the signal fluctuation properties. Figure 43.2 shows several cases where the signal within the ellipsoid will lead to wrong step detections. To avoid this kind of errors, the signal is filtered as shown by the red line in Fig. 43.2.

To reduce the influence of sensor errors, two constraints are implemented during the step detection procedure, that is, (1) the time interval during one step should be larger than the threshold δt; (2) the variance of accelerometer outputs during one step should be larger than the threshold δa. The threshold δt and δa rely on the walking dynamic status and will be further discussed in the experiment section.

The step length is used to update user's location when one step is finished. It is shown that step length is influenced by the walking frequency, variance of the accelerometer signal during one step period, as well as the ground inclination [2, 5, 6]. It can be assumed that step length will not change significantly during a short period. Thus it can be calculated by averaging the estimated step length of previous steps within a moving window

$$s_k = \frac{1}{N}\sum_{i=1}^{N} \hat{s}_{k-i} \tag{43.2}$$

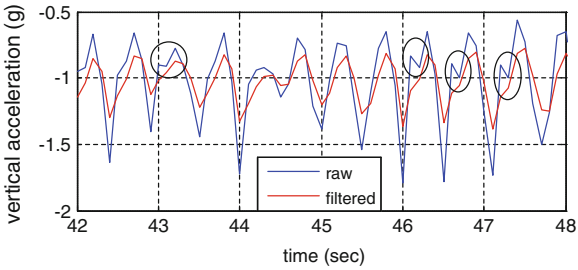

Fig. 43.2 Accelerometer outputs raw and filtered measurements (Output rate = 10 Hz)

where N is the window length depending on the walking frequency and environment, and $\hat{s}_{k-i}$ is the step length estimated by the integrated position solution at step $k - i$ and $k - i - 1$.

The position updated by step detection is then used to form the measurement model of Kalman filter. The measurement noise is computed based on the error propagation algorithm and given as

$$\begin{cases} \sigma_{x_k}^2 = \sigma_{x_{k-1}}^2 + \sigma_{s_k}^2 * (\cos\psi_k)^2 + (s_k * \sin\psi_k)^2 * \sigma_{\psi_k}^2 \\ \sigma_{y_k}^2 = \sigma_{y_{k-1}}^2 + \sigma_{s_k}^2 * (\sin\psi_k)^2 + (s_k * \cos\psi_k)^2 * \sigma_{\psi_k}^2 \end{cases} \tag{43.3}$$

where σ_*^2 is the variance of corresponding variant "*". $\sigma_{x_{k-1}}^2, \sigma_{y_{k-1}}^2$ are derived from the Kalman filter estimation, $\sigma_{s_k}^2$ is obtained from Eq. (43.2), as well as $\sigma_{\psi_k}^2$ is set to zero when going straight and derived from Kalman filter time update during turning.

43.3 Heading Angle Constraint from Walking Status Detection

The heading angle changes gradually during turning and keeps constant when going straight forward, without considering any external disturbance or measurement noises. However, the low-cost MEMS INS cannot maintain a stable heading angle solution even in short period when user is walking straight forward. One enhanced option is to take use of magnetometer. But the magnetic measurement is easily disturbed by external interference sources, thus cannot always provide believable reference to heading angle.

Assumed the initial heading angle is known, the strict heading constraint can be obtained by judging whether the user is walking straight forward, and then the heading angle update will be only implemented during turning period. Figure 43.3 shows the gyroscope measurements on the down direction axis during a walking test with an "L" trajectory and the output rate is 10 Hz. The red line is the raw measurements. It shows a significant distinguish among different walking status, where the signals within first 60 s are stable and correspond to the static period.

Then the user starts to walk forward and this leads to a remarkable fluctuation on the output signals. During the 80th to 90th second large negative drifts occur, illustrating a turning left period. The signal properties during different walking status can be expressed by

$$\begin{cases} E(\omega_i) = 0, \quad D(\omega_i) = \sigma_\omega^2, \quad i = 1, \ldots, m, m+t+1, \ldots n \\ E(\omega_i) = \omega_0, \quad D(\omega_i) = \sigma_\omega^2, \quad i = m+1, \ldots, m+t \end{cases} \tag{43.4}$$

where ω_i is the angular rate measurement along the vertical axis at the ith epoch. "E" and "D" are expectation and variance function, respectively. ω_0 is a value which is not equal to zero, and σ_ω^2 is a positive value. Equation (43.4) indicates between 1th and mth epoch, the user was walking straight forward, and then during the epoch of $m+1$ and $m+t$, the user was turning, after that the user kept straight until the end.

Due to the influence of noises, the different walking status cannot be simply distinguished by a threshold. Here a moving window is used to resample the signal by averaging the measurements within the window, so that the random noise can be largely mitigated.

$$\omega_i' = \frac{\sum_{i=i-k+1}^{i} \omega_i}{k} \tag{43.5}$$

where k is the length of filtering window, ω_i' is the filtered value of ω_i. Combining with Eq. (43.4) it can be deduced that

$$\begin{cases} E(\omega_i') = 0, & i = 1, \cdots, m \\ E(\omega_i') = \frac{i-m}{k}\omega_0, & i = m+1, \ldots, m+k(k \le t) \\ E(\omega_i') = \omega_0, & i = m+k+1, m+t(k \le t) \\ E(\omega_i') = \frac{k-(i-m-t)}{k}\omega_0, & i = m+t+1, \ldots, m+t+k-1(k \le t) \\ E(\omega_i') = 0, & i = m+t+k, \ldots, n(k \le t) \end{cases} \tag{43.6}$$

where $D(\omega_i') = \frac{\sigma_\omega^2}{k}, i = 1, \ldots, n$. Equation (43.6) shows the expectation of the filtered angular rate measurement does not reduce to zero immediately after turning is finished. Thus the influence of this period should be subtracted from the detected period.

As an illustration, the blue line in Fig. 43.3 is the smoothed measurement with a window size of ten, where the signal remains between -8 and 8°/s during going straight forward period and will sway to as lower as -60°/s during turning left period. Figure 43.4 shows an inverse case when the user walked back along the same trajectory and turned right at around 110th second.

The window size and the threshold will impact the performance of the walking status detection. A small window size cannot effectively reduce the random noises. While a large window size leads to a more obvious delay to the detection. Similarly, a small threshold will misidentify some going forward epochs as turning status, while larger threshold will delay the detect when turning start and end the

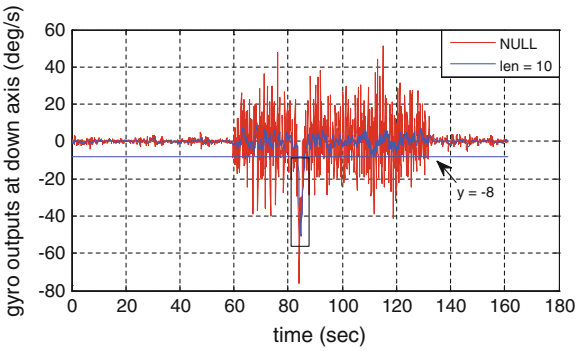

Fig. 43.3 Gyroscope outputs at down axis (10 Hz)

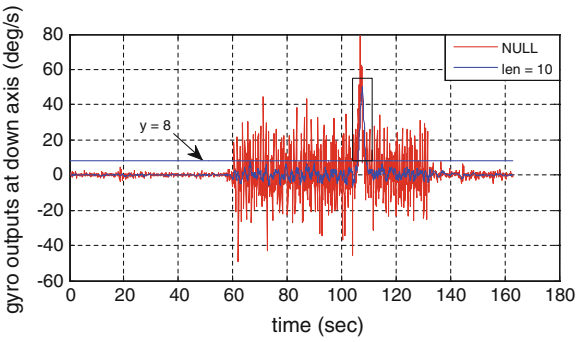

Fig. 43.4 Gyroscope outputs at down axis (10 Hz)

turning period much earlier. Thus, epochs near the beginning or the end of the turning cannot be detected. Practical experiments show that a smaller threshold is required when a larger smoothing window size is used. The window size and threshold not only depend on the gyroscope output rate, but also rely on the walking speed as well as other personal walking properties. By repetitively walking along the "L" trajectory 20 times, a window size of 10 for 10 Hz data and a threshold of 8°/s are selected during the walking status detection procedure.

43.4 Experiment and Analysis

43.4.1 Experiment Description

Experiments were conducted on the campus of University of New South Wales, Sydney, Australia. Data were collected in both outdoor and indoor environments. Indoor experiments were conducted inside the Electrical Engineering Building. The test devices used in this paper are shown in Fig. 43.5. The nAX5, a small MEMS-INS/GPS device, was used to collect Inertial Measurement Unit (IMU) and GPS data, with the GPS antenna fixed to the top of the device. The IMU

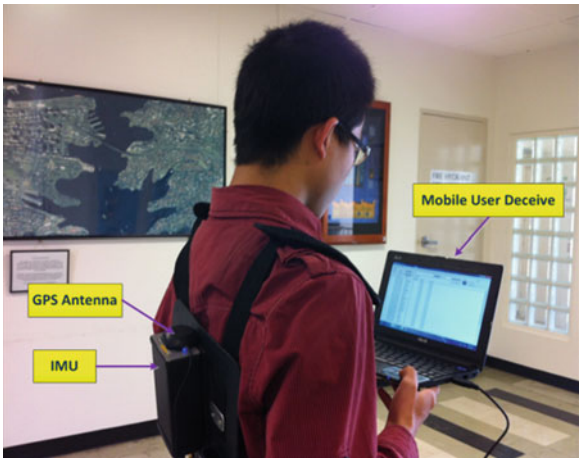

Fig. 43.5 Experiment setup: a laptop used to store data, IMU and GPS antenna

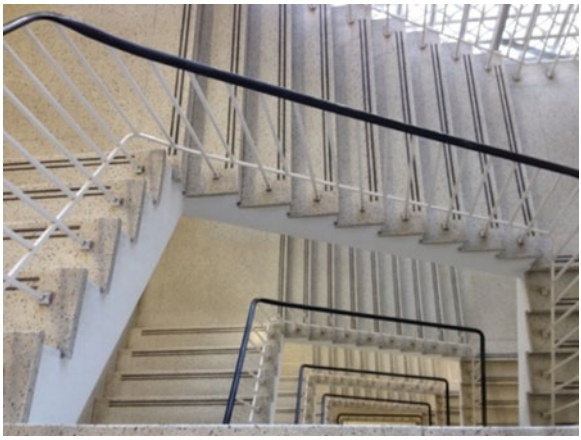

Fig. 43.6 Stairs inside Electrical Engineering Building, UNSW

outputs contained three orthogonal acceleration and angular velocities tagged with GPS time (http://www.navextech.com). For these tests the output rate of the nAX5 IMU was configured as 10 Hz.

To assess the performance of step detection and walking status detection, tests were conducted at following different circumstances:

(1) Walking straight forward
(2) Walking straight forward with a 90° turn, either left or right
(3) Walking along a rectangular lawn, without stairs
(4) Walking straight forward with a up-down stairs without turning
(5) Walking along with turning stairs

The first four circumstances above are common in both outdoors and indoors, while the last circumstance shown in Fig. 43.6 is typical inside buildings, such as offices, theaters, shopping malls and others.

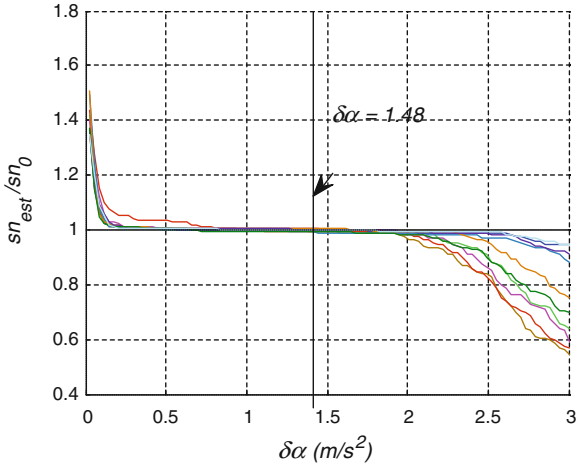

Fig. 43.7 Step detection accuracies along with δa (sn_{est}/sn_0 is the ratio of detection number and real number)

43.4.2 Step Detection Verification

To assess the accuracy of the step detection algorithm, data were collected at the above five circumstances. The number of steps during one test were recorded and compared with the estimation results.

In the step detection algorithm, the threshold of time interval δt can be calculated by the walking speed. To determine the threshold δa, the accuracies of the step detection according to different δa are shown in Fig. 43.7, where the tests were conducted under different circumstances (1) and (2) and the same trajectory was repeated five times to ensure the estimation stability.

Figure 43.7 indicates that the value of δa will influence the step detection estimation accuracy. Smaller δa results in an overestimation while large δa lead to a underestimation of the step number. To further investigate the detection successful rate according to the value of δa, the numbers of wrong step according to those tests in Fig. 43.7 are listed in Table 43.1. Due to the influence of signal errors, a threshold of δa for an entire correct detection is not existed. Therefore, it is inevitable to accept a small number of wrong steps during the step detection procedure. Large sample of tests has proved that a value of $\delta a = 1.48$ is optimal and can limit the number of wrong steps within 1.

To analyse the influence of walking distance on the step detection estimation accuracy, the step detection results under circumstance (3) are shown in Table 43.2, with the walking circles increase from 1 to 4. Results in Table 43.2 shows that the number of wrong step does not increase remarkably with the increase of walking distances. It indicates there is not a linear relationship between the walking distance and the step detection accuracy. Thus, the estimation accuracy of step detection can be guaranteed during long performance period. It can be further assumed that the wrong step detection mainly happen during the period of start and stop walking.

Table 43.1 δa threshold according to wrong step numbers

Test no.	Number of wrong steps		
	−1	0	1
1	0.27–0.48	0.51–1.38	1.41–1.56
2	0.42–0.45	0.48–1.35	1.38–1.74
3	0.81–0.93	0.96–1.08	1.11–1.98
4	0.45–1.44	1.47–1.83	1.86–1.89
5	0.33–0.45	0.48–1.23	1.26–1.48
6	0.24–0.54	0.57–1.74	1.77–2.04
7	0.42–1.62	1.65–1.77	1.80–2.28
8	0.27–1.26	1.29–1.92	1.95–2.13
9	0.36–0.63	0.66–0.69	0.71–1.65
10	0.21–0.81	0.84–1.8	1.83–2.58

Table 43.2 Step detection results with different walking distance (detected number/real number)

Circle no.	Test no.				
	1	2	3	4	5
1	175/175	176/175	178/178	175/176	176/176
2	349/350	351/351	347/348	350/350	349/350
3	518/519	518/518	516/517	519/520	517/518
4	689/690	687/688	688/689	689/689	686/687

Table 43.3 Step detection results with multiple pauses (detected number/real number)

Stop no.	Test no.				
	1	2	3	4	5
0	175/175	176/175	178/178	175/176	176/176
1	179/181	180/180	179/179	179/178	181/181
2	181/183	182/184	182/183	183/184	183/185
3	182/184	181/184	182/185	181/183	180/183

To show the impact of pause on the step detection accuracy, the results of the same trajectories but with multiple pauses during one circle under circumstance (3) are listed in Table 43.3. It further proves that the possibility of wrong detection at the epochs of start or stop walking is rather higher than during the walking.

The step detection results of the five different circumstances presented in Sect. 43.4.1 are illustrated in Table 43.4. It can be seen that the number of wrong steps under circumstance (1)–(4) are no larger than 1. This means the detection algorithm with proper thresholds of δa and δt can be applied under different situations and the estimation accuracies can be guaranteed. The last line in Table 43.4 shows that the step detection accuracy under circumstance (5) is quite lower than others. The number of wrong steps can reach to 3 within 170 steps, which is almost twice of those under circumstance (1)–(4). This is because under this environment, a

Table 43.4 Step detection results under different circumstances (detected number/real number)

Case no.	Test no.				
	1	2	3	4	5
(1)	146/147	148/149	148/149	147/147	146/147
(2)	151/150	149/148	150/150	146/147	149/148
(3)	175/175	176/175	178/178	175/176	176/176
(4)	100/100	100/100	99/100	100/100	101/100
(5)	158/161	160/157	163/165	160/160	165/168

person is required to turn immediately after finishing one segment of stairs. This leads to an inevitable tiny pause, which is the main reason of the wrong detection.

43.4.3 Assessment of the Walking Status Detection

To assess the performance of turning detection, tests were conducted under circumstance (2), (3), and (5). In each test, the step indexes were recorded, by which the real time slot of turning can be noted.

Figure 43.8 shows the detection result in one test. The blue line is filtered angular rate measurements at the vertical direction. With the threshold of −8°/s, the period of turning is detected as demonstrated by the two vertical blue lines. The reference period of turning was recorded by the step indexes and demonstrated by the two vertical red lines. The difference between the estimation and reference value is 0.4 s. The detected turning period is 0.2 s earlier than the reference. This is mainly caused by the slight delay on the detected steps with the use of filtered data.

To statistically assess the turning detection performance, the tests conducted repeatedly under circumstance (2), (3), and (5). The detected time at turning start and end epochs for (2) and (3) are listed in Tables 43.5 and 43.6, where the figures before and behind "/"are the detected time epochs and the corresponding reference values, respectively.

Table 43.5 shows that during five repetitive tests, the errors of detected turning period are all less than 0.4 s. In most cases, reference time epochs are slightly later than detected epochs. Since the reference turning periods are record by step index, the accuracy of the reference is about one step, an estimation error around 0.4 s is reasonable.

Table 43.6 shows the turning detection results when walking along a rectangular lawn, so there are four times of turning during one test. In these five tests, 22.5 % of the estimated time epochs are the same as their reference values, 50 % of the estimation errors are not larger than 0.1 s, 60 % are less than 0.2 s, 85 % are not larger than 0.3 s, and 15 % of these errors are 0.4 s. This further demonstrated that the proposed turning detection method can perform well under these circumstances.

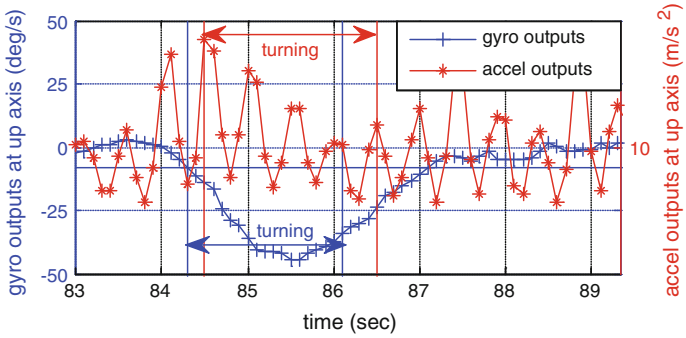

Fig. 43.8 Gyroscope outputs for turning detection

Table 43.5 Turning detection results under circumstance (2)

	Test no.				
	1	2	3	4	5
Start	84.3/84.5	83.6/84	85.3/85.5	83.2/83.5	82.6/82.9
End	86.1/86.5	85.1/85.4	87.2/87	84.7/85	84.6/84.8

Table 43.6 Turning detection results under circumstance (3)

Turn no.		Test no.				
		1	2	3	4	5
1	Start	34.3/34.4	58.5/58.5	33.8/33.7	41/41.2	35.4/35.3
	End	36/35.9	60.1/59.9	35.6/35.7	42.6/42.7	37.6/37.2
2	Start	42.3/42.3	66.1/66.4	42/42.3	48.7/48.7	43/43.3
	End	43.7/43.8	67.5/67.9	43.8/43.8	50.1/50.1	44.7/44.7
3	Start	71.9/72.1	95.9/96.2	72.6/72.9	78.6/78.9	73.1/73.1
	End	73.4/73.5	97.3/97.6	73.9/74.3	80/80.3	74.4/74.4
4	Start	83.7/83.9	107.7/108.1	84.3/84.2	89.8/90.1	84.5/84.8
	End	85.4/85.8	109.4/109.5	85.8/85.7	91.4/91.6	86.2/86.6

To investigate the turning detection performance during climbing a spiral stairs, the filtered angular rate measurements at vertical axis under circumstance (5) are shown in Fig. 43.9. There were 18 times of turning when climbing the stairs from lower ground level to level 4 of the building.

Figure 43.9 shows there are 18 peaks which demonstrate the 18 times of turning clearly. This means the filtered angular rate measurement along vertical axis can obviously indicate the approximate time period of turning. However, because the turning periods under this circumstance is quite shorter than walking on a plane ground, the detection accuracy is relatively lower. Further investigation is still

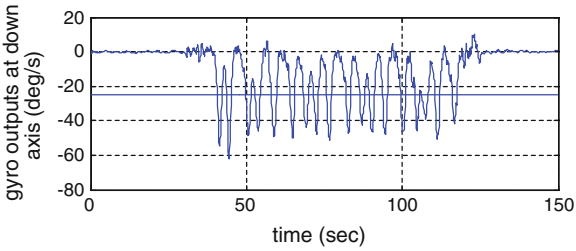

Fig. 43.9 Gyroscope outputs for turning detection (window length = 10)

required to improve the turning detection accuracy under this kind of complex environment.

43.5 Concluding Remarks

This paper presents algorithms of walking status detection based on inertial sensor's properties under different application environments. Firstly step detection is implemented by using the accelerometer outputs along the vertical direction. Then the turning periods can be detected by the angular rate measurements along the vertical direction. The performance of the algorithms have been investigated and verified by repeated tests under different environments, in both indoors and outdoors. It shows that the error of step detection is less than 2 and does not grow with the increase of walking distance during one stop tests. Besides, the accuracy will degrade if there are multiple pauses during walking. On the other hand, the turning detection algorithm performs quite well when walking on a plane ground. Comparably the detection errors when climbing spiral stairs are much larger. Further research will improve the turning detection accuracy under this type of complex environments.

References

1. Borenstein J, Ojeda L, Kwanmuang S (2009) Heuristic reduction of gyro drift in IMU-based personnel tracking systems. In: Proceedings SPIE, vol 7306. p 73061H
2. Cho SY, Park CG (2006) MEMS based pedestrian navigation system. J Navig 59(01):135–153
3. Godha S, Lachapelle G (2008) Foot mounted inertial system for pedestrian navigation. Meas Sci Technol 19(7):075202
4. Jiménez AR, Seco F, Prieto JC, Guevara J (2010) Indoor pedestrian navigation using an INS/EKF framework for Yaw drift reduction and a foot-mounted IMU. In: 2010 7th Workshop on positioning navigation and communication (WPNC), IEEE, New York, pp 135–143
5. Ladetto Q, Merminod B (2002) Digital magnetic compass and gyroscope integration for pedestrian navigation. In: 9th Saint Petersburg international conference on integrated navigation systems, Saint Petersburg, Russia, pp 111–120

6. Levi RW, Judd T (1996) U.S. Patent 5,583,776, Washington, DC, U.S. Patent and Trademark Office
7. Suh YS, Park S (2009) Pedestrian inertial navigation with gait phase detection assisted zero velocity updating. In: ICARA 2009: 4th International conference on autonomous robots and agents, 2009, IEEE, New York, pp 336–341
8. Yun X, Bachmann ER, Moore H, Calusdian J (2007) Self-contained position tracking of human movement using small inertial/magnetic sensor modules. In: IEEE international conference on robotics and automation, IEEE, New York, pp 2526–2533

Chapter 44
Stochastic Modelling and Estimation of Inertial Sensors

Youlong Wu, Jinling Wang, Xiaoming Wang and Muwaffaq Alqurashi

Abstract The Global Navigation Satellite System (GNSS) and Inertial Navigation System (INS) are two main navigation systems with complementary characteristics. In some GNSS challenged environments, due to signal jamming or blockage, INS becomes stand-alone navigation system. INS is a dead reckoning based system, and its performance will gradually degrade with time. This performance degradation is mainly caused by the deterministic errors and stochastic errors according to their sources. Therefore, precise modelling inertial sensors are the first and the most important step for the inertial navigation system. Deterministic errors are due to manufacturing and mounting defects and can be calibrated out from the raw measurements. On the other hand, stochastic errors are the random errors which cannot be removed from the measurements and should be modelled as processes. Therefore, the better identification of the stochastic errors is critical for navigation. Previous work on analysing and modelling inertial sensors is based on the computing the Allan variance of inertial sensors output and using least squares fitting or reading results from the Allan variance log–log plot directly. This paper presents a methodology for estimating the stochastic errors using segmented weighted algorithm. Firstly, individual noise is simulated and the noise spectral density can be obtained through the least square to validate each noise type. Secondly, the simulation studies with the combination of different noise types are

Y. Wu (✉) · X. Wang
School of Mechanical Engineering, Nanjing University of Science and Technology, Nanjing 210094, China
e-mail: youlong.wu@hotmail.com

X. Wang
e-mail: 202xm@163.com

Y. Wu · J. Wang · M. Alqurashi
School of Civil and Environmental Engineering, University of New South Wales, Sydney, NSW 2052, Australia
e-mail: jinling.wang@unsw.edu.au

M. Alqurashi
e-mail: alqurashi.m@student.unsw.edu.au

J. Sun et al. (eds.), *China Satellite Navigation Conference (CSNC) 2014 Proceedings: Volume III*, Lecture Notes in Electrical Engineering 305,
DOI: 10.1007/978-3-642-54740-9_44,

carried out to compare with the traditional method. The proposed algorithm demonstrates remarkable improvement, especially in estimate the long-term errors compared with the traditional method. Field test results also confirm the effectiveness of the new method.

Keywords Allan variance · Stochastic modelling · Inertial sensors

44.1 Introduction

An inertial navigation system (INS) is a dead-reckoning system that provides velocity, position and attitude independent of external electronic and magnetic signals [1]. However, the accuracy of an inertial navigation solution degrades with time. This is mainly caused by the error properties of inertial sensors. Based on different error sources, the inertial sensor errors can be divided into deterministic and stochastic errors [2]. The deterministic errors, including biases, scale factors and misalignments, can be removed by specific calibration procedures through the rate table [3]. One the other hand, the compensation for the stochastic errors usually employs a Kalman filter to estimate the sensors' noise component [4]. Therefore, before the calibration, the characterization of random noise of the inertial sensor should be well estimated [5]. This paper will focus on the accurate estimation of stochastic errors performance.

In time and frequency metrology, the power spectral density has been proposed to measure frequency stability in the frequency domain. As discussed in [6], it has been found empirically that random fluctuations in standards can be modelled by a power law of the power spectral density. However, to analyse a long-term characteristic of the sensor, the processing of huge amount of data is necessary. In this case, determination of the power spectral density is very computationally intensive and the results are difficult to extract [7]. Additionally, Allan variance has been widely used in time and frequency metrology as a substitute for the classical variance to characterize the stability of clocks or frequency standards in the time domain [6]. Because of the close analogies to inertial sensors, this method has been applied to analyse the error characteristics of any precision measurement instrument [8].

In [5] and [8, 9], power spectral density and Allan variance methods are given to analyse the stochastic sensors errors. By these two methods, the spectral densities of the noise components can be obtained by least squares fitting or from the Allan variance log–log plot directly. However, Allan variance data values can span several orders of magnitude, the noise character such as quantization (Q), angle random walk (ARW), bias instability (BI), rate random walk (RRW) and rate ramp (RR) are easily affected by each other. This leads a poor estimation performance. In this aspect, correct noise parameters in the inertial sensors leads to better performance for the GNSS/INS integrated navigation system.

This paper is focused on the identification of the stochastic error in the inertial sensors and obtained more accurate noise parameters. The structure of the paper is organized as follows: Sect. 44.2 describes the mathematical definition of the Allan variance and relationship between the Allan variance and the noise power spectral density. In Sect. 44.2, a new method was proposed to estimate the noise parameters. Section 44.3 provides a simulation study for estimating the noise and a navigation demonstration was carried out to validate the method. Section 44.4 concludes the paper.

44.2 Modelling Inertial Sensors

44.2.1 Sensor Error Components

The output of post calibration inertial sensor which is stationary can be described by the following equation:

$$y(t) = u(t) + n(t) + b(T) + N(T, t) \tag{44.1}$$

where $y(t)$ is the sensor measured output, $u(t)$ is the real value that the sensor supposed to measure (i.e. real rotation rate and real acceleration), $b(T)$ is the bias which is probably dependent on the temperature, $n(t)$ is the time varying component noise, T is the temperature, $N(T, t)$ is the error induced by all environmental factors.

In Eq. (44.1), it is generally assumed that $n(t)$ is the sum of the following components [8]:

$$n(t) = Q(t) + N(t) + B(t) + K(t) + R(t) + M(t) + S(t) \tag{44.2}$$

where $Q(t)$, $N(t)$, $B(t)$, $K(t)$, $R(t)$, $M(t)$ and $S(t)$ are the coefficients for the quantization noise, angle random walk, bias instability, rate random walk, rate ramp, markov process and sinusoidal error. These noise power spectral densities needed to be well estimated before using in the GPS/INS integration Kalman filter. In the following section, these error components will be modelling through the Allan variance.

44.2.2 Allan Variance

As mentioned, Allan variance is a method of analysis in time domain. It describes the variance of data as a function of averaging time. In order to compute the Allan variance associated with a record of IMU data, the angular rates are recorded at a

constant time interval τ_0, a collection of N data points can be reformed to be $K = N/M$ clusters where M is the number of samples per cluster. Then, the Allan variance σ^2 statistic for this data set is described as [8]:

$$\sigma^2(\tau) = \frac{1}{2}\left\langle \left(\bar{\omega}_{k+1}(M) - \bar{\omega}_k(M)\right)^2 \right\rangle \tag{44.3}$$

where $\langle\ \rangle$ is denoted as the infinite time average, $\tau = M\tau_0$ is the correlation time.

For a finite number of samples N, the Allan variance can be estimated as [8]:

$$\sigma^2(\tau) \cong \frac{1}{2(K-1)} \sum_{k=1}^{K-1} \left(\bar{\omega}_{k+1}(M) - \bar{\omega}_k(M)\right)^2 \tag{44.4}$$

The Allan variance can be used to investigate stochastic processes, by taking use of its relation with PSD. This relation is [8]:

$$\sigma^2(\tau) = 4 \int_0^\infty S_x(f) \frac{\sin^4(\pi f \tau)}{(\pi f \tau)^2} df \tag{44.5}$$

where $S_x(f)$ is the PSD of the random process, f is the frequency, the Allan variance is proportional to the total power output of the random process when passed through a filter with the transfer function of the form $\sin^4(x)/x^2$. This particular transfer function is the result of the method used to create and operate on the clusters.

If different spectral noise components are described by different spectral density power laws, different noise type can be distinguished from the log–log plot of Allan variance versus sampling period allows by the slope of plot in particular time regions, as well as the magnitudes of these noise components can be determined. If not considering the markov noise and sinuous noise, there exist five main error sources, as for instance quantization noise, white noise, bias instability, rate random walk, and ramp noise. Individual noise process can be distinguished on the Allan variance log–log plot by their characteristic slope. The noises, their Allan variances, PSDs and curve slope are listed in Table 44.1. For example, on the Allan variance log–log plot the angle random walk is associated with a region of slope $-1/2$.

Assuming all the stochastic processes are independent to each other, the total Allan variance is the sum of the Allan variance for each noise type [6, 8]:

$$\begin{aligned} \sigma^2(\tau) &= \sigma_Q^2(\tau) + \sigma_N^2(\tau) + \sigma_B^2(\tau) + \sigma_K^2(\tau) + \sigma_R^2(\tau) \\ &= \frac{3Q^2}{\tau^2} + \frac{N^2}{\tau} + \frac{B^2 2ln2}{\pi} + \frac{K^2\tau}{3} + \frac{R^2\tau^2}{2} \end{aligned} \tag{44.6}$$

where, Q, N, B, K and R are the coefficients for the quantization noise, white noise, bias instability, rate random walk and rate ramp.

Table 44.1 Stochastic error sources in inertial sensors

Noise types	Allan variance	Parameters	PSD	Slope
Quantization noise	$3Q^2/\tau^2$	Q	$(2\pi f)^2 Q^2 T$	-1
Angle random walk	N^2/τ	N	N^2	$-1/2$
Bias instability	$2B^2 ln2/\pi$	B	$B^2/2\pi f$	0
Angular rate random walk	$K^2\tau/3$	K	$K^2/(2\pi f)^2$	$+1/2$
Rate ramp	$R^2\tau^2/2$	R	$R^2/(2\pi f)^3$	$+1$

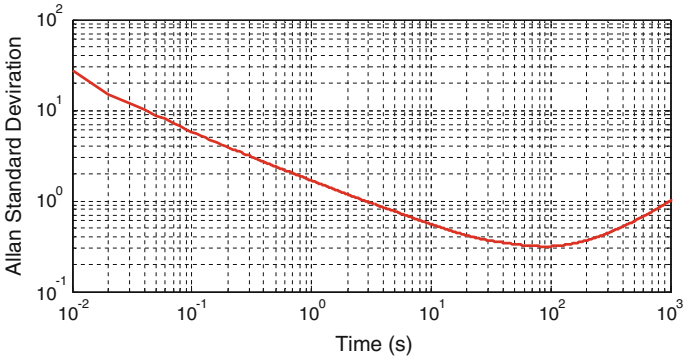

Fig. 44.1 Allan variance log–log plot for CMIGITS

In practice, the Allan variance is based on a finite number of independent clusters, so its accuracy depends on the additional number of cluster averages. In general, the accuracy of the computation is given by [8]:

$$\sigma(\delta) = \frac{1}{\sqrt{2\left(\frac{N}{m} - 1\right)}} \times 100\ \% \tag{44.7}$$

Previous works about modelling inertial sensors mainly rely on Allan variance analysis. It assumes that different error sources were independent to each other. Based on this assumption, the various error sources can be identified from the Allan variance slopes, which can be determined by line fitting with several straight lines [5]. However, when we tested the Allan variance log–log plot for CMIGITS sensors we found that the errors sources have slopes that are not completely equal to any one of the theoretical slopes as listed in Table 44.1. This is caused by the correlation relationships among different error sources. As shown in Fig. 44.1, it can be noted that angle random walk (ARW) and rate random walk (RRW) are dominant sources in the tactical-grade sensors. In this paper, only these two sources are considered.

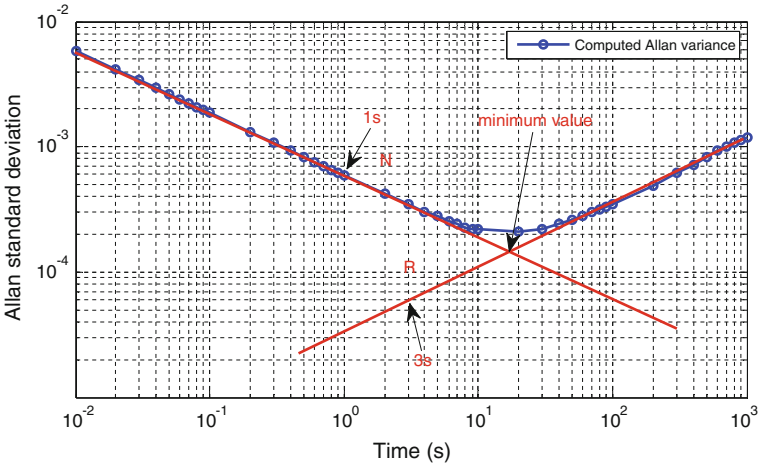

Fig. 44.2 Allan variance log–log plot

If only ARW and RRW exist in the sensors, the Eq. (44.6) can be simplified as

$$\sigma^2(\tau) = \frac{N^2}{\tau} + \frac{K^2\tau}{3} \tag{44.8}$$

By differentiating and setting the result to zero, it can be seen the minimum of the Allan variance plot occurs at

$$\tau = \sqrt{3}\frac{N}{K} \tag{44.9}$$

The minimum value of the plot is

$$\sigma^2(\tau) = \sqrt{\frac{4}{3}}\frac{N}{K} \tag{44.10}$$

Assuming ARW value is 10 times than RRW value, it can be obtained the minimum Allan variance value occurs at $\tau_0 = 1.73$ s according to Eq. (44.9). Notice in Fig. 44.2, for values of τ smaller than τ_0, the Allan variance plot is identical with the line due to the ARW term, which depends on N. For values of τ much larger than τ_0, the Allan variance is identical with the line due to the RRW term, which depends on K. For values of τ close to τ_0, the Allan variance depends on both N and K. Therefore, in order to get a good estimate of these two random processes, the observation should be divided into two segments near the τ_0.

Figure 44.3 illustrates that the computed Allan variance values error is getting larger with the increase of the cluster times. It is noted that smaller errors corresponds to the shorter-term noise, which guarantee the estimation accuracy of

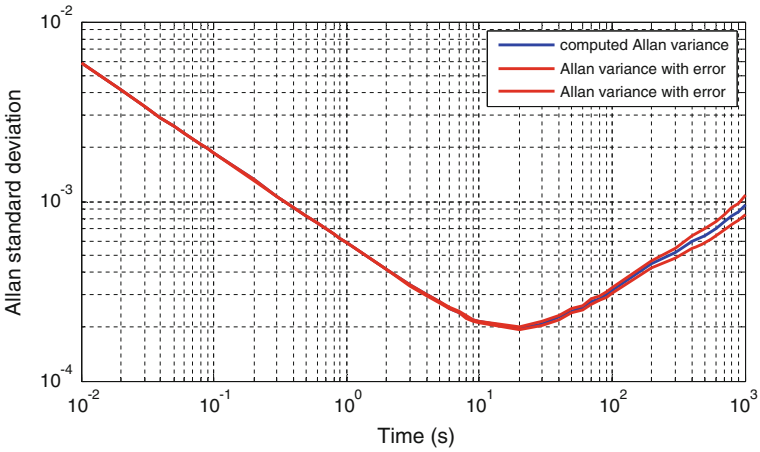

Fig. 44.3 Allan variance values with error

ARW. For long-term noise, the computed Allan variance accuracy is degraded. Therefore the RRW term is largely affected. In order to get a good estimate of RRW, one must use values greater than τ_0, and the optimal weights should be carried out.

The Gauss-Markov model of uncorrelated observation equation is

$$v = A\hat{x} - l \tag{44.11}$$

where v is n by 1 vector of residuals, A is the n by t design matrix, x is the vector of t unknown, and its estimated value is $\hat{x}$, 1 is the n by 1 measurement vector. The n by n positive definite variance covariance matrix, which implies full rank, $\sum$ of the measurements is given by

$$D(l) = \Sigma = Q = P^{-1} \tag{44.12}$$

where Q is the n by n cofactor matrix, and P is the n by n corresponding weight matrix. It can be obtained from the Eq. (44.7) according to the cluster times.

The optimal estimates for the states parameters $\hat{x}$

$$\hat{x} = \left(A^{\mathrm{T}}PA\right)^{-1}A^{\mathrm{T}}Pl \tag{44.13}$$

After getting the coefficients for the main stochastic errors, a better error model can be applied in the GPS/INS integrated navigation system.

44.3 Simulations and Analysis

44.3.1 Simulation Study

In order to compute the total Allan variance, the simulation was implemented to verify the estimation accuracy of individual noise. A 10 h data set with 100 Hz sample frequency was generated for ARW and RRW, respectively. Figures 44.4 and 44.5 show examples of different types of data and Allan variance log–log plots used to determine the noise characteristics of inertial sensors. The circles are the computed Allan variance points. The red line is the corresponding least-squares estimation result. The estimated values of ARW and RRW is given in Table 44.2. It shows the estimated values are coincident to the given true value.

The combination of ARW and RRW errors are simulated to validate the proposed method. The ARW noise value is chosen as 5.8682e−004, and RRW noise value is successively chosen as 5.8682e−003, 5.8682e−004 and 5.8682e−005, so that ARW noise value is larger than, equal to, and smaller than RRW noise value, respectively.

A log–log plot of the Allan variance is shown in Fig. 44.6. The estimated results are summarized in Table 44.3. For these different combinations, the value of N is almost the same with its true value, while the value of K is quite different. When the value of K is larger than N, value from conventional method is 8.3 % larger than the true value of K, while value from propose method is 1.8 % larger than its true value. When K equals to N, estimated result from conventional method is 14.5 % smaller than the true value of K, while result from propose method is 4.5 % smaller than its true value. When K is smaller than N, value from conventional method is 10.7 % larger than the true value of K, while value from propose method is 0.7 % larger than true value. All these comparison verify the superior performance of the proposed method over the conventional method.

44.3.2 Experimental Test

To further evaluate the performance of the proposed method, static and dynamic test were carried out. Firstly, CMIGITS inertial sensors were used to collect static data to analyse the stochastic error sources using Allan variance method. The noise parameters were obtained from the conventional method and proposed method. Secondly, the CMIGITS were operated in a field test and the dynamic data was collected. A loosely-coupled GPS/INS system with 21 states, including 9 states for position, velocity and attitude error and 12 states for accelerometer bias, gyro bias, velocity random walk and gyro rate random walk, was performed to assess the impact of the noise parameters on the navigation results. The CMIGITS specifications are listed in Table 44.4.

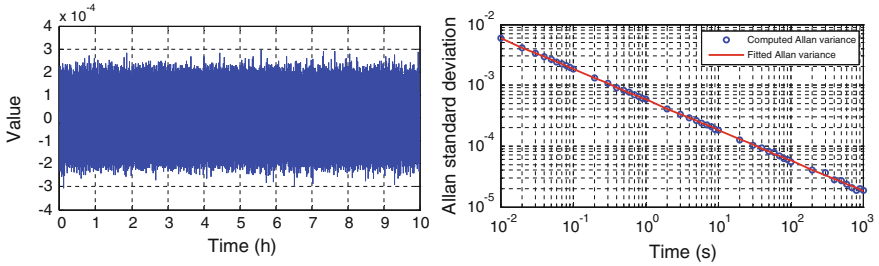

Fig. 44.4 ARW properties in time and Allan variance domains using numerical example

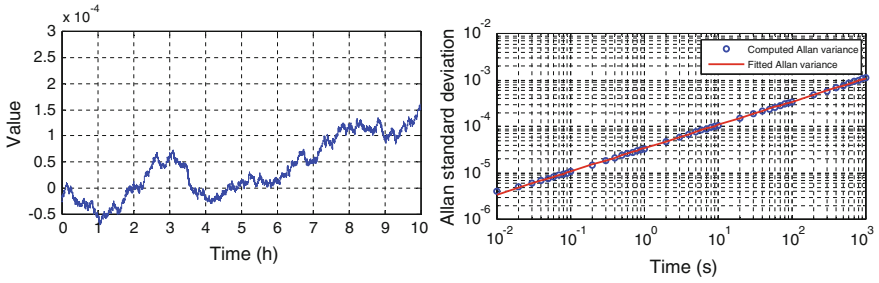

Fig. 44.5 RRW properties in time and Allan variance domains using numerical example

Table 44.2 Statistics of estimated values

	N	K
True	5.8682e−004	5.8682e−006
Estimated	5.8682e−004	5.8636e−006
Slope	−0.5087	0.4930

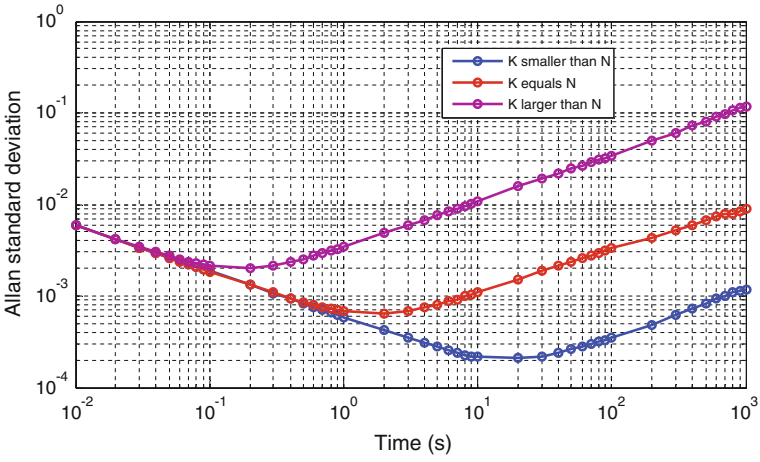

Fig. 44.6 Allan variance results

Table 44.3 Estimated value

	K	*K*	*K*
True	5.8682e−003	5.8682e−004	5.8682e−005
Conventional	6.3542e−003	5.0191e−004	6.4952e−005
Proposed	5.9762e−003	5.6072e−004	5.9082e−005

Table 44.4 Technical specifications of CMIGITS

Noise type	Values
Gyro bias	5 deg/h
Angular random walk	0.035 deg/root-h
Accelerometer bias	500 μg
Velocity random walk	60 μg/root-Hz

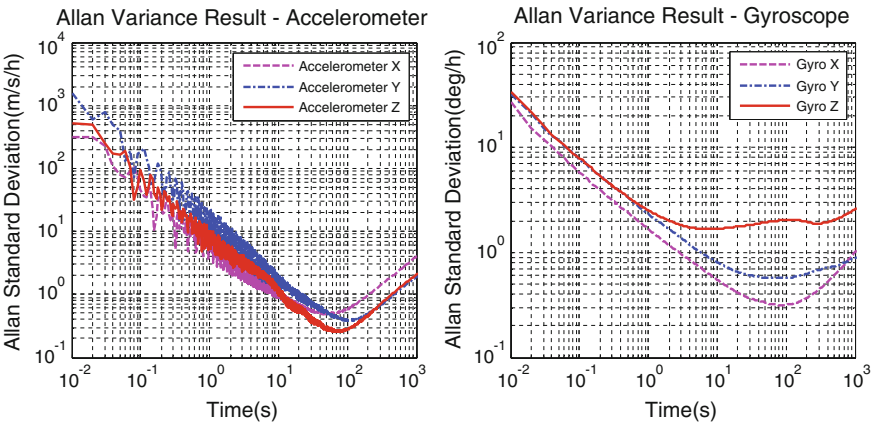

Fig. 44.7 Allan variance log–log plot for inertial sensors

The results of the Allan variance log–log plot for inertial sensors are shown in Fig. 44.7. It can be seen that two main noise sources present in the accelerometers and gyros data are ARW and RRW. The dominant error in the long cluster times is RRW with the slope of 1/2. By getting the coefficients for the main stochastic errors from these two methods, the error model can be applied in the GPS/INS integrated navigation system.

The integration system was first operated in GPS/INS integration mode. After obtaining stable navigation solutions, the GPS signal was cut off intentionally for 100 s and the system was operated in the INS stand-alone mode during this period. With the Google Maps as a coarse reference, the navigation results for these two models are compared in Fig. 44.8. It can be noted the trajectory based on proposed method (marked in green colour) is much closer to the road compared with that

Fig. 44.8 Trajectory comparisons

from conventional method (marked in red colour). The horizontal position accuracy has improved 15 m. This verifies that the stochastic modelling can be estimated much better by using the proposed method compared with the conventional method, in terms of the navigation accuracy.

44.4 Conclusion Remarks

This paper presents a method to estimate the spectral density of angle random walk and the rate random walk. A performance comparison between conventional method and proposed method was conducted using both simulated and real data. The results show conventional method can give an accurate estimate for angle random walk but not for rate random walk, while proposed method can give a better estimation for these two noises when the interactive influences are considered. Furthermore, from the results of the field tests, a similar conclusion can be drawn. After getting the coefficients for the main stochastic errors, a better error model can be applied into the GPS/INS integrated navigation system, which largely enhances the capability of bounding the inertial sensor errors during GPS blockage.

References

1. Noureldin A, Karamat TB, Eberts MD et al (2009) Performance enhancement of MEMS-based INS/GPS integration for low-cost navigation applications. IEEE Trans Veh Technol 58(3):1077–1096
2. Groves PD (2008) Principles of GNSS, inertial, and multisensor integrated navigation systems. Artech House, Massachusetts
3. Park M, Gao Y (2008) Error and performance analysis of MEMS-based inertial sensors with a low-cost GPS receiver. Sensors 8(4):2240–2261
4. Sadi F, Klukas R (2013) New jump trajectory determination method using low-cost MEMS sensor fusion and augmented observations for GPS/INS integration. GPS Solutions 17(2):139–152
5. Han S, Wang J (2011) Quantization and colored noises error modeling for inertial sensors for GPS/INS integration. IEEE Sens J 11(6):1493–1502
6. IEEE Standard Specification Format Guide and Test Procedure for Single-Axis Interferometric Fiber Optic Gyros (1997) New York, USA
7. Ng LC, Pines DJ (1997) Characterization of ring laser gyro performance using the Allan variance method. J Guid Control Dyn 20(1):211–214
8. EI-Sheimy N, Hou H, Niu X (2008) Analysis and modeling of inertial sensors using Allan variance. IEEE Trans Instrum Meas 57(1):140–149
9. Zhao Y, Horemuz M, Sjöberg LE (2011) Stochastic modelling and analysis of IMU sensor errors. Arch Photogrammetry Cartography Remote Sens 22:437–449

Chapter 45
The Acceleration Sensitive Coefficient Calibration of the Crystal Oscillator Based on the GPS Carrier Control Principle

Yijun Hang, Rongbing Li, Jianye Liu, Li Xing and Yi Wang

Abstract In acceleration and vibration environment, to weaken frequency instability influence of the crystal oscillator on GPS carrier loop and rectify frequency compensation, researchers usually adopt the solution of crystal oscillator frequency acceleration compensation. The vital basis of compensating frequency errors is how to obtain accurately corresponding sensitive parameters of crystal oscillator. In the traditional calibration approach of acceleration sensitivity coefficient, indispensably using precise frequency reference and measurement equipment makes the calibration process expensive and complex, that fails to be widely applied in GPS navigation system. Combined a precise frequency reference of GPS satellites with the carrier tracking loop principle, the paper analyzes the acceleration frequency errors transmission mechanism of crystal oscillator in the *carrier tracking loop*, and designs an adaptive weighted EKF to handle frequency bias observed values synchronously in multiple tracking loops, which reduces frequency bias estimating noise and separates frequency offset and frequency drift rate, from the receiver's frequency bias observation in the crystal oscillator. And on this basis, acceleration sensitivity coefficients of crystal oscillator calibrate on the super tight combination navigation board by 2g flipping calibration method. The experiments show that the method is able to effectively calibrate acceleration sensitivity coefficients of crystal oscillator, which is the solution base of compensating crystal oscillator acceleration frequency errors on related GPS technology research.

Keywords GNSS · Carrier tracking loop · Crystal oscillator · Acceleration sensitive coefficient

Y. Hang (✉) · R. Li · J. Liu · L. Xing · Y. Wang
Nanjing University of Aeronautics and Astronautics, Nanjing 210016, China
e-mail: hangyijun@nuaa.edu.cn

Y. Wang
Beijing Institute of Automation Control Equipment, Beijing 100074, China

J. Sun et al. (eds.), *China Satellite Navigation Conference (CSNC) 2014 Proceedings: Volume III*, Lecture Notes in Electrical Engineering 305,
DOI: 10.1007/978-3-642-54740-9_45,

45.1 Introduction

With the increasing development of satellite navigation technology and special navigation requirements of high dynamic carriers such as ultra-high speed of sound aircrafts, domestic and overseas research institutions and companies has carried out extensive researches on receiver signal loop tracking technology in high dynamic environment, the main of which is how to ensure the reliability of receiver signal tracking loop in the high-dynamic condition [1, 2].

GPS signal loop includes both carrier tracking loop and code tracking loop, whether in the ordinary receivers or deep integration receivers. Since the carrier frequency is generally much higher than the code frequency, the changes of the carrier frequency are more rapid and complex in the high-dynamic condition, which makes the stability control of the carrier loop more difficult than the code loop in the GPS signal loop control [3–5].

On the pre-exiting papers about receiver carrier loop control methods and theory researches, the researches mainly focus on the influences of both receiver exercise stress and loop control on loop stability control. And the receiver exercise stress influence on GPS signal is also considered in related stimulating verification [6–8].

When the receiver is practically designed and used, receiver's *crystal oscillator* as the local clock benchmark of *carrier tracking loop,* in the condition of accelerated motion, poses the same influences on loop tracking stability as the Doppler changes of GPS signal produced by traditionally researching exercise stress [9, 10]. As a result, the effective solutions for weakening the exercise stress influence on receiver's loop are to research the frequency error transmission characters of receiver's *crystal oscillator* in the condition of accelerated motion, calibrate and compensate accelerating sensitive coefficients of the *crystal oscillator* frequency. How to precisely calculate accelerating sensitive coefficients of the GPS navigation system is the vital precondition, for compensating accelerating sensitive frequency. In the traditional calibration approach of acceleration sensitivity coefficient, indispensably using precise frequency reference and measurement equipment makes the calibration process expensive and complex, that fails to be widely applied in GPS navigation system.

The paper has researched the work principle and errors transmission characters of *crystal oscillator*, and then analyzed main error sources of the *crystal oscillator*. With the respect to the problems of large frequency bias observation noise and complex coupling errors in GPS tracking loop, the adaptive weighted EKF algorithm is proposed, which sufficiently utilizes frequency bias observation provide by multiple tracking loop, and separates frequency bias term and frequency bias drift term from observations. Based on this, the accelerating sensitive coefficients are calibrated on biaxial high precision turntable by 2g flipping calibration method. The experiments show that, by the proposed solutions, the frequency bias term is effectively extracted from loop observations, and the influences on calibration caused by frequency bias drift and loop control noise is restrained, which implement the calibration of sensitive coefficients changing over acceleration in the

crystal oscillator of GPS carrier loop. The adopted methods in the paper is operated conveniently and economical, with no need for extra equipment, so it is able to widely spread and applied in GPS navigation systems.

For the past few years, based on the FPGA + DSP open hardware experiment platform of GPS super tight integration navigation system, the Navigation Research Center (NRC) of Nanjing University of Aeronautics and Astronautics (NUAA) has researched carrier loop control methods of super tight integration navigation system, analyzed *crystal oscillator* error transmission process in the *carrier tracking loop*, and acquired better research progression on the aspects of super tight integrated loop control and integrated filter technology.

45.2 Crystal Oscillator Errors Modelling and Transmission Mechanism Research on GPS Carrier Loop

45.2.1 Work Principle and Errors Model of Crystal Oscillator

In ideal situations, when the *crystal oscillator* operates normally, its output is the single sinusoidal signal, the frequency of which is called crystal's carrier frequency indicated as f_{c0} (CF for short, namely nominal frequency). As the acceleration, temperature and other conditions are changing, the carrier frequency output of *crystal oscillator* will change. f_c is the current frequency given by (45.1):

$$\begin{aligned} f_c &= f_{co} + \Delta f_c \\ \Delta f_c &= f_{c0} a_b \Gamma_a + \delta f_T \Delta T_c + \delta f_c + \int \delta \dot{f}_c + v f_c \end{aligned} \tag{45.1}$$

In (45.1), Δf_c represents the frequency difference of *crystal oscillator* synthetically produced by main error sources, called as frequency bias between output frequency and nominal frequency of *crystal oscillator*. According to different errors incentive mode and error characteristics, the frequency error sources of *crystal oscillator* are divided into four types as follows:

1. Long-period frequency bias δf_c [ppb/year]—describing slowly changing frequency offsets over time.
2. Short-period drift [ppb/s]—describing short-period random and unstable frequency characters of the *crystal oscillator*, such as frequency jitter noise $v f_c$ and short-cycle frequency offset rate $\int \delta \dot{f}_c$, etc.
3. Sensitive coefficients of temperature drift δf_T [ppm]—indicating frequency difference by the changes of the *crystal oscillator* frequency with the temperature changing.

4. *Acceleration sensitive coefficient* Γ_a [ppb/g]—indicating the coupling relationship between the changes of the *crystal oscillator* frequency and motional acceleration.

When the continuous running time of the *crystal oscillator* is shorter, and the changes of surrounding temperature are small, we consider the long-period frequency bias and temperature drift errors as the constants, which would not affect the tracking stability of receiver carrier loop during the GPS loop tracking process.

Researches show that, the main influence factors of GPS carrier loop tracking stability is short-period random errors and acceleration's sensitive coefficients errors. Therefore, by combing long-period frequency offset with temperature drift errors, and with respect to *acceleration sensitive coefficient* errors, the output frequency combined model is shown as follows:

$$f_c = f_{co}(1 + a_b\Gamma_a) + \delta f_c + \int \delta \dot{f}_c + \nu f_c \tag{45.2}$$

where $a_b(\, a_{bx} \quad a_{by} \quad a_{bz}\,)_{1\times 3}$ respectively represents the X, Y and Z axis acceleration of the *crystal oscillator*, the unit of which is gravity acceleration g. $\Gamma_a(\, \Gamma_{ax} \quad \Gamma_{ay} \quad \Gamma_{az}\,)_{3\times 1}$ is *acceleration sensitive coefficient* of the *crystal oscillator* frequency, and the unit is ppb/g.

45.2.2 Research on the Frequency Errors Transmission Mechanism of the Crystal Oscillator in the GPS Tracking Loop

where f_o is the local carrier frequency of the receiver, called as channel tracking control frequency. By above deduction, we get the relationship among tracking frequency f_o, carrier Doppler frequency, the frequency error of the *crystal oscillator* Δf_c and the RF front-end down-conversion clock multiplier factor M_{IF} given by (45.3):

$$f_o = f_{dop} + f_{IF} + M_{IF}\Delta f_c \tag{45.3}$$

In the traditional receiver carrier control loop, the loop control output of whether second order or third order phase-locked loop contains not only the frequency offset but also the integral frequency offset drift. As a result of the different control parameters setting, or the noise ratio change of the satellite signal, the output frequency of the carrier loop control system usually includes a larger control noise, which has no effect on signal loop tracking control, but will bring bigger errors to *acceleration sensitive coefficient* calibration method of the *crystal oscillator* based on signal control loop data frequency, as shown in Fig. 45.1. Frequency difference between the loop output frequency and the calculated Doppler frequency can be expressed as: $f_o - f_{dop}$.

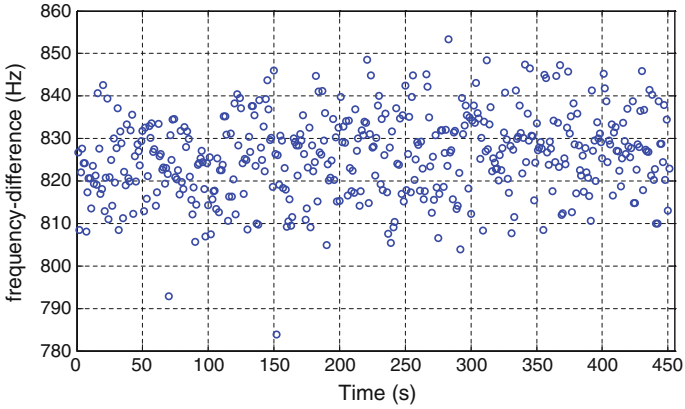

Fig. 45.1 Data distribution of original frequency difference

From Fig. 45.1, we can find that this frequency difference signal is very volatile, where the largest fluctuation is even more than 50 Hz. From the whole distribution of the frequency difference, there is a small drift process. Therefore, in order to accurately estimate the acceleration sensitivity coefficients of the *crystal oscillator* under the condition of different frequency deviation of acceleration input, observation signal noise should be filtered out and frequency difference and the integral frequency offset drift should be separated from observations firstly.

45.3 Acceleration Sensitive Coefficient of the Crystal Oscillator Calibrated Method Research Based on Adaptive Weighted EKF

45.3.1 State Model of Adaptive Weighted EKF

According to above analysis, when establish the state equation, frequency difference and frequency change is chosen as the state:

$$X_k = \begin{pmatrix} \delta f_c & \delta \dot{f}_c \end{pmatrix}^T \tag{45.4}$$

In the process of modeling, we use first-order Markov model to describe the change rule of the *crystal oscillator* frequency difference δf_c. The state transfer model of δf_c is described as follows, where ΔT is the sampling interval time:

$$\delta f_{c/k+1} = \delta f_{c/k} - \frac{\Delta T}{T_1}\delta f_{c/k} + \delta \dot{f}_{c/k}\Delta T + v_1 \tag{45.5}$$

In addition, the state update model of the *crystal oscillator* frequency drift can be established according to the first-order Markov process given by (45.6):

$$\delta\dot{f}_{c/k+1} = \delta\dot{f}_{c/k} - \frac{\Delta T}{T_2}\delta\dot{f}_{c/k} + v_2 \tag{45.6}$$

where T_1, T_2 is correlation time of the first-order Markov process, v_1, v_2 respectively represents frequency difference and Gaussian white noise of frequency drift. According to above model, building complete filtering equation is given by (45.7), where $\phi_{k/k-1}$ is state-transition matrix, Γ_{k-1} is noise-coefficient matrix and is noise matrix.

$$X_k = \phi_{k/k-1}X_{k-1} + \Gamma_{k-1}W_{k-1} \tag{45.7}$$

45.3.2 Observed Model of Adaptive Weighted EKF

According to the *crystal oscillator* error transmission mechanism in the receiver carrier loop, in receiver static case, the output frequency of carrier loop minus the calculated Doppler frequency which can acquire frequency drift observation of the *crystal oscillator*.

In order to further reduce the state estimation deviation, by making full use of the frequency difference observation of different GPS satellites, we set up the adaptive weighted observation equation with N carrier frequency difference, and the observation is expressed in (45.8).

$$Z_k = \begin{pmatrix} f_{o1} - f_{dop1} \\ f_{o2} - f_{dop2} \\ \vdots \\ f_{on} - f_{dopn} \end{pmatrix} \tag{45.8}$$

Taking one group of the transfer relationship between the observation and the state as an example, the observation model is set up in (45.9).

$$f_{oi} - f_{dopi} = \delta f_c + \delta\dot{f}_c\Delta T + v_i, \quad i = 1 \sim N \tag{45.9}$$

The discretization observation equation is given by (45.10), where $H_{k/k-1}$ is the observation transfer matrix, G_k is the observation noise coefficient matrix, and V_k is the observation noise matrix.

$$Z_k = H_{k/k-1}X_k + G_kV_k \tag{45.10}$$

where according to the channels' noise ratio of GPS carrier, the observation noise value can be adjusted to improve the filtering accuracy.

Table 45.1 Calculation positions of the crystal oscillator

Axis	X	Y	Z
Input acceleration	+g	+g	+g
Frequency difference	Δf_{x+}	Δf_{y+}	Δf_{z+}
Input acceleration	−g	−g	−g
Frequency difference	Δf_{x-}	Δf_{y-}	Δf_{z-}

45.3.3 2g Flipping Acceleration Sensitive Coefficient Calibration Algorithm Based on Biaxial Turntable

Based on the design of the filter processing algorithm, during the calibration process, we also have to exert incentive accelerations on the different axis of the *crystal oscillator*, in order to incent the axis' frequency offset when there is a coaxial acceleration.

As a result, when the calibration experiment is carried out, the GPS receiver is installed on the biaxial high precision turntable. And then the position of the *crystal oscillator* is replaced in a different angle position according to Table 45.1, which makes three axial *crystal oscillator* of the receiver and the gravitational acceleration coincident or reversed respectively, in order to exert twice gravitational acceleration successively. Thus, we can incent the *acceleration sensitive coefficient* variation of the frequency offset in the receiver loop output signal.

By calculating the frequency offset output variation with the exerting acceleration variation, we calculate each axial acceleration sensitivity coefficient, that is, each axial acceleration sensitivity coefficient of the *crystal oscillator* can be calculated in (45.11).

$$\begin{aligned} \Gamma_x &= \frac{\Delta f_{x+} - \Delta f_{x-}}{2f_{L1}} \\ \Gamma_y &= \frac{\Delta f_{y+} - \Delta f_{z-}}{2f_{L1}} \\ \Gamma_z &= \frac{\Delta f_{z+} - \Delta f_{z-}}{2f_{L1}} \end{aligned} \tag{45.11}$$

45.4 Design and Calibration Validation Experiment of GPS Receiver Based on FPGA + DSP

45.4.1 Design of GPS Receiver System Based on FPGA + DSP

We use FPGA + DSP open architecture design for the GPS receiver experiment platform, based on which, the required loop tracking frequency and the Doppler estimated data can be calculated by extracting the calibration observation in the

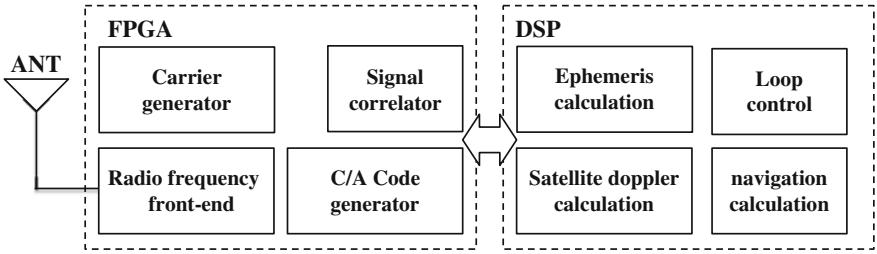

Fig. 45.2 Structure of system module

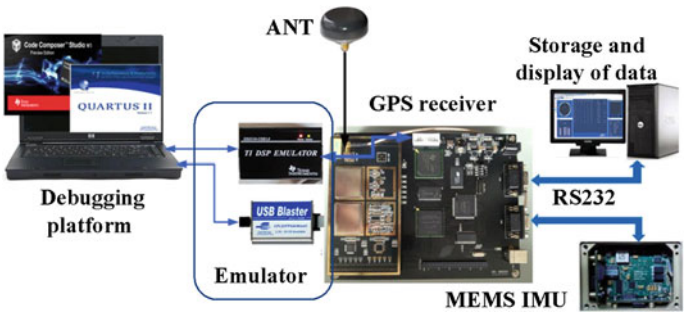

Fig. 45.3 Open experiment platform of GPS

program. The structure of system module of the GPS receiver is shown in Fig. 45.2.

As shown in Fig. 45.2, the receiver signal processing module primarily includes two signal processing units, where the FPGA processing unit contains four modules, such as the RF front-end data acquisition module, carrier and code signal generation module, and signal related module. In DSP signal processing unit, there is data code synchronization and ephemeris decoding module, satellite Doppler frequency calculation module, loop control module and navigation solution module.

In the calibration experiments, loop frequency control variations and Doppler frequency calculation value shown in Fig. 45.3 is stored and processed, by serial ports sending to the calibration experiment required estimation of control and satellite value can be sent to the upper computer. Figure 45.3 is the physical connection diagram of the GPS experiment system platform based on FPGA + DSP open architecture.

This experiment system is mainly composed of debugging and simulation equipment, GPS signal processing board, a serial port to receive, display and storage devices.

Fig. 45.4 Experimental system installed on the turntable

45.4.2 Calibration Experiment and Results Analysis

We define three axial orthogonal coordinate of the *crystal oscillator* installed on the GPS receiver loop board, and then install the loop board on the biaxial high precision turntable. The frequency output of the *crystal oscillator* in different directions can be measured, through the control turntable is staying for a period of time in the position shown in Table 45.1, where the turntable calibration installation is shown in Fig. 45.4.

Figure 45.5 is contrast curves of frequency offset signal before and after filter the eleventh collected GPS signal in the static case, the noise ratio of which 40 dB-Hz. Before filter, the variance of the original frequency difference signal is about 93.6 Hz, and after filter, the variance of the original frequency difference signal frequency drops to 1.7 Hz. Not only the signal noise is greatly reduced, that is the foundation for subsequent calibration data processing, but also the frequency drift rate of the *crystal oscillator* can be calculated.

By calculating filter data means, the accurate frequency difference can be obtained, when coaxial gravitational acceleration is input as shown in Table 45.2.

According to the characteristic of GPS signals, RF carrier frequency is $f_{L1} = 1{,}575.42$ MHz, and then from Table 45.2 and (45.1), the acceleration sensitivity coefficient calibration results of the *crystal oscillator* are shown in Table 45.3.

Calculated results of Table 45.3, *acceleration sensitive coefficient* in the Z axis is larger. Thus, if this error was not compensated, a larger frequency error would be produced in the *carrier tracking loop,* under the high dynamic situation, which would affect the stability of the carrier loop tracking control.

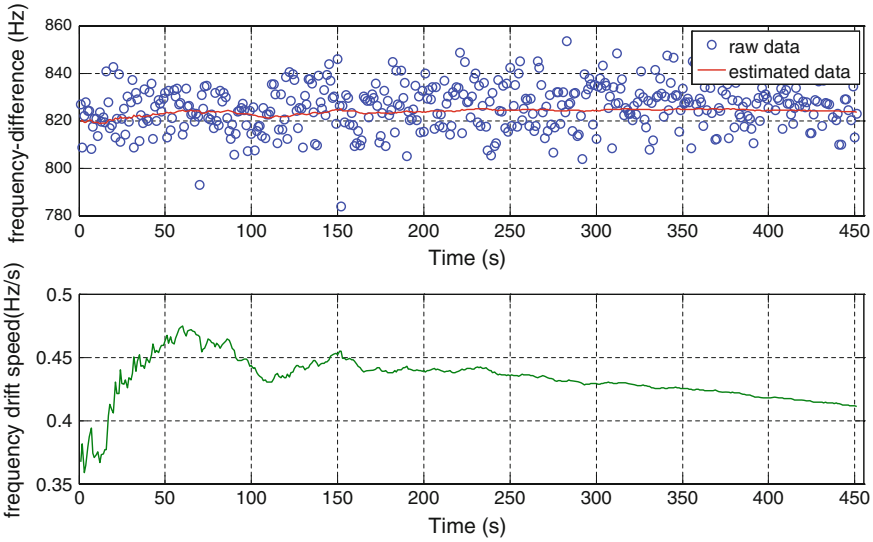

Fig. 45.5 Contrast curves of frequency offset signal before and after filter

Table 45.2 Processing results of calculation data

Axis	X	Y	Z
Input acceleration	**+g**	**+g**	**+g**
Frequency difference	819.9646	801.4141	792.9928
Input acceleration	**−g**	**−g**	**−g**
Frequency difference	822.7904	807.7643	810.5261

Table 45.3 Calculated results of acceleration sensitive coefficient

Axis	X(Hz)	Y(Hz)	Z(Hz)
Frequency drift due to acceleration	$\Delta f_{x+} - \Delta f_{x-}$	$\Delta f_{y+} - \Delta f_{y-}$	$\Delta f_{z+} - \Delta f_{z-}$
	−2.8258	−6.3502	−17.5333
Oscillator g-sensitivity values	**X (ppb/g)**	**Y (ppb/g)**	**Z (ppb/g)**
	−0.89754	−2.01695	−5.56895

45.5 Conclusion

The paper build output frequency error models of, research the frequency error transmission mechanism of the *crystal oscillator* the GPS receiver *carrier tracking loop*, design the adaptive weighted EKF filter based on the frequency deviation of GPS tracking loop, deal with the influence of the loop noise and frequency difference drift rate on frequency difference estimation precision. On this basis, the

2g flip *acceleration sensitive coefficient* calibration algorithm is proposed, the *acceleration sensitive coefficient* calibration is experimented on by open GPS super tight integration development platform, which accurately estimate the corresponding acceleration sensitive parameters of the *crystal oscillator*.

The paper research lays the foundation for acceleration sensitive error compensation technology of the *crystal oscillator* output frequency in the GPS receiver, and improves the *crystal oscillator* frequency instability of GPS navigation system in high dynamic situation. It is the important reference to research on the carrier tracking control optimization technology of the receiver and super tight integrated navigation system in high dynamic situation.

Acknowledgments This work was partially supported by the National Natural Science Foundation of China (Grant No. 61374115, 61273057), the innovation of graduate student training project in Jiangsu province (Grant No. CXZZ12_0159), and the Industry-Academy-Research Fund Project supported by AVIC.

References

1. Bhaskar S, Curran JT, Lachapelle G (2012) Effect of oscillator quality on ultra-tight GPS/INS aided carrier phase tracking. In: ION GNSS12 conference, session A1, Nashville, TN
2. Xie F, Liu J, Li R et al (2013) Deeply SINS/GPS integrated navigation algorithm based on tracking loop correlation measurements. J Chin Inertial Technol 21(004):472–477
3. Ji L, Shan Q, Tang Q, Lin M (2012) The acceleration effects on crystal oscillators and research on compensating technique. J Astronaut Metrol Meas 32(2):37–41
4. Lashley M, Bevly DM, Hung JY (2009) Performance analysis of vector tracking algorithms for weak GPS signals in high dynamics. IEEE J Sel Top Sign Process 3(4):P8–20
5. Huang J, Li R, Liu J et al (2012) High dynamic self-adjusting software receiver loop tracking technology research. In: The 3rd China satellite navigation electronic corpus academic conference—S07 BEIDOU/GNSS user terminal technology
6. Julier SJ, Uhlmann JK (2004) Unscented filtering and nonlinear estimation. Proc IEEE 92:401–422
7. Seo J, Walter T, Chiou T-Y, Enge P (2009) Characteristics of deep GPS signal fading due to ionospheric scintillation for aviation receiver design. Radio Sci 44(1):16–22
8. Henkel P, Giger K, Günther C (2008) Multi-carrier vector phase locked loop for robust carrier tracking. In: Proceedings of the European Navigation Conference (ENC), Toulouse, France
9. Gao G, Datta-Barua S, Walter T, Enge P (2007) Ionospheric effects for wideband GNSS signals. In: ION annual meeting, Cambridge (MA), USA
10. Angus J (2006) RAIM with multiple faults. J Inst Navig 53(4):249–257

Chapter 46
GPS/GLONASS/COMPASS Combined Positioning Based on CNMC

Zhang Yize, Chen Junping, Wu Bin, Wang Jiexian, Yang Sainan and Duan Bingbing

Abstract GLONASS and COMPASS system have become important part of GNSS system in the past few years. With the construction and improvement of these systems, multi-system combined solutions will greatly improve the accuracy in GNSS positioning. The current research of multi-system positioning mainly focuses on the combination of GPS and GLONASS systems, while the data of COMPASS has not combined with other systems. This paper focuses on the GPS/GLONASS/COMPASS multi-system combined positioning. Experiments using the data of GPS/GLONASS/COMPASS capable stations were conducted for positioning. Results show that the accuracy of triple-system positioning is better than that of single or combination of two systems. To reduce the noise of the pseudorange, a real-time algorithm called CNMC is applied. The smoothed GNSS pseudorange is then used for combined positioning. Results show that this method can improve the reliability of the estimated parameters and improve the positioning precision by about 30–60 %, depending on the precision of the satellite orbits and clocks. A station differential strategy is proposed to reduce the effect of orbits and clocks, which is proved to dramatically improve positioning precision.

Keywords Multi-system positioning · Code noise and multipath correction (CNMC) · Multipath effect · Station differencing

Z. Yize (✉) · W. Jiexian · D. Bingbing
College of Surveying and Geo-Informatics, Tongji University, Shanghai, China
e-mail: zhyize@163.com

Z. Yize · C. Junping · W. Bin · Y. Sainan · D. Bingbing
Shanghai Astronomical Observatory, Chinese Academy of Science, Shanghai, China

J. Sun et al. (eds.), *China Satellite Navigation Conference (CSNC) 2014 Proceedings: Volume III*, Lecture Notes in Electrical Engineering 305,
DOI: 10.1007/978-3-642-54740-9_46,

46.1 Introduction

As GPS, GLONASS, Galileo and COMPASS have become the four mainly global positioning systems in the past few decades, the inter-compatibility and inter-operation among these systems have become big issues. Traditional multi-system application mainly focuses on GPS/GLONASS combined positioning. Results show that the combined system positioning precision is better than single system both in pseudorange and phase [1–3]. The COMPASS system has put into operation and starts to provide official service by the year 2012 [4]. According to the design of the COMPASS system, the positioning accuracy is 25 m horizontally and 30 m vertically in 2012, and the service coverage area is regional (mainly in Asia). By the year of 2020, the global COMPASS system will be in full operation with positioning accuracy of within 10 m [5]. A lot of study on COMASS positioning performance has been discussed in recent few years [6–9]. However, the COMPASS combined positioning with GPS or GLONASS, or even a triple-system combined positioning is rarely discussed so far. Based on this background, we study the GPS/GLONASS/COMPASS combined positioning in this paper.

The COMPASS Navigation Satellite System (CNSS), also named Beidou-2, is China's second-generation satellite navigation system, which is capable to provide positioning, navigation and timing (PNT) service to users on a continuous worldwide basis. Unlike the other systems, COMPASS utilizes the Geostationary Orbit (GEO) and Inclined Geosynchronous Satellite Orbit (IGSO) satellites for a better regional service [6]. However, the constellation of GEO satellites makes the multipath effect on them much more serious than that of IGSO or MEO satellites [8]. Many algorithms have been discussed to correct the multipath effect [7, 8, 10]. Results demonstrate that these methods are able to correct multipath effect in different level. In this paper, we use a method called Code Noise and Multipath Correction (CNMC) to estimate the multipath effect and make the pseudorange smoother. Then the smoothed GNSS pseudorange can be used for multi-system GNSS positioning.

However, the smooth level of the pseudorange data greatly depends on the precision of satellite orbits and clocks, which is usually up to meter-magnitude for navigation ephemeris. For COMPASS system, it is worse than GPS and GLONASS. To eliminate this error, a station differencing strategy is used here.

The paper is organized as following: a brief introduction is given in Sect. 46.1; Sect. 46.2 focuses on the multi-system GNSS positioning model; Sect. 46.3 introduces the algorithm of CNMC, the station differencing strategy is also discussed in this part; Experiments and results on CNMC are listed and discussed. Section 46.4 gives the conclusions.

46.2 GPS/GLONASS/COMPASS Combined Positioning

Considering the multipath effect, we start with the GNSS pseudorange and carrier phase observation equations expressed in meters as follows:

$$\begin{cases} P_1 = \rho - c \cdot \delta^j + c \cdot \delta_i + \delta_{trop} + \frac{1}{f_1^2}\delta_{iono} + Mp_1 + \varepsilon_{p1} \\ P_2 = \rho - c \cdot \delta^j + c \cdot \delta_i + \delta_{trop} + \frac{1}{f_2^2}\delta_{iono} + Mp_2 + \varepsilon_{p2} \\ L_1 = \rho - c \cdot \delta^j + c \cdot \delta_i + \delta_{trop} - \frac{1}{f_1^2}\delta_{iono} + M\phi_1 + amb_1 + \varepsilon_{\phi 1} \\ L_2 = \rho - c \cdot \delta^j + c \cdot \delta_i + \delta_{trop} - \frac{1}{f_2^2}\delta_{iono} + M\phi_2 + amb_2 + \varepsilon_{\phi 2} \end{cases} \tag{46.1}$$

where P_1, P_2, L_1 and L_2 are the pseudorange and carrier phase observations in each band, ρ is the geometric distance between the satellite and receiver, δ^j and δ_i mean the clock corrections in satellite and receiver, δ_{trop} and δ_{iono} are the tropspheric and ionospheric delays, $Mp_1, Mp_2, M\phi_1$ and $M\phi_2$ are the multipath effects in pseudorange and carrier phase, f_1, f_2 is the frequency, ε_{p1}, ε_{p2}, $\varepsilon_{\phi 1}$ and $\varepsilon_{\phi 2}$ are the observation noise.

To eliminate the ionospheric delay, the Ionospheric-Free (IF) combined is applied, so the expression of pseudorange in Eq. (46.1) can be rewritten as:

$$P_{IF} = \rho - c \cdot \delta^j + c \cdot \delta_i + \delta_{trop} + Mp_{IF} + \varepsilon_{pIF} \tag{46.2}$$

In GPS/GLONASS/COMPASS combined positioning, the system time offset should be taken into account [2, 3], so the receiver clock parameter δ_i is different for different system. We conduct a field experiment in Shanghai using Trimble NET R9 receiver, which can receive triple-system GNSS data. Then the multi-system GNSS observations are used for kinematic positioning. In the positioning processing, only the coordinate of the receiver and the receiver clocks in different systems are estimated.

The kinematic pseudorange positioning statistics for different combinations are listed in Table 46.1. DOP value is a very important factor to specify GNSS geometry effects on user positioning accuracy [9]. We compare the DOP value for each system and combined triple-system in Fig. 46.1. Due to the constellation of GEO and IGSO satellites, the mean DOP value of COMPASS is much bigger than that of GPS or GLONASS, and that is why the RMS of single COMPASS positioning is worse in horizontal than the other two systems. However, any kind of combination of different systems improves the positioning accuracy, especially for a GPS/GLONASS/COMPASS combination. We can also see from Fig. 46.1 that the DOP value is somehow more stable for COMPASS, which is due to the fact that the GEO and IGSO satellites, visible for the regional area most of the time, are the main contributor to the current COMPASS constellation. Both for GPS and COMPASS, there are sometime DOP value jumps, which is because the missing data for one satellite at that epoch indicating bad quality of data.

Table 46.1 Kinematic pseudorange positioning precision for different GNSS combination

Combination	RMS			
	N/m	E/m	U/m	3-D/m
G	1.374	3.884	3.532	5.427
R	1.970	3.773	5.018	6.580
C	7.585	3.045	7.265	10.935
R + C	3.299	1.605	3.196	4.865
G + R	3.625	2.852	4.753	4.754
G + C	3.116	0.819	2.513	4.086
G + R + C	2.317	1.003	1.976	3.206

C stands for COMPASS, *G* for GPS, *R* for GLONASS

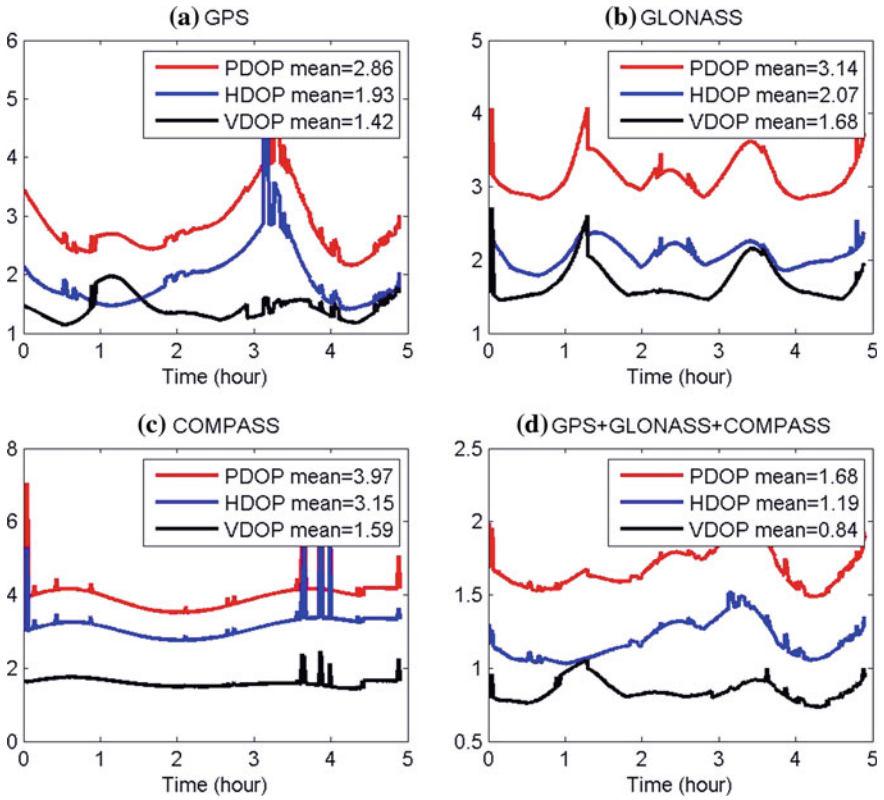

Fig. 46.1 The DOP value for different systems of a GNSS station in Shanghai (DOY 350, 2012)

46.3 Carrier Phase Smoothed Pseudo-range

To smooth the pseudorange with carrier phase, algorithm such as Hatch Filter [11], RNXSMT [12] or CNMC [8] are usually applied. Hatch Filter uses the epoch-differenced IF (Ionospheric-Free) combination phase to smooth IF combination pseudorange. This algorithm is simple and easy to realize. However, it doesn't take the multipath effect into account. In other words, it considers the epoch-differenced multipath effects as the same value for the pseudorange and phase observations. Hatch Filter is a real-time algorithm, which is widely used when the multipath effect is small enough and can be neglected. However, the multipath effect in pseudorange is much more serious for COMPASS system, especially for GEO and IGSO satellites. The RNXSMT algorithm is a post-processing method, which is not suitable for real-time positioning. In this part, we adopt the CNMC algorithm for real-time COMPASS combined positioning.

46.3.1 CNMC Algorithm

The theory and details on CNMC can be found in relevant bibliography [8]. We only give the formulas here.

Taking the L1 band for example, the multipath effect in pseudorange for dual-frequency observations in Eq. (46.1) can be written as follows:

$$\begin{cases} Mp_1 = P_1 - L_1 - 2\frac{f_2^2}{f_1^2 - f_2^2}(L_1 - L_2) - CAmb_1 \\ Mp_2 = P_2 - L_2 - 2\frac{f_1^2}{f_1^2 - f_2^2}(L_1 - L_2) - CAmb_2 \end{cases} \tag{46.3}$$

where $CAmb_1$ and $CAmb_2$ is the combined ambiguities.

$CAmb_1$ and $CAmb_2$ can be get from a real-time formula. Take L1 band as example, if no cycle slip happens in an observation arc, it can express as follows:

$$CAmb_1(t_n) = \frac{n-1}{n} CAmb_1(t_{n-1}) + \frac{1}{n}[P_1(t_n) - L_1(t_n) - 2\frac{f_2^2}{f_1^2 - f_2^2}(L_1(t_n) - L_2(t_{n-1}))] \tag{46.4}$$

From Eqs. (46.3) and (46.4), the multipath effect can be estimated in a real-time way. At the first epoch, the multipath effect is initialized as zero. With the increase of the arc, the combined ambiguity will be more and more precise. At the same time, the multipath effect could be derived more precisely. However, when a cycle slip happens, a new initialization will be restarted. So the effectiveness of this algorithm is subject to the data quality [8].

Having known the multipath effect in pseudorange, it can be added to the raw pseudorange observation to get "cleaned" pseudorange. In some way, the CNMC is a carrier phase smoothed pseudorange method in fact.

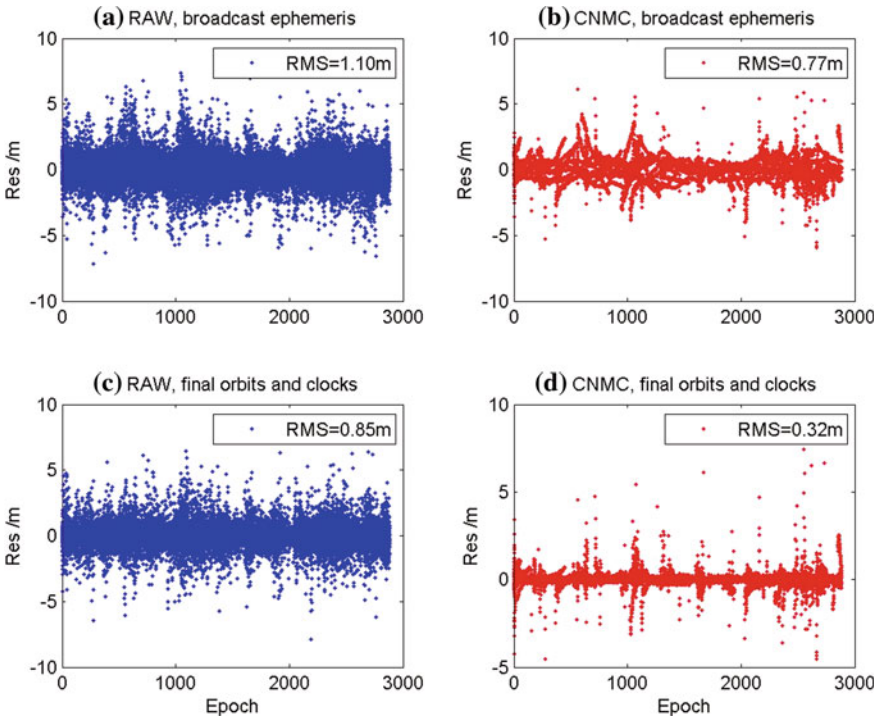

Fig. 46.2 The residuals of GPS observations for raw and smoothed pseudorange using different products (SHAO, DOY 298, 2012)

Here we use the GPS data of the IGS station at Shanghai (SHAO) to verify the CNMC algorithm. The broadcast ephemeris and IGS final orbits with satellite clocks are respectively applied. Figure 46.2 shows the effect of CNMC algorithm. From (a) and (b) in Fig. 46.2 we can see that the quality of the smoothed pseudorange is improved by 30 % compared with the raw data. This improvement can reach up to 62 % using IGS final products. It indicates that CNMC reduces the noise of pseudorange and make it smoother. However, the smooth level greatly depends on the precision of the satellite orbits and clocks.

46.3.2 CNMC Application and Improvement Based on Station Differencing

As it is discussed and concluded above, the CNMC algorithm greatly depends on the data quality and the precision of satellite orbits and clocks. However, for real-time users, it is hard to get the final precise products, especially for satellite clocks. Station differencing method, which could reduce the impact of satellite orbits and clocks, could be used in combination with the CNMC algorithm.

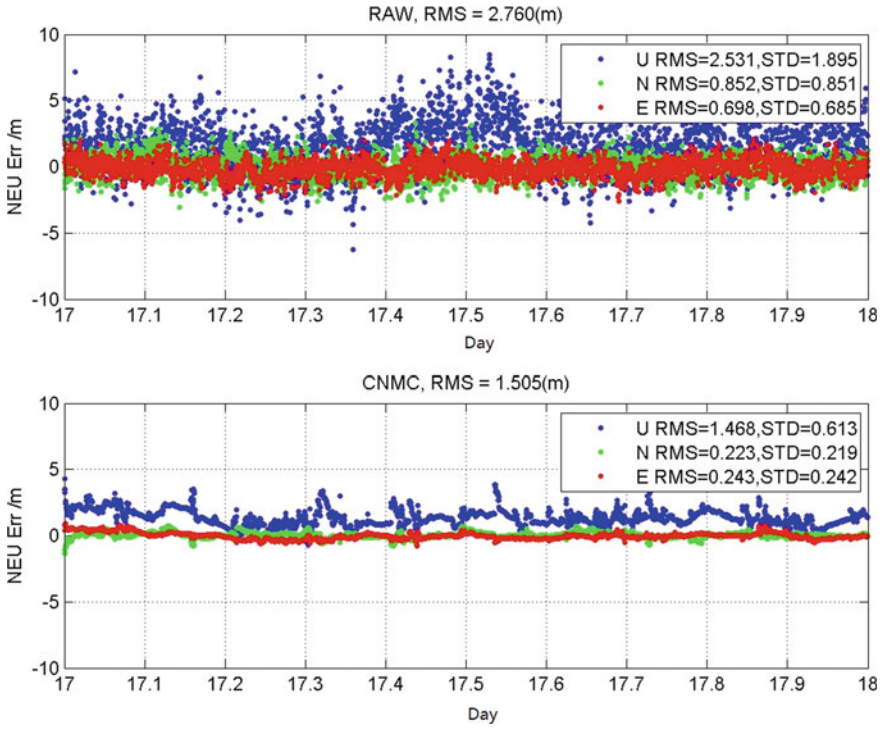

Fig. 46.3 The GPS/COMPASS combined positioning error of different strategies; *Upper* using RAW observations; *Lower* using smoothed observations

Data of two stations in Shanghai, parting 1,000 m in between, is used. Both stations are capable to receive mixed GPS and COMPASS data. We use two strategies in data analysis: (1) Station differencing without data smoothing (2) Station differencing with data smoothing using CNMC algorithm. The GPS/COMPASS kinematic positioning results for these two strategies are shown in Fig. 46.3. From the figure we can see that CNMC algorithm makes the positioning error smoother and the precision is improved by 45.5 %, which proves that CNMC algorithm is effective in station differencing.

Using the CNMC algorithm, multipath effect in P1 and P2 can be estimated in real-time. Here we list the multipath of 2 GEO, 2 IGSO and 2 MEO satellites, which is available in Fig. 46.4. It can be seen from the figure that the multipath effect can be more than 1 m for most satellites. Multipath of GEO satellites (C03 and C04) is smaller and more stable than that of IGSO and MEO satellites. For IGSO and MEO satellites, multipath is much serious in the periods of arising and descending.

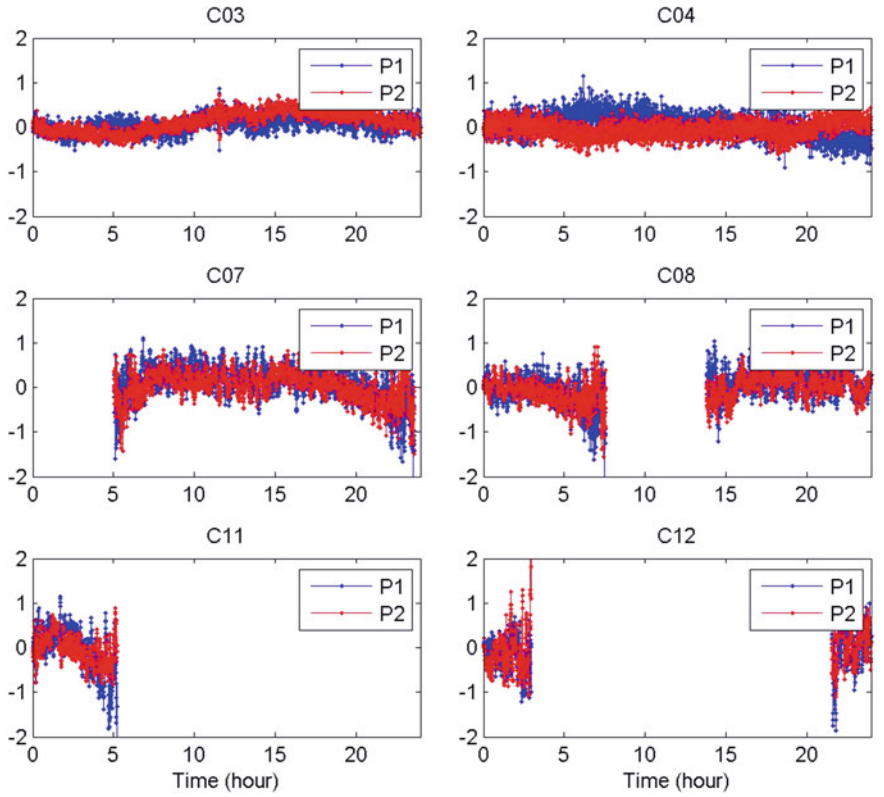

Fig. 46.4 The multipath (in meters) of different COMPASS satellites

The accuracy of user positioning could be further improved by adding the equivalent satellite clock corrections, which are differential information for authorize users [9]. It is a strategy that fixes station coordinates and calculates the user range error caused by satellite orbits, clocks and other errors and these information is sent to authorize users via GEOs. The equivalent satellite clock correction is normally derived using pseudorange observations, thus its quality depends on pseudorange. Figure 46.5 shows the equivalent satellite clock correction for three COMPASS satellites using raw and smoothed COMPASS data. From the figure we can see that after removing multipath effects using the CNMC algorithm, the noise of the equivalent satellite clock correction is much smaller and more stable. This indicates that the CNMC algorithm can be used in wide area difference system.

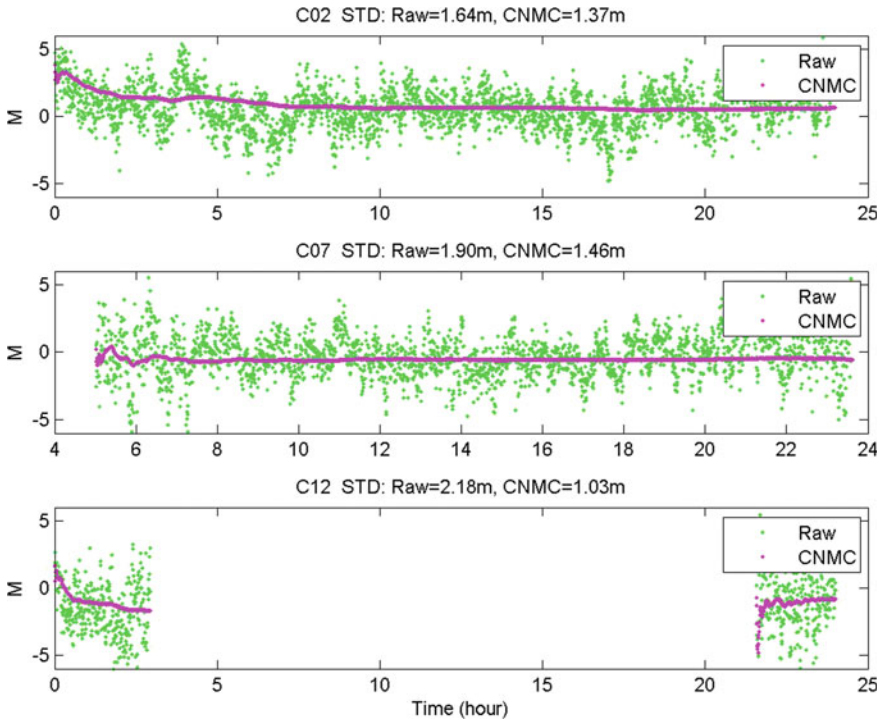

Fig. 46.5 Multipath effect on equivalent satellite clock corrections

46.4 Conclusions

In this paper, we discuss the positioning model of multi-system GNSS positioning, an example of combined GPS/GLONASS/COMPASS positioning proves that the accuracy of triple-system positioning is better than that of single or double system. The CNMC algorithm of eliminating multipath effect and smoothing the pseud-orange is discussed. We found that the effective of the CNMC algorithm greatly depends on the precision of satellite orbits and clocks. The station differenced strategy is used to further eliminate the error caused by satellite. The CNMC algorithm also improves the precision of the estimation of equivalent satellite clock corrections.

Acknowledgments This paper is supported by the 100 Talents Programme of The Chinese Academy of Sciences, the National High Technology Research and Development Program of China (Grant No. 2013AA122402), the National Natural Science Foundation of China (NSFC) (Grant No. 11273046 and 40974018), and the Shanghai Committee of Science and Technology (Grant No. 12DZ2273300, 13PJ1409900).

References

1. Pei X, Chen J et al (2012) Application of inter-system hardware delay bias in GPS/GLONASS PPP. In: China satellite navigation conference 2012 proceedings, lecture notes in electrical engineering, p 160. doi:10.1007/978-3-642-29175-3_34
2. Zhang X, Guo W et al (2010) Study on precise point positioning based on combined GPS and GLONASS. Geomatics Inf Sci Wuhan Univ 35(1):9–12
3. Meng X, Guo J et al (2010) GPS/GLONASS and their combined precise point positioning. Geomatics Inf Sci Wuhan Univ 35(12):1409–1413
4. COMPASS website. http://www.beidou.gov.cn/
5. China Satellite Navigation Office (2011) Development of Beidou Navigation Satellite System. Munich satellite navigation summit
6. Zhou S, Cao Y et al (2012) Positioning accuracy assessment for the 4GEO/5IGSO/2MEO constellation of COMPASS. Sci Chin Phys Mech Astron 55(12):2290–2299
7. Chen L, Zhao Q et al (2012) Preliminary analysis on pseudorange data quality and positioning accuracy of Beidou satellite navigation system. In: China satellite navigation conference 2012 proceedings, lecture notes in electrical engineering, p 159. doi:10.1007/978-3-642-29187-6_3
8. Wu X, Zhou J et al (2012) Multipath error detection and correction for GEO/IGSO satellites. Sci Chin Phys Mech Astron 55(7):1297–1306
9. Cao Y, Hu X et al (2012) The wide-area difference system for the regional satellite navigation system of COMPASS. Sci Chin Phys Mech Astron 55(7):1307–1315
10. Geng T (2009) Real-time precise orbit determination theory for navigation satellite and its experimental application based on regional reference stations. PhD thesis, Wuhan University
11. Hatch R (1982) The synergism of GPS code and carrier measurements. In: Proceedings of the 3rd international geodetic symposium on satellite Doppler positioning
12. Hugentobler U, Dach Rolf et al (2004) Bernese GPS software version 5.0 draft. Univ Bern 2004:91–95

Chapter 47
Research on Ultra-Tight Integration Technology for GNSS/SINS Integrated Navigation Systems

Geng Feng

Abstract GNSS/SINS deep integration relative to the tight integration can further improve navigation accuracy and noise immunity of high dynamic environment, and it is the future direction of development. A deep integrated navigation technology based on vector delay lock loop is researched. First, in the baseband signal preprocessing unit, Unscented Kalman Filter (UKF) is adopted to pre-filter the satellite signal, reduce the signal update rate, and the nonlinearity between I/Q signals and navigation state variables. By utilized base band signal pre-filter technology, the measurement equations of deeply integrated filter are simplified, and the calculation amount is also reduced significantly. For the heterogeneous sensor data fusion problem, in the deeply integrated filter design, an improved Unscented Particle Filter (UPF) algorithm based on the sequential importance sampling is proposed. The simulation studies show that the techniques researched here are effective. Comparing the tight integration technology, the position, velocity and attitude accuracy of navigation system are improved.

Keywords Integrated navigation · Deep integration · GNSS · SINS · Vector delay lock loop · UPF

47.1 Introduction

At present, the GNSS/SINS Integrated Navigation has got great attention and been widely used. As we all know, although GNSS can provide users with all-weather land, sea and space, full time, continuous three-dimensional position, three-dimensional velocity and time information, but its dynamic performance is poor,

G. Feng (✉)
20th Research Institute, China Electronics Technology Group Corporation, Xi'an, China
e-mail: gengfeng36@163.com

J. Sun et al. (eds.), *China Satellite Navigation Conference (CSNC) 2014 Proceedings: Volume III*, Lecture Notes in Electrical Engineering 305,
DOI: 10.1007/978-3-642-54740-9_47,

the satellite signal is vulnerable to electromagnetic interference. SINS is a autonomous navigation system, which has a good hidden, anti-interference ability, but navigation errors accumulate over time. Through the GNSS/SINS Integrated Navigation, it can not only overcome the disadvantage of the low long-term precision of SINS, but also improve dynamic performance and anti-jamming ability of GNSS.

GNSS/SINS ultra-tight integration is a new integration method, originated in Spilker's "vector tracing" [1]. It uses satellite more "primitive" information with respect to the tight combination method, and by global optimization design, it can accurately correct the SINS device errors, get the best signal tracking bandwidth, and improve the overall performance of navigation system. Comparing the tight combination method, GNSS/SINS ultra-tight integration can further improve navigation accuracy and anti-jamming capability under high dynamic environment, and is the future direction of GNSS/SINS Integrated Navigation system [2]. At the beginning of this century, Draper Laboratory has begun to research the GNSS/SINS deep integration navigation system theory and technology [3]. In 2006, Honeywell company and Rockwell Collins company jointly developed the anti-impact, anti-interference INS/GPS ultra-tight integration navigation, guidance and flight control management module, positioning accuracy 5 m (CEP), 2,000 g shock resistant, withstand 58 dB of interference [4].

In this paper, a GNSS/SINS ultra-tight integrated navigation technology was researched. First, an incoherent deep integrated architecture based on vector delay lock loop was proposed. Second, in the satellite baseband signal preprocessing, an unscented Kalman filtering technique (UKF) was used. UKF is a non-linear distribution approximation method using sampling strategy, and with respect to the extended Kalman filter technology, it has better performance. Since the measurement noise covariance matrix of SINS and GNSS does not match with each other, for the data fusion problem between heterogeneous sensors, an unscented particle filtering technique based on the sequential importance sampling was utilized in the ultra-tight integrated filter designing.

47.2 GNSS/SINS Ultra-Tight Integrated Navigation System Architecture

The main task of the deep integration system is to maintain code phase and carrier frequency lock. Depending on the carrier phase tracking methods, deep integration method can be divided into two categories: coherent and incoherent deep integration. Compared with the coherent deep integration algorithms, incoherent combination algorithm does not need to estimate carrier phase error, only need to track each satellite pseudo code phase and carrier frequency. Compared with the carrier phase tracking, pseudo code phase and carrier frequency tracking can be run in the environment of low carrier to noise ratio [5].

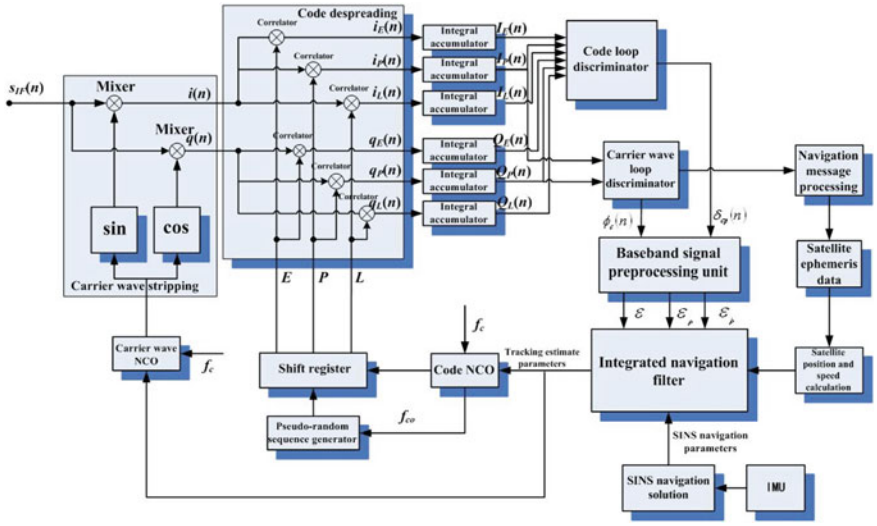

Fig. 47.1 GNSS/SINS ultra-tight integrated navigation system structure diagram

The structure of GNSS/SINS deep integrated navigation system based on the incoherent algorithm is shown in Fig. 47.1. This system mainly includes the vector tracking and integrated navigation information processing. In the vector tracking structure, the channel filter and main filter are used for signal tracking, while the main filter also burdened with navigation information processing task.

After the phase discriminating, the in-phase, orthogonal signal outputted by the correlator, as the measurement information of channel filter, can be used to estimate the PN code phase and carrier frequency tracking error. The channel filter state estimation after scaling are used as the measurement information input to the main filter, to estimate the error state of the integrated navigation system. The main filter receives the measurement information of the GNSS tracking channel and SINS, The state variables are updated and navigation error parameters are feedbacked to SINS system to be corrected.

According to the corrected SINS navigation parameters and satellite ephemeris data, integrated navigation system determines GNSS pseudo code phase and carrier frequency, used to drive the numerical control oscillator in the receiver, generating a local copy of the input signal, to maintain the GNSS signal tracking.

47.3 Vector Delay Lock Loop

Vector tracking loop (Vector Delay Lock Loop, VDLL) [6] can reduce the tracking noise, and make the phase detector is not easy to enter the nonlinear interval. When part of the signal is temporarily loses lock, the VDLL can still work

normally. By navigation filter, VDLL can make each signal channel integrate, so as to realize the information interaction between channels, easy to achieve global optimization of all satellite signals. VDLL is one of the effective ways to improve measurement accuracy and reliability of the satellite signals.

In the vector tracking loop, the satellite signal PN code phase and carrier frequency will be tracked. And signal tracking loop is closed through the deep integrated navigation filter. The deep integrated navigation filter according to the navigation parameters and satellite ephemeris data estimates the received signal pseudo distance, pseudo distance variation and pseudo range rate, and the information estimated are sent to the carrier and pseudorandom code NCO of the local signal generator.

The estimated pseudo distance information is used to adjust the pseudo code phase of code NCO, and pseudo range rate information is used for the transmission rate adjustment for carrier and pseudo code NCO. The vector tracking process did not estimate the carrier phase, so the carrier phase in carrier NCO without adjustment, still run by independent Costas carrier phase tracking loop way. The outputs for the correlators of each integral reset cycle are used for generating pseudo code phase, carrier frequency, the channel filter update. The channel filter obtains the pseudo code phase and carrier frequency, which transformed into pseudo distance, pseudo distance variation, pseudo range rate information to input into the deep navigation filter, used for navigation error state update [7].

47.3.1 The Cumulative Outputs of Correlator

Not considering the noise case, intermediate frequency signal model for receiver RF front-end output [8]:

$$S_{IF} = A \cdot D(kt_s) \cdot C(kt_s) \cdot \cos(\omega_{IF} \cdot kt_s + \varphi) \tag{47.1}$$

Among them, A is the signal amplitude, $D(\cdot)$ is navigation data bit level value, the value ± 1, $C(\cdot)$ is C/A code, ω_{IF} is the IF signal frequency, φ is carrier phase. IF signal inputs are multiplied with the in-phase, orthogonal signals of local carrier, and then filter the high frequency components, the two branch output, as follows:

$$S_I = 0.5 \cdot A \cdot D(kt_s) \cdot C(kt_s) \cdot \cos(\varphi_e) \tag{47.2}$$

$$S_Q = 0.5 \cdot A \cdot D(kt_s) \cdot C(kt_s) \cdot \sin(\varphi_e) \tag{47.3}$$

where, φ_e is the phase difference between the local carrier and input signal, $\varphi_e = kt_s \cdot (\omega_{IF} - \omega_L) + (\varphi - \varphi_L)$, t_s is sampling interval, k is counting points, ω_L and φ_L are the local carrier angle frequency and phase. The output signals of two

branches respectively correlate with the instant code(P), lead code(E), lag code(L) generated by the local pseudo code generator, and accumulate during the pre-monitoring integral time. Assuming the integral interval, the carrier frequency difference and phase difference are approximately constant, and then take the mean, the correlator outputs are:

$$I_{PS} = 0.5 \cdot A \cdot D_i \cdot R(\varepsilon_i) \cdot (\pi\delta fT)^{-1} \sin(\pi\delta fT) \cdot \cos(\pi T\delta f + \delta\varphi) \tag{47.4}$$

$$I_{ES} = 0.5 \cdot A \cdot D_i \cdot R(\varepsilon_i - \delta) \cdot (\pi\delta fT)^{-1} \sin(\pi\delta fT) \cdot \cos(\pi T\delta f + \delta\varphi) \tag{47.5}$$

$$I_{LS} = 0.5 \cdot A \cdot D_i \cdot R(\varepsilon_i + \delta) \cdot (\pi\delta fT)^{-1} \sin(\pi\delta fT) \cdot \cos(\pi T\delta f + \delta\varphi) \tag{47.6}$$

$$Q_{PS} = 0.5 \cdot A \cdot D_i \cdot R(\varepsilon_i) \cdot (\pi\delta fT)^{-1} \sin(\pi\delta fT) \cdot \sin(\pi T\delta f + \delta\varphi) \tag{47.7}$$

$$Q_{ES} = 0.5 \cdot A \cdot D_i \cdot R(\varepsilon_i - \delta) \cdot (\pi\delta fT)^{-1} \sin(\pi\delta fT) \cdot \sin(\pi T\delta f + \delta\varphi) \tag{47.8}$$

$$Q_{PS} = 0.5 \cdot A \cdot D_i \cdot R(\varepsilon_i + \delta) \cdot (\pi\delta fT)^{-1} \sin(\pi\delta fT) \cdot \sin(\pi T\delta f + \delta\varphi) \tag{47.9}$$

Among them, δ is the local C/A code lead-lag interval, T is pre-detection integration time, δf and $\delta\varphi$ is the carrier frequency difference and phase difference between local reference signal and input signal at the starting time of integration interval, R(·) represents correlation function for the C/A code, and its maximum value is 1.

47.3.2 The Code and Carrier Wave Loop Discriminating

The code loop discriminator adopts like-coherent dot-product power algorithm. This algorithm is affected by the signal amplitude, can be normalized, and although in the phase correction range, its linear performance is worse than the envelope algorithm and the coherent dot-product power algorithm, but its calculation load is lower. The specific algorithm is as follows:

$$\begin{aligned} \delta_{cp} &= 0.5[(I_E - I_L)I_P + (Q_E - Q_L)Q_P] \\ &= 0.25A^2R(\Delta\varphi)(R(\Delta\varphi - \delta) - R(\Delta\varphi + \delta)) \end{aligned} \tag{47.10}$$

The carrier tracking loop phase discrimination method adopts two quadrant arctangent function Costas PLL algorithm:

$$\phi_e = \arctan\left(\frac{Q_p}{I_P}\right) = \frac{\arctan(-\sin(2\pi\delta f(k-1)t_s + \Delta\varphi))}{\cos(2\pi\delta f(k-1)t_s + \Delta\varphi)} \tag{47.11}$$

47.3.3 Baseband Signal Preprocessing Unit

Baseband signal preprocessing unit is used to estimate the tracking error. The state variables of preprocessing filter mainly include pseudo code phase error, carrier phase error and carrier frequency error, and also include the carrier amplitude and frequency change ratio error. The preprocessing filter model can be expressed as:

$$\dot{\mathbf{X}}_c = \mathbf{F}_c\mathbf{X}_c + \mathbf{W}_c \tag{47.12}$$

where, $\mathbf{X}_c = [\,\varepsilon \quad \delta\varphi \quad \delta f \quad \delta a \quad A\,]$ are the state variables of pre-processing filter, ε is pseudo code phase error, $\delta\varphi$ is carrier phase error, δf is carrier frequency error, δa is the carrier frequency error, A is the amplitude of the signal, $\mathbf{F}_c$ is the coefficient matrix, $\mathbf{W}_c$ is the noise matrix.

$$\mathbf{F}_c = \begin{bmatrix} 0 & 0 & f_{ca}/f_{L1} \cdot k_p & 0 & 0 \\ 0 & 0 & 2\pi & 0 & 0 \\ 0 & 0 & 0 & 1 & 0 \\ 0 & 0 & 0 & 0 & 0 \\ 0 & 0 & 0 & 0 & 0 \end{bmatrix} \tag{47.13}$$

Among them, $k_p = f_s$, f_{ca}, f_{ca} is C/A code transmission frequency, f_s is the sampling frequency.

Pre-processing filter measurement information are the phase detection results about pseudo code and carrier phase, the measurement equations can be expressed as:

$$Z_1 = 0.25A^2R(\Delta\varphi)(R(\Delta\varphi - \delta) - R(\Delta\varphi + \delta)) \tag{47.14}$$

$$Z_2 = \frac{\arctan(-\sin(2\pi\delta f(k-1)t_s + \Delta\varphi))}{\cos(2\pi\delta f(k-1)t_s + \Delta\varphi)} \tag{47.15}$$

In the preprocessing filter design, the Unscented Kalman Filter (UKF) algorithm [9, 10] is utilized. UKF is a non-linear distribution approximation method using sampling strategy. The numbers of UKF particle sampled point (generally known as Sigma-point) are small, and the specific numbers depend on the selected sampling strategy. The most commonly used is $2n + 1$ Sigma point's symmetric sampling, n is the state variable dimension. The calculation load of UKF and EKF is quite, but the performance is better than EKF. For the additive noise characteristics of linear system model and the nonlinear measurement model of pre-filter, the state equations and measurement equations of the pre-processing filter are discretized, and then the nonlinear system model can be expressed as:

$$\mathbf{X}_{k+1} = f(\mathbf{X}_k) + \mathbf{w}_k \tag{47.16}$$

$$\mathbf{Z}_{k+1} = h(\mathbf{X}_k) \tag{47.17}$$

where, $\mathbf{w}_k$ is the unrelated Gauss white noise. The Weighted sequence based on the symmetric sampling $\mathbf{w}$ and Sigma-point χ is as follows:

$$\chi_0 = \hat{x},\ \boldsymbol{\chi}_i = \hat{x} + \left(\sqrt{(n+\kappa)\mathbf{P}}\right)_i^T,\ \boldsymbol{\chi}_{i+n} = \hat{x} + \left(\sqrt{(n+\kappa)\mathbf{P}}\right)_i^T,\ i = 1, 2, \ldots, n \tag{47.18}$$

$$w_0^m = \frac{\kappa}{n+\kappa},\ w_0^c = w_0^m + 1 + \beta - \alpha^2,\ w_i^m = w_i^c = \frac{1}{2(n+\kappa)}, \quad i = 1, 2, \ldots, n \tag{47.19}$$

Among them, $\hat{x}$ is the mean of $\mathbf{X}_k$ initial distribution, $\mathbf{P}$ is covariance matrix, κ is a scalar, used to control the distance between each point and the mean, $\kappa = n(\alpha^2 - 1)$, α is the scale parameter ($10^{-4} \leq \alpha \leq 1$), β is used to reduce the effects of high order matrix, for the Gauss distribution, the optimal value $\beta = 2$, $\left(\sqrt{(n+\kappa)\mathbf{P}}\right)_i$ is the i-th row (or column) of the root mean square matrix obtained by Cholesky decomposition.

Time update equations:

$$\dot{\boldsymbol{\chi}}_{i,k|k-1} = f\left(\dot{\boldsymbol{\chi}}_{i,k-1|k-1}\right), \quad i = 1, 2, 3, \ldots, 2n \tag{47.20}$$

$$\hat{\mathbf{X}}_{k|k-1} = \sum_{i=0}^{2n} w_i^m \dot{\boldsymbol{\chi}}_{i,k|k-1} \tag{47.21}$$

$$\mathbf{P}_{k|k-1} = \sum_{i=0}^{2n} w_i^c \left(\dot{\boldsymbol{\chi}}_{i,k|k-1} - \hat{\mathbf{X}}_{k|k-1}\right)\left(\dot{\boldsymbol{\chi}}_{i,k|k-1} - \hat{\mathbf{X}}_{k|k-1}\right)^T + \mathbf{Q}_k \tag{47.22}$$

Measurement update equations:

$$\mathbf{Z}_{i,k|k-1} = h\left(\dot{\chi}_{i,k|k-1}\right) \tag{47.23}$$

$$\hat{\mathbf{Z}}_{k|k-1} = \sum_{i=0}^{2n} w_i^m \mathbf{Z}_{i,k|k-1} \tag{47.24}$$

$$\mathbf{P}_{zz} = \sum_{i=0}^{2n} w_i^c \left(\mathbf{Z}_{i,k|k-1} - \hat{\mathbf{Z}}_{k|k-1}\right)\left(\mathbf{Z}_{i,k|k-1} - \hat{\mathbf{Z}}_{k|k-1}\right)^T \tag{47.25}$$

$$\mathbf{P}_{XZ} = \sum_{i=0}^{2n} w_i^c \left(\dot{\boldsymbol{\chi}}_{i,k|k-1} - \hat{\mathbf{X}}_{k|k-1}\right)\left(\mathbf{Z}_{i,k|k-1} - \hat{\mathbf{Z}}_{k|k-1}\right)^T \tag{47.26}$$

$$\mathbf{K}_k = \mathbf{P}_{XZ}(\mathbf{P}_{zz})^{-1} \tag{47.27}$$

$$\hat{\mathrm{X}}_{\mathrm{k|k}} = \hat{\mathrm{X}}_{\mathrm{k|k-1}} + \mathbf{K}_{\mathrm{k}}\left(\mathbf{Z}_{\mathrm{k}} - \hat{\mathbf{Z}}_{\mathrm{k|k-1}}\right) \tag{47.28}$$

$$\mathbf{P}_{\mathrm{k|k}} = (\mathbf{I} - \mathbf{K}_{\mathrm{k}}\mathbf{H}_{\mathrm{k}})\mathbf{P}_{\mathrm{k|k-1}} \tag{47.29}$$

47.4 GNSS/SINS Ultra-Tight Integrated Navigation Filter Model

Each channel's pre-processing filter estimates the tracking error states, and according to pseudo code phase, carrier frequency error estimation information, as well as the reference information of the carrier and pseudo codes NCO, calculate the corresponding pseudorange, distance variation, pseudo range rate, and as the measured information, input to the integrated navigation filter; The SINS system, according to the ephemeris data decoded by GNSS receiver, calculates the satellite position, velocity, and then, by the use of these navigation parameters, calculates the distances between the satellite and receiver, the variations of distance, and as the measured information, input into the integrated filter; The integrated filter, according to pseudorange, pseudorange variation, pseudorange rate information inputted by GNSS tracking channels and SINS, updates the navigation error states; After the information fusion processing, integrated system feedbacks the error estimation information to SINS to revise the corresponding element errors and navigation parameters, on the other hand, integrated system, according to the corrected position, speed and other navigation parameters, combined with satellite parameters, calculate the pseudorange and pseudorange rate information between the receiver and satellites, and then transfer to the pseudocode and carrier NCO of GNSS receiver, to adjust the local pseudo code phase and carrier frequency, while the local carrier phase, according to the channel phase error estimation, is adjusted.

47.4.1 System Error Equations

In the earth centered fixed coordinate frame, the error states of the deep integrated navigation filter include SINS errors and GNSS errors, that is $\mathbf{X} = [\,\mathbf{X}_{\mathrm{SINS}} \quad \mathbf{X}_{\mathrm{GNSS}}\,]^{\mathrm{T}}$. System error equations are as follows:

$$\dot{\mathbf{X}} = \begin{bmatrix} \dot{\mathbf{X}}_{\mathrm{SINS}} \\ \dot{\mathbf{X}}_{\mathrm{GNSS}} \end{bmatrix} = \begin{bmatrix} \mathbf{F}_{\mathrm{SINS}} & 0 \\ 0 & \mathbf{F}_{\mathrm{GNSS}} \end{bmatrix} \begin{bmatrix} \mathbf{X}_{\mathrm{SINS}} \\ \mathbf{X}_{\mathrm{GNSS}} \end{bmatrix} + \begin{bmatrix} \mathbf{G}_{\mathrm{SINS}} & 0 \\ 0 & \mathbf{G}_{\mathrm{GNSS}} \end{bmatrix} \begin{bmatrix} \mathbf{W}_{\mathrm{SINS}} \\ \mathbf{W}_{\mathrm{GNSS}} \end{bmatrix} \tag{47.30}$$

$$\dot{\mathbf{X}}_{\mathrm{SINS}}(t) = \begin{bmatrix} \Delta\dot{\mathbf{R}}^{e} \\ \Delta\dot{\mathbf{V}}^{e} \\ \dot{\boldsymbol{\varepsilon}}^{e} \\ \Delta\dot{\boldsymbol{\omega}}^{b} \\ \Delta\dot{\mathbf{f}}^{b} \end{bmatrix} = \begin{bmatrix} 0 & \mathbf{I}_{3\times3} & 0 & 0 & 0 \\ \mathrm{N}^{e} & -2\Omega_{ie}^{e} & -\mathrm{F}^{e} & 0 & \mathrm{C}_{b}^{e} \\ 0 & 0 & -\Omega_{ie}^{e} & \mathrm{C}_{b}^{e} & 0 \\ 0 & 0 & 0 & -\mathrm{A} & 0 \\ 0 & 0 & 0 & -\mathrm{B} & 0 \end{bmatrix} \begin{bmatrix} \Delta\mathbf{R}^{e} \\ \Delta\mathbf{V}^{e} \\ \boldsymbol{\varepsilon}^{e} \\ \Delta\boldsymbol{\omega}^{b} \\ \Delta\mathbf{f}^{b} \end{bmatrix} + \begin{bmatrix} 0 & 0 \\ 0 & 0 \\ 0 & 0 \\ \mathbf{I}_{3\times3} & 0 \\ 0 & \mathbf{I}_{3\times3} \end{bmatrix} \begin{bmatrix} \mathrm{W}_{\omega} \\ \mathrm{W}_{f} \end{bmatrix} \tag{47.31}$$

$$\dot{\mathbf{X}}_{\mathrm{GNSS}} = \begin{bmatrix} 0 & 1 \\ 0 & -\mathrm{T}_{ru}^{-1} \end{bmatrix} \mathbf{X}_{\mathrm{GNSS}} + \begin{bmatrix} \mathrm{w}_{tu} \\ \mathrm{w}_{tru} \end{bmatrix} \tag{47.32}$$

Among them, $\mathbf{X}_{\mathrm{SINS}}$ is the error state vector associated with SINS, including the position error, velocity error, attitude error, gyro and accelerometer errors, $\mathbf{X}_{\mathrm{GNSS}}$ is the error state vector associated with GNSS, including the clock equivalent distance error and clock frequency equivalent rate error (first order Markov process, T_{ru} the relevant time), $\mathbf{X}_{\mathrm{GNSS}} = [\,\Delta\mathrm{l}_{u} \quad \Delta\mathrm{l}_{ru}\,]^{\mathrm{T}}$. $\mathbf{F}_{\mathrm{SINS}}$ and $\mathbf{F}_{\mathrm{GNSS}}$ is the coefficient matrix for SINS and GNSS error state equation, $\mathbf{W}_{\mathrm{SINS}}$ and $\mathbf{W}_{\mathrm{GNSS}}$ represents the random error vector for SINS and GNSS, $\mathbf{W}_{\mathrm{SINS}} = [\,\mathrm{W}_{\omega} \quad \mathrm{W}_{f}\,]^{\mathrm{T}}$, $\mathbf{W}_{\mathrm{GNSS}} = [\,\mathrm{w}_{tu} \quad \mathrm{w}_{tru}\,]^{\mathrm{T}}$. $\Delta\mathbf{R}^{e}$, $\Delta\mathbf{V}^{e}$ and $\boldsymbol{\varepsilon}^{e}$ is the position error vector, velocity error vector, and misalignment angle vector. $\Delta\boldsymbol{\omega}^{b}$ and $\Delta\mathbf{f}^{b}$ is the gyro error vector and accelerometer error vector. $\mathbf{F}^{e}$ is the anti-symmetric matrix of the specific force in the earth centered fixed coordinate system. $\mathbf{C}_{b}^{e}$ is the direction cosine matrix, the body coordinate system to the earth centered fixed coordinate. Ω_{ie}^{e} is the anti-symmetric matrix of the earth's rotation angular velocity ω_{ie}^{e}. $\mathbf{A}$ and $\mathbf{B}$ is gyro and accelerometer error coefficient matrix. $\mathbf{R}^{e}$ is the position vector, $\mathbf{R}^{e} = [\,\mathrm{x} \quad \mathrm{y} \quad \mathrm{z}\,]^{\mathrm{T}}$. The calculation formula about $\mathbf{N}^{e}$ is as follows:

$$\mathbf{N}^{e} = \frac{\mathrm{GM}}{\mathrm{r}^{3}} \begin{bmatrix} -1+\frac{3\mathrm{x}^{2}}{\mathrm{r}^{2}} & \frac{3\mathrm{xy}}{\mathrm{r}^{2}} & \frac{3\mathrm{xz}}{\mathrm{r}^{2}} \\ \frac{3\mathrm{xy}}{\mathrm{r}^{2}} & -1+\frac{3\mathrm{y}^{2}}{\mathrm{r}^{2}} & \frac{3\mathrm{yz}}{\mathrm{r}^{2}} \\ \frac{3\mathrm{xz}}{\mathrm{r}^{2}} & \frac{3\mathrm{yz}}{\mathrm{r}^{2}} & -1+\frac{3\mathrm{z}^{2}}{\mathrm{r}^{2}} \end{bmatrix} + \begin{bmatrix} \omega_{ie}^{2} & 0 & 0 \\ 0 & \omega_{ie}^{2} & 0 \\ 0 & 0 & 0 \end{bmatrix} \tag{47.33}$$

where, GM represents the product of Earth's gravitational constant and the mass, $\mathrm{r} = \sqrt{\mathrm{x}^{2}+\mathrm{y}^{2}+\mathrm{z}^{2}}$.

47.4.2 System Observation Equations

In GNSS/SINS deep integrated navigation system, the pseudorange error, pseudorange error change and pseudo range rate variation are selected as the observation information. Assuming that m visible stars can be observed at the t moments, then, the measurements of the integrated navigation filter contain m groups of the preprocessed baseband data. The results of each pre-processing unit include the pseudorange error $\varepsilon_{\rho}^{(\mathbf{i})}$ of receiver to the satellite i-th, pseudorange error change $\Delta\varepsilon_{\rho}^{(\mathbf{i})}$ and pseudo range rate variation $\Delta\varepsilon_{\dot{\rho}}^{(\mathbf{i})}$, that is, the i-th satellite measurements are as follows:

$$\mathbf{Z}_{\mathrm{i}} = \begin{bmatrix} \varepsilon_{\rho_{\mathrm{c}}}^{(\mathrm{i})} & \Delta\varepsilon_{\rho_{\mathrm{c}}}^{(\mathrm{i})} & \Delta\varepsilon_{\dot{\rho}_{\mathrm{c}}}^{(\mathrm{i})} \end{bmatrix}^{\mathrm{T}}$$

Estimated by the position information $\begin{bmatrix} \mathrm{x_{SI}} & \mathrm{y_{SI}} & \mathrm{z_{SI}} \end{bmatrix}$ of SINS, the pseudorange of receiver to the i-th satellite $\begin{bmatrix} \mathrm{x_s^{(i)}} & \mathrm{y_s^{(i)}} & \mathrm{z_s^{(i)}} \end{bmatrix}$ is as follows:

$$\rho_{\mathrm{SI}}^{(\mathrm{i})} = \sqrt{\left[\left(\mathrm{x_{SI}} - \mathrm{x_s^{(i)}}\right)^2 + \left(\mathrm{y_{SI}} - \mathrm{y_s^{(i)}}\right)^2 + \left(\mathrm{z_{SI}} - \mathrm{z_s^{(i)}}\right)^2\right]} \tag{47.34}$$

Assuming that, the receiver true position coordinate vectors is $\begin{bmatrix} \mathrm{x} & \mathrm{y} & \mathrm{z} \end{bmatrix}$, then, the pseudorange measured by receiver is

$$\rho_{\mathrm{G}}^{(\mathrm{i})} = \mathrm{r_i} + \Delta\mathrm{l_u} + \mathrm{v}_{\rho}^{(\mathrm{i})} \tag{47.35}$$

After linearization, the pseudorange observation equation of the receiver to the i-th satellite is as follows:

$$\varepsilon_{\rho_{\mathrm{c}}}^{(\mathrm{i})} = \rho_{\mathrm{SI}}^{(\mathrm{i})} - \rho_{\mathrm{G}}^{(\mathrm{i})} = \mathrm{e}_1^{(\mathrm{i})}\Delta\mathrm{x} + \mathrm{e}_2^{(\mathrm{i})}\Delta\mathrm{y} + \mathrm{e}_3^{(\mathrm{i})}\Delta\mathrm{z} + \Delta\mathrm{l_u} + \mathrm{v}_{\rho_{\mathrm{c}}^{(\mathrm{i})}} \tag{36}$$

In the formula (36), $\mathbf{e}^{(\mathbf{i})} = \begin{bmatrix} \mathrm{e}_1^{(\mathrm{i})} & \mathrm{e}_2^{(\mathrm{i})} & \mathrm{e}_3^{(\mathrm{i})} \end{bmatrix}$ is the unit vector between the carrier and the satellite line-of-sight direction, $\mathrm{e}_1^{(\mathbf{i})} = (\mathrm{x} - \mathrm{x_s^{(i)}})/\mathrm{r}^{(\mathrm{i})}$, $\mathrm{e}_2^{(\mathbf{i})} = (\mathrm{y} - \mathrm{y_s^{(i)}})/\mathrm{r}^{(\mathrm{i})}$, $\mathrm{e}_3^{(\mathbf{i})} = (\mathrm{z} - \mathrm{z_s^{(i)}})/\mathrm{r}^{(\mathrm{i})}$, $\mathrm{r}^{(\mathrm{i})} = \sqrt{(\mathrm{x} - \mathrm{x_s^{(i)}})^2 + (\mathrm{y} - \mathrm{y_s^{(i)}})^2 + (\mathrm{z} - \mathrm{z_s^{(i)}})^2}$, and $\mathrm{v}_{\rho_{\mathrm{c}}^{(\mathrm{i})}}$ is the measurement noise.

Assuming that, the line-of-sight unit vector matrix between satellites n and the ground station is as follows:

$$\mathbf{u} = \begin{bmatrix} \mathrm{e}_1^{(1)} & \mathrm{e}_2^{(1)} & \mathrm{e}_3^{(1)} \\ \vdots & \vdots & \vdots \\ \mathrm{e}_1^{(\mathrm{n})} & \mathrm{e}_2^{(\mathrm{n})} & \mathrm{e}_3^{(\mathrm{n})} \end{bmatrix}_{\mathrm{n}\times 3} \tag{47.37}$$

Then, the pseudorange error vector of the satellites n is:

$$\boldsymbol{\varepsilon}_{\rho_c} = \left[\varepsilon_{\rho_c}^{(1)} \quad \cdots \quad \varepsilon_{\rho_c}^{(n)} \right]^T = \mathbf{u}\Delta\mathbf{R}^e + \mathbf{h}\Delta l_u \tag{47.38}$$

where, $\mathbf{h} = [\,1 \quad \cdots \quad 1\,]_{n\times 1}^T$.

Assuming that, the pre-detection integration time of the vector tracking loop is T, the initial time in an integral period is t_0, then, the variation of the pseudo-range error $\Delta\boldsymbol{\varepsilon}_{\rho_c}$ is:

$$\Delta\boldsymbol{\varepsilon}_{\rho_c} = \Delta\mathbf{u}\Delta\mathbf{R}^e + \mathbf{u}_{t0}T\Delta\mathbf{V}^e - \frac{1}{2}\mathbf{u}_{t0}\mathbf{a}_\times^e T^2\boldsymbol{\varepsilon}^e - \frac{1}{2}\mathbf{u}_{t0}\mathbf{C}_b^e T^2\Delta\mathbf{a}^b + \mathbf{h}T\Delta l_{ru} \tag{47.39}$$

where, $\Delta\varepsilon_{\rho_c} = [\,\varepsilon_{\rho_{SI}}^{(1)} - \varepsilon_{\rho_G}^{(1)} \quad \cdots \quad \varepsilon_{\rho_{SI}}^{(n)} - \varepsilon_{\rho_G}^{(n)}\,]^T$, $\Delta\mathbf{u} = \mathbf{u}_t - \mathbf{u}_{t_0}$, $\mathbf{a}_\times^e$ is the anti-symmetric matrix of the acceleration vector under the earth centered fixed coordinate system. Similarly, the pseudo range rate variation $\Delta\boldsymbol{\varepsilon}_{\dot{\rho}_c}$ can be obtained

$$\Delta\boldsymbol{\varepsilon}_{\dot{\rho}_c} = \Delta\mathbf{u}\Delta\mathbf{V} + \mathbf{u}_{t_0}\mathbf{a}_\times^e T\boldsymbol{\varepsilon}^e + \mathbf{u}_{t_0}\mathbf{C}_b^e T\Delta\mathbf{a}^b \tag{47.40}$$

In summary, the total observation equation of the integrated navigation system can be expressed as:

$$\mathbf{Z} = \left[\varepsilon_{\rho_c}^{(1)} \quad \cdots \quad \varepsilon_{\rho_c}^{(n)} \; \Delta\varepsilon_{\rho_c}^{(1)} \quad \cdots \quad \Delta\varepsilon_{\rho_c}^{(n)} \; \Delta\varepsilon_{\dot{\rho}_c}^{(1)} \quad \cdots \quad \Delta\varepsilon_{\dot{\rho}_c}^{(n)} \right]^T = \mathbf{H}\mathbf{X} + \mathbf{V}$$

$$\mathbf{H} = \begin{bmatrix} \mathbf{u} & 0_{n\times 3} & 0_{n\times 3} & 0_{n\times 3} & 0_{n\times 3} & \mathbf{h} & 0_{n\times 1} \\ \mathbf{u} & \mathbf{u}_{t0}T & -0.5\mathbf{u}_{t0}\mathbf{a}_\times^e T^2 & 0_{n\times 3} & -0.5\mathbf{u}_{t0}\mathbf{C}_b^e T^2 & 0_{n\times 3} & \mathbf{h}T \\ 0_{n\times 3} & \mathbf{u} & \mathbf{u}_{t_0}\mathbf{a}_\times^e T & 0_{n\times 3} & \mathbf{u}_{t_0}\mathbf{C}_b^e T & 0_{n\times 1} & 0_{n\times 1} \end{bmatrix}_{3n\times 17} \tag{47.41}$$

47.5 GNSS/SINS Ultra-Tight Integrated Navigation Filter Design

In the multi-sensor centralized fusion structure, there are mainly three kinds of filtering methods, namely, the parallel filtering, data compression filtering and sequential filtering. Parallel filtering operation process will lead to high dimension matrix multiplication and inverse operation, the load of calculation is large; Data compression filtering is mainly used for the data fusion problem between homogeneous sensors. As the data fusion between heterogeneous sensors, the measurement noise covariance matrices of GNSS and SINS are mismatch between each other, so should not use data compression filtering approach. Sequential filtering takes the observation values of each sensor at k-th moments as new

independent measurements, and the new independent measurements will be filtered through the sequential manner. Because it is not like the parallel filtering, for all the observations, expanding the dimensions, so there is no increase in computational complexity, and the target states update independently by use of the sensor observation values, does not exist measurement noise covariance matching problem between the sensors. Therefore, this article uses sequential filtering method in GNSS/SINS integrated navigation filter design, and filtering algorithm utilizes the unscented particle filter (UPF) algorithm.

The unscented particle filter (UPF) algorithm [11], uses unscented Kalman filter (UKF) to generate an approximate Gaussian distribution as an important density function. In each iteration of the sequential importance sampling algorithm, it is combined with Markov chain Monte Carlo, so that the particles can be moved to different places, and thereby, avoid degradation caused by the particle filter. The whole calculation procedure is as follows:

Initialization:

$$\overline{\mathbf{x}}_0^{\mathrm{a}} = \left[\overline{\mathbf{x}}_0^{\mathrm{a}} \quad 0 \quad 0\right]^{\mathrm{T}},\ \mathbf{P}_0^{\mathrm{a}} = \begin{bmatrix} \mathbf{P}_0 & 0 & 0 \\ 0 & \mathbf{Q} & 0 \\ 0 & 0 & \mathbf{R} \end{bmatrix} \tag{47.42}$$

Characteristic samples calculation:

$$\mathbf{X}_{t-1}^{\mathrm{a}} = \left[\mathbf{x}_{t-1}^{\mathrm{a}} \quad \mathbf{x}_{t-1}^{\mathrm{a}} + \sqrt{(n+\kappa)\mathbf{P}_{t-1}^{\mathrm{a}}}\right] \tag{47.43}$$

Time updating:

$$\mathbf{X}_{t|t-1}^{\mathrm{x}} = \mathrm{f}\left(\mathbf{X}_{t-1}^{\mathrm{x}}, \mathbf{X}_{t|t-1}^{\mathrm{v}}\right),\ \overline{\mathbf{x}}_{t|t-1} = \sum_{i=0}^{2n} w_i^{(m)} \mathbf{X}_{i,t|t-1}^{\mathrm{x}} \tag{47.44}$$

$$\mathbf{Y}_{t|t-1}^{\mathrm{x}} = \mathrm{h}\left(\mathbf{X}_{t|t-1}^{\mathrm{x}}, \mathbf{X}_{t-1}^{\mathrm{v}}\right),\ \overline{\mathbf{y}}_{t|t-1} = \sum_{i=0}^{2n} w_i^{(m)} \mathbf{Y}_{i,t|t-1}^{\mathrm{x}} \tag{47.45}$$

$$\mathbf{P}_{t|t-1} = \sum_{i=0}^{2n} w_i^{(m)} \left[\mathbf{X}_{i,t|t-1}^{\mathrm{x}} - \bar{\mathbf{x}}_{t|t-1}\right] \left[\mathbf{X}_{i,t|t-1}^{\mathrm{x}} - \bar{\mathbf{x}}_{t|t-1}\right]^{\mathrm{T}} \tag{47.46}$$

Measurement updating:

$$\mathbf{P}_{x_t y_t} = \sum_{i=0}^{2n} w_i^{(m)} \left[\mathbf{X}_{i,t|t-1}^{\mathrm{x}} - \overline{\mathbf{x}}_{t|t-1}\right] \left[\mathbf{Y}_{i,t|t-1}^{\mathrm{x}} - \overline{\mathbf{y}}_{t|t-1}\right]^{\mathrm{T}} \tag{47.47}$$

$$\mathbf{P}_{y_t y_t} = \sum_{i=0}^{2n} w_i^{(m)} \left[\mathbf{Y}_{i,t|t-1}^{\mathrm{x}} - \overline{\mathbf{y}}_{t|t-1}\right] \left[\mathbf{Y}_{i,t|t-1}^{\mathrm{x}} - \overline{\mathbf{y}}_{t|t-1}\right]^{\mathrm{T}} \tag{47.48}$$

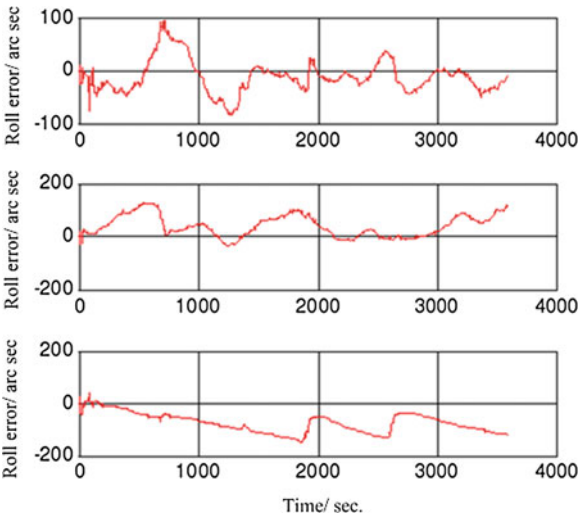

Fig. 47.2 The ultra-tight integration attitude angle error *curve*

$$\mathbf{K}_t = \mathbf{P}_{x_t y_t} \mathbf{P}_{y_t y_t}^{-1} \tag{47.49}$$

$$\overline{\mathbf{x}}_t = \overline{\mathbf{x}}_{t|t-1} + \mathbf{K}_t \left(\overline{\mathbf{y}}_t - \overline{\mathbf{y}}_{t|t-1} \right), \ \mathbf{P}_t = \mathbf{P}_{t|t-1} - \mathbf{K}_t \mathbf{P}_{y_t y_t} \mathbf{K}_t^{\mathrm{T}} \tag{47.50}$$

47.6 GNSS/SINS Ultra-Tight Integrated Navigation Simulation and Analysis

Gyro drift is 0.01°/h, accelerometer bias is 10^{-4} g. Gyro noise includes white noise, a first-order Markov process and stochastic constant, and accelerometer noise includes white noise and a first-order Markov process. Gyro random constant is 0.1/h, gyro white noise variance is 0.1/h, the first-order Markov noise variance of gyroscope is 0.1/h, accelerometer first-order Markov noise variance is 10^{-4} g.

Let the receiver clock drift equivalent velocity error is a first-order Markov process, the driving white noise variance is 0.1 m/s, the receiver clock bias equivalent range error variance is set to 10 m of white noise.

Missile track parameters come from the simulator. The missile did maneuver in climbing process, contains a high-speed turn, level flight and other typical maneuver. The simulation time is 3,600 s, the update frequency of SINS is 50 Hz, and the GNSS data update frequency is 1 Hz, information fusion period is 1 s. The initial level attitude angle error is 100 arc s, the heading angle error is 150 arc s, velocity error is 0.6 m/s, longitude and latitude error is 20 m, the height error is 30 m, the particle number is 1,200. The integrated navigation error curves are shown as in Figs. 47.2, 47.3 and 47.4.

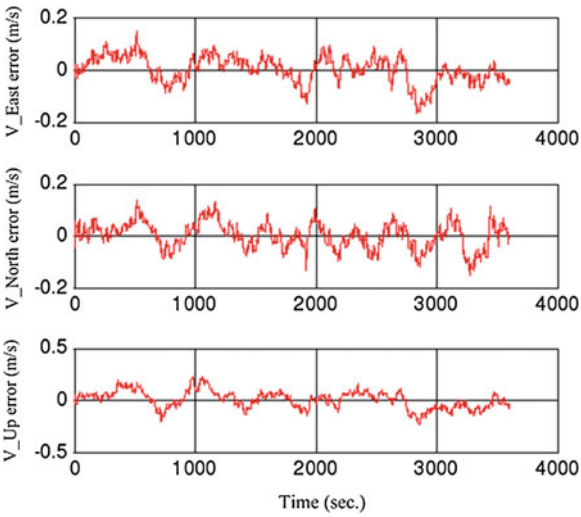

Fig. 47.3 The ultra-tight integration velocity error *curve*

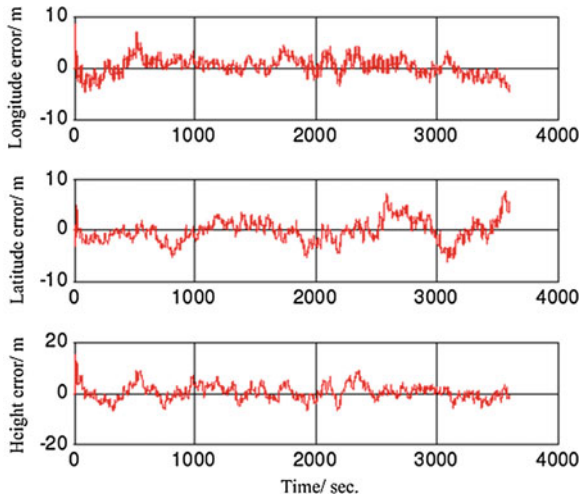

Fig. 47.4 The ultra-tight integration position error *curve*

In the same simulation conditions, the navigation accuracy comparison of the tight integrated navigation and deep integrated navigation is shown as in Table 47.1.

According to the navigation accuracy comparison of the deep integrated navigation and tight integrated navigation, the overall accuracy is roughly equal, the position accuracy is better than 4 m, speed accuracy is better than 0.08 m/s, the attitude angle accuracy is better than 50 arc s. But the deep integrated navigation relatively has higher precision, position accuracy is better than 3 m, speed accuracy is better than 0.06 m/s, the attitude angle accuracy is better than 40 arc s.

Table 47.1 The tight integration and ultra-tight integration accuracy comparison

Performance parameters		Tight integration	Deep integration
Position errors (RMSE)	Longitude (m)	3.74	2.53
	Latitude (m)	3.05	2.613
	Height (m)	3.104	2.816
Speed errors (RMSE)	North (m/s)	0.077	0.051
	East (m/s)	0.044	0.038
	Up (m/s)	0.073	0.055
Attitude errors (RMSE)	Roll (arc sec)	35.75	31.05
	Pitch (arc sec)	42.14	36.12
	Yaw (arc sec)	48.3	38.64

47.7 Conclusion

This paper proposes an incoherent deep integration architecture based on vector tracking loop. In the satellite baseband signal preprocessing, an unscented kalman filter(UKF) technique is adopted. UKF is a method of nonlinear distribution approximated by sampling strategy, Compared with the extended kalman filter, has better performance, can reduce the satellite signal update rate, better to weaken the nonlinear between I/O signals and navigation states. Because the observation noise covariance matrices of SINS and GNSS do not match, therefore, for the data fusion problem between heterogeneous sensors, in the deep integration filter design, an unscented particle filtering technique based on the sequential importance sampling is adopted. The simulation results demonstrate that the proposed technology is effective, and comparing with tight integration, deep integration can achieve better position, velocity and attitude accuracy.

References

1. Kaplan DE, Hegarty JC (1996) Understanding GPS: principles and applications. Artech House, Boston
2. Lashley M, Bevly DM, Hung JY (2010) Analysis of deeply integrated and tightly coupled architectures. In: 2010 IEEE/ION position location and navigation symposium, California, pp 382–396
3. Landis D, Thorvaldsen T, Fink B, Sherman P et al (2006) A deep integration estimator for urban ground navigation. In: 2006 IEEE/ION, position, location, and navigation symposium, pp 927–932
4. Buck TM, Wilmot J, Cook MJ (2006) A high G MEMS based deeply integrated INS/GPS guidance, navigation and control flight management unit, in position, location, and navigation symposium, 2006 IEEE/ION
5. Gustafson ED, Dowdle RJ, Elwell J (2004) Deeply-integrated adaptive GPS-based navigator with extended-range code tracking. US, No.6731237

6. Petovello MG, Lachapelle G (2006) Comparison of vector-based software receiver implementations with application to ultra-tight GPS/INS integration. ION GNSS 2006, Fort Worth TX
7. Benson D (2007) Interference benefits of a vector delay lock loop (VDLL) GPS receiver. In: Proceedings of the 63rd annual meeting of the ION, pp 749–756
8. Ziedan NI (2006) GNSS receivers for weak signals. Artech House Inc, Boston
9. Nunes FD, Marçal JMS (2010) Low-complexity VDLL receiver for multi-GNSS constellations. In: ESA workshop on Satellite Navigation Technologies and European workshop on GNSS signals and signal processing, pp 1–8
10. Jwo D-J, Chung F-C (2010) Fuzzy adaptive unscented Kalman filter for ultra-tight GPS/INS integration. In: Proceedings of the 2010 international symposium on computational intelligence and design, pp 229–235
11. Cheng Q, Bondon P (2008) A new unscented particle filter. Acoust Speech Signal Process 2008:3417–3420

Chapter 48
Integrated XNAV/Inter-Satellite Measurement Navigation Algorithm for Spacecraft Formation

Liu Ye, Anxi Yu, Jianfeng Cao and Geshi Tang

Abstract Due to the increasing requirement of autonomous navigation for spacecraft formation, an integrated navigation algorithm based on XNAV and inter-satellite measurement is suggested. First, the navigation system architecture is established according to the formation flying dynamics and observed principle. Then, the navigation filter is presented. The filter has a multi-estimated architecture by virtue of the non-correlation of formation state, which can improve the navigation observability and computed efficiency. Meanwhile, a novel cubature Kalman filter is suggested which is more stable and suitable for high dimensional system. Furthermore, a covariance adaptive strategy based on recursive random weighting is developed for the deficiency of low sample rate in XNAV. Finally, simulation results validated the efficiency and effectiveness of the integrated navigation architecture and algorithm. The algorithm here is universal and can benefit researches on the autonomous navigation for spacecraft formation, especially for the vehicles flying in high earth orbit or interplanetary.

Keywords Formation flying · Integrated navigation · X-ray pulsar · Cubature Kalman filter · Random weighted

This work was supported by the National Natural Science Foundation of China (67072115,11203003,61304233).

L. Ye (✉) · J. Cao · G. Tang
Science and Technology on Aerospace Flight Dynamic Laboratory, Beijing, China
e-mail: liuye_new@sina.com

A. Yu
College of Electronic Science and Engineering, NUDT, Changsha, China

J. Sun et al. (eds.), *China Satellite Navigation Conference (CSNC) 2014 Proceedings: Volume III*, Lecture Notes in Electrical Engineering 305,
DOI: 10.1007/978-3-642-54740-9_48,

48.1 Introduction

GPS and inter-satellite measurements (ISM) are the commonly instruments for the formation flying spacecraft [3]. However, this is not suitable for autonomous formation flight in high earth orbit or interplanetary.

By detecting the different arrival time of the same pulsar signal between the spacecraft and the reference point, the the X-ray pulsar-based navigation (XNAV) can provide high accuracy positioning and timing services autonomously [6]. Therefore, some researches have been focused on the autonomously long time navigation for constellation by XNAV [5, 8]. Even some differential strategies [9] are proposed for eliminating the common errors. Some integrated navigation systems are also presented, such as integrated XNAV and inertial measurement units [2], where the latter device was introduced for system dynamics modelling.

But due to the low SNR of pulsar signals, longer observation time is required to obtain better measurements in XNAV. Furthermore, the pulsar number and kinds of error sources, such as pulsar time model, reference celestial body's ephemeris and propagated delay [12], may also limit the utilization of XNAV in formation flight. Huang and Chen pint out the potential enhancement of cross-link measurement for XNAV and give some beneficial theoretical and simulate analysis results [5]. However, the integrated navigation systems faced to many difficulties, such as asynchronous observation, high dimension and nonlinear state estimation and real-time requirement et al. Therefore, navigation algorithm with high accuracy, stability and computing efficiency are urgently required.

The paper is aim to obtain a real-time algorithm for the integrated XNAV and ISM navigation. The navigation system architecture is derived firstly by the dynamic character and observed principles of the spacecraft formation. Then, a novel navigation algorithm is suggested by integrated utilization of multi-estimated technique [6], cubature Kalman filter (CKF) [1] and random weighted strategy [4]. Simulated validation is discussed in detail finally. Thanks to these strategies, the algorithm is very suitable for the nonlinearly high dimensional formation state estimation, and can debate the deficiency of longer observation time and less available pulsars in XNAV too.

48.2 Navigation System Architecture

According to the observed mechanics and sample rate of the measurement, the proposed navigation system architecture can be summarized in Fig. 48.1.

During the primary stage, XNAV is only applied to estimate absolute orbit for individual spacecraft. Then, a rude relative orbit computed by the difference of absolute orbit and is transferred to inter-satellite instruments as directional guidance. Until there is a stable output of absolute orbit, we can estimate accurate absolute and relative orbits simultaneously by fusion of XNAV and ISM. The

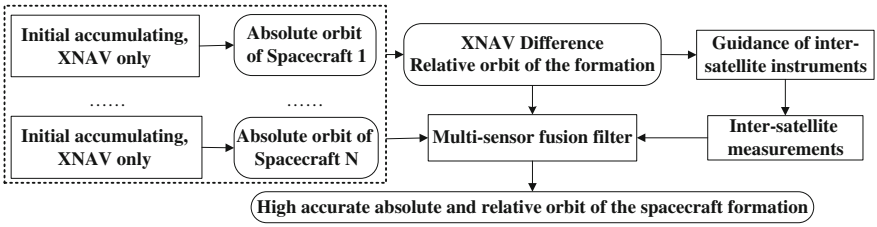

Fig. 48.1 Architecture of the proposed integrated navigation system

fusion system is solved by real-time filter here, thus the foundational dynamic model and the measurement equation of the formation should be constructed.

48.2.1 System Dynamics

Let $\boldsymbol{r}$ and $\boldsymbol{v}$ be position and velocity respectively, the spacecraft's acceleration can be computed as follow

$$\boldsymbol{a}(t) = -\mu \boldsymbol{r}(t)/r^3(t) + \boldsymbol{a}_b[\boldsymbol{r}(t), \boldsymbol{v}(t)] + \boldsymbol{a}_d(t) \tag{48.1}$$

where μ is the gravitational constant of the central celestial bodies, $\boldsymbol{a}_b(\boldsymbol{r})$ is the perturbing item which is determined by the space environment and requirement of navigation accuracy [8], and $\boldsymbol{a}_d$ is the potential maneuver acceleration. Then the dynamic model of the formation with N spacecraft at time step k is

$$[\boldsymbol{r}_{i,k}, \boldsymbol{v}_{i,k}]^T = [\boldsymbol{r}_{i,k-1}, \boldsymbol{v}_{i,k-1}]^T + \int_{t_k}^{t_{k+1}} [\boldsymbol{v}_i(t), \boldsymbol{a}_i(t)]^T dt + \boldsymbol{u}_{i,k},\ i = 1, \cdots, N, \tag{48.2}$$

Furthermore, relative orbit between spacecraft i and spacecraft j can be calculated as $\delta \boldsymbol{r}_{ij,k} = \delta \boldsymbol{r}_{i,k} - \delta \boldsymbol{r}_{j,k}$ and $\delta \boldsymbol{v}_{ij,k} = \delta \boldsymbol{v}_{i,k} - \delta \boldsymbol{v}_{j,k}$ without the introduction of Hill equation. For XNAV, the clock errors of each spacecraft should also be solved online. These clock errors are often assumed to be a polynomial motion process

$$\boldsymbol{\tau}_{i,k} = \boldsymbol{B}_i \boldsymbol{\tau}_{i,k-1} + \boldsymbol{w}_{i,k}, \quad i = 1, \cdots, N \tag{48.3}$$

where $\boldsymbol{B}$ is the polynomial coefficient and $\boldsymbol{w}_k$ is noise vector. For example, in the second order clock error model, $\boldsymbol{\tau}_k$ is composed by clock bias and drift frequency.

48.2.2 System Measurements

The foundation of XNAV is to observe the time of arrival (TOA) of a pulsar's signal. Then the TOA difference between the spacecraft and reference point is picked up as the observed vector of XNAV. The reference point is often selected as the solar system barycentre or the centroid of the earth. And the TOA to the reference point is calculated by an accurate pulsar timing model [7].

Let $\boldsymbol{n}$ be the direction of the pulsar and Δt be the TOA difference, the measurement equation of XNAV can be formula as follow

$$\Delta t = \boldsymbol{n} \cdot \boldsymbol{r}(t)/c + t_{rel} + \tau + v \tag{48.4}$$

where c is the speed of light, t_{rel} contains relative effect, annual parallax effect and higher order effects eat al., v is noise vector including those errors which cannot be modeling calibrated.

The inter-satellite instruments available can be divided into radio and optical signal, both of them can provide the distance and angular measurement between the space vehicles. Assume that spacecraft B is observed by spacecraft A, then the ISM equation have the form as

$$[\rho_{AB}(t), A_{AB}(t), E_{AB}(t)]^T = g(\boldsymbol{L}_A(t) \cdot \delta \boldsymbol{r}_{AB}(t)) + \varepsilon_{AB}(t) \tag{48.5}$$

where $\boldsymbol{L}_A$ is the transfer matrix from inertial coordinate system to orbit coordinate system of A, and $g(\cdot)$ is the transfer formulas from Cartesian coordinate to spherical coordinate.

The Eqs. (48.2)–(48.5) defined the basic architecture of the integrated navigation system. The system state need to be estimated are unknown position, velocity and clock error et al. Thus, this is a typical nonlinearly high dimensional real-time system. Furthermore, long term observed pulse data should be assembled into one pulse profile in XNAV for its low SNR, which makes the sample period of XNAV is up to 300–1,000 s or even longer. This is very slow than the presently inter-satellite radio or optical signal with sample rates about 0.1–20 Hz. That is to say an asynchronously fusion is required in the integrated navigation system. Therefore, the following context will be focused on the navigation algorithm for the deficiency of accuracy, robustness and computing efficiency.

48.3 Navigation Algorithm

48.3.1 Asynchronous Measurement Fusion

Referring to the multi-senor measurement fusion technology [11], the integrated navigation can utilize an augmented measurement by observations of XNAV and

ISM to achieve the most information usage. But the asynchronously observed problem should not be ignored.

Take a uniform expression of (48.4) and (48.5) as $\boldsymbol{Z}_k = H(\boldsymbol{r}_k, \boldsymbol{v}_k) + \boldsymbol{\varepsilon}_k, k = 1, \cdots, n$, and set maker vector $\boldsymbol{s} = [1, \cdots, 1]_{1\times n}$, we construct the full index observed vector $\boldsymbol{Z}_k$ before the startup of the navigation filter first. During the tracking stage, let $\boldsymbol{s}_i = 0$ if the ith component in $\boldsymbol{Z}_k$ is not observed. Then take $\boldsymbol{s}$ as the index of $\boldsymbol{Z}_k$, we can obtain the time-variable measurement equation for the navigation system as

$$\boldsymbol{Z}_{\boldsymbol{s}=1,k} = H_{\boldsymbol{s}=1}(\boldsymbol{r}_k, \boldsymbol{v}_k) + \boldsymbol{\varepsilon}_{\boldsymbol{s}=1,k} \tag{48.6}$$

One should note that if XNAV and ISM are both observed, absolute and relative orbit can be solved synchronously by the navigation filter. However, when there is only ISM available, relative orbit is solved by the filter according to predicted absolute orbit, and is used to modify the estimation of absolute orbit.

48.3.2 Filter Architecture by Multi-estimation Technique

Although spacecraft fly nearby during the formation flight, there is no correlation between different spacecraft's state. By virtue of this separability, we introduced the multi-estimated architecture [6] for filter design here. Taking a formation with two satellites A and B as example, the system in (48.2)–(48.5) at time step k can be solved by two sub systems running alternately as follow

$$\begin{cases} \begin{cases} [\boldsymbol{r}_{A,k}, \boldsymbol{v}_{i,k}]^T = [\boldsymbol{r}_{A,k-1}, \boldsymbol{v}_{A,k-1}]^T + \int_{t_k}^{t_{k+1}} [\boldsymbol{v}_A(t), \boldsymbol{a}_A(t)]^T dt + \boldsymbol{u}_{A,k} \\ \boldsymbol{\tau}_{A,k} = \boldsymbol{B}_A \boldsymbol{\tau}_{A,k-1} + \boldsymbol{w}_{A,k} \end{cases} \\ \begin{cases} \Delta t_{As} = \boldsymbol{n}_s \cdot \boldsymbol{r}_A(t)/c + t_{As,rel} + \tau_{As} + v_A s, \quad s = 1, \cdots, M \\ [\rho_{AB}(t), A_{AB}(t), E_{AB}(t)]^T = g(\boldsymbol{L}_A(t) \cdot (\bar{\boldsymbol{r}}_{B,k|k-1} - \boldsymbol{r}_{A,k})) + \varepsilon_{AB}(t) \end{cases} \end{cases} \tag{48.7}$$

$$\begin{cases} \begin{cases} [\boldsymbol{r}_{B,k}, \boldsymbol{v}_{i,k}]^T = [\boldsymbol{r}_{B,k-1}, \boldsymbol{v}_{B,k-1}]^T + \int_{t_k}^{t_{k+1}} [\boldsymbol{v}_B(t), \boldsymbol{a}_B(t)]^T dt + \boldsymbol{u}_{B,k} \\ \boldsymbol{\tau}_{B,k} = \boldsymbol{B}\boldsymbol{\tau}_{B,k-1} + \boldsymbol{w}_{B,k} \end{cases} \\ \begin{cases} \Delta t_{Bs} = \boldsymbol{n}_s \cdot \boldsymbol{r}_{Bs}(t)/c + t_{Bs,rel} + \tau_{Bs} + v_{Bs}, \quad s = 1, \cdots, N \\ [\rho_{AB}(t), A_{AB}(t), E_{AB}(t)]^T = g(\boldsymbol{L}_A(t) \cdot (\boldsymbol{r}_{B,k} - \hat{\boldsymbol{r}}_{A,k|k})) + \varepsilon_{AB}(t) \end{cases} \end{cases} \tag{48.8}$$

Absolute orbit and clock error of Satellite A is firstly solved by operating a filter (such as CKF) in system (48.7) with predicted state of Satellite B as control input. Then orbit and clock error of Satellite B is filter utilizing the estimated state of Satellite A as control input. At each sample time, there are fourteen variables under estimated and $M + N + 3$ observed data for system filter. In the sub filters, the state dimension is seven accompanied with observed vector dimension $M + 3$ and $N + 3$ respectively. Obviously, the observability, as well as robustness and computing, is improved by the multi-estimated architecture.

Furthermore, according to the uncorrelated between orbit and clock error, systems (48.7) and (48.8) can also be divided into two sub systems running alternately.

48.3.3 State Estimation by Cubature Kalman Filter

For the nonlinear state estimation problem, the unscented Kalman filter (UKF) utilizes unscented transforms of several determined samples to approximate a nonlinear system and is more accurate and stable than the traditional extended Kalman filter (EKF). Though being widely applied, the origin UKF will be unstable in high dimension system because of its unequal weighting strategy which may make one sample carries more weighting than others. Therefore, the recently developed CKF which derived through the rigorous spherical-radial cubature rule has been paid more attention [1]. The equal weighting cubature points (less than the UKF) in CKF can give more stable and accurate filter performance than the EKF and UKF. Therefore, we introduce the CKF to the navigation systems here.

Take system (48.7) as example. Let $\boldsymbol{X} = [\boldsymbol{r}, \boldsymbol{v}, \boldsymbol{\tau}]^T$ and $\boldsymbol{Y} = [\Delta t_1, \cdots, \rho(t), A(t), E(t)]^T$ be the state and observed vector, and assume the estimated state $\hat{\boldsymbol{X}}_{k-1|k-1}$ is obtained with covariance $\boldsymbol{P}_{\boldsymbol{X},k-1}$, then the filter implementation at time step k is as follow.

- State update. According to the state equation in (48.7), let $\overline{\mathrm{x}}^i_{k|k-1}$ be the predicted state samples from cubature points $\overline{\mathrm{X}}^i_{k-1} = \boldsymbol{P}^{1/2}_{\boldsymbol{X},k-1}\boldsymbol{\xi}_i + \hat{\boldsymbol{X}}_{k-1|k-1}$, $i = 1, \cdots, L$, $L = 14$ and $\boldsymbol{P}_{\boldsymbol{u}}$ be the state noise covariance, then the predicted state and covariance are

$$\begin{cases} \bar{\boldsymbol{X}}_{k|k-1} = \sum_{i=0}^{L} \overline{\mathrm{x}}^i_{k|k-1}/L \\ \bar{\boldsymbol{P}}_{\boldsymbol{X},k} = \sum_{i=0}^{L} (\overline{\mathrm{x}}^i_{k|k-1} - \bar{\boldsymbol{X}}_{k|k-1})(\overline{\mathrm{x}}^i_{k|k-1} - \bar{\boldsymbol{X}}_{k|k-1})^T/L + \boldsymbol{P}_{\boldsymbol{u}} \end{cases} \tag{48.9}$$

- Measurement update. According to the observed equation in (48.7), let $\overline{\mathrm{Y}}^i_{k|k-1}$ be the predicted measurement samples from cubature points $\overline{\mathrm{X}}^i_{k|k-1} = \bar{\boldsymbol{P}}^{1/2}_{\boldsymbol{X},k-1}\boldsymbol{\xi}_i + \bar{\boldsymbol{X}}_{k|k-1}$, $i = 1, \cdots, L$, $L = 14$ and $\boldsymbol{P}_{\boldsymbol{n}}$ be the observed noise covariance, then the predicted measurement and covariance are

$$\begin{cases} \overline{\boldsymbol{Y}}_{k|k-1} = \sum\limits_{i=0}^{L} \overline{\mathrm{Y}}^i_{k|k-1}/L \\ \overline{\boldsymbol{P}}_{\boldsymbol{Y},k} = \sum\limits_{i=0}^{L} (\overline{\mathrm{Y}}^i_{k|k-1} - \bar{\boldsymbol{y}}_{k|k-1})(\overline{\mathrm{Y}}^i_{k|k-1} - \bar{\boldsymbol{Y}}_{k|k-1})^T/L + \boldsymbol{P}_{\boldsymbol{n}} \\ \bar{\boldsymbol{P}}_{\boldsymbol{XY},k} = \sum\limits_{i=0}^{L} (\overline{\mathrm{X}}^i_{k|k-1} - \bar{\boldsymbol{x}}_{k|k-1})(\overline{\mathrm{Y}}^i_{k|k-1} - \bar{\boldsymbol{Y}}_{k|k-1})^T/L \end{cases} \tag{48.10}$$

- State filter. Under the Kalman filter framework, we can calculated the estimated state and covariance with gain matrix $\boldsymbol{K}_k = \bar{\boldsymbol{P}}_{\boldsymbol{xy},k}\bar{\boldsymbol{P}}_{\boldsymbol{y},k}^{-1}$ as follow

$$\begin{cases} \hat{\boldsymbol{X}}_{k|k} = \bar{\boldsymbol{X}}_{k|k-1} + \boldsymbol{K}_k(\boldsymbol{Y}_k - \bar{\boldsymbol{Y}}_{k|k-1}) \\ \boldsymbol{P}_{\boldsymbol{X},k} = \bar{\boldsymbol{P}}_{\boldsymbol{X},k} - \boldsymbol{K}_k\bar{\boldsymbol{P}}_{\boldsymbol{Y},k}\boldsymbol{K}_k^T \end{cases} \tag{48.11}$$

where the vector set $\{\boldsymbol{\xi}_i\}$ is calculated according to the cubature rule

$$\{\boldsymbol{\xi}_i\} = 0.5\sqrt{L}[1, 0, \cdots, 0; \cdots;\ 0, 0, \cdots, 1;\ -1, 0, \cdots, 0; \cdots;\ 0, 0, \cdots, -1] \tag{48.12}$$

48.3.4 Measurement Covariance Adaptive by Random Weighting

There are complicated errors in real XNAV systems [12], and some of the errors have not modeling exactly. Therefore, measurement covariance adaptive is required in high accurate navigation task. As above, XNAV have to perform a long term signal accumulation for its low SNR, which makes the data set for covariance adaptive could not be long. This is a typical small test data statistical problem, where the random weighting techniques may have good application.

Let the residual set be $\{\boldsymbol{\Delta}_i, i = 1, \cdots, L\}$ with mean value $\bar{\boldsymbol{\Delta}}$ and $\boldsymbol{\varepsilon}_i = \boldsymbol{\Delta}_i - \bar{\boldsymbol{\Delta}}$, then covariance estimation with equal weighting is $\boldsymbol{S}(L) = \sum_{i=1}^{L} \boldsymbol{\varepsilon}_i \cdot \boldsymbol{\varepsilon}_i^T/(L-1)$. According to the random weighting principle, taking M random weight sets as $\{v_{ij}, i = 1, \cdots, N\}, j = 1, \cdots, M$, the covariance estimation can be given by

$$\boldsymbol{\sigma}(L) = 2\boldsymbol{S}(L) - (1/M)\sum_{j=1}^{M}\left[\sum_{i=1}^{L} v_{ij}(\boldsymbol{\varepsilon}_i \cdot \boldsymbol{\varepsilon}_i^T)/L\right] \tag{48.13}$$

where $\{v_{ij}, i = 1, \cdots, N\}$ are Dirichlet vectors which is generated by difference of series with uniform distribution in [0, 1]. This can be seen as the equal weighing $1/(L-1)$ is replaced by the random weight v_{ij} in M test data sets.

Take a note $\boldsymbol{D}_i = \boldsymbol{\varepsilon}_i \cdot \boldsymbol{\varepsilon}_i^T$, then $\boldsymbol{S}(L)$ can be modified as

$$\boldsymbol{S}(L) = \sum_{i=1}^{L+1} \boldsymbol{D}'_{ii}/L, \quad \boldsymbol{D}'_i = \begin{cases} \boldsymbol{D}_i, & i \le L \\ \boldsymbol{S}(L), & i = L \end{cases} \tag{48.14}$$

Correspondingly, the equation (48.13) can be modified similarly as

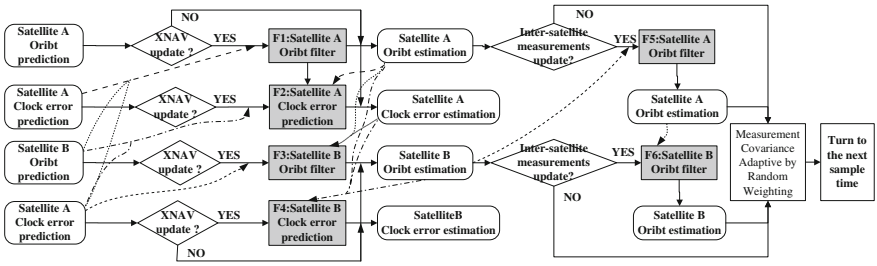

Fig. 48.2 Data processing diagram of the integrated navigation algorithm

$$\boldsymbol{\sigma}(L) = 2\boldsymbol{S}(L) - (1/M)\sum_{j=1}^{M}\left[\sum_{ii=1}^{L} v_{ij}\boldsymbol{D}_i\right] - (1/M)\sum_{j=1}^{M} v_{Lj}\boldsymbol{S}(L) \tag{48.15}$$

when the number of samples changes to $L + 1$, we have

$$\boldsymbol{S}(L+1) = \sum_{i=1}^{L+1}\boldsymbol{D}_i/L = \boldsymbol{S}(L) + [\boldsymbol{D}_{L+1} - \boldsymbol{S}(L)]/L \tag{48.16}$$

That is to say the $\boldsymbol{D}'_{L+1}$ in (48.14) is replaced by $\boldsymbol{D}_{L+1}$ here. Similarly, we have

$$\begin{aligned}\sigma(L+1) &= 2S(L+1) - (1/M)\sum_{j=1}^{M}\left[\sum_{i=1}^{L+1} v_{(L+1)j}D_i\right] \\ &= \sigma(L) + \left(2/L - \sum_{i=1}^{L+1} v_{(L+1)j}/M\right)\cdot[D_{L+1} - S(L)]\end{aligned} \tag{48.16}$$

This is just the recursive random weighting adaptive estimation of the measurement covariance.

48.3.5 Data Processing Diagram of the Navigation System

In summary, the navigation data for two satellite formation flight can be dealt with a multi-estimated architecture by several sub filters noted F1–F6 as in Fig. 48.2. Those filters update asynchronously and can be implemented by CKF or other algorithms according to their structure respectively. The dashed lines show the information exchange which are taken as control input vectors between those sub filters. Similarly, the F1 and F2 can be emerged as one filter for the navigation of Satellite A. The same is to F3 and F4 for Satellite B. One can note that when there

is new measurement, the corresponding noise covariance will be calculated by the random weighting of the filter residual before the next filter cycle.

48.4 Simulation

A representative simulation of two satellite formation flight is executed to validate our findings in this section. The reference orbit elements are referred to the ENVISAT and is given as

Satellite A: $(a, e, i, \Omega, \omega, M) = (7159\ \text{km},\ 0,\ 98.549^\circ, 133.01^\circ, 90^\circ,\ -49.46^\circ)$
Satellite B: $(a, e, i, \Omega, \omega, M) = (7159\ \text{km},\ 0,\ 98.549^\circ, 133.01^\circ, 86.94^\circ, -46.38^\circ)$

Their dynamic models are established in the equatorial inertial coordinate system. Clock error of 1 us is introduced to both satellites. In XNAV, the reference space point is chosen at the centroid of the earth and the pulsars used in XNAV are given in Table 48.1. Cross-link radio signal sampling at 0.1 Hz is involved for the inter-satellite distance and angular measurement with noises 1m and $5''$ respectively. The filter is initialized by analytic solution according to the measurement of the first four pulsars in XNAV.

The estimated error (while tracking is stable) with XNAV measurement only of the EKF, UKF and CKF are shown in Table 48.2. The EKF becomes divergence and exhibits a very poor accuracy. The CKF has a better orbit estimation (P, V) than the UKF. But because the state dimension is one in the clock error filter, the CKF has no superiority to the UKF and possesses a little worse tracking result. Besides, the CKF has one sample less than the UKF and thus takes less time costs.

Introduce the measurement covariance adaptive step without simulation scenarios change. Estimated results of Satellite A by Sage filter [10] and random weighting (RW) with different number of samples N are shown in Figs. 48.3 and 48.4. Both of the algorithms perform better while the sample numbers increase. And they achieve a similar accuracy when $N = 30$. But the RW is more accurate for small sample test data cases (N is small), especially in the clock error estimation (Fig. 48.5).

To illustrate the overall performance of the navigation system, Figs. 48.6, 48.7 and 48.8 shows the tracking error with and without ISM. There is no ISM during the first 1,000 s for the filter divergence purpose. Take a note that the filter with and without multi-estimated architecture as DKF and JKF respectively. As we can see, the DKF and JKF have the same tracking accuracy. But the DKF is much efficiency, for example when introduce ISM, the time costs in the DKF is 100 s, while it's 150 s in the JKF. The figures also show the contributions of the ISM. Besides the extremely improvement of the relative orbit (baseline), the absolute orbit estimations become more smooth and accurate too.

Table 48.1 Parameters of navigational X-ray pulsars

Pulsar	Crab	B1937 + 21	B1821 − 24	B1957 + 20	B0531 + 21	B0540 − 69
Galactic longitude (°)	83.63	294.91	276.13	29.90	184.56	279.72
Galactic latitude (°)	22.01	21.58	−24.87	20.80	−5.78	−31.52
Range accuracy (m)/500 s	380	380	380	380	380	380

Table 48.2 Estimated error of different filter algorithm

Error	P_A (m)	V_A (m/s)	τ_A (us)	P_B (m)	V_B (m/s)	τ_B (us)	Time cost (s)
EKF	2.3e6	9,317	24.40	2.4e6	51,066	39.4	100
UKF	106	0.10	0.39	139	0.14	0.41	12.3
CKF	62.7	0.05	0.48	101	0.09	0.42	12.1

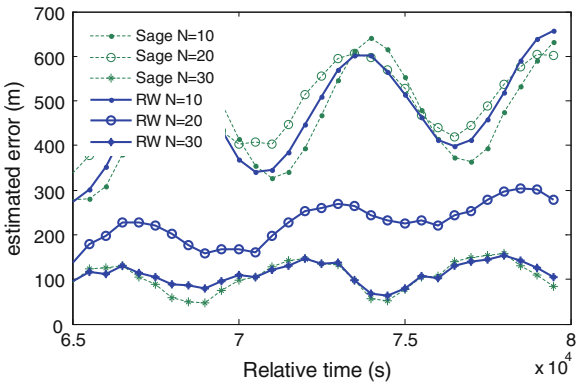

Fig. 48.3 Estimated position of different adaptive algorithm (satellite A, N: samples No.)

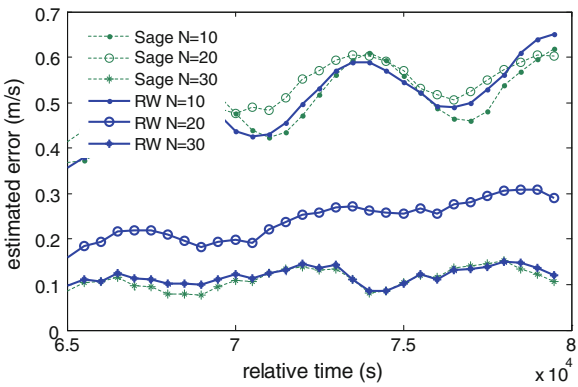

Fig. 48.4 Estimated velocity of different adaptive algorithm (satellite A, N: samples No.)

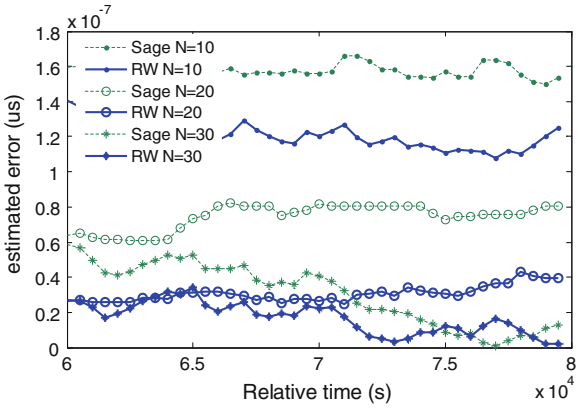

Fig. 48.5 Estimated clock error of different adaptive algorithm (satellite A, N: samples No.)

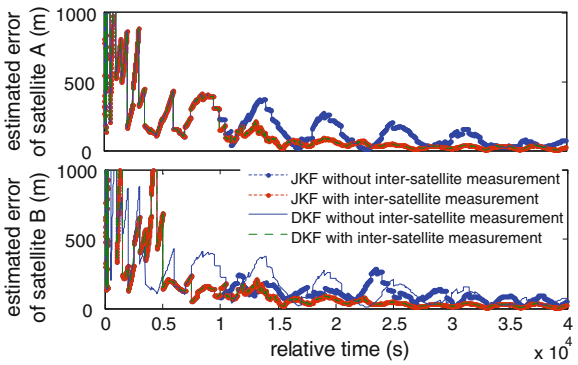

Fig. 48.6 Estimated absolute orbit of different filter

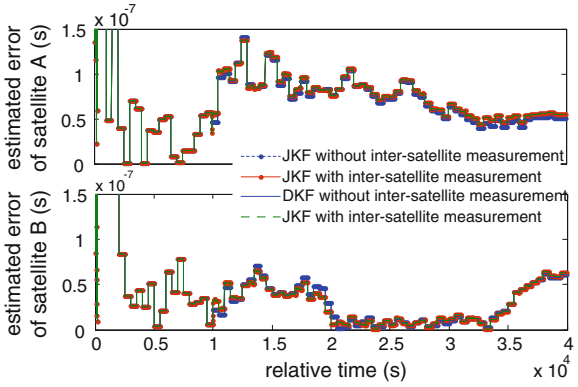

Fig. 48.7 Estimated Clock error of different filter

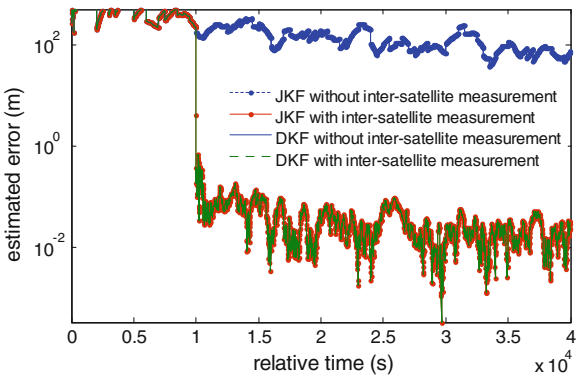

Fig. 48.8 Estimated relative orbit of different filter

48.5 Conclusion

For the autonomous navigation requirement for spacecraft formation, integrated navigation system architecture is established utilizing XNAV and ISM. Furthermore, according to the nonlinearity, high dimension and strong dynamic asynchronous observation character, navigation filter is mainly studied by integrated several benefit estimated technology.

The multi-estimated architecture utilizes several sub filters running alternately with low state dimension to improve the observability, which is more suitable when not enough pulsars is available or the observe geometry is not very good in XNAV. Taking equal weighting samples by the spherical-radial cubature rule, the CKF has a better accuracy and stability than the traditional EKF and UKF for the nonlinearly high dimensional state estimation. A recursive random weighting strategy is also derived for measurement covariance adaptive estimation. The strategy has standout applications for small sample test data cases, and thus is very suitable for the low sample rate in XNAV for real-time requirements.

While the simulation results preferred the algorithms here, real XNAV system will be more complicated with kinds of errors which may not be modeling exactly. Therefore, when applied in those cases, performances of the filter here should be lucubrated. Moreover, the filter designing techniques here are universal, and thus can be extended into other nonlinear system solving problem. Those all will form part of our ongoing researches in this area.

References

1. Chang Lu bin, Baiqing Hu, Li Li (2013) Unscented type Kalman filter: limitation and combination. IET Signal Process 7(3):167–176
2. Emadzadeh AA, Spever JL (2011) Relative navigation between two spacecraft using X-ray pulsars. IEEE Trans Control Syst Technol 19(5):1021–1035

3. Flechtner F (2003) Relative baseline determination for a tandem SAR mission using GPS code and phase measurements. GFZ Technical Note
4. Falin W, Xiaohong S, Yan Z et al (2012) Relative navigation for formation flying spacecrafts using X-ray Pulsars. IEEE Position location and navigation symposium, Myrtle Beach, SC
5. Ping S, Zhonggui C, Guangji Q (2009) Orbit dynamics about X-ray pulsar-based navigation. Sci China Technol Sci 39(3):556–561
6. Ray PS, Sheikh SI, Graven PH et al (2008) Deep space navigation using celestial X-ray sources. ION NTM 2008, San Diego, CA
7. Shesheng G, Zhihua F, Yongmin Z et al (2008) Random weighting estimation of parameters in generalized Gaussian distribution. Inf Sci 178(9):2275–2281
8. Wei Z, Yidi W, jiang W (2013) Analysis of the performance of X-ray pulsar-based navigation system. The 4th Chinese satellite navigation conference, Wuhan, 2013
9. Xianlin H, Zhengming C, Hongqiang L et al (2010) High accuracy autonomous navigation of GNSS using X-ray pulsar based navigation. IEEE Aerospace conference, Big Sky, MT
10. Yang Y, Wen Y (2003) Integrated robust filter for precision orbit determination. Sci China Ser D 3(11):1112–1119
11. Ye L, Xi-long S, Ju-bo Z et al (2010) A self-calibration filter based on semi-parameter modeling and DUKF. ICSP10, Beijing
12. Yu A (2003) Research on multisensor measurement fusion technology. NUDT, Changsha

Chapter 49
Study on Intelligent Setting of Initial Alignment for GNSS/INS Integration

Linlin Gong, Quan Zhang, Qingli Li, Lin Gao and Xiaoji Niu

Abstract The main purpose of inertial navigation system (INS) alignment is attitude initialization. Alignment precision and alignment time affect the performance of navigation solution directly. Alignment can be static or kinematic. A proper alignment method should be applied to the initial conditions, and meet the requirement of high accuracy and short time. There has been much interest in alignment method in current research works related to the Global Navigation Satellite System (GNSS)/INS or INS initialization, whereas few works focus on the intelligent setting. For the inexperienced beginners, manual setting of the initial alignment method has large difficulty and low success rate, and takes large work load. An improper alignment setting can seriously affect the performance of navigation processing. Therefore, the intelligent setting of alignment for GNSS/INS integration is a concern in our paper. That is, the proper alignment method can be automatically determined by vehicle dynamics auto-detected by analyzing the inertial measurement unit (IMU) and GNSS data, and combining with the grade of inertial navigation system. To verify the feasibility of intelligent judgment, the large amounts of datasets (including different grade systems and dynamics) were processed by GINS, which is newly developed GNSS/INS data processing software, and alignment results were statistical analyzed. The results prove the correctness and reliability of the intelligent judgment of alignment. This work can not only reduce the difficulty for using, and improve the efficiency of data processing, but also ensure the success rate for the beginners, and it can further promote the applicability of the GNSS/INS data processing software.

Keywords Initial alignment · Intelligent setting · Dynamics auto-detection · Probability threshold method · GINS

L. Gong · Q. Zhang · Q. Li · L. Gao · X. Niu (✉)
GNSS Research Center, Wuhan University, Wuhan 430079, China
e-mail: xjniu@whu.edu.cn

L. Gong
e-mail: happylin@whu.edu.cn

J. Sun et al. (eds.), *China Satellite Navigation Conference (CSNC) 2014 Proceedings: Volume III*, Lecture Notes in Electrical Engineering 305,
DOI: 10.1007/978-3-642-54740-9_49,

49.1 Introduction

Inertial navigation system (INS) is a three-dimensional dead-reckoning navigation system. An inertial navigation system usually contains three mutually orthogonal gyros and three accelerometers, known as the inertial measurement unit (IMU). Unlike many other types of navigation system, inertial navigation systems are entirely self-contained within the vehicle. The principal advantages of INS are continuous operation, low short-term noise and high data update rate. However, the time-dependent growth of systematic errors is a major concern in INS. Therefore, they are usually integrated with Global Navigation Satellite System (GNSS) [1–3]. GNSS/INS integrated systems can provide high-rate precise positioning and attitude information.

INS is a kind of dead-reckoning (DR) based navigation system. A vital factor in achieving accurate navigation is the initialization of the INS before the start of navigation. The initial position and velocity can be easily obtained from GNSS or other aiding sensors, while the attitude initialization, also known as alignment, requires specific initial alignment algorithms to deal with [4]. Therefore, accurate alignment is crucial, and poor initial alignment accuracy will end up with poor navigation [5]. Due to the importance of INS initial alignment, many researchers have investigated this topic. The aim of initial alignment is the determination of the Direction Cosine Matrix (DCM) C_b^n, i.e. the coordinate transformation matrix from body frame to navigation frame [6, 7]. Several methods are available and can be divided into different types, such as the stationary alignment and in-motion alignment methods according to the moving conditions of carrier [5, 8, 9]. However, most researchers were mainly interested in the alignment method, and very few works focus on the intelligent setting of initial alignment. For the inexperienced beginners, manual setting of the initial alignment method has large difficulty and low success rate. An improper alignment setting can seriously affect the performance of navigation processing. Therefore, in this work, we concentrate on the intelligent setting of alignment for GNSS/INS integration.

In our work, a proper alignment method can be automatically determined by vehicle dynamics auto-detected by analyzing the IMU and GNSS data, and combining with the grade of inertial navigation system. This method can meet the requirement of high accuracy and short time. To verify the feasibility of intelligent judgment, the large amounts of datasets were processed, and alignment results were statistical analyzed. The results prove the correctness and reliability of the intelligent judgment of alignment.

49.2 Initial Alignment Method

To start the navigation, the initial position and velocity as well as the attitude should be determined first. Generally the position and velocity can be initialized by other aiding sensors (e.g. GNSS), while the attitude initialization may use the

inertial sensor outputs. Traditionally the process of attitude initialization is called initial alignment [4, 10]. Based on the different requirements of alignment and the dynamic conditions, different alignment methods are applied. This paper focuses the topic on the intelligent setting of alignment, and the automatic setting of stationary and in-motion alignment will be discussed in detail.

49.2.1 Stationary Alignment

Generally, the process of initial alignment for INS in stationary mode consists of two stages i.e. the coarse alignment and the fine alignment [5]. The coarse alignment aims at getting the coordinate transformation matrix from body frame to navigation frame and providing a fairly good initial condition for the fine alignment. Since INS is self-contained, coarse alignment of INS can be done in stationary mode by sensing the local gravity and the Earth's rotation [2, 6, 11], that is leveling and gyrocompassing. The process of leveling is to initialize the roll and pitch using the accelerometer outputs, and gyrocompassing is to initialize the heading information using the gyro outputs [2, 7]. Here the analytical coarse alignment is adopted, and we can get the initial coordinate transformation matrix from body frame to navigation frame i.e. C_b^n in one steps as follows [7, 9]:

$$C_b^n = \begin{bmatrix} \frac{-\tan\varphi}{g} & \frac{1}{\omega_e \cos\varphi} & 0 \\ 0 & 0 & \frac{-1}{g\omega_e \cos\varphi} \\ \frac{-1}{g} & 0 & 0 \end{bmatrix} \begin{bmatrix} \left(f^b\right)^T \\ \left(\omega_{ib}^b\right)^T \\ \left(f^b \times \omega_{ib}^b\right)^T \end{bmatrix} \tag{49.1}$$

where f^b and f^n is the specific force vector in the body frame and navigation frame respectively, ω_{ib}^b and ω_{ib}^n is the angular rate vector of body frame relative to inertial frame in the body frame and navigation frame respectively, g is local gravity, ω_e is the Earth rotation rate, and φ is latitude.

The accuracy of this method can be estimated by Eqs. (49.2), (49.3) and (49.4) [7]:

$$\delta\emptyset = \frac{\delta f_y}{g} \tag{49.2}$$

$$\delta\theta = \frac{1}{2}\left(-\frac{\delta f_x}{g} + \frac{\delta f_z}{g}\tan\varphi - \frac{\delta\omega_z}{\omega_e}\sec\varphi\right) \tag{49.3}$$

$$\delta\Psi = -\frac{\delta f_y}{g}\tan\varphi + \frac{\delta\omega_y}{\omega_e}\sec\varphi \tag{49.4}$$

where $[\delta\emptyset \quad \delta\theta \quad \delta\Psi]$ is the estimated attitude accuracy of this method, $[\delta f_x \quad \delta f_y \quad \delta f_z]$ is the accelerometer bias, and $[\delta\omega_x \quad \delta\omega_y \quad \delta\omega_z]$ is the gyro bias.

Followed by the coarse alignment, the small misalignment angles between reference frame and the body frame are computed accurately in the fine alignment stage [5]. Usually, the fine alignment is applied using the EKF with a small heading uncertainty (SHU) model [9]. Here no more detailed information about fine alignment is provided.

49.2.2 In-Motion Alignment

When the INS is initialized in motion, the information from an external source, such as GPS velocity, can be used for in-motion alignment. For most land vehicles, the roll can be initialized to zero. Then the GPS velocities can be used to initialize the pitch and heading, which can be computed as follows [2, 9, 12]:

$$\theta = \tan^{-1}\left(\frac{-v_D}{\sqrt{v_N^2 + v_E^2}}\right) \tag{49.5}$$

$$\Psi = \tan^{-1}\left(\frac{v_E}{v_N}\right) \tag{49.6}$$

where v_N, v_E and v_D are north, east and down GPS velocity, respectively, θ and Ψ are the pitch and heading, respectively.

The accuracy of the pitch and heading initialized by GPS velocities can be estimated by Eqs. (49.7) and (49.8) [12]:

$$\sigma_\theta^2 = \frac{v_N^2 \cdot v_D^2}{\left(v_N^2 + v_E^2 + v_D^2\right)^2 \cdot \left(v_N^2 + v_E^2\right)}\sigma_{v_N}^2 + \frac{v_E^2 \cdot v_D^2}{\left(v_N^2 + v_E^2 + v_D^2\right)^2 \cdot \left(v_N^2 + v_E^2\right)}\sigma_{v_E}^2 + \frac{v_N^2 + v_E^2}{\left(v_N^2 + v_E^2 + v_D^2\right)^2}\sigma_{v_D}^2 \tag{49.7}$$

$$\sigma_\psi^2 = \frac{v_E^2}{\left(v_N^2 + v_E^2\right)^2}\sigma_{v_N}^2 + \frac{v_N^2}{\left(v_N^2 + v_E^2\right)^2}\sigma_{v_E}^2 \tag{49.8}$$

where σ_X denotes the standard deviation of (X).

49.3 Vehicle Dynamic Auto-Detecting

In GPS/INS integrated navigation system, the zero velocity update (ZUPT) can serve as an extra measurements to correct the errors. It is an important and efficient method of bounding the error growth in inertial navigation. Also, the ZUPT is

usually applied in the pedestrian navigation system [3, 13–16] and the vehicle navigation system [17] to improve the performance of the systems. In our work, the zero velocity intervals can be applied to detect the vehicle dynamic in initial alignment of INS, which can be auto-added in the ZUPT module to reduce the error drift.

As we know, a proper alignment method should be applied to the initial conditions. Generally, when vehicle has sufficient speed the in-motion alignment method is to be used, and the stationary alignment is carried out when the vehicle is in stationary mode. So before choosing the alignment method, the raw data should be analyzed manually and the vehicle dynamics will be detected. Usually, the manual setting of ZUPTs and initial alignment mode is of low efficiency and is difficult for the inexperienced users. For this reason, the zero velocity auto-detecting method is of essential and significant.

There are many different zero velocity detection algorithms before, and the threshold method is usually used [13–16]. That is, a threshold value is determined first according to the feature of different detectors. Then analyze the detectors of raw measurements and check the vehicle state. If the IMU measurement is less than the threshold value in the analysis temporal window, then the zero velocity intervals is decided. The subtle difference between the threshold methods of zero velocity detection algorithms is mainly the type of detectors. For example, in [13] three detectors are used, while in [16] the norms of gyroscope and accelerometer output are used. The threshold method is easy to realize and used widely, while the result appears to be too absolute and lack flexibility only based on the value of threshold.

Hence, in our work, the method based on probability threshold is proposed for zero velocity auto-detection. The flow chart of the probability threshold method is presented in Fig. 49.1.

For a certain type of IMU, a set of sample data is processed first, the target of which is to get the probability curve of stillness for different STD (standard deviation). The probability of stillness is obtained by the STD of zero velocity intervals which are determined manually. Then the zero velocity detection of test data can be conducted, the process of which is as follows [18]:

- Calculate the STD value within the analysis temporal window, the length of which is 1 s.
- Get the probability of stillness for different STD value based on the probability curve of sample data.
- Compare the probability with the probability threshold of stillness and determine the dynamic of vehicle

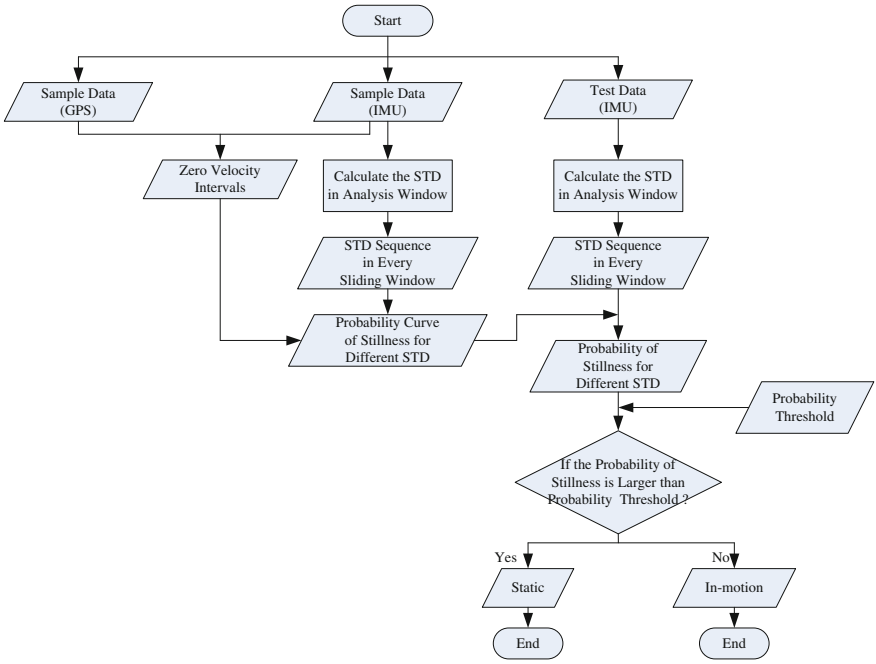

Fig. 49.1 Flow chart of the probability method in zero velocity detection

49.4 Intelligent Setting of Initial Alignment

49.4.1 Intelligent Setting of Stationary Alignment

As discussed in Sect. 49.2.1, the coarse alignment under static conditions is accomplished by leveling and gyrocompassing. The method is carried out by sensing the local gravity and Earth's rotation. In stationary mode, the true components of gravity in the north and east directions are nominally zero, so the roll and pitch can be initialized by accelerometers measurements. The process of gyrocompassing aims to find the initial heading by sensing the earth rotation. Based on the relationship between the heading angle and gyro measurements and the Eq. (49.4), the azimuth error can be roughly estimated as follows:

$$\delta\Psi \approx \frac{\delta\omega_y}{\omega_e \cos\varphi} \tag{49.9}$$

where $\delta\omega_y$ is the bias of east gyro. Given that the RMS error of gyro average value is proportional to the square root of the alignment time, the azimuth error can be

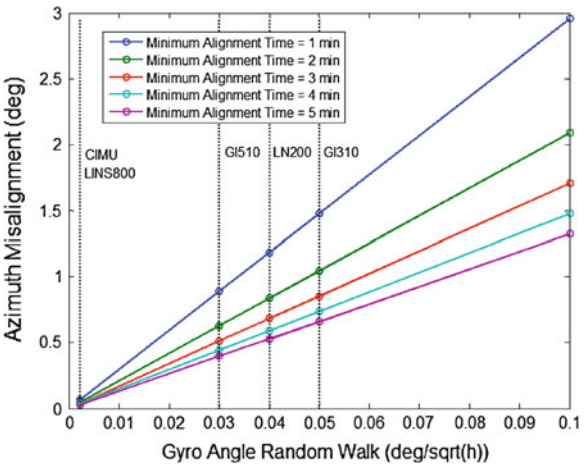

Fig. 49.2 The effect of azimuth accuracy on Gyro ARW along with alignment time (Latitude = 30°)

roughly estimated as Eq. (49.10) [19], and the effect of azimuth accuracy on gyro angle random walk (ARW) along with alignment time is shown in Fig. 49.2:

$$\delta\Psi = \frac{ARW}{\omega_e \cos\varphi\sqrt{T}} \tag{49.10}$$

From Fig. 49.2, it is clear that using the average of measurements for a few minutes in stationary mode can get a better accuracy of azimuth. For the high-end tactical grade or higher grade IMUs, 1 min of alignment time can ensure the azimuth accuracy level remains within ±1.5°, and 5 min can ensure it within ±0.7°.

Based on above analysis, for the high-end tactical grade or higher grade IMUs, the attitude can be initialized by analytic coarse alignment as Eq. (49.2) when vehicle has sufficient stationary time (see Fig. 49.3). The initial attitude uncertainty of this method can be estimated by Eqs. (49.3) (49.4) and (49.5), and the initial position and velocity uncertainty can be set based on the position and velocity standard deviation (STD) from GPS measurements file within the alignment time. For the low-cost IMUs, whose gyro bias and noise lever are near or larger than the value of the Earth's rotation, the approach of analytic coarse alignment on stationary mode cannot be used, and it is the same when the stationary condition is insufficient. Then, the in-motion alignment should be used in these conditions.

49.4.2 Intelligent Setting of In-Motion Alignment

In our work, in-motion alignment is used when the vehicle has sufficient speed. Assuming the land vehicles traveling on the plane road, the down velocity is zero.

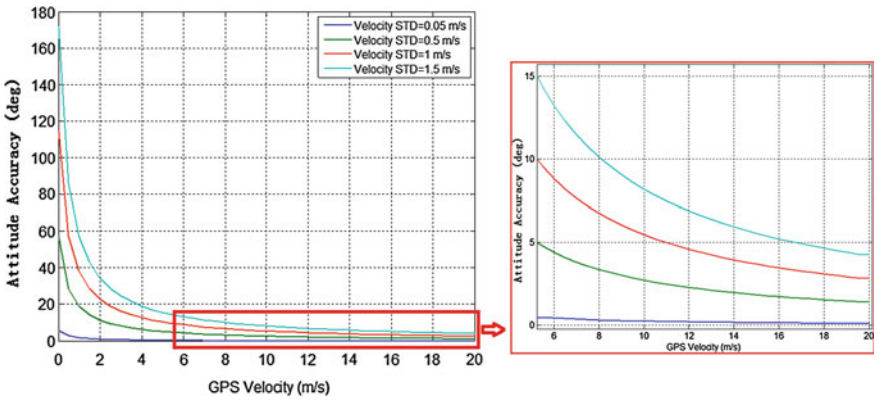

Fig. 49.3 Effect of attitude accuracy on GPS velocity

And the velocity STD of GPS in north, east and down is considered as the same, i.e. σ. Then (49.8) and (2.9) can be simplified to (49.11):

$$\sigma_{\psi}^2 = \frac{\sigma^2}{v_N^2 + v_E^2} \tag{49.11}$$

Based on (4.7), the accuracy of attitude initialized by GPS velocities depends on the vehicle velocity, and the greater the velocity is, the better the accuracy. Figure 49.3 shows the relationship between the GPS velocity and the accuracy of attitude.

From Fig. 49.3, it can be seen that the accuracy of attitude deteriorates rapidly with GPS velocity when it is less than 4 m/s. And the azimuth accuracy level remains within $\pm 15°$ when the GPS velocity is larger than 6 m/s. Therefore, when the vehicle has sufficient velocity, the in-motion alignment can be applied. And the velocity threshold can be chose based on the conditions of GPS velocity accuracy as well as the attitude accuracy needed. Because the in-motion alignment is applied by GPS velocity, it also can be used in the land vehicle applications with low-cost IMU integrated with GPS systems. Also, in the condition that the stationary time is insufficient, this method can be used until the vehicle has sufficient speed. And the attitude uncertainty can be estimated based on the Sect. 49.2.2. The initial position and velocity uncertainty can be set based on the STD from the GPS measurements file at the start of the initialization time.

49.5 Experiments

In this section, the method of vehicle dynamic auto-detecting as well as the intelligent setting of initial alignment method proposed above is verified using experiment data. In our experiments, a representative land vehicle test was

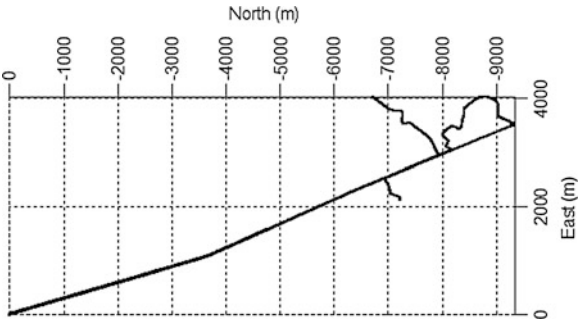

Fig. 49.4 Trajectory of land vehicle test

Table 49.1 Performance of IMUs

	LINS800	GI310	Mti-G
Gyro bias STD (deg/h)	0.005	0.5	3,600
Accel. bias STD (mGal)	25	25	2,000
ARW (deg/sqrt(h))	0.0022	0.05	3
VRW (m/s/sqrt(h))	0.00075	0.1	0.12

conducted in the open-sky area of Wuhan on 19 June 2013, which contained various scenarios, as shown in Fig. 49.4.

Three different grades of IMUs are used in this paper, that are a navigation grade IMU (LINS800), a tactical grade (GI310) and a typical MEMS IMU (Mti-G). The performance of the three IMUs are listed in Table 49.1.

The initial condition is an important factor to affect the intelligent setting of initial alignment, so the results of the success rate in zero velocity detecting will be presented first. Followed it the results of stationary alignment and in-motion alignment are given to verify the feasibility and correctness of intelligent setting for initial alignment. One of the requirements of initial alignment is high accuracy. Finally the results of alignment accuracy are presented in 5.3.

49.5.1 Success Rate of Dynamic Detecting

In Sect. 49.3, the method of vehicle dynamic auto-detecting was discussed. The initial alignment mode is chose based on the vehicle dynamic; hence the success rate of intelligent setting depends largely on the dynamic detecting. As a reference, the zero velocity intervals are determined by manually analyzing the raw data, which can be considered as a true value. The zero velocity intervals are easily detected manually because the noise and abnormal data is easy to be spotted directly. Then compared the intelligent setting with the manual setting, the statistic rate of correct is given in Table 49.2. Simultaneously Table 49.2 presented the success rate of threshold method too.

Table 49.2 Statistic results of success rate in dynamic detecting [18]

	False positive (%)	False negative (%)
Probability threshold method	1.81	2.91
Standard threshold method	1.91	3.20

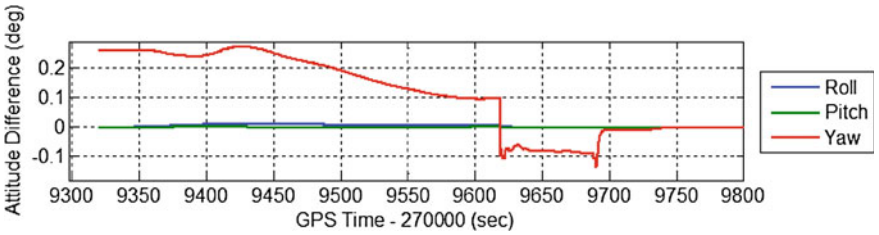

Fig. 49.5 Difference between the intelligent and manual setting in stationary alignment

The results in Table 49.2 show that the true positives is as high as 98.19 % and the false negative is under 3 %, which is better and more reliable than the results of threshold method. Hence, the intelligent setting method has high credibility and can meet with the requirements for land vehicle applications.

49.5.2 Feasibility of Intelligent Setting

The intelligent setting of initial alignment can greatly improve the efficiency of data post-processing of the GPS/INS integrated systems, as well as increase the success rate of alignment for the inexperienced beginners. But the premise is that the intelligent setting method is reliable and feasible. Next the result of difference between the intelligent setting and manual setting is to be discussed. For reasons of space, the result of a typical tactical grade IMU i.e. GI310 is presented (see Fig. 49.5).

Figure 49.5 shows the difference between the intelligent setting and manual setting. To aviod to display the large GPS time, the GPS time is adjusted by the function of floor, i.e. floor (time(1, 1)/10,000) * 10,000, which is processed similarly in Fig. 49.6. From Fig. 49.5, slight difference in the roll and pitch between the results of two sets, and the biggest difference in yaw is about 0.3°. Based on (49.3) to (49.5), the theoretical attitude accuracy of GI310 is 0.0015° in roll, 1.1067° in pitch and 2.2119° in heading. The difference between the intelligent and manual setting is much less than the alignment accuracy of GI310. Hence, the method of intelligent setting in stationary alignment can be feasible and reliable.

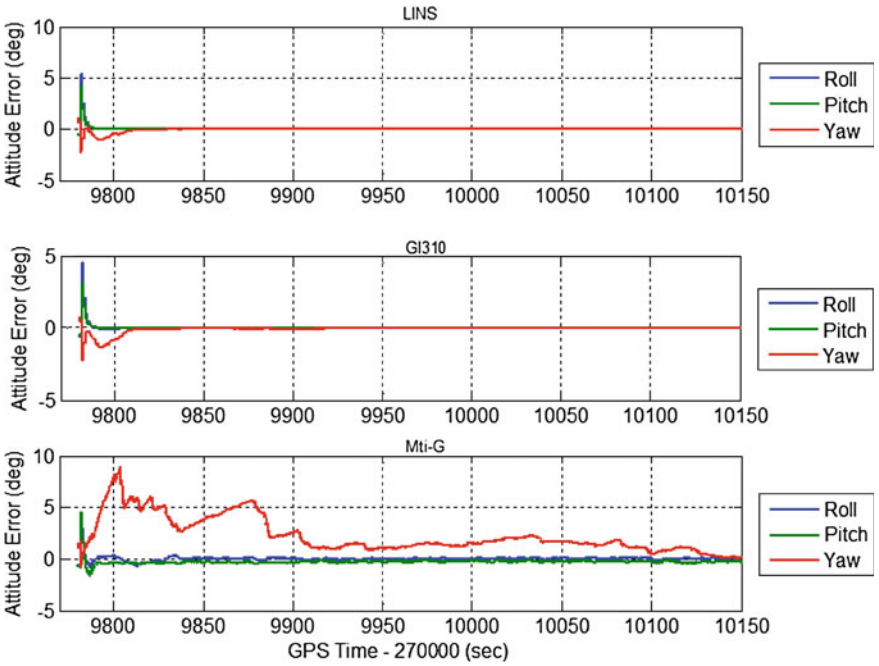

Fig. 49.6 Attitude accuracy of different systems in in-motion alignment

49.5.3 Accuracy of Intelligent Setting

In Sect. 49.5.2, the feasibility and reliability have been proved. Next the alignment accuracy of intelligent setting in different grade IMUs will be evaluated. To estimate the accuracy of initial alignment, the solution of backward smoothing from a higher grade IMU (LINS800) is used to provide a reference result of initial alignment. Table 49.3 lists the statistic summary of the attitude errors in stationary alignment process.

From Table 49.3, it is obvious that the heading error is much larger than the roll and pitch errors. The horizontal accuracy of LINS is within 0.003°, and that of GI310 is within 0.04°. Yet the vertical accuracy of LINS is about 0.4° and the GI310 is 1.6°. This is a common feature of the high grade navigation systems that the accuracy in vertical directions is worse than the accuracy in horizontal direction.

Similarly, the result of in-motion alignment is shown in Table 49.4 and Fig. 49.6. Here the reference data is the backward smoothing solution of LINS.

In in-motion alignment, the attitude is initialized based on the GPS velocity. The GPS data file we used in three grades of GPS/INS system is the same. No difference is exists in attitude estimating between the test data and the reference data at the start moment of the initial alignment, which is listed in Table 49.4. And

Table 49.3 Statistic values of attitude errors in stationary alignment

		Roll error (deg)	Pitch error (deg)	Heading error (deg)
LINS	RMS	0.0018	0.0016	0.3729
	Max	0.0021	0.0027	0.4029
GI310	RMS	0.0071	0.0089	1.3545
	Max	0.0390	0.0187	1.6171

Table 49.4 Attitude difference in in-motion alignment

	Pitch (deg)	Heading (deg)
Alignment result	−1.7099	163.5005
Reference	−2.2851	164.4944
Difference between result and reference	0.5752	0.9939
Theoretical accuracy	2.8142	1.5523

Table 49.4 represents the result of the LINS, GI310 and Mti-G at the start of the process of alignment. The theoretical accuracy in Table 49.4 is calculated based on the (49.8) and (2.9). The in-motion alignment method used in this paper can only estimate two of the attitude (see Sect. 49.2.2), so in Table 49.4 only the results of pitch and heading are given. From Table 49.4, it is clear that the attitude accuracy is better than the theoretical expectation accuracy. Based on (49.8) and (2.9), the attitude accuracy is influenced by the GPS velocity STD provided by the result of differential GPS. Besides the attitude accuracy of start moment, Fig. 49.6 shows the error of different systems in in-motion alignment.

Based on the analysis of Table 49.4, there are no differences in the accuracy of three grades of IMUs at the start moment of alignment. In Fig. 49.6, it is clear that the error drift is increasing first, which results from the instable state of the Kalman Filter in the first few minutes of navigation. And then the attitude error starts converging. The extent of drift and the convergence rate depend on the grade of IMUs, which can be seen in Fig. 49.6. Comparing the result in Fig. 49.6, the accuracy of LINS and GI310 are remarkably superior to the accuracy of Mti-G. And as a result of the difference in the IMU grade, the convergence rate of Mti-G has low convergence speed.

Comparing the result in in-motion alignment and that in stationary alignment, the accuracy of stationary alignment is better than in-motion alignment. Hence, except for the low-cost IMUs, the stationary alignment is recommended in the post-processing of GPS/INS integrated navigation system. So, before collecting data, the vehicle should be in stationary state for a few minutes to get a better post-processed accuracy.

From the above analysis, the intelligent setting of initial alignment can be applied based on the grade of IMU and the condition of vehicle. For the inexperienced beginners, the use of intelligent setting can greatly increase the success rate in improve the efficiency of data post-processing of the GPS/INS integrated systems, as well as increase the success rate of alignment for the inexperienced beginners.

49.6 Summary

This paper proposes a method of intelligent setting for initial alignment. This is a practical technique and has been integrated in GINS software, which is newly developed GNSS/INS data processing software by MAP Company of Wuhan. The results prove the correctness and reliability of the intelligent judgment of alignment. The method of intelligent setting can not only greatly increase the success rate of the data processing in GPS/INS integrated systems, but also improve the efficiency of GPS/INS data processing. Simultaneously, the application of intelligent setting for initial alignment can further promote the applicability of the GNSS/INS data processing software. Besides, a new zero velocity detection method is used to detect the vehicle dynamics automatically, that is the probability threshold method. The false positive and false negative is smaller than that of the standard threshold method. The method of zero velocity auto-detection can be also applied in ZUPTs technique in improving the accuracy of GPS/INS integrated systems.

References

1. Wang J, Dai L, Tsujii T, Rizos C, Grejner-Brzezinska D, Toth C (eds) (2001) GPS/INS/Pseudolite integration: concepts, simulation and testing. In: Proceedings of the 14th international technical meeting of the Satellite Division of the Institute of Navigation (ION GPS 2001)
2. Groves PD (2013) Principles of GNSS, inertial, and multisensor integrated navigation systems
3. Titterton D (2004) Strapdown inertial navigation technology, IET
4. Han S, Wang J (2010) A novel initial alignment scheme for low-cost INS aided by GPS for land vehicle applications. J Navig 63(04):663–680
5. Ali J, Jiancheng F ()2006 Alignment of strapdown inertial navigation system: a literature survey spanned over the last 14 years. School of instrumentation Science and Optoelectronics Engineering, Beijing University of Aeronautics and Astronautics, Beijing, p 100083
6. Yi J, Zhang L, Shu R, Wang J (2011) Initial alignment for SINS based on low-cost IMU. J Comput 6(6):1080–1085
7. Shin E-H, El-Sheimy N (2001) Accuracy improvement of low cost INS/GPS for land applications. Department of Geomatics Engineering, University of Calgary
8. Ma L, Wang K, Shao M (2013) Initial alignment on moving base using GPS measurements to construct new vectors. Measurement
9. Shin E-H (2005) Estimation techniques for low-cost inertial navigation. UCGE report, p 20219
10. Bekir E (2007) Introduction to modern navigation systems. World Scientific
11. Fang JC (1996) A fast initial alignment method for strapdown inertial navigation system on stationary base. IEEE Trans Aerosp Electron Syst 32(4):1501–1504
12. Godha S (2006) Performance evaluation of low cost MEMS-based IMU integrated with GPS for land vehicle navigation application. UCGE report, p 20239
13. Skog I, Handel P, Nilsson J-O, Rantakokko J (2010) Zero-velocity detection—an algorithm evaluation. IEEE Trans Biomed Eng 57(11):2657–2666

14. Park SK, Suh YS (2010) A zero velocity detection algorithm using inertial sensors for pedestrian navigation systems. Sensors 10(10):9163–9178
15. Mather C, Groves P, Carter M (eds) (2001) A man motion navigation system using high sensitivity GPS, MEMS IMU and auxiliary sensors. In: Proceedings of the 19th international technical meeting of the Satellite Division of the Institute of Navigation (ION GNSS 2006)
16. Foxlin E (2005) Pedestrian tracking with shoe-mounted inertial sensors. IEEE Comput Graph Appl 25(6):38–46
17. Davidson P, Hautamäki J, Collin J (eds) (2008) Using low-cost MEMS 3D accelerometers and one gyro to assist GPS based car navigation system. In: Proceedings of 15th Saint Petersburg international conference on integrated navigation systems, May 2008
18. Li Q (2013) A parking detection method based on inertial sensors. Wuhan, China
19. Niu X (2013) Princple and algorithm of inertial navigation system: initial alignment of INS. Wuhan, China (GNSS Research Center, Wuhan University, GNSS Research Center WU)

Chapter 50
Error Calibration of Tri-axial Magnetometer Based on Particle Swarm Optimization Algorithm

Feng-xi Wu, Bing Hua and Guo-hua Kang

Abstract A particle swarm optimization (PSO) algorithm-based error calibration method is presented for tri-axial magnetometer. The calibration of bias error and scale factor error in tri-axial magnetometer is completed. The specific algorithm derivation is shown in this paper and the error calibration optimization function is defined. The simulation results show that, the convergence speed of particle swarm optimization algorithm is fast with high accuracy. This method makes the tri-axial magnetometer measurement error reduce to 0–150 nT from 400–1,500 nT, which demonstrates the feasibility of the method.

Keywords Particle swarm optimization · Tri-axial magnetometer · Error calibration · Measurement error

Foundation item: National Natural Science Foundation of China (No. 61203188)Natural Science Foundation of Jiangsu Province (BK2011729)Youth Foundation of Natural Science Foundation of Jiangsu Province (SBK201343261)

F. Wu (✉)
College of Automation Engineering, Nanjing University of Aeronautics and Astronautics, Nanjing 210016, China
e-mail: wfx123@nuaa.edu.cn

B. Hua · G. Kang
College of Astronautics, Nanjing University of Aeronautics and Astronautics, Nanjing 210016, China
e-mail: huabing@nuaa.edu.cn

G. Kang
e-mail: kanggh@nuaa.edu.cn

J. Sun et al. (eds.), *China Satellite Navigation Conference (CSNC) 2014 Proceedings: Volume III*, Lecture Notes in Electrical Engineering 305,
DOI: 10.1007/978-3-642-54740-9_50,

50.1 Introduction

Geomagnetic navigation has been a research focus of the vehicle navigation. As the sensor for estimation of attitude, the measurement precision of the tri-axial magnetometer is significant in geomagnetic navigation [1]. The tri-axial magnetometer errors include bias error, scale factor error, orthogonal error and so on. The bias error and scale error will be offset with changing of time and the environment. So they are the main destabilizing factors of magnetometer.

At present, the methods of error correction for the tri-axial magnetometer are based on the Kalman filter, FLANN or etc. The means proposed in the Refs. [2] and [3] demand the magnetic reference value which is obtained difficulty and do not consider the affection of the interference magnetic field. Therefore, they are applied to the practical application hardly.

This paper proposes a new method for tri-axial magnetometer error correction based on particle swarm optimization algorithm, which calibrates the bias error and scale factor error by PSO. The sensor error model is established. As a parameter optimization problem, the error calibration is solved. So the optimization objective function is derived in this paper. Finally, the simulation analysis on this method is completed.

50.2 Error Analysis and Modeling

The measurement error of tri-axial magnetometer is composed of bias error, scale factor error, orthogonal error, measurement noise, hard iron error, soft iron error and alignment error. The first three kinds belong to the instrument error. The others are the environmental interference error which can be decomposed into bias error and scale factor error with reflected in the sensor [4, 5, 6]. In the ideal orthogonal condition, the bias error and scale factor error are calibrated based on the particle swarm optimization algorithm in this thesis.

Based on the above analysis, the output of the tri-axial magnetometer is expressed as:

$$\widetilde{\mathbf{H}} = \mathbf{K} \cdot \mathbf{H} + \mathbf{e_z} \tag{50.1}$$

In which, $\widetilde{\mathbf{H}}' = \begin{bmatrix} \widetilde{H_X} \\ \widetilde{H_Y} \\ \widetilde{H_Z} \end{bmatrix}$ is actual measured value, $\mathbf{K} = \begin{bmatrix} K_X & 0 & 0 \\ 0 & K_Y & 0 \\ 0 & 0 & K_Z \end{bmatrix}$ corresponds to scale factor in each axis, $\mathbf{H} = \begin{bmatrix} H_X \\ H_Y \\ H_Z \end{bmatrix}$ is theoretical true value and $\mathbf{e_z} = \begin{bmatrix} \Delta H_X \\ \Delta H_Y \\ \Delta H_Z \end{bmatrix}$ is bias error in each axis.

50.3 PSO

The particle swarm optimization (PSO) is an evolutionary computation technique. The based idea is to find the optimal solution by collaboration and information sharing of the groups' individual.

The PSO algorithm randomly initializes a swarm of particles—random solution, and then finds the optimal solution by iteration. In the each iteration, particles are updated through two extremes (P_{besti}, G_{best}). The particles are manipulated according to the following time-transition equations:

$$\begin{aligned} V_i[k+1] =, & wV_i[k] + C_1\gamma_1(P_{besti}[k] - P_i[k]) \\ & + C_2\gamma_2(G_{best}[k] - P_i[k]) \end{aligned} \tag{50.2}$$

$$P_i[k+1] = P_i[k] + V_i[k] \tag{50.3}$$

where $V_i[k]$ and $P_i[k]$ respectively represent the velocity vector and position for particle i at time k; $P_{besti}[k]$ represents the best position in its past experience—local optimum; $G_{best}[k]$ is the best position among all particles in the population. γ_1 and γ_2 are two random functions with a range [0, 1]. C_1 and C_2 are the cognitive and the social parameter respectively. w represents the inertia weight.

The main parameters of PSO include: population size m, the inertial weight w and the cognitive and the social parameter and the maximum speed $V_{\max}$. The population size is decided by the complexity of the issues. The inertia weight w is employed to control the impact of the precious history of velocities on the current velocity. A large inertia weight facilitates global exploration, while with a small one the particle is more intended to do local exploration. The acceleration constant C_1 and C_2 represent the weighting of the stochastic acceleration terms that pull each particle toward positions of P_{besti} and G_{best}. Low values of C_1 and C_2 allow particles to roam far from target regions before being tugged back. Conversely, high ones result in abrupt movement toward, or past, target region. Generally, $C_1 = C_2 = 2$. The maximum velocity $V_{\max}$ determines the resolution, or fineness, with which regions between the present position and the target position are searched. If $V_{\max}$ is too high, particles might fly past good solutions. If $V_{\max}$ is too small, on the other hand, particles may not explore sufficiently beyond locally good regions. In fact, they could become trapped in local optima, unable to move far enough to reach a better position in the problem space [7, 8].

50.4 Derivations of Calibration Algorithm and Best Cost Function

From the formula (50.1),

$$\widetilde{H_X} = K_X H_X + \Delta H_X, \widetilde{H_Y} = K_Y H_Y + \Delta H_Y, \widetilde{H_Z} = K_Z H_Z + \Delta H_Z \tag{50.4}$$

where K_X, K_Y, K_Z and ΔH_X, ΔH_Y, ΔH_Z can be considered to be constant during a short period of time. In addition, $H_X^2 + H_Y^2 + H_Z^2 = B_0^2$, where B_0 represents the local magnetic field.

Equation (50.4) can be rewritten as follows:

$$\frac{\widetilde{H_X}}{K_X} = H_X + \frac{\Delta H_X}{K_X}, \frac{\widetilde{H_Y}}{K_Y} = H_Y + \frac{\Delta H_Y}{K_Y}, \frac{\widetilde{H_Z}}{K_Z} = H_Z + \frac{\Delta H_Z}{K_Z}$$

Then,

$$\frac{\widetilde{H_X}^2}{K_X^2} + \frac{\widetilde{H_Y}^2}{K_Y^2} + \frac{\widetilde{H_Z}^2}{K_Z^2} = (H_X + \frac{\Delta H_X}{K_X})^2 + (H_Y + \frac{\Delta H_Y}{K_Y})^2 + (H_Z + \frac{\Delta H_Z}{K_Z})^2$$

that is simplified as:

$$\frac{\widetilde{H_X}^2}{K_X^2} + \frac{\widetilde{H_Y}^2}{K_Y^2} + \frac{\widetilde{H_Z}^2}{K_Z^2} = B_0^2 + (\frac{\Delta H_X^2}{K_X^2} + \frac{\Delta H_Y^2}{K_Y^2} + \frac{\Delta H_Z^2}{K_Z^2}) + 2H_X\frac{\Delta H_X}{K_X} + 2H_Y\frac{\Delta H_Y}{K_Y} + 2H_Z\frac{\Delta H_Z}{K_Z}$$

As K_X, K_Y, K_Z and ΔH_X, ΔH_Y, ΔH_Z can be considered to be constant during a short period of time, we assume that $\frac{\Delta H_X^2}{K_X^2} + \frac{\Delta H_Y^2}{K_Y^2} + \frac{\Delta H_Z^2}{K_Z^2} = \Delta B^2$, which is substituted in the above equation.

Thus,

$$\frac{\widetilde{H_X}^2}{K_X^2} + \frac{\widetilde{H_Y}^2}{K_Y^2} + \frac{\widetilde{H_Z}^2}{K_Z^2} = B_0^2 + \Delta B^2 + 2H_X\frac{\Delta H_X}{K_X} + 2H_Y\frac{\Delta H_Y}{K_Y} + 2H_Z\frac{\Delta H_Z}{K_Z} \tag{50.5}$$

In two different postures, following can be obtained by using the Eq. (50.5):

$$\begin{aligned}&\frac{\widetilde{H_{X1}}^2 - \widetilde{H_{X2}}^2}{K_X^2} + \frac{\widetilde{H_{Y1}}^2 - \widetilde{H_{Y2}}^2}{K_Y^2} + \frac{\widetilde{H_{Z1}}^2 - \widetilde{H_{Z2}}^2}{K_Z^2} \\ &= 2(H_{X1} - H_{X2})\frac{\Delta H_X}{K_X} + 2(H_{Y1} - H_{Y2})\frac{\Delta H_Y}{K_Y} + 2(H_{Z1} - H_{Z2})\frac{\Delta H_Z}{K_Z}\end{aligned} \tag{50.6}$$

where

$$H_{X1} - H_{X2} = \frac{\widetilde{H_{X1}} - \widetilde{H_{X2}}}{K_X}, H_{Y1} - H_{Y2} = \frac{\widetilde{H_{Y1}} - \widetilde{H_{Y2}}}{K_Y}, H_{Z1} - H_{Z2} = \frac{\widetilde{H_{Z1}} - \widetilde{H_{Z2}}}{K_Z}.$$

Therefore,

$$\begin{aligned} &\frac{\widetilde{H_{X1}}^2 - \widetilde{H_{X2}}^2}{K_X^2} + \frac{\widetilde{H_{Y1}}^2 - \widetilde{H_{Y2}}^2}{K_Y^2} + \frac{\widetilde{H_{Z1}}^2 - \widetilde{H_{Z2}}^2}{K_Z^2} \\ &= 2\frac{\widetilde{H_{X1}} - \widetilde{H_{X2}}}{K_X^2}\Delta H_X + 2\frac{\widetilde{H_{Y1}} - \widetilde{H_{Y2}}}{K_Y^2}\Delta H_X + 2\frac{\widetilde{H_{Z1}} - \widetilde{H_{Z2}}}{K_Z^2}\Delta H_Z \end{aligned} \tag{50.7}$$

That can be rewritten as follow:

$$\begin{aligned} &2(\widetilde{H_{X1}} - \widetilde{H_{X2}})K_Y^2K_Z^2\Delta H_X + 2(\widetilde{H_{Y1}} - \widetilde{H_{Y2}})K_X^2K_Z^2\Delta H_Y \\ &+ 2(\widetilde{H_{X1}} - \widetilde{H_{X2}})K_X^2K_Y^2\Delta H_Z - (\widetilde{H_{X1}}^2 - \widetilde{H_{X2}}^2)K_Y^2K_Z^2 \\ &- (\widetilde{H_{Y1}}^2 - \widetilde{H_{Y2}}^2)K_X^2K_Z^2 - (\widetilde{H_{Z1}}^2 - \widetilde{H_{Z2}}^2)K_X^2K_Y^2 = 0 \end{aligned} \tag{50.8}$$

According to the Eq. (50.8), multiple groups of equations can be obtained with raw outputs of tri-axial magnetometer in different attitudes. As calibrating six parameters (K_X, K_Y, K_Z and ΔH_X, ΔH_Y, ΔH_Z), this paper select outputs of the magnetometer in 12 different attitudes obtaining 6 groups of equations. Mark each equation as f_i.

Let us assume

$$f = f_1^2 + f_2^2 + \cdots + f_5^2 + f_6^2 \tag{50.9}$$

that is defined as the best cost function on calibrating problem. Thus the PSO algorithm is set to searching the minimum.

50.5 Simulation

In order to demonstrate feasibility of applying the PSO algorithm to error calibration of tri-axial magnetometer, simulation experiments are carried out. Varieties of measurement are simulated according to the formula (50.1). In simulation, we assume that $B_0 = 4 \times 10^5$ nT.

Setting the range of parameters is essential for controlling computations of the algorithm. In the experiment, the range of K_X, K_Y and K_Z is [0.99, 1.05] according to actual situation. Meanwhile, it is vital to set the range of ΔH_X, ΔH_Y and ΔH_Z. If the range is too wide, the amount of computation will be increased significantly. The follow is the way to determine the range of bias error. K_X, K_Y and $K_Z$in the Eq.

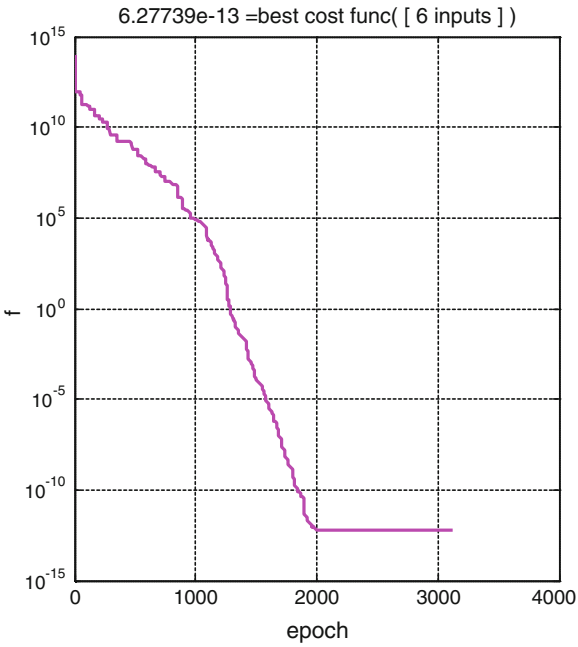

Fig. 50.1 The best cost function

Table 50.1 The results of parameters calibration

Parameters	$[\Delta H_X \quad \Delta H_Y \quad \Delta H_Z \quad K_X \quad K_Y \quad K_Z]^T$			
Setting	500 300 400 1.02 1.01 1.03	450 350 450 1.02 1.02 1.03	600 600 600 1.01 1.02 1.01	600 500 650 1.03 1.02 1.01
The results	499 300 400 1.01990 1.00991 1.02990	450 349 449 1.02562 1.02562 1.03568	600 599 599 1.00924 1.01923 1.00924	600 500 650 1.02737 1.01740 1.00742

(50.8) are assumed as the constant 1. Thus, there are only three unknown numbers in the 6 groups of equations (f_i). $\Delta H'_X$, $\Delta H'_Y$ and $\Delta H'_Z$ will be resolved by the least squares. These values will be the center of the bias error range with the variation amplitude ± 200 nT.

The parameters of the PSO are:

(1) The size of the population m: 50.
(2) The inertia weigh$w$: initial inertia weight 0.9 and final inertia weight 0.4 (the better results can be achieved with dynamic inertia weight).

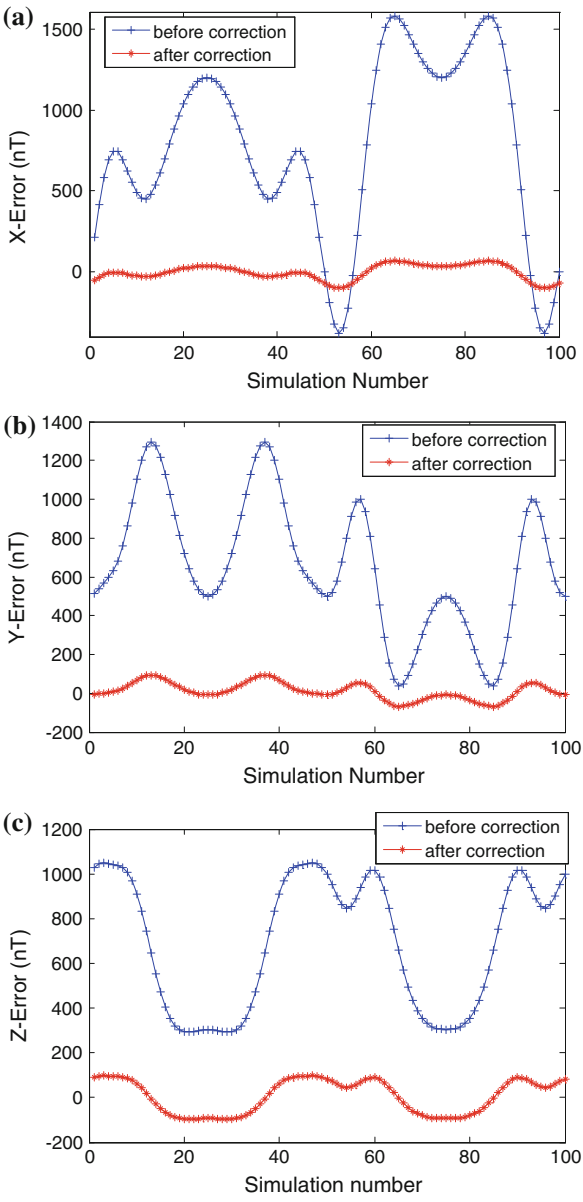

Fig. 50.2 Comparison of measurement errors *before* and *after correction* in each axis. **a** X-axis magnetometer error. **b** Y-axis magnetometer error. **c** Z-axis magnetometer error

(3) $C_1 = C_2 = 2$.

(4) Terminate criterion: maximum number of iterations: 4,000; If the gradient of global optimums obtained in two consecutive iterations is less than 10^{-25}, terminate runs; If the gradient does not change over 1,000 consecutive iterations, terminate runs.

As shown in Fig. 50.1, the convergence speed of particle swarm optimization algorithm is fast with high accuracy. In fact, the PSO has converged in approximately 2,000th iteration.

The Table 50.1 shows the feasibility of the proposed PSO algorithm. The bias errors can be calibrated with high precision and calibration of scale factors has the reasonable accuracy with a certain range.

As can be seen in Fig. 50.2, the PSO algorithm-based error calibration method can significantly improve the measurement accuracy of the tri-axial magnetometer. Specifically, X-axis error is reduced from 500–1,500 nT to 0–150 nT; Y-axis from 400–1,200 nT to 0–150 nT; Z-axis from 400–1,500 nT to 0–150 nT. The measurement accuracy of all axes has been effectively improved.

50.6 Conclusion

In this paper, a new feasible method is proposed for error calibration of tri-magnetometer. The error calibration regarded as the parameter optimization problem is resolved. The PSO algorithm is applied to solve the parameter optimization problem. Meanwhile, the best cost function is derived. The simulation shows that the PSO is capable to solve error calibration of tri-magnetometer. The convergence speed of the PSO is fast with high accuracy. Finally, the measurement accuracy of tri-axial magnetometer is improved with correction. In practical application, this method can be effectively applied.

References

1. Wu D, Huang S, Zhao W (2009). Research on correction of tri-axial magnetometer based on FLANN. Chin J Sci Instr 30(3):449–453
2. Hao D, Sheng T, Chen X (2011) The error correction of three-axis magnetometer measurement. Spacecraft Environ Eng 28(5):463–466
3. Pang H, Pan M, Chen D, Luo S, Luo F (2012) Error calibration of three axis magnetometer based on UKF and equipment. Chin J Sci Instr 33(8):1800–1805
4. Meng J (2011) Research on error analysis and calibration of three-axial magnetometers. Harbin Institute of Technology, pp 1–10
5. Huang L, Jing W (2008) Spacecraft attitude determination and three-axis magnetometer calibration. J Astronaut 29(3): 854–859
6. Li C, Yang SX (2009) An adaptive learning particle swarm optimizer for function optimization. In: IEEE congress on evolutionary computation, Trondheim, Norway, pp 381–388
7. Zhen Z, Wang D, Li M (2009) Improved particle swarm optimizer based on adaptive random learning approach. In: IEEE congress on evolutionary computation, Trondheim, Norway, pp 1045–1048
8. Xia J, Qin Y, Jia J (2009) Application of particle swarm optimization algorithm in transfer alignment. J Chin Inertial Technol 17(5):513–516

Chapter 51
GNSS/INS/VKM Vehicle Integrated Navigation System

Gong-min Yu, Jian Xiong, Hang Guo and Ji-xu Wang

Abstract When the vehicle is in the process of moving, the GNSS signals may be unlocked or lost star which will make GNSS/INS integrated navigation system not reliable enough for driving. To solve this problem, I put forward a kind of vehicular integrated navigation scheme constructed by GNSS, INS and vehicle kinematics model. This integrated navigation strategy depends on GNSS information to determine the condition: when GNSS information is available, it will use GNSS aided inertial navigation system; When the GNSS information is invalid, the kinematics model and constraint condition of the vehicle aided inertial navigation system will start to work; The results of simulation show that this method can provide high precision position information speed when GNSS information is valid, and the position error can be effectively suppressed when GNSS failure, which will ensure the precision, reliability and continuous of navigation information of vehicle navigation system.

Keywords Vehicle kinematic model · Constraint condition · INS · Integrated navigation

51.1 Introduction

Global Positioning System (GPS), all-weather, low cost, and high Positioning accuracy has been widely used in the field of vehicle navigation [1], but for the street, and other complex areas, the GPS information can be cut off easily and the

G. Yu (✉) · J. Xiong · J. Wang
Department of Process Equipment and Measuring and Control Engineering, Nanchang University, Nanchang, China
e-mail: 568651142@qq.com

H. Guo
Academy of Space Technology, Nanchang University, Nanchang, China

J. Sun et al. (eds.), *China Satellite Navigation Conference (CSNC) 2014 Proceedings: Volume III*, Lecture Notes in Electrical Engineering 305,
DOI: 10.1007/978-3-642-54740-9_51,

loss of continuous Positioning capability. Generally, the low-cost Micro mechanical Inertial Measurement Unit (MIMU) can be use to constructed SINS/GPS integrated navigation system to improve positioning accuracy in the complex areas, and improve the continuous positioning and fault tolerance for vehicle navigation use [2–4].

However, it cannot guarantee the inertial navigation system provide accurate and reliable navigation information for autonomous vehicle when GPS signal failure for a long time [5]. Therefore, it is not enough to guarantee the reliability of the integrated system only by GPS [6]. Study the vehicle constraint condition aid the low-cost inertial navigation system [7, 8]. Study the vehicle motion constraints improve the navigation accuracy. The vehicle constraint condition aid the low-cost inertial navigation system is studied by Klein [9].

In the paper, We mainly studies the influence of navigation accuracy when GPS signal loss, and put forward a new method of using the vehicle kinematic model aided inertial navigation system to improve the navigation accuracy when GPS signal loss. The strategy of integration is presented whose judging condition is whether GPS information is valid or not. The simulation results show that this method can restrain the pure inertial navigation error accumulated over time effectively, and improve the positioning accuracy, and satisfies the requirement of vehicle navigation in complex environments.

51.2 Analysis of the Vehicle Motion

51.2.1 Vehicle Kinematic Model

Vehicles on the road is a relatively complex kinematics process. There are exist the following relations between radius of turning circle R, steering angle of front wheel and wheel base l when steering [10]:

$$R = \frac{l}{\tan \delta} \tag{51.1}$$

The model establish only in the ideal case, the car turning radius depends on the steering angle of front wheel entirely and have nothing to do with vehicle speed and tire cornering, the ground is flat or not. Generally, Assume that the road is flat, a simplified vehicle motion model is shown in Fig. 51.1. In the figure, M is the axis of the rear of the vehicle. In t_k, the state of the vehicle expression with a set of coordinates $(x_k, y_k, z_k, \theta_k)$, θ_k is the Angle relative to the X axis. M_k and M_{k+1} are the Two consecutive location of vehicle, I is the center of the circle. $\Delta = \rho \cdot \omega$, Δ is the distance of M had gone from t_k to t_{k+1}, ω is yaw velocity, ρ is the radius of turning circle.

It is easy to get the following equations by analyzing the geometrical relation of different variables of the figure:

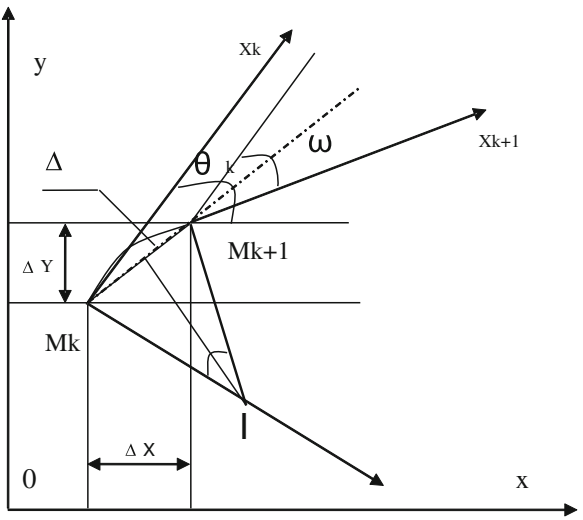

Fig. 51.1 vehicle kinematic model

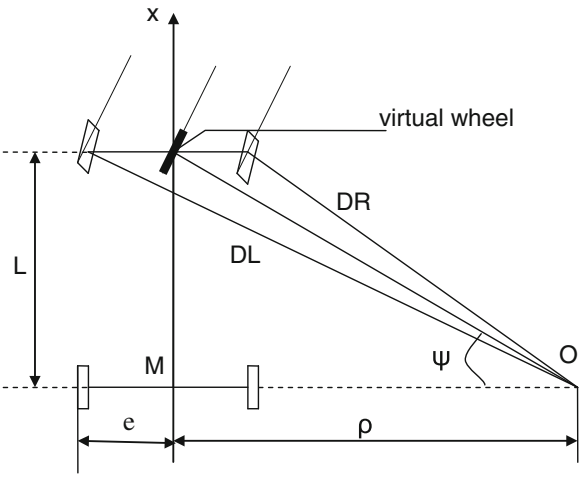

Fig. 51.2 Four-wheel steering model

$$\begin{cases} x_{k+1} = x_k + \Delta * \cos(\theta_k + \omega/2) \\ y_{k+1} = y_k + \Delta * \cos(\theta_k + \omega/2) \\ z_{k+1} = z_k \\ \theta_{k+1} = \theta_k + \omega \end{cases} \tag{51.2}$$

For four-wheel vehicle model [11], as shown in Fig. 51.2. Where, e is a half of the wheel tread, L is wheel base, ψ is the steering angle of virtual front wheel which can instead of steering angle of front wheel approximatively, and, Assuming no vehicles sliding between two sampling points, e and L keep constant.

We can get the following formula by the figure of each variable in the relationship:

$$\tan(\psi) = \frac{L}{\rho} \tag{51.3}$$

$$\begin{cases} \Delta_{RR} = \omega \cdot (\rho + e) \\ \Delta_{RL} = \omega \cdot (\rho - e) \end{cases} \tag{51.4}$$

where, Δ_{RR} is the distance of right rear wheel, Δ_{RL} is the distance of left rear wheel.

Above all, we can get the following equation:

$$\begin{cases} x_{k+1} = x_k + \left(\frac{\Delta_{RR}+\Delta_{RL}}{2}\right) \cdot \cos\left(\theta_k + \frac{\Delta_{RR}-\Delta_{RL}}{4 \cdot e}\right) \\ y_{k+1} = y_k + \left(\frac{\Delta_{RR}+\Delta_{RL}}{2}\right) \cdot \sin\left(\theta_k + \frac{\Delta_{RR}-\Delta_{RL}}{4 \cdot e}\right) \\ z_{k+1} = z_k \\ \theta_{k+1} = \theta_k + \frac{\Delta_{RR}-\Delta_{RL}}{2 \cdot e} \end{cases} \tag{51.5}$$

51.2.2 Constraint Condition

Vehicle kinematic model can provide the vehicle's position and the speed of the driving direction information, but can't provide the speed of the vertical driving direction information. In ideal conditions, under the condition that Vehicle move on the ground and no sideslip [12, 13], the speed is zero in x-axis and z-axis in body coordinate, in fact, it can be express by gaussian white noise [14].

$$\begin{cases} V_{bx} - v_x = 0 \\ V_{bz} - v_z = 0 \end{cases} \tag{51.6}$$

where, V_{bx}, V_{bz} is the velocity components on the direction of x, z in the body coordinate system, v_x, v_z are gaussian white noise with mean zero, variance eσ_x^2 and σ_z^2.

Assume that the vehicle speed is $V_b(t)$ in the forward direction, and transition to the navigation coordinate system, The speed observation kinematics model of aided inertial navigation system can be expressed as follows:

$$V_1 = C_b^n * \begin{bmatrix} v_x \\ V_b(t) \\ v_z \end{bmatrix} \tag{51.7}$$

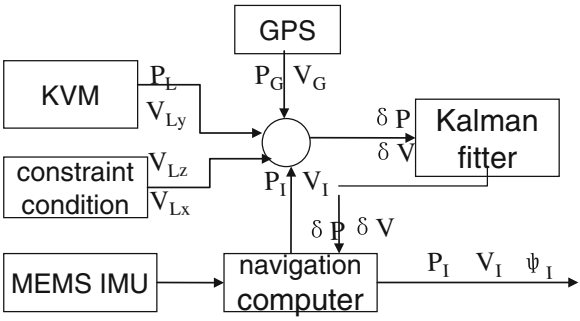

Fig. 51.3 Scheme of integration strategy

51.3 Design of Integrated Navigation Strategy

As shown in Fig. 51.3, GPS and INS correct the error of inertial navigation real-time for by using feedback correction. The mode of the integrated navigation system can be divided into two kinds according to the GPS information is valid or not. The system work in mode one when GPS information is valid. With the method of integrated of INS and GPS, which its state error equation of INS error propagation characteristics s described 9 d. three of position error, velocity error, attitude error are included:

$$X_g = [\varphi_E \quad \varphi_N \quad \varphi_U \quad \delta V_E \quad \delta V_N \quad \delta V_U \quad \delta L \quad \delta\lambda \quad \delta h] \tag{51.8}$$

where, φ_E, φ_N, φ_U are the error equations of attitude angle, ΔV_E, ΔV_N, ΔV_U are the velocity errors in ENU, ΔL, $\Delta\lambda$, Δh are the position errors.

Reference system state equation was:

$$\dot{X}(t) = F(t)X(t) + G(t)W(t) \tag{51.9}$$

where, $F(t)$ was coefficient matrix compared with the nine basic navigation errors. $G(t)$ was error coefficient matrix, $W(t)$ was dynamic noise matrix of the system.

Take the position and velocity of the inertial navigation system and output information and GPS location, speed observation output difference as the observed quantity.

$$Z(t) = \begin{bmatrix} P_N - P_G \\ V_N - V_G \end{bmatrix} \tag{51.10}$$

where, P_N, V_N are the position and velocity from INS. P_G, V_G are the position and velocity from model. Measurement equation can be written as:

$$Z(t) = H(t)X(t) + V(t) \tag{51.11}$$

$$H(t) = \begin{bmatrix} & R_M & 0 & 0 & & & \\ 0_{3\times3} & 0 & R_N \cos L & 0 & & 0_{3\times3} & \\ & 0 & 0 & 1 & & & \\ & & & & 1 & 0 & 0 \\ 0_{3\times3} & & 0_{3\times3} & & 0 & 1 & 0 \\ & & & & 0 & 0 & 1 \end{bmatrix} \tag{51.12}$$

where, R_M, R_N are the radius of curvature in meridian and curvature in prime vertical, L is latitude. Observation noise $V(t)$ is random white noise, which related to the simulation precision of the device. Measurement noise covariance matrix is $R(t) = diag(R_p(t), R_v(t))$, among them, R_p and R_v are the noise variance matrix of position and velocity observation.

The system working in mode 2 when GPS information is lost. Taking consider of constraint condition of vehicles using kinematics model aided INS to restrain navigation error. According to the vehicle kinematic relations recursive movement of the vehicle state information, the information is not affected by the interference of external environment, and more reliable. Therefore, the use of the information and the position and velocity information from INS output difference as observed quantity, can estimate error of inertial navigation system, effectively. Thus to calibration of inertial navigation, restrain the error drift of inertial navigation, improve vehicle navigation precision and reliability, can be used as a GPS/INS integrated navigation system of backup effectively.

The position and forward velocity are described by vehicle kinematics model. The velocity of the other two directions can be get from the constraint conditions which can make difference with the position and velocity from navigation computer's output, as observation equation. The system' observation should be change correspondingly:

$$Z(t) = \begin{bmatrix} P_N - P_L \\ V_N - V_L \end{bmatrix} \tag{51.13}$$

Adjust the corresponding observation noise $V(t)$ and measurement noise covariance matrix $R(t) = diag(R_p(t), R_v(t))$, get the corresponding valuation to correction navigation computer, which can restrain the error of inertial navigation from divergence.

51.4 Simulation and Analysis

In order to study rationality and feasibility of the scheme, we carry on the simulation. The simulation path are based on a closed area real road. The path view of Fig. 51.4 on the Google Earth. Driving direction be shown in Fig. 51.4 A starting point, B for the end. The simulation condition be setted to: vehicles by 20 m/s

Fig. 51.4 The vehicle driving route in Google Earth

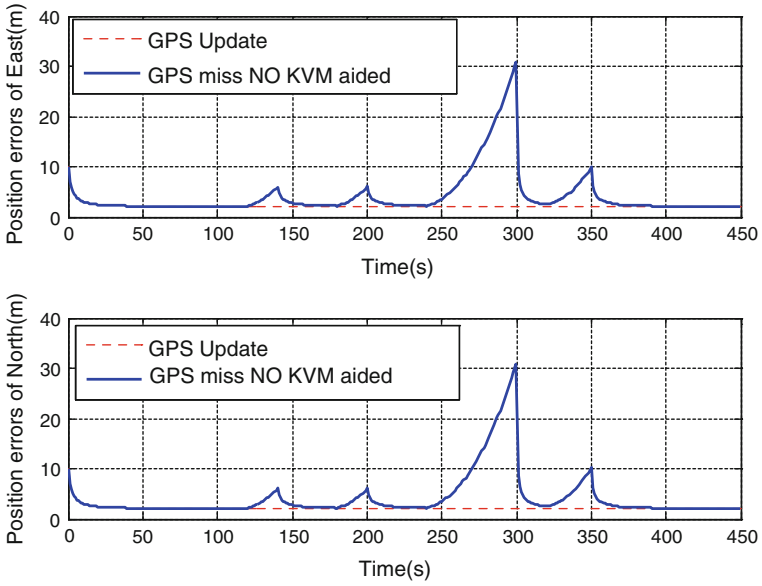

Fig. 51.5 Position errors from no KVM aided and GPS update

uniform motion, the simulation time is 450 s. Assuming that acceleration measurement noise is white noise random measurement, with the standard deviation of 1×10^{-3} g. Gyroscope measurement noise is the random constant drift and random white noise, the standard deviation are (50°)/h. GPS simulation error on the east, north, the up three directions respectively by 10, 10, 20 m, velocity simulation error is 0.5, 0.5, 0.5 m/s. Differential odometer output error was white noise with standard deviation 0.1 m/s, the constant error is 0.1 m/s, yawing angle standard deviation is 0.05 rad/s. The simulation step is 0.02 s.

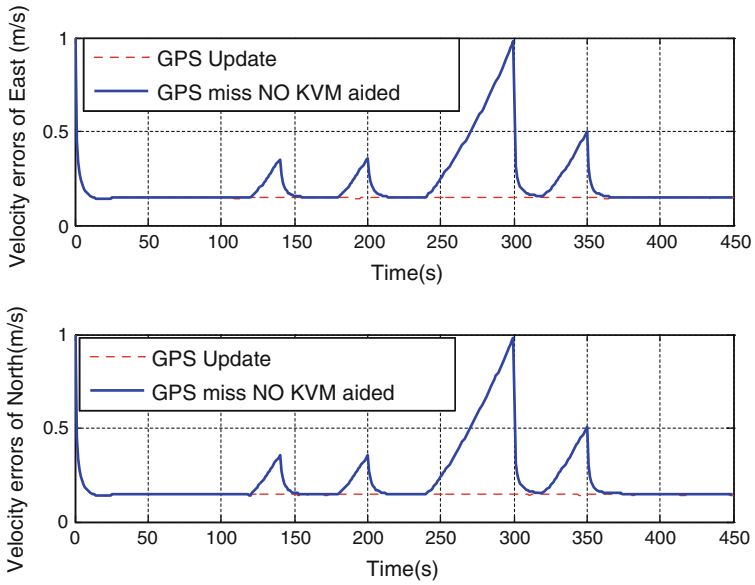

Fig. 51.6 Velocity errors from no KVM aided and GPS update

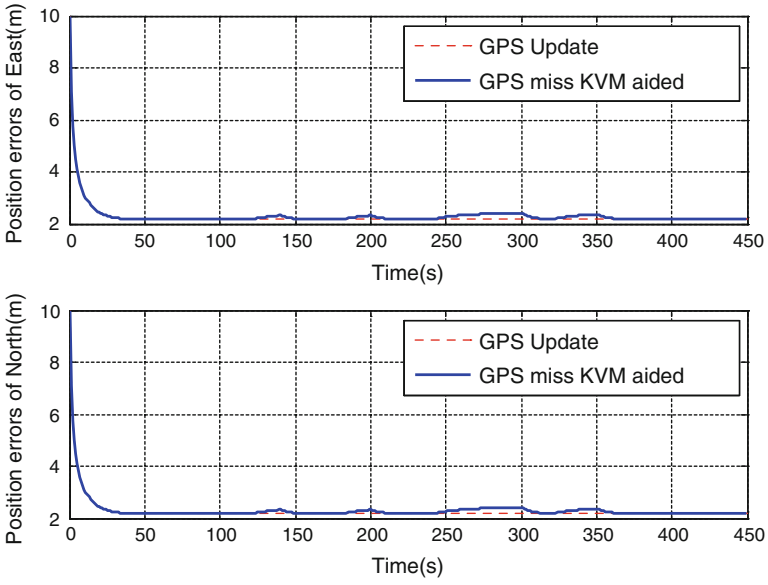

Fig. 51.7 Position errors from KVM and GPS update

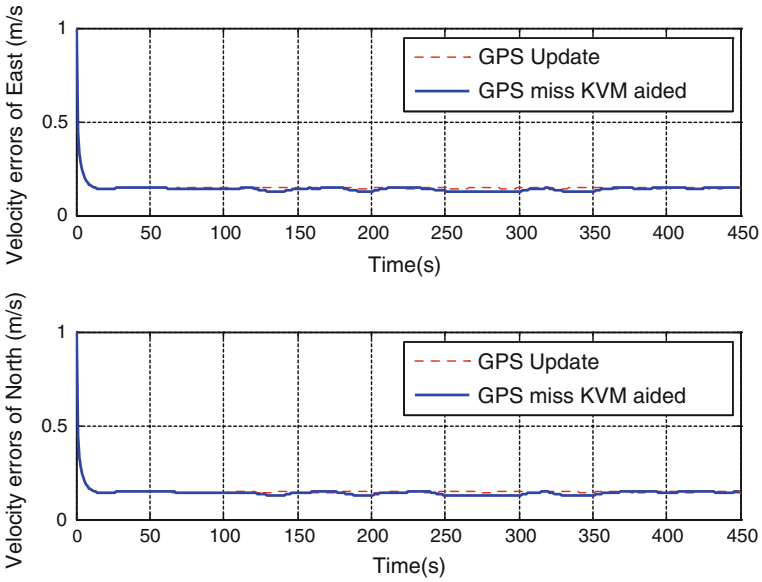

Fig. 51.8 Velocity errors from KVM and GPS update

Assume that the GPS information intermittent loss of lock. Disable GPS measurement information 4 times, 180 and 120, 240 and 320 s respectively, the duration is 20, 20, 60, 30 s respectively. Navigation system works on mode 1 to mode 2 when GPS is not valid.

Figures 51.5, 51.6 was the position, velocity error comparison in the east, north with GPS is valid or not. In Figs. 51.5, 51.6, the full line is the position and velocity errors when GPS is not valid with no aid. The dot dash line is the position and velocity errors when GPS is valid. Obviously, the GPS/INS integrated navigation system is higher positioning accuracy when GPS is valid with 2.2 m position errors 0.15 m/s velocity errors in East and North. The precision of integrated navigation system is mainly decided by GPS precision, integrated navigation error spread quickly when GPS is not valid with position error reached 30 m, velocity error reached 1.0 m/s and can't provide positioning effectively.

Figures 51.7, 51.8 gives the position, velocity errors curve get from kinematic model aided when GPS is not valid in the east and north. In Figs. 51.7, 51.8, the full line is the position, velocity errors get from kinematic model when GPS is not valid while the dot dash line is the errors when GPS is valid. Obviously, the kinematics aided method can restrain the error of the navigation system drift when GPS is not valid, with position error 2.5 m and velocity error 0.2 m/s. Accuracy is a bit poor than GPS and also can meet the demand of vehicle positioning. The kinematics model aided method can reduce the navigation error when GPS failure effectively, ensure the continuity of navigation information.

51.5 Conclusion

The paper aim at the problem that vehicle integrated navigation system positioning is not reliable when GPS signal block intermittently, the vehicle kinematics model and constraint condition were brought in, and design the corresponding integrated navigation strategy. And a simulation was carried out. The simulation results show that this method can restrain inertial navigation error when GPS failure effectively, and get higher positioning accuracy. This method can be used as a backup of GPS/INS integrated navigation system when GPS unlock, to ensure the navigation precision and navigation information continuous.

References

1. Han S, Wang J (2010) Land vehicle navigation with the integration of GPS and reduced INS: performance improvement with velocity aiding. J Navig 63(1):153–166
2. Zhang J-Z, Zhang H-T (2009) Vehicle dynamic stability control based on GPS. In: 2009 international conference on information engineering and computer science, ICIECS 2009, Wuhan, China, pp 1–4
3. Bryson M, Sukkarieh S ()2004 Vehicle model aided inertial navigation for a UAV using low-cost sensors. In: Proceedings of the Australasian conference on robotics and automation, Canberra, Australia
4. Li B, Li Y, Liu Y, Li X (2012) Optimized arithmetic of INS/GPS multi-sensor integrated navigation system used in vehicle. Piezoelectrics Acoustooptics 34(1):37–41
5. Qin H, Cong L, Sun X (2012) Accuracy improvement of GPS/MEMS-INS integrated navigation system during GPS signal outage for land vehicle navigation. J Syst Eng Electron 23(2):256–264
6. Dissanayake G, Sukkarieh S, Nebot E et al (2001) The aiding of a low-cost strapdown inertial measurement unit using vehicle model constraints for land vehicle applications. IEEE Trans Robot Autom 17(5):731–747
7. Yuan G, Liang H, He K, Wang W (2010) Design of integrated navigation algorithm based on low-cost vehicular navigator. J Chin Inertial Technol 18(6):69–74
8. Fu Q, Qin Y, Li S, Wang H (2012) Inertial navigation algorithm aided by motion constraints of vehicle. J Chin Inertial Technol 20(6):640–643
9. Klein I, Filin S, Toledo T (2011) Vehicle constraints enhancement for supporting INS navigation in urban environments. Navigation 58(1):7–15
10. Martinez JL, Mandow A, Morales J, Garcia-Cerezo A, Pedraza S (2004) Kinematic modeling of tracked vehicles by experimental identification. In: Proceedings of 2004 IEEORSJ international conference on intelligent robots and systems, Sendal, Japan
11. Hernandez JI, Kuo C-Y (2003) Steering control of automated vehicles using absolute positioning GPS and magnetic markers. IEEE Trans Veh Technol 52(1):150–160
12. Klein I, Filin S, Toledo T (2010) Pseudo-measurements as aiding to INS during GPS outages. Navigation 57(1):25–34
13. Jo K, Chu K, Lee K, Sunwoo M (2010) Integration of multiple vehicle models with an IMM filter for vehicle localization. In: 2010 IEEE intelligent vehicles symposium (IV), San Diego, CA, USA, pp 746–751
14. Yang C, Jiang J, Huang C (2009) J Bomb Arrow Guidance 29(6):270–273

Chapter 52
Research on A-GPS Rapid Positioning Algorithm Based on Doppler Positioning

Zhiyong Huang, Dongqing Zhao, Yijun Tian and Hao Wu

Abstract The time to first fix (TTFF) of conventional GPS receiver need one minute or more in the case of autonomous cold start, when in weak signal environments like indoors or urban canyons, even tens of minutes are difficult to achieve the TTFF. Assisted Global Positioning System provided ephemeris, a priori time and a priori position for a A-GPS receiver through the cellular network base station to solve the weak signal positioning problem, the process of observation satellite and decoding ephemeris move to A-GPS reference station and a location server to complete. From initial acquisition to frame synchronization need to go through its correlation lock, phase lock, the bit synchronization process, When the signal is very weak that cannot achieve frame synchronization and demodulation satellite TOW, the conventional algorithm cannot achieve positioning solution. The A-GPS fast positioning algorithm combine the Doppler positioning and reconstructing full pseudoranges method presented in this paper, reconstructing full pseudoranges method elimination the common bias implied in integer millisecond pseudoranges to avoiding the integer millisecond ambiguity problem in reconstructing launch time method due to common bias and measurement error, Doppler positioning solution guarantees to provided a initial position and time error less than 0.5 light-ms, so the A-GPS rapid positioning resolved in the coarse time and rough location condition.

Keywords TTFF · A-GPS · Frame synchronization · Doppler positioning · Reconstructing full pseudoranges

Z. Huang (✉) · D. Zhao · Y. Tian · H. Wu
Institute of Mapping and Surveying, Information Engineering University, Zhengzhou, China
e-mail: lanruo_hzy@sina.com

J. Sun et al. (eds.), *China Satellite Navigation Conference (CSNC) 2014 Proceedings: Volume III*, Lecture Notes in Electrical Engineering 305,
DOI: 10.1007/978-3-642-54740-9_52,

52.1 Introduction

Conventional GPS receiver autonomous cold start Time To First Fix (TTFF) takes about 1 min, when in urban canyons (urban canyons) and other weak signal conditions cannot achieve the location [1]. Assisted Global Positioning System provided ephemeris, a priori time and a priori position for a A-GPS receiver through the cellular network base station to solve the weak signal positioning problem [2]. Since A-GPS satellite receiver in advance to know the PRN you want to search, Doppler frequency shift and code-delay, the three-dimensional search space is identified, the process of acquisition and tracking time-consuming is decreased, time to first fix takes only a few seconds or so. Further, since the A-GPS receiver is designed in advance to know which frequency to be searched, allowing configuration of the receiver becomes longer accumulate, thereby increasing the specific energy of the reception in each of the frequency [1]. This increases the sensitivity of the A-GPS receiver, and allow it to capture weaker signals.

Time To First Fix is point to the time from the receiver start to obtain the first GPS positioning results, it includes the receiver capture, track, bit synchronization and frame synchronization and decoding navigation message as well as the positioning operation and a series of process to multiple satellite signal. When in weak signal environments like indoors or urban canyons, since the navigation data demodulation bit error rate (BER) [3] is too high, the receiver can only obtain the value of the pseudo code-phase and the Doppler frequency shift by the process of acquisition, and cannot accomplish bit synchronization, the frame synchronization and demodulating the navigation message [4]. Since the receiver can accomplish only part of the pseudoranges measurement, the signal transmission time can recover only part, and the specific location of the satellite cannot be obtained when transmitting a signal, the problem is also known as “coarse-time navigation”.

The transmission time of the transmitted signal changes between 64 and 89 ms since GPS satellites at different distances from the ground, in coarse-time problem that we only know sub-millisecond pseudoranges, and how to reconstructing all of the pseudoranges measurements to achieve location solution. To solve this problem, Syrjarinne first proposed the “recovery time” [5] the notion that the use of auxiliary means to restore the complete signal transmission time, however, when the signal is weak, due to the cross-correlation peak leak detection alarm rate [6] is too high, causing the method is difficult to achieve; Sirola improved enhanced triangulation method, a new function using the lambda-fraction [7, 8] to eliminate the satellite signal transmission time ambiguity method, however, when the signal transmission time to eliminate ambiguities, the receiver clock offset equivalent distance of most of them have been eliminated; Roland Kaniuth propose a Snapshot algorithm, but there is an integer millisecond ambiguity problem of the algorithm [1]; van Diggelen presents a full reconstruction of the pseudoranges [9] to solve the problem of coarse-time navigation positioning algorithms to solve the problem of integer millisecond flipped, but the algorithm requires a priori position and time error is less than 0.5 light-milliseconds.

A A-GPS fast positioning algorithm based on the Doppler positioning, using only the Doppler frequency shift measurement obtained by the acquisition process and pseudo code-phase, positioning results can be obtained quickly, greatly reducing the TTFF [10]. Pseudoranges reconstruction algorithms achieve approximate location, priori time and assisted ephemeris via A-GPS server, can quickly achieve stable ocation results. However, when the receiver is in roaming beyond mode and cannot get rough coordinates. The results accuracy based of Doppler shift measurements positioning algorithm is limited, but it can provide the pseudoranges reconstruction algorithm priori coordinates and time, and the total error is generally less than 150 km. When the receiver is in motion mode, Doppler positioning results deserve to large errors, then you can set constraints conditions by iterative calculation, ensure to achieve proper reconstruction of the whole pseudoranges values.

52.2 The Basic Principle of the Algorithm

52.2.1 Reconstructing Pseudoranges Algorithm

There isn't fine time assistance (fine time assisted means accuracy is better than 10 ms, GSM, UMTS, WCDMA time accuracy 1–2 s, CDMA microsecond time accuracy) for assisted GPS receiver under most circumstances, then, you can decode TOW to get it, but it takes a few seconds. And in the case of weak signals environments, for a long time will not decode ephemeris, unable to obtain TOW. The relative motion of the satellite caused a rough time navigation of issue, you can calculate the relative speed of each satellite, using the navigation equations to solve the user's location X_u (x_u, y_u, z_u), the receiver public bias b and coarse error tc. That is to say, time can be calculated to obtain, without relying on the decode to get it, which would also reduces the time to first fix.

The 4 steps of navigation are as follows, tc is coarse-time error.

1. Estimate the satellite state through the assisted ephemeris and time information.
2. By the receiver approximate position and satellite coordinates to get the pseudoranges forecasts $\hat{\rho}$.
3. By the pseudo code-phase values $z^{k,chip}$ obtained by measuring to get the actual reconstruction of the full pseudoranges.
4. According to the deviation between predicted and measured pseudoranges, and to adjust the transcendental state, denoted by $\delta\rho = \rho - \hat{\rho}$. Therefore, the update vector $\delta x = \left[\delta_x, \delta_y, \delta_z, \delta_b, \delta_{\mathrm{tc}}\right]^T$ is a vector update a priori x, y, z, b, tc, while the $\hat{\rho}$ is impacted by δ_{tc}, and the relationship between $\hat{\rho}$ and δ_{tc} is:

$$\hat{\rho}_{(\hat{t}_{tx})} - \hat{\rho}_{(t_{tx})} = \hat{\rho}_{(\hat{t}_{tx})} - \hat{\rho}_{(\hat{t}_{tx}+\delta_{tc})} = -v \cdot \delta_{tc} \tag{52.1}$$

Among the formula, t_{tx} Represents the actual time of transmission $\hat{t}_{tx}$ Represents the rough time estimate of t_{tx} . $v = \left(\vec{e} \cdot \vec{v} - \dot{\delta}_t\right)$ is the pseudoranges rate. For each satellite, the relationship between $\delta\rho^{(k)}$ and x is:

$$\delta\rho^{(k)} = \rho^{(k)} - \hat{\rho}^{(k)} = -e \cdot \delta x_{xyz} + \delta_b + v^{(k)} \cdot \delta_{tc} + \varepsilon^{(k)} \tag{52.2}$$

For k satellites, Matrix equation can be obtained:

$$\delta\rho = H\delta x + \varepsilon \tag{52.3}$$

Therefore, As long as there are five or more satellites, you can get five-state closure solution of the coarse-time assisted. When constructing a priori residuals, as sub-millisecond pseudoranges measurements (i.e., pseudo code-phase measurements) $z^{k,chip}$ exist an unknown public bias b (the main difference is the receiver clock) And measurement error ε, True geometric distance's expectations from the receiver to the satellite is r, pseudoranges $\hat{\rho}^{(k)}$ exist a priori position and time error r_d, When combined with unknown of the public biases and expectation pseudoranges $\hat{\rho}^{(k)}$ close to 1 ms, modulo easily lead deflection of 1 ms. Let z values for the sub-millisecond pseudoranges true value:

$$z^{k,chip} = z + b + \varepsilon \tag{52.4}$$

$$\hat{\rho}^{(k)} = r + r_d \tag{52.5}$$

$$\delta\rho^{(k)} = (z^{k,chip} - \hat{\rho}^{(k)})\,[1\text{ ms}] = (z - r + b - r_d + \varepsilon)\,[1\text{ ms}] \tag{52.6}$$

The above algorithm exists for the integer millisecond ambiguity problem, you can use the selected reference star to contain the same approach error term to resolve it, A superscript (0) to indicate the reference satellite and with (k) represents other satellites. Calculates of all satellites to the expectation pseudoranges and assign an integer value $N^{(0)}$ to the reference satellite based on reference satellite pseudorange value, so the full pseudorange is $(N^{(0)} + z^{(0)})$ ms. Geometric distance $r_d^{(0)}$ Contains errors from the a priori position and time errors, the relationship between the reconstruct of full pseudoranges and geometric distance is:

$$N^{(0)} + z^{(k,chip)(0)} = r^{(0)} + b + \varepsilon^{(0)} = \hat{r}^{(0)} - r_d^{(0)} + b + \varepsilon^{(0)} \tag{52.7}$$

If assign a integer values for all measurement value, so that they contain the same common bias, to k satellites we get the following equation.

$$N^{(k)} + z^{(k)} = r^{(k)} + b + \varepsilon^{(k)} = \hat{r}^{(k)} - r_d^{(k)} + b + \varepsilon^{(k)} \tag{52.8}$$

Because they contain the same common bias, make two equations subtraction, we get:

$$N^{(k)} = N^{(0)} + z^{(0)} - z^{(k)} + (\hat{r}^{(k)} - r_d^{(k)} + b + \varepsilon^{(k)}) - (\hat{r}^{(0)} - r_d^{(0)} + b + \varepsilon^{(0)}) \tag{52.9}$$

$$(N^{(k)} + z^{(k)}) - (N^{(0)} + z^{(0)}) = (\hat{r}^{(k)} - r_d^{(k)} + b + \varepsilon^{(k)}) - (\hat{r}^{(0)} - r_d^{(0)} + b + \varepsilon^{(0)}) \tag{52.10}$$

If $(-r_d^{(k)} + \varepsilon^{(k)} + r_d^{(0)} - \varepsilon^{(0)}) < 0.5$ light-ms, You can get the right $N^{(k)}$.

$$N^{(k)} = \text{round}\left(N^{(0)} + z^{(0)} - z^{(k)} + \hat{r}^{(k)} - \hat{r}^{(0)}\right) \tag{52.11}$$

52.2.2 Doppler Positioning Algorithm

As already deduced from the pseudoranges linear navigation Eq. (52.3), on both sides to the time differential, derive:

$$\frac{\partial \delta\rho}{\partial t} = \frac{\partial(\rho - \hat{\rho})}{\partial t} = \frac{\partial(H\delta x)}{\partial t} + \varepsilon' \tag{52.12}$$

$$\frac{\partial \rho}{\partial t} - \frac{\partial \hat{\rho}}{\partial t} = H\frac{\partial(\delta x)}{\partial t} + \frac{\partial(H)}{\partial t}\delta x + \varepsilon' \tag{52.13}$$

assume: $y = \frac{\partial \rho}{\partial t}$ is Doppler measurement vector; $\hat{y} = \frac{\partial \hat{\rho}}{\partial t}$ is predicted Doppler measurement vector, calculated by assisted ephemeris or almanac. Therefore, $\partial y = y - \hat{y}$. The right of polynomial equations can be calculated to obtain. The first polynomial can be obtained from the receiver speed of classical linear equations:

$$H\frac{\partial(\delta x)}{\partial t} = H\frac{\partial}{\partial t}\begin{bmatrix} \delta_x \\ \delta_y \\ \delta_z \\ \delta_b \\ \delta_{tc} \end{bmatrix} = H\begin{bmatrix} \delta_{x'} \\ \delta_{y'} \\ \delta_{z'} \\ \delta_{b'} \\ \delta_{tc'} \end{bmatrix} \tag{52.14}$$

In the above formula, $\delta_{x'}$, $\delta_{y'}$, $\delta_{z'}$ is a priori status update status to receiving end speed. $\delta_{b'}$ is a status update of priori frequency offset, $\delta_{tc'}$ is a priori status update of coarse-time error. The relationship between the location update and the Doppler measurements value is:

$$\frac{\partial H}{\partial t}\delta x = \begin{bmatrix} -\partial e^{(1)}/\partial t & 0 & \partial v^{(1)}/\partial t \\ \vdots & \vdots & \vdots \\ -\partial e^{(k)}/\partial t & 0 & \partial v^{(k)}/\partial t \end{bmatrix} \begin{bmatrix} \delta_x \\ \delta_y \\ \delta_z \\ \delta_b \\ \delta_{tc} \end{bmatrix} = \begin{bmatrix} -\partial e^{(1)}/\partial t & \partial v^{(1)}/\partial t \\ \vdots & \vdots \\ -\partial e^{(k)}/\partial t & \partial v^{(k)}/\partial t \end{bmatrix} \begin{bmatrix} \delta_x \\ \delta_y \\ \delta_z \\ \delta_{tc} \end{bmatrix} \tag{52.15}$$

Three-dimensional vector $[\partial e^{(k)}/\partial t]$ and $[\partial v^{(k)}/\partial t]$ are as follows:

$$\frac{\partial e^{(k)}}{\partial t} = \frac{\partial}{\partial t}\left(\frac{X_s^{(k)} - X_u}{\left|X_s^{(k)} - X_u\right|}\right) \tag{52.16}$$

$$\frac{\partial v^{(k)}}{\partial t} = \frac{\partial}{\partial t}\left(e^{(k)} \cdot v^{(k)}\right) = \partial e^{(k)}/\partial t \cdot v^{(k)} + e^{(k)} \cdot a^{(k)} \tag{52.17}$$

In the above formula, $X_s^{(k)}$ is the position of the k satellite, X_u is priori position information of receiver. Omit the superscript (k), and r represents the range of the receiver and the satellite: $r = |X_s - X_u|$.

$$\frac{\partial e}{\partial t} = \frac{\partial}{\partial t}\left(\frac{X_s - X_u}{r}\right) = \left(\frac{\partial(x)}{\partial t} - e \cdot (e \cdot v)\right)\frac{1}{r} \tag{52.18}$$

Take the formulas (52.15) (52.16) and (52.18) into Eq. (52.13), we get:

$$\partial y = \begin{bmatrix} -e^{(1)} & 1 & v^{(1)} \\ \vdots & \vdots & \vdots \\ -e^{(K)} & 1 & v^{(K)} \end{bmatrix} \begin{bmatrix} \delta_{x'} \\ \delta_{y'} \\ \delta_{z'} \\ \delta_{b'} \\ \delta_{tc'} \end{bmatrix} + \begin{bmatrix} -\partial e^{(1)}/\partial t & \partial v^{(1)}/\partial t \\ \vdots & \vdots \\ -\partial e^{(k)}/\partial t & \partial v^{(k)}/\partial t \end{bmatrix} \begin{bmatrix} \delta_x \\ \delta_y \\ \delta_z \\ \delta_{tc} \end{bmatrix} + \varepsilon' \tag{52.19}$$

The above formula is the equation contains 9 states (3 receiver position parameters, three speed parameters, one frequency offset parameters, the coarse-time error parameters, the change rate of coarse-time error parameters) on the instantaneous Doppler measurements of linear equations. If the receiver is stationary, the change rate of coarse-time error is ignored, so reducing the amount of the unknown on formula (52.19) to five, and therefore the position of the receiver can be obtain by five satellites' Doppler measurements.

$$\partial y = \begin{bmatrix} -\partial e^{(1)}/\partial t & 1 & -\partial v^{(1)}/\partial t \\ \vdots & \vdots & \vdots \\ -\partial e^{(k)}/\partial t & 1 & -\partial v^{(k)}/\partial t \end{bmatrix} \begin{bmatrix} \delta_x \\ \delta_y \\ \delta_z \\ \delta_{b'} \\ \delta_{tc} \end{bmatrix} + \varepsilon' = H_D \begin{bmatrix} \delta_x \\ \delta_y \\ \delta_z \\ \delta_{b'} \\ \delta_{tc} \end{bmatrix} + \varepsilon' \tag{52.20}$$

The least squares equation results is:

$$\delta\hat{x} = \left(H_D^T H_D\right)^{-1} H_D^T \delta y \tag{52.21}$$

When the positioning error is less than 100 km, the time error is less than 1 min, which can success provided rough coordinates and time to the pseudoranges reconstruction algorithm. when under the special conditions and cannot met the calculate, execute the iterative calculation by setting constraints can be quickly fixed correctly integer millisecond pseudoranges ambiguity.

52.2.3 The Constraints Based on Doppler Positioning Algorithm

From the above derivation shows that, when the Doppler positioning provides total error of less than 0.5 light-millisecond, the pseudoranges reconstruction algorithm can get the correct positioning results. When not satisfied, you can set the following two constraints.

52.2.3.1 Coarse-Time Error Constraints

GPS satellite position and velocity is actually a time-dependent function, once the navigation data decoding and time of week (TOW) decoding is not completed, it cannot obtain an accurate signal transmission time. When the cellular network time assistance is exist, it's generally able to meet the positioning requirements. While in roaming beyond mode, coarse-time error is larger, it may lead to a larger satellite position and velocity errors. Then by the constraints, calculate a Doppler residuals every 1 s epoch, which making the Doppler residual value is the minimum is the alternatives time to seek.

$$MIN[\partial y(t, X_u)] = |y+| \frac{v_s^{(t)}}{\lambda} \cdot \left(\frac{X_s^{(t)} - X_u}{\left| X_s^{(t)} - X_u \right|} \right) \tag{52.22}$$

In the above formula, X_r is the distance between the user's location to the Earth's center of mass, R is the earth radius, the user's location X_u is only requires the difference absolute value between X_r and R does not exceed 200 km, any rough coordinates can meet this requirement on Earth, that:

$$6{,}170 \text{ km} \leq |X_r - R| \leq 6{,}570 \text{ km} \tag{52.23}$$

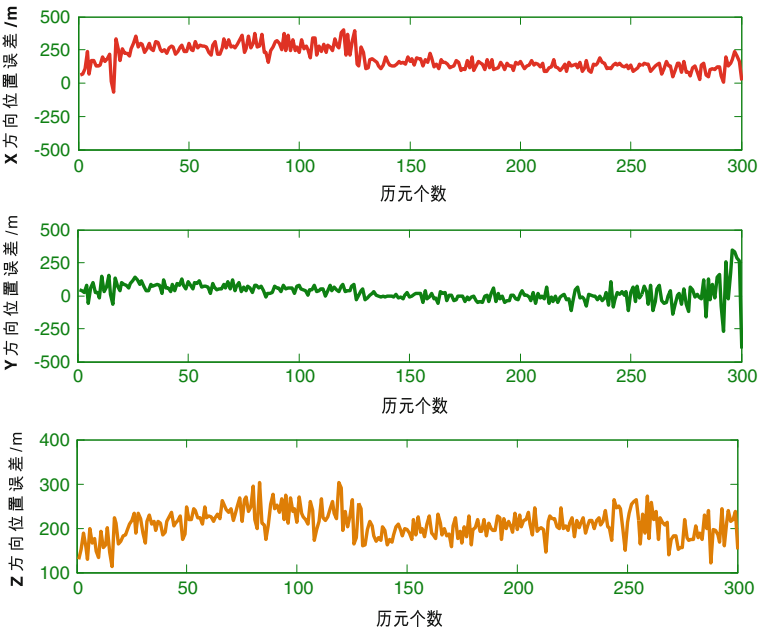

Fig. 52.1 *Curve* Doppler positioning error in three directions

52.2.3.2 Integer Millisecond Ambiguity Constraints

When the receiver moves at a higher speed, the coordinate error based on a Doppler positioning may be greater than 150 km, the integer millisecond ambiguity problem now exists. You can solve this problem by ambiguity search method, since 1 ms pseudorange value equivalent 150 km, ambiguity search space is generally small, typically several times will be able to search for the correct pseudorange values each satellite.

If search three times each satellite, for the eight visible satellites, the total number of searches is 3^8 times. So the integer milliseconds N is a alternative value which derived minimum of rough coordinate corrections. At this time we ask coarse-time error does not exceed 1 s, use common clock generally meet the accuracy requirements.

$$MIN[\delta x(N^{(k)})] = \sqrt{\delta_x^2 + \delta_y^2 + \delta_z^2} \tag{52.24}$$

.

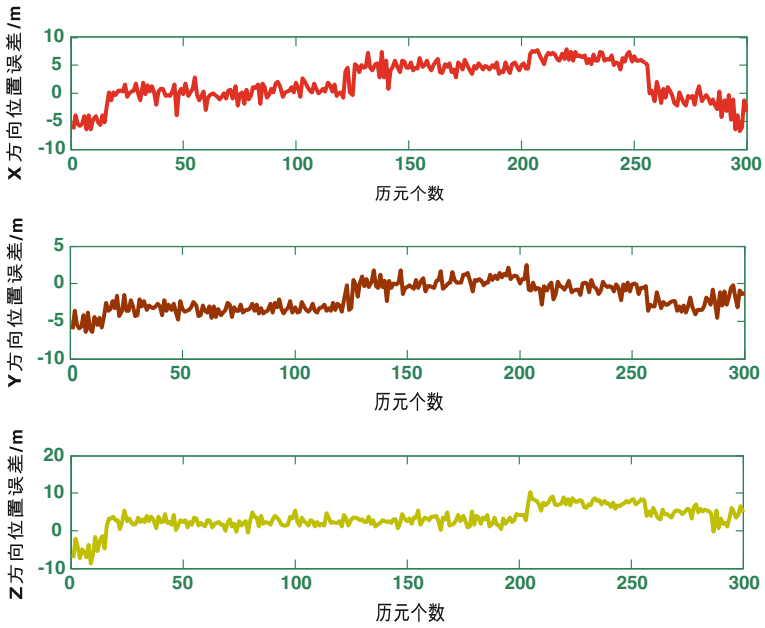

Fig. 52.2 *Curve* Reconstructing pseudoranges position error in three directions of A-GPS positioning algorithm

52.2.4 The Data Operation Process

From the above we can see that the Doppler-based A-GPS rapid positioning algorithm solver positioning process are as follows [11]:

Step 1 The equipment obtained assisted ephemeris from the reference receiver or A-GPS location server [using extended ephemeris in roaming beyond mode Ephemeris Extension (EE)], and the orientation of the currently visible satellites, elevation and other information is known;

Step 2 A-GPS receiver capture the satellite quickly by assisted ephemeris, acquisition code-phase and Doppler shift measurements;

Step 3 Using Doppler positioning to get a coarse position, and provide a rough coordinate and time for the pseudoranges reconstruction algorithm;

Step 4 Using the pseudoranges reconstruction algorithm to get the full value of the pseudoranges observation, and with prediction rough geometric distance subtract obtain pseudorange residuals, get iterative solution of a five state equations;

Table 52.1 3D RMS of Doppler and reconstructing pseudoranges positioning algorithm

Three-dimensional position RMS	X/m	Y/m	Z/m
Doppler positioning	202.3214	75.4579	210.9335
Reconstruct pseudorange positioning	4.0018	2.6244	4.4273

Step 5 Construct a posteriori residuals statistics about location, when the calculated full pseudoranges is correct, posteriori residuals is very small, whereas is very large. Re-do positioning and integer milliseconds ambiguity search by the above two constraints, if you still cannot get the correct solution, then need to adjust the priori rough coordinates and time, return to Step 3 until the correct solution to solve.

52.3 Analysis of Experimental Data

In order to verify the effectiveness of the algorithm, select IGS reference stations in Germany PTBB station [Brunswick, the Cartesian coordinates of the real space (3844059.9135, 709661.3700, 5023129.5945)] Fixed observations 300 epochs May 27, 2013 were simulation calculation. During the simulation calculation, using real pseudorange observation to get the millisecond pseudorange values, using the real end Doppler observations instead of obtained Doppler frequency shift in the process of acquisition.

$$z^{k,chip} = (\rho^{(k)}/c)\ [1\ ms] \tag{52.25}$$

First, using the Doppler to calculation the position, let coarse-time error to be 1 s, and Arbitrary given an rough coordinates of the earth, calculations show that after several iterations can be effectively converge. As the initial approximate coordinates of pseudoranges reconstruction algorithm, get the following Three-dimensional position RMS TAB of A-GPS pseudoranges reconstruction positioning and Doppler positioning algorithm. In addition, the 300 epoch of Doppler positioning and pseudoranges reconstruction positioning algorithm of the three directions location error graph are drawn as Figs. 52.1, 52.2 (Table 52.1).

52.4 Conclusions

The satellite positioning technology in weak signal environment has become the focus of research international navigation industry technology, which combined GPS positioning technology and wireless communications platform to develop A - GPS positioning system is considered to be one of the most application

prospect of research direction [2]. Assisted GPS can greatly extend the application range of conventional GPS, and can greatly shorten the Time To First Fix (TTFF). In this paper, based on the Doppler positioning of A-GPS rapid positioning algorithm can be further applied to traditional GPS cannot be in A weak signal environment. The algorithm only needs to be done on GPS signal pseudo code-phase and Doppler frequency shift measurement, without complete synchronization and frame synchronization and demodulation navigation message. Paper presents a Doppler positioning and calculation process of pseudoranges reconstruction algorithm, was deduced A-GPS rapid positioning algorithm based on Doppler positioning of constraint conditions, and the feasibility of the algorithm was validated by the simulation data. Validation show that the Doppler positioning algorithm positioning accuracy is about 200 m, with no need for initial coordinate, Able to provide reliable initial value for pseudoranges reconstruction algorithm. The pseudoranges reconstruction algorithm positioning accuracy is Better than 10 m, closer to traditional GPS localization algorithm.

As the "BeiDou second generation" services in the Asia Pacific region, Independent research on assisted BeiDou satellite navigation system is presented to (A-BDS) more pressing needs, in this paper, the proposed algorithm can be effectively applied to the assisted BeiDou satellite navigation system.

References

1. Van Diggelen F (2013) A-GPS: assisted GPS, GNSS, and SBAS (辅助GPS原理与应用. 孟维晓, 马永奎, 高玉龙, 译. 2013:54–59/65–68)
2. 宋成. 辅助型GPS定位系统关键技术研究. 国防科学技术大学, 2009:135–138
3. 谢钢. GPS原理与接收机设计 2009:266–270
4. 米斯拉, 恩格. Global positioning system signals, measurements, and performance. 全球定位系统-信号、测量与性能[M]. 罗鸣, 译. 2008:15-16/36-37
5. Syrjarinne J (2001) Studies of modern techniques for personal positioning. Ph.D. dissertation, Tampere University of Technology, Tampere
6. Syrjarinne J (2000) Possibilities for GPS time recovery with GSM network assistance. In: Proceedings of ION GPS, 2000
7. Sirola N (2001) A method for GPS positioning without current navigation data. Master of Science dissertation, Tampere University of Technology, Tampere
8. Akopian D, Syrjarinne J (2002) A network aided iterated LS method for GPS positioning and time recovery without navigation message decoding. In: PLANS 2002, Palm Springs, CA, pp 77–84
9. van Diggelen F (2011) Method and apparatus for computing position using instantaneous Doppler measurements from satellite. U.S. patent 7987048B2
10. Chen H-W et al (2013) A new coarse-time GPS positioning algorithm using combined Doppler and code-phase measurements. GPS Solutions 10(22):5–7
11. 陈陌寒,巴晓辉,王云, 等.辅助式GPS接收机的快速定位算法研究[J].科学技术与工程, 2011, 11(10):2220–2224

Chapter 53
A Method of Spread Spectrum Positioning Signal Generation Based on Storage-Broadcast for Base Station Positioning System

Zhuang Yuan, Zhongliang Deng, Yuezhou Hu, Le Yang, Kun Zhai and Qian An

Abstract With the development of the world, Location based service (LBS) is becoming more and more important. Relative to widely used and accordingly mature GNSS technology, Pseudolite Positioning System can offer seamless outdoor and indoor positioning. However, the construction/maintenance cost of pseudolite is high and restricts its application. At present most of pseudo satellite base station use spread spectrum navigation and positioning signal system like GNSS. It usually adopts the direct sequence spread spectrum signal transmitter, whose architecture includes information modulation, spread spectrum modulation and frequency modulation to realize the generation of positioning signal. A positioning signal generation algorithm of pseudolite positioning system with good flexibility is presented here. It is based on the way of storage-broadcast, which firstly store digital spread spectrum sequence signal processed in advance, then choose the corresponding position signal phase to broadcast, lastly modulate to generate baseband positioning signal on account of navigation message. This method can easily change the spread spectrum code sequence and signal system, has good flexibility and can be used as a general positioning signal generator. Actual design and application show that the method can satisfy the demand of location system for baseband positioning signal.

Keywords Pseudolite positioning · Storage-broadcast · Spread spectrum positioning signal

Z. Yuan (✉) · Z. Deng · Y. Hu · L. Yang · K. Zhai · Q. An
School of Electronic Engineering, Beijing University of Posts and Telecommunications, Beijing, China
e-mail: eyz12315@163.com

J. Sun et al. (eds.), *China Satellite Navigation Conference (CSNC) 2014 Proceedings: Volume III*, Lecture Notes in Electrical Engineering 305,
DOI: 10.1007/978-3-642-54740-9_53,

53.1 Introduction

Location Based Service (LBS) has been widely accessed into people's life. At present, Global Navigation Satellite System (GNSS), represented by Beidou, GPS and Galileo has been widely used in the field of military and civilian applications. Yet the satellite signal is easily affected by buildings, trees and terrain, causes the outdoor blind area of signal coverage. It's even more difficult to receive the GNSS signal indoor. Those limit the application of GNSS. Pseudolite positioning systems can effectively avoid the problem [1].

Pseudolite positioning system use pseudolites to take the role of satellites in GNSS, terminals can get their location information by receiving signals broadcasted by a number of base stations. Those base stations used to broadcast positioning signal are called pseudolites. Generally, those pseudolites take the way similar to satellites to generate positioning signal, this results in its high cost and complex hardware structure, thereby restrict the development of pseudolite positioning system [2, 3].

On the basis of the analysis of the base station in pseudolite positioning system, this paper put forward an improved storage-broadcasting method used for generating of positioning signal. The basic principle, design and implementation of hardware/software are given. The feasibility of this method is verified through experiment verification.

53.2 Traditional Pseudolite Structure

At present most of pseudo satellite base station use spread spectrum navigation and positioning signal system like GNSS. It usually adopts information modulation, spread spectrum modulation and frequency modulation to realize the generation of positioning signal. There would be a controller to control the process of signal processing.

Signal generated by pseudolites contains the following three parts [4]:

- Carrier signal.
- Navigation messages. As for the satellites of GNSS system, the navigation messages include the information of satellite orbit, satellite clock, ionosphere, and the rough almanac information of the satellite. However, as for the pseudolite, the navigation messages might include the geographical location information of the base station, the time information, and other information required by resolving.
- Spread spectrum code sequence, according to different navigation positioning signal system design, there would be one or more of spread spectrum code sequence, used for modulation of navigation message (Fig. 53.1).

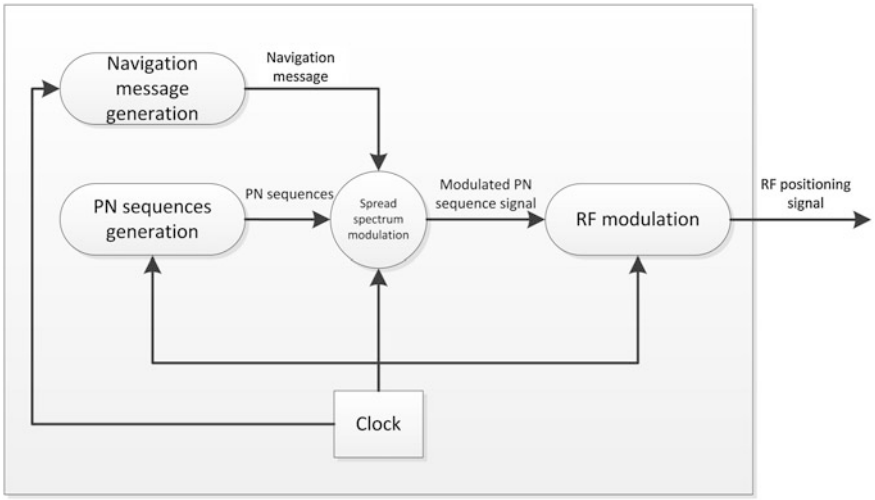

Fig. 53.1 Principle diagram of signal generation for traditional pseudolite

Traditional pseudolites first generate navigation message according to the information collected or configuration information, then navigation message is modulated with the spread spectrum code sequence generated by Spread Spectrum Code Sequence Generator, finally positioning RF signal is modulated. Visible, in signal processing of traditional pseudolite two types of digital signal (navigation message signal and spread spectrum code sequence signal) need to be generated, and two modulation processes (spread spectrum modulation and RF modulation) need to be finished. In addition, the matching between different clock frequency need to be taken into consider while designing signal processing [5, 6].

53.3 The Method of Positioning Signal Generation Based on Storage: Broadcast

Traditional pseudolite need to generate two digital signals and to complete two signal modulation processes during positioning signal generation process. All those processes would take up a lot of hardware resources, a controller is also need to implement strict sequential control. If we can simplify these processes, the complexity and cost of base station could be reduced. Because navigation message need to generated on the basis of collected information, the generation of it cannot be simplified, Yet the spread spectrum code sequence of positioning base station would not change in a short time, so the generation of spread spectrum code sequence can be optimized. The process of spread spectrum modulation can be optimized too.

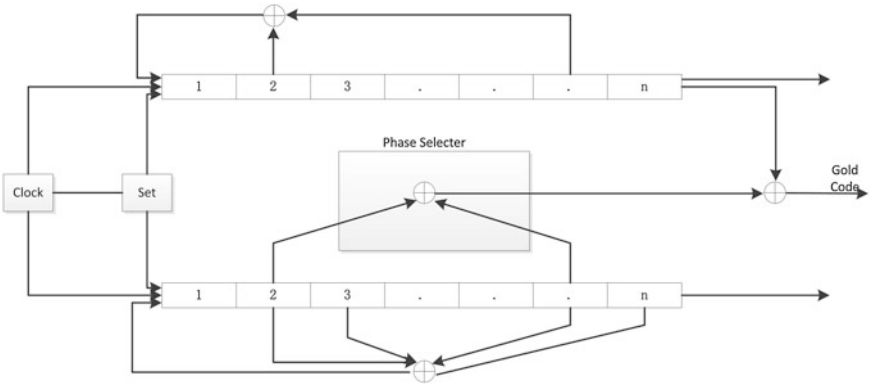

Fig. 53.2 Generation of gold code sequence

The spread spectrum code sequence used by base station is a kind of deterministic signal which has the characteristic of white noise. Gold sequence is usually used. Because it owns the statistical characteristics similar to white noise, it is sometimes called Pseudo Random Noise (PRN) sequence. Gold sequence is generated by linear feedback shift register, it is the sum of the two longest code sequences.

For register of length n, it can produce cycle for $2 * n - 1$ pseudo random code. Traditional pseudo satellites use hardware to implement registers of length n as well as the corresponding multipliers, use controller to implement the time sequence control and register address selection, so as to realize the output of Gold sequence (Fig. 53.2).

In order to save hardware resources of base stations and reduce the design complexity, the process of Gold sequence generation can be done outside the base station, then the Gold sequence can be stored in storage and read by address of storage. Gold sequence generation can be achieved by the upper computer, which only need a little time to finish. Data would be generated in binary format, which is easy to store in the storage of base station.

At the same time, we can invert Gold sequence generated and store it in storage, then if there appears jump in navigation message, we need only to set pointer from address of normal sequence to that of inverted Gold sequence. Thus the spread spectrum modulation of navigation message can be achieved by address offset (Fig. 53.3).

Through the above methods, without reducing the performance of modulation, we reduce the software and hardware resources cost of computation, sequential control at the expense of sacrificing part of storage space. The contrast of resources consumed by spread spectrum signal generation process in new method and traditional method is shown in Table 53.1.

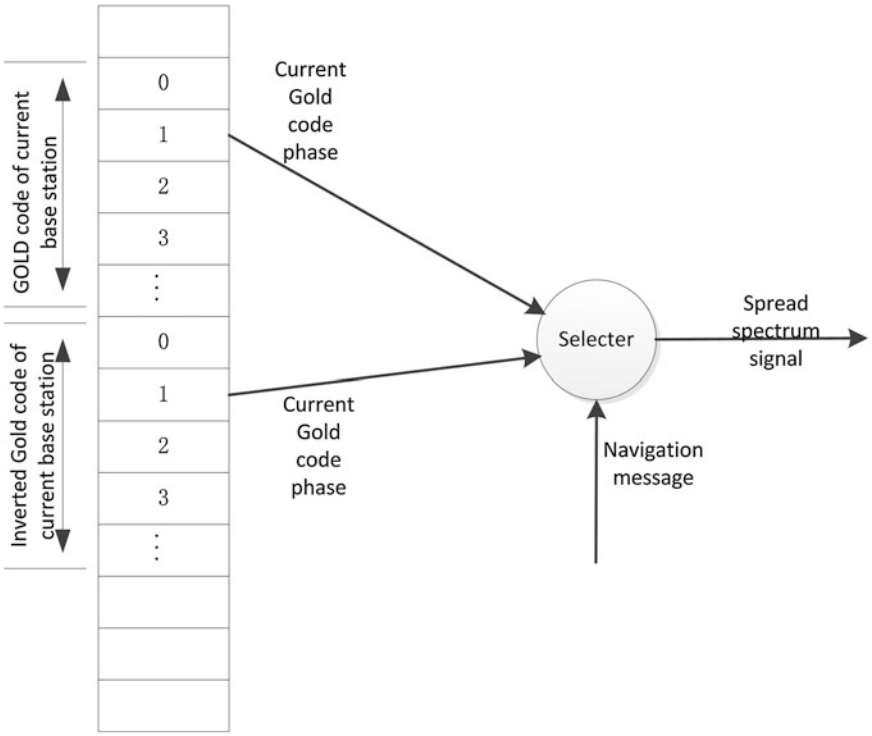

Fig. 53.3 Generation process of the spread spectrum modulated signal based on storage-broadcast

Table 53.1 Contrast of resources consumed of two methods

Resources	Storage-broadcast method	Traditional method
Linear shift register	0	$\geq 2 * n$
Adder	0	≥ 2
Sequential control	Simple	Complex
Memory	$2 * (2n - 1)$	Less

n is the length of linear shift register

53.4 Design and Implementation of Positioning Base Station Based on Storage-Broadcast Signal Generation

According to the above proposed positioning signal generation method, we set up a base station positioning experiment prototype. In order to save the development cycle, we used MCU as the core to control digital signal processing, and carrier

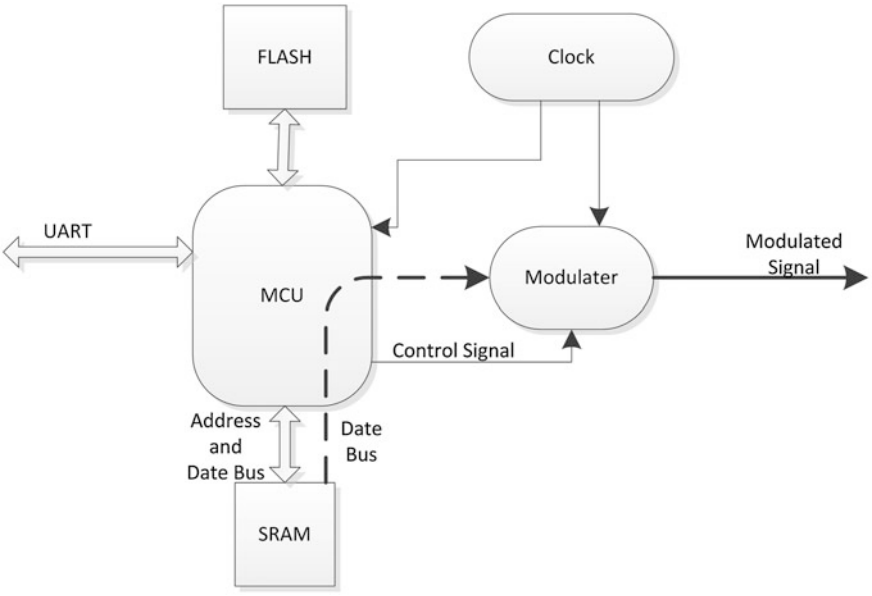

Fig. 53.4 Principle diagram of new pseudolite

modulation is realized by integrated circuit modulator. System principle block diagram is shown in Fig. 53.4.

Base station can communicate with the upper computer through universal asynchronous serial port (UART). Gold code sequence is stored in the FLASH in advance. In initialization process, the base station writes the Gold sequence and inverted Gold sequence required to an SRAM, then the MCU control the SRAM address according to the navigation information and the code piece counter, so as to realize the output of modulated spread spectrum positioning signal. The output of digital baseband signal would be sent to the modulator after converted to analog signal by DA convertor.

53.5 Experimental Results

Figure 53.5 shows the waveform of navigation message, Fig. 53.6 is the waveform of modulated spread spectrum signal, Fig. 53.7 shows spectrum of the final output RF signal from base station.

The experimental results show that the designed base station system can realize positioning signal generation and broadcast very well.

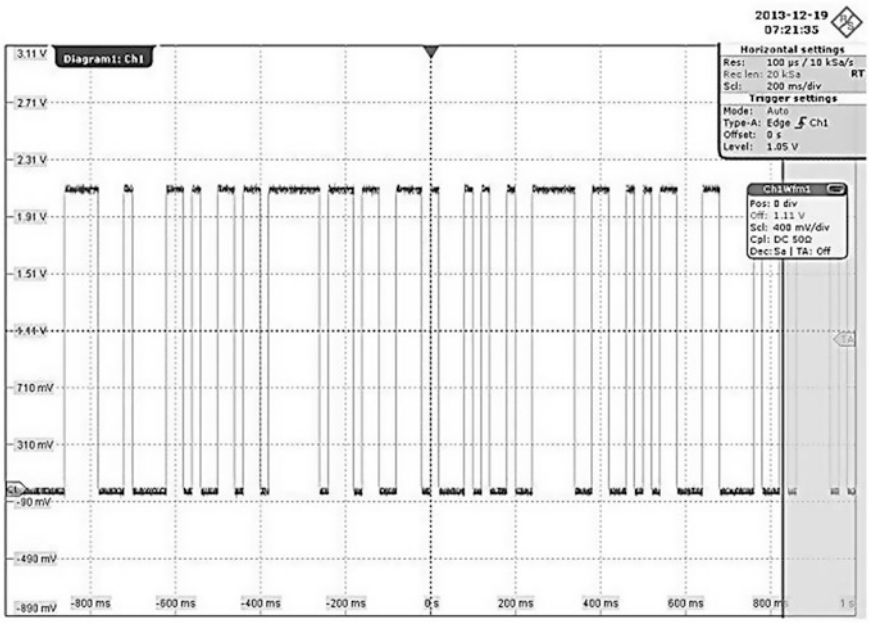

Fig. 53.5 Waveform of navigation message

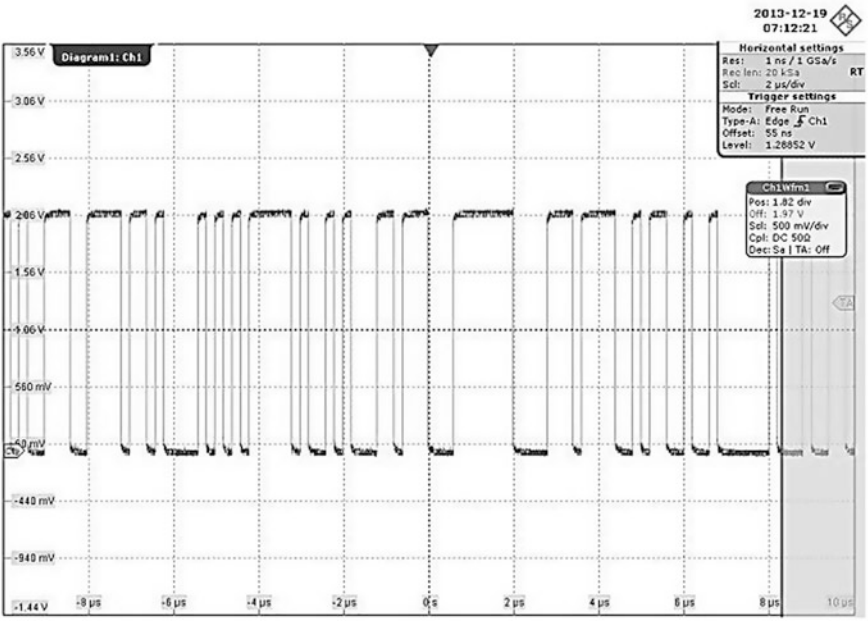

Fig. 53.6 Waveform of modulated spread spectrum signal

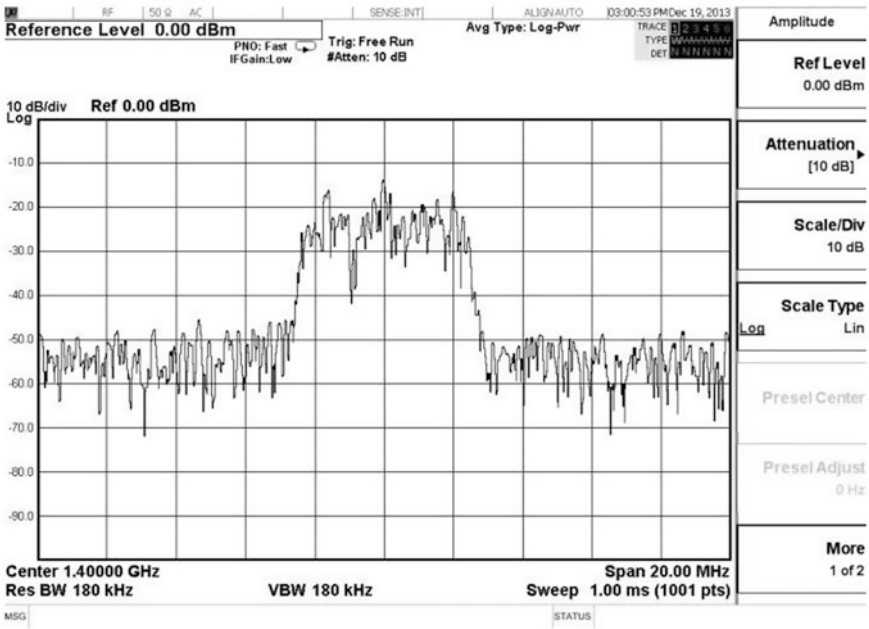

Fig. 53.7 Spectrum waveform of RF signal

53.6 Conclusion

In this paper, a pseudolite with new signal processing structure was proposed and realized. Firstly, the paper introduced the base station in pseudo satellite positioning system and analyzed the traditional pseudolite signal processing method and architecture, then put forward the spread spectrum positioning signal generation method based on storage—broadcast. Finally, the feasibility of this method is verified by experiment, proved that this method can effectively reduce the complexity of pseudolite design.

References

1. Wang HH, Zhai CR, Zhan XQ, He Z (2008) Outdoor navigation system using integrated GPS and pseudolite signals: theoretical analysis and simulation. In: Proceedings of the 2008 IEEE international conference on information and automation, Zhangjiajie, China, pp 1127–1131
2. Liu C, Gao JX, Yu ZY, Wang J (2012) An optimal pseudolites location model of GPS/pseudolites integrated relative positioning. J Chin Univ Min Technol 41(1):120–126
3. Wang YB, Zhan XQ, Xu HL, Wan XG (2012) Research and design of pseudolite in-door positioning navigation system. Comput Meas Control 20(3):793–796

4. Yi WY, Dong XR, Meng FY, Guo J (2010) GNSS single frequence software receiver development and applications. National Defense Industry Press, Beijing
5. Mao ZH, Zhan XQ, Xu HL (2010) Design and implementation of base band and IF of low-cost GPS L1 pseudolite. Comput Meas Control 18(4):875–877
6. Song Q, Zhang B, Li SJ (2013) Study of configuration technology of ground pseudolite. Comput Meas Control 21(3):743–746

Chapter 54
Indoor Positioning Algorithms Based on Multidimensional Information

Qian An, Zhongliang Deng, Xiaohong Zhao, Keji Wang and Fengli Ruan

Abstract With the development of internet, the LBS market will increase fast. Outdoor LBS has been widely used with the support of four satellite navigation system. Indoor positioning technology as an important field of location service has get more and more attention of people. The positioning technology based on wireless network make up for the deficiency of the existing navigation system. With a wide range and low cost of application, the mobile base station signal is of high popularization value in study indoor positioning technology. In this paper, a certain amount of feature points are collected which contains multi-dimensional characteristic information such as Time Difference of Arrival (TDOA) and Received Signal Strength Indication (RSSI) and so on, then make pre-processing of multidimensional positioning information of feature points by signal path division filtering, and then choose specific feature points by matching multidimensional information, these selected points are used to revise positioning information received, and calculate positioning coordinates by Newton iteration method. Meter-level position precision can be reached through the positioning mechanism talked above.

Keywords Indoor position · Feature points · Multi-dimensional characteristic information · Newton's iterative method

54.1 Introduction

With the growing of mobile Internet, the Location Based Severs (LBS) have developed a lot in recent years. And the demand of location services is increasing because there is more large buildings in the world. For example, Areas such as public security, counter-terrorism systems, production safety, networking, special

Q. An (✉) · Z. Deng · X. Zhao · K. Wang · F. Ruan
School of Electronic Engineering, Beijing University of Posts and Telecommunications, Beijing 100876, China
e-mail: anqian126@126.com

J. Sun et al. (eds.), *China Satellite Navigation Conference (CSNC) 2014 Proceedings: Volume III*, Lecture Notes in Electrical Engineering 305,
DOI: 10.1007/978-3-642-54740-9_54,

caring populations, and smart city, require the use of accurate indoor location information.

In TDOA location systems, because that signals often have reflection, refraction and multipath phenomena due to the complexity of indoor positioning environment. Use specially set sensors to receive ranging information broadcasted from multiple signal nodes, and design a specific algorithm model to process position calculating, by improving the weight of nodes that are less affected by NLOS in the whole ranging measurement, the optimized positioning result is got. However, only when ranging information of multiple signals nodes are received that this model can show a good effect. In positioning system that use BSs as signal sources, the number of BS is limited, thus bringing the limited improvement result of the positioning precision [1].

According to the statistical features of NLOS, design algorithms to estimate the errors in ranging measurements brought about by NLOS, so as to reconstruct the corresponding TDOA in LOS channel. As the NLOS change usually is unobvious in adjacent area, the NLOS compensation methods based on statistical model cannot play the role well, in addition, the positioning error could be very large [2].

Fingerprinting positioning technique requires a small amount of information, as well as overcomes the influence of NLOS, hence, meter scale positioning precision could be reached. However, a large amount of work needs to be down to get the transcendental fingerprint information, from this aspect, fingerprinting is inappropriate for a wide range of use [3].

Also as we can see, Newton's iteration method is widely used for planning the non-holonomic path of Space Robot 1, the research on optimization of traffic billing of Campus Area Network, and Matrix Inversion in Zhang Neural Network [4]. Besides all these areas, this classical Newton algorithm is also popular among the field of Location Based Service (LBS) [5].

54.2 Generated Database of Multidimensional Signal

When acquiring feature point information, since the multipath changes caused by signal diffraction, scattering and reflection, the feature values may fluctuate among different path values. In this case, the measured feature values should be processed. Therefore, how to improve the quality of a characteristic point signal become a key breakthrough and the filtering method is also very important. To solve the low accuracy problem in positioning technologies, it is necessary to find an effective filtering method for feature information collection.

The data processing of feature points mainly refers to that collecting location data, and then excluding data of large errors, isolating multi-path information, and finally representative information of the current feature point can be acquired. The multidimensional feature acquisition system is shown in Fig. 54.1. The processing of feature information in TDOA can be divided into following steps: Remove signal with less data. If the collected data of the signal from a station is less than a specific threshold, removing this set of data.

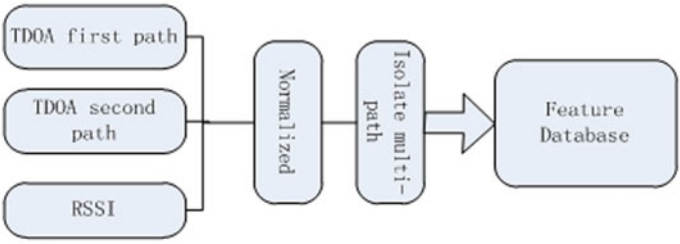

Fig. 54.1 Multi-dimensional characteristic information

Normalization the data based on the most and second strongest respectively. The value after normalization is a data for TDOA. Put the normalized TDOA data through sub path filtering. Because TDOA may fluctuate in the vicinity of the value of different paths in complex indoor environment, different paths need to be separated through corresponding algorithm. This paper presents a practical and effective routing algorithm whose data processing can be divided into several units. Store the better of the two sets of data. Select the data of less TDOA paths to be stored in the database, which can effectively reduce multipath phenomenon caused by bad station selection.

Firstly, arranging the acquired signal of feature points ascending order, and wherein the number of each group is determined automatically by the amount of data collected. Secondly, subtracting the data in first group and last group, and determine whether they are from the same path based on the absolute values of difference.

Based on the above method, the standard deviation of each path can be calculated after excluding the multipath signal of feature points. And if the standard deviation is larger than a threshold or the number of data is too small, the diameter is deleted for its big error. Then put each diameter in sliding window filter, and select the most stable part of the data to go through the mean filter, the final result is just eigenvalues of the diameter. Finally, the importance of the effective diameter derives from the amount of data, and the data amount proportional of each path can be stored for subsequent feature matching.

54.3 Select Feature Points and Amend Position Error

Suppose the number of BSs involved in positioning is more than 3, the ith BS coordinates are (X_i, Y_i, Z_i), $i = 1, 2...m$ MS coordinates is (x, y, z), thus the distance between BS and MS is as follows:

$$R = \sqrt{(X_i - x)^2 + (Y_i - y)^2 + (Z_i - z)^2} \tag{54.1}$$

Then the difference of distance from MS to BS can be obtained by Eq. (54.2):

$$R_{ij} = R_i - R_j \tag{54.2}$$

But in real channel environment, TDOA is shown as:

$$TDOA = c * t = Los + e_{Nlos} + n_{i,j} \tag{54.3}$$

where c denotes the electromagnetic wave propagation velocity, and t is the measured time delay value, e_{Nlos} denotes error caused by transmission and, n_{ij} means the measurement error which obey Gaussian distribution and have been well solved [3].

54.3.1 Select Feature Point

In positioning process, the positioning will achieve higher accuracy when the feature point matching is more accurate, so it is necessary to effectively match the characteristic points.

In the feature point matching process, by filtering, separating normalizing the received location information, we can get a set of position information that can be used for matching feature point.

$$FP = \{Tdoa_{1,1}, Tdoa_{2,1}...Tdoa_{4,1}, Tdoa_{1,2}, Tdoa_{1,2}, Tdoa_{2,2}...Tdoa_{4,2}, Rssi_1, Rssi_2...Rssi_4\}$$

this is the multi-dimensional information of feature points in the database. Assuming that there are four base stations in the positioning system, $Tdoa_{i,j}$ denotes the diameter of the feature point in the jth TDOA path for the ith base station, and $Rssi_i$ is field strong values of it. This paper uses Euclidean distance to match TDOA and RSSI information respectively. Where the Euclidean distance formula is shown as:

$$EucDis_{Rssi} = \sqrt{\sum_{i=1}^{n} \left(Rssi_{p,i} - Rssi_{f,i}\right)^2} \tag{54.4}$$

$Rssi_{p,i}$ means Rssi of position point, $Rssi_{f,i}$ means Rssi of feature point.

Because multipath of Tdoa, match feature point according to the following rules: first calculate Euclidean distance of one base station Tdoa:

$$Dis_{i,j} = Tdoa_{p,i} - Tdoa_{f,i,j} \tag{54.5}$$

the $Dis_{i,j}$ means the difference between the ith Tdoa of position point and the ith road and the jth diameter of feature points. $Tdoa_{p,i}$ maens the ith TDOA, $Tdoa_{f,i,j}$

means the ith road and the jth diameter of feature points. Compare the ith $Dis_{i,j}$, select the smallest $Dis_{i,j}$ as Dis_i

$$EucDis_{Tdoa} = \sqrt{\sum_{i=1}^{n} Dis_i^2} \tag{54.6}$$

calculate the Tdoa Euclidean distance between position point and feature point by use the Eq. (54.6).

Based on a lot of experimental data, we can see that Tdoa is more obvious than the Rssi on the degree of differentiation, So first according to the Euclidean distance of Tdoa sorting to select nine minimum Euclidean distance of the feature points, then according to weighting average the Euclidean distance of TDOA and Rssi, we select three feature points with the shortest Euclidean distance [3].

By multidimensional information matching, we can reduce the sampling density feature points, and improve the accuracy of matching.

54.3.2 Amend Position Error

In transmission environment, BS signal arrive at the receiver through reflection, diffraction and so on.

Set the following BS coordinates: $BS_1(x_1, y_1, z_1)$, $BS_2(x_2, y_2, z_2)$, $BS_3(x_3, y_3, z_3)$, $BS_4(x_4, y_4, z_4)$

Use the equation bellow to get the NLOS error:

$$\begin{aligned} Los_A = Los_{A1} - Los_{A2} = &\sqrt{(x_1 - x_A)^2 + (y_1 - y_A)^2 + (z_1 - z_A)^2} \\ &- \sqrt{(x_2 - x_A)^2 + (y_2 - y_A)^2 + (z_2 - z_A)^2} \end{aligned} \tag{54.7}$$

$$\begin{aligned} NLos_A = NLos_{A1} - NLos_{A2} = &\sqrt{(x_3 - x_A)^2 + (y_3 - y_A)^2 + (z_3 - z_A)^2} \\ &- \sqrt{(x_4 - x_A)^2 + (y_4 - y_A)^2 + (z_4 - z_A)^2} \end{aligned} \tag{54.8}$$

Use the equation bellow to get the TDOA NLOS error:

$$TdoaError = Los - Nlos \tag{54.9}$$

we found that the differences of the three NLOS errors were small, in adjacent region. This is because points are close to each other in terms of geographical location, whereas in the wide region are relatively far away from each other.

Equation (54.7) is suitable for both the feature points and the positioning point. Due to the fact that BS location, feature points location, as well as the NLOS of feature points are known, we can get the TDOA error of feature points. By weighting feature points' TDOA error, we could get the TDOA error of the positioning point, below are the mechanism by which feature points are weighted,

the basic idea is to use the Euclidean distance between feature points' NLOS TDOA and positioning point's NLOS TDOA:

$$W_i = \left(\sum EucDis_j - EucDis_i\right) / \left(2 * \sum EucDis_j\right) \tag{54.10}$$

which $\sum W_i = 1$, W_i denotes the corresponding weights of feature point i, as we can see from Eq. (54.8), feature point with the shortest Euclidean distance obtains the biggest weight value. Then get the NLOS error of positioning point by the following equation:

$$TdoaError_p = \sum W_i * TdoaError_{fi} \tag{54.11}$$

In which $TdoaError_{fi}$ means the NLOS of the ith feature point, by using Eq. (54.9) we could get the LOS TDOA of the positioning point.

54.4 Newton's Iterative Method

When the unknown variables are 2 (x and y, z is given by other module, but this still is a 3D positioning scenario), MS could receive 4 BS signals, Newton's iterative method [6] is applied to solve the following equation:

$$\begin{cases} Los_1 = \sqrt{(x_2 - x)^2 + (y_2 - y)^2 + (z_2 - z)^2} - \sqrt{(x_1 - x)^2 + (y_1 - y)^2 + (z_1 - z)^2} \\ Los_2 = \sqrt{(x_3 - x)^2 + (y_3 - y)^2 + (z_3 - z)^2} - \sqrt{(x_1 - x)^2 + (y_1 - y)^2 + (z_1 - z)^2} \\ \vdots \\ Los_6 = \sqrt{(x_4 - x)^2 + (y_4 - y)^2 + (z_4 - z)^2} - \sqrt{(x_3 - x)^2 + (y_3 - y)^2 + (z_3 - z)^2} \end{cases} \tag{54.12}$$

with Los_i as the ith TDOA paths which is got from Portion B. And (x, y, z) represent the BS coordinates, z means the height of positioning point.

The total differential Eq. (54.1) is as follows:

$$\begin{aligned} \mathrm{d}Los_i = & \left(\frac{-(x_{i1} - x)}{\sqrt{(x_{i1} - x)^2 + (y_{i1} - y)^2 + (z_{i1} - z)^2}} + \frac{-(x_{i2} - x)}{\sqrt{(x_{i2} - x)^2 + (y_{i2} - y)^2 + (z_{i2} - z)^2}} \right) \mathrm{d}x \\ & + \left(\frac{-(y_{i1} - y)}{\sqrt{(x_{i1} - x)^2 + (y_{i1} - y)^2 + (z_{i1} - z)^2}} + \frac{-(y_{i2} - y)}{\sqrt{(x_{i2} - x)^2 + (y_{i2} - y)^2 + (z_{i2} - z)^2}} \right) \mathrm{d}y \end{aligned} \tag{54.13}$$

The matrix form of differential equation is below, set the coefficient matrix as A:

$$\begin{bmatrix} \mathrm{d}los_1 \\ \mathrm{d}los_2 \\ \vdots \\ \mathrm{d}los_6 \end{bmatrix} = A * \begin{bmatrix} \mathrm{d}x \\ \mathrm{d}y \end{bmatrix}, A = \begin{bmatrix} A_{11} & A_{12} \\ A_{21} & A_{22} \\ \vdots & \vdots \\ A_{61} & A_{62} \end{bmatrix} \tag{54.14}$$

$$A_{i1} = \frac{-(x_m - x)}{\sqrt{(x_m - x)^2 + (y_m - y)^2 + (z_m - z)^2}} + \frac{(x_n - x)}{\sqrt{(x_n - x)^2 + (y_n - y)^2 + (z_n - z)^2}} \tag{54.15}$$

When i = 1, m = 2, n = 1, then the other combination of are (2, 3, 1), (3, 4, 1), (4, 3, 2), (5, 4, 2), (6, 4, 3).

Step 1 Calculate $Los_i(n)$ using the equation below:

$$\begin{aligned} Los_i(o) = & \sqrt{(x_{k,1} - x(o))^2 + (y_{k,1} - y(o))^2 + (z_{k,1} - z)^2} \\ & - \sqrt{(x_{j,2} - x(o))^2 + (y_{j,2} - y(o))^2 + (z_{j,2} - z)^2} \end{aligned} \tag{54.16}$$

where $(x_{i,1}, y_{i,1}, z_{i,1})$ and $(x_{j,2}, y_{j,2}, z_{j,2})$ are the first and the second BS coordinates in the ith TDOA, means coordinates of the oth iteration. When o is 0, set as the x, y of feature point with the shortest Euclidean distance, so as to reduce the misconvergence of the result.

Step 2 get $\mathrm{d}Los_i(o)$

$$\mathrm{d}Los_i(o) = Los_i - Los_i(o) \tag{54.17}$$

Step 3 Transfer Eq. (54.14) as below, then use the Least Square Algorithm (LSA) to compute the generalized inverse matrix, and get $[\mathrm{d}x(o), \mathrm{d}y(o)]^T$

$$\begin{bmatrix} \mathrm{d}x(o) \\ \mathrm{d}y(o) \end{bmatrix} = \left[A(o)^T * A(o)\right]^{-1} * A(o)^T * \begin{bmatrix} \mathrm{d}Los_1(o) \\ \mathrm{d}Los_2(o) \\ \vdots \\ \mathrm{d}Los_6(o) \end{bmatrix} \tag{54.18}$$

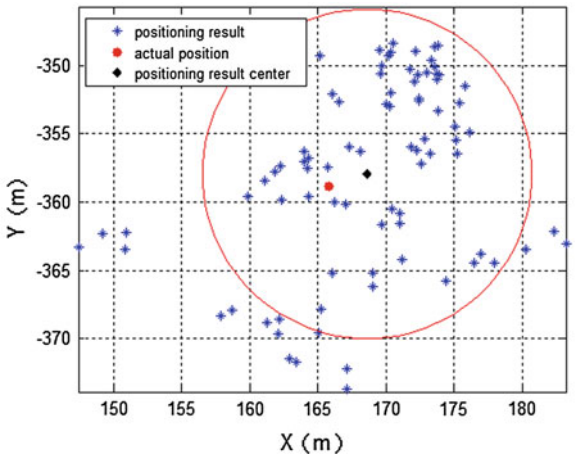

Fig. 54.2 Positioning results of method in this paper

Step 4 Process the $\mathrm{d}v(o)$ limiting condition below, Compare it with the selected threshold 0.01, if is no greater than the threshold, the final position will be $(x(o), y(o))$, else $\mathrm{d}v(o)$calculate the and as follows, then go back to Step 1.

$$\mathrm{d}v = \sqrt{\mathrm{d}x(o)^2 + \mathrm{d}y(o)^2} \tag{54.19}$$

$$x(o+1) = x(o) + \mathrm{d}x(o) \tag{54.20}$$

$$y(o+1) = y(o) + \mathrm{d}y(o) \tag{54.21}$$

54.5 Performance Analysis

In this section, the method we proposed is verified in the campus of Beijing University of Posts and Telecommunications (BUPT) in which we set up 4 BSs for positioning experiments. The coordinates of BSs are(530, −719, 76), (204, −498, 82), (495, −275, 98) and (123, −256, 84) and the testing region is within the area enclosed by 4 BSs.

Inside teaching building No. 4 used for testing, we collected 6 feature points, and use the proposed positioning method based on NLOS compensation in this paper and the Newton's iterative algorithm respectively. In the testing points, is a LOS TOA, the NLOS error of is about tens of meters, the NLOS error of and is about tens or hundreds of meters. Due to different gestures of MS, 3 or 4 base station signals could be received, thus we can get a total of 3 or 4 effective TOAs.

A set of typical positioning result is shown in Fig. 54.2, in which the red point refers to the actual positioning of the MS, black point refers to the center of the

positioning, blue points are the positioning results. As we can see from the figure, the center of the many positioning results is less than 2. 65 m away from the real position. The root mean square (RMS) error to the positioning results is 9.2 m, and 67 % of the positioning results fall within the circle with radius of 11 m and the black point as the center.

References

1. Gang C, Jia Q, Sun H, Zhang X (2010) Non-holonomic path planning of space robot based on Newton iteration. 8th World Congr Intell Control Autom (WCICA) 6534(6538):7–9
2. Guan W, Deng Z, Yu Y, Ge Y (2010) A NLOS mitigation method for CDMA2000 mobile location. 2nd IEEE Int Conf Netw Infrastruct Digit Content 668 (672):24–26
3. Moghtadaiee V, Dempster AG, Li B (2012) Accuracy indicator for fingerprinting localization systems. IEEE/ION Position Location Navig Symp (PLANS) 1204(1208):23–26
4. Zhang Y, Guo D, Yi C, Li L, Ke Z (2010) More than Newton iterations generalized from Zhang neural network for constant matrix inversion aided with line-search algorithm. 8th IEEE Int Conf Control Autom (ICCA) 9–11 June 2010, pp 399–404
5. Teramoto Y, Asahara A (2012) Wireless LAN based indoor positioning using radio-signal strength distribution modeling. Int Conf Indoor Positioning Indoor Navig (IPIN) 1(7):13–15
6. Liu N, Xu Z, Sadler BM (2012) Geolocation performance with biased range measurements. IEEE Trans Signal Process 60(5):2315–2329

Chapter 55
Exploration of BD2/SINS Deeply Integrated Navigation in CZ-7 Launch Vehicle Guidance System

Yi Tang, Wenan Zhong, Junming Shou and Wenfeng Hu

Abstract Long March 7 (CZ-7) launch vehicle is China's new generation of non-toxic, non-polluting, high performance, low cost and high thrust medium launch vehicle series. As an important part of launch vehicle flight control system, the main function of the guidance system is to control the center of mass motion using the motion parameters provided by navigation system, ensure that the launch vehicle along a predetermined trajectory. At present, CZ-7 launch vehicle guidance system used global navigation satellite system (GNSS) and the strapdown inertial navigation system (SINS) loosely integrated navigation mode. In the first flight phase of launch vehicle, the positioning antenna of satellite receiver disturbed largely, and launch vehicle injection accuracy is decided by the guidance accuracy of second flight phase, thus GNSS/SINS loosely integrated navigation mode used only in the second flight phase of launch vehicle. In order to further improve injection accuracy of CZ-7 launch vehicle, the BD2/SINS deeply integrated which applied in the CZ-7 launch vehicle guidance system are discussed in this paper. The system structure and applicability condition for BD2/SINS deeply integrated navigation are analysis briefly in the paper, based on the new characteristics of CZ-7 launch vehicle. The research results can provide a theoretical basis and technical support for the new launch vehicle guidance system.

Keywords BD2 · Strapdown inertial navigation system · Deeply integrated navigation · Launch vehicle · Guidance system

Y. Tang (✉) · W. Zhong · J. Shou · W. Hu
Unit 63810, Wenchang, Hainan, People's Republic of China
e-mail: tongygood@sohu.com

J. Sun et al. (eds.), *China Satellite Navigation Conference (CSNC) 2014 Proceedings: Volume III*, Lecture Notes in Electrical Engineering 305,
DOI: 10.1007/978-3-642-54740-9_55,

55.1 Introduction

Long March 7 (CZ-7) launch vehicle is China's new generation of non-toxic, non-polluting, high performance, low cost and high thrust medium launch vehicle series, has now entered the stage of early prototype development, will have a capacity of 13.5 t low-earth orbit [1]. CZ-7 launch vehicle mainly to meet the future needs of the space station launch cargo spacecraft will first flew in Hainan satellite launch center; when accumulate some reliability, it will used to launch manned spacecraft at the Jiuquan satellite launch center. Predicts 2021, CZ-7 launch vehicle technology mature and stable, will gradually replace the existing Long March 2, 3, 4 series, bear the mission in our country is about 80 % [1, 2].

As an important part of guidance system, the main function of launch vehicle flight control system is to use the navigation system to provide the launch vehicle motion parameters, to control the centroid movement of the launch vehicle body, ensure that the launch vehicle flying along the orbit. CZ-7 launch vehicle guidance system through the organic combination of SINS and GNSS navigation system, which adopts SINS navigation, the combined navigation system GNSS navigation is complementary, comprehensive use of the advantages of both, and realize the complementary advantages, improve the accuracy and reliability of the guidance system.

CZ-7 launch vehicle integrated guidance system using GNSS/SINS loosely integrated navigation mode. Loosely integrated navigation mode of main advantages are simple structure, easy to implement, can greatly improve the navigation precision of the system; Defect is integrated navigation observation noise associated with time, does not meet the Kalman filter for the basic requirement of the observation noise to white noise, and almost no redundant information, is not conducive to abnormal diagnosis, and the stochastic model of reform [3, 4]. Based on the analysis of CZ-7 launch vehicle guidance system basic structure, the structure of BD2/SINS deeply integrated navigation system was extracted in this paper, and its applicable condition is analyzed in brief.

55.2 CZ-7 Launch Vehicle Guidance System

Guidance system is an important part of launch vehicle flight control system, whose task is to accurately send the payload into predetermined orbit. In the process of rocket flight, duly issued a shutdown instructions, guidance and flight procedures, to ensure that the launch vehicle flying along a predetermined orbit [5].

CZ-7 launch vehicle guidance system uses "strapdown inertial measurement unit + satellite navigation receiver + onboard computer of launch vehicle" integrated navigation scheme [5]. In primary flight segment GNSS receiver positioning antenna interference large and accuracy of launch vehicle into orbit is determined mainly by the second flight segments, so the integrated navigation is used only in the second flight segment. The functional block diagram is shown in Fig. 55.1.

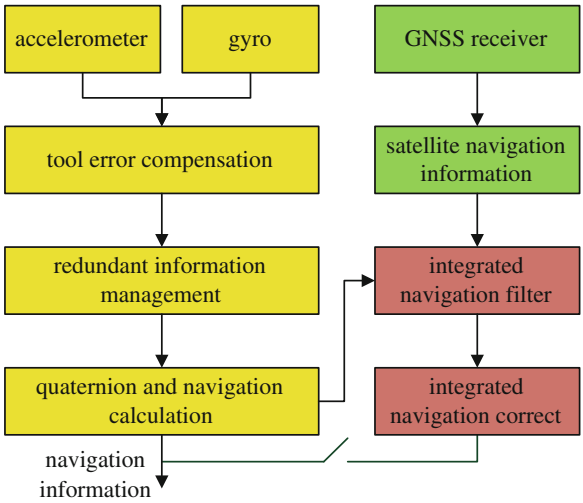

Fig. 55.1 CZ-7 launch vehicle guidance system s functional block diagram

In the process of launch vehicle flight, three orthogonal accelerometers and three orthogonal gyros in strapdown inertial measurement unit sensitive three directions of apparent acceleration and angular velocity information at launch vehicle body coordinate system, respectively, and provide apparent acceleration and angular velocity accumulative pulse count to the onboard computer of launch vehicle.

Through data bus, onboard computer of launch vehicle acquired the output information of strapdown inertial measurement combination, after the tool error compensation and redundant information management, get the body angle increment and apparent velocity increment information of launch vehicle to quaternion and navigation calculation, then get the rockets attitude, velocity and position information on inertial coordinate system.

Based on mission requirements, satellite navigation receiver receives the GNSS positioning information for data analysis, and obtain the location of the launch vehicle, speed, information, and then using the difference of inertial navigation parameter information and the satellite navigation parameters as input of least squares filtering, calculate the navigation parameters (position and velocity) correction, sent to the onboard computer of launch vehicle for navigation parameter correction.

55.3 Structure Design for BD2/SINS Deeply Integrated Navigation System

55.3.1 Different Integrated Structure Analysis

BD2/SINS integrated navigation for CZ-7 launch vehicle can be divided into loosely integrated, tightly integrated and deeply integrated navigation mode, all kinds of system structure of the integrated navigation mode is shown in Fig. 55.2 [6, 7].

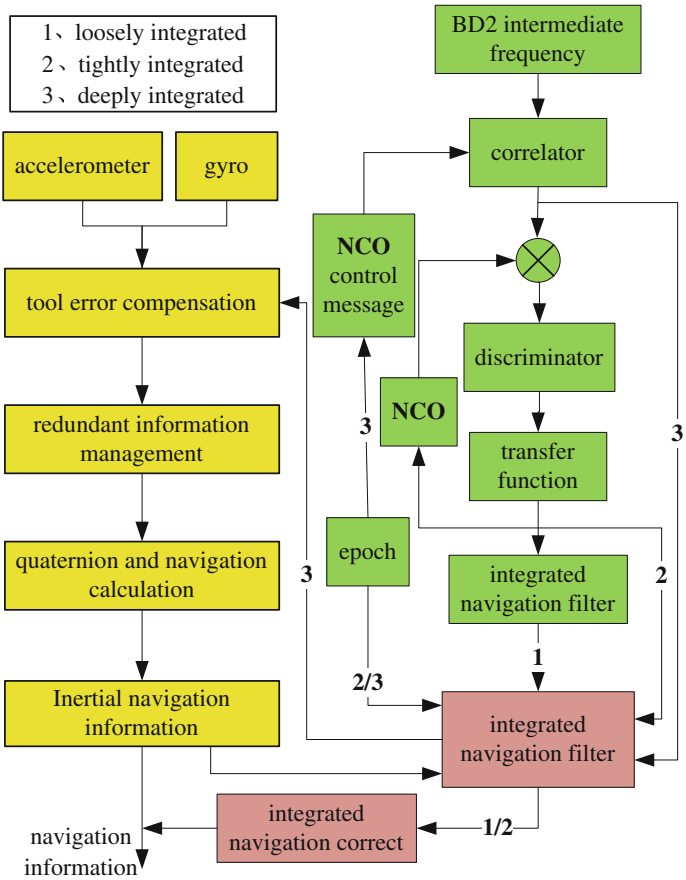

Fig. 55.2 CZ-7 launch vehicle 3 kinds integrated navigation frame

In Fig. 55.2, respectively, with the number 1, 2, and 3 arrows indicate BD2/SINS loosely integrated, tightly integrated and deeply integrated navigation information transmission process. Main difference between them is inertia and BD-2 receiver information of different fusion levels. In loosely integrated, tightly integrated and deeply integrated navigation filter, BD2 receiver observation information combined with inertial information is position/velocity, the pseudorange/pseudorange rate and baseband I/Q information, respectively.

Loosely integrated and tightly integrated navigation only BD2 receiver aided SINS, and deeply integrated navigation increases the SINS aided BD2 receiver information feedback loop of the internal information processing. SINS are not affected by dynamic constraints, deeply integrated navigation system using SINS information feedback loop real-time transfer vehicle dynamic information to the receiver, the receiver in the parameter design, without considering the influence of dynamic [8].

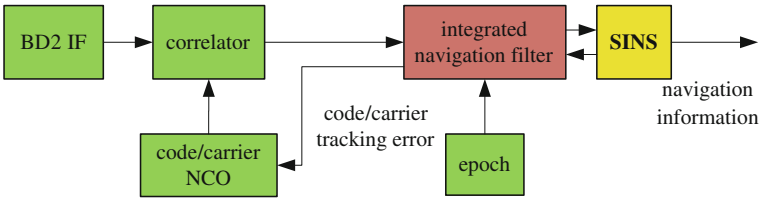

Fig. 55.3 Centralized BD2/SINS deeply integrated navigation system sketch map

Only baseband I/Q information has the property which observation noise are independent of each other, in the three kinds of integrated navigation filters observation information, in theory [9]. These processes which baseband I/Q information get pseudorange/pseudorange rate information using the discriminator and loop filter, and of at least four satellites pseudorange/pseudorange rate information get the speed/position information using least squares or navigation filter, destroys the baseband I/Q information measurement noise independence. Therefore, in the above three kinds of integrated navigation mode, only the deeply integrated navigation satisfies the precondition which Kalman filter as an optimal estimate [10].

In summary, deeply integrated navigation system has the global optimal characteristics of theory, and it can pass down the receiver loop equivalent bandwidth to enhance its anti-jamming performance or tracking sensitivity under the premise of three types of navigation mode to work properly.

55.3.2 BD2/SINS Deeply Integrated Navigation Model

55.3.2.1 Select the Structure for the Deeply Integrated Navigation System

From the perspective of information fusion, BD2/SINS deeply integrated navigation system can be divided into centralized and federated two structures.

Centralized BD2/SINS deeply integrated code /carrier tracking and SINS error estimates unified in one integrated navigation filter, shown in Fig. 55.3 [6, 11].

Centralized BD2/SINS deeply integrated navigation system directly to baseband I/Q information as observed quantity, although the navigation parameters and track parameters can be obtained the global optimal solution in theory, but it has the following two deadly limitations, making it difficult to pay to the engineering practice.

1. The large amount of calculation. Observation information and state variables are highly nonlinear in centralized BD2/SINS deeply integrated navigation system, involved in the implementation process nonlinear function for partial derivatives and high dimension matrix inversion and nonlinear filtering, etc., at

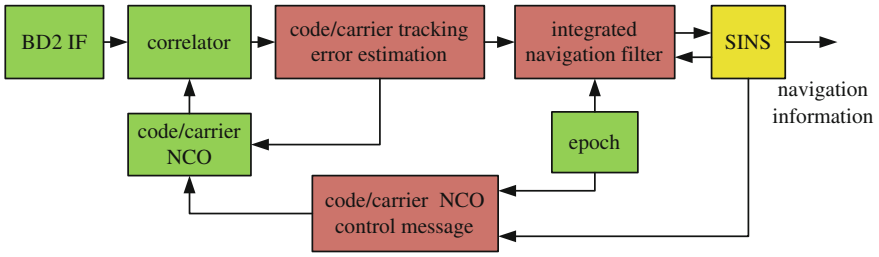

Fig. 55.4 Federated BD2/SINS deeply integrated navigation system sketch map

the same time considering the processing requirements of each channel correlator will make its computation amount is too big, can't satisfy the real-time requirements of launch vehicle.

2. Fault tolerance is poor. If the signal of a channel for BD2 receiver is destroyed by man-made or external factors, the baseband I/Q information of the channels are still as observation information into integrated navigation filter, thus affecting the accuracy of the filtering results.

In order to reduce the processing burden of integrated navigation filter in centralized BD2/SINS deeply integrated navigation system, Federated BD2/SINS deeply integrated navigation system is decomposed integrated navigation filter into two modules, former module complete code/carrier tracking error estimation, the integrated navigation filter of after module complete the estimate of the SINS error information, as shown in Fig. 55.4 [6, 7].

Compared with centralized BD2/SINS deeply integrated navigation system, due to the federated BD2/SINS deeply integrated navigation system code/carrier tracking error estimation module completed the code/carrier tracking process of high speed processing, so the function of the integrated navigation filter degrade into tightly integrated navigation filtering, which only in a low update rate, the estimate error of SINS by linear Kalman filter.

The observation information of integrated navigation filter in federated BD2/SINS deeply integrated navigation system is pseudorange errors, rate of pseudorange errors or of peudorange acceleration error, Similar to tightly integrated navigation system, this paper no longer discussed about this, but only discuss code/carrier tracking error estimation module.

55.3.2.2 Code/Carrier Tracking Error Estimation

Integrated the current research literature, the realization methods of the code/carrier tracking error estimation mainly include discriminator, pre filter and extended correlator [6].

Federated BD2/SINS deeply integrated navigation system based on discriminator directly to lead lag of normalized envelope code discriminator, second

quadrant arctangent carrier phase discriminator and four quadrant arctangent of carrier frequency discriminator output as integrated navigation filter observed quantity [12], as shown in the following

$$\begin{cases} \delta\tau = \frac{\sqrt{I_E^2+Q_E^2}-\sqrt{I_L^2+Q_L^2}}{\sqrt{I_E^2+Q_E^2}+\sqrt{I_L^2+Q_L^2}} \\ \delta\phi = ATAN\left(Q_p/I_p\right) \\ \delta f = \frac{ATAN2(dot,cro)}{t_2-t_1} \end{cases} \tag{55.1}$$

where, $\delta\tau$ is code phase tracking error, $\delta\phi$ is carrier phase tracking error, δf is Carrier frequency tracking error, I_E and Q_E are early in-phase and quadraphase channel information, I_L and Q_L are late in-phase and quadraphase channel information, I_P and Q_P are late in-phase and quadraphase channel information, $dot = I_{P1}I_{P2} + Q_{P1}Q_{P2}$, $cro = I_{P1}Q_{P2} - I_{P2}Q_{P1}$, the subscript 1 represents the correlator output after the first half of the integrate and dump operation, the subscript 2 represents the correlator output after the latter half of the integrate and dump operation, t_1 and t_2 are sampling time of I/Q information.

In three kinds of Federated model, the implement of federated BD2/SINS deeply integrated navigation system based on discriminator is the most convenient, but its damaged baseband I/Q information between the independence of the noise.

In Federated BD2/SINS deeply integrated navigation system based on the preliminary filter, code/carrier tracking error is estimated using preliminary filter firstly, the estimated information as integrated navigation filter observation. Finally control message of code/carrier numerical control oscillator (NCO) forming a closed loop by calculating Inertial information which corrected by inertial integrated navigation filter and satellite ephemeris. In Common preliminary filter models, the filter state selected as

$$X = [A \quad \delta\tau \quad \delta\phi \quad \delta f \quad \delta a]^T \tag{55.2}$$

where A is The normalized amplitude, δa is Carrier frequency change rate tracking error.

For the corresponding state equation is

$$\begin{bmatrix} \dot{A} \\ \delta\dot{\tau} \\ \delta\dot{\phi} \\ \delta\dot{f} \\ \delta\dot{a} \end{bmatrix} = \begin{bmatrix} 0 & 0 & 0 & 0 & 0 \\ 0 & 0 & 0 & \frac{\lambda_{carr}}{2\pi\lambda_{BD}} & 0 \\ 0 & 0 & 0 & 1 & 0 \\ 0 & 0 & 0 & 0 & 1 \\ 0 & 0 & 0 & 0 & 0 \end{bmatrix} \begin{bmatrix} A \\ \delta\tau \\ \delta\phi \\ \delta f \\ \delta a \end{bmatrix} + \begin{bmatrix} 1 & 0 & 0 & 0 & 0 \\ 0 & 1 & \frac{\lambda_{carr}}{2\pi\lambda_{BD}} & 0 & 0 \\ 0 & 0 & 1 & 0 & 0 \\ 0 & 0 & 0 & 1 & 0 \\ 0 & 0 & 0 & 0 & 1 \end{bmatrix} \begin{bmatrix} w_A \\ w_\tau \\ w_\phi \\ w_f \\ w_a \end{bmatrix} \tag{55.3}$$

where λ_{carr} is carrier wavelength, λ_{BD} is code length; w_A is noise of amplitude; w_ϕ is noise of carrier phase tracking error by clock excursion; w_f is noise of carrier frequency tracking error by clock excursion ratio; w_a is noise of carrier frequency

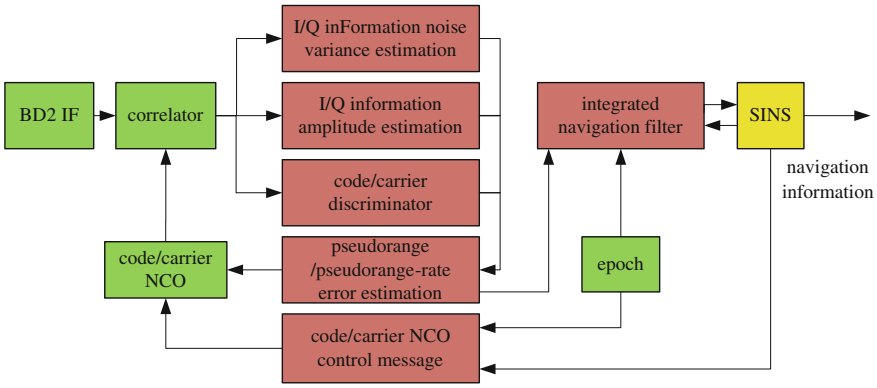

Fig. 55.5 Federated BD2/SINS deeply integrated navigation system based on extended correlator

ratio tracking error; w_τ is noise of code phase error by multipath, ionosphere, troposphere and code/carrier warp.

Observation information $\boldsymbol{Z}$ off for normalization of lead lag envelope code discriminator and the output of the second quadrant arctangent carrier phase discriminator, observation equations

$$Z = \begin{bmatrix} \delta\tau \\ \delta\phi \end{bmatrix} = \begin{bmatrix} \frac{\sqrt{I_E^2+Q_E^2}-\sqrt{I_L^2+Q_L^2}}{\sqrt{I_E^2+Q_E^2}+\sqrt{I_L^2+Q_L^2}} \\ ATAN(Q_P/I_P) \end{bmatrix} = \begin{bmatrix} 0 & 1 & 0 & 0 & 0 \\ 0 & 0 & 1 & 0 & 0 \end{bmatrix} X + \begin{bmatrix} v_1 \\ v_2 \end{bmatrix} \tag{55.4}$$

where v_1 and v_2 are noise of code and carrier discriminator.

In Federated BD2/SINS deeply integrated navigation based on the preliminary filter, state variables of preliminary filter has a linear relation with the observation information, so you just need to use linear Kalman filter to implementation code/carrier tracking error estimates.

The structure of federated BD2/SINS deeply integrated navigation system based on extended correlator as shown in Fig. 55.5, this structure estimate baseband I/Q information normalized amplitude, the information of baseband I/Q noise variance and pseudorange/rate of pseudorange error using different filter, respectively [6].

Implementation process for federated BD2/SINS deeply integrated navigation system based on extended correlator need to solve the synchronization problem of multiple information processing modules, in addition, independently estimated for the baseband I/Q information normalized amplitude and noise variance is not reasonable, because the influence of code/carrier tracking is the carrier to noise ratio [6].

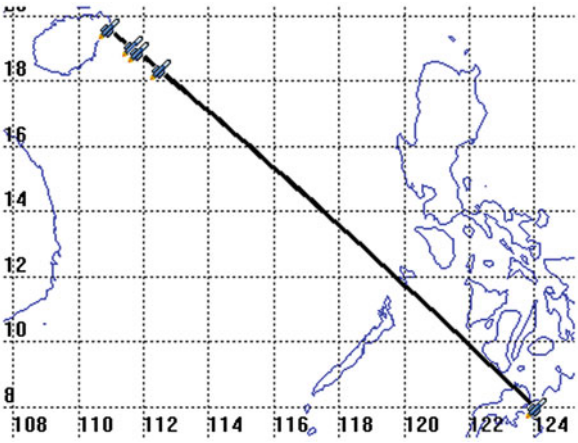

Fig. 55.6 Ground track of CZ-7 launch vehicle

55.4 BD2/SINS Deeply Integrated System Applicability Analysis

55.4.1 BD2/SINS Deep Integrated Navigation System Availability

As mentioned above, in CZ-7 launch vehicle primary flight segment GNSS receiver positioning antenna interference large and accuracy of launch vehicle into orbit is determined mainly by the second flight segments, so the integrated navigation is used only in the second flight segment. Therefore, we need to analysis the CZ-7 launch vehicle whether receive BD2 signals, as well as the satellite navigation and positioning accuracy is available in the second flight segment.

This paper uses 5GEO + 3IGSO + 12MEO BD2 regional navigation constellation, as an example of CZ-7 launch vehicle launch freight in Hainan Wenchang launch site, the satellite visibility and geometric dilution of precision (GDOP) is analysed at the whole process of flight segment. Figure 55.6 shows the Ground track of CZ-7 launch vehicle on freight state, the corresponding orbital inclination of the space station is about 42°, perigee/apogee altitude of 200 km/400 km [1].

Analysis shows that due to the geographical advantage of Hainan Wenchang launch site, during the whole flight process of CZ-7 launch vehicle, all GEO and IGSO satellites are visible. For the different launch time, the launch vehicle in flight process could observe 0–4 MEO satellite.

GDOP value can characterize the satellite constellation selection effect on positioning accuracy, under the same conditions of the observation error, the smaller the GDOP, the higher the positioning accuracy. Figure 55.7 shows the GDOP changes over time about the 5 cases which observed 0–4 MEO satellite.

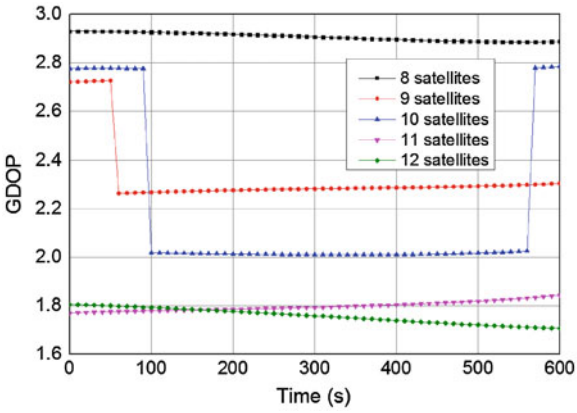

Fig. 55.7 GDOP for CZ-7 launch vehicle

The Fig. 55.7 shows that the worst situation is observed only five GEO satellites and 3 IGSO satellites, their GDOP value is about 2.9, and with the increase of the number of visible MEO satellite, GDOP value also showed a trend of decline. Usually when GDOP is greater than 6, we needs to be careful to use positioning result, thus the second flight segment of CZ-7 launch vehicle can use BD2/SINS deeply integrated navigation mode.

55.4.2 Software and Hardware Modification

Comparative Figs. 55.1 and 55.2, if CZ-7 launch vehicle guidance system use the BD2/SINS deeply integrated navigation, its modification on software and hardware mainly includes the following aspects:

1. Integrated navigation filter modification. BD2/SINS loosely integrated navigation send the correction calculate by the least squares filtering whose input is the difference of inertial navigation parameters information and satellite navigation information to the onboard computer of launch vehicle for navigation parameter correction. Federated BD2/SINS deeply integrated navigation system need to design two modules, first using the code/carrier tracking error estimation module estimate the code/carrier tracking error, and the estimated information as integrated navigation filter observation, to estimate the SINS error information.
2. Code/carrier NCO controls volume calculation. BD2/SINS deeply integrated navigation increased code/carrier NCO control volume calculation process. Using the inertial information adjusted by integrated navigation filter and satellite ephemeris calculate code/carrier NCO control.
3. The BD2/SINS error information assists SINS. BD2/SINS deeply integrated navigation increased the BD2/SINS error information assists SINS navigation

calculation. The errors accelerometer and gyroscope of SINS are through inertial navigation equation into the system, so the errors can be estimated through integrated navigation filter, and feedback correction SINS measurement.

55.5 Conclusion

In order to further improve injection accuracy of CZ-7 launch vehicle, the BD2/SINS deeply integrated which applied in the CZ-7 launch vehicle guidance system are discussed in this paper. The results showed that the secondary flight of CZ-7 launch vehicle can use BD2/SINS integrated navigation mode. Thesis research results can provide the development of a new type of vehicle guidance system to provide certain theoretical basis and technical support.

References

1. Ruixiang F, Yi R (2013) The evolution prospect of China's medium launch vehicle. Manned Spacefl 19(1):P1–P4
2. Dong L, Tangming C (2006) Development prospect of China's new generation of launch vehicles. Eng Sci 8(11):P33–P38
3. Xiaofeng H (2009) Algorithms for BD/MIMU integrated navigation system. National University of Defense Technology, Changsha
4. Xingling Z (2007) The performance comparison between loose coupling and tight coupling of GPS/INS integrated navigation system. Avion Technol 38(4):P1–P6
5. Shan MU (2003) Launch vehicle control system. National Defense Industry Press, Beijing
6. Yong L (2012) Research on the information matching problem and tracking algorithm in GNSS/INS deeply integrated navigation system. National University of Defense Technology, Changsha
7. Gao GJ (2007) INS-assisted high sensitivity GPS receivers for degraded signal navigation. Universtiy of Calgary, Calgary
8. Babu R. Mitigating the correlation in INS aided tracking loop measurements: a Kalman filter based approach. In: Proceedings of international technical meeting of the satellite division of the Institute of Navigation (ION GNSS), Long Beach, CA, 21–24 Sept 2004, pp 1566–1574
9. Parkinson B, Spilker JJ (1996) Global positioning system: theory and applications. AIAA, Washington, DC
10. Grewal MS, Andrews AP (2001) Kalman Filte ring: theory and practice using MATLAB. Wiley, New York
11. Fernandez-Prades C, Closas P, Vela-Valls J (2010) Nonlinear filtering for ultra-tight GNSS/INS integration. In: IEEE ICC, 2010
12. Lashley M, Bevly DM (2008) A comparison of the performance of a non-coherent deeply integrated navigation algorithm and a tightly coupled navigation algorithm. In: Proceedings of international technical meeting of the satellite division of the Institute of Navigation (ION GNSS), Savannah, GA, 16–19 Sept 2008, pp 2123–2129

Chapter 56
Cooperative Positioning for Mobile Phone

Qiang Chang, Qun Li, Hongtao Hou, Wangxun Zhang and Weiping Wang

Abstract Indoor positioning for mobile phone is important for many applications. The widely used mobile phone indoor positioning technique need to pre-located anchor nodes, or collect fingerprint for the indoor environment. Peer-to-Peer Hybrid Cooperative Positioning (P2P-HCP) is a novel indoor positioning technology to provide reliable, GNSS-like navigation performance in hostile, GNSS-challenged environments. A new P2P-HCP algorithm is proposed for mobile phone indoor positioning. In this algorithm, short-range communication is used to exchange location information. A novel data fusion algorithm is proposed to fuse both navigation satellite information and located neighboring phones' information to estimate position. Simulation result shows that the proposed algorithm offers a good performance in accuracy and coverage in indoor environment without any priority information or pre-located anchor nodes.

Keywords GNSS challenged environment · Cooperative positioning · Data fusion · Mobile phone

56.1 Introduction

In the second decades of the 21st century, smart mobile phone becomes more and more widely used as the development of hardware and software technique. Most of our common used mobile phone has equipped with quite a lot of sensors, such as light sensor, gravity sensor and so on. And the computation ability becomes more and more powerful. By installing variety of software, we can nearly do everything by using mobile phone. The combination of internet and mobile phone

Q. Chang (✉) · Q. Li · H. Hou · W. Zhang · W. Wang
College of Information System and Management, National University of Defense Technology, Changsha 410073, China
e-mail: cq.nudt@gmail.com

J. Sun et al. (eds.), *China Satellite Navigation Conference (CSNC) 2014 Proceedings: Volume III*, Lecture Notes in Electrical Engineering 305,
DOI: 10.1007/978-3-642-54740-9_56,

push us into the age of mobile internet. In the era of mobile internet, Location Based Service (LBS) developed dramatically. The integration of traditional service and location service brings about a great deal of innovation applications. All of these LBS applications have the same requirement: the user's position must be acquired at any place at any time. However, the widely used technique, such as GNSS [1], Wireless Sensor Networks (WSN) [2], AGNSS [3, 4] and fingerprint can't provide proper positioning performance for LBS applications.

Although most of the mobile phones are equipped with GNSS chips, but the phone users stayed in GNSS challenged environment at most of the time, such as urban canyons, heavy tree shadowed and indoor scenarios. More ever, the most widely used AGNSS positioning performs bad in accuracy in indoor environment. Wireless Sensor Networks (WSN) positioning is developed for indoor positioning and works well if there is some anchor sensors located in come critical position. But this technique needs to maintain fixed infrastructure, which means daily cost for the service. Fingerprint is another newly developed and well-performed indoor positioning technology, but we need to collect the signal characteristic at most point of the area and update the database frequently. So, there is no well-performed positioning technology for indoor mobile phone positioning.

Researchers starting to considering the possibility to improve GNSS receivers performance by allowing information exchange among users, and they develops a new Positioning technology, called Peer-to-Peer Cooperative Positioning [5–7] (P2P-CP), in which data and information are shared within clusters of GNSS receivers so as to improve individual receiver performance. This new Positioning technique would provide more accurate position in harsh environment, where the line-of-sight (LOS) between satellites and receiver antenna is often obstructed, and GNSS-based localization heavily degrades or completely fails. The principle of this technology is that all the GNSS receivers have to equip with terrestrial ranging and communication modular. The terrestrial ranging and communication modular respectively used for distance measurement and communication between nearby GNSS receivers, distributed algorithms are applied to fuse pseudorange and neighbouring nodes' distance to calculate the nodes' position. The effectiveness of P2P-CP is demonstrated by the simulation results, which show that P2P-CP gets equally precision compared with Assisted GNSS (AGNSS), but the time cost of P2P-CP is less than AGNSS.

The embedded sensors in most of mobile phones can be used for constructing the cooperative positioning networks. The GNSS chips in mobile phone are used for navigation satellite capture, and navigation signal analysis. Short range communication sensors, such as infrared modular, Bluetooth, and Near Field Connection (NFC), are used for distance measure and information exchange between neighbouring mobile phones. The CPU is used to data fusion. But distance measurement between neighbouring phones is difficult and inaccurate. More ever, it will cost a lot of energy during measuring [8, 9]. So, mobile phone based traditional P2P-CP is unpractical.

In this paper, we propose a new range-free peer to peer cooperative positioning algorithm (RF-P2P-CP), which is based on the basic principal of P2P-CP, but more suitable for mobile phone indoor positioning. The main different between RF-P2P-CP and P2P-CP is that no range measure is needed in our proposed algorithm. A new data fusion algorithm is developed to fuse satellites position, pseudorange, and neighbouring phones location to estimate the phone's location.

56.2 Related Works

Cooperative Positioning (CP) was originally proposed as an approach for acquiring real-time positioning information of mobile robots by Kurazume et al. They propose an approach called Cooperative Positioning System (CPS) [10] to overcome the shortcomings of Dead Reckoning and landmark method [11, 12]. The main concept of CPS is to divide the robots into two groups, A and B where group A remains stationary and acts as a landmark while group B moves and then group B stops and acts as a landmark for group A. Position identification experiments give a positioning accuracy of 0.12 % for position and 0.32° for attitude after the robots traveled a distance of 21.5 m.

Based on the concept of CPS, Garello et al. propose a new positioning paradigm by allowing information exchange among receivers to overcome the shortage of GNSS positioning in GNSS challenged environment. Their new positioning algorithm is called Peer-to-Peer Cooperative Positioning (P2P-CP) [6, 7]. In P2P-CP, receivers shares data with its neighbors in an unstructured way. This way of cooperation has the advantage of not requiring a fix infrastructure, allows scalability, and fosters the creation of heterogeneous time-varying networks with different receivers.

Based on the differing natures of the exchanged data, P2P-CP can be categorized as GNSS-only and Hybrid type.

GNSS-only P2P-CP requires the receivers possess GNSS receiver and communication system. The missing equations necessary for the PVT solution can be obtained by using the pseudorange measurements between the aiding peers and one or more satellites out of the user visibility. GNSS-only means the exchanging data only contains data generated in GNSS systems or obtained by processing GNSS signals. Examples include information about carrier-to-noise density ratio, doppler shift, pseudoranges, secondary code delay, and so on. GNSS data only approach is very similar to AGNSS, but this approach need no infrastructure and data center, this is a distributed implementation of AGNSS.

Hybrid P2P-CP approach focuses on receivers within GNSS-challenged environments equipped with a GNSS receiver, a terrestrial ranging modular, and a communication system. Range from the neighbors can be used to integrate satellites' pseudoranges and dramatically improved availability and accuracy of positioning in deep indoor environment [7].

But until now, P2P-CP has not come into practice yet. In this paper, we are going to propose a new type of peer to peer cooperative positioning algorithm, which is based on the basic principal of P2P-CP, but more suitable for mobile phone indoor positioning.

56.3 Peer to Peer Cooperative Positioning for Mobile Phone

56.3.1 Summarization of the Algorithm

Generally speaking, the mobile phones among short communication range are in the same elevation, or their elevations are very approximate to each other. So the hypothesis that we assume all the indoor mobile phone have the same elevation is reasonable and practical.

Considering the difficulty of distance measurement between mobile phones, our proposed algorithm needs no distance measurement, just like GNSS-only P2P-CP. The mobile phones broadcast their location to its neighboring phones.

The mobile phone used for our proposed positioning algorithm must contain GNSS chips, computation device, and short range communication modular. The GNSS chips are used to navigation signal capture and analysis. If the satellites in view exceed four, we can acquire the position of the mobile phone, if not, we only acquire satellites' pseudorange. The short range communication modular is used for exchanging locations. And the computation device is used for position estimation. The basic idea of our proposed algorithm is illustrated in Fig. 56.1.

In Fig. 56.1, phone P1 has four satellites in view, so the position can be acquired by the GNSS chips. P2 and P3 have not enough satellites to estimate location. But after P1 broadcast its position to them, both P2 and P3 will get their location according to our data fusion algorithm.

56.3.2 Details of the Algorithm

56.3.2.1 System Model

Let us consider a network with N mobile phones located in a square with 200 m long. The phones are equipped with GNSS chips, computation device, and short range communication modular. The phones move freely in the square. So the structure of the cooperative network changes frequently.

The mobile phones have three possible statuses, Self-Localized (SL), Assistant-Localized (AL) and Un-Localized (UL). The location of SL phones come from GNSS chips. The UL phones have no location information about themselves. The rest are AL phones.

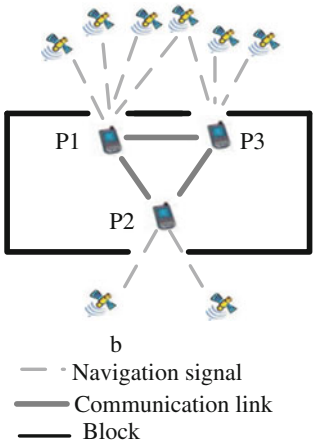

Fig. 56.1 Range free peer to peer cooperative positioning

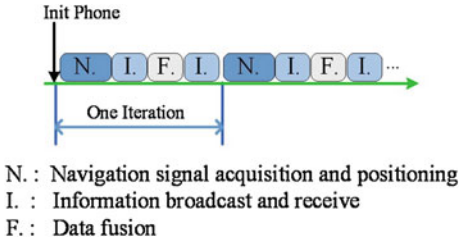

Fig. 56.2 Steps of the algorithm

Let $S_n^{(k)}$ denotes the satellites in view of phone n at time k, $S_n^k = \{s_1^k, s_2^k, \ldots\}$, and $s_i^k = \{s, Pse\}$, s is the ID of the satellite, Pse is the pseudorange between n and s. Let $L_n^{(k)}$ denotes the located neighbors of phone n at time $k, L_n^k = \{l_1^k, l_2^k, \ldots\}$, and $l_i^k = (x_i, y_i, z_i)$. The communication range is R. The SL phones only broadcast location information. The AL phones both broadcast and receive location. The UL phones only receive location from neighbors. The AL and UL phones estimate their location if enough information is acquired.

56.3.2.2 Basic Steps of the Algorithm

In order to implement a cooperative positioning algorithm, every phone has to execute three different sub-steps namely navigation signal acquisition and positioning, information broadcast and receive, and data fusion, see example depicted in Fig. 56.2.

The above mentioned sub-steps are detailed on next.

1. Navigation signal acquisition and positioning: in this step, the navigation signal can be acquired by GNSS chips. The chips analysis the signal to get the ID and

pseudorange. If the total number of satellites in view exceeds four, location can be acquired from the chips, and the phone status is set to SL. Else set status to UL.
2. Information broadcast and receive: in this step, the AL and SL phones broadcast location to their neighbors, AL and UL phoned receive information from located neighbors.
3. Data fusion: in this step, the AL and UL phones fuse different information to estimate their location, and set the status according to the algorithm below.

56.3.2.3 Basic Steps of the Algorithm

We develop a new data fusion algorithm for our cooperative positioning. Only AL and UL phoned need data fusion, we can divide these phoned in four types:

1. $|S_n^k| == 3, L_n^k > 0$

According to our hypnosis, the elevation equals to any of the localized neighbors, so we get below formulas

$$\begin{cases} (x - x_{s1})^2 + (y - y_{s1})^2 + (z_l - z_{s1})^2 = pse_{s1}^2 \\ (x - x_{s2})^2 + (y - y_{s2})^2 + (z_l - z_{s2})^2 = pse_{s2}^2 \\ (x - x_{s3})^2 + (y - y_{s3})^2 + (z_l - z_{s3})^2 = pse_{s3}^2 \end{cases} \tag{56.1}$$

where x_{si}, y_{si}, z_{si} and pse_{si} are the coordinates and of the pseudorange of the $i's$ satellite, x, y, z_l are the coordinates of the phone.

We use Maximum Likelyhood Estimate (MLE) to solve the formulas. This phone's status is set to AL.

2. $|S_n^k| == 2, L_n^k > 0$

Similar to the previous type, we get the elevation, and we have below formulas

$$\begin{cases} (x - x_{s1})^2 + (y - y_{s1})^2 + (z_{l1} - z_{s1})^2 = pse_{s1}^2 \\ (x - x_{s2})^2 + (y - y_{s2})^2 + (z_{l1} - z_{s2})^2 = pse_{s2}^2 \end{cases} \tag{56.2}$$

and

$$(x - x_{l1})^2 + (y - y_{l1})^2 \leq R \tag{56.3}$$

where x_{l1}, y_{l1}, z_{l1} are the coordinates of any localized neighbors.

Solve formulas (56.2), we get two possible locations for this phone, by considering the formula (56.3), the two possible locations is reduced to one, and thus the phone's status is set to AL.

3. $L_n^k > 0$

According to the communication range, we get below formulas

$$\begin{cases} (x - x_{l1})^2 + (y - y_{l1})^2 \le R \\ \vdots \\ (x - x_{lk})^2 + (y - y_{lk})^2 \le R \end{cases} \tag{56.4}$$

From formulas (56.4), we get

$$\begin{cases} x_{l1} - R \le x \le x_{l1} + R \\ \vdots \\ x_{lk} - R \le x \le x_{lk} + R \end{cases} \tag{56.5}$$

and

$$\begin{cases} y_{l1} - R \le y \le y_{l1} + R \\ \vdots \\ y_{lk} - R \le y \le y_{lk} + R \end{cases} \tag{56.6}$$

We can localize the phone according to the below equations:

$$\begin{cases} x = \dfrac{\min(x_{li}+R) + \max(x_{li}-R)}{2} \\ y = \dfrac{\min(y_{li}+R) + \max(y_{li}-R}{2}) \\ z = z_l \end{cases} \tag{56.7}$$

And thus the phone's status is set to AL.

4. else

The phone's status is set to UL.

The whole algorithm shows below:

Algorithm 56.1 **Range-free cooperative positioning algorithm**

Range-free cooperative positioning algorithm

0: $k = 0$, set all the phones' status to UL;
1: Navigation signal acquisition and positioning
  If $|S_n^k| \ge 4$
    status = SL
  Else
    status = UL
2: Information broadcast and receive

(continued)

(continued)

Range-free cooperative positioning algorithm

If status != UL
Broadcast location
Else
Receive neighbors information
3: Data fusion
If status != SL && $\left|S_n^k\right| == 3, L_n^k > 0$
Acquire location using Eq. (56.1), status != AL
Else if status != SL && $\left|S_n^k\right| == 2, L_n^k > 0$
Acquire location using Equation (56.2) (56.3), status = AL
Else if status != SL && $L_n^k > 0$
Acquire location using Equation (56.7), status = AL
Else if status != SL
status = UL
4: Information Broadcast
If status != UL
Broadcast location
5: $k = k + 1$,back to Step 1.

56.4 Performance Evaluation

Simulation tests were performed in order to evaluate the performance of the proposed algorithm. The experimental and simulation parameters showed in Table 56.1:

Figure 56.3 is the time trend of the located phone proportion in different algorithms. The proportion is defined as:

$$Proportion = \frac{N_{locatedphones}}{N_{totalphones}} \tag{56.8}$$

From the simulation we can see that, our newly proposed FR-P2P-CP algorithm greatly increased accuracy compared to GNSS only localization in challenged scenarios. In about three time slot, the proportion comes to at about 1. The accuracy increased too, because the un-localized phone acquired their position by the new algorithm.

Now, we will change the simulation parameters to search the hidden pattern of our algorithm.

Figure 56.4 illustrates some characters of different communication ranges.

From Fig. 56.4a, we can see that the longer communication range is, the larger the max proportion gets. From Fig 56.4b, we can see that when the communication range is about 7, the phones need the most steps to achieve max proportion.

Table 56.1 Simulation parameters

Simulation parameters	Parameter value
Size of the square	100 m × 100 m
Number of phones	200
Number of located phones	20
Communication range	20 m

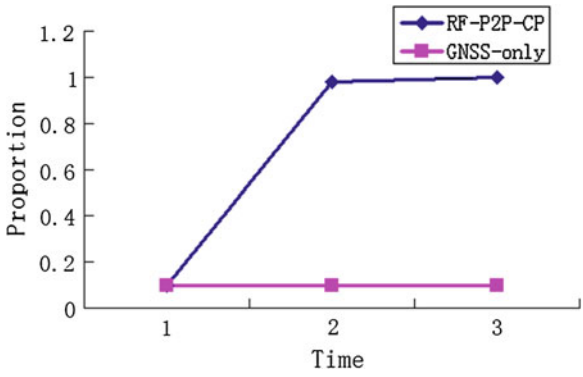

Fig. 56.3 Located phone proportion

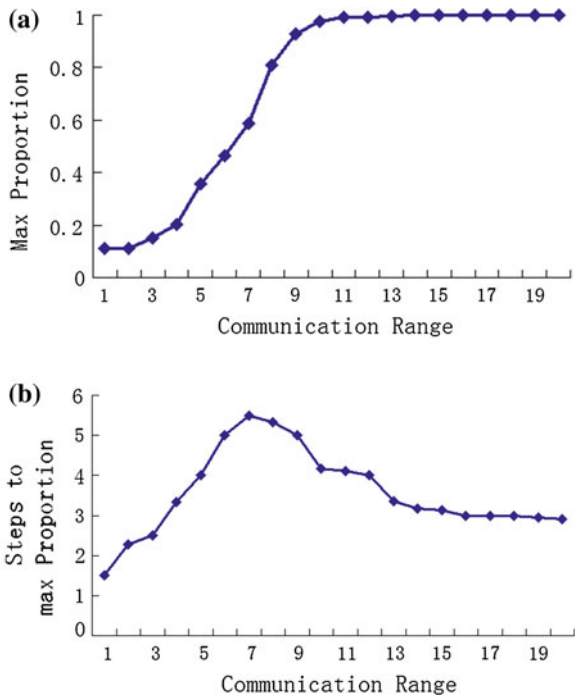

Fig. 56.4 Different communication range. **a** Max proportion in different range, **b** steps to the max proportion

56.5 Conclusion

In this paper, we propose a new range-free peer to peer cooperative positioning algorithm for mobile phone positioning in GNSS-challenged environment. And a new data fusion algorithm is developed to fuse satellites position, pseudorange, and neighbouring phones location to estimate the phone's location. The simulation result shows that the proposed algorithm increased both positioning availability and accuracy compared to GNSS only localization in challenged scenarios.

Acknowledgement Gratitude is acknowledged to National Natural Science Foundation for supporting this research under Contract No. 61074107, 60974074, and 71031007.

References

1. Kaplan ED, Understanding GPS (2006) Principles and applications. Artech House, London
2. Ren FY, Huang HN, Lin C (2003) Wireless sensor networks. J Softw 14(2):1148–1157
3. Van DF (2009) A-GPS: assisted GPS, GNSS, and SBAS. Artech House, London
4. Kraemer I, Eissfeller B (2009) A-GNSS, a different approach. Inside GNSS, 2009, pp 52–61
5. Politecnico DT (2011) Peer-to-peer positioning-final report. Universita di Bologna, Italy
6. Garello R, Samson J, Spirito MA, Wymeersch H (2012) Peer-to-peer cooperative positioning part one: GNSS-aided acquisition. Inside GNSS (March/April 2012) 55–63
7. Garello R, Corazza GE, Samson J (2012) Peer-to-peer cooperative positioning part two: hybrid device with GNSS & terrestrial ranging capability. Inside GNSS (July/August 2012) 56–64
8. Liu J, Priyantha B, Hart T, Ramos SH, Antonio AFL, Wang Q (2012) Energy efficient GPS sensing with cloud offloading. In: Proceedings of the 10th ACM conference on embedded network sensor systems, New York, USA, 6–9 Nov 2012
9. Paek J, Kim J, Govindan R (2010) Energy-efficient rate-adaptive GPS-based positioning for smart phones. In: Proceedings of the 8th international conference on mobile systems, applications, and services, New York, USA, 15–18 June 2010
10. Kurazume R, Hirose S, Nagata S, Sashida N (1996) Study on cooperative position system. IEEE international conference on robotics and automation, Minneapolis, USA, 22–28 Apr 1996
11. Fuke Y, Krotkov E (1996) Dead reckoning for a lunar rover on uneven terrain. In: IEEE international conference on robotics and automation, Minneapolis, USA, 22–28 Apr 1996
12. Becker C, Salas J, Tokusei K, Latombe J. Reliable navigation using landmarks. In: IEEE international conference on robotics and automation, Nagoya, Japan, 21–27 May 1995

Chapter 57
A Perspective on Cramér-Rao Bound for Hybrid GNSS-Terrestrial Cooperative Positioning

Shiwei Tian, Boyu Huang, Guangxia Li, Weiheng Dai, Jing Lv and Jiang Chang

Abstract Global Navigation Satellite System (GNSS) is the most popular technique in the area of navigation and positioning, due to its performance is satisfied for most applications in the open-sky environment. However, GNSS always fail to provide satisfactory performance due to signal blockage in some environments such as urban terrain, forests or indoor scenarios. The traditional method to resolve the above problem is to develop various augmented systems, or build some terrestrial-based wireless positioning system, working together with GNSS or independently. Cooperative positioning is a new paradigm around how devices can cooperate with each other to improve their ability to compute position, compared to traditional augmented methods, it does not required a fixed infrastructure, and even provide a better performance. Cooperative positioning is an effective way to improve the performance of positioning accuracy, availability, etc. The positioning accuracy is a fundamental metric for positioning system. In this contribution, we discuss the two expressions of Cramér-Rao Bound (CRB) on positioning accuracy, and the relationship between them. Meanwhile, we prove the conclusion that the fundamental positioning performance in cooperative positioning outperforms that in traditional (non-cooperative) positioning, rather than verification via numerical simulation.

Keywords Cooperative positioning · GNSS · CRB

S. Tian (✉) · G. Li · W. Dai · J. Lv · J. Chang
College of Communications Engineering, PLA University of Science and Technology, Nanjing 210007 Jiangsu, People's Republic of China
e-mail: tianxwell@163.com

B. Huang
Department of Electronic Engineering, TsingHua University, Beijing 100084, People's Republic of China

J. Sun et al. (eds.), *China Satellite Navigation Conference (CSNC) 2014 Proceedings: Volume III*, Lecture Notes in Electrical Engineering 305,
DOI: 10.1007/978-3-642-54740-9_57,

57.1 Introduction

Due to the characters of high positioning accuracy, global coverage and working all the days, GNSS is the most widely used positioning and navigation technology to date, and it has been widely used in numerous applications such as military sectors, civil and commercial applications. However, since the received GNSS signal is extremely low power, the satellite signals can be easily obstructed. For instance, GNSS-based techniques may fail to provide satisfactory service due to signal blockage in many environments, such as forests, urban terrain, or indoor scenarios. At the same time, GPS receivers are also susceptible to jamming and unintentional interference for this same reason [1].

Traditionally, there are three methods to solve the above problem, i.e., develop the GNSS system itself, develop techniques of integrated navigation and build various augmented systems, such as satellite-based systems, terrestrial augmentation systems. However, the above methods either rely on fixed infrastructure, or can not provide satisfactory service in some environments.

Driven by the success of cooperative techniques in many research areas, such as cooperative evolution and cooperative communication, cooperative techniques have been introduced in the research of positioning and navigation [2, 3]. Cooperative positioning methods have been recognized as part of an effort to improve the performance of GNSS receivers in hostile environments, relying on information exchange and/or direct measurements among devices (also referred to as agents hereafter). They can be used not only when GNSS is unavailable, but also in combination with GNSS, in order to improve the performance of positioning, such as positioning accuracy and availability [4]. Hybrid cooperative positioning is an emerging research topic [5].

Positioning accuracy is one of the most important metrics in positioning system, and it is always focused by users firstly as well. It is well known that the CRB sets a fundamental lower limit to the covariance of any unbiased estimator for a vector parameter [6], and CRB can serve as a theoretical tool to evaluate the fundamental positioning accuracy. In prior work, several contributions deal with CRB in case of cooperative positioning, e.g., [7] for wide-band systems, [8] for wireless sensor networks. Considering the unique features in hybrid positioning system, [5] deals with CRB in hybrid GNSS-terrestrial systems and present a numerical example.

In this paper, CRB in hybrid GNSS-terrestrial systems is analysed as well. Compared to [5], another form of the CRB is derived. Furthermore, an theoretic study on the relationship between CRB in cooperative positioning and CRB in traditional (non-cooperative) positioning is performed.

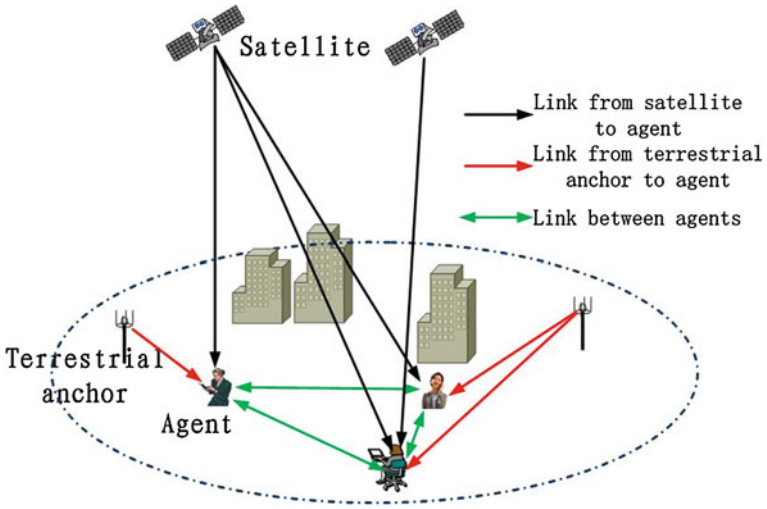

Fig. 57.1 Scenario for hybrid GNSS-terrestrial cooperative positioning

57.2 Problem Formulation

Consider a hybrid GNSS-terrestrial cooperative network including satellite nodes with know clock bias and known position, anchor nodes with known position but unknown clock bias, and agents with unknown clock bias and unknown position. Generally, bias in range measurements from satellite to terrestrial devices is considered, resulting from imperfect synchronization of device clock with respect to satellites. Nevertheless, the above bias in terrestrial range measurements is usually not considered. Figure 57.1 illustrates the scenario for hybrid GNSS-terrestrial cooperative positioning.

Let M be the set of agents, S the set of satellites, A the set of anchors; denote by S_m the set of satellites agent m can see, by A_m the set of anchors agent m can communicate with. Positional state of satellite $s \in S$, of anchor $a \in \mathrm{A}$, and of agent $m \in \mathrm{M}$, are indicated respectively by $\mathbf{x}_s = [x_s \quad y_s \quad z_s]$, $\mathbf{x}_a = [x_a\ y_a\ z_a]$, $\mathbf{x}_m = [x_m\ y_m\ z_m]$. The dimension of position vectors, indicated by D, may be 2 or 3. The variable b_m represents the clock bias of agent m, expressed in distance units. The information agent m obtained from satellites (denoted by $\mathbf{P}_{sm}$) and terrestrial anchors (denoted by $\mathbf{R}_{am}$) and from useful neighboring agents (denoted by $\mathbf{P}_m$) is denoted by $\mathbf{M}_m = \mathbf{P}_{sm} \cup \mathbf{R}_{am} \cup \mathbf{P}_m$, a set of unknowns $\mathbf{U}_m = [\mathbf{x}_m\ b_m]$ for agent m are to be determined.

In the above scenario, there exist the following two types of measurements:

- Range measurements, i.e., distance between agents and anchors $r_{am} = \|\mathbf{x}_a - \mathbf{x}_m\| + v_{am}$.
- Pseudorange measurements, i.e., distance between agents and satellites $\rho_{sm} = \|\mathbf{x}_s - \mathbf{x}_m\| + b_m + v_{sm}$.

where the symbol $\|\cdot\|$ denotes Euclidean distance, $m \in \mathrm{M}$, $a \in \mathrm{A}$, $s \in S$, v_{am}, v_{sm} are measurement noise. Without loss of generality, in the following of this paper, we only discuss on the situation when distance between agents and satellites is available, and the measurements between agents and anchors will not be considered.

57.3 CRB in Cooperative Positioning

Now, we revisit the overview of the CRB, which will help to reveal the essence of its calculation. All that is needed to calculate a CRB is the statistical model of the random measurements $p(\mathbf{X}|\boldsymbol{\theta})$, where $\mathbf{X}$ are the random measurements, and $\boldsymbol{\theta} = [\theta_1\, \theta_2 \ldots \theta_p]^T$ (superscript ^{T} indicates transpose) are the parameters that are to be estimated from the measurements. Any unbiased estimator $\hat{\boldsymbol{\theta}}$ must satisfy

$$\mathrm{cov}(\hat{\boldsymbol{\theta}}) \geq \mathbf{I}^{-1}(\boldsymbol{\theta}) \tag{57.1}$$

where $\mathrm{cov}(\cdot)$ indicates covariance of the estimator, the matrix inequality $\mathrm{cov}(\hat{\boldsymbol{\theta}}) \geq \mathbf{I}^{-1}(\boldsymbol{\theta})$ indicates that $\mathrm{cov}(\hat{\boldsymbol{\theta}}) \geq \mathbf{I}^{-1}(\boldsymbol{\theta})$ is positive semidefinite, superscript $^{-1}$ indicates inversion of the matrix, $\mathbf{I}(\boldsymbol{\theta})$ indicates the $p \times p$ Fisher information matrix (FIM), and it is defined as follows

$$[\mathbf{I}(\boldsymbol{\theta})]_{ij} = -E\left[\frac{\partial^2 \ln p(\mathbf{X}|\boldsymbol{\theta})}{\partial\theta_i \partial\theta_j}\right], \quad i = 1, 2, \ldots, p;\ j = 1, 2, \ldots, p \tag{57.2}$$

where $E[\cdot]$ indicates expected value.

Consider the problem of positioning, the parameters to be estimated are the positions $\mathbf{p} = [\mathbf{p}_1\, \mathbf{p}_2 \ldots \mathbf{p}_P]^T$ and clock bias $\mathbf{b} = [b_1\, b_2 \ldots b_P]^T$ of agents, where $\mathbf{p}_i = [x_i\ y_i\ z_i]^T$ for three-dimensional positioning, and $[\mathbf{p}_i,\ b_i]^T$ are parameters related to agent i, $1 \leq i \leq p$. Particularly, the parameters to be estimated can be indicated as $\boldsymbol{\theta} = [\mathbf{p}_1\, b_1\, \mathbf{p}_2\, b_2 \ldots \mathbf{p}_P\, b_P]^T$ or $\boldsymbol{\theta} = [\underbrace{x_1\, x_2 \ldots x_P}_{\mathbf{x}}\ \underbrace{y_1\, y_2 \ldots y_P}_{\mathbf{y}}\ \underbrace{z_1\, z_2 \ldots z_P}_{\mathbf{z}}\ \underbrace{b_1\, b_2 \ldots b_P}_{\mathbf{b}}]^T$, the above two representations will lead to different FIMs. However, the CRB for estimation of the parameters related to every agent should be equal in the two cases.

The former representation was utilized in [5]. In this paper, the second representation of parameters is used and the FIM will have the following form if partitioned into blocks

$$\mathbf{I} = \begin{bmatrix} \mathbf{I}_{xx} & \mathbf{I}_{xy} & \mathbf{I}_{xz} & \mathbf{I}_{xb} \\ \mathbf{I}_{xy}^T & \mathbf{I}_{yy} & \mathbf{I}_{yz} & \mathbf{I}_{yb} \\ \mathbf{I}_{xz}^T & \mathbf{I}_{yz}^T & \mathbf{I}_{zz} & \mathbf{I}_{zb} \\ \mathbf{I}_{xb}^T & \mathbf{I}_{yb}^T & \mathbf{I}_{zb}^T & \mathbf{I}_{bb} \end{bmatrix} \tag{57.3}$$

Let $H(k) = H(k\_GNSS) \cup H(k\_ter)$, where $H(k\_GNSS) = \{\text{s: s denotes the satellite that can be observed by agent k}\}$, $H(k\_ter) = \{\text{j: j denotes the agent that makes peer-to-peer measurement with agent k}\}$, $1 \le k, j \le p$. By convention, an agent cannot make peer-to-peer measurement with itself, thus $k \notin H(k\_ter)$. Let σ^2 denotes the variance of measurement noise, $I_{H(k\_ter)}(l) = \begin{cases} 1 & l \in H(k\_ter) \\ 0 & else \end{cases}$. The elements of (3) are

$$[\mathbf{I}_{xx}]_{k,l} = \begin{cases} \frac{1}{\sigma^2}\sum \frac{(x_k - x_i)^2}{\|\mathbf{p}_k - \mathbf{p}_i\|^2}, & i \in H(k), \ \ k = l \\ -\frac{1}{\sigma^2} I_{H(k\_ter)}(l) \frac{(x_k - x_l)^2}{\|\mathbf{p}_k - \mathbf{p}_l\|^2}, & k \ne l \end{cases}$$

$$[\mathbf{I}_{xy}]_{k,l} = \begin{cases} \frac{1}{\sigma^2}\sum \frac{(x_k - x_i)(y_k - y_i)}{\|\mathbf{p}_k - \mathbf{p}_i\|^2}, & i \in H(k), \ \ k = l \\ -\frac{1}{\sigma^2} I_{H(k\_ter)}(l) \frac{(x_k - x_l)(y_k - y_i)}{\|\mathbf{p}_k - \mathbf{p}_l\|^2}, & k \ne l \end{cases}$$

$$[\mathbf{I}_{xz}]_{k,l} = \begin{cases} \frac{1}{\sigma^2}\sum \frac{(x_k - x_i)(z_k - z_i)}{\|\mathbf{p}_k - \mathbf{p}_i\|^2}, & i \in H(k), \ \ k = l \\ -\frac{1}{\sigma^2} I_{H(k\_ter)}(l) \frac{(x_k - x_l)(z_k - z_l)}{\|\mathbf{p}_k - \mathbf{p}_l\|^2}, & k \ne l \end{cases}$$

$$[\mathbf{I}_{xb}]_{k,l} = \begin{cases} -\frac{1}{\sigma^2}\sum \frac{x_k - x_i}{\|\mathbf{p}_k - \mathbf{p}_i\|}, & i \in H(k\_GNSS), \ \ k = l \\ 0, & k \ne l \end{cases}$$

$$[\mathbf{I}_{yy}]_{k,l} = \begin{cases} \frac{1}{\sigma^2}\sum \frac{(y_k - y_i)^2}{\|\mathbf{p}_k - \mathbf{p}_i\|^2}, & i \in H(k), \ \ k = l \\ -\frac{1}{\sigma^2} I_{H(k\_ter)}(l) \frac{(y_k - y_l)^2}{\|\mathbf{p}_k - \mathbf{p}_l\|^2}, & k \ne l \end{cases}$$

$$[\mathbf{I}_{yz}]_{k,l} = \begin{cases} \frac{1}{\sigma^2}\sum \frac{(y_k - y_i)(z_k - z_i)}{\|\mathbf{p}_k - \mathbf{p}_i\|^2}, & i \in H(k), \ \ k = l \\ -\frac{1}{\sigma^2} I_{H(k\_ter)}(l) \frac{(y_k - y_l)(z_k - z_l)}{\|\mathbf{p}_k - \mathbf{p}_l\|^2}, & k \ne l \end{cases}$$

$$[\mathbf{I}_{yb}]_{k,l} = \begin{cases} -\frac{1}{\sigma^2}\sum \frac{y_k - y_i}{\|\mathbf{p}_k - \mathbf{p}_i\|}, & i \in H(k\_GNSS), \ \ k = l \\ 0, & k \ne l \end{cases}$$

$$[\mathbf{I}_{zz}]_{k,l} = \begin{cases} \frac{1}{\sigma^2}\sum \frac{(z_k - z_i)^2}{\|\mathbf{p}_k - \mathbf{p}_i\|^2}, & i \in H(k), \ \ k = l \\ -\frac{1}{\sigma^2} I_{H(k\_ter)}(l) \frac{(z_k - z_l)^2}{\|\mathbf{p}_k - \mathbf{p}_l\|^2}, & k \ne l \end{cases}$$

$$[\mathbf{I}_{zb}]_{k,l} = \begin{cases} -\frac{1}{\sigma^2}\sum \frac{z_k - z_i}{\|\mathbf{p}_k - \mathbf{p}_i\|}, & i \in H(k\_GNSS), \ \ k = l \\ 0, & k \ne l \end{cases}$$

$$[\mathbf{I}_{bb}]_{k,l} = \begin{cases} \sum \frac{1}{\sigma^2}, & i \in H(k\_GNSS), \ \ k = l \\ 0, & k \ne l \end{cases}$$

where $1 \le k, l \le p$.

Let **J** be the CRB matrix obtained by inversion of **I**, after removing rows and columns corresponding to non-estimable parameters. According to the CRB theorem, for any unbiased estimator $(\hat{\mathbf{x}},\ \hat{\mathbf{y}},\ \hat{\mathbf{z}},\ \hat{\mathbf{b}})$, it follows from

$$\operatorname{cov}\begin{bmatrix}\hat{\mathbf{x}}\\ \hat{\mathbf{y}}\\ \hat{\mathbf{z}}\\ \hat{\mathbf{b}}\end{bmatrix} \geq \mathbf{J} \tag{57.4}$$

In such case, the horizontal component, vertical component and bias component of the positioning accuracy for agent m can be respectively denoted as

$$\sigma_{CRLB-hor}(m) = \sqrt{\mathbf{J}(m,m) + \mathbf{J}(m+p, m+p)} \tag{57.5}$$

$$\sigma_{CRLB-vert}(m) = \sqrt{\mathbf{J}(m+2p, m+2p)} \tag{57.6}$$

$$\sigma_{CRLB-bias}(m) = \sqrt{\mathbf{J}(m+3p, m+3p)} \tag{57.7}$$

57.4 Theoretic Studies on the Superior Performance of the Accuracy in Cooperative Positioning

Generally speaking, based on the derived CRB in cooperative positioning, there are two methods to further demonstrate the relationship of the bound of traditional positioning and cooperative positioning: (1) study the relationship through mathematical methods; (2) study the relationship through numerical example. In reference [5], the latter method was utilized. In the authors' opinion, a systematic analysis of the former method is called for, and this section reports our efforts along this direction.

Considering Eqs. (57.5–57.7) in reference [5], let $\mathbf{A} = diag\{\mathbf{F}_1, \ldots, \mathbf{F}_M\}$, and $\mathbf{B} = \begin{bmatrix}\mathbf{F}_{11} & \cdots & \mathbf{F}_{1M}\\ \vdots & \ddots & \vdots\\ \mathbf{F}_{M1} & \cdots & \mathbf{F}_{MM}\end{bmatrix}$.

The the CRB matrix of traditional (non-cooperative) positioning can be expressed as:

$$\mathbf{J}_1 = \mathbf{A}^{-1} \tag{57.8}$$

And the the CRB matrix of cooperative positioning can be expressed as:

$$\mathbf{J}_2 = (\mathbf{A} + \mathbf{B})^{-1} \tag{57.9}$$

Note that for the matrix $\mathbf{A}$ and $\mathbf{A}+\mathbf{B}$ that CRB can be determined, it can be derived that matrices $\mathbf{A}$ and $\mathbf{B}$ are both positive definite.

Moreover, from the derivation of matrix $\mathbf{A}$ and $\mathbf{B}$, it can be seen that both the two matrices are symmetric.

Theorem 1 *For n-dimensional positive definite symmetric matrices* $\boldsymbol{A}$ *and* $\boldsymbol{B}$*, let* $\mathbf{J}_1 = \mathbf{A}^{-1}, \mathbf{J}_2 = (\mathbf{A}+\mathbf{B})^{-1}$*, then every element in the diagonal of* $\boldsymbol{J}_1$ *is larger than the corresponding element in the diagonal of* $\boldsymbol{J}_2$*.*

Proof Let $e_i = [0 \quad \cdots \quad 0 \quad 1 \quad 0 \quad \cdots \quad 0]^T$ denote a $n \times 1$ matrix, where all the elements are 0 except that the ith is 1, the proof of Theorem 1 is equal to prove:

$$e_i^T(\mathbf{A}+\mathbf{B})^{-1}e_i < e_i^T\mathbf{A}^{-1}e_i \tag{57.10}$$

$\forall i = 1, 2, \ldots, n$.

Equation (57.10) is equal to :

$$e_i^T\left[\mathbf{A}^{-1} - (\mathbf{A}+\mathbf{B})^{-1}\right]e_i > 0 \tag{57.11}$$

Note that in Eq. (57.11), the following equation is derived as:

$$\begin{aligned}
&\mathbf{A}^{-1} - (\mathbf{A}+\mathbf{B})^{-1} \\
&= \left[\mathbf{A}^{-1}\mathbf{A} - (\mathbf{A}+\mathbf{B})^{-1}\mathbf{A}\right]\mathbf{A}^{-1} \\
&= \left[\mathbf{I} - (\mathbf{A}+\mathbf{B})^{-1}\mathbf{A}\right]\mathbf{A}^{-1} \\
&= (\mathbf{A}+\mathbf{B})^{-1}[(\mathbf{A}+\mathbf{B}) - \mathbf{A}]\mathbf{A}^{-1} \\
&= (\mathbf{A}+\mathbf{B})^{-1}\mathbf{B}\mathbf{A}^{-1}
\end{aligned}$$

Then Eq. (57.11) is equal to:

$$e_i^T\left[(\mathbf{A}+\mathbf{B})^{-1}\mathbf{B}\mathbf{A}^{-1}\right]e_i > 0 \tag{57.12}$$

It can be easily proven that $\mathbf{A}^{-1} - (\mathbf{A}+\mathbf{B})^{-1}$ is symmetric, $(\mathbf{A}+\mathbf{B})^{-1}$ and $\mathbf{A}^{-1}$ are positive definite symmetric matrices. Then the problem in (57.12) is equal to prove that $(\mathbf{A}+\mathbf{B})^{-1}\mathbf{B}\mathbf{A}^{-1}$ is positive definite. The proof is given in the follow:

Assume matrices $\mathbf{E}$ and $\mathbf{F}$ are positive definite symmetric, the goal is to prove that $\mathbf{EF}$ is positive definite.

Utilizing Cholesky decomposition, we can obtain that $\mathbf{E} = \mathbf{P}^T\mathbf{P}, \mathbf{F} = \mathbf{Q}^T\mathbf{Q}$.

And $\mathbf{EF} = \mathbf{P}^T\mathbf{P}\mathbf{Q}^T\mathbf{Q}$, then, $\mathbf{QEFQ}^{-1} = \mathbf{QP}^T\mathbf{PQ}^T = \left(\mathbf{QP}^T\right)\left(\mathbf{QP}^T\right)^T$, it can be seen that $\mathbf{EF}$ is similar to $\left(\mathbf{QP}^T\right)\left(\mathbf{QP}^T\right)^T$.

Then we can draw the conclusion that $\mathbf{EF}$ is positive definite, from which we can obtain Theorem 1. □

From theorem 1, the benefits of cooperation can be shown. In cooperative case, the elements in the diagonal of CRB matrix are always smaller than that of traditional case, which indicates that the performance of theoretical positioning accuracy bound of every device is better due to cooperation.

57.5 Conclusions

Cooperative positioning is an effective way to improve the positioning performance in harsh environments. Fundamental positioning accuracy is focused in this paper, and CRB is utilized as a theoretic tool. We described the problem formulation for the hybrid GNSS-terrestrial cooperative positioning firstly, and then reviewed the calculation of CRB. We analyzed CRB on positioning accuracy in two forms, and derived an expression in one form. Since a systematic analysis, rather than solely numerical simulation is called for, we further perform a proof on the relationship of the bound on cooperative positioning and traditional positioning. To the best of our knowledge, the proof is derived for the first time.

Several issues we plan to address in future mainly include performing experiments related to cooperative positioning.

References

1. Quebe S, Campbell J, DeVilbiss S et al (2010) Cooperative GPS navigation. In: IEEE/ION PLANS, pp 834–837
2. Kurazume R, Nagata S, Hirose S (1994) Cooperative positioning with multiple robots. In: Proceedings of the IEEE international conference on robotics and automation, Los Alamitos, pp 1250–1257
3. Wymeersch H, Lien J, Win MZ (2009) Cooperative localization in wireless networks. Proc IEEE 97(2):427–450
4. Win MZ, Conti A, Mazuelas S et al (2011) Network localization and navigation via cooperation. IEEE Commun Mag 49(5):56–62
5. Penna F, Caceres MA, Wymeersch H (2010) Cramer-Rao bound for hybrid GNSS-terrestrial cooperative positioning. IEEE Commun Lett 14(11):1005–1007
6. Wang T (2012) Cramér-Rao bound for localization with a priori knowledge on biased range measurements. IEEE Trans Aerosp Electron Syst 48(1):468–476
7. Shen Y (2010) Fundamental limits of wideband localization–part II: cooperative networks. IEEE Trans Inf Theory 56(10):4981–5000
8. Larsson EG (2004) Cramér-Rao bound analysis of distributed positioning in sensor networks. IEEE Signal Process Lett 11(3):334–337

Chapter 58
A Cooperative Vehicular Technique for Direction

Dengyun Lei, Weijun Lu, Yanbin Zhang and DunShan Yu

Abstract Due to the shadowing in the urban environment, the GNSS receiver positioning accuracy is poor which is unable to meet the critical applications in vehicle network. To meet the accuracy of relative positioning in critical vehicles application, a variety of wireless ranging methods is being applied to the vehicle navigation. However, they not get the direction information between cars. In this paper, a method that combines wireless ranging and difference pseudorange is presented. This method increase the accuracy of direction information in the relative positioning and can be implemented in the case of only 2–3 shared satellites which expand the cooperation positioning application. Compared with traditional method, the variance of Azimuth is reduced by 50 %.

Keywords Pseudorange difference · Direction method · Cooperation position

58.1 Introduction

Global Navigation Satellite System (GNSS) is widely used in vehicle navigation. However, due to signal blocked and multipath interference in urban, the GNSS position bias is tens to hundreds meters, or even can not locating. Low positioning accuracy and availability limit the use of GNSS in vehicle safety systems, such as anti-collision detection, life safety. In order to meet the needs in critical areas, a series off point-point ranging method [1] is used to improve the ability of relative

D. Lei · Y. Zhang · D. Yu
Institute of Microelectronics, Peking University, Beijing, China
e-mail: dengyun.lei@pku.edu.cn

W. Lu (✉)
School of Electronics Engineering, Beijing University of Posts and Telecommunication, Beijing, China
e-mail: luwj526@gmail.com

J. Sun et al. (eds.), *China Satellite Navigation Conference (CSNC) 2014 Proceedings: Volume III*, Lecture Notes in Electrical Engineering 305,
DOI: 10.1007/978-3-642-54740-9_58,

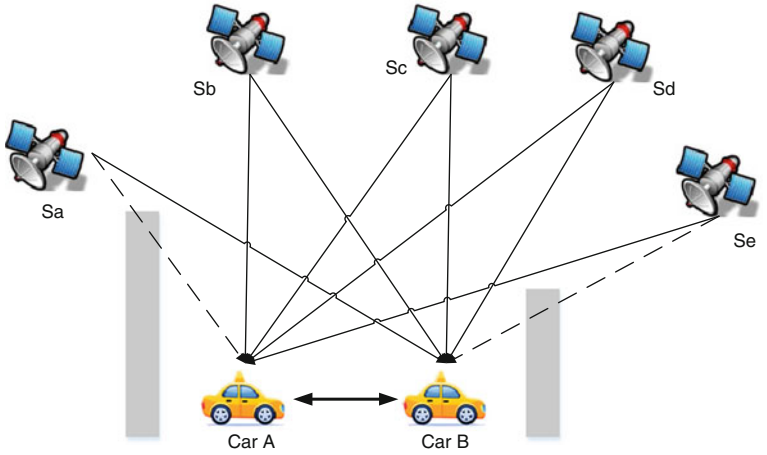

Fig. 58.1 Different satellite constellations in signal blocked environment

positioning between the vehicle. Those ranging method mainly based wireless network signal characteristics, including Received Signal Strength Indication [2] (RSSI), Angle of Arrival [3] (AOA), Time of arrival [4] (TOA) and Time Difference of Arrival (TDOA).

Those ranging technologies have made considerable progress. In addition to the ranging between vehicles, the direction information also plays a key role in the security field. Direction measurement often require special equipment which limits applications. In AOA method, the technique requires an antenna array to measure the signal arrival direction that is not widely adopted. TOA and TDOA technology itself can only measure the relative distance between vehicles. In order to measure the direction relationship between vehicles, multi-node network is often required, or a fixed node is needed. While, the topology of vehicle network changes rapidly, so the technology is greatly limited.

Cooperative Positioning (CP) as a new technology is also widely used in vehicle networking. GNSS technology can be obtained using the relative position vector between vehicles. Difference pseudorange method which can eliminate common errors between receiver and improve the measurement accuracy, has been widely adopted [5, 6]. Unlike DGPS algorithm, the program does not need to adjust the ambiguity solution and can quickly locate. The actual environment in urban is shown in Fig. 58.1, that the buildings on both sides block satellites and cause the shared satellite between receivers focused on the top and along roadside. Vehicle A, B can be located independently, but the CP method requires four or more shared satellites that can not be used.

In this paper, a novel direction method that use wireless ranging and difference pseudorange, is presented. The method can provide more reliable orientation information with 2 or 3 shared satellites.

58.2 Direction Model Based on Pseudorange Difference

In this section, the difference pseudorange method is described and then we built the system model for direction propose. In addition, the system bias is discussed.

58.2.1 Difference Pseudorange Model

The receiver measures signal transmission time between satellites and receiver and then the location is obtained using the triangulation method. Since the local time and satellite time the vehicle is not synchronized, the measurement distance is not the true distance. For a single satellite, the pseudorange can be expressed as:

$$P_a^s = R_{sa} + \Delta t_a + I_s + T_s + n_{sa} \tag{58.1}$$

where P_a^s is the pseudorange of satellite S and receiver A, R_{sa} is the distance between receiver and satellite, Δt_a is the timing difference, I_s is ionospheric delay error, T_s is tropospheric delay error, n_{sa} is noise.

Due to the distance of vehicle is close, the ionospheric and tropospheric delay error is same for vehicles. For a shared satellites, the satellites position and timing error is same. The pseudorange can be divided into two parts: common and non common error. The common error can be eliminated using single difference pseudorange method. The difference pseudorange is given:

$$\begin{aligned} S_{ab}^s &= P_a^s - P_b^s = (R_{sa} - R_{sb}) + (\Delta t_a - \Delta t_b) + (n_{sa} - n_{sb}) \\ &= \Delta R_{ab}^s + \Delta t_{ab} + n_{ab}^s \end{aligned} \tag{58.2}$$

where S_{ab}^s is the single difference pseudorange of satellite S, ΔR_{ab}^s is the distance difference, Δt_{ab} is the timing difference between receiver A and B, n_{ab}^s is the non-common error, including receiver noise and multipath error.

In Fig. 58.2, the relationship of receivers and satellite can be expressed as:

$$\vec{r} = \vec{S}_{sb} - \vec{S}_{sa} \tag{58.3}$$

Considering the distance between vehicle and satellites is larger than that of vehicles, $\vec{S}_{sa}$ and $\vec{S}_{sb}$ is considered in parallel. The S_{ab}^s is equal to the projection of $\vec{r}$ in $\vec{S}_{sa}$ (point D), as:

$$\Delta R_{ab}^s = \vec{r} \cdot (-1 \cdot \vec{S}_{sa} \Big/ R_{sa}) \tag{58.4}$$

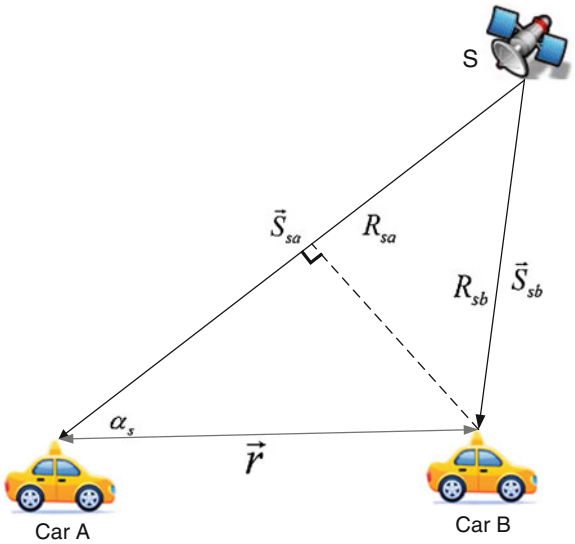

Fig. 58.2 One shared satellite of two cars

where α_s is the angle between $\vec{r}$ and $\vec{S}_{sa}$. $-1 \cdot \vec{S}_{sa} \Big/ R_{sa}$ is direction vector of the vehicle A and satellites S, express as:

$$\begin{cases} \mathrm{x_s} = \cos\theta_s \cos\varphi_s \\ \mathrm{y_s} = \cos\theta_s \sin\varphi_s \\ \mathrm{z_s} = \sin\theta_s \end{cases} \tag{58.5}$$

where θ_s and φ_s are elevation and azimuth of satellite respectively.

The system model can:

$$\begin{bmatrix} S_{ab}^{s1} \\ S_{ab}^{s2} \\ \vdots \\ S_{ab}^{sn} \end{bmatrix} = H \begin{bmatrix} \vec{r} \\ \Delta t_{ab} \end{bmatrix} \tag{58.6}$$

where:

$$H = \begin{bmatrix} -1 \cdot \vec{S}_{s1a} \Big/ R_{s1a}, 1 \\ -1 \cdot \vec{S}_{s2a} \Big/ R_{s2a}, 1 \\ \vdots \\ -1 \cdot \vec{S}_{sna} \Big/ R_{s4a}, 1 \end{bmatrix} \tag{58.7}$$

If the number of shared satellites is greater then four, the $\vec{r}$ can be given [6]:

$$\begin{bmatrix} \vec{r} \\ \Delta t_{ab} \end{bmatrix} = (H^T H)^{-1} H^T \begin{bmatrix} S_{ab}^{s1} \\ S_{ab}^{s2} \\ \vdots \\ S_{ab}^{sn} \end{bmatrix} \tag{58.8}$$

$\vec{r}$ is also equal to:

$$\begin{cases} \mathrm{x_r} = r\cos\theta_B \cos\varphi_B \\ \mathrm{y_r} = r\cos\theta_B \sin\varphi_B \\ \mathrm{z_r} = r\sin\theta_B \end{cases} \tag{58.9}$$

where θ_B is elevation of B, φ_B is azimuth, r is $|\vec{r}|$. The direction can be given by Eqs. (58.8) and (58.9).

58.2.2 Direction Method

The pseudorange difference method can give a accurate relative position, but it needs four shared satellites which maybe not satisfied in urban. Therefore, a new method is introduced using the distance information from wireless ranging method. The new method can provide direction information with 2 or 3 shared satellites.

Replacement of Eqs. (58.5) and (58.9) in (58.4) to establish the relationship between the vehicle position and pseudorange difference:

$$rf(\theta_B, \varphi_B, \theta_s, \varphi_s) = \Delta R_{ab}^s \tag{58.10}$$

where:

$$\begin{aligned} f(\theta_B, \varphi_B, \theta_s, \varphi_s) = {} & \sin\theta_B \sin\theta_s \\ & + \cos\theta_B \sin\varphi_B \cos\theta_s \sin\varphi_s + \cos\theta_B \cos\varphi_B \cos\theta_s \cos\varphi_s \end{aligned} \tag{58.11}$$

The relationship between direction and pseudorange with a shared satellites can be given:

$$rf(\theta_B, \varphi_B, \theta_s, \varphi_s) = S_{ab}^s - \Delta t_{ab} - n_{ab}^s \tag{58.12}$$

The timing difference Δt_{ab} can be removed using double difference method. The results is:

$$r\{f(\theta_B, \varphi_B, \theta_s, \varphi_s) - f(\theta_B, \varphi_B, \theta_p, \varphi_p)\} = S_{ab}^s - S_{ab}^p - n_{ab}^s + n_{ab}^p \tag{58.13}$$

The distance between vehicles can be given by wireless ranging, the unknown variables is azimuth and elevation. If the number of shared satellites is larger than 2, the following equation can be produced:

$$\begin{cases} r\{f(\theta_B, \varphi_B, \theta_1, \varphi_1) - f(\theta_B, \varphi_B, \theta_2, \varphi_2)\} = S_{ab}^1 - S_{ab}^2 - n_{ab}^1 + n_{ab}^2 \\ r\{f(\theta_B, \varphi_B, \theta_1, \varphi_1) - f(\theta_B, \varphi_B, \theta_3, \varphi_3)\} = S_{ab}^1 - S_{ab}^3 - n_{ab}^1 + n_{ab}^3 \end{cases} \tag{58.14}$$

Due to the symmetry of trigonometric functions, the azimuth is needed to be extended to [0, 360] range. That the characteristic of pseudorange difference or position result is used to constrain to 180°. The elevation angle is in the range [−90, 90]. The iterative method is used to slove this equation.

When there are only two shared satellites, only one double difference equation can be built. Considering the straight road, the elevation is 0° in most case. Equation (58.11) can be simplified as:

$$f(\theta_B, \varphi_B, \theta_s, \varphi_s) = \sin\varphi_B \cos\theta_s \sin\varphi_s + \cos\varphi_B \cos\theta_s \cos\varphi_s \tag{58.15}$$

58.2.3 System Error Analysis

Systematic errors include two aspects: the error of pseudorange measurement and wireless ranging error.

1. The error of pseudorange measurement

From Eq. (58.13), the measurement is the non-common error between two receivers, including code tracking error and multipath:

$$\varepsilon = n_{ab}^s - n_{ab}^p \tag{58.16}$$

Assuming the pseudorange non-common error meets normal distribution and satisfies independent of each other. ε satisfies the following distribution:

$$\varepsilon \sim N(0, (\sigma_a^s)^2 + (\sigma_b^s)^2 + (\sigma_a^p)^2 + (\sigma_b^p)^2) \tag{58.17}$$

where σ_a^s, σ_b^s, σ_a^p, σ_b^p are pseudorange measurement variance of receiver A or B to satellites S and P.

2. Wireless ranging error

The range between cars is measured by wireless signal, and its error meets the normal distribution:

$$\varepsilon_r \sim N(0, \sigma_r^2) \tag{58.18}$$

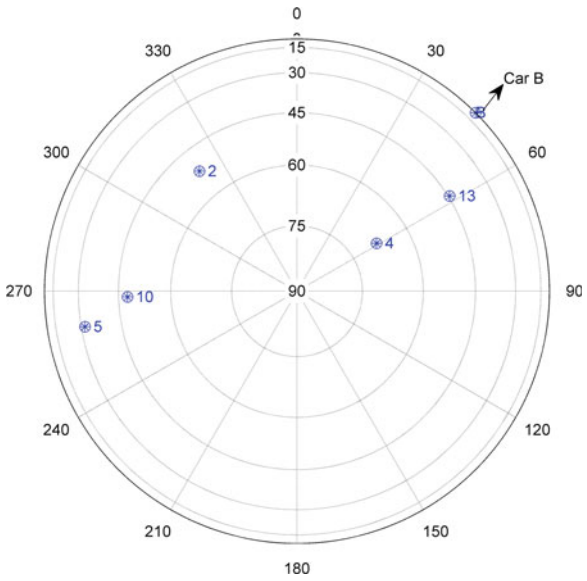

Fig. 58.3 Skyplot of satellites and *car B*

As the wireless signal is affected by the surrounding environment, ranging accuracy deviation will occur. In general, the ranging accuracy is evaluated by the ratio of variance and the real distance.

58.3 Testing and Analysis

In order to verify the effectiveness of the algorithm, different conditions and methods are used. The skyplot of test scenario is shown in Fig. 58.3. The visible satellites number of vehicle A are 2, 4, 10, 13 and that of vehicle B are 2, 4, 5, 10. The shared satellites number is 2, 4, 10. The two vehicles apart 28.3 m, with 45° azimuth, 0° elevation in view of A [7].

In traditional method, the position results is used to calculate the relative direction relationship. The results shown in Fig. 58.4 (the absolutely elevation is used). Since the pseudorange error, the position of vehicles may be overlapped. When this is occur, the azimuth is blur and this phenomenon can be seen in the center of Fig. 58.4.

Because of the high elevation of shared satellites which affected by less multipath effect, the accuracy of pseudorange is high. The common error is the main source error for vehicles. Using double difference method, the common error can be eliminated. As can be seen in Fig. 58.5, the measurement accuracy has improved significantly. Comparison of Figs. 58.5 and 58.6, it can be seen that with the decrease in the inter-vehicle distance measuring accuracy, the calculated azimuth value distribution is diffused and the variance increases.

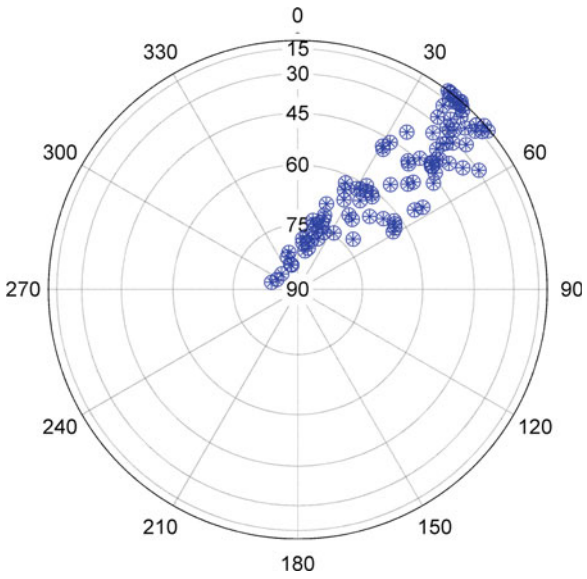

Fig. 58.4 Skyplot of car B using difference position

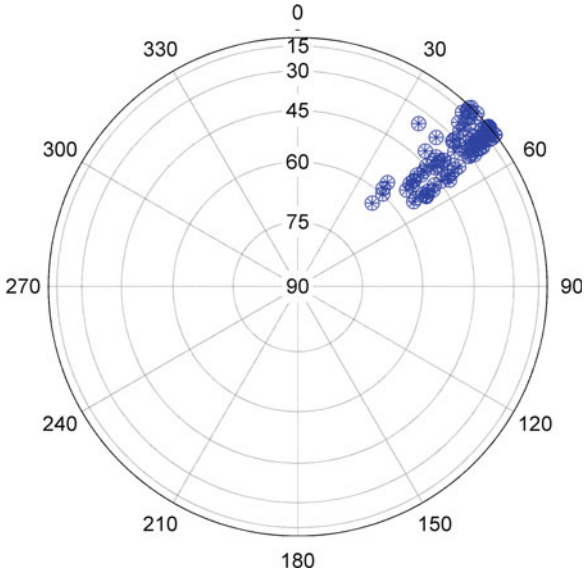

Fig. 58.5 Skyplot of car B using difference pseudorange ($\sigma_r = 0.1r$, $\theta_B = 0°$)

When the elevation increasing, the result of elevation is getting worse because of the distance is decreasing in horizontal plane same as both method in Figs. 58.7 and 58.8, but the performance of difference pseudorange method is better than traditional method.

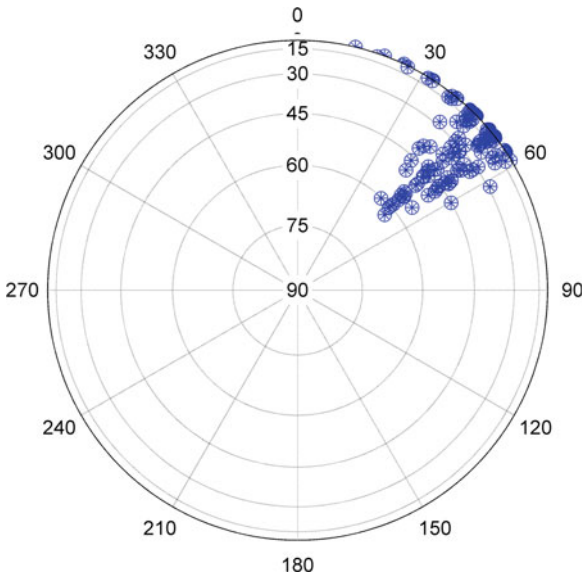

Fig. 58.6 Skyplot of car B using difference pseudorange ($\sigma_r = 0.2r$, $\theta_B = 0°$)

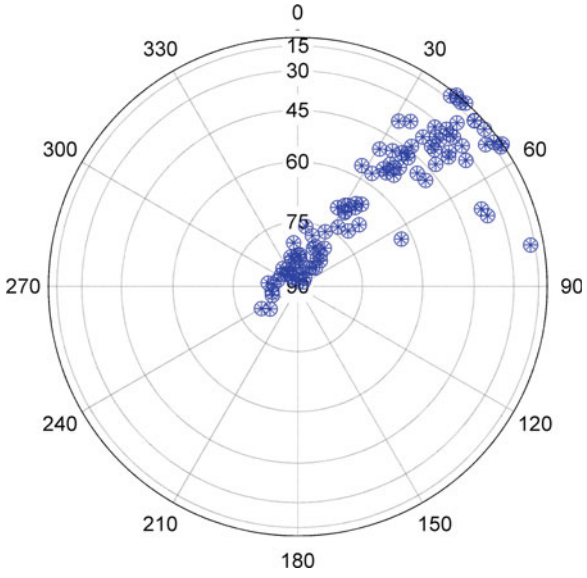

Fig. 58.7 Skyplot of car B using difference position ($\theta_B = 45°$)

Table 58.1 shows the mean and variance of the azimuth and elevation result under different circumstances. Comparing with the traditional method, the proposed method gives quite satisfactory azimuth. However, the elevation is not credible by both method with large variance.

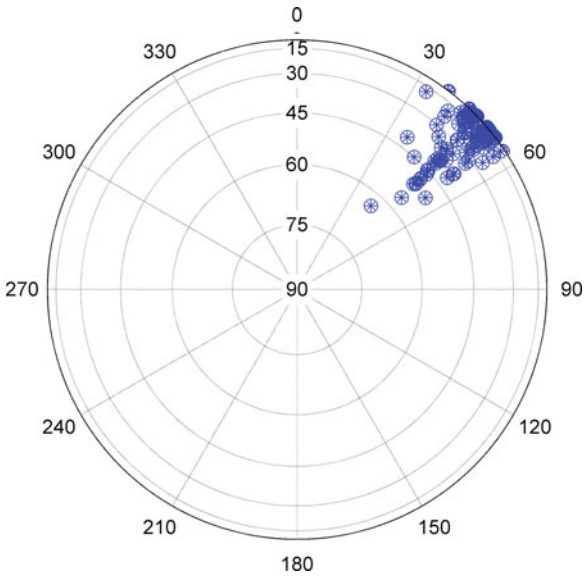

Fig. 58.8 Skyplot of car B using difference pseudorange ($\sigma_r = 0.1r$, $\theta_B = 45°$)

Table 58.1 Mean and variance of elevation and azimuth

Elevation (°)	Method	Azimuth (°)		Elevation (°)	
		Mean	Var	Mean	Var
0	Position-differ	32.28	13.4	27.99	51.19
	Pseudorange-diff σ r = 0.1r	49.97	3.42	−14.58	27.49
	Pseudorange-diff σ r = 0.2r	47.86	6.75	−20.61	27.83
45	Position-differ	38.99	20.26	51.57	44.90
	Pseudorange-diff σ r = 0.1r	47.11	8.01	−16.62	28.90

58.4 Conclusion

This paper presents a pseudorange difference method for measuring direction in vehicle networks. The pseudorange difference method can eliminate the common noise between receiver and get higher accuracy. Combing the pseudorange and wireless ranging information make the method suit in urban with 2–3 shared satellites. Compared with different position method, the performance and stability are improved using proposed method.

References

1. Alam N, Dempster AG (2013) Cooperative positioning for vehicular networks: facts and future. IEEE Trans Intell Syst 14:1–10
2. Xia HH (1996) Analytical model for predicting path loss in urban and suburban environments. In: Proceedings of IEEE international symposium PIMRC, Taiwan, vol 1, pp 19–23
3. Wang X, Wang Z, O'Dea B (2003) A TOA-based location algorithm reducing the errors due to non-line-of-sight (NLOS) propagation. IEEE Trans Veh Technol 52(1):112–116
4. Falsi C, Dardari D, Mucchi L, Win MZ (2006) Time of arrival estimation for UWB localizers in realistic environments. EURASIP J Appl Signal Process 2006:1–13
5. Alam N, Tabatabaei Balaei A, Dempster AG (2011) A DSRC doppler-based cooperative positioning enhancement for vehicular networks with GPS availability. IEEE Trans Veh Technol 60(9):4462–4470
6. Yang D et al (2012) A GPS pseudorange based cooperative vehicular distance measurement technique. In: Vehicular technology conference (VTC spring), Japan
7. Xiaomin M, Xianbo C, Hazem H R (2009) Performance and reliability of DSRC vehicular safety communication: a formal analysis. EURASIP J Wirel Commun Netw 2009:1–13

Chapter 59
A Method of Map Matching in Indoor Positioning

Fengli Ruan, Zhongliang Deng, Qian An, Keji Wang and Xiaoyang Li

Abstract Compared with Outdoor Vehicle Navigation, personal motion state is more complex. The spatial distribution of indoor space environment is relatively complex. The attributes of the room is different from the corridor. This paper studies indoor map matching technology based on personal motion state. The indoor environment abstract space model theory is proposed, in which the Spatial Data of indoor map is studied in detail. The information of the Inertial Measurement Unit from the mobile terminal is combined with the abstract space model to further correct the wireless positioning results. For each compact structure region of indoor space environment and multiple personnel movement state, the method of map-matching proposed in this paper is combined with personnel movement direction, wireless location results and IMU. The optimal positioning point estimation is generated by probabilistic matching algorithm. The proposed map-matching can further restrain the indoor positioning error, and for indoor wireless coverage blind spots, this method can protect the continuity of navigation, improve user experience in indoor positioning and navigation.

Keywords Indoor positioning · Map matching · Inertial measurement unit (IMU) · Indoor abstract space model

59.1 Introduction

Currently, map-matching technology has been widely used in Vehicle Navigation System. Even meter-level positioning error is still difficult to meet the requirements of indoor navigation. Different buildings, The general structure of the indoor space is different with Intensive room and corridor. From the user's point of view, people

F. Ruan (✉) · Z. Deng · Q. An · K. Wang · X. Li
School of Electronic Engineering, Beijing University of Posts and Telecommunications, Beijing 100876, China
e-mail: ruanfenglijiayou@163.com

J. Sun et al. (eds.), *China Satellite Navigation Conference (CSNC) 2014 Proceedings: Volume III*, Lecture Notes in Electrical Engineering 305,
DOI: 10.1007/978-3-642-54740-9_59,

in the hallway, and the people in the room, are two completely different status and experience. In this paper, accelerometer and electronic compass in phones are use to estimate a step size and identify direction. Points, lines, polygons feature in indoor map will be used to build a general indoor environment model, and a method of map matching combined with personal movement state and indoor environment model will be proposed. Experimental results show that this algorithm significantly reduces the positioning error in indoor positioning and navigation system.

59.2 Universal Indoor Structural Model

59.2.1 The key Data for Map Matching to Classify and Process

Although different forms of these objects are not the same, but their geometric characteristics are the same, they are all composed of points, lines, polygons.This paper summarizes the classification of these vector data to establish a common model for indoor map matching and provide reference for map-matching algorithm proposed after.

Point feature: The most critical point feature in the algorithm this paper proposed is the door. Doors can represent the spatial region accessibility. This article defaultly believe that people always pass in and out the room and other such spatial structure through the door. The point set is like:

$$P = \{(\mathrm{x_i}, \mathrm{y_i}) | \, \mathrm{x_i} \in \mathrm{R}, \, \mathrm{y_i} \in \mathrm{R}\} \tag{59.1}$$

Line feature: Map Road network is constituted by a set of two-dimensional sections, each section of road is composed of a series of nodes. The line set is like:

$$L = \{(P_0, P_1), (P_1, P_2), (P_2, P_3) \ldots (P_\mathrm{n}, P_{n+1}) \ldots | \, P_n \in P\} \tag{59.2}$$

Polygon feature: Closed polygon composed of n lines. The polygon is like:

$$Polygon = \{(L_0, L_1 \ldots L_\mathrm{n})\} \tag{59.3}$$

the starting point of L_0 and the terminal point of L_n is coincident.

In this paper, based on the position of the road network, these objects are divided into two categories corridor class and the class room. The space area existing road network is considered corridor class, and the space area is considered room class with no road network. Room class can be expressed as

$$Polygon_{room} = \left\{ Polygon \, | \sum L_{road} \not\subset Ploygon \right\} \tag{59.4}$$

Corridor class can be expressed as

$$Polygon_{\text{corridor}} = \Omega - Polygon_{room} \tag{59.5}$$

59.2.2 The Relationship Among the Various Elements in Indoor Structural Model

The relationship among each elements in interior space model this paper proposed refers to Fig. 59.1. In this model, the internal structure of a building can be simply an abstract $Polygon_{room}$ and $Polygon_{\text{corridor}}$. The key factor of dividing into two categories is whether the space area exists road network. Accessible rooms can be divided into categories such as offices, classrooms etc., inaccessible room categories such as patio, hollow, where person can not reach.

59.2.3 The Abstract Geometric Model of Indoor Structure

The indoor environment model presented in this paper is a simple model that abstracted from the spatial structure of the building. In Fig. 59.2 left, the map contains a very rich amount of information. And in Fig. 59.2 right, it is abstracted by the model of this article which contains only a point, line and plane vector information, and such information is sufficient to meet the needs of indoor map-matching algorithm.

59.3 Get People's Moving State

When people moving indoors, the state of movement is measured by the velocity and direction, which are detected by the frequency estimation step and the step speed reference technical personnel available, this technology has already shown very mature in research. The paper [2, 6] has given a detailed analysis, so we use its conclusions directly. Detection inertial measurement unit (IMU) in the direction of the movement has been a problem. The traditional detection methods must require inertial devices and pedestrian movement direction that remains fixed angle, which in practical applications, clearly has limitations. In paper [1, 4], the proposed method effectively solves the problem of people in the random direction to take the phone, this article will use its conclusions directly. This paper will estimate the state personnel movement, as one of the important factors indoor map matching algorithm mentioned in this article have important reference value.

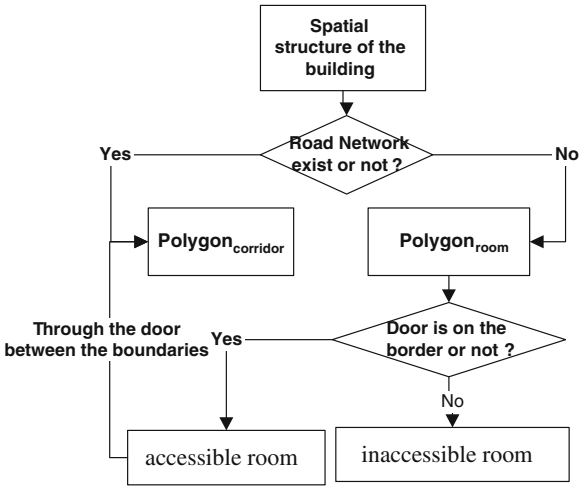

Fig. 59.1 Abstract model of the spatial structure of buildings

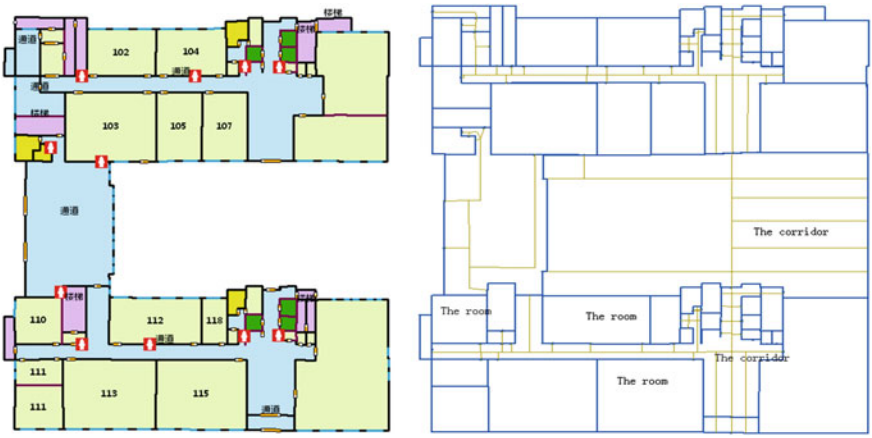

Fig. 59.2 Abstract structural indoor model process

59.4 The Algorithm of Indoor Map-Matching

Currently, the map-matching algorithm commonly used are: direct projection method, correlation algorithms, probability and statistics, fuzzy logic algorithm [3, 5].

59.4.1 Four Precondition Required in Indoor Map Matching Algorithm

(1) People can not inter inaccessible areas where that is inaccessible the room.
(2) People in the process of the corridor and the room switching, people can only perform switching through doors that connected the corridor and the room.
(3) Unify the coordinate system. The proposed map-matching algorithm using a local Cartesian coordinate system, unified to east as the X-axis, Y-axis to the north.

59.4.2 Factors to be Considered in Indoor Map-Matching Algorithm

(1) Direction of pedestrian movement.
(2) The positional relationship between the positioning data queue adjacent points, determines the positioning point in the room or the corridor each time.
(3) Distance between two points adjacent from positioning data queue.

59.4.3 Indoor Map Matching Flow

In Fig. 59.3 Indoor map matching process, the whole process of the indoor map matching, the specific role of each part are as follows:

(1) Get position point the direction of movement at the moment (Fig. 59.4). Usually the angle of movement direction is to the north as 0°, increasing with counterclockwise, less than 2π. The transforming relationship with Cartesian coordinate system:

when $0 \leq \theta \leq \frac{\pi}{2}$, refer to Fig. 59.4 left,

$$\psi = \frac{\pi}{2} - \theta \tag{59.6}$$

when $\frac{\pi}{2} < \theta < 2\pi$, refer to Fig. 59.4 right,

$$\psi = \frac{5\pi}{2} - \theta \tag{59.7}$$

θ is to the east as 0°, ψ is angle converted to Cartesian coordinates.
(2) Positioning error range:

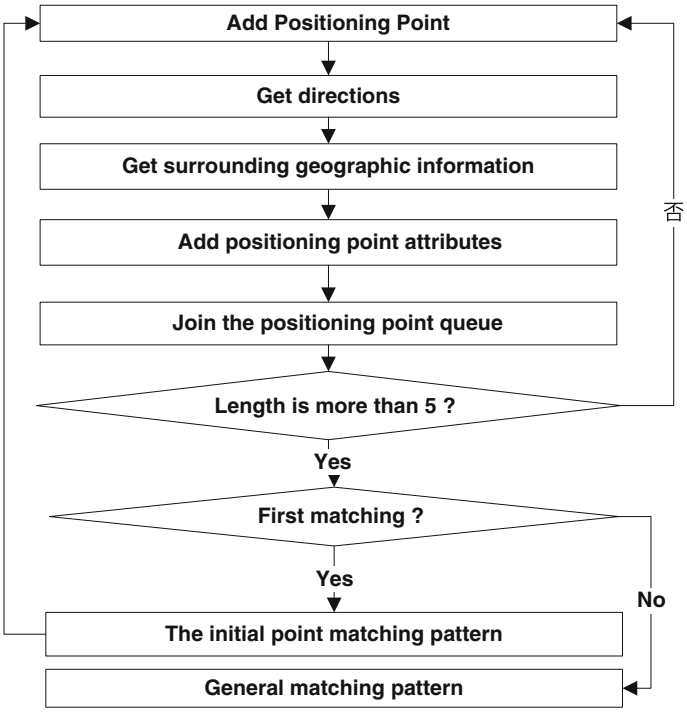

Fig. 59.3 Indoor map matching process

Fig. 59.4 Coordinate conversion

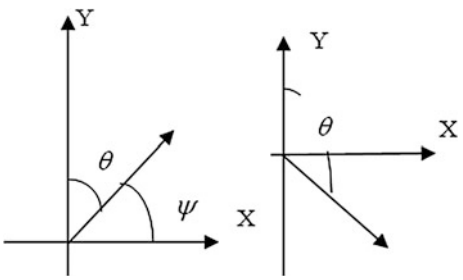

This range is used to search the surrounding geographic information, which is determined by the scope of the error ellipse. Refer to Fig. 59.5.

The Error variance is σ_x^2 on the X-axis, σ_y^2 on the Y-axis.

$$a = k\sqrt{\frac{1}{2}\left(\sigma_x^2 + \sigma_y^2 + \sqrt{(\sigma_x^2 - \sigma_y^2)^2 + 4\sigma_{xy}^2}\right)} \tag{59.8}$$

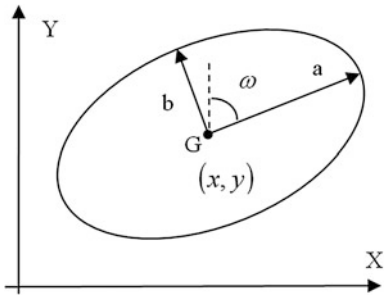

Fig. 59.5 Error oval map

$$b = k\sqrt{\frac{1}{2}\left(\sigma_x^2 + \sigma_y^2 - \sqrt{(\sigma_x^2 - \sigma_y^2)^2 + 4\sigma_{xy}^2}\right)} \tag{59.9}$$

$$\omega = \frac{\pi}{2} - \frac{1}{2}arc\,tan\left(\frac{2\sigma_{xy}}{\sigma_x^2 - \sigma_y^2}\right) \tag{59.10}$$

k is enlargement factor, k can be 3.03 when the Confidence of Oval error range is 99 %.

(3) The initial point matching mode: When a match for the first time, enter the mode. First, determine whether the position point queue length is greater than 5, otherwise continue to load position points and their attributes, when the length is greater than 5, remove the coarse value and averaging, get initial match point (x0, y0).

$$x_0 = \frac{1}{n}\sum_i^n x_i, \quad y_0 = \frac{1}{n}\sum_i^n y_i \tag{59.11}$$

(4) Track matching mode: In this mode two cases will be discussed based on the positional relationship between indoor models and geographic information.

① Positioning points which are adjacent are distributed in two same type regions of space. Refer to Fig. 59.8. Point P is positioning point and line AB is the candidate road. The distance between P and AB is:

$$d = \sqrt{(x - x_0)^2 - (y - y_0)^2} \tag{59.12}$$

The distance weight value is:

$$\omega_d = \frac{1}{1 + d} \tag{59.13}$$

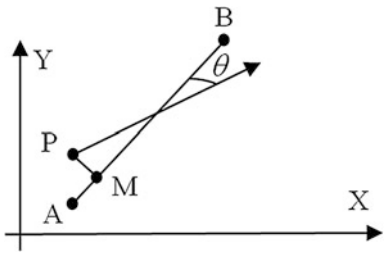

Fig. 59.6 Calculating weights in corridor

In Fig. 59.6. θ is the angle between the direction of positioning point and road. Direction weight value is:

$$\omega_\theta = \cos\theta \tag{59.14}$$

Calculate the distance weight value and direction weight value for all road in error range, select the max, and then positioning point will be projectioned on this road. When the weight value is less than threshold ω, the matched point is keeping with the current point.

② Neighbouring points are in different types of spatial region

Firstly, get two Accessible Boundary information spatial region, and decomposition into two parts, $Polygon_{\text{corridor}}$ and $Polygon_{room}$. The Algorithm needs two steps.

I Positioning point border-crossing judgment, in Fig. 59.7.

For example, the last point is in the corridor, and current point is in the room.If there is no doors in the border between the corridor and the room, positioning point is impossible in the room. Positioning point will be projectioned on the road in the corridor. If the door is available, calculate the vertical angle of the barriers where doors are on them. Take the absolute subtracting the value of positioning point angle and vertical barrier angle $\Delta\theta$. If $\Delta\theta$ is less than angle threshold $\frac{\Delta\phi}{2}$, the positioning point is in the room.Refer to Fig. 59.8.

II The best matching point estimation

Use probability match algorithm to estimate the best position. The formula is: $P_{\text{estimate}} = P_{current} + \nabla\sigma$, $P_{current}$ is the current positioning point,including direction. The Error length $\nabla\sigma$ obey Normal distribution:

$$\nabla\sigma \sim N(\varepsilon, \delta^2) \tag{59.15}$$

ε is the error mean wireless Location Information given and σ is error standard deviation. Refer to Fig. 59.9.

$$\nabla\sigma = \frac{1}{\sqrt{2\pi}\sigma} e^{-\frac{(x-\varepsilon)^2}{2\sigma^2}}, \quad x \in R \tag{59.16}$$

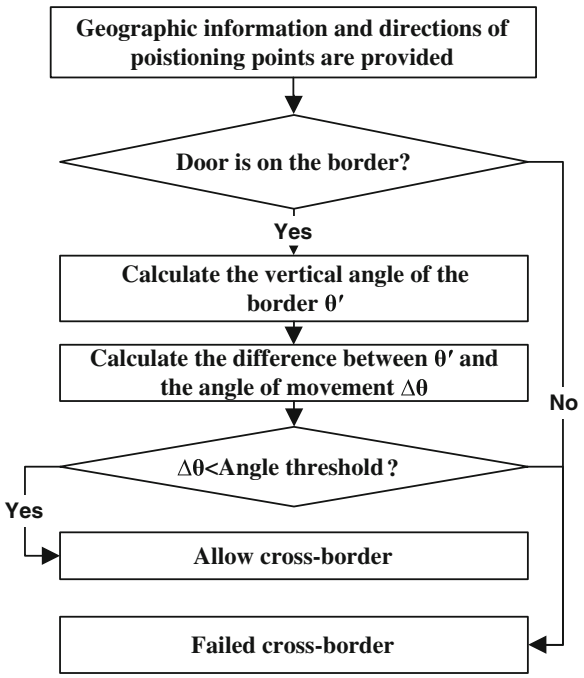

Fig. 59.7 Switch between different spatial categories

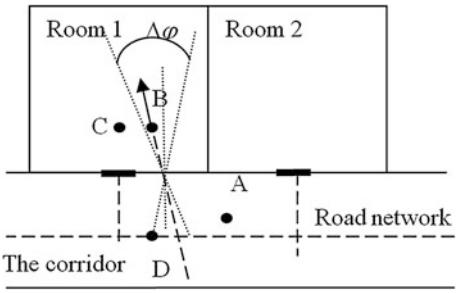

Fig. 59.8 Switch between different spatial categories

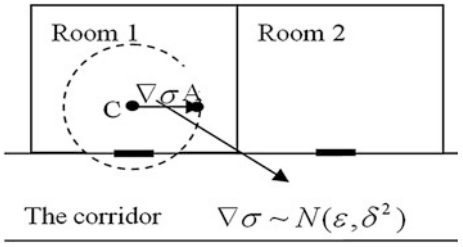

Fig. 59.9 Optimal matching point estimation

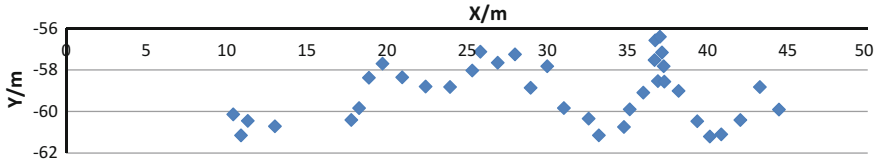

Fig. 59.10 Positioning points distribution before map matching

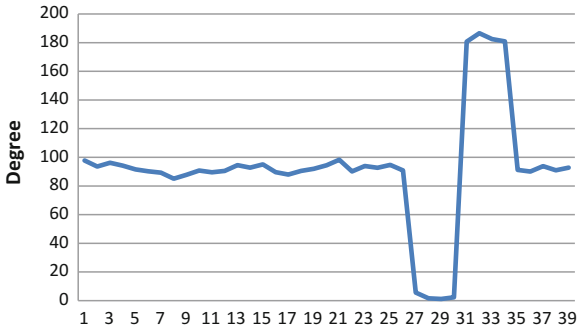

Fig. 59.11 Positioning points angle

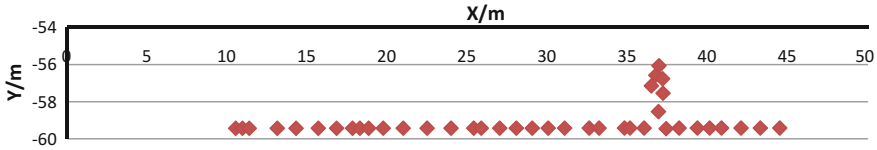

Fig. 59.12 Positioning points distribution after map matching

59.5 Application Examples and Results Analysis

As Figs. 59.10 and 59.11 show, positioning points coordinate and angles are from wireless positioning and sensors. After map matching, positioning points distribution is like Fig. 59.12. In Fig. 59.13, Number 1, the angle of position don't meet the conditions of border change. However, in the range of number 2, The room and the corridor is accessible, besides, $\Delta\theta$ is less than angle threshold $\frac{\Delta\phi}{2}$. In Fig. 59.10, in the range of 13 m $<$ x $<$18 m, signal appears blind area, and then the wireless location algorithm is failed to output the results. The map-matching algorithm this paper proposed makes the positioning points continuously output.

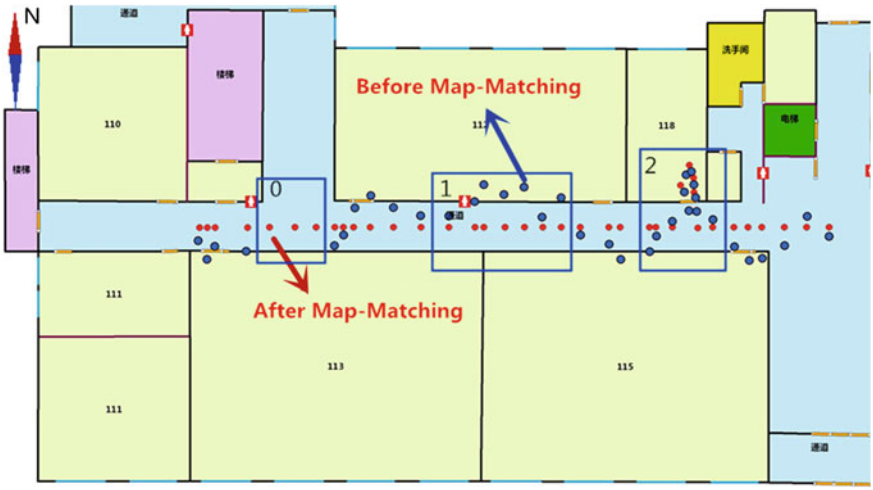

Fig. 59.13 Map matching results

References

1. Chen W (2010) Research on GPS/self-contained sensors based seamless outdoor/indoor pedestrian positioning algorithm. University of Science and Technology of China, AnHui
2. Bao H, Wong WC (2013). An indoor dead-reckoning algorithm with map matching. In: 9th International conference on wireless communications and mobile computing (IWCMC) 1–5 July 2013, pp 1534–1539
3. Jie SU, Dong-fang ZHOU, Chun-sheng Yue (2001) Real-time map-matching algorithm in GPS navigation. Acta Geod Cartogr Sin 30(3):252–256
4. Kamisaka D, Muramatsu S (2011) Design and implementation of pedestrian dead reckoning system on a mobile phone. IEICE Trans Inf Syst 94(6):1137–1146
5. Nan W, Yongfeng W, Jiren L (1999) A point-Based map-matching algorithm. J Northeast Univ (Nat Sci) 20(4):347–349
6. Song Y (2006) Research and application of map-matching algorithm with the inertial navigation sensor information. Beijing Jiaotong University, Beijing

Chapter 60
Pedestrian Dead Reckoning in Handheld Terminal with Inertial Measurement Unit

Keji Wang, Zhongliang Deng, Shengmei Luo, Yanpei Yu and Fengli Ruan

Abstract In this paper, using the pedestrian dead reckoning algorithm based accelerometer and electronic compass composition IMU to assist indoor positioning. Detection pedestrians step length and walking status. Currently detect direction of motion requires the user wear or holding IMU with a fixed posture, To address this issue, proposed terminal gesture recognition algorithm to solve cognitive difficulties problems of direction of movement when handheld terminal with any posture, to get the correct direction of movement. Then combination step count values, step length, direction of movement and wireless positioning results, this system can effectively improve the positioning performance.

Keywords Pedestrian dead reckoning PDR · Inertial navigation · Indoor positioning

60.1 Introduction

Compared with GNSS positioning technology, indoor positioning face more challenges. Including: (1) compared with outdoor electronic map, indoor electronic map has larger scale, more details, higher precision, positioning accuracy is more sensitive to the occurrence of slight jitter positioning results will obviously be reflected in the indoor electronic map, affect the user experience; (2) indoor positioning must correctly identify where the user is located, such as room, corridors, halls, etc. when positioned results close to the border of adjacent regions,

K. Wang (✉) · Z. Deng · Y. Yu · F. Ruan
Beijing University of Posts and Telecommunications, Beijing, China
e-mail: amazure@foxmail.com

S. Luo
Zhongxing Telecom Equipment, Guangzhou, Shenzhen, China

J. Sun et al. (eds.), *China Satellite Navigation Conference (CSNC) 2014 Proceedings: Volume III*, Lecture Notes in Electrical Engineering 305,
DOI: 10.1007/978-3-642-54740-9_60,

relying solely on wireless location technology prone to judging error or switch back and forth between the adjacent regions; (3) in the indoor environment, signal attenuation characteristics and signal distribution is more complex and vulnerable to environmental impact and easy to appear blind spots of wireless signal coverage. Need to use some methods such as pedestrian dead reckoning navigation—assisted positioning technology to protect the continuity and accuracy and enhance the user experience.

60.2 Pedestrian Dead Reckoning

Currently, IMU assisted positioning technology has been applied to indoor positioning [1]. Its basic idea is: acceleration has cyclical changes in walking process, using accelerometer to detection personnel step frequency; pedestrian step estimation model based on the use of walking in the steps of acceleration characteristics estimates; using electronic compass to get the direction of movement of pedestrians. Pedestrian dead reckoning technology in step frequency step length detection has been more mature, the difficulty lies in the direction of motion detection on the user. Current direction of motion detecting required user wear or hand in IMU with a fixed posture, the moving direction of the pedestrian walking is determined to maintain the relationship between the coordinate system in the IMU, and then measuring the relationship between the IMU coordinates and map coordinates via electronic compass, the direction of movement of the pedestrian conversion to the map coordinates. Reference [2], the IMU fixed on the shoe personnel, Ref. [3] The IMU is fixed at the waist personnel, Ref. [4] requires positioning must be oriented to pedestrians when the phone screen, keeping with the direction of movement of pedestrians fixed angle so that the normal direction of movement of pedestrians walking in the IMU coordinate system remain to determine the relationship, and then through the step frequency step length and heading angle, carried dead reckoning. Obviously, there are great limitations described above, due to the randomness of people carry mobile phones and other mobile positioning terminals, the method cannot be widely used mobile phone navigation service.

To solve these problems, this paper analyzes the basic principles of PDR techniques in Sect. 60.2; On this basis, Sect. 60.3 proposed detection algorithm based on the direction of movement of the terminal stance, tested the method in a pedestrian no fixed posture handheld terminal case under the direction of the pedestrian accurate measurement; Sect. 60.4, this method is used to assist in indoor wireless positioning system, effectively improve the positioning performance of the system. This paper uses electronic compass HMC5883L and accelerometer MMA8451Q which can be used in mobile phones and other types of common terminal.

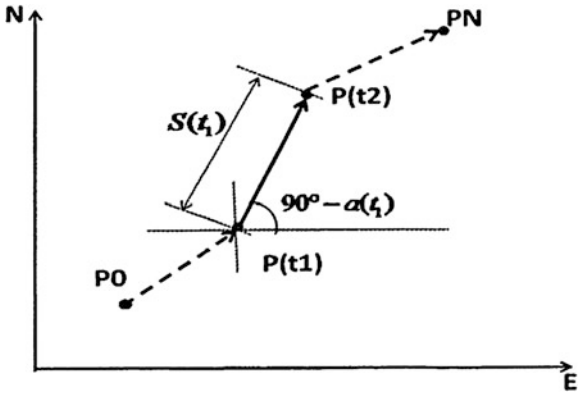

Fig. 60.1 Speculate track by displacement and heading

60.2.1 PDR Principle

Generally considered pedestrian movement a two-dimensional movement, the basic principle is the plane geometry method. Principle: In the case of sampling a short time that pedestrians do linear motion, that the starting point of the location information, the amount of displacement can be obtained within the first minute or the next moment the precise location information and sampling time carrier. The principle is shown in Fig. 60.1. Wherein S(t1) represents the speed between the time t1 to the time t2, a(t1) represents the period pedestrian heading. If known coordinates of the starting point of the pedestrian dead reckoning, you can coordinate the next time a pedestrian was determined by the coordinate transformation matrix.

PDR equation of location of the pedestrian can be expressed as:

$$\begin{cases} E_{k+1} = E_K + S_k \cdot \sin(a_k) \\ N_{k+1} = N_K + S_k \cdot \cos(a_k) \end{cases} \tag{60.1}$$

E_k and N_k represents the North and East coordinate in the ENU coordinate system when the K step of pedestrians, a_k indicates that the step heading, S_k represents the step size of the step.

60.2.2 Pedometer Design

Normal gait having a periodic, each gait cycle (Gait Cycle) can be divided into four phases: foot off the ground (Push-off)—Swing (Swing)—heel-strike (Heel Strike)—Stand (Stance) illustrated in Fig. 60.2.

When pedestrians moving forward, the acceleration shown in Fig. 60.3. The vertical acceleration signal waveform and the advancing direction of pedestrians

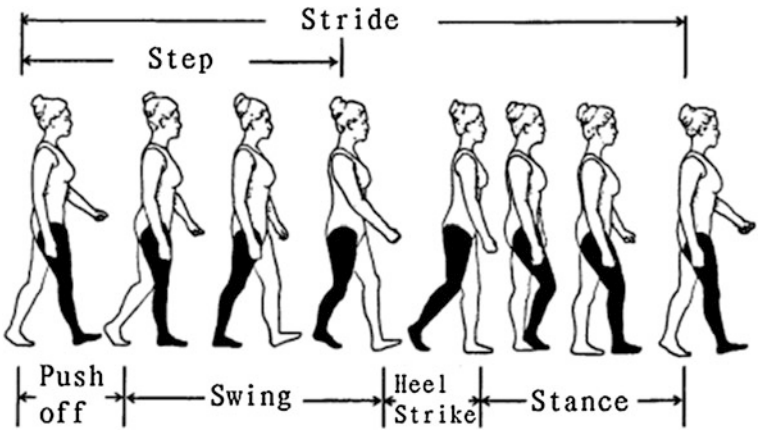

Fig. 60.2 Normal walking gait

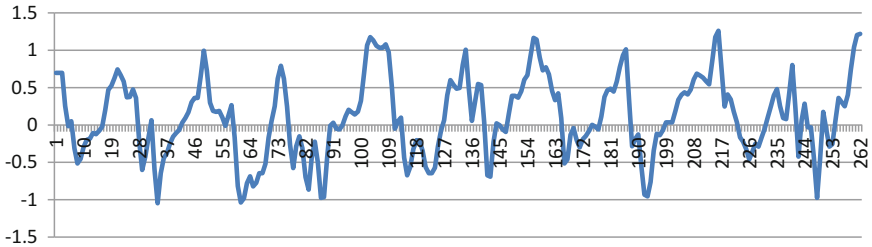

Fig. 60.3 Acceleration in forward direction

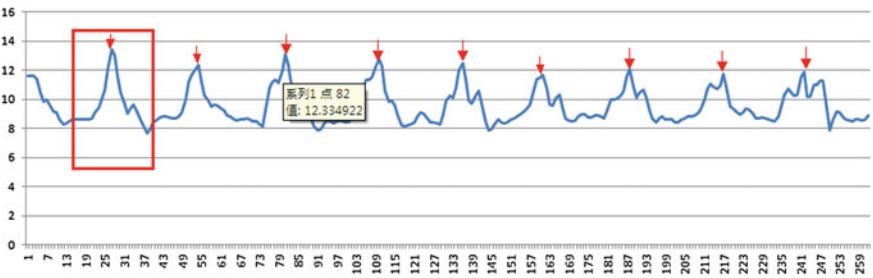

Fig. 60.4 Acceleration in vertical direction

can reflect the periodic gait, calculated using the number of steps of this feature information. Usually used as the count in the vertical direction acceleration detecting step basis in Fig. 60.4, the block move is a change in the acceleration period, the arrows pointing peak acceleration during swing.

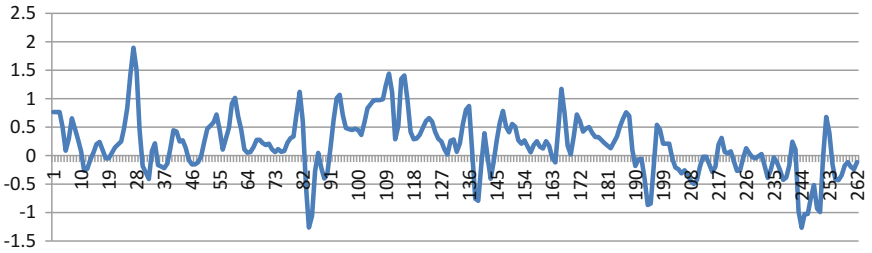

Pedometer algorithm based on the dynamic changes in the sampling frequency of the time window and dynamic acceleration thresholds, ensuring a more accurate pedometer results.

60.2.3 Projections Step Length

According to some researchers of the acceleration waveform pedestrians do a thorough research and found that pedestrians step length and acceleration waveforms with the following rules [5]:

(1) Natural walking stride frequency of 95–125 steps/min, step length range of 50–80 cm, different people step frequency and step length differences, and individual height, mood, habits, road conditions and so on; (2) Natural walking pedestrians little change step length, the standard deviation is small; (3) Peak of the acceleration signal, variance, statistical data and the step frequency step length a good correlation is generally greater than 0.6; (4) Under different road conditions, applicable in different step length the model, as in the plains, where applicable, the model does not apply to the ramp situation.

According to the above rules, the step length is generally estimated using the rules 1's value or using Eq. (60.2) to estimating step length of pedestrian.

$$Step\ Length \approx \sqrt[n]{(A_{\max} - A_{\min})} \times C \tag{60.2}$$

where n = 4, may be modified according to different conditions of the test results; A representative of the sum of the gravity axis, A_{max} is the maximum acceleration value a stride cycle, A_{min} is the minimum acceleration value a stride cycle; C is a constant;

Solving the constant C: N times before the test proceeds in steps cumulative total distance, and make every stride of A are the same, which can be obtained C.

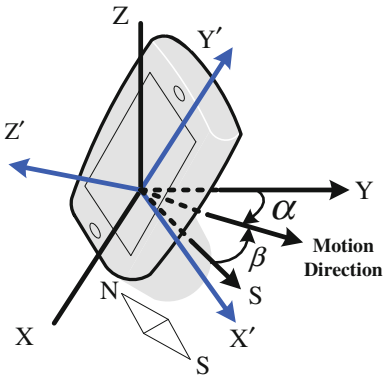

Fig. 60.5 Define the coordinate system

60.3 Projections Direction of Movement

60.3.1 Coordinate System Definition

X′, Y′, Z′ for the corresponding axis IMU in the terminal coordinate system is called the coordinate system A. X, Y, Z axis geographic coordinates, wherein the ground plane is parallel with the XY plane, the coordinate system is called B. A coordinate system to the coordinate system B can be rotated by a linear transformation realized IMU pitch angle (Pitch) and the roll angle (Roll). S is the geoid geographic coordinate system in the direction pointing due south, α is the angle between the direction of horizontal movement and Y axes, $\alpha \in [0°, 360°)$, β is the angle between the horizontal movement of pedestrians and south direction, $\beta \in [0°, 360°)$ (Fig. 60.5).

60.3.2 Terminal Gesture Recognition Algorithm

Solving the problem of pedestrian direction of motion can be described for the sake of horizontal movement and south direction angle β. The figure, the angle between the Y axis and south direction $Ac = \alpha + \beta$ can be carried out by an accelerometer tilt—compensated electronic compass measured. The direction of movement for the sake of solving the problem can be transformed with the horizontal direction of movement of the Y-axis angle α. In the α solving aspects. This article will angle α converting into solving positioning handheld terminal pitch angle (Pitch) and roll angle (Roll) four-quadrant arctangent, namely

Fig. 60.6 Two common held mode

$$\alpha = \arctan 2\frac{Roll}{Pitch} \tag{60.3}$$

Pitch for handheld positioning terminal where the pitch angle, Roll to roll angle of handheld positioning terminal, which is calculated pitch angle and roll angle has been very mature, not repeat them here.

The figure shows the actual direction of movement of pedestrians:

$$\beta = Ac - \alpha \tag{60.4}$$

Ac electronic compass direction in which the output value.

Generally pedestrian held terminal in two modes, portrait mode and landscape mode (Fig. 60.6).

When in the portrait mode according to the grip angle, the pitch angle variation range for the terminal Pitch $\in [0°, 90°)$, at this time the roll angle Roll $\approx 0°$ substituting into Eq. (60.3),

$$\alpha = 0°, \quad \text{that } \beta = Ac$$

In this case the value of the electronic compass direction is the unbiasedness direction of movement of pedestrians.

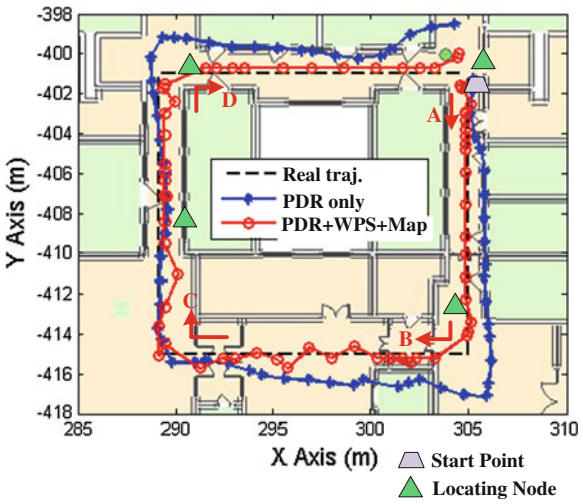

Fig. 60.7 *Curve* system result of standard experiment

When in the landscape mode according to the type of grip angle, such as horizontal and vertical grip, rolling angle range of the terminal Roll $\in [-90°, 90°]$, this time the roll angle Pitch $\approx 0°$ substituting into Eq. (60.3),

$$\begin{cases} \alpha = -90°, & (\text{roll} = -90°) \\ \alpha = 90°, & (\text{roll} = 90°) \end{cases}$$

Substituted α into the formula (60.4) can be obtained at this time the value of the direction of movement of pedestrians. That is the direction of movement of pedestrians at this time is the value of the electronic compass direction minus deviation angle α. Similarly, at any angle landscape mode and portrait mode can be used between the manner described in this section, said pedestrians heading values obtained after the correction.

60.4 Experimental Validations and Conclusion

60.4.1 Experimental Validations

Based on the method in Sect. 60.3.2, we make laboratory tests conducted handheld terminals, each walking in order α for different angles, walk 60 steps, the test results shown in Table 60.1.

Table 60.1 Angle detection test results

α (°)	Deviation (°)	Standard differential (°)	α (°)	Deviation (°)	Standard differential (°)
0	0.2	1.2	−15	2.3	3.5
15	3.8	4.7	−30	2.8	4.4
45	2.6	3.6	−45	3.3	6.2
60	3	5.4	−60	−0.6	3.5
75	−3.7	5.9	−75	−2.2	5.0
90	3.9	6.4	−90	−2.5	4.2

Test results show that the method can be used detecting a moving direction, when the person carrying the terminal in a different posture, the detection error of the mean results is better than 5°, Standard differential is better than 10°. The standard difference may be further reduced by filtering techniques.

Measurement error due to the velocity and direction of movement of the existence of cumulative features, PDR technology needs and wireless positioning system (WPS) combined. The wireless location system to eliminate the accumulated error PDR generated by the robustness and PDR improve positioning accuracy wireless location system to achieve long-term stability seamless precision positioning. In PDR auxiliary indoor positioning experiment, by the techniques mentioned above, based on a common electronic compass and accelerometer to any angle handheld terminal to identify the direction of movement of personnel. Combined pedestrian pedometer with step length [6], obtain the velocity and direction of motion information. To velocity, direction information and the results of the integration of wireless positioning system location, and further integration of indoor map-matching technology for experimental verification experiment of four wireless indoor positioning systems to locate nodes. During the test, people walking along the corridor week is divided into A, B, C, D four sections, each section using the angle of terminal carrying way. Experimental results are shown in Fig. 60.7.

Experimental results show that the technique is effective to identify the direction of movement of persons in the case of the pedestrian at any angle of the handheld terminal. When the simple use PDR, the error is relatively large. Use PDR, the wireless location system and map information can be obtained good indoor positioning effect, errors are controlled within 3 m.

60.4.2 Conclusion

This article describes the positioning inertial measurement unit based handheld terminal pedestrian dead reckoning methods, and focus on resolving the current difficulties in the use of hand-held terminal cognitive direction of movement of personnel issues, relationship model triaxial accelerometer and the direction of

movement, gesture recognition algorithm proposed terminal, and the result is converted to pedestrian direction of the settlement movement. After testing, the method can detect the direction of movement of personnel in the case of workers in a variety of portable terminal stance, combined with the step length pedometer-based measurement techniques, assisted acceleration changes indoor wireless positioning system characteristics, to achieve good positioning results.

References

1. Kuusniemi H, Liu J, Pei L et al (2012) Reliability considerations of multi-sensor multi-network pedestrian navigation. IET Radar Sonar Navig 6(3):157–164
2. Ruiz ARJ, Granja FS, Honorato JSP et al (2012) Accurate pedestrian indoor navigation by tightly coupling foot-mounted IMU and RFID measurements. IEEE Trans Instrum Meas 61(1):178–189
3. Alvarez JC, Alvarez D, Lopez A et al (2012) Pedestrian navigation based on a waist-worn inertial sensor. Sensors 12(8):10536–10549
4. Herrera EP, Kaufmann H, Secue J et al (2013) Improving data fusion in personal positioning systems for outdoor environments. Inf Fusion 14(1):45–56, 157–164
5. Chen W (2010) Research on GPS, self. contained sensors based seamless outdoor/indoor pedestrian positioning algorithm
6. Jimenez AR, Seco F, Prieto JC et al (2010) Indoor pedestrian navigation using an INS/EKF framework for yaw drift reduction and a foot-mounted IMU. In: Positioning Navigation and Communication (WPNC):135–143

Chapter 61
A Direct Phase Estimation Method of X-ray Pulsar Signal Without Epoch Folding

Hua Zhang, Lu-Ping Xu, Rong Jiao, Yang-He Shen and Jing-Rong Sun

Abstract X-ray Pulsar Navigation (XPNAV) is an attractive method for the future deep space autonomous navigation. Currently, techniques for the phase estimation of X-ray pulsar radiation involves maximization of generally non-convex object functions based on average profile from epoch folding method, which results in suppression of useful information and high computation. In this paper, a new maximum likelihood (ML) directly utilizing the measured Time of Arrivals (TOAs) is present. The x-ray pulsar radiation will be traded as a cyclostationary process and the TOAs of the photons in a period will be redefined as a new process, whose probability distribution function is the normalized standard profile of the pulsar. We proved the new process is equivalent to the general used Poisson model. Then, the phase estimation problem is recast as a cyclic shift parameter estimation process under ML estimation, and we also put forwards a parallel ML estimation method to improve the ML solution. Furthermore, numerical simulation results show how the herein described estimator present a higher precision and reduced computation complexity compared with the current estimators.

Keywords X-ray pulsar · Poisson model · Phase estimation · Maximum likelihood

H. Zhang (✉) · L.-P. Xu · R. Jiao · Y.-H. Shen · J.-R. Sun
School of Aerospace Science and Technology, Xidian University, Xi'an 710126, China
e-mail: zhanghua@mail.xidian.edu.cn

L.-P. Xu
e-mail: lpxu@mail.xidian.edu.cn

R. Jiao
e-mail: jrong_06@163.com

Y.-H. Shen
e-mail: yanghe_shen@163.com

J.-R. Sun
e-mail: jrsun@xidian.edu.cn

J. Sun et al. (eds.), *China Satellite Navigation Conference (CSNC) 2014 Proceedings: Volume III*, Lecture Notes in Electrical Engineering 305,
DOI: 10.1007/978-3-642-54740-9_61,

61.1 Introduction

Pulsars, especially millisecond pulsars (period below 20 ms), show extreme frequency stability of their pulse signals, which have been considered to be used for positioning purposes as early as 1974 [1]. In recent years, several studies demonstrated the feasibility for a spacecraft to perform self-positioning based on Time of Arrival (TOA) of pulse radiated by pulsars [2, 3]. Of all the different types of pulsars, X-ray pulsars are the most suitable ones for navigation application since their X-ray radiation contains the majority of energy from the X-ray pulsars' emission. Then, a small and light X-ray detector available can be employed for X-ray detection. X-ray Pulsar Navigation (XPNAV) has great potential to provide complete autonomous navigation solutions for deep space mission.

Recently, several researchers have investigated different applications of XPNAV for both absolute navigation [4, 5] and relative navigation [6]. It is shown that one key issue of XPANV is how to measure the TOA of X-ray pulses precisely. Hanson et al. have proposed an epoch folding method for phase estimation [7] based on the assumption of Gaussianity of the underlying signals. Emadzadeh *and Speyer* improved the results, and formulated the epoch folding procedure mathematically [8]. Besides, Emadzadeh et al. proposed a nonlinear least-squares (NLS) estimator of the pulse phase and a maximum likelihood pulsar phase estimator based on the statistical model of TOAs of photons, and studied its performance against the Crámer-Rao lower bound [8]. Both the estimators employ the grid discretization searching method in the direct search maximization procedure, which descends from a tradeoff between computation complexity and estimation accuracy. Li and Ke described a low signal to noise ratio (SNR) approximation pulsar phase estimator [9]. The low SNR approximation allows us to reduce the computation complexity, but causes the estimator performance to degrade for increased SNR values.

In this paper, we treat the phase estimation of pulsar signal as a general cyclic shift parameter estimation problem under multinomial distributed observations. In our previous works, the multi-component Gaussian fitting method is used to unambiguously and uniquely determine the profile characteristics such as the width of profile, the numbers and position of components [3, 10]. In the next sections, after introducing the basic signal model of X-ray pulsar, we will show that the commonly used Poisson model can be approximated by the multi-component Gaussian distribution. Then, we describe how to form an approximate, computationally efficient, ML pulsar signal phase estimator. Besides, the Crámer-Rao lower bound is presented to evaluate the performance of X-ray pulsars on phase and velocity estimation.

61.2 Time Sequence Model of X-ray Pulsar Signal

Due to the high cyclic stability of X-ray pulsar radiation, it can be characterized by a cyclo-stationary process. As explained above, the nature of the received photons will be expressed in terms of a Poisson point process.

Assuming t_0 the reference time and t_E the end time of one observation, we use $\{T_i\}_{i=1}^{E}$ to denote the ith sampling interval, where $T_i = t_i - t_{i-1}$. The photons of X-ray pulsar radiation falling in T_i is a random variable obeying the poisson distribution. The probability that k Poisson points occur in an interval of time T_i is provided by the relationship (61.1) [4, 8],

$$p(k = k_n) = \frac{\left[\int_{T_i} \lambda(t)dt\right]^{k_n}}{k_n!} \exp\left\{\int_{\mathrm{T_i}} -\lambda(t)dt\right\} \tag{61.1}$$

where $\lambda(t)$ is a nonlinear function versus t. $\lambda(t)$ represents the nonuniform density of X-ray pulsar radiation just as $\int_{T_i} \lambda(t)dt \underset{T_i \to 0}{\approx} \lambda(t)T_i$ and the $\lambda(t)T_i$ closely relates to the pulse phase evolution and pulse profile.

61.3 New Model of Pulsar Signal

Many exist literatures have measured the TOA of the X-ray pulsar signals using the average profile which is obtained by the *Epoch folding* method [3, 8, 10]. However, the average profile suppress any useful information about the parameters that may be contained in the photon TOAs. Here, to directly utilize the measured TOAs, a new X-ray pulsar signal model and an ML estimator are presented and formulated. We also proved the new model is equivalent to the aforementioned Poisson model.

61.3.1 Multi-Gaussian Fitting of X-ray Pulsar Profile

The shapes of the averaged pulsars profiles are very stable, which provide valuable information about the physical process of radio emission from pulsars [11]. Through investigating about 200 profiles of 18 pulsars obtained from 100-m radio telescope of the MPifR in Effelsberg, Kramer et al. found the Gaussian components decomposition method (GFSAP) fit the individual components well [12].

So, except for the physical significance, this method is also good at representing the pulsar profiles' structure and minutiae. Consequently, we describe this method by fitting a sum of Gaussian functions

$$h_g(\varphi_v) = \sum_{i=1}^{M} f_i(\varphi_v) \tag{61.2}$$

to the normalized average pulsar profile. In (61.2),

$$f_i(\varphi_v) = a_i \frac{1}{\sqrt{2\pi\delta_i^2}} \exp\left[-\frac{(\varphi_v - \mu_i)^2}{\delta_i^2}\right] \tag{61.3}$$

where i is the i-th component, a_i, μ_i and δ_i are scale factor, mean, and variance of the i-th Gaussian component.

61.3.2 New Model Based on GFSAP

Assume the recorded data starting at t_0, and Let t_{end} denote the end time, then the observation interval is $t_{obs} = t_{end} - t_0$. Furthermore, let t_i denote the time of arrival of the i-th photon and the photon sequence can be expressed as $\{t_i\}_{i=1}^{m} = \{t_1, t_2, t_3, \ldots, t_m\}$. The definition of aforementioned model in Sect. 2.1 indicates the recorded sequence arrives in an increasing order [8], that is

$$t_0 \le t_1 < t_2 < t_3 < \cdots < t_m \le t_{end} \tag{61.4}$$

From the recent literatures [3, 8], we note the fact that, due to the weakness of the pulsar signals, XPNAV must use the statistical arrival time of all the observed photons to solve the position of the spacecraft. In this point of view, some average method such as *epoch folding* method is proposed [7, 8], which folds all the time tags during the observation time back into a single time interval equal to one pulse period. It arouses us to make an assumption that, for the pulsar photon sequence, if n photons are captured in one period, it can be considered that the independent event of one photon, whose probability distribution function is the normalized pulsar profile, occurs n times in the period theoretically. This hypothesis is supported by the theorem as follows.

Theorem 1 *Let $h(\varphi)$ denote the normalized pulsar profile, and $\int_0^1 h(\varphi) = 1$. If there is only one photon even in one pulsar period, its arrival time follows the distribution whose probability distribution function is $h(\varphi)$.*

proof Without loss of generality, we assume $\lambda_b = 0$. Then, according to (61.6), the pulsar signal density can be rewrote as $\lambda_{s,\Delta} = \int_\Delta AK\eta\lambda_s h(\varphi)d\varphi$, where Δ is the time interval between the start time of the period and the TOA of the photon. Let P is the period of the pulsar. If there is one photon arriving in P, the probability of this event in the interval Δ can be given by

$$
\begin{aligned}
p(x(\Delta)=1|x(P)=1) & \\
&= \frac{p\{x(\Delta)=1, x(P)=1\}}{p\{x(P)=1\}} \\
&= \frac{p\{x(\Delta)=1, x(P-\Delta)=0\}}{p\{x(P)=1\}} \\
&= \frac{\lambda_{s,\Delta} e^{-\lambda_{s,\Delta}}}{\lambda_{s,P} e^{-\lambda_{s,P}}} e^{-\lambda_{s,(P-\Delta)}} \\
&= \frac{\int_{\Delta} h(\varphi) d\varphi}{\int_{P} h(\varphi) d\varphi}
\end{aligned}
\tag{61.5}
$$

Furthermore, because $\int_P h(\varphi)d\varphi = 1$, there is $p(x(\Delta)=1|x(P)=1) = \int_{\Delta} h(\varphi)d\varphi$. It is easy to find the probability mass of the instant time τ of the event in a period is given by

$$p(\tau) = h(\tau). \tag{61.6}$$

So, the **theorem 1** is tenable.

Based on **Theorem 1** and (61.6), a new generation method on pulsar signal will be presented in the following. Let τ_n denote the fractional part of the n-th photon, and N denote the cycle counts. There is

$$\tau_n = \frac{t_i - NP}{P} \tag{61.7}$$

If the pulsar frequency is an unknown constant due to the velocity of the spacecraft, the period should be amended as

$$\tau_n = \frac{t_i - NP_v}{P_v} \tag{61.8}$$

where $P_v = \frac{c}{c+v} P$, and v is the velocity of the spacecraft. Thus, according to **Theorem 1** and the Eq. (61.2), the probability of the TOAs of the photons in one period can be restated as

$$p(\tau_n) = h_g(\tau_n) \quad \tau_n \in [0,\ 1) \tag{61.9}$$

The Eq. (61.9) indicates that the distribution of the photon TOAs in the N-th cycle can be approximated by the probability using the normalized standard profile as its distribution function. To define the initial phase φ_0, rewrite the Eq. (61.3) as

$$
\begin{aligned}
f_i(\tau_n) &= a_i \frac{1}{\sqrt{2\pi\delta_i^2}} \exp\left[-\frac{(\tau_n - (\varphi_0 + \delta\mu_i))^2}{\delta_i^2} \right] \\
i &= 1, 2, \ldots, M
\end{aligned}
\tag{61.10}
$$

where $\mu_i = \varphi_0 + \delta\mu_i$, and $\delta\mu_i$ is the offset between the initial phase and the i-th part of the pulsar profile. Generally, φ_0 can be set to arbitrary value in [0, 1). In the following part, we set $\varphi_0 = \mu_0$, which means $\delta\mu_0 = 0$.

61.4 Phase Estimator Using GFSAP Model

61.4.1 ML Estimator of the Initial Phase

Employing the new probability model in Sect. 61.3.2, a maximum-likelihood estimation problem can be formulated to estimate φ_0. According to (61.9) and (61.10), the pdf of the sequence is given by

$$p\left(\{t_i\}_{i=1}^m; \varphi_0\right) = \prod_{i=1}^{m} h_g(\tau_i; \varphi_0). \tag{61.11}$$

Regarding the pdf given in (61.11) as the likelihood function, the ML estimator is provided by maximizing (61.11) with respect to the unknown parameter φ_0. Equivalently, the natural logarithm of the likelihood function can be maximized

$$\mathrm{LLF}(\varphi_0) = \sum_{i=1}^{m} \ln\left(h_g(\tau_i; \varphi_0)\right) \tag{61.12}$$

where LLF means the log-likelihood function. Then, the initial phase can be estimated by solving the following optimization problem:

$$\hat{\varphi}_0 = \underset{\varphi_0 \in [0,1)}{\operatorname{argmax}} \mathrm{LLF}(\varphi_0) \tag{61.13}$$

The derivation of the CLRB can refer to our previous works [10].

61.4.2 Numerical Searching Method

Generally, the GFSAP model must use multiple Gaussian components to fit the pulsar profile which has multiple peaks. Considering the phase estimation generally used in the iteration position determination procedure, the priori phase information can be acquired easily from previous determined position. Therefore, the Newton–Raphson iteration searching method can be utilized, whose iteration factor is given by

$$\vec{\theta}_{k+1} = \vec{\theta}_k + \left[J(\vec{\theta})\right]^{-1} \mathrm{pLLF}(\vec{\theta})\Big|_{\theta=\theta_k} \tag{61.14}$$

where $k = 0, 1, 2, \ldots$, $\text{pLLF}(\vec{\theta}) = \partial \ln p\left(\{t_i\}_{i=1}^{m}; \vec{\theta}\right)/\partial\vec{\theta}$. The iteration process stop when $\|\theta_{k+1} - \theta_k\| < \xi$, where ξ is the convergence threshold. The detail of the Newton–Raphson can refer to [13].

61.4.3 Improving the Searching Performance

Since the proposed model in Sect. 61.3 assumes the x-ray pulsar signals are cyclo stationary process, all the photon TOAs have the same probability distribution function. Consequently, $pLLF(\vec{\theta})$ can be recast as

$$pLLF(\vec{\theta}) = \sum_{l=1}^{L} \sum_{i=la+1}^{la+a} \frac{\partial ln\left(h_g(\tau_n; \vec{\theta})\right)}{\partial\vec{\theta}} \tag{61.15}$$

Equation (61.15) means that, the calculation process can be divided into L independent subprocesses which have a photons. According to (61.15), $\text{pLLF}(\vec{\theta})$ can be calculated by four steps as shown in Fig. 61.1

1. subdivide the photon sequence into L parts. Every part contains $[m/L]$ photons, where $[\cdot]$ means rounding operation.
2. For every part in step 1, calculate the pLLF function.
3. Add all the results in the step 2.

61.5 Numerical Simulation

Three typical pulsars, B0531−21, B1937+21, and B0329+54, whose parameters are given in Table 61.1, are selected to be applied to the three proposed methods. The profile of the three pulsars can be fitted by the Multi-Gaussian method. As an example, the Multi-Gaussian fit of the pulsar B0531+21 is given in Table 61.2 and plotted in Fig. 61.2.

The simulations are performed using the Monte Carlo technique with over 100 independent realization of TOAs for each observation time. It is assumed that the detector area A is 1 m^2 and the background photo rate is $\lambda_b = 0.05$ ph/(s.cm^2). The source arrival rate λ_s is shown in Table 61.1. The initial phase is chosen to be $\varphi_0 = 160 * \pi * \rho$, where ρ is the equal-length bins of the profile samples.

The procedure of the ML estimation simulation is described as follows. Firstly, based on the assumed parameters, namely the detector area A, the background photo rate λ_b, and the source arrival rate λ_s, the amount and the TOA of the detected photon rates are generated. Secondly, substituting the TOAs into the cost function presented in (61.12), the initial phase $\hat{\varphi}_0$ can be estimated by solving

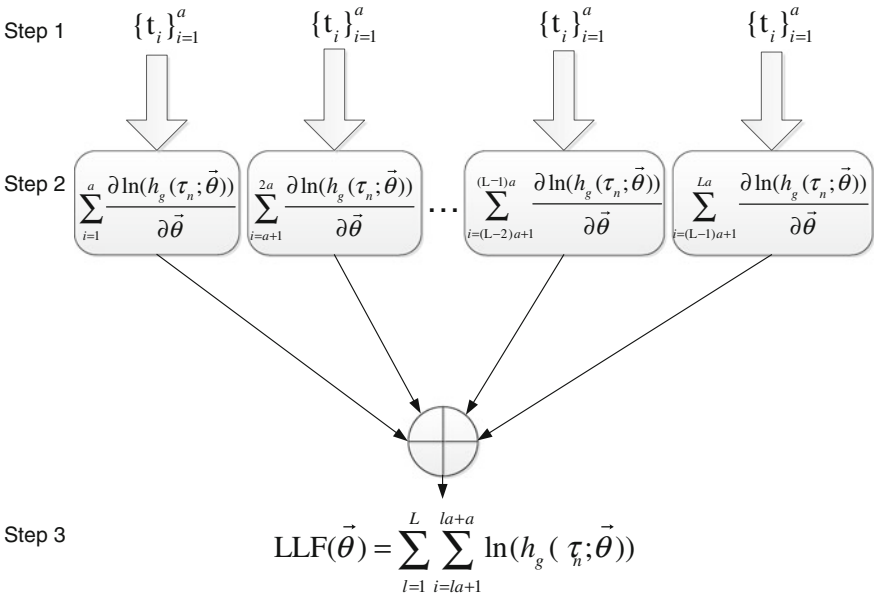

Fig. 61.1 The scheme of the parallel strategy

Table 61.1 Employed pulsars

Pulsar	Period (s)	Sampling interval (s)	Flux (2–10 keV) ph/cm^2/s	Qualify factor
B0531+21	0.0335	5.3e−4	1.54e+0	1.1601e+10
B1937+21	0.0016	1.5e−6	4.99e−5	4.7026e+5
B0329+54	0.7145	1.5e−3	5.15e−3	212.7541

Table 61.2 Multi-Gaussian fit of B0531+21

Parameters	C 1	C 2	C 3	C 4	C 5
Mean(μ)	3.584e−1	3.765e−1	3.572e−1	3.322e−1	3.5e−1
Var(δ)	1.708e−2	3.581e−3	3.971e−3	3.801e−3	4.533e−3
Scale(α)	4.298e−3	8.66e−4	8.826e−3	7.34e−4	1.603e−3

function (61.13). Then, using the Monte Carlo technique, we have obtained the estimated initial phase $\hat{\varphi}_0$ for 100 times during each observation time. At the same time, the mean square error (MSE) is described as follows:

$$MSE(\hat{\varphi}_0) = E\left[(\hat{\varphi}_0 - \varphi_0)^2\right]. \tag{61.16}$$

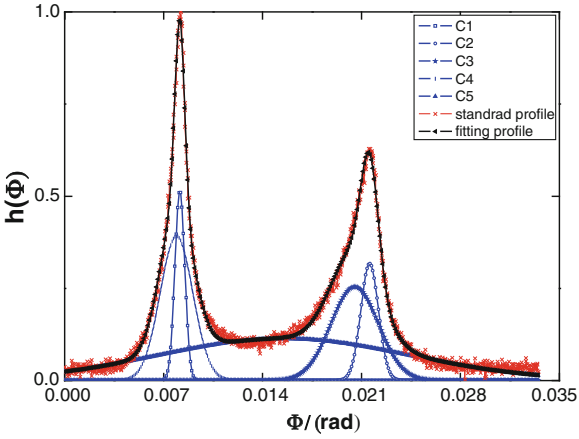

Fig. 61.2 Multi-Gaussian fit of the pulsar B0531+21

The MSE of the 100 estimated initial phases can be calculated. Lastly, as the observation time changes from 1 to 500 s, statistics of the root mean square (RMS) of the ML estimation error, which is plotted in Fig. 61.4, can be obtained.

The parallel ML estimation simulation is generally similar to the current ML estimation except for the construction of the cost function $\mathrm{pLLF}(\vec{\theta})$ as described in Sect. 4.5. The parallel ML estimator uses the parallel computation of the $\mathrm{pLLF}(\vec{\theta})$, which will reduce the computational complexity. In this simulation, we use independent parallel subprocesses of different amounts to show the superiority of the parallel ML estimator.

As a compared method towards the ML estimator and the improved ML estimator, the NLS e simulation is illustrated. Firstly, the generation of TOA is the same to the ML estimator. Secondly, knowing the TOA of the detected photon, the average profile is obtained by the Epoch folding method. Then we can obtain the estimated initial phase $\hat{\varphi}_0$ by maximizing the correlation function of the average profile and the standard profile. Also using the Monte Carlo technique, the MSE of 100 estimated initial phase $\hat{\varphi}_0$ have been calculated for each observation time. Lastly, changing the observation time changes from 1 to 500 s, statistics of RMS of the NLS estimation error can be obtained.

In Fig. 61.3, the cost functions of the three pulsars are plotted. It can be seen that the three pulsars, B0531−21, B1937+21, and B0329+54 have different extremum. It is also shown that the pulsars B0531−21 and B1937+21 have multiple extrema. As a result, a numerical searching method is applied in order to avoid getting trapped in local extrema.

In Fig. 61.4, three curves, the root mean square (RMS) of the ML estimator, the RMS of the NLS estimator, the square root of CRLB (φ_0) are plotted for each observation time. It is shown that, on one hand, the ML estimator and the NLS estimator are both asymptotically unbiased, compared against the CRLB (φ_0), on the other hand, that the ML estimator is more asymptotically efficient than the NLS estimator. As the observation time decreases, both the mean square errors in

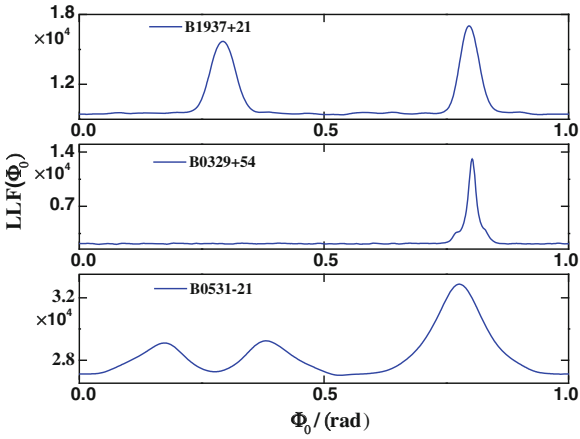

Fig. 61.3 Cost functions of three pulsars

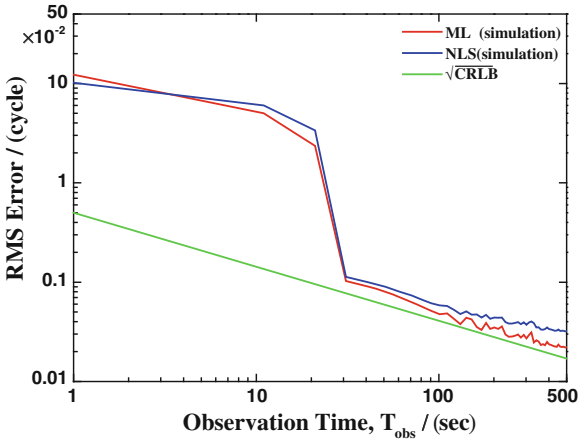

Fig. 61.4 RMS error of different simulation methods

Fig. 61.4 deviate from CRLB (φ_0) below the threshold point and on the contrary, they follow a more and more unbiased trend above the threshold point.

Although the current ML estimator has advantage over the NLS estimator on the asymptotically unbiased side, the operation time taken by the estimator should be taken into consideration. In Fig. 61.5, the CPU time, which Matlab R2011b takes to calculate one Monte Carlo realization, is plotted as a function of the observation time. The used processor is an Intel 3.2 GHz quad-core and the operating system is the Windows 7. It can be seen that the ML estimator takes more time than the NLS estimator, while the parallel ML estimator spends less time with the change of the parallel subprocess amount *L*. In this simulation, L is chosen to be three values, namely 2, 10, 20. When *L* is set to be two, the CPU time has decreased, but it is still longer than the CPU time of the NLS estimator. As soon as *L* is changed into 10, the parallel ML estimator takes almost the same time

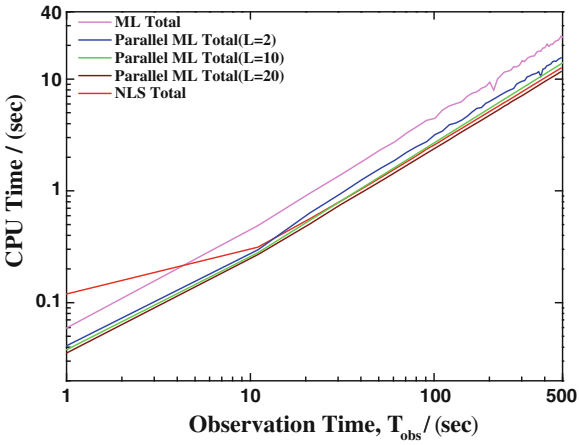

Fig. 61.5 CPU time of different simulation methods

as the NLS estimator. While L is set to be 20, the time taken by the parallel estimator is less than the NLS estimator although it is not obvious in Fig. 61.5. As a result, it does have significantly reduced computational complexity compared to the current ML estimator.

61.6 Conclusions

The X-ray pulsar signals were analyzed using the mathematic model and a new process of TOA was redefined. We use the maximum likelihood method to estimate the signal phase. A parallel ML estimation method was developed compared to the current ML estimator and the NLS estimator. It is proven that the current ML estimator and the parallel ML estimator are both more asymptotically efficient than the NLS estimator. However, the current ML estimator is computationally more than the NLS estimator. Since the parallel ML estimation reducing more computational complexity than the current ML estimator, it spends less time than the NLS estimator when the photons are divided into specific independent parallel subprocesses. As a result, the parallel estimator has advantages over the NLS estimator, not only on the asymptotically unbiased side, but also on the computational complexity.

References

1. Downs GS (1974) Interplanetary navigation using pulsating radio sources. NASA technical reports, pp 1–12
2. Sheikh SI (2005) The use of variable celestial X-ray sources for spacecraft navigation. http://adsabs.harvard.edu/abs/2005PhDT……..30S

3. Zhang H, Xu L, Xie Q (2011) Modeling and Doppler measurement of X-ray pulsar. Sci China Phys Mech Astron 54:1068–1076
4. Sala J, Urruela A, Villares X (2004) Feasibility study for a spacecraft navigation system relying on pulsar timing information. Eur Space Agency Adv Concepts Team 3:23
5. Sheikh SI, Pines DJ, Wood KS, Ray PS, Lovellette MN (2007) Navigational system and method utilizing sources of pulsed celestial radiation. http://www.google.com/patents?id=31J_AAAAEBAJ
6. Emadzadeh AA, Speyer JL (2011) Relative navigation between two spacecraft using X-ray pulsars. IEEE Trans Control Syst Technol 19:1021–1035
7. Hanson J, Sheikh S, Graven P, Collins J (2008) Noise analysis for X-ray navigation systems. In: Position, location and navigation symposium 2008 IEEEION, pp 704–713. doi:10.1109/PLANS.2008.4570028
8. Emadzadeh AA, Speyer JL (2010) On modeling and pulse phase estimation of X-ray pulsars. IEEE Trans Sign Proces 58:4484–4495
9. Li J-X, Ke X-Z (2011) Maximum-likelihood TOA estimation of X-ray pulsar signals on the basis of Poison model. Chin Astron Astrophys 35:19–28
10. Zhang H, Xu L (2011) An improved phase measurement method of integrated pulse profile for pulsar. Sci China Technol Sci 54:2263–2270
11. Xu X, Wu X (2003) Mean pulse analysis and spectral character study of pulsar PSR B2111+46. Sci China Series G 46:104–112
12. Kramer M (1994) Geometrical analysis of average pulsar profiles using multicomponent Gaussian fits ant several frequencies II Individual results. Astron Astrophys 107:527–539
13. Kay SM (1998) Fundamentals of Statistical signal processing, Volume 1: estimation theory, Prentice Hall PTR, New Jersey. http://www.lavoisier.fr/livre/notice.asp?ouvrage=1114518

Chapter 62
GNSS Satellite Clock Real-Time Estimation and Analysis for Its Positioning

Bingbing Duan, Junping Chen, Jiexian Wang, Yize Zhang, Jungang Wang and Li Mao

Abstract Real-time and high-precision Multi-GNSS positioning technical has been playing an important role in the determination of low earth orbiter (LEO) and monitoring of geologic hazards. The key concern should be on the achievement of the high-precision satellite orbit and clock products. In this paper, real-time clock estimation strategy was introduced. Based on the mean square root filtering method, dates via 35 global uniformly distributed IGS observations were used to estimate real-time satellite clock errors of GPS and CLONASS, which was proved 0.2 ns and 0.8 ns respectively. The outcomes were verified again via precise point positioning. Consequently, compared with the positioning accuracy via only GPS, that of GPS and GLONASS improved 26 % in X direction, 40 % in Y direction and 2 % in Z direction. The convergence time shorten 2 to 4 times as well.

Keywords GPS · GLONASS · Real-time clock estimation · Combination positioning · Mean square root filtering

62.1 Instruction

Precise point positioning (PPP) of Global navigation satellite system (GNSS) can achieve centimetre-level accuracy for static positioning and decimetre-level for kinematic respectively. Its precision depends mainly on the quality of satellite orbit

B. Duan (✉) · J. Wang · Y. Zhang · J. Wang · L. Mao
College of Surveying and Geo-informatics Building, Tongji University, Shanghai, China
e-mail: 410_duanbingbing@tongji.edu.cn

J. Chen
Shanghai Astronomical Observatory, Chinese Academy of Sciences, SHAO, ShangHai, China
e-mail: junping.chen@shao.ac.cn

J. Sun et al. (eds.), *China Satellite Navigation Conference (CSNC) 2014 Proceedings: Volume III*, Lecture Notes in Electrical Engineering 305,
DOI: 10.1007/978-3-642-54740-9_62,

and clock. At present, the precision of GPS broadcast ephemeris is 7 ns for clock error (http://igscb.jpl.nasa.gov/components/prods.html) while GLONASS is 15 ns, which is far from the requirement of precise positioning [1]. From November 5, 2000 (GPS Week 1087), International GNSS Service(IGS) began to offer ultra-rapid(IGU) services, but the predicting part is still not accurate enough (5 ns). Besides that, RTG (Real-time GIPSY) developed by JPL analysis center could estimate real-time GPS orbit and clock products based on 60 NASA global networks (http://galia.gdgps.net/igds). The precision is 1 ns and has about 4 seconds latency, but the production is secretive [2]. Natural Resources Canada(NRCan, http://www.cdgps.com) can also estimate real-time GPS clock using ultra-rapid orbit but need to be authorised [3]. Till now, almost all the real-time GPS clock products are paid and GLONASS clock products provided by CLONASS control center (MCC, ftp.glonass-iac.ru/MCC) and Shanghai Astronomical Observatory (SHAO, http://202.127.29.4/shao_gnss_ac/) could not satisfy the need of precise positioning. So, real-time clock products are needed for the real-time positioning.

62.2 Real-Time Satellite Clock Error Estimation Module

There are two main roles for clock in GNSS positioning, one is to record the emission time of satellite signal and another is to determine the transmission time between satellite and receiver antenna. For the former effect, we need the absolute time to calculate the orbit position. Thus, a precision better than 10–6 s will be enough [4]. For the latter using, it depends only on relative time and needs to choose a satellite or receiver clock as reference clock.

62.2.1 Observation Module

Ionosphere-free combination of pseudorange and carrier phase observations are used in the estimation of precise satellite clock error. It could be simplified as [5]

$$P_{IF}^{G,R} = \frac{f_1^2}{f_1^2 - f_2^2} P_1 - \frac{f_2^2}{f_1^2 - f_2^2} P_2 = \rho + c(dt_r - dt_s) + d_{trop} + \varepsilon(P_{IF}) \tag{62.1}$$

$$\begin{aligned} \Phi_{IF}^{G,R} &= \frac{f_1^2}{f_1^2 - f_2^2} \Phi_1 - \frac{f_2^2}{f_1^2 - f_2^2} \Phi_2 \\ &= \rho + c(dt_r - dt_s) + d_{trop} + \frac{c(f_1 N_1 - f_2 N_2)}{f_1^2 - f_2^2} + \varepsilon(\Phi_{IF}) \end{aligned} \tag{62.2}$$

where G, R denote GPS and GLONASS respectively; $P_{IF}^{G,R}$, $\Phi_{IF}^{G,R}$ are respectively the pseudo-range and carrier phase observation; ρ is geometrical distance; c is light speed; $f_{i=1,2}$ is frequency; dt_r is receiver clock offset; dt_s is satellite clock

Table 62.1 Parameters of clock error estimation

Name	Number	Initial value
Satellite clock error	One at each epoch and each satellite	Broadcast ephemeris
Receive clock error	One at each epoch and each receive	Pseudorange point positioning
Tropospheric delay	One at each receive and each hour	Module
Site coordinate	Each station has three	Pseudorange point positioning
Ambiguity	One at each station and satellite	D-value between Pseudorange and carrier phase observations

offset; d_{trop} is tropospheric delay; N_1, N_2 is the ambiguity of observations; $\varepsilon(P_{IF})$ and $\varepsilon(\Phi_{IF})$ are residuals.

In Eq. (62.2), clock parameter and ambiguity parameter are related and can not be estimated directly, but we can get satellite clock error through pseudorange equation. However, it could not be precise enough due to the precision of pseudorange observation. So, different weight should be given to the two kinds observations.

62.2.2 Error Correction and Pre-processing

Some errors need to be corrected in the precise point positioning. We eliminate the ionosphere error using ionosphere-free combination; For troposphere correction, we calculate an initial value at the Zenith direction using Saastmoinen module and regard the residual error as parameter in the normal equation; Using GMF (Global mapping function) as Mapping function [6]; For Antenna phase center correction, we use absolute phase center correcting module [7]; Then, Solid tide, pole tide, ocean tide and relativity effect, this paper refers to the International Earth Rotation Service (IERS); finally, wind up correction, We refer to the IGS standard module [8].

In the pre-processing we will come across ms jump correction, cycle slip and the estimation of initial value. For some GPS receivers, the time scale will drift due to the unstable of frequency. In order to keep the consistency of observations and time scale, we have to modulate the time scale of the receiver. Then, in order to detect whether there is any ms jump, we compare the D-value of pseudorange and carrier phase observations between epochs. Besides, we use LW and LG combination to detect cycle slips and use Bancroft method to estimate initial value based on pseudorange observations. The calculation parameters are shown in Table 62.1.

62.2.3 Method of Parameter Estimation

Least square estimation and kalman filtering theory are the most common methods for GNSS parameter estimation and the latter is more suitable for kinematic

positioning. However, researches have shown that the Kalman filter algorithm is sensitive to computer roundoff and that numeric accuracy sometimes degrades to the point where the results cease to be meaningful. we put the mean-root-square filtering method into GNSS parameter estimation and find out that it is more elegant in parameter estimation.

Recall the least square performance functional from document [5].

$$J(x) = \|A_i \delta x - l_i\|_2 = \min \tag{62.3}$$

Let H be an orthogonal matrix. Because of the property of orthogonal matrix, we can write

$$J(x) = \|HA_i \delta x - Hl_i\|_2 = \min \tag{62.4}$$

In fact, $J(x)$ is independent of H and this can be exploited. We shall show how H can be chosen using Household transformation in bibliography [9].

For an arbitrary matrix $A \in R^{m\times n}(m \geq n)$, there exists an orthogonal transformation $H \in R^{m\times m}$ such that

$$HA = \begin{bmatrix} s & \vdots & \\ & \vdots & \tilde{A} \\ 0 & \vdots & \end{bmatrix} \tag{62.5}$$

where s and $\tilde{A}$ are computed directly from A, and the matrix H is only implicit, computer mechanization requires no additional computer storage other than that used for A. We use the properties of the elementary Household transformation H that

$$Hl_i = l_i - \gamma \bar{u} \qquad \gamma = (l_i^T \bar{u})\bar{u} + v \tag{62.6}$$

where $\bar{u}$ is a unit vector of u, and u is the normal to the reference plane. v is that part of l_i that is orthogonal to u.This formula shows that storage of the matrix H is not necessary. So formula (62.4) can write

$$J(x)\left\| \begin{bmatrix} R \\ 0 \end{bmatrix} \delta x - \begin{bmatrix} z_1 \\ z_2 \end{bmatrix} \right\|_2 = \min \tag{62.7}$$

where $R \in R^{n\times n}$, is an upper triangular matrix, $Hl_i = \begin{bmatrix} z_1 \\ z_2 \end{bmatrix}$, $z_1 \in R^n$, $z_2 \in R^{m-n}$.

By reducing the least square performance functional to the form (62.5), we can see that the minimizing δx must satisfy

$$R\delta x - z_1 = 0 \tag{62.8}$$

These results are more elegant than is the brute force construction via the normal equation. More importantly, the solution using orthogonal transformation is less susceptible to errors due to computer roundoff.

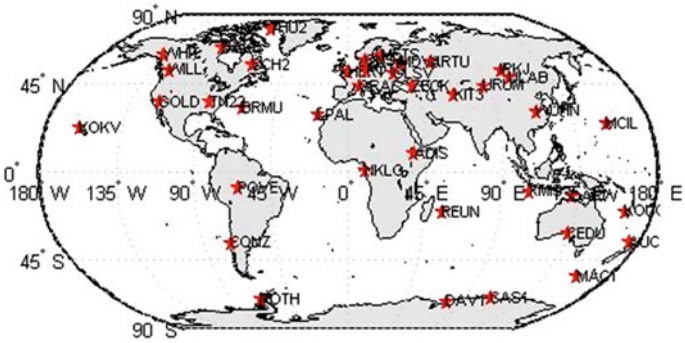

Fig. 62.1 Distribution of IGS station

62.3 Analysis of Examples

In the calculation, 35 global uniformly distributed IGS stations are used (Fig. 62.1) at 300 day, 2012. We fix the station coordinates refer to the snx file, use ultra-rapid orbit. The sampling interval is 30 s and satellite cutoff is 7°. All the calculation is based on the LTW_BS software that developed by SHAO.

We choose a atomic clock as reference clock in the estimation. So, when evaluate the precision of estimated clock error we have to compare the D-value of one reference satellite to others.

Figure 62.2 is a comparison of GPS clock estimation between single and multi-system, which shows that RMS of GPS clock could be 0.2 ns and the result are almost the same for the two situations. Figure 62.3 is the estimation of GLONASS clock error, which could easily find that RMS of GPS clock could be 0.8 ns and satellite R10, R11, R12 own a bad precision because of the their observations.

62.4 Real-Time Precise Point Positioning

In order to certify the reliability of the estimated satellite clock, we put the result together with orbit product from IGU into real-time precise point positioning.

Figures 62.4 and 62.5 depend on single system's estimated clock and multi-system estimated clock respectively, we can find that there is no obvious difference. Figure 62.6 is the result of combination of GPS and GLONASS, which denotes that the convergence time decreases a lot.

Table 62.2 is the result of 10 stations for real-time positioning, where we can find that result from GPS + GLONASS combination improved 26 % in X, 40 % in Y and 2 % in Z compared to that from single GPS system, and convergence time shorten 2 to 4 times.

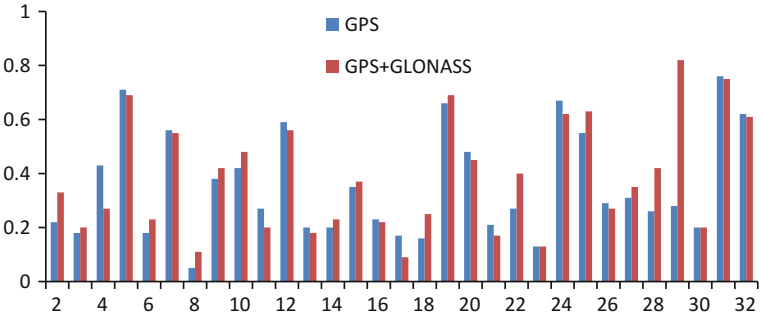

Fig. 62.2 Comparison of GPS clock estimation between single and multi-system RMS (ns)

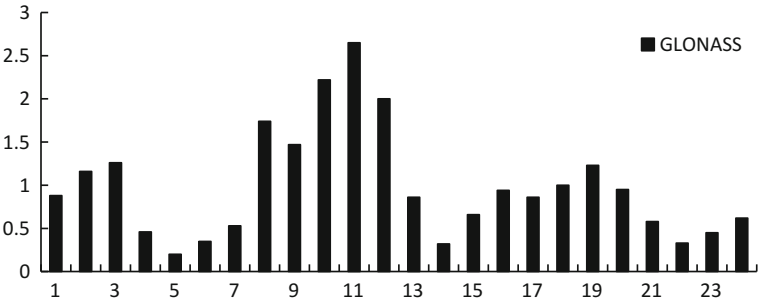

Fig. 62.3 Result of GLONASS clock estimated by multi-system

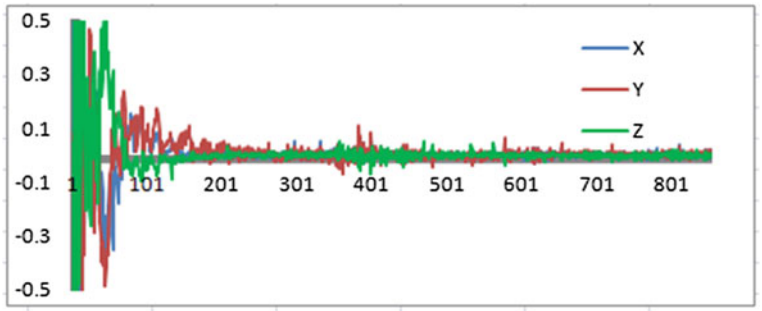

Fig. 62.4 GPS positioning based on single system's clock (m)

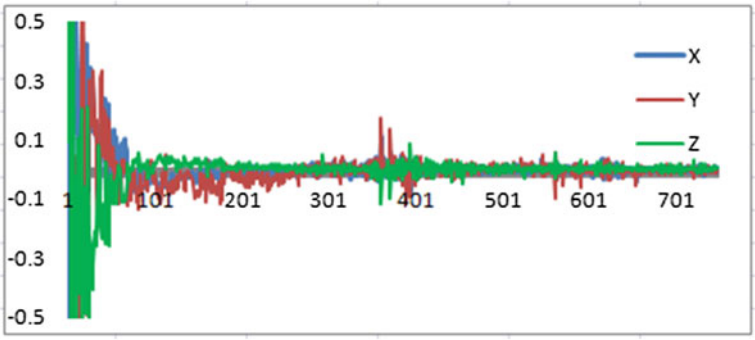

Fig. 62.5 GPS positioning based on multi-system's clock (m)

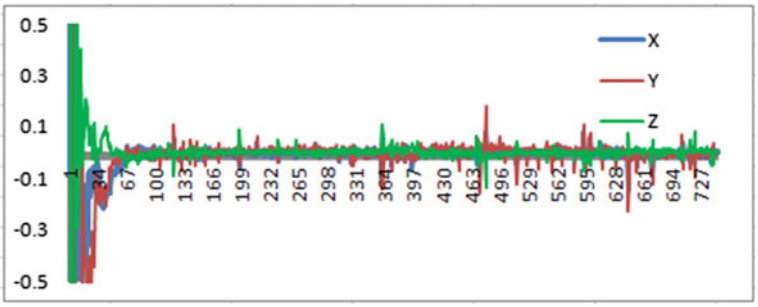

Fig. 62.6 GPS + GLONASS positioning based on multi-system's clock (m)

Table 62.2 Real-time kinematic positioning

站名	GPS (RMS)			GPS + GLONASS (RMS)			收敛至 0.1 m 时间(历元)	
	X	Y	Z	X	Y	Z	GPS	GPS + GLONASS
GOLD	0.043	0.046	0.040	0.017	0.024	0.017	120	33
GRAS	0.019	0.019	0.010	0.013	0.007	0.014	32	20
IRKJ	0.017	0.010	0.010	0.007	0.010	0.014	83	35
JPLM	0.025	0.043	0.024	0.015	0.019	0.014	55	36
KIT3	0.023	0.016	0.017	0.015	0.016	0.018	64	28
KOKV	0.017	0.041	0.009	0.025	0.023	0.017	48	29
KOSG	0.018	0.054	0.023	0.013	0.006	0.014	91	36
XMIS	0.011	0.012	0.016	0.009	0.008	0.011	78	38
THU2	0.010	0.009	0.018	0.009	0.006	0.021	103	32

62.5 Conclusion

This paper elaborates the observation modules, error correction modules, pre-processing and parameter estimation of GNSS clock estimation. First, do some experiment in the estimation of GPS and GLONASS clock error based on single and multi-system, and find that clock from single system and multi-system is almost the same in precision. Then, put the estimated clock products into real-time precise point positioning and conclude that result from GPS + GLONASS combination improve 26 % in X, 40 % in Y and 2 % in Z compared to that from single GPS system. Besides, the convergence time shorten 2 to 4 times.

Acknowledgements This paper is supported by the 100 Talents Programme of The Chinese Academy of Sciences, the National High Technology Research and Development Program of China (Grant No. 2013AA122402), the National Natural Science Foundation of China (NSFC) (Grant No. 11273046 and 40974018), the Shanghai Committee of Science and Technology(Grant Nos. 12DZ2273300,13PJ1409900) and National Natural Science Foundation of China (NSFC) (Grant NO. 41174023).

References

1. Guo J, Meng X, Li Z (2011) Accuracy analysis of GLONASS satellites broadcast ephemeris. J Geodesy Geodyn 31(1):12–16
2. Dach R, Hugentobler U et al (2007) Bernese GPS software version 5.0. Astronomical Institute, University of Bern, Bern, Switzerland
3. Dettmerring (2006) Real-Time GNSS-Policy Aspects[R].BKG, Frankfurt, Germany
4. Yidong Lou (2008) Research on real-time precise GPS orbit and clock offset determination. WuHan University, WuHan
5. Jiexian Wang (1997) GPS precise orbit determination and positioning. Tongji University Press, Shanghai
6. Boehm J, Niell AE, Tregoning P et al (2006) The global mapping function (GMF): a new empirical mapping function based on data from numerical weather model data. Geophys Res Lett 33(4):13–15
7. Dow JM, Neilan RE et al (2007) Galileo and the IGS:taking advantage of multiple GNSS constellations. Adv Space Res 39(10):1545–1549
8. Wu JT, Wu SC, Hajj GA et al (1993) Effects of antenna orientation on GPS carrier phase. Manuscripta Geod 18:91–93
9. Boehm J, Niell AE, Tregoning P, et al (2006b). The Global Mapping Function (GMF): a new empirical mapping function based on data from numerical weather model data. Geophys Res Lett 33(4):48–52

Chapter 63
Study of Toutatis Imaging Illumination and Integrity Based on Chang-E II Flyby Navigation Relation

Yanlong Bu, Geshi Tang, Cheng Yang, Ye Liu, Jinchao Xia, Chuankai Liu, Baofeng Wang and Ping Miao

Abstract On December 13, 2012, China's Chang'E II spacecraft successfully flew by the asteroid Toutatis, and obtained a series of clear optical images on Toutatis surface, which is China's first asteroid detection and also human's first close optical exploration on the asteroid. These optical images are of great benefit to build an accurate model of Toutatis surface, and to analyze physical properties of the asteroid. However, due to the acquired optical images can only reveal a partial surface of Toutatis, meanwhile influenced by light, one cannot visually determine whether the optical images reveal a complete side of Toutatis or not, in other words, how much part of the side was not photographed because of light shadows. In the paper, based on the Chang-E II flew over strategy, combined with the spacecraft's orbit, attitude and other navigation information, and through photographic measurement method, the angle between the direction of the sun light and the line of sight of Toutatis's surface feature points was accurately calculated, namely irradiation angle. Through precise calculation, irradiation angles of Toutatis surface feature points are 36.8°–39.0°, and furtherly, with the help of a pose simulation of a radar-observing-based shape model by NASA, we can get one important conclusion, that is during the fly by, the space borne optical camera got complete imaging for one side of Toutatis's surface, and there is no wide shadow on the images.

Keywords Chang'E II · Toutatis · Fly by · Optical imaging · Navigation information · Irradiation angle

Supported by NSFC(No. 41204026); DPFC(No.9140A24060712KG13290)

Y. Bu (✉) · G. Tang · C. Yang · Y. Liu · J. Xia · C. Liu · B. Wang · P. Miao
National Key Laboratory of Science and Technology on Aerospace Flight Dynamics, Beijing, China
e-mail: buyanlong@yahoo.com

Y. Bu
Beijing Aerospace Control Center, Beijing, China

J. Sun et al. (eds.), *China Satellite Navigation Conference (CSNC) 2014 Proceedings: Volume III*, Lecture Notes in Electrical Engineering 305,
DOI: 10.1007/978-3-642-54740-9_63,

63.1 Introduction

On December 13, 2012, Toutatis approached the Earth again [1, 2], and China's lunar detection spacecraft Chang'e II flew by the asteroid and successfully took optical pictures with the spaceborne surveillance camera under the ground command [3, 4]. This is the first close-range optical detection of Toutatis internationally and marks the start of China's asteroid detection.

When Chang'e II passed over Toutatis, the asteroid was 7 million kilometres far away from the earth, and the effective imaging time is only 100 s. All of the returned optical images are taken from the same point of view, and they are only different in scale, while the image surfaces are exactly the same. This causes a serious question for the scientific analysis of Toutatis images, namely whether the surface information of Chang'e II spacecraft optical image revealed the complete shape of this small body. However, this question cannot be answered only from the optical images.

In this paper, the navigation information of Chang'e II during flybys probing is applied to the process of illumination analysis of imaging plane. Combined with the absolute and relative position, attitude, and the conversion relations between the spacecraft, the sun and the asteroids in the space, the illumination condition on the imaging surface are studied. Although the truth cannot be acquired yet, this method can come to a reasonable conclusion theoretically.

63.2 Main Coordinate Systems

During the flyby, the observation systems and control systems on the earth are used to tracking and measure the movement of Chang'e II and Toutatis. The spacecraft's orbit is tracked through radio stations, and the asteroid's orbit is determined through ground optical telescope [5, 6]. All of the measurement information on the ground can be unified into the heliocentric inertial system.

Optical imaging is a direct relation in a close range between the spacecraft and Toutatis, so the images are reaction of the position and attitude of the asteroid relative to the camera plane in Chang'e II. This leads to a camera coordinate system, which is a relative motion coordinate system, defined as: the origin is located in the camera optical center, the axis Z is the camera optical axis, the axis X and the axis y are parallel to the imaging plane.

Besides, conversion between the heliocentric inertial frame and the camera coordinate system involves a body coordinate system of the spacecraft. There is a fixed conversion relation between the camera coordinate system and the body coordinate system.

63.3 Angle Between Line of Sight and Sun Vector

63.3.1 Sun Vector in the Camera System

To obtain the expression of sun vector in the camera system, the location of the sun in the camera system ${X_{Sun}}^{rs}$ must firstly be known, which needs go through a series of coordinate transformation. Those at least include transformation from the heliocentric inertial system to the spacecraft system and from the spacecraft system to the camera coordinate system. At the same time, the error between the theoretical value and the actual value in camera installation must be considered. Based on the above, the transformation formula is as following:

$$ {X_{Sun}}^{rs} = M_{pe} M_{bp} M_{ib} \left({X_{Sun}}^{i} - {X_s}^{i} \right) \tag{63.1} $$

where, ${X_{Sun}}^{i} = 0$, is the coordinate of the Sun centre in inertial system, ${X_s}^{i}$ is the coordinate of the spacecraft in the inertial system when imaging, M_{ib}, M_{bp}, M_{pe} are respectively transformation matrix from the heliocentric inertial system to the spacecraft system, from the spacecraft system to the theoretical camera system, and from the theoretical system to the actual system. M_{ib} could be calculated through the spacecraft's real-time telemetry attitude. M_{bp} is the fixed conversion determined by the installation matrix. Here, the asteroid space gesture does not be required strictly, so M_{pe} can be ignored.

Based on the actual remote measurement value by Chang-E II spacecraft, through calculating by formula (63.1), when imaging:

$$ {X_{Sun}}^{rs} = \begin{bmatrix} -87195778623 \\ 30838100336 \\ -120196288751 \end{bmatrix} (\mathrm{m}) \tag{63.2} $$

63.3.2 Toutatis Centroid in the Camera Coordinate System

Radio stations on the ground were used to track the spacecraft trajectory, and astronomical telescopes were used to observe the asteroid trajectory. The relative motion between the spacecraft and Toutatis can be gotten afterwards. During the 100 s of imaging time, the relative motion was very similar to a linear motion [7]. According to the relative motion relationship, the motion of Toutatis's centroid in the camera coordinate system can be parameterized described as follows:

$$\begin{aligned} x_M(t) &= 186.8t - 1858.9 \\ y_M(t) &= -14.4t + 5550.8 \\ z_M(t) &= 10725.1t + 25804.5 \\ 0 &\le t \le 100(s) \end{aligned} \tag{63.3}$$

where coefficients are acquired according to ground measurement results.

63.3.3 The Angle Between Line of Sight and the Sunlight Vector in the Camera Coordinate System

Here the line of sight in the camera coordinate system is defined as the vector from the camera optical center to the Toutatis's centroid. Since the optical center is located at the camera system origin, line of sight can be directly got according to the motion of the centroid described in Sect. 63.3.2. Hence, the angle between the line of sight and the sunlight vector at any imaging time can be calculated. Suppose centroid coordinates of the asteroid in the camera coordinate system is ${X_{a_i}}^{rs}, i = 1, 2, \ldots, n$, the angle between the line of sight and the sunlight vector θ_1 can be expressed as follows:

$$\theta_1 = \pi - \arccos\left(\frac{{X_{Sun}}^{rs} \odot {X_{a_i}}^{rs}}{norm({X_{Sun}}^{rs}) \cdot norm({X_{a_i}}^{rs})}\right) \tag{63.4}$$

63.4 Calculation of Effective Imaging Part

63.4.1 The Equivalent Cylindrical Rotary Body Modelling

Based on the many years' observations by the earth-base radars, NASA has built a basic shape model of Toutatis. It represents the general shape of the asteroid, despite local deviations from the real situation. For the analysis convenience, it is equivalent to a regular body that rotates around the long axis, or a cylindrical rotary body in this paper.

For the convenience of representation, the rotating coordinate system $O^{cy} - xyz$ is introduced in, with the origin locating in the center of the cylinder, and the z-axis as the main axis. Thus, cylinder can be described by formula (63.5):

$$\begin{cases} (x^{cy})^2 + (y^{cy})^2 = R^2 \\ -L/2 \le z^{cy} \le L/2 \end{cases} \tag{63.5}$$

where L is the length of the main axle, R is the rotating radius.

In the camera coordinate system, the coordinate of the rotator X_M^{rs} and its scale the can be controlled via the parameters. The main axis direction can be described by the main axis attitude angle. Thus the rotator formula in the camera system can be written as:

$$\begin{aligned} X_i^{rs} &= RX_i^{cy} + X_M^{rs}, \\ R &= C(\alpha)C(\beta)C(\gamma), \end{aligned} \tag{63.6}$$

The straight line formula of the main axis which passes through the model center X_M^{rs}, with the direction angles α, β, γ can be written as:

$$\frac{x - x_M^{rs}}{m} = \frac{y - y_M^{rs}}{n} = \frac{z - z_M^{rs}}{p} \tag{63.7}$$

where $[m, n, p]^T = \begin{bmatrix} -\sin(\beta) \\ \cos(\beta) \cdot \sin(\chi) \\ \cos(\beta) \cdot \cos(\chi) \end{bmatrix}$.

63.4.2 Calculating the Effective Imaging Part

In the camera coordinate system, let the light axis vector be l_{view}, the solar ray vector be l_{sun}, and the Toutatis's main axis vector be l_{4179}, then the effective imaging can be calculated by the following three steps.

63.4.2.1 Solar Ray Boundary Plane

The sun light boundary plane is calculated in the camera coordinate system, O^{rs}. In the O^{rs}system, the sun direction vector l_{sun}^{rs} can be determined by the sun coordinate X_{Sun}^{rs} and the cylinder center coordinate X_M^{rs}, like in formula (63.8):

$$l_{sun}^{rs} = \left(X_{Sun}^{rs} - X_M^{rs}\right)_{norm} \tag{63.8}$$

Calculate its normal vector $n_{sun-l_{cy}}^{rs}$ of the plane $s_{sun-l_{cy}}^{rs}$, which passes the main axis l_M^{rs}, and is co-planed with the solar ray (vector l_{sun}^{rs}), with the below formula,

$$n_{sun-l_{cy}}^{rs} = l_{sun}^{rs} \otimes l_M^{rs} = \begin{bmatrix} i & j & k \\ x_1 & y_1 & z_1 \\ x_2 & y_2 & z_2 \end{bmatrix} \tag{63.9}$$

Calculate the normal vector $n^{rs}_{(sun-l_{cy})\perp}$ of plane $s^{rs}_{(sun-l_{cy})\perp}$, which passes the main axis l^{rs}_{M} and perpendicular to plane $s^{rs}_{sun-l_{cy}}$, using the below formula,

$$n^{rs}_{(sun-l_{cy})\perp} = n^{rs}_{(sun-l_{cy})} \otimes l^{rs}_{M} \tag{63.10}$$

Calculate the plane $s^{rs}_{(sun-l_{cy})\perp}$, which passes the point X^{rs}_{M}, and with $n^{rs}_{(sun-l_{cy})\perp}$ as its normal vector, using the below formula:

$$\left(n^{rs}_{(sun-l_{cy})\perp}\right)^{T}\left(X - X^{rs}_{M}\right) = 0 \tag{63.11}$$

63.4.2.2 The Line of Sight Boundary Plane

Calculate the line of sight boundary plane in the camera coordinate system O^{rs}. Strictly speaking, any position on the Toutatis surface can correspond to a line of sight vector. Yet the analysis and calculation is extremely complex. Because the distance from the spacecraft to Toutatis at the picturing time is extremely larger than the dimension of Toutatis itself, the line of sight vector l^{rs}_{view} can be represented by the parallel lights passing the origin and the centroid X^{rs}_{M}, like below

$$l^{rs}_{view} = \left(X^{rs}_{M}\right)_{norm} \tag{63.12}$$

Follow the below formula, and calculate the normal vector $n^{rs}_{view-l_{cy}}$ of the plane $s^{rs}_{view-l_{cy}}$, which passes the cylinder main axis l^{rs}_{M} and co-planes with the line of sight (directory vector l^{rs}_{view}):

$$n^{rs}_{view-l_{cy}} = l^{rs}_{view} \otimes l^{rs}_{M} = \begin{bmatrix} i & j & k \\ x_1 & y_1 & z_1 \\ x_2 & y_2 & z_2 \end{bmatrix} \tag{63.13}$$

And calculate the normal vector $n^{rs}_{(view-l_{cy})\perp}$ of the plane $s^{rs}_{(view-l_{cy})\perp}$, which passes the cylinder main axis l^{rs}_{M} and is perpendicular to the plane $s^{rs}_{view-l_{cy}}$:

$$n^{rs}_{(view-l_{cy})\perp} = n^{rs}_{(view-l_{cy})} \otimes l^{rs}_{M} \tag{63.14}$$

Follow the below formula, calculate the plane $s^{rs}_{(view-l_{cy})\perp}$, which passes the point X^{rs}_{M}, and with $n^{rs}_{(view-l_{cy})\perp}$ as its normal vector:

$$\left(n^{rs}_{(view-l_{cy})\perp}\right)^{T}\left(X - X^{rs}_{M}\right) = 0 \tag{63.15}$$

63.4.2.3 The Angle Between the Sunlight Boundary Plane and the Line of Sight Boundary Plane

After the above calculation, the angle between the sunlight boundary plane and the line of sight boundary plane can be calculated through the angle between the two normal vectors $n^{rs}_{(sun-l_{cy})\perp}$ and $n^{rs}_{(view-l_{cy})\perp}$, with below relationship:

$$\cos(\theta_2) = \pi - \frac{n^{rs}_{(sun-l_{cy})\perp} \cdot n^{rs}_{(view-l_{cy})\perp}}{\left\| n^{rs}_{(sun-l_{cy})\perp} \right\| \cdot \left\| n^{rs}_{(view-l_{cy})\perp} \right\|} \tag{63.16}$$

The effective imaging part of the Toutatis is directly determined by the angle θ_2 between the two boundary planes. The part within θ_2 is being lightened up by the sun, and shot by the camera at the same time, which makes it visible on the image. Other parts are called as shadow parts or camera non-displayable parts, which are invisible on the image.

63.5 Results and Analysis

63.5.1 Angle Between the Line of Sight Vector and the Sun Light Vector

Use formula (63.4) in Sect. 63.3.3 to calculate the angle θ_1 between the line of sight vector and the sun light vector. Use formula (63.2) to determine the sun light vector ${X_{Sun}}^{rs}$ in the camera coordinate system. Use formula (63.3) to determine the Toutatis centroid movement relationship in the camera coordinate system. Then θ_1 follows the below curve during the overflight imaging period.

From Fig. 63.1, during the overflight imaging period, the angle between the line of sight vector and the sun light vector moves slowly and stably in the range of $[36.8^\circ, 39^\circ]$, which indicates that for each picture, the illumination angle on Toutatis keeps nearly the same.

63.5.2 Toutatis Effective Imaging Part

Use formula (63.3) to determine the Toutatis centroid movement relationship in the camera coordinate system. Use the method in Sect. 63.4.2 to calculate the angle θ_2 between the sunlight boundary plane and the line of sight boundary plane. In the calculation, the strict attitude of the Toutatis main axis in the camera system is not available, but according to the direction of Toutatis on the optical image, its

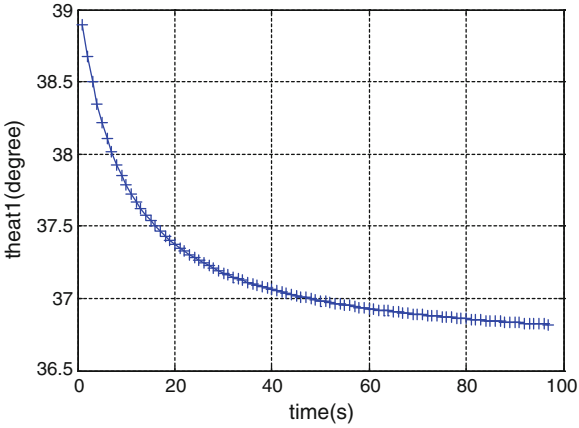

Fig. 63.1 Illumination angle curve during the overflight imaging period

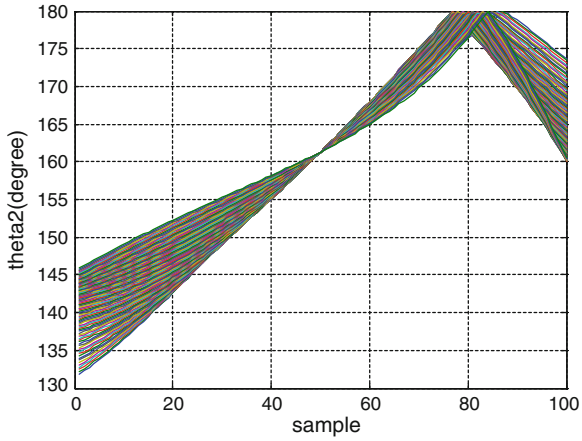

Fig. 63.2 The range of the angle between the sunlight boundary plane

direction angle α, β, γ range in the camera system can be acquired. Then calculate θ_2 within this range, and get the range of the effective imaging part.

The direction angle α is used describes how the rotary body rotates around the main axis. It has no impact on θ_2. So let α be a certain value, and let the range of β, γ be $[-135°, -45°]$. Then take 100 samples with equivalent steps. And the range of θ_2 under different sampling is shown in Fig. 63.2.

From Fig. 63.2, within the given range of the direction angle, θ_2, the angle between the sunlight boundary plane and the line of sight boundary plane always falls into the region of $[130°, 180°]$. That means the effective imaging part is 72–100 % of all the sun lightened area. Or to say the Toutatis optical image taken by Chang'E-II represents 72–100 % of the asteroid's on side surface. So this was a very successful optical probing.

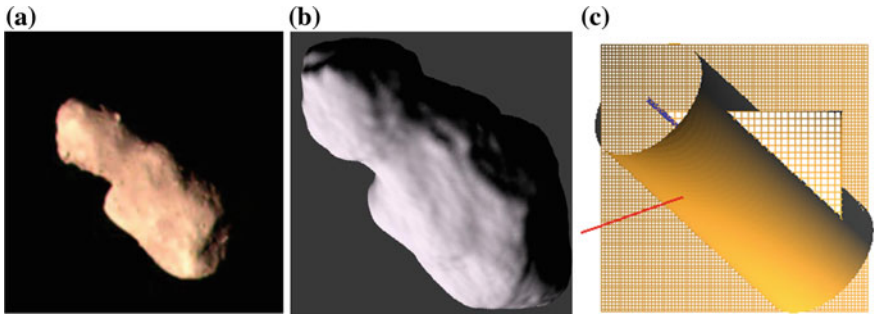

Fig. 63.3 Verification of the calculation results, **a** Chang'e II optical image, **b** NASA shape model based illumination simulation, **c** calculated illumination in the paper

63.5.3 Comparison with the NASA Shape Model

The above conclusion is verified through a radar-observing-based shape model constructed by NASA [8, 9]. Firstly, the azimuth angles of Toutatis in the camera coordinate system are estimated out through comparison between the shape model and optical images. Then the effective imaging range is calculated based on the equivalent rotating body model. Then the shadow part calculated based on the rotary model (as shown in Fig. 63.3b) and the shadow simulated on the NASA model (as shown in Fig. 63.3c) are compared. After comparison, calculated shadow is consistent with the radar model. At the same time, we draw an important conclusions: during the flyby, Chang'e II almost get a complete surface of Toutatis'one side.

In particular, in theory, if we can get the accurate attitude of Toutatis in the camera system when imaging, the rigorous calculation of the angle between sun light boundary plane and the sight boundary plane can be realized, then an accurate estimation of the effective imaging range will be made.

63.6 Summary

In this paper, backgrounded by the flyby detection of Chang'e II to Toutatis, combined with all of the space navigation information when imaging such as orbit and attitude of the spacecraft and the asteroid, an important scientific problem is studied, which is illumination on the optical images. Through precise calculation, irradiation angles of Toutatis surface feature points are 36.8°–39.0°, and furtherly, with the help of a pose simulation of a radar-observing-based shape model by NASA, we can get one important conclusion, that is during the fly by, the space borne optical camera got complete imaging of one side of Toutatis's surface, and there is no wide range of shadow on the images.

References

1. Hudson RS, Ostro SJ (1995) Shape and non-principal axis spin state of asteroid 4179 Toutatis. Sci New Ser 270(5233):84–86
2. Mueller BEA, Samarasinha NH, Belton MJS (2002) The diagnosis of complex rotation in the lightcurve of 4179 Toutatis and potential applications to other asteroids and bare cometary nuclei. Icarus 158:305–311
3. http://www.space.com/18933-chinese-probe-asteroid-toutatis-flyby.html
4. http://www.planetary.org/multimedia/space-images/small-bodies/change-2-images-of-toutatis.html
5. Scheeres DJ, Ostro SJ, Hudson RS et al (1998) Dynamics of orbits close to asteroid 4179 Toutatis. Icarus 132:53–79
6. Wang J, Jiang X, Bai J (2013) Ground based optical observation of asteroid 4179. Sci China Technol Sci Ser 43:618–622
7. Tang G, Bu Y, et al (2013) Optical-image-based precise estimation of chang'e II fly-by distance to Toutatis. In: The 64th International Astronautical Congress
8. Ostro SJ, Hudson RS et al (1999) Asteroid 4179 Toutatis: 1996 radar observations. Icarus 137:122–139
9. Hudson RS, Ostro SJ, Scheeres DJ (2003) High- resolution model of Asteroid 4179 Toutatis. Icarus 161:346–355

Chapter 64
Tightly Coupled SLAM/GNSS for Land Vehicle Navigation

Jiantong Cheng, Jonghyuk Kim, Zhenyu Jiang and Weihua Zhang

Abstract Simultaneous Localization and Mapping (SLAM) algorithm takes the advantages of online map building without any prior environment information and simultaneously location determining with the generated map. This paper proposes an innovative navigation algorithm, tightly coupling of SLAM and GNSS. If GNSS signals are available, the GNSS raw measurements are fused with SLAM measurements to correct the errors of the system's pose as well as reducing the uncertainty of the map. In the GNSS-denied environments, the system operates at the stand-alone SLAM to provide continuous navigation solutions. Considering the computational cost problem, Compressed Extended Kalman Filter (CEKF) is employed to the multi-sensor data fusion. The simulation of the proposed algorithm is implemented in the simulated large-scale environment. Results demonstrate that the proposed technique provides a high accuracy of trajectory tracking in complex environments, and improves greatly the performance of data association and loop-closure detection.

Keywords Simultaneous localization and mapping · Compressed extended Kalman filter · Tightly coupled · GNSS

J. Cheng (✉) · Z. Jiang · W. Zhang
College of Aerospace Science and Engineering, National University of Defense Technology, Changsha 410072, China
e-mail: jiantong.cheng@gmail.com

J. Kim
College of Engineering and Computer Science, Australian National University, Acton ACT 0200, Australia
e-mail: jonghyuk.kim@anu.edu.au

J. Sun et al. (eds.), *China Satellite Navigation Conference (CSNC) 2014 Proceedings: Volume III*, Lecture Notes in Electrical Engineering 305,
DOI: 10.1007/978-3-642-54740-9_64,

64.1 Introduction

Autonomous navigation system is a key component of autonomous land vehicles. Several sorts of approaches have been investigated to provide continuous and reliable navigation information for autonomous land vehicles [1–3]. Dead Reckoning (DR) is a kind of completely autonomous navigation system which doesn't rely on any outside information [4]. Inertial Measurement Units (IMU) and odometer are mostly applied for DR system. However, the stand-alone DR error is time depended so that its accuracy degrades dramatically along with the operation time. The Global Navigation Satellite System (GNSS) is a space satellites-based, absolute positioning system, which takes advantages of long-term stability and high accuracy. However, it is prone to jamming and takes a low update rate. In particular, the GNSS signals are easily blocked in urban. The integration of DR and GNSS incorporates both systems' benefits and has been widespread used in the practical application [5, 6].

A new concept of terrain-based navigation, SLAM, was originally introduced by Smith and Cheeseman [7]. The essential SLAM problem asks if it is possible for a mobile robot to incrementally map an unknown environment while simultaneously determining its location with utilizing the generated map [8, 9]. In past years, a variety of different methods have been addressed to solve the SLAM problem [10–13]. Therefore, SLAM can be considered as a solved-problem at theoretical and conceptual level. However, data association and the loop-closure detection are still substantial challenges for SLAM practical application in complex environments. The failed data association directly affects the result of loop-closure detecting. Nearest neighbour (NN) is a basic and useful approach for data association [8] and has been extensively used in solving the SLAM problem. However, NN holds a low reliability in clutter environments corresponding to these robust techniques, the joint compatibility branch and bound (JCBB) [14], combined constraint data association (CCDA) [15] and multi-hypothesis data association [16]. Regarding the loop-closure problem, several approaches appearing were discussed in [17] which proposed a robust loop-closure verification method with the RRR algorithm. This method improves the performance of detecting and removing outlier loop-closures to recover the correct map estimation. Although the robustness of data association and loop-closure detection gets arisen, no approach can guarantee 100 % accuracy. Furthermore, the computational load is also an underlying problem.

To augment the feasibility and reliability of SLAM operating in environments with large loop manoeuvres, the integration of SLAM and GNSS is an alternative approach. Kim and Sukkarieh [18] firstly used SLAM to aid GNSS/INS for unmanned aerial vehicle (UAV) system, which performs features-based mapping utilizing the GNSS/INS solutions when the GNSS observation is available. Vice versa, the INS error is corrected with using the generated map when the GNSS signals aren't accessible. However, the loosely coupled integration was applied in that proposed system. For the land vehicle, the running environment may be the

urban district or even the forest area where it is hard to track four or more satellites simultaneously. To overcome this problem and make well use of the GNSS observations, this paper proposes tightly coupled SLAM/GNSS integration algorithm. In case of only three or less satellites available, the GNSS raw measurements can still aid SLAM system to reduce the system's uncertainty. Considering the problem of the high computational load, CEKF is employed in the SLAM update. Furthermore, CEKF is developed to fuse the GNSS measurements with the SLAM measurements.

The paper is organised as follows. In Sect. 64.2, the problem of tightly coupled odometer and laser sensor-based SLAM/GNSS is shortly formalized. Multi-sensor data fusion based CEKF is addressed in Sect. 64.3. In Sect. 64.4, simulation and results are provided to verify the performance of the proposed algorithm. Finally, Sect. 64.5 presents conclusions and future work.

64.2 Tightly Coupled SLAM/GNSS Integration

The tightly coupled integration with SLAM and GNSS incorporates both systems' benefits and overcomes their individual drawbacks. Compared with the loosely coupled integration, this system has distinct advantages. All external information gets fully used for the vehicle localization.

64.2.1 SLAM Problem

A solution of the SLAM problem is the online estimation of the trajectory of the vehicle and the relative location of all landmarks without any prior knowledge about the environment. In filter-based SLAM, landmarks are augmented as the system's state variables with the land vehicle's current pose. Then, up to the time instant k, the solution of the SLAM problem can be defined as the computation of the probability distribution

$$P(\mathbf{X}_v(k), \mathbf{m}(k) | \mathbf{U}_{0:k}, \mathbf{Z}_{0:k}, \mathbf{X}_v(0)) \tag{64.1}$$

where $\mathbf{X}_v(k)$ is the state vector presenting the location $\mathbf{L}_v = [x_v, y_v]'_k$ and orientation $\phi_{v,k}$ of the vehicle at the time stamp k; $\mathbf{m}(k) = [\mathbf{m}_1, \ldots, \mathbf{m}_n]_k$ is the set of observed landmarks and $\mathbf{m}_n$ is the location of the nth landmark; $\mathbf{U}_{0:k}$ and $\mathbf{Z}_{0:k}$ are the system control inputs and observations respectively. Popular methods like Kalman filter (KF) or particle filter (PF) are usually used to solve Eq. (64.1). While CEKF [11], a variant of EKF, is adopted in this paper.

When the vehicle is equipped with odometer and laser-sensor as shown in Fig. 64.1, and the motion model is known at advance [11], Eq. (64.1) can be

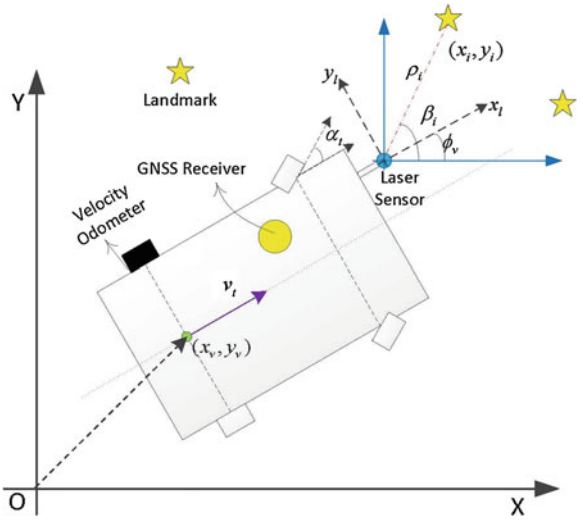

Fig. 64.1 System setups with odometer, GPS receiver and laser scanner

conducted as the linearized state equation of the vehicle pose given by Eq. (64.2) with all landmark observations equations given by Eq. (64.3).

$$\mathbf{X}_v(k+1) = \Phi_v(k+1,k)\mathbf{X}_v(k) + \mathbf{U}_v(k) + \mathbf{w}_v(k) \tag{64.2}$$

where $\Phi_v(k+1, k)$ is the state transition matrix; $\mathbf{U}_v(k)$ is the system control input operated at time k driving the vehicle to the next state at time $k+1$; $\mathbf{w}_v(k)$ is the process noise with zero mean and covariance $\mathbf{Q}_v$. Considering the static assumption of all landmarks in the environment, the sate equation of all observed landmarks can be defined as

$$\mathbf{m}(k+1) = \mathbf{m}(k) \tag{64.3}$$

According to Eqs. (64.2) and (64.3), the full state equation can be presented as

$$\mathbf{X}(k+1) = \Phi(k+1,k)\mathbf{X}(k) + \mathbf{U}_k + \mathbf{W}_k \tag{64.4}$$

where, $\mathbf{X} = [\mathbf{X}_v; \mathbf{m}]$ is the full state vector, and the whole system transition matrix is $\Phi = blkdiag(\Phi_v, \mathbf{I})$ in matlab language; $\mathbf{U} = [\mathbf{U}_v, 0]$ and $\mathbf{W} = [\mathbf{w}_v, 0]$.

For the range and bearing-based SLAM, the observations are the relative ranges from the range sensor to the landmarks and the sensor bearing measurements. As shown in Fig. 64.1, the discrete observations toward the ith landmark is $\mathbf{Z}^s_{k,i} = [\rho_i, \beta_i]'$. If m landmarks are observed at time stamp k, the observation equations can be written as

$$\mathbf{Z}^s_k = \mathbf{H}^s_k\mathbf{X}(k) + \varepsilon^s_k, \quad \varepsilon^s_k \sim (0, \mathbf{R}^s_k) \tag{64.5}$$

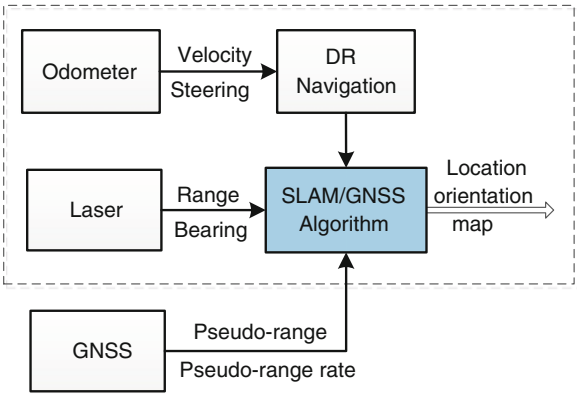

Fig. 64.2 The architecture of the tightly coupled SLAM/GNSS system

where $\mathbf{Z}_k^s = [\rho_1, \beta_1, \ldots, \rho_m, \beta_m]'$ is the observation vector with the dimension of $2 \times m$; $\mathbf{H}_k^s$ is the observation matrix that relates the state vector to the measurements; and ε_s^k is the measurement residual error vector. Based on CEKF, the SLAM problem can be solved according to the above state and observation equations in theoretical level.

64.2.2 Structure of Tightly Coupled

Tightly coupled SLAM/GNSS integration combines the SLAM system's observation with the GNSS raw measurements, while the prediction process keeps unchanged. Therefore, only the observation equation [Eq. (64.5)] should make some relative modifications. In the loosely coupled system, GNSS measurements are processed to compute the GNSS receiver's position and velocity. In the tightly coupled system, each pseud-orange or pseud-orange rate is applied to construct an observation equation directly. Therefore, it can aid the SLAM system all the time when any satellite is accessible. Figure 64.2 depicts the architecture of the tightly coupled SLAM/GNSS system.

If there are M visible satellites at the time instant k and the satellite's errors are corrected according to the ephemeris, the satellite measurement equations can be shown as Eqs. (64.6) and (64.7), respectively.

$$\mathbf{Z}_{k,\rho}^g = \mathbf{H}_{k,\rho}^g \mathbf{L}_v(k) + \delta \mathbf{b}_r + \varepsilon_{k,\rho}^g, \quad \varepsilon_{k,\rho}^g \sim (0, \mathbf{R}_{k,\rho}^g) \tag{64.6}$$

$$\mathbf{Z}_{k,\dot{\rho}}^g = \mathbf{H}_{k,\dot{\rho}}^g \mathbf{V}_v(k) + \delta \mathbf{d}_r + \varepsilon_{k,\dot{\rho}}^g, \quad \varepsilon_{k,\dot{\rho}}^g \sim (0, \mathbf{R}_{k,\dot{\rho}}^g) \tag{64.7}$$

where $\mathbf{Z}_{k,\rho}^g = [\rho_1^g, \ldots, \rho_M^g]$ and $\mathbf{Z}_{k,\dot{\rho}}^g = [\dot{\rho}_1^g, \ldots, \dot{\rho}_M^g]$ are M pseudo-range and M pseudo-range rate observations respectively; $\mathbf{H}_{k,\rho}^g$ and $\mathbf{H}_{k,\dot{\rho}}^g$ separately stand for corresponding measurement matrices with the dimension of $M \times 3$; $\mathbf{L}_v(k)$ and

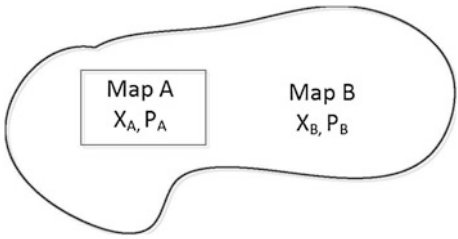

Fig. 64.3 Local and neighbour maps

$\mathbf{V}_v(k)$ means correspondingly the location and velocity of the vehicle; δt_r is the receiver's clock offset and δd_r is the receiver's clock drift; $\epsilon^g_{k,\dot{\rho}}$ and $\varepsilon^g_{k,\dot{\rho}}$ are corresponding residual errors with covariances $\mathbf{R}^g_{k,\rho}$ and $\mathbf{R}^g_{k,ho}$, respectively.

64.3 Data Fusion Based on CEKF

EKF is commonly used in the integration of GPS/DR. However, the time-cost of an EKF update in the SLAM problem is quadratic with the number of the landmarks logged in the map. Submapping-based CEKF was proposed to reduce the computational complexity in [11]. This section develops the CEKF for the tightly coupled SLAM/GNSS integration data fusion.

As shown in Fig. 64.3, the global map is partitioned to local map A and neighbour map B. The state vectors are defined as $\mathbf{X}_A$ with covariance $\mathbf{P}_A$ and $\mathbf{X}_B$ with covariance $\mathbf{P}_B$ respectively. Considering the consistency of the local map prediction and update between EKF and CEKF, only the prediction and update of the neighbour map are discussed here. When the vehicle runs in the local map and takes these initial conditions $\phi_1 = \mathbf{I}$, $\theta_1 = 0$, $\psi_1 = 0$, the CEKF algorithm can be presented as prediction and update steps.

Prediction

$$\phi(k+1,1) = \Phi_A(k)\phi_k \tag{64.8}$$

Update

$$\phi_{k+1} = [\mathbf{I} - \xi(k+1)]\phi(k+1,1) \tag{64.9}$$

$$\theta_{k+1} = \theta_k + \phi^T(k+1,1)\zeta(k+1) \tag{64.10}$$

$$\psi_{k+1} = \psi_k + \phi^T(k+1,1)\kappa(k+1)\phi(k+1,1) \tag{64.11}$$

where ϕ_{k+1} relates $\mathbf{P}_{AB}(k,k)$ to $\mathbf{P}_{AB}(k+1,k+1)$; θ_{k+1} relates $\mathbf{X}_B(k,k)$ to $\mathbf{X}_B(k+1,k+1)$; ψ_{k+1} relates $\mathbf{P}_B(k,k)$ to $\mathbf{P}_B(k+1,k+1)$;$\xi(k+1) = \mathbf{P_A}(k+1,k)\kappa(k+1)$, $\kappa(k+1) = \mathbf{H_A}^T\mathbf{S}^{-1}\mathbf{H_A}$ and $\zeta(k+1) = \mathbf{H_A}^T\mathbf{S}^{-1}\upsilon$. A detailed

expression of these parameters can be found in [11]. While the vehicle is moving into the neighbor map, one full update is conducted as follows.

$$\mathbf{P}_{AB}(k+1,k+1) = \phi_{k+1}\mathbf{P}_{AB}(1,1) \tag{64.12}$$

$$\mathbf{P}_{B}(k+1,k+1) = \mathbf{P}_{B}(1,1) - \mathbf{P}_{AB}^{T}(1,1)\psi_{k+1}\mathbf{P}_{AB}(1,1) \tag{64.13}$$

$$\mathbf{X}_{B}(k+1,k+1) = \mathbf{X}_{B}(1,1) + \mathbf{P}_{AB}^{T}(1,1)\theta_{k+1} \tag{64.14}$$

where $\mathbf{P}_{AB}(1,1)$, $\mathbf{X}_{B}(1,1)$ and $\mathbf{P}_{B}(1,1)$ are corresponding parameters of the last full update. In Eq. (64.2), the velocity of the vehicle isn't selected as the component of the state vector. Only the pseudo-range measurements are considered as the observations of the GNSS in the tightly coupled system. Without introducing confusion and for simplicity, the time mark is omitted in the following context. If the GNSS measurements are available, Eq. (64.6) can be rewritten as

$$\mathbf{Z}^{g} = \left[\mathbf{H}_{A}^{g}, \mathbf{H}_{B}^{g}\right]\begin{bmatrix}\mathbf{X}_{A}\\ \mathbf{X}_{B}\end{bmatrix} + \delta\mathbf{b}_{r} + \varepsilon^{g}, \quad \varepsilon^{g} \sim (0, \mathbf{R}^{g}) \tag{64.15}$$

where $\mathbf{H}_{A}^{g}$ and $\mathbf{H}_{B}^{g}$ are the local map and the neighbour map observation matrices, respectively. Furthermore, the landmarks in the neighbour map don't introduce effects into the vehicle motion and the GNSS observations, therefore $\mathbf{H}_{B}^{g} = 0$. The kalman filter gain of the GNSS observations follows that

$$\mathbf{W}_{g} = \mathbf{P}(k+1,k)\mathbf{H}^{g,T}\mathbf{S}_{g}^{-1} = \begin{bmatrix}\mathbf{P}_{A}(k+1,k)\mathbf{H}_{A}^{g,T}\mathbf{S}_{g}^{-1}\\ \mathbf{P}_{BA}(k+1,k)\mathbf{H}_{A}^{g,T}\mathbf{S}_{g}^{-1}\end{bmatrix} = \begin{bmatrix}\mathbf{W}_{A}^{g}\\ \mathbf{W}_{BA}^{g}\end{bmatrix} \tag{64.16}$$

where the innovation covariance is

$$\mathbf{S}_{g} = \mathbf{H}^{g}\mathbf{P}(k+1,k)H^{g,T} + \mathbf{R}^{g} = \mathbf{H}_{A}^{g}\mathbf{P}_{A}(k+1,k)\mathbf{H}_{A}^{g,T} + \mathbf{R}^{g} \tag{64.17}$$

Using Eqs. (64.15) and (64.16), the update of the neighbour map can be written as

$$\mathbf{P}_{AB}^{g} = (\mathbf{I} - \mathbf{W}_{A}^{g}\mathbf{H}_{A}^{g})\mathbf{P}_{AB}^{s} \tag{64.18}$$

$$\mathbf{P}_{B}^{g} = \mathbf{P}_{B}^{s} - \mathbf{W}_{BA}^{g}\mathbf{H}_{A}^{g}\mathbf{P}_{AB}^{s} \tag{64.19}$$

$$\mathbf{X}_{B}^{g} = \mathbf{X}_{B}^{s} + \mathbf{W}_{BA}^{g}(\mathbf{Z}^{g} - \mathbf{H}_{A}^{g}\mathbf{X}_{A}) \tag{64.20}$$

where the superscripts g and s mean the update results with the GNSS measurements and the laser-based SLAM measurements, respectively. By inducing

Eqs. (64.12)–(64.14) into Eqs. (64.18)–(64.20), the update of these auxiliary variables (i.e. ϕ_{k+1}, θ_{k+1} and ψ_{k+1}) with the GNSS measurements can be rewritten as

$$\phi_{k+1}^{g} = (\mathbf{I} - \mathbf{W}_{A}^{g}\mathbf{H}_{A}^{g})\phi_{k+1}^{s} \tag{64.21}$$

$$\theta_{k+1}^{g} = \theta_{k+1}^{s} + \phi_{k+1}^{s,T}\mathbf{H}_{A}^{g,T}\mathbf{S}_{g}^{-1}(\mathbf{Z}^{g} - \mathbf{H}_{A}^{g}\mathbf{X}_{A}) \tag{64.22}$$

$$\psi_{k+1}^{g} = \psi_{k+1}^{s} + \phi_{k+1}^{s,T}\mathbf{H}_{A}^{g,T}\mathbf{S}_{g}^{-1}\mathbf{H}_{A}^{g}\phi_{k+1}^{s} \tag{64.23}$$

Finally, the update of neighbour map B can be accessed by Eqs. (64.12) to (64.14) with using above equations.

64.4 Simulation and Results

64.4.1 Experiment Setup

As shown in Fig. 64.4, 100 landmarks are randomly manually generated and the simulation environment is set up as an approximate 500 × 500 m area. The vehicle starts at the position of [0, 0] and ends at the initial location after moving over this trajectory (approximate 1.6 km) three rounds anticlockwise. Therefore, a large loop is conducted in this simulation. In this experiment, the vehicle runs at a constant velocity at 5 m/s measured by a velocity odometer with the output frequency of 40 Hz. An angular encode is simulated to provide the vehicle steering angle output with the same update rate as the velocity odometer. The measurements of landmarks are performed by a simulated laser sensor with 180° angular scanning range and a maximum distance range of 30 mat 5 Hz. To simulate the system errors, the standard deviations of the velocity and steering are 0.3 m/s and 3°, respectively. Correspondingly, the measurement noise levels of ranges and bearings are 0.5 m and 1.5°.

The GNSS observations are simulated according to the well-known GPSoft software. For simplicity, the receiver clock error and drift are not considered in this experiment. The noise of measuring pseudo-range is produced with the standard deviation of 2 m and the output frequency of 1 Hz. Furthermore, to simulate the GNSS denied scenario, the GNSS signals are available only when the vehicle locates in the areas, $x_v > 200$ or $y_v > 200$. The number of accessible satellites in this area is 2.

64.4.2 Results Analysis

To clearly assess the performance of the proposed algorithm, the solutions of the stand-alone SLAM system, the tightly coupled DR/GNSS integration and the

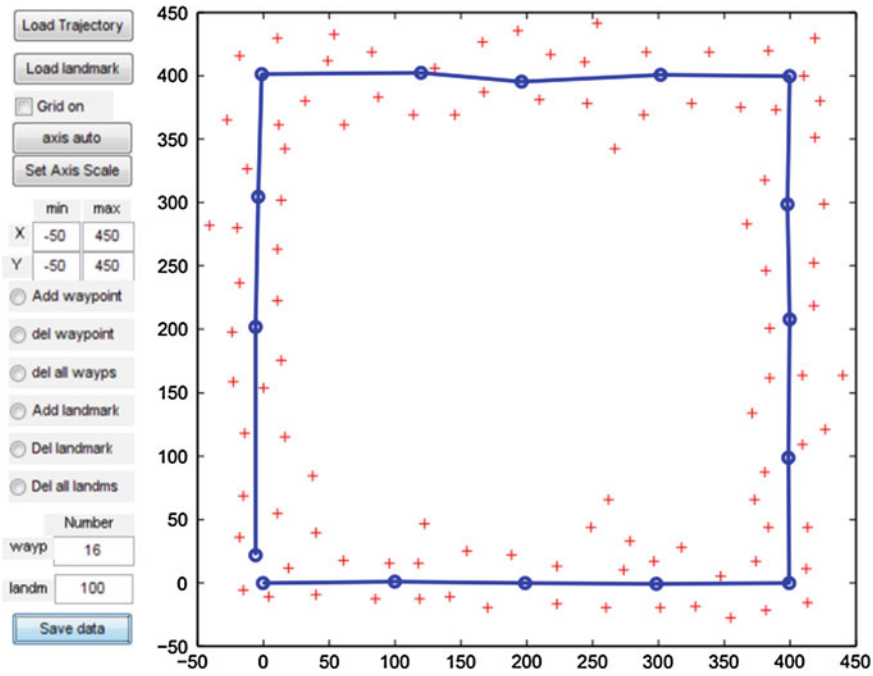

Fig. 64.4 Simulation environment with landmarks (*cross points*) and the trajectory (*solid line*)

tightly coupled SLAM/GNSS integration are shown in Figs. 64.5, 64.6 and 64.7, respectively. Correspondingly, the positioning errors of each system are presented in Fig. 64.8.

It can be seen from Figs. 64.5 and 64.8 that the stand-alone SLAM system can estimate the vehicle's position accurately and track the landmarks well at the initial period. However, the error grows quickly and the reliability of the data association reduces greatly over the vehicle moving. Finally, 257 landmarks are incrementally created in the estimated map shown as circles in Fig. 64.5, and the estimation of the map diverges due to the terrible data association. Furthermore, the detection of the first loop-closure also fails after the large loop traverse. Therefore, the generated map can't aid the DR system correctly when the vehicle revisits the environment. The maximum error of the estimated trajectory reaches up to 129.70 m. The jumps of the estimated trajectory at the second and third rounds occur when the data association gives out the judgments of some landmarks re-observed. However, it is hard to determine whether these judgments are acceptable without a prior knowledge of the data association. In Fig. 64.6, the DR system tracks the vehicle motion well with the aid of the GNSS observations. However, the performance of this system degrades dramatically when the GNSS signals become unavailable, and the error arrives 68.85 m.

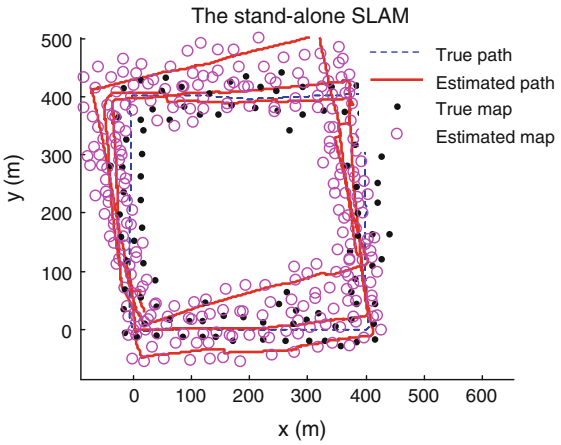

Fig. 64.5 Navigation results of the stand-alone SLAM system

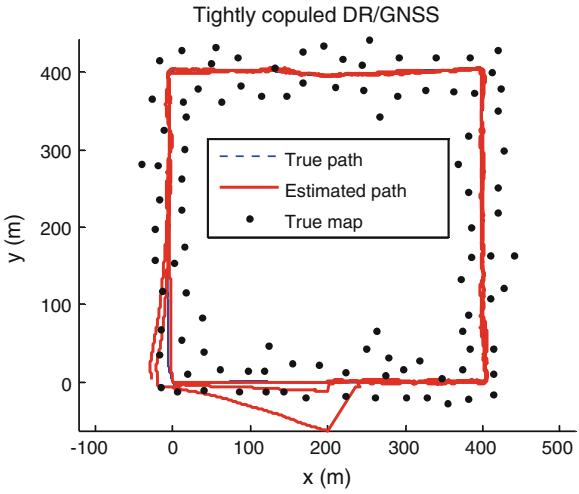

Fig. 64.6 Navigation results of the tightly coupled DR/GNSS integration

The tightly coupled SLAM/GNSS integration outputs a much smoother trajectory as shown in Fig. 64.7. It can be seen that the estimated map describes the true environment accurately. The uncertainty of the landmarks is illustrated in Fig. 64.9. At the first loop, the proposed algorithm operates as the stand-alone SLAM before the GNSS signals arrive as shown in the sub-figure of Fig. 64.7, where both trajectories nearly overlap together. On the other hand, it can be concluded that the performance of the DR system gets improved under the aid of the generated map as expected. When the GNSS signals become accessible, the error of the vehicle location gets corrected at once, and the uncertainty of the map gets reduced greatly. Subsequently, the new landmarks can also hold low uncertainties before the loop-closure. The vehicle position error is also constrained at a low level when the GNSS signals get lost again, and the maximum error is no larger than 7 m in the whole

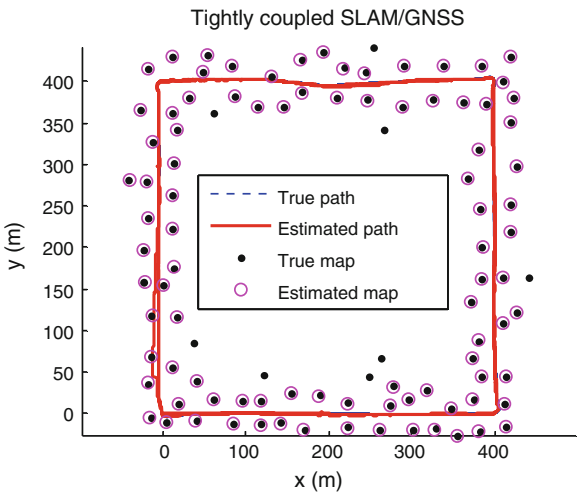

Fig. 64.7 Navigation results of the tightly coupled SLAM/GNSS integration

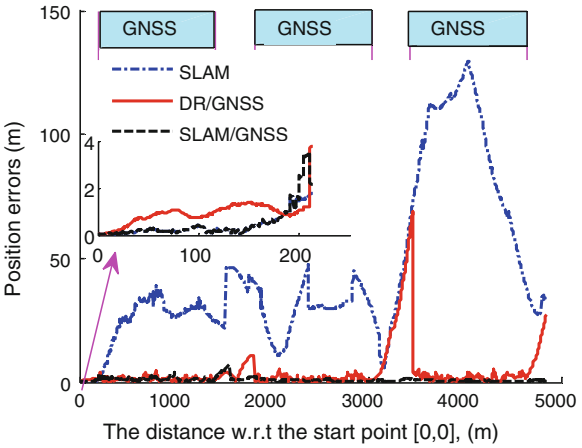

Fig. 64.8 Position errors of three navigation systems

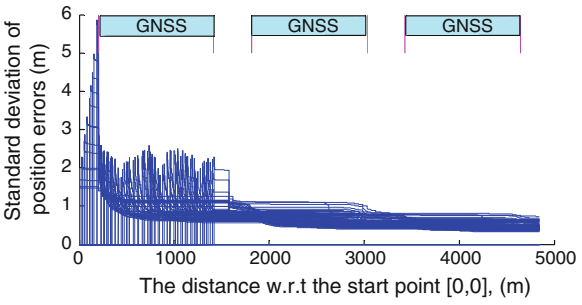

Fig. 64.9 Standard deviation of position errors of the estimated landmarks

experiment. In particular, the error is less than 1.6 m at the second and third rounds regardless of whether the GNSS observations are available or unavailable.

64.5 Simulation and Results

In this paper, the tightly coupled SLAM/GNSS integration algorithm is proposed to provide continuous and reliable navigation for the land vehicle in the GNSS signal partly blocked environment. By analyzing the structure of the proposed system, CEKF is developed for the multi sensor data fusion. Simulation results have verified that by tightly coupling SLAM with GNSS, the performance of SLAM locating in the large loop maneuver is further enhanced. In particular, the accuracy of the mapping gets improved distinctly. Therefore, when the map is constructed with a low uncertainty after the first loop, the vehicle can get a high quality navigation solution even if the GNSS signals are not available.

Acknowledgments The first author appreciates China Scholarship Council (CSC) for supporting his study at the Australian National University. The authors would like to thank Dr Tim Bailey for his original code of the simulation environment generating.

References

1. Sukkarieh S (2000) Low cost, high integrity, aided inertial navigation systems for autonomous land vehicles. The University of Sydney
2. Dissanayake G, Sukkarieh S, Nebot E et al (2001) The aiding of a low-cost strapdown inertial measurement unit using vehicle model constraints for land vehicle applications. IEEE Trans Robot Autom 17(5):731–747
3. Georgy J, Karamat T, Iqbal U et al (2011) Enhanced MEMS-IMU/odometer/GPS integration using mixture particle filter. GPS Solutions 15(3):239–252
4. Godha S (2006) Performance evaluation of low cost MEMS-based IMU integrated with GPS for land vehicle navigation application. UCGE Report (20239)
5. Stephen S, Stephan T, Michael C et al (2012) Flight results from the SHEFEX2 hybrid navigation system experiment. In: AIAA guidance, navigation, and control conference
6. Noureldin A, Karamat TB, Georgy J (2013) Fundamentals of inertial navigation, satellite-based positioning and their integration. Springer, Heidelberg
7. Smith RC, Cheeseman P (1986) On the representation and estimation of spatial uncertainty. Int J Robot Res 5(4):56–68
8. Bailey T, Durrant-Whyte H (2006) Simultaneous localization and mapping (SLAM): part II. IEEE Robot Autom Mag 13(3):108–117
9. Durrant-Whyte H, Bailey T (2006) Simultaneous localization and mapping: part I. IEEE Robot Autom Mag 13(2):99–110
10. Dissanayake MG, Newman P, Clark S et al (2001) A solution to the simultaneous localization and map building (SLAM) problem. IEEE Trans Robot Autom 17(3):229–241
11. Guivant JE, Nebot EM (2001) Optimization of the simultaneous localization and map-building algorithm for real-time implementation. IEEE Trans Robot Autom 17(3):242–257

12. Montemerlo M (2003) FastSLAM: a factored solution to the simultaneous localization and mapping problem. Carnegie Mellon University
13. Thrun S, Liu Y, Koller D et al (2004) Simultaneous localization and mapping with sparse extended information filters. Int J Robot Res 23(7–8):693–716
14. Neira J, Tardós JD (2001) Data association in stochastic mapping using the joint compatibility test. IEEE Trans Robot Autom 17(6):890–897
15. Bailey T (2002) Mobile robot localisation and mapping in extensive outdoor environments. University of Sydney
16. Bar-Shalom Y (1987) Tracking and data association. Academic Press, New York
17. Latif Y, Cadena C, Neira J (2013) Robust loop closing over time for pose graph SLAM. Int J Robot Res 32(14):1611–1626
18. Kim J, Sukkarieh S (2005) 6DoF SLAM aided GNSS/INS navigation in GNSS denied and unknown environments. J Global Positioning Syst 4(1–2):120–128